Application of Deep Eutectic Solvent Nanofluid as Electron Exchange Mediator in Microbial Fuel Cell

Y.L. Chong[1,*], R. G. Walvekar[1], W. Y. Wong[1], Y. H. Ong[1], K.W. Lee[2], M. Ghasemi[3], T. Jafary[3]

[1]*School of Engineering, Taylor's University, Malaysia*
[2]*School of Biosciences, Taylor's University, Malaysia*
[3]*Fuel Cell Institute, Universiti Kebangsaan Malaysia, Malaysia*

[*]youliang.chong@gmail.com

ABSTRACT

Microbial fuel cells (MFCs) generate electricity by converting organic wastes in the absence of oxygen. However, MFC power plant is still far from realisation. The major breakthrough of microbial fuel cells happened when adding a little neutral red (NR) that was later named, electron mediator. Electron mediator boosts the output of electricity generation by acting as an electron bridge that breaks through the lipids of the microbes and shuttles them to the electrode. In this study, a deep eutectic solvent is chosen to be the electron mediator in replace of neutral red (NR). Choline chloride-ethylene glycol (ChCl-EG) mixed deep eutectic solvent (DES) is chosen because of its good electrical conductivity, low viscosity and low cost compared to methylene blue. Carbon nanotubes (CNTs) are also dispersed in the deep eutectic solvent making it a nanofluid and the effects were observed. The objective is then to investigate on the optimum ratio (1:1.75 to 1:2.5) of choline chloride-ethylene glycol and the presence of carbon nanotubes to generate the largest power output. Results showed that addition ChCl-EG ratio of 1:2 is optimal for power output even though the power is 1 magnitude lower than NR as the mediator. The dispersion of CNT into DES mediated anolyte showed destructive result showing power output even lower than without any mediator.

Keywords:

Microbial fuel cell; Deep eutectic solvent; Electron exchange mediator; *Escherichia Coli*; Bio electricity generation

1. Introduction

Microbial Fuel Cells (MFCs) take advantage of the ability of microbes to produce small amount of electrons under anaerobic respiration conditions. However, most of the microbes do not have the ability to transport the electrons produced in it directly to the electrode, there is the need of an electron shuttle or electron mediator that picks up the electrons from inside the microbes and transport it to the electrode. [1][2] The most common mediator that is being used is expensive, non-biodegradable ionic liquids (ILs) such as methylene blue (MB) and neutral red (NR). [3] The price of IL is expensive because it often needs to be purified and are only produced in small quantity for laboratory use. Furthermore, its toxicity towards the environment is a major reason of it being eliminated as an electron exchange mediator in MFC. Hence, this project urges for a better choice of mediator compared to the ILs. And this choice is to use deep eutectic solvent (DES) that has proven to have functionalities of ILs yet does not come with its drawbacks. Compared to IL, DES can be prepared simply by mixing. Recently, DESs had been found to possess good electrical properties. Researchers have found uses for it in the electroplating industry. The biodegradability of DES in nature interests the industry in search for greener materials.

A basic setup of MFC is shown in **Figure 1.1** where DES, instead of IL is mixed with water and organic matter. The organic matter consists of glucose substrate that fuels the microbes to metabolize. Microbes that are in the anaerobic chamber digest glucose substrate and produce electrons and hydrogen ions, H^+. The electrons, e^- with the help of an electron exchange mediator (DES) are being transported to the anode and flows through an external circuit. When a load or a resistor is put in between the electrodes, a voltage can be observed indicating that electricity is being generated. Electrolyte solution in the anode chamber is named anolyte whilst in the cathode chamber is called catholyte.

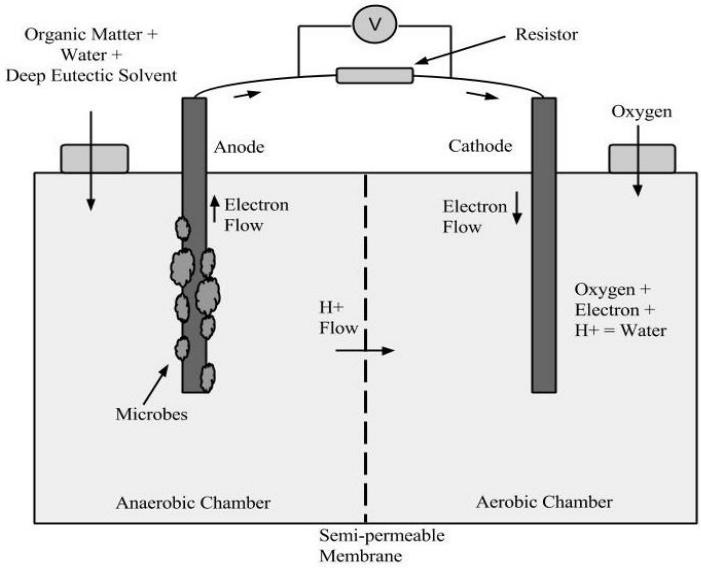


Figure 1.1: Schematic of Typical MFC Design
(Drawn with modifications after Sharma) [4]

The objective of this study was to compare the MFC power generation using DES as electron mediator with conventional mediator. Then, CNT was added into the DES mediated system to observe the effects power generation of CNT addition in the anolyte. This project will contribute researches by opening a new window for a better, greener mediator by means of electron transfer from microbes to electrodes. At the same time, configurations that generates the largest electricity output is desired to be competitive with IL mediated MFCs.

In a MFC consist of multiple components working together to produce electricity. With two electrodes (anode and cathode) on each side connected through a wire, they are dipped into separated electropositive and electronegative solutions (anode compartment and cathode compartment). The tendency of nature to achieve balance so called potential difference in between cathode and anode is the driving force of the system. [5]

The anode compartment usually consist of the solid electrode itself, the substrate that is the “fuel” of the system, the microbes under anaerobic conditions, turns substrate into electrons (e^-), hydrogen ions (H^+) and carbon dioxide (CO_2), and sometimes an additional mediator that boosts the electron transfer from the microbes

to the electrode. The anode compartment has to be in anaerobic condition in order for the microbes to produce electrons. [6] This is to prevent oxygen (O_2) in the air from picking up any generated electrons before the electrons even flow through the wire. O_2 has the maximum reduction potential and hence it accepts electrons better than any other biological substance. [7]

The produced electrons then flow from the anode compartment to the cathode compartment through an external wire. If a load is put in between the electrodes, an electricity generation can be observed. [8] On the other hand, H^+ is unable to flow through the solid copper wire. It is allowed to flow through a proton exchange membrane (PEM) and then into the cathode compartment. The PEM prevents anything other than protons from flowing through it. Then at the cathode compartment is where electrons are received and combined with H^+ and O_2 to produce water. [7] **Equation 1.1** and **1.2** shows the reaction that takes place in the MFC. [9] [10]

$$C_6H_{12}O_6 + 6H_2O \xrightarrow{Microbes} 24H^+ + 24e^- + 6CO_2 \text{ (Anode)} \qquad \textbf{(1.1)}$$

$$4e^- + 4H^+ + O_2 \rightarrow 2H_2O \text{ (Cathode)} \qquad \textbf{(1.2)}$$

Adding mediator to microbes that does not have micropili acts as an electron shuttle that will immerse into the external layer of the microbe, pick up then transport the electron to the electrode. In the processes of taking the electrode, the mediator undergoes a reduction reaction and returns to its original state only after releasing the electrons to the anode. Researches have proved that adding mediators artificially to the anode chamber where the microbes are, increases performance of MFCs no matter if the biocatalyst is capable of direct electron transfer or not. [11] [12]

DESs are made of simple mixtures of quaternary salt with a hydrogen bond donor (HBD) or a metal halide. The quaternary salts are such as ChCl and methyl triphenyl phosphonium bromide. On the other hand HBDs can be glycerol and EG. In this project, ChCl-EG mixture is chosen as the DES after various studies. Abo-Hamad et al., (2015) have provided a list of properties of different mixtures of DES that eased the selection for mediator usage in MFCs. The common yet high profile ChCl-EG mixture at 1:2 ratios has an electrical conductivity of 7.61mScm^{-1}. This DES appeared

to have the highest electrical conductivity when compared to various other mixtures. Furthermore, viscosity is only 37cP that is about one magnitude lower compared to most of the DES. Higher conductivity and lower viscosity eases the transport of electrons in the electrolyte solution that in return reduce ohmic losses in the MFC, which ultimately leads to higher power output. [13]

Sharma have shown that the use of multiwall carbon nanotubes (MWCNTs) excel over single wall CNTs (SWCNTs) when being used in the anode of MFCs. [8] In his research, CNT based electrodes as well as dispersing them in the IL mediated solution shown an increase in power density. So far, this work has been regarded as the highest open circuit potential (OCP) of 0.91V and power density of 2470mW/m^2 of a single unit MFC in the research field so far. In MFC, the most common use of CNTs was to coat them on the carbon electrodes. Only few made attempt to disperse the CNTs into the aqueous anode medium.

2. RESEARCH METHODOLOGY

2.1 DES Preparation

Using hotplate stirrer and stored in Schott bottles, the range of ratio of ChCl to EG that will be prepared are, 1:1.75, 1:2, 1:2.5 calculated on mass basis. The needed mass of both ChCl and EG is then mixed with magnetic stirrer for approximately 4 hours at 90^0C inside the Schott bottles sealed with parafilm on the hot plate stirrer. [14] ChCl is very reactive with air and easily contaminated. Hence it shall be weight and handled very quickly to be sealed up. The mixture turns from cloudy to colorless when mixed well. Eye and breathing personal protective equipments (PPEs) should be worn when weight the ChCl and EG to prevent any chemical inhalation. 0.04% v/v DES was added to the anolyte. It was then increased to 0.67%v/v and 13.3%v/v to observe the effect of change in DES concentration to the power generation of MFC.

2.2 Nanofluid Preparation

Any fluid that is added with nanoparticles is known as nanofluid. Using methods from Sharma, the DES produced is firstly diluted with distilled water in order to prepare the fluid base at 0.04%v/v. [7] 0.32g/L of MWCNT is then added into the aqueous DES and then ultrasonicated using the Syclon Ultrasonicator (SKL-IIDN) for half an hour. Its sole purpose is to prevent agglomeration of the MWCNT in aqueous solutions.

2.3 Microbes Preparation

Using microbe preparation method in respect to Sharma. [3] E. Coli BL21 strain were cultured overnight using Luria Bertani broth (10g/L Peptone, 5g/L Yeast Extract, 10g/L Sodium Chloride) at 37^0C in an incubator. Then 10%v/v of the cultured medium was transferred into anodic medium.

2.4 Conducting Experiment

A two-compartment MFC with a total of 300mL volume was used as the container. The anode compartment consists of 55mM glucose, 37g/L Luria Bertani Broth, 0.04%v/v DES, 100mM phosphate buffer and 10%v/v liquid cultured E. Coli. The cathode compartment consists of 100mM phosphate buffer solution. Both compartments were separated with Nafion 212 membrane. Anode used was plain carbon felt with area of 16cm^2 (4x4cm) while cathode used was carbon felt coated with 0.5mg/cm^2 platinum. The power density and polarization curves are plotted using a potentiostat (Autolab PGSTAT128N).

3. RESULTS AND DISCUSSION

Three chambers with the same initial setup were used without any mediator. However, it is shown that chamber 1 works better than chamber 2 following by chamber 3 at least at the initial stage. The maximum power density in respect of anode of chamber 1 without any mediator reached 49mW/m^2 followed by chamber 2 with 37.7mW/m^2 and chamber 3 with 23.4mW/m^2. This results shows that each individual chambers even though set up as similar as possible, has minor difference unique to each other. The difference in these three control set also proved to have affect to the following results.

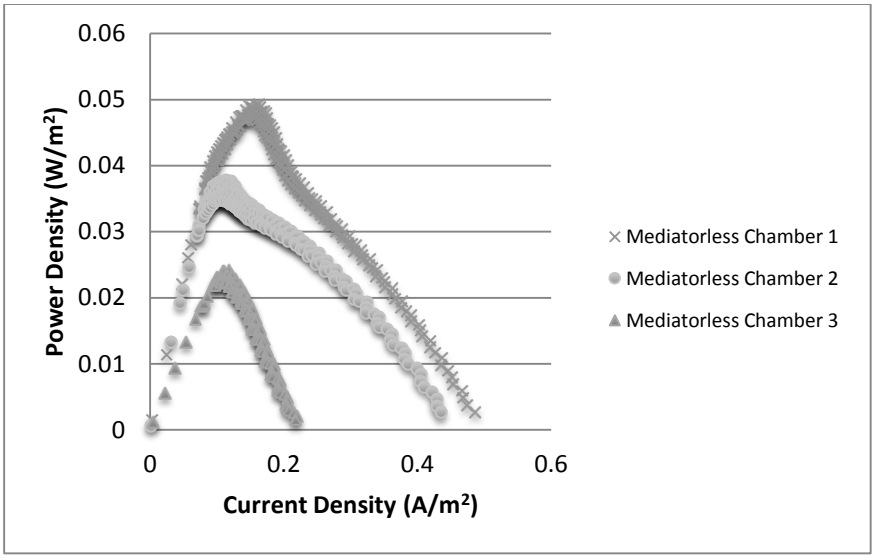


Figure 3.1 Power Density of Mediatorless Chambers 1, 2 and 3.

Using Neutral Red as mediator shows about 793.7mW/m^2 power density, which is twice the power density (386mW/m^2) of NR mediated with plain graphite electrode used by Sharma. [3] Results show that NR mediated chamber is about 10 times higher than all the other mediated chambers. When NR is taken away from comparison, all the other results gave power density in the same order of magnitude ranging from 20mW/m^2 to 80W/m^2 as shown in Figure 3.2. Although DES has high electrical conductivity, it was unable to penetrate the lipid layers of the microorganisms as easily as NR. It is because ChCl-EG based DES is hydrophilic, resulting in less hydropressure acting towards the surface of the lipid membranes.

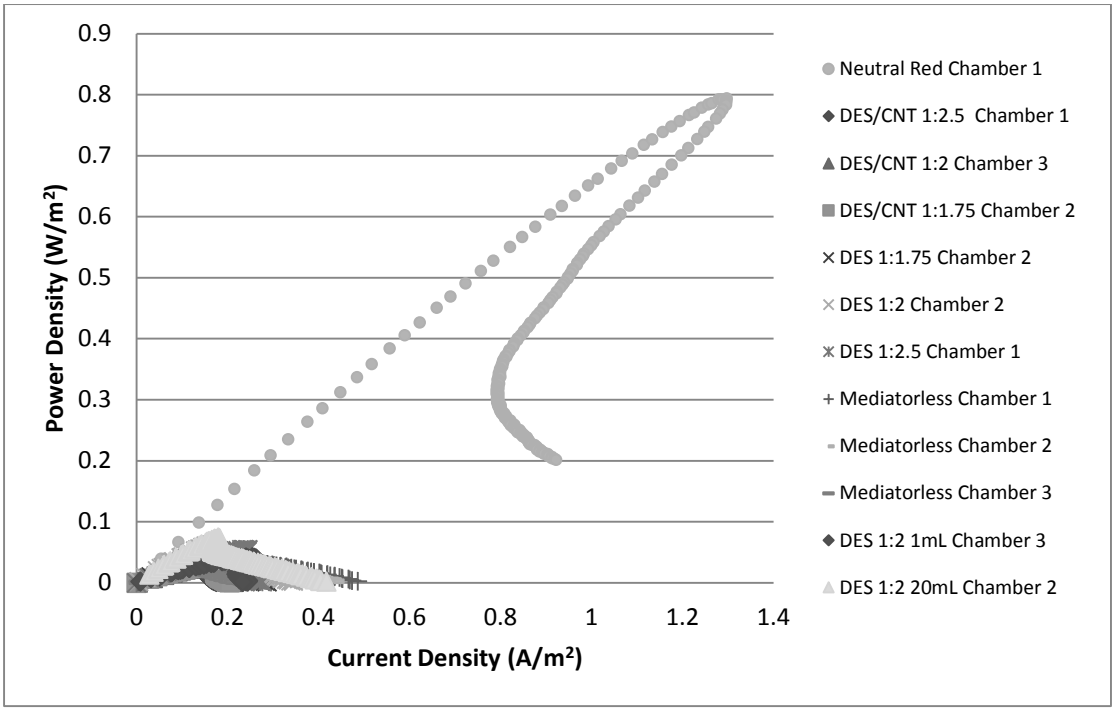


Figure 3.2 Overall Power Density Curve.

Difference in ratio of ChCl to EG also proved to have different output although very small. As of figure 3.3, DES 1:2 showed the best power output (62.5mW/m^2) while 1:1.75 (52.5mW/m^2) and 1:2.5 (54.7mW/m^2) showed similar results. Hence, we could conclude that DES 1:2 is the best ratio. It is speculated that ratio 1:2 provides complete mixing of ChCl and EG as compared to 1:1.75 and 1:2.5. It was found that ratio 1:1.75 constantly recrystallizes into its salt form where ChCl is abundant to EG.

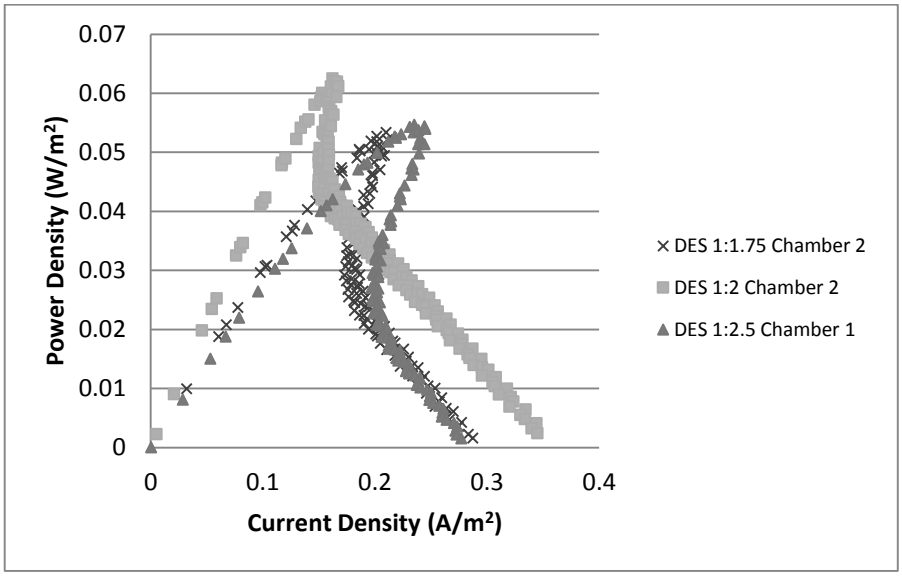


Figure 3.3 Power Density Curve of Different DES Ratio.

Since ratio 1:2 was the best ratio to be used, it was used to further compare with the presence of CNT. Addition of CNT into the system unexpectedly decreased the power density to even lower than non-mediated MFC. This result contradicts with Sharma's findings where addition of CNT improved the power density even further. [3] The adverse effect of CNT might be caused by the absence of functional group added to the CNT since most of the researchers often treat the CNT beforehand. Figure 3.4 showed that highest power density was obtained using DES 1:2 ratio, about twice the non-mediated MFC. This shows that DES is successful in improving the power output of MFC despite much lower compared to NR.

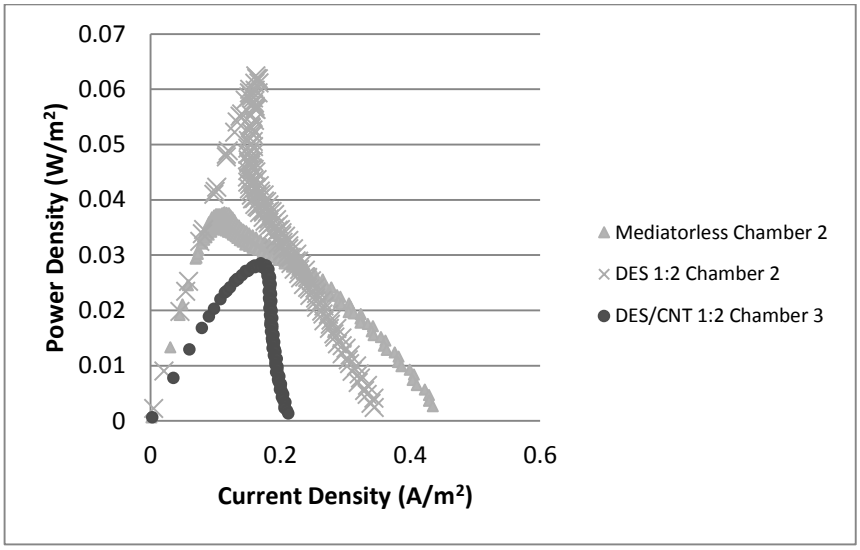


Figure 3.4 Power Density Curve Comparing Mediatorless, DES 1:2 Mediated and DES/CNT 1:2 Mediated MFC.

Different concentration of DES 1:2 (0.6mL (0.4%v/v), 1mL (0.67%v/v), and 20mL 13.3%v/v) was used in the system (Figure 4.5). 20mL DES in the system showed higher power (73.9mW/m^2) compared to 0.6 mL (62.5mW/m^2) and 1mL (41.9mW/m^2) showed to lowest results. The lower power density shown by 1mL DES 1:2 was justified that chamber 3 was being used for the experiment. It is expected to be in between 0.6mL and 20 mL range if chamber 2 was being used. Hence, the higher the concentration of DES would provide a higher power density.

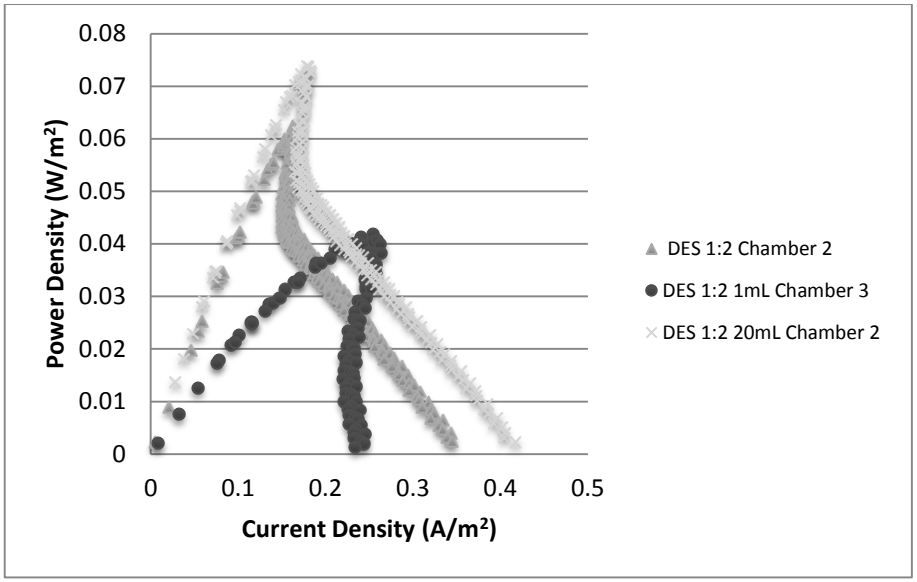


Figure 3.5 Power Density Curve Comparing Mediatorless, DES 1:2 Mediated and DES/CNT 1:2 Mediated MFC.

Table 3.1 is a summary of open circuit potential (OCP) and maximum power density. Generally, NR showed the highest OCP and also maximum power density as expected. The OCP of all DES mediated results were higher than the maximum obtained by Rahimnejad of 0.25V using methylene blue as the mediator. [11] Furthermore, DES mediated MFC were comparable to that of Zou whom obtained 89mW/m^2 using NR mediator. [16]

Table 3.1 Summary Table of Open Circuit Potential and Maximum Power Density.

Electron Mediator	Chamber	OCP (V)	Maximum Power Density (mW/m^2)
Mediatorless	1	0.469	49.0
	2	0.433	37.7
	3	0.256	23.4
NR	1	0.723	793.7
DES 1:1.75	2	0.315	52.7
DES 1:2	2	0.439	62.5
DES 1:2.5	1	0.289	54.7
DES/CNT 1:1.75	2	0.245	29.9
DES/CNT 1:2	3	0.219	28.5
DES/CNT 1:2.5	1	0.289	31.0
DES 1:2 1mL	3	0.238	41.9
DES 1:2 20mL	2	0.488	73.9

4. CONCLUSION AND FUTURE WORK

Thus far, it is concluded that DES does increase the power output of MFC. However the amount of increase is in within the same order of magnitude, which is insignificant when compared to NR as the mediator. On the other hand, it was found that the higher the concentration of DES in the anolyte, the higher the power density. Addition of CNT into anolyte decreases the power output of MFC. It was discussed that the CNT have to be treated with additional functional group for it to increase the power density of the MFC.

This is the very first attempt to use DES in MFC. Hence, much more can be expected in the future. Altering the operating conditions or the DES itself allows a collection of a large range of information. For instance, the hydrophobicity should also be considered when selecting the right DES to be used as the mediator. The same experiment can also be repeated using a mix culture of microbes to observe if it does enhance as much as a single culture. Even more, using waste water that consists of a diverse type of substrate and microbes to replicate a real waste water treatment plant will bring the use of DES in MFC a step closer to be industrialized.

ACKNOWLEDGEMENT

This research work was financially supported by the research funds from School of Engineering, Taylor's University. A token of appreciation also had to be given to the Fuel Cell Institute, Universiti Kebangsaan Malaysia for the generous lending of equipment and materials.

REFERENCES

[1] Stirling, J.L., Bennetto, H.P., Delaney, G.M., Mason, J.R., Roller, S.D., Tanaka, K. (1983). Microbial fuel cells. *Biochem Soc Trans*, 11:451–3.

[2] Bennetto, H.P. (1984) Microbial fuel cells. *Life Chem Rep*, 2:363–453.

[3] Sharma, T., et al. (2008). Development Of Carbon Nanotubes And Nanofluids Based Microbial Fuel Cell. *International Journal of Hydrogen Energy,* 33.22: 6749-6754.

[4] Sharma, T., et al. (2010). Biocatalysts In Microbial Fuel Cells. *Enzyme and Microbial Technology,* 47.5: 179-188.

[5] Venkata, M., S., et al. (2008). Bioelectricity Production From Wastewater Treatment In Dual Chambered Microbial Fuel Cell (MFC) Using Selectively Enriched Mixed Microflora: Effect Of Catholyte. *Bioresource Technology* 99.3: 596-603.

[6] Du, Z., Li, H., and Gu, T. (2007). A State Of The Art Review On Microbial Fuel Cells: A Promising Technology For Wastewater Treatment And Bioenergy. *Biotechnology Advances,* 25.5: 464-482.

[7] Nelson, David, L., et al. (2005). Lecture Notebook For Lehninger Principles Of Biochemistry*, Fourth Edition*. New York.

[8] Venkata, M., and Srikanth, S. (2011). Enhanced Wastewater Treatment Efficiency Through Microbially Catalyzed Oxidation And Reduction: Synergistic Effect Of Biocathode Microenvironment. *Bioresource Technology,* 102.22: 10210-10220.

[9] Venkata, M., et al. (2014). Microbial Fuel Cell: Critical Factors Regulating Bio-Catalyzed Electrochemical Process And Recent Advancements. *Renewable and Sustainable Energy Reviews,* 40: 779-797.

[10] Wang, C., Chen, W., and Huang, R. (2010). Influence Of Growth Curve Phase On Electricity Performance Of Microbial Fuel Cell By Escherichia Coli. *International Journal of Hydrogen Energy,* 35.13: 7217-7223.

[11] Rahimnejad, M., et al. (2011). Methylene Blue As Electron Promoters In Microbial Fuel Cell. *International Journal of Hydrogen Energy,* 36.20: 13335-13341.

[12] Park, D. H., and Zeikus, J. G., (2002). Improved Fuel Cell And Electrode Designs For Producing Electricity From Microbial Degradation. *Biotechnology and Bioengineering,* 81.3: 348-355.

[13] Cheng, S., Liu, H., and Bruce, E.L., (2006). Increased Power Generation In A Continuous Flow MFC With Advective Flow Through The Porous Anode And Reduced Electrode Spacing. *Environmental Science & Technology,* 40.7: 2426-2432.

[14] Bagh, F.S., Ghareh, et al. (2013). Electrical Conductivity Of Ammonium And Phosphonium Based Deep Eutectic Solvents: Measurements And Artificial Intelligence-Based Prediction. *Fluid Phase Equilibria* 356: 30-37.

[15] Hassan, Sedky, H.A., Kim, Y. S., and Oh. S., (2012). Power Generation From Cellulose Using Mixed And Pure Cultures Of Cellulose-Degrading Bacteria In A Microbial Fuel Cell. *Enzyme and Microbial Technology* 51.5: 269-273.

[16] Zou, Y.J., Sun, L. X., Xu, F., and Yang, L.N., (2007). E. coli microbial fuel cell using new methylene blue as electron mediator. *Chem J Chin Uni* 28(2):510-3.

Production of Reducing Sugar by Cellulolytic Bacteria from Activated Sludge

Kok Leng Chuah[1*], Ying Hui Ong[1], Li Wan Yoon[2]

[1,2]School of Engineering, Taylor's University

[2]School of Engineering, Taylor's University

[2]Department of Chemical Engineering, Faculty of Engineering, University of Malaya

[*]corresponding email: Chuahkl1993@gmail.com

Abstract

In the world of rapid growing population along the years, there is an increase in the amount of food demands. Agricultural foods such as corn, sugarcane, wheat and others act as the source of food supply which in turn produces agricultural wastes. Sugarcane bagasse is one of the agricultural wastes from the sugar factories after the extraction process which is rich in the lignocellulosic materials. It consists of 42% cellulose, 25% hemicelluloses, 20% lignin and remaining of ash, wax and proteins. Hence, the research aims to determine the suitability of bacteria in activated sludge to generate reducing sugar from sugarcane bagasse through a solid state fermentation and also to increase the amount of reducing sugar produced through physical and alkali pretreatment. During the solid state fermentation stage, enzymatic hydrolysis occurred when the excessive sludge from Indah Water is combined with the high cellulose content sugarcane bagasse. Through enzymatic hydrolysis process, reducing sugar will be formed due to the breaking of β-glycosidic bonds by the endoglucanases, exoglucanases and β-glucosidases enzyme. The amount of reducing sugar produced will also increase when the bagasse are subjected to alkali pretreatment due to the increase in porosity. The concentration of cellobiose was detected by using High Performance Liquid Chromatography (HPLC). Cellobiose is a disaccharide form of reducing sugar. From the results obtained, it is clearly illustrated that the alkali pretreated bagasse posses a higher cellobiose concentration than untreated bagasse. On day 1, both treated and untreated bagasse shows the highest amount of reducing sugar with concentration of 36.32ppm and 27.76ppm. The amount of reducing sugar remain fluctuates on the subsequent days but it increases significantly at day 5. Hence, it proved that alkali pretreatment enhance the amount of cellobiose production with low number of fermentation days required. A Fourier Transform Infrared Radiation (FTIR) was carried out to determine the chemical structure of untreated and treated sugarcane bagasse before and after fermentation.

Keywords: sugarcane bagasse, cellulolytic bacteria, activated sludge, solid state fermentation, reducing sugar.

1. Introduction

Agricultural wastes are abundantly generated through the increase in human population along the years. Some examples of agricultural wastes are woody plant, sweet sorhum bagasse, sugarcane bagasse, corn sobs and others. Sugarcane bagasse is one of the major waste sources from the sugar factories after the process of sugar extraction. However, the pressing process of sugarcane bagasse does not fully extract out the sugar contents that are presence in the lignocellulosic content which can be further studies. In sugarcane bagasse, the lignocellulosic content is mainly formed by 42% cellulose, 25% hemicelluloses, 20% lignin and remaining of ash, wax and proteins [1]. Hence, sugarcane bagasse which has a high amount of cellulose could be subjected to an additional fermentation process and enzymatic digestion in order to extract valuable reducing sugar from the agricultural wastes.

On the other hand, activated sludge is the most common product produced after the aeration and settling tank in the Waste Water Treatment Plant (WWTP). **Fig.1** illustrates the activated sludge process that take place in the WWTP. Incineration, dumping at sea and landfill are among the few techniques currently used to treat the excess activated sludge. In many countries along the world, the generation of excessive activated sludge process had become a challenge to resolve it as this issue had brought heavy impacts to the companies. The removal of excessive activated sludge process consume about 50-60% of total operating cost of a plant which makes the operation less economical [2]. Besides that, an additional pretreatment cost is required to ensure that the concentration of toxic waste emissions through the 3 methods mentioned above is below the permissible level of environmental law and regulations [2].

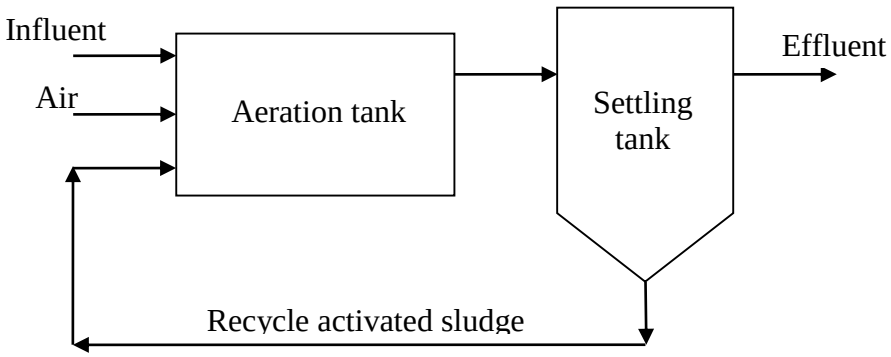


Figure 1. Activated sludge process

In enzymatic digestion of cellulose material, cellulase enzyme plays an important role in breaking the β-1,4 linkage between the long glucose chain [3-4]. Cellulase enzyme is a type of inducible enzyme produced from a complex microorganism's community such as activated sludge which involve of bacteria and fungi during the growth on cellulosic material of the bagasse [1]. Endoglucanases, exoglucanases and β-glucosidases are the most essential type of cellulase enzyme for the production of single glucose molecule [3-4]. Endoglucanases is the enzyme that breaks on the β-glycosidic bonds that is presence in the polysaccharide to form glucans chains [5]. Then, exoglucanases will convert the glucans into disaccharide molecules

known as β-cellobiose [5]. Finally, the β-glucosidases will break the bond in disaccharide molecule to produce single glucose unit [5].

A fermentation medium is essential to cultivate the microorganisms for the production of cellulase enzyme so that enzymatic digestion can occur. Fermentation can be classified as Solid State fermentation (SSF) and Submerged Fermentation (SmF). SSF is a fermentation process in the absent of free water but there is sufficient moisture content within the substrate which cater for the growth of microorganisms [6]. SmF on the other side require large amount of free water in order for the fermentation to take place. **Table 1** below shows the comparison pro and cons of SSF and SmF. Although SSF posses more advantages than SmF but there is yet to be proven [6].

Table 1. Comparison of Solid State Fermentation and Submerged Fermentation.

Fermentation techniques	Advantages	Disadvantages
Solid State Fermentation (SSF) [7,8]	• Similar natural habitat to the microorganisms, especially fungi • Save cost • Reduce energy consumptions • Higher enzyme production • Increase fermentation productivity	• Scale up issue • Hard to maintain the moisture content
Submerged Fermentation (SmF) [7,9]	• Able to control the parameters	• More cost to recover product

Sugar is the one of the products formed from the fermentation process of the biomass. It can be classified as monosaccharide or disaccharide whereby disaccharide is the combination of two monosaccharides with β-1,4 linkage in between. Reducing sugar is typically a type of sugar that has free aldehyde group and is able to be oxidized to form carboxylic acid [10]. Glucose, fructose, maltose and lactose are some examples of reducing sugar. There are many application of glucose in either biochemical pathway, carboxylate platform or even in the chemical pathway [11-13]. Alcohol type biofuels such as butanol, ethanol and others are mainly produced from glucose through the biochemical pathway [11]. In the chemical pathway, glucose acts as a precursor for high value products such as succinic acid and bioplastics [12]. Glucose can also be used as a substrate for producing drop-in biofuels through carboxylate platform [13].

In order to generate more reducing sugar from the fermentation process, pretreatment is often the alternative way. Pretreatment process helps to remove the lignin and hemicelluloses content that are presence in the lignocellulosic material of the agricultural wastes [14-15]. Besides that, pretreatment also play an important role in reducing the crystallinity and polymerization of cellulose content [16]. As a consequence, there will be an increase in surface area in contact that eases the enzymatic hydrolysis process. There are 4 main types of pretreatment process, namely chemical pretreatment, physical pretreatment, biological pretreatment and physio-chemical pretreatment. Biological pretreatment is not the best option as the degradation

rate of microorganisms on the lignocellulosic part is very time consuming [17]. On the other hand, physio-chemical pretreatment will introduce the formation of inhibitor such as furfural that inhibits the formation of glucose [18]. Thus, physical pretreatment and chemical pretreatment are the most common option. Physical pretreatment of grinding, milling, shredding and chipping process causes the plant cell wall to rupture and also dissociate the tissues [19]. In the studies, it was found that alkali pretreatment is the most efficient method [20].

From the challenges of excessive activated sludge produced from the WWTP and also the abundant sugarcane bagasse generated from sugar factories, reducing sugar can be produced through the mixing of both wastes via solid state fermentation. Hence, the objectives of this research are to determine the suitability of bacteria presence in Indah Water activated sludge to generate reducing sugar through a Solid State Fermentation process and also to increase the amount of reducing sugar produced through combination of physical and alkali pretreatment process.

2. Methodology

2.1 Materials

Sugarcane bagasse which is an agro-industrial waste was collected from the night market seller near Jalan Seruling 57, Klang, Selangor. On the other hand, activated sludge was taken from Indah Water Sdn Bhd for the purpose of utilizing the available bacteria during the sugarcane bagasse fermentation process. All chemicals required were provided by the laboratories in Taylor's University.

2.2 Preparation of Sugarcane bagasse

Sugarcane bagasse was rinsed with water to remove any impurities that is presence on the surface of sugarcane bagasse. Then, the excessive water will be drained off while bagasse will be arranged on the baking tray. The rinsed bagasse will be subjected to drying at 60^{o}C for 24 hours in the oven (Memmert, Germany). Dried bagasse was grinded into fine particle using the electric grinder (KGC Scientific, China). Bagasse size of range from 425-825 µm was selected through the sieving process using a mechanical siever (Tyler, United State).

2.3 Alkali pretreatment

Dried bagasse was pretreated in a Scott bottle using 0.62M sodium hydroxide solution. The alkali pretreatment process was carried out under temperature between the range of 121-128^{o}C for 30 minutes using an oil bath [2]. Solid loading of 9%w/v was selected for the pretreatment condition. After the pretreatment process, sodium hydroxide was rinsed off with excessive water to greatly reduce the pH to about 7 or 8. Then, citrate buffer was added to further lower down the pH to 5. Excessive liquid was removed and the pretreated bagasse was dried in oven for another 24 hours at 60^{o}C.

2.4 Fermentation and separation process

The fermentation process was conducted on untreated and pretreated bagasse for 6 days. 2g of bagasse was mixed up with 20ml of activated sludge in the Erlenmeyer flask. Mandel's medium of 2g/L KH_2PO_4, 0.3g/L $CaCl_2.2H_2O$, 1.4mg/l $ZnSO_4.7H_2O$, 1.6mg/L $MnSO_4.2H_2O$, 0.2% (v/v) Tween 80, 1.4g/L $(NH_4)_2SO_4$, 0.3g/L urea, 1g/L peptone, 0.3g/L $MgSO_4.7H_2O$, 5mg/L $FeSO_4.7H_2O$ and 2mg/L $CoCl_2.6H_2O$ were added in as nutrient and also provide 70% moisture to the bagasse mixture [3], [4]. The samples were covered with single hole stopper and kept in an orbital shaker. The orbital shaker (Yih-Der, China) was maintained at 30^oC and 150rpm for throughout the entire fermentation period.

One sample of each fermented untreated and pretreated products were taken out from orbital shaker on each day. 20ml of 50mM (pH 4.8) citric acid was added into each Erlenmeyer flask [5]. Extracted liquid from each sample was transfer to the rotary shaker (Yih-Der, China) and agitate at 150rpm for an hour. Supernatant liquid was extracted by placing both samples in the centrifuge (Labogene, Denmark) of 4^oC, 3500rpm for 20 minutes [2]. Particles that were settling down were discarded. A filtration process was essential to ensure most of the impurities were removed from the supernatant liquid. A 0.2μm filter was used to eliminate large particle that might affect the analytical testing readings.

2.7 Analytical method

A HPLC (Agilent, United State) model of PL1170-6830 was used to analyze the reducing sugar that available in supernatant liquid. 0.005M sulfuric acid was used as the mobile phase along the Agilent Hi-Plex H column at flow rate of 0.7ml/min. The column was remained at 60^oC while Refractive Index Detector (RID) was set at 55^oC [6]. The analysis time was set at 15 minutes for each sample run. Besides that, FTIR (Perkin Elmer, United State) was used to study on the changes of chemical structure in lignocellulosic content of sugarcane bagasse when subjected to pretreatment and also the effects of fermentation on these structures. After the background scan, solid samples were placed and tighten on the diamond. The spectrum was taken with 16 scans between the ranges of 650 to 4000cm^{-1}. Methanol is used to clean the diamond before and after each sample test to prevent cross contamination between samples.

3. Results and Discussions

3.1 High Performance Liquid Chromatography analysis

The results obtained from the HPLC analysis were plotted in the **Fig. 2** below. The results show a fluctuation in the concentration of reducing sugar produced throughout the 6 days of solid state fermentation period. On the first day, both treated and untreated sugarcane bagasse produced the highest amount of reducing sugar with 36.32ppm and 27.76ppm. There are greater amount of reducing sugar observed in the sample of treated sugarcane bagasse as compared to untreated bagasse on day 1. One of the reasons might be the structural changes in lignocellulosic content during the combination pretreatment process. Untreated bagasse is reported to have high crystallinity of cellulose with low surface in contact which resulted in a lower performance of cellulase enzyme [7], [8]. Hence, size reduction through grinding process helps to rupture the plant cell wall to increase the total accessible surface area [9]. When the accessible surface area increases, the efficiency of cellulase enzyme increases. Alkali pretreatment method on the other hand causes the swollen of biomass and also removal of lignin and hemicellulose content simultaneously [10]. Another

reason might be the addition of Mandel's medium on day 0 which enhanced the bacteria activity by producing more cellulase enzyme to break the cross linkage bonds [8].

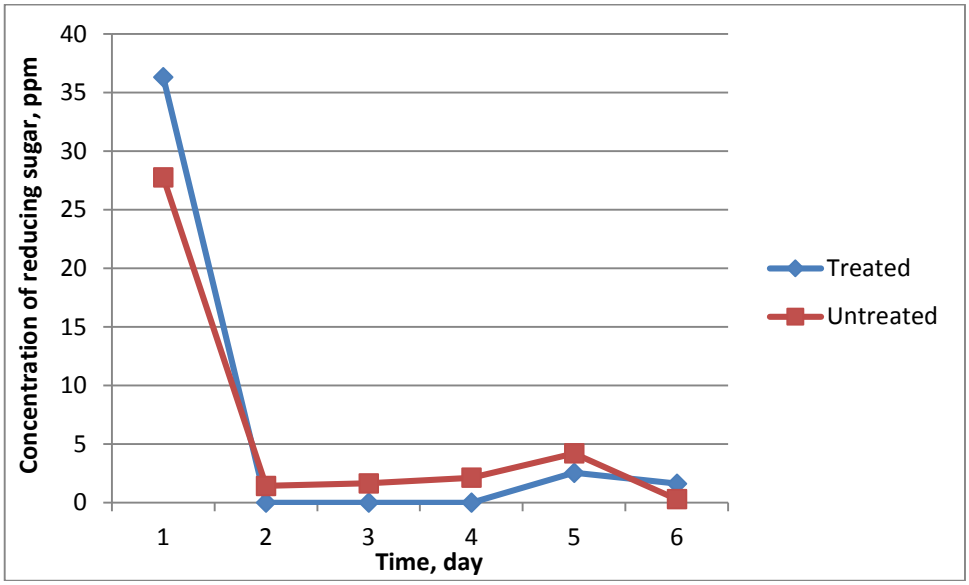


Figure 2: HPLC results for treated and untreated sugarcane bagasse for 6 days.

On the second day, there is a drastic drop on the amount of reducing sugar. Activated sludge with high number of different microorganisms will actively consume on the Mandel's medium added. Thus, more reducing sugar is consumed by the cellulolytic bacteria and some other bacteria for growing purpose which leads to lower reducing sugar content. However, there is a slight different trend in the amount of reducing sugar between the treated and untreated sugarcane bagasse from day 2 to day 4. Untreated bagasse posses an increasing trend while treated bagasse shows a minimal concentration of cellobiose.

At day 5, the production of reducing sugar by the cellulolytic bacteria through enzymatic hydrolysis process is sufficient to overcome consumption of reducing sugar. The concentration of reducing sugar for treated and untreated sugarcane bagasse is 2.55ppm and 4.21ppm respectively. Although it was reported that treated bagasse has the higher tendency of producing reducing sugar during the fermentation but the results obtained between day 2 to day 5 shows a different outcomes. It might be due to the production of different enzymes from other bacteria. Cellulase enzymes are generally produced from cellulolytic bacteria of *Bacillus*, *Thermomonospora*, *Bacteriodes*, *Microbispora*, *Clostridium thermocellum*, *Bacteroides cellulosolvens* and others [11]. This enzyme is important for the production of cellobiose and glucose molecules. In the mixed microorganism's community, enzyme such as xylase and lactase might be generated instead of cellulase.

As the fermentation process goes on, the amount of reducing sugar decreases. One of the reasons might be the depletion of nutrient contents in the fermentation medium. When cellulolytic bacteria get insufficient nutrients, the cellulase production process slows down which directly affect the generation of reducing sugar. In short, it can be conclude that the combination of alkali and physical pretreatment produce the highest amount of reducing sugar in 1 day of fermentation. Thus, it helps to save on the

total operating cost of an industry with the benefits of short fermentation duration needed.

3.3 Fourier Transform Infrared Radiation analysis

The FTIR was carried out on the untreated bagasse before fermentation, untreated bagasse after fermentation, treated bagasse before fermentation and also treated bagasse after fermentation. The results obtained was plotted in Fig. 3 below to study the effect of pretreatment on the lignocellulosic content of sugarcane bagasse. The spectrums produced in each region are indicating different chemical structures.

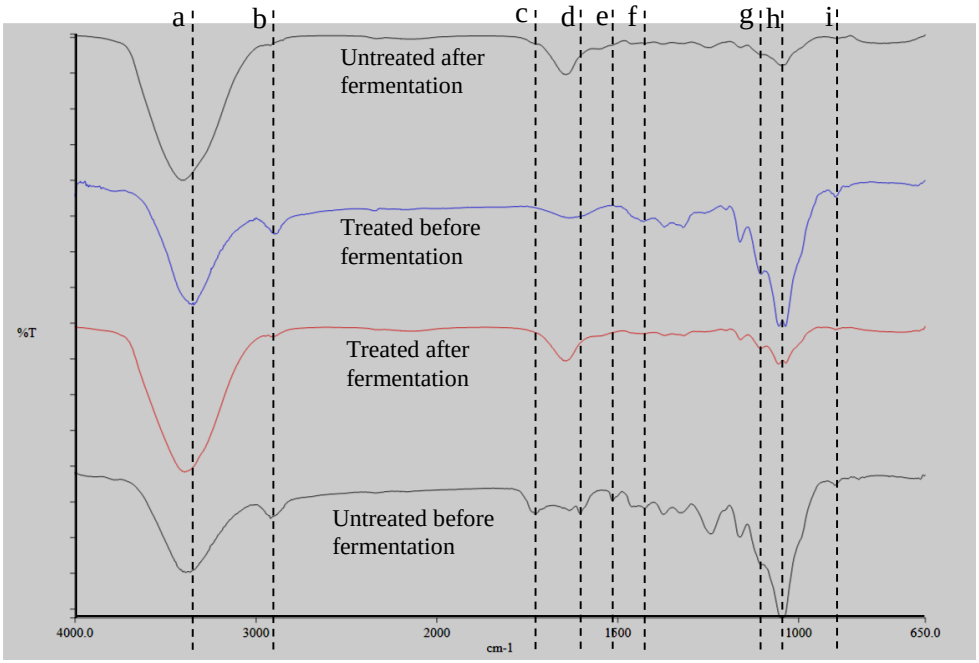


Figure 3: FTIR spectrum results at (a) 3353.14cm^{-1} (b) 2912.58 cm^{-1} (c) 1729.30 cm^{-1} (d) 1605.30 cm^{-1} (e) 1514.48 cm^{-1} (f) 1423.67 cm^{-1} (g) 1104.07 cm^{-1} (h) 1049.76 cm^{-1} (i) 897.99 cm^{-1}.

Based on the spectrum results obtained, there are significant differences between the untreated bagasse before fermentation, untreated bagasse after fermentation, treated bagasse before fermentation and treated bagasse after fermentation. The peaks formed at 3353.14cm^{-1} are representing the hydroxyl bonds which presence in the lignocellulosic content of sugarcane bagasse [2]. On the other hand, the peaks at 2912.58cm^{-1} are indicating the C-H stretching [2]. Hydroxyl bonds and C-H stretching are the essential structures needed to build up the glucose polymer chain in the lignocellulosic content. However, there are no significant effects on these two peaks after the combination pretreatment process.

There is a significant peak at 1729.30cm^{-1} on the untreated bagasse before fermentation. This peak is representing the 4-O-methyl-D-glucuronic linkages in uronic ester that is presence in the hemicelluloses, xylan and lignin [12]. Saphonification process took place during alkali pretreatment process had lead to the reduction in the cross linkage bonds [8], [13]. Thus, it can clearly see that the intensity of peak at 1729.30cm^{-1} reduces. The same trend goes to the peak at 1605.3cm^{-1} and 1514.48cm^{-1}

which represent the aromatic skeleton vibrations in lignin content [12], [14]. Hence, the result correlate well with the research done by Sun, saying that alkali pretreatment is able to remove the lignin content presence in lignocellulosic material of sugarcane bagasse [10].

The assigned peak for crystalline cellulose appears at 1423.67cm^{-1} [2]. Although the intensity of peak remains the same before and after pretreatment but both intensity reduces after fermentation process. This might happen because of the enzymatic hydrolysis process that is taken place during the fermentation process which causes CH_2 scissoring on crystalline celluloses. Hence, it is easier to be solubilized. On the other hand, amorphous cellulose presence at peak of 897.99cm^{-1} [2], [12], [15]. After the fermentation process, it is believed that most of the β-1,4 linkage had been hydrolyzed by the generated cellulase due to the low spectra intensity [16]. However, there is still a minor peak observed in the untreated bagasse after SSF. Through the alkali pretreatment process, cellulose degradation took place as a consequence of swollen biomass [17].

Apart from that, C-O-C bonds at β-1,4 linkage and C-O stretching are indicated by the peaks at 1104.07cm^{-1} and 1049.76cm^{-1} [12], [18]. The intensity of both peaks greatly reduces after SSF process which shows the degradtion of cellulose content by cellulase enzyme in the enzymatic hydrolysis process [18]. As a summary, the results correlate well with the researches mentioning that alkali pretreatment reduces the lignin content, solubilized the cellulose and saponify the ester bonds in hemicellulose [8], [13], [17].

4. Conclusion

As a conclusion, reducing sugar of cellobiose could be produced from both alkali pretreated and untreated sugarcane bagasse. However, there are greater amount of reducing sugar produced in the alkali pretreated samples compared to untreated samples of similar particle size. On the first day of fermentation, the concentration of cellobiose was 36.32ppm for treated bagasse and 27.76ppm for untreated bagasse. Since cellobiose is produced through the solid state fermentation using Indah Water activated sludge and the amount generated increases with sodium hydroxide pretreatment, the objectives of this research were met. As a future work, more research parameters are needed to ensure higher amount of cellobiose is produced within a short fermentation period. Besides that, the research can be further study to induce formation of glucose as end product.

Acknowledgement

The author would like to express the author's appreciation to the family members, project supervisor, friends and laboratory technicians of Taylor's University for the helps and guidance provided throughout the entire research project.

References

[1] R. C. Kuhad, R. Gupta, and A. Singh, "Microbial cellulases and their industrial applications.," *Enzyme Res.*, vol. 2011, p. 280696, 2011.

[2] L. W. Yoon, G. C. Ngoh, and A. S. M. Chua, "Simultaneous production of cellulase and reducing sugar through modification of compositional and structural characteristic of sugarcane bagasse," *Enzyme Microb. Technol.*, vol. 53, no. 4, pp. 250–256, 2013.

[3] J. Ouyang, Z. Dong, X. Song, X. Lee, M. Chen, and Q. Yong, "Improved enzymatic hydrolysis of microcrystalline cellulose (Avicel PH101) by polyethylene glycol addition," *Bioresour. Technol.*, vol. 101, no. 17, pp. 6685–6691, 2010.

[4] M. Yang, J. Zhang, S. Kuittinen, J. Vepsäläinen, P. Soininen, M. Keinänen, and A. Pappinen, "Enhanced sugar production from pretreated barley straw by additive xylanase and surfactants in enzymatic hydrolysis for acetone–butanol–ethanol fermentation," *Bioresour. Technol.*, vol. 189, pp. 131–137, 2015.

[5] R. R. Singhania, R. Saini, M. Adsul, J. K. Saini, A. Mathur, and D. Tuli, "An integrative process for bio-ethanol production employing SSF produced cellulase without extraction," *Biochem. Eng. J.*, pp. 8–11, 2015.

[6] S. Ball, S. Bullock, L. Lloyd, K. Mapp, and a Ewen, "Analysis of carbohydrates , alcohols , and organic acids temperature effects on invert Sugar," 2011.

[7] S. Behera, R. Arora, N. Nandhagopal, and S. Kumar, "Importance of chemical pretreatment for bioconversion of lignocellulosic biomass," *Renew. Sustain. Energy Rev.*, vol. 36, pp. 91–106, 2014.

[8] R. Singh, A. Shukla, S. Tiwari, and M. Srivastava, "A review on delignification of lignocellulosic biomass for enhancement of ethanol production potential," *Renew. Sustain. Energy Rev.*, vol. 32, pp. 713–728, 2014.

[9] A. Barakat, F. Monlau, A. Solhy, and H. Carrere, "Mechanical dissociation and fragmentation of lignocellulosic biomass: Effect of initial moisture, biochemical and structural proprieties on energy requirement," *Appl. Energy*, vol. 142, pp. 240–246, 2015.

[10] S. Sun, S. Sun, X. Cao, and R. Sun, "The role of pretreatment in improving the enzymatic hydrolysis of lignocellulosic materials," *Bioresour. Technol.*, pp. 960-8524, 2015.

[11] Y. Sun and J. Cheng, "Hydrolysis of lignocellulosic materials for ethanol production: A review," *Bioresour. Technol.*, vol. 83, no. 1, pp. 1–11, 2002.

[12] M. D. Harrison, Z. Zhang, K. Shand, I. M. O'Hara, W. O. S. Doherty, and J. L. Dale, "Effect of pretreatment on saccharification of sugarcane bagasse by complex and simple enzyme mixtures," *Bioresour. Technol.*, vol. 148, pp. 105–113, 2013.

[13] F. C. Lunelli, P. Sfalcin, M. Souza, E. Zimmermann, V. Dal Prá, E. L. Foletto, S. L. Jahn, R. C. Kuhn, and M. a. Mazutti, "Ultrasound-assisted enzymatic hydrolysis of sugarcane bagasse for the production of fermentable sugars," *Biosyst. Eng.*, vol. 124, pp. 24–28, 2014.

[14] L. Liu, J. Sun, M. Li, S. Wang, H. Pei, and J. Zhang, "Enhanced enzymatic hydrolysis and structural features of corn stover by FeCl3 pretreatment," *Bioresour. Technol.*, vol. 100, no. 23, pp. 5853–5858, 2009.

[15] N. C. Carpita and D. M. Gibeaut, "Structural models of primary cell walls in flowering plants: consistency of molecular structure with the physical properties of the walls during growth.," *Plant J.*, vol. 3, no. 1, pp. 1–30, 1993.

[16] Y. Cao, Y. Cao, H. Tan, and H. Tan, "Effects of cellulase on the modification of cellulose," *Carbohydr. Res.*, vol. 337, pp. 1291 –1296, 2002.

[17] A. T. W. M. Hendriks and G. Zeeman, "Pretreatments to enhance the digestibility of lignocellulosic biomass," *Bioresour. Technol.*, vol. 100, no. 1, pp. 10–18, 2009.

[18] R. E. Abraham, C. J. Barrow, and M. Puri, "Relationship to reducing sugar production and scanning electron microscope structure to pretreated hemp hurd biomass (Cannabis sativa)," *Biomass and Bioenergy*, vol. 58, pp. 180–187, 2013.

Retained total phenolic content (TPC) and antioxidant activity of betel leaves extract from fresh and recycled solvent using solvent extraction and ultrasonic-assisted extraction methods

Si Wen Loo[1], Rebecca Xiao Yien Lim[1*], Chien Hwa Chong[1]

[1]*School of Engineering, Taylor's University, Malaysia*

[*]XiaoYien.Lim@taylors.edu.my

Abstract
Betel leaf, also known as *Piper betle* Linn is well-known for its therapeutic purposes. Since ancient times, betel leaf is widely used to overcome body odor, itchiness and injuries, eliminate bad breath, treat ulcers as well as used for manufacturing medicines and food additives. Its extract has shown antioxidant, anti-inflammatory and antimicrobial properties. This research aims to investigate the best extraction method based on the antioxidant property. Besides, the project also aims to evaluate the stability of bioactive compounds in betel leaves extract, mainly hydroxychavicol (HC) under different light intensities. Betel leaves were freeze dried and extracted by using two different methods, solvent extraction and ultrasonic-assisted extraction (UAE) using fresh and recycled ethanol as solvent. The recycled solvent has a composition of 50 wt% used and 50 wt% fresh ethanol. Betel leaves extracted using recycled ethanol solvent were exposed to two different light intensities, light and dark condition. The total phenolic content of the betel leaves extracts was analyzed using fast blue BB (FBBB) reagent while the antioxidant activity of the extracts was investigated using 2,2-diphenyl-1-picrylhydrazyl (DPPH) free radical scavenging assay. High performance liquid chromatography (HPLC) was used to determine the chemical profiles and composition of HC. Ultrasonic-assisted extraction using fresh ethanol solvent extract showed highest extraction yield of 12% and total phenolic content of 216 mg/g of gallic acid equivalents (GAE). All the extracts had shown inhibition on the antioxidant assay with UAE using fresh ethanol solvent extract showing the highest antioxidant activity of 68%. The HPLC analysis revealed that HC was detected in all the extracts and the concentration was highest in the UAE using fresh ethanol solvent extract with a concentration of 213 ng/µl. These results indicate that HC contribute to the antioxidant property of betel leaves.

Keywords: betel leaf, recovered solvent, ultrasonic-assisted extraction, total phenolic content, antioxidant, hydroxychavicol

1. Introduction

Herbal medicines have been widely used to treat different types of diseases [1]. Even though modern pharmaceutical companies have developed a wide range of treatment, traditional medicinal plants still make an important contribution to the world health. Traditional herbal medicines are still widely used since ancient times to date as modern medicines have greater toxic side effect [2]. The World Health Organization (WHO) estimates that about 4 billion people, representing 80% of the world population, are still depending on herbal medicines as major healthcare essentials [3]. Since the chemical constituents found in the herbal plants are part of the physiological functions of the plants, it is acknowledged to be more compatible with human body. Therefore, the use of phytochemicals of plant extracts is crucial in pharmaceutical industry [4], [5].

Betel leaf, also known as *Piper betle Linn*, belongs to the family of Piperaceae [6]. It is one of the most important medicinal plants in Asiatic region used for many medicinal purposes [7]. This plant is native to central and eastern Malaysia and has been nurtured for more than 2500 years ago throughout Malaysia and Asia [8]. Betel leaf is known to possess many medicinal properties. It has shown capability to improve appetite, used as mouth freshener and antiseptic, industrial raw material for manufacturing medicines, tonics and food additives [9]. Betel leaf possesses various properties such as antioxidant, anti-inflammatory, antimicrobial, antidiabetic, anticancer and antifertility [10]–[16].

In general, plant contains a variety of bioactive compounds. Bioactive compounds in plants are responsible for health promotion and disease prevention [17]. Betel leaf contains phytochemicals such as eugenol, hydroxychavicol, allypyrocatechol and chavibetol [18]. In this research hydroxychavicol was studied as it was reported to contribute to a lot of bioactivities in betel leaves [19]–[21], which includes the antioxidant activity. Antioxidant is capable of preventing or slowing the process of oxidation of other molecules. It helps to destroy the free radicals that damage cells and promote growth of healthy cells [22]. Since HC possesses antioxidant property, the antioxidant activity of betel leaves extract was investigated in this research.

In extraction process, it is unavoidable that large amount of organic hazardous solvents are used and thus increases the cost of solvent waste disposal. Therefore, it is necessary to produce better and more environmental friendly extraction methods. Besides, in industry with large scale of production, it is more cost effective to operate by recycling used solvent. However, studies done on recycled solvent were limited. In this research, recycled solvent with a composition of 50 wt% used ethanol and 50 wt% fresh ethanol was used to investigate the antioxidant property of betel leaves extract and concentration of. Ethanol solvent was selected as it was reported by Nouri *et al.* that ethanol solvent was the most effective solvent and showed the highest amount of total phenolic content and antioxidant activity [23].

Besides that, two types of extraction techniques were used in this research, which include solvent extraction and ultrasonic-assisted extraction. There were limited studies done on the usage of ultrasonic-assisted extraction in betel leaves extraction. According to Dhanani *et al.*, the phenolic content obtained from solvent

extraction using ethanol solvent was higher as compared to UAE [24]. From the study done by Ma *et al.*, the total phenolic content obtained from UAE using ethanol solvent was much higher than solvent extraction [25]. However, these studies were not done on betel leaves. Thus, this research intended to investigate if the usage of UAE results in higher antioxidant activity and greater concentration of HC than the conventional solvent extraction for betel leaves extraction. This is because ultrasonic-assisted extraction uses lesser amount of solvent and shorter amount of extraction time [26].

Betel leaves extracted using recovered solvent were exposed to two different light intensities, light and dark condition, during storage before undergoing further analysis on the total phenolic content, antioxidant activity and concentration of HC. This is because phytochemicals degrade after a period of time and the stability of phytochemicals during storage depends very much on the light exposure [27]. As there were limited studies done on the effects of light intensity during storage of betel leaves extract, the antioxidant activity and concentration of HC of the recycled ethanol solvent extracts, which were exposed to different light intensities were investigated.

Therefore, the objectives of this study were to investigate the total phenolic content, antioxidant property and concentration of HC in betel leaves extract using fresh and recycled ethanol solvent. In addition, it was also aimed to identify the best extraction method used in betel leaves extraction based on the total phenolic content, antioxidant property and concentration of HC analyzed. Last but not least, the effects of light intensity on the composition of bioactive compounds in betel leaves extracted using recycled ethanol solvent were studied as well.

2. Materials and Methods

2.1 Materials

Betel leaves were purchased from Sirih Enterprise located in Banting, Selangor. Deionized water was obtained from School of Biosciences, Taylor's University. Ethanol was purchased from HmBG. HPLC grade methanol and gallic acid were obtained from Merck. Sodium hydroxide was purchased from Friendemann Chmidt. Fast blue BB (FBBB), 2,2-diphenyl-1-picrylhydrazyl (DPPH) as well as hydroxychavicol standard were purchased from Sigma-Aldrich.

2.2 Drying Process

Betel leaves were cleaned up using distilled water. The drying process was performed following the method in Górnaś *et al.* with slight modifications [28]. Betel leaves were dried at -50^{o}C and 0.08 mbar for 24 hours using freeze dryer (77500 Series, Labconco, USA). Drying of leaves remove excess moisture and avoid decomposition of phytochemicals as well as contamination of microbial [29]. Then, the dried leaves were blended using an electrical blender (EBM-9182, Elba, Malaysia) to increase the surface area for greater contact with solvent during extraction process. After blending, the dried leaves were sieved using a coarse sieve shaker (RX-812-1, Tyler, USA) in order to obtain even leaves size of 500 μm. Dried betel leaves were stored at 4^{o}C until further use.

2.3 Extraction Process

In this research, ethanol was used as the solvent in the extraction process. Fresh and recycled ethanol solvent at a composition of 50 wt% used ethanol and 50 wt% fresh ethanol were used. Recycled solvent was obtained by recovering the solvent during evaporation process and using it for the subsequent extraction process. Hence, solvent recovered was of the same processes. The extraction processes were carried out using solvent extraction method and ultrasonic-assisted extraction method.

2.3.1 Solvent Extraction

The extraction process was carried out based on the methods in Pin *et al.* and Pradhan *et al.* with slight modifications [30], [31]. The extraction was done by simple maceration process using water bath with occasional stirring at a temperature of 50°C to avoid degradation of phytochemicals. Dried betel leaves were mixed with solvent at a ratio of solvent to solid of 30.0 ml to 1.0 g. This process was carried out for 6 hours. After extraction, rotary evaporator (RV 10 BASIC, IKA, Germany) was used to remove excess solvent and obtain crude extract. Due to limitation of equipment, the evaporation was carried out at 80°C. Crude extracts were stored at 4°C until further analysis. The extraction yield is expressed as the percentage ratio of crude extracts obtained to the amount of raw materials used.

$$Yield = \frac{W_d}{W_s} \times 100\% \quad (1)$$

Where W_d is the weight of dried extracts (g) and W_s is the weight of raw materials (g).

2.3.2 Ultrasonic-Assisted Extraction (UAE)

The extraction process was carried out following the method in Pin *et al.* and Feng *et al.* with slight modifications [30], [32]. The extraction process was done using ultrasonic bath (S60H, Elmasonic, Germany) at a temperature of 50°C to avoid degradation of phytochemicals. Dried betel leaves were mixed with solvent at a ratio of solvent to solid of 30.0 ml to 1.0 g. This process was carried out for 30 minutes. After extraction, rotary evaporator (RV 10 BASIC, IKA, Germany) was used to remove excess solvent and obtain crude extract. Due to limitation of equipment, the evaporation was carried out at 80°C. Crude extracts were stored at 4°C until further analysis. The extraction yield is expressed as the percentage ratio of crude extracts obtained to the amount of raw materials used.

$$Yield = \frac{W_d}{W_s} \times 100\% \quad (2)$$

Where W_d is the weight of dried extracts (g) and W_s is the weight of raw materials (g).

2.4 Light Intensity

Betel leaves extracted using recovered ethanol solvent were exposed to two different light intensities. Clear petri dish and petri dish wrapped with aluminum foil were used to vary the light intensity in order to create a light and dark condition during storage.

2.5 Analysis of Betel Leaves Extracts

2.5.1 Concentration of Hydroxychavicol via High Performance Liquid Chromatography (HPLC)

The HPLC analysis was performed based on the method in Singtongratana *et al.* with slight modifications [33]. The analysis was carried out using a HPLC (1220 Infinity LC, Agilent Technologies, USA) Hypersil GOLD C_{18} column (250 x 4.6 mm). The mobile phase consisted of 70% HPLC grade methanol, 30% deionized water and analysis was performed under isocratic conditions at temperature of 28^{o}C, flow rate of 0.7 ml/min and wavelength of 280 nm. The 3.0 mg of betel leaves extract was dissolved in 3.0 ml of ethanol [19]. Then, the mixture was filtered using a syringe filter (diameter: 25 mm, pore size: 0.20 μm, membrane: regenerated cellulose, Sartorius, Germany) before undergoing HPLC analysis.

2.5.2 Total Phenolic Content (TPC) via Fast Blue BB (FBBB) Assay

The assay was performed following the method in Medina and Lester *et al.* with slight modifications [34], [35]. Gallic acid standard with concentrations of 10, 50, 100, 200 and 250 ppm were prepared in distilled water. Then, 0.1 ml of 0.1% FBBB was added to the gallic acid standards and mixed for 1 minute before adding 0.1 ml of 5% sodium hydroxide. The reaction was allowed to complete for 90 minutes at room temperature. The absorbance of the mixture was observed at 420 nm by using UV-Vis spectrophotometer (Genesys 10S, Thermo Scientific, USA). After obtaining the standard calibration, 1.0 mg of betel leaves extract was dissolved in 20.0 ml of distilled water. The reaction mixture was prepared by replacing the gallic acid standards with test solution. The absorbance of the test solution was recorded and referred to the calibration curve to obtain the equivalent concentration of gallic acid. Hence, the total phenolic content of the sample was expressed as gallic acid equivalents.

2.5.3 Antioxidant Assay via 2,2-diphenyl-2-picrylhydrazyl (DPPH) free radical scavenging assay

The assay was performed following the method in Pin *et al.* with slight modifications [19]. DPPH stock solution was prepared at a concentration of 1.0 mM in methanol. Betel leaves extract of 2.0 mg was mixed with 4.0 ml of methanol and 1.0 ml of DPPH and kept in a universal bottle. The mixture was agitated and left for 30 minutes at room temperature. Then, absorbance of the mixture was observed at 520 nm by using the UV-Vis spectrophotometer. The negative control of this assay is

methanol while positive control is prepared by replacing betel leaves extract with gallic acid.

The percentage of inhibition is calculated as:

$$\%\ inhibition = \frac{Ab_{C,-ve} - Ab_S}{Ab_{C,-ve} - Ab_{C,+ve}} \times 100\% \quad (3)$$

Where Ab_s is the absorbance of sample, $Ab_{c,-ve}$ is the absorbance of negative control and $Ab_{c,+ve}$ is the absorbance of positive control.

3. Results and Discussion

3.1 Extraction Yield

Fig. 1 shows the comparison of extraction yield for both solvent extraction and ultrasonic-assisted extraction using fresh and recycled ethanol solvent at a composition of 50 wt% used ethanol and 50 wt% fresh ethanol. The extraction yield obtained using UAE was higher than solvent extraction. Besides that, fresh ethanol solvent shows greater extraction yield as compared to recycled ethanol solvent as well. The extraction yield for UAE ranges from 10% to 12% whereas solvent extraction had an extraction yield of 6% to 9.5%. Dhanani *et al.* reported a similar finding for *Withania somnifera* extraction yield, in which the extraction yield for UAE and solvent extraction using fresh ethanol solvent were 10% and 9%, respectively [24]. The decrease in extraction yield for UAE of this finding might be due to the extraction time used, which was 20 minutes. Another study by Bampouli *et al.* on the extraction of *Pistacia lentiscus* var. *chia* leaves had reported that the extraction yield for both UAE and solvent extraction was similar, which was around 12% [36]. The difference in extraction yield for both UAE and solvent extraction was not huge with a difference of 2.5% for both extraction processes using fresh ethanol solvent, indicating that ultrasonication combined with ethanol solvent lead to similar extraction yield but significantly shorter time. Also, the improved extraction yield for ultrasonic-assisted extraction may be due to the cavitation effects caused by high intensity ultrasound [37].

In addition, there were decreases in extraction yield for recycled ethanol solvent for both extraction methods. The quality of recycled solvents is a critical factor in controlling the quality of the resulting extracts obtained [38]. Therefore, the differences in extraction yield could be due to the quality difference between fresh ethanol solvent and recycled ethanol solvent due to the presence of impurities in recycled solvent. Fig. 2 shows the HPLC chromatogram of the recycled solvent obtained and this chromatogram has indicated that there was presence of contaminants in the solvent, causing reduction in the extraction yield when compared to fresh solvent. Besides that, the difference in extraction yield of solvent extraction using recycled ethanol solvent and fresh ethanol solvent was much larger than the difference of UAE. This could be due to the propagation of sound waves during sonication and hence enhances the mass transport of solvent into plant cells [39]. To date, there were limited studies done on the usage of recycled solvent on the extraction of plants.

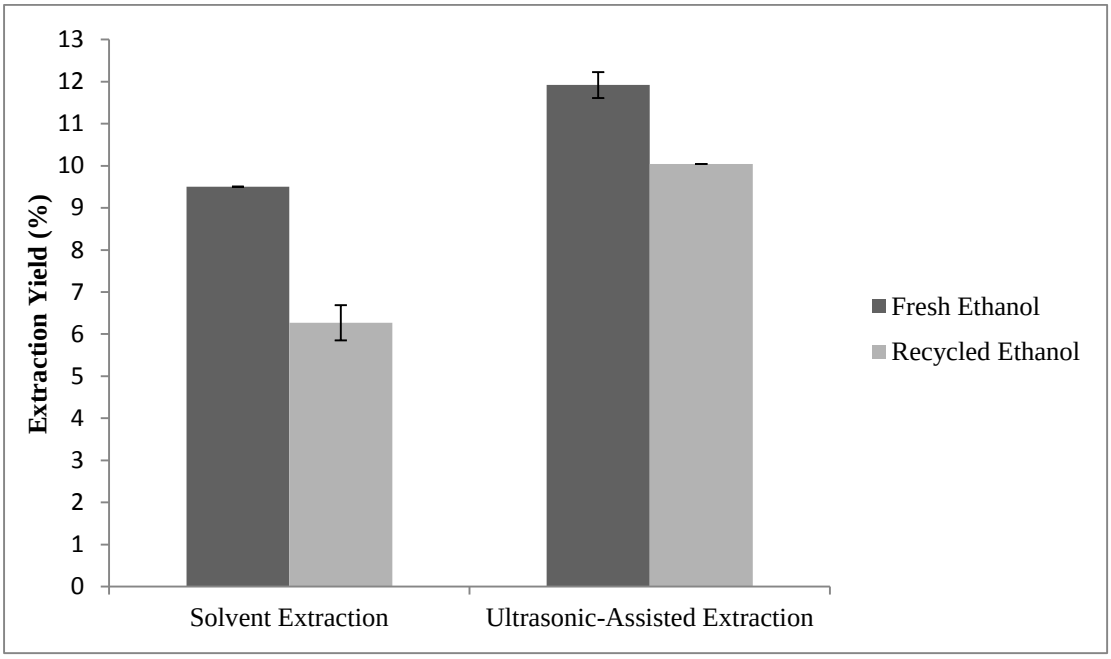


Figure 1. Extraction yield of betel leaves extract

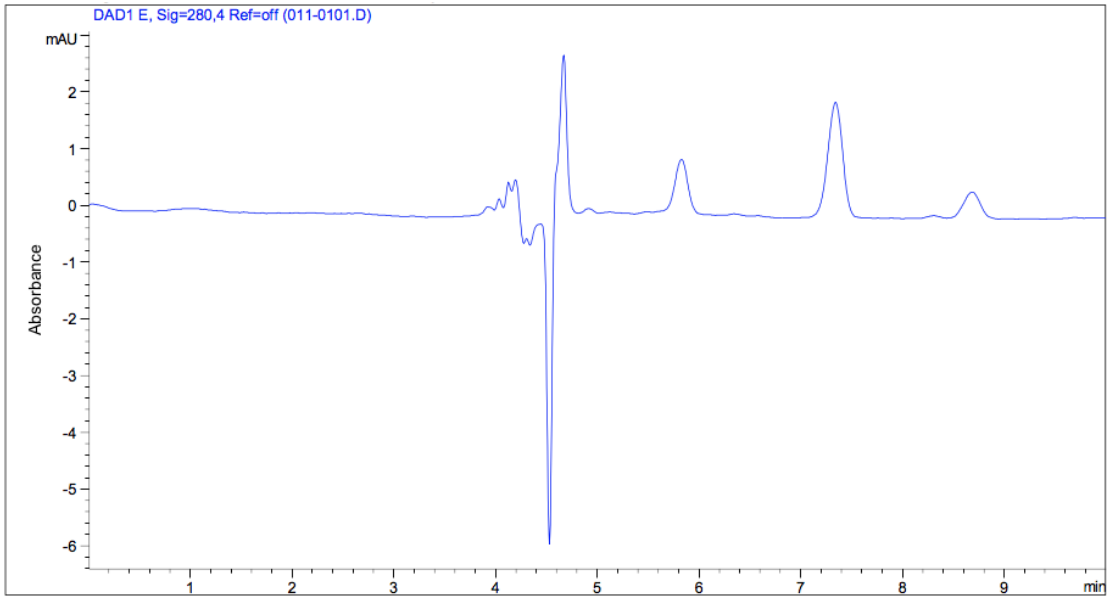


Figure 2. HPLC chromatogram of recycled ethanol

3.2 Total Phenolic Content (TPC)

The presence of phenolic compounds, especially phenolic acids derivatives and flavonoids are often related to the antioxidative and pharmacological properties. Hence, the investigation on total phenolic content of betel leaves extract is crucial. Fig. 3 shows the TPC of the betel leaves extracted using the solvent extraction and UAE methods. The extracts obtained using the recycled solvents were exposed to two different light intensities (dark and light condition). This is because the differences in extraction yield for fresh and recycled ethanol solvents were less than 4% as shown in Fig. 1. This signifies that there were areas of development for the usage of recycled ethanol solvent. As light intensity has an effect on the bioactivities of bioactive compounds, it was intended to investigate the effects of different light intensities on extracts that were obtained from recycled ethanol solvent.

The TPC in the extracts obtained through UAE were higher than the extracts obtained from the solvent extraction method. The highest phenolic content found in the UAE method was 216 mg GAE/g dried extract while the highest phenolic content found in solvent extraction was 193 mg GAE/g dried extract and these results were obtained using fresh ethanol solvent. According to Nouri *et al.*, the TPC of betel leaves extract obtained from solvent extraction using fresh ethanol solvent was 196 mg GAE/g dried extract, which was comparable with the result obtained from this study [23]. However, there were limited studies done on the extraction of betel leaves using ultrasonic-assisted extraction.

There were a few researches done on the comparison of different extraction techniques on the total phenolic content. These studies were in agreement with the results obtained from this study, in which the TPC of UAE was slightly higher than conventional solvent extraction. However, these studies were done on other plants, which were *Citrus sinensis* peel [40], *Achyranthes aspera* [41], blueberry leaves [42], *Hippophae Rhamnoides L.* and *Lippia Citriodora* [43]. The possible reason to this occurrence could be due to the high frequency sound waves during sonication that helped to extract targeted compounds more effectively as compared to solvent extraction that depends mainly on the solubility of the phytochemicals in the solvent [24].

On top of that, the TPC of recycled ethanol solvent for both solvent extraction and UAE methods were lower than the TPC of the fresh ethanol solvent extraction. This might be due to the potential differences in quality between fresh solvent and recycled solvent that could lead to significant differences in the bioactive compound composition of the extracts [38]. Furthermore, the TPC of recycled ethanol solvent stored in environment with light exposure were lower than the TPC of fresh ethanol solvent stored in dark condition. This is because bioactive compounds are destabilized by heat, light exposure, enzymes and dissolved oxygen [27]. However, the TPC of the UAE method using the recycled ethanol solvent that was exposed to light was not much different from the extract stored in dark condition.

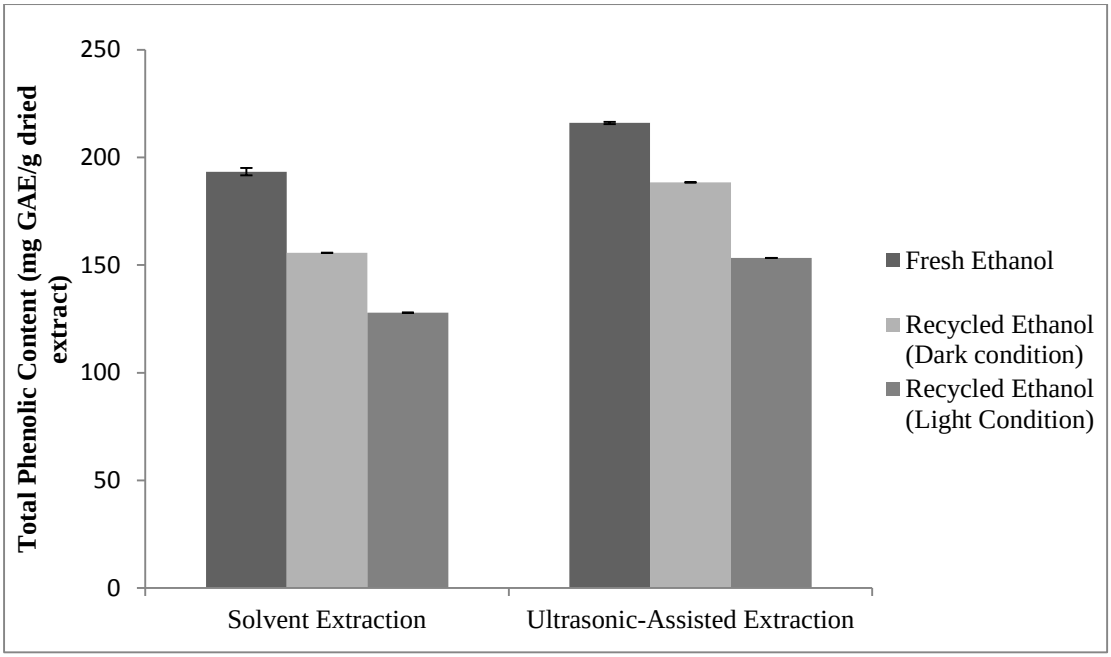


Figure 3. Total phenolic content of betel leaves extract

3.3 Antioxidant Activity

The percentage inhibition of antioxidant activity of betel leaves extracted using different methods are shown in Fig. 3. For UAE, the highest percentage inhibition of antioxidant activity was 68.3% whereas the highest percentage inhibition of antioxidant activity for solvent extraction was 59.6%. According to Nouri *et al.*, the percentage inhibition of antioxidant activity of betel leaves extract obtained from solvent extraction using fresh ethanol solvent was 89.95% [23]. It is slightly higher as the extraction process was carried out for 24 hours whereas the extraction process done in this study was 6 hours. By reducing 18 hours of extraction duration, percentage inhibition of antioxidant activity was still as high as 59.6%.

By comparing Fig. 3 and Fig. 4, it can be deduced that there is a positive correlation between the total phenolic content and antioxidant activity of the extracts. This is because phenols are significant plant constituents because of the scavenging ability of phenols on free radicals due to presence of hydroxyl groups [44], [45]. Thus, causing direct contribution of phenolic content of plants to the antioxidant activity. Numerous studies had been carried out on the relationship between TPC and antioxidant activity of plant extracts, which results in high linear correlation [45]–[50]. According to a few studies, UAE of different plants resulted in greater percentage inhibition of antioxidant activity as compared to solvent extraction [24], [36], [40]–[43], [51].

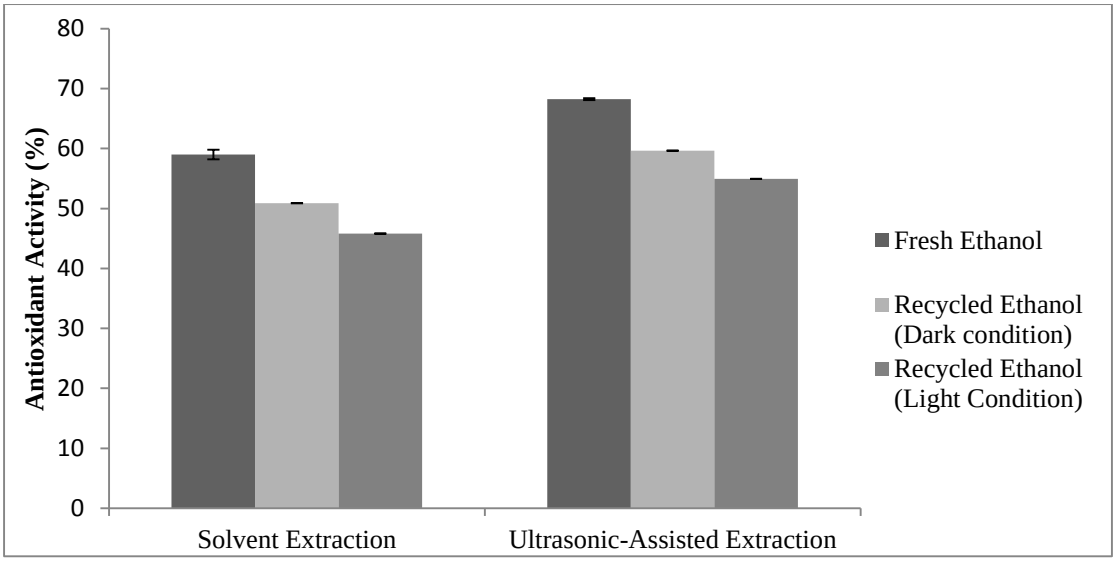


Figure 4. Antioxidant activity of betel leaves extract

3.4 Concentration of Hydroxychavicol (HC)

Retention of HC was investigated in this study as it was reported that huge amount of bioactive compounds can be found in betel leaves, which contribute to the antioxidant activity [19]–[21]. According to Pin *et al.*, there was reduction in the concentration of HC when betel leaves were dried at 80^{o}C as compared to 70^{o}C [29]. Concentration of HC was reduced to as much as 29%. Fig. 5 shows the concentration of HC in the betel leaves extracted using solvent extraction and UAE. The highest concentration of HC detected was from the UAE using fresh ethanol solvent extract with a concentration of 213 ng/µl. The main purpose of the analysis on the concentration of HC was to study the relationship of HC in contributing the antioxidant activity of betel leaves extract. Furthermore, the total phenolic content and antioxidant activity mentioned in Sec. 3.2 and Sec. 3.3 show a similar trend as the concentration of HC analyzed. This indicates that HC had great contribution on the antioxidant activity.

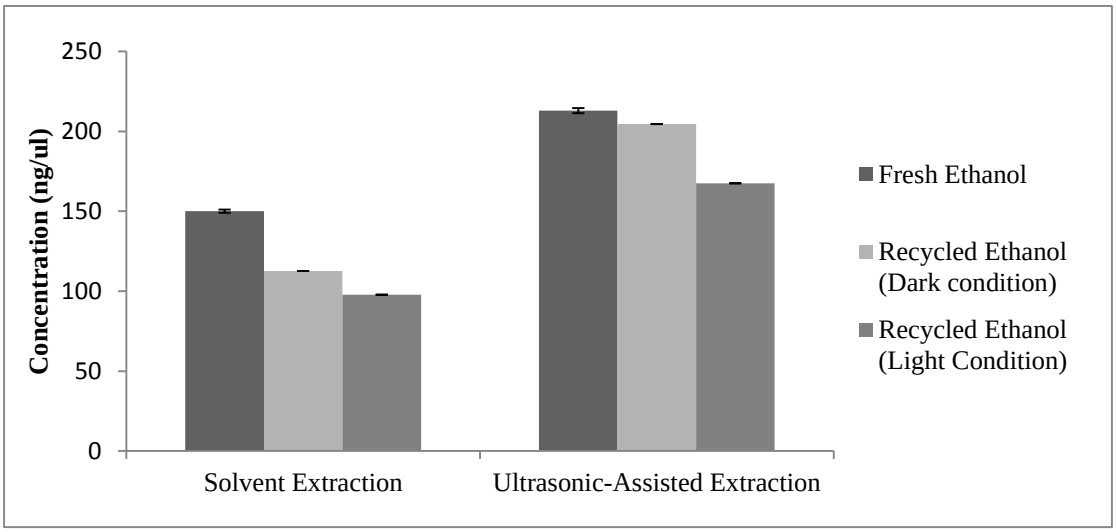


Figure 5. Concentration of HC in betel leaves

4. Conclusions

The selection of extraction technique had great effect on the extraction yield, total phenolic content, antioxidant property and concentration of hydroxychavicol in betel leaves extract. In this research, UAE had proven to be the best extraction method as it resulted in highest extraction yield, total phenolic content, antioxidant property and concentration of hydroxychavicol. For the ethanol solvent used during extraction process, fresh ethanol solvent had shown better results as compared to recycled ethanol solvent. This is because on average, the extraction yield of fresh ethanol solvent was higher by 3%, total phenolic content was greater by 26 mg GAE/g dried extract, antioxidant property had a higher percentage inhibition of 7% and concentration of hydroxychavicol was greater by 23 ng/ µl.

References

[1] Y. S. Pathare and V. D. Wagh, "Herbal Medicines and Nutritional supplements used in the treatment of Glaucoma : A Review," *Res. J. Pharm. Biol. Chem. Sci.*, vol. 3, no. 1, pp. 331–339, 2012.

[2] P. S. Patil and R. Shettigar, "An Advancement of Analytical Techniques in Herbal Research," *J. Adv. Sci. Res.*, vol. 1, no. 1, pp. 8–14, 2010.

[3] G. Bodeker, K. K. . Bhat, J. Burley, and P. Vantomme, *Medicinal plants for forest conservation and health care*. 1999.

[4] R. Nair, T. Kalariya, and S. Chanda, "Antibacterial Activity of Some Selected Indian Medicinal Flora," *Med. Exp.*, vol. 29, pp. 41–47, 2005.

[5] A. C. Akinmoladun, E. O. Ibukun, E. Afor, E. M. Obuotor, and E. O. Farombi, "Phytochemical constituent and antioxidant activity of extract from the leaves of Ocimum gratissimum," *Sci. Res. Essay*, vol. 2, no. 5, pp. 163–166, 2007.

[6] D. Pradhan, K. a Suri, D. K. Pradhan, and P. Biswasroy, "Golden Heart of the Nature: Piper betle L.," *J. Pharmacogn. Phytochem.*, vol. 1, no. 6, pp. 147–167, 2013.

[7] P. Guha, "Betel Leaf: The Neglected Green Gold of India," *J. Hum. Ecol.*, vol. 19, no. 2, pp. 87–93, 2006.

[8] L. Arambewela, K. G. a Kumaratunga, and K. Dias, "Studies on Piper betle of Sri Lanka," *J. Natl. Sci. Found. Sri Lanka*, vol. 33, no. 2, pp. 133–139, 2005.

[9] S. Sripradha, "Betel Leaf - The Green Gold," *J. Pharm. Sci. Res.*, vol. 6, no. 1, pp. 36–37, 2014.

[10] S. Sharma, I. A. Khan, I. Ali, F. Ali, M. Kumar, A. Kumar, R. K. Johri, S. T. Abdullah, S. Bani, A. Pandey, K. A. Suri, B. D. Gupta, N. K. Satti, P. Dutt, and G. N. Qazi, "Evaluation of the antimicrobial, antioxidant, and anti-inflammatory activities of hydroxychavicol for its potential use as an oral care agent," *Antimicrob. Agents Chemother.*, vol. 53, no. 1, pp. 216–222, 2009.

[11] P. Srimani, G. Mandal, S. Ganguly, P. Sana, R. Sen, R. De, A. Chatterjee, M. Bhattacharyya, U. Chaudhuri, S. K. Bandyopadhyay, and M. Chatterjee, "Antioxidant effect of ethanolic extract of Piper betle Linn. (paan) on erythrocytes from patients with HbE-beta thalassemia," *Indian J. Biochem. Biophys.*, vol. 46, no. 3, pp. 241–246, 2009.

[12] B. Majumdar, S. G. Ray Chaudhuri, A. Ray, and S. K. Bandyopadhyay, "Effect of ethanol extract of Piper betle Linn leaf on healing of NSAID-induced experimental ulcer--a novel role of free radical scavenging action.," *Indian J. Exp. Biol.*, vol. 41, no. 4, pp. 311–315, 2003.

[13] N. Dasgupta and B. De, "Antioxidant activity of Piper betle L. leaf extract in vitro," *Food Chem.*, vol. 88, no. 2, pp. 219–224, 2004.

[14] L. S. R. Arambewela, L. D. a M. Arawwawala, and W. D. Ratnasooriya, "Antidiabetic activities of aqueous and ethanolic extracts of Piper betle leaves in rats," *J. Ethnopharmacol.*, vol. 102, no. 2, pp. 239–245, 2005.

[15] A. J. Amonkar, M. Nagabhushan, A. V. D'Souza, and S. V Bhide, "Hydroxychavicol: A New Phenolic Antimutagen From Betel Leaf," *Food Chem. Toxic*, vol. 24, no. 12, pp. 1321–1324, 1986.

[16] P. M. Ranjan, M. Manjushree, M. Sabita, and S. Samira, "Antifertility Effect of Alcoholic Extract of Piper betle Linn on Female Albino Rats," *Int. Res. J. Pharm.*, vol. 4, no. 1, pp. 218–220, 2013.

[17] M. Saxena, J. Saxena, R. Nema, D. Singh, and A. Gupta, "Phytochemistry of Medicinal Plants," *J. Pharmacogn. Phytochem.*, vol. 1, no. 6, pp. 168–182, 2013.

[18] M. S. Baliga, F. Fazal, M. Rashmi Priya, V. S. Ratnu, and M. P. Rai, *Betel leaf (Piper betel Linn): The wrongly maligned medicinal and recreational plant possesses potent gastrointestinal and hepatoprotective effects*, 1st ed. Elsevier Inc., 2013.

[19] K. Y. Pin, A. L. Chuah, A. A. Rashih, M. P. Mazura, J. Fadzureena, S. Vimala,

and M. a. Rasadah, “Antioxidant and anti-inflammatory activities of extracts of betel leaves (Piper betle) from solvents with different polarities,” *J. Trop. For. Sci.*, vol. 22, no. 4, pp. 448–455, 2010.

[20] N. Kumar, P. Misra, A. Dube, S. Bhattacharya, M. Dikshit, and S. Ranade, “Piper betle Linn. A maligned pan-asiatic plant with an array of pharmacological activities and prospects for drug discovery,” *Curr. Sci.*, vol. 99, no. 7, pp. 922–932, 2010.

[21] T. Nalina and Z. H. a Rahim, “The crude aqueous extract of Piper betle L. and its antibacterial effect towards Streptococcus mutans,” *Am. J. Biochem. Biotechnol.*, vol. 3, no. 1, pp. 10–15, 2007.

[22] P. Chakraborty, S. Kumar, D. Dutta, and V. Gupta, “Role of Antioxidants in Common Health Diseases,” *Res. J. Pharm. Technol.*, vol. 2, no. 2, pp. 238–244, 2009.

[23] L. Nouri, A. Mohammadi Nafchi, and A. A. Karim, “Phytochemical, antioxidant, antibacterial, and α-amylase inhibitory properties of different extracts from betel leaves,” *Ind. Crops Prod.*, vol. 62, pp. 47–52, 2014.

[24] T. Dhanani, S. Shah, N. a. Gajbhiye, and S. Kumar, “Effect of extraction methods on yield, phytochemical constituents and antioxidant activity of Withania somnifera,” *Arab. J. Chem.*, 2013.

[25] Y. Q. Ma, J. C. Chen, D. H. Liu, and X. Q. Ye, “Simultaneous extraction of phenolic compounds of citrus peel extracts: Effect of ultrasound,” *Ultrason. Sonochem.*, vol. 16, no. 1, pp. 57–62, 2009.

[26] R. Hendryani, M. Lutfi, and L. C. Hawa, “Antioxidant Extraction from Dried Red Betel Leaf (Piper crotatum) using Ultrasonic Assisted Extraction as Pre-Treatment (Study Comparative of Solvent and Extraction Time),” *J. Bioprocess Commod. Trop.*, vol. 3, no. 2, pp. 33–38, 2015.

[27] B. K. Tiwari, N. P. Brunton, and C. S. Brennan, “Stability of phytochemicals during storage,” in *Handbook of Plant Food Phytochemicals: Sources, Stability and Extraction*, 2013.

[28] P. Górnaś, E. Šnē, A. Siger, and D. Segliņa, “Sea buckthorn (Hippophae rhamnoides L.) leaves as valuable source of lipophilic antioxidants: The effect of harvest time, sex, drying and extraction methods,” *Ind. Crops Prod.*, vol. 60, pp. 1–7, 2014.

[29] K. Y. Pin, T. G. Chuah, a. A. Rashih, C. L. Law, M. a. Rasadah, and T. S. Y. Choong, "Drying of Betel Leaves (Piper betle L.): Quality and Drying Kinetics," *Dry. Technol.*, vol. 27, no. 1, pp. 149–155, 2009.

[30] K. Y. Pin, T. G. Chuah, T. S. Y. Choong, a A. Rashih, M. a Rasadah, and C. L. Law, "Modelling of Extraction Kinetics of Hydroxychavicol From Betel (Piper Betle L .) Leaves," in *Proceedings of the 1st International Conference on Natural Resources Engineering & Technology*, 2006, no. July, pp. 146–152.

[31] D. Pradhan, P. Biswasroy, and K. A. Suri, "Variation in the percentage content of hydroxychavicol in different extracts of Piper betle L. by altering the extraction parameters," *Int. J. Adv. Sci. Tech. Res.*, vol. 2, no. 4, pp. 517–530, 2014.

[32] S. Feng, Z. Luo, B. Tao, and C. Chen, "Ultrasonic-assisted extraction and purification of phenolic compounds from sugarcane (Saccharum officinarum L.) rinds," *LWT - Food Sci. Technol.*, pp. 1–7, 2014.

[33] N. Singtongratana, S. Vadhanasin, and J. Singkhonrat, "Hydroxychavicol and eugenol profiling of betel leaves from Piper betle L. obtained by liquid-liquid extraction and supercritical fluid extraction," *Kasetsart J. - Nat. Sci.*, vol. 47, no. 4, pp. 614–623, 2013.

[34] M. B. Medina, "Determination of the total phenolics in juices and superfruits by a novel chemical method," *J. Funct. Foods*, vol. 3, no. 2, pp. 79–87, 2011.

[35] G. E. Lester, K. S. Lewers, M. B. Medina, and R. a. Saftner, "Comparative analysis of strawberry total phenolics via Fast Blue BB vs. Folin–Ciocalteu: Assay interference by ascorbic acid," *J. Food Compos. Anal.*, vol. 27, no. 1, pp. 102–107, 2012.

[36] A. Bampouli, K. Kyriakopoulou, G. Papaefstathiou, V. Louli, M. Krokida, and K. Magoulas, "Comparison of different extraction methods of Pistacia lentiscus var. chia leaves: Yield, antioxidant activity and essential oil chemical composition," *J. Appl. Res. Med. Aromat. Plants*, vol. 1, no. 3, pp. 81–91, 2014.

[37] H. Li, L. Pordesimo, and J. Weiss, "High intensity ultrasound-assisted extraction of oil from soybeans," *Food Res. Int.*, vol. 37, no. 7, pp. 731–738, 2004.

[38] E. M. Agency, "Reflection paper on the use of recovered / recycled solvents in the manufacture of herbal preparations for use in herbal medicinal products / traditional herbal medicinal products," 2013.

[39] T. Jerman, P. Trebše, and B. Mozetič Vodopivec, "Ultrasound-assisted solid liquid extraction (USLE) of olive fruit (Olea europaea) phenolic compounds," *Food Chem.*, vol. 123, no. 1, pp. 175–182, 2010.

[40] B. Nayak, F. Dahmoune, K. Moussi, H. Remini, S. Dairi, O. Aoun, and M. Khodir, "Comparison of microwave, ultrasound and accelerated-assisted solvent extraction for recovery of polyphenols from Citrus sinensis peels," *Food Chem.*, vol. 187, pp. 507–516, 2015.

[41] V. Upadhya, S. R. Pai, and H. V. Hegde, "Effect of method and time of extraction on total phenolic content in comparison with antioxidant activities in different parts of Achyranthes aspera," *J. King Saud Univ. - Sci.*, vol. 27, no. 3, pp. 204–208, 2015.

[42] W. Routray and V. Orsat, "MAE of phenolic compounds from blueberry leaves and comparison with other extraction methods," *Ind. Crops Prod.*, vol. 58, pp. 36–45, 2014.

[43] A. Roidaki, P. Zoumpoulakis, and C. Proestos, "Comparison of Extraction Methods for the Determination of Antioxidant Activity in Extracts of Hippophae Rhamnoides L . and Lippia Citriodora. The Effect of Seasonal Collection," *Austin J. Nutr. Food Sci.*, vol. 3, no. 1, pp. 1–8, 2015.

[44] M. Tosun, S. Ercisli, M. Sengul, H. Ozer, T. Polat, and E. Ozturk, "Antioxidant properties and total phenolic content of eight Salvia species from Turkey," *Biol. Res.*, vol. 42, pp. 175–181, 2009.

[45] M. S. Stanković, "Total Phenolic Content , Flavonoid Concentration and Antioxidant Activity of Marrubium peregrinum L . Extracts," *Kragujev. J. Sci.*, vol. 33, pp. 63–72, 2011.

[46] G. Clarke, K. Ting, C. Wiart, and J. Fry, "High Correlation of 2,2-diphenyl-1-picrylhydrazyl (DPPH) Radical Scavenging, Ferric Reducing Activity Potential and Total Phenolics Content Indicates Redundancy in Use of All Three Assays to Screen for Antioxidant Activity of Extracts of Plants from the M," *Antioxidants*, vol. 2, pp. 1–10, 2013.

[47] M. Amzad Hossain and M. D. Shah, "A study on the total phenols content and antioxidant activity of essential oil and different solvent extracts of endemic plant Merremia borneensis," *Arab. J. Chem.*, vol. 8, no. 1, pp. 66–71, 2015.

[48] V. Katalinic, M. Milos, T. Kulisic, and M. Jukic, "Screening of 70 medicinal plant extracts for antioxidant capacity and total phenols," *Food Chem.*, vol. 94, no. 4, pp. 550–557, 2006.

[49] R. Borneo, a. E. León, A. Aguirre, P. Ribotta, and J. J. Cantero, "Antioxidant capacity of medicinal plants from the Province of Córdoba (Argentina) and their in vitro testing in a model food system," *Food Chem.*, vol. 112, no. 3, pp. 664–670, 2009.

[50] S. Dudonne, X. Vitrac, P. Coutiere, M. Woillez, and J.-M. Merillon, "Comparative Study of Antioxidant Properties and Total Phenolic Content of 30 Plant Extracts of Industrial Interest Comparative Study of Antioxidant Properties and Total Phenolic Content of 30 Plant Extracts of Industrial Interest Using DPPH , ABTS , FRAP," *J. Agric. Food Chem.*, vol. 57, pp. 1768–1774, 2009.

[51] V. Kothari, A. Gupta, and M. Naraniwal, "Comparative study of various methods for extraction of antioxidant and antibacterial compounds from plant seeds," *J. Nat. Remedies*, vol. 12, no. 2, pp. 162–173, 2012.

Characterisation of DES Based CNT Nanofluid

A.H. Mariam[1*], W. Rashmi[1], Y.C. Yan[1], K. Shahbaz[2], M. Khalid[3]

[1]*Energy Research Group, Department of Chemical Engineering, School of Engineering, Taylor's University, No. 1 Jalan Taylors, Subang Jaya, Malaysia*

[2]*University of Auckland, Auckland 1010, New Zealand*

[3]*Manufacturing and Industrial Process Division, University of Nottingham Malaysia Campus, 43500 Semenyih, Selangor, Malaysia*

[*]Corresponding Author *mariam_hafeez@hotmail.com*

Abstract

Commercial coolants used in many of the industrial cooling applications such as water and ethylene glycol possess very low thermal conductivity and therefore a need to develop efficient heat transfer fluid arises to improve the cooling. Due to advancement in nanotechnology, stable nanofluids are developed by dispersing high thermal conductivity nanoparticles in base fluid which shows its potential to replace conventional coolants. In this research Deep Eutectic Solvents (DESs) are introduced as an alternative to the commonly used base fluids due to their unique solvent properties such as high thermal stability, biodegradability and non-flammability. Different molar ratios (1:3-1:5) of salt (choline chloride) and HBD (triethylene glycol) were mixed and heated at 90-120 ℃ until a clear solution of DES was obtained. MWCNTs with different concentrations (0.01-0.08 wt %) were dispersed into DES without the addition of surfactant and homogenized for 4 hours using ultrasonic bath. Stability study was then carried out through visual observation and UV-vis spectrophotometer for 22 days. Resulting nanofluids were characterised using optical microscopy to study dispersion and effect of temperature on suspensions was also investigated. The results showed that DES was unable to stabilise CNT suspensions as it was not able to overcome strong Van der Waals force between nanoparticles. Through visual observation sedimentation of CNT was observed starting day 5 whereas UV-Vis showed decline in CNT concentration with respect to time. However, the clusters formed were of uniform size distribution observed on day 1 and day 11. It was also found that at 25 ℃ CNT suspensions are uniform whereas at 40 ℃ loose bundles of CNT are formed due to change in interaction between CNTs and base fluid. Brownian motion of particles would have further increased the entanglement of CNTs at higher temperature. Clusters formed were loose and slight shake could easily re-disperse the nanoparticles into base fluid.

Keywords: nanofluids, deep eutectic solvents, carbon nanotubes, nanofluid stability.

1. Introduction

Heat transfer plays an important role in many industries and processes such as automobiles, aerospace, chemical processes, energy systems, electronic chip cooling, air conditioning, refrigeration, heat pumps, and many more [1]. Heat transfer fluids which are also known as coolants are used to remove heat from the systems. Water is commonly used coolants but it has drawback as it freezes or boils at extreme temperatures. However, commercially available coolants contain a mixture of water and ethylene glycol (EG) because adding EG, commonly known as anti-freeze decreases the freezing point and increases the boiling point of water (base fluid). Using EG in heat transfer fluid broadens its operating range on both ends of the temperature scale [2]. In countries with extreme climate conditions mixture of water and EG is used in car radiator which prevents the coolant from freezing when it is cold and evaporating when it is hot. Recently, mixtures of 50:50 ratios of water and EG are used for better performance but they possess low thermal conductivity. Therefore a need for new efficient heat transfer fluid arises to improve the cooling of the systems.

The base fluid is an important factor in heat transfer enhancement. The commonly used base fluids are water, engine oil and EG which have very low thermal conductivity compared to solid materials. Recently ionic liquids (ILs) have become dominant replacements for commonly used base fluids. IL is a salt with poorly coordinated ions resulting in a solvent with a melting point below 100 ℃. Typically they are composed of organic nitrogen containing heterocyclic cations and inorganic anions [3]. Some of its characteristics which have drawn attention of researchers from various fields are high thermal stability, high ionic conductivity, low vapour pressure and wide temperature range for liquid phase [4]. However despite of various attractive features, the application of ILs has been less favourable due to high cost and difficulty to synthesise which includes expensive raw materials and long preparation and purification procedures [5].

New green solvents known as deep eutectic solvents (DES) are alternatives to ionic solvents. They are made by mixing salts and hydrogen bond donors (HBD) such as amine, alcohol and acid which are able to produce a eutectic mixture [6]. DESs possess similar physical and chemical properties to ILs but have low cost, are biodegradable, non-toxic and easy to synthesise [7]. Because of these conditions DES are able to replace traditional solvents and ILs. Some of its applications include in extraction and synthesis in chemical processing and medium for metal deposition.

Liu *et al* [8] found that nanofluids have potential for effective heat transfer applications [8]. Thus, conventional coolants can be replaced by nanofluids for cooling. Nanometre sized particles in the range of 1-100 nm called nanoparticles are dispersed in the base fluid to form stable nanofluid which was first termed by Choi in 1995 [9] at Agronne National Laboratory, USA. Based on the type material of nanoparticles can be categorized into three types namely metallic (Al, Ag, Au, Cu), metal oxides (Al_2O_3, TiO_2, CuO) and carbon based (carbon nanotubes, fullerenes, graphene etc) which have distinguishable particle shapes such as spherical, cylindrical and sheet-like. Recent investigations highlight that suspending the nanoparticles in heat transfer liquids enhances the thermal conductivity of the fluid and hence the heat transfer performance of the system is drastically improved. The thermal conductivity

of conventional base fluid such as water and EG is below 1 W/m.K whereas as seen in Table 1 the thermal conductivity of solid particles is very high compared to the base fluid. Hence addition of solid particles to base fluid can enhance the thermal conductivity of the fluid.

Table 1. Thermal Conductivity of Solid Particles and Base Fluid at 27 ℃

	Material	Thermal Conductivity (W/m.K)	Reference
Metallic	Aluminium	237	[10]
	Silver	429	[9]
	Gold	318	[11]
	Copper	401	[9]
Non-metallic	Aluminium oxide	40	[10]
	Copper oxide	76.5	[11]
	Carbon nanotubes (MWCNTs)	3000	[10]
Base fluid	Water	0.613	[11]
	Engine oil	0.145	[11]
	Ethylene glycol	0.253	[11]

From Table 1 it can be observed that CNTs have high thermal conductivity compared to metal or metal oxide nanomaterials hence its addition to base fluid will increase the thermal conductivity of the nanofluid. Due to its high thermal properties CNTs have potential applications in fields such as refrigeration, automotive and aerospace. Murshed and Nieto De Castro [10] reviewed literature data and reported that the thermal conductivity of CNT-nanofluids enhances with increase in CNT concentration and increases higher with temperatures that make an attractive feature as these nanofluids can be used at higher temperatures.

However the dispersion and stability of CNTs in base fluid is a challenge as they have the tendency to agglomerate due to high Van der Waals force and strong affinity between the CNT particles [12]. Agglomerations of CNTs can cause clogging in the pipes and micro-channels as well as increase the sedimentation rate which decreases the thermo-physical properties such as thermal conductivity and viscosity [13]. There are various methods found in literature to disperse and stabilise nanoparticles which includes surface modification, surface coating and sonication. In surface modification also called functionalisation, nanoparticles are oxidized using acid to attach hydroxyl (OH), carboxylic (COOH) or amine (NH_2) functional group to the surface through covalent bond [12]. Functionalizing nanoparticles increases the interaction between nanoparticles and based fluid. However, due to high temperature and acidic conditions during functionalisation nanoparticles structures are often damaged [14]. Powerful sonication can damage and shorten the nanoparticles which in turn will decrease their mechanical properties [15]. Surface coating is the addition of surfactant or dispersant which stabilises the nanofluid by forming a protective layer around nanoparticles and acting as a barrier between them preventing agglomeration. The drawback of adding surfactant is that it decomposes at high temperature and is not suitable for high temperature applications. On the other hand ILs with special ionic structures has the ability to stabilise various nanoparticles without addition of

surfactant [16,17]. ILs and DES have been used as electrolyte, solvents for nanomaterials synthesis, exfoliation, and dispersants [18]. As DES has advantages over ILs and it possesses similar physical and chemical properties it has a potential to be used in nanotechnology for various applications. The literature available for use of DES as dispersant is limited compared to ILs.

From literature it is found that no research work has been carried out on dispersing CNT into DES (ChCl and TEG) base fluid to form nanofluid as a heat transfer fluid which drives the motivation to perform this research. Studies have shown that nanofluids which are made by dispersing nanoparticles in base fluid have high thermal properties compared to base fluids without particles. CNTs have high thermal conductivity compared to metal or metal oxide nanomaterials hence its addition to base fluid will increase the thermal conductivity of the nanofluid. Moreover, it is found that DES compared to IL is an environmental friendly and cheap alternative to base fluids which has potential to form stable nanofluids by forming strong hydrogen bonds. DES is formed by mixing a salt and HBD which results in a eutectic mixture. The freezing point of DES is suppressed below the freezing point of individual components due to strong hydrogen interactions. TEG has higher boiling point compared to EG which shows it has a potential to be used in high temperature application. As no research work is done for DES based CNT nanofluid, the stability of the nanofluid is uncertain. To fill these gaps in literature, this research is carried to study the stability of DES based CNT nanofluid.

2. Methodology

2.1 Materials

For synthesis of DES, choline chloride ($C_5H_{14}ClNO$) and triethylene glycol ($C_6H_{14}O_4$) were purchased from Merck Sdn Bhd with high purity (>99%). MWCNTs with purity of ≥95% were purchased from Chinese Academy of Science, China. The MWCNT has an average length of 35 μm and outer diameter of 20 nm.

2.2 Synthesis of DES

In this research work choline chloride was used as a quaternary salt and trietheylene glycol as HBD to prepare DES. Synthesis was carried out by mixing different molar ratios of salt to HBD (1:3-1:5) based on research work done by Shahbaz *et al* [19]. Firstly, salt and HBD were weighed accurately according to molar ratios using electronic weigh balance (BEL Engineering MG164A, Italy) as the DES was prepared on mass basis. Then salt-HBD combinations were added into 100 ml Schott bottles respectively along with cylindrical magnetic stirrer bar which were then wrapped around the cap using Parafilm to prevent atmospheric moisture from entering as it can increase the water content in DES and also because DES is hygroscopic and will absorb water molecules from the atmosphere. Then the bottles containing salt-HBD were placed on a hot plate stirrer at 80 ℃ with approximate agitation of 300 rpm until a homogeneous clear liquid was obtained [5]. If the salt did not dissolve at 80 ℃ then the temperature was increased for 10 minutes not exceeding 120 ℃ to avoid decomposition of DES. Table 2 shows the combinations of salt:HBD used in this research to prepare DES and their abbreviations.

Table 2. Combinations and Abbreviation of Synthesised DES

Salt	HBD	Molar ratio (Salt:HBD)	Abbreviation
Choline Chloride	Triethylene Glycol	1:3	DES 1
		1:4	DES 2
		1:5	DES 3

2.3 Preparation of Nanofluid

CNT was measured using electronic weigh balance (BEL Engineering MG164A, Italy) with resolution of 0.0001g. Then it was added into scintillation vials with different synthesised DES to produce nanofluids with different concentration (in weight percentage) of 0.01, 0.04 and 0.08 wt%. This range is selected because CNT is expensive so concentration is maintained as low as possible. Also if the concentration is increased above 0.1 wt%, nanofluid will become too saturated and the viscosity will increase which is not desired in this research. After CNTs were added into DES, the suspensions underwent homogenization also known as sonication using Soltec Ultrasonic Bath (5300 EPS3, Italy) for 4 hours with frequency of 35 kHz [12]. Sonication was done to provide uniform and homogeneous colloids. Vibrations produce help break the clusters of particles hence prevent the agglomeration of CNT particles in the nanofluids. Samples were then allowed to be cooled because during homogenization process the temperature of the samples increases due to the vibration. Table 3 shows combinations and abbreviations for synthesised DES based CNT nanofluids.

Table 3. Compositions and Abbreviation of Synthesised DES Based CNT Nanofluids

DES	Abbreviation		
	CNT Concentration (wt%)		
	0.01	0.04	0.08
DES 1	1A	1B	1C
DES 2	2A	2B	2C
DES 3	3A	3B	3C

2.4 Stability Study

In stability study there were two types of analysis performed. Visual observation and microscopy is qualitative analysis whereas UV spectrophotometry is quantitative analysis. For stability study, nanofluids were stored at room temperature in a cabinet so they were not subjected to fluctuating temperature and light.

After sonication, the nanofluids were added into cuvettes and concentration of nanofluids was measured over a period of 22 days using UV-Vis Spectrometer (Perkin Elmer Lambda 35, USA). Blank samples consisted of base fluid without CNT which is pure DES so that when the absorbance value of nanofluid is measured, absorbance of base fluid is eliminated and is of CNT only. One nanofluid sample and its blank were used to identify the absorbance spectrum of CNT. A peak in the spectrum was obtained at wavelength of 382 nm which agrees with the literature [20]. A calibration curve of absorbance against concentration was plotted to obtain the concentration of CNT. The stability of the nanofluids was studied by measuring the

concentration of CNT over a period of days and observing if there is any decrease in concentration indicating sedimentation.

Simultaneously the nanofluids formed were left in scintillation vials for 22 days for visual observation with the aid of photograph capturing which was carried out to monitor the suspension of the particles and to check if there are sediments or agglomerates in the nanofluids [13].

For further characterisation, the dispersion of CNTs was studied using optical microscope (Swift Digital Microscope M10DB-MP, USA) at magnification of 4X for nanofluid samples on day 1 and day 22. This was done to examine change in size and dispersion of particles. Formation of clusters and non-uniform dispersion indicates an unstable nanofluid.

3. Results and Discussion

3.1 Stability Study

3.1.1 UV-Vis

The stability of DES based CNT nanofluids was studied for 22 days using UV-vis after the CNT was dispersed into DES and sonicated for 4 hours. Stable nanoparticles are dispersed uniformly in the nanofluid after sonication however if it is unstable, the nanoparticles start to sediment. Based on Fig. 1 the concentration of CNT in nanofluids decreases as days increase which indicates sedimentation of CNT is occurring in nanofluids. This is due to strong Van der Waals force between the CNT nanoparticles causing agglomeration and sedimentation. This also shows that ChCl and TEG based DES is unable to disperse CNT nanoparticles. In Fig. 1(a) the concentration of 1C increases for first 5 days and then decreases rapidly coming to a constant concentration. This is because in UV-vis, light is passed through the fluid at one point and in case of 1C the CNT is sedimenting at a slower rate so when the absorbance value is measured, the top layer sedimentation is at the point where light is passed through hence a higher CNT concentration is obtained. Due to high concentration of CNT, 1C sediments earlier than the other two nanofluids with lower CNT concentration. Similarly in Fig. 1(b) and (c) for all nanofluids with different CNT concentrations, a decline was seen in the CNT concentration which indicates an unstable nanofluid sedimented over a short period.

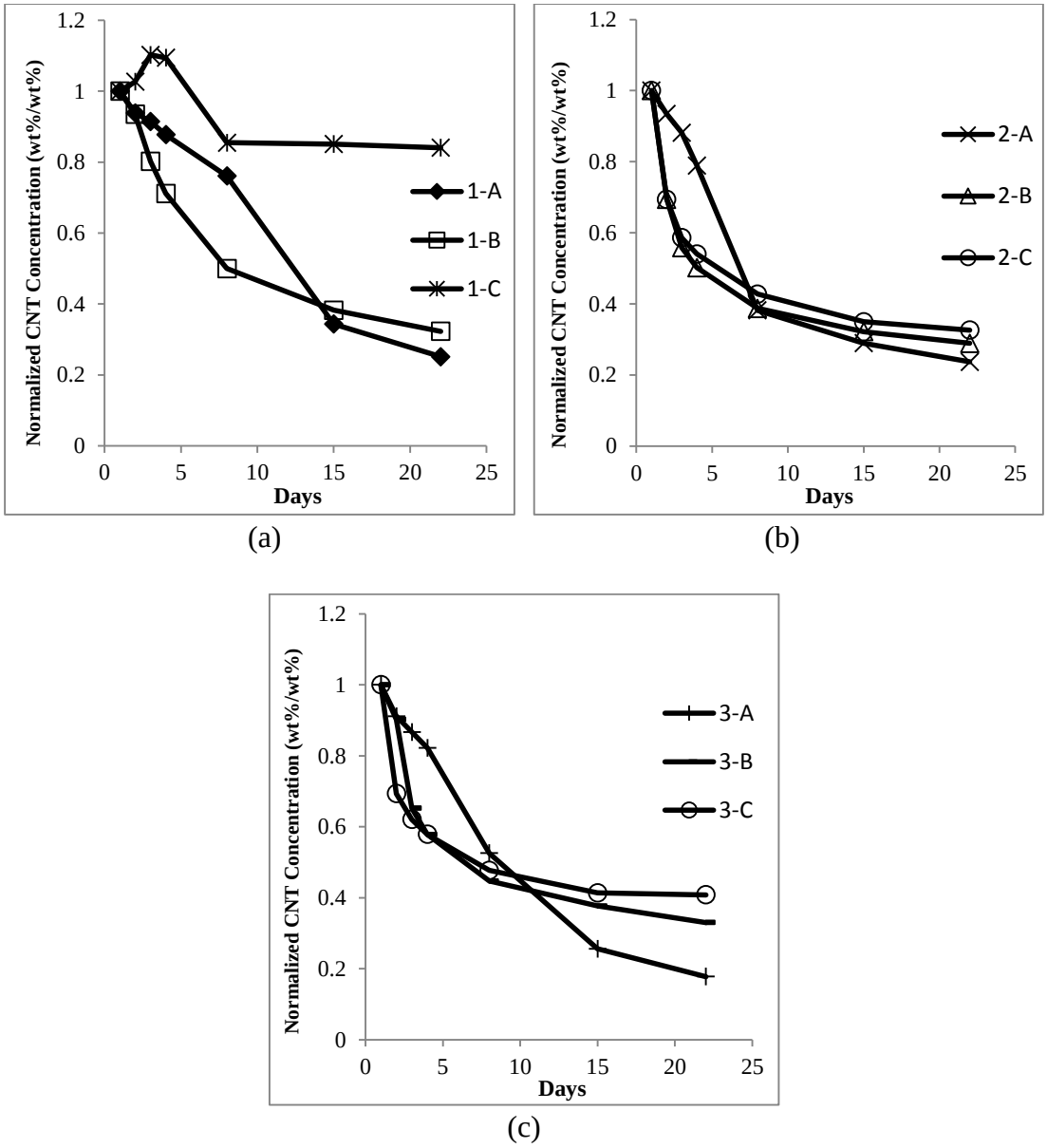


Figure 1. Stability of Nanofluids with Respect to Days

3.1.2 Visual Observation

Fig. 2 to Fig. 4 show visuals of nanofluids from day of sonication to 22 days later. In Fig. 1(a), Fig. 2(a) and Fig. 3(a) it can be seen that sonication is able to disperse CNT uniformly in DES as no sediments are observed. However as the days pass by, the nanofluids start to settle which is visible from visuals on day 5. This clearly indicates that the polarity of DES is not able to stabilize non-polar CNT hence sedimentation of suspensions occurs. Due to high Van der Waals force and high surface area, CNTs agglomerate to reduce surface energy [15] and the weight of the bundles increases which leads to faster sedimentation [12, 20]. Loose CNT bundles were formed in nanofluids which sedimented completely in 22 days as can be seen in Fig. 2(g), Fig. 3(g) and Fig. 4(g).

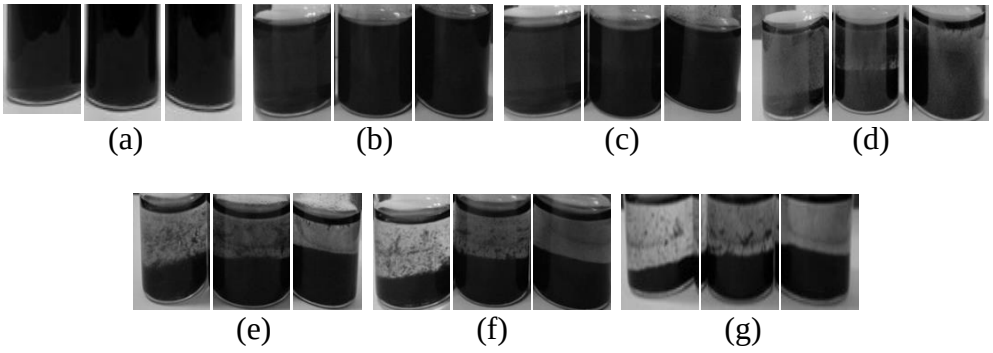


Figure 2. Visual Observation (from left to right) of 1A, 1B and 1C, (a) Day 0 (b) Day 1 (c) Day 3 (d) Day 5 (e) Day 8 (f) Day 15 (g) Day 22

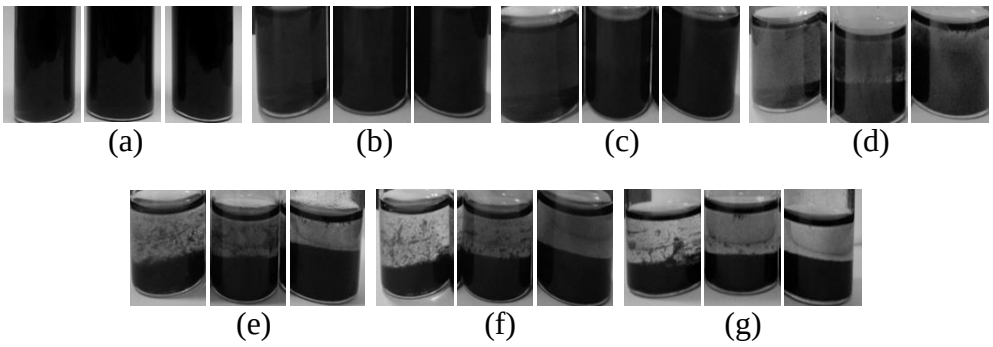


Figure 3. Visual Observation (from left to right) of 2A, 2B and 2C, (a) Day 0 (b) Day 1 (c) Day 3 (d) Day 5 (e) Day 8 (f) Day 15 (g) Day 22

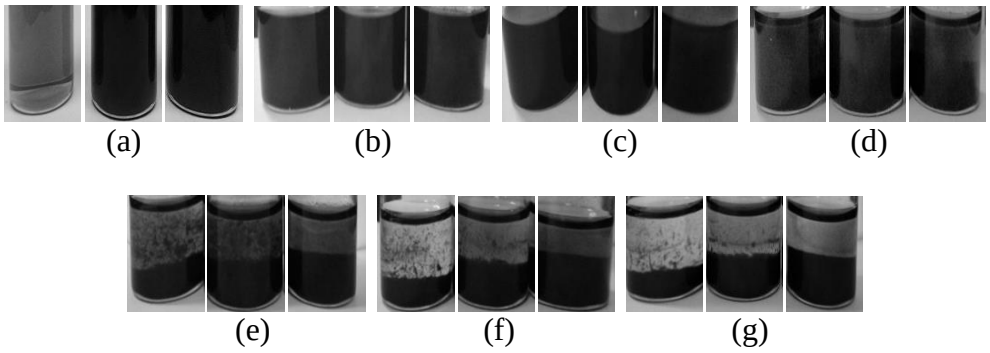
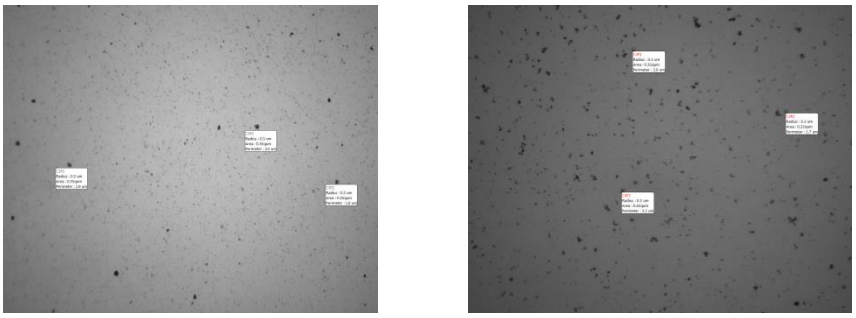


Figure 4. Visual Observation (from left to right) of 3A, 3B and 3C, (a) Day 0 (b) Day 1 (c) Day 3 (d) Day 5 (e) Day 8 (g) Day 15 (g) Day 22

3.1.3 Optical Microscopy

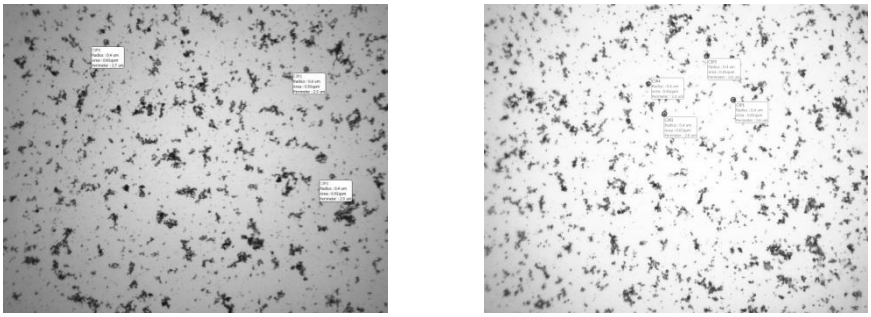
To study the CNT dispersions in nanofluids with different CNT concentrations, optical microscopy was used for a set of nanofluid (1A, 1B and 1C) on day 1 and then after 11 days to visualise the cluster size. Fig. 5(a) shows uniform dispersion of CNT with very few clusters measuring 0.3 μm whereas 11 days later the number of clusters increased due to strong Van der Waals force between nanoparticles but the size remained same as 0.3 μm. In Fig. 6(a) it can be seen that the number of clusters

formed in 1B is higher compared to 1A and the size of the clusters is 0.4 μm. This is because the concentration of CNT in 1B is higher than 1A and as the nanofluid is unstable CNTs will aggregate forming larger clusters. Fig.7 shows dispersion of 0.08wt% of CNT in DES 1 on day 1 and day 11. The size of the clusters formed in 1C is 0.5 μm which is larger than the clusters formed in 1A and 1C. As explained before, it is due to the high concentration of CNT and strong Van der Waals force between them which makes CNT prone to aggregation. The size of the clusters remained same after 11 days however the dispersion of clusters was not uniform as seen in Fig. 7(b).



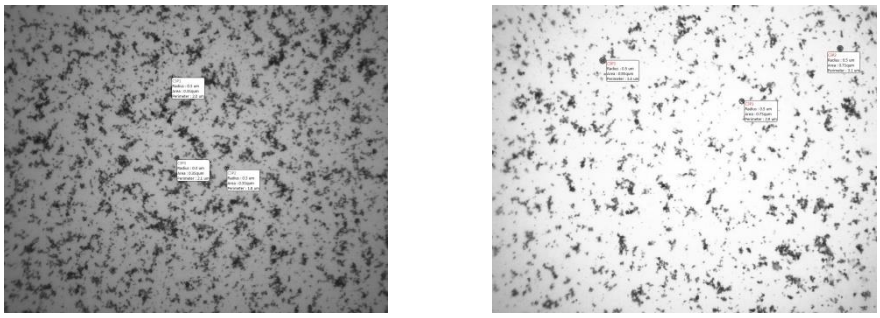
(a) (b)

Figure 5. Dispersion of 1A (a) Day 1 (b) Day 11



(a) (b)

Figure 6. Dispersion of 1B (a) Day 1 (b) Day 11

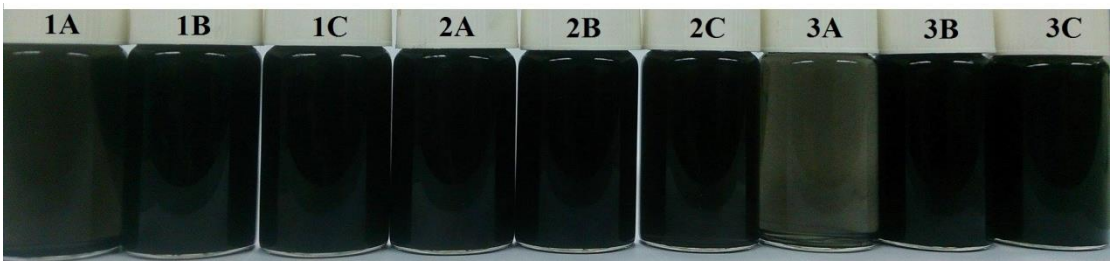


(a) (b)

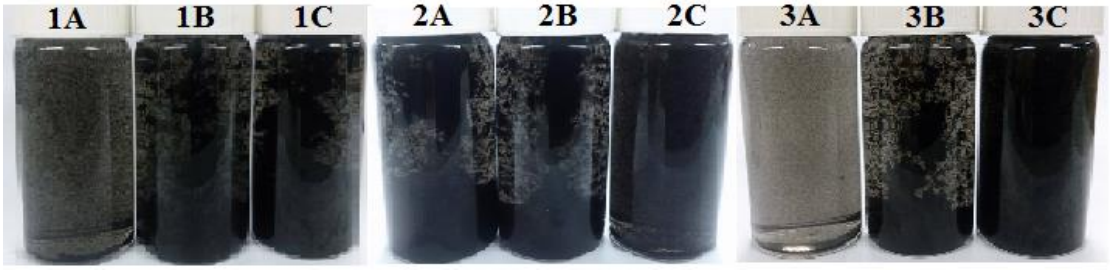
Figure 7. Dispersion of 1C (a) Day 1 (b) Day 11

3.1.4 Effect of Temperature

The effect of temperature on the dispersion of nanofluids was investigated at two different temperatures, 25 ℃ and 40 ℃. Visual inspection was done after placing the samples in waterbath for 1 hour. It was observed that CNT suspension is better at 25 ℃ as seen in Fig. 8(a). On the other hand, at higher temperature loose bundles of CNTs and faster sedimentation were observed as seen in Fig. 8(b). Similar observation was obtained by Dumee [15] who studied effect of temperature on CNT nanofluids. This indicates that temperature is a vital parameter in dispersion of nanofluids. Formation of bundles at higher temperature is due to change in interaction between CNT nanoparticles [15]. In addition, particles were observed to show movement at high temperature which increased contact between CNTs causing entanglement. At high temperature Brownian motion of the particles increases which leads to movement of particles in fluid resulting in increase in entanglement.



(a)



(b)

Figure 8. Effect of Temperature, (a) 25 ℃ (b) 40 ℃

4. Conclusions

In this study, stability of nanofluids with different CNT concentration dispersed in ChCl based DES with different salt and HBD combinations were studied using UV-vis, visual observation and optical microscopy. The results show that ChCl and TEG based DES is unable to overcome the strong attractive forces between CNT nanoparticles and stabilize CNT dispersions which lead to sedimentation in all prepared nanofluids in a short period. Also effect of temperature on nanofluid suspension was investigated at two different temperatures (25 ℃ and 40 ℃). It was found that at higher temperature loose bundles of CNT are formed due to change in CNT/CNT interaction and movements caused by Brownian motion of nanoparticles. This leads to entanglement of CNTs and hence agglomeration occurs. The findings from this research work can be used to further study on using DES with different salt as dispersant in CNT nanofluids. Also in future work, the effect of adding surfactant in ChCl based DES can be studied for CNT stabilisation and the enhancement of

thermal properties. Moreover CNT can be functionalised and dispersed in DES to perform stability study and measurement of thermo-physical properties. Lastly the effect of temperature higher than 40 ℃ can be used to inspect the effect on CNT bundles in DES nanofluid.

References

[1] V. Trisaksri and S. Wongwises, "*Critical review of heat transfer characteristics of nanofluids*," *Renew.* Sustain. Energy Rev., vol. 11, no. 3, pp. 512–523, 2007.

[2] S. M. Peyghambarzadeh, S. H. Hashemabadi, S. M. Hoseini, and M. Seifi Jamnani, "*Experimental study of heat transfer enhancement using water/ethylene glycol based nanofluids as a new coolant for car radiators*," Int. Commun. Heat Mass Transf., vol. 38, no. 9, pp. 1283–1290, 2011.

[3] A. A. Shamsuri and D. K. Abdullah, "*Ionic Liquds: Preparations and Limitations*," Makara Sains, vol. 14, no. 2, pp. 101–106, 2010.

[4] A. Matic and B. Scrosati, "*Ionic liquids for energy applications*," MRS Bull., vol. 38, no. 07, pp. 533–537, 2013.

[5] K. Shahbaz, F. S. Mjalli, M. A. Hashim, and I. M. AlNashef, "*Prediction of deep eutectic solvents densities at different temperatures*," Thermochim. Acta, vol. 515, no. 1–2, pp. 67–72, 2011.

[6] M. A. Kareem, F. S. Mjalli, M. A. Hashim, and I. M. AlNashef, "*Phosphonium-Based Ionic Liquids Analogues and Their Physical Properties*," J. Chem. Eng. Data, vol. 55, no. 11, pp. 4632–4637, 2010.

[7] Y. Dai, J. van Spronsen, G.-J. Witkamp, R. Verpoorte, and Y. H. Choi, "*Natural deep eutectic solvents as new potential media for green technology*," Anal. Chim. Acta, vol. 766, pp. 61–8, 2013.

[8] M.-S. Liu, M. C.-C. Lin, I.-T. Huang, and C.-C. Wang, "*Enhancement of Thermal Conductivity with CuO for Nanofluids*," Chem. Eng. Technol., vol. 29, no. 1, pp. 72–77, 2006.

[9] S. U. S. Choi and J. A. Eastman, "*Enhancing thermal conductivity of fluids with nanoparticles.*"

[10] S. M. S. Murshed and C. a. Nieto De Castro, "*Superior thermal features of carbon nanotubes-based nanofluids - A review*," Renew. Sustain. Energy Rev., vol. 37, pp. 155–167, 2014.

[11] Y. Li, J. Zhou, S. Tung, E. Schneider, and S. Xi, "*A review on development of nanofluid preparation and characterization*," Powder Technol., vol. 196, no. 2, pp. 89–101, 2009.

[12] W. Rashmi, A. F. Ismail, I. Sopyan, A. T. Jameel, F. Yusof, M. Khalid, and N. M. Mubarak, "*Stability and thermal conductivity enhancement of carbon*

nanotube nanofluid using gum arabic," J. Exp. Nanosci., vol. 6, no. 6, pp. 567–579, 2011.

[13] A. Ghadimi, R. Saidur, and H. S. C. Metselaar, "*A review of nanofluid stability properties and characterization in stationary conditions*," Int. J. Heat Mass Transf., vol. 54, no. 17–18, pp. 4051–4068, 2011.

[14] W. H. Chang, I. W. Cheong, S. E. Shim, and S. Choe, "*The dispersion stability of multi-walled carbon nanotubes in the presence of poly(styrene/α-methyl styrene/acrylic acid) random terpolyme*r," Macromol. Res., vol. 14, no. 5, pp. 545–551, 2006.

[15] L. F. Dumee, "*Carbon-nanotube-based membranes for water desalination by membrane distillation*," Victoria University, Melbourne, Australia, 2011.

[16] M. L. Polo-Luque, B. M. Simonet, and M. Valcárcel, "*Functionalization and dispersion of carbon nanotubes in ionic liquids*," TrAC Trends Anal. Chem., vol. 47, pp. 99–110, 2013.

[17] A. Wittmar and M. Ulbricht, "*Dispersions of Various Titania Nanoparticles in Two Different Ionic Liquids*," Ind. Eng. Chem. Res., vol. 51, no. 25, pp. 8425–8433, 2012.

[18] A. Abo-Hamad, M. Hayyan, M. A. AlSaadi, and M. A. Hashim, "*Potential applications of deep eutectic solvents in nanotechnology*," Chem. Eng. J., vol. 273, pp. 551–567, 2015.

[19] K. Shahbaz, F. S. Mjalli, M. a. Hashim, and I. M. Alnashef, "*Eutectic solvents for the removal of residual palm oil-based biodiesel catalyst*," Sep. Purif. Technol., vol. 81, no. 2, pp. 216–222, 2011.

[20] Y. Hwang, J. K. Lee, C. H. Lee, Y. M. Jung, S. I. Cheong, C. G. Lee, B. C. Ku, and S. P. Jang, "*Stability and thermal conductivity characteristics of nanofluids*," Thermochim. Acta, vol. 455, no. 1–2, pp. 70–74, 2007.

[21] M. Farbod, A. Ahangarpour, and S. G. Etemad, "*Stability and thermal conductivity of water-based carbon nanotube nanofluids*," Particuology, 2014.

Calculation of Blood Flow inside Human Arteries with Stent

Adrian K.W. Khoo [*], Thein Chung Ket[1]

[1]*Department of Mechanical Engineering, Taylor's School of Engineering*

[*]adriankhookahwei@gmail.com

Abstract

Atherosclerosis is a type of cardiovascular disease that stands as the principal cause of mortality where there is an accumulation of lipids and migration of inflammatory cells and vascular smooth muscle cells that form a thick layer of plaque. The treatment for atherosclerosis has been in favour of non-invasive methods since the introduction of stent insertion. Stenting treatment is being developed and improved because of the potential this technology possesses for shorter procedure times and cheaper cost through upgraded design or materials. One major factor that affects the formation of atherosclerosis plaque is the regions of low wall shear stress for blood. Recent studies have brought to light the issue of incomplete stent apposition and the significant role it plays in tandem with shear stress to cause atherosclerosis. This research focuses on investigating the relationship between the severity of incomplete stent apposition and the haemodynamic changes of blood flow in coronary arteries. The paper also discusses the significance of wall shear stress as an indicator for analysing arterial conditions which can lead to thrombosis or restenosis. SolidWorks will be used to model the fully defined stent and artery. The stent model is based on conventional designs that employ the balloon deployment method for insertion. The artery wall and stent struts are designed with rigid and no slip conditions. Computational fluid dynamic simulation will be used to visualize the blood flow through the artery with and without stent malapposition. The expected outcome of this paper will highlight the changes in shear stress due to incomplete stent apposition. Atherosclerosis plaque deposited in the arteries is predicted to disrupt blood flow which will allow for cases of late stent thrombosis or restenosis to occur after stent insertion. This paper presents a more accurate representation of shear stress in coronary arteries implanted with stent.

Keywords: Atherosclerosis, Coronary Stents, Stent malapposition, Wall shear stress, Computational Fluid Dynamics.

1. Introduction

The significance of technological advancement in treatments for atherosclerosis or formation of arterial plaque can be attributed to the increasing trend of coronary artery disease contraction [1]. In modern times, coronary stents have shown enormous progress in development which has seen the invention of drug-eluting stents (DES) that not only provide mechanical vascular support but also distributes medicine to artery at location of insertion for appropriate healing of the artery. The advantages of DES over the traditional bare metal stents (BMS) include shorter procedural times and a lower chance for restenosis to occur [2]. However, recent studies have begun to question the sustainability of DES with regards to the patient's health when late stent thrombosis and hypersensitivity reactions became increasingly common in patients with DES implantation [3]. The new generation of DES proved highly successful with low risk of long term adverse clinic effects [4].

Although stent implantation is now the leading treatment for atherosclerosis, newer studies have highlighted the detrimental effects of incomplete stent apposition (ISA), which can only be detected through intravascular ultrasound (IVUS) and optical coherence tomography due to the requirement of the ability to scan for high resolution cross-sectional images. It is important to take note that although it is difficult to tie ISA with late stent thrombosis, research finds that the risk of late stent thrombosis or very late stent thrombosis is significantly higher in the presence of ISA [5]. Foin et al. suggest that ISA causes a disturbance in blood flow due to increased shear stress [6].

Before this generation, in-depth research would not be possible without highly technologically advanced software such as computational fluid dynamics (CFD). CFD can be used to analyse the haemodynamic changes in human blood due to coronary stent implantation by relating the effects of wall shear stress (WSS) to ISA which inevitably is related to late stent thrombosis. The results could possibly be used for future reference during the engineering of a more optimized stent design.

Since the introduction of CFD, the analysis of coronary stents in blood have been mainly based on simplified models of stent. E. Poon et al. recently concluded numerical analysis of the effects of ISA on blood flow using a simplified stent model [7]. The study concludes that ISA bares an effect on the WSS despite employing a simplified model with WSS almost always being higher than the threshold along the artery, hence exposing patients to a higher risk of late stent thrombosis. Additional findings note that long distances between stent struts may cause chaotic flow to occur and thus leading to increased wall shear stress.

In this study, the haemodynamic changes are analysed with the presence of stent. The significance of ISA on the effects of haemodynamic change is investigated more thoroughly through the use of realistically designed stent model. This study will also determine if the severity of ISA is a significant factor to consider during analysis. This study will help expand our knowledge on the relationship between ISA and haemodynamic changes in order to assist with future development of more efficient solutions to ISA, thrombosis or stent restenosis by improving coronary stent insertion techniques or designs.

The research by Nakazawa et al. shows that arterial lesions accumulated more prevalently at regions with low rate of shear [8]. The shear stress negatively affects the

endothelial layer of the artery which in turn promotes lipoprotein uptake, up regulation of leukocyte adhesion molecules and leukocyte endothelial transmigration which altogether hastens atherosclerosis [8]. Wall shear stress has been proven to have substantial associations to stent restenosis due to excessive neointimal hyperplasia [9]. This study will investigate the effects of WSS on realistic stent designs in the presence of ISA.

2. Methodology

2.1 Realistic Stent Model in Idealised Coronary Artery

The geometry of the artery and stent are modelled as shown in Figure 1. The coronary artery has a fixed diameter of 3mm. In this study, a realistic stent model was designed based on test parameters for optimization [10].

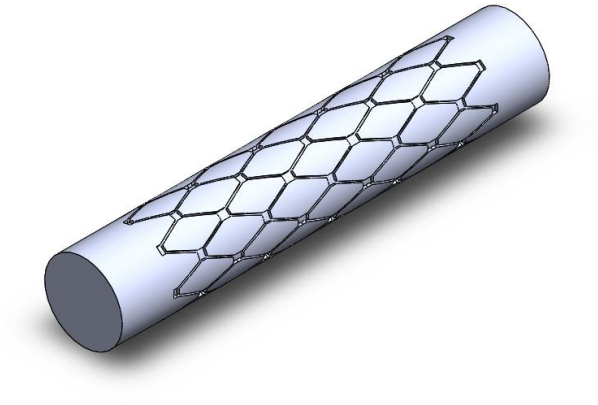


Figure 1. Geometry of artery with coronary stent modelled using SolidWorks.

The strut length, height and angle were calculated to give the optimal number of strut circumferential repetitions for a 3mm large artery. CFD simulates flow by analysing the geometry as a fluid zone. In tandem with this theory, the coronary stent pattern was debossed from the artery wall by $T = 0.1mm$, which is equal to the thickness of the stent as shown in Figure 2.

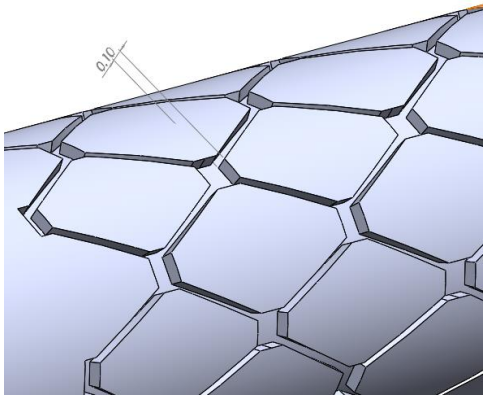


Figure 2. Dimension of the strut thickness is measured to be 0.1mm.

The mesh of the model was generated by ANSYS Workbench and initially contained 11 million tetrahedral cells as seen in Figure 3 and 4. The element quality (<,

aspect ratio and skewness of elements were checked to be well within the recommended levels. However a grid resolution study was carried out and determined that the amount of time needed to solve such a complex geometry is intangible and bore no significance to haemodynamic change.

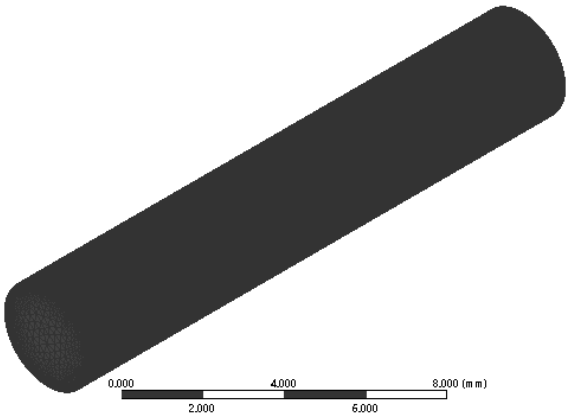


Figure 3. Mesh of the artery with coronary stent that contains 11million elements.

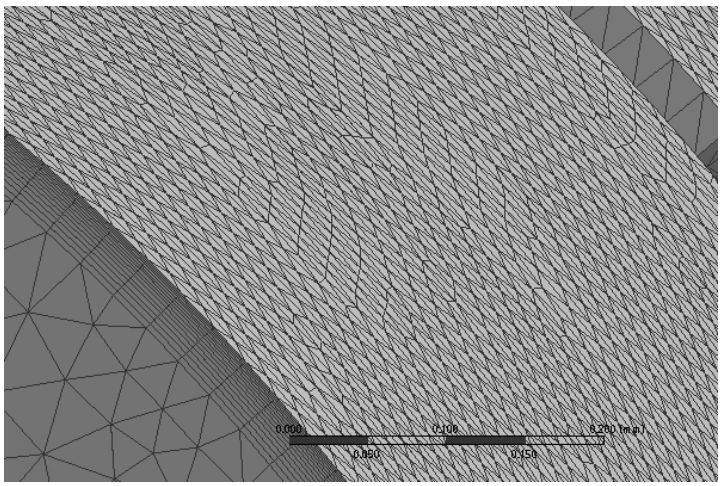


Figure 4. Enhanced view of the tetrahedral mesh for the geometry.

A simpler mesh was opted for that still satisfied the element quality conditions with skewness <0.97 and element quality $\cong 1$ as checked by ANSYS Meshing. Inflation was applied with first layer thickness of 0.001mm as boundary in order to have a clearer visualization of flow near the walls. Body sizing of 0.1mm was applied. The cross-section of the simpler mesh can be seen in Figure 5. The velocity profile used for inlet was based on the study of pulsatile waveform by M. Sinnot [11].

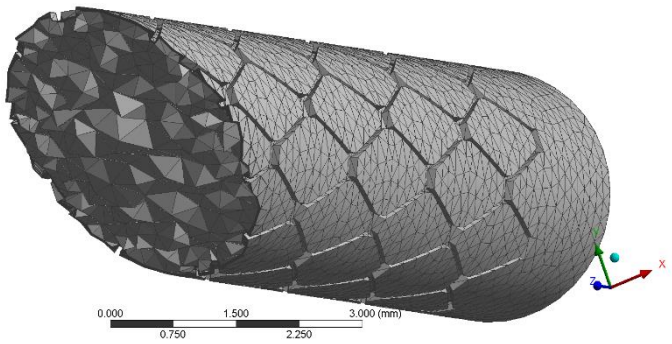


Figure 5. Cross-section cut of the simpler mesh for coronary artery with stent.

The velocity profile was programmed to simulate a patient undergoing diastole followed by systole blood flow. Diastolic blood flow was assumed to be 3.61 m/s, which is roughly 5 times the resting blood velocity reported by Nagel et al. [12]. Figure 6 shows the pulsatile waveform programmed and applied to the inlet of the model.

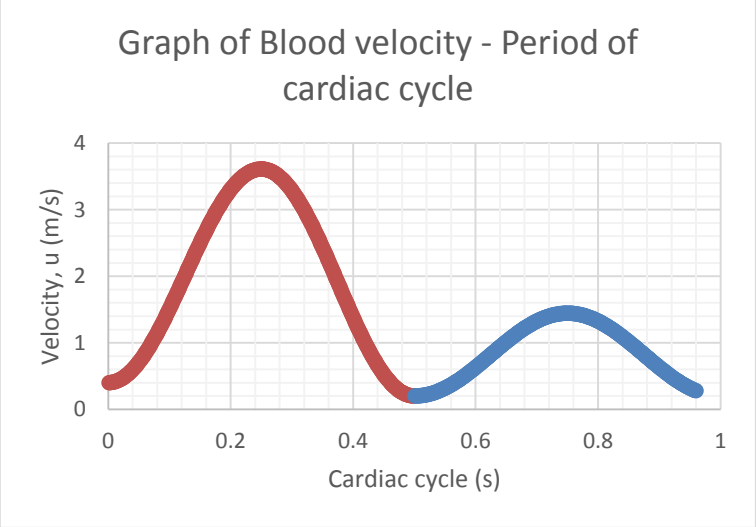


Figure 6. Pulsatile velocity profile for inlet boundary condition.

2.2 Computational Fluid Dynamics

The blood flow inside human arteries was analysed using the CFD software, ANSYS Fluent. The material properties of blood were set based on the assumption that blood is a Newtonian fluid. M. Siebert et al. states that the modelling of blood flow is complex due to the nature of blood at different shear rates. At shear rates less than $100s^{-1}$, blood behaves as a non-Newtonian fluid but behaves as Newtonian fluid when shear rates are above $100s^{-1}$ [13]. As Foin et. al demonstrates, the shear rate of blood exceeds its threshold in the presence of ISA [6]. Therefore, to simplify and standardise the calculations made for CFD, the entire study is carried out with the assumption that blood is Newtonian and flow is laminar. Carreau model is employed to define the viscosity of the fluid with values referenced from the research of M. Siebert et al. [13]

In real scenarios, arteries have hyperelastic properties that allow them to stretch and contract as pressure is applied to them. Simplification of the artery walls and stent

are done in this study by assuming that the artery wall is rigid and has a no slip condition. The blood flow is computed by Fluent through solving the Navier-Stokes equations. The solution was calculated using the PISO algorithm which is reliable for pressure-velocity calculations. The solution controls were manipulated with relaxation factors for pressure and momentum to be at 0.3 and 0.3 respectively. Lower relaxation factors allow a faster time for convergence of the results and the convergence criteria was reduced to 10^{-2} in order to sustain convergence for the complex simulation [14]. The time step size was set to 0.0015s with 540 time steps per cardiac cycle and 7 iterations per time step as 7 iterations were tested to have convergence during the first period of time steps.

3. Results

The CFD analysis is plotted instantaneously after 1 cardiac cycle using contours for WSS and vectors for velocity while comparing the residual and area-weighted shear stress graphs in order to identify convergence in the results. As the simulation of the flow is 3-dimensional, the views captured for analysis are isometric and right-side view. The velocity applied in this simulation is for blood flow under normal resting conditions.

3.1 Fully Expanded Coronary Stent

Figure 6 & 7 represents the WSS contours and velocity vectors respectively when the coronary stent is expanded to the artery wall and have no malapposition (MD = 0mm). The WSS contours maintain a consistent value along the radial direction. WSS decreases as it approaches the stent struts maintains a region of lower WSS within the stent struts.

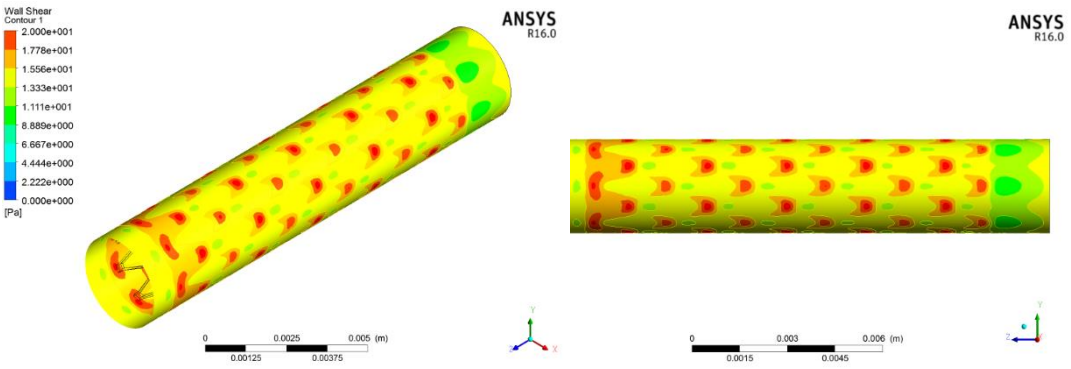


Figure 6. WSS Contours of artery wall with fully expanded stent. Shear stress increases again after the flow passes the stent region.

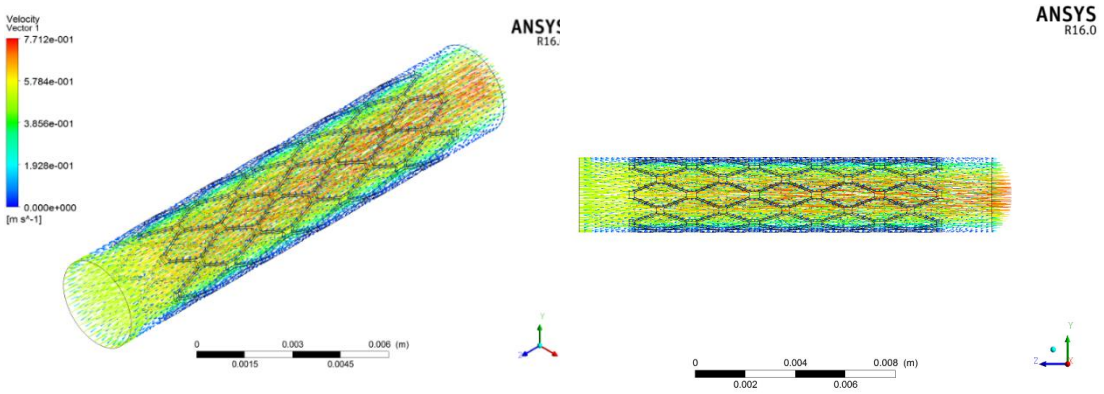


Figure 8. Velocity vector of the interior of the artery. Velocity is near zero at artery walls. Velocity is seen decreasing towards the struts and highest at center.

3.2 Incompletely Expanded Stent

The case of incompletely expanded stent is investigated. The 2 cases selected for study are when malapposition distances are 0.25mm and 0.5mm respectively. Assume that 0.25mm is a common value for ISA to occur while 0.5mm represents a severe case. As shown in Figure 9 & 10, the WSS contours of artery with stent malapposition of 0.25mm (MD = 0.25mm) is exhibits difference in shear stress distribution which can be observed as different trends.

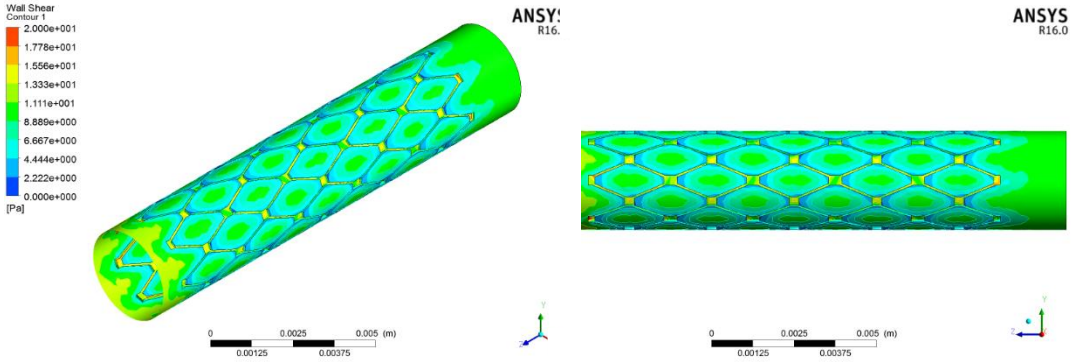


Figure 9. WSS Contours of artery wall with malapposed stent (MD = 0.25mm). Areas of high wall shear stress are located prominently around artery wall.

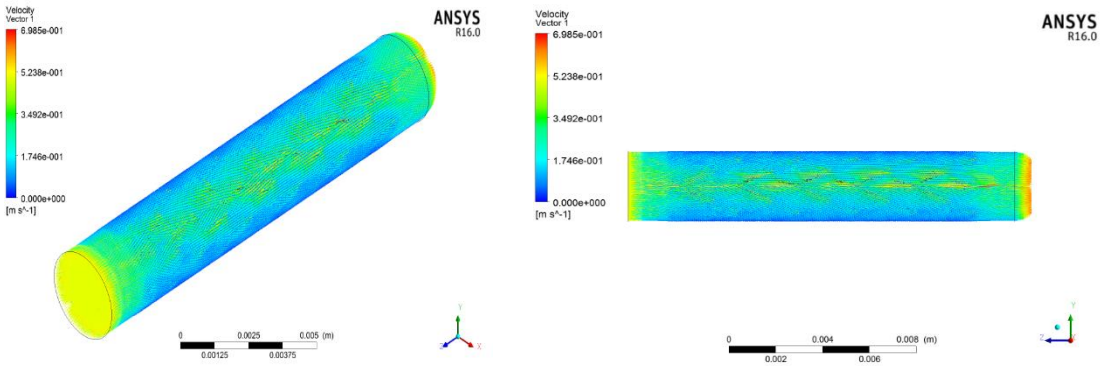


Figure 10. Velocity vector of the interior of the artery with malapposed stent (MD = 0.25mm).

The study of assumed large stent malapposition is carried out with a malapposition distance of 0.5mm (MD = 0.5mm) as seen in Figure 11 & 12. The artery wall contour shows evenly distributed wall shear stress throughout the surface and only decreases at the surface of the stent.

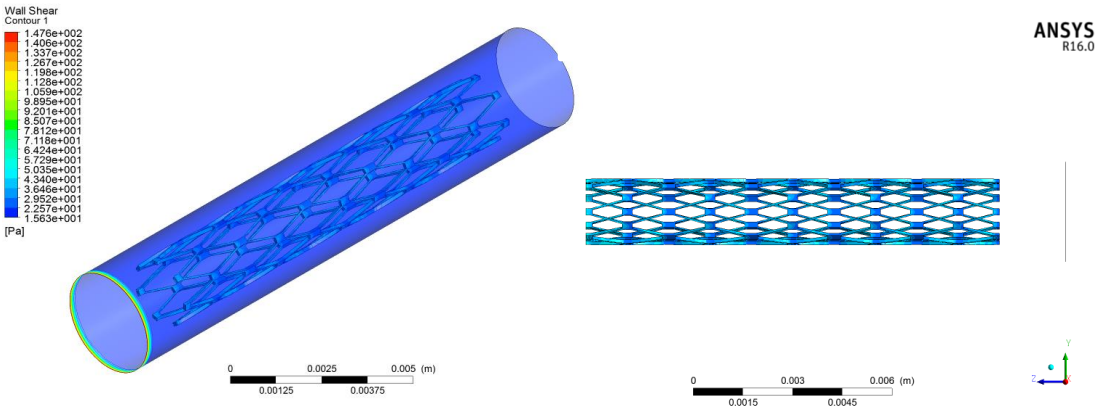


Figure 11. WSS Contour of artery wall with malapposed stent (MD = 0.5mm). Areas of WSS are seen around the stent but unclear around artery wall.

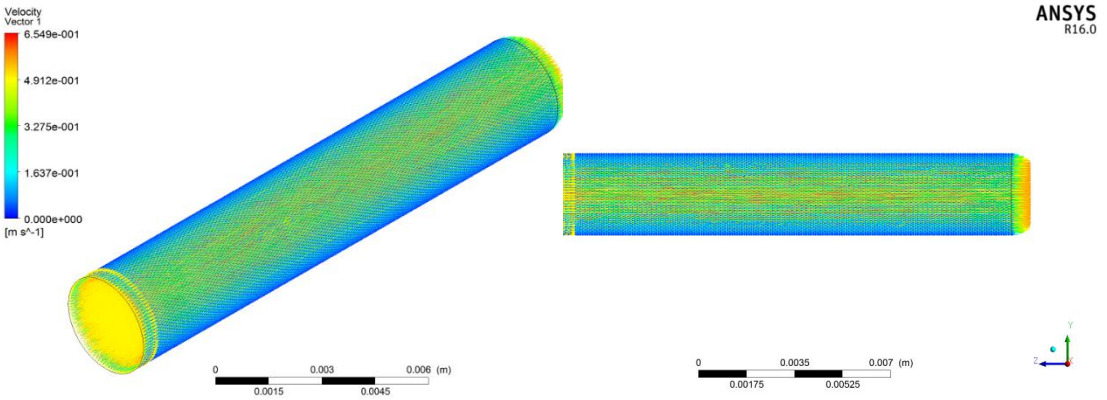


Figure 12. Velocity vector of the interior of the artery with malapposed stent (MD = 0.5mm)

By comparing the WSS in the graph as shown in Figure 13, there is a clear difference in the values of WSS for completely expanded and incompletely expanded stents. The stent when completely expanded shows a highest WSS of approximately 70 Pa with most of the distribution ranging around 10 Pa. However, the malapposed stent (MD = 0.25mm) shows a highest WSS of 100 Pa with plots of WSS distributed around 70 to 40 Pa as well while the other (MD = 0.5mm) has a highest WSS of 160 Pa. The overall WSS distribution of a stent with ISA is significantly greater than a fully expanded one.

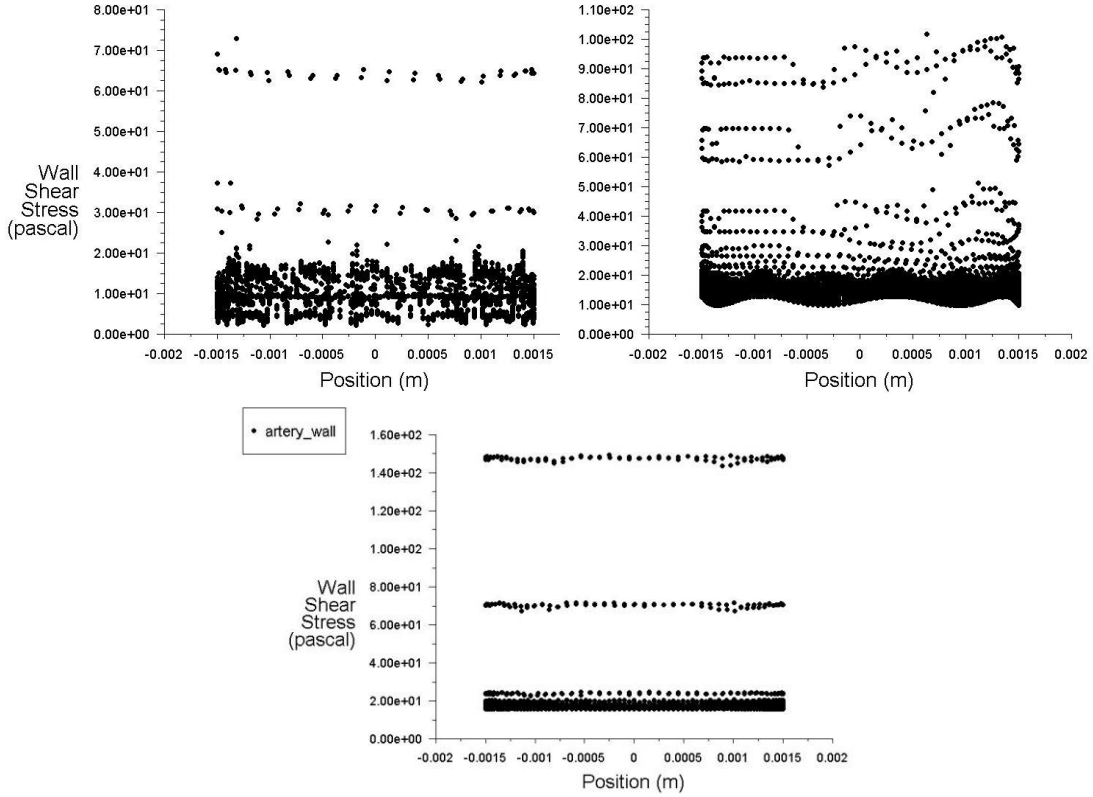


Figure 13. X-Y plot of WSS against Position in artery wall. [Left] WSS of fully expanded stent. [Right] WSS of malapposed stent. (MD = 0.25mm). [Bottom] WSS of malapposed stent. (MD = 0.50mm)

4. Conclusions

4.1 Discussion

By using CFD, a methodical approach can be taken to study the consequences of ISA to haemodynamics of human blood. Existing studies on computational analysis of realistic coronary stents are few as most researches simplify the stent struts to square or ring shapes. The basis and results of those studies provide the foundation for more attempts at in-depth analysis.

The flow of blood in human arteries display haemodynamic changes in the form of WSS stress and blood velocity. The distribution of WSS is constant throughout the radial axis. The overall values of wall shear stress increase with the presence of incomplete stent apposition and increases further along with ISA. Another trend that is worth taking note of is the decrease in maximum blood velocity with the increase of ISA. This information could prove useful for future computational analysis on realistic stent models.

4.2 Limitations and Recommendations

In this study, the velocity profile for inlet can be improved further by programming a pulsatile velocity for conditions of rest and during exercise. This could bring other realistic conditions into simulation to observe haemodynamic changes during those scenarios. It is also worth noting that the accuracy of results can be further improved through the use of the extremely high quality mesh at 11 million elements. The higher quality mesh will allow for convergence to occur quicker at a high convergence criterion, therefore allowing for a more accurate result. The further decrease in skewness and aspect ratio is also a case for study as the high quality mesh is undetermined to effect the results significantly or not. However, the limitations of time and computing power are constraints enough for this study.

Furthermore, the coronary artery was modelled as a rigid structure with ideal properties. The structural model of the artery was designed without curvature and hyperelastic properties which neglect the conditions of stenosis. The exemption of this criteria can be a major factor in WSS analysis as distensibility and the effects of intramyocardiac pressure are neglected [15]. In addition to that, the coronary stent model designed for research was only based on one commercial design. In the medical world, the design for coronary stents is constantly being optimised and future design may provide different results for this analysis. It is important that the results of this research is utilised for reference of more advanced future studies and interpreted with care.

Acknowledgment

The authors would like to acknowledge the support of the Faculty of Engineering, University of Melbourne for providing the title for this research.

References

[1] S. Mendis, P. Puska, and B. Norrving, “Global atlas on cardiovascular disease prevention and control,” *World Heal. Organ.*, pp. 2–14, 2011.

[2] G. Mani, M. D. Feldman, D. Patel, and C. M. Agrawal, “Coronary stents: A materials perspective,” *Biomaterials*, vol. 28, no. 9, pp. 1689–1710, 2007.

[3] B. O’Brien and W. Carroll, “The evolution of cardiovascular stent materials and surfaces in response to clinical drivers: A review,” *Acta Biomater.*, vol. 5, no. 4, pp. 945–958, 2009.

[4] C. Costopoulos, A. Latib, S. Ferrarello, T. Naganuma, A. Sticchi, F. Filippo, F. Giannini, S. Basavarajaiah, M. Kawaguchi, C. Naim, A. Candreva, M. Carlino, A. Chieffo, M. Montorfano, and A. Colombo, “First- versus second-generation drug-eluting stents for the treatment of coronary bifurcations,” *Cardiovasc. Revascularization Med.*, vol. 14, no. 6, pp. 311–315, 2013.

[5] G. F. Attizzani, D. Capodanno, Y. Ohno, and C. Tamburino, “Mechanisms, pathophysiology, and clinical aspects of incomplete stent apposition,” *J. Am. Coll. Cardiol.*, vol. 63, no. 14, pp. 1355–1367, 2014.

[6] N. Foin, J. L. Gutierrez Chico, S. Nakatani, R. Torii, R. Lee, S. Sen, R. Petraco, P. Wong, C. Di Mario, Y. Onuma, J. E. Davies, and P. W. Serruys, "TCTAP A-083 Incomplete Stent Apposition Causes High Shear Flow Disturbances and Delay in Neointimal Coverage as a Function of Strut to Wall Detachment Distance: Implications for Stent Optimization," *J. Am. Coll. Cardiol.*, vol. 65, no. 17, p. S43, 2015.

[7] E. K. W. Poon, P. Barlis, S. Moore, W.-H. Pan, Y. Liu, Y. Ye, Y. Xue, S. J. Zhu, and A. S. H. Ooi, "Numerical investigations of the haemodynamic changes associated with stent malapposition in an idealised coronary artery," *J. Biomech.*, vol. 47, no. 12, pp. 2843–2851, 2014.

[8] G. Nakazawa, S. K. Yazdani, A. V. Finn, M. Vorpahl, F. D. Kolodgie, and R. Virmani, "Pathological Findings at Bifurcation Lesions. The Impact of Flow Distribution on Atherosclerosis and Arterial Healing After Stent Implantation," *J. Am. Coll. Cardiol.*, vol. 55, no. 16, pp. 1679–1687, 2010.

[9] J. R. Buchanan, C. Kleinstreuer, S. Hyun, and G. a. Truskey, "Hemodynamics simulation and identification of susceptible sites of atherosclerotic lesion formation in a model abdominal aorta," *J. Biomech.*, vol. 36, no. 8, pp. 1185–1196, 2003.

[10] T. J. Gundert, A. L. Marsden, W. Yang, and J. F. LaDisa, "Optimization of Cardiovascular Stent Design Using Computational Fluid Dynamics," *J. Biomech. Eng.*, vol. 134, no. 1, p. 011002, 2012.

[11] M. Sinnott, P. W. Cleary, and M. Prakash, "An investigation of pulsatile blood flow in a bifurcation artery using a grid-free method," *Proc. Fifth Int. Conf. CFD Process Ind.*, no. December, pp. 1–6, 2006.

[12] E. Nagel, T. Thouet, C. Klein, S. Schalla, A. Bornstedt, B. Schnackenburg, J. Hug, E. Wellnhofer, and E. Fleck, "Noninvasive Determination of Coronary Blood Flow Velocity With Cardiovascular Magnetic Resonance in Patients After Stent Deployment," *Area*, pp. 1738–1743, 2003.

[13] M. W. Siebert and P. S. Fodor, "Newtonian and Non-Newtonian Blood Flow over a Backward- Facing Step – A Case Study," *Proc. COMSOL Conf. 2009 Bost.*, 2009.

[14] R. Balossino, F. Gervaso, F. Migliavacca, and G. Dubini, "Effects of different stent designs on local hemodynamics in stented arteries.," *J. Biomech.*, vol. 41, no. 5, pp. 1053–61, 2008.

[15] C. Chiastra, S. Morlacchi, D. Gallo, U. Morbiducci, R. Cárdenes, and F. Migliavacca, "Computational fluid dynamic simulations of image-based stented coronary bifurcation models Computational fluid dynamic simulations of image-based stented coronary bifurcation models," 2013.

A Study of Segmented Single and Dual Inlets Parallel Configuration Designs in Proton Exchange Membrane Fuel Cell using CFD approach

Ahmad Syabil Ahmad Zorin*, Mohd Hardie Hidayat Mohyi

School of Engineering, Taylor's University, Malaysia

*syabilzorin@gmail.com

Abstract

This research was studied to compare the flow field design of single inlet and dual inlets segmented parallel designs in Proton Exchange Membrane Fuel Cell (PEMFC). Design of the flow field is a major contributor in the performance of a fuel cell. By changing the flow field design, it effect the pressure drop and the distribution flow which both contribute in the performance of the fuel cell. Single inlet segmented parallel design and dual inlets segmented parallel designs are initially used in the study of the pressure drop and the distribution flow in the bipolar plates. Dimension and the active area for the bipolar plates are made similar. This is to allow the designs to be compared. Study of the pressure drop and distribution flow in the flow fields of the PEMFC bipolar plates are done by simulating it using Computational Fluid Dynamics (CFD) simulation fluent and is modelled using Solidworks software. Engineering simulation software, ANSYS allow simulation of the two designs of flow field, velocity distribution and pressure to be illustrate. Simulation of the design is done in purpose of obtaining optimum flow field designs. Modification in terms of the design is made later on to obtain optimum pressure drop and distribution flow across the channels. Modified single inlet segmented parallel and modified dual inlets segmented parallel designs will be model and compared with initial design in terms of pressure and the velocity distribution across the bipolar plates.

Keywords: Proton Exchange Membrane Fuel Cell, Computational Fluid Dynamics, Bipolar plates, flow field designs, segmented parallel flow field.

1. INTRODUCTION

PEMFC is fundamental in fuel cells as it is the main components that causes the production of power generated.it is a semi-permeable membrane that allows proton ions to pass through it, which is the hydrogen ions. During the stage where hydrogen ions pass through the membrane, electrons will be passing through the circuit, which contain the load, for example, light bulbs, engine and many more. Hence, energy is produce.

PEMFC has still a lot of area to be improve in terms of its design. This is to increase the efficiency of the PEMFC. Several challenges that is encountered in increasing the efficiency of the PEMFC is located in the designing of PEMFC. This is because, design of the manifold of the PEMFC effect the flow distribution of reactant in PEMFC. For this project, we will only focus on parallel design of PEMFC. Based on the article written by Jayanti et al (2005), parallel-channel PEMFC is among the most common design which is being used in fuel cell. However, he stated that there are main problems regarding single parallel-channel PEMFC. The problems are the flow distribution and also the pressure drop. It has been stated in his article, that the result of study of single parallel channel PEMFC shows that some of the parts of the tube or path does not contain any reactant in it. This may be due to unsymmetrical bifurcation of the reactant when passing through pipes [2]. Because of this, electrolysis process in PEMFC could not be optimized. To obtain high energy due to optimized electrolysis process, two factors need to be considered. This two factors are the distribution flow of the reactants and pressure drop at the outlet from the inlet [2].

Stable distribution flow is important in any field of industries. For example in chemical reactor, in heat sink and even in medical industry. “Agricultural irrigation” stated, stabilized flow distribution means high products with the use of low water. By achieving this stable flow distribution, it means low in terms of maintenance, power pump used, vibration, noise and heat energy released. Other than that it also cause better heat transfer in the system [3]. Thus it is very important to achieve this steady distribution flow in PEMFC. As for the pressure loss, pressure loss in a fuel cell shows the efficiency of the fuel cell. Efficient [2].

By taking these two problems into consideration, modelling of single and dual inlet segmented parallel PEMFC will be done in Solidworks CAD software and analytical simulation will be tested using ANSYS CFD simulation software. Thus from this initial designs, improved designs of PEMFC with better distribution and efficiency can be made.

2. Theoretical Framework

2.1. Basic of Proton Exchange Membrane Fuel Cell

Fuel cell is basically an electrolysis process that harvests the electrical energy from hydrogen fuel and also air which is oxygen. During the electrolysis, electron that is separated from hydrogen ions need to go to the electrode, through the circuit and to the second electrode. This event will cause energy to be generate. The operation was

been firstly demonstrated by William Grove in 1839. In the demonstration of electrolysis, energy is used to electrolyze water to hydrogen and oxygen via electric current, which the experiment is set as in figure 2. After the gasses are collected, the power source is replaced with ammeter which results in the movement of the needle due to electric current passing through it. It demonstrates that electron are produced due to the electrolysis of hydrogen and oxygen in water [1]. This is the basic of fuel cell on generating energy. The path that is taken by electrons and also hydrogen ions in PEMFC is shown in the figure 1.

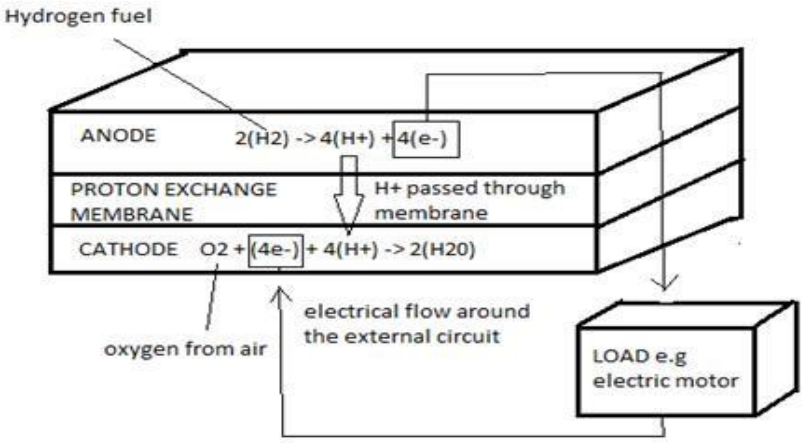


Figure 1: Basic Fuel cell components. Path of electron is shown by the arrow

2.2. Flow Field Designs

PEMFC is the component that is responsible in flowing the reactant of the fuel cell. Thus, the design of the PEMFC is important in making the fuel cell efficient in generating energy. Based from the article written by Jayanti et al (2005). It stated that PEMFC is used to ensure reactant can flow efficiently, so that electrolysis process can be optimized. There are various types of designs regarding the manifold of PEMFC, for example there are serpentine design, there are parallel design, and there are Z- type design and many more. The various design of the PEMFC is shown in figure 2. All of this various designs is due to this two factor which are:

- Distribution flow of reactants
- Pressure drop from inlet to outlet.

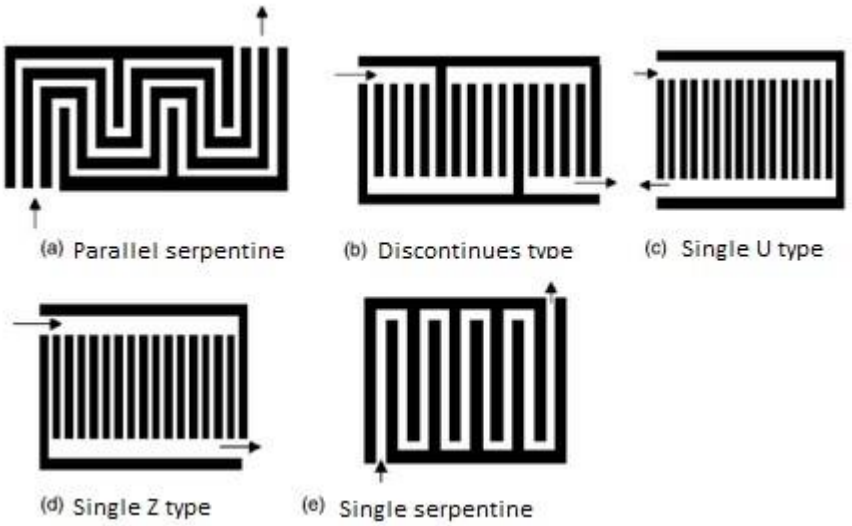


Figure 2: Various designs of PEMFC available[2]

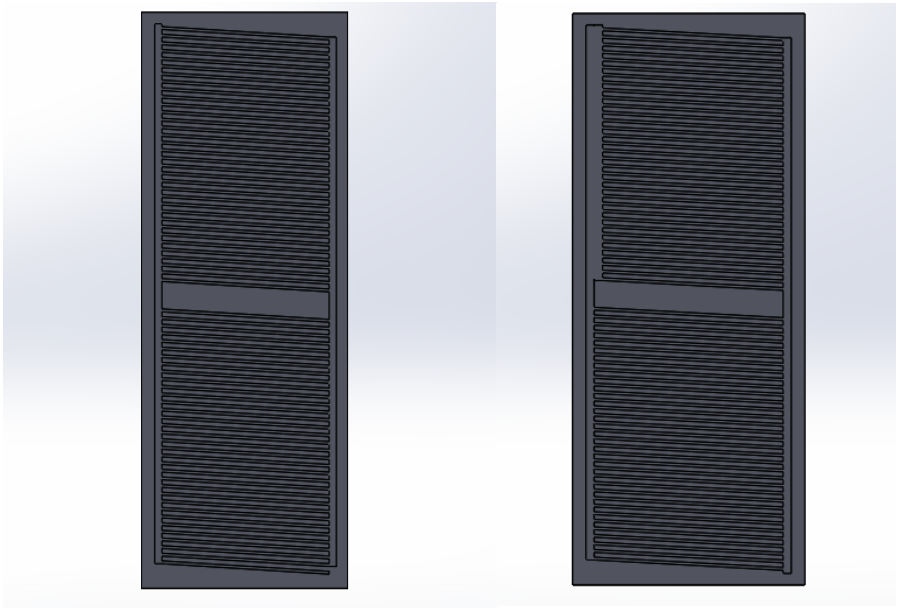
Author of the journal of Power sources, Kee et al (2002) has demonstrated analytical problems regarding PEMFC designs available. For example, huge pressure loss occurred on serpentine design when demonstrating the flow field design. As for parallel U shape design, "muldistribution flow" occurred [2]. Parallel PEMFC design which is also known as "Conventional design", is used by researchers to be analyzed. Article written by Jayanti et al (2005) demonstrated a modification in the conventional U type design that was used in their experiment. The conventional PEMFC is modified by adding a central rib. This small modification cause a lot of difference in the results compared to the normal conventional U type design [2]. The result is done by using CFD software. This modification shows a good improvement in the distribution flow of the reactant compared to the previous design [2]. As for the journal of Hydrogen Energy written by Li et al (2010), it studies on the design of multiple bifurcation structure of flow channels in manifold of PEMFC. In this article, it stated that by making changes on the edges of the turns of the bifurcation it can improve the distribution flow of the reactant in the PEMFC. In this article, it investigated 3 types of design, which are first sharp edge bifurcation design, circular bifurcation design and also round edge bifurcation design. The analysis of the 3 designs were made using CFD simulation and actual experimental analysis. For the CFD simulation, design were constructed in Solidworks CAD software and later sent to CFD simulation for the analysis to be done. As for the experimental models, it was been constructed by using polymer material. The analysis is done to measure the flow distribution in all channels. This two methods is then compared. Based from the result, it shows that the distribution flow for the round edge has better distribution flow compared to the two other designs. The reactant flow uniformly in the path from the inlet to the outlet. Thus this also conclude that the design of the PEMFC affect the distribution flow of the reactant [3].

However, in the article written by Jayanti en al (2005), for parallel design PEMFC, there is a massive volumetric flow rate occur in the inlet and outlet, hence causes the flow distribution to be bad, thus making the fuel cell not efficient. Kee et al (2002) is one of the researchers that research on the PEMFC of single parallel design, was the first researcher that discover on the "muldisfuction" of the distribution flow in PEMFC by providing mathematical analysis. Due to this, further study by other

researcher has been made, for example Jayanti et al (2005), did a further study on the flow distribution of parallel design of PEMFC where it modified the conventional design to multiple U-type parallel design and multiple Z- type parallel design [2]. Therefore, all of this modification in terms of design shows that, there are still room for improvement in terms of PEMFC design manifold. The reason of the optimization of design is to increase the efficiency of the fuel cell and also obtain a stable distribution flow of the reactant.

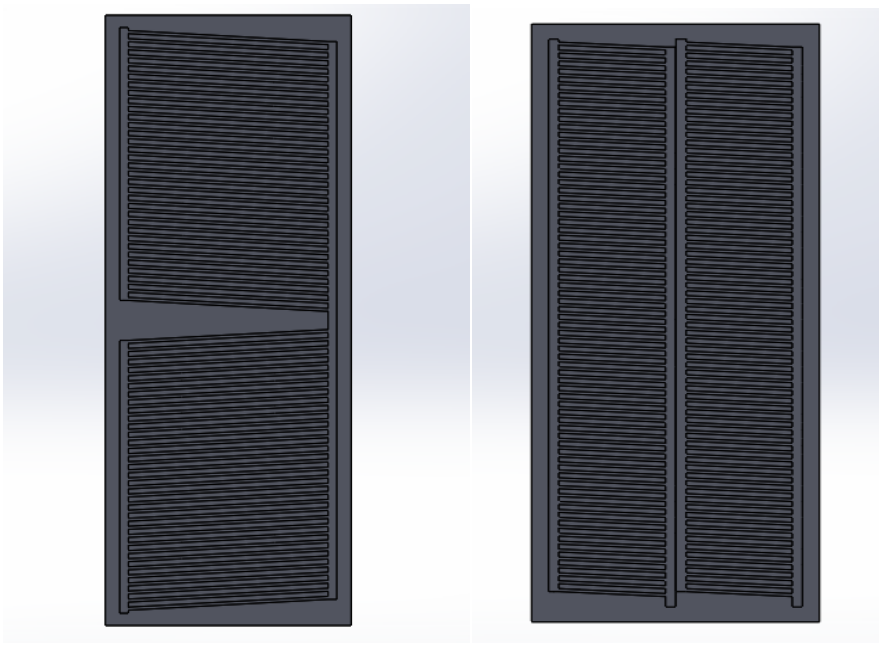
3. Methodology Framework

3.1. Flow Field Designs



Design A: 1 inlet and 1 outlet Design B: 2 inlets and 1 outlet

Figure 3: Bipolar plate initial designs for segmented parallel PEMFC



Design C: 1inlet and 1 outlet Design D: 2 inlets and 2 outlets

Figure 4: modified design of bipolar plates segmented parallel design

There are 2 initial design and 2 modified design of PEMFC that were used in this report. The two initial designs are compared and later on, modification is been made to the design. Thus, the new modified design is being compared.

a) Design A: Initial Single inlet segmented parallel design

As shown in figure 3 design A, single inlet segmented parallel PEMFC design has 1 inlet and 1 outlet for the reactant to go in and out. As the reactant moves in the PEMFC, it will bifurcate to all of the channels in the PEMFC. To increase the efficiency of the PEMFC, the separation of reactant through all of the channels need to be ensure. This is because, based from research written by Jayanti et al (2005), it stated that the distribution of reactant through the channels for single parallel PEMFC design is bad. Therefore the detail in designing the single inlet segmented parallel PEMFC design for this report need precise. As can see from the figure XXX the channels that the reactant will flow is slightly slanted by few degrees. This is because, by making the channels slanted, this will cause gravitational force to be included due to the force balancing. Thus, by including gravitational flow, the reactant will pass through the channels from the inlet to the outlet more fluent compared to single parallel design without slanted feature. Other than that blockage of the reactant through the channels also hardly occurred due to the slanted feature of the PEMFC design. As compared to the normal single parallel PEMFC design, there is no segmented feature included in it. For this design, segmented is included. This also to optimize the distribution flow of the reactant passing through the channels.

b) Design B: Initial Dual inlet segmented parallel design

Based from figure 3 design B, the obvious difference between single and dual inlet design is for dual inlet, there are 2 inlet and one outlet. The reason of this two inlets is to increase the volume of reactant that passing through the PEMFC in one period of time. As the volume of reactant that passing through a PEMFC in one moment of time increase, the PEMFC's volume occupied by the reactant also increase. Hence it optimized the distribution flow. As for the inlet, we can see two inlets going in at the same location which is the upper left of the PEMFC. One of the inlet will focus on the upper segment of the PEMFC. Meaning all of the reactant will only touch and go through the upper inlet. As for the second inlet, it will only focus on the 2nd segmented, which is at the bottom of the PEMFC. The purpose of this design is to increase the volume of reactant that enter the channels. The channel will be slightly slanted by 3 degree in the design. This will help in fluidity flow of the reactant across the channels. Fixed dimension is used in both dimension so that it will be easy for comparison between both of the design.

c) Design C: Modified single inlet segmented parallel design

Based from figure 4 design C, the first segmented is the same as the initial design. However, at the second segment, the angle of the channels is -3 degree. Therefore the reactant passed through the first segment and then move to the second segment. Even though the design is different, the total volume for the modified single inlet segmented bipolar plate are still in the range of 20% acceptance level when compared to the initial volume. Therefore, the design is acceptable and the result can be compared.

d) Design D: Modified dual inlet segmented parallel design

The length of the modified design is half the length of the initial dual inlets design as shown in figure 4 design D. However, the segmented is in the middle, making the channels from top to bottom for each segments increase. Based from the article written by A.Manso et al (2012), it stated that length of the channels and number of channels of PEMFC is the major influence in PEMFC performance.

3.2. Boundaries and dimension

Dimension of the flow fields are made to be approximately exact with one another. This is to ensure that the activation area is similar. Due to this, the bipolar plates can be compared. The parameters for example the mass flow rate use is fixed in all designs. For the flow of the reactant, Laminar flow will be used in this simulation. This is because laminar flow is well develop and easy to be calculate. This has been proven by various scholars that research on PEMFC. For example, for journal written by Jayanti et al (2005) and Li et al (2010), both of this journals used Laminar flow in their experimental on PEMFC. Turbulent flow is not recommended because of its unpredictability. Thus making it hard to calculate and analyzed. Therefore, in this report, Renolds, Re number of $Re < 2400$ will be used for simulation of the PEMFC design model. Parameters of the bipolar plates is as shown in table 1.

Table 1: PEM fuel cell dimension and operating condition

	Design A	*Design B*	*Design C*	*Design D*
Active volume (mm^3)	2663.57	2898.35	2646.02	3028.29
Bipolar plate dimension	170mm x 75mm x 2mm			
Rib width	1.68mm			
Channel depth	1mm			
Degree Angle of channels	3 degree			
Inlet and outlet depth	0.5mm			
Mass flow rate single inlet	3.0 x10^7 kg/s			
Mass flow rate dual inlets	1.5x10^7 kg/s			

3.3. Meshing

Meshing is include in the pre-processing stage in simulation. In preprocessing states, mashing size is state, inlets and outlets are set, and boundaries and condition of the simulating model are define [11]. Post processing stage is where result is generated. For the result to be accurate, mashing of the model need to be good, therefore meshing of the model is very important. One of the indicator of a good mesh is the number of mesh elements. The higher the number of mesh, the better the result will be [11].the number of element mesh for a model is also depend on the computer used. Normal computer will not be able to handle meshing up until 500 000 element. This is due to the limitation of the computer itself. Even though it can mesh up to 500 000 elements or more, it will take tremendous amount of time to mesh and to generate data [11]. Other than meshing element, meshing size also influence data generated by CFD. The smaller the size of mesh, the higher the number of element able to be in a model. Therefore, result will be accurate. Tetrahedron meshing type is used in the simulation. This is because the mesh size is constant throughout the flow field models. Therefore the result will be better. One of the indicator that can show either the mesh is good or not is by checking the skewness. For best meshing, skewness need to be below 0.8. This indicate the mesh properties used for the flow field design is acceptable, thus further calculation can be proceed. Table 2 shows the properties of mesh for all of the designs.

Table 2: meshing properties of flow field designs

	Design A	*Design B*	*Design C*	*Design D*
Mesh element	3,697,164	3,714,851	3,677,692	3,737,602
Skewness (Max)	0.974	0.966	0.985	0.963
Mesh type	Tetrahedron			
Mesh size	0.001			

4. Result and Discussion

4.1. Initial Design : Single inlet design

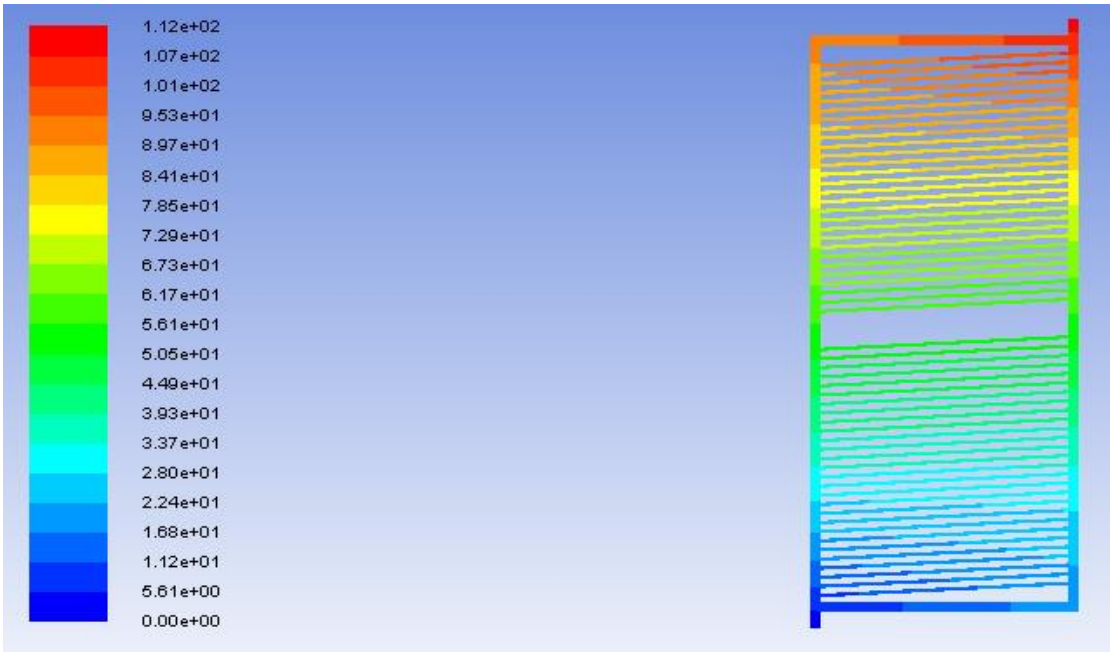


Figure 5: pressure spread for design A

Figure 5 shows the pressure distribution across the PEMFC manifold single inlet initial design. for this single inlet and single outlet PEMFC design, the maximum pressure act on the model is 112Pa. as it goes from the inlet to the outlet, it shows that the pressure decrease gradually. The indication of pressure inlet is higher than the outlet also shows indicates that the water produced from the reaction will be push down from the inlet and will be from near the outlet. This is good considering less water will be accumulate in the middle of the plates and cause flooding, which can

decrease the efficiency of the PEMFC [7]. Pressure spread across the inlet to the outlet of the design is illustrate nicely in figure xxx. It can be seen the pressure at the inlet is where the maximum pressure is located at and as it goes from the inlet to the channels and across the outlet, the pressure gradually decrease.

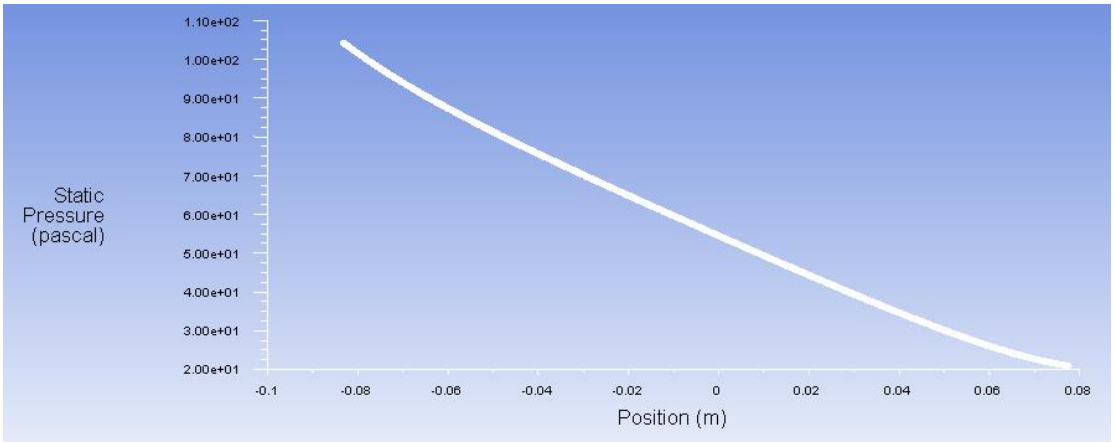


Figure 6 pressure at inlet length section

Graph shown in figure 6 focus on the pressure occurred at the inlets end to end before it enter the channels. Range indicator at the Y axis shows that the pressure start with high pressure value and decrease as pressure goes down to the bottom inlet section. Parabolic graph is also seen in the graph as it goes down the bottom inlet section. This parabolic graph is due to head loss occurred along the length of the inlet section. Length of the design plays an important roles in head loss that occurred in the PEMFC. As the length increase, the head loss occur from initial point to the end point also increase [6]. This result match previous studied carried by Santamaria et al (2013), where decrease in pressure can be seen across the inlet length section. Result also shows that at the inlet section, pressure value does not reach 0 Pa. this is due to non-opening at the end of inlet length section, therefore atmospheric boundary condition does not affect the pressure at this point.

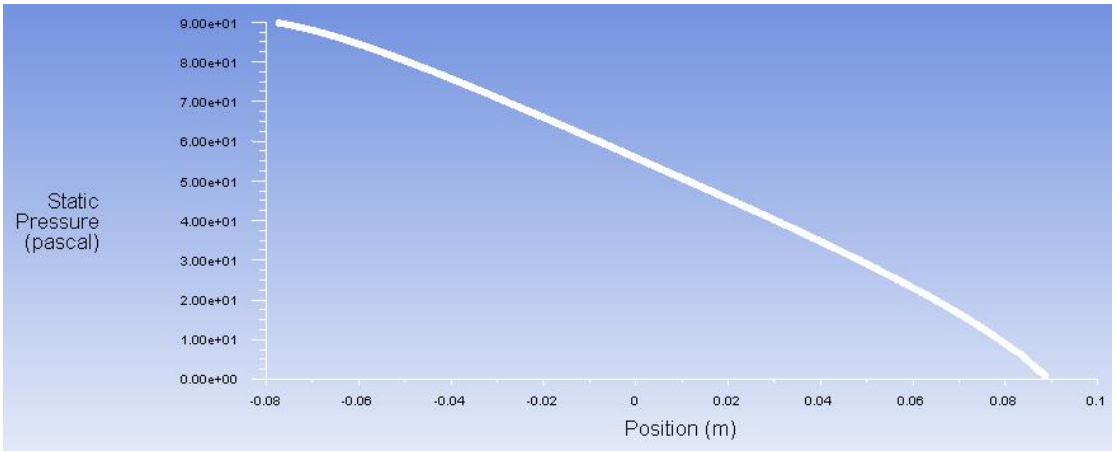


Figure 7: pressure at outlet inlet length section

Pressure at the outlet is illustrate in the graph shown in figure 7. As can be seen, the pressure reduce as it goes down the length to the outlet. However, the minimum pressure value at the outlet section is 0 Pa. this low amount of pressure is due to the atmospheric boundary condition at the outlet section. Comparison of the pressure

occurred in inlet top/bottom section and outlet top/bottom section can be seen in figure 8. From this graph, better understanding on the pressure difference occurred in the inlet section and outlet section can be seen. White line represent the pressure acting on the inlet length section while red line represent the pressure acting along the outlet length section. Pressure at the outlet section start relatively low compared to the pressure start at the inlet. This is due to the pressure loss occurred as reactant travel from inlet and across the channel to the initial outlet position [7].

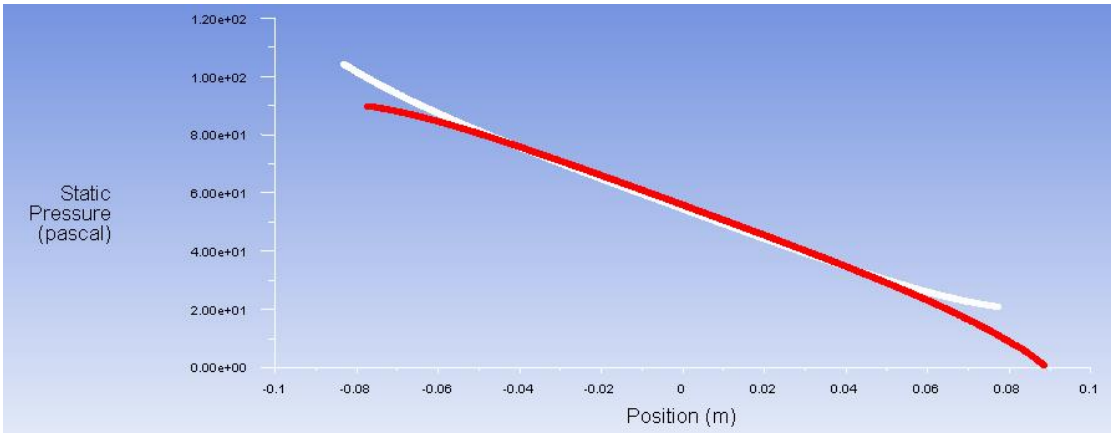


Figure 8 : comparison between pressure at inlet and outlet section length

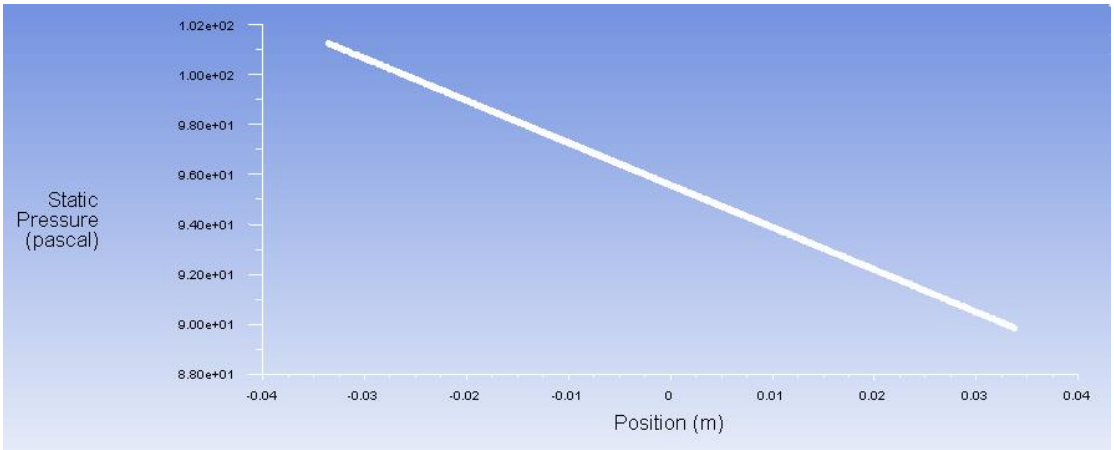


Figure 9 : pressure in top segmented first channel

Across the channels, pressure loss occurred as reactant enter the channels to the exit of the channels. The graph, as seen in figure 9, is the pressure loss occurred in the first channel of the PEMFC manifold design. Difference in pressure that occurred in the channels is not as huge as the pressure loss that occurred in the inlet or outlet length section. These is because of the size of the channel and also the velocity occurred in the channel. The area cross section of the channels are small in comparison with the inlet and the outlet. This difference of area can affect the velocity of the reactant as it flows through the PEMFC manifold. Low velocity cause pressure loss occurred to be low. Therefore, pressure loss occurred in the channels can be seen low due to the low velocity which caused by small cross section area of the channels [19].

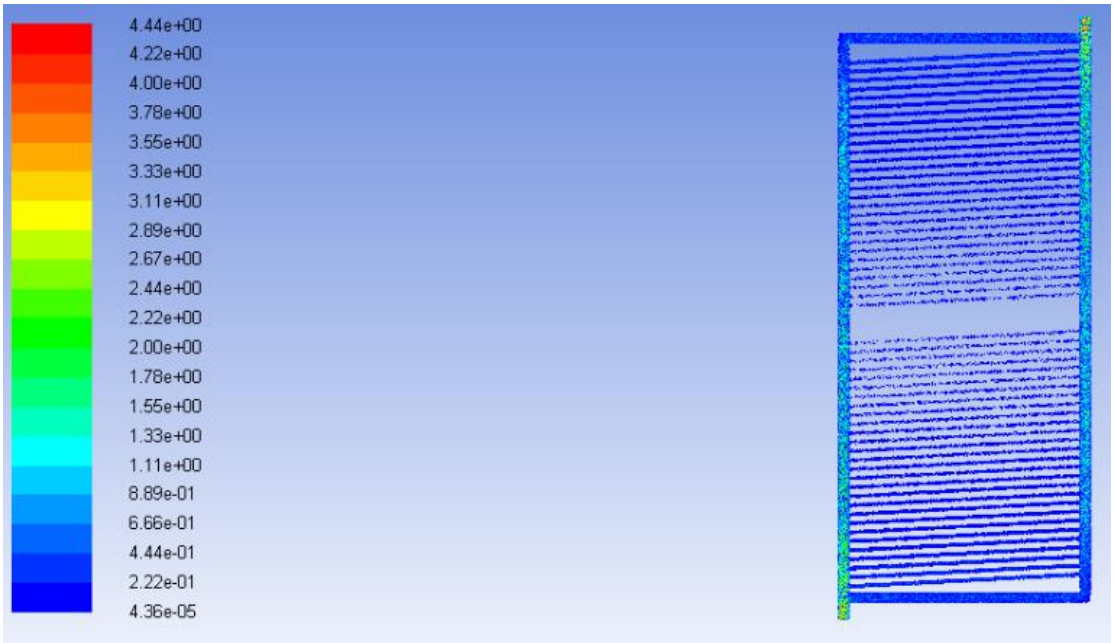


Figure 10 : design A velocity vector

Figure 10 illustrate the velocity distribution occurred across initial PEMFC manifold design. Figure shows that the velocity is maximum at the inlet and at the outlet. Low velocity can be seen at the channels of the PEMFC manifold. These support the claim that is mention on the relationship on pressure with velocity where velocity of the reactant effect the pressure occurred in in PEMFC manifold [7], [19].

4.2 Initial Design : Dual inlet design

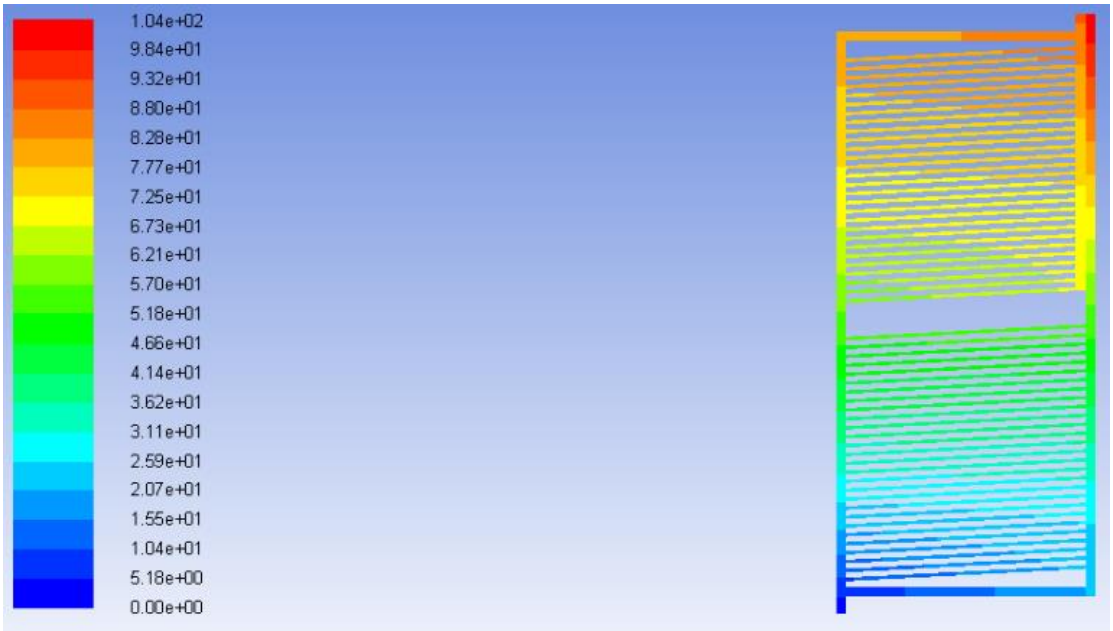


Figure 11 : Pressure spread for design B

Overall spread pressure that can be seen for dual inlet design is shown in figure 11. The pressure spread quite similar to as we saw with single inlet pressure. Hence,

the pressure spread for dual inlet is acceptable. As for the dual inlets, inlet 1 will cover the top segmented channels while the inlet 2 cover the bottom segmented section.

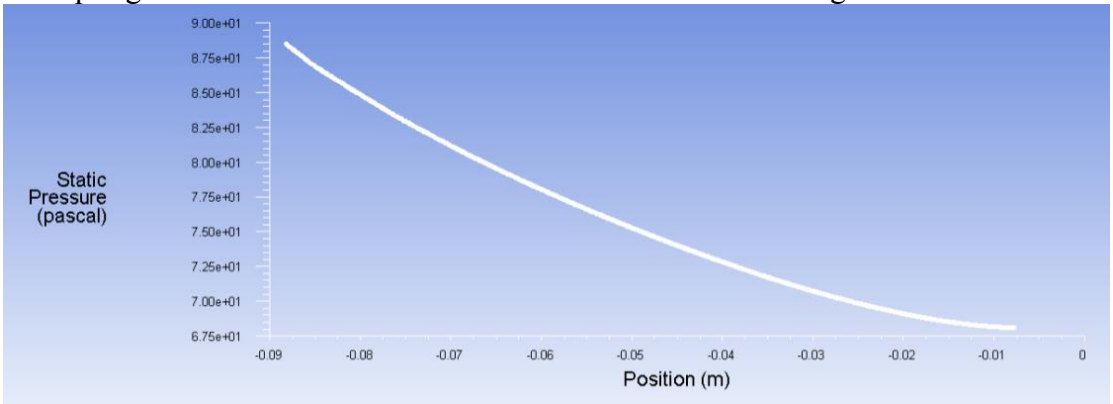


Figure 12 : pressure at inlet 1 length section for design B

As compared between inlets to the inlet length at the bottom segmented section, there are difference in head loss between both. In figure 12, the graph represent the pressure at the top segmented inlet length section. As compared to the graph that represent pressure at the bottom inlet length section, there are significant difference in the head loss between both of the graph. This is because for the inlet 1 length section has shorter length compared to the inlet 2 length section. Inlet 2 length section has twice the length as inlet 1 length. Hence, there affect the pressure loss occurred. Pressure loss for inlet 1 top to bottom section is approximately half of the pressure loss occurred at the inlet 2 top to bottom length. Lengths at the top segmented.

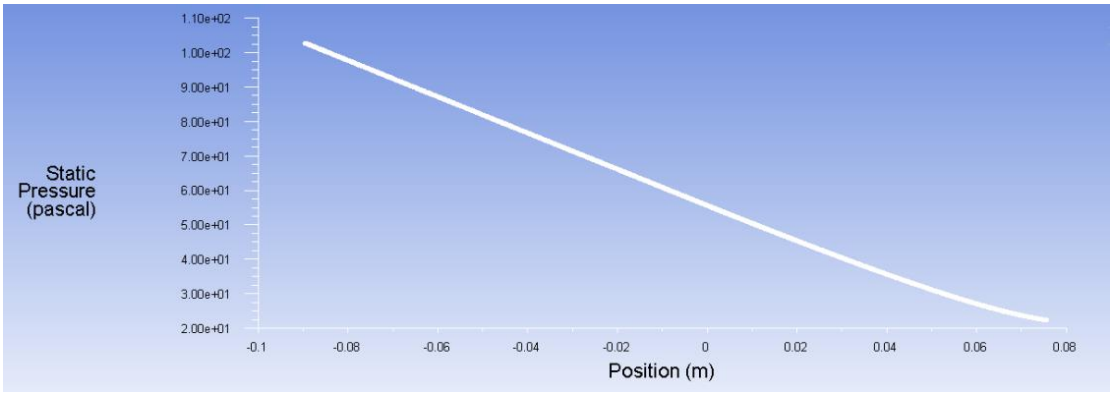


Figure 13 : pressure at inlet 2 length section for design B

Comparison between channel in top segmented and bottom segmented is been made in figure 14. This is to verify the difference of pressure value that is allocate at that particular location. Due to the difference in length travel by reactant to the 2 channels, difference in pressure can be seen. As predicted, pressure for bottom segmented has a low spread compared to pressure at the top segmented. However, the head loss for both are approximately exact. Head loss can be seen base from the gradient of the graph where both of the channels has similar gradient. This is because the length and area of the channels are still the same. Due to the exact dimension, the velocity of the reactant at the channels will still be the same, thus, head loss is the same. The pressure at the inlet of both channels are different due to the difference in the length of inlet top to bottom section.

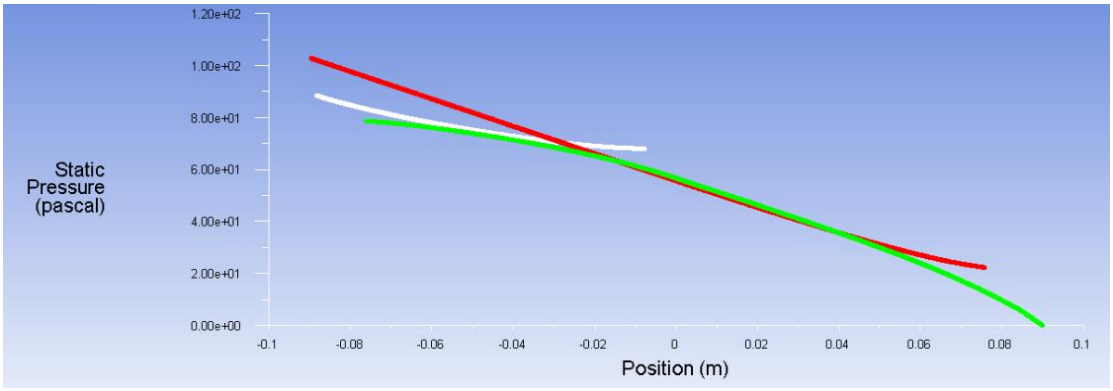


Figure 14 : pressure inlets and outlet comparison in design B

Figure 14 shows the comparison of gradient at the inlets and outlet across the PEMFC manifold. 3 lines can be seen indicating inlet 1, inlet 2 and outlet. White line indicate pressure at inlet 1, which cover only inlet length section until the top segmented part. Read line indicates pressure along inlet 2 until the entrance of channels at the bottom segmented part, whereas, green line indicates the outlet length section part. Similar parabolic graph lines is obtain for dual inlets segmented parallel design as compared to single inlet parallel segmented design's graph. These consistency shows that the result obtain is acceptable. Value for outlet line reach 0 Pa due to the boundary condition set during simulation.

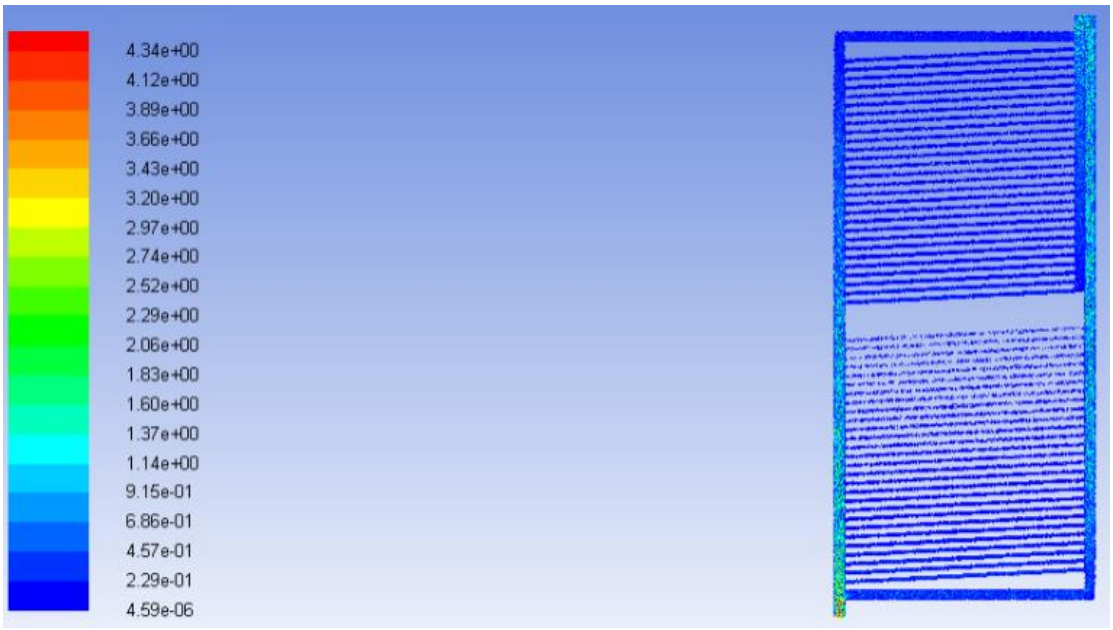
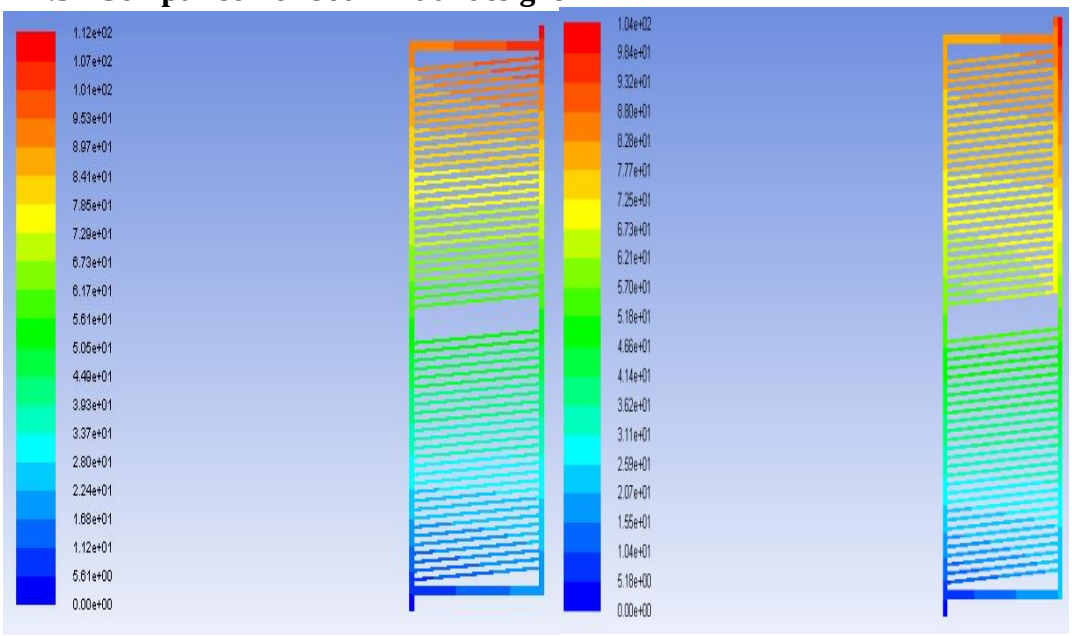


Figure 15: velocity vector for design B

As for the velocity distribution, figure 15 shows that the velocity of the reactant start with high velocity. These high velocity is due to the large cross section area of the inlet section. Reactant will lose its momentum as it enters the channels. Decrease in velocity is due to the small cross section area of the channels. However, as it enter the outlet section, the velocity increase towards the outlet. This is due to the ideal condition where no energy is loss during this process. Velocity from the channels outlet to the PEMFC outlet will increase until it reach the exact value as the velocity at the inlet.

4.3 Comparison of both initial designs



Design A **Design B**

Figure 16: comparison of pressure spread for both initial designs

Comparison is made between both of the designs to determine the difference that influence the result obtain in both of the designs. Comparison between the inlet section pressure and the outlet section pressure for both designs can be seen in figure 16. Based on the figure, difference in the pressure spread for single inlet segmented PEMFC design and dual inlets segmented PEMFC design can be seen. Pressure drop for single inlet segmented PEMFC design is higher compared to the pressure drop occurred on the dual inlet segmented PEMFC design. The reason for the pressure drop is due to the number of inlets available. Dual inlets consist of 2 inlets, which means the reactant has more area to flow into the inlets. Due to this, low volume of mass is forced in a single inlet. This will caused less pressure to be built in the manifold. As for single inlet, there will be more volume per mass that is pushed in the inlet. This will increase the pressure act on the inlet, and across the PEMFC manifold. Hence, increasing the pressure. Pressure drop in fuel cell is important as it controls the production of water in a fuel cell. Hydrogen and oxygen will react at the proton exchange membrane and form electrical energy and water. Water that is formed need to be remove. This is because as water increase in a fuel cell, it can lower the performance of the fuel cell due to less reactive contact area. Other than that, uncontrolled water production in a fuel cell can also cause short circuit of fuel cell. These two issues can decrease the rate of energy production and the efficiency of the fuel cell. Therefore, pressure drop is needed in a fuel cell.

Pressure drop in a fuel cell need to be low as possible. This is because high pressure drop indicates high velocity in a fuel cell. Due to this high velocity, the rate of reaction between hydrogen and oxygen to react and produce electrical energy and water, will be low. Therefore, low productivity will cause low efficiency of fuel cell performance.in case of this project, it shows that dual inlets segmented PEMFC design has better design compared to the single inlet segmented PEMFC design. However, the

difference between both of the designs is small. Therefore there will not be drastic difference in terms of both of the designs fuel cell performance.

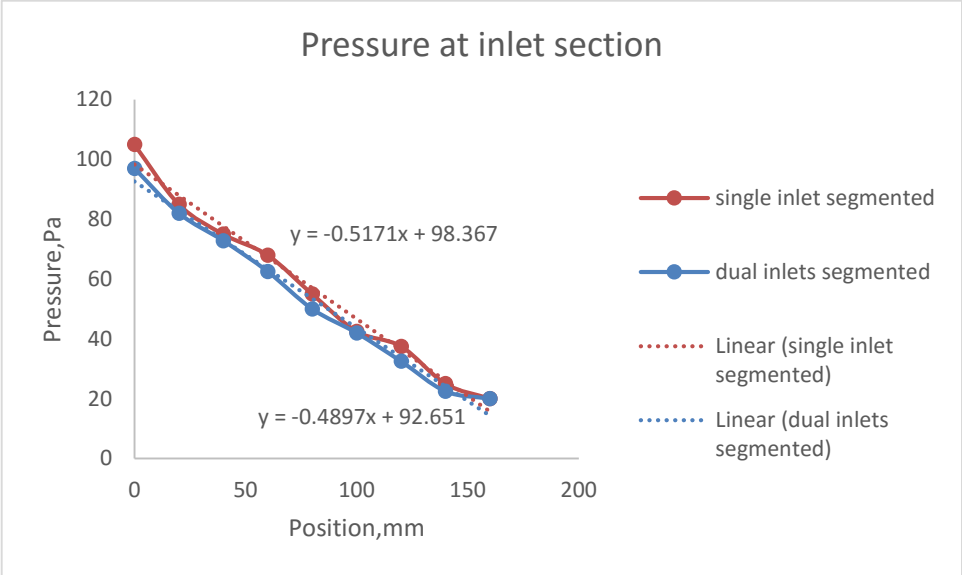


Figure 17 : pressure comparison for both initial designs at inlet length section

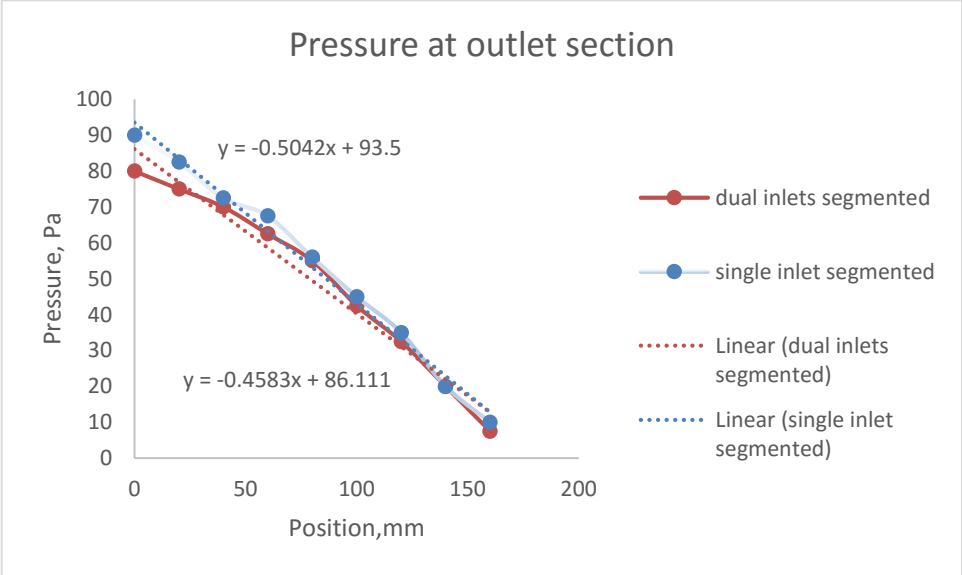
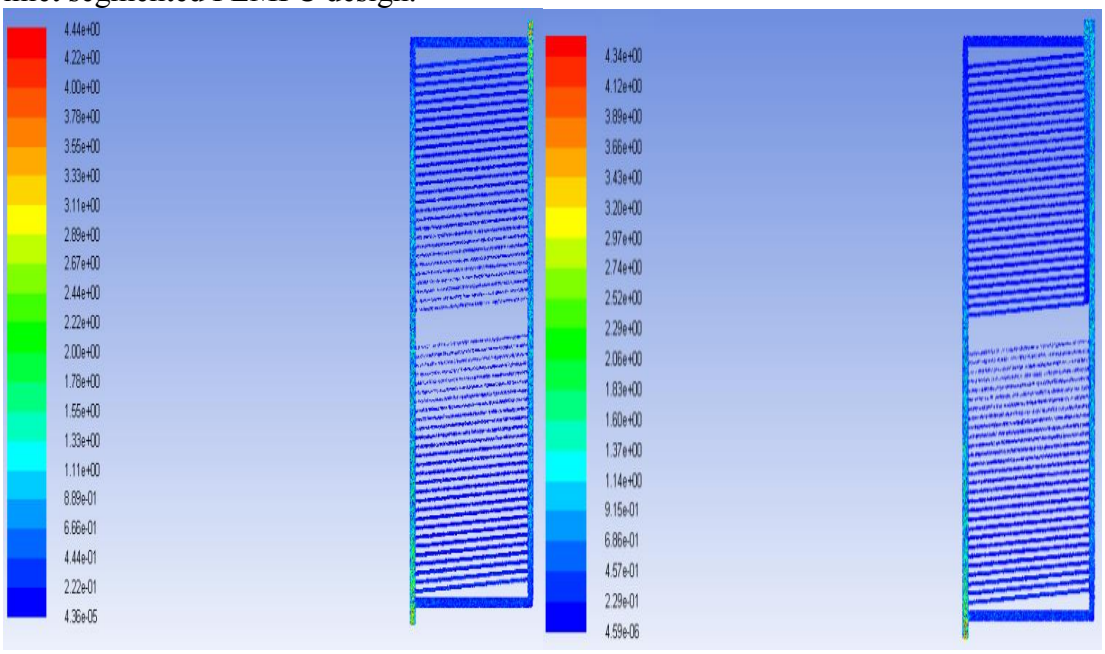


Figure 18 : pressure comparison for both initial designs at outlet length section

Graph of pressure of both designs for the inlet and outlet has been plotted and illustrate. This is to show clearly the difference in both designs. For single inlet segmented PEMFC design, graph shows that the value plotted is higher compared to dual inlets segmented PEMFC design. Output section pressure graph also shows a similar trend as the inlet pressure section graph. In figure 17 and figure 18, it shows pressure plot for dual inlets segmented design has lower pressure compared to single inlet design. These can be seen from the gradient of the path line form in the graph. Gradient represent the pressure drop from one certain point to the other. It shows that pressure in outlet section for dual inlet, the gradient is 0.4583, whereas the gradient for single inlet design is 0.5042. Similar value of gradient is obtain on pressure acting in inlet length section. Gradient for dual inlets design is 0.4897 and 0.5171 for single inlet

PEMFC design. Hence proving that the pressure drop in single inlet is higher than in dual inlet segmented design. These evidence clearly shows that pressure drop in dual inlets segmented design is lower compared to the single inlet segmented design. Lower pressure drop indicates better design as it indicates lower loss of energy in PEMFC [22]. Hence, dual inlets parallel segmented design is a better design in comparison to single inlet segmented PEMFC design.



Design A **Design B**

Figure 19: velocity vector comparison between both initial designs

As for the velocity distribution, it shows that the velocity spread for both of the designs are similar. For single inlet segmented PEMFC design, the maximum velocity is 4.44 m/s and for dual inlets segmented PEMFC designs, the maximum velocity is 4.34m which is slightly slower. These difference in velocity is due to the number of inlets available. In figure 19, difference colour in the inlets for single and dual inlet segmented design are seen at the inlet section. This indicate that single inlet segmented PEMFC design has higher velocity acting in its inlet. The velocity of reactant in the dual inlets segmented PEMFC design is lower due to the number of channels available. However, the difference in velocity is too little to be able to compare and see the difference.

4.4 Modified Design : single inlet design

Modified design for single and dual inlet has been made and compared. Changes in the designs can be seen in comparison to the initial designs. Evaluation on the result for each design and comparison is made in the following section

Graph for single inlet design shows a different pattern in comparison with the initial single design. This is due to the angle of the channels and the path reactant flows.

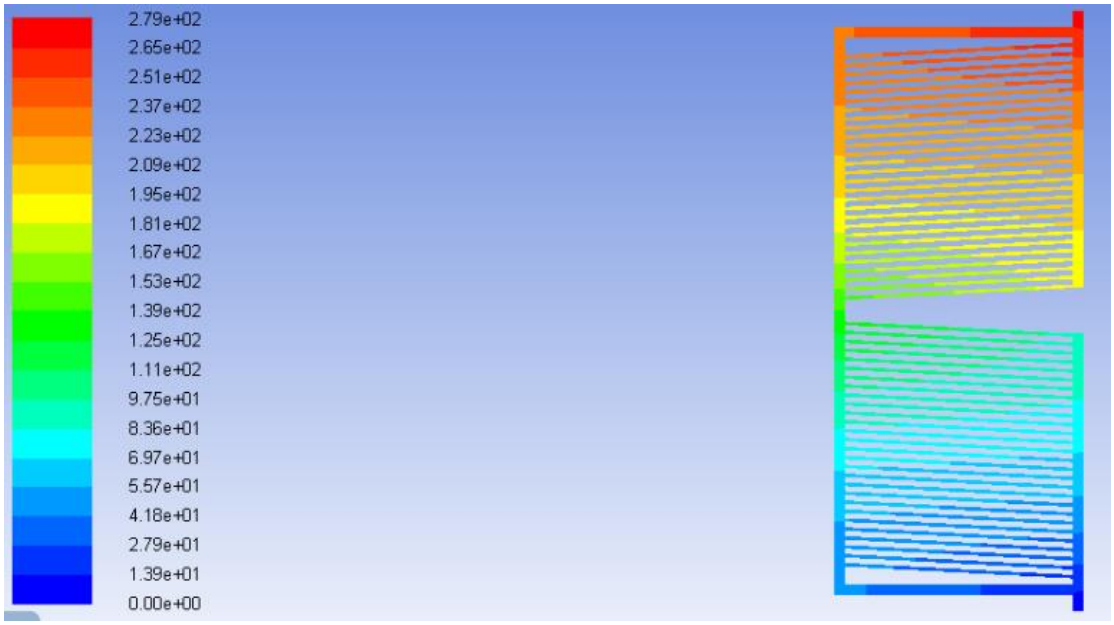


Figure 20 : Pressure spread for design C

Based from figure 20, it shows the pressure spread along the manifold design. It can be seen that the maximum pressure for this designs is the highest in comparison to the other previous designs. This high pressure is due design of the manifold. Reactant that enter the inlet can only distribute in the first segmented due to the design. Therefore, high mass per volume will accumulate at the first segmented. This will cause the pressure to increase. Later on, the reactant will flow to the second segmented channels and to the outlet. As mentioned before, pressure is the fundamentals in designing PEMFC manifold design. Large amount of pressure will cause large amount of stress acting on the manifold, therefore higher possibility of damage will occurred to the design. Other than that, more energy is needed to pump the reactant into the manifold. Due to this extra energy needed, hence higher maintenance required for this fuel cell designs. Therefore, single inlet modified design has the worst pressure spread among the previous designs.

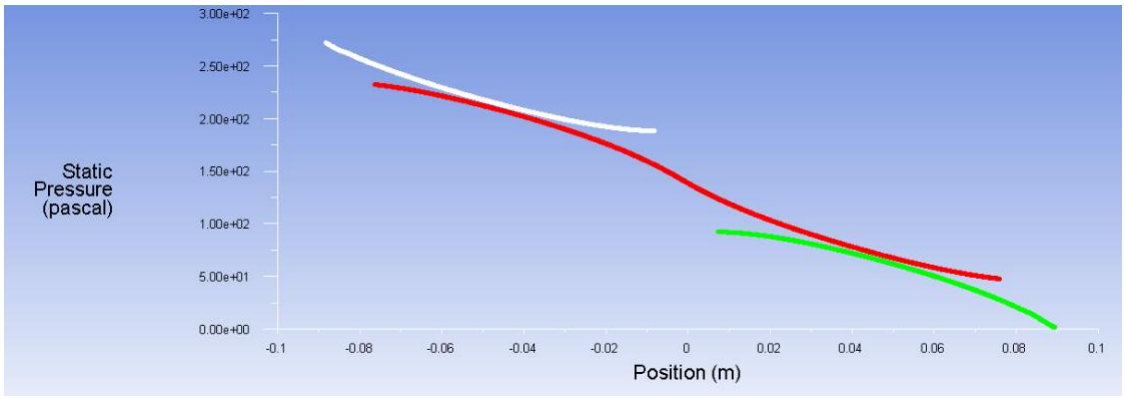


Figure 21 : pressure inlet and outlet section length comparison for design C

Figure 21 shows the pressure that act on the inlet and outlet length sections. White line represent the pressure acting on the top segmented inlet length section, green line signify pressure at the bottom segmented outlet section, and red line shows the pressure acting at the left top to bottom length section. As can see the graph is different

in comparison to the previous designs' graph. This is due to the design of the manifold. Reactant that enter the manifold only distribute at the first segmented. It will move to the channels and to the left side of the section then enter the bottom segmented part vie from the left. Hence, producing pressure graph pattern as seen in figure 21. When comparing this design with the previous designs, maximum pressure acted on the previous design is approximately equal to the pressure acting on the second segmented part of this single modified design. These means that, the pressure that act on this design is twice the value compared to the previous design. Therefore this design is not recommended to be used in fuel cell. High maintenance and high possibility of damaging fuel cell due to the high value of pressure, will lower the efficiency and cost of operation for these fuel cell design.

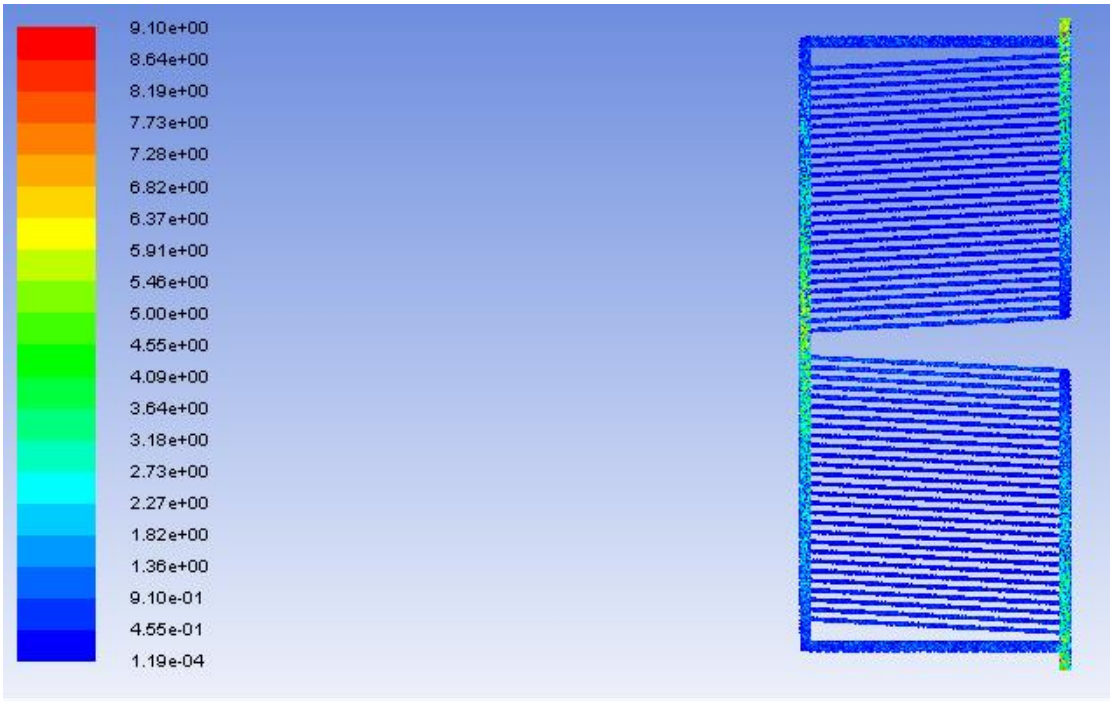


Figure 22 : velocity vector for design D

Figure 22 shows the velocity spread for single inlet segmented modified design. It can be seen that the reactant velocity is twice higher than the velocity of the reactant flow in the other two designs. Read dots in the figure indicates maximum velocity whereas blue indicates lowest or minimum velocity. One significant difference that can be seen in this velocity flow is the change in velocity. As can see from this single inlet parallel modified design, reactant enter the inlet with high velocity and enter the first segmented channels with low velocity. When it leaves the top segmented channels, the velocity increase back. However, reactant need to flow to the next segmented, which is at the bottom part before it flow to the outlet and leave the manifold. This required the flow to decrease in velocity again as it enter the channels.

Figure shows that velocity is high at the middle neck pathway. This high velocity indicates the pressure at that particular location is higher in compared to other parts. This will cause the manifold to burst due to high pressure. Hence, it will cause short circuit and instantly damaging the fuel cell. Due to this it is not advisable to proceed with this design in fuel cell.

4.5 Modified design: Dual inlet design

Dual inlet segmented parallel PEMFC design has 2 inlets and two outlets. The segmented part can be seen in the middle of the design. Pressure and the velocity is studied and the result is shown in the following section.

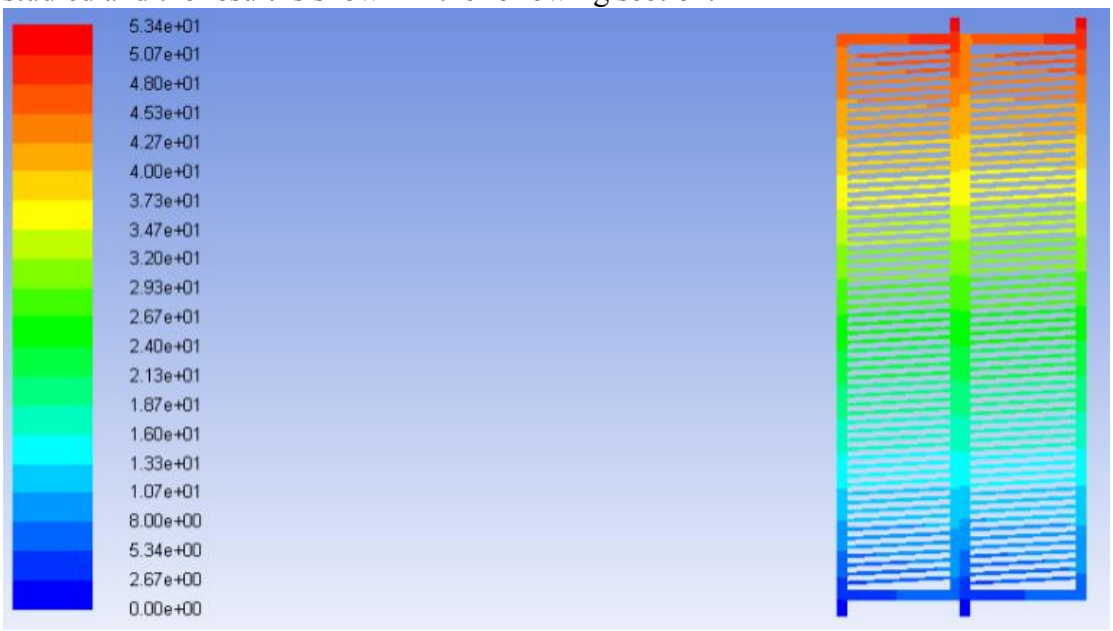


Figure 23 : pressure spread for design D

For modified dual inlet noticeable difference can be seen in the pressure act on the PEFC manifold. Based from the pressure spread in PEMFC dual inlets modified design shown in figure 23, the maximum pressure act in this design is 53.4 Pa. These result shows the lowest range of pressure in comparison to all of the previous designs. As mention earlier, low pressure in a manifold indicates good reactant flow. Low pressure also indicates low energy needed to pump in reactant in the manifold, therefore low maintenance is needed. Due to low maintenance, cost of operational for this design can be assume low. Distribution of pressure in this design indicates a good pressure distribution. It shows that pressure gradually decrease as it flows towards the outlet. This is good for the water removal process. High pressure will push the water produced toward the low pressure area. Water will later on be removed via outlet.

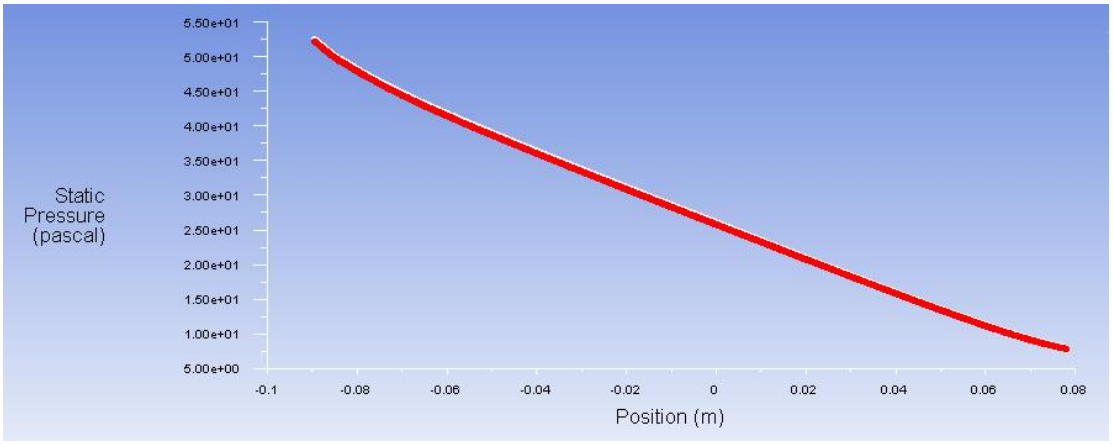


Figure 24: pressure comparison at inlets section length for design D

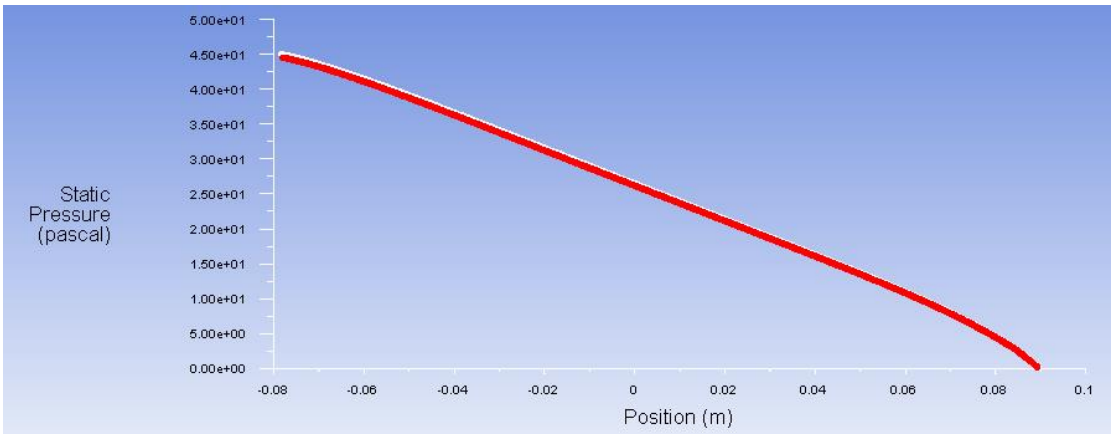


Figure 25 : pressure comparison at outlet section length for design D

Dual inlets modified design consist of 2 inlets ad 2 outlets. The pressure that act on both segmented are the same due to its symmetrical dimension and design. This claim can be seen as both of the outlets and inlets are compared in figure 24 and figure 25. White line represent pressure along inlet 1 length section and red line shows the pressure for inlet 2 length section. The pressure as it travels from its initial position is the same in both segmented. Pressure in channels for both segmented section also is compared. It shows that, the value of pressure for both channels is similar due to the symmetrical design of both parts. This can be seen in figure 26. Position of the lines in the graph are in a different location due to the location of the channels studied. Again, pressure range for dual inlets segmented parallel PEMFC design is smaller compared to other previous designs. These shows that it has the best pressure spread compared to other designs.

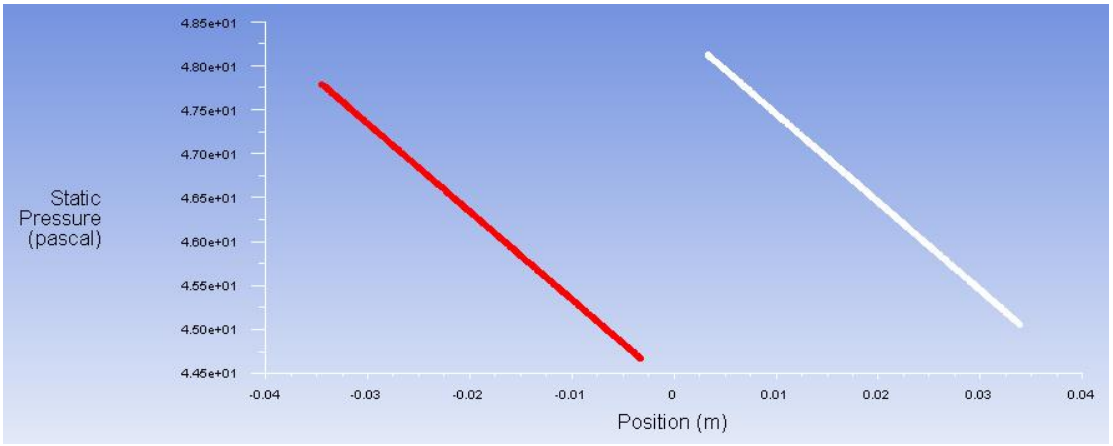


Figure 26: pressure comparison at top and bottom segmented part channel of design D

Pressure in channels for both segmented section also is compared. It shows that, the value of pressure for both channels similar due to symmetrical dimension. The difference is the position where the channels are located.

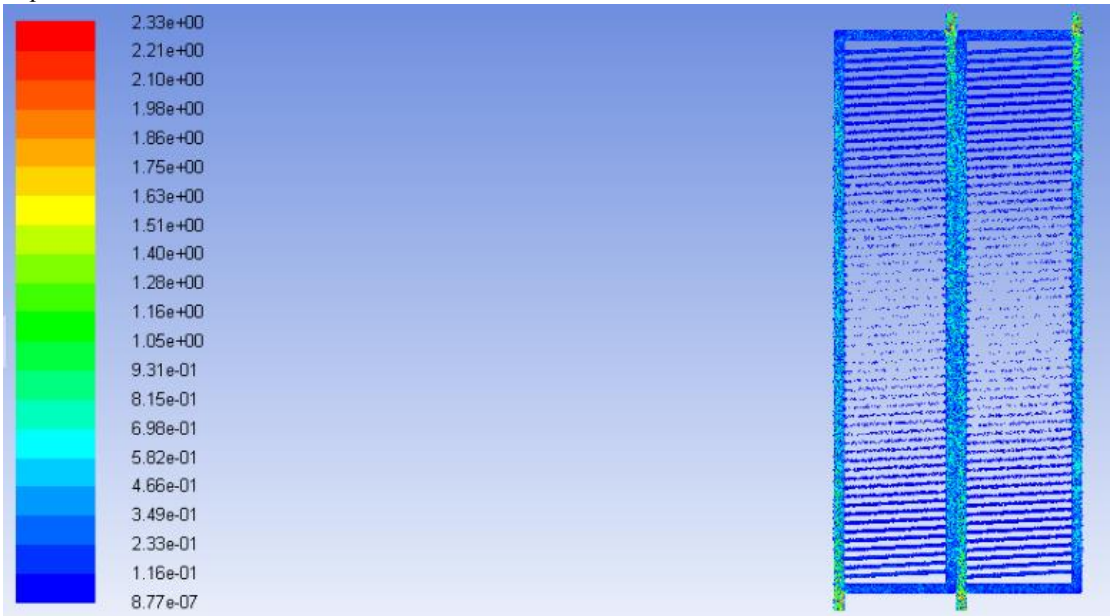


Figure 27: velocity vector for design D

As for velocity distribution of dual inlets modified PEMFC design, figure 27 indicates that the velocity of reactant in the design is low. Maximum velocity in this design is half lesser compared to the velocity for the initial designs and 4 times lesser in comparison with single inlet modified PEMFC design. As mention earlier, due to low velocity of the reactant, rate of reaction between hydrogen and oxygen will increase, henceforth, more electrical energy is produce.

4.6 Comparison between both modified designs

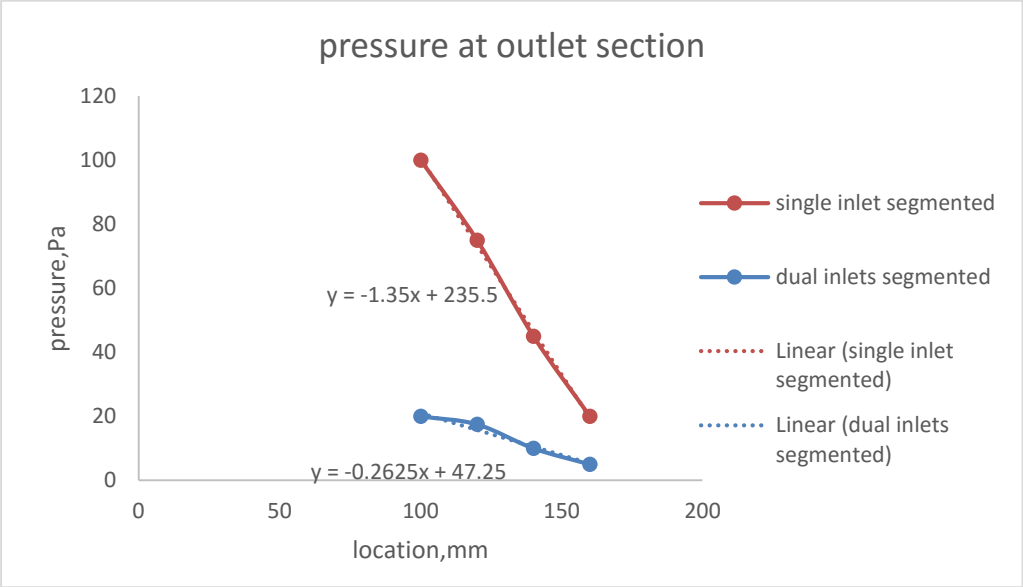


Figure 28 : pressure comparison at outlet length section for design C and D

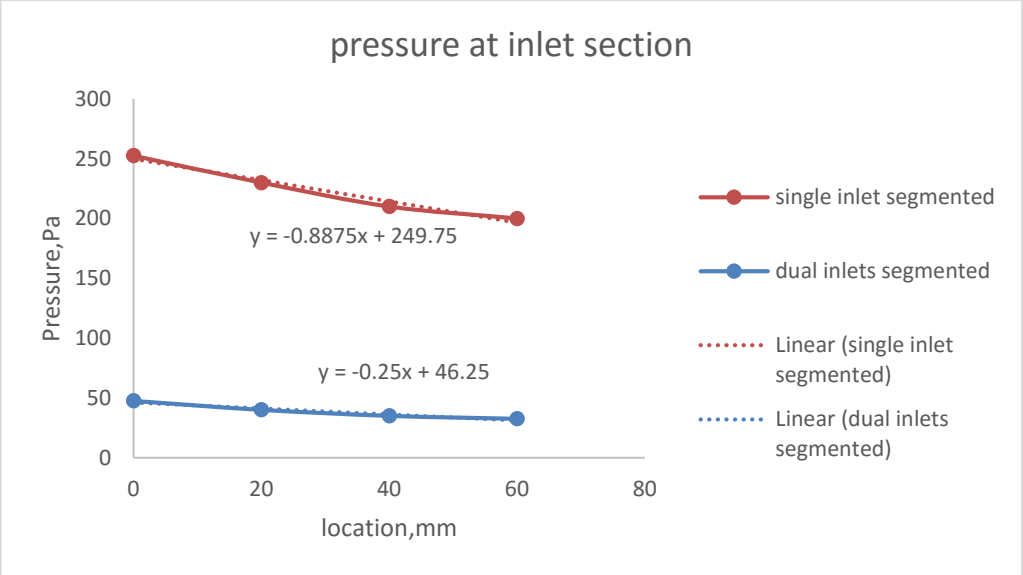


Figure 29: pressure comparison at inlet section length for design C and design D

Comparison for the modified design focus on the pressure and the velocity of the reactant passing through the manifold. Comparison for pressure is represent by the graph of pressure at inlet section and graph of pressure along the inlet length. Based from graph 28 and graph 29. Range of position that is studied in the graph for single inlet modified design is smaller due to inlets and outlets sections. Significant difference can be seen between the pressure acting in single inlet segmented modified design and dual inlet segmented modified design. The difference in pressure between both of this design is approximately more than 100Pa. based from the gradient generated in the graphs, difference between the gradient for both designs are approximately more than 0.5. These value of gradient shows the pressure drop acting in the designs manifold for single inlet segmented design is too large. Based from all of the evidences, it shows that single inlet modified design is clearly not a good design and will not be procced in studying this design. Due to its large amount of pressure acting on the manifold, it will lower the efficiency of the PEMFC fuel cell due to maintenance and damage.

5. Conclusion

Pressure drop and velocity in each designs has been study and it shows that dual inlets segmented parallel PEMFC design gives a better pressure distribution that leads to good amount of pressure drop and also better velocity range compared to single inlet segmented parallel PEMFC. This results is due to the dual inlet features where it reduce the pressure occurred at the inlet, thus giving a better distribution flow of the reactants in the bipolar plates. However modification design can be further made to obtain a higher efficient design of bipolar plates. Modification In the diameter of the inlets and outlets, length of the channels or round cornering at the end of the channels can be done

to enhance the design of bipolar plate. Due to these modification, increase in efficiency of PEMFC can be achieved.

References

[1] J. Larminie, and A Dicks, *fuel cell system explained,* Second Edition. West Sussex,UK:John Wiley & Sons Ltd, 2003

[2] S. Maharudrayya, S. Jayanti, and A. P. Deshpande, "Preure drop and flow distribution in multiple parallel-channel configurations used in roton-exchange membrane fuel cell stacks", *Journal of Power Sources*, No. 157, pp. 358-367, July 2005

[3] H. Liu, P. Li, and V. Lew, "CFD study on flow distribution uniformity in fuel distributors having multiple structural bifurcations of flow channels", *International Journal of Hydrogen Energy,* No. 35, pp. 9186-9198, June 2010

[4] K. I. Sainan, R. Atan, and W. A. W. Mohammed, "Analysis of PEM Fuel Cell Flow Field Design and Operation for Effective Water Removal" 2010

[5] I. Sabir, J. Park, and X.Li, "A flow channel design procedure for PEM fuel cells with effective water removal," *Journal of Power Sources*, vol. 163, pp. 933-942, 2007.

[6] A. D. Santamaria, N. J. Cooper, M. K. Becton, and J. W. Park," Effect of channel length on interdigitated flow-field PEMFC performance: A computational and experimental study,"*International Journal of Hydrogen Energy*, vol. 38, pp. 16253-16263, 2013.

[7] A.P. Manso, F.F. Marzo, J. Barranco, X. Garikano and, M. G. Mujika, "Influence of geometric parameters of the flow fields on the performance of a PEM fuel cell. A review," *International Journal of Hydrogen Energy*, vol. 37, pp. 15256-15287, 2012.

[8] M. Zerouala , S. B. Bouzidab , H. Benmoussac, and H. Bouguettaia, "Numerical study of the effect of the inlet pressure and the height of gas channel on the distribution and consumption of reagents in a fuel cell (PEMFC)," *Energy Procedia*, vol. 18, pp. 205 – 214, 2012.

[9] L. Chen, T. Cao, Z. H. Li, Y. L. He, and W. Q. Tao, "Numerical investigation of liquid water distribution in the cathode side of proton exchange membrane fuel cell and its effects on cell performance," *International Journal of Hydrogen Energy*, vol. 37, pp. 9155-9170, 2012.

[10] J. Scholta, G. Escher, W. Zhang, L. Kuppers, L. Jorissen, and W. Lehnert, "Investigation on the influence of channel geometries on PEMFC performance," *Journal of Power Source*, vol. 155, pp. 66-71, 2006.

[11] N. M.C. Martins, N. J.G. Carriço, H. M. Ramos, and D. I.C. Covas, "Velocity-distribution in pressurized pipe flow using CFD: Accuracy and mesh analysis," *Computers & Fluid*, vol.105, pp. 218- 230, 2014.

[12] D. L. Gutierrez, A. H. Guerrero, B. R. Alvarado, I. P. Raya, and A. A. Ordaz, "Performance analysis of a proton exchange membrane fuel cell using tree-shaped design for flow distribution," *International Journal of Hydrogen Energy*, vol. 38, pp.14750-14763, 2013

[13] B.R. Sivertsen and N. Djilali, "CFD-based modelling of proton exchange membrane fuel cells," *Journal of Power Sources,* vol. 141, pp. 65-78,2005

[14] P. A.C. Changa, J. St-Pierre, J. Stumper, and B. Wetton, "Flow distribution in proton exchange membrane fuel cell stacks," *Journal of Power Sources,* vol. 162, pp. 340-355, 2006

[15] N. M.C. Martins, N. J.G. Carriço, H. M. Ramos, and D. I.C. Covas, "Velocity-distribution in pressurized pipe flow using CFD: Accuracy and mesh analysis," *Computers & Fluids,* vol. 105, pp. 218-230, 2014

[16] J. Glandt, S. Shimpalee, W. K. Lee, and J. W. V. Zee, "Modeling the effect of flowfield design on PEM fuel cell performance" 2002

[17] K. I. Sainan, R. Atan, H. Husain and W. A. N. W. Mohamed, "Computational Model Analysis on a Bipolar Plate Flow Field Design of a PEM Fuel Cell" 2011

[18] N. Bunmark, S. Limtrakul, M. W. Fowler, T Vatanathama, and J. Gostick, "Assisted water management in a PEMFC with a modified flow field and its effect on performance," *International Journal of Hydrogen Energy*, vol. 35, pp.6887-6896, 2010

[19] E. Carcadea, M. Varlam, I. Stefănescu, L. Pătularu, A Marinoiu, V Tanislav, and S. Enache, "Effects Of Flow Field On PEM Fuel Cell Performance," *Progress of Cryogenics and Isotopes Separation*, vol.

[20] B. ZareNezhad, and M. M. Sabzemeidani, "Predicting the Effect of Cell Geometry and Fluid Velocity on PEM Fuel Cell Performance by CFD Simulation," *Journal of Chemical Technology and Metallurgy,* vol. *50,* pp. 176-182, 2015

[21] Y. Yi, T. Z. kai, Z. Z. Gang, and P. Mu, "Gravity effect on the performance of PEM fuel cell stack with different gas manifold positions," *International Journal Of Energy Research,* Vol.36, pp. 845-855, 2011

[22] V. Radhakrishnan, and P. Haridoss, "Effect of GDL compression on pressure drop and pressure distribution in PEMFC flow field," *International Journal of Hydrogen Energy*, vol. 36, pp.14823-14828, 2011

[23] A. Kabza, *Fuel Cell Formulary,* 2015

Investigation and Analyse of Bone-Implant using Finite Element Analysis

Ahmed Saeed Abood Bahagari[1*], Thein Chung Ket[2], Leong Wai Yie[3]

[1]*Taylor's University Lakeside Campus, Malaysia*

[*]chungket.thein@taylors.edu.my

Abstract

Dental implant is an essential treatment choice to replace a posterior single or different missing tooth. For quite a long time were encouraged to put their coveted aside and acknowledge the limits of a FPD (Fixed Partial Dentures). The essential motivation to propose or perform a treatment ought not to be identified with treatment time, expenses, or trouble of the methodology however rather ought to consider the best conceivable long duration solution for every person. The purpose of this project is to research and investigation the impact of implant core geometric on forces distribution and to examine over-load hazard at the implant as well as the mandibular molar area. A 3D-finite element model of ITI standard implant was used. Therefore, the three instances of forces applied on the top surface of the dental implant. The Von Mises maximum value occurred at the bottom of the implant while the minimum existed in the top of the implant. The load transfers along the implant from the top to the bottom and into the material in which the implant is located. The deformation result of the simulation showed that the deformation of the titanium implant is slightly small. The load transfers along the implant from the top to the bottom and into the material in which the implant is located. The deformation result of the simulation showed that the deformation of the titanium implant is slightly small. Based on the information collected from this investigation, improve the design of implant is the main influence factor on the stability function

Keywords: Dental implant, Stress distribution, finite elements analysis,

1. Introduction

Numerous individuals, whether because of disregard, injury, bad fortunes or simply getting older, will lose many or the majority of their teeth. Lost teeth can have a critical effect on your appearance, as well as on your fearlessness and general wellbeing. Missing teeth can have an emotional effect on an individual's appearance. Individuals with terrible or lost teeth regularly abstain from grinning, and attempt to cover their mouths when they grin. They regularly evade social or business circumstances in light of the fact that they are humiliated about their teeth. Numerous pass up a great opportunity for critical exercises and other life practices due to their terrible teeth, their lost teeth, or their sick fitting dentures. Other than appearance, wasted teeth can have a huge effect on an individual's fearlessness. Individuals with missing teeth regularly express an inclination of jawbone impairment: As soon as a tooth is lost from gum infection or an extraction, the supporting bone in the jaw starts to disintegrate. This procedure is called resorption. The more extended a tooth is lost, the more prominent the bone misfortune. Thus, more of the jawbone breaks down until it gets to be emaciated and perceptibly smaller: that they have lost their liveliness, or their capacity to talk out in the open or to be dynamic. It is just after their teeth are lost that abundant individuals understand that a good health of mouth is important for keeping up a decent personal satisfaction

Teeth give a bigger number of capacities than simply the capacity to bite. They are essential for the soundness of the gums, jaw, and other teeth too. The following impacts of lost teeth can be adverse to long period oral and therapeutic wellbeing [1].

- **An off-nibble relationship**: Having holes where teeth are lost influences the way the jaw closes. Case in point, a neighboring tooth may tilt or float into an open space left by a missing tooth bringing about the contradicting jaw line to have chomp relationship issues. TMJ (intense and ceaseless agony and issues with the jaw joint) may be created by tooth misfortune. Moreover, sustenance can get to be caught in open spaces, expanding the danger of rot and gum ailment.

- **Jawbone impairment**: As soon as a tooth is lost from gum infection or an extraction, the supporting bone in the jaw starts to disintegrate. This procedure is called resorption. The more extended a tooth is lost, the more prominent the bone misfortune. Thus, more of the jawbone breaks down until it gets to be emaciated and perceptibly smaller.

- **Nutrition:** As teeth are missing, it gets to be harder to consume and bite nourishment. Studies have demonstrated that 29% of denture wearers consume just mellow or crushed nourishments and half keep away from all types of food.

Dental implant offers an alternate choice to consider truly when substituting lost teeth. Consequently, dental implants are completely put in the bone in request to substituting the root base of the tooth and permit the establishment of a dental prosthesis. Dental implant was enhanced lately, supplying patients with unparalleled levels of adequacy, accommodation, and reasonableness. This is one of the primary

reasons why such a large number of dental specialists propose dental implant as their favored strategy to substitute missing teeth. Titanium dental implants can offer several profits. Since they give osseointegration which is defined as an immediate structural and useful association between requested, the bone and the surface which carrying the implant, is basic for implant dependability, and is considered an essential for implant stacking and long period clinical accomplishment of endosseous dental implants [2]. The jawbone, they are more steady than dentures. Patients with dental implants may have the capacity to talk and consume more effectively without facing the danger of their dentures dislodging. Dentures oblige substitution when the gum tissue psychologists and changes the fit; implants are not influenced by this issue. The upkeep and cleanliness of dental implants are less demanding than with dentures. An alternate purpose behind proceeded with development of the worldwide business sector for dental implants is that dental implants offer a successful treatment for edentulism and on account of the climbing interest for nonessential dentistry worldwide over all age bunches [3].

A fundamental implant framework could be constructional of three different parts: these distinctive structural parts may take the structure of either one, a few separate parts. Figure 1 demonstrates three different parts diagrammatically and how they are connected with each other [4]**.**

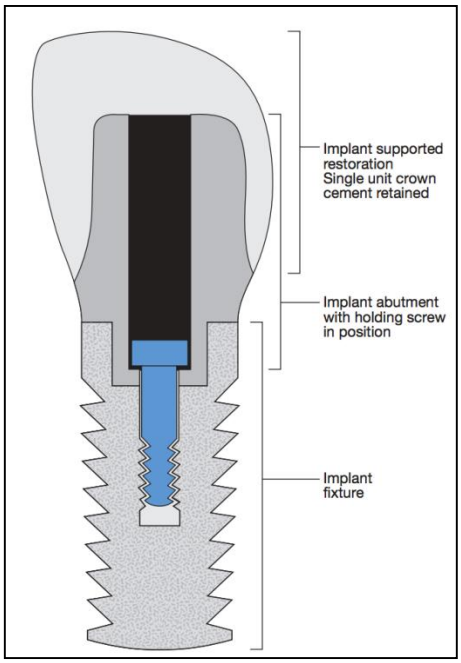


Figure 1: Dental implant with three different parts

The bone implant interface consists of three parts. Firstly, the segment that is osseointegrated with bone is normally alluded to as the implant fixture and gives maintenance and backing for the prosthesis. Secondly, the abutment is the part that is associated with the fixture and navigates the overlying delicate tissue to give an association between the fixture and the overlying restoration. Lastly, the last part of the framework is the restoration which additions backing as well as maintenance from the fixture through the abutment [4].

Therefore, the biologic reaction of issue that needs to be addressed forces and determination of implant positions influence implant lifespan. Since forces are exchanged to bone through implant, cautious arranging and execution of the fixture insertion are significant factors in accomplishment the forces distribution in the bone. Subsequently, the exchange of useful loads and going with stress appropriation in the implant prosthesis gathering rely on upon the material properties and locative shape arrangement model of every part [5]. Stress analysis of dental implant is indispensable for the examination stress in the bone and most extreme moorage achievement. Erroneous load or overloading might feel pain in the bone and subsequent implant lack. Meanwhile clinical definition of stress distribution in bone is unrealistic, in this manner; substitution strategy ought to be utilized. Consequently, Finite Element (FE) analysis, which is an authoritative procedure, is utilized to focus the data about stress in implant-bone structure.

The objective for this research is to investigate the impact of implant core geometric on forces distribution and to examine hazard at the implant. The mandible has constructional characteristic for an outside layer of high elastic modulus cortical bone and an internal layer of spongy cancellous bone with low elastic modulus. In addition, the mechanical cortical bones properties are not the same as these of cancellous bones [6]. Lastly, the result of the forces distribution and deformation in the implant bone has been obtained and analysed by Finite Elements Analysis (FEA).

2. Materials and Methods

To assess the stress distribution in the bone implant and the bone, dental implant was directed by a finite element analysis (FEA). In this manner, the 3D-finite element demonstrated utilizing designing software (SolidWorks) and simulated utilizing ANSYS as shown figure 2. The use of titanium alloys is due to their excellent corrosion resistance. Based on galvanic series, titanium is the fourth high corrosive resistance element in the series [7]. Additionally, that is a direct result of their strength, a high strength into weight ratio and low modulus of elasticity. Titanium keeps on being generally utilized as a part of biomedical applications. [8]. Thus, titanium (Ti-6AI-4V) implant is the first decision for dental implant. Figure 1 demonstrates both threaded dental implants were breaking down: ITI Implant and ITI Implant Plus (by Institute Straumann, AG). Figure 3 demonstrates that ITI implant has total length (l) of 12.8 mm, max diameter (d) of 4.8 mm; thread pitch (p) of 1.15 mm and thread depth (x) of 0.25 mm. Figure 4 demonstrates that ITI implant has total length (l) of 12.8 mm, max diameter (d) of 6.5 mm; thread pitch (p) of 0.98 mm and thread depth (x) of 0.2 mm.

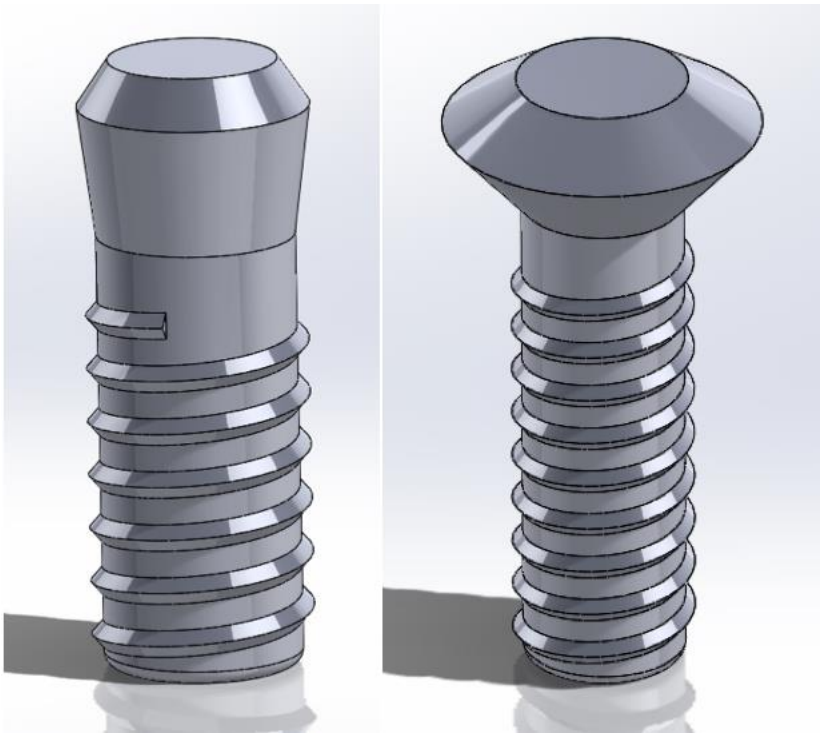


Figure 2: 3D modelling of both Implants

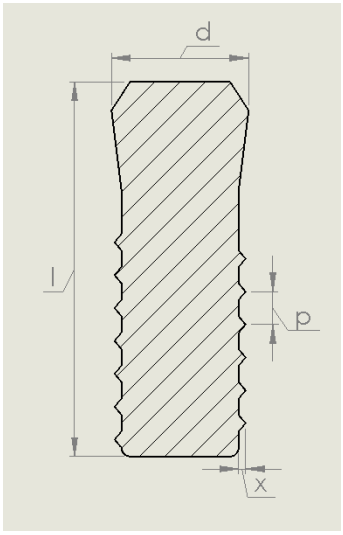


Figure 3: Dental implant dimensions

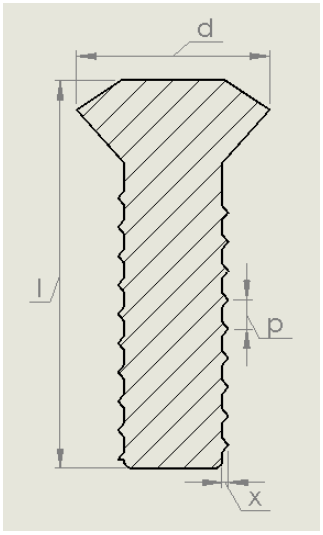


Figure 4: Dental implant plus dimensions

Furthermore, implant material assumed to have a homogenous volume and a linearly elastic isotropic conduct. Also, titanium alloy has Poisson's ratio of 0.36 and a Young's modulus of 96 GPa. In addition, the mandibular bone has two different components where the outer cortex is cortical while the centre is cancellous bone [6]. Figure 5 shows the mandibular bone components with inserted dental implant. Table 1 shows the mechanical properties of the implant and the mandibular bone [9-10].

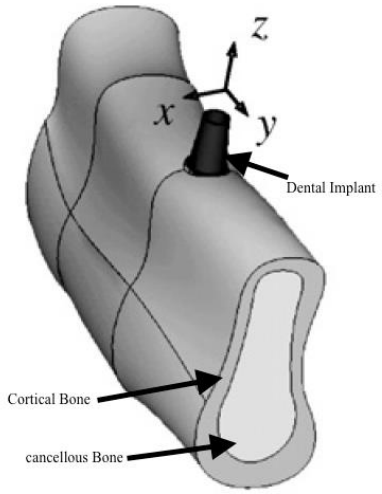


Figure 5: The mandibular Bone components with inserted dental implant

Table 1: Mechanical material properties

Material	Modulus of elasticity/GPa	Poisson ratio, υ
Titanium	96	0.36
Cortical bone	13.70	0.30
Cancellous bone	1.37	0.30

2.1 Loads and Boundary condition

Static structure investigations of implants ought to be directed to guarantee that the design is safe. According to previous researchers work, table 2 demonstrates the three instances of forces connected on the top surface of the dental implants. Complete osseous joining in the middle of implant and living tissues was assumed and in addition the bone section thought to be settled at the base. Figure 6, and 7 show the forces applied and the boundary condition which considered in the simulations for both designs. Therefore, bone implant and the mandibular piece will be anatomized to estimate the stress distribution so that will help to understand the risk of overloading on the implant. As well as, the Von-Mises stress (σ_{VM}) will be utilized to indicate the level of the stress on the implants. Therefore, its yield is completely perfect with a finite element method utilized for consolidating the majority of the parts containing the bone implant model and for producing and understanding the discrete finite element meshes.

Table 2: The three load cases

Load case	Vertical force (N)	Oblique force With 45 degree (N)
One	100	50
Two	200	100
Three	300	150

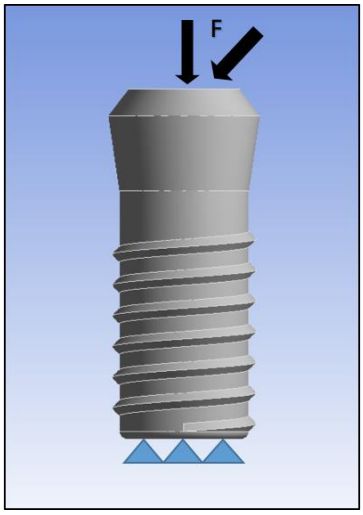


Figure 6: The loads and boundary condition on the implant (30 % of BIC)

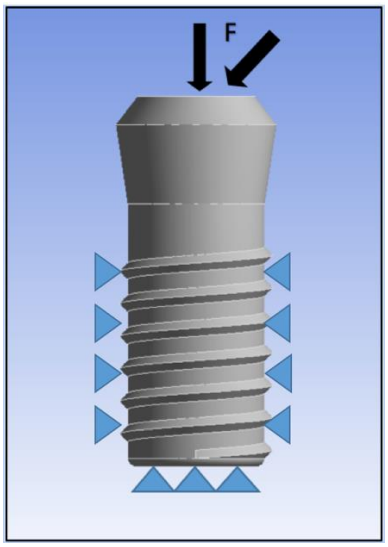
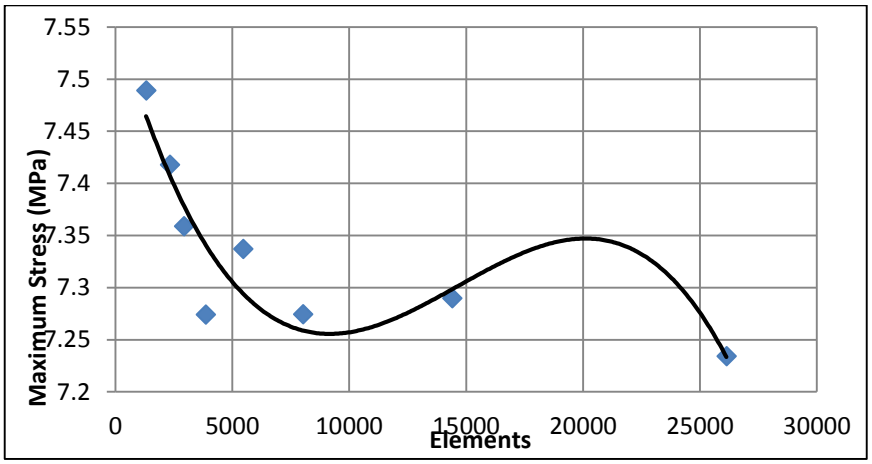


Figure 7: The loads and boundary condition on the implant (70 % of BIC)

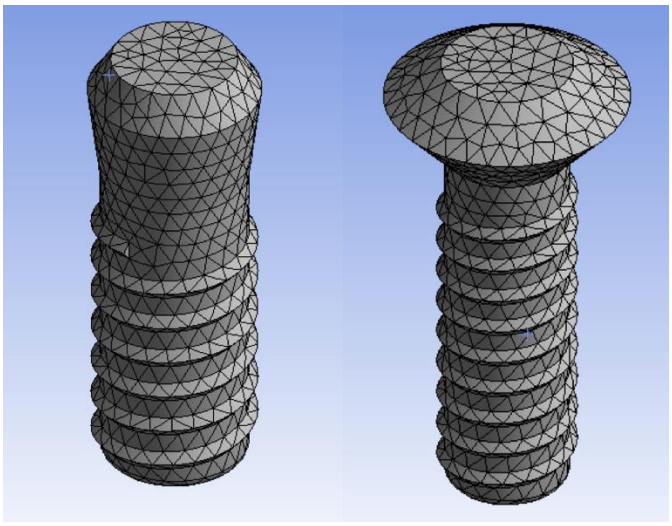
2.2 Convergence analyse

3D-finite element models were directed to convergence test to guarantee that the quantity of element discretization has been utilized is sufficient. As there are no suitable test results in the literature to contrast our outcomes with approve the finite element model, many distinct models for the dental implant with changing quantities of element were compared and the outcomes of the convergence was inspected utilizing the maximum tensile stress under a vertical force condition. The outcomes and the quantity of elements are appeared in graph 1. From the graph, the convergence for the models was gone after the accompanying mesh size which is 0.6 mm with pyramid shape for type of meshing. The most suitable type of element for both dental implant designs is in 3-Dimensional as shown in figure 8. It is because the bone implant must be considered as solid material to obtain relevant maximum stress

results. Table 3 shows the amount of elements and nodes constructed in ANSYS for both implants.



Graph 1: Convergence Analyze



(A) (B)

Figure 8: Bone implant meshing, A: ITI Implant and B ITI Implant Plus

Table 3: The amount of elements constructed in ANSYS for both implants

Type of implant	No. of element	No. of node
ITI Implant	8026	12401
Implant Plus	6843	10928

3.0 Results

In this investigation, Von Mises stress was chosen due to the complicated nature of the bone shape. In any case, in this study, the bone is delegated fragile and an isotropic material, in this way, standard stress is valuable to examine the work. For the dental implant Von Misses stress might be critical to understand the stress happened. Subsequently Von Mises stress circulation is approaching. The subsequent Von Mises stress qualities, processed in the bone implant of the framework under the three load cases. This study is basically of stress level qualities in the mandibular

bone. For this reason, Von Mises stress investigation was figured for the bone implant of the framework in the three load cases.

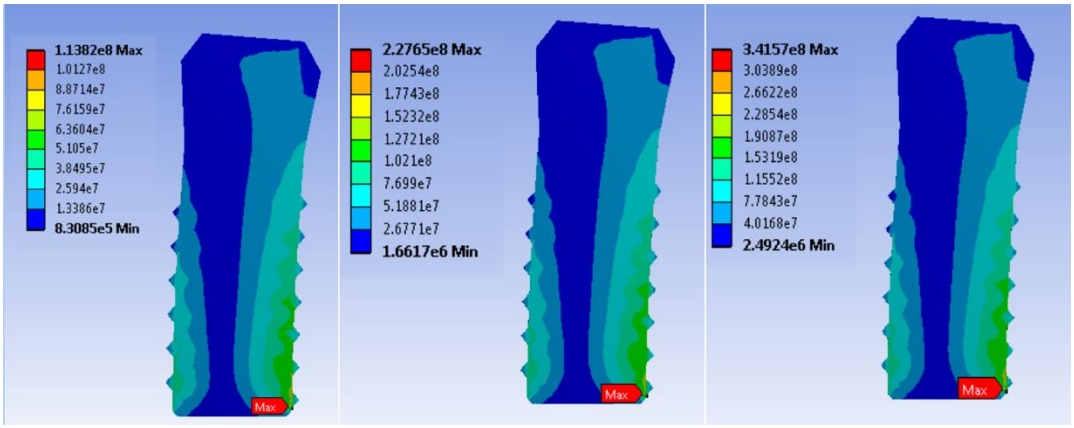
3.1 First case of boundary condition

3.1.1 ITI Standard Implant

The peak value of Von Mises stresses that took a place at the implant for first boundary condition case are given in table 4. Figure 9 demonstrates the stress distribution in the implant fixture in static loading. Maximum stress in all load cases were situated at the bottom region of the implant. The peak value of Von Mises stresses for the implant in all loading cases were 113.8, 227.6 and 341.5 MPa, respectively. For the static loading, the peak values of Von Mises stress in the implant structure for all load cases were 24.6%, 49.26% and 73.9% of the yield strength, respectively. Comparing the peak values of stress at the implant body of static loading condition were less than the Commercially Pure (CP) titanium which has yield strength of 462 MPa [11]

Table 4: The peak values of Von Mises stress in load cases for the first boundary condition

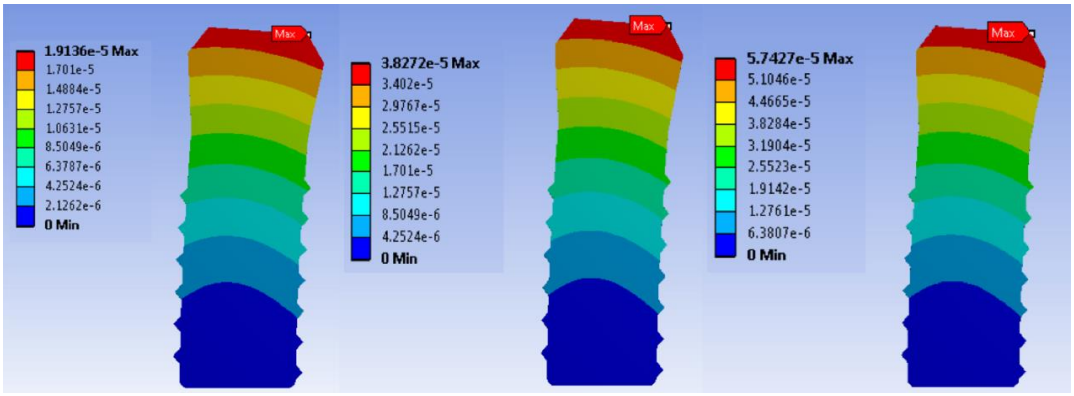
Load Case	Loads		Maximum Equivalent (Von Mises) stress (MPa)
	Vertical (N)	oblique (N)	
A	100	50	113.8
B	200	100	227.6
C	300	150	341.5



(A) (B) (C)

Figure 9: The Von Mises stress on the implant, (A) load case one, (B) load case two and (C) load case three

Deformation that occurred at the implant for first boundary condition case forces are presented in figure 10. The maximum deformation value in the bone implant for all load cases are 1.701×10^{-5}, 3.827×10^{-5} and 5.742×10^{-5} m. Based on the trend of results in table 5, the deformation values increase proportional to the forces applied on bone implant. For all cases, most of deformation occurs at the top part of the bone implant.



(A) (B) (C)

Figure 10: The deformation on the implant, (A) load case one, (B) load case two and (C) load case three

Table 5: Deformation in load cases for the first boundary condition

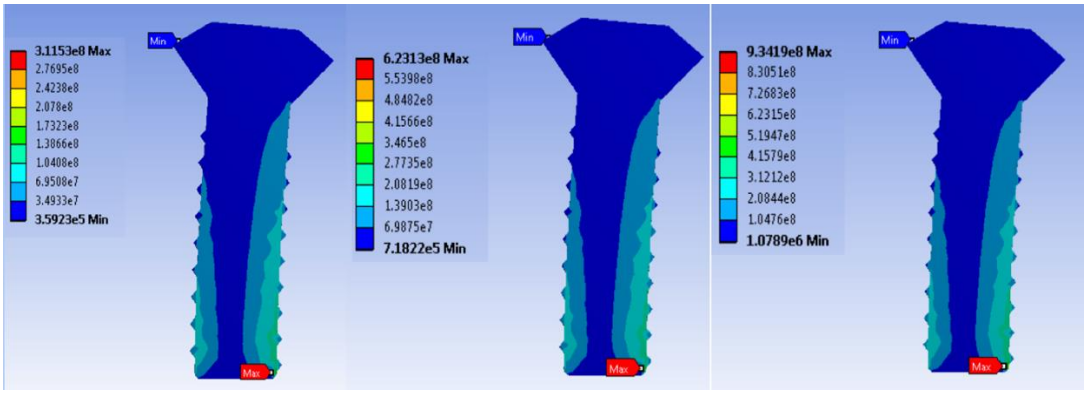
Load Cases	Load		Deformation (m)	Deformation (μm)
	Vertical (N)	Oblique (N)		
A	100	50	1.701×10^{-5}	17.01
B	200	100	3.827×10^{-5}	38.27
C	300	150	5.742×10^{-5}	57.42

3.1.2 ITI Standard Implant Plus

The peak value of Von Mises stresses that took a place at the implant for first boundary condition case are given in table 6. Figure 11 demonstrates the stress distribution in the implant (Plus) fixture in static loading. Maximum stress in all load cases were situated at the bottom region of the implant. Maximum Von Mises stresses for the implant in all loading cases were 311.5, 623.1 and 934.2 MPa, respectively. For the static loading, the peak values of Von Mises stress within the implant body for all load cases were 67.4%, 134% and 202%. of the yield strength, respectively. Maximum stress values at the implant body of static loading condition were less the Commercially Pure (CP) titanium which has yield strength of 462 MPa [11]

Table 6: The peak values of Von Mises stress in load cases for first boundary condition case

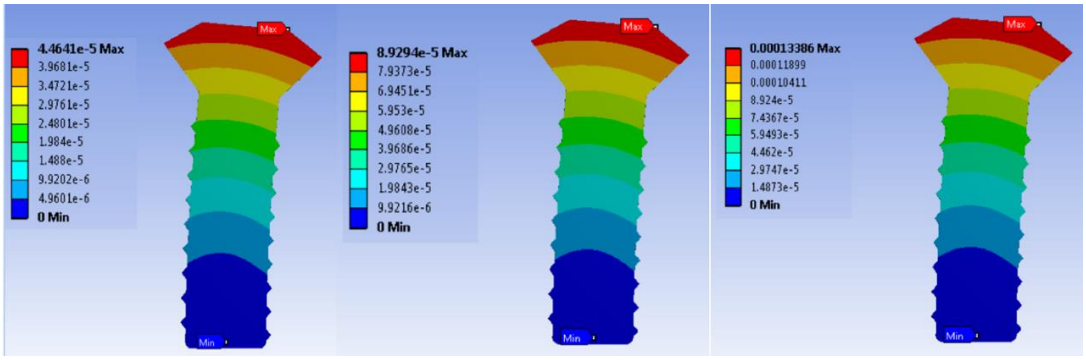
Load Case	Loads		Maximum Equivalent (Von Mises) stress (MPa)
	Vertical (N)	Oblique (N)	
A	100	50	311.5
B	200	100	634.2
C	300	150	934.2



(A) (B) (C)

Figure 11: Maximum Von Mises stress on the implant, (A) load case one, (B) load case two and (C) load case three for first boundary condition case

Deformation that occurred at the implant (Plus) for first boundary condition case forces are presented in figure 12. The maximum deformation value in the bone implant for all load cases are 4.4641×10^{-5}, 8.929×10^{-5} and 1.338×10^{-4}m. Based on the trend of results in Table 7, the deformation values increase proportional to the forces applied on bone implant. For all cases, most of deformation occurs at the top part of the bone implant.



(A) (B) (C)

Figure 12: Maximum deformation stress on the implant, (A) load case one, (B) load case two and (C) load case three for first boundary condition case

Table 7: Deformation in load cases for first boundary condition case

Load Case	Loads		Deformation (m)	Deformation (μm)
	Vertical (N)	Oblique (N)		
A	100	50	4.464×10^{-5}	44.64
B	200	100	8.929×10^{-5}	89.29
C	300	150	1.338×10^{-4}	133.8

3.2 Second case of boundary condition

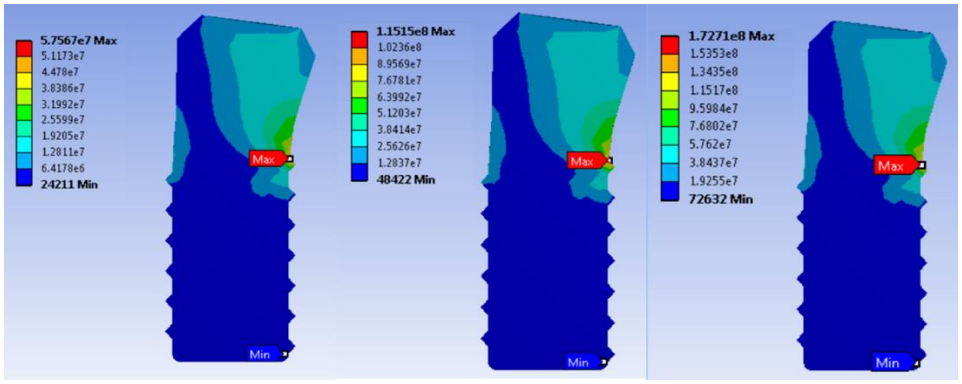
3.2.1 ITI Standard Implant

The peak values of Von Mises stress that took a place at the implant for second boundary condition case are given in table 8. Figure 13 demonstrates the stress distribution in the implant fixture in static loading. Maximum stress in all load cases were situated at the first thread of the implant. Maximum Von Mises stresses for the

implant in all loading cases were 57.5, 115.2 and 172.7 MPa, respectively. For the static loading, the maximum stress values within the implant body for all load cases were 12.45%, 24.9% and 37.4%. of the yield strength, respectively. The peak values of Von Mises stress within the implant body of static loading condition were less than the Commercially Pure (CP) titanium which has yield strength of 462 MPa [11]

Table 8: The peak values of Von Mises stress in load cases for second boundary condition

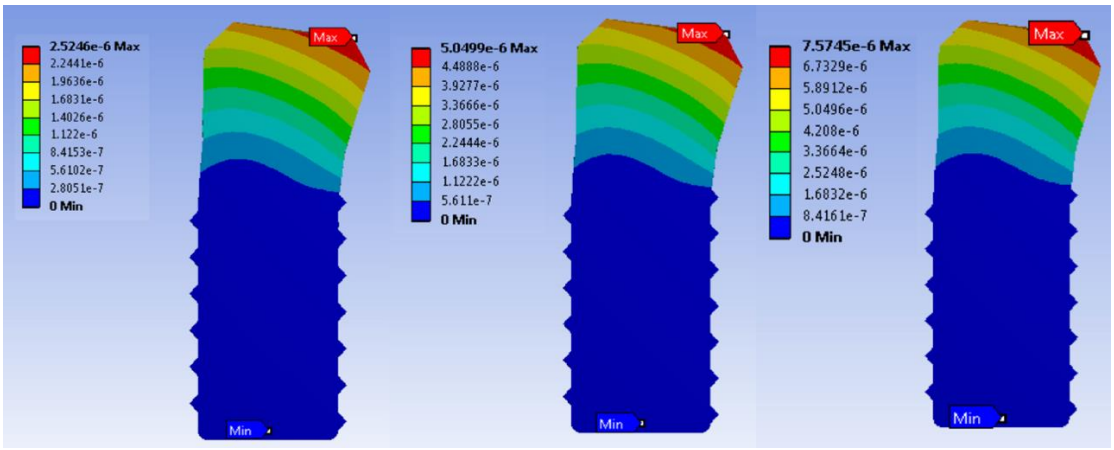
Load Cases	Loads		Maximum Equivalent (Von Mises) stress (MPa)
	Vertical (N)	oblique (N)	
A	100	50	57.5
B	200	100	115.2
C	300	150	172.7



(A) (B) (C)

Figure 13: The Von Mises stress on the implant, (A) load case one, (B) load case two and (C) load case three

Deformation that occurred at the implant for second boundary condition case forces are presented in figure 14. The maximum deformation value in the bone implant for all load cases are 2.5246×10^{-6}, 5.0499×10^{-6} and 7.5745×10^{-6}m. Based on the trend of results in Table 9, the deformation values increase proportional to the forces applied on bone implant. For all cases, most of deformation occurs at the top part of the bone implant.



(A) (B) (C)

Figure 14: The deformation on the implant, (A) load case one, (B) load case two and (C) load case three

Table 9: The deformation in load cases for the second boundary condition

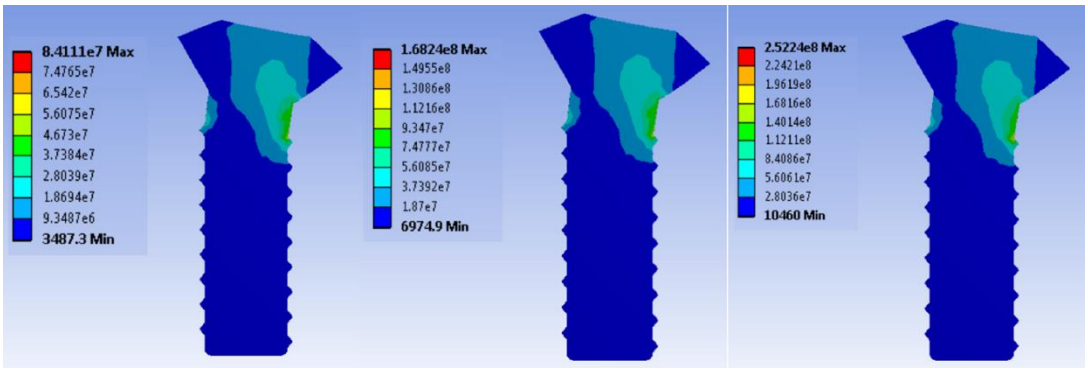
Load Case	Loads		Deformation (m)	Deformation (μm)
	Vertical (N)	Oblique (N)		
A	100	50	2.5246×10^{-6}	2.5246
B	200	100	5.0499×10^{-6}	5.0499
C	300	150	7.5745×10^{-6}	7.5745

3.2.2 ITI Standard Implant Plus

The peak value of Von Mises stresses that took a place at the implant (Plus) for second boundary condition case are given in table 10. Figure 15 demonstrates the stress distribution in the implant (Plus) fixture in static loading. Maximum stress in all load cases were situated at the first thread of the implant. Maximum Von Mises stresses for the implant in all loading cases were 84.1, 168.2 and 252.2 MPa, respectively. For the static loading, The peak values of Von Mises stress within the implant body for all load cases were 18.2%, 36.4% and 54.5%. of the yield strength, respectively. The peak values of Von Mises stress within the implant body of static loading condition were less than the Commercially Pure (CP) titanium which has yield strength of 462 MPa [11]

Table 10: The peak values of Von Mises stress in load cases for second boundary condition case

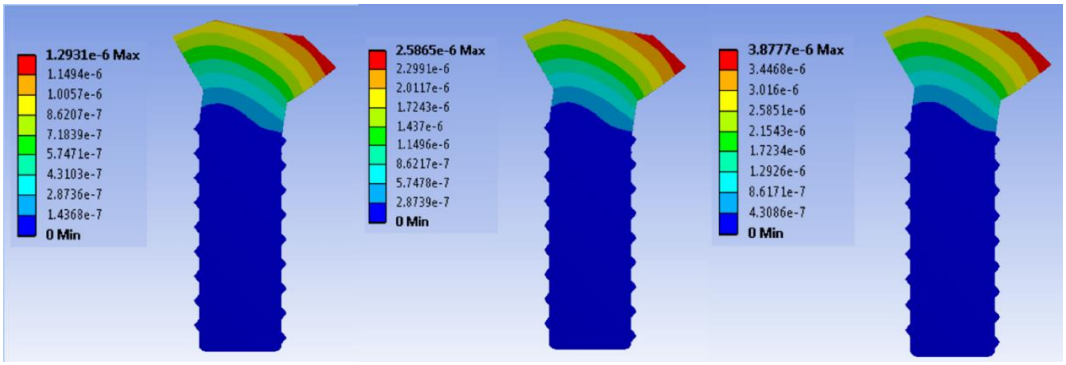
Load Cases	Loads		Maximum Equivalent (Von Mises) stress (MPa)
	Vertical (N)	Oblique (N)	
A	100	50	84.1
B	200	100	168.2
C	300	150	252.2



(A) (B) (C)

Figure 15: Maximum Von Mises stresses on the implant (plus), (A) load case, (B) load case and (C) load case for second boundary condition case

Deformation that occurred at the implant for second boundary condition case forces are presented in figure 16. The maximum deformation value in the bone implant (Plus) for all load cases are 1.293×10^{-6}, $2.5865\times10^{-6}$and 3.8777×10^{-6}m. Based on the trend of results in Table 11, the deformation values increase proportional to the forces applied on bone implant. For all cases, most of deformation occurs at the top part of the bone implant.



(A) (B) (C)

Figure 16: Maximum deformation stress on the implant, (A) load case one, (B) load case two and (C) load case three for second boundary condition case

Table 12: Maximum deformation in load cases for the second boundary condition

Load Case	Loads		Deformation (m)	Deformation (μm)
	Vertical (N)	Oblique (N)		
A	100	50	1.293×10^{-6}	1.293
B	200	100	2.5865×10^{-6}	2.5865
C	300	150	3.8777×10^{-6}	3.8777

4 Discussion

The finite element technique is recommended to be utilized as a part of stress investigation in both industry and science. It is utilized for examining hip joints, knee prostheses and dental implants. The outcomes of the FEA calculation rely on upon numerous individual factors, comprehensive of properties of the material, interface fixed area, interface definition, furthermore on the general approach to deal with the model. It is clear that the introduced model was just an estimate of the clinical condition. The utilization of a 3D model simulation with the non-symmetric loading by the masticatory power on a dental implant brought about a more agreeable outcome of "clinical reality" than that accomplished with 2D models utilized in different investigations.

Demonstrating the definite complexity of the implant geometry, comprehensive of the thread helix of the fixture, was important for finite element examination. Modeling the exact implant will help to analyse the force distribution among the thread. Therefore, while using FEA to dental implants, it is essential to consider not just vertical force and horizontal forces but and a combined force due to performed more realistic occlusal directions.

Overload at the done implant interface most probably will cause crestal bone loss disease and early implant failure after forcing results [12]. This phenomenon could be more understandable by the analysis of FE of force distribution in the bone. the mechanical distribution of stress with the dental implant happens at the bone contact [13]. Thus, when the contact area of the bone is small with implant body, the greater the overall stress.

4.1 Stress distribution

The elements of implant are essentially subject to the immediate holding with the encompassing bones. The long-term achievement of an implant is dictated by reliability and stability of the implant bone interface, and the achievement or failure of an implant is dictated by the way that the stresses at the bone-implant interface exchange to the encompassing bones [11]. With a specific end goal to guarantee the long term stability of an implant, the implant

ought to be planned as per two primary standards. In the first place, the load ought to be minimized to prevent from surpassing its physiological resistance as overloading could bring about bone resorption or fatigue failure of the implant. Then again, under loading might cause disuse atrophy and subsequent bone loss [14]. Second, boundary condition or the interface area among the bone and dental implant ought to be expanded to reduce the bone interface stress. The structural characteristic for the mandible demonstrates an external layer of thick cortical bone and an internal layer of loose cancellous bone. Both the modulus of elastically and mechanical strength of cortical bone (10-18 GPa) are higher than those of cancellous bone (1.3-4 GPa) [11].

In this study, the vertical force and oblique were combined and applied to analyse the stress distribution through dental implant. Based on the figures 9, 11, 13 and 15 the maximum Von mises stress for all load cases is located at the same position with respect to each boundary condition cases. In order to fulfill the objective of this study, the location of the maximum stress concentration is managed to be shifted closer to the cortical bone by increasing the boundary condition or interface area among the bone and implant. Therefore, the position of maximum stress concentration is shifted from bottom part to the first thread of the implant which is based on research finding where the maximum stress concentration from the implant body to first or second thread of dental implant [15].

4.2 Deformation

The wider surface of the top head implant was not substantial for the deformation increase under vertical force. On the other hand, it is relevant for oblique forcing. According to the literature, the micro-movement of the dental implant is limited due to the elastic limit of the bone, which takes place between 3 to 5 μm vertically as well as from 10 to 50 μm horizontally. In case the deformation across these limits, the 'osseointegration' might fail [16].

4.2.1 ITI Standard Implant

Based in the result in table 5 for the first boundary condition, the deformations which are 17.01 and 38.27 μm were within the limit for A and B load cases. Thus, it is safe to apply the force without causing a failure. While, the deformation in load case C is exceed the limit of the bone. Thus, the force applied in load case C is considered overload, also it may cause fracture. Furthermore, based in the result in table 9 for the second boundary condition, the deformation in all load cases is less than 10 μm. Through this result, it is not safe to utilized the implant under the second boundary condition.

4.2.2 ITI Standard Implant Plus

Based on the result in table 7 for the first boundary condition, the deformation which is 44.64 μm was within the limit for load case A. But the deformation in load case B and C which are 89.29 and 133.8 μm were exceed the limit. On the other hand, and based on the result in table 12 for the second boundary condition, the deformation in all load cases is exceed the elastic limit.

Based on the forces applied on the implant, it found that the vertical load applied on the implant is not the main reason behind the deformation which is in agreement with the result of an earlier study [16]. Furthermore, the deformation due to stress concentration for the oblique load was nearly twice from load case A to load case B. At the same time, the deformation was one and a half from load case B to load case C. This might be understood by the theoretical analysis of previous research which proposed that vertical loads are more appropriate for uniform stress distribution in the implant [17]. Furthermore, the stress

concentration of the oblique forces is increased in implant and bone and generate a severe or bad moment in effected area [18].

5.0 Conclusion

In conclusion, two commercial implants were used. Thus, the 3D finite element models of dental implant were done using design software which is SolidWorks 14.0. Furthermore, FEA has been selected as the best appropriate technique to numerically, demonstrate to it by ANSYS software. So, the analysis system that being used was Static Structural. Thus, the most suitable type of meshing element for both dental implant designs is in 3-Dimensional due to the complexity of the geometry. It is to ensure the feasibility and smooth meshing process by eliminating sophisticated curves in the bone implant design. There are two cases of boundary condition as well as three load cases were investigated. The finite element method has limitations inherent to computerized simulation: for instance, the properties of the chosen materials were assumed as isotropic, homogeneous, and linear, contrasting from the clinical cases of bone tissue. Whereas, this methodology is based on findings in literature of bone biomechanics.

In finite element model investigation, both dental implants were tested under two different boundary conditions while the rest of parameters were constant. The first boundary condition showed that the maximum stress concentration is located at the bottom of both implant. Therefore, the cancellous bone experienced more stress than the cortical bone. on the other hand, the second boundary condition showed that the maximum stress concentration is located at the first thread in both implants. Therefore, the implant with a bigger diameter showed better stress distribution compare to the smaller diameter implant. On the other hand, the result of the deformation of the bigger diameter implant is less than the smaller diameter implant in all boundary condition cases.

Reference

[1] P. E. Petersen, "Oral Health," in *International Encyclopedia of Public Health*, H. K. Heggenhougen, Ed., ed Oxford: Academic Press, 2008, pp. 677-685.

[2] S.Anil, P.S. Anand, H. Alghamdi and J.A. Jansen (2011). Dental Implant Surface Enhancement and Osseointegration, Implant Dentistry - A Rapidly Evolving Practice, Prof. Ilser Turkyilmaz (Ed.) ISBN: 978-953-307-658-4.

[3] Carlos Nelson Elias (2011). Factors Affecting the Success of Dental Implants, Implant Dentistry – A Rapidly Evolving Practice, Prof. Ilser Turkyilmaz (Ed.), ISBN: 978-953-307-658-4, InTech, DOI: 10.5772/18746.

[4] B. Reinhardt and T. Beikler, "Chapter 4 - Dental Implants," in *Advanced Ceramics for Dentistry*, J. Z. Shen and T. Kosmač, Eds., ed Oxford: Butterworth-Heinemann, 2014, pp. 51-75.

[5] B. Şimşek, E. Erkmen, D. Yilmaz, and A. Eser, "Effects of different inter-implant distances on the stress distribution around endosseous implants in posterior mandible: A 3D finite element analysis," *Medical Engineering & Physics*, vol. 28, pp. 199-213, 4// 2006.

[6] van OSTERWYCK H, DUYCK J, VANDER S, VANDER P G, DECOOMANS M, LIEVEN S, PUERS R, NAERT L. The influence of bone mechanical properties and implant fixation upon bone loading around oral implants [J]. Clin Oral Implants Res, 1998, 9(6): 407−412.

[7] R. Winston Revie, Herbert Henry Uhlig, (2011). Uhlig's Corrosion Handbook, 3rd Edition, John Wiley & Sons, pp. 233-245, DOI: 10.1002/9780470872864

[8] F. Mollica, L. Preziosi and K. Rajagopal, *Modeling of biological materials*. Boston, Mass.: Birkhäuser, 2007.

[9] Rho JY, Ashman RB, Turner CH. Young's modulus of trabecular and cortical bone material: Ultrasonic and microtensile measurements. J Biomech. 1993;26:111-119.

[10] Kitamura E, Stegaroiu R, Nomura S, et al. Influence of marginal bone resorption on stress around an implantda three-dimensional finite element analysis. J Oral Rehabil. 2005;32:279-286.

[11] L. CHEN, H. HE, Y. LI, T. LI, X. GUO and R. WANG, 'Finite element analysis of stress at implant–bone interface of dental implants with different structures', *Transactions of Nonferrous Metals Society of China*, vol. 21, no. 7, pp. 1602-1610, 2011

[12] M. Aljuboori and R. Saini, 'Crestal Bone Regeneration in Defective Bone Implants', *International Journal of Experimental Dental Science*, vol. 3, pp. 95-97, 2014.

[13] S. Fawzi, 'The Effect of Dental Implant Design on Bone Induced Stress Distribution and Implant Displacement', *International Journal of Computer Applications*, vol. 74, no. 17, pp. 15-21, 2013.

[14] T. KITAGAWA, Y. TANIMOTO, K. NEMOTO and M. AIDA, 'Influence of Cortical Bone Quality on Stress Distribution in Bone around Dental Implant', *Dental Materials Journal*, vol. 24, no. 2, pp. 219-224, 2005.

[15] R. Chowdhary, A. Halldin, R. Jimbo and A. Wennerberg, 'Evaluation of Stress Pattern Generated Through Various Thread Designs of Dental Implants Loaded in a Condition of Immediately After Placement and on Osseointegration—An FEA Study', *Implant Dentistry*, vol. 22, no. 1, pp. 91-96, 2013.

[16] S. Moraes, F. Verri, J. Junior, D. Almeida, C. Mello and E. Pellizzer, 'A 3-D Finite Element Study of the Influence of Crown-Implant Ratio on Stress Distribution', *Brazilian Dental Journal*, vol. 24, no. 6, pp. 635-641, 2013.

[17] G. Kumar, L. Kovoor and V. Oommen, 'Three-dimensional finite element analysis of the stress distribution around the implant and tooth in tooth implant-supported fixed prosthesis designs',*Journal of Dental Implants*, vol. 1, no. 2, p. 75, 2011.

[18] J. Rubo and E. Capello Souza, 'Finite-Element Analysis of Stress on Dental Implant Prosthesis',*Clinical Implant Dentistry and Related Research*, vol. 12, no. 2, pp. 105-113, 2009.

Design of the Shape and Size of Test Model used in Wind Tunnels at Low Subsonic Speeds

Amir Karimi*, Abdulkareem Shafiq Mahdi Al-Obaidi

School of Mechanical Engineering, Taylor's University, Malaysia

*karimitabassi.amirjavad@sd.taylors.edu.my

Abstract
Wind tunnels are devices that aid researchers in analyzing the effects and nature of air movement around and over objects. Among other purposed, wind tunnels have mainly been employed in the safety and improvement of air transportation vehicles like airplanes and spacecraft by testing various models to observe the flow velocity and whether the conditions affecting the flow may be improved by changing shape and size of the test models. In order to accurately measure the aerodynamic characteristics of a prototype, it is necessary that its shape and size must be similar to the model. The aim of this paper is to design a test model shape and size for the test section of the Taylor's Wind tunnel using analytical and experimental methods. The main objective of this research is to discover the optimum scale of a low speed wind tunnel model without affecting the flow conditions around the model. The expected results of velocity and pressure distribution around the test model at different angles of attack are analytically obtained using continuity and Bernoulli's equations.One of the most common instruments used in experimentation is the Hot Wire Anemometer & Data Logger which are used to measure flow velocity in the test section. The analytical and experimental results are then compared in the form of tables and graphs to assess the reliability and accuracy of each method. The final design should be an accurately scaled down model of the airfoil prototype produced for testing at Taylor's University low speed wind tunnel. The whole procedure for designing the optimum airfoil model is then noted in the form of a user manual to guide the wind tunnel's users.

Keywords: Low speed wind tunnel, optimal test model, aerodynamic characteristics, analytical and experimental methods. Bernoulli's equation

1. Introduction

1.1. Background Research

The field of wind engineering is one that has been continuously developing over the years. Structures known as wind tunnels have been directly and indirectly involved in the progression of wind engineering. Wind tunnels are devices that allow engineers to move air over objects or vehicles and to visualize its movement patterns and other physical attributes based on its aero dynamical properties. Air transport is increasingly evolving and is currently the most popular type of transportation for long distances. Therefore, it is of utmost importance that planes are able to perform at their peak while providing a safe atmosphere for the passengers inside. One of the tools that assist in achieving these tasks is a wind tunnel [1]. The wind tunnel has a number of various functions. It can be used to investigate scale models of aircrafts in order to observe their reactions during periods of take off, cruising and landing [2]. Engineers are able to carry out tests on new materials such as wood, steel and alloys as well as various shapes to employ as aircraft parts for the improvement of airplanes and their safety. The wind tunnel operates by possessing powerful fans on one side which move air through the tube. The model which is to be tested is secured in the test section of the tunnel and the air that moves around the object. This assists the user in obtaining an image that portrays the nature of fluid flow around a scaled model of a real object. This act is known as flow visualization [3]. Observation of air movement may be carried out by smoke or dye or even by attaching a thread to the object being tested.

Wind tunnel tests play a significant role in determining the reaction of structures to wind as numerical calculations are deemed unfavorable in most situations. However, in order to obtain an accurate prediction of the response, the test model must be correctly defined in terms of its shape and size. This task may prove to be challenging as the length of the manufactured test model is considerably scaled down from the actual prototype. This goes on to show that to obtain reliable experimental results, there are a number of conditions that have to be met and extra experimental analysis to be carried out on larger scales of the test models. This is because some elements of the model could alter the aerodynamic behavior of the model. Dimensional analysis is the main tool used for this practice. The laboratory results gained from the model can be applied to the real prototype as long as similar key dimensional parameters between them are maintained [4]. Verifying the quality of flow in the wind tunnel test section is a critical feature that is based on the maximum achievable speed, flow uniformity and turbulence levels. The test section must be able to attain a controlled flow in order to display the required flow performance and quality parameters [5].

Scaling of wind tunnel data to conditions associated with free flight requires the consideration of several phenomena. These phenomena include model support interference effects as well as lower Reynolds numbers. Eckert and Hegen [6] studied the wall effects of a low speed wind tunnel on a military transporter A400M aircraft model. A 1:9 scaled model of the A400M was produced in order to generate measurements for the aircraft's control characteristics and low speed capabilities. These areas could not be studied under normal sizing of the prototype due to impracticality. Rolston [7] predicted that for an aircraft of high capacity, an increment of 1% in drag would result in the requirement of 3 additional tones of fuel at constant range. Moreover, the drag increment would cause a range reduction of 120

km to occur with the plane at its maximum takeoff weight. This is particularly important as it depicts the severe drawbacks that could occur if the scaling and modeling of the aircraft was not handled properly.

Wang et al. [8] investigated scaling effects in wind tunnel modeling. The purpose of this research was to discover how models of different scales reacted to velocity profiles. The results showed that the scale ratio of the roughness height is equal to the scale ratio of the boundary thickness. More importantly, the results depicted that the most similar and precise velocity profiles in the wind tunnel occured at a boundary layer scale ratio of 200-400 while turbulence intensity was apparent at a scale ratio of 200-600. The scaled models were also used to study the pressure effects on scaling. Based on the observation, it was concluded that a 10-15% difference in pressure coefficients would be present if the wrong scale ratio of either the boundary layer thickness or roughness height was used.

Albert et al. [9] did a comprehensive study on the granular drag of several distinct shapes through a spherical granular medium and on how the shape of that object affected jamming. The shapes studied included a sphere, a semi-sphere, a teardrop, a cone and a disk. In order to make sure that the experiment was conducted fairly and that the results were accurate, the different shapes were made from the same material (aluminum or brass) and their surfaces were similarly prepared and sand-blasted. It was discovered that relative to effects of shape on fluid drag, changing the geometry of the dragged object had a small impact on the drag force. They came to this conclusion by relating the diameter and depth of the sphere in the medium to the drag experienced on the sphere. The diameter dependance to the drag could be classified as quadratic but the depth dependence displays distinct nonlinearity. While the geometrical factors had little on the drag force, they are responsible for producing the magnitude deviations in the depth dependence functions. It was concluded that the streamlining of the object is one of the most influential geometrical factors on the decrease and increase of drag on the object. This conclusion was valid since the disc and semi-sphere shapes produce more drag than the sphere and teardrop shapes. Another geometrical factor that affects the drag force is the length of the dragged object in the flow direction. It was found out that drag has a linear relationship with the disc length and that it increases when the latter increases.

Measurements involving force undergo some data reduction to acknowledge the effects of Reynolds and Mach numbers on the model being tested. The most important tests are the ones that present diagnostic information the properties of air flow around and thru the model. In order for a wind tunnel experiment to be valid, both these numbers must correspond with flight conditions. Reynolds number refers to the ratio of inertial forces to viscous ones and it is used to dictate whether the flow will be laminar or turbulent. At high Reynolds numbers (>2100), the inertial forces will be greater than viscous forces and the flow will be turbulent. Alternatively, viscous forces will be greater than inertial ones at low Reynolds numbers (<1100) and a laminar flow will be present [10]. The laminar flow transits to a turbulent flow when the ratio of the density of fluid, velocity, diameter and fluid viscosity is the same. Reynolds number is important as it defines the aerodynamic properties of lifting surfaces and enables these properties such as lift and drag to be applied to real life full scale prototypes from the wind tunnel test models.

Laitone [11] tested rectangular platform wings at very small Reynolds numbers in a low speed and turbulence wind tunnel. NACA 0012 lift and drag measurements were analyzed with regards to cambered and thin flat plates. The test results revealed that a thin plate with a 5% circular arc camber was the optimum profile for Reynolds numbers below 70000. This was due to the fact that this specific thin plate profile generated the best lift-drag ratio at all levels of turbulence, and produced the highest lift coefficient at all the angles of attack tested. The aforementioned research is critical to the work being done in this work as the model tested is based off NACA 0012.

The NACA 0012 was chosen due to its use in many different constructions. The airfoil is used in the B-17 Flying Fort include aircrafts such as the B-17 Flying Fortress and Cessna 152 and the Sikorsky S-61 SH-3 Sea King helicopter [12]. One of the factors analyzed in this study is the effect of the angle of attack on the flow characteristics around the airfoil. A research study was carried out by Critzos et al [13] to display the NACA 0012 airfoil aerodynamic characteristics at various angles of attack ranging from 0 ° to 180 °. A low Reynolds number (1.8×10^0) and roughness for both leading and trailing edges were used. The highest lift coefficient was produced at an angle of attack of 5° for the airfoil's rounded edge. The lift coefficients attained for angles of attack from 25 ° to 125 ° were not dependent on the roughness and low Reynolds number. The surface roughness however, affected drag coefficients at 90 ° angle of attack with 2.08 and 2.02 being the values for smooth and rough airfoil surfaces respectively.

1.2. Objectives

The aim of this paper is to design an optimal test model shape and size for the test section of Taylor's Wind tunnel using analytical and experimental methods. This is first accomplished by obtaining the velocity at different areas of an empty wind tunnel test section. Next, a scaled down NACA 0012 model is placed inside the test section of the wind tunnel. Next, through the use of similarity rules and Bernoulli's equations, the various velocities present at different sections of the test model is obtained analytically. Finally, the velocity experiment is repeated with the model present inside the test section. This would allow the identification of the boundary layer surrounding the model and how it would change according to the velocity. This in turn can be used to obtain the lift and drags achieved by the airfoil and reach the final goal by ultimately finding the best size and shape of the model that will minimize the disruption of flow in the Taylor's low speed wind tunnel. Lastly, a user manual on designing an optimal model for low speed wind tunnel testing is produced for Taylor's Wind Tunnel users.

2. Research Methodology

2.1 Experimental Approach

2.1.1 Obtaining relation between velocity and fan frequency

There are a few experiments that have to be performed prior to experimentally obtaining aerodynamic characteristics of the wind tunnel model. One of these experiments is to discover how altering the wind tunnel's fan frequency would affect

the velocity of a specific point in the test section. Since the actual testing of model inside the test section would be carried out at a constant inlet velocity, the results of this experiment would allow the user to determine that value by accordingly adjusting the frequency of the fan.

The Taylor's wind tunnel is a standard open circuit type with a rectangular test section (Fig. 1). The structure measures 0.303m by 0.303 m in cross section and possesses a length of 0.885 m.



Figure 1. Taylor's Low Speed Wind Tunnel Test Section

A HVACR Datalogger plus a hotwire was used to measure the flow velocity at different frequencies and record the results. The steps of this procedure are described in the following:

1) Before the switch of the wind tunnel is turned on, all the equipment for measuring must be obtained and the walls in the test section must be secured as tightly as possible. This is to ensure that air would not escape the test section and affect the readings.
2) The anemometer is switched on and the tip of the hot wire is passed through the pre-mentioned hole in the center of the bottom cover. The hot wire must be held as vertical as possible perpendicular to the wind flow in the test section.
3) The wind tunnel is switched on and its frequency is set using the remote control on the device. This experiment was started with the lowest possible frequency that the wind tunnel could be set; 5Hz.
4) While the hot wire is inside the test section, the velocity of the wind is displayed on the DAQ for that particular frequency. It must be noted that the DAQ is only able to provide a range of values based on the current air standards and no definitive value is available. Therefore, in order to get the most accurate reading, the most common range that was displayed by the DAQ was noted and an average value was calculated.
5) The frequency of the wind tunnel was increased to 10 Hz and step 4) is repeated at 10 Hz, 15 Hz, 20 Hz, 25 Hz, 30 Hz and 35 Hz.
6) The hotwire is slowly removed from the bottom cover and placed safely in the cover. The wind tunnel frequency is lowered down to its minimum value before being switched off.

The results were tabulated (Table 1) at the end of the experiment.

Table 1. Results of frequency against velocity.

Frequency (Hz)	Average Velocity (m/s)
0	0
5	3.05
10	6.20
15	9.30
20	12.65
25	15.70
30	18.95
35	22.50

2.1.2 Obtaining velocity distribution in test section without test model

The next experiment that was done was to discover the different velocities present at each section of the test section. This is useful as it would help visualize the difference in velocity and the boundary layer present when the experiment is carried out with a test model inside. This would ultimately help in deducing which parts of the airfoil affect the velocity inside the test section. The test section (Fig. 3) is marked and split into 5 equal quadrants for x, y and z-axes. This would add up to 125 velocity readings across the surface area of wind tunnel for all three axes. Average values of each of the readings were taken to ensure reliability. The experiment was performed similar to the previous one and all the same precautions and steps were followed. The only difference was the addition of an adjustable height clamp. This was used to ensure that the anemometer remained still when taking readings at different heights in the test section. The readings were done two separate fan frequencies, which meant that the inlet velocities for each case were different. A representation of a graph for the velocity at x=1 at a speed of 9.3 m/s (Fig. 2) is shown below:

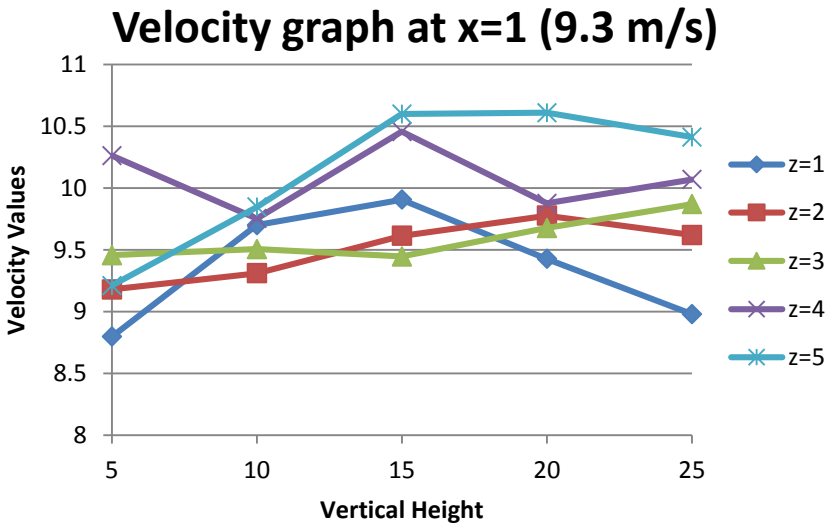


Figure 2. Velocity values in test section at section x=1

From the above graph it can be concluded that the highest velocity achieved at x=1 (0.177 m) from the left side of the wind tunnel, occurs at a vertical height of 15 cm at the end most of z-axis.

2.2 Analytical Approach

During flight, there are four main forces that are exerted on an aircraft. These include thrust, weight, drag and lift. The analytical method focuses on drag and lift. The airfoil's shape is one of the main contributors to lift. Generally, the design of an airfoil shape should offer high values of lift with low drag. There are a number of steps involved for deciding the best shape and size of the wind model analytically. Firstly, the airfoil's dimensions and nomenclature would have to be identified (Fig. 3).

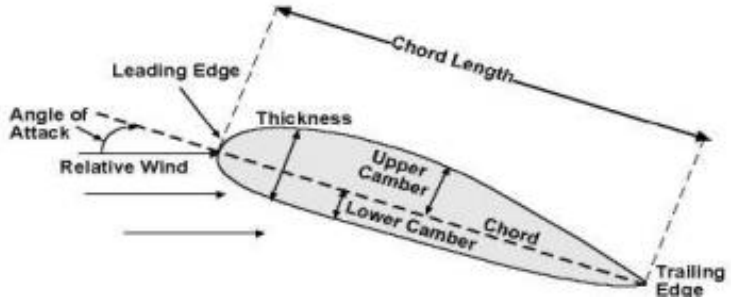


Figure 3. Main specifications of Airfoil [16]

Next, one of the most significant equations in airfoil calculations, the Bernoulli's equation is defined in Eq. (1).

$$p_1 + \frac{1}{2}\rho {v_1}^2 + \Upsilon Z_1 = p_2 + \frac{1}{2}\rho {v_2}^2 + \Upsilon Z_2 \quad (1)$$

Here, p is the pressure at a specific point, v is the fluid flow velocity, ρ is the density of the fluid, and z is the elevation above a reference point. However in this case, the heights are the same level and $z_1 = z_2$, the two parts of the equation cancel each other out and Eq. (1) may be written as Eq. (2).

$$\Delta p = \frac{1}{2}\rho {v_2}^2 - \frac{1}{2}\rho {v_1}^2 \quad (2)$$

Another equation that is used in the calculation is the mass flow rate equation (known as Continuity equations):

$$\dot{m} = \rho v A \quad (3)$$

In this case $\dot{m}$ represents mass flow rate while ρ, v and A signify the fluid density, inlet velocity and surface area respectively. Since the inlet velocity, fluid density and surface area are all fixed, this means that mass flow rate is constant. Therefore, the equation can be re-arranged to analytically provide the velocity at each point of a model that is placed in the center of the test section. The re-arranged equation is shown in Eq. (4).

$$v = \frac{\dot{m}}{\rho A} \tag{4}$$

The area in above equation can represent either the difference between the upper or lower area of the test section from the airfoil. With this in mind, the velocities for both the top and bottom of the airfoil, known as v_{top} and v_{bottom} may be calculated. The model that is to be tested is the NACA 0012. The first digit depicts the maximum camber as a percentage of the chord while the second digit describes the distance between maximum camber to the leading edge of the airfoil in terms of ten percents of the chord. The last two digits show the airfoil's maximum thickness as chord percentage. Since the first two digits are zero, the NACA 0012 is a symmetrical airfoil.

The readings for velocity at different angles of attacks were taken. It is important to note that when the angle of attack changes from 0 °to 2 °for example, the difference in height for the upper or lower half of the test section changes as well. The formula for calculating this is defined in Eq. (5).

$$h_{new} = h_{upper} - l\sin\alpha \tag{5}$$

Here, h_{new} represents the new height (or thickness) after the height of the new angle of attack has been subtracted, $h_{upper}$is the height from the center to the top of the test section, l is half the length of the chord and α is the angle of attack. Similarly, the lower surface is obtained by subtracting the combination of the upper surface and the maximum thickness of airfoil at a certain point from the height of the test section. Fig. 5 below is an illustration of Eq. (5).

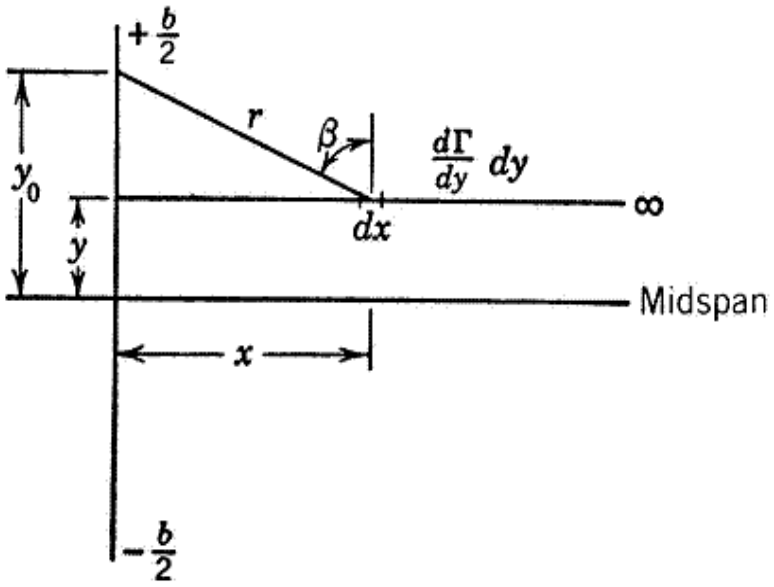


Figure 5. Calculating Height Difference of Airfoil Surface and Test Section [17]

3. Results & Discussions

3.1 Experimental Approach

3.1.1 Velocity and fan frequency results

The linear regression depicting the nature of dependency for both fan frequency and average wind velocity is Fig. 6.

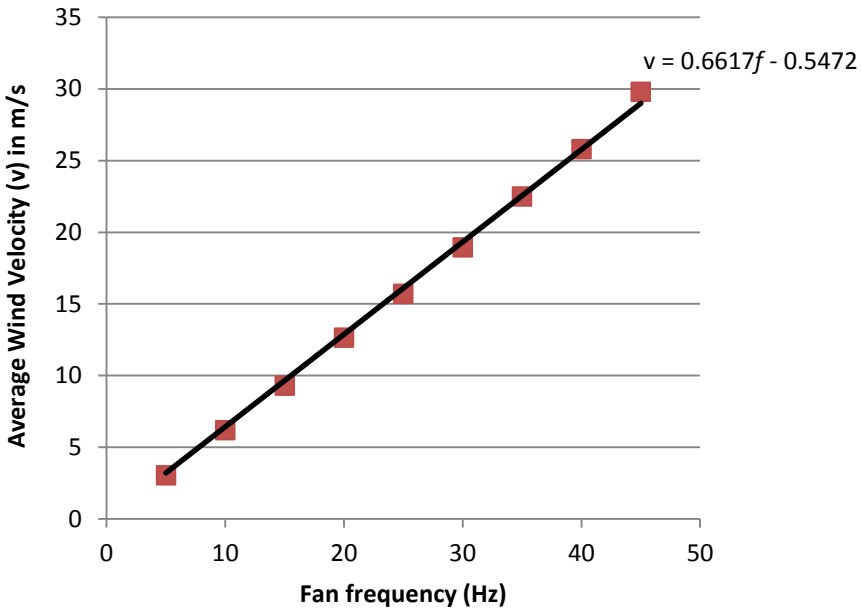


Figure 6. Average Wind Velocity against Fan Frequency.

As it can be observed from the graph, velocity and frequency in the test section of the wind tunnel are directly proportional to each other. It is physically known that if frequency is zero, velocity will also be equal to zero. Due to the graph having a slope of 0.6444, an increment of the frequency by 1 Hz will cause the flow velocity to increase by 0.6444. Another interesting thing to note is that an increment of 5 Hz brings about an approximate increase of 3 m/s in the value of the velocity each time.

However, this value increases to an increment of 4 m/s at higher frequencies as there are other factors at play as well. The graph drawn is one of linear regression and is well suited to the nature of the experiment. The y-intercept obtained in this graph is -0.5472 m/s. The reason for this less accurate result may be due external factors affecting the quality of the equipment such as the wind tunnel, the hotwire and data acquisition system. The fan frequency may possess a slight delay which may affect the overall reading of the experiment to differ from the actual results due to the long duration between re-calibration. The experimental result of a similar test done in 2009 [14] is shown in Fig. 7..

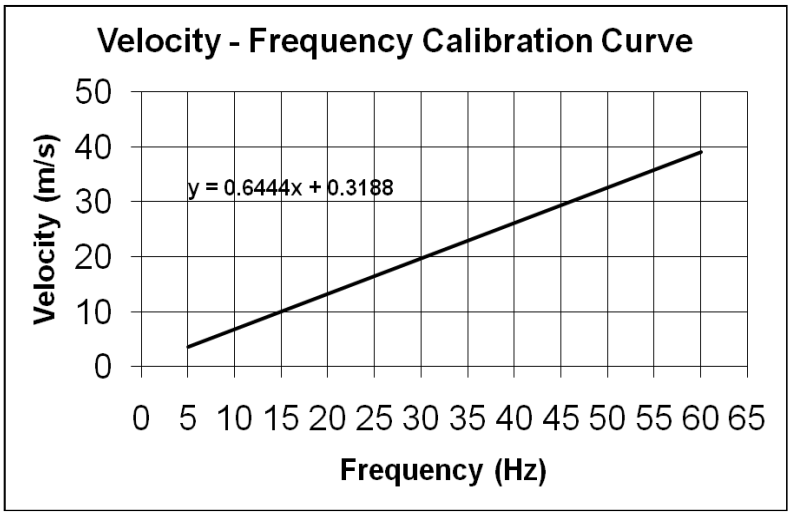


Figure 7. Velocity and Frequency of previous experiment [14].

From this figure, it is know that there is a difference between the results obtained in terms of slope and the y-intercept. Fig. 8 shows the combination of these two graphs for easy comparison.

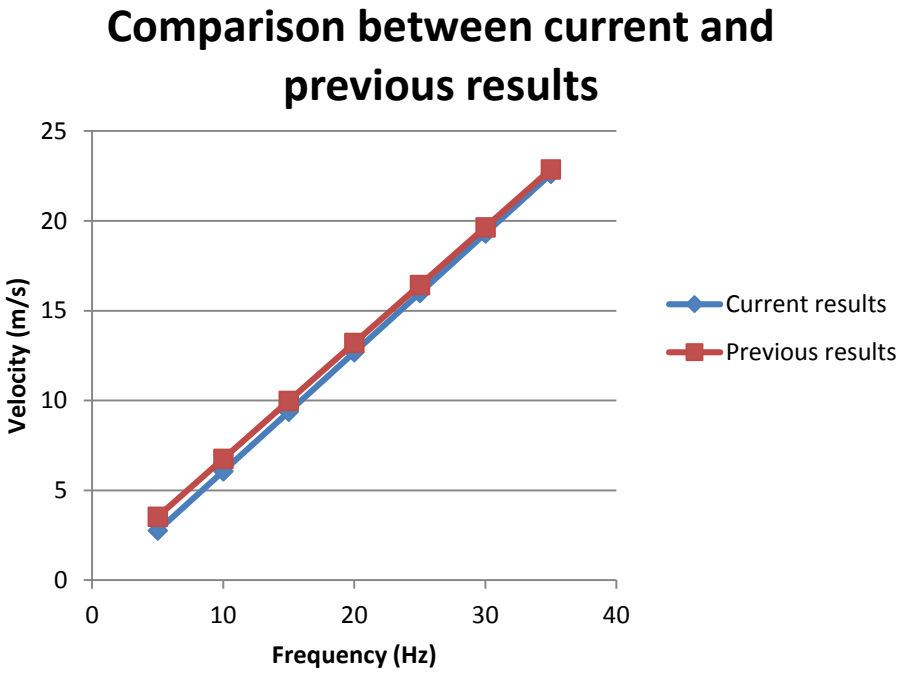


Figure 8. Comparison of current and previous results

Since the slope of both the graphs are the same, the percentage difference is measured to be around 2.58.

$$Percentage\ Difference = \frac{0.6617 - 0.6444}{0.6717} \times 100\%$$

$$= 2.58$$

These results display that the reliability of both experiments is very high and the equipment that is used to obtain these measurements is very dependable since the previous experiment was done 6 years ago. There is still a considerable amount of difference between the linear regression constants of the two experiments. The reason for this may be due to the difference in environmental conditions that occur during various periods of time. These environmental conditions include surrounding temperature and pressure. Another possible explanation for this error is due to the movement, reassembly and configuration of the wind tunnel from Taylor's College to Taylor's University. The steps taken in the reassembly process might have been different and not done as before resulting in gaps and leakage of air flow.

3.1.2 Velocity distribution results

After obtaining all the velocities at different points in the test section, a graph was produced showing the deviation of velocity from the original inlet velocities of 9.3 m/s and 15.7 m/s (Fig. 9).

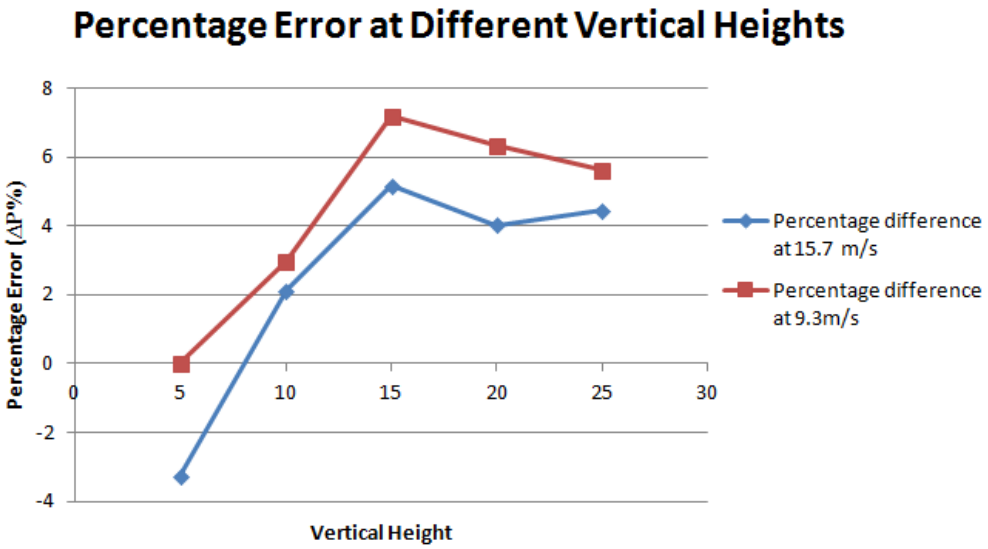


Figure 9. Velocity and Frequency of previous experiment

The above graphs display the nature of the velocity values based on the vertical positioning of the hot wire anemometer at different spots in the test section. Naturally, a higher fan frequency is expected to produce a higher flow velocity and this is conclusive with the results produced. The main issue is the discrepancy of results when it comes to comparison of results between different x and z values. It is generally known that at the center line the flow is steadier. Thus, it is expected that there is no big fluctuation in the value of the flow velocity from the reference value (9.3 m/s). The positions closest to the test section walls should produce the highest difference compared with the reference velocity due to the boundary conditions affecting air flow. However, this does not prove to be the case for other results produced. For example, the velocity value of graph x=1 is the highest for z=5 when compared to the rest of the z-values. The positioning of z=5 is the closest to the side

wall which brings up some uncertainty. Although the readings were taken as an average of 3 repeating measurements with separate times, the overall data obtained is very close to each other and the results are often inaccurate and clustered. This could be due to the fact that the boundary conditions inside the test section may not have settled when the frequency of the wind tunnel is changed to get readings. Moreover, even at constant frequency settings, the values of the velocity showed that the flow is not steady. This is because even slight changes of atmospheric conditions affect the flow conditions in the test section.

Three other graphs were made based on the first ten graphs. The graphs of vertical height against average velocity for both 9.3 m/s and 15.7 m/s were constructed. The average value of z for each vertical height is taken for each point. Then from those two graphs, a final graph depicting average velocities for both flows is produced. This graph is made by taking the values of x=5 and averaging them for 9.3 m/s and 15.7 m/s respectively. This step is then repeated for values of x=10, 15, 20 and 25. The final graph shows two lines each representing one velocity. From here, the percentage error may be found using Eq. (6):

$$\frac{vread - v}{v} \times 100\% \quad (6)$$

The average percentage error value for 9.3m/s is calculated as 4.44% and the average percentage value for 15.7m/s is calculated as 3.8%. From these average percentage errors, it can be concluded that the results have a high value of precision and accuracy since the values are very small.

3.2 Analytical Approach

In this section the NACA 0012 points and their respective thicknesses are shown (Table 2). Also, the upper and lower heights, areas and velocities are calculated based on the Eq. (1), (2), (3), (4) and (5) presented in the research methodology. These preliminary conditions were used in the calculation of the velocities and pressure distribution:

Density of air, ρ = 1.225 kg/m^3

Width of model = 0.1 m

Surface area of test section, A = 0.092 m^2

Fan frequency set at 15 Hz, according to previous experiments, this causes the inlet velocity to be at 9.3 m/s. The calculation was done for angles of attack of 0 °, 4 °, 8 °, -4 ° and -8 °.

Table 2. NACA 0012 airfoil data and calculation results

Distance along model (m)	Half thickness (Thickness) (m)
0	0

0.01	0.003653
0.02	0.005093
0.03	0.0058
0.04	0.006
0.05	0.005827
0.06	0.00532
0.07	0.00448
0.08	0.00332
0.09	0.001867
0.1	0.00012

A sample for the results obtained for 0 ° angle of attack is tabulated (Table 3). Fig. 10 and 11 show the pressure and velocity differences of the upper and lower surfaces of NACA0012 airfoil.

Table 3. NACA 0012 results for 0 ° angle of attack

Distance along model (m)	Upper Area (m^2)	Lower Area (m^2)	Upper Surface Velocity (m/s)	Lower Surface Velocity (m/s)	Pressure Difference Bottom (kg/ms^2)	Pressure Difference Top (kg/ms^2)
0	0.04590	0.04609	18.6387	18.56146	1.759711	-1.75971
0.01	0.04479	0.04498	19.0992	19.01813	1.893106	-1.89310
0.02	0.04436	0.04455	19.2870	19.20439	1.949395	-1.94939
0.03	0.04414	0.04433	19.3806	19.29717	1.977849	-1.97784
0.04	0.04408	0.04427	19.4073	19.32358	1.985999	-1.98599
0.05	0.04413	0.04433	19.3842	19.30073	1.978947	-1.97894
0.06	0.04429	0.04448	19.3170	19.23408	1.958471	-1.95847
0.07	0.04454	0.04473	19.2066	19.12466	1.925164	-1.92516
0.08	0.04489	0.04509	19.0563	18.97558	1.880399	-1.88039
0.09	0.04590	0.04553	18.8713	18.79209	1.826263	-1.82626
0.1	0.04586	0.04605	18.6535	18.57612	1.76389	-1.76389

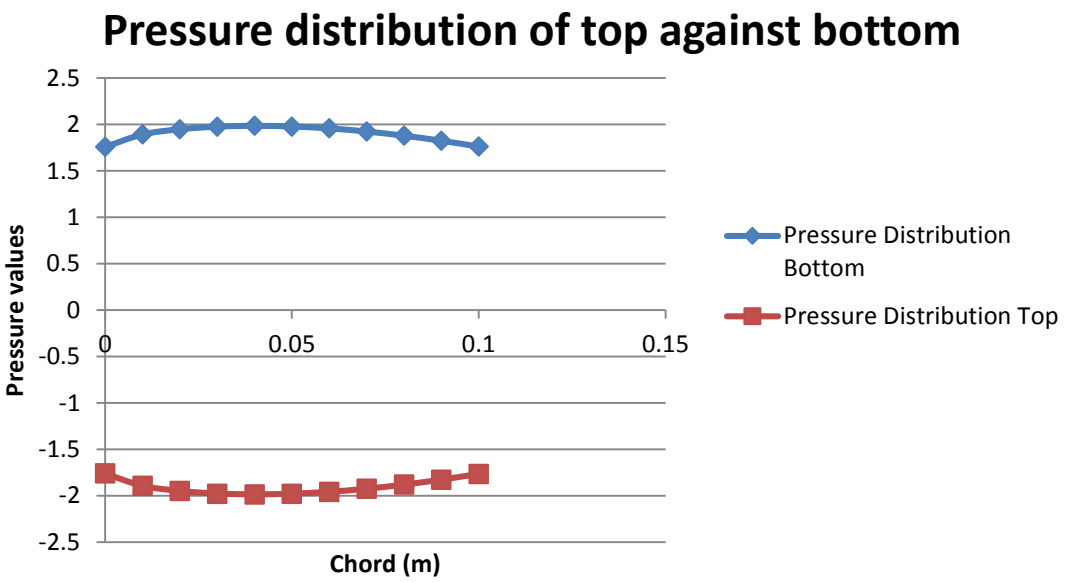


Figure 10. NACA 0012 Pressure distribution at zero angle of attack.

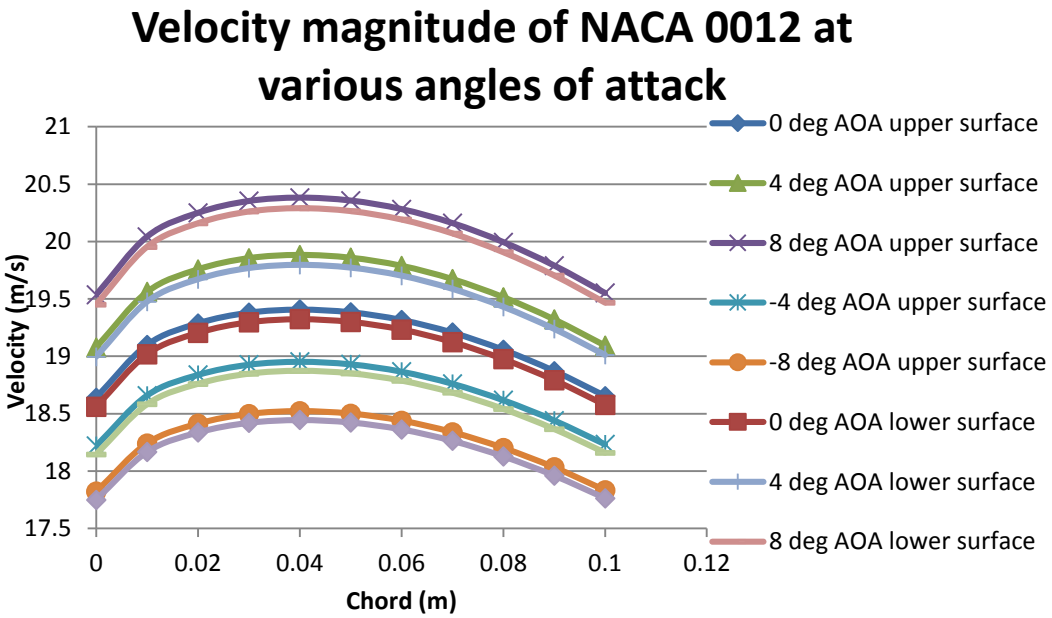


Figure 11. Velocity Distribution Graph

When an object moves through a fluid, there is a difference in velocity occurring around the object's surface. This in turn, causes difference in pressure along the airfoil according to Bernoulli's rule. Determining the relative velocity between an object and the flow is important since it is one of the factors that dictate lift, one of the key aerodynamic forces. Lift and drag equal to the square of the velocity and they are directly related to it. Another factor influencing lift in a wing is the angle of attack which is directly proportional if low angles of attack (0-10 °) are considered. This may be observed in Figure. above which shows the 8 ° angle of attack to have the highest relative velocities as compared to the other angles of attack. However this is not the case for higher angles of attack would create a layer of air around the airfoil, known as boundary layer. The separation of this boundary layer from the airfoil at high

angles of attack is one of the main causes of loss of lift. The critical angle of attack is known as the angle of attack in which the most amount of lift is produced. Increasing the angle of attack up to the critical angle will cause the lift coefficient to increase. However, if the angle of attack is further increased beyond the critical angle, the lift will start to decrease. Generally, the critical angle of attack for most airfoils, including the NACA 0012 is between 15°-20° [14]. As it can also be observed, the upper surfaces of airfoil have a slightly higher velocity than lower surfaces at low angles of attack. Due to the fact that the maximum camber occurs at 30-40% of the chord, this is also why the velocity is highest at these points of the airfoil.

The pressure distribution graph in (Fig. 9) represents the outline of the boundary layer achieved by the airfoil at this angle of attack. As it can be observed the bottom surface of the airfoil has higher existing pressures than the top of the airfoil. This is the reason why the curves resemble the shape of the NACA 0012 airfoil. Lift is provided by having wing pressure below the wing to be higher than the wing pressure above the wing, effectively creating a net force upwards. The airfoil geometry such as the thickness distribution, the camber line and incidence determine the pressure distribution on an airfoil's surface. Angle of incidence refers to an angle between the wing chord line and a reference axis along the fuselage. In order for the lift force to be generated by the presence of pressure difference, there must be a non-uniform spreading of pressure along a wide area of the airfoil. This may be achieved by making sure that both vertical and horizontal pressure difference are preserved as well as turning the flow downward and changing its velocity, in accordance with the Bernoulli's principle. Newton's second law and the fact that surface flow along the airfoil has downward-sloping contours also signify the presence of pressure difference [15].

4. Conclusions and Future Work

The velocity versus frequency test showed that the relationship between the frequency and velocity is linear. This experiment also helped to establish a set inlet velocity which may be used for the rest of the following tests. The velocity distribution test displayed the velocity values across the cross section of the test section and gave an outline of which sections were affected the most. This would help in visualizing on where to place the test model in order to not disrupt the flow. It also provides a benchmark to test against the results of the same experiment with the presence of a test model. The percentage difference is used to differentiate the velocity deviations from the inlet velocity across different points. The analytical results show that velocity of the upper surface of the airfoil is always higher than the velocity at the lower surface. Applying Bernoulli's rule this also dictates that the upper surface must have lower pressure than the bottom and therefore a lifting force is generated. These outcomes will eventually allow the calculation of lift and drag of the airfoil at different angles of attack. With that information, the scaling for the best model size and shape may be recommended to future users. For future works, the experimental analysis will be carried out with the model inside the test section. This has not been achievable until now due to ongoing maintenance of the Taylor's wind tunnel. The maintenance involves obtaining new test section walls to replace the old walls that have surface inconsistencies such as dents and holes present in them due to

prolonged use. It is important to remove these, as the results of future experiments will be affected by them.

References

[1] Hitt, D. 'What Are Wind Tunnels?', *NASA*, 2014. [Online]. Available: http://www.nasa.gov/audience/forstudents/5-8/features/what-are-wind-tunnels-58.html#.VT6HRyGqpBc. [Accessed: 04- Oct- 2015].

[2] Singh, M., Singh, N., Yadav, S.K. (2013). Review of Design and Construction of an Open Circuit Low Speed Wind Tunnel, *Global Journal of Researches in Engineering: Mechanical and Mechanics Engineering*, vol.13, no. 5.

[3] Ristić, S. (2007). Flow Visualisation Techniques in Wind Tunnels Part I – Non optical Methods, *Scientific Technical Review*, vol.57, no.1, pp. 39-50.

[4] Allori, D., Bartoli, G., Mannini, C. (2013). Wind tunnel tests on macro-porous structural elements: A scaling procedure, *Journal of Wind Engineering and Industrial Aerodynamics*, vol. 123, pp. 291-299.

[5] Hernandez, M.G., Lopez, A.M., Perales, J.M., Wu, Y., Xiaoxiao, S.(2013), Design Methodology for a Quick and Low-Cost Wind Tunnel, *Wind Tunnel Designs and Their Diverse Engineering Applications*.

[6] Eckert, D. L., Hegen, G. H. (2006). *Dnw's method to correct for support and wall interference effects on low speed measurements with a large propeller powered transport aircraft model.* Paper presented at 25th International Congress of the Aeronautical Sciences.

[7]Rolston, S. (2001). High reynolds number tools and techniques for civil aircraft design - an overview of the HiReTT programme, *Air & Space Europe*, vol. 3, no. 3-4, pp. 109-111.

[8] Wang, Z., Plate, E., Rau, M., Keiser, R. (1996). Scale effects in wind tunnel modeling. *Journal of Wind Engineering and Industrial Aerodynamics*, vol. 61, no. 2-3, pp. 113-130.

[9] Albert, I., Sample, J., Morss, A., Rajagopalan, S., Barabási, A., Schiffer, P. (2001). Granular drag on a discrete object: Shape effects on jamming, *Physical Review E*, vol. 64, no. 6

[10] Holman, J. P. (2002). *Heat Transfer*. McGraw-Hill. p. 207.

[11] Laitone, E. (1997). Wind tunnel tests of wings at Reynolds numbers below 70 000, *Experiments in Fluids*, vol. 23, no. 5, pp. 405-409.

[12] Douvi Eleni, C. (2012). Evaluation of the turbulence models for the simulation of the flow over a National Advisory Committee for Aeronautics (NACA) 0012 airfoil, *J. Mech. Eng. Res.*, vol. 4, no. 3.

[13] Critzos, C.C., Heyson, H.H., Boswinkle Jr., R.W. (1955). Aerodynamic characteristics of NACA 0012 airfoil at angles of attack from 0 to 180 degrees, NACA TN 3361.

[14] Lee, C. S., Tan, K., Lee, H. I., Singh, K., Foo, T. (2009). *Velocity – Frequency Calibration Curve,* Subang Jaya, Selangor Darul Ehsan, Taylor's University, School of Engineering

[15] MacLean, D. (2012) *Understanding aerodynamics*. Weinheim: Weley-VCH.

[16] Pakalnis, S. *Main Specifications of Airfoil*. 2006.

[17] Chklovski, T. *Calculating Height Difference of Airfoil Surface and Test Section*.

EURECA2015 – Conference Paper
Paper 2ME5

Computational Studies of the Bell-Mouth Structure on the Performance of the Outdoor Unit of a Split Air-Conditioner

Cassandra Low Zhiu Yee[1], Lim Chin Hong[1*], Yan Yao Chen[2], Yap Kim Haw[2]

[1]*School of Engineering Taylor's University, Malaysia*
[2]*Panasonic Appliances Air Conditioning R&D Malaysia Sdn. Bhd.*

[*]chinhong.lim@taylors.edu.my

Abstract

Split type air-conditioners are commonly used among residential and commercial buildings. Energy efficient air-conditioners are highly in demand for consumers. The performance criteria for every manufactured air-conditioner needs to meet the requirements of Minimum Energy Performance Standard (MEPS). The criteria for MEPS should have at least 2 star rating. The outdoor unit of a split-type air conditioner consists of three main surrounding structures, which are the heat exchanger, bell-mouth, compressor and discharged grille. The objective of this study is to conduct a wind tunnel experiment on the original bell-mouth and validate the CFD model. Bell-mouth is designed to extract air purposes within air-conditioner ventilation system. Mesh dependency study was done and the study shown that the configuration of 1/8 of overall mesh size for thickness of first layer of the boundary layer, rate of change of thickness of 1.1 and mesh size of 1/3 of minimum distance between blade tip and bell-mouth yield the best numerical results. Experiment was conducted at the wind tunnel at Panasonic Malaysia and CFD simulations were run on the bell-mouth with a cooling fan. Both numerical and experimental results were compared. The numerical results at flowrate less than 20 m^3/min are well in the range of 70% of accuracy between numerical and experimental results. However, when flowrate is higher than 20 m^3/min, the accuracy between numerical and experimental results are less than 70%. The boundary conditions of volumetric flow rate at the inlet and SST k- ω turbulence model are to be used for design of experiment simulations.

Keywords: computational fluid dynamic (CFD), bell-mouth, split-type air-conditioner, aerodynamic, Cradle SC/Tetra

1. Introduction

The outdoor unit of a split-type air conditioner consists of four main structures, which are the heat exchanger, bell-mouth, compressor and discharged grille. Bell-mouth is designed to extract and guide air for the air-conditioner ventilation system. The airflow from the indoor unit passes through the heat exchanger in radial direction and streams out of outdoor unit in an axial direction. Cooler air is released into the room with air extracting out from the ventilation system. Thus, as air extracted from ventilation system increases, the amount of cooler air released into the room is increased. Figure 1.1 shows a bell-mouth design on a commercial split-type air conditioner.

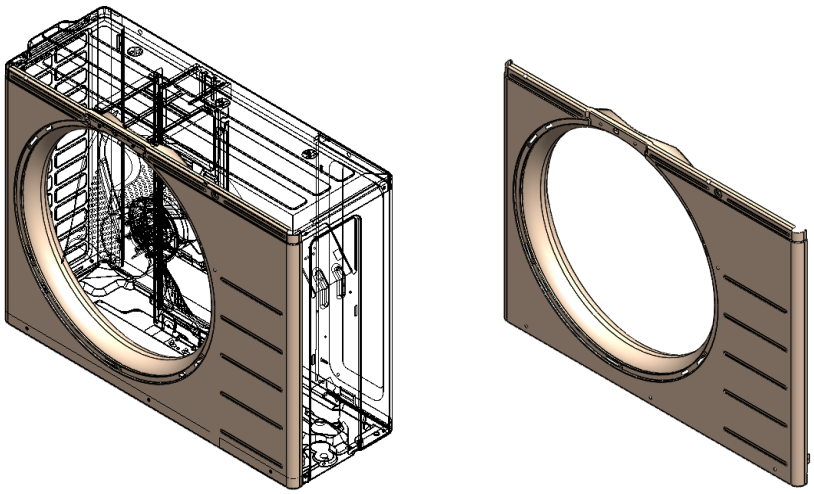


Figure 1.1: Illustration of the location of the bell-mouth

There are a few related studies on the performance of an air conditioner outdoor unit. including acoustic and aerodynamic of the bell-mouth,. Maaloum et al. [1], Tian et al. [2] and Hu et al. [3] studied on acoustic performance while Wu et al. [4] and Zhao et al. [5] studied on both aerodynamic and acoustic performance of the bell-mouth. The presence of a contoured duct shows great improvement of minimizing acoustic emissions [1] and double contoured duct was design and acoustic emissions were further minimize [3]. Tian et al. [2] further studied on the outdoor unit and found that the grilles have large affect the acoustic performance. Rectangular grille was replaced by circular grille which demonstrates better results in lowering acoustic emission. This result shows that grille pattern could be an impact to the acoustic performance of an outdoor unit. Furthermore, not only the presence of grille and duct could reduce the noise level, noise reduction can be also be reduced by modifying fan. Zhao et al. [5] suggested that flanging out-edge blade is more effectual in reducing noise level. Aerodynamic performance can be improve by using double contoured duct as suggested by [3]. Wu et al. [4] proposed two improved profile of vortex tongue that can increase flow rate while band sound pressure level remains lower but the two improved design weren't mentioned in the study.

From Phan et al. [6], the authors studied the effect of surrounding structure of an air conditioner towards the airflow performance. However, airflow performance in this study is in term of sound and air-throw direction. The surrounding structures that being studied were the partition for compressor, radius of nozzle and depth of nozzle.

Parameters studies were done by using DOE and Pareto principle and concluded that the depth of nozzle is the main effect of reducing noise level between the 3 factors. Further analysation on other surrounding structures such as radius of bell-mouth, fan guard design and motor mounting bracket and results show that the presence of inlet radius reduced sound by 1.25%, fan guard design reduced the sound pressure level by 4.23% and motor mounting bracket reduced sound pressure level by only 0.5%. To conclude the research, the recommended design according to the results obtained is to have nozzle depth of 47 mm and radius of 43 mm, spiral grille and motor mounting bracket flanged outward causes the sound pressure level of the outdoor unit to reduce about 5.9%. Chamfered bell-mouth outlet radius was further proposed to improve the air-throw direction as flow separates at the chamfered corner and creates an axial flow out of the outdoor unit. This study also conform with [2] as Tian et al. concluded that circular grille has an effect on reducing the sound level.

Wang et al. [7] also done a study on up-flow of outdoor unit by redesigning bell-mouth profile. Fan of outdoor unit was first analysed and concluded that the cause of poor aerodynamic performance was due to complex vertical flow field that was found near the rotor tip. Bell-mouth was redesigned by lengthening both upstream and downstream. CFD simulations was done on 3 different design which are redesigned bell-mouth with 2 blade fan, original bell-mouth with 3 blade fan and redesigned bell-mouth with 3 blade fan. By comparing the results, the redesigned bell-mouth shows an improvement of 1.2% of flow rate. 3 blade fan do show higher flow rate, however, the flow loss increases due to high work capacity needed in which lowering the efficiency of the fan. Although the redesigned bell-mouth shows an improvement but the study cannot be implemented onto an air conditioner outdoor unit due to restricted space of an outdoor unit.

The objective of this project is to simulate flow around the air-conditioner bell-mouth with the cooling fan in wind tunnel with application of computational fluid dynamics analysis and experiment. In this study, pressure difference across wind tunnel is used to determine whether there is an improvement on the airflow. Three-dimensional (3D) computational fluid dynamics (CFD) simulation based on cradle SC/Tetra is used to study the impact of the bell-mouth on the outflow of the outdoor unit. The reason of using 3D instead of 2D is because of the presence of the fan which produces turbulence and causes air to flow in all direction. Besides that, Lit et al. [9] did researches by comparing 2D and 3D simulations of circulating fluidized bed risers and concluded that 2D only can be used for qualitative studies and 3D is for quantitative studies on flow behaviour.. By the end of this project, the improvement on the bell-mouth's profile and configurations to increase the aerodynamic performance and outflow of outdoor unit of air-conditioner.

2. Research Methodology

According to Figure 2.1, the project starts with conducting CFD simulation done on the bell-mouth. The original designs of bell-mouth and wind tunnel was provided by Panasonic Appliances Air Conditioning R&D Malaysia. Cradle SC/Tetra software is used to run simulation. Mesh dependency was conducted on the bell-mouth

in order to obtain the optimum mesh size and configuration, including thickness of first layer and rate of thickness of the boundary layers for the CFD model.

Rate of thickness of the boundary layer is the rate of change in prism layer thickness from the wall. Prism layer thickness increases away from the walls when the value is greater than 1. Thickness of first layer originally by default about one-half of the size of the tetrahedral mesh near the boundary walls. The optimum combination of bell-mouth mesh size, thickness of the first boundary layer and rate of change of thickness that shows airflow is independent from the mesh will be chosen for future reference. After mesh dependency was done, CFD simulations were run by controlling pressure at the inlet of the wind tunnel and obtain the inflow flow rate. Pressure difference across the wind tunnel against volumetric flow rate (P-Q) graph is drawn.

Experiment is conducted in parallel with the CFD simulations. Experiments are conducted in the wind tunnel located at PAPARADMY1. Experimental results obtained from wind tunnel are compared to the CFD simulation results. P-Q graph will be drawn and compared with computational result. The reason of plotting P-Q graph is because different flow rate in the wind tunnel will cause different pressure difference. The accuracy between numerical and experimental results are targeted to reach at least 70%, which is recommended by the industry standards.

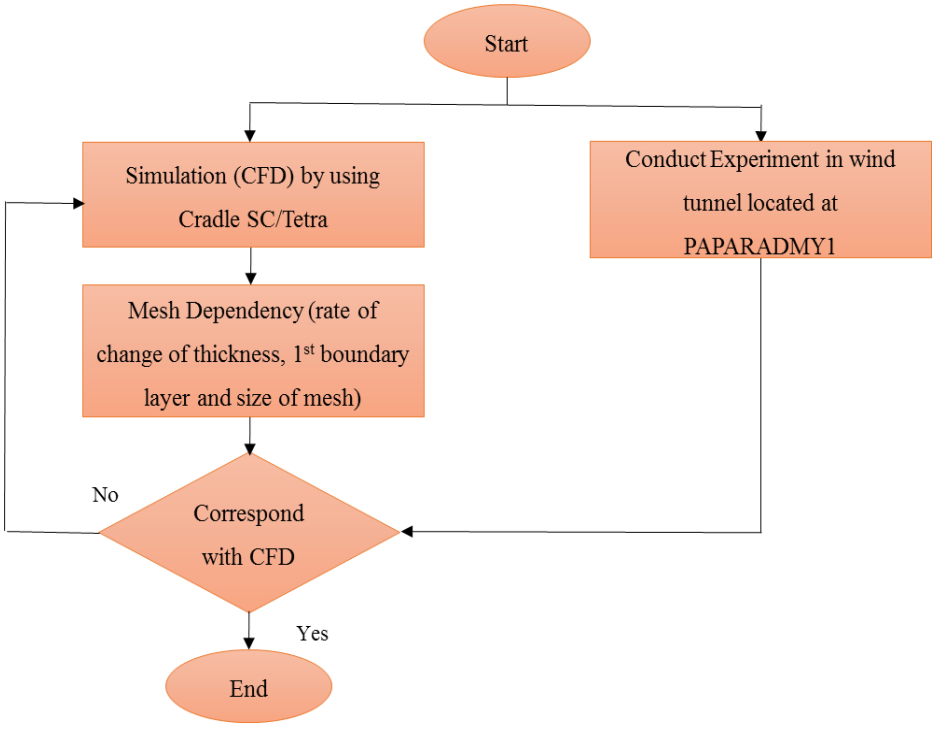


Figure 2.1: Flowchart of research methodology

The limitations for this project are computational resources to run the CFD simulations and unavailability of wind tunnel for this project. In PAPARADMY1, there is only one computer that can be used to run simulation and simulation only can run one at a time. Also, the availability of wind tunnel is unpredictable. Besides that, the scanned model for the fan only done on the beginning of the semester and causes the scheduled plan postponed.

2.1 Governing Equations

Reynolds Averaged Navier-Strokes (RANS) equations consists of continuity equation, momentum equation and energy equation. There are only continuity and momentum equation involve in this study [10]. RANS on each direction are to be solved and continuity equation is as follows

$$\frac{\partial \rho}{\partial t} + \frac{\partial}{\partial x_i}(\rho u_i) = 0 \qquad (1)$$

where ρ represents fluid density and u_i is the velocity component in each direction of x, y, and z. Furthermore, momentum equation also needs to be solved and the equation as follows

$$\frac{\partial}{\partial t}(\rho u_i) + \frac{\partial}{\partial x_j}(\rho u_i u_j) = -\frac{\partial P}{\partial x_i} + \frac{\partial}{\partial x_j}\left[\mu\left(\frac{\partial u_i}{\partial x_j} + \frac{\partial u_j}{\partial x_i}\right) - \frac{2}{3}\mu\frac{\partial u_i}{\partial x_i}\right] + \frac{\partial\left(\overline{u_i' u_j'}\right)}{\partial x_j} + \rho g_i \qquad (2)$$

where g_i represents gravitational acceleration, μ represents viscosity and $\overline{u_i' u_j'}$ is related to turbulence model.

2.2Meshing

Cradle SC/Tetra is used to run simulations on the bell-mouth. The mesh size has significant effect on the numerical results hence, it is important to investigate the best mesh size for the study of bell-mouth design. Mesh dependency varies the mesh size until the airflow is independent from the mesh, in which the numerical simulation solution converges.

Figure 2.2 shows the mesh near the bell-mouth. The five layers shown in Figure 2.3 is called inflation. These are the boundary layers that are going to be used for mesh dependency study.

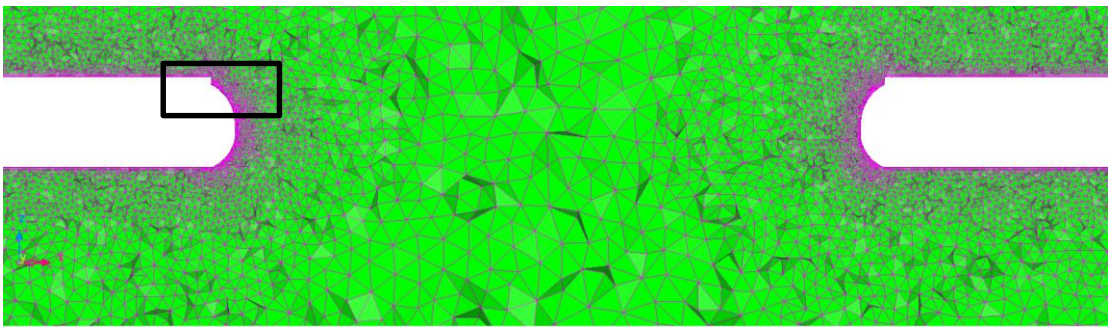


Figure 2.2: Mesh at the bell-mouth

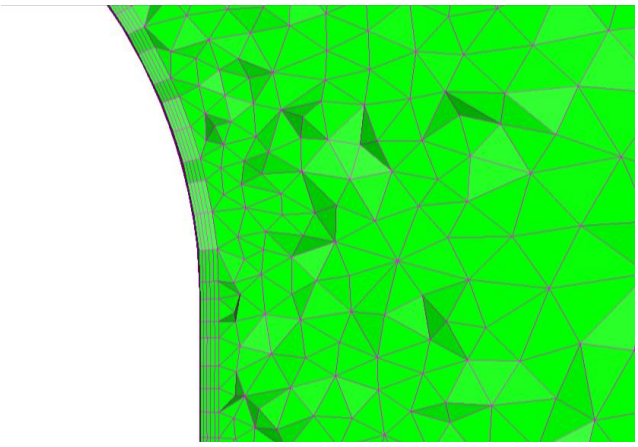


Figure 2.3: Inflations at the bell-mouth (zoom in on the black box in Figure 2.2)

Table 2.1 shows the number of mesh elements in each case. From the table below, as the quality of mesh improves, the size of mesh decreases and the number of element increases.

Table 2.1: Mesh Dependency (varying mesh sizes)

Bell-mouth mesh size	Thickness of First Layer of Boundary Layer		Rate of change of thickness	
	1/2 of overall mesh size	1/4 of overall mesh size	1.1	1.3
1/2 of minimum distance between fan and bell-mouth (Coarse)	7.49 mil elements	7.49 mil elements	7.50 mil elements	7.55 mil elements
1/3 of minimum distance between fan and bell-mouth (Fine)	15.97 mil elements	16.31 mil elements	16.35 mil elements	16.45 mil elements
1/4 of minimum distance between fan and bell-mouth (Extra Fine)	24.48 mil elements	25.05 mil elements	25.12 mil elements	25.29 mil elements

For this mesh dependency, wall y^+ function is used as guidance in selecting appropriate configuration. Wall y^+ commonly known as non-dimensional distance [11]. It is used to determine quality of mesh. Figure 2.4, Figure 2.5 and Figure 2.6 show wall y^+ on the bell-mouth. The range of y^+ that is used to study for this project is less than 5. The red colour shows the region y^+ is 5. Orange to green region is y^+ of 4 – 3 while green to blue region is y^+ of 3 – 0. It is best to have the range of 3 – 0 on the outlet of the bell-mouth so that optimum results can be obtained. From Figure 2.5a and Figure 2.5b, it is obvious that the y^+ on the outlet of the bell-mouth decreases from 5. It is the same goes to Figure 2.4 and Figure 2.6. This shows that the smaller the thickness of first layer of boundary layer, y^+ on the outlet of the bell-mouth decreases. From Figure 2.5c and Figure 2.5d, it also shows that y^+ on the outlet of the bell-mouth decreases from 5. Thus, as the rate of thickness increases, y^+ on the outlet of the bell-mouth decreases. It is also the same goes to Figure 2.4 and Figure 2.6. These conclude that extra fine mesh is more suitable as y^+ near the outlet of bell-mouth is in the range of 3 – 0. However, rate of thickness of 1.3 is not recommended as the thickness is too big and causes inaccuracy of results. On the other hand, extra fine mesh is not suitable to be used in future due to high computational cost, so fine mesh is used to do mesh

dependency study. Furthermore, $y^+<5$ are on the outlet of the bell-mouth thus enhanced wall function will be use.

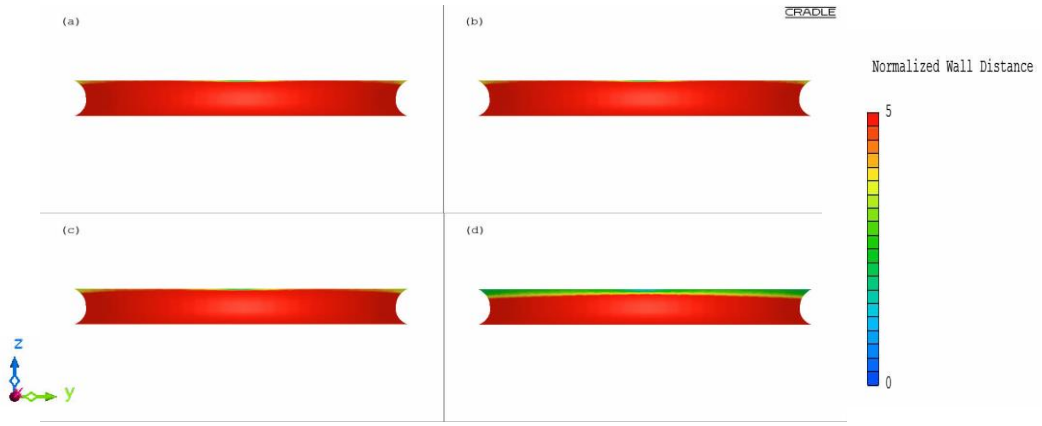


Figure 2.4: y+ < 5 (coarse) (a) ½ of overall size (b) ¼ of overall size (c) 1.1 rate of thickness (d) 1.3 rate of thickness

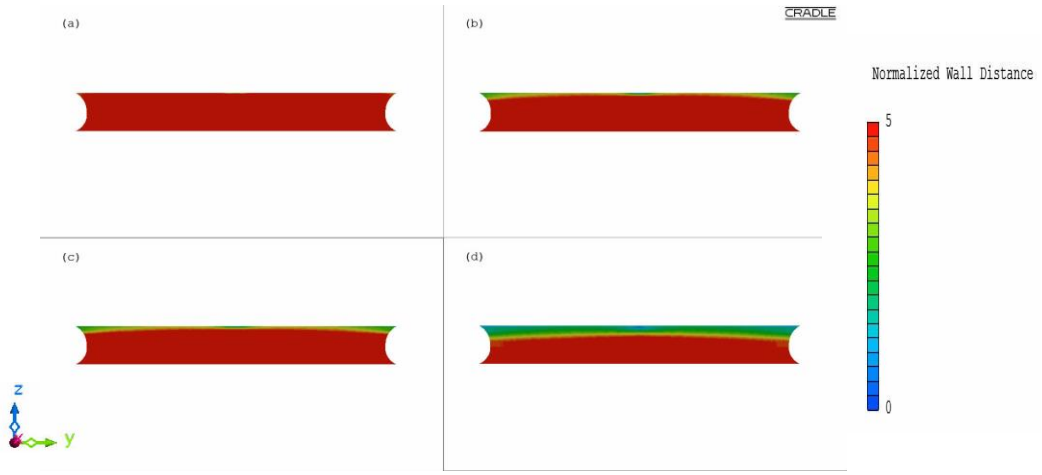


Figure 2.5: y+ < 5 (fine) (a) ½ of overall size (b) ¼ of overall size (c) 1.1 rate of thickness (d) 1.3 rate of thickness

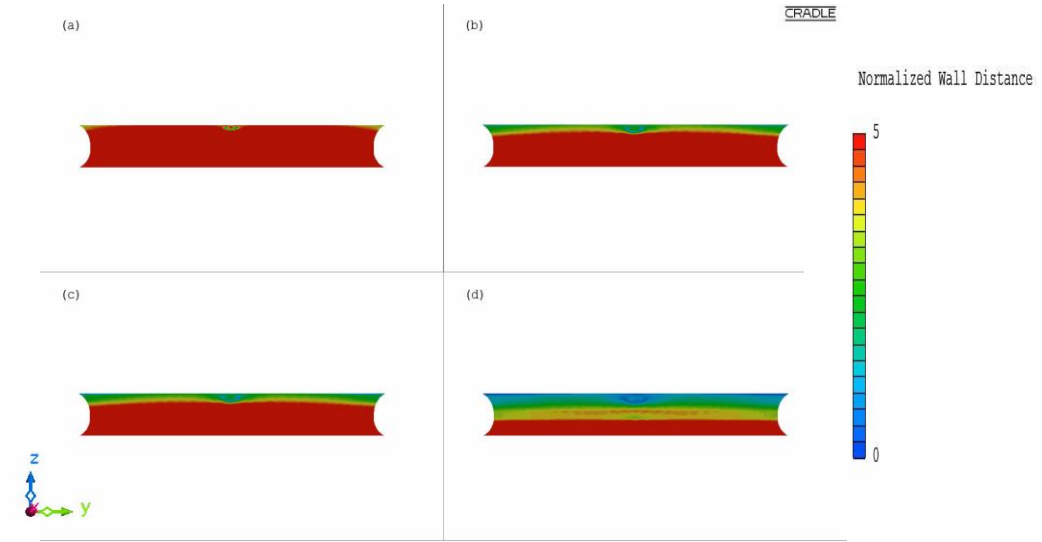


Figure 2.6: y+ < 5 (extra fine) (a) ½ of overall size (b) ¼ of overall size (c) 1.1 rate of thickness (d) 1.3 rate of thickness

The mesh was further simulated where thickness of first layer of boundary layer was altered while rate of change of thickness remains default as 1.1 and mesh size remain as 1/3 of minimum distance between blade tip and bell-mouth. It was done to choose the best configurations for further reference. This will be a guide when fan is involved for meshing and simulation.

Table 2.2 shows the number of elements for each case. Each case was then input with four different inflow flow rate which are 42.68 m^3/min, 40.14 m^3/min, 36.8 m^3/min and 32.68 m^3/min respectively. Pressure difference was calculated by using the difference in pressure at the inlet and outlet. Different inflow flow rate affect the pressure on the inlet and outlet. High velocity flowing through the bell-mouth will cause high pressure at that point. After the flow pass through the bell-mouth, velocity is still high thus causing the pressure at the bell-mouth outlet to decrease to approximate 0 Pa.

Table 2.2: Mesh Dependency (varying first layer of boundary layer)

Case	First layer of Boundary Layer	No. of elements
1	1/4 of overall mesh size	15.97 mil
2	1/6 of overall mesh size	16.47 mil
3	1/8 of overall mesh size	16.57 mil
4	1/10 of overall mesh size	16.64 mil

According to Figure 2.7, pressure difference increases as inflow flow rate increases. Thus, pressure difference is directly proportional to inflow flow rate. From Figure 2.7, case 4 is the optimum result, as the pressure difference is 0.8% (shown in Table 2.3) from case 3. Thus, percentage difference for case 1, 2, and 3 were compared to case 4. There is a percentage difference of 3.8% when comparing case 1 to 4 while 2% when comparing case 2 to 4. Besides, since the pressure difference for both cases are similar, this would mean that the flow is independent from the mesh since case 3.Considering time and computational factors, it can be conclude that case 3 is the optimum configuration.

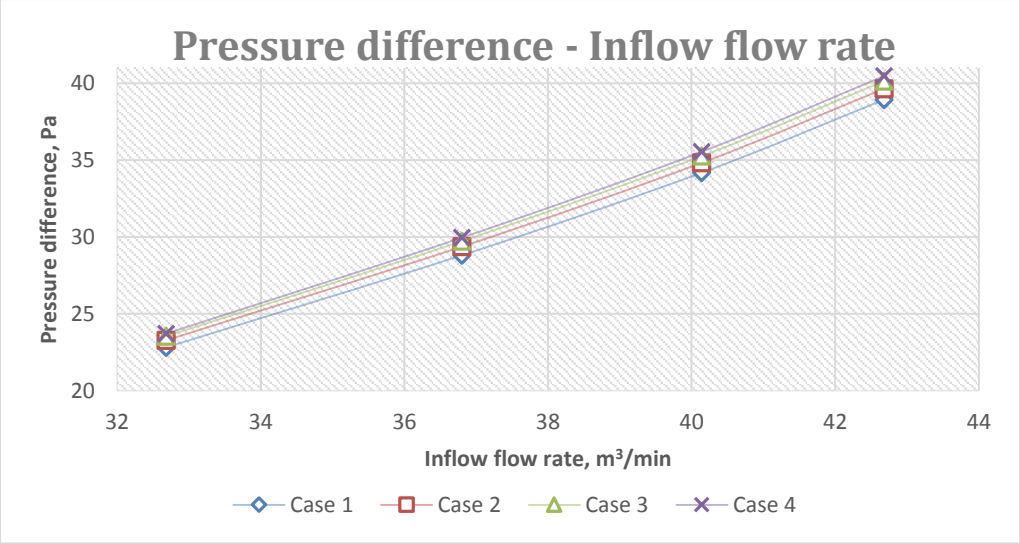


Figure 2.7: Pressure Difference against Inflow Flow Rate

Table 2.3: Percentage difference between case 1, 2, 3, and 4

Case comparison	Percentage %
4->1	3.8
4->2	2.0
4->3	0.8

2.3 Boundary Conditions

The flow used to study this project is turbulent flow. K-ε turbulence model is chosen by Edmunds et al. [12] and Alaimo et al. [13] because of its simplicity, modest computational cost and stability. However, from Cable [14], SST k-ω turbulence model could calculate both near wall and far field areas. Thus, it is preferable to use in this project. From mesh dependency study, it was stated that enhanced wall function is suitable to use in this study. [12,14] implemented multiple reference frame (MRF) because these studies involve fixed and rotating domain. This project will involve a fixed and rotating domain when fan is incorporate into wind tunnel model. The rotating domain in this study is the fan which runs at a rotation speed of 860 rpm. The static region around the fan is considered as fixed domain. MRF is also known as discontinuous mesh in Cradle SC/Tetra.

In this study, no-slip boundary is to be set on stationary wall. The surfaces of the fan are set to mesh velocity is equal to wall velocity. Both inlet and outlet boundary are set to pressure [16]. Turbulence energy of 0.01 m^2/s^2 and turbulence dissipation of 0.01 m^2/s^3 are set at the inlet boundary. Steady analysis is used with 10,000 cycles. The simulation is stopped when it reaches steady state and finishes 10,000 cycles.

2.4 Experimental Setup

Experiments were conducted concurrently with the CFD simulation in the wind tunnel located at PAPARADMY1. Figure 2.8 is located at the testing case shown in Figure 2.9. The wind tunnel consists of an inlet where airflows in, a testing zone to put the testing case of the outdoor unit, an outlet , two pressure sensors and two temperature sensors. The dimension of the wind tunnel is 7000 mm by length, 2800 mm by height and 3300 mm by width. Change in pressure of the wind tunnel has to be as close as 0 Pa when calibrating steady airflow in the wind tunnel because 0 Pa is equivalence to atmospheric pressure of the wind tunnel. Stroboscope is used to obtain the three-blade fan's revolutions per minute (RPM). After calibration was done, experiment starts by decreasing the pressure change of the wind tunnel to -5 Pa and wait for 15 – 30 minutes for the airflow to reach steady state. The air flows from chamber 1 to chamber 2. The steady volumetric flow rate at the outlet is recorded. Experiment is repeated by decreasing the change in pressure in interval of 5 which are -10 Pa, -15 Pa, -20 Pa, -25 Pa, -30 Pa and -35 Pa. Experiment is repeated to ensure the results are the same and within the range of 1 from the first experiment. Figure 2.10 shows the results obtained from wind tunnel experiment. Experimental results obtained from wind tunnel are compared to the simulation result. The experimental pressure difference against volumetric flow rate (P-Q) graph are compared with computational results. The accuracy of the CFD models is targeted to reach at least 70%, which is recommended by the industry standards.

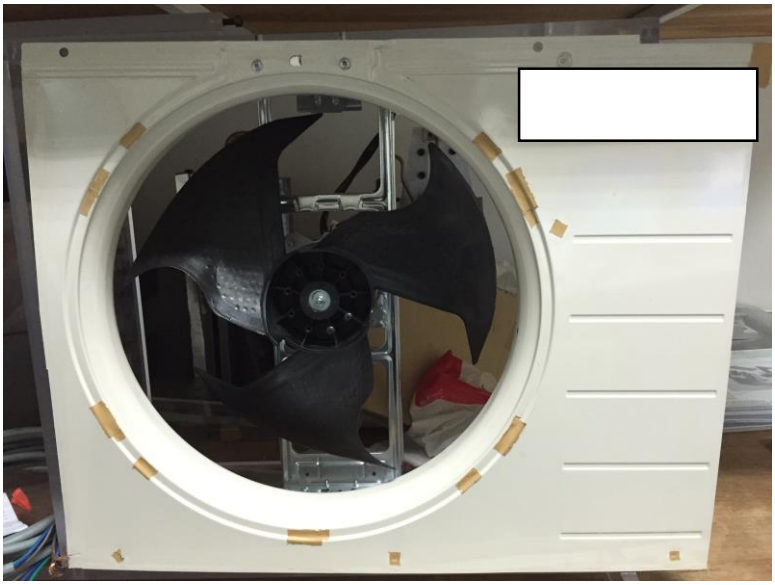


Figure 2.8: Bell-mouth with fan attached to outdoor unit casing

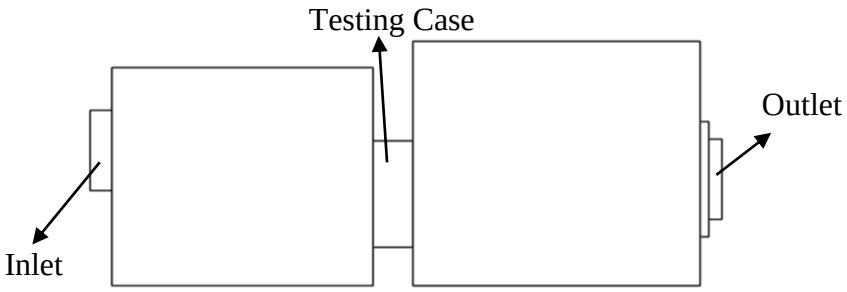


Figure 2.9: Illustration of the wind tunnel

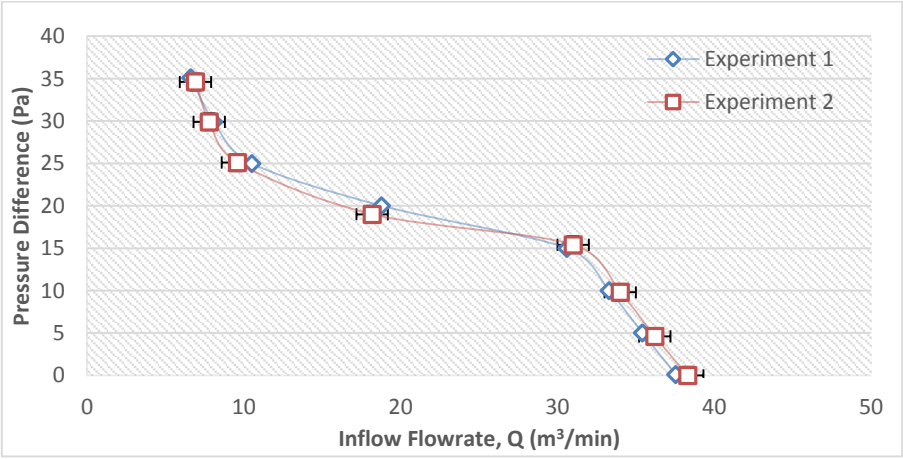


Figure 2.10: Experiment results

3. Results and Discussion

Figure 3.1 shows the comparison between numerical and experimental results. The pressure inputs at the inlet are constricted according to the pressure difference obtained from the experiment. The pressure at the inlet is known just by observing the pressure difference obtained from wind tunnel experiment. From Figure 3.1, it can be concluded that the trend of pressure control is different from experiment trend. It shows that the trend of pressure control do fluctuates but not experiment trend. Thus, this boundary condition is not approachable for this project.

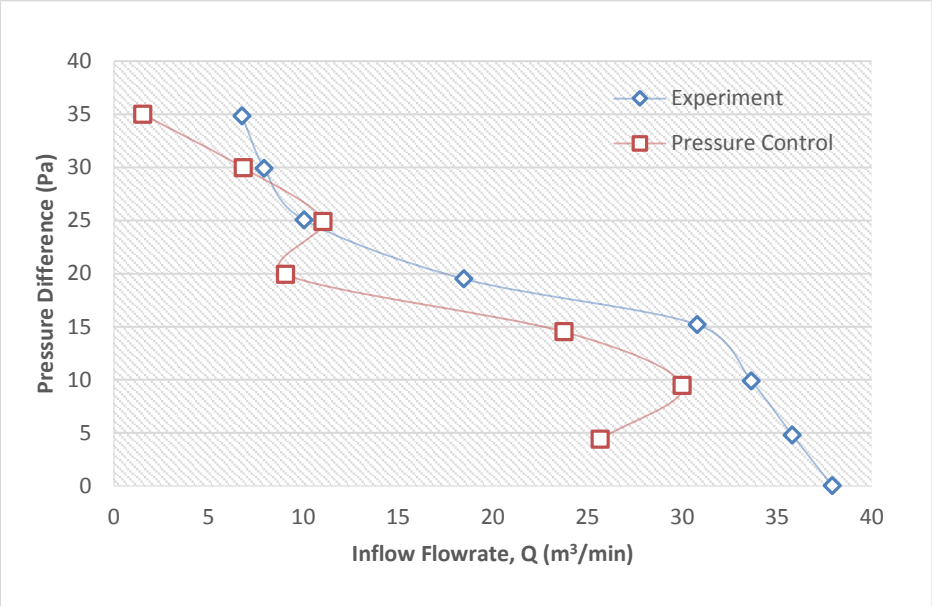


Figure 3.1: P-Q graph (pressure control)

Further analysation on simulations boundary conditions was done to improve the simulation models. The boundary conditions was modified by specifying volumetric flow rate at the inlet and different turbulence models was used in order to obtain a better trend curve. Standard k- ε, RNG k- ε and SST k- ω turbulence models are simulated to obtain better numerical results. From Figure 3.2, it can be seen that the fluctuations reduced and showed better similarity to experimental curve after the proposed changed of boundary condition. Following, all three turbulence models shown similar trend curves and research was done by comparing the three turbulence models and from Cable [14], SST k- ω turbulence model is a better turbulence model to be used for later simulation. Cable [14] mentioned that SST k- ω turbulence model involves both k- ε and k- ω calculations and calculates near and far wall areas.

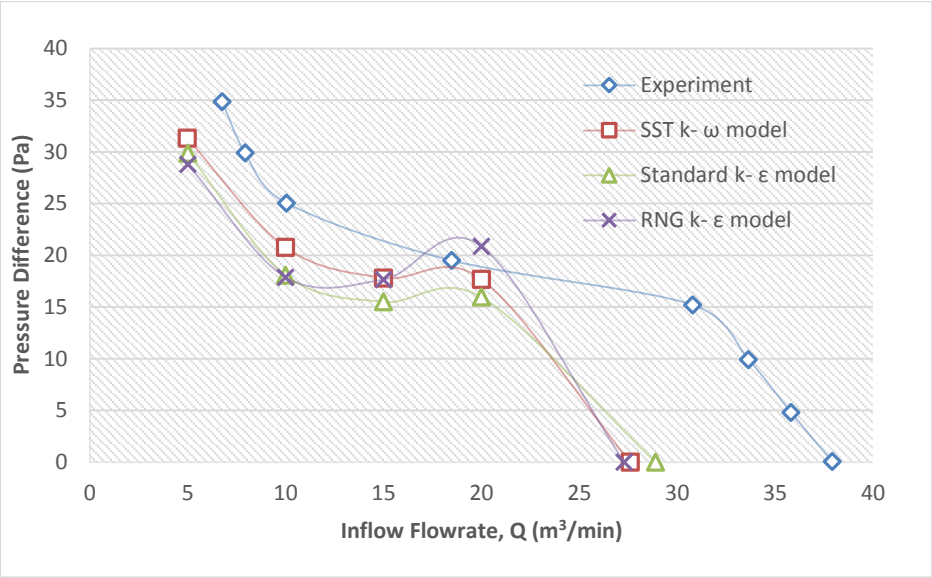


Figure 3.2: P-Q graph (different turbulence models)

Figure 3.3 shows that when flow rate is below 20 m^3/min, the trend of pressure difference is similar to experiment trend. However, as the flow rate increases, the trend is out of the range of 70% accuracy between numerical and experimental results. This might due to the turbulence occurred when pressure difference is being calculated. From Figure 3.3, the pressure difference across wind tunnel decreases as flow rate increases. This theory agrees well with Bernoulli's principle. When high velocity flowing through bell-mouth, low pressure occurred at the outlet of the bell-mouth. According to Figure 3.4, the air flow in z-direction and high pressure approximate -20 Pa when flow encounter with fan and at the inlet of bell-mouth. When the fan force the air out rotational speed 860 rpm, pressure suddenly increases to approximately 1 Pa which is the atmospheric pressure. This leads to when there is low pressure at the outlet of bell-mouth, high flow rate will flow out of the outdoor unit.

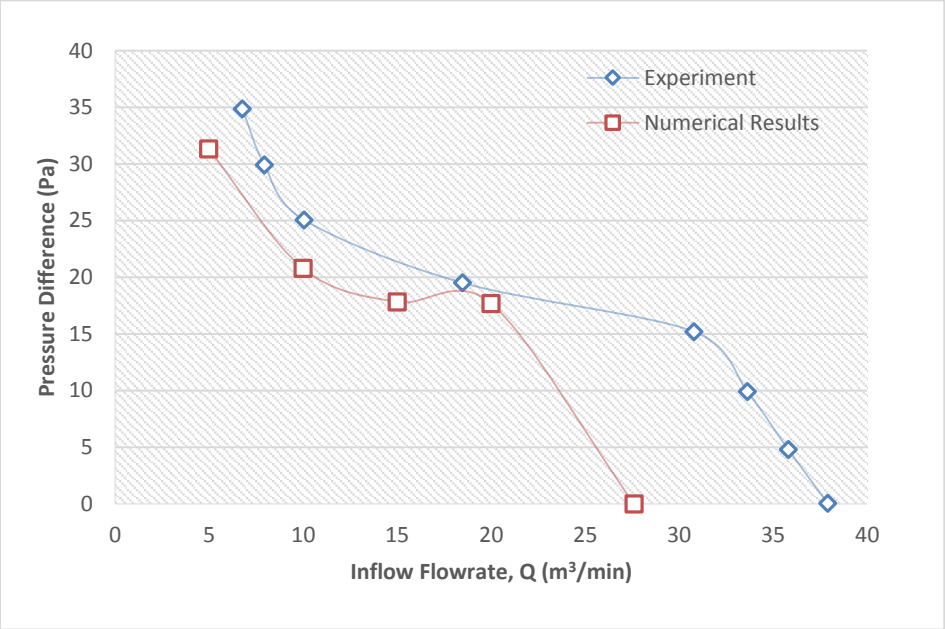


Figure 3.3: P-Q graph



Figure 3.4: Pressure contour at flow rate of 20 m^3/min

In conclusion, the numerical results with controlled flow rate and SST k- ω turbulence model is the approachable way for this project. Design of experiment results are to be compare with this numerical results.

Design of experiment will be done in coming weeks. This project could not be done on time due to time limitations and resources limited when it comes to running simulations. Further simulation will be done by using the same boundary conditions for design of experiment. Different parameters on the bell-mouth to be studied in near future.

4. Conclusions

From mesh dependency study, it was concluded that 1/8 of overall mesh size for thickness of first layer of the boundary layer, rate of change of thickness of 1.1 and mesh size of 1/3 of minimum distance between blade tip and bell-mouth are the most optimum configurations. Simulations were further run with different pressure input at inlet and compared to experimental results. Different approaches were done to investigate the discrepancy between the CFD models and experimental results. It concluded controlled flow rate with SST k- ω turbulence model was the best approach. This boundary condition is to be used for design of experiment simulations. Simulations can be run by using transient analysis to increase the accuracy but due to time limitations and high computational cost, it is recommended for future work.

Acknowledgement

This project has benefited from the support of Panasonic Appliances Air Conditioner R&D Malaysia by providing wind tunnel for experiments and Cradle SC/Tetra software for CFD simulation.

References

[1] A. Maaloum, S. Kouidri, F. Bakir, and R. Rey, “Effect of inlet duct contour and lack thereof on the noise generated of an axial flow fan,” *Appl. Acoust.*, vol. 64, no. 10, pp. 999–1010, 2003.

[2] J. Tian, H. Ouyang, and Y. Wu, “Experimental and numerical study on

aerodynamic noise of outdoor unit of room air conditioner with different grilles," *Int. J. Refrig.*, vol. 32, no. 5, pp. 1112–1122, 2009.

[3] J. Hu and G. Ding, "Effect of deflecting ring on noise generated by outdoor set of a split-unit air conditioner," *Int. J. Refrig.*, vol. 29, no. 3, pp. 505–513, 2006.

[4] C. J. Wu, D. P. Liu, and J. Pan, "A study of the aerodynamic and acoustic performance of an indoor unit of a DC-inverter split air-conditioner," *Appl. Acoust.*, vol. 73, no. 4, pp. 415–422, 2012.

[5] X. Zhao, J. Sun, and Z. Zhang, "Prediction and measurement of axial flow fan aerodynamic and aeroacoustic performance in a split-type air-conditioner outdoor unit," *Int. J. Refrig.*, vol. 36, no. 3, pp. 1098–1108, 2013.

[6] E. Phan, T. Z. E. Wei, M. Hamdi, and A. Shukor, "A Study of Effects of Surrounding Structures towards Airflow Performance in the Outdoor Unit of Split-type Air-conditioners," in *International Conference on FLUID MECHANICS*, 2009.

[7] H. Wang, J. Tian, H. Ouyang, Y. Wu, and Z. Du, "Aerodynamic performance improvement of up-flow outdoor unit of air conditioner by redesigning the bell-mouth profile," *Int. J. Refrig.*, vol. 46, pp. 173–184, 2014.

[8] "Bernoulli's Principle," *ModTech*. [Online]. Available: http://theory.uwinnipeg.ca/mod_tech/node68.html. [Accessed: 11-Oct-2015].

[9] T. Li, S. Pannala, and M. Shahnam, "CFD simulations of circulating fluidized bed risers, part II, evaluation of differences between 2D and 3D simulations," *Powder Technol.*, vol. 254, pp. 115–124, 2014.

[10] S. Z. Roshan, S. Alimirzazadeh, and M. Rad, "RANS simulations of the stepped duct effect on the performance of ducted wind turbine," *J. Wind Eng. Ind. Aerodyn.*, vol. 145, pp. 270–279, 2015.

[11] S. M. Salim and S. C. Cheah, "Wall y+ Strategy for Dealing with Wall-bounded Turbulent Flows," *Int. MultiConference Eng. Comput. Sci.*, vol. II, 2009.

[12] M. Edmunds, R. Malki, a. J. Williams, I. Masters, and T. N. Croft, "Aspects of tidal stream turbine modelling in the natural environment using a coupled BEM–CFD model," *Int. J. Mar. Energy*, vol. 7, pp. 20–42, 2014.

[13] A. Alaimo, A. Esposito, A. Messineo, C. Orlando, and D. Tumino, "3D CFD

Analysis of a Vertical Axis Wind Turbine," *Energies*, vol. 8, no. 4, pp. 3013–3033, 2015.

[14] M. Cable, "An Evaluation of Turbulence Models for the Numerical Study of Forced and Natural Convective Flow in Atria by A thesis submitted to the Department of Mechanical and Materials," no. May, p. 148, 2009.

[15] X. Ye, P. Li, C. Li, and X. Ding, "Numerical investigation of blade tip grooving effect on performance and dynamics of an axial flow fan," *Energy*, vol. 82, pp. 556–569, 2015.

[16] W. H. Lam, G. a. Hamill, and D. J. Robinson, "Initial wash profiles from a ship propeller using CFD method," *Ocean Eng.*, vol. 72, pp. 257–266, 2013.

Stability Improvement of Graphene Oxide Nanofluid by Optimizing Homogenization Factors

Fazrin Azwar bin Abdul Karim [1*], Azadeh Ghadimi[2]

[1,2]*Department of Mechanical Engineering, School of Engineering, Taylor's University, Malaysia*

[*]fazrin.azwar25@gmail.com

Abstract

The investigation of nanofluid materials is one of the example of solutions made to tackle ongoing engineering challenges; specifically the high cost of thermal management size increment to provide heat dissipation, which encourage the production of nanofluid as a cheap but effective novelty coolant. Using Graphene Oxide (GO) nanofluid as the area of research interest; the overall process of homogenizing and stabilizing GO nanofluid will be experimented, characterized, analyzed and improved based on three distinct homogenization factor; GO concentrations (0.005-0.010 wt.%), homogenizer's RPM (660-1500 RPM) and the homogenization period (60-180 min). As a cost-effective method of acquiring GO nanoparticles, filtering and drying used GO samples was showcased a feasible option to be executed. Finally, the collection of sediment balance method (SBM) readings as well as UV-Vis dimensions plays a major role on obtaining the optimization values via DOE software for the overall stability of GO nanofluid.

Keywords: Nanofluid, Homogenization Factors, Stability, Graphene Oxide

1. Introduction

The advancements of engineering and technologies developments have led to the exponential growth of production and investigation of nanofluid materials. This is due nanofluids' image of being one of the cost effective solutions made to tackle ongoing engineering challenges such as alternative coolant for the high cost of thermal management size increment to provide heat dissipation [1]. Historically, the term 'Nanofluid' was defined by researchers named Choi and Eastman to refer the condition in which nano-sized particles; nanofibres or metal or non-metal nanoparticles, were dispersed within a fluid medium; with the properties of possessing high thermal conductivity boost [2].

Based on the nanofluid definition, two primary techniques of producing nanofluids can be implemented using 'Single Step Method' and 'Two Step Method' [3]. The 'Single Step Method' is also known as the Vacuum Evaporation onto a Running Oil Substrate (VEROS) process. One of the benefits of the respective method is the minimization of the nanoparticle agglomeration. However, this particular technique is very minimal in terms of general practice due to the process's high degree of complexity to be implemented plus the method is majorly effective towards low vapor pressure fluids [4]. Meanwhile, 'Two Step Method' is a technique that incorporates the combination or direct mixing of separately yielded nanoparticles and base fluids; with the controlling of surfactant addition and ultrasonication treatment, to form nanofluid. Conversely; with a simpler and cost-effective experimental setup, comes one of the main drawbacks of the respective process which is the low amount of stability level of nanofluid produced due high number of nanoparticles aggregation; diminishing the nanofluid high suspension characteristics.

Thus, using Graphene Oxide (GO) nanofluid as the area of research interest; the overall stability and homogenization of GO nanofluid will be experimented, inspected, analyzed and improved based on the optimization of three distinct homogenization factor; GO concentrations, homogenizer's revolution per minute (RPM) and the homogenization period. The project is specifically conducted on both the analytical and experimental analysis terms; where the analytical investigation involves the practice of Design of Experiment (DOE) software, utilizing the experimental design of three levels Box-Behnken Design (BBD) and Responses Surface Methodology (RSM) for the responses optimization. Meanwhile, the experimental method of analysis is achieved through the production GO nanoparticle and nanofluid via Simplified Hummer's method and Two Step Method. This particular research also aims to contribute towards the body of knowledge which is the study of nanofluid and its' applications via verifying or validating the results to be obtained with other literature works of the same field.

1.1 Objectives

The objectives of this research are:

1. To yield and characterize the Graphene Oxide in the form of nanoparticles.
2. To synthesize GO nanofluid based on three parameters; homogenization period, homogenizer RPM and concentration of GO.
3. To investigate the level of stability of GO nanofluid via two responses capturing and evaluation of sedimentation balance method and UV-Vis Spectrophotometer readings
4. To conceive and repeat the optimized run for a stable GO nanofluid based on the accumulated responses via DOE software optimization feature.

2. Theoretical Framework

2.1 Production and Characterization of GO Nanoparticles

There are two early documented methods associated with the synthesis of GO which are Hummer's method and Brodie's method. Each method utilized different types of acid chemical treatment to oxide the graphite material. However, Botas *et al*. research on the modified version of the two method reveal the critical difference on the type and numbers of functional group formed on the molecular structure of the synthesized GO [5]. Figure 1 shows the modified Hummer's method leading Brodie's method in terms of oxygen weight percentage as well as higher percentage for three functional group of epoxy, carboxyl and hydroxyl. Figure 1 also includes the RAMAN spectrometer reading as the characterizing tool for GO in terms of reading the degree of disorder of lattice; caused by oxidation. Thus, this particular literature clearly strengthen the case for the project to consider adopting modified Hummer's method in order to narrow the identification for the most suitable method to synthesize GO.

Table 1 – Main characteristics of samples.

	Elemental analysis (wt.%)					XPS								S_{BET}[a]	Raman		
	C	H	O	N	S	C/O	O (%)	C (%)	Csp^2 (%)	Csp^3 (%)	C–OH (%)	C–O–C (%)	C(O)OH (%)	(m^2g^{-1})	I_D/I_G[b]	W_D[c] (cm^{-1})	W_G[d] (cm^{-1})
GO-H	48.0	2.2	47.8	0.0	2.0	1.8	35.2	64.8	32.2	12.8	36.2	14.3	4.4	–	0.88	1348	1592
TRGH-700	87.8	0.8	11.1	0.0	0.3	9.2	9.8	90.2	74.6	15.1	8.5	0.6	1.2	390	0.91	1354	1592
TRGH-1000	97.9	0.1	1.1	0.0	0.9	57.8	1.7	98.3	82.4	13.9	3.6	0.0	0.0	300	1.28	1335	1570
TRGH-2000	99.5	0.0	0.5	0.0	0.0	332.3	0.3	99.7	88.9	9.6	1.5	0.0	0.0	140	0.09	1350	1580
GO-B	70.1	0.9	28.2	0.0	0.0	2.9	25.7	74.3	39.2	14.5	32.4	11.2	2.7	–	0.88	1332	1565
TRGB-700	90.1	0.2	9.7	0.0	0.0	13.1	7.1	92.9	75.0	13.1	9.2	1.8	0.9	660	0.86	1353	1578
TRGB-1000	98.0	0.3	1.6	0.1	0.0	25.3	3.8	96.2	77.3	14.1	8.6	0.0	0.0	570	1.10	1335	1570
TRGB-2000	99.3	0.0	0.7	0.0	0.0	37.5	2.6	97.4	81.8	13.0	5.3	0.0	0.0	140	0.33	1364	1588

[a] BET surface area.
[b] Ratio of intensities of band D and G in the Raman spectra.
[c] Position of band D in the Raman spectra.
[d] Position of band G in the Raman spectra.

Figure 1. Data of Functional Groups of GO Nanoparticles Treatments

Finally, Ban *et al*. reported on the findings of producing GO nanoparticles by applying the simplified Hummer's method as oppose to the modified process [6]. The main advantage of the simplified process over the modified is the similarity of oxidation values but through an easier and cost-effective way. Figure 2 shows the comparison of X-Ray Powder Diffraction (XRD) readings of previously mentioned Botas *et al*. against Ban *et al*. readings. Few observations can be made such as that both data display peak shifting around the approximated 10.5˚ with the recorded interlayer distance of 0.800 nm for simplified method meanwhile modified process logged at 0.846 nm of interlayer distance.

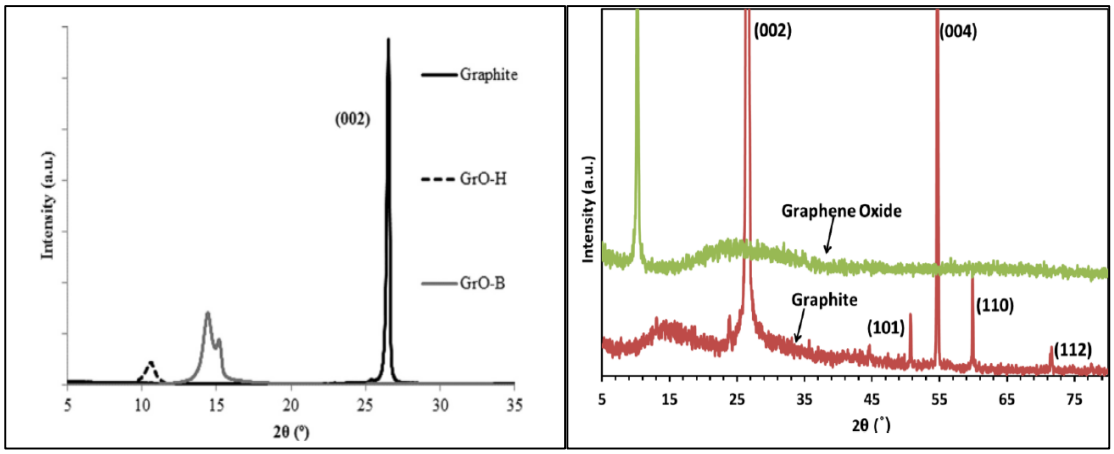


Figure 2. XRD Data Comparison of Modified (Left) and Simplified (Right) Hummer's Method.

In summary, based on the two well discussed literatures; the project is to be initiate with the implementation of the simplified Hummer's method as part of the research methodology to synthesize the GO nanoparticles. This is mainly due to the process ability to be compatible with the project scope; especially the cost-effective nature of the method and the availability of the instruments for Graphene and GO characterization made available at Taylor's University facilities.

2.2 Homogenization Factors and Stability of GO Nanofluid

For this sub-section; the focus lies upon reviewing the literatures on types of homogenization factors executed and the overall stability of GO nanofluids. For instance, Mehrali *et al*. has performed the investigation on the production, classification, and thermal conductivity of the nitrogen-doped graphene (NDG) nanofluid with distinct homogenization factors such as different types of surfactant addition plus vary range of sonication time [7]. The findings showcase a length of six month worth of stable nanofluid with factors of 60 minutes of probe ultrasonication and surfactant addition of X-100 compound. The interaction between the factors ensures the enhancement of thermal conductivity coinciding with stability improvement of the nanofluid. The only critical point to be stated out is that the manufactured nanofluid of nitrogen-doped graphene is based on entirely different chemical composition with the project's scope which concentrates on the Graphene Oxide nanofluid composition as well as other research like [8] and [9].

Besides, Lee *et al*. decided to focus on the particular heat transfer properties of GO nanofluid with a singular homogenization factors of continuous bath sonication of graphene oxide plus water; for a period of three hours, based on the two step method where water is chosen as the base fluid [10]. A critical observation that was developed upon reviewing this literature is the lack of focus on improving the overall stability of diluted GO nanofluid of the value 0.01% percentage before commencing on the critical heat flux (CHF) enhancement test; which may contribute towards the overall quality of the CHF experiment setup. Another research team of Zhang *et al*. also carried distinct CHF experiment setup but with the range of extremely diluted GO nanosheets (GONs) nanofluid concentration factors from 0.0001% till 0.001% to a similar outcome as Lee *et al*. group's literature [11]. Conversely; when a comparison is made, Zhang *et al*. project is less significant due to the smaller scope of the project and the low count of quantitative data for extra analysis.

Mehrali *et al*. once again managed to make sure that the team's chosen nanoparticle; graphene nanoplatelets (GNP), undergoes both thermo physical plus stability testing [2]. The data collected displays the GNP ability to be moderate in terms of heat transfer properties and the aptitude to stable for extended duration of time even though this projects purposely choose to control only the extent of the nanofluid ultra-sonication. Unfortunately, the developed nanofluid originated from GNP is established to be both lacking in similarities in terms of molecular structure but also less superior in terms of thermal conductivity enhancement; especially when compared with the readings of GO nanoparticles suspended within ethylene glycol (EG) base fluid [2].

Baby and Ramaprabhu also published a research with regards towards the graphene structured oxidation process into the thermal exfoliate graphene oxide (TEG) based on thermal exfoliation method [12]. The TEG nanofluid also undertaken the homogenization factor practices of the regulatory of the pH value range of mixture solution from pH 6 till 7 whereas the ultra-sonication process is controlled by the homogenization period allocated while the range of frequency being fixed. In summary, the literature shows that TEG nanofluid is clearly not homogeneous and stable as oppose to the functionalized-TEG nanofluid. This is mainly because of the UV-vis spectrophotometer inspection instrument displays absorption flattening reading since TEG is known to be non-homogeneity with the particles in deionized water (DI) for the UV test [12]. Hence, this showcase the stability increment inspection device must also be compatible with the nanofluids produced in order to avoid low quality data reading for additional analysis purposes.

Hajjar *et al*. also established that Graphene Oxide nanosheets ably accomplish long term stability in water; due to the sheet's hydrophilic surfaces. This homogenous dispersion is gain via pure ultra-sonication and different concentration of GO in form weight percentage [13]. As for the stability inspection tool, the sediment photo capturing method was used for this study and resulted in the no sedimentation of GO nanoparticles accumulated at the bottom of the fluid container. However, this publication is lacking the interaction of two factors out of three determined homogenization factors of the project; in order to further providing enhanced stability of the GO nanofluid.

Meanwhile, Dreyer *et al*. concluded the extensive research on the chemistry background of GO. Some key highlights such as the avoidance of damaging GO platelets when opting for mechanical stirring GO within polar organic medium or water as oppose to faster delivery output of sonication process [14]. Figure 3 displays the photo capturing technique of dispersed GO nanoparticles within 14 particular base fluid with a fixed ultrasonication period of 60 minutes.

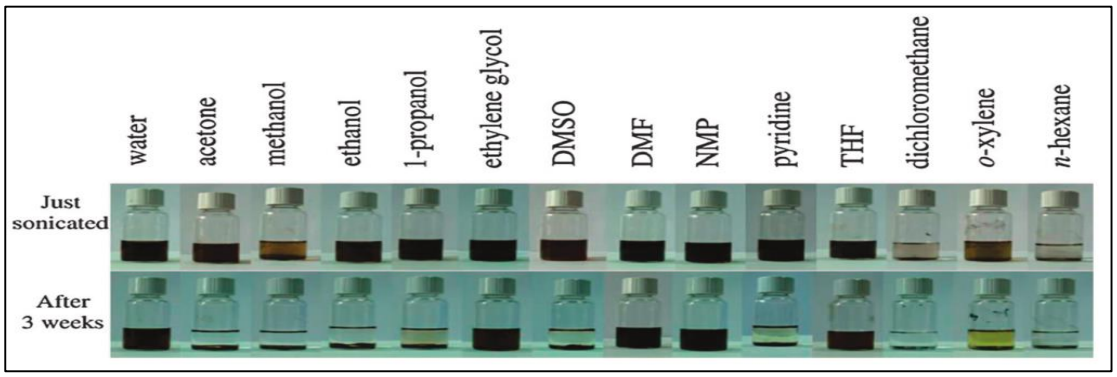


Figure 3. Different Periods of Photo Capturing of 14 Types of GO Nanofluid

Generally, the publication deals with the characterization of GO molecular composition which helps researchers to explore for future application of synthesized GO nanofluid. Unfortunately, the literature underprovide the overall GO nanofluid stability inspection stage which also contributes on the chemistry background of the GO.

Furthermore, Ijam *et al.* investigated on the thermos-physical properties, electrical conductivity and most significantly the stability of GON nanofluid with the distinct ratio combination base-fluid of DI/ethylene glycol [15]. The overall research showcase noteworthy nanofluid stability of up to 2 months of duration; via UV-Vis spectrophotometer data capturing, as well as about 1664% increase in terms of electrical conductivity for a specific parameter of 25 ℃ and 0.1% of weight percentage. The investigation however only dedicated on dispersion of GO in nanosheets form as oppose to nanoparticles.

Khoshvaght-Aliabadi *et al.* as well as Srinivas Rao and Srivastava publications managed to highlight on the usage of magnetic stirrers with distinct homogenization period as a form of homogenizing apparatus for the nanoparticles [16,17] respectively. Nevertheless, the lack of GO nanoparticles treatment for the investigation is an opportunity to be analyzed with.

Finally, two specific publications were reviewed to further explore on all three of the project's homogenization factors; concentration of GO, homogenizer RPM and homogenization period [18,19]. In comparison, both literature choose to implement the stirrer as one of the form of homogenizing the nanofluid synthesized. A critical observation can be made towards both research as the experimented material is not similar to the project's scope of optimizing GO nanofluid stability. Consequently, table 1 shows the compilation of the homogenization factors and stability inspection methods implemented for selected literature covered.

Table 1. Comparison of Homogenization Factors and Stability Inspection Method

Publication	Base Fluid	Concentration of Nanoparticles	Homogenizing Apparatus	Homogenizer RPM & Period	Stability Inspection Method
Mehrali *et al.* [7]	Distilled Water (DW)	0.01-0.06 wt.% of NDG	Ultrasonic Bath & Probe	N/A & 15-120 min.	UV-Vis Spec. & Zeta Potential
Lee *et al*. [10]	Water	0.01 vol.% of GO	Ultrasonic Bath	N/A & 180 min.	Zeta Potential
Zhang *et al*. [11]	Water	0.0001-0.0010 wt.% of GONs	N/A	N/A	UV-Vis Spec.
Baby and Ramaprabhu [12]	Water & EG	0.005-0.056 vol.% of TEG	Sonicator	30kHz & 30-45 min.	UV-Vis Spec.
Hajjar et al. [13]	DI	0.05-0.25 wt.% of GO	Ultrasonic Washing	60kHz & N/A	Thermal Conduct. Data & UV- Vis Spec.
Ijam *et al.* [15]	DI/EG	0.01-0.10 wt.% of GO	Ultrasonic Bath	40kHz & 60 min.	UV-Vis Spec.
Khoshvaght-Aliabadi *et al.* [16]	Water	0.1 & 0.3 vol.% of Copper	Magnetic Stirrer & Ultrasonic	N/A, 24kHz & 180 min., 120 min.	Thermal Conduct. Data
Srinivas Rao and Srivastava [17]	DI	0.005-0.03 vol.% of Aluminum oxide	Magnetic Stirrer	N/A & 16-18 hrs.	Thermal Conduct. Data
Park *et al.* [18]	Sodium-Water	0.214 vol.% of Titanium	Overhead Stirrer	660 RPM & 120 min.	N/A
Hwang *et al.* [19]	DI	0.5 wt.% of Carbon Black	Overhead Stirrer	1500 RPM & 120 min.	Zeta Potential

In summary, GO nanofluid is well recognized to being capable of experiencing increment in terms of stability with respect to the homogenization parameters optimization. Conversely, the lack of usage of magnetic stirrer based homogenizer by the research community shows the uncovered possibilities on optimizing the homogenization factors of Graphene Oxide nanofluid. Hence, the research gap is to execute the DOE software with regards on the optimization of three homogenization factors; homogenizer RPM, concentration of GO and homogenization period, which to ensure an increment of the overall stability of nanofluid.

3. Research Methodology

3.1 Production and Characterization of GO Nanoparticles

In this specific stage, the procured 2.5 kilogram of graphite powder via Sigma-Aldrich Inc. is acquired and characterized. This is to ensure that appropriate steps are taken to predict the outcome of upcoming physical and chemical treatment of the graphite while reducing the number of errors of experimentation. Some example of graphite or graphene characterization instruments which have not been covered are the scanning electron microscope (SEM), transmission electron microscope (TEM) and Fourier Transform Infrared Spectroscopy (FTIR). SEM and TEM device provides qualitative and quantitative readings in terms of image capturing with exact scale of graphene while FTIR displays the identification of functional groups within layers of both graphene and GO [20,21].

Next, the project is sustained through the oxidization of the graphite material with chemical mixture of sulfuric acid and gradual addition of potassium permanganate; based on the simplify Hummer's method, in order to yield GO nanoparticles [7,9]. Figure 5 shows the required steps for achieving GO nanoparticles of three grams of weight. Finally, the GO nanoparticles will be undergone through extensive characterization test of FTIR (Perkin Elmer-spectrum 100 model) and XRD (EMPYREAN, PANALYTICAL).

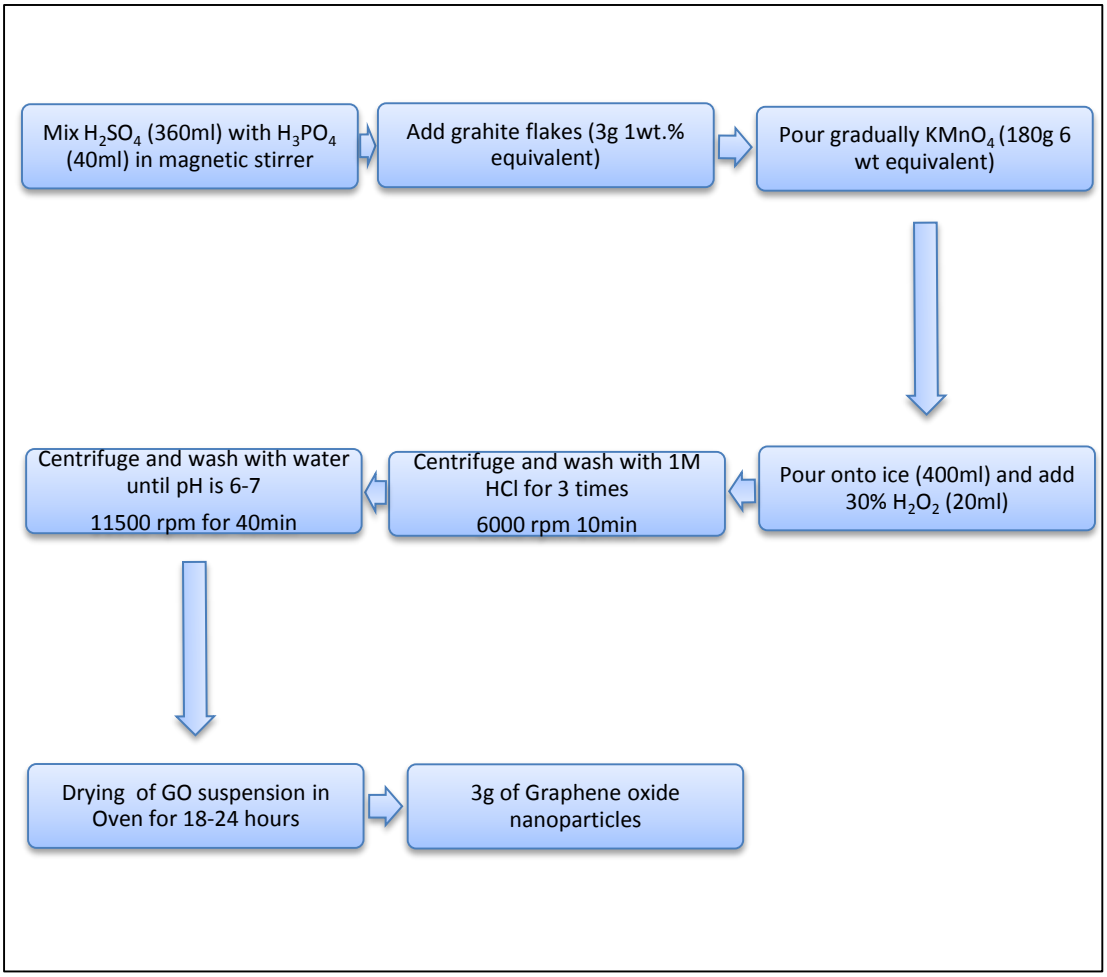


Figure 3. Overall Flowchart of Simplified Hummer Method for GO Synthesis

3.1 DOE Setup, Synthesis and Stability Inspection of GO Nanofluid

The first task for this stage are to run the DOE software with the main application of the BBD and RSM experimental method. Definitively, RSM is the usage of factorial design to achieve accurate magnitude, direction and information response capturing based on the preset factor effects [22]. BBD is define to be an independent quadratic design which promotes the quadratic effect of identified significant factors via no placement of points positioning at the respective vertices of the experimental region. BBD is particularly is beneficial towards the project as it considers the limited but precise project scope. Thus, the combination of the two experimental methods will result in the DOE software initiation of 3 factors, 3 levels, and 2 responses for a number of 15 runs each. Table 2 demonstrates the finalized table of runs by DOE software.

Table 2. Finalized Table of Factors and Responses by DOE software

Run	Factor 1: Homogenizer RPM	Factor 2: Concentration of GO (wt. %)	Factor 3: Homogenizer Period (min)	Response 1: SBM (%)	Response 2: UV-Vis Reading
1	1500	0.0075	60		
2	1500	0.0050	90		
3	660	0.0100	90		
4	1080	0.0050	60		
5	1080	0.0075	90		
6	1500	0.0100	90		
7	660	0.0050	90		
8	1080	0.0075	90		
9	1080	0.0100	60		
10	660	0.0075	120		
11	1500	0.0075	120		
12	660	0.0075	60		
13	1080	0.0050	120		
14	1080	0.0075	90		
15	1080	0.0100	120		

The second undertaking is the synthesis of the GO nanofluid via executing the two-step method where the initially yielded GO nanoparticles are dispersed in the base fluid of DI; based on the randomized 15 runs. Ultimately, the decision to implement two-step technique is preferred rather than one-step method as a cost-efficient process and widely practiced for majority of the literature reviewed such as [12], [13] and [23]. Moreover, the availability of a magnetic stirrer (WiseStir, SMHS-3) as a homogenizer with the maximum capability of 1500 RPM is capitalized. Lastly, the range of 0.005-0.010 of weight percentage (wt.%) is determined due to limiting the project's scope as well as preserving the amount of GO particles synthesized for the overall project.

Finally, the stability inspection is completed based on the readings of the UV-Vis spectrophotometer (THERMO SCIENTIFIC, Genesys 10S) and the implementation of sediment balance method (SBM). Firstly, the main interest of utilizing UV-Vis is the instrument ability to measure the degree of nanofluid stability via acquiring the peak absorbance wavelength of the homogenized nanoparticles [4]. Secondly, SBM is commonly performed to quantify the stability level of any nanofluid due to easiness is capturing the results. Sedimentation of the nanoparticles occurred because of the difficulty in breaking the aggregated nanoparticles [24]. Hence, the measurement of the sedimentation weight is converted into a suspension fraction (F_s) whereby $F_s = (W_0 – W)/ W_0$ [25]. Specifically, W_0 is the overall weight of all nanoparticles measured while W is the weight of the particular sediment at a certain period.

4. Results and Discussions

With respect, the overall length of the particular investigation was planned to be concluded by the end of 13 weeks from 24th August till 23rd November 2015. The results recorded up to this exact period were the filtration and drying process of GO nanoparticles from previously used samples and the three distinct SBM measurements of run 6, 12 and 13. Unfortunately, the overall response collection and optimization for the DOE software were not completed because of the time limitation.

4.1 Filtration and Drying of GO Nanoparticles

The task of filtering and drying used GO nanoparticles from previously used samples was originated to counter the mismanagement of lacking resources in terms of graphite for scheduled execution of simplified hummer's method. The particular situation presented an opportunity to practice the reusability of nanoparticles; specifically GO, as the process involves the filtering using filter paper (Whatman, Grade 1) and 60°C drying for minimum 2 hours of 13 DI base fluid samples; ranging from 0.005 to 0.03 volume percentage (vol.%) of GO.

The overall conversion value of the particular 13 samples from total vol. % to total mass of GO used by the 13 samples is equal to 0.687 grams. Consequently, the filtering and drying process resulted in the collection of 0.347 grams worth of GO nanoparticles. This shows the cost-effective and viability of both process since a value of 50.5% was guaranteed using only conventional filter paper and oven drying. Based on the particular literature, the oven drying method is categorized as bulk drying method; suitable for laboratory scale projects [26]. Figure 4 displays the overall setup and results of the experimental filtration and drying of GO.



Figure 4. Filtering Experiment Setup (Left) and Results after Oven Drying (Right)

4.2 SBM Data

For this specific sub-section; based on Table 2, three measurements of SBM were collected and analyzed based on distinct numbered runs of 6, 12 and 13 respectively. For instance, Figure 5 highlights the significant steps of weighting 'run 6' before and after 40 minutes period. Next, the overall data is tabulated as shown in table 3.



Figure 5. Original 'run 6' mass (Left) and after 40 minute period 'run 6' (Right)

Table 3. Finalized Table of Factors and Responses by DOE software

Run	Sample	Factor 1: Homogenizer RPM	Factor 2: Concentration of GO (wt. %)	Factor 3: Homogenizer Period (min)	Response 1: SBM (%)
6	1st	1500	0.0100	90	0.0957
12	2nd	660	0.0075	60	0.1010
13	3rd	1080	0.0050	120	0.0989

Therefore, the 2nd sample recorded the highest percentage of SBM reading in comparison to sample 1st and 3rd. This signifies low level of stability exhibited by the 2nd sample since the sedimentation phenomena represent the contrary nature of nanoparticles to suspend in colloidal forms within the base fluid as well as not to agglomerate with other respective nanoparticles.

5. Conclusions

In conclusion, the overall primary knowledge and responses collection of GO nanofluid stability investigation have been understood and still ongoing respectively. Future works must be performed such as the quality improvement on the literature review component with respect to both nanofluid stability as well as homogenizing factors.

The potential of reusing nanoparticles via filtration and drying method can assist in terms of adhering to a more cost-effective and sustainable future for nanomaterials industry. Finally, the DOE software for optimizing the results of the three experimented factors should produce a positive pattern upon project completion.

References

[1] N. A. C. Sidik, H. A. Mohammed, O. A. Alawi, and S. Samion, “A review on preparation methods and challenges of nanofluids,” Int. Commun. Heat Mass Transf., vol. 54, pp. 115–125, May 2014.

[2] M. Mehrali, E. Sadeghinezhad, S. T. Latibari, S. N. Kazi, M. Mehrali, M. N. B. M. Zubir, and H. S. C. Metselaar, “Investigation of thermal conductivity and rheological properties of nanofluids containing graphene nanoplatelets.,” Nanoscale Res. Lett., vol. 9, no. 1, p. 15, 2014.

[3] A. Ghadimi, R. Saidur, and H. S. C. Metselaar, “A review of nanofluid stability properties and characterization in stationary conditions,” Int. J. Heat Mass Transf., vol. 54, no. 17–18, pp. 4051–4068, Aug. 2011.

[4] S. Mukherjee and S. Paria, “Preparation and Stability of Nanofluids-A Review,” IOSR J. Mech. Civ. vol. 9, no. 2, pp. 63–69, 2013.

[5] C. Botas, P. Álvarez, P. Blanco, M. Granda, C. Blanco, R. Santamar á, L. J. Romasanta, R. Verdejo, M. a. L ópez-Manchado, and R. Menéndez, “Graphene

materials with different structures prepared from the same graphite by the Hummers and Brodie methods," Carbon N. Y., vol. 65, pp. 156–164, Dec. 2013

[6] F. Y. Ban, S. R. Majid, N. M. Huang, and H. N. Lim, "Graphene Oxide and Its Electrochemical Performance," vol. 7, pp. 4345–4351, 2012.

[7] M. Mehrali, E. Sadeghinezhad, S. Tahan Latibari, M. Mehrali, H. Togun, M. N. M. Zubir, S. N. Kazi, and H. S. C. Metselaar, "Preparation, characterization, viscosity, and thermal conductivity of nitrogen-doped graphene aqueous nanofluids," J. Mater. Sci., vol. 49, no. 20, pp. 7156–7171, Jul. 2014.

[8] A. Ghozatloo, M. Shariaty-Niasar, and A. M. Rashidi, "Preparation of nanofluids from functionalized Graphene by new alkaline method and study on the thermal conductivity and stability," Int. Commun. Heat Mass Transf., vol. 42, pp. 89–94, Mar. 2013.

[9] M. Mehrali, E. Moghaddam, S. F. S. Shirazi, S. Baradaran, M. Mehrali, S. T. Latibari, H. S. C. Metselaar, N. A. Kadri, K. Zandi, and N. A. A. Osman, "Synthesis, mechanical properties, and in vitro biocompatibility with osteoblasts of calcium silicate-reduced graphene oxide composites.," ACS Appl. Mater. Interfaces, vol. 6, no. 6, pp. 3947–62, 2014.

[10] S. W. Lee, K. M. Kim, and I. C. Bang, "Study on flow boiling critical heat flux enhancement of graphene oxide/water nanofluid," Int. J. Heat Mass Transf., vol. 65, pp. 348–356, Oct. 2013.

[11] L. Zhang, L. Fan, Z. Yu, and K. Cen, "An experimental investigation of transient pool boiling of aqueous nanofluids with graphene oxide nanosheets as characterized by the quenching method," Int. J. Heat Mass Transf., vol. 73, pp. 410–414, Jun. 2014.

[12] T. T. Baby and S. Ramaprabhua, "Investigation of thermal and electrical conductivity of graphene based nanofluids," J. Appl. Phys., vol. 108, no. 12, p. 124308, 2010.

[13] Z. Hajjar, A. M. Rashidi, and A. Ghozatloo, "Enhanced thermal conductivities of graphene oxide nanofluids," Int. Commun. Heat Mass Transf., vol. 57, pp. 128–131, Oct. 2014.

[14] D. R. Dreyer, S. Park, C. W. Bielawski, and R. S. Ruoff, "The chemistry of graphene oxide.," Chem. Soc. Rev., vol. 39, no. 1, pp. 228–240, Jan. 2010.

[15] A. Ijam, R. Saidur, P. Ganesan, and A. M. Golsheikh, "Stability, thermo-physical properties , and electrical conductivity of graphene oxide-deionized water / ethylene glycol based nanofluid," Int. J. Heat Mass Transf., vol. 87, pp. 92–103, 2015.

[16] M. Khoshvaght-Aliabadi, H. Shabanpour, A. Alizadeh, and O. Sartipzadeh, "Experimental assessment of different inserts inside straight tubes: Nanofluid as working media," Chem. Eng. Process. Process Intensif, vol. 97, pp. 1–11, 2015.

[17] S. Srinivas Rao and A. Srivastava, “Interferometry-based whole field investigation of heat transfer characteristics of dilute nanofluids,” Int. J. Heat Mass Transf., vol. 79, pp. 166–175, 2014.

[18] G. Park, S. J. Kim, M. H. Kim, and H. S. Park, “Experimental study of the role of nanoparticles in sodium–water reaction,” Nucl. Eng. Des., vol. 277, pp. 46–54, Oct. 2014.

[19] Y. Hwang, J.-K. Lee, J.-K. Lee, Y.-M. Jeong, S. Cheong, Y.-C. Ahn, and S. H. Kim, “Production and dispersion stability of nanoparticles in nanofluids,” Powder Technol., vol. 186, no. 2, pp. 145–153, Aug. 2008.

[20] M. B. Moghaddam, E. K. Goharshadi, M. H. Entezari, and P. Nancarrow, “Preparation, characterization, and rheological properties of graphene–glycerol nanofluids,” Chem. Eng. J., vol. 231, pp. 365–372, Sep. 2013.

[21] W.W. Liu, S.P. Chai, A. R. Mohamed, and U. Hashim, “Synthesis and characterization of graphene and carbon nanotubes: A review on the past and recent developments,” J. Ind. Eng. Chem., vol. 20, no. 4, pp. 1171–1185, Jul. 2014.

[22] A. Ghadimi, “*Stability and Thermal Conductivity of Low Concentration Titania Nanofluids*,” University of Malaya, Kuala Lumpur, 2013.

[23] K. S. Suganthi and K. S. Rajan, “Temperature induced changes in ZnO–water nanofluid: Zeta potential, size distribution and viscosity profiles,” Int. J. Heat Mass Transf., vol. 55, no. 25–26, pp. 7969–7980, Dec. 2012.

[24] D. W. Oh, A. Jain, J. K. Eaton, K. E. Goodson, and J. S. Lee, "Thermal conductivity measurement and sedimentation detection of aluminum oxide nanofluids by using the 3ω method," Int. J. Heat Fluid Flow, vol. 29, pp. 1456–1461, 2008.

[25] H. Zhu, C. Zhang, Y. Tang, J. Wang, B. Ren, and Y. Yin, "Preparation and thermal conductivity of suspensions of graphite nanoparticles," *Carbon N. Y.*, vol. 45, pp. 226–228, 2007.

[26] Z. Pakowski, "Modern methods of drying nanomaterials," Transp. Porous Media, vol. 66, no. 1–2, pp. 19–27, 2007.

Linear Dynamic FEA Simulation of Air-conditioner Rubber Bushing

Gavin Neo Hung Ming[1], Ch'ng Shiau Ying[1]*, Yap Kim Haw[2]

[1]*School of Engineering, Taylors University Lakeside Campus, Malaysia*
[2]*Panasonic Appliances Air-conditioning R&D Malaysia Sdn. Bhd, Malaysia*

gavinhungming.neo@sd.taylors.edu.my, *shiauying.chng@taylors.edu.my

Abstract
This paper focuses on utilizing an experimental approach to determine the frequency dependent Young's Modulus for rubber bushing provided by Panasonic Appliances Air-conditioning R&D Malaysia Sdn. Bhd (PAPARADMY 1) and validate it through a simulation and experimental approach. The project is a joint industrial project between Taylors University and PAPARADMY 1. Firstly, Dynamic Mechanical Analysis (DMA) was performed on rubber specimens to obtain the storage modulus and loss modulus for the rubber bushing experimentally within a frequency range of 5 Hz to 100 Hz at isothermal temperature. From the storage modulus and loss modulus, the frequency dependent Young's Modulus and material damping of rubber can be calculated. Following that, ANSYS Mechanical APDL 15.0 was used to perform modal analysis and spectrum analysis simulation for the rubber bushing. A coding approach was used to model the properties of rubber in ANSYS Mechanical APDL as the current User Interface (UI) is unable to model frequency dependent material properties. Base excitation experiment was carried out to validate the Finite Element model developed. It is found that the results from the simulation and experiment are similar with a difference of approximately 5 Hz between the simulation and experimental peaks due to sources of error which are explained for this research.

Keywords: Rubber Bushing, Dynamic Mechanical Analysis, ANSYS Mechanical APDL, Spectrum Analysis, Base Excitation

1. Introduction

Rubber is a common material that is used in our everyday life. Rubber can come in many different forms which include natural rubber and synthetic rubber such as Isoprene Rubber (IR), Silicone Rubber (SiR), Styrene Butadiene Rubber (SBR), Polychloroprene (CR) and Perfluoroelastomer (FFKM) [1]. The many different forms of rubber are being utilized widely for various applications such as car tyres, hoses, rainwear, shoes, insulation and many others. Within such a wide range of topics, the topic of interest is specifically focused on investigating the properties of rubber bushing which is used to mount the compressor of air-conditioning units at Panasonic Appliances Air Conditioning Malaysia Sdn. Bhd. (PAPAMY 1) as a means to dampen the vibrations from the compressor.

Puşcă et al. [2] has purposed that natural rubber is an elastomer which basically means that it does not follow the linear elastic model for most materials and the Young's Modulus of rubber varies with frequency and temperature. PAPARADMY 1 is responsible for performing Finite Element Analysis (FEA) simulations on various different air-conditioner components. NX Nastran is used to perform design work and analysis by PAPARADMY 1. There are various types of simulations being performed such as modal analysis to calculate the natural frequencies and mode shapes of the air-conditioning components. The natural frequency of the components must be above the threshold of 100 Hz as the operating frequency of the air-conditioning system varies between 5 Hz to 100 Hz. This is due to coincide between natural and operating frequency which will induce resonance and severely damage the air-conditioning components.

Al-Alili et al. [3] has mentioned in his paper that heating, ventilating and air conditioning (HVAC) systems have been present since a long time ago and is a culmination of technology to guarantee the comfort of humans within an indoor environment. HVAC systems consists of several different engineering principles which mainly include fluid mechanics, thermodynamics and heat transfer. Abdullah et al. [4] also mentioned that an integral part of the HVAC system is the air conditioning system which works on the basis of refrigeration cycle and is responsible for the cooling of a particular zone.

Based on Zhenying et al. [5] the refregeration cycle of an air-conditioning unit is categorized into 4 steps. The high pressure liquid refrigerant will first enter the expansion valve. The valve will restrict the flow of the refrigerant and thus lowers the pressure of the refrigerant as it leaves the expansion valve. After the expansion valve, the refrigerant will then enter the evaporator as a low pressure liquid. Heat exchange process occurs at the evaporator where the refrigerant will absorb the heat of surrouding air and changes state from liquid to gas. The refrigerant will then enter the compressor as a hot low pressure gas. Within the compressor, the refrigerant is compressed to increase its pressure and is then moved to the condensor. Within the condensor, heat transfer process happens again where the refrigerant will give out its heat to the surroundings and condenses back to liquid form. The high pressure liquid refrigerant will enter the expansion valve again where the cycle is repeated. The refrigeration cycle of the air-conditioning unit can be simplified in the form of the diagram as shown in Fig. 1 below:

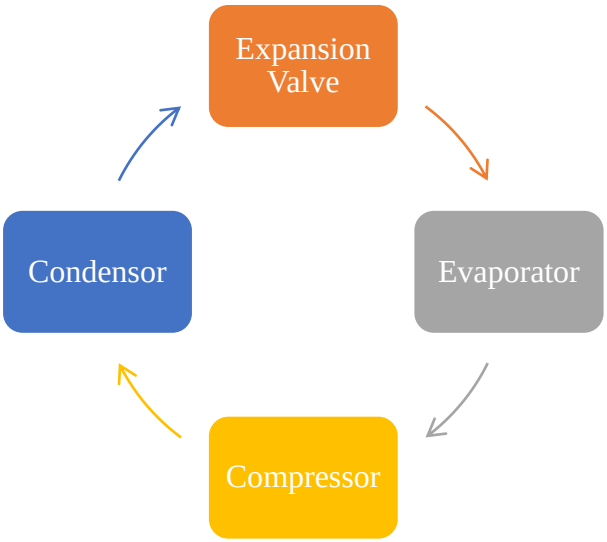


Figure 1. HVAC Refrigeration Cycle [5]

Compressors are used to compress the refrigerant to a higher pressure and is usually installed outside of the household. This is due to the compressors giving out loud noises during operation. There are many different types of compressor such as the reciprocating compressor, screw compressor, rotary compressor, centrifugal compressor and many others [6]. Rotary compressors are used in Panasonic brand AC. Rotary compressors operate on a simple compression mechanism and only require a low cost to produce. It is adopted mainly for AC units with cooling of 69,000 Btu/hour [6-7].

The main concern of this research is targeted at the compressor used for compressing the refrigerant to a higher pressure. During operation, compressors are known to give out loud noises. A sound intensity measurement study was done and the vibrating cylinder heads of the compressor have been identified as the dominant noise source for the compressor [6-7]. Roozen et al. [6] has purposed that the noise level of the compressor in his research was found out to be within a range of 70 decibels (dB) to 96.6 dB. Exposure to sound levels of approximately 85 dB will initially cause a temporary lost in hearing which is known as temporary threshold shift (TTS). However, prolonged exposure to this level of sound would cause the TTS to become permanent threshold shift (PTS) which is permanent hearing loss [1].

The results of Swan's study states that the solution to this problem is to implement a damper to reduce the vibrations of the compressor. A rubber bushing is used as a damper for the compressor which dampens the energy transmitted through the bushing. Rubber has been used for various purposes since a long time ago and there is a very large demand for rubber be it natural or synthetic within various industries across the globe. Natural rubber is widely used as a vibration isolator due to it having a low Young's Modulus which is capable of sustaining deformations and isolating vibrations. Not only that, it also has high tensile properties and is cheap which makes it the ideal choice to reduce the vibrations of the compressor [2,8]. The compressor is mounted onto the rubber bushing and this will dampen the noise of the compressor.

Based on Sauerbrunn & Zemo [9], Dynamic Mechanical Analysis offers an insight to the mechanical and thermal properties of rubber and is able to provide information such as the glass transition temperature and damping behaviours of materials for a large range of temperatures and frequencies. The data of interest which can be obtained from DMA test are the storage modulus, loss modulus and tan delta of rubber. Storage modulus is a measurement of the energy stored by the rubber and is shown in Eq. (1) below:

$$Storage\ Modulus, E' = \frac{\sigma_0}{\varepsilon_0}\cos\delta \tag{1}$$

Loss modulus is the energy which is dissipated as heat and is shown in Eq. (2):

$$Loss\ Modulus, E'' = \frac{\sigma_0}{\varepsilon_0}\sin\delta \tag{2}$$

By dividing Eq. (2) by Eq. (1), Eq. (3) which is the material damping will be obtained as shown below:

$$\tan\delta = \frac{E''}{E'} \tag{3}$$

The complex Young's Modulus can be expressed as shown in Eq. (4) below:

$$E^* = E' + iE'' \tag{4}$$

where,
E' = Storage Modulus
E'' = Loss Modulus
E^* = Complex Young's Modulus
σ_0 = Initial Stress
ε_0 = Initial Strain
δ = Phase Lag between Stress and Strain
i = Imaginary Unit

For this research, a DMA plot for frequencies of 5 Hz to 100 Hz is to be obtained. A typical temperature plot for DMA is shown below in Fig. 2.

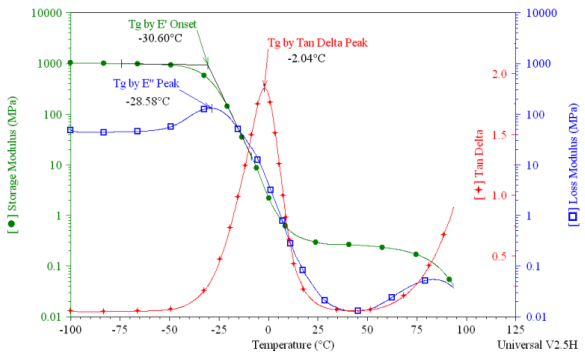


Figure 2. Typical DMA Graph of Viscoelastic Polymer [10]

Generally, hyperelastic material models are used to define the characteristic of rubber. Several popular models which are used frequently include the Neo-Hookean model, Mooney-Rivlin model and Arruda-Boyce model. These models are mainly used to predict the non-linear stress and strain properties for materials which are facing huge deformations. The curves of these models do not follow the linear elastic curve as purposed in Hooke's Law. Instead, Al-Bahkali et al. [11] mentioned that the stress and strain curve will only follow the linear elastic curve up to a certain point before it becomes non-linear . However, for this research the rubber can be modeled as a linear isotropic material. This is because the strain on the rubber damper applied through vibration of the compressor is very small. In other words, the rubber will never go past its yield point. Thus, the entire case falls under the linear region of the hyperelastic models and the rubber bushing can be modeled as a linear isotropic material which follows Hooke's Law as mentioned by Namani et al. [12] in his journal paper. Also, the strain which was applied in DMA testing was small and also falls within the linear region of the material model. Thus, the results obtained from the testing are valid and able to be used in a linear isotropic material model.

2. Research Methodology

2.1 Obtaining Rubber Specimens from PAPARADMY 1

The natural rubber specimens was obtained from PAPARADMY 1 with length of 25mm, width of 5mm and thickness of 0.5mm. The period to manufacture and obtain the rubber was 2 weeks.

2.2 DMA Testing of Rubber Specimens

TA Q800 DMA analyzer was used to perform the DMA analysis for the rubber specimens. A film tension clamp was used instead of a compression clamp to perform the experiment due to budget limitations. The test was carried out with a constant applied strain of 15 μm and isothermal room temperature of 26^{o}C. A frequency sweep ranging from 5 Hz to 100 Hz was performed to obtain the properties of the rubber specimen. The rubber was clamped to a fixed upper clamp and a 'floating' bottom clamp. The bottom clamp will oscillate upwards and downwards which will apply the strain of 15 μm to the rubber at different frequencies. The response of the rubber specimen is then measured by the analyzer. The test was repeated to obtain an average reading. The experimental setup for the DMA test is shown in Fig. 3 below:

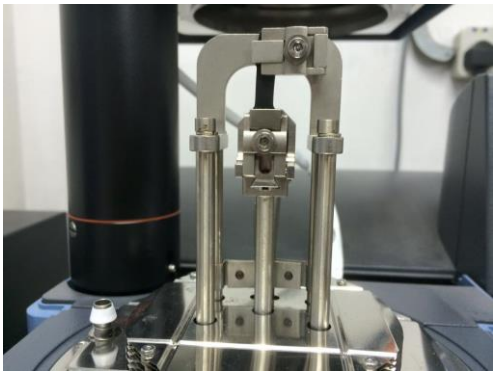


Figure 3. Experimental Setup for DMA Test (Film Tension Clamp)

2.3 Designing Fixture and Weight for Rubber

The second part of the research involves performing a modal analysis and spectrum analysis on the rubber bushing and performing a base excitation experiment to validate the FE model developed. Thus, it is required to design and manufacture a stainless steel fixture and weight for the rubber bushing to hold it in place on the shaker for the experiment. The fixture will be connected to a stainless steel jig previously manufactured by PAPARADMY 1. The jig will be connected to the base of the shaker through the usage of M12 bolts. The function of the weight is to provide a compressive force on the rubber bushing similar to the function of the mass shown below in Fig. 4:

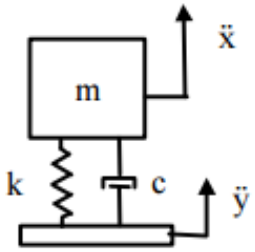


Figure 4. Single DOF Representation of Rubber Bushing System

Three parts were designed which are the fixture, fixture base and the weight. The fixture will be connected to the fixture base by M5 thread. The fixture base will be connected to the base of the jig by M4 bolts and the weight will be fitted tightly to the rubber bushing. The assembly is shown below in Fig. 5:

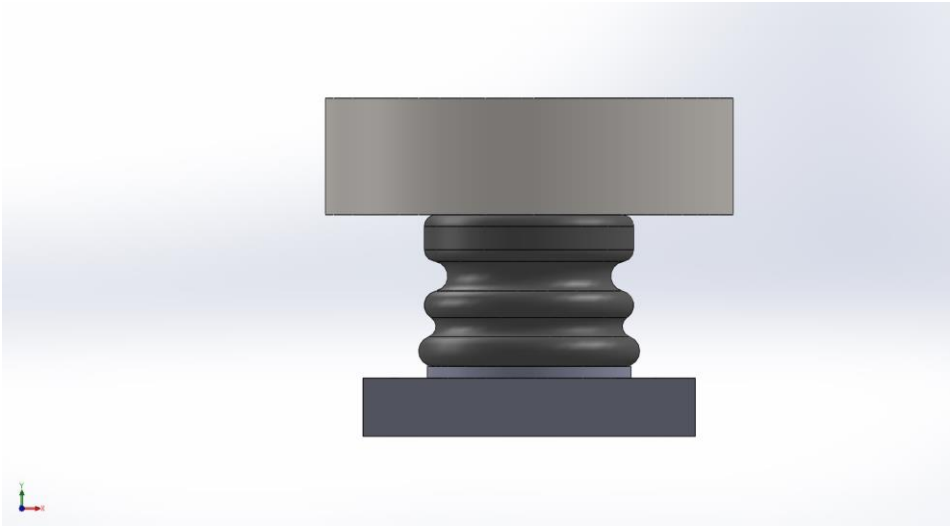


Figure 5. Front View of Assembly

2.3 Rubber Modelling in Mechanical ANSYS APDL

ANSYS Workbench was used to model the rubber bushings based on the experimental results obtained through DMA. ‘Bonded’ contact was used with the two M4 holes defined as fixed supports. Two different meshing methods were considered.

The first method was to use tetrahedral mesh on every component of the assembly whereas the second method was to use hex-dominant mesh on every component of the assembly with the exception of the fixture which was a tetrahedral mesh.The effect of mesh size was also analyzed by performing a mesh convergence analysis at the end of simulation. By inspecting different meshing methods and mesh sizes, it is found that the optimum method to be used is the second method with mesh size of 3 mm. This is because the second method has a significantly lower number of elements as compared to the first method. A lower number of elements results in shorter computation time and thus is preferred over its counterpart. Not only that, the first method has a very high element skewness of 0.99 which will greatly affect the accuracy of the results. It is also noted that a reduction in element size will also reduce the element skewness. However, this comes at the trade-off of increased computation time due to larger number of elements. As such, a 3 mm mesh size was selected rather than a 2 mm mesh size as there is a significant increase in the number of elements from 10105 to 27205. The increase in computation time from 3 mm to 2 mm mesh size is significantly longer with not much improvement to the accuracy of results. The element skewness of 0.9239 is acceptable as well because a further reduce in element size to 2 mm will increase the number of element significantly. The mesh details are shown in Fig. 6, Fig. 7 and Table 1 below:

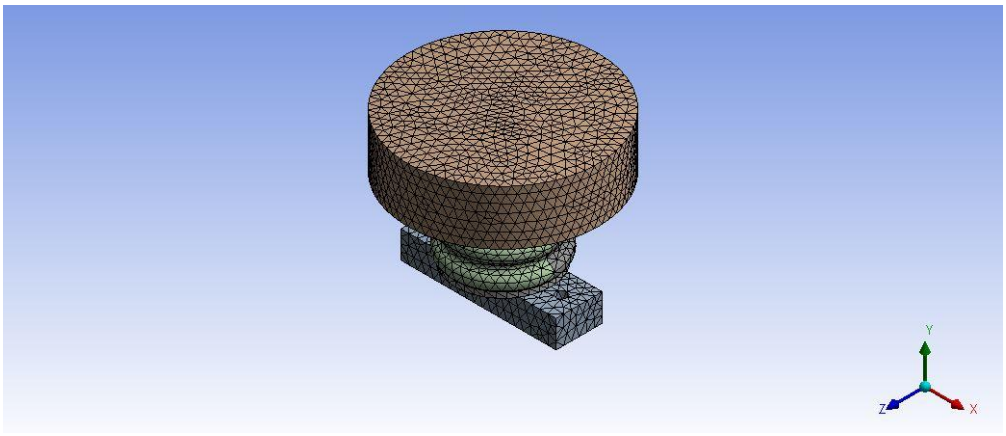


Figure 6. Meshing Method 1(3 mm Tetrahedral)

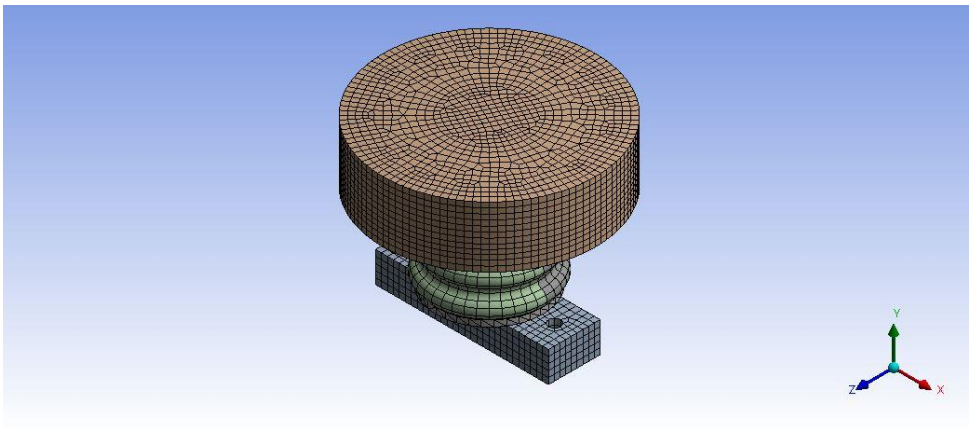


Figure 7. Meshing Method 2 (3 mm Hex Dominant + Tetrahedral Fixture)

Table 1. Number of Elements and Skewness for Meshing Methods 1 and 2

Mesh Size (mm)	**Method 1**		**Method 2**	
	No. of Elements	Skewness	No. of elements	Skewness
6	8178	0.9999	2777	0.9888
5	11627	0.9999	3589	0.9938
4	19229	0.9999	5518	0.9561
3	39636	0.9993	10105	0.9239
2	122372	0.9973	27205	0.8570

The assembly model was imported from ANSYS Workbench to ANSYS Mechanical APDL. The material properties are applied through a coding approach as the current User Interface (UI) does not support frequency dependent material properties. The rubber bushing is modeled as a linear isotropic material as the strain applied by the compressor on the rubber bushing is very small and is within the linear range of hyper elastic model and following Hooke's Law. PAPARADMY 1 had also provided other details which were modeled including Poisson ratio of 0.45, density of 1150 kg/m^3 and structural damping ratio of 0.5 for the rubber bushing. The rubber bushing can be represented as having the properties of both spring and damper in a single DOF system. Thus, both the Young's Modulus which represents the material stiffness and tan delta which represents the material damping needs to be included. As such, MPDELE and TBDELE commands are first used to clear any previous material properties assigned to the rubber bushing from ANSYS Workbench. MP and TB commands are used to define the frequency dependent material properties of rubber. Both modal analysis and spectrum analysis are carried out to investigate the acceleration response of the rubber bushing. The input force for the spectrum analysis is based on ISO 13355 Vibration Test Profile [13]. The acceleration response is calculated for both the base and the top of the assembly and is in the form of a curve. It is expected that there is a peak at the vertical mode shape frequency for the acceleration response measured at the top. The vibration test profile is shown below in Table 2:

Table 2. ISO 13355 Vibration Test Profile

Frequency (Hz)	Level (g^2/Hz)
3	0.0005
6	0.012
18	0.012
40	0.001
200	0.0005
Overall level, g rms	0.59

2.4 Base Excitation Experiment

The rubber bushing, weight and fixture were assembled together. The components were fitted tightly together and fixed in place. A uniaxial accelerometer was attached to the center of the weight to measure the acceleration response at the top. The assembly is shown below in Fig. 8:

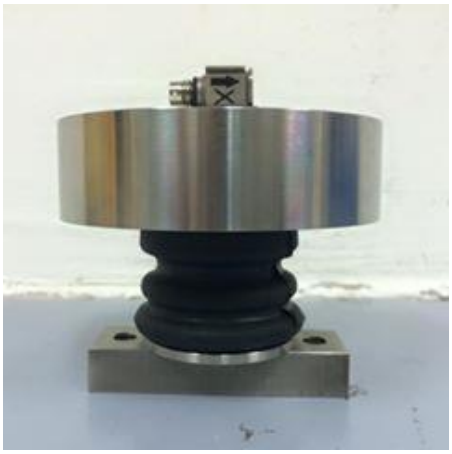


Figure 8. Rubber Bushing Assembly

The assembly was then screwed to the base of the PAPARADMY 1 jig by M4 bolts. The jig was then screwed to the shaker by using 6 M12 bolts. An accelerometer was attached to the base of the jig to measure the acceleration response at the base. ISO 13355 Vibration Test Profile was used. The vibrations of the shaker was observed through the controller. The vibrations will fall outside the upper and control limits at the beginning and gradually stabilize close to the center line. The measurements for the accelerometer were only recorded once the vibrations from the shaker has stabilized. The experimental setup is shown below in Fig. 9:

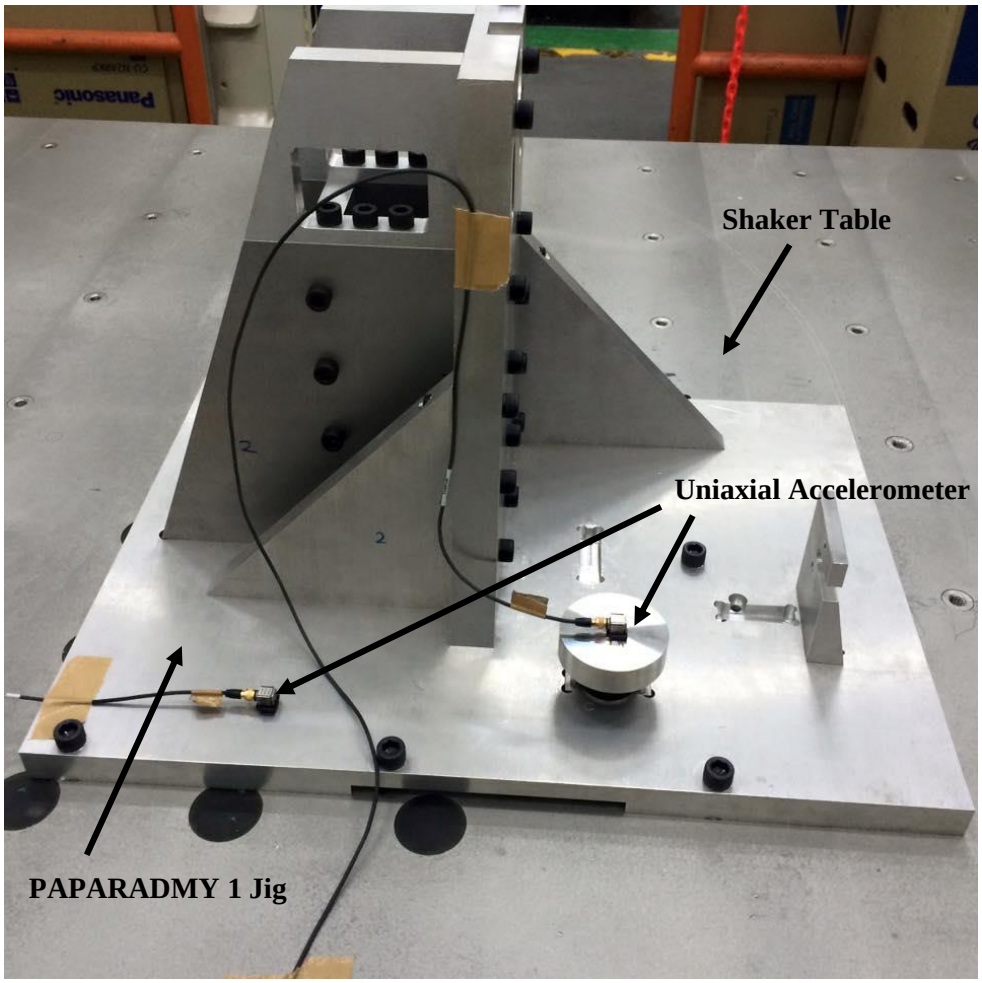


Figure 9: Experimental Setup of Base Excitation Experiment

3. Results and Discussion

3.1 Dynamic Mechanical Analysis (DMA)

DMA was performed on the rubber specimens obtained from PAPARADMY 1 to determine its material properties. The experiment was repeated to obtain three sets of results for storage modulus and loss modulus. There were some variations between the three sets of data as the temperature was rising slowly from 26°C to 29°C throughout the experiments. Due to budget constraints, nitrogen gas was not used as a cooling medium like it was supposed which caused the temperature to rise gradually from the heat generated by the DMA machine. This caused some slight variations in the data obtained as shown in Fig. 10 and Fig. 11 below:

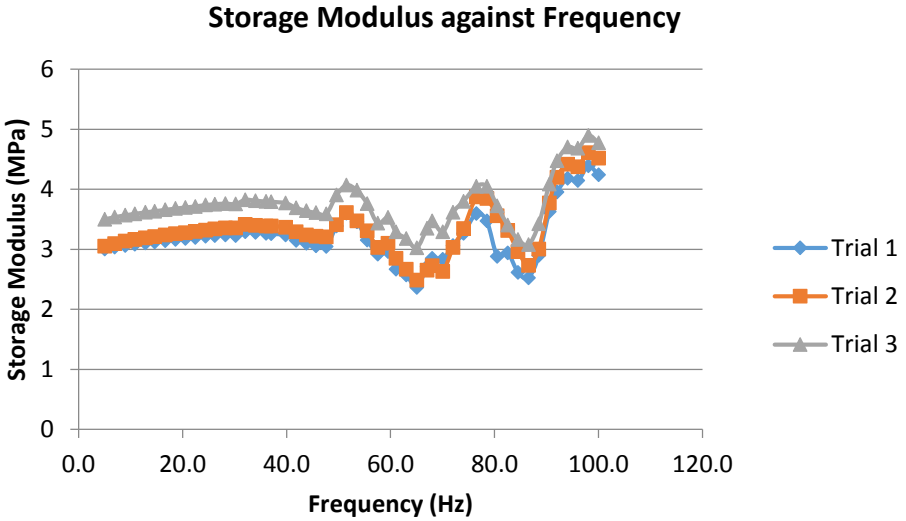


Figure 10. Graph of Storage Modulus against Frequency for DMA Results

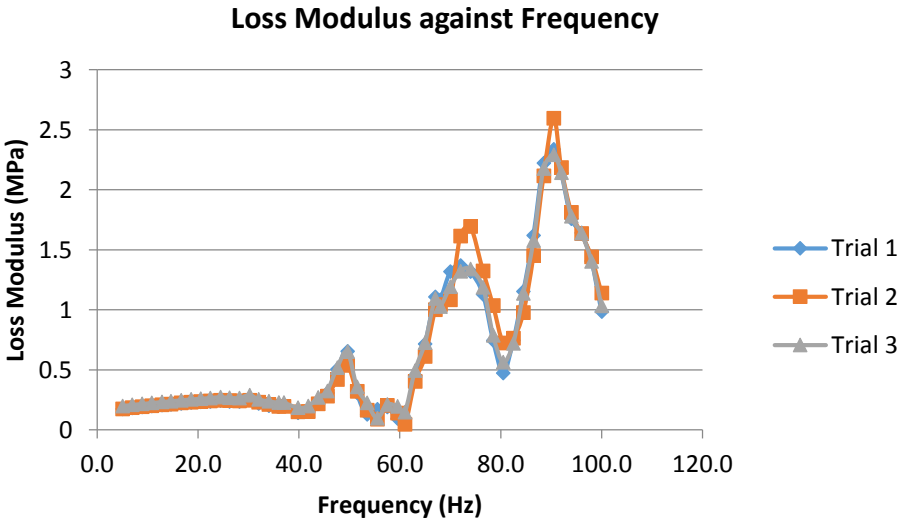


Figure 11. Graph of Loss Modulus against Frequency for DMA Results

Based on the storage modulus and loss modulus obtained from DMA, the tan delta which represents the material damping of rubber can be calculated as well based on Eq. (3). The tan delta of the rubber specimen is shown below in Figure 12:

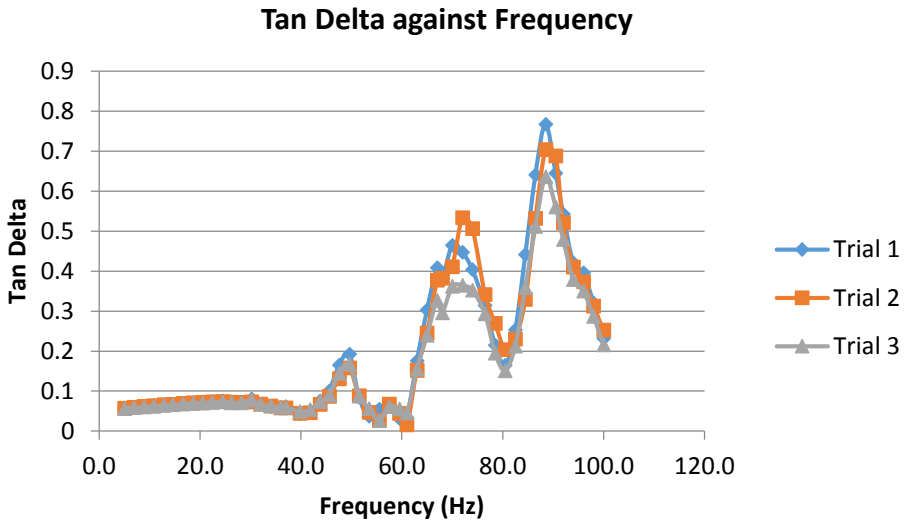


Figure 12. Graph of Tan Delta against Frequency for DMA Results

The average storage modulus and loss modulus were calculated and shown below in Fig. 13. Following that, the frequency dependent Young's Modulus was calculated based on Eq. (4) and shown below in Fig. 14. The average tan delta representing the material damping of rubber was also calculated and shown in Fig. 15:

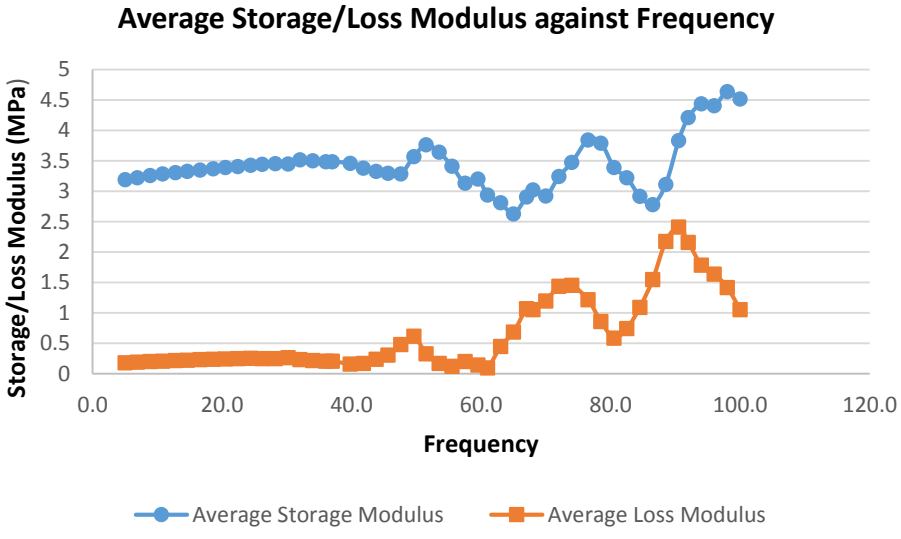


Figure 13. Graph of Average Storage/Loss Modulus against Frequency

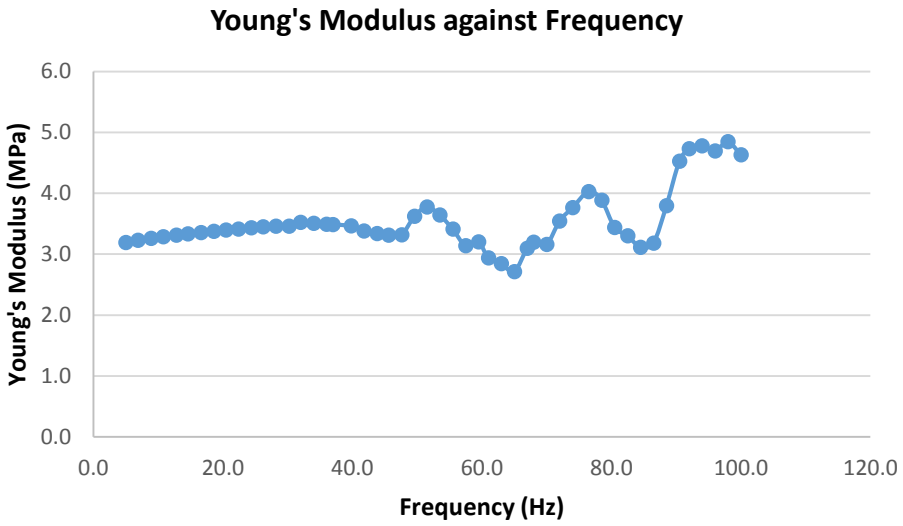


Figure 14. Graph of Young's Modulus against Frequency

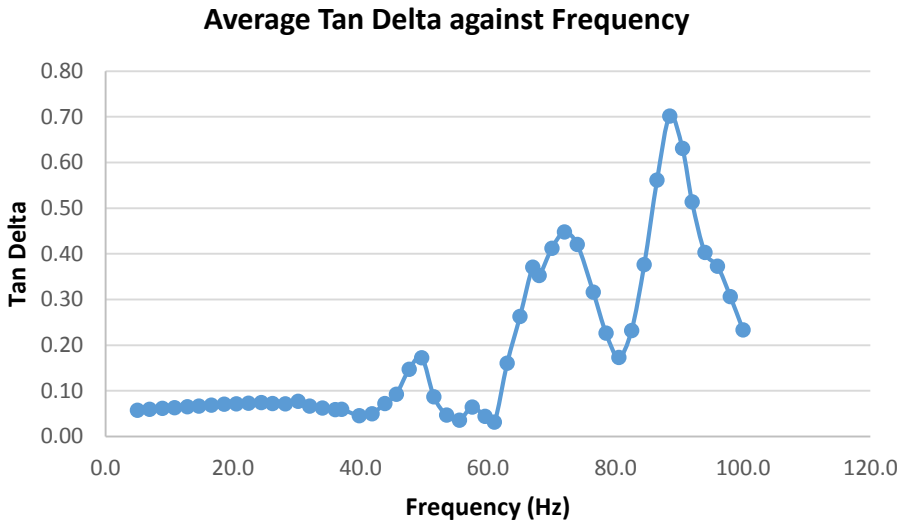


Figure 15. Graph of Average Tan Delta against Frequency

3.2 Modal Analysis and Spectrum Analysis

Based on the analysis performed, the acceleration response was calculated for both the base and the top of the assembly. The base excitation was input based on ISO 13355 Vibration Test Profile. Six mode shapes were determined to be within the frequency range of 5 Hz to 100 Hz with the vertical mode shape as mode shape 6 at 40 Hz. The base excitation is in the vertical direction which means that there is an expected peak at 40 Hz for the acceleration response curve. The modes of the assembly are shown in Table 3 below. Also, the acceleration response for the base and top calculated from simulation are shown in Figure 16:

Table 3. Rubber Bushing Assembly Mode and Frequencies

Mode Number	Frequency (Hz)
1	9.1503
2	10.279
3	12.398
4	37.367
5	38.073
6	40.683
7	315.55
8	324.28

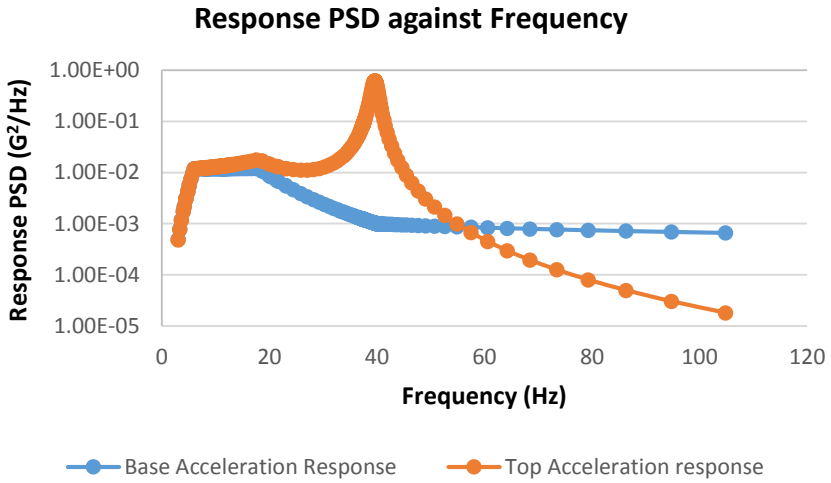


Figure 16. Graph of Response PSD against Frequency (Simulation)

3.3 Base Excitation Experiment

The response PSD curves for the base and top of assembly which were recorded by the accelerometers were plotted and compared with the simulation results from Fig. 16 and is shown below in Fig. 17 and Fig. 18.

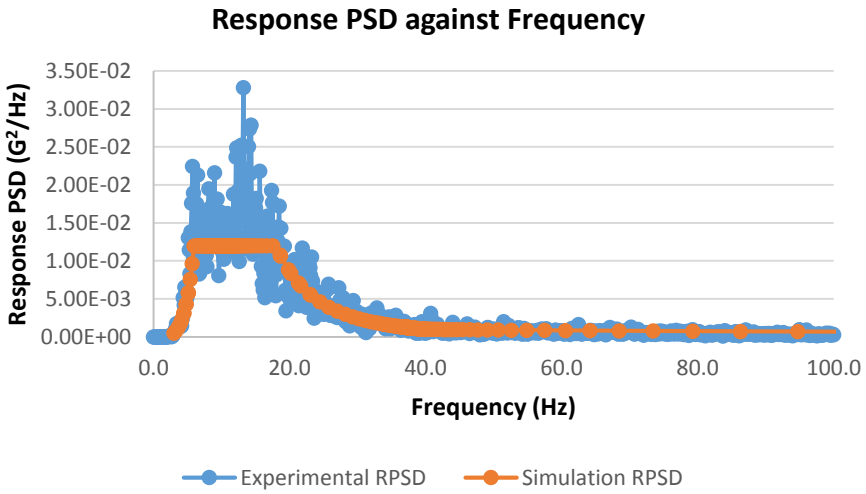


Figure 17. Graph of Comparison of Response PSD against Frequency (Base)

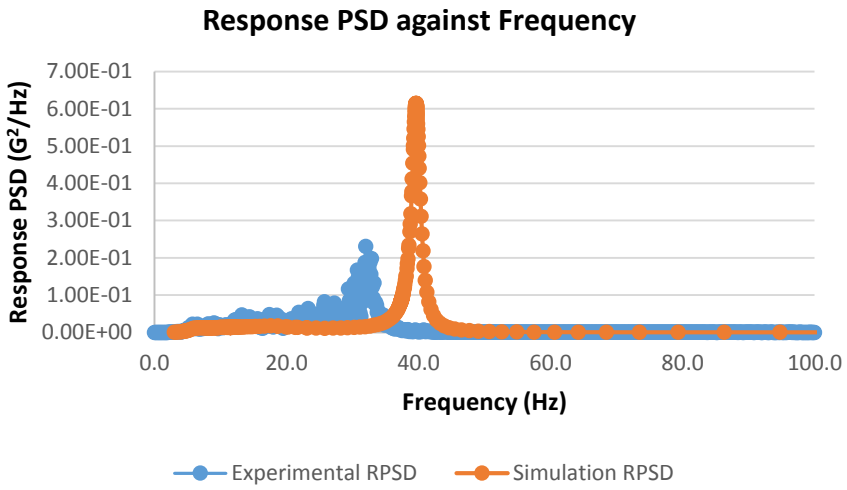


Figure 18. Graph of Comparison of Response PSD against Frequency (Top)

Also, ISO 13355 Vibration Test Profile is plotted against the real-time excitation curve of the shaker and is shown below in Fig. 19:

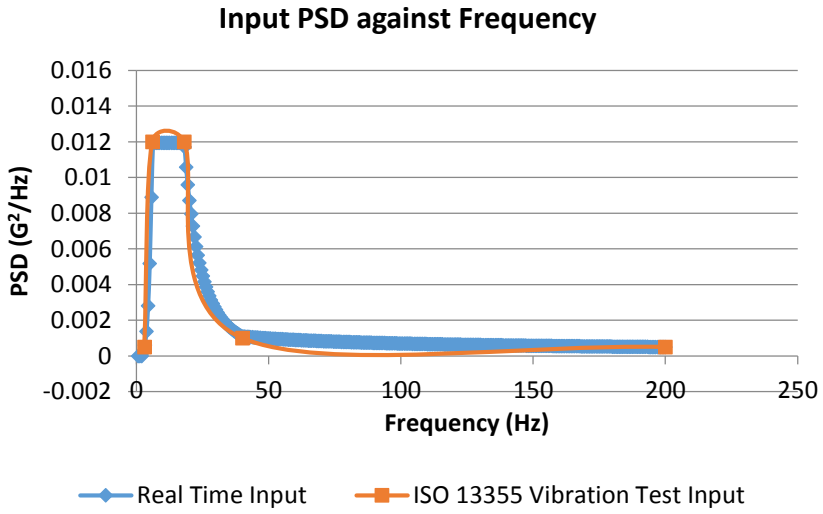


Figure 19: Graph of Input PSD against Frequency

3.4 Error Analysis

Based on the comparisons between simulation and experimental results, it is seen that the trends of the graph and almost similar with a difference of approximately 5 Hz between the peaks of the response PSD curves. This can be attributed to several causes such as temperature fluctuations when performing DMA, tension clamp instead of compression clamp used to perform DMA, jig not being fully rigid and 'bonded' to the shaker as defined in the simulation and also the actual base excitation varies slightly as compared to the ISO 13355 Vibration Test Input in the simulation.

4. Conclusion

Based on the research performed, the dynamic properties of rubber bushing have been found through an experimental approach of Dynamic Mechanical Analysis. The frequency dependent Young's Modulus is also calculated based on Eq. (4) as mentioned in the literature. A modal analysis and spectrum analysis has been performed to determine the acceleration response of the rubber bushing under a base excitation. The base excitation input is based on ISO 13355 Vibration Test Input. The base excitation experiment was carried out and the FE model was validated with a difference of 5 Hz between the peaks of the simulation and experiment results. All relevant results and findings have been presented and the material properties and methodologies will be used by PAPARADMY 1 for future simulations.

References

[1] Taneja, MK 2014, 'Noise-induced hearing loss', *Indian Journal Of Otology*, 20, 4, pp. 151-154, Academic Search Complete, EBSCO*host*, viewed 29 April 2015.

[2] Puşcă, A, Bobancu, Ş, & Duţă, A 2010, 'MECHANICAL PROPERTIES OF RUBBER - AN OVERVIEW', *Bulletin Of The Transilvania University Of Brasov, Series I: Engineering Sciences*, 3, 52, pp. 107-114, Academic Search Complete, EBSCO*host*, viewed 30 April 2015.

[3] Al-Alili, A, Yunho, H, & Radermacher, R 2014, 'Experimental Investigation of a Hybrid Air Conditioner for Hot and Humid Climates', *ASHRAE Transactions*, 120, 1, pp. 1-9, Food Science Source, EBSCO*host*, viewed 1 May 2015.

[4] Abdullah, H, Nitamakwuavan, S, & Jalaludin, A 2012, 'Energy studies on central and variable refrigerant flow air-conditioning systems', *AIP Conference Proceedings*, 1440, 1, pp. 486-490, Academic Search Complete, EBSCO*host*, viewed 1 May 2015.

[5] Zhenying, Z, Lili, T, Yanhua, C, & Lirui, T 2014, 'Effect of an Internal Heat Exchanger on Performance of the Transcritical Carbon Dioxide Refrigeration Cycle with an Expander', *Entropy*, 16, 11, pp. 5919-5934, Academic Search Complete, EBSCO*host*, viewed 30 April 2015.

[6] Roozen, N, van den Oetelaar, J, Geerlings, A, & Vliegenthart, T 2009, 'Source Identification and Noise Reduction of a Reciprocating Compressor; a Case History', *International Journal Of Acoustics & Vibration*, 14, 2, pp. 90-98, Computers & Applied Sciences Complete, EBSCO*host*, viewed 30 April 2015.

[7] Metwally, S, Khalil, M, & Abouel-seoud, S 2011, 'Noise evaluation of automotive A/C compressor', *International Journal of Energy & Environment*, 2, 3, pp. 505-514, Academic Search Complete, EBSCO*host*, viewed 29 April 2015.

[8] Lopes Pacheco, J, Bavastri, C, & Pereira, J 2015, 'Viscoelastic Relaxation Modulus Characterization Using Prony Series', *Latin American Journal of Solids & Structures*, 12, 2, pp. 420-445, Academic Search Complete, EBSCO*host*, viewed 29 April 2015.

[9] Sauerbrunn, S, & Zemo, M 2004, 'DMA of rubber in immersion environments', *Rubber World*, 229, 4, pp. 36-41, Business Source Complete, EBSCO*host*, viewed 1 May 2015.

[10] Turi, EA, 1997. *Thermal Characterization of Polymeric Materials*. 1st ed. Brooklyn, New York: Academic Press.

[11] Al-Bahkali, E, Erchiqui, F, Moatamedi, M, & Souli, M 2013, 'Deployment of a Neo-Hookean membrane: experimental and numerical analysis', *International Journal Of Multiphysics*, 7, 1, pp. 41-52, Academic Search Complete, EBSCO*host*, viewed 29 April 2015.

[12] Namani, R et al. 'Elastic Characterization Of Transversely Isotropic Soft Materials By Dynamic Shear And Asymmetric Indentation'. J Biomech Eng 134.6 (2012): n. pag. Print.

[13] 'Standard Test Method For Random Vibration Testing Of Shipping Containers'. *ASTM International* D4728.01 (2015): n. pag. Print.

Validation on the Simplified Model of the Bias Two-Wheeler Tire Characteristics Using Finite Element Analysis

Goh Kok Chong[1], Thein Chung Ket[1]*, Ch'ng Shiau Ying[1]

[1]*School of Engineering, Taylor's University, Malaysia*

*chungket.thein@taylors.edu.my

Abstract

Rubber is a complex material that has the ability to stretch at least twice its original length and return to its initial dimension. Indeed, the behavior of rubber is unpredictable at different conditions. The characteristics to such ability of rubber is analysed through finite element analysis on a bias tire model. Modelling and simulation of the two-wheeler bias tire model were executed using finite element analysis. Arruda-Boyce model was used to simulate the tire behaviour using FEA. The simulation model is verified through inflation and footprint analyses. The first validation of the inflation analysis shows that there is a good agreement between both simulation and actual tire. It was then further validated through footprint analysis. In footprint analysis, tire model was validated through footprint dimension and stress distribution. For the footprint's dimension, the average percentage error of footprint width was within acceptable range. However, the footprint height was slightly larger compared to actual tire footprints. In terms of footprint stress distribution, the stress intensity of simulation footprints was similar to the actual tire footprints. Moreover, the tire model experienced buckling during footprint simulation which resulted in presence of hole in the middle of footprint. The occurrence of buckling was due to softness of the tire model which is not reflected to the actual tire properties. Deformation characteristic of tire model were identified despite the occurrence of buckling. As a result, through inflation and footprint analysis, deformation behaviour of tire layer was identified and analysed.

Keywords: Finite Element Analysis, Bias Two-Wheeler Tire, Arruda-Boyce.

1 Introduction

1.1 Background

Tires are vital part of an automobile as it serves as a platform for automobile to travel with stability. Applying brakes to the tire will generate friction and wear out the tire surface thread. Hence, it is a necessity to change the tires of a vehicle when the threads of the tires are worn out so that the vehicle will not skid during accelerating and braking. In short, the safety of driver and passengers in an automobile depends on the performance of the tires.

Motorcycle is a two-wheeled automobile which is generally available in every country. According to the research conducted by Malaysian Institute of Road Safety (MIROS), the number of motorcycle accident has rocketed up from 79,816 to a shocking number of 120,156 from year 2000 to 2010 [1]. Among the motorcycle accident cases, one of the main causes of the accident is due to performance of the tire as stated by Malaysian Institute of Road Safety (MIROS). Although it is a small percentage, the amount of lives lost is bad for the population of a country. Therefore, research and analysis of the motorcycle tire also known as the two-wheeler tire has been done over the years to understand the behavior of the tire in order to improve based on the parameters which affect the performance of a tire.

Motorcycle tire, also known as two-wheeler tire consist mainly of two types, namely, radial and bias tire. The distinguishable feature between these tires is the belts construction in one of the tire layer. In this paper, bias tire will be emphasized.

Generally, a bias tire comprises of 4 layers: the first (outer) layer is the thread, second layer is the thread base, third layer is the cord rubber ply and the fourth (inner) layer is the liner as shown in
Figure1. In order to understand the behavior of a tire as a whole, it is important to investigate and understand deformation on each and every layer of the tire. Deep understanding of the simplified bias two-wheeler tire can be developed through analysis and simulation to investigate the contour deformation of the tire.

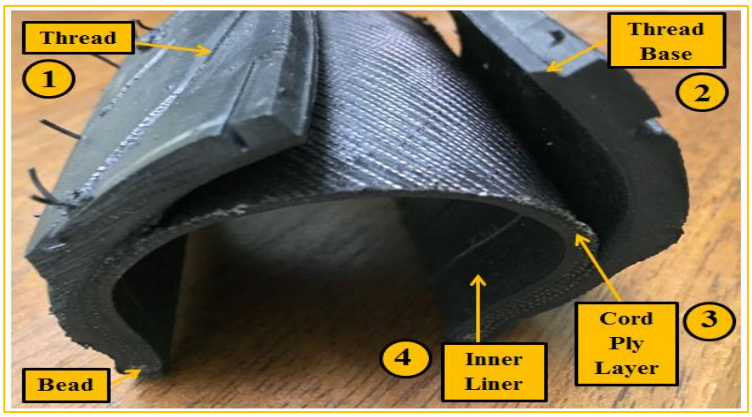


Figure 1: Structure of Bias Tire

The main objective of this project is to model and simulate the two-wheeler tire using finite element analysis. In order to validate the tire model, a series of analyses were conducted.

1.2 Two-Wheeler Tire

A bias ply tire is constructed with carcass running at 30^0 to 45^0 angle of the tread centre line [2]. Sidewalls and crown of a bias tire are constructed in a way that multiple rubber plies overlapped each other hence making them dependent on each other [3]. On the other hand, structure of bias tire enables transmission of sidewall flex to the thread and deformation of footprint [3]. As a result, the bias tire will slip and have less contact with the ground causing significant ground damage and decreased power transmission from engine [3]. Bias tire is much stiffer and hence it hardly absorbs shock and bumps on the road. The application of bias tire is normally applicable on motorcycle that transports heavy loads so that the side walls will not damage easily as bias tire has thicker and stiffer side walls. Due to tire performance which causes the rise of motorcycle accident rate for the past decade, improvements on the bias tire are needed to be analysed. Therefore, this research focus on the validation of the bias two-wheeler tires characteristics.

The bias tire comprises of 4 layers (see Fig. 1): the first (outer) layer is the thread, second layer is the thread base, third layer is the cord rubber ply and the fourth (inner) layer is the liner. The third layer is the cord rubber ply consists of another two layers of nylon cable that embedded into the tire. This nylon cable which acts as a cord which has an angle of 33^0 and 36^0, respectively. Both cord ply layers have alternate direction between plies; hence the name bias. The alternate direction cords provide bias tire with greater strength as stress of tire is distributed in both angle direction.

In short, the bias tire is one of the most common tires used by motorcyclists. Therefore, by conducting simulations and validating with experiment results, understanding of deformation on each layer of the bias tire can be achieved. As a result, improvements of the bias tire can be made to enhance the performance and vast amount of motorcycle accident rates can be reduced.

1.3 Actual Tire Performance

The characteristics of tires can be tested through experiments using testing machines. Testing machines such as the static load machine are used to obtain the strain results of the tire by applying different amount of stress. The strain results then can be analysed and the tire performance can be improved through modification.

However, experiments involving usage of testing machines are able to obtain tire results which can be used to improve limited areas of the tire. As a result, potential improvements of the tire are not able to achieve. In order to improve the performance of a tire as a whole, the behavior of the tire layers must be studied and understood. This can be achieved through simulations using finite element analysis. Through simulations, results can be obtained from each layer of the tire and analysis could be done through studying the deformation process of each layer.

1.4 Hyperelastic Model

In ANSYS simulation software, selection of material for the simulated model is important as different material will generate different results despite the same simulation process. Tire is made of rubber and the tire model generated in ANSYS will be simulated as hyperelastic material. Hyperelastic material is chosen because it represents similar properties as rubber such as non-linearly elastic, isotropic and incompressible.

In terms of stored energy function, rubber is known as hyperelastic material [4]. Rubber is assumed to be incompressible and it is isotropic in terms of elastic behavior according to theory proposed by Rivlin [4]. Since hyperelastic material is considered incompressible, the incompressible constant, d is assumed to be zero. Hyperelastic material characteristics can be represented in the form of simulation model by providing value of coefficient to the formula. Results retrieved from uniaxial, biaxial and shear test are used to determine the coefficients in these functions [4].

Performing a finite element analysis (FEA) on a hyperelastic material is difficult due to nonlinearity, large deformation, and material instability [5]. It is vital to select the appropriate hyper elastic material model before performing finite element analysis to avoid limitation in analysis and simulation. Several models have been compared in terms of number of parameters to generate model, stability under large strain and strain percentage. Hyperelastic models are being compared based on the parameters required to form the equation for the model and the range of strain percentage the model can withstand. The maximum strain percentage of a hyperelastic model has to be at least 300% to understand the stress-strain behavior of models such as tire. Because tire which is made of rubber is able stretch up to 700% of its original length.

The Arruda-Boyce model is one of few recently developed models that are applicable to hyperelastic material. It is a statistical mechanic-based model whereby assumed rubber is randomly oriented long molecular chain. It is an 8 chain model of the non-Gaussian statistical treatment that applied in large deformation of model. The equation for Arruda-Boyce model is shown in Eqn. (1) [4]:

$$U = \mu \sum_{i=1}^{5} \frac{C_i}{\lambda_m^{2i-2}} \left(\overline{I_1} - 3^i\right) + \frac{1}{D}\left[\frac{{J_{el}}^2 - 1}{2} - Ln(J_{el})\right] \quad (1)$$

where U is the strain energy potential, μ is the shear modulus, C_i is the material constant, λ_m is the locking stretch, $\overline{I_1}$ is the first invariant of deviatoric strain, D is the incompressibility constant and J_{el} is the elastic volume ratio.

The Arruda-Boyce model requires 5 materials constant, C, which can be generated from ANSYS. Arruda-Boyce model is able to generate up to 300% strain percentage. According to Cioroianu et al., Arruda-Boyce model is applicable in bio-polymer collagen network [6] which is one of the suitable models for to simulate polymer such as rubber material. According to Vegard Tømmernes, Arruda-boyce model is stable at large deformation due to its physical background [7]. There are many models such as Mooney-Rivlin, Yeoh, Ogden etc. that can represent rubber but

Arruda-boyce is one of the most suitable models in this research. Although the strain percentage is less than that of Ogden model, maximum strain percentage generated by Arruda-Boyce model is able to fit the tire model's strain percentage. Moreover, the material constants required to generate this formula is less than other models except for Neo-Hookean model. Thus with limited data of uniaxial test of tire, material constant still can be generated to fit in Arruda-Boyce model. Table 1 shows the comparison of the hyperelastic models.

Table 1: Comparison of Hyperelastic Models

Model	Number of parameter	Test	Strain Percentage (%)
Neo-Hookean	• 1 shear modulus, μ • Incompressibility constant, d	Uniaxial	• 30-40%
Yeoh	• 3 material constants, C • 3 incompressibility constants, d	Uniaxial	• 200-300%
Ogden	• 3 material constants, α • 3 shear modulus, μ	Uniaxial	• 700%
Mooney-Rivlin	• 2, 3, 5 and 9 material constants, C	Uniaxial	• 2 parameters : < 100% • 5 and 9 parameters : 100-200%
Arruda-Boyce	• 5 material constants, C	Uniaxial	• 300%

The study of the two-wheeler bias tire's behaviour is validated using commercial finite element analysis software. ANSYS is used to predict behavior of product and shows the operation of manufacturing processes in reality surroundings [8]. Finite element analysis provides detailed modelling and analysing features which will beneficial in this research.

Bias tire which will be simulated was modelled using ANSYS ADPL 15.0. The dimension of the modelled bias tire is based on the actual two-wheeler tire provided by Continental Tyre Sdn Bhd. The modelled bias tire used in this study will be simulated and analysed using ANSYS ADPL 15.0 as well. SOLID 186 were used to model the hyperelastic material which is a 20 nodes element type.

Boundary conditions are set based on the type of simulation to be tested on the subject. Besides setting the boundary conditions for the tire model, the selected material to simulate the tire model is also a vital step. The suitable material to simulate a tire model is hyperelastic material which is discussed in the following sub-section.

1.5 Validation of Simulation Results

In order to validate the characteristic of the bias tire model, analysis of the tire layers need to be done. Inflation and footprint simulations will be simulated on the tire model. Results generated from simulations will be analysed and compared with actual tire performances.

Tire circumference can be determined from inflation simulation which will be compared and validated through actual tire circumference. The tire model will be further validated through footprint analysis if the accuracy within the acceptable range.

Footprint results from simulation are compared with actual tire footprint in terms of footprint dimension and footprint stress distribution. Footprint results are validated if comparison between actual footprint and tire model footprint are below specific difference percentage.

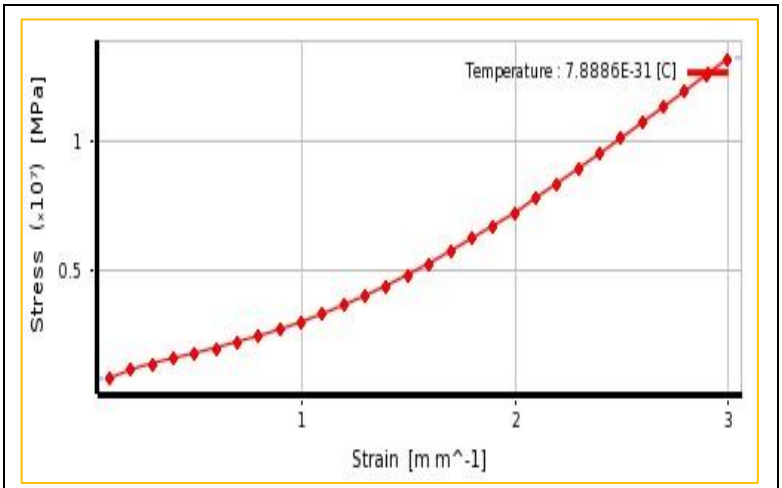
2 Research Methodology

This project comprises of 2 parts, namely, modeling using FEA followed by simulation using FEA. First phase of the project is mainly on improving the tire model through application of modelling and simulation techniques. Second phase of the project is on analysis of tire model layers through inflation and footprint simulation as well as validating the simulation results with actual tire results.

2.1 Modeling using Finite Element Analysis

2.1.1 Finite Element Model Parameter

The stress and strain results of the tire are obtained from uniaxial test which is conducted using tensile test machine in Continental Tyre Sdn Bhd laboratory. The results are later inserted to ANSYS Workbench to generate the stress-strain curve and the material parameters of the tire as shown in Figure 2. The generated material parameters reflect the properties of Arruda-Boyce hyperelastic model. The material parameters are then inserted to the equation of hyperelastic model to generate the model in ANSYS ADPL 15.0. In order to generate the tire model, modeling and simulation techniques are applied.



Arruda-Boyce		
Initial Shear Modulus Mu	1.604E+06	MPa
Limiting Network Stretch	-2.6635	
Incompressibility Parameter D1	0	Pa^-1

Figure 2: (Top) Stress Strain Curve and (Bottom) Material Constants

2.1.2 Finite Element Model

In order to validate the characteristic of the bias tire, modelling of the inner layer which is the cord ply layer has to be done to simulate and study the deformation of the layer. The cord ply layer of the tire consist of 2 layer of nylon ply embedded into rubber at alternate angle of 33^0 and 36^0 respectively. The technique to be applied in the modelling the cord ply layer is rebar element modelling. The cord ply layer are modelled by rebar elements which are superimposed to elements describing the matrix rubber elements so that it stabilize the tire and follow all deformations of the rubber element during simulations [9]. In addition, partial tire model of 20^0 is generated instead of a full tire model. Because simulation process of a full model is much more time consuming and takes up memory space of a computer.

After tire model is generated, meshing of tire model is necessary. Accuracy of simulation results is dependent on the mesh size. Because meshing the tire model with smaller mesh size is able to divide the tire model into more components known as elements. Hence, more elements are analysed to generate more accurate results. Convergence test was conducted on inflation simulation of tire model, where by different mesh size was simulated to generate different sets of stress results. Through convergence test, optimum meshing size of 1 mm were indicated and used for inflation and footprint simulation. Moreover, mesh type has huge influential on the accuracy of simulation results depending on the model. Although mesh shape of hexahedral is more accurate compared to tetrahedral, both type of mesh were used on the tire model to generate optimum results.

The tire model will be simulated in ANSYS using selected hyperelastic model which is Arruda-Boyce model. Before selecting the appropriate hyperelastic model, it

is necessary to compare several models. The comparison of the model will be based on stability of the model under large deformation and the fitment of stress and strain graph plotted using ANSYS Workbench. After the refinement model is completed, it is necessary to run the simulation.

2.2 Simulation Using Finite Element Analysis

This section comprises of inflation and footprint analysis. Inflation analysis will be conducted first then followed by footprint inflation. Results of inflation and footprint simulation will be compared and validated with actual footprint results.

2.2.1 Inflation Analysis

The objective of inflation simulation is to inflate the tire at a specific pressure and analyse the results generated which is the tire circumference. ANSYS ADPL 15.0 will be used as the simulation program to simulate inflation test on the existing modelled tire. Specific inflation pressures of 190, 210, 230, 250 and 270 kPa are applied to the inner liner tire as boundary condition as shown in Fig. 3 (Left). Boundary condition of fixing the inner side walls is applied to restrict movement of the tire as inflation pressure is applied as shown in Fig. 3 (Right). Tire displacements results are viewed in x-component as maximum displacement generating the tire circumference occur in x-axis direction. Resulted maximum displacement due to the inflation will be used to calculate the circumference of the tire with the formula as shown in Eq. (2).

$$Cir = \pi(D_i + 2D_f) \tag{2}$$

where Cir is the circumference, D_i is the initial diameter and D_f is the maximum deformation. Tire circumference results generated by Arruda-Boyce tire model are compared and validated with actual tire circumference.

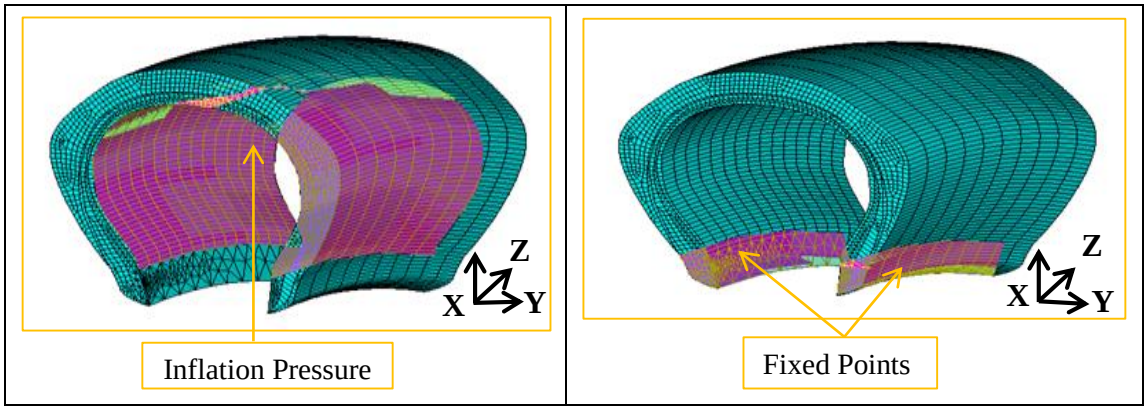


Figure 3: Pressure applied to Inner Liner Layer (Left) and Fixed Tire Side Walls (Right)

2.2.2 Footprint Analysis

Footprint simulation involves compressing a flat plate against a tire at a specific force. Result generated from this simulation will be a footprint on the flat plate's surface. A work plane is then created in ANSYS to capture the footprint. The

capturing method is done by altering the work plane on the same level as the flat plate's surface after compression. In short, the main objective of the footprint simulation is to analyse the footprint generated by hyperelastic models and validate with actual tire footprint.

In ANSYS ADPL 15.0, uniform force could not be applied to an area of a model. Thus, displacement is applied as force indicator. For example, the flat plate compress against the rubber block by 0.006408 m to generate compressive force of 801 N. Determination of compressive force through flat plate displacement is based on the experimental graph of vertical load against vertical tire deflection provided by Continental Sdn Bhd.

Complex rubber shape such as a tire behaves differently when subjected to compressive force. Hence, footprint generated is captured and analysed differently for rubber of various shapes. Before proceeding to footprint simulation of tire model, method of capturing footprint is verified through footprint block test. Similar to the tire footprint simulation, the footprint block test involves a rubber block compressed by a flat plate at a specific force as shown in
Figure 4.

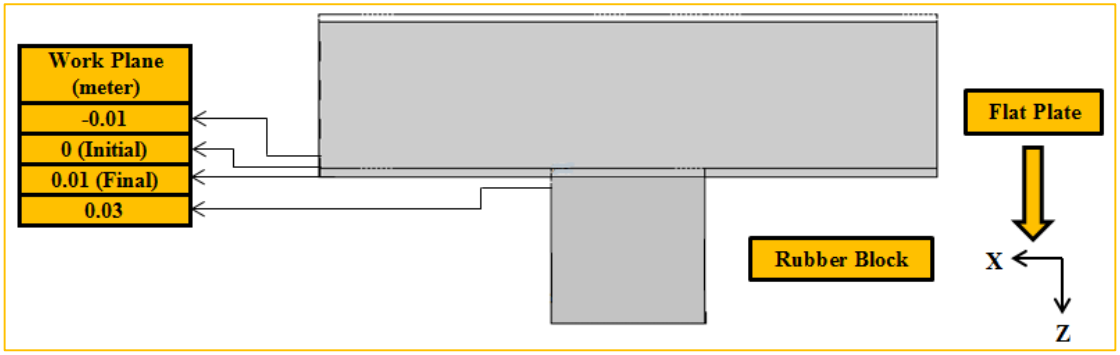


Figure 4: Footprint Block Test

After compressing the flat plate against the rubber block, the work plane is altered to 9 levels along the flat plate and rubber block. After analysing the footprints captured, conclusion made was footprint captured at the exact level as the flat plate's surface is the most accurate among the other footprints. Therefore, the proper method of capturing the footprint is verified.

After verifying the footprint capturing method, footprint simulation on tire model can be proceeded. Tire model with different inflation pressures of 190, 210, 230, 250 and 270 kPa is compressed with a flat plate in negative x-axis direction as shown in
Figure5. The flat plate is compressed against the tire at a specific displacement to generate desired compressive force. 5 sets of indicated compressive forces and respective displacements are shown in

Table **2**. As the displacement of flat plate increased, the compressive force generated is greater. After the compression, work plane is adjusted on the same level as the contact surface to capture the footprint. Footprints generated by Arruda-Boyce model

are compared and validated with actual tire footprint in terms of footprint dimension and stress distribution.

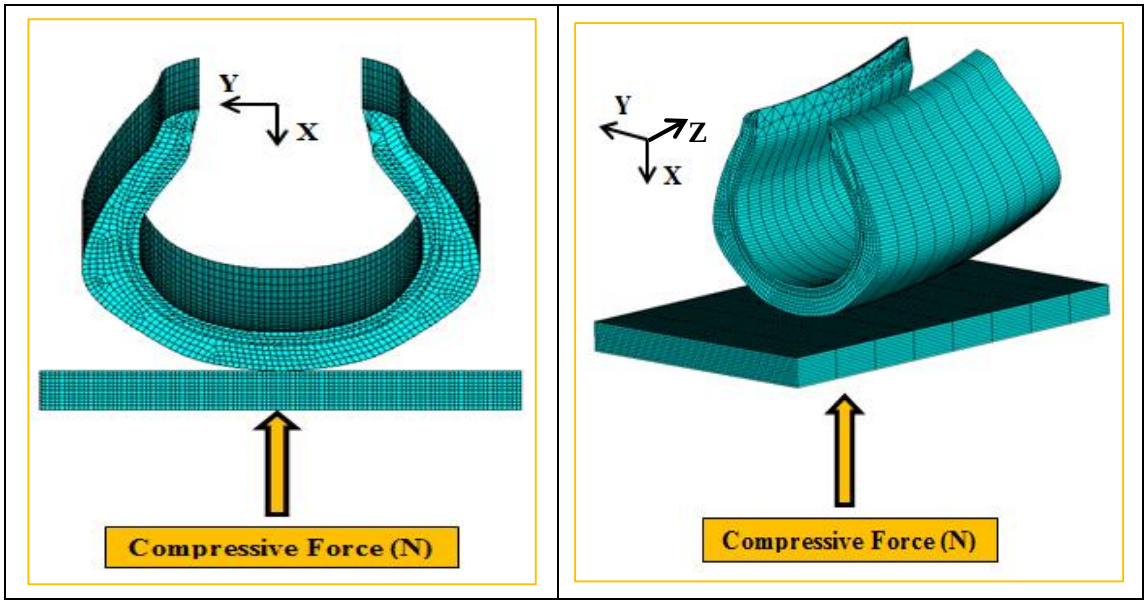


Figure 5: Footprint Simulation (Left) Front View, and (Right) Isometric View

Table 2: Flat Plate Displacements and Indicated Compressive Forces

Flat Plate Displacement (m)	Compressive Force (N)
0.006408	801
0.008008	1001
0.100160	1252
0.012536	1567
0.015032	1879

Methodology of this project is summarized in a flow chart as shown in Fig. 6.

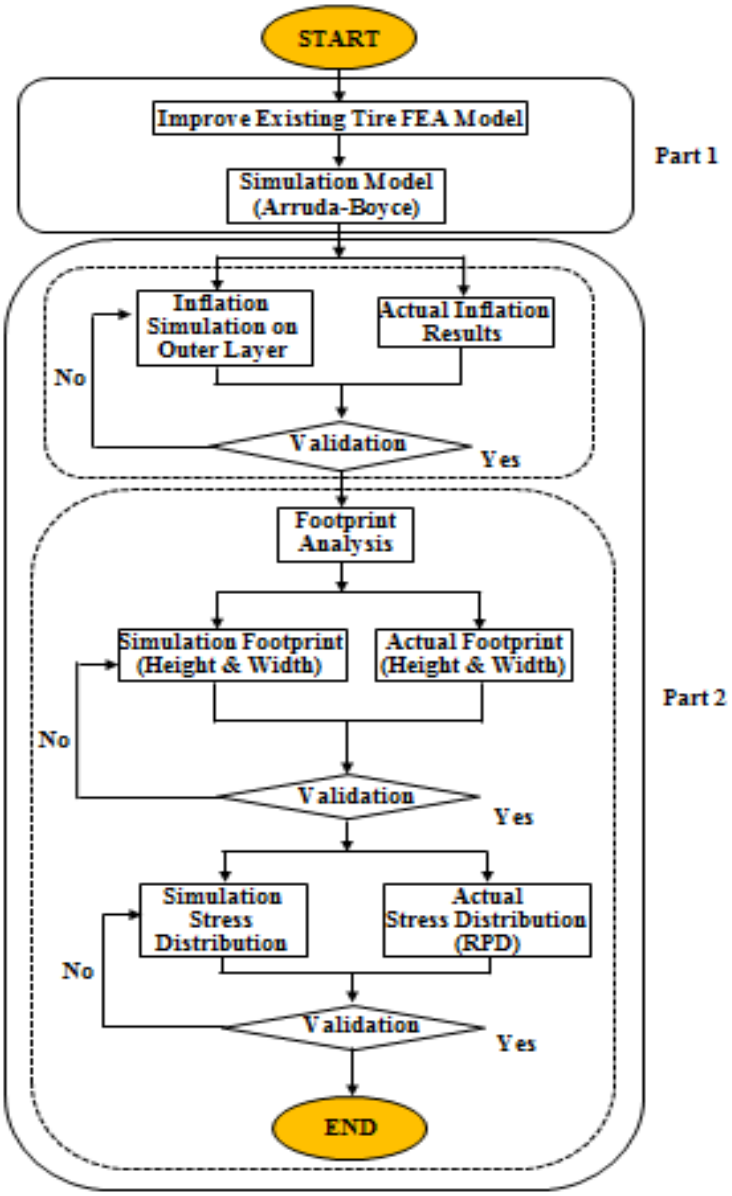


Figure 6: Project Flow Chart

3 Results and Discussion

3.1 Inflation Analysis

To validate the simulation model, inflation analysis was performed. Boundary conditions of pressures are applied to the inner liner tire layer as well as fixing the sidewalls of the tire model. Tire displacement is the result of applied pressure at 230 kPa in x-axis direction as shown in Figure7.

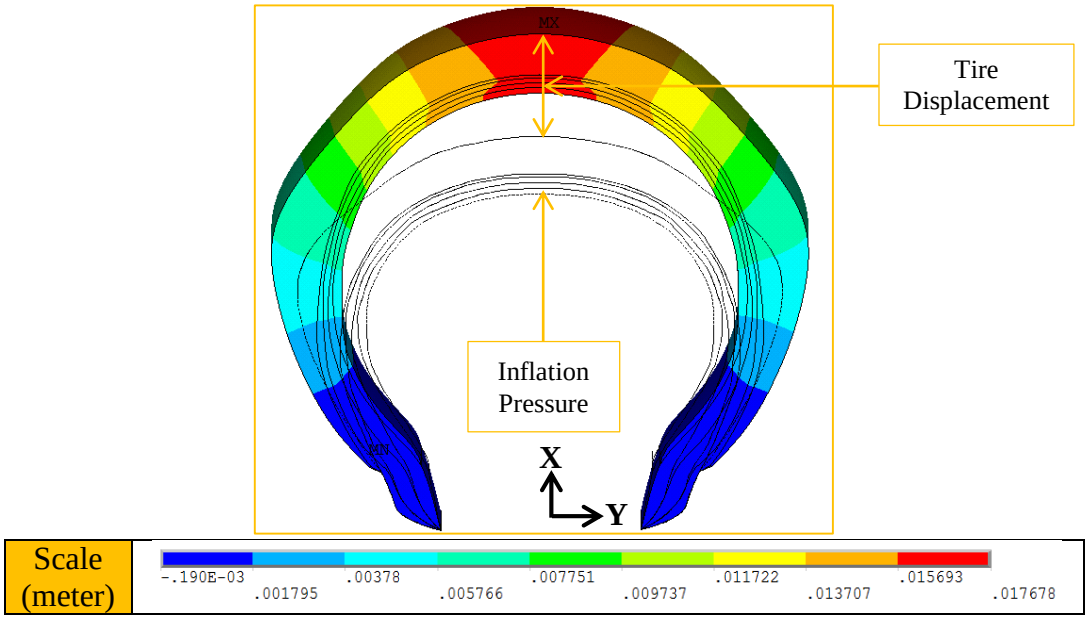


Figure 7: Tire Displacement and Inflation Pressure

Displacements generated by tire model are inserted to Eqn. 2 (Refer to section 2.2.1) to determine the tire circumference. Figure8 show that the graph of simulation circumference is plotted against pressure and compared it with the actual. The simulation model is used Arruda-Boyce method to predict the circumference. In addition, the models experienced a similar result as actual tire at lower pressure such as 190, 210 and 230 kPa with respective difference error of range from 2 % to 4 %. However, as the pressure increased to 250 and 270 kPa, the simulation circumference started to deviate from the actual tire circumference with difference error of range from 4 % to 6 %. Although the error percentage of Arruda-Boyce increases as the inflation pressure increases but it is able simulate with stability and results generated do not deviate drastically. The average error percentage of circumferences generated by Arruda-Boyce model is about 3.41%. Therefore, the simulation results are within acceptable range and the model will be furthered validate through footprint analysis.

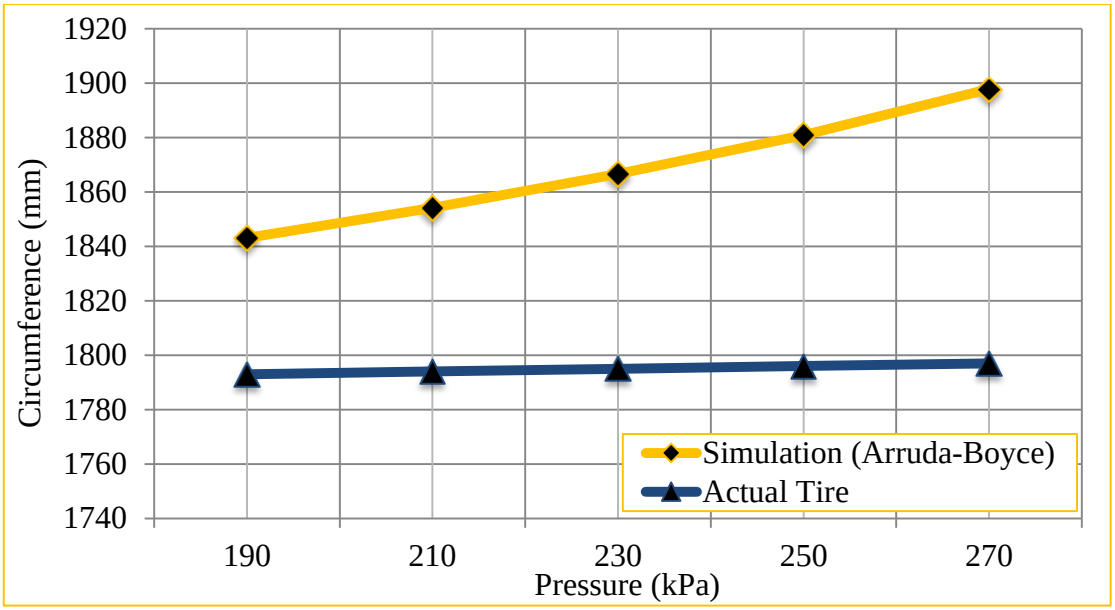


Figure 8: Graph of Tire Circumference against Pressure

3.2 Footprint Analysis

Footprint simulation is the extract by compressing the flat plate against the tire model. Inflated tire model of 230 kPa is subjected to compressive force of 801, 1001, 1252, 1567 and 1879 N. The footprint is capture at the surface of the plane. Contour distribution footprints of the simulation model are compared with the actual tire as shown in Figure 9.

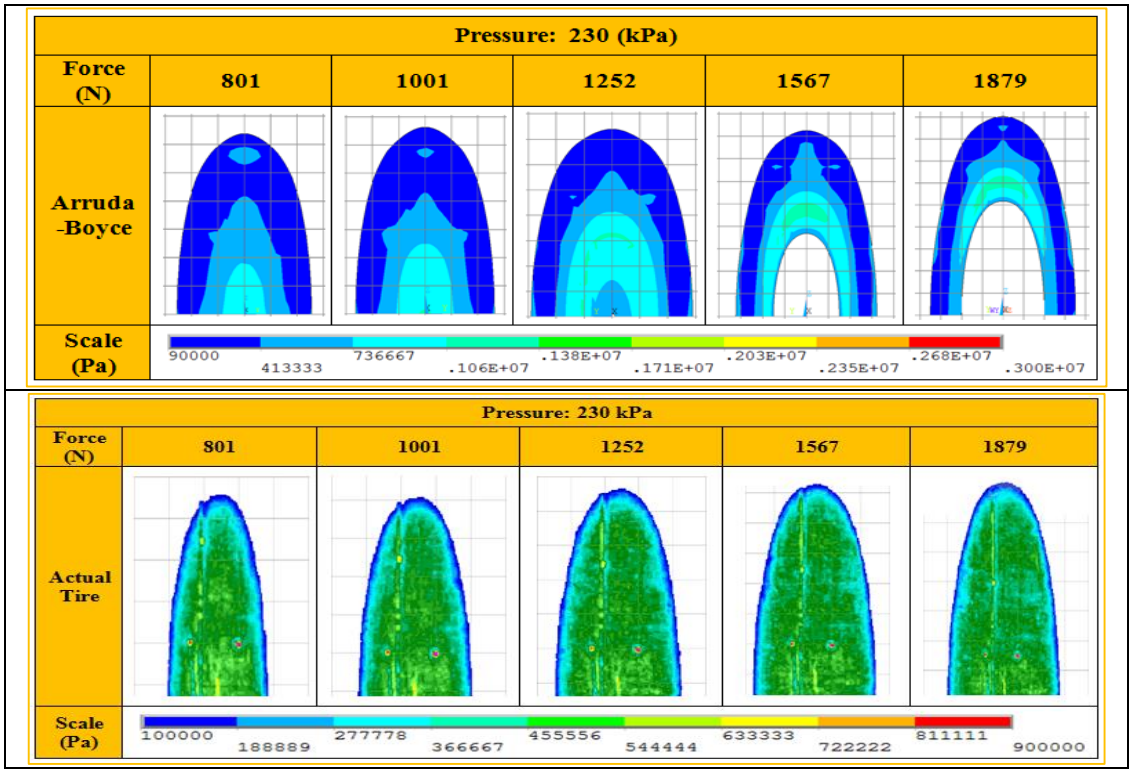


Figure 9: Simulation model (Top) and Actual tire (Bottom) footprints

Footprints for Arruda-Boyce model and actual tire have similar trend of increasing dimension as compressive force increased. This is because at higher compressive force, there is greater contact area between flat plate and tire surface resulting in bigger dimension footprint. Moreover, footprints shape of simulation and actual tire have similar shape.

Footprints width and height of Arruda-Boyce model and actual tire are measured and plotted in a graph as shown in Fig. 10. As shown in
Figure 10, footprint dimension of Arruda-Boyce model at lower compressive force footprint deviated from the actual tire results. However, at high compressive force footprint dimension generated is similar to actual tire. In terms of footprint width, simulation tire have average difference error of 14.3 %. Average difference error of footprint height for simulation tire is 30.1 %. This result suggested that Arruda-Boyce model has better capability and stability in simulating at higher force. After validating the footprint dimension, comparison and validation of footprint stress distribution can be proceeded.

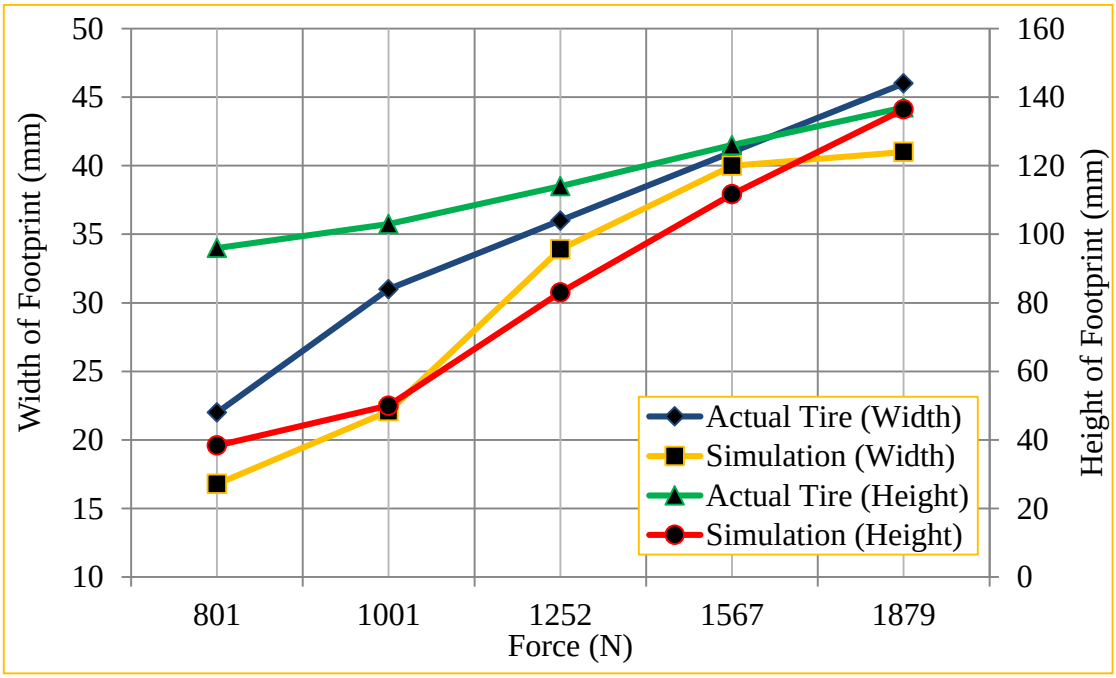


Figure 10: Footprint Width and Height of Simulation and Actual Tire

In terms of footprint stress distribution, simulation and actual footprints shows similarity in footprint stress intensity. This result shows that Arruda-Boyce model has similar structural strength properties as actual tire. This is because the stress intensity of footprint is affected by the structural and the strength properties of a tire. As a result, with similar structural and strength properties as tire, stress from compressing flat plate is able to distribute similarly as tire on the generated footprint.

A hole was found in the middle of the simulation footprints when the force is 1567 N and 1879 N as shown in Fig. 9. This is because the structural strength of the tire is lower than the actual tire performance. Hence, this phenomenon is known as buckling. Occurrence of buckling is due to instability when subjected to high compressive forces or stress which resulted in structural failure of tire model. In

footprint simulation, as the tire model buckled after compression, the tire model is not in full contact with the flat plate. Therefore, it is not able to capture a full footprint on the flat plate's surface as shown in Fig. 11. In this research, the occurrence of buckling in tire model was due to limitation in modeling method which will be remodeled in the next phase.

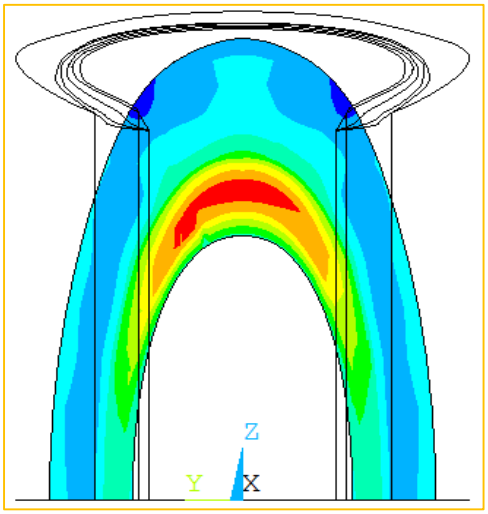


Figure 11: Buckled Arruda-Boyce model Footprint (230 kPa, 1879 N)

4 Conclusion

The objective of this project is to validate the characteristic of tire model through simulations using finite element analysis. The scope is breakdown into two parts along with specific tasks and objectives to achieve the overall goal.

Objective of part 1 is to generate the tire model. Hence tasks assigned to achieve this objective are application of modelling and simulation techniques. Tire model is modelled with element type of SOLID 186 which generated more detailed tire model. Besides that, tetrahedral and hexahedral shape meshes were combined in meshing of the tire model to achieve optimum performance. Through convergence test of inflation simulation, optimum meshing size of 1 mm was determined and applied in simulation to generate maximum analysis performance. Comparisons of several hyperelastic models were made to select the appropriate model as material to simulate the tire. Arruda-Boyce model was selected as it is able to simulate up to greater strain percentage and required lesser material parameters to generate the hypereleastic model compared to other models. As a result, tire model was generated and objective for part 1 was achieved.

Goal of part 2 is to validate and analyse the deformation behavior of tire layer through inflation and footprint analysis. Results generated from simulation of the Arruda-Boyce tire model are compared and validated with actual tire results. In inflation simulation, the generated model proved to be a successful one as the circumference of the tire model is similar to the actual tire although there is a slight difference which is due to error in modelling. Error percentage of inflation simulation results was minor and within acceptable range. Thus, tire model was validated in the

aspect of inflation analysis. Footprint simulation results of Arruda-Boyce tire model were compared with actual tire footprints in terms of footprint dimension and stress distribution. Footprint dimension generated by Arruda-Boyce model was inaccurate at low compressive force but increased in accuracy at high compressive force. Compared to actual footprint width, average difference of simulation's footprint width was minor within acceptable range. Conversely, average difference of simulation's footprint height was deviated from actual tire. This might be due to flaws in modelling of the cord-ply tire player. Besides that, footprint stress distribution of Arruda-Boyce model and actual tire shows similarity in the aspect of stress intensity. In addition, footprint simulation results show that there was presence of hole in the middle of footprint due to buckling for several compressive forces. Although the actual footprints do not show presence of buckling, occurrence of buckling was identified in simulation footprint and analysed. Reasoning behind buckling is instability of tire structure when subjected to high compressive force. In this case, structure failure of Arruda-Boyce tire model was due to limitation in modelling method of cord-ply layer which resulted in weaker tire structure strength compared to actual. Outcomes of the task executed met the objectives for this part of the project as tire model was validated in terms of footprint dimension and stress distribution.

More importantly, through validation of inflation and footprint analysis, accurate tire layer deformation behavior was determined and analysed. Meeting the objectives set in both parts of the project ensured the buildup to project success and completion.

Acknowledgement

I wish to express my gratitude to Taylor's University for providing the resources and materials to complete this research project. I would also like to thank Continental Tyre Sdn Bhd for the opportunity to conduct research and experiment on this collaborative project with Taylor's University. To Mr. Jonathan Lim from Continental Sdn Bhd, I am grateful for the experience gained through this project as I have learned a lot from his feedbacks and comments on this project to keep improving. To Ms. Tan Huey Meing from Continental Tyre Sdn Bhd, I am thankful for her help and support provided throughout the completion of this project. I would like to thank my family and friends for showing their support during the course of this project. Most of all, I am blessed to have Dr. Thein and Dr. Ch'ng as my supervisor and co-supervisor for this project as they have dedicated themselves by guiding me with patience to overcome countless barriers in completion of this project.

References

[1] MIROS, "Statistics and Accident Characteristics Involving Motorcycles in Malaysia", *MIROS*, Apr. 15, 2015. [Online]. Available: http://www.miros.gov.my/c/document_library/get_file?uuid=9d24d742-5abd-481d-abf5-9128c1384128&groupId=26426. [Accessed: Apr. 20, 2015].

[2] MICHELIN, "RADIAL VS. BIAS TECHNOLOGY", *MICHELIN*, Dec. 24, 2004. [Online]. Available: http://www.michelinag.com/Innovating/Radial-vs.-Bias-technology. [Accessed: Apr. 20, 2015].

[3] ANSYS, "About ANSYS, Inc.", ANSYS, (n.d). [Online]. Available: http://www.ansys.com/About+ANSYS. [Accessed: Apr. 20, 2015].

[4] Aidy Ali, M. Hosseini and B. Sahari, "A Review of Constitutive Models for Rubber-Like Materials", *American J. of Engineering and Applied Sciences*, vol. 3, no. 1, pp. 232-239, 2010.

[5] M. Stuparu, "HUMAN HEART VALVES. HYPERELASTIC MATERIAL MODELING", *SERIA MECANICĂ*, vol. 47, no. 61, 2002.

[6] A. Cioroianu et al., "An Improved Non-Affine Arruda-Boyce Type Constitutive Model for Collagen Networks," *Biophysical Journal*, vol. 104, no. 2, pp. 511a, January 2013.

[7] Vegard Tømmernes, "Implementation of the Arruda-Boyce Material Model for Polymers in Abaqus," *Noewegian University of Science and technology, Department of Structural Engineering*

[8] Canonsburg, T. D. (2013). ANSYS Mechanical APDL Introductory Tutorials, *15317*(November), 724–746.

[9] H. H ̈olscher et al., "Modeling of Pneumatic Tires by a Finite Element Model for the Development a Tire Friction Remote Sensor", *Computers & Structures*, vol. 82, December 2004.

Preparation and Characterization of Cu-, Fe-, Ag-, Zn- and Ni- Doped Gelatin Nanofibers for Possible Applications in Antibacterial Nanomedicine

Tamrin Nuge[1], Tshai Kim Yeow[1*], Lim Siew Shee[1], Norshariza Nordin[2], Md Enamul Hoque[1]

[1]*Department of Mechanical, Materials and Manufacturing Engineering, University of Nottingham Malaysia Campus, Jalan Broga, 43500 Semenyih Selangor, Malaysia.*

[2]*Faculty of Medicine and Health Science, University Putra Malaysia, Lorong Asam Jawa 1, 43400 Serdang Selangor, Malaysia.*

[*]Kim-Yeow.Tshai@nottingham.edu.my

Abstract

A facile and efficient approach to prepare metal nanoparticles doped electrospun (espun) gelatin from metal salts precursors was successfully developed. The incorporation of metal ions with antimicrobial activity into electrospun gelatin is an attractive approach to control the inflammatory reaction and prevent infection in wound. In this study, metal salts precursors $AgNO_3$, $Fe(NO_3)_3.9H_2O$, $Cu(NO_3)_2.3H_2O$, $Zn(NO_3)_2.6H_2O$ and $Ni(NO_3)_2.6H_2O$ were reduced to metal nanoparticles with acetic acid as a solvent and reducing agent. The agglomeration of nanoparticles was inhibited by the gelatin polymer matrix. Electrospinning of both neat electrospun gelatin and metal-nanoparticles/Ge-espun resulted in the formation of smooth fibers with average diameters of ~280 nm and ~ 40 nm - 150 nm, respectively. The efficacy of metal nanoparticles/Ge-espun against bacteria commonly found on the wounds: *Escherichia coli* (Gram negative: ATCC 25922), *Pseudomonas aeruginosa* (Gram negative: ATCC 27853); and *Staphylococcus aureus* (Gram Positive: ATCC 25023) were tested with different metal loading by measuring the inhibition of colony forming units. The results indicated a broad spectrum of antibacterial activity showed by Ag/Ge-espun, followed by Fe/Ge-espun and Zn/Ge-espun. An interesting finding on the efficacy of Cu/Ge-espun and Fe/Ge-espun against the Gram's positive bacteria is worth exploring to further investigate the potential application of metal-based antibiotics against the antibiotic-resistant bacterial strains.

Keywords: Electrospinning, Antibacterial Activity, Metal-nanoparticles, Electrospun.

1. Introduction

In recent years, electrospinning has gained much attention as a useful method to prepare fibers in nanometer diameter range. The unique combination of high specific surface area, extremely small pore size, flexibility and superior mechanical performance makes electrospun nanofiber a preferred material for many applications especially in biomedical fields such as enzymes immobilization, tissue engineered scaffolds and drugs deliveries [1]. In an electrospinning process, a polymer solution held by its surface tension and a high voltage is applied to the liquid solution at the end of a capillary tube. Charge is induced on the liquid surface by an electric field. Mutual charge repulsion causes a force directly opposite to the surface tension. As the intensity of the electric field is increased, the hemispherical surface of the solution at the tip of the capillary tube elongates to form conical shape known as the Taylor cone [2]. When the electrical field reaches a critical value at which the repulsive electric force overcomes the surface tension force, a charge jet of the solution is ejected from the tip of the cone [3]. Since this jet is charged, its trajectory can be controlled by an electric field. As the jet travels in the air, the solvent evaporates, leaving behind a charged polymer fiber which lays itself randomly on a collecting metal plate. Thus, continuous fibers are laid to form nonwoven fabric.

Overall, this is a relatively robust and simple technique to produce nanofibers from a wide variety of polymers including gelatin. Gelatin is a natural biopolymer derived either by partial acid (gelatin type A) or alkaline hydrolysis (gelatin type B) of animal collagen from skins, bones and tendons [4]. The differences in collagen sources and preparation techniques make gelatin present a structure with variable physical properties and chemical heterogeneity [5]. Due to its natural abundance and inherent biodegradability in physiological environments, gelatin is widely used in food, cosmetic, pharmaceuticals and medical applications [6]. Gelatin can be processed into hydrogels, three dimensional (3D) microporous scaffolds and electrospun into non-woven nanofibrous matrices due to its inherent properties such as triple helix conformational structure [6]. The electrospun gelatin nanofibers are ideal materials to be used as scaffolds for cell and tissue culture, carriers for tropical /transdermal delivery of drugs and wound dressing. Owing to its remarkable properties, such as high surface area to volume ratio, high porosity of the electrospun

matrices and flexibility for surface functionalization (via pendant free amine groups), the electrospun gelatin matrices are of interest here [7].

The high water absorption capacity and ability to activate macrophages and homeostasis in bleeding wounds are highly desired properties for wound dressing [8]. More recent strategies on controlling the inflammatory reaction and preventing infection in wounds are achieved via the incorporation of metal-based antibiotics into nanofibrous matrix [9]. Wound infection delays wound closure, diminishes tensile strength of the healing wound tissue, increases the length of hospital stay and cost, and increases the patient's risk of bacteremia, sepsis, multisystem organ failure and death [10]. With the increased prevalence and the emergence of antibiotic-resistant bacterial strains, there is mounting need to reduce and eliminate wound infection using methodologies that limit the ability of bacteria to evolve into further antibiotic resistant strains.

Klinkajon and Supaphol [11] investigated the use of copper (II) ions in hydrogel alginate dressing. The results showed that the copper (II) ions exhibited bacterial disinfection and displayed potentiating effect on prothrombotic coagulation and platelet activation. Additional work by Chaturvedi and coworkers demonstrated that the copper ions were successfully impregnated onto PVA-based cryogels nanocomposites and exhibited high antibacterial activity against Gram-positive and Gram negative bacteria. The nanocomposites also offered fair blood compatibility and good mechanical strength [12]. A study by Lin et al. [13] aimed to investigate the efficacy of silver containing dressings on controlling wound infection and wound healing. Silver ions and silver based compounds are known to have broad antibacterial spectrum (highly toxic to 16 major species of bacteria) [14] and are relatively safe, which makes silver an excellent choice for clinical care and consumer products. The impregnation of silver ions onto scaffolds could enhance reduction in the levels of pro-inflammatory cytokines [15] and inhibit the activities of interferon gamma and tumor necrosis factor alpha which are involved in inflammation [16]. Recent investigations have been extended to study other metal nanoparticles such as Zn, Ni and Fe that could have antibacterial activity and are economically cheaper than Ag and Au.

This works describes the preparation and characterization of electrospun gelatin chelates with metal ions (Cu^{2+}, Zn^{2+}, Ag^{+}, Ni^{2+} and Fe^{3+}) by electrospinning technique to explore the role of metal-based antibiotics as potential antibacterial agents. In the present study, the chelation of metal ions in the gelatin solution was extensively investigated, with the aim of understanding the effects of aging time on chelation. The nanofibers features produced during the electrospinning were studied and the efficacy of the doping process onto the nanofibers was characterized systematically. In order to evaluate the antibacterial activity, the electrospun nanofibers doped with metal ions were subjected to antibacterial screening against three bacterial strains that are commonly found on burn wounds, of which two were gram negative (*Escherichia coli* and *Pseudomonas aeruginosa*) and one Gram positive *Staphylococcus aureus*.

2. Experimental Details

2.1 Materials

Gelatin powder and silver nitrate ($AgNO_3$) were purchased from Merck (Germany). Iron nitrate ($Fe(NO_3)_3.9H_2O$), copper nitrate ($Cu(NO_3)_2.3H_2O$) and nickel nitrate ($Ni(NO_3)_2.6H_2O$ were purchased from Systerm®. Zinc nitrate ($Zn(NO_3)_2.6H_2O$) was purchased from R&M chemicals (UK). The solvent used was analytical grade glacial acetic acid obtained from Fisher Chemical (UK) and deionized distilled water (ddH_2O) which was filtered by Milli-Q integral water purification using 0.22 µm Millipak membrane filter. All chemicals were of analytical grade and used without further purification.

2.2 Preparation and characterization of gelatin solutions containing metal ions

The metal ions chemical reagents were first dissolved in a quantity of 10 % (w/v) in 90:10 glacial acetic acid/distilled water, respectively. 1 % (v/v) of the metal ion mixtures were then transfer into the 18 % (w/v) gelatin solution of acetic acid/ddH_2O at the ratio of 90:10. The mixture was then stirred to homogenize and allow the chelation of metal ions into the gelatin/acetic acid/water solution. In this system, gelatin was used as a stabilizer and dispensing agent for the metal ions. The gelatin solution containing metals ion were stirred for a varied period in order to investigate the effect of aging time on the formation of metal ions. The diffusion of

metal ions into the gelatin/acetic acid/water solution was confirmed by monitoring the surface plasmon absorption band using UV-Vis Lambda 35 spectrophotometer (Perkin Elmer, USA).

2.3 Preparation of neat and doped electrospun gelatin matrices

The neat gelatin solution and the metals ion-containing gelatin solution that had been aged for 12 hours were fabricated into nanofibers matrices by electrospinning. The experimental set-up used for electrospinning process (Fig.1) consisted of a syringe and a needle, a ground electrode (aluminum collector plate of 20 cm × 20 cm wrapped with aluminum sheet) with a distance of 10 cm from the needle and a high voltage adjustable DC power supply (Gamma High Voltage Research, USA). A positive voltage (15 kV) was applied to the gelatin solutions. The solutions were delivered via syringe pump to control the mass flow rate. The feed rate was maintained at 0.42 ml/h throughout the study. As the electrical potential was applied, a jet was created. The resulting nanofibrous matrices were collected on an aluminum plate after 18 hours of electrospinning process. After the process, all the matrices collected with the aluminum foils on the collector were kept at room temperature for 24 hours before being place in a vacuum drying oven for a couple of days for drying treatment. After the aluminum foil was carefully peeled off, the specimens' thickness were measured using a digital micrometer, having a precision of 1 µm. The thickness of the neat and the metals-ion containing gelatin matrices were between 320 µm to 340 µm.

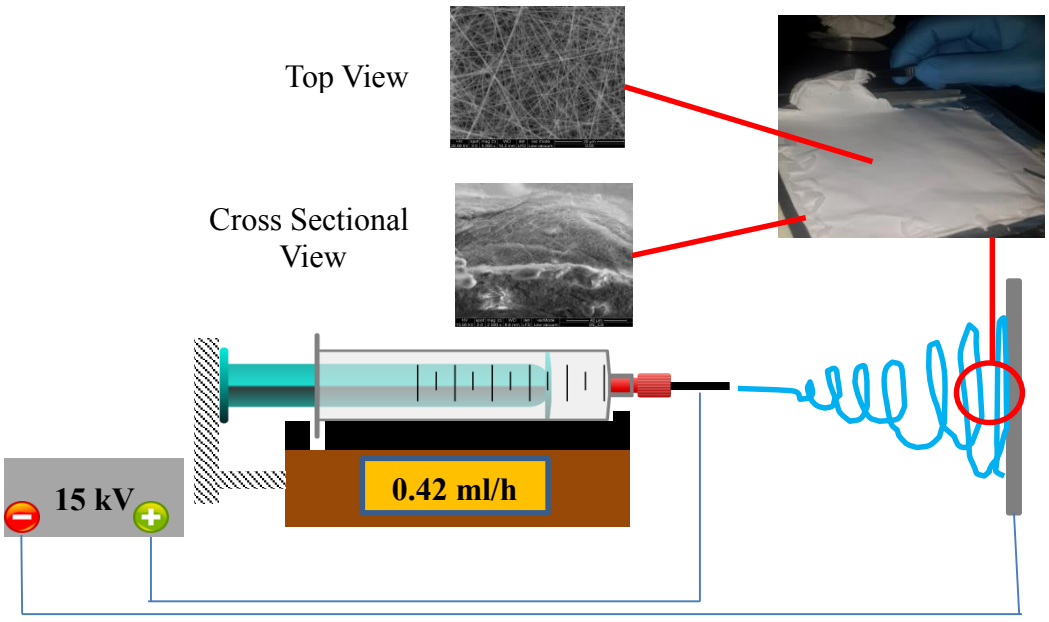


Figure 1. Schematic of electrospinning system

2.4 Characterization

The nanofibers morphology was observed under scanning electron microscopy (SEM) using a FEI Quanta 400 F (USA) with acceleration voltage of 20 kV. Before SEM observation, a small section of the nanofiber mat was cut at three different positions and placed on the SEM sample holder. The diameter of at least 100 different positions on the nanofiber mat was analyzed using image visualization software ImageJ developed by Upper Austria University of Applied Sciences and available for free at http://imagej.nih.gov/ij/download.html.

2.5 Antibacterial Evaluation

The antibacterial activity of the electrospun gelatin with both the neat and loaded metal nanoparticles were tested against bacteria commonly found on wounds: *Escherichia coli* (Gram negative: ATCC 25922), *Pseudomonas aeruginosa* (Gram negative: ATCC 27853); and *Staphylococcus aureus* (Gram Positive: ATCC 25023). The assessment was conducted based on the discs diffusion method of the US Clinical and Laboratory Standard Institute (CLSI). Both the neat and metal loaded gelatin matrices were cut into circular disks (7 mm in diameter). The bacteria were cultured on Luria Bertani agar (Merck, Germany) in a plastic petri dish. The nanofibrous disks were placed in the middle of culture and then incubated at 37 ℃ for 24 hours. If inhibitory concentration was reached, there would be no bacteria growth and could be observed as a clear zone around the disc specimens. These were photographed for further evaluation.

3. Results and Discussion

3.1 Formation of metal nanoparticles in gelatin solutions and effect of aging time

The liquid phase chemical reduction technique discovered by Faraday more than 150 years ago has been widely used for the production of metal nanoparticles. The chemical reduction method is based on mixing of a reducing agent with a metal salt precursor in the presence of stabilizing agents (ligands, polymers and surfactant). The stabilizing agent is confined to prevent the undesirable particle agglomeration and the formation of stable nanoparticles depends on the properties of stabilizing

agent [17]. In this study, the metal salts were reduced to metal nanoparticles with acetic acid as a solvent and reducing agent. The gelatin polymer matrix was used as stabilizer to prevent further growth and particle agglomeration of metals. The metal ions were reduced directly into metal nanoparticles through a series of steps including nuclei formation, crystal growth via diffusion mechanism to give primary particles and spontaneous self-organization of primary particles to form clusters. The formation of metal nanoparticle nuclei was postulated to originate from ionic interactions between metal ions and amino, carboxyl and hydroxyl groups on gelatin. The metal nanoparticles – gelatin matrix clusters can be expressed according to Eq. (1);

$$x\mathrm{M}^{\mathrm{n}+} + \mathrm{n}xe^{-} + \mathrm{Gelatin} \rightarrow \mathrm{M}_n^0\,(\mathrm{Cluster}) \qquad (1)$$

The reduction of metal ions into metal nanoparticles in metal salts-containing gelatin solutions at different aging time could be visualized from the solution color intensity, from light color of the neat solution to dark color after the completion of aging. The UV/visible absorption spectra of metal salt- containing gelatin solution that had been aged for various time of intervals after preparation are displayed in Fig. 2. The surface plasmon absorption bands for $Cu(NO_3)_2$ –containing gelatin solutions exhibit two peaks in the range of 370 nm to 390 nm and 690 nm to 710 nm (Fig. 2A). Upadhyaya et al. [18] observed the same pattern described that the spectral shift was due to the complexation between Cu^{2+} ions and stabilizing agents (polyaniline) and depended on the concentration of Cu^{2+} ions. Evidently, an increase in the aging time resulted in the observed color change in solution from blue to yellowish green and finally to dark green. It can be assumed that the cupric ions were bound to gelatin chains. Similar redox behavior was observed with Fe^{3+}, Ni^{2+} and Zn^{2+} ions in this study.

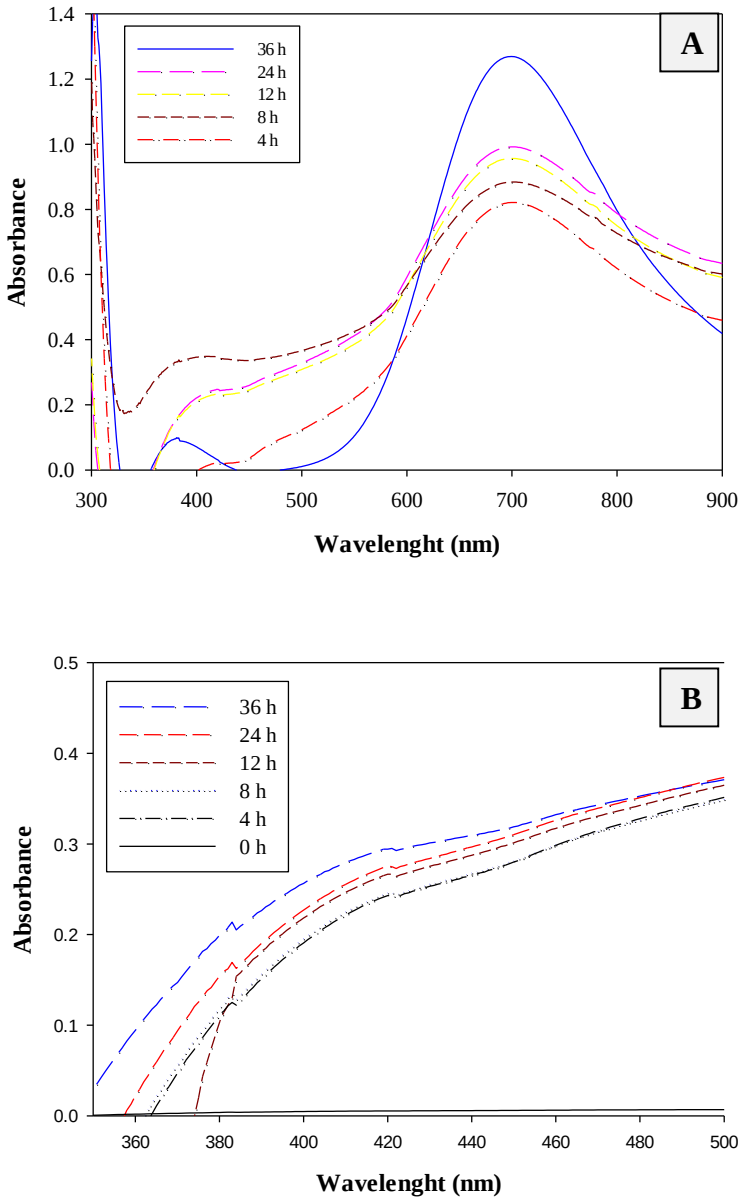


Figure 2. Surface plasmon absorption band of aged (A) $Cu(NO_3)_2$ and (B) $AgNO_3$ containing gelatin solution using UV-Vis spectrophotometer at different time intervals. The concentration of gelatin solution was 18% (w/v) and the metal salt precursor was 1 % (w/w) based on the weight of gelatin.

The reduction of Ag^+ to Ag^0 (silver nanoparticles) by acetic acids and the formation of silver nanoparticles-gelatin matrix follows the following schemes (Eq. (2) and Eq. (3)) [19]:

$$H_2N - COOH + AgNO_3 \leftrightarrow H_2N - COOAg + HNO_3 \quad (2)$$

$$H_2N - COOH + AgNO_3 \leftrightarrow AgHN - COOH + HNO_3 \quad (3)$$

Silver nanoparticles have a surface plasmon resonance absorption in the UV-visible region and the band arises from the coherent existence of free electrons in the conduction band due to small particle size [20]. The band shift is dependent on the particle size, chemical surrounding, adsorbed species on the surface and dielectric constant [19]. Fig. 2B shows the UV-Vis spectra gradually increased over time and the peak position was slightly shifted to a longer wavelength. This indicates that the number of Ag^+ ions that converted into silver nanoparticles increased with an increase of reaction time. The absorption peaks were observed at 382 nm and 420 nm, which correspond to two particle population of silver nanoparticles.

3.3 Morphology of metal nanoparticles /gelatin- electrospun nanofibers

While electrospinning has proven to be a versatile and powerful means of fabricating nanofibers, the applicability to obtain smooth, uniform fibrous structure is not straightforward. The morphology and diameter of electrospun fibers are dependent on a number of parameters including properties and composition of the polymer solution such as viscosity, concentration, conductivity and surface tension [21]. The optimum parameters for fabricating smooth and uniform neat electrospun gelatin nanofibers were discussed in our previous work [22].

Fig.3 shows the selected SEM images of the samples generated using electrospinning from gelatin solution and gelatin solutions containing different metal salts as a precursor. The conductivities of the metal nanoparticles-gelatin solutions linearly increased, while the viscosities and surface tensions did not change with increase content of metal salts. Since the metal salts increased the charge density in gelatin solutions, stronger stretch forces were imposed on the ejected jets under the

electrical field, resulting in substantial formation of finer ultrafine fibers [23]. The average diameter of neat electrospun gelatin and electrospun loaded with metal nanoparticles are shown in Fig. 3. Smooth and uniform nanofibers with average diameter of 280.60 ± 35.92 nm were observed on the neat electrospun gelatin (Fig. 3A). The fiber diameters tended to decrease, when the nanometals loaded onto the fibers. The average diameters of Ag/Ge-espun and Cu/Ge-espun were 147.33 ± 96.43 nm and 41.43 ± 8.05 nm, respectively (Fig. 3B and 3C). The average diameters of Fe/Ge-espun, Ni/Ge-espun and Zn/Ge-espun were ranging from 45.21 ± 12.43 nm to 102.05 ± 26.12 nm (data not shown). Wide variation of nanofiber size was observed on the Ag/Ge-spun. The diameter of Ag/Ge-spun obtained was much smaller compared to the study reported by Rujitanaroj et al. [24] with the diameter ranging from 280 ± 40 nm.

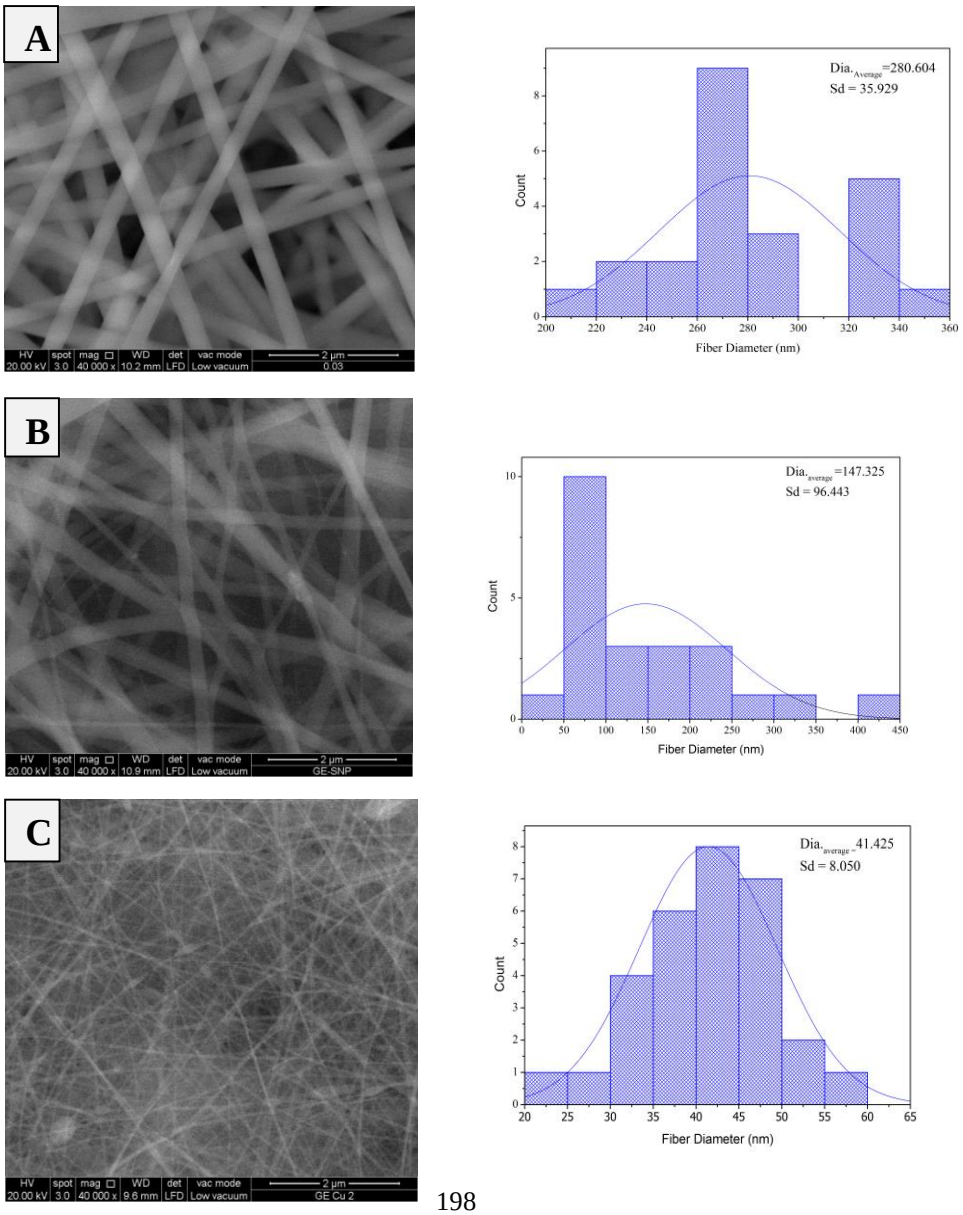


Figure 3. Selected SEM micrograph of the electrospun gelatin nanofibers and diameter distribution of (A) neat electrospun gelatin (B) Ag/Ge-espun (C) Cu/Ge-espun.

The presence of metal nanoparticles in the nanofibers was further assessed with energy-dispersive X-ray (EDX) spectroscopy analysis. The assessment proved the presence of metal nanoparticles in electrospun. The quantitative analysis of the presence of metal nanoparticles in electrospun gelatin is highlighted in the Table 1. The EDX pattern of elements detected in nanofibers is available as **supplementary data**.

Table 1. Quantitative EDX analysis of the presence of nanometals in the electrospun gelatin nanofibrous matrix.

Metal nanoparticles/Ge -espun	**Elements (w/w)%**				
	Ag	**Cu**	**Fe**	**Ni**	**Zn**
Neat-espun	-	-	-	-	-
Ag/Ge-espun	0.41	-	-	-	-
Cu/Ge-espun	-	0.44	-	-	-
Fe/Ge-espun	-	-	0.42	-	-
Ni/Ge-espun	-	-	-	0.45	-
Zn/Ge-espun	-	-	-	-	0.41

3.4 Antimicrobial activity

The antibacterial activity is a demonstration of release of metal ions from nanofiber matrix. Metal nanoparticles exhibit relatively large surface area, thus increasing their contact with bacteria. Fig. 4 shows the results of antibacterial efficacy of gelatin electrospun loaded with metal nanoparticles against some common bacteria found on wounds*: Escherichia coli* ATCC 25922, *Pseudomonas aeruginosa* ATCC 27853, and *Staphylococcus aureus* ATCC 25023. The antibacterial activity is based on the disc diffusion method and expressed as a ratio of clear inhibition of microorganisms in contact with all metal nanoparticles loaded on the nanofibers and

the neat electrospun gelatin. It should be noted that the initial diameter of all the specimens was fixed at 0.7 cm. The relative zone of inhibition was calculated from Eq. (4).

$$\text{Relative Zone of Inhibition} = \frac{\text{B}-\text{A}}{\text{A}} \times 100 \quad (4)$$

where A and B are the diameter of the clear inhibitory zone of the neat electrospun and the clear inhibitory zone of electrospun loaded with metal nanoparticles, respectively.

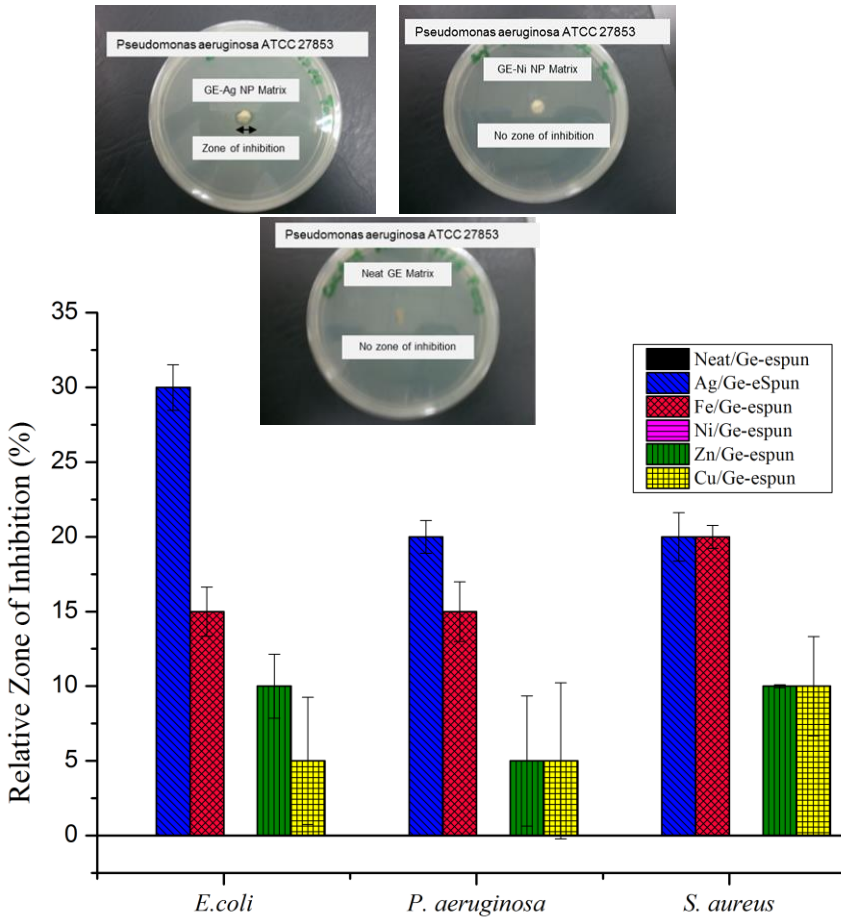


Figure 4. Bar diagram showing the antibacterial effect of the different metal loaded electrospun gelatin on commonly found bacteria on wounds. *Notes*: E.coli – Escherichia coli ATCC 25922; P. aeruginosa – Pseudomonas aeruginosa ATCC 27853; S. aureus – Staphylococcus aureus ATCC 25023

According to the data obtained, no antibacterial activity was detected for the neat Ge-espun nanofibers and Ni/Ge-espun against the bacteria tested. The poor inhibition by the Ni/Ge-espun was contradicted with the study reported by Popova et al. They found that the nickel ion complexes with ligands manifested good antibacterial activity against the tested bacteria, especially towards the Gram's positive strains [25]. In the recent years, focus on the bimetallic complexes of Ni with other metal nanoparticles has gained more attention in the area of dental materials. Argueta-Figueroa reported that the Ni-Cu complexes showed broad antibacterial spectrum and potentially being employed in dentistry for formulation of bone cements, irrigating the root canal and devices coating [26].

Evident bacteria inhibition zones were observed on the Ag/Ge-espun, Fe/Ge-espun, Zn/Ge-espun and Cu/Ge-espun. Metal nanoparticles except nickel exhibited broad spectrum antimicrobial activity. The bacterial inhibition zone on Ag/Ge-espun nanofiber was the greatest but its antibacterial efficacy reduced towards the *S. aureus* (gram positive bacteria). This can be explained by the difference in structure of the envelope of Gram-positive and Gram-negative bacteria. Gram positive bacteria have a thick peptidoglycan layer below the cell membrane that protects bacteria from external stresses and is believed to reduce the penetration of silver nanoparticle [27]. In contrast, the Fe/Ge-espun and Cu/Ge-espun displayed greater inhibition on Gram positive bacteria than Gram negative bacteria. The same pattern was also reported by Klinkajon and Supaphol [11] on the ability of the cooper alginate hydrogel to inhibit Gram positive bacteria. This can be explained due to the greater abundance of amines and carboxyl groups on cell surface of Gram positive bacteria and greater affinity of cooper towards these groups [28]. The cooper ions are targeting the antisense that involves in gene coding and lead to DNA molecules disruption [29]. In the case of Fe/Ge-espun, the bacterial inhibition was driven by iron chelation by the chelator. Based on this concept, the higher the iron binding constant to the chelator (Ge-espun), the stronger the predicted antimicrobial activity [30]. The composition of the microorganism's cell wall and the physical nature of the iron chelator also affect the inhibition of the bacterial growth [31]. The exact mechanism behind bactericidal effect of iron nanoparticles is not known and needs to be studied further.

4. Conclusion

In this work, copper, iron, nickel, silver and zinc were successfully impregnated onto electrospun gelatin nanofibers using electrospinning technique from 1% (v/v) solutions of their salts precursor and 18% (w/v) of gelatin solution. The presence of the metal nanoparticles was confirmed using the surface plasmon absorption band and energy-dispersive X-ray (EDX) spectroscopy. The amount of metal nanoparticles increased with the increase of aging time. Both neat and metal nanoparticles/Ge-espun were spun into smooth nanofibers matrices. The average diameter of nanofiber tended to decrease with nanometals loaded fibers. The average diameter of metal nanoparticles ranged from 40 nm to 150 nm. Wide variation of nanofiber diameter was observed on the Ag/Ge-espun. Metal nanoparticles doped gelatin nanofibers manifested good antibacterial effects except Ni/Ge-espun. The nanocomposite of Ag/Ge-espun showed greater inhibition against the Gram's negative bacteria but exhibited lower efficacy on the Gram's positive bacteria. In contrast, the Cu/Ge-espun and Fe/Ge-espun displayed high efficacy on the Gram's positive bacteria. Bimetallic complexes of Ag-Cu doped electrospun gelatin could be explored in the future for potential metal-based antibiotics that could prevent the emergence of antibiotic-resistant bacterial strains.

Acknowledgement

The authors would like to thank the researcher in the Faculty of Engineering and the Faculty of Science, University of Nottingham Malaysia Campus for the facilities and the helpful discussion. This study was supported by a research grant (NER40002) from the Ministry of Higher Education (MOHE) and partially supported by the Faculty of Engineering, University of Nottingham Malaysia Campus.

References

[1] Ziabari, M., Mottaghitalab, V., Haghi, A. ., and McGovern, S. T., 2009, "Control of Electospun Nanofiber Diameter Using Distance Transform Method: A Novel Approach," Electrospun Nanofibers and nanotubes Research Advances, A.. Haghi, ed., Nova Science Publishers, Inc, New York, pp. 69–94.

[2] Teo, W. E., and Ramakrishna, S., 2006, "A review on electrospinning design and nanofibre assemblies.," Nanotechnology, **17**(14), pp. R89–R106.

[3] Fong, H., Chun, I., and Reneker, D. ., 1999, "Beaded nanofibers formed during electrospinning," Polymer (Guildf)., **40**(16), pp. 4585–4592.

[4] Schrieber, R., and Gareis, H., 2007, Gelatine Handbook: Theory and Industrial Practice, Wiley-VCH Verlag GmbH & Co. KGaA, Germany.

[5] Schrieber, R., 2007, "From Collagen to Gelatin," Gelatin Handbook, Wiley-VCH Verlag GmbH & Co. KGaA, Germany, pp. 113–114.

[6] Hoque, M., Nuge, T., Yeow, T. K., and Nordin, N., 2013, "Electrospinning of Gelatin Nanofibre: Current Trends in Tissue Engineering Applications," J. Appl. Mech. Eng., **02**(04), p. 9873.

[7] Nuge, T., Hoque, M., Yeow, T., Nordin, N., and Chowdhury, M., 2013, "Electrospun Gelatin Composite Nanofibres : A Review On Structural and Mechanical Characterizations," Regen. Res., **2**(2), pp. 39–42.

[8] Gao, Y., Bach Truong, Y., Zhu, Y., and Louis Kyratzis, I., 2014, "Electrospun antibacterial nanofibers: Production, activity, and in vivo applications," J. Appl. Polym. Sci., **131**(18), p. 40797.

[9] Yang, H., Gao, P. F., Wu, W. B., Yang, X. X., Zeng, Q. L., Li, C., and Huang, C. Z., 2014, "Antibacterials loaded electrospun composite nanofibers: release profile and sustained antibacterial efficacy," Polym. Chem., **5**(6), p. 1965.

[10] Mohiti-Asli, M., Pourdeyhimi, B., and Loboa, E. G., 2014, "Skin tissue engineering for the infected wound site: biodegradable PLA nanofibers and a novel approach for silver ion release evaluated in a 3D coculture system of keratinocytes and staphylococcus aureus.," Tissue Eng. Part C. Methods, **20**(10), pp. 790–7.

[11] Klinkajon, W., and Supaphol, P., 2014, "Novel copper (II) alginate hydrogels and their potential for use as anti-bacterial wound dressings.," Biomed. Mater., **9**(4), p. 45008.

[12] Chaturvedi, A., Bajpai, A. K., Bajpai, J., and Sharma, A., 2015, "Antimicrobial poly(vinyl alcohol) cryogel–copper nanocomposites for possible applications in biomedical fields," Des. Monomers Polym., **18**(May 2015), pp. 385–400.

[13] Lin, Y. H., Hsu, W. S., Chung, W. Y., Ko, T. H., and Lin, J. H., 2014, "Evaluation of various silver-containing dressing on infected excision wound

healing study," J. Mater. Sci. Mater. Med., **25**, pp. 1375–1386.

[14] Prabhu, S., and Poulose, E. K., 2012, "Silver nanoparticles : mechanism of antimicrobial action , synthesis , medical applications , and toxicity effects," Int. nano Lett., **2**(32), pp. 1–10.

[15] Tian, J., Wong, K. K. Y., Ho, C.-M., Lok, C.-N., Yu, W.-Y., Che, C.-M., Chiu, J.-F., and Tam, P. K. H., 2007, "Topical Delivery of Silver Nanoparticles Promotes Wound Healing," ChemMedChem, **2**(1), pp. 129–136.

[16] Shin, S.-H., Ye, M.-K., Kim, H.-S., and Kang, H.-S., 2007, "The effects of nano-silver on the proliferation and cytokine expression by peripheral blood mononuclear cells.," Int. Immunopharmacol., **7**(13), pp. 1813–1818.

[17] Bonnemann, H., and Richards, R. M., 2001, "Nanoscopic metal particles - synthetic methods and potential applications," Eur. J. Inorg. Chem., (10), pp. 2455–2480.

[18] Upadhyaya, M., Ahmed, N., Deka, R., and Kakati, D. K., 2012, "Studies on Cu +2 ion doped polyaniline," Iran. Polym. J. (English Ed., **21**(9), pp. 601–607.

[19] Sharma, V. K., Yngard, R. A., and Lin, Y., 2009, "Silver nanoparticles: Green synthesis and their antimicrobial activities," Adv. Colloid Interface Sci., **145**(1-2), pp. 83–96.

[20] Jeong, L., and Park, W. H., 2014, "Preparation and characterization of gelatin nanofibers containing silver nanoparticles.," Int. J. Mol. Sci., **15**(4), pp. 6857–79.

[21] Haghi, A. ., and Zaikov, G., 2011, "Polymeric Nanofibre fabrication Via Electrospinning Process," Advances in Nanofibre Research, iSmithers, Shropshire, pp. 11–39.

[22] Hoque, M. E., Nuge, T., Yeow, T. K., Nordin, N., and Prasad, R. G. S. V, 2014, "Gelatin Electrospun Nanofibre Scaffold for Potential Wound Healing Application," 9th International Materials Technology Conference and Exhibition.

[23] Madhumathi, K., Sudheesh Kumar, P. T., Abhilash, S., Sreeja, V., Tamura, H., Manzoor, K., Nair, S. V., and Jayakumar, R., 2010, "Development of novel chitin/nanosilver composite scaffolds for wound dressing applications," J. Mater. Sci. Mater. Med., **21**(2), pp. 807–813.

[24] Rujitanaroj, P. O., Pimpha, N., and Supaphol, P., 2008, "Wound-dressing materials with antibacterial activity from electrospun gelatin fiber mats containing silver nanoparticles," Polymer (Guildf)., **49**(21), pp. 4723–4732.

[25] Popova, T. P., Alexandrova, R. I., Tudose, R., Mosoarca, E. M., and Costisor, O., 2012, "Antimicrobial activity in vitro of four nickel complexes," Bulg. J. Agric. Sci., **18**(3), pp. 446–450.

[26] Argueta-Figueroa, L., Morales-Luckie, R. A., Scougall-Vilchis, R. J., and Olea-Mejía, O. F., 2014, "Synthesis, characterization and antibacterial activity of copper, nickel and bimetallic Cu–Ni nanoparticles for potential use in dental materials," Prog. Nat. Sci. Mater. Int., **24**(4), pp. 321–328.

[27] Quirós, J., Borges, J. P., Boltes, K., Rodea-Palomares, I., and Rosal, R., 2015, "Antimicrobial electrospun silver-, copper- and zinc-doped polyvinylpyrrolidone nanofibers," J. Hazard. Mater., **299**, pp. 298–305.

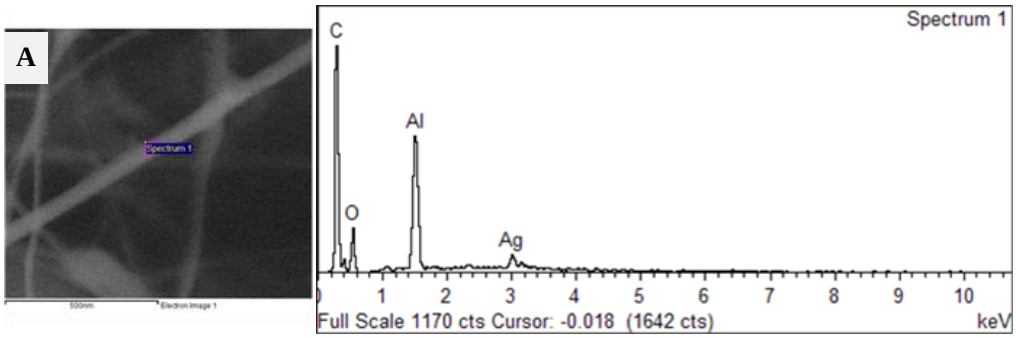
[28] Ruparelia, J. P., Chatterjee, A. K., Duttagupta, S. P., and Mukherji, S., 2008, "Strain specificity in antimicrobial activity of silver and copper nanoparticles," Acta Biomater., **4**(3), pp. 707–716.

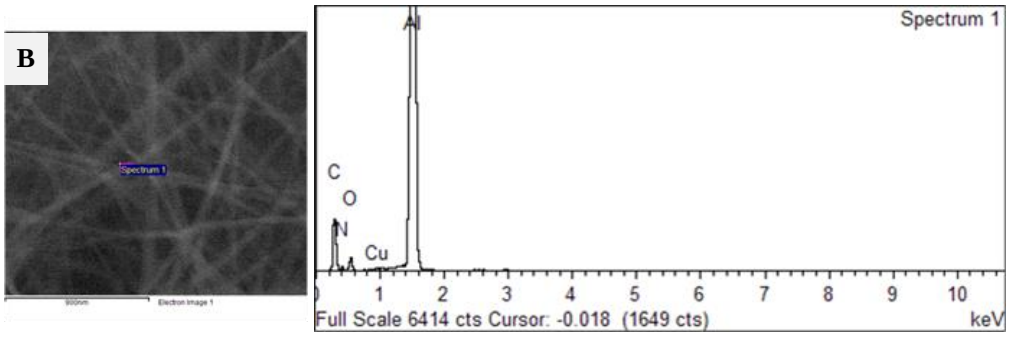
[29] Bai, H., Sang, G., You, Y., Xue, X., Zhou, Y., Hou, Z., Meng, J., and Luo, X., 2012, "Targeting RNA polymerase primary σ 70 as a therapeutic strategy against methicillin-resistant Staphylococcus aureus by antisense peptide nucleic acid," PLoS One, **7**(1), pp. 1–10.

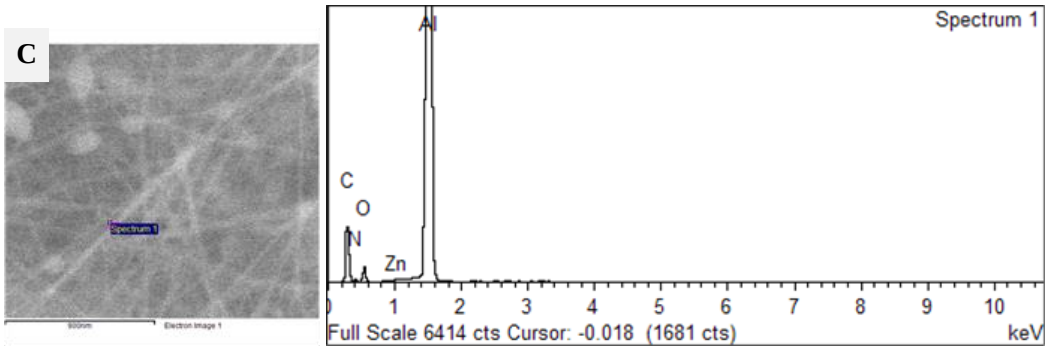
[30] Qiu, D.-H., Huang, Z.-L., Zhou, T., Shen, C., and Hider, R. C., 2011, "In vitro inhibition of bacterial growth by iron chelators.," FEMS Microbiol. Lett., **314**(2), pp. 107–11.

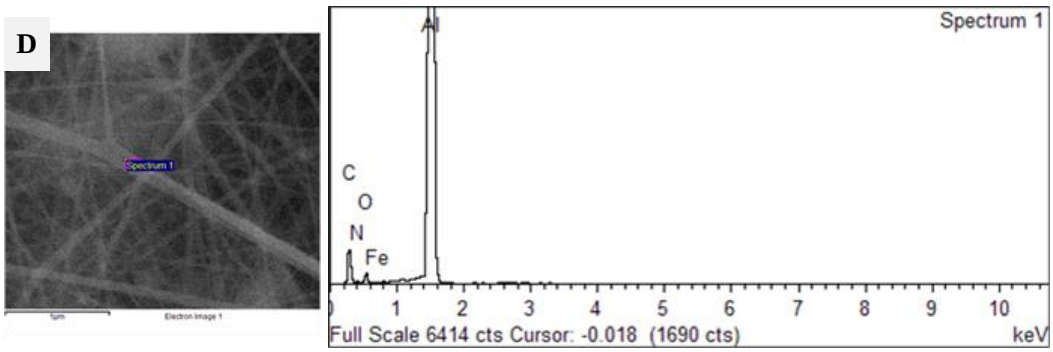
[31] Chew, B. P., Tjoelker, L. W., and Tanaka, T. S., 1985, "In Vitro Growth Inhibition of Mastitis Causing Bacteria by Phenolics and Metal Chelators," J. Dairy Sci., **68**(11), pp. 3037–3046.

SUPPLEMENTARY DATA









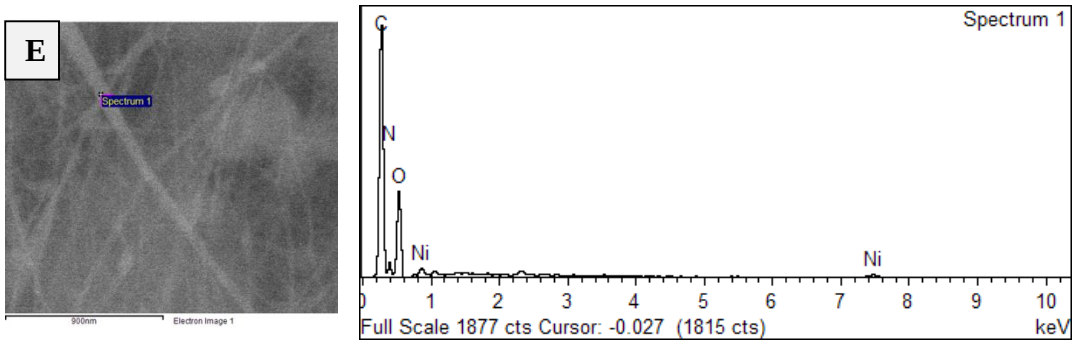


Figure 1. Energy dispersive X-ray analysis of (A) Ag/Ge-espun; (B) Cu/Ge-espun; (C) Zn/Ge-espun; (D) Fe/Ge-espun and (E) Ni/Ge-espun.

Performance of Electrical Grounding System at Low Moisture Content Condition

Chin Chee Tung, Siow Chun Lim
School of Engineering, Taylor's University, Malaysia
CheeTung.Chin@sd.taylors.edu.my, ChunLim.Siow@taylors.edu.my

Abstract
The paramount of an effective grounding system is to safeguard building, equipment and human beings from electric hazard in the event of earth faults. Effective grounding system is a crucial feature and yet concepts of electrical grounding system are still less likely to be emphasized which leads to electric hazards. Soil resistivity plays a major factor in designing the grounding system along with the contact resistance between the grounding electrode and soil and the arrangement of the electrodes in a grounding system to ensure ground electrodes have sufficiently low resistance to minimize potential shock. It is more difficult and complex to design and install a grounding system in an area where the soil resistivity is high due to the low moisture content of the soil. Moisture content and compression level of soil are the major components that govern the soil resistivity. The objective of this study is to investigate the effect of the moisture content and compression level of soil on the performance of an electrical grounding system at low moisture content. Hence, quantitative study has been conducted. Clay and fine sand samples were dried in the oven at 110 ± 5 ℃ to ensure the water content on both samples is 0% before proceeding to the experiment. The soil resistivity of the samples at various moisture content and compression level was then calculated respectively in a laboratory setup. From the soil resistivity results, the ground resistance was computed starting from the simplest grounding system configuration to horizontal buried strip configuration. From the computed ground resistance, it was found that the ground resistance decreased with the increased of moisture content and compression level of soil respectively in which this further justified that such factors were having influences on the overall effectiveness of the grounding system.

Keyword: Soil resistivity, Grounding system, Soil compaction, Ground electrode, Low moisture content.

1. Introduction

The objective of electrical grounding system is to ensure effective protection of system or equipment in the event of earth fault currents by disconnecting the source of energy from the system or equipment to avoid impacts of excessive currents produced under earth fault conditions [1]. Electrical grounding system is utilized to drain off unwanted flow of electrical charges such as fault and lightning induced currents to the earth or return to the generator via earth mass [2]. In other words, the function mechanism of an electrical grounding system is to provide protective grounding, functional grounding in electrical power systems and lightning protection that serves to not only safeguard building and equipment but also more importantly to protect people [3-4].

Although an effective grounding system is referred as one of the most crucial features in the event of electrical design and installations, yet concepts of electrical grounding in electrical industry are still less likely to be emphasized or rather misunderstood despite knowing that failure of achieving effective grounding may lead to serious damages including fatalities [5]. In this context, there were 64 accidents related to electricity involving 27 fatalities throughout Malaysia in year 2014 [6-7]. Among the major causes of these disastrous events was due to the poor consideration of safety work procedures in the event of installation and maintenance [7]. As a result of these accidents, the design of electrical grounding has been seriously taken into considerations as it is the major parameter that affects the behavior of earth fault in an electrical power system [8-9].

However, there are chances that the electrical grounding system may not perform satisfactorily due the connection of the system to earth is not adequate for the particular installation. That being said, the ground connection plays a crucial role in ensuring the whole electrical safety grounding system performs satisfactorily and one of the most fundamental designs of the system is to ensure the ground electrodes have sufficiently low resistance for grounding to minimize potential for shock and limit transient overvoltage. Ideally, the lower the ground resistance, the better the grounding system in terms of adequately meeting the requirements. Yet, the value of ground resistance varies from different installations as larger systems with higher levels of fault current requires lower ground resistance than smaller systems which yield lower level of fault current. In general, ground resistance ranging from 1 ohm to 5 ohm is suitable for large commercial installations and industrial plant substations and building as stated in IEEE 142-2007 green book [10].

Referring to [11-14], it is well known that soil resistivity plays a key factor in determining the design of an effective electrical grounding system and lightning protection system due to the fact that the soil resistivity will affect the depth of a grounding electrode to be driven in order to attain low ground resistance. The soil resistivity varies widely depending on the geological structure of the ground due to the several factors that govern the parameter of the soil resistivity and the most significant ones are moisture content, chemical composition, soil compaction, temperature, vertical thickness, depth and divisions. That being said, the design of the ground electrode is highly dependent on the profile of soil resistivity in order to achieve low ground impedance [12]. However it is important to realize that at low frequency, the ground impedance can be represented by a single resistor which means capacitive and inductive reactance are assumed to be negligible. Hence, ground impedance is equal to ground resistance on low frequency behavior of grounding system.

Under ordinary soil condition where the moisture content in the soil is relatively high, the grounding configurations required are usually simpler due to the low resistivity of soil. However, this is not true when the moisture condition of the soil is low in which the soil resistivity is high. When the soil resistivity is high, it is more difficult to design and install a grounding system where its ground resistance is low enough to dispose the unwanted current during the ground fault. This is because the computation of ground resistance for an effective grounding system is greatly affected by the soil resistivity. That being said, in order to achieve a low ground resistance in a high resistivity soil, a more complex of grounding configuration is usually required.

Unlike the enormous amount of research which has been conducted on studying the relationship of moisture content and compression level of soil to the soil resistivity respectively, there is still limited research done on the influence of moisture content and compression level of soil to the performance of an electrical power grounding system especially at low moisture content [1-5, 12, 14]. Hence, investigation is conducted to determine the influence of these two factors to the electrical grounding system at low moisture content condition. Therefore in this research topic, two different types of soil samples which are clay and fine sand would be measured at various moisture composition and different compression level respectively in a laboratory setup to study the influence of these two factors on the computation of ground resistance of a typical electrical power grounding system during low frequency behavior. In nature, the sand and clay can hold up to 88% and 50% of moisture weightage respectively. Hence, moisture content below 10% is regarded as low for these two types of soil [15].

The obtained soil resistivity measurement values are then compared with the values from literature. On the other hand, the ground resistance is calculated based on the obtained measurement values of soil resistivity and hence is computed accordingly starting from the simplest grounding system configuration.

1.1 Research Contribution

Based on surveyed literature [2, 11-14], most of the studies conducted stop at the stage of soil resistivity. The researchers did not proceed further to discuss the effects of factors that govern the soil resistivity on the performance of an electrical grounding system especially at low moisture content. One related research is to study the relationship of soil resistivity with moisture content. However, the impact of moisture content on the performance of a grounding system has yet to be discussed and addressed quantitatively. This implies the necessity of conducting this research study in order to investigate the factors that affect the soil resistivity and how these factors possess a direct impact to the overall effectiveness of a grounding system.

This investigation serves to contribute to the electrical grounding system field by providing a quantitative study on the variation of moisture content and compression level of soil in designing the most adequate electrical grounding system when the soil is of low moisture content condition. In this context, the value of ground resistance at different moisture content and compression level of soil is determined and hence can be used as a reference value in the event of designing and installing an effective grounding system. That being said, this research topic links the study of factors that affect the soil resistivity conducted by other researchers to the performance of a grounding system.

2. Literature Review

Grounding system is necessary for any electrical power system and soil resistivity is one of the major factors that determine its performance. These factors also include the size and geometry of the ground electrode connected to the system.

2.1 Soil Resistivity

There are four main types of soils that can be commonly found in Malaysia and it can be grouped into clay and clay soil, peat soil, acid sulphate soils and sandy soil [16]. Soil can be generally characterized based on its composition, color, texture, soil water, organic matter, structure and chemistry as stated in [17]. Soil resistivity is an indication of a soil's ability to conduct flow of current and is determined by the transport of ions dissolved in moisture. Soil resistivity can be defined as resistance measured between the opposite sides of a cube of soil with a side dimension of 1 meter [12]. Besides, soil resistivity has a direct effect on the resistance of a grounding system and is largely determined by the composition of soil itself according to [1].

According to [18], there are other factors affecting the soil resistivity other than the type of soil itself. These factors include temperature, moisture, salt content and compactness of the soil. The relationship of these factors towards the soil resistivity respectively can be explained by referring to the graph as shown in Figure 1. Figure 1 illustrates the effects of moisture content, temperature and salt content upon soil resistivity. It can be clearly seen that with the increment of percentage in salt content, moisture and temperature, the soil resistivity decreases. On the other hand, it is observed that the effect on soil resistivity is minor once the moisture content exceeds approximately 22% as shown in IEEE Std-80-2000 [19]. Moisture content is one of the main factors governing the parameter of the soil resistivity, this is due the flowing of electricity in soil is essentially electrolytic. This can be further proven by referring to Figure 1 where the soil resistivity of sand soil increases abruptly whenever the moisture content accounts for less than 15% of the soil weight. This is due to the presence of moisture content allowing the conduction of electricity through movement of ions in pore water [20].

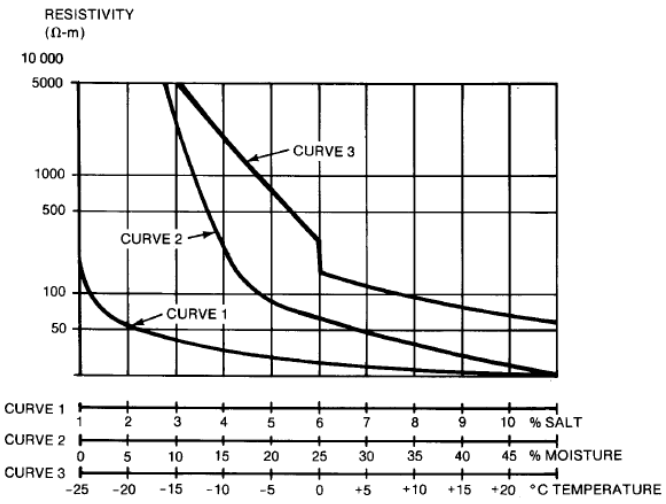


Figure 1. Effects of moisture, temperature and salt content upon resistivity on sand soil [19]

3. Research Methodology

The methodology consisted of quantitative investigation regarding (i) the influence of moisture content on the performance of an electrical power grounding system and (ii) the influence of compression level of soil on the performance of an electrical power grounding system. The measurement values of soil resistivity at (i) and (ii) were then compared with the values from literature. From the obtained results at (i) and (ii), the ground resistance was computed starting from the simplest grounding system configuration. This research topic was conducted quantitatively in a laboratory experimental setup to study the influence of moisture content and compression level of soil to ground resistance at low moisture content. Laboratory experiment was chosen over on-site measurement because in the latter, moisture content and compression level cannot be controlled. Soil resistivity of two types of soils, clay and fine sand at various moisture content and compression level respectively were recorded and quantitative analysis of the factors influencing the parameters of ground resistance were done. An overall flow chart as shown in Figure 2 was constructed to provide an overview to this research topic.

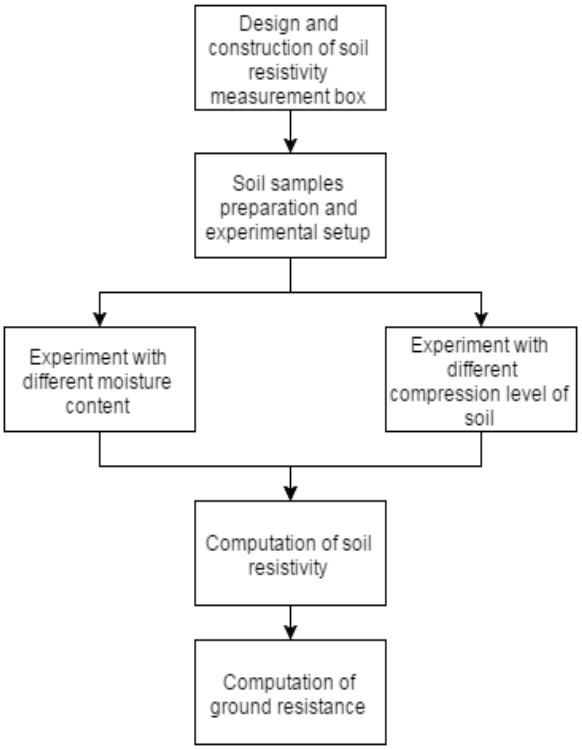


Figure 2. Flow chart of the overall research topic

3.1 Design and Construction of Soil Resistivity Measurement Box

The design of the soil resistivity measurement box is referred to [21] and design sketches of the soil resistivity measurement box are shown in Figure 3. The required tools and materials for the construction of soil resistivity measurement box were acrylic sheet, screws, aluminium conductive plate, washers, rubber, washer and nut set. The outer part of the soil box was constructed using acrylic sheet as it provides good electrical insulation, greater impact resistance than glass, crack resistance and chemical resistance. The purpose of using acrylic sheet is to prevent the

soil box from cracking sideways when the soil in it is compressed during the investigation of soil resistivity at various compression levels. The aluminium conductive plates in this context acted as electrode to allow conduction of electrical current. Referring to Figure 3, the electrode was locked using screws at both side of the soil box respectively. This allowed the experiments of measuring the soil resistance to be easily carried out as the Kelvin clips from the LCR meter could be connected to the screws at both side of the soil box respectively.

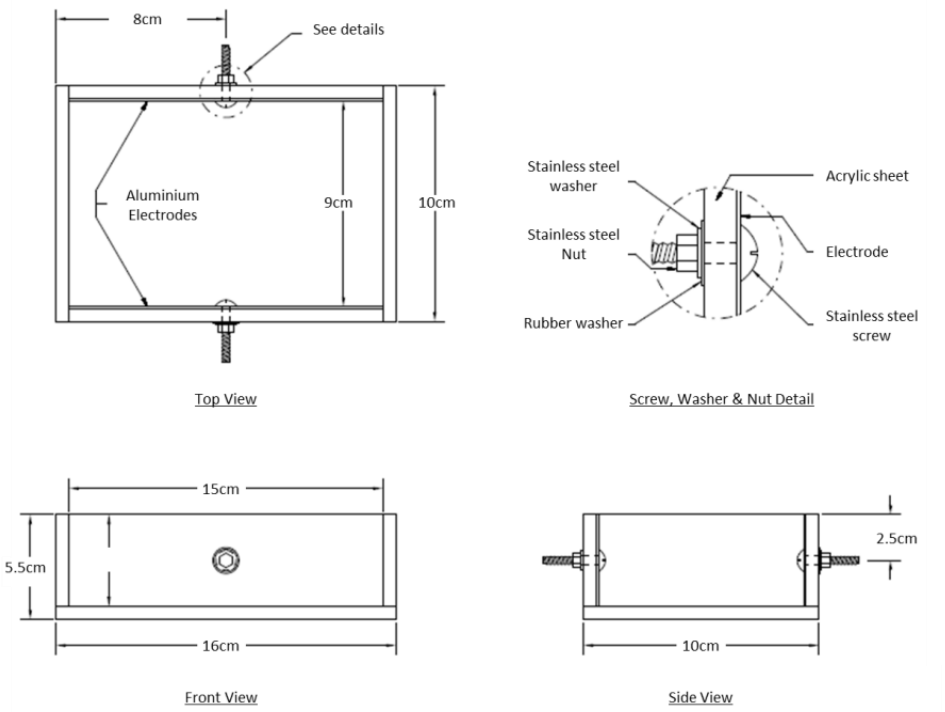


Figure 3. Design sketches of the soil resistivity measurement box in top view, front view, side view and detailed illustration of screwm washer and nut [21].

3.2 Soil Samples Preparation and Experimental Setup



Figure 4. Experimental setup process flow

In this process, LCR meter was used to measure the resistance of the soil and then later computed to soil resistivity by multiplying to the soil box factor. The types of soil samples prepared for the investigation were clay and sand. The purpose of conducting the research study using these two types of soils is due to the difference of texture and composition in the soils hence ground resistance from two different types of soils can be computed and analyzed. 500g of each type of soil was used to conduct the experimental study. The soil box was designed in a smaller scale to ensure the current is able to flow through the soil. This is because the further the distance between the electrodes, the ability of current to flow through the soil is weaker hence the soil resistance reading obtained in the LCR meter might be inaccurate. Usage of 500g of soil was to ensure the soil filled in the volume of the soil box hence

increasing the contact of the soil with the electrodes in order to obtain a more stable soil resistance value. The experimental setup process flow was prepared as shown in Figure 4.

Before proceeding to the experimental stage, the clay and sand samples were dried in the oven at 110±5 ℃ for 16 hours to obtain constant mass of the soil samples as stated in ASTM D2216 [22].

The volumetric water content (VWC) of wet soil is spatial and temporal in nature. Hence, it is difficult to obtain a predefined VWC. Therefore, volumetric water content test was done to reduce the error while commencing the experiment. The preparation of volumetric water content test was accomplished in 3 steps starting from calculating the bulk density of the dry soil then followed by calculating the approximate amount of water to achieve the target percentage and adding water to the dry soil. The actual volumetric water content of the soil was calculated hereafter [23]. The bulk density of the dry soil can be expressed as:

$$\rho_{bulk} = \frac{mass\ of\ dry\ soil}{volume\ of\ dry\ soil} \tag{1}$$

The approximated volume of water to be added to the soil samples to achieve the target moisture content can be calculated by referring to equation (2) which is expressed as:

$$Volume\ of\ water = VWC \times \frac{mass\ of\ soil}{bulk\ density\ of\ the\ soil} \tag{2}$$

After adding the calculated amount of water to the soil, the actual VWC of the soil can be obtained by referring to equation (3).

$$VWC_{actual} = \frac{Volume\ of\ water}{Total\ volume\ of\ wet\ soil} \tag{3}$$

Figure 5 refers to the experimental setup of the investigation where the Kelvin clips from the LCR meter were connected to the two ends of the screws as shown in Figure 5. From this, the soil resistance value was obtained from the LCR meter as shown in Figure 6.

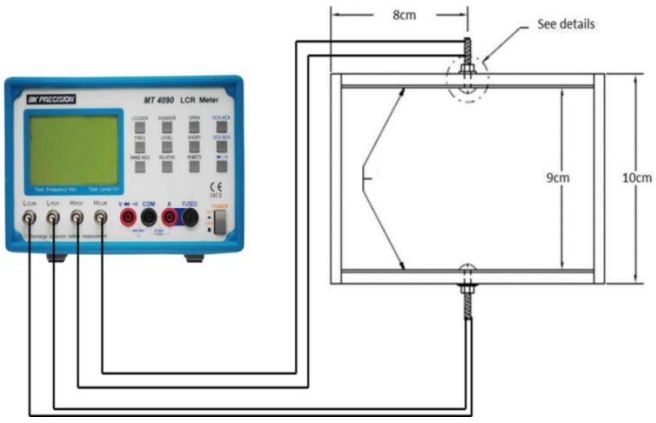


Figure 5. Connection of LCR meter to the soil resistivity measurement box

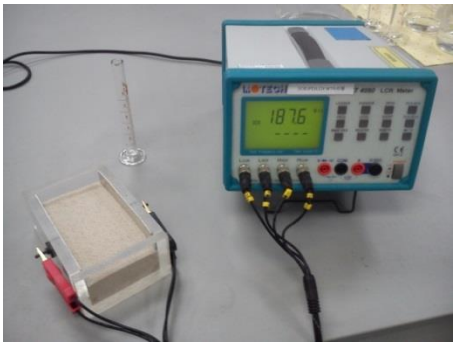


Figure 6. Actual experiment setup

3.3 Experiments with Different Moisture Content

Due to the maximum weightage of moisture content that clay and sand can hold in nature is 50% and 88% respectively. Hence, moisture content below 10% on these types of soil is considered significantly low. The experiment was conducted at moisture content from 1% to 10% based on the percentage of water used for 500g of original oven dried soil to investigate the soil behavior at low moisture content. For example, a constant volume of water based on the target volumetric moisture content was added consistently and mixed thoroughly into the oven dried soil and the soil resistance value reading from the LCR meter was recorded. The test was then repeated at the same procedure until the volumetric water content reaches 10%. In this context, a constant pressure of 30 kPA was applied before taking any reading from the LCR meter to reduce the error due to different compaction level of the soil. The purpose of conducting the experiment at a range of 1% to 10% is due to the significant changes of soil resistivity at this range based on the surveyed literature [1, 19].

3.4 Experiments with Different Compression Level of Soil

The variation of soil compression level was done using the Newton Weights to compress the soil sample in the soil box. The soil samples were exposed to the applied pressure of 5, 10, 15, 20, 25, 30, 35 and 40 kPA successively and the soil resistance reading on the LCR meter were recorded for each applied pressure.

3.5 Computation of Soil Resistivity

Do notice that the readings obtained from the LCR meter was soil resistance and in order to convert it to soil resistivity the soil box factor (SBF) was taken into consideration when calculating the soil resistivity as stated in [21]. The soil resistivity can then be computed by multiplying the SBF with the soil resistance reading obtained in the LCR meter. The SBF can be expressed as:

$$SBF = \frac{A}{D} \tag{4}$$

Where A = area of one electrode in m^2, D = distance between electrodes in m.

$$\rho = SBF \times R_{soil} \tag{5}$$

Where ρ = soil resistivity in Ωm, R = soil resistance in Ω. At this stage, the soil resistance obtained from the moisture and compression experiments was converted to the soil resistivity and the ground resistance can be computed hereafter. Graphs of soil resistivity against moisture content and applied pressure on soil were plotted to provide a better understanding on the relationship between these three values.

3.6 Computation of Ground Resistance

The final and most crucial process in the methodology of this research topic is to compute ground resistance based on the measurement value of soil resistivity obtained. From the surveyed literature, most of them may have provided the relation of soil resistivity with moisture content and compression level respectively. However, relationship between ground resistance with moisture content and compression level respectively has yet to be demonstrated in a quantitative manner.

The connection to ground of a system in general contains complex impedances, resistance, capacitance and inductance. These resistive, capacitive and inductive components determine the current-carrying capabilities of a grounding system. That being said, ground impedance determines the effectiveness of a grounding system [18]. Vertical single ground rod is one of the most commonly used grounding electrode system for grounding due to its simplicity in approximating the grounding resistance at low frequency especially at 50 or 60 Hz [24]. Ground impedance is usually measured at low frequencies in an electrical power system and it can be represented by a single resistor under such condition [24-25]. Figure 7 refers to the low frequency equivalent circuit for vertical ground rod.



Figure 7. Low frequency equivalent circuit [24]

As mentioned in [1], a grounding electrode has a direct impact on the parameters of the ground resistance. It is affected by the contact resistance between the rod and soil, resistance of the conductor to the connection and the most significant factor is the resistance in the surrounding earth to current flow.

Referring to [1, 18, 26], to compute ground resistance, soil resistivity throughout the volume is assumed to be uniform in this context though it is seldom case in nature. Due to the fact that equations for systems of electrodes are complex, hence it is often expressed only as an approximation and the most common one is the single ground electrode (rod) system and can be expressed as follow:

$$R = \frac{\rho}{2\pi l}\left(ln\frac{4l}{r} - 1\right) \quad (6)$$

Where R = resistance in ohms of the ground rod to the soil, l= grounding electrode length, r = grounding electrode radius, ρ = average resistivity in Ωm

Referring to equation (6), the ground resistance can be computed with given grounding electrode length and radius and using soil resistivity as the main factor in varying the computation of ground resistance. Once computation for single vertical rod was done, the work can be extended for other common ground electrode configuration such as multiple vertical driven electrodes, plates and horizontal buried strip configurations. Hence, possible conclusion can be drawn on the extent of influence of variation of moisture content and compression strength on different ground electrode configuration.

4. Result and Discussion

In this section, ground resistance of different grounding configurations is computed. Ground resistance of a single driven rod can be approximated by referring to equation (6). According to IEEE Std 142-2007, for grounding system consists of 2 to 24 rods having one rod length distance from each other in a line, hollow, triangle or square will provide ground resistance divided by number of rods and multiplied by the factor F as tabulated in Table 1 [10].

Table 1. Multiplying factors for multiple rods

Number of rods	F
2	1.16
4	1.36
8	1.68
16	1.92
24	2.16

In this context, 3 m length with a diameter of 12.7mm of copper rod is used to compute the ground resistance where the 3 m length meets the code requirement of minimum standard length buried and the small diameter of 12.7 mm rod has an advantage in meeting the driving requirements [27]. For plate type of ground configurations, area of 1.9 m^2 is commonly used [10]. For the evaluation of plate type ground configuration, the equation is expressed as:

$$R_p = \frac{\rho}{4}\sqrt{\frac{\pi}{A}} \tag{7}$$

R_P is the ground resistance Ω, ρ is soil resistivity (Ωm) and A is the area of plate in m^2 [10].

If the computed ground resistance from multiple driven rods and plate configuration does not meet the NEC of 25Ω for ground rods [27], a horizontal buried strip grounding configurations can be implemented and it is expressed as:

$$R = \frac{\rho}{P\pi L}\left(ln\frac{2L^2}{wh} + Q\right) \tag{8}$$

R is the ground resistance Ω, ρ is soil resistivity (Ωm) and L is the length of strip conductor (m), h is the depth of electrode (m), w is the width of conductor (m), P and Q are the coefficient for different arrangements of electrode. In this case, the

coefficient for *P* and *Q* for four lengths of strip conductors at 90℃ is 8 and 3.6 respectively [1].

4.1 Effect of Moisture Content on Ground Resistance

Moisture content is one of the major factors that govern the soil resistivity and affect the performance of an electrical grounding system. Referring to Figure 8, it is noticed that the soil resistivity decreases with the increment of moisture content for both clay and sand. This is due to the presence of moisture content facilitates the movement of ions in pore water hence allowing the conduction of electricity [19]. The soil resistivity of sand at 0% moisture content is not included in the results as the resistivity is too high to be measured in such moisture condition.

In general, the average resistivity of clay is lower than sand however based on the obtained results as shown in Figure 8, it is seen that at low moisture condition, the resistivity of clay is greater than sand. This can be explained by referring to literature [28], it is more difficult to remold clay clods at low compaction and dry of optimum water content in which it results in relative large interclod pores of clay in low moisture condition. In such condition, the pores are usually filled with air which is dielectric and the contacts between the inter particles are poor thus this indicates the high soil resistivity of clay in low moisture condition. In contrast, at high compaction and wet of optimum water content, it is easier to remold the clay clods hence the pores become smaller in size and more saturate in which the dielectric air filled pores are reduced whereas the water filled pores increased. Under such condition, the contacts of the inter particle is strong and hence reduces the resistivity of the soil. Referring to [29], due to the level of porosity of clay is higher than sand, the tendency of clay in the absorption of water is greater than sand. Thus, it can be stated that the clay resistivity is significantly more moisture-dependent than sand resistivity. Referring to Figure 8, it is seen that the clay resistivity continues to drop and it is significantly lower than sand resistivity when the moisture content surpasses 10%. Such statement can be justified by referring to [12, 28] where the findings show that clay resistivity is significantly lower than sand resistivity.

Contrary to common understanding that clay has lower soil resistivity, it is not the case when moisture content is low. In fact in all relevant standards such as IEEE Standard-80, IEEE Standard-81 and IEEE Standard-142, the average value and the range of value of clay resistivity is given without specifying at what moisture content or at what range of moisture content. Resistivity-moisture content curve is only available for sand and rarely for clay [10, 18-19].

Figures 9 and 10 refer to the computed ground resistance of clay and sand samples on different grounding configurations. It is noticed that due to the high soil resistivity caused by the low moisture content, the ground resistance computed by a single driven rod and plate configuration is nowhere in meeting NEC requirements of grounding. Hence, multiple driven rods are considered and even with 24 rods driven, the ground resistance is still appear to be high in low moisture content. Therefore, it is necessary to implement the horizontal strips configuration where the ground resistance of this configuration is highly dependent on the length of the conductor and has minor effect on the width and the depth of the strip as stated in [1]. With such implementation it is noticed that even at low moisture content, the computed ground resistance is much lower compared to other configurations. However, such configuration is very expensive due to the long length of the copper strips conductor and it is difficult to bury into the ground. That being said, such implementation will

only be applied in the event of very high soil resistivity whereas in ordinary soil condition multiple driven rods grounding configuration is sufficient.

Besides, it is noticed that the computed ground resistance drops abruptly with slight increase on moisture content in both soil samples and it continues to drop with an increment of moisture content. Referring to Figures 9 and 10, it can be clearly seen that the 4 horizontal strips configuration is not affected by the moisture content as much as the others configurations. Hence, implementing a 4 horizontal buried strips in a high moisture content soil is considered as excessively designed where such complex design can actually be easily replaced by a simpler grounding configuration. That being said, a less expensive grounding configuration such as single ground rod can be used and this further implies the influence of moisture content on the performance of an electrical grounding system.

From the findings, the ground resistance computed based on the resistivity of clay is higher than sand. Hence it can be stated that clay is not as effective as sand as a grounding medium for moisture content lower than 10% due to its high resistivity. However, type of clay used may also be influential as resistivity value of different types of clay varies.

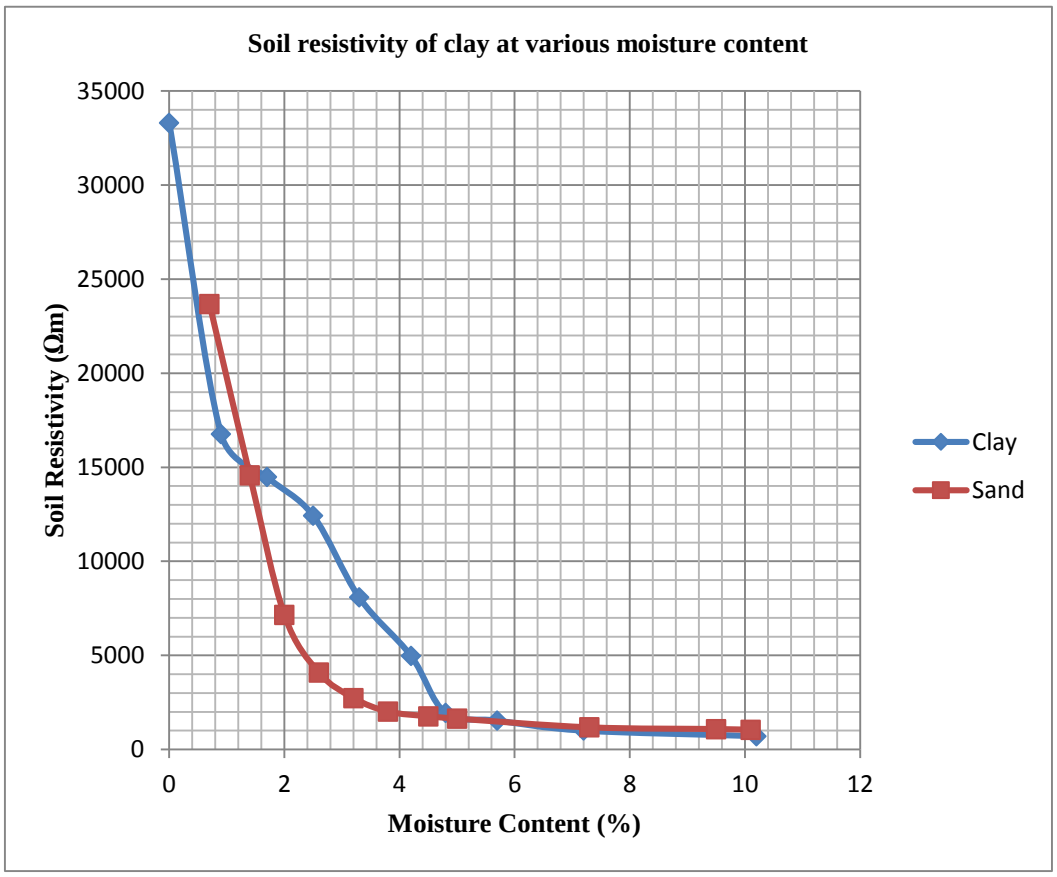


Figure 8. Soil resistivity of clay and sand at various moisture content

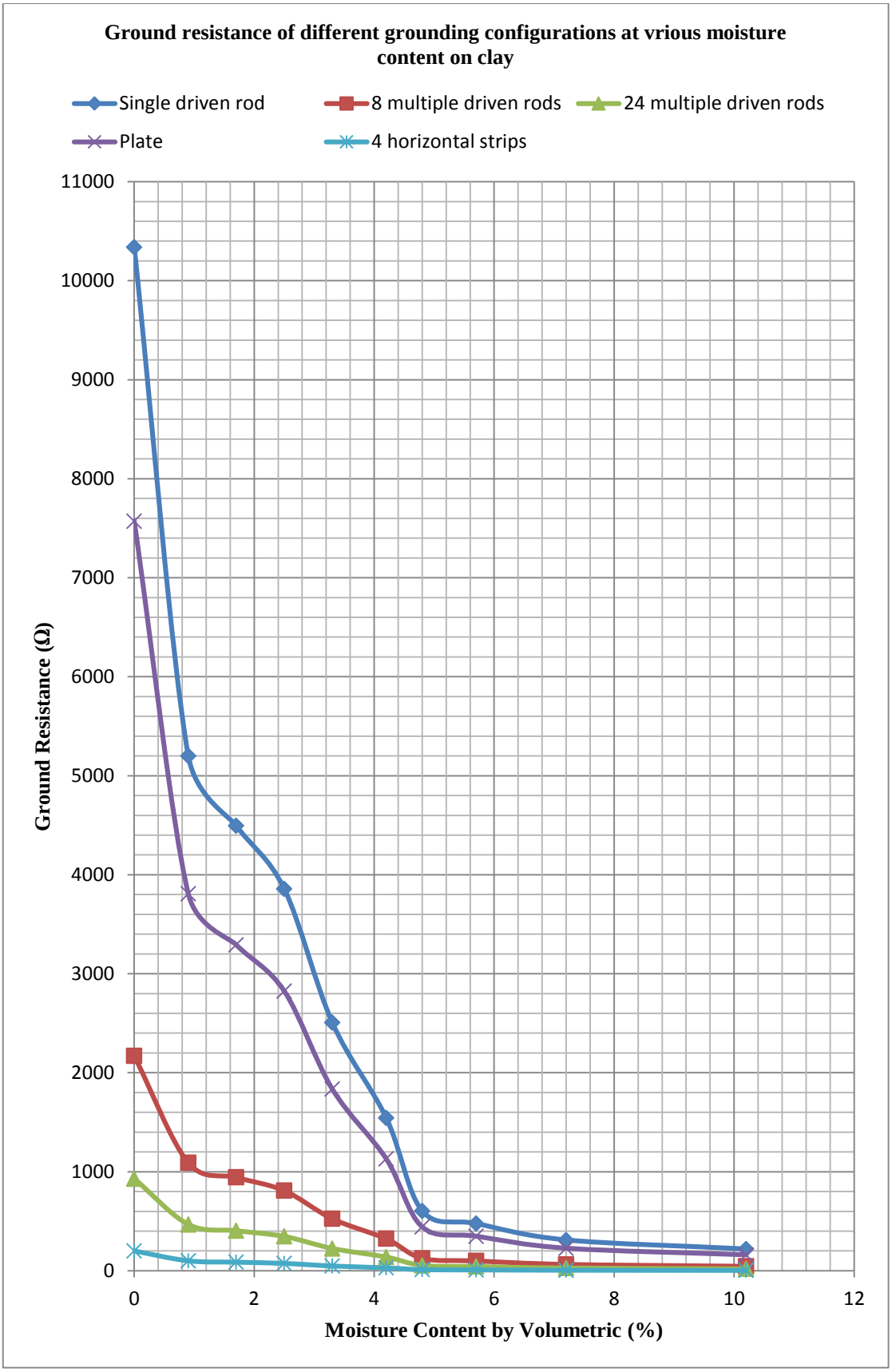


Figure 9. Ground resistance of different grounding configurations on clay

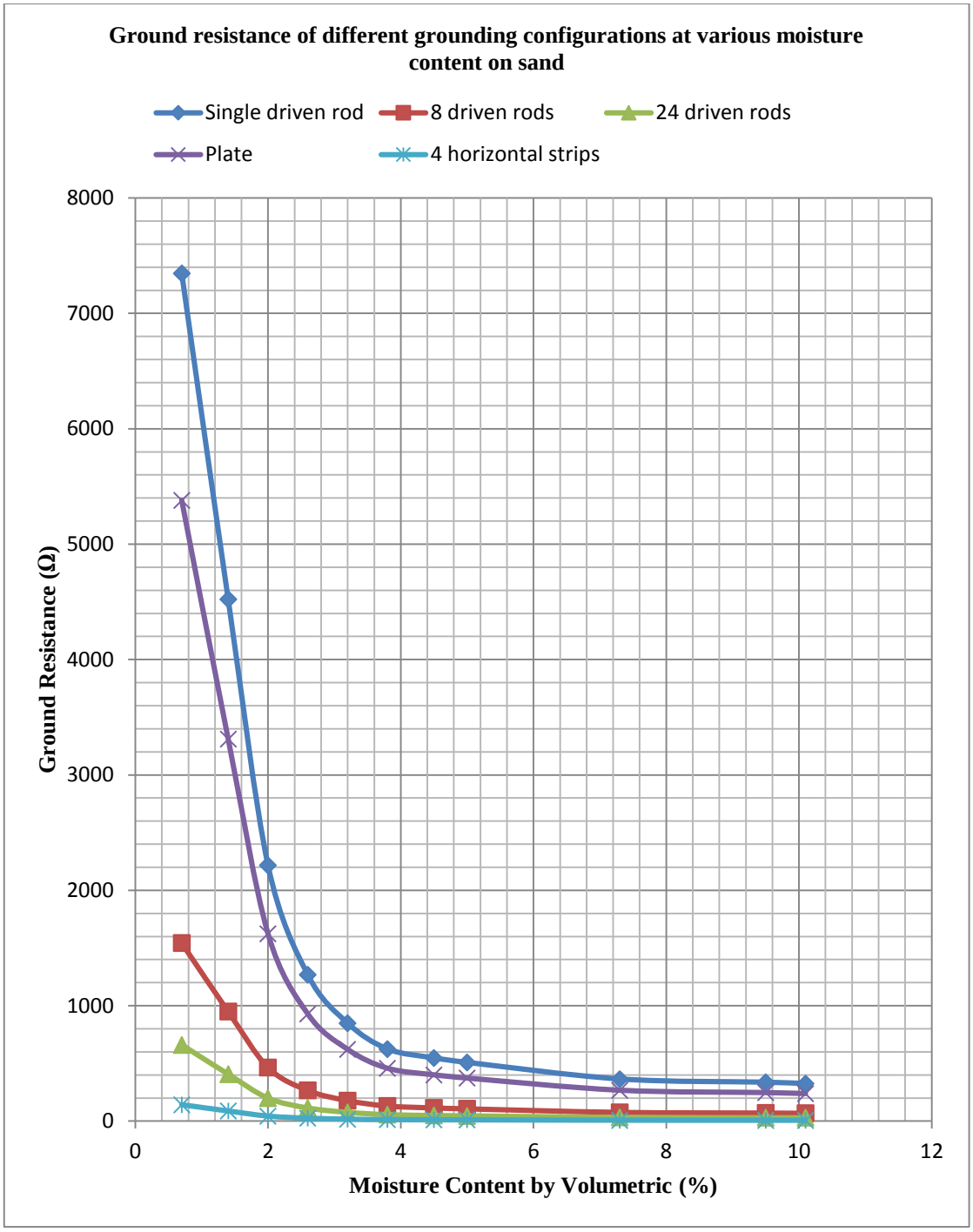


Figure 10. Ground resistance of different grounding configurations on sand

4.2 Effect of Compression Level of Soil on Ground Resistance

In this context, constant moisture content of 2.7% was applied to both clay and sand while conducting the experiment. This is to study the effect of compaction effort at low moisture content as change in compaction effort at high moisture content soil does not significantly affect the soil resistivity as stated in [28].

In the event of soil compaction, the soil particles are pressed together resulting in the reduction of pore space between them. There are few large pore contained in

heavily compacted soils in which it will reduce the rate of both water infiltration and drainage from the compacted layer hence this explains that it is effective for water to move through the soil due to the presence of large pores when it is saturated [30]. Referring to Figure 11, a decrease in the compression level of soil will lead to an increase in the soil resistivity and this is due to the low density of soil causing the soil porosity to be filled with air whereas an air filled void possess a higher resistivity than water filled void [31]. Besides, it is noticed that the soil resistivity of clay drops abruptly even in 10 kPA of applied pressure. This is could be due to the particle size of the clay is smaller than the sand and the porosity level of clay is higher than sand [31]. That being said, clay particle absorb more water than sand particle. In this context, the air void ratio is reduced hence it is easier to become saturated in which it reduces the resistivity. According to [32], air void ratio is affected by the degree of compaction and when the compaction effort increases, the soil resistivity decrease.

However, the soil resistivity of clay is still greater than sand is because of the moisture content of the soil is very low. If the moisture content increases, it will reach to a point where the soil resistivity of clay is lower than the sand as shown in Figure 8 [28, 30].

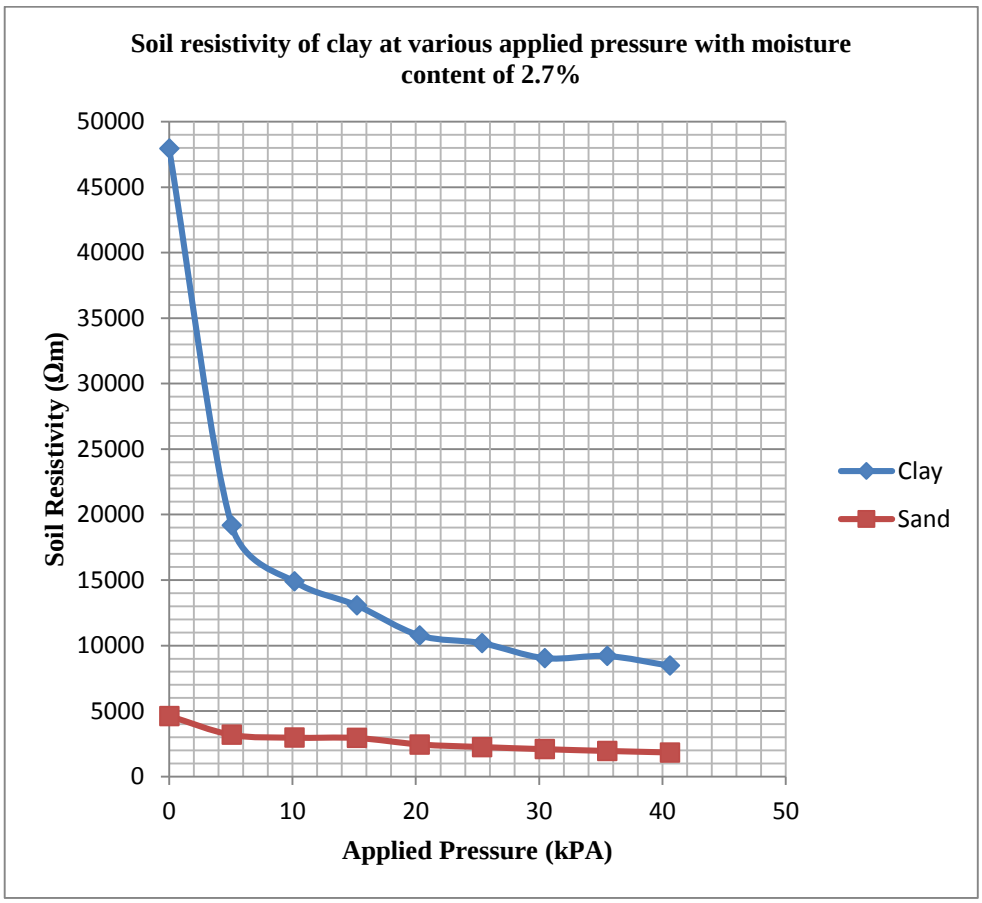


Figure 11. Soil resistivity of clay and sand at various applied pressure

Referring to Figures 12 and 13, it is noticed that level of soil compression has a direct influence towards the computation of ground resistance where the ground resistance drops abruptly with the increase in applied pressure to the soil. This is because by referring to the equation (6), (10) and (11), the soil resistivity plays a major role in determining the computed ground resistance and the soil resistivity

varies at different soil compression. In this context, due to low compression level of soil, it is necessary to implement 4 horizontal buried strip configuration based on equation (11). However such implementation may not be required when the compression level of soil is high and this can be proven by referring to Figures 13 and 14 where the changes of ground resistance computed based on the 4 horizontal buried strip configuration are very minor. That being said, at very high level of soil compression, a typical grounding system such as parallel multiple driven rods configuration is sufficient in order to achieve the NEC standard ground resistance.

Besides, the change in the soil resistivity due to the increase of compression level of clay is more significant that sand. However, due to the low moisture content, the effectiveness of clay as a grounding medium is lower than sand. Again, this is only for low moisture content and at wet and high compaction effort optimum moisture content, clay is essentially a better grounding medium than sand as clay can be further compressed to saturation that results in the reduction of resistivity [28].

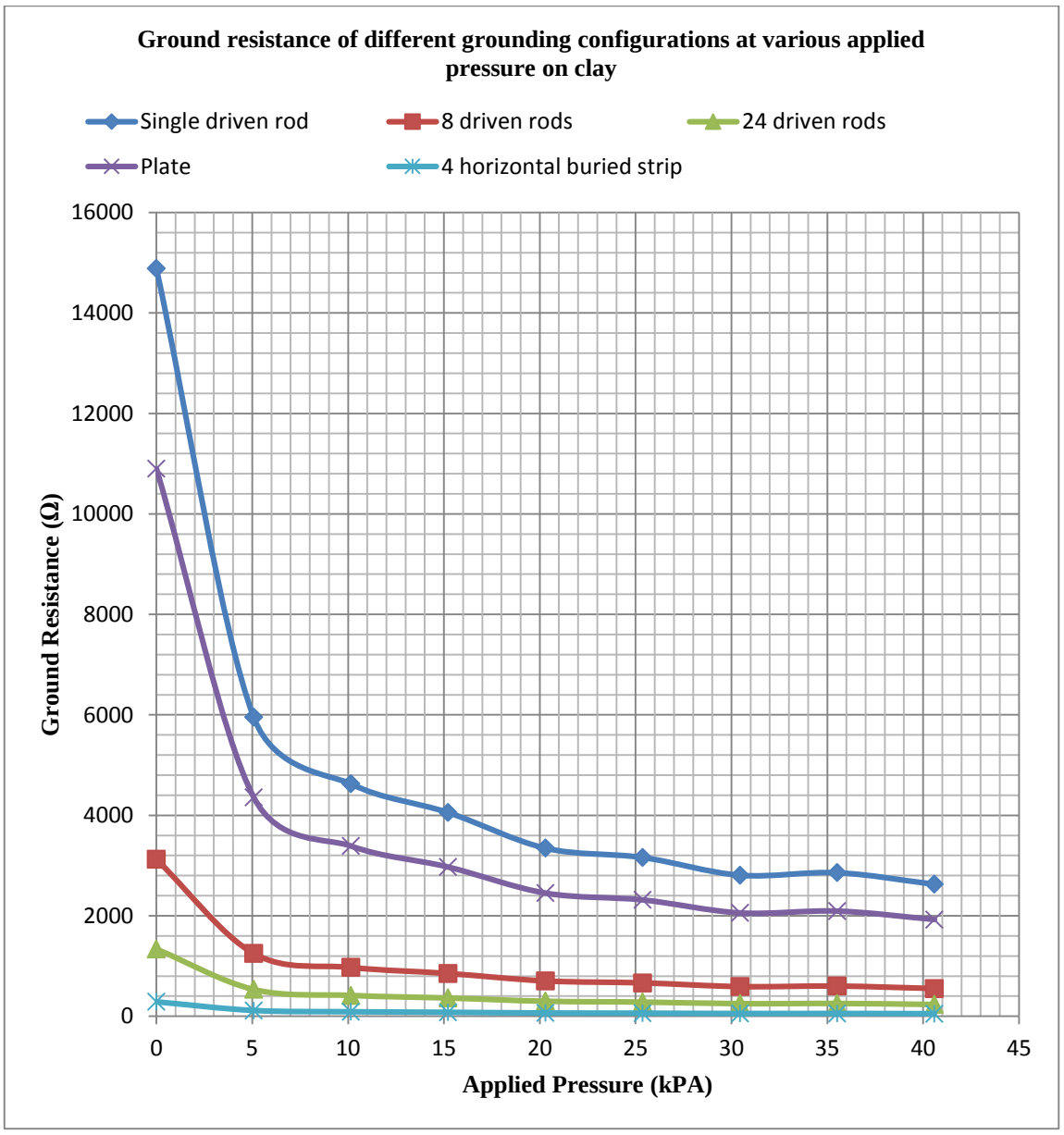


Figure 12. Ground resistance of different grounding configurations on clay

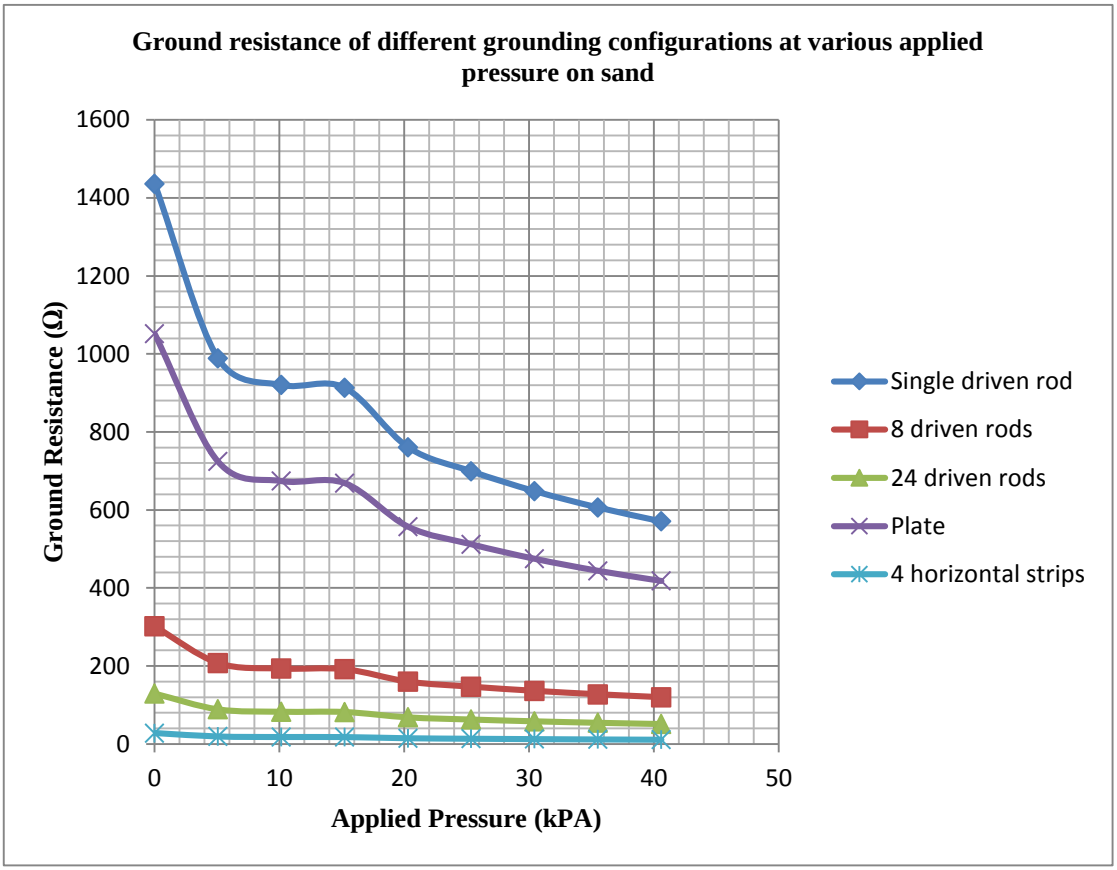


Figure 13. Ground resistance of different grounding configurations on sand

6. Conclusions

Effect of moisture content and compression level of soil on the computation of ground resistance respectively at low moisture content have been discovered and analyzed quantitatively. This investigation only focuses on low frequency behavior of a grounding system hence capacitive and inductive reactance are neglected. The performance of an electrical grounding system is highly dependent on the value of ground resistance and the ground resistance is governed by the soil resistivity. In this research, it is noticed that both clay and sand decrease in resistivity when the moisture content and the applied pressure increase respectively. This indicates that the ground resistance will decrease too.

From the findings, it is noticed that the resistivity of clay is higher than sand at low moisture content and low compression level. This is possibly because it is difficult for the clay clods to remold at low moisture content. Hence, the pores are large and filled with dielectric air resisting the conduction of current. In this condition, the soil resistivity of the clay is greatly increased to a point that it is greater than sand. However, it is noticed that at moisture content of 10% and more, the clay resistivity drops and becomes lower than the sand. This is due to increase in the presence of water causing the clay clods to be easily remolded and because clay is more moisture-dependent than soil, it absorbs more water filling the void and the resistivity of water filled void is much lower than dielectric air filled void. In this context, the water facilitates the flow of current causing the overall resistivity to be lower. It is noticed

that at 10% moisture content, the effect of moisture content on the sand is minor and this is because the porosity of the sand is lower and the tendency of sand in becoming saturated is easier than clay. When soil is saturated, further increment of moisture content has minor effect on its resistivity.

Besides, results show that the effect of level of compression in clay is greater than sand where the resistivity of clay decreases abruptly when the level of compaction increases. This is due to the particle size of clay is smaller than sand and the porosity is higher resulting in greater air void ratio. Hence the contact between the inter particle for the clay can be increased more with higher compaction whereas due to small air void ratio of sand, a higher compaction will not yield any significant effect on it.

From the experiment, the approximated single ground rod resistance computed at low moisture content and compaction is nowhere meeting the requirement of the NEC standard. As for the horizontal buried strip configuration, even at such condition, the computed ground resistance is low enough to meet the requirement. However at high moisture content and soil compaction, the difference of the computed ground resistance between the single rod driven configuration and horizontal buried strip condition is very low.

Based on this research, conclusion can be drawn that at either lower moisture content or compression level of soil, a more complex grounding configuration is needed such as the horizontal buried strip electrode to assure the ground resistance computed meets the requirement of the NEC standard. However, when the soil condition is of higher moisture content or more compact, simpler grounding configurations such as single driven rod or multiple driven can be considered to achieve the NEC standard of ground resistance value. Thus it can be concluded that the effectiveness of clay as a grounding medium is lower than sand at low moisture and low compaction level. However, at moisture content greater than 10%, the clay as a grounding medium is more effective due to its low resistivity.

This research study can be further extended to investigate the performance of grounding system on different types of soil samples under the same condition applied in this research. While computing the ground resistance based on different grounding configurations, the ground potential rise of the grounding system will vary hence it is necessary to perform a ground potential rise evaluation to assure the potential rise is of tolerable step and touch voltage.

References

[1] BS 7430 : 1998, Code of Practice for Earthing. ISBN 0-580-28229-5.

[2] S. C. Lim, C. Gomes, M. Z. A. Ab Kadir. (2013). Electrical earthing in troubled environment. *International Journal Of Electrical Power And Energy Systems*, 47117-128.

[3] R. Venhuizen. (2012). A systems approach to earthing. *Earthing & EMC*. Copper Development Association.

[4] H. Markiewicz, A. Klajn. (2004). Earthing systems – basic constructional aspects. *Earthing & EMC*. Copper Development Association.

[5] H. N. Amadi. (2015). Effective earthing system in the corrosive soil of Niger Delta. *International Journal of Emerging Science and Engineering (IJSESE), Volume-3 Issue-6.* ISSN: 2319-6378

[6] "13 electrical accidents with seven fatalities in Sabah," Borneo Post, September 19, 2014. [Online]. Available: http://www.theborneopost.com/2014/09/19/13-electrical-accidents-with-seven-fatalities-in-sabah/ [Accessed: June 12, 2015]

[7] "27 deaths caused by electricity-linked accidents last year – TNB." Astro Awani, April 12, 2015. [Online]. Available: http://english.astroawani.com/malaysia-news/27-deaths-caused-electricity-linked-accidents-last-year-tnb-57714 [Accessed: June 12, 2015]

[8] A. Nouri, H. M and Al-Ayoubi. (2011). Investigation into substation grounding and its implementation on Gaza substation. *Energy and Power Engineering, 3, 593-599.*

[9] A. A. Mehta, S. N. Singh, M. K. Singhal. (2012). Earthing system design for small hydropower (SHP) station – a review. *IACSIT International Journal of Engineering and Technology, Vol. 4, No. 3*.

[10] IEEE SDT-142 (Green Book). IEEE Recommended practice for grounding of industrial and commercial power systems; 2007.

[11] F. H. Slaoui, F. Erchiqui. (2010). Evaluation of grounding resistance and inversion method to estimate soil electrical grounding parameters. *International Journal of Multiphyscis Volume 4 Number 3*, 201-215.

[12] M. Kizlo, A. Kanbergs. (2009). The causes of the parameters changes of soil resistivity. *Power and Electrical Engineering*. ISSN 1407-7345.

[13] S. C. Lim, C. Gomes, M. Z. A. Ab Kadir. (2013). Characterizing of bentonite with chemical, physical and electrical perspectives for improvement of electrical grounding systems. *Int. J. Electrochem. Sci.*, 11429-11447.

[14] V. L. Coelho, A. Piantini, H. A. D. Almaguer, R. A. Coelho, W. do C. Boaventura, J. O. S. Paulino. (2014). The influence of seasonal soil moisture on the behavior of soil resistivity and power distribution grounding systems. *Electric Power Systems Research 118*. 76-82.

[15] K. E. Saxton, W. J. Rawls. (2006). Soil water characteristic estimates by texture and organic matter for hydrologic solutions. *Soil Sci. Soc. AM. J., Vol 70.*

[16] C. C. Wong, C. C. Peng. (1998). Country pasture Malaysia. *Grassland and Pasture Crops.*

[17] K. A. Lemke. (2013). Soil characteristics. *Geoprahy The Physcial Environment*.

[18] IEEE SDT-81. IEEE Guide for Measuring Earth Resistivity, Ground Impedance, and Earth Surface Potentials of a Ground System; 1983.

[19] IEEE SDT-80. IEEE Guide for Safety in AC Substation Grounding; 2000.

[20] F. I. Siddiqui, S. B. A. S. Osman. (2012). Integrating geo-electrical and geotechnical data for soil characterization. *International Journal of Applied Physics and Mathematics, Vol. 2, No. 2.*

[21] Test procedure for measuring the resistivity of soil materials. *Measuring the Resistivity of Soil Materials.* Texas Department of Transportation; 1999.

[22] ASTM D2216: Standard test methods for laboratory determination of water (moisture) content of soil and rock by mass. American Society for Testing and Materials, Philadelphia. PA.

[23] M. Nabipoor. (2011). *Soil prepration procedure for accurate volumetric water content test*. Taylor's University, Malaysia.

[24] L. Grcev, M. Popov. (2005). On high-frequency circuit equivalents of a vertical ground rod. *IEEE Transactions on Power Delivery, Vol. 20, No. 2*.

[25] P. Llovera, J. A. Lliso, V. Fuster, A. Quijano. (2008). Improved methodology for high-frequency low-current measurement of grounding rod impedance. *IEEE Transactions on Power Delivery, Vol. 23, No. 4*.

[26] C. Arnoux. Understanding Ground Resistance Testing, Workbook Edition 7.0.

[27] NFPA 70, National Electrical Code® (NEC®).

[28] G. Kibria. (2011). *Determination of GeotechnicalProperties of Clayey Soil from Resistivity Image (RI).* The University of Texas at Arlington.

[29] R. Whitlow, *Basic Soil Mechanics*, 4th Edition. England: Pearson Prentice Hall, 2011.

[30] J. DeJong-Hughes, J. Moncrief, W. B. Voorhees, J.B. Swan. (2001). Soil compaction. *Agriculture Tillage*.

[31] S. Kowalczyk, M. Maslakowski, P. Tucholka. (2014). Determination of the correlation between the electrical resistivity of non-cohesive soils and the degree of compaction. *Journal of Applied Geophysics*. 43-50.

[32] W. McCarter. (1984). The electrical resistivity characteristics of compacted clays. *Geotechnique*, 32(2), 263.

The Application of Image Processing for In-Store Monitoring

Lau Kah Heng, Chew Wei Jen

[1]*School of Engineering, Taylor's University, Lakeside Campus, Box.47500 Subang Jaya, Malaysia*
**kahheng.lau@sd.taylors.edu.my*

Abstract

Merchandizers and customer goods companies are increasingly paying attention on in-store monitoring and to improve sale and profit by finding efficient and convenient ways to identify their customer's interest. Therefore, the application of image processing through video surveillance for in-store monitoring is proposed as the solution for understanding customer's shopping behaviour as well as monitoring the attendance of employees in real time. In this paper, an integrated system involving face detection, face recognition, and people tracking algorithms is developed. A database of training images of known faces is generated for testing the face detection and face recognition algorithms while a video which recorded pedestrian walking on a corridor is used as the input for the people tracking algorithm. Viola-Jones is implemented for face detection technique, Eigenfaces face recognition technique is implemented to perform employee's attendance checking while background subtraction and Kalman filter techniques are used in the people tracking-by-detection algorithm. Results show that the proposed counting algorithm combining with people tracking algorithm is able to provide relevant data for customer's shopping behaviour study.

Keywords: In-store monitoring, face detection, face recognition, human tracking, counting algorithm.

1. Introduction

Merchandizers and customer goods companies are increasingly paying attention to in-store monitoring systems. To improve sale and profit, companies are always finding the efficient and convenient ways to identify their best standard in-store product placement by knowing customers' interest. However, traditional methods of in-store monitoring such as frequent point-of-sale visiting, conducting surveys, and focusing on best-selling product are time consuming, costly and sometimes inaccurate while biometric technique is often afflicted with privacy issue. Therefore, we focus on the application of image processing through video surveillance for in-store monitoring as the solution for understanding customer's shopping behavior as well as monitoring the attendance of employees in real time. It offers in-store monitoring by tracking customers without their intervention using tracking-by-detection method and shorter data collection time. The motivation of this project is that the current existing systems implemented in the market does not clearly mentioned how they separate human tracking into customer tracking and employee tracking and this might cause the employees to be mistreated as the customers as well and the results would be inaccurate. RetailNext [1], an in-store analytic provider claimed to be the industry-first in-store monitoring with the exclusion of employees from video traffic counts using assigned Wi-Fi tracking tags. However, their system are used for reporting on the paths which customers and employees took and the interaction where their paths crossed. For focusing on the customer traffic in our project, the interaction between employees and customers is an irrelevant factor in our in-store monitoring system.

Therefore, our solution to the study is to develop a customer tracking system with the employee exclusion by integrating Viola-Jones [2] face detection, Eigenfaces [3] face recognition, and people tracking using background subtraction and foreground detection, and Kalman filtering [4] techniques. The objective of this project is to integrate face detection, face recognition, and people tracking features into one customer tracking based in-store monitoring system, and the system provides accurate data collection, with employee exclusion, which is used for further customer shopping behaviour study.

For literature review, methods for face detection, face recognition, and people tracking are discussed and compared in this section. We should point out that the project scope is limited to indoor video surveillance where lighting or illuminance is sufficient and consistent. Small training set or database of training images of faces of classmates are generated for testing the face recognition algorithm. Location of camera is set at the entrance of simulated environment so that frontal view of face detection is achieved. All the setup above will be the justification of the chosen method for face detection, face recognition, and people tracking.

1.1 Face Detection

Face detection is the first and foremost feature in the system to research about. It detects faces from an image or video frame before proceeding to face recognition. Face detection algorithm is just an object detector that looks for features like eyes, nose, and lips to identify a face. Firstly, Paul Viola and Michael Jones [2] created a rapid object detector named Viola-Jones algorithm. The framework of their algorithm is

categorized into three stages that are Integral Image, AdaBoost Training Algorithm, and Cascaded Classifier. Viola-Jones algorithm does not use image differencing and skin colour detection to achieve high framerate of face detection. They proved that their algorithm can process images extremely fast while having high face detection rate but it only detects faces in the frontal view. Face detection study by Kim et al. [5] proposed a face detection technique based on colour segmentation, image segmentation, and image matching method. It has high true detection rate and low false detection rate. However, it requires image matching which is computationally expensive. Due to the need of application of face detection that requires fast detection of non-static subject and fairly short detection window period as people enter the door and passby within few seconds,Viola-Jones algorithm is suitable method that has fast computional speed.

1.2 Face Recognition

Face recognition is the process of identifying one or more people from images or videos by analyzing and comparing the patterns to the image database. Usually face recognition requires facial feature extraction and it finds the best match from the database by comparing between the input and the database. Jon Kruger,et al. [3] introduced Eigenface system as one of the popular face recognition techniques used in computer vision. Eigenface uses PCA to simplify the initial Eigenface basis to a relative small set of vectors from a large dimentional space. From PCA, the differences and similarities between the images in the database can be obtained. Eigenface method is more effective than feature-based face recognition due to its face classification based on general facial patterns which provide more information for analysis while old methods work on particular features of the face only. Peter N. Belhumeur et. al. proposed Fisherfaces [6] face recognition algorithm based on Fisher's Linear Discriminant [7]. Fisherfaces maximizes the ratio of between-class scatter to that within-class scatter and projects away variation in illumination and facial expression, making itself insensitive to both variations. Both Fisherfaces and Eigenfaces reduce the image space to a low dimensional subspace and has the same computational requirements. The authors claimed that their method has lower error rates than those of Eigenfaces. However, the major drawback is that it encounter issue with small dataset size and the within-class scatter matrix become singular. K. Srinivasa Reddy, et. al. proposed a local feature method based face recognition with technique named Significant Non-Uniform Linear Binary Pattern (SNULBP) [8]. Fundamentally, the proposed method derived from LBP which use local information extracted from intensity images. One of the advantages of using LBP is its local computationally efficient nature and robustness in representing local features and illumination variation. However the drawback is that it considers a huge number of NULBP's under one label in which causes some lost information. By comparing the three methods, Eigenfaces method is the most suitable algorithm used in face recognition for in-store monitoring as its nature of face classification based on general facial patterns yields more information to be analyzed, resulting in a more accurate recognition rate. As indoor lighting is assumed to be constant and sufficient at all times, sensitivity to illumination variation seems to be insignificant in indoor application.

1.3 Tracking-by-detection Technique

Tracking-by-detection technique involves moving object detection and tracking method. There are three common methods in moving object detection, namely temporal

differencing, background subtraction, and optical flow. Gottipati [9] commented that temporal differencing is good in detecting moving object in dynamic environment but very bad at choosing all the right pixel features. Background subtraction gives the most complete pixel features among other methods but seriously affected by illumination variations and vigorous acitivities. Dealing with camera motion, optical flow performs the best in detecting moving objects but with complex computation and cannot perform in real time without specific hardware. Choosing based on the criteria or project scope as mentioned earlier, background subtraction is the choice of moving people detection method as illumination is constant in indoor and people are expected to walk around instead of running.

1.3.1 Background Subtraction

Background subtraction simply subtracts each new frame from the reference image and adjusts the result by using specific threshold. The reference image is a time-averaged background image while the resulting image displays binary segmenetation which represent regions of moving objects. The drawbacks of this method is that it requires a training period where the background image is absent of foreground object, and also suffers from gradual illumination changes. Adaptive background modelling techniques are introduced to solve these issues. Friedman and Russell [10] used adaptive parametric mixture model of three Gaussian distributions to model each pixel in the video frame. Koller *et al* [11] implemented Kalman filter on every pixel to track the background illumination changes, and also introduced a selective update scheme which selects only the probable background values and update them into the estimate of the background. Its only major disadvantage is that it cannot solve the problem arising from object being introduced or removed from the scene. To tackle these problems, Grimson *et al* [12] introduced an adaptive non-parametric Gaussian mixture model which modelled each pixel based on multiple-colour background. Their work is less affected by the subtle repetitive motions such as moving trees. In fitting a Gaussian mixture model, the common optimisation scheme used is the Expectation Maximisation (EM) algorithm which ensures the convergence to a local maximum in a seach space. In order to generate new Gaussian kernels to the existing mixture model, Grimson *et al* used deterministic thresholding.

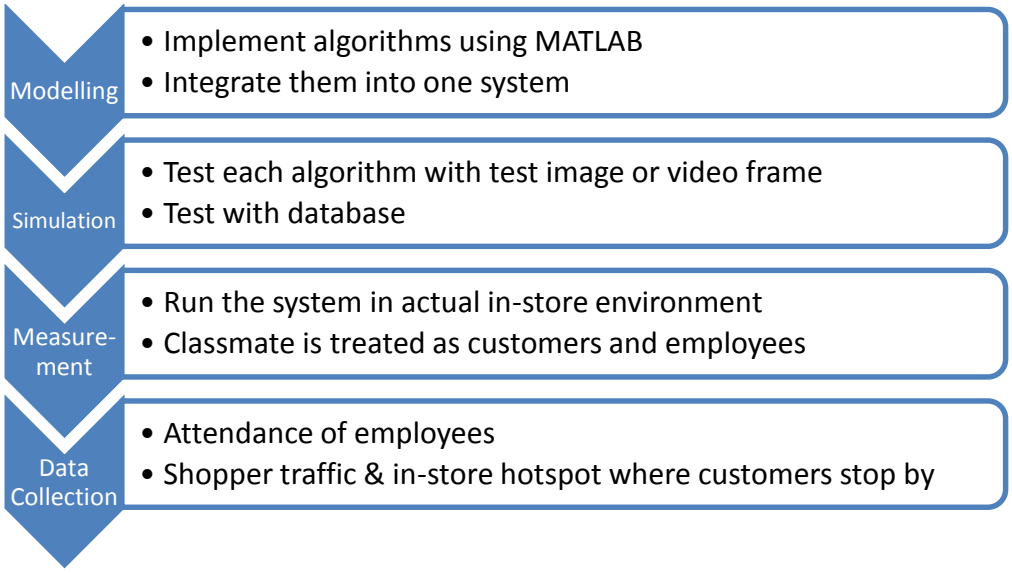
1.3.2 Adaptive Gaussian Mixture Model

Grimson *et al* modelled each background pixel by using a mixture of *K* Gaussian distributions. Typically K is a number range from 3 to 5. In this background model, different Gaussians represent different colours. The mixture adds weight parameters representing time proportions that those colours remain in the scene. The colours that remain longer and more static are the probable background colours. In the colour space, static single-colour objects form compact cluster while moving objects form spreading cluster because of different reflecting surfaces during the motion. *Fitness* is the term used for the measurement of the cluster. A selective update scheme is used for the background model to adapt to illumination changes and run in real time. The *fitness* value will measure each pixel value against the existing model components. The update scheme will update the first matched model component. If there is no match for the next model component, a new Gaussian component with a large covariance matrix, a small weighting parameter and a mean at that pixel.

1.3.3 Kalman filter

Kalman filter has been extensively used in the field of autonomous or assisted navigation. Kalman filter is a set of equation that solve discrete-data linear filtering problem recursively. It estimates the past, present, and future state and minimizes the least-mean square error. According to [12], Kalman filter helps in adding prediction to each Gaussian in their model, resulting more robust tracking in illumination variation.

2. Methodology



This section describes the project flow which includes steps, namely modelling, simulation, measurement and data collection. First, we implement the methods of our customer tracking system which are face detection, face recognition, and people tracking using MATLAB software. All the methods are integrated into one system to develop a complete in-store monitoring. Next, the simulation is tested with a set of database of test images using Viola-Jones face detection algorithm and Eigenfaces face recognition algorithm. Video frames are used to test the people tracking algorithm. The video recording is done using Logitech HD Webcam c615 with the specification of Full HD 1080p video capture (up to 1920 by 1080 pixels). For better computational speed, the video to be tested for the people tracking is recorded in the resolution of 640 by 360 pixels. The process of measurement is carried out where the developed in-store monitoring system is run in actual in-store environment using network cameras in real time manner. Lastly, the data collected will be the attendance of the employees, number of customers entering the store, in-store hotspot where customers stop by, and customer staying time. According to [13], customer staying time is the key parameter for zone management in in-store monitoring. Different staying time indicates different possible customer's behaviour or activity. The staying time is divided into 4 categories. Firstly, staying for less than 1 minute indicates "passing by" behaviour. Secondly, staying time between 1 to 5 minutes indicates that customer stops and looks at the product but there is still unnecessary for the employee to attend the customer. Thirdly, staying time between 5 to 10 minutes tells that the customer interacted with an employee and were actively browsing the product in that zone. Lastly, staying for more than 10 minutes indicates that the customer has the intention to buy. The output result is then exported

to Microsoft Excel spreadsheet as the data collected for further study of customer's shopping behavior as future work.

2.1 Overall Configuration of Developed System

To show how the developed system operate, a flowchart of overall configuration developed system is illustrated as shown in Fig. 1. At the beginning of the system operation, input video frame is first captured from the pre-setup camera located at the entrance of the simulated environment. The video frame is then fed into the face detection algorithm to produce a preprocessed output frame with face detected. The output frame will be compared with the training images in the database in the face recognition algorithm and undergone the identification process. The identification process determines whether the subject of the output frame is employee or customer. If the mentioned subject is determined as employee, the system will update the attendance of recognized employee and a specified input is outputted to the employee excluding algorithm where specific label is tagged on the employee. While the employee will still being tracked, with the specific tag on the employee, this will prevent triggering the customer counting algorithm and data collecting from employee in the people tracking. If the subject fails to match with any training images, it will be classified as customer and the people tracking stage works as normal. In the counting algorithm, one or more region of interest (ROI) is set up to output the number of people passing through and the staying time in that region.

2.2 Face Detection Stage

The flowchart of face detection process is shown in Fig. 2. Since the system will be using a video camera as the input source, the system will capture the image by snapshotting or taking a video frame based on desired image shown in Fig. 3(a). From the captured image, integral image can be created by computing the value of each pixel in the rectangle feature from Haar filter. Next, the integral image is then passed through a series of weak classifiers based on Adaboost training algorithm. Adaboost is an efficient feature selector where each round of weak classifier selects optimal feature given by the previous selected features. Cascaded classifier is then used to focus on the region of interest only to speed up the detector process. The output of the cascaded classifier is a successfully detected face. Once the position of the detected face is determined, a rectangle box or bounding box is drawn to locate the face in the output image using the information such as the upper left corner pixel coordinate, [x, y], width and height of the box shown in Fig. 3(b). To preprocess the output image, it will need to be converted to grayscale and normalized by resizing it to the size of 100 by 100 as shown in Fig. 3(c) and Fig. 3(d). The image conversion is needed because only one layer of image in the 3-layer of RGB image is needed to reduce the computation speed while image normalization is required so that same size of image is used for creating database as well as image matching for later stage of face recognition.

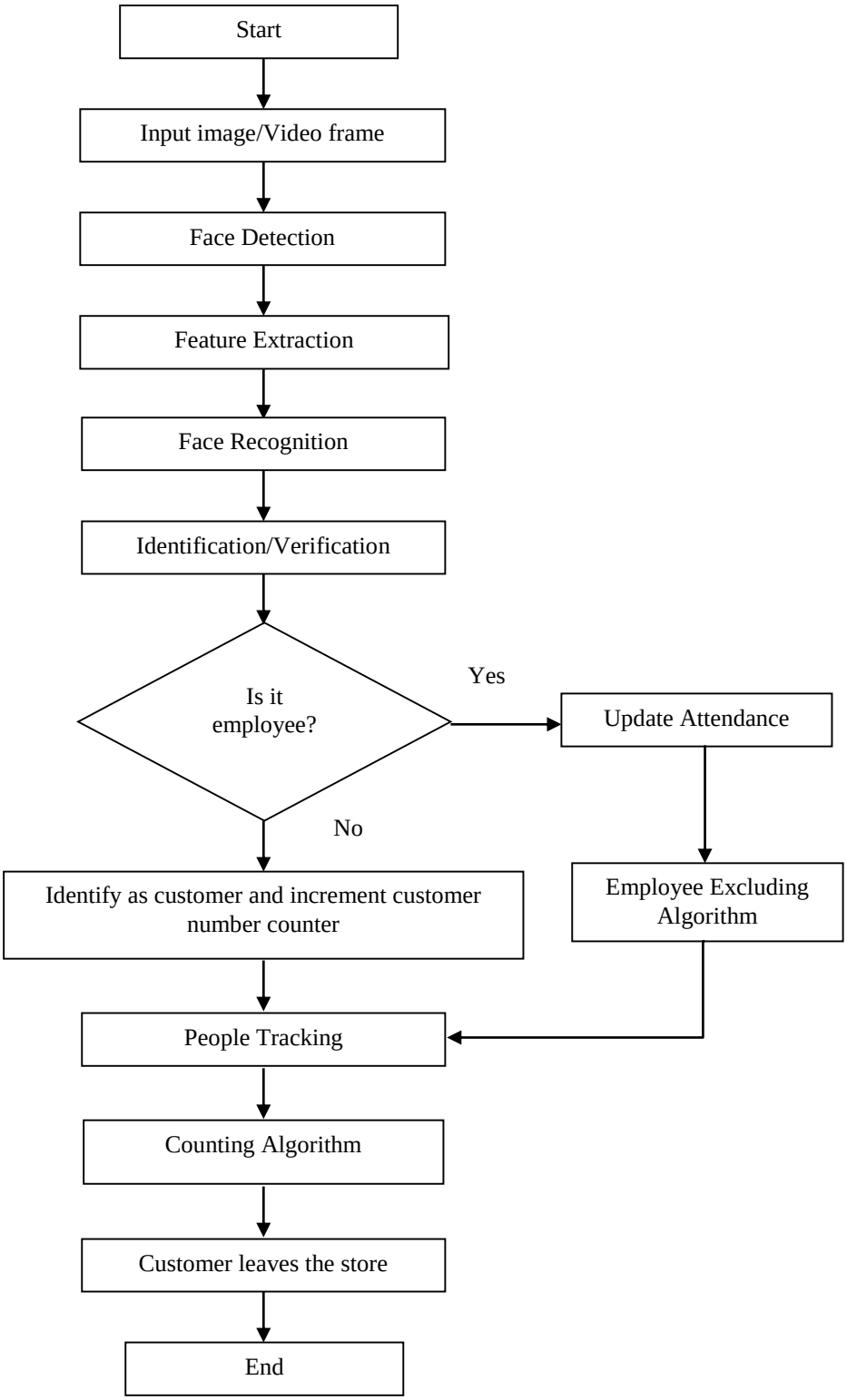


Figure 1: Overall application design.

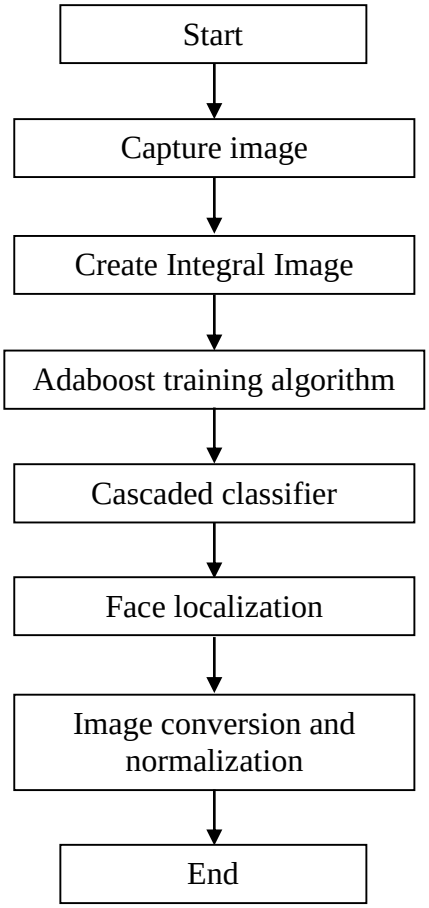


Figure 2. Viola-Jones Face detection algorithm flowchart.

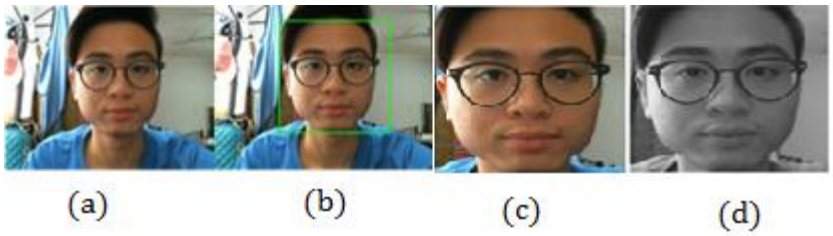


Figure 3. (a) Captured Image. (b) Output Image with bounding box. (c) Cropped image. (d) Cropped image converted to grayscale.

2.3 Face Recognition Stage

The flowchart of Eigenfaces face recognition process is shown in Fig. 4 and explained below. Before starting face recognition, a set of face images of known faces is collected to create a database. To create Eigenfaces, the average of face in the face space, N where each face images is converted into vectors, Γn, is calculated. Each face's difference from the average face is computed and formed a covariance matrix (C) for the database. From the result of the computation, Eigenfaces can be obtained from the eigenvectors of C. PCA is used to reduce the large dimensional space and find top Eigenfaces.

After database is setup, an input test image or video frame is fed into face detection algorithm and the output image will undergo feature extraction. The information from the feature extraction is used to compare with the top Eigenfaces in the database using classifier to determine whether the input matches any of the known faces in the database.

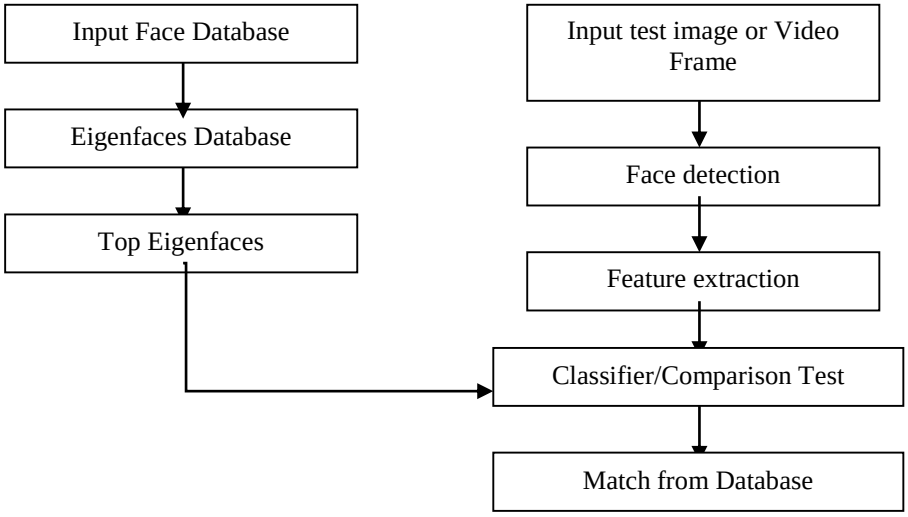


Figure 4. Eigenfaces face recognition flowchart.

2.4 People Tracking Stage

According to the flowchart shown in Fig. 5, our people tracking stage is divided into two parts, one is the detection of moving object and the other one is motion-based tracking. Background subtraction algorithm based on Gaussian mixture models is used for moving object detection. By background subtraction technique, it can detect foreground object from the video frame from stationary camera by comparing it to background model to determine whether individual pixels belong to background or foreground. Foreground is represented by pixels with value of 1 whereas background is represented by pixel with value of 0. To eliminate noise, morphological operation is implemented in the foreground mask and the holes are filled to form blob. Connected pixel or so called blob in the foreground mask is considered as moving object. Since the video is captured indoor, moving object are more likely to human. Lastly, blob analysis is applied on the blobs and output their characteristic such as area, centroid, and bounding box.

Motion-based tracking involves detection of moving objects in each frame and associating the detection of the same object over time. Kalman filter is introduced to deal with the motion of the object's track. It predicts the track's location in each frame and correct the estimate of the object's location with new detection. In any given frame, some of the detections are assigned to tracks but other detections and tracks still remain unassigned. The assigned tracks will be updated according to corresponding detection while unassigned tracks remain invisible and unassigned detection is given a new track. If the unassigned tracks remain invisible for specific number of frame which exceeds the threshold, the tracks will be deleted.

When creating new track, the employee excluding algorithm will obtain input from the face recognition stage indicating whether the person coming into the store is employee or customer. A specific tag will be labelled on the particular track if the track belongs to an employee. With this specific tag, employee remains invisible to the counting algorithm even though one is being tracked. If the track belongs to a customer, normal tag will be assigned to the track.

For the counting algorithm, a region of interest (ROI) is set up for assigned tracks to trigger the counter. Once the counter is triggered, the label of the assigned tracks and the number of frames that assigned tracks stay within the ROI are recorded.

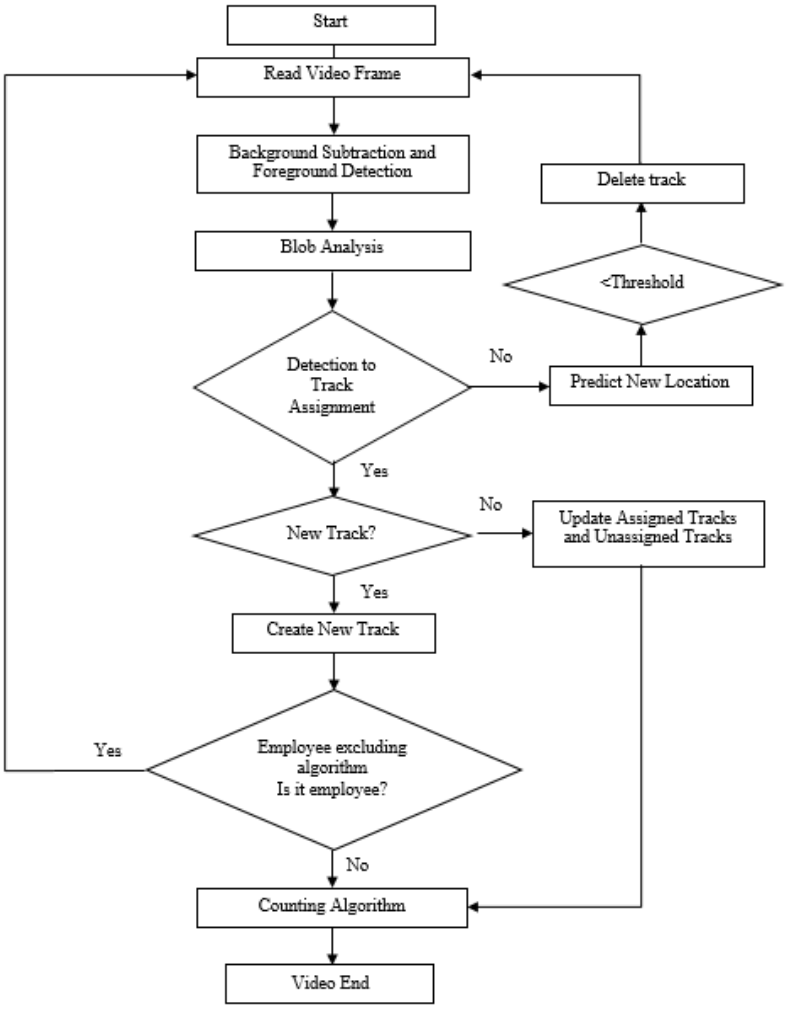


Figure 5. People tracking, counting algorithms, and employee excluding algorithm flowchart.

3. Experiment Result

In this section, we present and discuss the result for each of the three aforementioned algorithms. Before testing these algorithms, creating a database of known faces is the first task to start with. Face detection algorithm and image preprocessing are required to perform this task. After database is created, the face

recognition algorithm is evaluated by taking one training image from the database and comparing with the rest of the training images. The recognition rate of the algorithm is discussed. Lastly, people tracking algorithm is tested with a recorded video from webcam. The result of detecting moving people and the counter are analyzed and discussed.

3.1 Face Detection Result

A set of raw training images of 11 subjects each having 5 images are taken by camera as shown in Fig. 6(a). Each images in the series of 5 training images of each subject represents subject without spectacles, subject with spectacles or different light intensity, subject with different facial expression such as smile, subject with slight bottom pose, lastly subject with slight top pose respectively. After the raw training images are fed into the face detection algorithm, the output images with green bounding boxes showing the detected faces are displayed in Fig. 6(b). All raw training images are successful with face detected. This shows Viola-Jones face detection algorithm is robust and has high detection rate. To produce the final training images for database as shown in Fig. 7, the detected face must be cropped from the output images shown in Fig. 6(b), converted to grayscale with single layer selected and normalized to size of 100 by 100.



(a) (b)

Figure 6. Examples of (a) Raw training images. (b) Output images with detected faces.

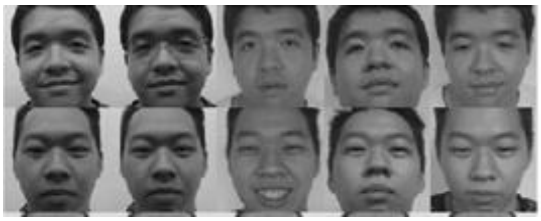


Figure 7. Examples of database with cropped, converted and normalized images.

3.2 Face Recognition Result

To test the face recognition algorithm, one training image of each of the subject is picked from the database one at a time and the rest of the image are used for training. Each time the training is done with 54 training images and the selected image is used to test the algorithm. Firstly, an average face is calculated by subtracting the mean of all training images from themselves. Then, the eigenvectors of the correlation matrix is calculated and the weight of each training images are stored into the eigenspace. Now the selected image is also subtracted from the mean and compared to find the nearest

match from the eigenspace. Based on the result shown in Fig. 8, 9 out of 11 subjects are matched correctly which gives a recognition rate of 81.82%. This proves that Eigenfaces method is good face recognition algorithm.

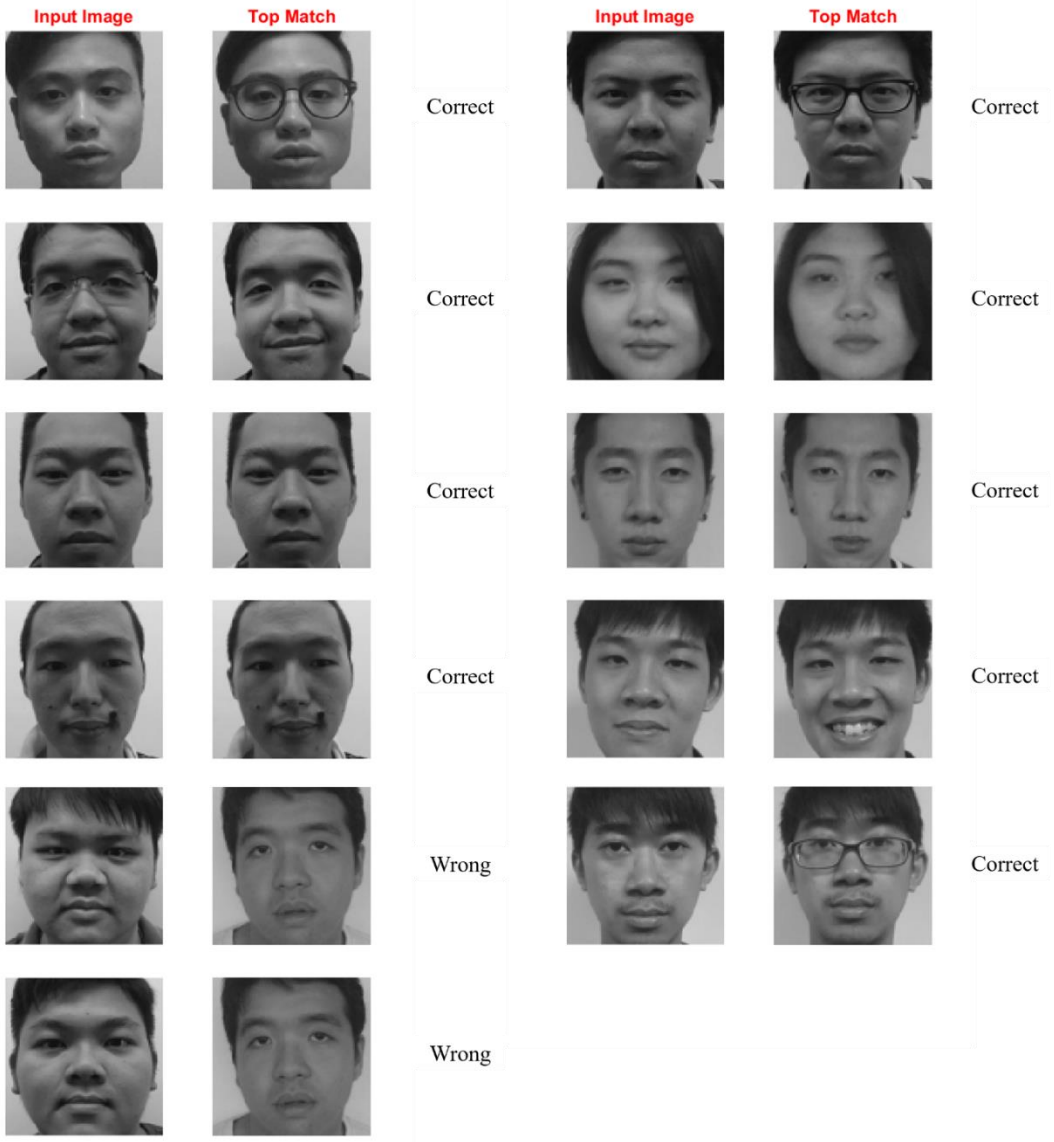


Figure 8. Face recognition algorithm result tested with all input subjects.

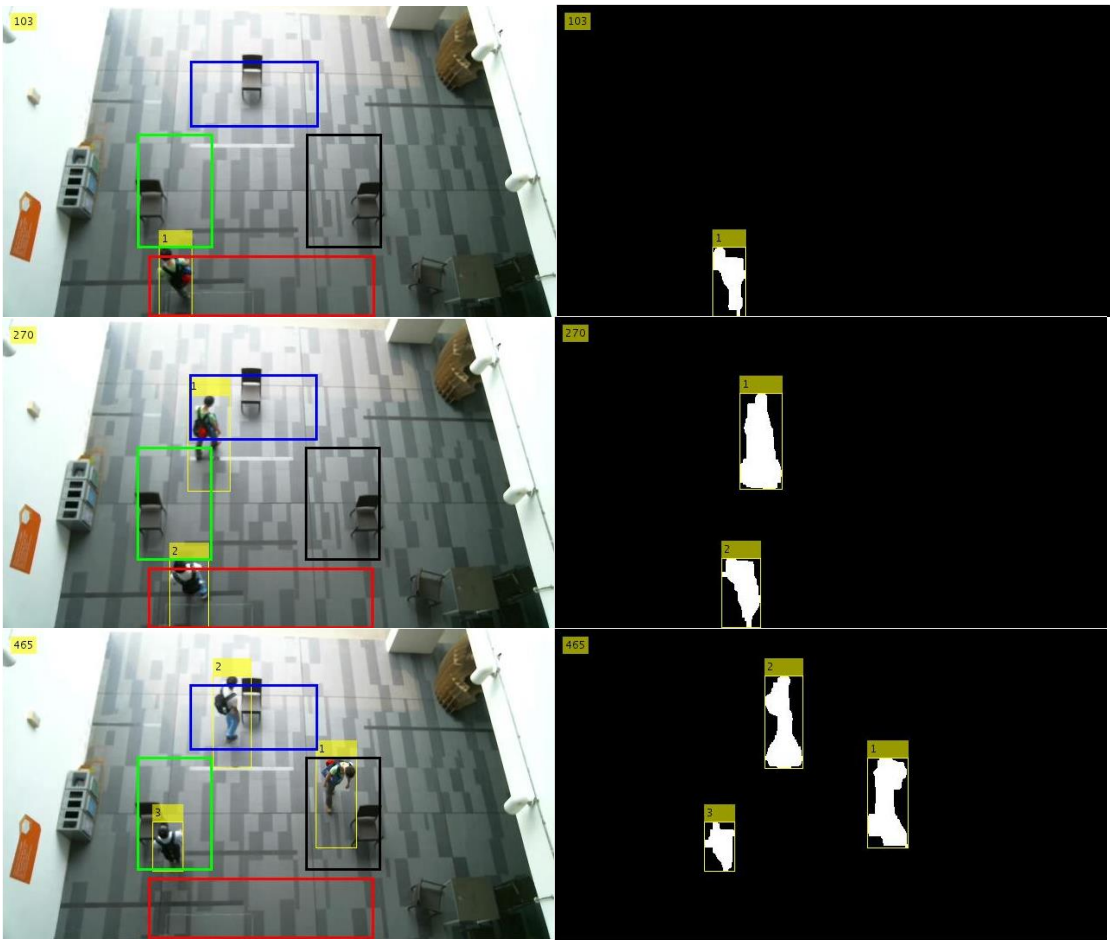
3.3 People Tracking Algorithm Result

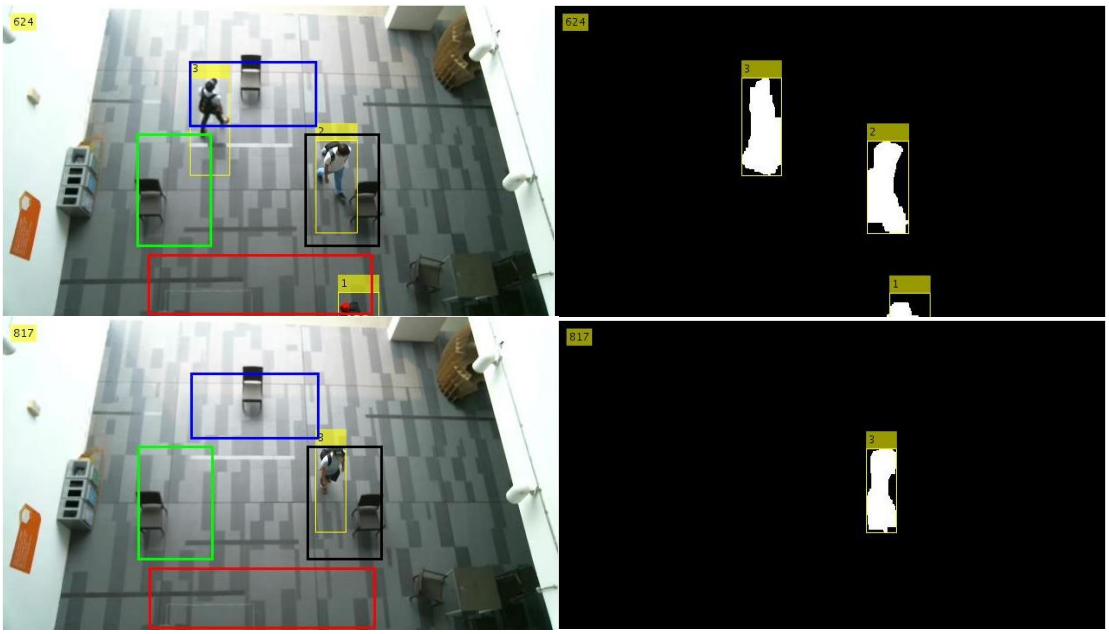
The people tracking algorithm is tested using a video with the size of 640 by 360. The video is captured at the location with fairly good illuminance and few pedestrians as subjects of interest. The video is viewed as original frame and foreground mask as shown in Fig. 9(a) and 9(b) respectively. This video is dedicated to be testing with and without employee excluding algorithm. For better tracking result, the motion of the subject in this video scene is planned accordingly. 4 different regions of interest (ROI) in the form of bounding box are drawn on the original video frame as shown in Fig. 9. Red, green, blue, and black bounding boxes indicate ROI 1, ROI 2, ROI 3, and ROI 4 respectively. At the start of the video, the first person will appear from the bottom of the video frame, entering bounding box from ROI 1, to ROI 2, to ROI 3, then to ROI

4, lastly back to ROI 1, and then left the video scene at the bottom of the frame. This motion is followed by second subject and third subject.

Fig. 9 shows the video frames of different subject entering different ROI. At frame 103, subject labelled number 1 was entering the video scene and was in ROI 1. At frame 270, subject 2 appeared from ROI 1 and about entering ROI 2 and subject 1 was in ROI 3. At frame 465, subject 3 appeared and located at ROI 2, subject 2 at ROI 3 and subject 1 at ROI 4. At frame 624, subject 1 was leaving the scene through ROI 1, subject 2 was at ROI 4 and subject 3 was at ROI 3. At frame 817, subject 1 and subject 2 were left the scene and subject 3 reached at ROI 4. Table 1 shows the data collected from counting algorithm without employee excluding algorithm which shows the staying time of the particular subject in particular ROI in term of number of frame. Table 2 shows the data collected when subject 1 is considered as an employee.

By comparing the result from Table 1 and Table 2, the data collected from subject 1 in Table 1 is not shown in Table 2. The count of number of frame for subject 2 and subject 3 does not change in both tables. This shows that employee excluding algorithm works accordingly as planned. Fig. 10 shows the screenshot of the export of data collected from the video with and without subject 1 excluded to Microsoft Excel spreadsheet.





(a) (b)

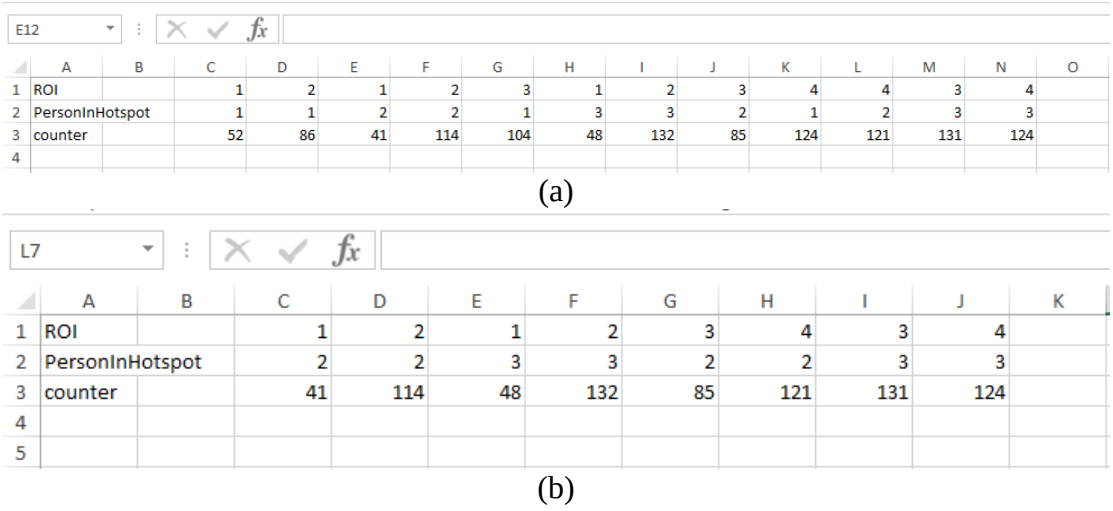
Figure 9. Tracking results of the people tracking with video 2. (a) Original frame. (b) Foreground mask. (Frame number: 103, 270, 465, 624, and 817 respectively.)

Table 1. Counting algorithm results of video 2 without employee excluding algorithm.

ROI	Subject	Count
1	1	52
2	1	86
1	2	41
2	2	114
3	1	104
1	3	48
2	3	132
3	2	85
4	1	124
4	2	121
3	3	131
4	3	124

Table 2. Counting algorithm results of video 2 with subject 1 excluded.

ROI	Subject	Count
1	2	41
2	2	114
1	3	48
2	3	132
3	2	85
4	2	121
3	3	131
4	3	124



E12

	A	B	C	D	E	F	G	H	I	J	K	L	M	N	O
1	ROI		1	2	1	2	3	1	2	3	4	4	3	4	
2	PersonInHotspot		1	1	2	2	1	3	3	2	1	2	3	3	
3	counter		52	86	41	114	104	48	132	85	124	121	131	124	
4															

(a)

L7

	A	B	C	D	E	F	G	H	I	J	K
1	ROI		1	2	1	2	3	4	3	4	
2	PersonInHotspot		2	2	3	3	2	2	3	3	
3	counter		41	114	48	132	85	121	131	124	
4											
5											

(b)

Figure 10. Data collected from video 2 exported to Microsoft Excel. (a) Data collected from video 2 including subject 1. (b) Data collected from video 2 without subject 1.

From the results obtained, it shows that the system proposed was able to identify the location that are frequently visited by customers.

4. Conclusions

In conclusion, we integrated Viola-Jones Algorithm and Eigenfaces method using Principal Component Analysis as the face detection and face recognition algorithms respectively to differentiate between employees and customers and check the attendance of the employees. Furthermore, background subtraction and foreground detection technique incorporating with Kalman filter are used in tracking-by-detection algorithm on tracking customer in-store movement to provide relevant data for customer's shopping behavior study. The novelty of this project is that the customer tracking feature of this project is able to identify customers from the people in the store with employee excluded and our system provides accurate data collected for better and more accurate customer's shopping behavior studies. Future work of this project will be implementing the face detection and face recognition in real time and provides input from face recognition into people tracking with employee excluding algorithm.

References

[1] RetailNext, Inc., March, 2015. "What Every Retailers Must Know About Traffic 2.0". [Online]. Available: http://home.retailnext.net/rs/314-HEV-582/images/What_Every_Retailer_Must_Know_About_Traffic_2.0.pdf?mkt_tok=3RkMMJWWfF9wsRonuqXNZKXonjHpfsX56uokWq6xlMI%2F0ER3fOvrPUfGjI4ATcFrI%2BSLDwEYGJlv6SgFSbHBMahlzLgIUxM%3D
[Accessed: 14 May 2015]

[2] Viola, Paul A. and Jones, Michael J. "Rapid Object Detection using a Boosted Cascade of Simple Features", IEEE CVPR, 2001.

[3] M.A. Turk, A.P. Pentland, “Face Recognition Using Eigenfaces.” Proceedings of the IEEE Conference on Computer Vision and Pattern Recognition, 3-6 June 1991, Maui, Hawaii, USA, pp. 586-591.

[4] G. Welch and G.Bishop, July 24, 2006. “An Introduction to the Kalman Filter”. Technical Report: TR95-041, Department of Computer Science, University of North Carolina.

[5] Inseong Kim, Joon Hyung Shim, and Jinkyu Yang. “Face detection”. [E-journal] Available: https://web.stanford.edu/class/ee368/Project_03/Project/reports/ee368group02.pdf [Accessed: 15 April 2015].

[6] N. Belhumeur, Peter, Hespanha, Joao P., and J. Kriegman, David. “Eigenfaces vs. Fisherfaces: Recognition Using Class Specific Linear Projection”. IEEE Transactions on Pattern Analysis and Machine Intelligence, Vol.19, No.7, July 1997.

[7] Bhattacharyya, Suman Kumar, and Rahul, Kumar. “Face Recognition by Linear Discriminant Analysis”. International Journal of Communication Network Security, ISSN:2231-1882, Vol-2, Issue-2, 2013.

[8] Reddy, K. Srinivasa, Krishna, V. Venkata, and Reddy, B. Eswara. “Facial Recognition using the Combination of Significant Non-Uniform Local Binary Patterns”. GVIP Journal, ISSN: 1687-398X, Vol. 15, Issue 1, ICGST, Delaware, USA, June 2015.

[9] Gottipati. Srinivas Babu. “Moving Object Detection Using MATLAB”. International Journal of Engineering Research & Technology (IJERT), ISSN: 2278-0181, Vol. 1 Issue 6, August – 2012.

[10] Friedman N., Russell S, 1997. “Image Segmentation in Video Sequences: A Probabilistic Approach” in The Thirteenth Conference on Uncertainty in Artificial Intelligence”. Brown University, Providence, Rhode Island, USA: Morgan Kaufmann Publishers, Inc., San Francisco, 1997.

[11] Koller D, Weber J. ,Huang T. ,Malik J. ,Ogasawara G. ,Rao B. ,Russell S., 1994. “Towards robust automatic traffic scene analysis in realtime” in Proceedings of the 33rd IEEE Conference on Decision and Control (Cat. No.94CH3460-3). IEEE. Part vol.4, 1994.

[12] Stauffer, Chris; Grimson, W.E.L., 1999. "Adaptive background mixture models for real-time tracking," in *Computer Vision and Pattern Recognition, 1999. IEEE Computer Society Conference on.* , vol.2, no., pp.252 Vol. 2, 1999.

[13] Ronny, M., September, 2013. “Chapter 6: Browsing Behavior,” in Behavior Analytics in Retail. Bloomington, USA. AuthorHouse, 2013.

Design and Construction of an Asynchronous Instruction Fetch Logic

Ng Jun Yit[1]*, Edwin Chung Chin Yau[2]*

[1]*Research Student, School of Engineering, Taylor's University, Malaysia*
[2]*Associate Professor, School of Engineering, Taylor's University, Malaysia*

*JunYit.Ng@sd.taylors.edu.my, *ChinYau.EdwinChung@taylors.edu.my

Abstract

The advancing of technology had led to a higher demand on a faster computer. However, in the current technology, all the available CPUs on the market are still implemented using a synchronous based design even though that the asynchronous based design has many potential benefits which could alleviate a dozen of challenges faced with synchronous based system such as clock skew and synchronization failure. Although much improvement had been made towards the design of asynchronous system, it is still a challenge to describe a simple process of CPU in full asynchronous mode. The objectives of the paper are to describe instruction fetch logic of CPU in asynchronous mode using Signal Transition Graph and apply theories of timing constraint extraction to the process. This comes down to the question whether STG is enough to describe the synthesized logic and if it is not, what are the possible amendments can be made to improve the technique. Besides, to prove the validity of the timing constraint extraction is another research challenge. The digital logic of instruction fetch will be designed at the very first step. After that, the logic will be translated into STG and further developed with software into a net-list which holds all the Boolean equations that described the behavior of signals. At the end of the day, there will be a workable asynchronous instruction fetch logic that proven to be free of glitches and hazards.

Keywords: Asynchronous, Instruction Fetch, Sequential Logic, Timing, Signal Transition Graph (STG), Self Timed Circuit, Petri Net, Petrify Tool.

1. Introduction

The demand for a better and faster computer is always increasing. Human will never be satisfied for what they have, they will always ask for more even though the current throughput have already fulfilled their requirements. So they want a larger RAM, larger hard disk space, powerful motherboard and most importantly faster processor. In the field of computing, the processor is often known as Central Processing Unit (CPU) or microprocessors.

CPU is the brain of a computer. All the operations are being processed and performed by the CPU. The typical components of a CPU are the arithmetic logic unit (ALU), control unit (CU) and register sets. ALU is to perform calculations for example addition. CU controls the transfer of information between different registers and calling ALU when necessary. The register sets includes special function registers like Program Counter (PC) and Instruction Register (IR) [1] [2].

As described in Von Neumann machines [3] [4], the CU fetches the instruction from the main memory by using the address in PC. While doing this, CU increments PC by 1. The PC will points to the instruction of the address that the PC is currently holding. The instruction will be read and sent back to the IR. CU will decodes this instruction and determines the operation to execute. The process is repeated after the CPU executes the operation.

In the current technology of microprocessors, all the mentioned operations are executed completely in synchronous behavior which the temporal control over the activities is centralized by a global clock. Synchronous systems are characteristically vulnerable to synchronization failure due to metastable failure while accepting asynchronous input [5]. Besides that, synchronous systems also have the issue in clock skew as the advancement in Very-Large-Scale-Integration (VLSI) had led to faster and larger circuits [6]. Furthermore, synchronous systems are seems to have reached a limit in maximum speed at which a synchronous system can function reliably. In order to eliminate these timing difficulties and to achieve the faster speed, more and more designers are now turning their attention on asynchronous design [5] [6].

At the opposite side, the activities of an asynchronous system are not monitored by a global clock but instead dispersed throughout the self-timed circuits. With the elimination of a global clock, the trouble of concerning about clock skew is no longer exists. Nonetheless, the necessity to synchronize the asynchronous inputs is removed, avoiding any chances of synchronization failure [7]. However, designing an asynchronous system is still a tough task to be achieved by engineers as the challenges lie within such as circuit hazards, critical races, and glitches [6].

Although the techniques for the synthesis of asynchronous sequential logic from Signal Transition Graph (STG) and the avoidance of hazards in the synthesized logic are fairly well understood, it is still a challenge just to describe a simple function in asynchronous mode. Therefore, it is hoped that this paper would provide a fundamental research which the STG is able to describe a realistic circuits like instruction fetch.

1.1 Literatures Review

The following section describes the fundamental knowledge required to study and reproduce the work on asynchronous based design system. The basic of asynchronous based design will be firstly described. After that, the working principle of Signal Transition Graph (STG) method will also being described. The STG based design will be compared to other techniques for the reason of choosing STG. The source for various design technique is quite old because there have not been many researchers focus on the asynchronous based design recently. Lastly, the theory of timing constraints is explained using a simpler example for better understanding.

1.1.1 Signal Transition Graph (STG)

Synchronous based designs will always accompanied by a clock, all of the registers, operations are will be performed at the edge of the clock. The basic idea of asynchronous based design is to remove the clock which is beneficial such as removing clock skew and synchronization failure. Signal transition graph is a graphical approach to describe the behaviour of sets of input-output transition without any kind of circuit expression. It models a system using nodes, and the transition happens during the firing of a signal. The starting token will be specified and will move accordingly to the transition of the signals [8].

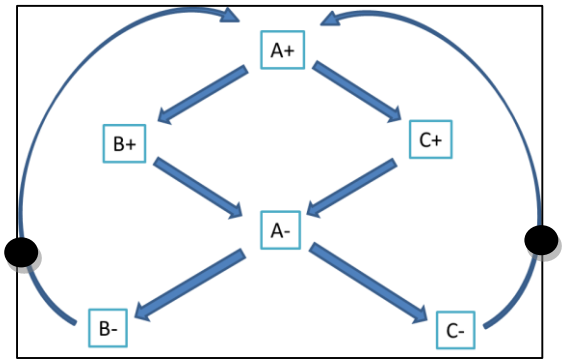


Figure 1: Example of STG

Figure 1 shows one simple example of STG. The black dots indicate the starting point of a system. Starting from black dots, the next firing is the A+, so the tokens moved to in between A+→B+ and A+→C+. Next firing will be C+ and B+ concurrently, noted that both C+ and B+ is pointing towards A-, this means that the firing of A- will only waits until both firing of B+ and C+ had been completed. The STG is useful in describing this situation where in asynchronous based design, there will be signals waiting to be fired only a certain conditions are met.

1.1.2 Other Techniques

There are other techniques that were used to describe asynchronous circuit behaviour such as Communicating Sequential Process (CSP). In CSP, the behaviour of a process is called an event and there are processes that define the behaviour such as stop and skip. The events are instantaneous and during an activity with duration, there will be two events representing start and end. At some moment in time, the behaviour can be recorded as the sequence of all events which has participated, and this moment of time is called trace [9].

Let *s* be the possible trace between the transition of P to Q. The transition formulation will be: P $-s\rightarrow$ Q. The *s* is the possible trace that can happen which leads the process of Q from P. There are other algebra expressions in describing using CSP method which are deterministic choice and non-deterministic choice [9]. The main idea of using CSP is that all the translation is fully done by hand. There might be situation where many transitions happen at the same time where using CSP might give different results depending on the translator. Other than that, if the circuits contain more signals, it will be difficult to translate using CSP algebra by hand.

In the other hand, there is a method called sequence (SEQ) module or Q-module in short. In this method, the Q-module performs a complete handshake first on one port A and then on the second port B upon receiving request of port C for example [9]. In simpler term, it checks for all the data whether it is ready, and then the module will pulse when all data are ready. With this method, there will be more circuits needed to check for the data validity only then the operations will go on. This is definitely asynchronous but it does not serve the benefits of it which it gives double the space, double the area. This leads to a lower throughput of the system where it is pointless to implement asynchronous based design.

In the case of STG, it is chosen mainly because it describes the behaviours in its purest forms with easy to view graphic. The movement of the transition can be described only using signals where other might needs other condition for single transition. Therefore, STG is chosen to be used for the circuit description.

1.1.3 Theory of Timing Constraints

The theorems of timing constraints were proposed by Chung and Kleeman [10] in 1995 where there is no further research on this particular area. The following theorem shows in the next page will be briefly described here.

Theorem 1 is saying in the transition of s1 to s2, exist a smallest subspace Cp with all the permutations σ where the transition stays 1, it is 1 within the subspace, if not it is – (dash). Theorem 2 is the definition a hazard free circuit where inside the subspace Cp, if the all the signals remain constant during the transition s1 to s2, either it stays 1 or 0, it is free from hazards.

Theorem 3 is describing where hazards happen. For some transition s1 to s2, there exists a subspace Cc which is the intersection of Cp and set of expression. The Cc describe is the conflict where hazards happen. This theorem is saying that the path of transition s1 to s2 will be limited to a path where it does not go inside this subspace with conflict Cc.

Theorem 1:

Let a state graph $\Phi_J = \langle S, T, \delta, s_o \rangle$ *and its corresponding n-space, the smallest subspace, C_P, which contains the transition* $s_1[\sigma\rangle s_2$ *from state s_1 to s_2 and all permutations of* σ *is described as:*

$$C_P(i) = \begin{cases} s_1(i) & \text{if transition } i\pm \notin \sigma \\ -(undefined) & \text{otherwise} \end{cases} \quad (1.1.3.1)$$

$s_1[\sigma\rangle s_2$ *denotes the path from s_1 to s_2 associated with the firing of transition sequence* σ *from state s_1, while $C_P(i)$ and $s_1(i)$ denote the logical state of signal i in C_p and s_1.*

Theorem 2:

The combinational logic that derived from a well-developed STG which implements function (f) with distinctive state coding using techniques for hazard-free design is free from circuit hazards if and only if:

$$\forall \sigma \in T^*; s_1, s_2 \in S : s_1[\sigma\rangle s_2 \quad (1.1.3.2)$$

If f remains constant during the transition $s_1[\sigma\rangle s_2$ *from s_1 to s_2* $\Rightarrow$ *only 1s or only 0s are contained within the tiniest subspace containing path* $s_1[\sigma\rangle s_2$ *in the K-space of function f.*

Theorem 3:

Given transition $s_1[\sigma\rangle s_2$ *for some* $s_1, s_2 \in S$ and $\sigma \in T^*$, *if the existence of subspace C is:*

$$s_i \notin C \ \forall \text{ state } s_i \in s_1[\sigma\rangle s_2 \quad (1.1.3.3)$$

$$C_C = C_P \cap C \neq \varnothing \quad (1.1.3.4)$$

Then

$$\forall \sigma' \in T^* : \left(\delta(s_1, \sigma') = s_2 \wedge |\sigma'| = |\sigma| \wedge \tau \in \sigma' \Leftrightarrow \tau \in \sigma\right)$$
$$\sigma' | T_C = \sigma | T_C \Rightarrow s'_j \notin C \quad \forall s'_j \in s_1[\sigma'\rangle s_2 \quad (1.1.3.5)$$

Where (3.4.6)

$$T_C = J_C \times \{+, -\}, \quad (1.1.3.6)$$

$$J_C = \{j \in J \mid C_P(j) = '-' \wedge C_C \neq '-'\} \text{ and} \quad (1.1.3.7)$$

$\sigma | T_C$ denote the projection of sequence σ onto the set of transition T_C

Therefore, given transition $s_1[\sigma\rangle s_2$ *and subspace C where C_P covering transition* $s_1[\sigma\rangle s_2$ *shares a common region with subspace C, if transition* $s_1[\sigma\rangle s_2$ *only traverses through a path which does not enter subspace C, then the transition* $s_1[\sigma\rangle s_2$, *permutation of transition* $s_1[\sigma\rangle s_2$ *will also be limited to a par which does not enter subspace C if* $\sigma' | T_C = \sigma | T_C$.

2. Methodology

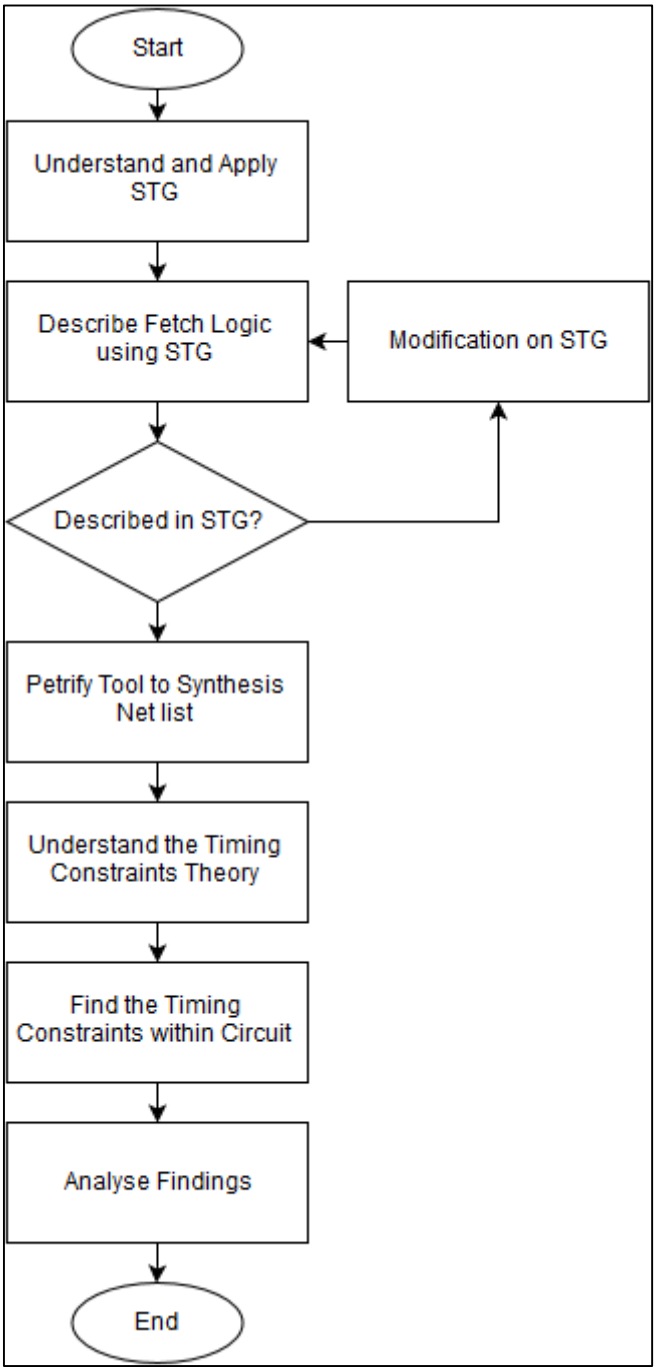


Figure 2: Flowchart of Research Design

Figure 2 shows the process of methodology during the research project. At first, it is required to understand the concept of signal transition graph. There will be literature review on the topic including comparison of methods. As the concept had been described in previous section, the understanding of the STG will not be mentioned in this section. Next, the process of using STG to describe the architecture and the control logic will be described in details. Petrify tool is a tool which is able to translate STG into a set of Boolean expression. It will mainly on the application part. Next is the timing constraint theory, as the theory was described, so only the application of the theory will be shown in this methodology flow.

2.1 Architecture

The instruction fetch as mentioned earlier is a process of fetching the data from the memory into instruction register while the program counter points to the address correspondingly. Figure 3 shows the architecture of the fetch process where this project will be using.

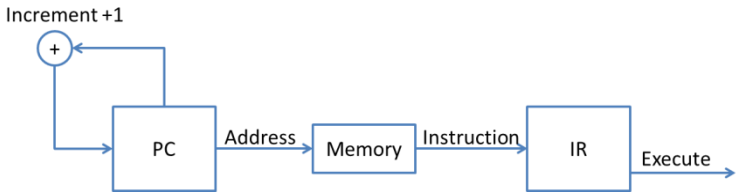


Figure 3: Instruction Fetch Architecture

The architecture will be fixed while only the sequential logic that controls all the registers and memory will be designed in asynchronous mode. As shown in Figure 4, the sequential logic will controls the flow of data. All the design including the architecture was designed from scratch, so there will be no reference on technique or methods from other sources. When the logic is developed, the design is translated into Net list using Petrify tool [7].

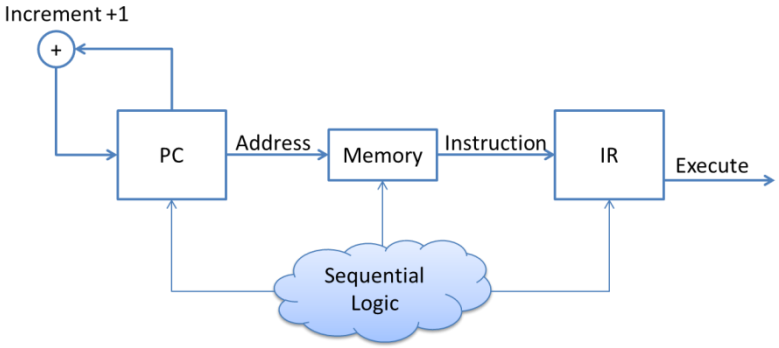


Figure 4: Designing the Sequential Logic

2.2 Signal Transition Graph Description (STG)

The sequential logic will be designed in the form of signal transition graph (STG). In STG, the signal will not be triggered or latched unless the previous signals have completed their tasks. For example, a+ will be triggered only after b+ and c+ have triggered and completed their task. Therefore, the properties of STG can be used to describe the behavior of signals that controls the architecture.

There is a loop in design methodology where the sufficiency of STG to describe a realistic implementation like instruction fetch will be tested. In Figure 5, all the control signals have been added so that the sequential logic will be implemented. There are request for increment of address (Req), acknowledgement that the increment has been completed (Ack), input enable of PC (IE-PC), output enable of PC (OE-PC), requesting data from the memory (Data Req), data is ready to be sent (Data Rdy), input enable of memory (IE-M) and input enable of IR (IE-IR). As seen in Figure 5, there are total of eight signals with two inputs and 6 outputs for the control logic. So these eight signals will be used in producing signal transition graph.

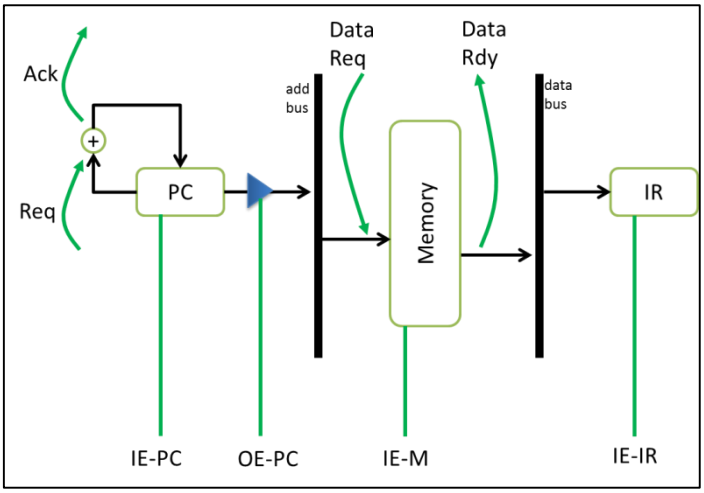


Figure 5: Architecture with Control Signals

Now, the next step is to describe the behavior of the circuits step by step. The black color dots are the starting tokens. When the Drdy is high, it means the data is ready to be latched by the instruction register (IR), so IRir goes high. After IR had received the data, all the other signals go low including output enable of PC (OEpc), input enable of memory (IEm) and data request (Dreq). After that, the input enable of IR (IEir) goes low because it does not need to take in any new data. The data ready and data request (Dreq & Drdy) are connected with a delay element, so it goes low after data request goes low. Then the next cycle begin with new address of PC, so input enable of PC (IEpc) goes high to take in new address. This is followed by the OEpc, IEm and Dreq to go high, the address be pointed in the memory and wait for the data to be ready (Drdy).

There is a small loop inside where Req- is the next step of IEpc+. This is the loop of incrementing. Starting from token, the input enable PC is low because the instruction register (IR) is handling the data. When the IR had received the data (IEir+), the address starts to increment by requesting (Req). When the address has completed incrementing, it will triggers a signal called acknowledge. With Ack+, the input enable of PC goes high (IEpc), changes its address to the incremented value. The loop is repeated with the low signal of request and acknowledge.

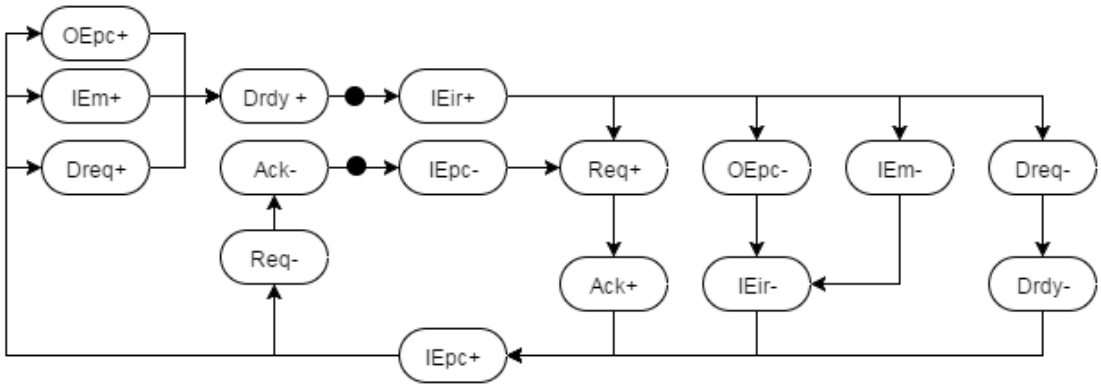


Figure 6: STG Design

2.3 Petrify Tool for Synthesis

The Petrify [7] tool will be used to synthesize the Boolean expression of the described STG. The tool is obtained from the Website of Technical University of Catalonia [11]. The tool runs as an executable file where command prompt or linux terminal equivalent must be used to run the program.

Figure 7 shows the input typed by the user to be used by the Petrify tool. Inside the command prompt, the following line is inserted:

./petrify4.1 -no -mc -eqn xyz_1.eqn arb32.g

The ./ is to execute the tool, -no means no output file would be generated, -mc means to generate monotonous covers. –eqn is a function to generate the Boolean equation which suits the need for the project. The .g file is the input file while the .eqn file is the generated result.

```
.model me32
.outputs a b c d e f
.inputs g h
.graph

h+ f+
g- b-
f+ a+ c- e- d-
b- a+
a+ g+
c- f-
e- f-
d- h-
g+ b+
f- b+
h- b+
b+ c+ e+ d+ a-
c+ h+
e+ h+
d+ h+
a- g-

.marking {<h+,f+> <g-,b->}
.end
```

Figure 7: Input File for Petrify

Table 1: The Relationship of Symbols to Signals

No.	Symbols	Signals	Description
1	a	Req	Request for increment
2	b	IEpc	Input enable of program counter
3	c	OEpc	Output enable of program counter
4	d	Dreq	Data request of memory
5	e	IEm	Input enable of memory
6	f	IEir	Input enable of instruction register
7	g	Ack	Acknowledgement of incremented address
8	h	Drdy	Data ready to be fetched

For easier input file while typing, the signals are replaced with symbols of a – h. Therefore, table 1 is generated for easy understanding of the relationship between symbols and signals. It is also for easy viewing of each specific function.

2.4 Apply Timing Constraint

From previous synthesis, it is found that the Boolean expressions for each output signals are as shown (Figure 8):

```
[a] = b' (X + a);
[b] = g (X' + b);
[c] = X' (a' + b);
[d] = X' (a' + b);
[e] = X' (a' + b);
[f] = f (e + c) + h e;
[X] = X (a' + b + h) + f;
```

Figure 8: Boolean Expression from Petrify

One of the Boolean will be shown step by step where the rest will be only showing the result. Taken signal a as example. In signal [a], there are only three terms in the expression. The signals are therefore {abX}.

[a] = b' (X + a);

Since the Boolean only involve the signal a, b and X, the rest of the signals are removed on the STG and the STG become:

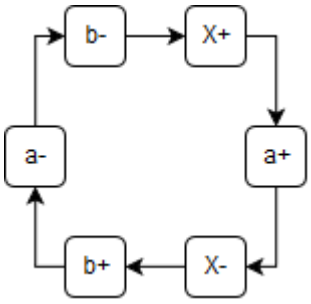


Figure 9: STG after Removing

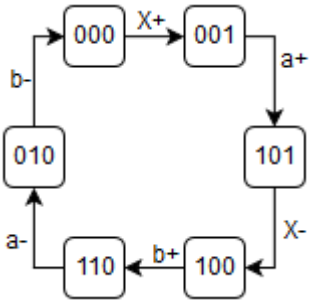


Figure 10: State Graph Formed from STG

Table 2: Truth Table of signal a

ab\X	0	1
00	0	1
01	0	x
11	0	x
10	1	1

In Figure 9, the STG had been simplified because not all the signals had been used in this STG, it is not necessary to include them. Therefore, the signals can be translated into state graph easily now. After the state graph in Figure 10 had been formed, the truth table in Table 2 can be now created. The following sets and resets are formed from the truth table.

Sets = [-01],[10-]
Resets = [-1-],[0-0]

Now to find the path of transition s1 to s2, it is necessary for the path to stays one. So, starting from 001, Cp is the transition of a+→X-, giving Cp = [-0-].

Cc = Cp ∩ Resets

Cc = [000]

000 is the region where conflicts happen, looking at the transition a+ → X-, a+ is moving away from the conflict where X- is moving into the conflict zone. Therefore, the timing constraint here is a+ > X- denotes that a+ has to be faster than X-. This is how the timing constraint being extracted.

3. Results and Discussions

```
# EQN file for model me32
# Generated by ./petrify-intel 4.2 (compiled 19-Jul-07 at 12:36 PM)
# Outputs between brackets "[out]" indicate a feedback to input "out"
# Estimated area = 25.00

INORDER = g h a b c d e f X;
OUTORDER = [a] [b] [c] [d] [e] [f] [X];
[a] = b' (X + a);
[b] = g (X' + b);
[c] = X' (a' + b);
[d] = X' (a' + b);
[e] = X' (a' + b);
[f] = f (e + c) + h e;
[X] = X (a' + b + h) + f;
# The initial state is unstable. No reset information generated.
# Signal b enabled in the initial state.
# Signal f enabled in the initial state.
```

Figure 11: Equation Generated by Petri Net

Figure 11 shows that the STG is enough to describe a realistic circuit like instruction fetch within the minimum scope of interest. The timing constrains for the output signals are shown in following table:

Table 3: Timing Constraints Found

Signals	Timing
[a]	a+ > X-
[b]	NA
[c]	a- > b-
[d]	a- > b-
[e]	a- > b-
[f]	f+ > h- f+ > e-

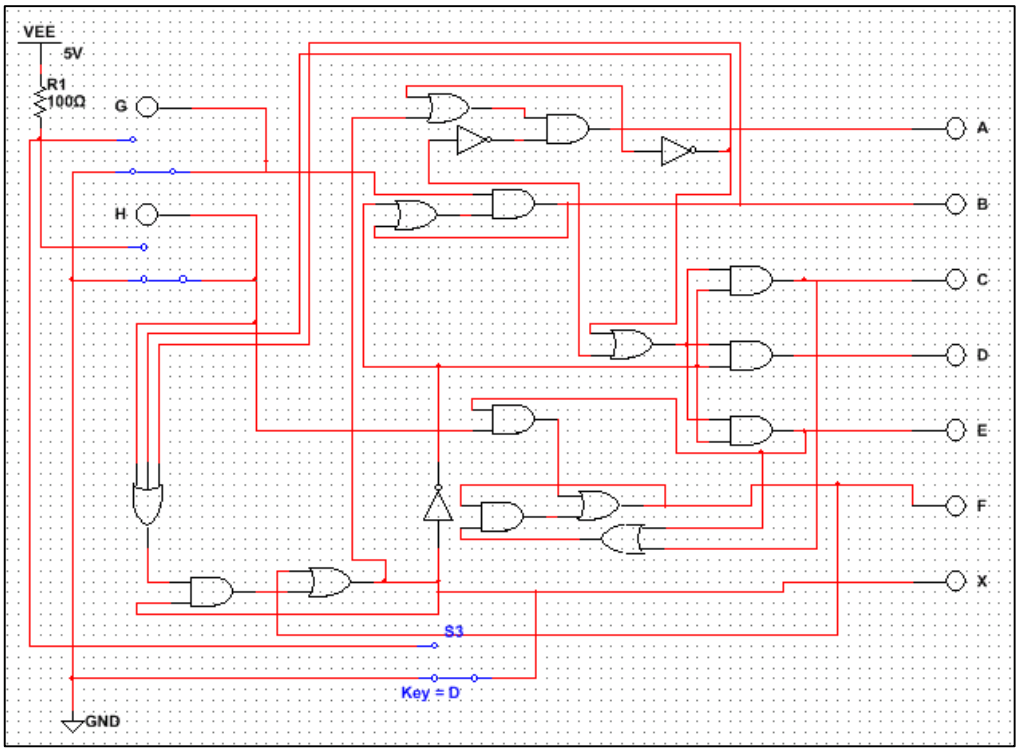


Figure 12: Sequential Logic of Control

As shown in Figure 12 is the completed design with timing checked. It is proven that the theory can extract the timing constraint. Since the timing constraint had been found, the condition where conflicts happened can be avoided by making adjustment.

4. Conclusion

This project will provide a fundamental knowledge to further advancement in this area. The hardware limitation of the semiconductor chips are seen to be reaching very soon. The first research question is on the STG where the STG had shown positive results which it can describe a practical application in this case the instruction fetch logic. Other than that, the timing constraint theory had successfully found the timing required to avoid hazards from happening. There are much more to be completed as the limit of STG and timing constraint theory had not been found. Insertion of one or more signals might bring to a failure to the system where this both technique would not work. This is the area of improvement needed to be researched on.

References

[1] N.Sharma, *Computer Architecture*. New Delhi, India: Pinnable Technology, 2009.

[2] J.L.Hennessy, D.A.Patterson and A.C.A.Dusseau, *Computer Architecture: A Quantitative Approach*, 4th ed. Amsterdam, Boston: Morgan Kaufmann, 2007.

[3] H.Lee and R.J.Baron, *Computer Architecture*. USA: Addison-Wesley Publishing Company, 1994.

[4] G.Blanchet and B.Dupouy, *Computer Architecture*. London: Iste, 2013.

[5] E.C.Y.Chung, "Synthesis of Hazard-free Metastable-robust Self-timed Digital Circuits from Live-Safe-Simple Signal Transition Graph," *Monash University*, 1995.

[6] M.Imai and T.Nanya, "Performance Comparison between Self-timed Circuits and Synchronous Circuits Based on the Technology Roadmap of Semiconductors," Res. Cent. Adv. Sci. Technol., Univ. of Tokyo, Japan, 2008.

[7] K.Michael, K.Alex, L.Luciano, and Y. Alexandre C.Jordi, "Petrify: A Tool for Manipulating Concurrent Specifications and Sysnthesis of Asynchronous Controllers," *IEICE TRANS. INF. SYST.*, vol. E80-D, no. 3, 1997.

[8] J.Sparso and S.Furber, *PRINCIPLES OFASYNCHRONOUS CIRCUIT DESIGN– A Systems Perspective*. Boston, London: Kluwer Academic Publishers, 2007.

[9] P.A.Beerel, R.O.Ozdag and M.Ferretti, *A Designer's Guide to Asynchronous VLSI.*: Cambridge University Press, 2010.

[10] E.C.Y.Chung and L.Kleeman, "Synthesis of Hazard-free Metastable-robust Self-timed Digital Circuits from Live-Safe-Simple Signal Transition Graph," *Monash University*, Australia, 1995.

[11] University of Politècnica de Catalunya. (1999) Petrify: a tool for synthesis of Petri Nets and asynchronous circuits. [Online]. http://www.cs.upc.edu/~jordicf/petrify/

Pretreatment of Oil Palm Mesocarp Fibre for Application as a Fuel Source in Direct Carbon Fuel Cells

Noor Clinton Faiz Otten[1*] Nida Jafri[1], Wong Wai Yin[1,] Veena A. Doshi[1],

[1]*School of Engineering Taylor's University, Malaysia*

[*]noorclintonfaizotten@sd.taylors.edu.my

Abstract

Fuel Cell technology continues to advance in order to meet the growing global demands for clean and sustainable energy. Direct carbon fuel cells (DCFC) use rich carbon fuels such as coal in a chemical reaction of carbon and oxygen to produce CO_2 and electricity. The efficiency of DCFCs greatly out does a majority of internal combustion engines and coal-powered generators to provide clean energy without any particulates and NOx and SOx pollutants in the process. To further improve the DCFC in sustainability and build upon its efficiency, biochar, a fuel made from biomass is able to recycle waste materials such as oil palm mesocarp fibre (OPMF) to produce clean, cheap, sustainable fuel that replace coal in a DCFC. However, biomass has impurities that require pretreatment before applying the process of pyrolysis to generate biochar. Research needs to be done to investigate and improve the properties of biomass OPMF in order to match the standard of coal fuels with the purpose to improving sustainability and innovation of the direct carbon fuel cell. Chemical and thermal pretreatment of biomass by using hydrochloric acid and potassium hydroxide are methods to improve raw MF, removing impurities that will inhibit the biochar produced from pyrolysis of biomass. Analysis such as BET to calculate Surface Area, XRD to measure degree of graphitization & crystallinity, TGA to measure thermal heat properties, proximate and ultimate analysis is used to generate data and discover the characterization of biochar made from oil palm mesocarp fibre and whether it will be an innovative & sustainable fuel source for direct carbon fuel cells.

Keywords: Pretreatment, Oil Palm Mesocarp Fibre, Pyrolysis, Biochar, Direct Carbon Fuel Cell

1. Introduction

Global energy demand has drastically growth over the years due to increase in population, industry and technology over the past decade. According to the International Energy Agency, energy consumption is expected to increase by 54% by 2030 and 70% of that growth will occur in developing countries such as China, India, Indonesia, Myanmar, & Malaysia [1]. This calls for newer energy resources, as fossil fuels are unsustainable to meet this growing demand.

Direct carbon fuel cells uses the same concept of a hydrogen fuel cell but differs by using pure carbon and oxygen as a fuel sources to produce electricity and carbon dioxide (CO_2). While hydrogen fuel cells are more commonly used fuel cells, hydrogen gas is used, which can be less economical as carbon can exist as solid for easier transport while the production of hydrogen gas can be expensive and difficult to store safely. Even though CO_2 is a product of the DCFC, the high efficiency of DCFCs produces same amount of energy with less carbon emissions than traditional combustion processes and without combustion, the amount of polluting emissions such as NO_x, SO_x and CO is reduced dramatically [2].

The production of biochar plays a big role in transforming DCFCs into environmentally friendly energy generators from renewable energy sources. By investigating the qualities of biomass as an alternative fuel source, this allows DCFCs to run carbon neutral. Carbon neutral is a term used to qualify a process that does not contribute to the accumulation of Carbon Dioxide present in our atmosphere. For example, in oil palm plantations, the oil palm trees absorb CO2 as they grow and produce oil palm as illustrated in Figure 1.

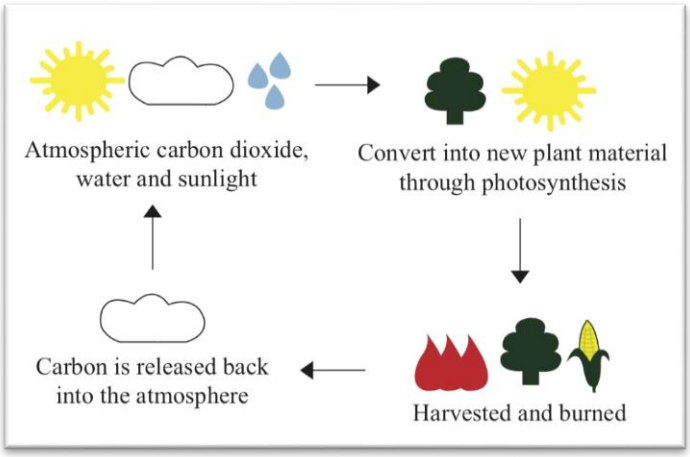


Figure 1. Carbon Neutral Cycle For Agricultural Biomass [2]

Biomass is an attractive alternative as global coal reserves are shrinking and increasing in price. The largest coal reserves are located primary in countries outside of Malaysia hence imported energy. By utilising local biomass produced in abundance, dependence on foreign energy sources can be reduced. In simple terms, DCFCs are generator of the future energy by reducing CO_2 emissions and for sustainable high efficient energy.

Overall, investigations must be made to discover the potential of mesocarp fibre from oil palm waste as a biochar fuel source in order to unlock the untapped potential of biochar in order to replace non-renewable fuel sources such as coal in a DCFC process and to test the real world application biochar as a fuel in DCFCs on efficiency and rate of energy production.

2. Theoretical Framework

This research will cover the following objectives; to produce biochar from oil palm mesocarp fibre through a combination of chemical and thermal pretreatments as well as to determine the physiochemical properties of biochar derived from oil palm mesocarp fibre.

2.1 Direct Carbon Fuel Cells

A direct carbon fuel cell uses solid carbon fuel (coal, coke, biomass) and air to produce CO_2 and free moving electrons in a chemical reaction. DCFCs have the advantage of a near 100% thermodynamic efficiency and a practical efficiency of about 80%, far higher than other hydrogen fuel cell technologies and coal fired generators due to the high operating temperatures DCFCs produce [3]. In this process, carbon reacts with carbonate CO_3^{2-} anions to produce CO_2 and free electrons at the anode, while oxygen from free flowing air undergoes oxidation to reform carbonate anions at the cathode. Overall reaction of carbon atoms and oxygen to produce CO_2 in an electrochemical reaction as in illustrated in Equations (2.1), (2.2) and (2.3) [2].

$$C + 2CO_3^{2-} \rightarrow 3CO_2 + 4e^- \quad \text{(Equation 2.1)}$$
$$O_2 + 2CO_2 + 4e^- \rightarrow 2CO_3^{2-} \quad \text{(Equation 2.2)}$$
$$C + 2O_2 \rightarrow CO_2 \quad \text{(Equation 2.3)}$$

With a pure product of CO_2 being produced from the reaction, this allows CO_2 sequestration processes to run easily and more efficiently without other by-product components needing to be removed from the product stream [3]. Throughout this process contaminants present such as elements of ash and sulphur from the fuel can hinder the process and performance of a DCFC. To ensure continuous operation, these contaminants must be minimized. These advantages prove an economical point of view to use DCFCs in energy generation.

2.2 Oil Palm Mesocarp Fibre

Biomass can be converted into solid, carbon rich fuel source and is widely accepted that it does not contribute to the greenhouse effect due to the CO_2 neutral conversion due to the renewability of biomass. The focus on biomass as an alternative to fossil energy has increased tremendously in recent times because of global warming problems originating mostly from fossil fuels combustion. There are hundreds of biomass varieties in several biomass groups and categories; woody biomass, herbaceous typed and agricultural based biomass, aquatic sourced biomass, & animal and human produced biomass wastes [4].

Oil palm plantations play a major role in the national economy of Malaysia. Based on a study by M. Umar Et al [5], the oil palm industry contributes up to 85.5% of the total biomass production in Malaysia and according to the Malaysian Palm Oil Board, the national annual product of oil palm biomass stands at an average of 80 million tonnes of dry biomass with an expected production of 100 million tonnes by year 2020 [5]. This gives the nation the grand opportunity to use biomass generated by oil palm plantations and refineries as a prime source of sustainable energy, all

made locally. Crude oil palm results in biomass as empty fruit bunches (EFB), oil palm kernel shell (POKS), and oil palm mesocarp fibre (OPMF) [6]. Current research focus has been given to EFB and POKS with little or rare studies conducted on the potential of OPMF, this leaves a gap to study further as it is ideal to utilize the entire spectrum of biomass produced from this large-scale industry leaving no waste materials unused.

OPMF originates the outer layer of the oil palm fruit surrounding the kernel of the fruit. It is produced from the screw process of the fresh fruit that separates the mesocarp from nut show in Figure 2 [7]. OPMF is categorized as an agricultural waste type biomass due to the large quantities produced from the industry. OPMF is rich in volatile matter originating from the biological proximity of the fibre from the oils of the POKS. Mesocarp fibre is similar to woody based biomass in terms of carbon content but ash content of OPMF is higher than wood. The fixed carbon content of OPMF is also on par to those of other biomass sources especially POKS and EFB. This shows that OPMF can be used as a source of carbon. However, the ash content of OPMF needs to be reduced to ensure longer DCFC life time cycles.

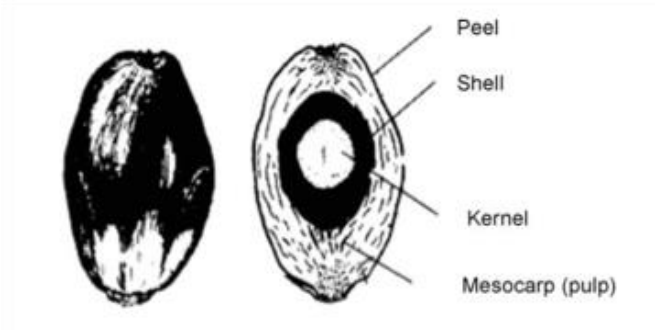


Figure 2. Cross-section of oil palm fruit with mesocarp fibre

Though OPMF is poised as a suitable biomass for carbon fuel production, it is the high content of ash that sets a difference of performance as a fuel in a DCFC as compared to coal. Currently, the biomass is only used as a fuel for the steam boiler on-site at most plantations to reduce the use of electricity to heat steam to sterilize oil palm fruit filled bunches. This approach to utilize the waste material is considered too simple method of using the resource. Even more, the use of OPMF in reboilers have caused major issues at plantations as the ashes produced causes corrosion effects throughout the exhaust system resulted from the high volatile matter composition of OPMF producing deposits that damage plantation equipment [5]. Nevertheless, by means of pretreatments for OPMF to remove its ash content enables the resource to be used as a fuel without compromise.

2.3 Pretreatments of Biomass

Pretreatment in the context of biomass is the process of removing impurities such as ash content from raw biomass before converting into fuel for power generation applications and can be categorised as chemical treatments such as acid and alkali solutions, physical treatments such as heat or grinding and biological treatments by using different types of micro-bacteria and enzymes to improve a biomass's outcome product. With ash content being the main priority of pretreatment,

the key to removing a majority of the content is to study the composition of ash in OPMF and applying the right pretreatment to reduce it.

According to M. Asadieraghi Et al [8] on an ash content analysis study of OPMF determines that the composition is as shown in Table 1 [8]. The study shows the amount of ash removed as well as its composition after several different acid solutions pretreatments for at a concentration of 2M and a residence time of 48hrs. This shows the large weight percentage of K_2O and SiO_2 has been dramatically reduced after pretreatment of hydrochloric acid (HCl) as well as compared to other acid pretreatments done [8].

Table 1. Ash removal of acid treated OPMF

Ash Content	Al_2O_3	CaO	Fe_2O_3	K_2O	MgO	Na_2O	PsO_5	SiO_2	ZnO
Raw OPMF	2.71	20.83	9.67	15.55	4.20	0.25	6.76	26.05	0.30
Acid treated OPMF	4.88	32.42	10.49	4.19	3.37	0.50	3.54	6.45	0.22

Other pretreatments such as heat treatment all focus primary on increasing fixed carbon content of the biomass than reducing ash content. Many studies show that high temperatures of pyrolysis result in an increase of fixed carbon content, reducing the amount of volatile matter and reducing ash content as well [10].

Alkali pretreatments primarily focus on surface area improvement and reduce degree of graphitization. Solutions such as NaOH and KOH have show results in reducing ash content as well, by removing metallic oxides found in biomass [11]. Alkali treatments are also less harsh to the structure of biomass than the effects of acid treatment.

2.4 Biochar Characterization

Biochar is charcoal derived from biomass materials by removing the moisture while retaining the fixed carbon content of the biomass. Numerous studies have investigated the effects of temperature, the presence of oxygen during pyrolysis and the reaction time on different types of biomass to determine their optimum parameters for pyrolysis. Though most biochar produced focuses on carbon yield for applications energy production from combustion, biochar produced for DCFC focuses on a balance of several other traits including carbon yield. The traits of an ideal biochar fuel for DCFC are the yield of carbon produced, ash content present, the surface area of the carbon, and the degree of graphitization, all after the pyrolysis process.

2.4.1 Carbon Yield

Carbon yield is the amount of carbon present after pyrolysis of biomass. This is calculated using equation (2.4) and (2.5), the yield is amount of biochar produced from the a set amount of biomass used while the carbon yield is the amount of carbon by weight present in the yield [12]. Carbon yield determines the amount of fuel that will be utilised ranging of 75-90% by weight of the biochar for OPMF.

A study by F. Abnisa Et al [12] shows that higher temperatures produce less yield but begin to constant in value as the volatiles of the biomass have evaporated leaving only fixed carbon [12]. This study was conducted with temperatures of 300-800℃ with optimum conditions being 400-500℃ for maximum yield. Carbon yield of the biochar is important as it determines the total quantity of fuel that can be produced from biomass and should be maximized during the process. A list of chemical compositions sourced from various journals that have studied the fibre is listed in Table 2 [4, 7, 9, 10].

Table 2. Carbon Yield of Various Biomass/Fuel

Biomass/Fuel	Ultimate Analysis (dry basis) wt.%						Reference
	C	O	H	N	S	Ash	
OPMF	51.50	40.10	6.60	1.50	0.30	8.30	[4]
Woody Based (Mean Values)	52.10	41.20	6.20	0.40	0.08	3.50	[9]
Coal	78.20	13.60	5.20	1.50	0.20	20.90	[9]
EFB	45.53	43.40	5.46	0.45	0.04	5.12	[7]
POKS	46.68	42.01	5.86	1.01	0.06	4.38	[7]
Rice Straw	43.68	39.72	5.70	0.97	0.21	9.72	[10]

2.4.2 Ash Content

As mentioned earlier, ash content of the biomass composition influences the amount of ash present in biochar. As carbon yield signifies quantity of carbon fuel that can be produced, ash content influences the quality of the fuel. OPMF contains an ash content of 8.4% weight, which inhibits the performance of DCFC as the presence of the ash poisons the anode catalyst, reducing the overall lifetime of the DCFC [8].

2.4.3 Surface Area

Surface area is yet another trait of quality for biochar, as DCFC relies on a reaction of CO_3^{2-} to produce free moving electrons as the rate of reaction depends on the amount of surface area present in the biomass for it to occur. Pyrolysis is the primary process to improve the surface area of biochar, during the process volatiles evaporate leaving physical pores behind in the surface. The more pores occur, the further increase in the surface area. More specific parameters include the diameter size of the pores. A. Shaabana, Sian-Meng Sea have studied the effects of slow pyrolysis on the surface area of biomass, concluding that higher temperatures and longer residence type can dramatically increase the BET surface area of the produced biochar at temperatures of 700^{o}C [13].

Though the aim is to increase the surface area, higher temperatures will reduce the yield of the biochar, hence a temperature below 700℃ is better to maximize both traits with minimal compromise. Other than pyrolysis, chemical treatments can have an influence on the surface area of a biomass before pyrolysis after removing the ash content of the biochar due to the removal of the impurities from the surface, leaving gaps and pores in the biomass.

2.4.4 Graphitization

Degree of graphitisation is related to the surface area of the biochar. As more pores form across the surface, the graphitisation of the biochar increases. Graphitisation is the process of forming uniform size of pores by using a template to form macro-porous and meso-porous pores on the surface of the biochar. An example would be using an iron rich solution to dot on the surface to form filled pores of size of the iron ions, afterwards removing the iron ions to leave pores of fixed shape and size [14]. Since a chemical treatment with HCl will be used, the study for graphitisation will observe the effects of acid on mesopore and macro-pore formation as well as the formation of micropores by pyrolysis.

3. Methodology

3.1 Sample Preparation

Raw oil palm mesocarp fibre biomass was acquired from the Seri Ulu Langat Palm Oil Mill Sdn. Bhd located in Dengkil, Selangor. The biomass is washed with distilled water and dried in an electric oven at 105^{o}C for 24 hours to preserve and remove any moisture content from the biomass. The biomass is grinded and then sieved to obtain uniformed sized biomass between 0.5mm to 2.0mm. The pH level is measured as a reference for pretreated samples. All samples untreated and pretreated are kept moisture free in a desiccator.

3.2 Acid Pretreatment

Acid pretreatment is conducted by preparing 1M of hydrogen chloride (HCl) solution by adding 500ml of 2M HCl stock solution and deionized water to a total volume of 1L in a volumetric flask. 5g of untreated biomass are weight into a 250ml glass beaker before 50ml of HCl solution is added into flask. The beaker contents are stirred with a magnetic stirrer for 2-hours. Beaker contents are washed with deionized water until reference pH is achieved and then dried in an electric oven at 105^{o}C for 24 hours. This procedure is repeated with conditions of 1M & 6 hours, 0.5M & 2 hours, and 0.5M & 6 hours.

3.3 Alkali Pretreatment

Figure 3 shows a setup for the alkali pretreatment. Untreated biomass is mixed with potassium hydroxide (KOH) solution in a round bottom flask attached to a reflux glass column and heated with a silicone oil bath. Tap water flows through the reflux, condensing any KOH evaporation. This ensures the concentration of KOH is kept constant throughout the experiment.

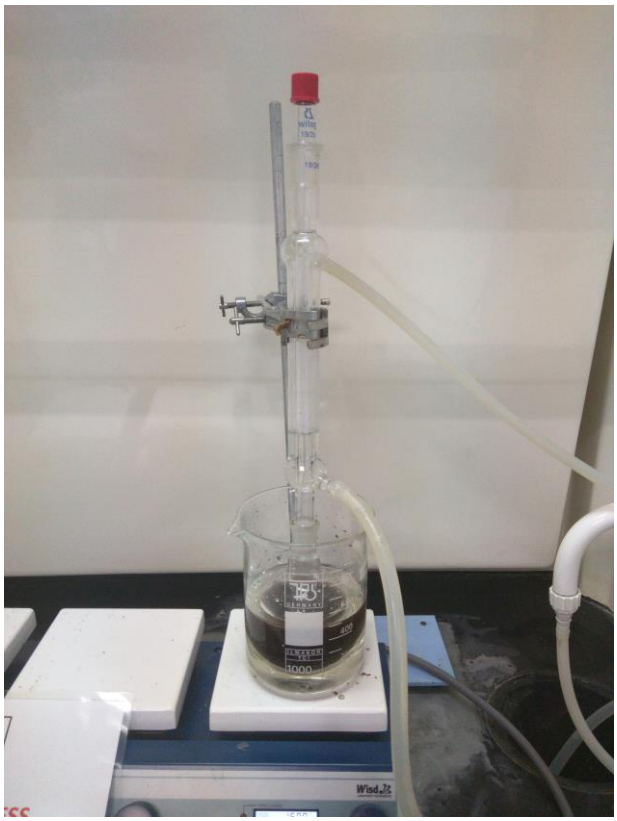


Figure 3: KOH Treatment Setup

1M of Potassium Hydroxide solution is prepared by adding 56.1g of KOH tablets with deionized water in a 1L volumetric flask. 5g of untreated biomass are weight into a 250ml round bottom flask before 50ml of KOH solution is added into flask. The flask is placed into the setup, heating the flask contents with a silicone oil bath and kept well mixed using a magnetic stirrer. Temperature of the contents is measure until a steady 85C is achieved.

The setup runs continuously for 10hrs with a reflux and the temperature checked periodically. After 10hrs, heating is turned off and the contents are left to cool before pouring into a 500ml beaker and washing the pretreated biomass with deionized water. pH level of the biomass mixture is checked until it has returned back to reference pH levels. The sample is then dried in an electric oven at 105^{o}C for 24 hours.

3.4 Pyrolysis Treatment

Figure 4 shows the pyrolysis setup with a split tube furnace, nitrogen gas supply, and a pressure pump to prevent backflow caused by the heating of the furnace.

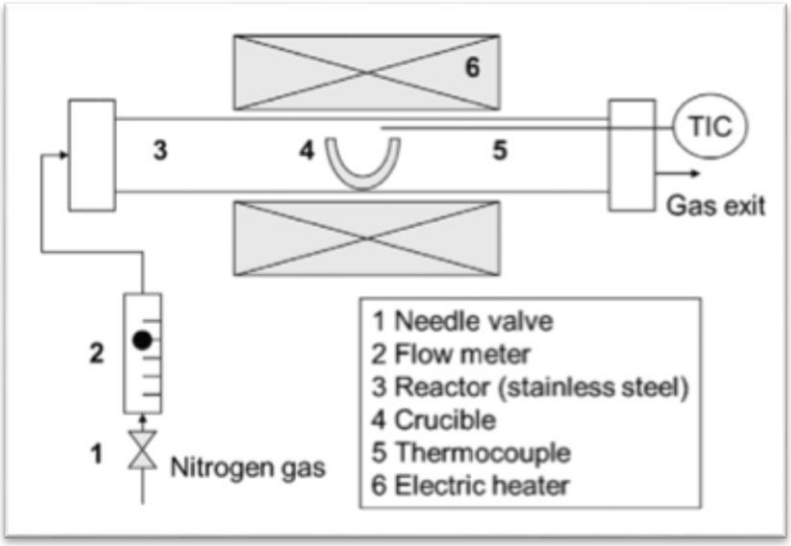


Figure 4. Pyrolysis setup with Split Tube Furnace

Pyrolysis conditions are set to inert conditions. Using ceramic crucibles, samples are placed into the glass tube and the furnace turned on. The sample is heated to 500^{o}C with a holding time of 30 minutes at a heating rate of 10C/min. After the pyrolysis, the furnace is left to cool and the samples is collected and kept in the desiccator. This procedure is repeated for all samples pretreated with alkali and acid.

3.5 Proximate Testing

Proximate analysis was conducted according ASTM E 897-88 to investigate the ash content of samples after chemical pretreatment and after pyrolysis. Samples are weighed at 1.0g and dried at 105^{o}C for 1 hour to remove inherit moisture. After which, samples are put into a muffle furnace at 750^{o}C for 1 hour at a heating rate of 10^{o}C/min.

4. Results and Discussion

4.1 Proximate Analysis

Results are tabulated and graphed to observe the trend shown in Table 3. The data obtained showed a trend of decreasing ash content after each chemical treatment with pyrolysis. Pyrolysis of untreated sample shows a reduction in ash after heat treatment of 500ºC for 30 minutes. Pyrolysis as a treatment has been shown to remove volatile matter when treated with inert conditions of nitrogen gas. According to a study by A. Veksha Et al, ash content of biomass pyrolysis reduces with the decrease of volatile compounds of the biomass [11].

Table 3. Decrease of Ash Content for Untreated Pyrolysis OPMF

	Ash Content		
Raw OPMF	Before Pyrolysis	After Pyrolysis	Reduction wt.%
	7.0%	3.8%	46%

Figure 5 shows the ash reduction trend of acid treated samples before and after pyrolysis. Ash content of the biomass reduces significantly after acid pretreatment. This can conclude that acid treatment removes metallic ash compounds found in POMF. However, after pyrolysis, pretreatments with 1M of HCl show improvement after pyrolysis while lower concentrations show a slight increase. Increased residence time also improves the effectiveness of lower concentrated acid pretreatments. The decrease in ash content is parallel to a study conducted by M. Asadieraghi Et al [8].

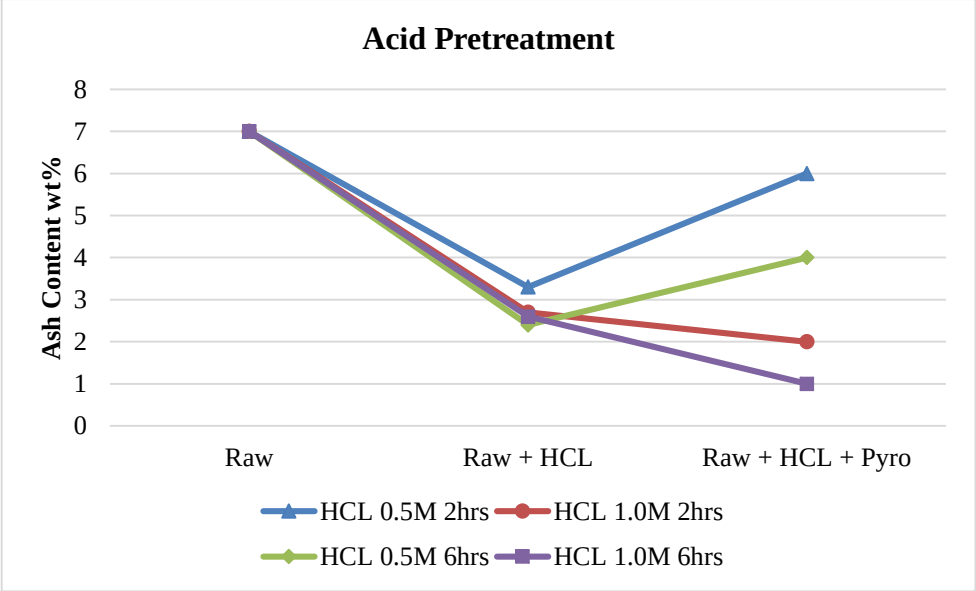


Figure 5. Graph trend for acid pretreated biomass and biochar

Pretreatment with KOH also proves to reduce ash content, however the results show less effectiveness than acid pretreatment of biomass. KOH is commonly used to improve surface area of biochar after pyrolysis and to produce activated carbon [11]. Pretreatment of mesocarp fibre with 1M of KOH solution and 10 hours of residence time at a temperature of 85ºC with reflux conditions have shown an improvement with ash content wt% reduced from 7.0% to 2.7% and increase to 3% after pyrolysis.

4.2 XRD Analysis

X-ray diffraction is method to show the crystallinity of a sample. Peaks are formed on a graph as the change of in degree occurs. In Figure 6 shows XRD results for untreated, acid pretreated, alkali pretreated biochar and raw OPMF. The highest peak, common to all four samples show the cellulose structure of the biomass fairly unchanged after treatment and pyrolysis. Pyrolysis samples differ from raw with the second peak.

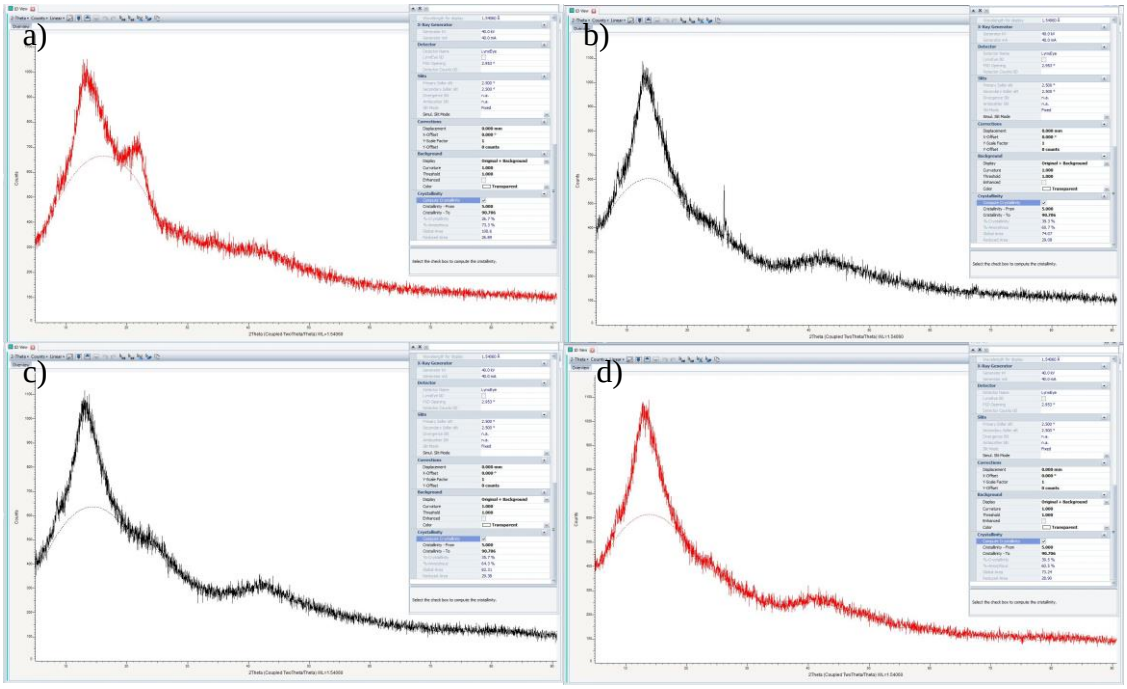


Figure 6. XRD Results for a) Raw Mesocarp Fibre, b) Untreated Pyrolysis c) Acid Pretreated Pyrolysis, & d) Alkali Pretreated Pyrolysis

From the XRD results, untreated and acid pretreated pyrolysis share the same degree of crystallinity at 39% while alkali pretreated pyrolysis shows 34% crystallinity. Pyrolysis reduces the second peak of the XRD analysis of raw mesocarp fibre due to volatile matter present in the biomass as the other graphs show similar pattern for the second peak. According to a study by A. Elleuch Et al [15], biochar with lower degree of crystallinity improves electrical conductivity of carbon fuel and the DCFC, alkali pretreated pyrolysis samples have less degree of graphitization than acid pretreated samples as fuel for DCFC.

4.3 Pyrolysis Yield

Yield of samples was also recorded and tabulated to observe the amount of biochar produced per gram of biomass used for pyrolysis. Mesocarp fibre primarily consists of volatile matter, at 400ºC volatile matter is released from the biomass, reducing its weight drastically. After the pyrolysis process, biochar remains with a maximum amount of carbon. Table 4 shows the weight of biomass before and after pyrolysis to show a yield of 32%, at average 0.32g of biochar per 1g of biomass.

Table 4. Weight of biomass & biochar before and after pyrolysis

Pretreatment Conditions	Crucible (Empty)	Crucible (After Pyrolysis)	Biochar Produced (g)	Yield wt%
Raw Pyrolysis 1	52.91	55.36	2.45	0.34
HCL 1M 2hrs	52.96	53.93	0.97	0.32
HCL 0.5M 2hrs	54.09	54.70	0.61	0.32
HCL 1M 6hrs	52.94	53.91	0.97	0.30
HCL 0.5M 6hrs	54.10	55.14	1.04	0.31
KOH 1M 10hrs 85ºC Reflux	53.00	53.73	0.73	0.34
Pyrolysis Yield Average	0.32			

5. Conclusion & Future Work

Pretreatments of biomass have been conducted using acid, alkali and pyrolysis treatments of mesocarp fibre. Acid pretreatment is showing a decrease of ash content from 7.0% to 2.2% and the increase of crystallinity from 26.7% to 39.6%. This is comparable with untreated pyrolysis reducing ash content from 7.0% to 3.8% with a crystallinity of 40%. KOH treatments have reduced ash content of the biochar from 7.0% to 3.0% with a crystallinity of 34% after pyrolysis. Alkali pretreatments give better for XRD results as a DCFC fuel with the current analysis completed. Pyrolysis yields conclude a 32% yield rate consistent with other research done on mesocarp fibre specifically. Pretreatments of biomass show promise for ash content removal & decrease of degree of graphitization, further analysis in CHNS, BET, & TGA will show other characteristics of the biochar untreated and pretreated. BET is important to show the bigger picture on the effects of acid and alkali pretreatments on mesocarp fibre biochar

When the effects of pretreatment of mesocarp fibre are concluded with CHNS, XRD, BET and TGA analysis, different stages and order of pretreatment and post-treatment can be conducted to further optimize the quality of mesocarp fibre biochar. Current samples can be used with a DCFC to test for practical results of the carbon fuel. With collaboration, further data can be recorded by testing each pretreated sample of biochar with a DCFC to measure the amount of electricity produced.

Acknowledgment

Gratitude and thanks is due to the individuals who have help in the process of this research, this includes Taylor's School of Engineer staff, Taylor's Lab technicians for their supervision and assistance as well as the guidance of supervisors for this final year project.

Reference

[1] H. Lean and R. Smyth, 'Disaggregated energy demand by fuel type and economic growth in Malaysia', *Applied Energy*, vol. 132, pp. 168-177, 2014.

[2] S. Giddey, S. Badwal, A. Kulkarni and C. Munnings, 'A comprehensive review of direct carbon fuel cell technology', *Progress in Energy and Combustion Science*, vol. 38, no. 3, pp. 360-399, 2012.

[3] C. Munnings, A. Kulkarni, S. Giddey and S. Badwal, 'Biomass to power conversion in a direct carbon fuel cell', *International Journal of Hydrogen Energy*, vol. 39, no. 23, pp. 12377-12385, 2014.

[4] S. Vassilev, D. Baxter, L. Andersen and C. Vassileva, 'An overview of the chemical composition of biomass', Fuel, vol. 89, no. 5, pp. 913-933, 2010.

[5] M. Umar, P. Jennings and T. Urmee, 'Sustainable electricity generation from oil palm biomass wastes in Malaysia: An industry survey', Energy, vol. 67, pp. 496-505, 2014.

[6] Y. Uemura, W. Omar, T. Tsutsui and S. Yusup, 'Torrefaction of oil palm wastes', *Fuel*, vol. 90, no. 8, pp. 2585-2591, 2011.

[7] Y. Uemura, W. Omar, T. Tsutsui, D. Subbarao and S. Yusup, 'Relationship between Calorific Value and Elementary Composition of Torrefied Lignocellulosic Biomass', *Journal of Applied Sciences*, vol. 10, no. 24, pp. 3250-3256, 2010.

[8] M. Asadieraghi and W. Wan Daud, 'Characterization of lignocellulosic biomass thermal degradation and physiochemical structure: Effects of demineralization by diverse acid solutions', Energy Conversion and Management, vol. 82, pp. 71-82, 2014.

[10] R. Xiao, X. Chen, F. Wang and G. Yu, 'Pyrolysis pretreatment of biomass for entrained-flow gasification', Applied Energy, vol. 87, no. 1, pp. 149-155, 2010.

[11] A. Veksha, W. Zaman, D. Layzell and J. Hill, 'Enhancing biochar yield by co-pyrolysis of bio-oil with biomass: Impacts of potassium hydroxide addition and air pretreatment prior to co-pyrolysis', *Bioresource Technology*, vol. 171, pp. 88-94, 2014.

[12] F. Abnisa, W. Daud, W. Husin and J. Sahu, 'Utilization possibilities of palm shell as a source of biomass energy in Malaysia by producing bio-oil in pyrolysis process', Biomass and Bioenergy, vol. 35, no. 5, pp. 1863-1872, 2011.

[13] A. Shaaban, S. Se, M. Dimin, J. Juoi, M. Mohd Husin and N. Mitan, 'Influence of heating temperature and holding time on biochars derived from rubber wood sawdust via slow pyrolysis', Journal of Analytical and Applied Pyrolysis, vol. 107, pp. 31-39, 2014.

[14] J. Tang, J. Liu, N. Torad, T. Kimura and Y. Yamauchi, 'Tailored design of functional nanoporous carbon materials toward fuel cell applications', Nano Today, vol. 9, no. 3, pp. 305-323, 2014.

[15] A. Elleuch, A. Boussetta, J. Yu, K. Halouani and Y. Li, 'Experimental investigation of direct carbon fuel cell fueled by almond shell biochar: Part I. Physico-chemical characterization of the biochar fuel and cell performance examination', *International Journal of Hydrogen Energy*, vol. 38, no. 36, pp. 16590-16604, 2013.

Preparation and Properties Study of PLA/Waste Tea-Leaf Fiber Composite

Pavin Prahaladar[1], Ming Meng Pang[1], Kim Yeow Tshai [2]

[11]*School of Engineering Taylor's University, Lakeside Campus, No1, Jalan Taylor's, 47500 Subang Jaya, Malaysia*

[22]*University of Nottingham Malaysia Campus, Department of Mechanical, Materials & Manufacturing Engineering, Jalan Broga, 43500 Semenyih, Selangor Darul Ehsan, Malaysia*

[*]pavin28_15@hotmail.com

Abstract

Polylactic acid PLA is a type of aliphatic polymer known because it is a biopolymer which has a rigid characteristic. It is derived from renewable resources such corn starch, tapioca roots or sugarcane. However, one of its major downside is that PLA is very brittle and has poor elongation at break. For this research, waste tea leaves are proposed as a potential combination with the PLA matrix. Half of the tea leaves were treated with an ultrasonic machine to aid the dispersion of the tea leaf fibre in the PLA matrix. The compounding process of the PLA composite was carried out using an internal mixer at a temperature of 180℃ and a rotor speed of 50rpm. Then, the composite was molded into sheet with 1mm thickness using compression moulding at 180℃ and pressure of 150 bar. PLA composite with the treated tea leaf fiber loading absorbs more water compared with the PLA with the untreated fiber loading. This could be due to the ultrasound treatment which increased the dispersion of the tea leaves fiber in the PLA matrix. Furthermore, the PLA/Tea leaf blend showed very good adhesion between the fiber and the matrix with the treated fiber displaying a better result. TGA analysis showed that increasing fiber loading decreases the thermal stability of the composite due to lower degradation temperature. However, very little residue waste is left behind when the PLA/Tea leaf composite is incinerated.

Keywords: Polylactic acid (PLA), Waste Tea-leaf fiber,

1.0 Introduction

Polylactic acid (PLA) is a biodegradable thermoplastic aliphatic polyester, which developed from renewable resources, such as corn and rice starch. PLA synthesis involves the formation of dextrose from the conversion of corn and rice. Dextrose is further converted to lactic acid through fermentation process. Lactic acid is further purified and converted into a polymeric form of PLA through polymerization. Some of the more notable advantages of PLA are its renewability, biocompatibility, processability and its energy saving. Since it's manufactured from renewable raw materials, this reduces our dependency on fossil fuels. One of the few drawbacks of PLA is that it's too brittle in nature thus limiting its area of applications. However, it still can be processed into different shapes through surface modification. Besides that, it is very costly which is why it is seldom used in the plastic industry [1].

Waste tea leaves are proposed as a suitable natural fiber to reinforce PLA. Waste tea leaves is the left over leaves that are disposed of by restaurants and factories once the tea essence has be drained from it. By incorporating waste tea leaves into PLA it can help lower the production cost of biodegradable polymer which is very high. Moreover, using the waste tea leaves can be a form of waste management to help reduce the rate of disposal of waste tea leaves. This research can also help diversify the usage of waste tea leaves in the scientific research field. An example of an existing application of waste tea leaves is the investigation of its sound absorption properties. Sezgin Ersoy et al [2] investigated the sounds absorption properties of industrial tea-leaf fiber waste material. Results showed that waste tea leaves showed better sound absorption when compared with polyester and polypropylene based non-woven fiber material. In general, there are three types of tea which include black, green and oolong tea. For this investigation black tea is chosen to reinforce the PLA matrix due to the fact that Malaysians in general uses about 80% of black tea. Example of black tea includes English tea and BOH tea while the most common green tea is Japanese tea. BOH's plantations in Malaysia account for nearly 70% of the country's annual tea production which is around 4000 tons of tea [3].

The aim of this study was to study the thermal properties of the PLA/Waste tea leaf composite through Thermogravimetric analysis (TGA) and Differential Scanning Calorimetry (DSC) as well as its water absorption capacity sine tea leaves is hydrophilic. The morphology was studied using the scanning electron microscope

(SEM). An ultrasound machine was used to treat half of the tea leaves specimen because a better dispersion of the waste tea leaves in the PLA matrix can be obtained.

2.0 Methodology

2.1 Materials

The materials used were polylactic acid 3051D (PLA) and waste tea leaves. Nature Works LLC provided the PLA with a glass transition temperature of 55 - 60 ℃ and a melting temperature of 170 ℃. The waste tea leaves were obtained from restaurants in Klang Valley.

2.2 Method

2.2.1 Melt Blending with Internal Mixer

The internal mixer (Haake Polylab System E93) was used to melt blend the mixture of PLA and waste tea leaves following the formulation listed in Table 1 below. The parameters of the internal mixer were set at temperature 180 ℃ and a rotor speed of 50 rpm. Once both parameters have been set, the PLA/Waste tea leaves mixture was poured inside and left for 10 minutes.

2.2.2 Compression Moulding

The 1mm thickness sheet was produced by compression moulding. The PLA/Waste tea leaves mixture was compressed at a temperature of 180 ℃ and pressure 150 bar using a hot press machine (Moore E53). Once the hot press plates have reached the desired temperature, the mold was placed in between them. The mold then undergoes a pre-heating process for 3 minutes. Once that is done, pressure is applied for 7 minutes. Then the machine is allowed to cool down to 60 ℃ before the sheet is removed. The polymer obtained has a dimension of 12cm x 15 cm with a 0.1cm thickness.

2.2.3 Filler Treatment

Some of the waste tea leaves were placed in beaker wrap with plastic wrap to be placed inside an ultrasonic machine. The purpose of this was to increase the dispersion of the tea leaf particles and compare its properties with the non-treated tea leaves. The tea leaves were treated at a frequency of 10 Hz for 30 minutes.

Table 1: Formulation of PLA and Waste tea leaves

Formulation
Neat PLA
PLA blend with 10% untreated waste tea leaves
PLA blend with 20% untreated waste tea leaves
PLA blend with 10% treated waste tea leaves
PLA blend with 20% untreated waste tea leaves

2.3 Testing and Characterization

2.3.1 Differential Scanning Calorimetry

The heat resistance level of the PLA/Waste tea leaf composite as well as the crystallinity was measured using DSC. Each sample are heated up from room temperature to about 200 ℃ followed by cooling at a rate of 10 ℃/min in the presence of nitrogen [4].

2.3.2 Thermogravimetric Analysis

The decomposition temperature of the PLA/Waste tea leaf composites is measured using TGA. Each sample will be heated up from 30 ℃ to 800 ℃ at a steady rate of 10 ℃/min [4].

2.3.3 Scanning Electron Microscopy

The surface and fracture morphology of the PLA/Waste tea leaf composite is observed using the Field emission SEM (model FEI Quanta 400F FESEM). . Each composite sample is sputtered coated with gold to prevent electrical discharge prior to being tested.

3.0 Results and Discussion

3.1 FTIR Analysis

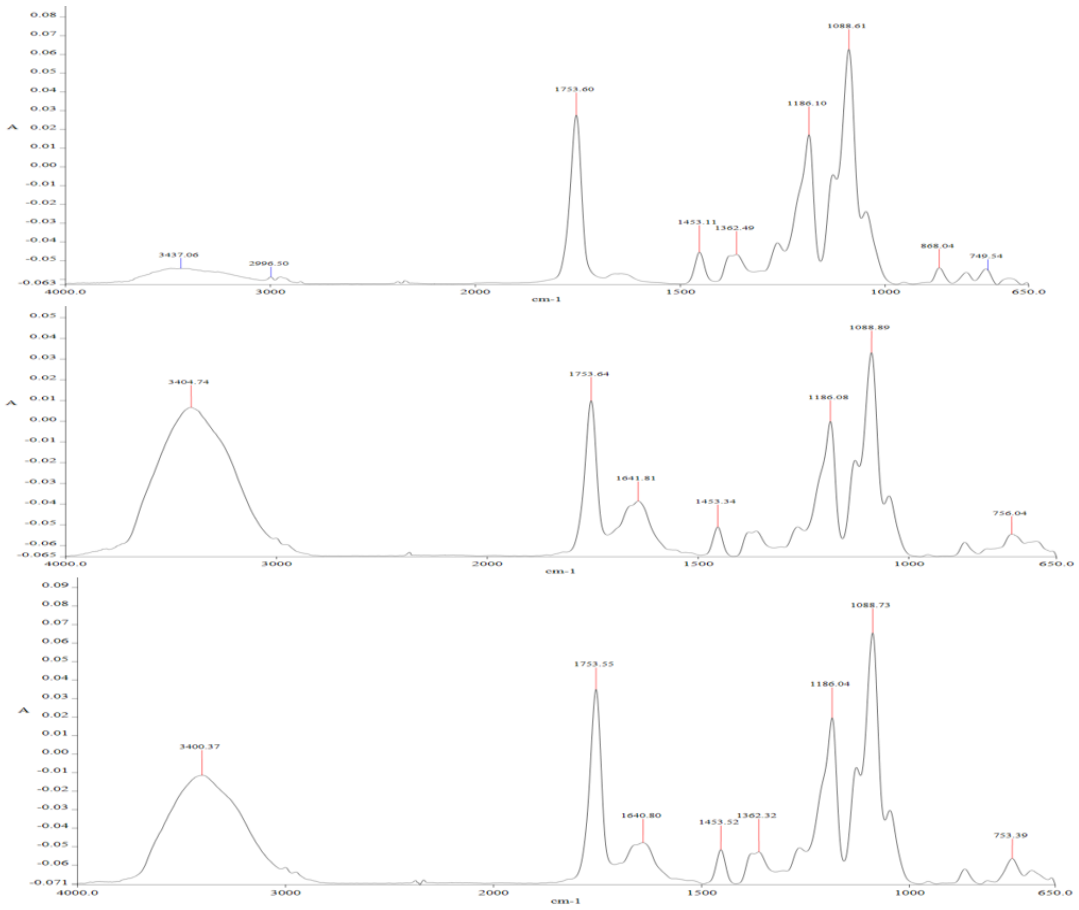


Figure 3.1.1 FTIR spectra of treated and untreated PLA/Tea leaf composite soaked in water

The various chemical composition of the treated and untreated PLA/Tea leaf composite (10% T, 10% T and 20%UT) soaked in water were analyzed using with FTIR as shown in Figure 3.1. It can be observed in both treated and untreated specimens have similar FTIR spectra due to their similar chemical composition. The hydrophilic tendency of the tea leaves can be seen in the absorption around 3300 – 3400 cm^{-1}. This is an indication of strong hydrogen-bonded stretching present in aliphatic or aromatic alcohols which are also subsequently present in their main component The peak around 1640 cm^{-1} shows H-O-H bonding due to the water absorbed by the specimens [5]. The peak around 1735 cm^{-1} signals that stretching vibrations of the C=O function of the acetyl and ester group of the hemicellulose or waxes and natural fatty components [6].

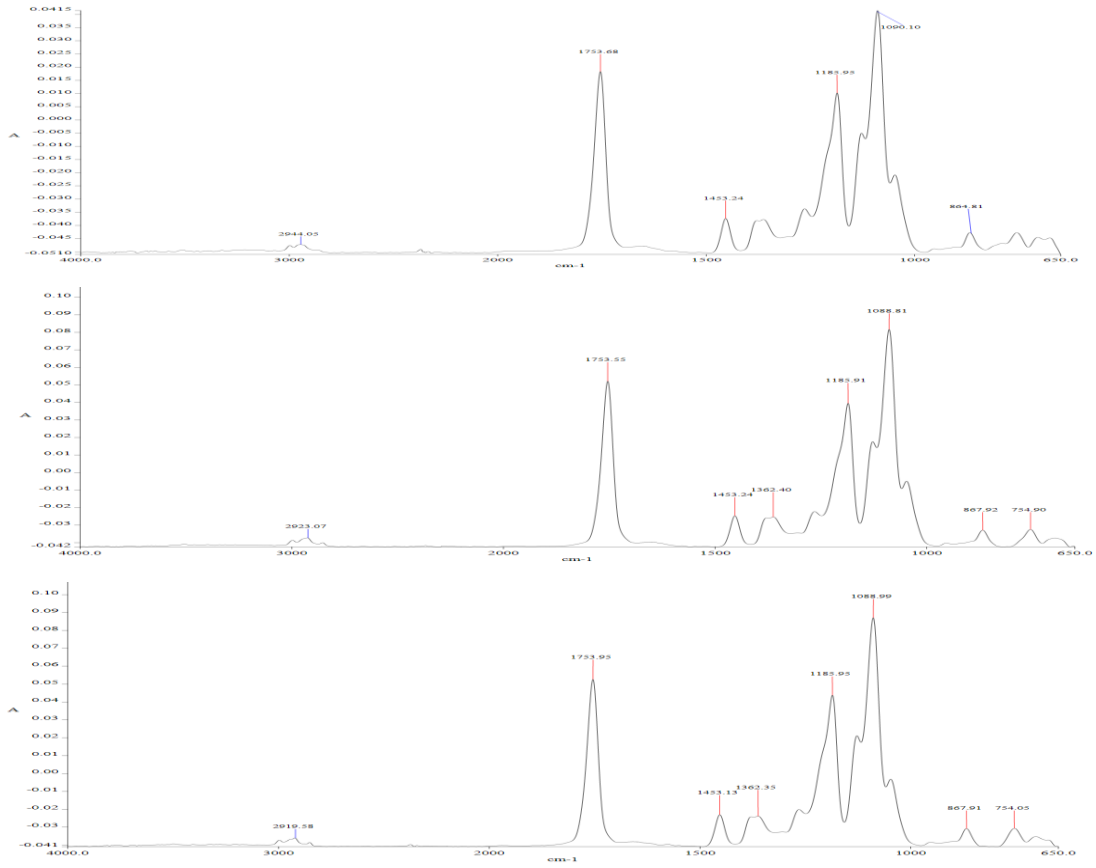


Figure 3.1.2 FTIR spectra of treated and untreated PLA/Tea leaf composite

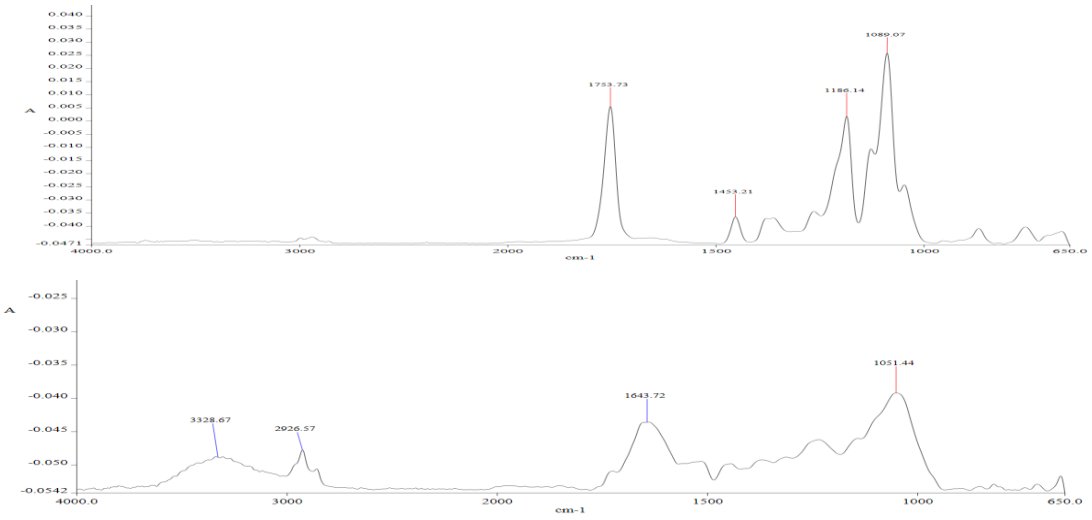


Figure 3.1.3 FTIR spectra of pure PLA sample and tea leaves

Figure 3.1.2 shows the analysis of the samples (10% T, 10% T, and 20% UT) that weren't soaked in water shows the presence of C-O stretch and O-H bend at peaks around 1290 – 1460 cm^{-1}. The peaks around 700 – 1160 cm^{-1} could be due the presence of the isomers catechin and epicatechin.

3.2 Water Absorption Test

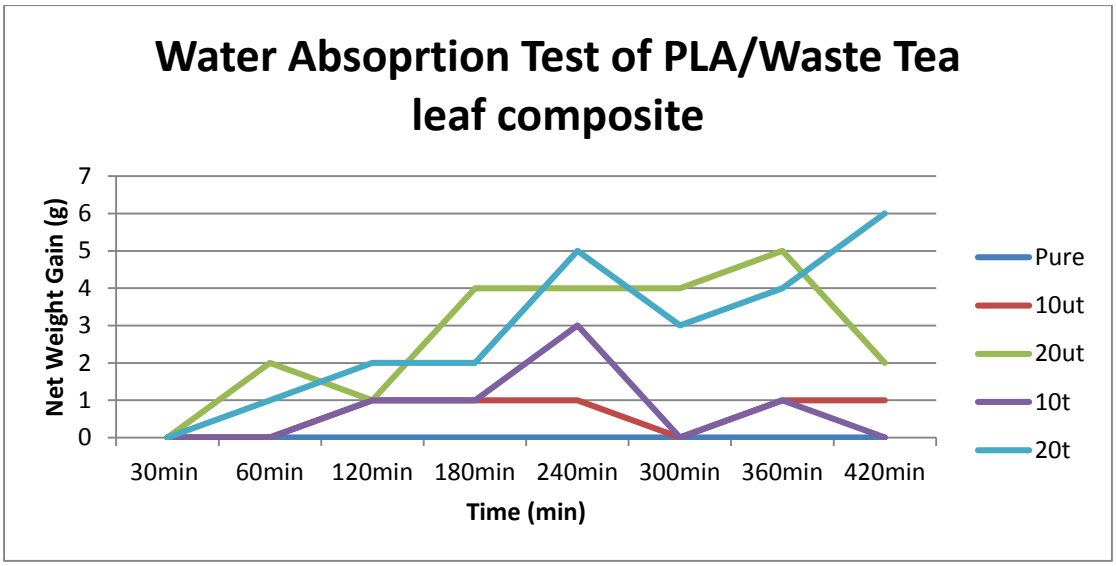


Figure 3.2.1 Comparison of water absorption for ultrasound treated and untreated PLA/Waste tea leaf composite

Figure 3.1 shows the net weight gain of water for each sample with a 7 hour period. As seen above, the amount of water absorbed by the composite increased with increased tea leaf composition. This is because the PLA itself is hydrophobic while the tea leaves are hydrophilic [7]. 10% untreated tea leaf (10ut) fiber loading reached the saturation point first compared with the others as it can be seen that there was no net gain higher than 1. On the other hand, both 20% untreated tea leaf fiber (20ut) and 10% treated fiber (10t) exhibited negative weight gain. This is an indication that desorption process is taking place. The same however can't be said for 20% treated tea leaf fiber (20t) which continued to absorb more water even after experiencing a negative weight gain. This could be due to the fact that a higher dispersion of the tea leaves in the PLA matrix is achieved. Therefore, a higher surface area of the tea leaves is exposed to absorb more water. This can be further supported by the net weight gain value of 3 for the 10% treated tea leaf fiber loading at the 4 hour mark.

$$Net\ Weight\ Gain = Weight\ of\ sample\ after\ being\ immersed\ in\ water - Initial\ weight\ of\ sample$$

3.3 Thermogravimetric Analysis (TGA)

The TGA results for the treated and untreated waste tea leaves are shown in Table 3.31 and in figures 3.3.1 and 3.3.2. As can be demonstrated in the TGA results for waste tea leaves in Figure 3.3.1, the first peak indicates close to 100 ℃ indicates weight loss due to the removal of water molecules absorbed by the waste tea leaves. The second stage is attributed to the degradation of hemicellulose, cellulose and partial lignin in the temperature range of 270 ℃ to 360 ℃. Finnally the degardation of the ligning residue happens from 360 ℃ till 600 ℃ [8]. The balance residual weight of the tea leaf left is 34.15% which could be due to the presence of inorganic matter. As seen in Table 3.3.1, neat PLA has a degradation temperature of 351.3 ℃ while the PLA/Tea leaf blends shows a decrease in the onset temperature at 338.7 ℃, 332.7 ℃ and 333.7 for fiber content of treated 10 and 20wt% and untreated 20wt%. Therefore, increasing the fiber content decreases the composite thermal stability due to the lower degradation temperature of the waste tea leaves at 278.7 ℃. However, it should be noted that the PLA/Tea leaf blends left behind minimal residue around 3% – 5%.

Table 3.3.1 TGA Data for PLA and PLA/Tea Leaf Blends in N_2 Atmosphere

Samples	Onset Temperature (℃)	Residual Weight (%)
Pure PLA	351.3	0 – 1
Waste tea leaves	278.7	~ 34
PLA blend with 10% treated waste tea leaves	338.7	3 – 4
PLA blend with 20% treated waste tea leaves	332.7	3- 4
PLA blend with 20% untreated waste tea leaves	333.7	4 - 5

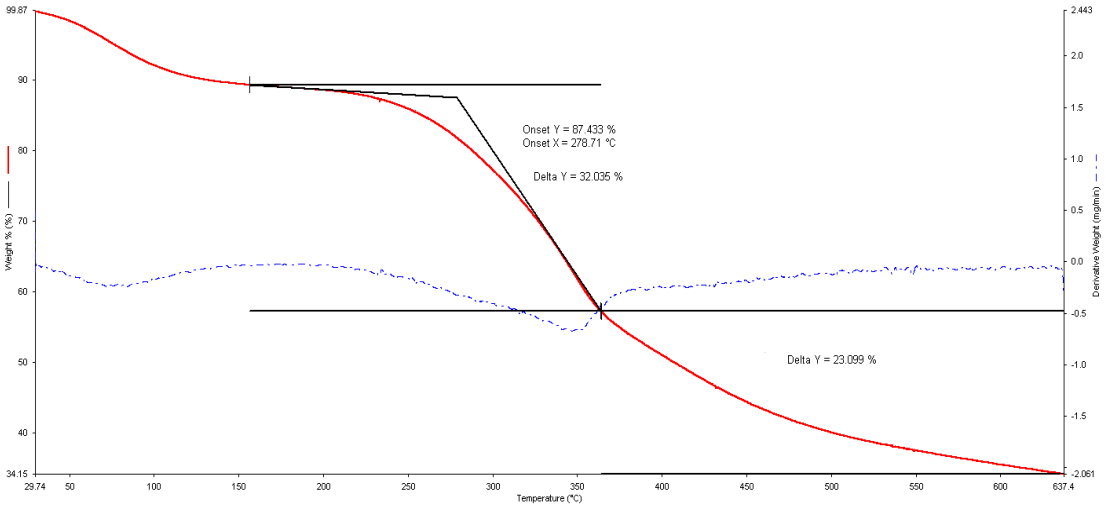


Figure 3.3.1 TGA Analysis of Tea leaves

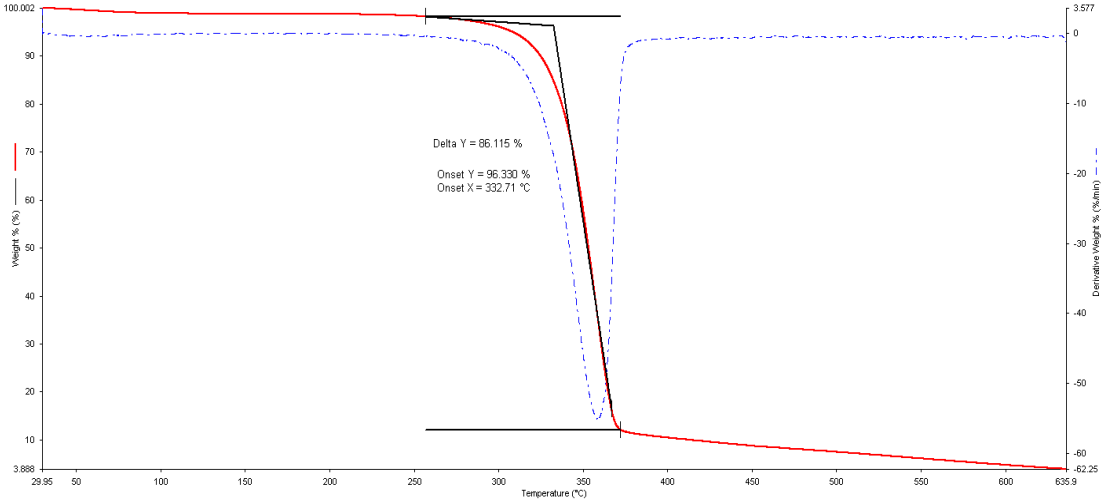


Figure 3.3.1 TGA Analysis of PLA blend with 20% treated tea leaves

3.4 Scanning Electron Microscope (SEM)

As it can be seen in Figure 3.4.1 to Figure 3.4.3, the presence of PLA on the tea leaf specimen in the fiber pullouts indicate a good adhesion between the PLA and the tea leaves. Both treated and untreated tea leaves show good adhesion between the fiber and the matrix. Moreover, the treated sample showed a better adhesion between the fiber and the matrix. This could be due the sonication of the tea leaves prior to moulding resulting in a better dispersion of the tea leaves increasing the amount of exposed surface area. This helps justify the waster absorption test results. Previous study by Heinemann and Fritz showed that natural fiber and PLA will have a good adhesion because of the hydrophilic property of the natural fiber. This is because PLA has slightly polar oxygen atoms which could form hydrogen bonds to the hydroxyl groups of the natural fibers [9].

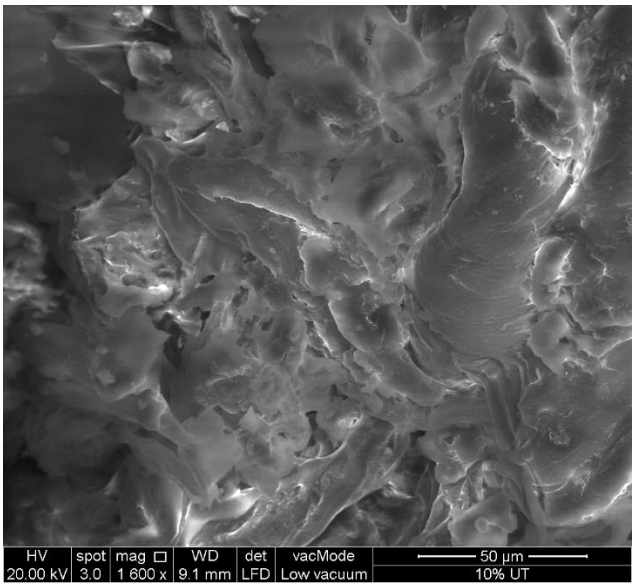


Figure 3.4.1 SEM image of PLA blend with 10% treated tea leaf fiber

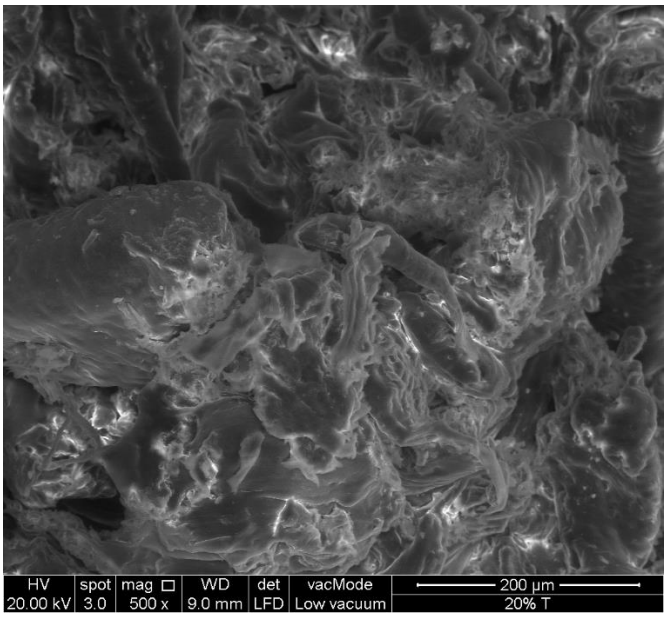


Figure 3.4.2 SEM image of PLA blend with 20% treated tea leaf fiber

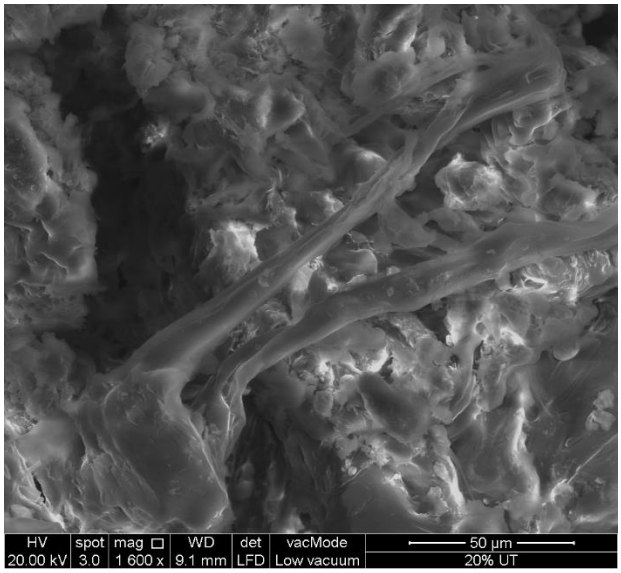


Figure 3.4.3 SEM image of PLA blend with 20% untreated tea leaf fiber

4.0 Conclusion

PLA with 10 and 20wt% treated and untreated tea leaf fibers were made using an internal mixer followed by a hot press. A pure PLA sample sheet was also made for comparison purposes. The water absorption test was performed accordingly in compliance with the international standard on all the samples.

PLA composite with the treated tea leaf fiber loading absorbs more water compared with the PLA with the untreated fiber loading. This could be due to the ultrasound treatment which increased the dispersion of the tea leaves fiber in the PLA matrix. Furthermore, the PLA/Tea leaf blend showed very good adhesion between the fiber and the matrix with the treated fiber displaying a better result. TGA analysis showed that increasing fiber loading decreases the thermal stability of the composite due to lower degradation temperature. However, very little residue waste is left behind when the PLA/Tea leaf composite is incinerated.

Acknowledgment

The authors I would like to thank are Taylor's University Malaysia as well as SIRIM Berhad and University of Nottingham Malaysia Campus for its financial and equipment support.

References

[1] L. Xiao, B. Wang, G. Yang, and M. Gauthier, "Poly (Lactic Acid) -Based Biomaterials Synthesis, Modification and Applications," pp. 248–257, 2006.

[2] S. Ersoy and H. Küçük, "Investigation of industrial tea-leaf-fibre waste material for its sound absorption properties," Appl. Acoust., vol. 70, no. 1, pp. 215–220, 2009.

[3] G. P. Harold N, "Green tea composition, consumption and polyphenol chemistry," pp. 334–500, 1992.

[4] Chun, K.S. & Husseinsyah, S. Polylactic acid/corn cob eco-composites: Effect of new organic coupling agent. Journal of Thermoplastic Composite Materials, 2013.

[5] T. P. T. Tran, J.-C. Bénézet, and A. Bergeret, "Rice and Einkorn wheat husks reinforced poly(lactic acid) (PLA) biocomposites: Effects of alkaline and silane surface treatments of husks," Ind. Crops Prod., vol. 58, pp. 111–124, 2014.

[6] Sun, R., Lawther, J.M., Banks, W.B., 1995. Influence of alkaline pre-treatments on the cell wall components of wheat straw. Ind. Crops Prod. 4 (2), 127–145.

[7] Amor IB, Ghallabi Z, Kaddami H, Raihane M, Arous M, Kallel A. Experimental study of relaxation process in unidirectional (epoxy/palm tree fiber) composite.
J Mol Liq 2010;154:61–8.

[8] S. Polat, E. Apaydın, and A. E. Pütün, "TGA- FTIR study on the thermal decomposition of tea waste," pp. 420–431, 2013.

[9] Heinemann M, Fritz H-G. Polylactid – Struktur, Eigenschaften und Anwendungen. 19. Stuttgater Kunststoff-Kolloquium 2005.

Uric Acid Adsorption By Activated Carbon Fibre (ACF) Derived From Empty Fruit Bunch(EFB)

Saravanakumar.R[1*],Lee Ting[2*]

[1] *School of Engineering, Taylor's University*

[*]saravanakumar.rajentheran@sd.taylors.edu.mmy

Abstract

Uric acid adsorption is an important process in the hemodialysis machine to treat the patients with kidney failure. It has drawback in term separation of the high molecular weight of solutes from the blood. Hemodialysis is the only optional for kidney failure person to survive, other than the kidney transplant which is very hard to acquire for the donor. It was suggested that the problem can be resolved with the use of high porous structure membrane in the dialysis machine. Activated carbon fiber derived from empty fruit bunch from palm oil was used in the project. The project was purpose to find the best ACF from different chemical activation treatment such as sulphuric acid, potassium hydroxide, phosphoric acid and also sodium hydroxide. Different type chemical activation would lead to the formation of different functional group. Functional group play an important role in the determining the efficiency of the adsorption processes as they alter the surface chemistry of the Activated Carbon. Chemical activation would be require lower temperature than the physical activation. Cellulosic backbone can be tarnished due to the reaction between the chemical and the carbon residue. Potassium hydroxide can be considered as better activating agent compared to Phosphoric acid due to its lower demand for energy. The chemical activation using the Potassium hydroxide and Sodium Hydroxide would produce activated carbon with high specific area (<1000 m^2/g). .The characterization test such as BET, UV-vis spectrometer and FTIR was used to determine the characteristic of the adsorption process and as well as the adsorbent. The samples activated with different chemicals was used in the adsorption of the uric acid. Performance of the uric acid adsorption in each sample was analyzed with the help of test mention earlier. The best sample was used in the adsorption of the urea.

Keywords: Activated Carbon Fibre, Micropore and Mesopore structures, Functional group.

1. Introduction

Adsorption can be explained as a process where the desired components or undesired components is separated from the mixture of solution or gas by the help of the adsorbents. Adsorption process has been practiced since biblical times, as in the decolourisation of sugar solution using bone char and also in the battlefield to save the life of soldiers by adsorbing the nerve gases. The application of the adsorption process had grown significantly as it is now being applied widely either in private or commercial application .Example of the application would be in waste water treatment, air filtration, and aerospace industries to inerting the fuel system ,supplying oxygen to the pilot and eliminating carbon dioxide or odour.

The application has also being applied in the medical field to find the cheap and efficient material or adsorbent for the dialysis process .Kidney dialysis is a process where the dirty blood containing the harmful wastes, salt and excess fluid from the body using urination process. The dialysis process can be categorized into hemodialysis and Peritoneal dialysis. Each of process differ in term of the operation, where the hemodialysis is operated by dialyzer and dialyzing machine. Perioneal dialysis is operated by the help of the special cleaning solution filled in the abdomen for the filtration process. In the machines, semi-permeable membrane is used as a medium to filter the waste products. Body waste such as uremic toxins are passed through the semipermeable membrane to the dialysate fluid with preserving the movement of the minerals such as sodium and potassium in balance level. The polymeric membrane was not able to fulfil the requirement to remove the uremic toxin such as the p-cresol , urea and the creatine [Wernet et al.,2005]. The continue research to find the sutitable to fill the requirement has been begun by the Barzin and his co- workers (Barzin et al.,2004) and development on wearable artificial kidney is already done by Gura and his co-workers (Gura et al.,2009). The material for the membrane must be chemically inactive , high adsorption efficiency ,biocompatibility and non-toxic .The permanent solution was to perform kidney transplant and it has limitation in order to find the compatible donor with suitable blood type with the recipient.

The empty fruit bunch (EFB) was chosen as the material as the abundance in the country as the biomass waste material and also it can be obtain n a cheaper price. Adsorbate can be described as a solid components which is having a porous structure that make it to be very special. The adsorbent to be used in this project would be activated carbon fibre (ACF) which is transformed from the empty fruit bunch .The adsorbate or the components to be adsorbed using the would be uric acid. The keen importance of finding the artificial kidney is increasing as the number of people or patient infected with kidney related illness is increasing. Around 2.5 million people suffered from the kidney related illness. Every year the number of the people affected increase from 5000 to 6000 patient per year. . About 10% of the dialysis patient die every year because they fail to find the organ donor for them (Annie Freeda Cruez 2014).

2. Material and Methods

2.1 Material

2.1.1 Empty Fruit Bunch (EFB)

Empty fruit bunch was chosen as the material to produce the activated carbon fibre (ACF).The EFB was chosen as the material due to certain reasons such as the high carbon content, small inorganic content .economical material and can provide the source of raw material at a steady level. Our country is one of the biggest producer and exporter of the oil palm at a value of 47% of total worl oil palm production (Umar et al., 2013). There are various type of waste material being produced from the oil palm (Table 1).Empty fruit bunch (EFB) is the waste that is being produced at a high amount at 31.6 MT per year. This waste can be altered to activated carbon fibre (ACF).There are researchers had already begun their researches on different type of biomass waste such as Sugar cane bagasse (Valix et al., 2008), bamboo (Hameed et al., 2007), coconut shell (Yang et al., 2010), sawdust (Malik, 2003), Empty fruit bunch fibre (Foo and Hameed, 2011) and several others.

Table 1: Shows the waste generated from the palm oil plantation (Abdullah et al., 2013)

N0	Type of Waste	Capacity produced /year (MT)
1	Empty fruit bunch (EFB)	31.6
2	Oil palm fronds (OPF)	48
3	Mesocarp fiber (MF)	17.8
4	Oil palm trunks (OPT)	15
5	Palm kernel shell (PKS)	8.3

Right now the biomass waste from palm oil is used as feedstock for the boilers in the oil palm mill or disposed in the open area as the natural decomposition to provide fertilizer for the land. This action has its effects to the environment as the burning in the boiler produce air pollution and the decomposition produce greenhouse effect.

EFB is made up of cellulose, hemicelluloce and lignin respectively (Figure 1). The cellulose in the EFB which are long, thin and straight are responsible for the microfibrils formation in the EFB (Fahma et al., 2010).Other than that, EFB has higher carbon content the other biomass waste from oil palm (Foo and Hameed, 2009).Certain research result was used as an evidence for the choose of the material for the ACF production. Alam and co –workers has used the AC for phenol adsorption (Alam et al., 2009) and Hameed and co-workers have produce the AC from EFB with BET surface area of 1141 m^2/g (Hameed et al., 2009) which was then used in the adsorption of 2,4,6- trichlorophenol. Potassium hydroxide has been used as chemical activating agent to produce EFB based AC. It has BET surface area of 807 m^2 /g (Foo and Hameed, 2011).This results can be used as a supporting evidence to prove that the EFB can be used to synthesis low cost carbon.



Figure 1 : Shows empty fruit bunch (EFB)

2.1.2 Uric acid

It has a molecular formula of $C_5H_4N_4O_3$ and has certain physical properties such as colourless, odourless, tasteless and insoluble in water. It also has a systematic name of 2/6/8-trioxypurine.This uremic toxins can be divided into three categories such as low, middle and high molecular weight solutes. Figure 2, show the molecular structure of the uric acid with a molecular mass of 168.1103 (The Human Metabolome Database 2007).

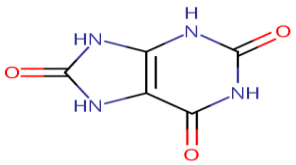


Figure 2 : Structure of the uric acid (The Human Metabolome Database 2007).

2.2 Method

2.2.1 Production of Activated Carbon Fibre (ACF)

There are series steps in the production of the activated carbon fibre from the EFB. There are major steps in the production of ACF which would be from cleaning of EFB, carbonization, activation and finally the adsorption of uric acid. In the cleaning step, the EFB was cleaned with 5% nitric acid .The EFB treated with nitric acid was immersed for around 20 minutes and rinsed with distilled water till the pH of the EFB is pH 7.The cleaned EFB was left to dry in the oven at temperature of 100 ^oC for overnight to remove the moisture content. 12g of EFB was treated with different type of chemical activating agents such as sulphuric acid, sodium hydroxide, potassium hydroxide and phosphoric acid at a mass of 9g.

2.2.2 Carbonization

Carbonization process was taken place at this stage with continuous flow of nitrogen gas at a rate of 100ml/min at a temperature of 10^0C /minute. The temperature of the process was maintained at the range of 400^{o}C for about 1 hour and then it was left to cool to room temperature with continuous supply of nitrogen gas. After that, the mass of the carbonized material was measured and the recorded. The char obtained was then washed with distilled water and left to dry in the oven at 100^0C for overnight.

2.2.3 Activation

The process was performed at temperature of 900^0C with continuously supply of nitrogen gas 100ml/min from room temperature till 900^0C.Once the temperature is reached, the flow of nitrogen gas is switched to carbon dioxide. The specimen was maintained at the temperature of 900^0C and the gas flow was switched to nitrogen after 1 hour. The condition was maintained till it reached the room temperature. After that, the mass of the ACF (Figure 3) was obtained to determine the weight loss.



Figure 3 : Activated Carbon Fibre

2.2.4 Adsorption

Produced ACF was tested its performance of adsorption with the uric acid. A small amount of the uric acid was mixed with the ACF. The concentration of uric acid before and after the mixing was taken using the UV-Vis spectrometer. The mixture of ACF and uric acid was left to dry and the mass was recorded. Other test such as the BET and FTIR was performed.

3. Result and Discussion

3.1 Burn off Analysis

Table 2 : Result of burn-off analysis

Sample	H2SO4 (%)	H3PO4 (%)	NaOH (%)	KOH (%)
Initila EFB (g)	12	12	12	12
Carbonization	5.85	6.51	9.86	8.11
Activation	3.21	3.2	3.6	3.8
Degree of mass loss, Θ (%)	73.25	73.3	70	68.3

Burn of analysis was calculated using the formula (1) shown below.

$$\Theta = (w_0\text{-}w) / w_0 \times 100 \qquad (1)$$

Where,

w_0 = Initial mass of raw material (g)

w = Final mass of the activated carbon fibre formed (g)

Each of the specimen has mass loss more than 60%.The cellulose, hemicelluloce and lignin respectively are burn off completely with preserving the carbon content.

4. Conclusion

Activated carbon fibre (ACF) from empty fruit bunch with different chemical activating agent such as H_2SO, NaOH, KOH, and H_3PO_4 can was produced successfully. EFB is a good material to be converted to ACF for the adsorption of the uric acid.

References

Annie Freeda Cruez, 2014, " 2.5 Mil Malayisan suffer from kidney disease", The sun daily 25 FebruaryAvailable from : <http://www.thesundaily.my/news/968646>.[5 May 2015].

Barzin, J, Feng, C, Khulbe, K C, Matsuura, T, Madaeni, S S & Mirzadeh, H (2004). Characterization of polyethersulfone hemodialysis membrane by ultrafiltration and atomic force microscopy. *Journal of Membrane Science*, 237**,** 77-85.

Fahma, F, Iwamoto, S, Hori, N, Iwata, T & Takemura, A (2010). Isolation, preparation, and characterization of nanofibers from oil palm empty-fruit-bunch (OPEFB). *Cellulose*, 17**,** 977-985

Foo, K Y & Hameed, B H (2011). Preparation of oil palm (Elaeis) empty fruit bunch activated carbon by microwave-assisted KOH activation for the adsorption of methylene blue. Desalination, 275, 302-305.

Hameed, B H, Din, A T M & Ahmad, A L (2007). Adsorption of methylene blue onto bamboo-based activated carbon: Kinetics and equilibrium studies. Journal of Hazardous Materials, 141, 819-825.

Valix, M, Cheung, W H & Zhang, K (2008). Role of chemical pre-treatment in the development of super-high surface areas and heteroatom fixation in activated carbons prepared from bagasse. Microporous and Mesoporous Materials, 116, 513-523.

Malik, P K (2003). Use of activated carbons prepared from sawdust and rice-husk for adsorption of acid dyes: a case study of Acid Yellow 36. Dyes and Pigments, 56, 239-249

Yang, K, Peng, J, Xia, H, Zhang, L, Srinivasakannan, C & Guo, S (2010b). Textural characteristics of activated carbon by single step CO2 activation from coconut shells. *Journal of the Taiwan Institute of Chemical Engineers*, 41**,** 367-372

Development of Palm Kernel Shell for CO_2 capture

Suryan Nair

BEng (Honours) in Chemical Engineering, School of Engineering, Taylor's University, Malaysia

nair.suryansukumaran@sd.taylors.edu.my

Abstract
Among the CO_2 capture technologies that can be employed to minimize CO_2 emissions into the atmosphere from industrial processes is through activated carbons (AC) especially that derived from palm kernel shells (PKS), which is a common waste product in the palm oil industry that exhibits properties best suited for adsorption. By mostly focusing on chemical activation, it is meant to determine the better chemical for impregnation (between KOH and $ZnCl_2$) and the activation method to employ. To do this, two samples are activated with potassium hydroxide (KOH) using different methods while another sample was activated with $ZnCl_2$ labelled Z1. The first activation method employed for KOH activation involved carbonisation first, followed by chemical impregnation, which resulted in sample K1, while the second activation method involved mixing the raw material with the KOH, followed by heat treatment, resulting in sample K2. Then, these three samples are then portioned into three parts that are sent for Brunauer-Emmett-Teller (BET) analysis, CO_2 adsorption, and SEM analysis to obtain both qualitative and quantitative data such as surface area and micro pore volume, adsorption capacity and pore structure. In conducting this project, the results obtained indicate that K1 could adsorb more CO_2 than Z1 due to greater BET surface area and microporosity, which was also affirmed by the honeycomb structure of the pores. However, more focus and time should have been placed on the cleaning of sample Z1 after chemical activation as metallic deposits were likely major contributors to blockages in the pores of the sample.

Keywords: Palm Kernel Shell, Activated Carbon, Carbon Dioxide Capture, Potassium Hydroxide, Zinc (II) Chloride.

1. Introduction

Carbon dioxide (CO_2) capture is a subset of the carbon dioxide capture and storage process. This process involves the separation of CO_2 from industrial and energy-related sources, the transport of CO_2 to a storage location (i.e. geological formations, in the ocean, in mineral carbonates, industrial use) to ultimately achieve long-term isolation of CO_2 from the atmosphere. CO_2 is a common pollutant/product from large point sources (i.e. fossil fuel power plants). In large quantities, CO_2 emissions into the atmosphere are a known contributor to global warming and ocean acidification as it is a greenhouse gas. Capture technologies such as activated carbons are used to minimize such effects from taking place (Abanades, 2005).

Activated carbon (AC) is charcoal that is obtained from plant and animal matter and undergoes processing. Activated carbons have high micro porosity and surface. These properties make AC useful to adsorb a variety of unwanted materials such as heavy metals, dyes, organic materials and much more (Salleh, 2010). The best way to ensure the activated carbon selectively adsorbs unwanted materials (in this case, CO_2) is to firstly choose the appropriate charcoal, then choose the right methods of processing, which is called the activation method. These activation methods include physical activation, chemical activation and physiochemical activation (physical reactivation). The charcoal used in this instance is obtained from palm kernel shells (PKS). PKS comes from palm fruit, which is in abundance in areas like Malaysia. PKS was used as the low ash content, high number of fixed carbons, hardness, and the ease of access in terms of availability and cost, make it a suitable activated carbon. This then leads to questioning, how are the adsorption capabilities of PKS activated carbons compare between different chemical activation means for selective CO_2 adsorption?

In order to answer the research question posed, a set of objectives have to be made to cater for it. Those objectives are shown below:

1) Determine and compare the behaviour and the selective adsorptive capabilities of CO_2 between different chemical activation methods.
2) Determine and compare the effectiveness of chemical activation via KOH and $ZnCl_2$ in the selective adsorption of CO_2.

PKS are a product of the oil palm industry and have regularly been used as a source of fuel to generate steam and/or electricity for mill processes (Elham, 2001). The Department of Statistics of Malaysia, Statistics of Oil Palm, Coconut, Tea and Cocoa estimated that the oil palm industry produced annually about 1.44 million tonnes of PKS as waste (Salleh, 2010). Therefore, to help minimise wastage produced by the oil palm industry as a result of supply exceeding that of the demand, the possiblities of PKS for other uses must be explored, especially since it is easily available to obtain (Salleh, 2010). Its availability in Malaysia is demonstrated by the fact that about 4.98 Mt/yr is produced. PKS are made up of high carbonaceous material (which forms charcoal after thermal work is applied) as well as a number of volatile compounds such as methanol, phenol, acetic acid, gases, etc. PKS charcoal has low ash content/inorganic content (2.5%), adequate hardness and a fairly high fixed carbon (35.09%) (Elham, 2001). These properties make PKS a suitable charcoal, which can in turn form an excellent activated carbon adsorber (Elham, 2001). An

instance of the effectiveness of PKS activated carbon in the selective adsorption of CO_2 is shown in the fact that the adsorption capacity is 36% greater than that of the palm kernel chars.

The potential of PKS activated carbons in the selective adsorption of CO_2 must be further explored in order to find more ways to further maximise the selective adsorption capabilities using a resource such as PKS. A starting point to this would be to find ways to develop and improve the Brunauer-Emmett-Teller (BET) surface area, porosity, in particular the microporosity, as well as the surface chemistry of the activated carbon sample, in this case it will be PKS (Nasri et al. 2014).

Many technologies are employed in the removal of CO_2 such as freeze drying, chemical separations such as absorption, membrane separation and adsorption (Lee et al. 2013). The prominent and commonly used method of CO_2 capture used in industries in this day and age is the absorption of CO_2 using amines (Nasri et al. 2014). The other means include using adsorbers such as silica, metal oxides, metallic oxide frameworks, zeolites and activated carbons (Nasri et al. 2014).

Adsorption should be the direction that should be looked into as liquid absorption using amines can have great energy demands and deterioration of the amine solvent and absorption can occur (Nasri et al. 2014). In terms of adsorption, it is a good idea to rely more on activated carbons as opposed to the other methods as they are more expensive, often requiring multiple fabrication procedure as well as diminishing in adsorption capacities after repeated runs (Nasri et al. 2014).

Physical, chemical and physiochemical activation is employed to increase the number of pores of the AC, as well as increase the size of the existing pores necessary for adsorption (Titirici, 2005). The three types of pores that develop in the AC are micropore (<2 nm), mesopore (2–50 nm) and macropore (>50 nm). The size and amount of pores present in the AC will affect its overall porosity, the total surface area that is available for adsorption as well as the size of molecules that can diffuse into the solid (Nasri et al. 2014). Generally, the total porous volumes in activated carbons are comprised of microporous and mesoporous volumes (Purnomo et al.2012). For the most part, gaseous pollutants are able to occupy space in the micropore region, (i.e. <2nm), thus, activated carbons can sufficiently adsorb them (Mohamad Nor et al. 2013). This suggests that the focus is in making sure that the microporosity of the system is more developed than the mesoporosity of the system.

In terms of physical activation, the use of steam is able to yield activated carbon with a relatively greater surface area than using CO_2 due to the smaller molecular volume of water that is able to better diffuse within the available pores in the char. The effectiveness of steam activation can be seen in the fact that the activation process is two or three times faster than using CO_2, assuming the same conversion (Mohamad Nor et al. 2013). However, a study on physical activation demonstrated that using a carbon dioxide stream the activation process promoted the development of microporosity, whereas the use of steam enhanced the mesoporosity (Jung et al. 2014).

When referring to chemical activation, it involves the usage chemicals such as acids, bases, or salts that are impregnated in the raw material. This is followed by

washing to remove the chemical activating agent and the inorganic reaction products, and then heat treatment occurs right after (Titirici, 2005). Another way chemical activation occurs is by having carbonisation take place first, followed by chemical impregnation and activation (Abechi et al. 2013). It is important to note that no results indicate which method gives a better outcome in terms of the selective adsorption of CO_2, therefore the area of chemical activation sequence should be further investigated. The chemicals that work best for CO_2 adsorption include KOH and amines (Chuang, 2008). It is also shown that zinc (II) chloride ($ZnCl_2$) has been used with PKS to selectively adsorb methane, another gaseous pollutant (Arami-Niya et al. 2010). The possibility of $ZnCl_2$ as an activation chemical in the selective adsorption of CO_2 should be looked into.

The impregnation of chemicals such as KOH into activated carbons works because it helps fragment the cellulose and other components of the raw material, which include hemicellulose and lignin (Titirici, 2005). KOH impregnation causes the removal of carbon atoms from the carbon matrix to form carbonates, as well as the reduction of the hydroxide forming metal atoms (Titirici, 2005) help to increase the micro pore volume which proves useful in the selective adsorption of CO_2.

Similar to KOH, $ZnCl_2$ is also a dehydrating agent for the raw materials as it greatly influences the heat treatment that follows after. This is because tars are less likely to be formed during the carbonisation phase, thus generating more yield and porosity in the activated carbon sample (Arami-Niya et al. 2010). It also allows for greater movement of the volatile compounds between the pores in the raw sample, which allows for greater amounts of these compounds to be released (Arami-Niya et al. 2010). This is because the activation expands the raw material, breaking the lateral bonding within the sample, which creates cavities that develop the microporosity as mentioned earlier (Yahya et al. 2015). On top of that, using $ZnCl_2$ stabilises the volatile matter in the raw sample, thus providing a higher carbon yield (Yahya et al. 2015). It is shown that a $ZnCl_2$ to PKS weight ratio that ranges from 0.15g:1g to 0.53g:1g gives the most micropores, while a higher ratio can decrease the number of micropores formed (Arami-Niya et al. 2010). Even though KOH is more frequently used than $ZnCl_2$ in chemical activation as it is more environmentally friendly (Abechi et al. 2013), it is yet to show its usefulness in the selective adsorption of CO_2.

Between physical and chemical activation processes, chemical activation is the preferred choice as typically it uses lower temperatures, lower heat treatment times. Besides that, it only consists of one stage and the yields for selective adsorption are usually higher (Titirici, 2005). However, the disadvantage that comes with chemical activation is that additional cleaning and washing treatment is usually required after the heat treatment, especially in order to manage the high levels of acidity or alkalinity that is present in the activated carbon sample (Titirici, 2005). Also, secondary pollution becomes commonplace with chemical activation, especially when the column needs to be replaced (Rashidi et al. 2012).

2. Methodology

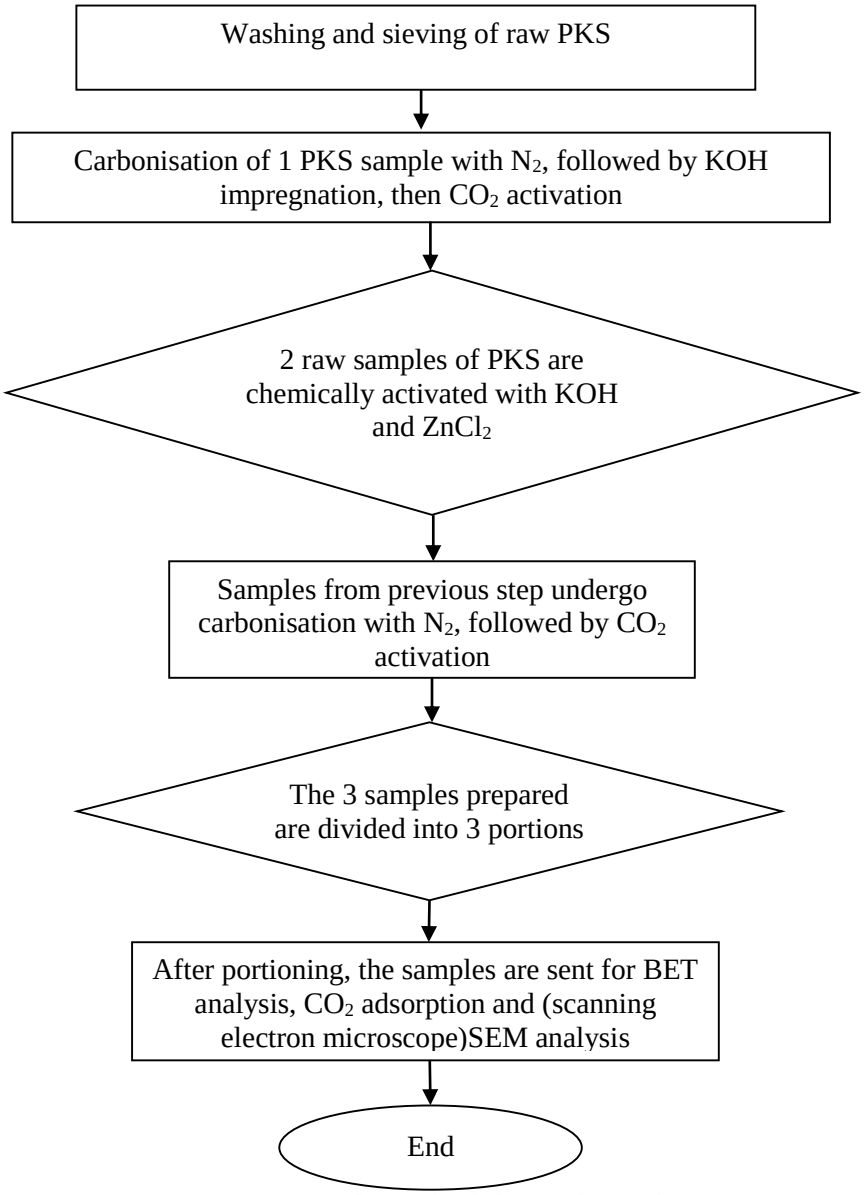


Figure 1: Research Methodology Flow Chart

Figure 1 shows the flowchart of the research methodology involved with this project. This flowchart will be referenced throughout the methodology portion.

2.1 Preparation of activated carbon samples

As shown in Figure 1, the raw PKS was washed with distilled water thoroughly in order to get rid of foreign substances, such as dust and dirt. To ensure the purity of the samples, the distilled water had to have no visible dust or dirt after washing. Then, the sample was dried at 105 ℃ for 24 hours in an oven to remove any remaining water content in the char (Arami-Niya et al. 2012). It was important to ensure that the char is as pure as possible so as to not impede on the adsorption capability. While prior research of this nature suggested to grind the char samples to approximately 2mm, this was not be practical as incidents of the available adsorption column failing due to adsorbents being too small for the column have been noted,

therefore it was wise to make sure this was not repeated. So in order to maintain consistency, the dried PKS samples were sieved to obtain raw samples that were 4mm and higher.

Then, a sample of raw PKS went through carbonisation using N_2 at 400 ℃ for 1 hour at a heating rate of 15 ℃/min. After that, KOH solution was mixed with the char at a KOH pellet to charcoal ratio of 3:1 by weight (Titirici, 2005) and a PKS to KOH solution ratio of 20g:200cm^3 was used (Abechi et al. 2013). This was to better develop the microporosity of the PKS sample (Purnomo et al. 2012). This mixture was stirred at 80 ℃ for 2 hours, drained, and left to dry at a temperature of 105 ℃ for 24 hours to remove excess moisture from the mixture with the help of an oven. After that, the char went through activation with a CO_2 stream at 800 ℃ for 45 minutes at a heating rate of 15 ℃/min. It was important to make sure that the temperature and time stayed at these values as great decrements in yield percentage could occur due to excessive burn-off (Abechi et al. 2013). After this was done, the solid mixture was washed with distilled water to minimize the alkalinity of the solid mixture, and left to dry at 120 ℃ overnight in an oven (Abechi et al. 2013). This sample was labelled as K1.

Then, 2 raw samples of PKS were impregnated with KOH and $ZnCl_2$ solution. While the impregnation of KOH remains the same as the previous sample, the $ZnCl_2$ to PKS ratio used was 0.5g:1g and the $ZnCl_2$ solution to PKS ratio was 2ml:1g. Once these samples were prepared, they went through the same carbonisation and activation steps as done with sample K1, with carbonisation occurring before activation. The sample that was impregnated with KOH was labelled K2, while the sample activated with $ZnCl_2$ was labelled Z1. With this step completed, the three AC samples developed were each divided into three portions for BET analysis, CO_2 adsorption and SEM analysis.

2.2 Analysis of Results

Once these samples were prepared, they were then sent to a separate lab where BET analysis, CO_2 adsorption and SEM analysis were be done, as the apparatus needed for the analysis was not readily available in the university. This was done to obtain quantitative and qualitative results with regards to the selective adsorption of CO_2.

The BET test was conducted using N_2 adsorption at 77 K with the help of the Micromeritics ASAP 2020 Analyzer. The focus of the BET analysis was to obtain data which included the micro pores size and surface area of the samples. These values were obtained via an N_2 adsorption and desorption cycle (Arami-Niya et al. 2010).

Then, the samples went through the CO_2 capture process, where a small amount of the prepared sample was heated up to a desired temperature and under a desired constant flow rate of N_2 gas for a specific amount of time. This test was run with the help of the Micromeritics 3Flex Version 3.01. After this time, the N_2 gas flow was switched off and CO_2 gas flow under the same conditions was turned on for a specific amount of time for adsorption to occur. Once the adsorption phase was

completed, desorption takes place with N_2 gas under the same conditions with a specified time span.

SEM analysis was done to obtain more qualitative data. This would relate the pore structures and surface of the activated sample to the amount of CO_2 adsorbed. To run this analysis, the samples were placed in an aluminium tub to ensure that electrons can reflect to provide sufficient data (Mohd Din et al. 2009).

3. Results and Discussion

The result and discussion section is divided into four main sections which include CO_2 adsorption capacity, BET analysis, SEM analysis and burn-off and yield analysis. This is done in order to elaborate on the qualitative and quantitative data pertaining to the samples prepared with regards to selective CO_2 adsorption, especially for samples K1 and Z1 as K2 was not prepared yet.

3.1 CO_2 Adsorption Performance

Figure 4.3 shows the isothermal linear plot, which plots the amount of CO_2 adsorb against the relative pressure of the CO_2 stream, under a constant temperature of 0 ℃. While both samples show a similar behavior, it is shown that sample K1 has a higher uptake of CO_2 than that of sample Z1 as shown by the greater slope in the graph formed. It also shows that at a relative pressure of 0.03, sample K1 has 86.45cm^3/g of CO_2 adsorbed while sample Z1 has 57.65 cm^3/g of CO_2 adsorbed. Where this is concerned, previous literature showed that physically activated palm kernel shells at the same relative pressure adsorbed 36.9cm^3/g of CO_2 (Nasri et al. 2014), which is significantly lower than that what was obtained from the analysis of both samples. This shows that the results are consistent with the literature as chemical impregnation was used for both samples, which gives the samples a higher adsorption capacity for CO_2. This also shows the effectiveness of $ZnCl_2$ in developing activated carbons for CO_2 adsorption.

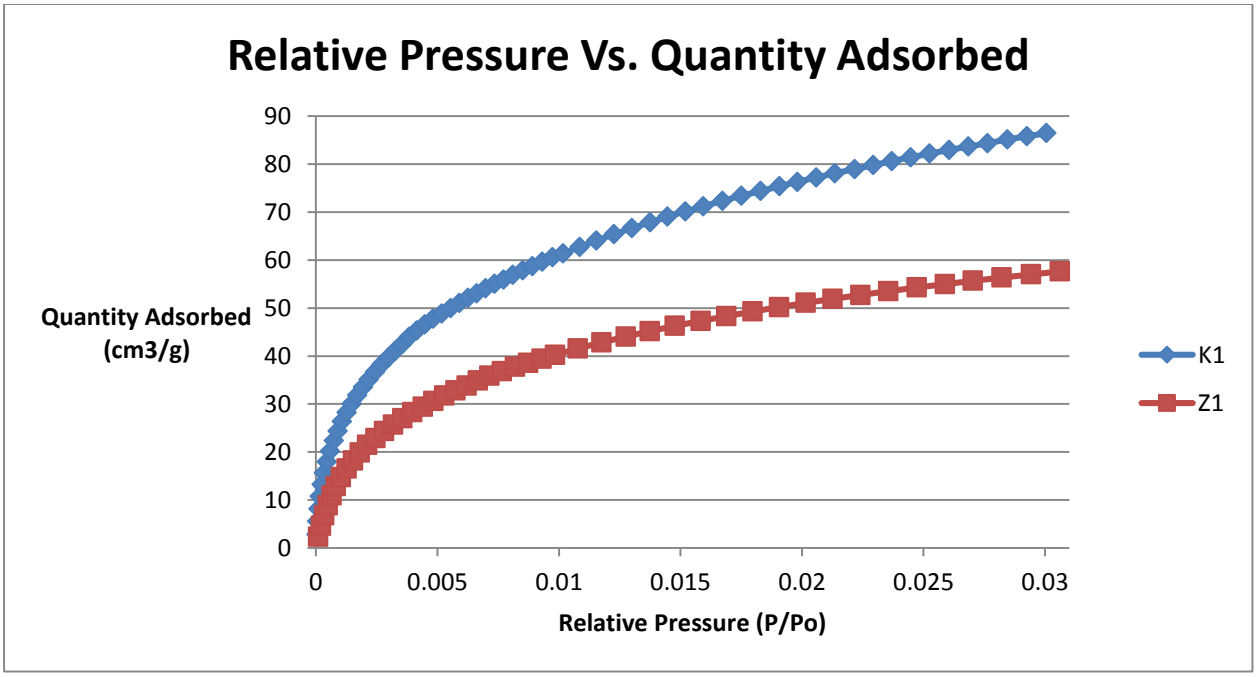


Figure 2: Graph of Relative Pressure Vs. Quantity Adsorbed

Besides this, it is shown that K1 has a wt% CO_2 of 16.974 at a relative pressure of 0.03 while Z1 has a wt% CO_2 of 11.32 at the same relative pressure as shown in Table 1. This either shows that K1 has a microporosity that is more developed or that there are interferences in the pores of Z1, likely due to zinc deposits. Since both values are close, it shows once again the potential of $ZnCl_2$ in developing highly porous activated carbons.

Table 1. BET test results for sample K1 and Z1

Relative Pressure (P/P_0)	Weight (%)	
0.03	K1	Z1
	16.97	11.32

3.2 BET analysis

From the BET study conducted, results such as BET surface area (S_{BET}), total pore volume (V_{total}) as well as micropore (V_{micro}) and mesopore (V_{meso}) volume was listed in the table in order to study the changes in pore characteristics of both samples. From the data as shown in Table 4.2, a S_{BET} of 621.323 m^2/g and 352.657 m^2/g are obtained for both K1 and Z1 samples respectively. For sample Z1, the sample seems to have a BET surface area that has a significantly lower value than 1307.7m^2/g, which was the value obtained from previous literature (Arami-Niya et al. 2010). This is likely due to the greater release of volatiles in the precursor based on the chemical impregnation used in the preparation (Arami-Niya et al. 2010). It also shows micropore area of K1 and Z1, which are 472.3538 m^3/g and 304.2301 m^3/g respectively, as well as a V_{micro} of K1 and Z1, which are 0.189650 cm^3/g and 0.120862 cm^3/g respectively based on a t-plot. For sample K1, the V_{micro} obtained is greater than that which was obtained in the literature involving activated carbons of the same nature, which was 0.063cm^3/g (Abechi et al. 2013). This is because the literature used a smaller impregnation ratio than what is used in sample K1, thus the results obtained are consistent. For sample Z1, the V_{micro} obtained is smaller than that which was obtained in the literature involving activated carbons of the same nature, which was 0.67m^3/g (Arami-Niya et al. 2010). This suggests that there are major interferences in the pores of sample Z1, likely from metallic deposits from the chemical impregnation, such as zinc. Another source of interference can likely be due to the fact that the N_2 flow rate used was too fast. This results in the flowing gas having insufficient contact time with the raw precursor, resulting in incomplete release of volatile matter from the precursor (Lua et al. 2001). Knowing this, it is best to ensure that the flow rate is kept at 300cm^3/min (Foo & Hameed 2013).

From the analysis, it is also shown that based on the graph of incremental pore volume against pore width shown in Figure 2, the majority of the pore volume for both samples fall under the pore width of 8.58 angstrom based on the highest peaks of both samples (0.057 cm^3/g and 0.04154cm^3/g for K1 and Z1 respectively. This shows that both samples are highly microporous (pore width<2nm or 20 angstrom). It is important to note that both K1 and Z1 have an additional high peak at a pore width of 15.91 angstrom, with Z1 having a higher pore volume value (0.03354cm^3/g) at this additional peak than K1 (0.00902cm^3/g). This further suggests a greater micropore

structure for both samples. Also based on this graph, it can be seen that K1 has a higher mesoporosity than Z1 as the pore volumes are much higher at pore widths greater than 20 angstrom. The presence of mesopores in this instance is likely due to the activating agent breaking down the pore walls whilst serving its purposes of removing the volatiles from the precursor (Ting et al. 2014). This goes to show that K1 has a higher overall porosity than Z1.

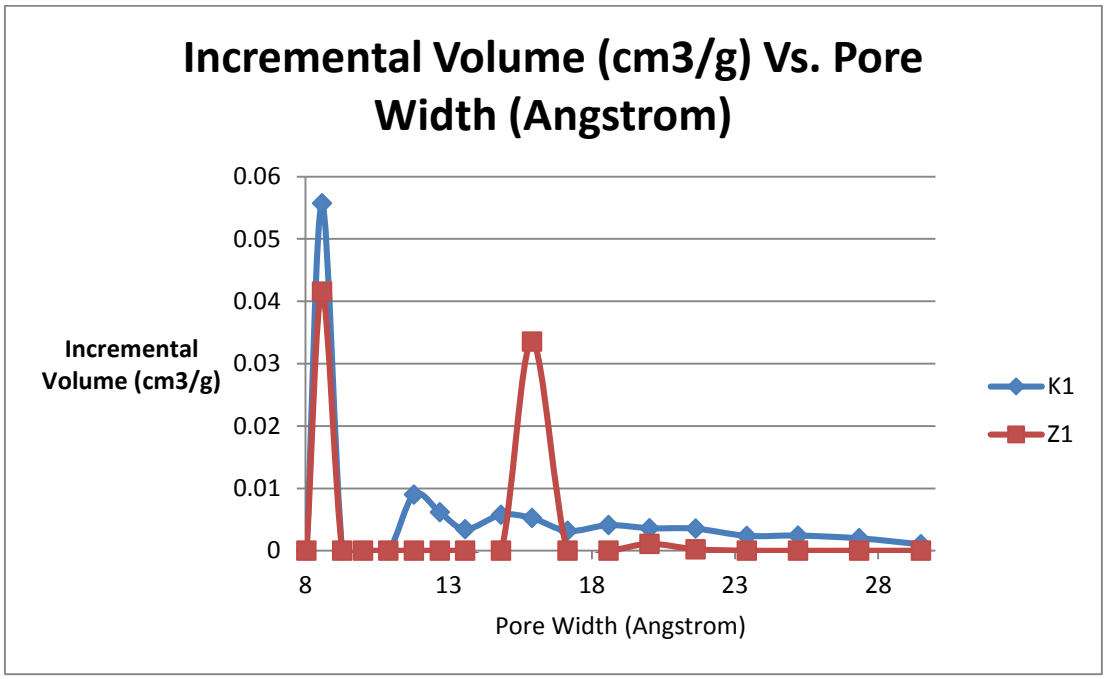


Figure 3: Graph of Incremental Volume Vs. Pore Width

Table 2 shows a summary of the results obtained from the BET analysis. This easily suggests that K1 has a larger surface area as well as microporosity. However, the likelihood of interferences in sample Z1 is also shown as the difference in values are very great.

Table 2. BET test results for sample K1 and Z1

Carbon Parameters	K1	Z1
Total Surface Area, S_{BET} (m^2/g)	621.323	352.657
Micropores Volume, V_{micro} (cm^3/g)	0.18965	0.0070
Micropore Area (m^2/g)	472.3538	304.2301
Average Pore Diameter, D_{avg} (Angtrom)	8.58	8.58

3.3 SEM analysis

Figure 4.8 shows the SEM photograph of sample K1. From the photograph, it can be seen that the surface of the sample has a well distributed honeycomb structure. This result is consistent with past literature that shows SEM photographs of PKS activated with the same procedure (Abechi et al. 2013). This already shows that KOH and CO_2 are useful in obtaining activated carbon samples with well-developed pores on its surface, leading to a high adsorption capacity of CO_2, which is also consistent with previous literature (TAN et al. 2008).

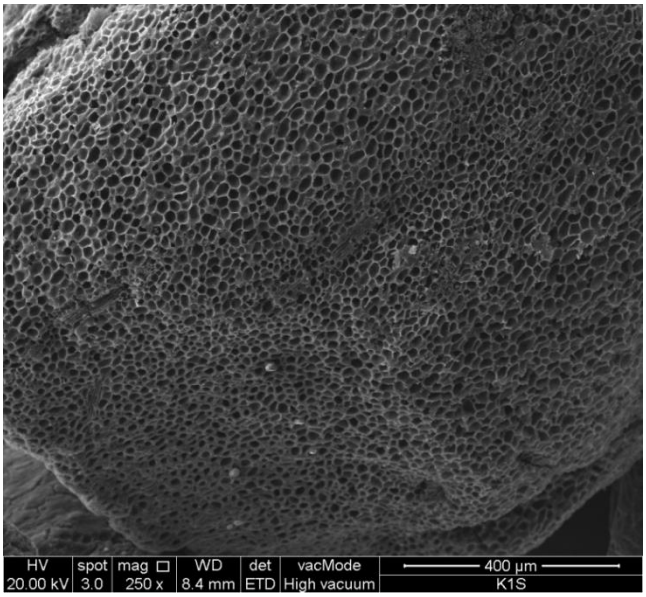


Figure 4.8: SEM photograph of sample K1

Figure 4.9 shows the SEM photograph of sample Z1. From the photograph, it is seen that the overall porosity and the development of the porosity is weaker than that of sample K1. However, it is important to note that large amounts of white deposits were found in the available pores of the sample. This is likely due to the formation of zinc deposits in the sample which were not washed off after the chemical activation. Had more time and focus been allocated to removing the zinc deposits after chemical activation, the CO_2 adsorption capabilities as well as the BET surface areas might change slightly and reflect the results shown in the literature discussed previously.

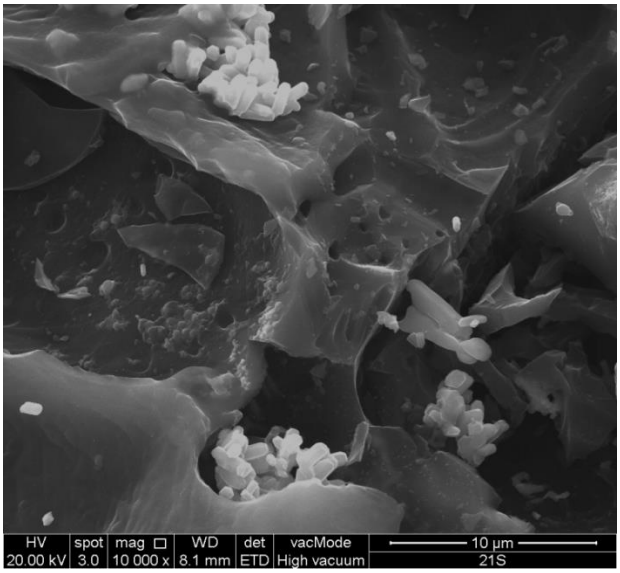


Figure 4.9: SEM photograph of sample Z1

3.4 Burn-off

From Table 1, it can be seen that sample K1 has the highest burn-off percentage. This means that the yield of the sample produced is also the lowest. This shows that $ZnCl_2$ is more useful at developing activated carbons of higher yield. The yield of sample K1 is much lower than 19.2%, which was the yield obtained in previous literature (TAN et al. 2008). This is likely because of the much higher flow rate of N_2 gas during carbonization. As discussed earlier, this likely caused the incomplete release of volatile matter and the formation of tars on the sample (Lua et. al. 2001). It is important to note that the burn-off of sample Z1 is significantly higher than that which was suggested by previous literature, which stated that a sample with a $ZnCl_2$ to PKS ratio of 0.15, that undergoes CO_2 activation after, has a burn-off percentage of 0% (Arami-Niya et al. 2010). This is likely because the impregnation ratio used in the literature was too low to have an effect on the sample and develop the microporosity, thus making physical activation more difficult to conduct.

Table 1. Burn-off for samples prepared

Sample	Initial raw weight (g)	Initial char weight(g)	Final weight(g)	Burn-off(%)	Yield (%)
K1	22.93	9.64	1.69	82.46887967	7.370257
Z1	13.92	13.64	5.25	61.51026393	37.71552

4. Conclusion

In conducting this project, the results obtained indicate that K1 could adsorb more CO_2 than Z1 due to greater BET surface area and microporosity, which was also affirmed by the honeycomb structure of the pores. However, more focus and time should have been placed on the cleaning of sample Z1 after chemical activation as metallic deposits were likely major contributors to blockages in the pores of the sample.

References

Abanades, J. C, et al., 2005. *Carbon Dioxide Capture and Storage: Summary for Policymakers*. Montreal: Intergovernmental Panel on Climate Change.

Abechi, S.E. et al., 2013. Preparation and Characterization of Activated Carbon from Palm Kernel Shell by Chemical Activation. *Research Journal of Chemical Sciences*, 3(7), pp.54–61.

Arami-Niya, A. et al., 2012. Production of microporous palm shell based activated carbon for methane adsorption: Modeling and optimization using response surface methodology. *Chemical Engineering Research and Design*, 90(6), pp.776–784. Available at: http://www.sciencedirect.com/science/article/pii/S0263876211003868 [Accessed June 1, 2015].

Arami-Niya, A., Daud, W.M.A.W. & Mjalli, F.S., 2010. Using granular activated carbon prepared from oil palm shell by ZnCl2 and physical activation for methane adsorption. *Journal of Analytical and Applied Pyrolysis*, 89(2), pp.197–203. Available at: http://www.sciencedirect.com/science/article/pii/S0165237010001178 [Accessed September 28, 2015].

Foo, K.Y. & Hameed, B.H., 2013. Utilization of oil palm biodiesel solid residue as renewable sources for preparation of granular activated carbon by microwave induced KOH activation. *Bioresource technology*, 130, pp.696–702. Available at: http://www.sciencedirect.com/science/article/pii/S0960852412018500 [Accessed May 23, 2015].

Jung, S.-H. et al., 2014. Production and characterization of microporous activated carbons and metallurgical bio-coke from waste shell biomass. *Journal of Analytical and Applied Pyrolysis*, 109, pp.123–131. Available at: http://www.sciencedirect.com/science/article/pii/S0165237014001624 [Accessed May 26, 2015].

Lee, C.S. et al., 2013. Impregnation of palm shell-based activated carbon with sterically hindered amines for CO2 adsorption. *Chemical Engineering Journal*, 219, pp.558–564. Available at: http://www.sciencedirect.com/science/article/pii/S1385894712014325 [Accessed May 8, 2015].

Mohamad Nor, N. et al., 2013. Synthesis of activated carbon from lignocellulosic biomass and its applications in air pollution control—a review. *Journal of Environmental Chemical Engineering*, 1(4), pp.658–666. Available at: http://www.sciencedirect.com/science/article/pii/S2213343713001826 [Accessed March 6, 2015].

Mohd Din, A.T., Hameed, B.H. & Ahmad, A.L., 2009. Batch adsorption of phenol onto physiochemical-activated coconut shell. *Journal of hazardous materials*, 161(2-3), pp.1522–9. Available at: http://www.sciencedirect.com/science/article/pii/S0304389408006808 [Accessed May 2, 2015].

Nasri, N.S. et al., 2014. Assessment of porous carbons derived from sustainable palm solid waste for carbon dioxide capture. *Journal of Cleaner Production*, 71, pp.148–157. Available at: http://www.sciencedirect.com/science/article/pii/S095965261300824X [Accessed April 2, 2015].

Rashidi, N.A. et al., 2012. Activated Carbon from the Renewable Agricultural Residues Using Single Step Physical Activation: A Preliminary Analysis. *APCBEE Procedia*, 3, pp.84–92. Available at:

http://www.sciencedirect.com/science/article/pii/S2212670812001224 [Accessed June 1, 2015].

TAN, I., AHMAD, A. & HAMEED, B., 2008. Optimization of preparation conditions for activated carbons from coconut husk using response surface methodology. *Chemical Engineering Journal*, 137(3), pp.462–470. Available at: http://www.sciencedirect.com/science/article/pii/S1385894707003075 [Accessed April 3, 2015].

Ting, L. et al., 2014. Activated carbon fibre - The hybrid of carbon fibre and activated carbon. *Review on Advanced Material Science*, 36, pp.118–136. Available at: http://www.ipme.ru/e-journals/RAMS/no_23614/03_23614_lee.pdf [Accessed November 13, 2015].

Yahya, M.A., Al-Qodah, Z. & Ngah, C.W.Z., 2015. Agricultural bio-waste materials as potential sustainable precursors used for activated carbon production: A review. *Renewable and Sustainable Energy Reviews*, 46, pp.218–235. Available at: http://www.sciencedirect.com/science/article/pii/S1364032115001392 [Accessed March 23, 2015].

Signal Processing for Feature Extraction

Quah Pooi Chi, Leong Wai Yie
School of Engineering, Taylor's University, Malaysia
PooiChi.Quah@sd.taylors.edu.my, WaiYie.Leong@taylors.edu.my

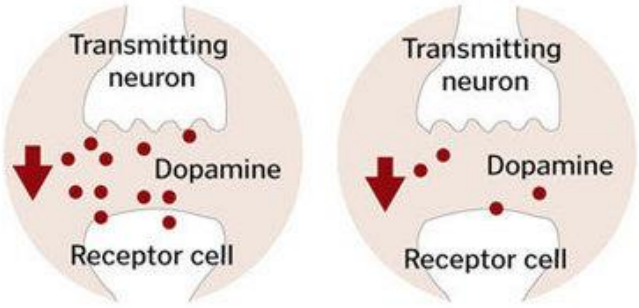
Abstract

Parkinson's disease (PD) is a growing disease in Malaysia. This disease affects mostly elderly people aged around 60 and above. Men are one and half times more likely to have PD than women. Many do not realise until they are diagnosed with PD. An estimated of 7 to 10 million people worldwide are living with PD. The loss of dopamine in substantia nigra in the brain is the main cause of PD. Insomnia and Bradykinesia are the most common symptoms for every PD patient. These symptoms affect their quality of life. A total of 49 participants took part in an experiment where 21 of them were healthy participants and 24 of them were PD patients. Out of these 24 PD patients, 15 suffered from Bradykinesia and 9 experienced Insomnia. Electroencephalogram (EEG) was used extensively to collect data. The data were then processed and evaluated using Haar and Daubechies wavelet to segregate PD patients from healthy adults. Index of Orthogonatility and distortion measurement were calculated to compare the performance of Haar and Daubechies wavelet. Beisde that, Discrete Wavelet Transform (DWT) was used together with the Haar and Daubechies properties to decompose the signals and extract features. The expected outcome for this project is mainly to have a better recognition of the signals collected from PD patients and to identify the similar features in the signals.

Keyword: Parkinson's disease, Electroencephalogram (EEG), Insomnia, Bradykinesia, Feature Extraction, Wavelet Transform

1. Introduction

Parkinson's disease (PD) is a common disorder of the nervous system that affects people later in their lives with tremors, movement instability and rigidity in their limbs. The true reasons for causing PD is still unknown, but many experts and researchers believe that PD could be caused by factors such as genetic, environment, drugs or repeated head injuries. [1]. However, PD was characterised primarily by the damage in the substantia nigra (SN) which lead to high chances of contracting PD [2, 3]. Symptoms of PD can be classified into two different categories, motor symptoms and non-motor symptoms. The loss of dopamine in SN causes motor symptoms which affects the mobility of the patients such as tremor, slowness and stiffness. Bradykinesia is one of the common symptoms in motor symptoms category. Bradykinesia means slow movement that affects the patient's mobility and causes difficulty in the person's walking stride. Patients suffer from Bradykinesia mostly walk in a very slow pace because it reduces the synchronous movement between the legs and the body and the chances of falling are higher than healthy adults [4, 5]. Figure 1 shows the comparison of the amount of Dopamine between healthy patient and Parkinson's Disease patient. Healthy patient has considerable more Dopamine compared to Parkinson's Disease patient.



Healthy Patient Parkinson's Patient

Figure 1. Compare the amount of Dopamine between healthy patient and Parkinson's Disease Patient [10].

Besides motor symptoms, non-motor symptoms such as constipation, insomnia, mood disorders and orthostatic hypotension may happen in the early stages of PD [6]. These symptoms are more serious than the motor symptoms because non-motor symptoms cannot be observe easily. Insomnia happens in the early stages of PD even before motor symptoms appear and according to Jerry Siegel [7], his study discovered that patient with PD and narcolepsy are likely linked together as both show the symptoms of lack of hypocretin (Hcrt) cells in the brain.

It is estimated that most PD patients are aged between 50 – 90 [8, 9] and according to a Dutch study [11], there are 1.4% of chances of getting PD for those aged between 55 to 60 years old and 4.3% for those who aged between 85 to 94 years old. Currently, there is no lab test available to diagnose PD but only positron emission tomography (PET) scan is available to do the imaging test to identify the low level of dopamine in the brain which is the key of developing PD. Currently not many clinics or hospitals employ PET scan as the cost is still prohibitive [12]. A more common and cheaper diagnosis method available now for PD is neurological interview; any neurologists normally can do this by observing the patients' movement, coordination and balance. The diagnosis might also include some mental and emotional tests [13 -

14]. However, these diagnoses are judgmental in nature and the results might not be very accurate.

Thus, in order to obtain more accurate results which involve less subjectivity in the diagnosis, for this project, Electroencephalogram (EEG) was used on PD patients to analyse their brain waves and compare to healthy adults. According to Harrison [15], the first EEG of human brain was created in Jena, Germany by a German psychiatrist, Hans Berger, in 1924. EEG is able to record and measures three kinds of activities, which are bioelectrical events produced by a single neuron, spontaneous activity and evoked potentials. Figure 2 shows the 10 – 20 international electrodes placements system that are used to capture EEG from PD patients [15]. As for this study, 3 EEG channels were used which are F3 or F4, C3 or C4 and O1 or O2, referred to A1 or A2.

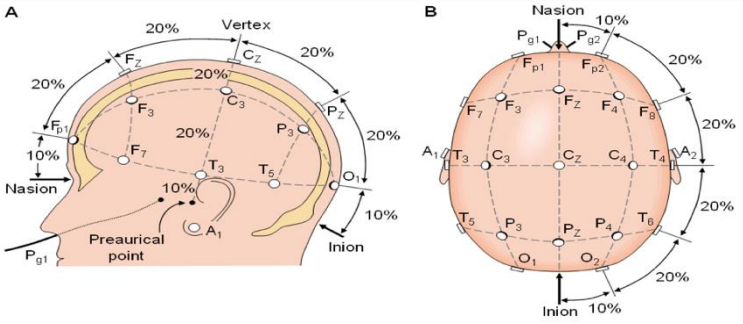


Figure 2. 10 - 20 International Electrodes Placement [15]

2. Literature Review

Neurological interview is the most commonly used method to diagnose PD patients. Unified Parkinson's disease Rating Scale (UPDRS) is the most popular tool in neurological interview [16 - 17]. UPDRS is a complete set of tool to determine the stages of the PD that consists of motor test, non-motor test and Activity Daily Living (ADL) test. Table 1 shows the PD progression stages [18 - 19]. However, the test results are very subjective because they rely fully on the experience of the neurologist [20].

Table 1. Parkinson's Disease Progression [19]

Stages	Description
Stage 0	No signs of disease
Stage 1	Unilateral disease
Stage 1.5	Unilateral disease plus axial involvement
Stage 2	Bilateral disease, without impaired balance
Stage 2.5	Bilateral disease, with impaired balance
Stage 3	Mild to moderate bilateral disease, some postural instability; physically dependent
Stage 4	Severe disability; still able to walk or stand unassisted
Stage 5	Wheelchair-bound or bedridden

In a recent study by Costa et al. [21], Sample Entropy (SampEn) was introduced to replace Approximate Entropy (ApEn) in the field of biomedical signal

analysis due to the inadequacies found in ApEn such as prejudice and the full dependence on sample length. SampEn characterises the consistency of the stride signal and each of the coarse-grained time series was calculated to ease the understanding process for the dynamic properties of time-varying stride [22]. Based on M. Aboy [23], SamEn is much more suitable for biomedical signal analysis because it can avoid counting self-matches to eliminate the ApEn bias, independent on the time series length and is more consistent. Eq. (1) shows the mathematic form of SampEn where *m* is the embedding dimension, *r* is the tolerance, *N* is the data point, *A* is the number of template vector pairs that have $d[X_{m+1}(i), X_{m+1}(j)] <$ r of length $m+1$, B is the number of template vector pairs that have $d[X_m(i), X_m(j)] < r$ of length m.

$$SampEn(m, r, N) = -log\frac{A^m}{B^m} \tag{1}$$

Furthermore, based on Ari Ylikoski [24], PD patients share a lot of similar symptoms with narcolepsy patients. Narcolepsy disease patients are unable to control their sleep and wakefulness. They have symptoms of Rapid Eye movement (REM), sleep dysregulation, and sleep paralysis [25 - 26]. These symptoms are sleep related phenomena which are very similar to non-motor symptoms of PD. These are caused by the loss of Hcrt cell in the brain and base on Thannickal TC and Fronczek R [27 - 28], 28% of the Hcrt cell is loss in stage 1 and the loss keeps increasing until 68% in stage 4. The stages are measured on the Hoehn and Yahr rating scale [19].

3. Methodology

Wavelet transform (WT) was used as the main signal processing technique for this project. Base on S. Lütfü [29], WT is the most frequently used technique in engineering and biomedical field because it can be used to detect, classify and analyse nonlinear and non-stationary data. There are several wavelet functions available. However, Discrete Wavelet transform (DWT) was selected for this project together with the most popular wavelet properties, Haar and Daubechies wavelet.

3.1 Discrete Wavelet Transform (DWT)

Eq. (2) and Eq. (3) show the mathematical equations for Continuous Wavelet Transform (CWT) and DWT. The DWT only uses discrete value in the time-domain of the signal. The reason behind choosing DWT is because it is simpler to implement compared to CWT and DWT delivers informative data on both analysis and synthesis of the original signals within a short span of time [30].

$$\psi_{s,\tau} = \frac{1}{\sqrt{|s|}}\int x(t)\,\psi\left(\frac{t-\tau}{s}\right)dt \tag{2}$$

$$\psi_{m,n} = \frac{1}{\sqrt{a_o^m}}\left(\frac{t - nb_o a_o^m}{a_o^m}\right)dt \tag{3}$$

Eq. (2), the ψ is the mother wavelet, *s* is the scale factor, τ is the translation factor and the factor $s^{-1/2}$ is for energy normalisation across the different scales, *t* is the time sampling and let *x(t)* be the signal that will be analysed [30]. For Eq. (3), the ψ is the mother wavelet; *m* and *n* control the wavelet dilation and translation respectively,

$a_o > 1$ for specified fixed dilation step parameter and the $b_o > 0$ is the location parameter [30]. Figure 3 shows the level 3 Sub-band Coding Algorithm.

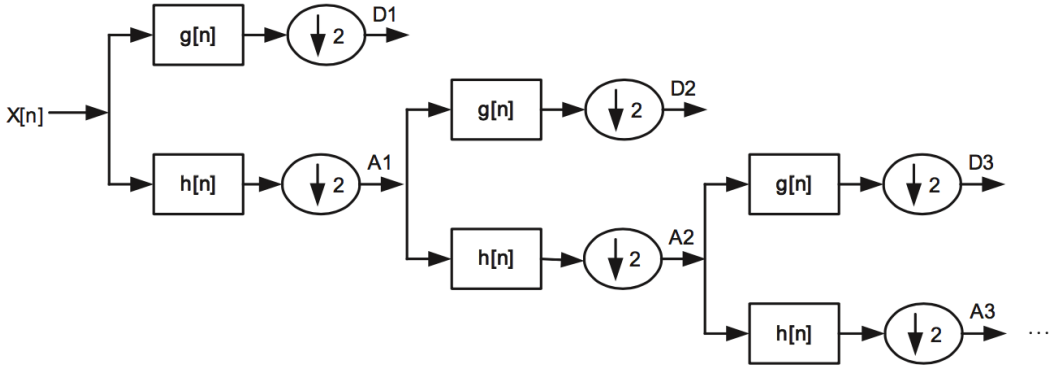


Figure 3: Level 3 Sub-band Decomposition of DWT [30]

3.2 Haar Wavelet

In 1909, the first DWT Haar wavelet was invented by Alfred Haar [30]. It uses scaling function together with wavelet to break up or reconstruct signal. Eq. (4), Eq. (5) and Eq. (6) show the wavelet analysis that are based on Haar wavelet scaling function.

$$\psi(x) = \begin{cases} 1, if\ 0 \le x < 1 \\ 0, \text{elsewhere} \end{cases} \tag{4}$$

$$\psi(x) = \begin{cases} 1, 0 \le x < \frac{1}{2} \\ -1, \frac{1}{2} \le x < 1 \\ 0, \text{otherwise} \end{cases} \tag{5}$$

$$\psi(x) = \emptyset(2x) - \emptyset(2x-1) \tag{6}$$

3.3 Daubechies Wavelet

In 1987, Daubechies Wavelet was invented by Ingrid Daubechies [30] and it is compactly supporting orthonormal wavelets and smoothness when processing the original signal so it makes discrete wavelet analysis practicable. For example, Eq. (7) shows the equation of Daubechies level 4 where ϕ is the scaling function [31].

$$\phi(x) = \frac{1+\sqrt{3}}{4}\phi(2x) + \frac{3+\sqrt{3}}{4}\phi(2x-1) + \frac{3+\sqrt{3}}{4}\phi(2x-1) + \frac{1-\sqrt{3}}{4}\phi(2x-1) \tag{7}$$

4. Experiment Setup



Figure 4: Flow chart for overall project.

Figure 4 shows the different stages required to be carried out in this project. The first stage is Data Collection for stride signal data and the sleep EEG signals. Data shared by Harvard Medical Faculty Care Group contained the stride time signal that they captured from a group of PD patients suffering from Bradykinesia. These 15 patients consist of 10 men and 5 women from the age of 44 to 79 years old with a mean age of 66.8. For comparison purpose, 16 healthy adults were asked to join in this experiment which included 2 men and 14 women from the age of 20 to 74 years old with a mean age of 39.9. The stride signals were obtained by placing eight force-sensitivity sensors under their feet.

Sleep EEG data for this project were obtained from a database provided by PhysioBank [32]. The database included EEG data from 9 patients, 4 males and 5 females form the age of 47 to 82 with a mean age of 60.8, suffering from Insomnia. For comparison purpose, a total of 9 healthy adults consist of 2 males and 7 females from the age of 23 to 42 with a mean age of 33.3 were used as a control group. Sleep EEG data were obtained by using the Activiwave EEG that are able to record various biomedical waveforms such as electromyography (EMG), electrocardiogram (ECG) and EEG. The placement of the electrodes used to capture the signals follow the 10 – 20 electrodes international placement system as shown in figure 2.

The second stage is the signal processing using different properties of Wavelet, Haar and Daubechies wavelet to extract the coefficients and features from the acquire signals. In this stage, Wavelet Toolbox in MATLAB® came into play. Wavelet Toolbox is packed with many wavelet-based algorithms for signal processing and signal extraction.

Numerical analysis for Haar and Daubechies Wavelet were computed in the Signal analysis stage. To check the efficiency and accuracy of a signal, the index of Orthogonality was used. Index of orthogonality checks for the signal leakage after the signals were processed. The higher the index of orthogonality, the higher the amount of data loss in a signal. In addition, distortion measurement was calculated to measure the performance for Haar and Daubechies Wavelet. Beside that, sleep bands were extracted using Daubechies Wavelet.

5. Result and Discussion

5.1 Index of Orthogonality

Data collected which is 15360 times of samples from C4 channel with 100Hz samples were used to run on Haar Wavelet and Daubechies Wavelet. Table 2 show the Index of Orthogonality of the algorithms.

Table 2. Index of Orthogonality for Haar and Daubechies Wavelet

Decomposition Method	Index of Orthogonality
Haar	0.9987
Daubechies	0.2097

For a better accuracy and efficiency of the results, the value of the index of orthogonality must be as close to zero as possible because the higher the value of index of orthogonality, the higher the data leakage. Table 2 shows that Haar have the most data leakage compared to Daubechies when decomposing those signals.

5.2 Stride Time Signal

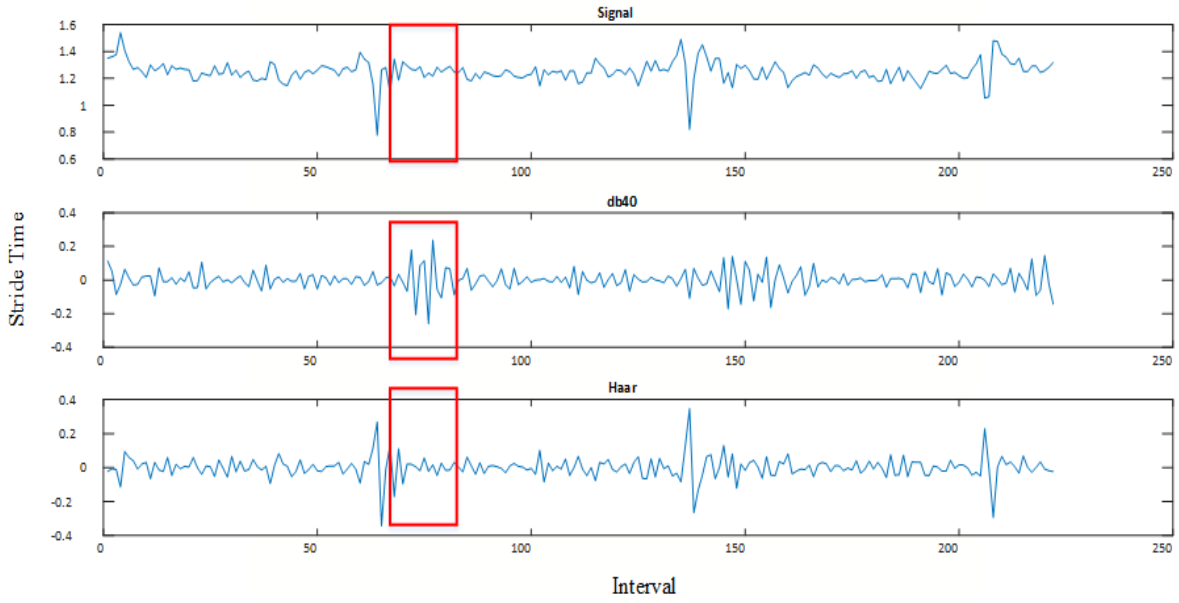


Figure 5. PD Patient Stride Time Signal

Figure 5 shows the stride time signal processed by the Haar and Daubachies Wavelet. It is clear that the original signals have very high and low amplitude and it it very difficult to analyse because the waveforms were not uniform. However, after applying the Haar and Daubechies Wavelet, it can be seen that the waveform has a minimum difference between the maximum and minimum peak. This means that the waveform is uniform compared to the original. There is obvious difference in the waveform by comparing the Haar and Daubachies wavelet. The red boxes in Figure 5 highlight the extra features from Daubachies Wavelet that have three peak regions compare to no peak in the Haar Wavelet. Thus, this can be concluded that Daubachies Wavelet retained more information compare to Haar Wavelet and this supports my initial result of Index of Orthogonality.

5.3 Sleep EEG

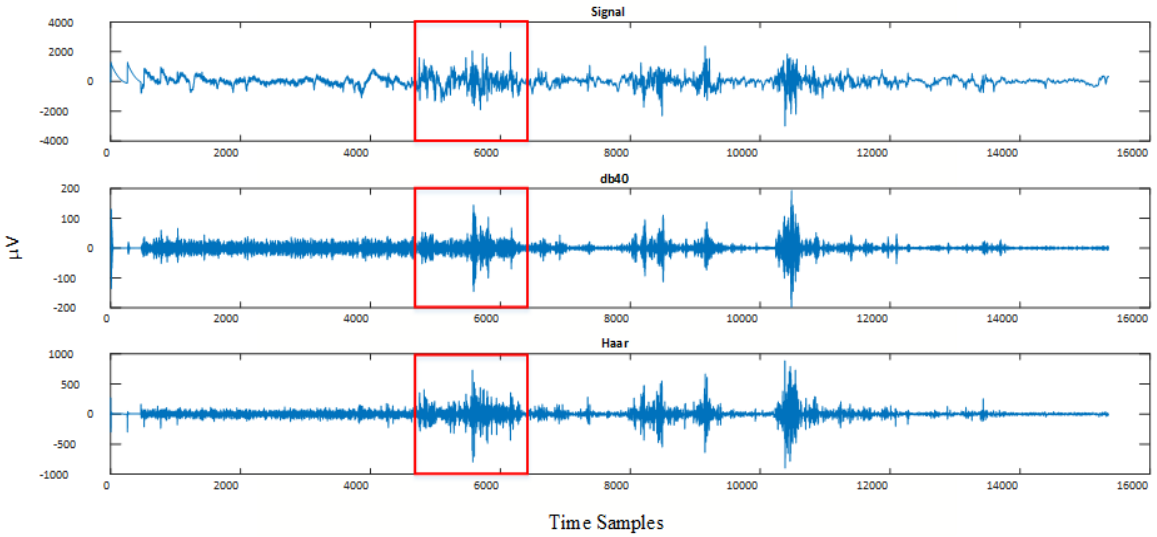


Figure 6.Insomnia EEG signals

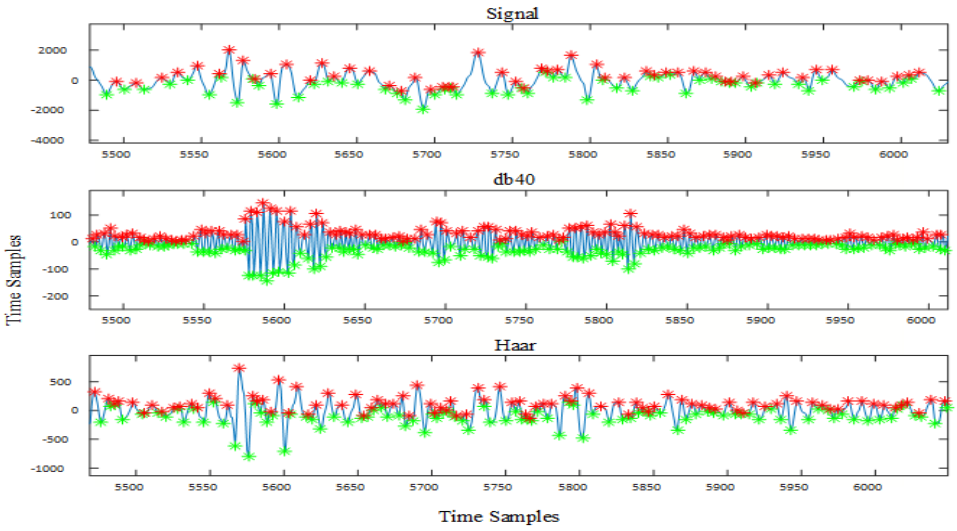


Figure 7. Zoomed Insomnia EEG signals with maxima and minima indication

Figure 6 shows the EEG data from a PD patient suffering from Insomnia. The red box highlights a part that has the most noticeable change in all the three signals. The original EEG contains local minima that are above zero and local maxima that are below zero. It means that the EEG waveform is very inconsistence and it is difficult to analyse the data. Figure 7 shows the zoomed insomnia EEG signals after applying the Haar Wavelet and Daubachies Wavelet. Improvement for all local maxima are above zero as indicated in red colour and local minima are below zero as indicated in green colour. Theses improvements decreased the amplitude and uniformed the waveform. From this result, Daubachies Wavelet has lower amplitude compared to Haar Wavelet which means Daubachies Wavelet waveform is much more uniform compared to Haar Wavelet. However, Haar Wavelet has higher peak region compared to Daubachies Wavelet. Hence, Daubachies has a uniform waveform but does not manage to retain the data.

5.4 Distortion Measurement

Nevertheless, one example will not be sufficient to make the conclusion. Thus Table 3 shows a set of more complete results for distortion measurement that include Energy Retainer, signal to noise ratio (SNR), standard deviation (SD), Cross Correlation and the execution time. SNR is the ratio between the signal strength and the noise cause by external interruption. SNR must be as high as possible. The higher the SNR, the higher is the signal efficiency. SD is to measure how much the signal fluctuates from the mean. Thus, lower SD means less signal fluctuation and more uniform signal. Cross-Correlation is to estimate the degree of two series signals. When the value is close to 1, there are similarity to each other. When the value is 0, it indicates no correlation between the two signals.

Table 3. Distortion Measurement

Transformer	Energy Retainer	SNR (db)	SD	Cross Correlation	Execution time(sec)
Haar	62.8779	13.3075	74.4938	0.153138	0.862
db10	70.2663	25.6716	17.9438	0.004212	0.256
db20	73.7798	26.5144	16.2844	0.010606	0.562
db30	75.6821	26.8055	15.7478	0.00108	0.637
db40	76.8615	26.9736	15.4458	0.003023	0.642

5.5 Sleep Band Extraction

Extracting sleep stages is a very common feature for sleep study. Wavelet will be used to extract the frequency bands of sleep from the original Sleep EEG data as shown in Figure 8. The reason to extract these data is to monitor the brain activities in different stages. Figure 8 shows the five stages of the sleep frequency bands.

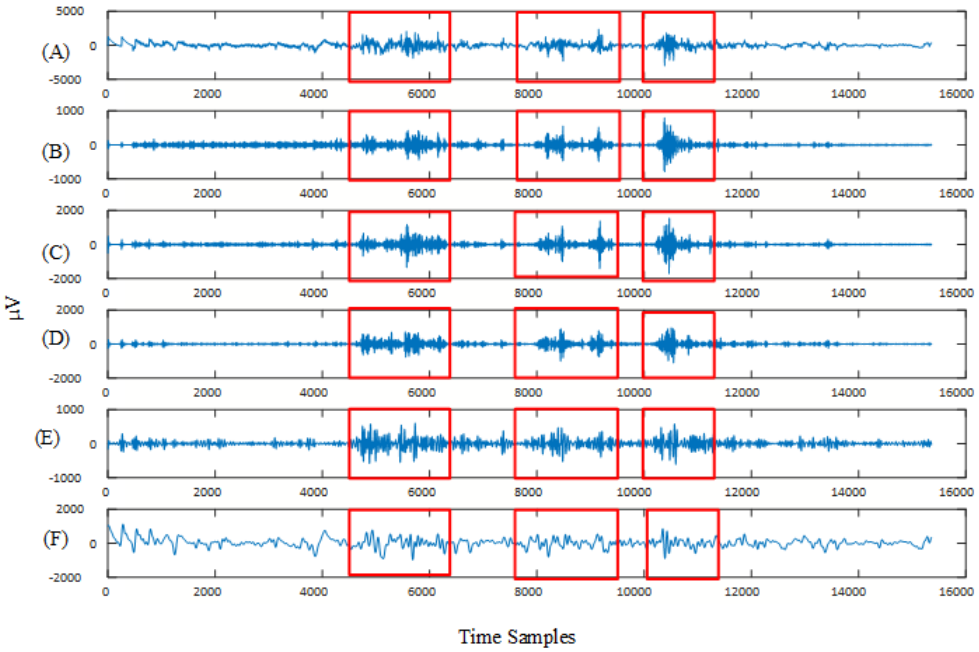


Figure 8. Frequency Bands for Sleep EEG

Daubechies wavelet filtered out the original EEG signal into half. Since the original sleep EEG signal from PD patient show in Fig.8 (A) is sampled at frequency is 100Hz, therefore, the frequency will be filtered from 100Hz to 50Hz for Gamma band (B), 50Hz to 25Hz for Beta band (C). For alpha band (D) is 25Hz to 12.5Hz and for Theta band (E) is 12.5Hz to 6.5Hz. Special case for the delta band (F) will be obtained from the reconstructed coefficient of the theta band. In addition, Fig. 8 also used the red box to highlight some features in the sleep band. Those features exist because of movement, dream or snoring while sleeping.Table 4 concludes the sleep stages of the PD patients after extracted the sleep EEG signal [33].

Table 4. Sleep stages [33]

Sleep Stages	Frequencies	Description
Awake	31-100Hz (Gamma Band) 16-30Hz (Beta Band)	At this stage, the patient is in a highly awake and consciousness state.
Stage 1 and 2	8-15Hz (Alpha Band)	At Alpha stage, the patient starts to enter sleep stage number 1. In this stage, the patient experiences drowsiness or pre-sleep. Slow rolling of eye movements will be exhibited in this stage.
Stage 3	4-7Hz (Theta band)	At Theta stage, the patient will be in a deep relaxation state. At this stage, the EEG signal will obviously show an appearance of the sleep spindles or some called it the K complexes. Therefore, spindle is the characteristic feature in stage 3.
Stage 4 and REM Stage	0.1-3Hz (Delta Band)	At Delta stage, the patient will be in a deep sleep and unconscious state and Rapid Eye movement (REM) will occur. When REM occurred, the patient's body will be well paralyzed and the patient will likely to have dreams. Desynchronised EEG is the characteristic featured in this stage.

6. Conclusions

This paper shows the signal processing using the Haar and Daubechies Wavelet. Both algorithms are used to analyse on the stride time signal that obtain from a PD patients suffer from Bradykinesia and sleep EEG signals from the PD patients suffer from Insomnia. The milestone achieved is associating the Index of Orthogonality, Energy retainer, SNR (db), standard deviation (SD), Cross Correlation and the execution time and sleep band. Both methods successfully show certain features regarding the stride time signal and sleep EEG signal that were important. In conclusion, this report shows the view that Daubechies Wavelet is more accurate and consistent than Haar Wavelet when compared to the Index of Orthogonality.

Challenges that faced when conducting this project is that there are no many programs available to read raw EEG data, thus using MATLAB® and sourcing for program is needed. Secondly is to identify the key features of the data because usually the data is not uniform and normally interrupted. Thus, more time is required to analyse the EEG data.

There are still rooms for improvements in this project. Firstly, it is better to conduct the actual experiment on a PD patient in order to get a pure raw EEG data. This can be done by recruiting PD patients to join in the experiment. Secondly, to gather as much data as possible. More data will translate to more accurate results.

References

[1] H. Shafique, A. Blagrove, A. Chung, and R. Logendrarajah, 'Causes of Parkinson's disease: Literature Review', *Journal of Parkinsonism and Restless Legs Syndrome*, vol. 1, no. 1, pp. 5–7, Dec. 2011.

[2] M. C. Staff, 'Parkinson's disease Definition', *Mayoclinic*, Jul. 2015.

[3] J. Meara, 'The Drug Treatment of Parkinson's Disease in the Elderly', *Drugs and the Older Population*, pp. 399–419, Jul. 2000.

[4] 'Bradykinesia and rigidity:: Parkinson's Victoria – We're in this together', 01-Jan-2003. [Online]. Available: http://www.parkinsonsvic.org.au/parkinsons-and-you/bradykinesia-and-rigidity/. [Accessed: 10-Oct-2015].

[5] A. E. Gabbey, 'Healthline.' [Online]. Available: http://www.healthline.com/symptom/gait-abnormality. [Accessed: 10-Oct-2015].

[6] W. Poewe and K. N. Chaudhuri, *The non-motor symptoms complex of Parkinson's disease*. New York: Oxford University Press, USA, 2009.

[7] 'Parkinson's Disease and Sleep.' [Online]. Available: https://sleepfoundation.org/sleep-topics/parkinsons-disease-and-sleep. [Accessed: 10-Oct-2015].

[8] J. G. Nutt and G. F. Wooten, 'Diagnosis and Initial Management of Parkinson's Disease', *New England Journal of Medicine*, vol. 353, no. 10, pp. 1021–1027, Sep. 2005.

[9] A. Elbaz, J. H. Bower, D. M. Maraganore, S. K. McDonnell, B. J. Peterson, J. E. Ahlskog, D. J. Schaid, and W. A. Rocca, 'Risk tables for parkinsonism and Parkinson's disease', *Journal of Clinical Epidemiology*, vol. 55, no. 1, pp. 25–31, Jan. 2002.

[10] 'Early Onset Parkinson's Disease: Symptoms and Treatments', 10-Oct-2015. [Online]. Available: http://www.newhealthadvisor.com/Early-Onset-Parkinson's-Disease.html. [Accessed: 10-Oct-2015].

[11] M. C. de Rijk, M. M. B. Breteler, G. A. Graveland, A. Ott, D. E. Grobbee, F. G. A. van der Meche, and A. Hofman, 'Prevalence of Parkinson's disease in the elderly: The Rotterdam Study', *Neurology*, vol. 45, no. 12, pp. 2143–2146, Dec. 1995.

[12] F. Molinet-Dronda, B. Gago, A. Quiroga-Varela, C. Juri, M. Collantes, M. Delgado, E. Prieto, M. Ecay, E. Iglesias, C. Mar ń, I. Pe ñuelas, and J. A. Obeso, 'Monoaminergic PET imaging and histopathological correlation in unilateral and bilateral 6-hydroxydopamine lesioned rat models of Parkinson's disease: A longitudinal in-vivo study', *Neurobiology of Disease*, vol. 77, pp. 165–172, May 2015.

[13] L. Zhao, L. Verhagen-Metman, J. H. Kim, C. C. Liu, and F. A. Lenz, 'EMG activity and neuronal activity in the internal globus pallidus (GPi) and their interaction are different between hemiballismus and apomorphine induced dyskinesias of Parkinson's disease (AID)', *Brain Research*, vol. 1603, pp. 50–64, Apr. 2015.

[14] G. S. Watson, B. A. Cholerton, R. G. Gross, D. Weintraub, C. P. Zabetian, J. Q. Trojanowski, T. J. Montine, A. Siderowf, and J. B. Leverenz, 'Neuropsychologic assessment in collaborative Parkinson's disease research: A proposal from the National Institute of Neurological Disorders and Stroke Morris K. Udall Centers of Excellence for Parkinson's Disease Research at the

University of Pennsylvania', *Alzheimer's & Dementia*, vol. 9, no. 5, pp. 609–614, Sep. 2013.

[15] Y. Harrison and J. A. Horne, 'Occurrence of "microsleeps" during daytime sleep onset in normal subjects', *Electroencephalography and Clinical Neurophysiology*, vol. 98, no. 5, pp. 411–416, May 1996.

[16] C. G. Goetz, 'Unified Parkinson's Disease Rating Scale (UPDRS) and The Movement-Disorder Society Sponsored-unified Parkinson's Disease Rating Scale (MDS-UPDRS)', *Encyclopedia of Movement Disorders*, pp. 307–309, 2010.

[17] Á. Jobbágy, P. Harcos, R. Karoly, and G. Fazekas, 'Analysis of finger-tapping movement', *Journal of Neuroscience Methods*, vol. 141, no. 1, pp. 29–39, Jan. 2005.

[18] K. L. Chou, J. Zamudio, P. Schmidt, C. C. Price, S. A. Parashos, B. R. Bloem, K. E. Lyons, C. W. Christine, R. Pahwa, I. Bodis-Wollner, W. H. Oertel, O. Suchowersky, M. J. Aminoff, I. A. Malaty, J. H. Friedman, and M. S. Okun, 'National Parkinson Foundation Hospitalization Survey', *PsycTESTS Dataset*, Oct. 2014.

[19] C. Owen, 'Parkinson's Disease Staging - Neurosurgical Service - Massachusetts General Hospital.' [Online]. Available: http://neurosurgery.mgh.harvard.edu/functional/pdstages.htm#UPDRS. [Accessed: 10-Oct-2015].

[20] B. Post, M. P. Merkus, R. M. A. de Bie, R. J. de Haan, and J. D. Speelman, 'Unified Parkinson's disease rating scale motor examination: Are ratings of nurses, residents in neurology, and movement disorders specialists interchangeable?', *Movement Disorders*, vol. 20, no. 12, pp. 1577–1584, 2005.

[21] M. Costa, C.-K. Peng, A. L. Goldberger, and J. M. Hausdorff, 'Multiscale entropy analysis of human gait dynamics', *Physica A: Statistical Mechanics and its Applications*, vol. 330, no. 1–2, pp. 53–60, Dec. 2003.

[22] J. S. Richman and J. R. Moorman, 'Physiological time-series analysis using approximate entropy and sample entropy', Am J Physiol Heart Circ Physiol, vol. 278, no. 6, pp. H2039–H2049, Jun. 2000.

[23] M. Aboy, D. Cuesta-Frau, D. Austin, and P. Mico-Tormos, 'Characterization of Sample Entropy in the Context of Biomedical Signal Analysis', *2007 29th Annual International Conference of the IEEE Engineering in Medicine and Biology Society*, Aug. 2007.

[24] A. Ylikoski, K. Martikainen, T. Sarkanen, and M. Partinen, 'Parkinson's disease and narcolepsy-like symptoms', *Sleep Medicine*, vol. 16, no. 4, pp. 540–544, Apr. 2015.

[25] 'American Academy of Dental Sleep Medicine Continuing Education Offerings', *Sleep and Breathing*, vol. 12, no. 3, pp. 287–288, Jul. 2008.

[26] M. Partinen, B. R. Kornum, G. Plazzi, P. Jennum, I. Julkunen, and O. Vaarala, 'Narcolepsy as an autoimmune disease: the role of H1N1 infection and vaccination', *The Lancet Neurology*, vol. 13, no. 6, pp. 600–613, Jun. 2014.

[27] T. C. Thannickal, Y.-Y. Lai, and J. M. Siegel, 'Hypocretin (orexin) cell loss in Parkinson's disease', *Brain*, vol. 130, no. 6, pp. 1586–1595, Apr. 2007.

[28] K. Suzuki, M. Miyamoto, T. Miyamoto, and K. Hirata, 'Parkinson's Disease and Sleep/Wake Disturbances', *Current Neurology and Neuroscience Reports*, vol. 15, no. 3, Feb. 2015.

[29] 'Fundamentals of Wavelet Transform', *Chemical Analysis*, pp. 99–146, Apr. 2004.

[30] P. S. Addison, 'The Illustrated Wavelet Transform Handbook', -*Infinity*, 2002.
[31] S. Malik and V. Verma, 'Comparative analysis of DCT, Haar and Daubechies Wavelet for Image Compression', *International Journal of Applied Engineering Research*, vol. 7, no. 11, 2012.
[32] M. G. Terzano, L. Parrino, A. Sherieri, R. Chervin, S. Chokroverty, C. Guilleminault, M. Hirshkowitz, M. Mahowald, H. Moldofsky, A. Rosa, R. Thomas, and A. Walters, 'Atlas, rules, and recording techniques for the scoring of cyclic alternating pattern (CAP) in human sleep', *Sleep Medicine*, vol. 2, no. 6, pp. 537–553, Nov. 2001.
[33] M. Hirshkowitz, K. Whiton, S. M. Albert, C. Alessi, O. Bruni, L. DonCarlos, N. Hazen, J. Herman, E. S. Katz, L. Kheirandish-Gozal, D. N. Neubauer, A. E. O'Donnell, M. Ohayon, J. Peever, R. Rawding, R. C. Sachdeva, B. Setters, M. V. Vitiello, J. C. Ware, and P. J. Adams Hillard, 'National Sleep Foundation's sleep time duration recommendations: methodology and results summary', *Sleep Health*, vol. 1, no. 1, pp. 40–43, Mar. 2015.

Collision Avoidance using Nature-Inspired Bat Algorithm

*Raefi Azrani Bin Ropee Adman, Aravind C.V**

Computer Intelligence Applied Research Cluster
Taylor's University, School of Engineering, Malaysia

*aravindcv@ieee.org

Abstract

Smart transportation in a futuristic safety in traffic is a key hold towards building sustainability towards the smart city concept. The priority in such a system is the collision avoidance and the vehicle involved within a space need to communicate to each other via wirelessly. Collision avoidance in vehicle control and safety measure in order to prevent the user from experiencing any type of collision, e.g. front to front, front to back or side to side collision. For most cases it is due to the user inability to predict accurately in the areas that involve uncertainty while the vehicle is still in use. Based on the research, statistics shows that why accidents happen on the road is because vehicle tend to collide with another due to the blind spot in which the driver have very limited vision of overviewing their parameter. The second factor through collision with a random object caused due to human error. Besides that, the collision is due to the proximity and rear impact through sudden variations in the driving mode conditions. The purpose of this research is to identify the framework of collision in urban transportations, simulate the environment and apply the intelligence technique from nature-inspired metaheuristic algorithm and implement the proposed algorithm to the developed framework to investigate the safety concerns, a feature that is core of next generation smart city.

Keywords: safety, collision avoidance, vehicle control, metaheuristic algorithm, nature, smart transportation.

1. Introduction

Cities and communities around the globe are facing intractable issues such as massive growth in population and it is predicted that an increase of 75% of growth by 2050 [1], and increase of greenhouse-gas emissions will definitely contribute to the deprecation in our comfort of living. In the recent years, a mixture of different industry has joined forces in creating in a worldwide Smart City movement [2]. The increment of high demand for intelligence and sustainable environment has struck us as a contributor to move towards a higher positive impact living [1]. Majority of the researcher believe by adapting the Smart City concept can lead us to achieving such goals. The conceptualization of Smart City varies from people to people, city-to-city and country-to-country, depending on development level of the nation and its willingness for change [4]. But in general, Smart City is defined as developed urban area that uses digital technology and information to communicate in order to enhance the quality and performance of its citizens and economy, to reduce the cost of operation and to manage resource consumption effectively [3]. Smart City covers in the areas of public service, building, mobility, energy and water system. In which, each of the area contribute to the sustainability of the city towards making it more efficient and cheaper place to live in.

In spite of the advancement in the road system, accident still happened among the car driver in the world. From 2007 to 2013, the report shows reaching about 500,000 cases of accident still happening in Malaysia alone [5] as shown in the figure below.

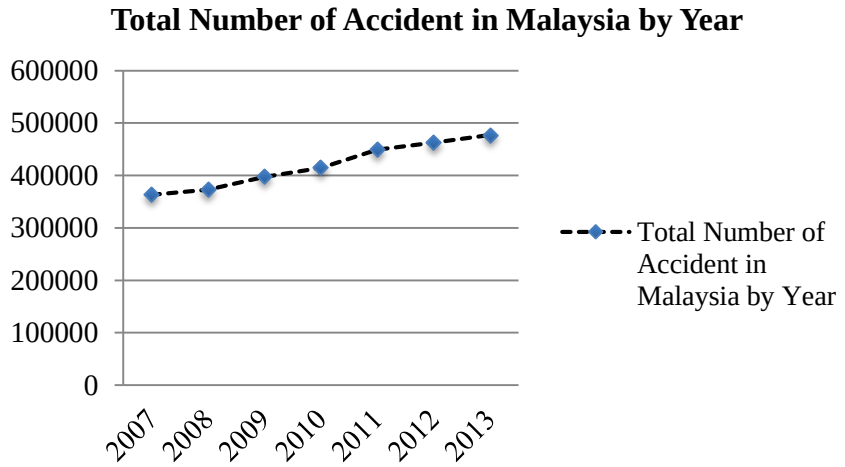


Figure 1. The Total Number of Accident in Malaysia from year 2007 to 2013

Based on Malaysian Automotive Association (MAA) statistic data, the growth of car sales is higher than the country's population growth of about 1.5% every year and the road expansion will be difficult to keep up with the growth of cars. Malaysia

has the highest number of new registered vehicles in the world with more than 680,000 new vehicles each year. 88% of the populations are dependent on private vehicles and 12% on public transport. Private vehicles become an important transport mode and traffic jams have become a thorn in urban living. The heavy traffic jams are costing the nation a huge price in terms of our safety, mobility and productivity [6].

Recent trend shows that collision avoidance system is one of the major areas of study in vehicle control and safety measure in order to prevent the user from experiencing any type of injuries. For most cases, accident happens due to the user inability to predict accurately in the areas that involve uncertainty. Research suggests that, the main reason why accidents happen on the road is between two vehicles colliding with another. The second factor is when the vehicle hitting a random object. Follow by side impact, rear impact and so on. All of these cases have a common ground to it, in which the user of the vehicle has the tendency to collide with another object while in motion [5]. The percentage of categories accident can be seen on the graph below.

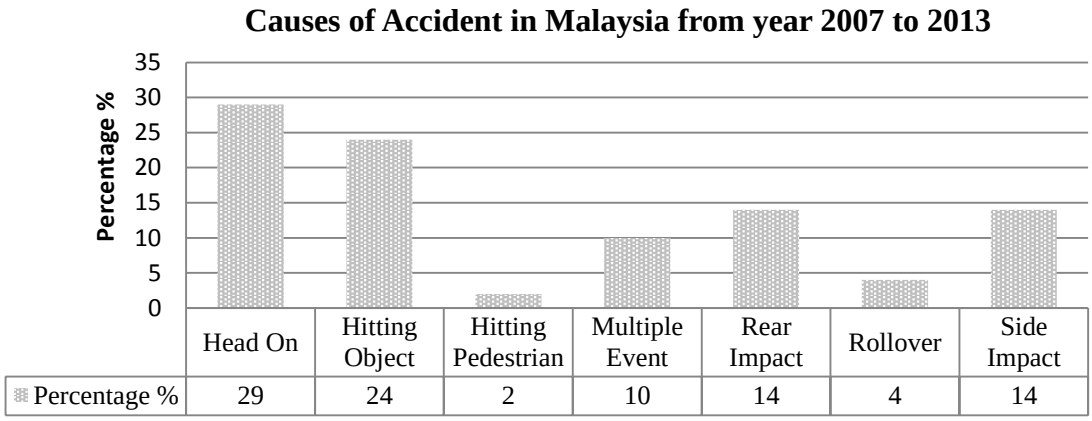


Figure 2. Causes of Accident in Malaysia from year 2007 to 2013

This research work is focused on optimizing the algorithm techniques. In this paper, in order to achieve such objective, an optimize version of a Nature-inspired Metaheuristic algorithms is purposed. It is to be implemented or adapt into the safety system, which uses ultrasonic sensors. The aim, when the vehicle is presented with one or more obstacle within its parameters, it could be either be stationary on in dynamic motion, the vehicle need to avoid it at all cost when come to near impact autonomously

2. Comparison of Collision Avoidance Methods

For an optimization safety system, it needs to satisfy the requirement of avoiding any harmful situation such as collision among objects or vehicle while in motion autonomously. The following literature content focuses comparing various collision method and algorithms that is to be implement and act as the core

personality of how does the electrical safety system should operate by adapting from the natural-inspired metaheuristic algorithms.

Table 1: Collision Avoidance Methods

Method	Description	Drawbacks	Ref.
Vehicle Cyber Physical System (VCPs)	Predict the collision by determine the vehicle motion behavior, its location, driver behavior and road geometry.	The system reflects on the driver's behavior and pattern, and the road geometry that to certain extends it is inconsistent and would be more difficult for the system to predict and assess the risk later on.	[7]
Forward Collision Avoidance Technology (FCAT)	A hybrid model that follows the behavioral characteristics of an Ant and a Bat.	When comes to application, the implementation of Ant's algorithm in to the vehicle or the moving object cannot react properly or expectedly when there is a sudden object in front of it.	[8]
In-Wheel Collision Avoidance Warning System (IVCAWS)	A warning system which aids the driver in preventing any such collision when the vehicle is on the road or near to impact to any object.	As the reliability of the system increases the performance of the system decreases. This is because the driver's relied on his or her own judgment rather than the system itself.	[9]
Dedicated short-range Communication (DSRC)	By analyzing the timing of the event, the system can predict the situation and communicate with another vehicle in order to prevent the collision.	Despite the system can predict the risk involve when the driver drive the vehicle, the system does not control on how the vehicle should react to the situation.	[10]

Table 2: Natural-Inspired Metaheuristic Algorithms

Algorithm	Application	Limitations	Ref.
Ant Colony Optimization (ACO)	Optimize the best route between two points of distance.	The solution is based on the number of iterations, thus, the best route may or may not be the most inefficient route to cross since it is depends on the popularity of the route.	[11]
Particle Swarm Optimization (PSO)	Solution for multivariable condition.	The algorithm can only function if and only if the next agent is equipping with the same logic.	[12]
Harmony Search (HS)	Adapting to the condition or requirement.	The algorithm depends crucially on memory capacity.	[13]
Bee Algorithm (BA)	Evaluation and comparing process.	Required a master and slave condition.	[14]
Original Bat's Algorithm (OBA)	Positioning.	The variable of a different condition may be the same resulting in same solution.	[15]

These algorithms can contribute for creating a proper system that can prevent any collision among objects or vehicles. However, for this project the algorithm that is applicable to be implemented in the car system would be OBA, since it emphasis on the best positioning approach for a vehicle to move while in motion.

3. Theoretical Framework

3.1 Original Bat's Algorithm

The bat-inspired algorithm is an adaptation from the characteristics of the echolocation of microbats. The bat's echolocation is mostly used to determine its pin point location to the point of its surrounding such as rocks, wall or other bats. Furthermore, it is also used to differentiate between foods or objects and also to direct its movement accordingly without colliding with the other bats. The microbats move in such randomness with velocity, at position, with a fixed frequency, and by varying

its wavelength, and loudness [15], it can determine the potential danger that is about to happen or how it located its preys. The following figure shows the original bat's algorithm.

3.1.1 Bat's Movement

The movement of the bats is set or define by certain type of rules where the positions and velocity, in the d-dimensional search space is consider as the influencer on how does the bat's move. In order for the bats to create a path for them to move efficiently, the next action steps needed to be constantly updated so that the next move will be better that the previous one. From the equation that was developed by X.Yang [30, 31], showcase how to determine the new location point based on the previous decision where the position, and velocity, is obtain at any given time;

$$f_i = f_{min} + (f_{max} - f_{\min})\beta \quad (1)$$

$$V_i^t = V_i^{t-1} + (X_i^t - X_*)f_i \quad (2)$$

$$X_i^t = X_i^{t-1} + V_i^t \quad (3)$$

Where β ε [0.1] is categories as the random vector that is drawn from a uniform distribution. Furthermore, is defined as the current best location after comparing the solution with all the other bats.

For the local search part, it is generated based on the current best solution and the new solution is generated locally using random walk.

$$X_{new} = X_{old} + \varepsilon A^t \quad (4)$$

Where ε ε [-1, 1] is taken randomly and $A^t = \langle V_i^t \rangle$ is determine by the average loudness of all the bats at that time.

3.1.2 Loudness and Pulse Emission

The loudness and rate, r_i of pulse emission are determined by the number of iterations. This can be calculated by the following equation:

$$A_i^{t+1} = \alpha A_i^t \quad (5)$$

$$\gamma_i^{t+1} = \gamma_1^0 - \exp(-\gamma t) \quad (6)$$

Where α and γ are constants.

From here, the loudness and emission rates can be updated if and only if the new solution is somewhat improve. Because of such characteristics the bats are moving accordingly to the most optimal movement at that time and place.

3.2 Implementation of Bat's Algorithm in the Collision Avoidance System of a Vehicle

In theory, the variation on how bats differentiate object is influence by the frequency difference. Where, object that is in stationary, reflect a constant or fix bandwidth or frequency. This is determining by their echolocation capability, whereas, for a prey or predator that is in dynamic movement, give out difference vive of frequency. For example, if the object is approaching towards the bat, the reflected wave produces a more intense frequency and if the object is going away from the bat, it reflects a lighter wave.

For application purpose, the behavior of the bat is look at 3 main condition that are stationary, approaching and receding obstacle. The figure below shows a more illustrate concept of the BA adaption.

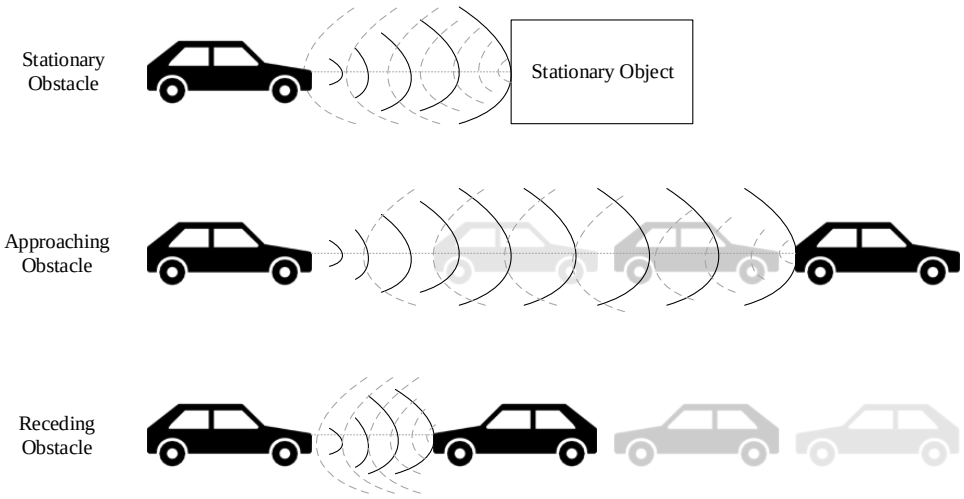


Figure 3. Adaptation of BA in Vehicle

From Figure 3, shows 3 different cases when detecting an object around it. By applying modern technology devices, an ultrasonic sensor has the most similarity to producing radar of wave like a bat. So, the first case show when a vehicle detects a stationary object when using an ultrasonic sensor, whereas for case 2 and 3 shows how the vehicle sees and react upon detection of a moving vehicle. To further explain, for a stationary obstacle, the car system only detect if and only if there is an obstacle nearby it. For an approaching and receding obstacle, the vehicle detects earlier on and warns the system of the upcoming obstacle before proceeding to the action steps.

4. Research Methodology

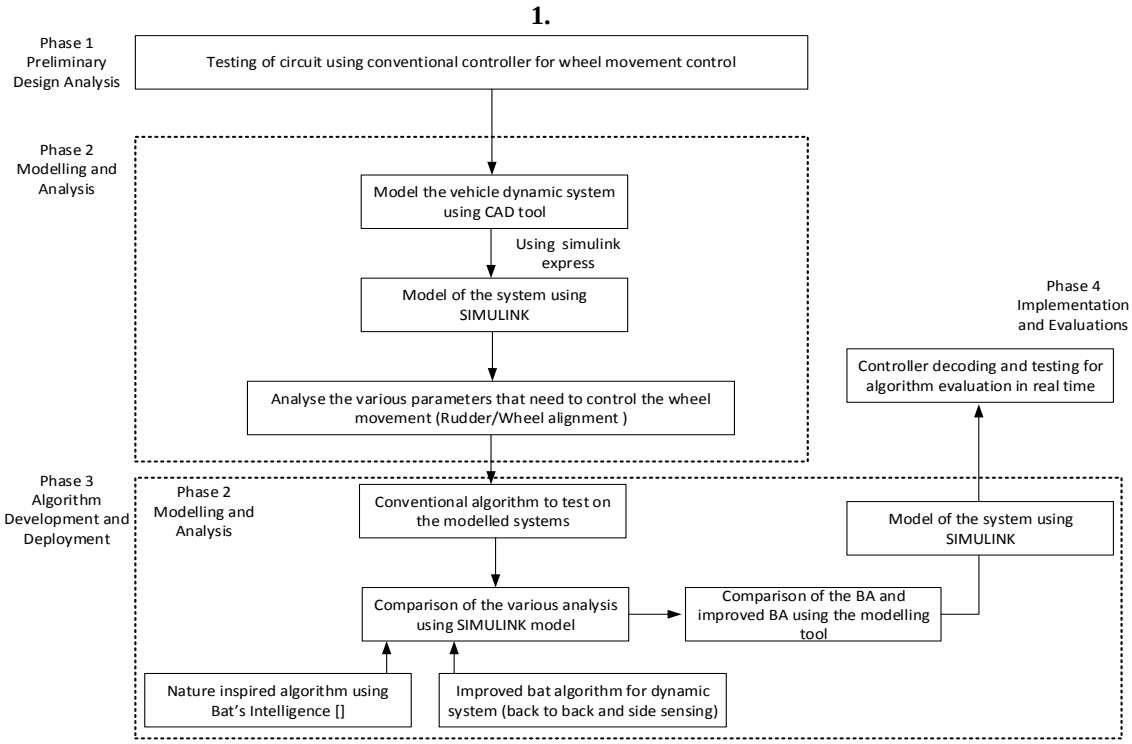
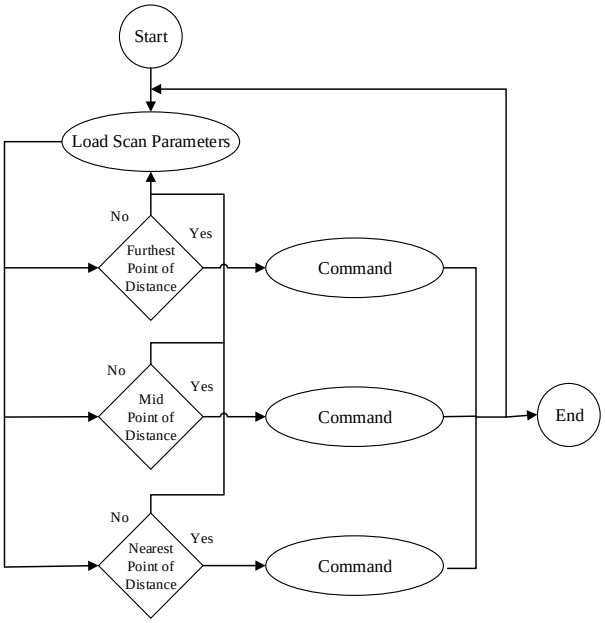


Figure 4. Project Work Flow

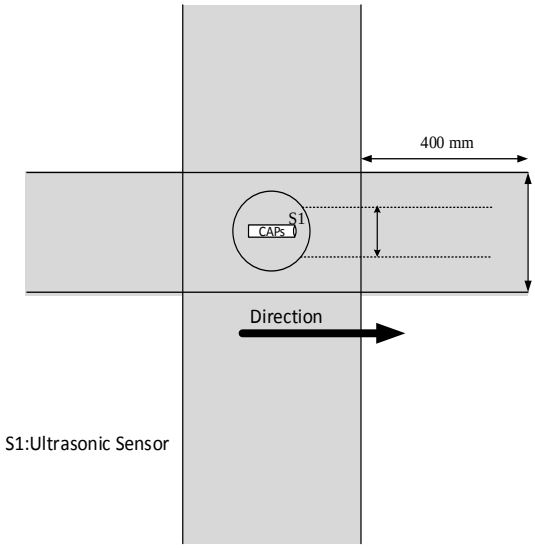
The research was conducted by two approach methods. Firstly was to extract a CAD model using Solidworks. After that, it was to manufacture a prototype robot based on the CAD model that can function according to intended logic. Finally, the logic control will be implemented into the electronic system where it will be tested and the overall performance will be compare with the existing algorithm. The comparison is mostly focuses on the effectiveness of it avoiding any such collision with the intended use of it application.

4.1 Implementation of BA in the Mobile Unit System

From Figure 4, the implementation of the BA using Ardunio is set in deferent priority points. The point is set as the Nearest Point of Distance (NPD), Mid. Point of Distance (MPD) and Furthest Point of Distance (FPD). The NPD area functions as the highest alert level, whereas the MPD and FPD act as an early system warning.



(b) Bat's Algortithm Adaptation Flow Chart



(a) Bat's Algortithm Adaptation using Ardurnio

Figure 5. Implementation of BA in the Mobile Unit System

4.2 Experimental Design for Collision Avoidance

Table 3: Case Condition

Case Condition	**Description**
Robot detect a stationary object and stop	When the robot detect an object, it will stop instantaneously and will not move until there is no object is detected by the robot
Robot detect a stationary object and slow down	When the robot detect an object in front of it, the speed of the motor will slow down until a certain rage it will stop
Robot detect a stationary object and over pass	Robot pass through a stationary object by delaying one of the motor and regain back it speed after a certain distance

5. Fabrication of the Mobile Unit Prototype Model

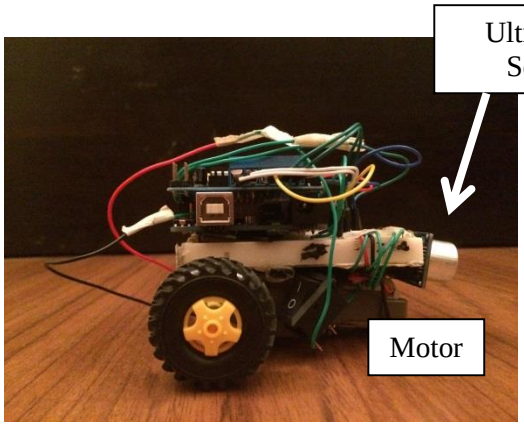


Figure 6: Top View of the Prototype Model

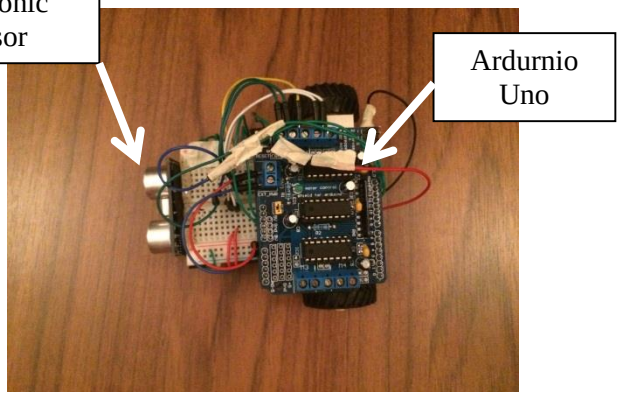


Figure 7: Side View of the Prototype Model

6. Behavior Evaluations

Case 1: Mobile unit detects a stationary object and stop

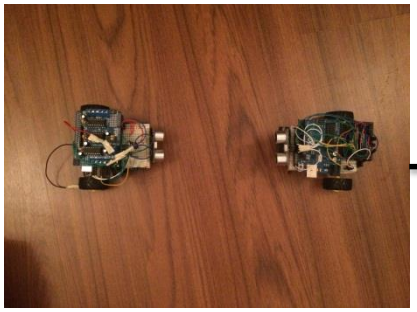


Figure 7: Robot Detect an Object

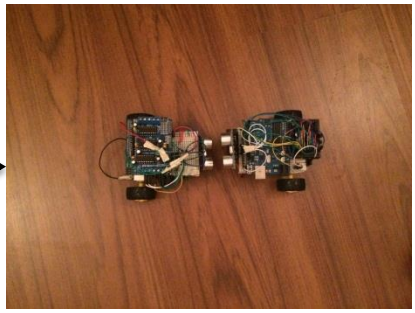


Figure 8: Robot Stop after reach a certain Distance

Case 2: Robot Detects a Stationary Object and Slow Down

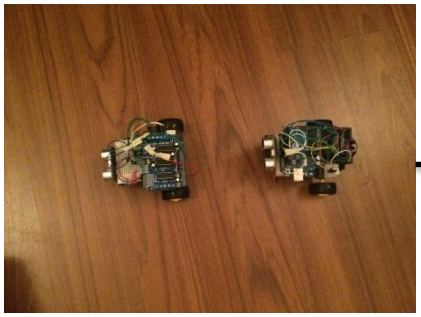


Figure 8: Robot Detect an Object

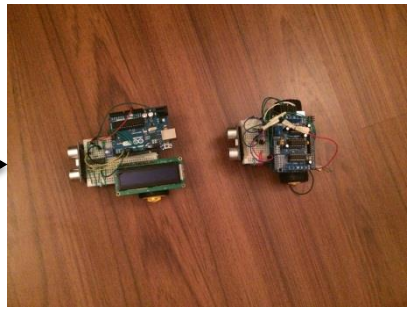


Figure 9: Robot detect an Object and Speed is Reduce

From Figure 7 to 9, when the robot detects an object, it delays the signal to both of the motor making the speed of the robot to slow down. As it reaches to a certain distance (the second distance parameter) the signal to the motor from Ardunio will stop. Making the robot is at halt until the obstacle is clear

Case 3: Robot Detects a Stationary Object and Over Pass



Figure 10: Robot Detect an Object



Figure 11: Robot Delay Right Motor

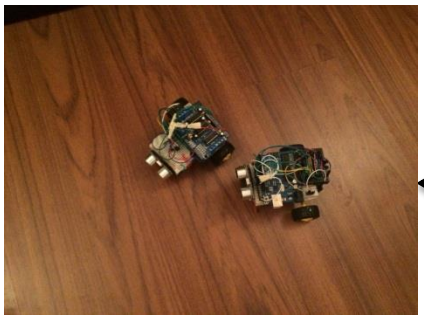


Figure 13: Robot Overcome the Obstacle



Figure 12: Robot Continue to Move

From Figure 4.7 to 4.10, it shows how the robot over pass the obstacle in front of it while in motion. At Figure 4.8, the signal from the Ardunio board delays the output signal of the motor 2 (right wheel), thus because of the delay the robot can turn to the right. After that, motor 1 is delay in order to readjust the position of the robot. Finally, at Figure 4.10 shows that the robot continue to move in a straight line. The drawback of this system is that the position of the original robot is not maintained. More complicated coding is needed in order for the robot to gain back to its original line while avoiding an obstacle in a straight line.

7. Conclusion

The research focused on the concept of designing an algorithm and adapting to the application that can be used as safety precaution for the user upon driving on the road specifically towards four-wheel vehicles. The original mobile unit with BA with one sensor is sufficient enough to act as an avoidance system but because of the limited view point for its external detection the movement is not efficient enough to avoid the obstacle fully. The modification that was made from the original mobile unit shows the performances have significantly improved. The modification contribute the system to generate a more optimize solution for the unit to position itself without hitting any obstacle around it. Thus, increase the performance of avoiding the obstacle. In order to fulfill the objectives, the BA optimizes which was implemented in the modified model can function as a safety system for 4 wheel vehicle. The next step is to focus on application and the scalability of the application.

References

[1]Ieee.org, 'Smart Cities Community, IEEE', 2015. [Online]. Available: https://www.ieee.org/membershipcatalog/productdetail/showProductDetailPage.html?product=CMYSC764. [Accessed: 29- Oct- 2015].
[2] S. Huston, ',ÄòSmart City,Äô - Contemporary Frameworks and Antiquity', SSRN Electronic Journal.
[3] V. Albino, U. Berardi and R. Dangelico, 'Smart Cities: Definitions, Dimensions, Performance, and Initiatives', Journal of Urban Technology, vol. 22, no. 1, pp. 3-21, 2015.
[4] Smart City Guidelines, 1st ed. India: Ministry of Urban Development Government of India, 2015.
[5] T. Toroyan, M. Peden and K. Iaych, 'WHO launches second global status report on road safety', Injury Prevention, vol. 19, no. 2, pp. 150-150, 2013.
[6]Statistics.gov.my, 'Department of Statistics Malaysia Official Portal', 2015. [Online]. Available: https://www.statistics.gov.my/index.php. [Accessed: 29- Oct- 2015].
[7] M. Staubach, 'Factors correlated with traffic accidents as a basis for evaluating AdvancedDriverAssistanceSystems', Accident Analysis & Prevention,vol.41,no. 5, pp. 1025-1033, 2009.
[8] M. Maltz and D. Shinar, 'Imperfect in-vehicle collision avoidance warning systems can aid distracted drivers', Transportation Research Part F: Traffic Psychology and Behaviour, vol. 10, no. 4, pp. 345-357, 2007.
[9] A. Tang and A. Yip, 'Collision avoidance timing analysis of DSRC-based vehicles', Accident Analysis & Prevention, vol. 42, no. 1, pp. 182-195, 2010.
[10] Q. Hossain, M. Uddin and M. Hasan, 'Collision avoidance technique using bio-mimic feedback control', 2014 International Conference on Informatics, Electronics & Vision (ICIEV), 2014.

[11] Xin-She Yang,'Nature-Inspired Metaheuristic Algorithms Second Edition', 2nd ed. University of Cambridge: Luniver Press, 2010.
[12]Intechopen.com, 'Swarm Optimization | Swarm Intelligence | InTechOpen', 2015. [Online].Available:http://www.intechopen.com/books/swarm_intelligence_focus_on_ant_and_particle_swarm_optimization. [Accessed: 17- March- 2015].
[13]J. Fourie, S. Mills and R. Green, 'Harmony filter: A robust visual tracking system using the improved harmony search algorithm', Image and Vision Computing, vol. 28, no. 12, pp. 1702-1716, 2010.
[14]'Artificial Bee Colony Algorithm and Its Application to Generalized Assignment Problem', pp. 113-143.
[15] I. Fister, I. Fister, X. Yang, S. Fong and Y. Zhuang, 'Bat algorithm: Recent advances', Computational Intelligence and Informatics (CINTI), 2014 IEEE 15th International Symposium on, pp. 163-167, 2014.

Design of Edge-fed Micro Strip Antenna for Wireless Application

Shawn Yong Zhan Hao, Lee Chia Ping
School of Engineering, Taylor's University, Malaysia
Yong.ShawnZhanHao@sd.taylors.edu.my , ChiaPing.Lee@taylors.edu.my

Abstract
An edge-fed Micro Strip Patch Antenna design that enhances the bandwidth to operate from 5.2GHz to 5.8GHz is presented in this paper. The proposed antenna design is simulated in CST Microwave Studio software and its simulated results comply with the return loss of *S11*<-10dB and impedance of 50Ω. Details and parameters of the antenna design and correlated results are discussed thoroughly in this paper. However, the challenge in designing the antenna would be the narrow bandwidth characteristics of micro strip patch antennas itself. Therefore, the simulated results of this antenna design give a better understanding of design parameters of a micro strip antenna and their effects on bandwidth enhancement. Furthermore, the antenna has achieved the optimal designated frequency range, impedance and return loss making it to be used for wireless applications.

Keyword: Return Loss, Impedance, Bandwidth, Micro strip Patch Antenna.

1. Introduction

Micro strip Patch Antenna is an electrical and electronic device governs to send, transmit and receive microwave signals, satellite signals, and telecommunication signals. Therefore, micro strip antennas are easily fabricated as it can be mounted onto a circuit board with ease using modern printed circuit technology. Its conducting patch is etched onto the ground plane of micro strip antenna separated by dielectric substrate. The conducting patch of the micro strip antenna is manufactured from commonly used material such as copper. For proper input impedance matching, the patch shape and antenna feeding are vital, as antennas are versatile in terms of resonant frequency and radiation pattern. Figure 1 and Figure 2 below shows the basic micro strip patch antenna design geometry.

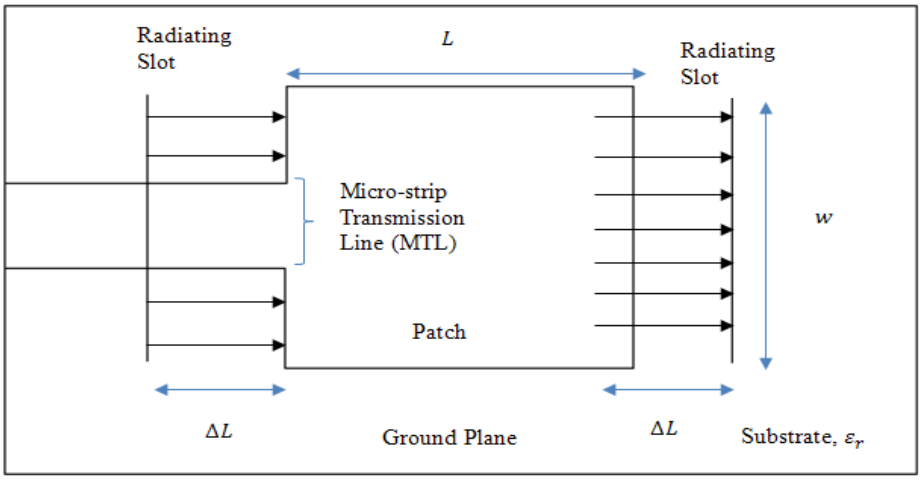


Figure 1: Basic Micro strip Patch Antenna geometry (top view).

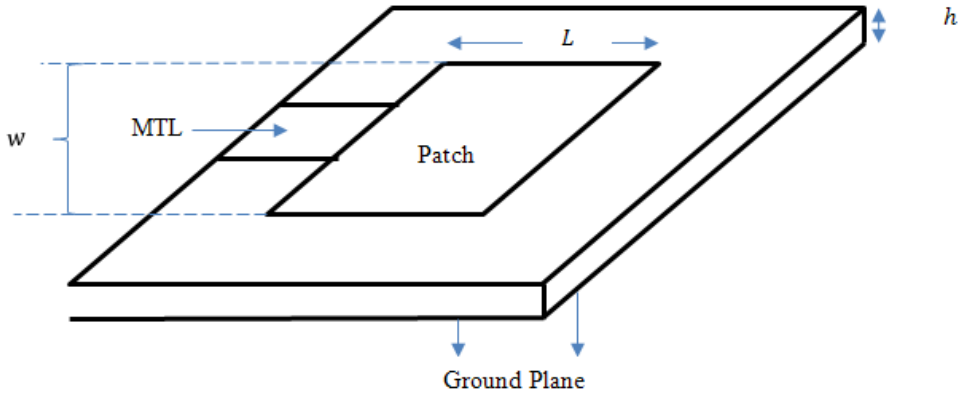


Figure 2: Basic Micro strip Patch Antenna geometry (diagonal view).

In contacting feeding such as edge-fed antenna feeding technique, the Radio Frequency (RF) power is directly being fed to the radiating patch via micro strip transmission line (MTL). It is then being connected using a coax cable or micro strip line for direct connection as the input source. The input impedance affects the impedance matching depending on the location of the connection within the patch

boundaries. Therefore, the design parameters are the most important factor in achieving the project objectives. The performance can be further analyzed and evaluated using Transient Simulation Solver (Time Domain) or Frequency Domain Solver in CST Microwave Studio. The motivation behind this paper work is to experiment different design parameters using edge-fed technique to improve its bandwidth for satisfactory micro strip antenna performance. The overall simplicity in structure and low cost manufacturing gives productive insights and opportunities in the telecommunication world. Due to the massive growth and improvement in communication systems to date, antennas are frequency used for wireless applications. Thus, the demand for micro strip antennas, also commonly referred to as patch antennas, is relatively high.

2. Literature Review

Research has shown that the impedance bandwidth of operation can be adjusted and modified by modifying the thickness of grounded substrate [1]. Generally, greater substrate width or thickness develops greater bandwidths but it also increases the possibility of higher order mode of excitation that leads to several surface wave losses. These undesirable losses contribute to the distortion of micro strip antenna performance and low antenna efficiency [2, 3]. Another consequence of integrating a thicker substrate is that the width of the micro strip feedline gets wider and larger [4]. This is then again contributing to the unwanted distortions in the radiation pattern and overall antenna performance. This is due to the patch layout being compromised and it creates undesirable grating lobes, which is known as unwanted beams of radiation being emitted. Therefore, the Identical Dual Patch Micro strip with Air Gap (IDMA) technique has been conducted to mitigate such issue [5]. This design technique improves the bandwidth of the micro strip antenna without increasing the substrate thickness of the antenna.

According to the research done by S. Panwar [6, 7], the researcher analyzes the surface area of an antenna in order to improve the bandwidth characteristics. The author modifies the rectangular patch and introduces an H-patch antenna design by increasing the notches on the surface of the patch. The dual U-slotted H-patch increases the total surface area of the patch resulting in an increased of capacitance and resistance through the patch layout [7].

Based on M. Kiroriwal and S. Rawat [8], the researchers use a different type of antenna geometry whereby the patch of the antenna has a 90° angle cut from the center using coaxial-fed feeding technique. The proposed design is being simulated through an IE3D Electromagnetic Simulator and the bandwidth of the antenna has improved to 11.15% as compared to the conventional rectangular micro strip patch antenna [9].

3. Methodology

The execution of project begins with Part 1 of the flow chart as shown in Figure 3. The research phase for this project commences with understanding and justifying the methods of micro strip antenna feeding techniques. For simplicity and flexibility in antenna design, the edge-fed feeding technique is used for this paper work. During the Part 1 of the flow chart, it mainly focuses on literature reviews and

comparison of simulated results from researchers. It enhances the basic antenna design methodology and understanding of its performance from different design parameters before proceeding into part 2 of this research project.

The Part 2 of the flow chart focuses on experiment and designing phase. It begins with parametric calculation of parameters for the antenna design. Then, the antenna is designed using CST Microwave Studio. After running the simulation process, validation on simulated results are conducted. The return loss of the antenna design has to fall below *S11*< -10dB and has an impedance of 50 Ω. If the simulated results are not desirable, the research project again ventures into experiment of different design parameters stage in a looping process. Before the completion of this project, the desirable and acceptable results are being analyzed and studied.

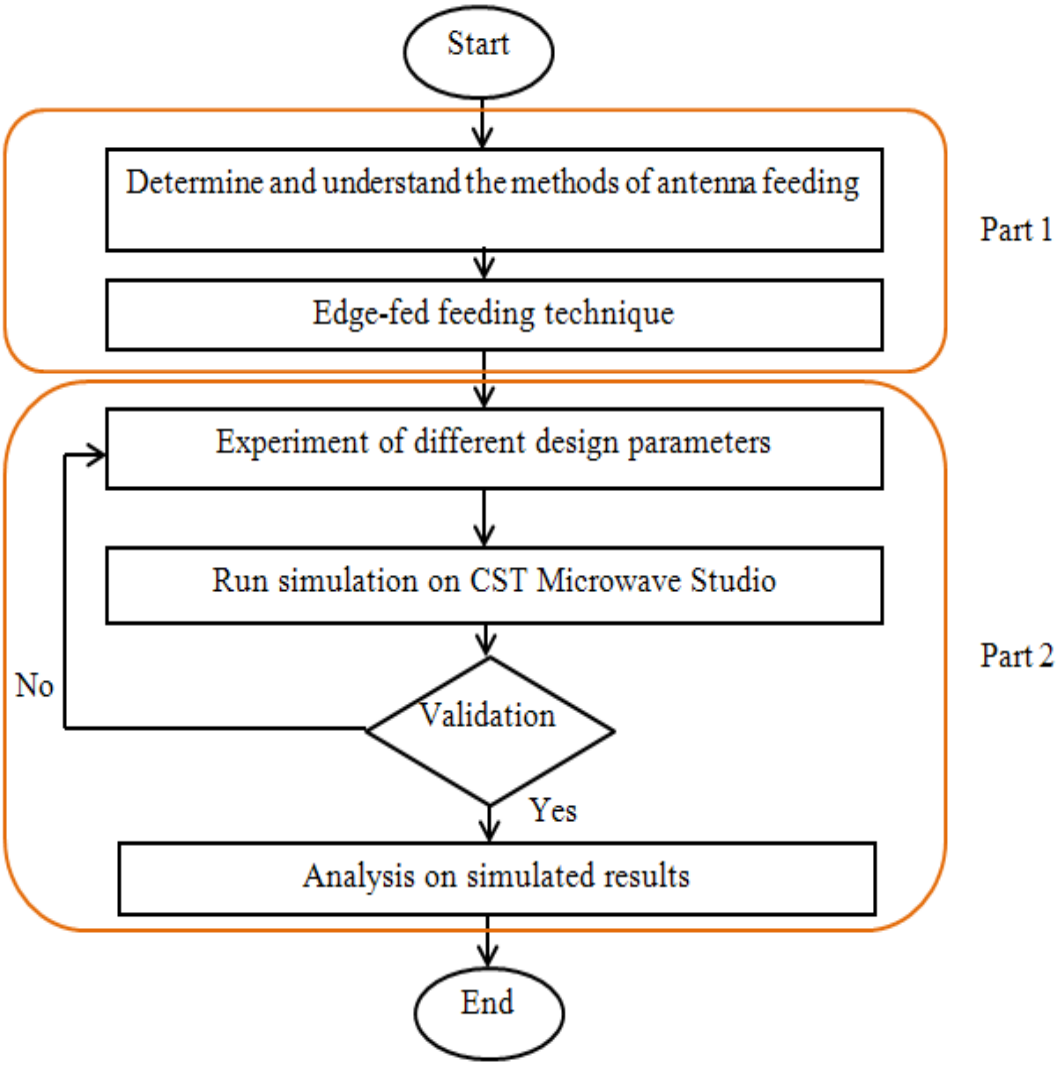


Figure 3: Flow chart

4. Result and Discussion

4.1 Antenna Design Geometry

A micro strip patch antenna with low dielectric constant has a normal or moderate bandwidth but large in terms of size [10]. In short, the dielectric values of substrate when increases, the bandwidth of the antenna decreases [11]. The substrate design of the antenna for this antenna design is FR-4 with relative permittivity and dielectric constant of $\varepsilon_r = 4.3$ and loss tangent of 0.025. For an antenna to exhibit optimal performance, the substrate of the antenna should have a low loss tangent value in order to reduce the dielectric loss; and an isotropic dielectric constant for minimizing changes in circuit impedance [12]. The material chosen for the patch design is copper. The entire geometry for the antenna design shows an enhancement in bandwidth by using FR-4/Cu layer configuration. The FR-4 substrate is placed directly under the patch and above the ground plane with 1mm thickness. The length of the patch regulates the operational frequency of the micro strip patch antenna and the length of the entire antenna should have a length that is one-half of the wavelengths within the medium of the substrate [13]. The dimensions of the antenna design are shown in Figure 4 and Table 1 respectively.

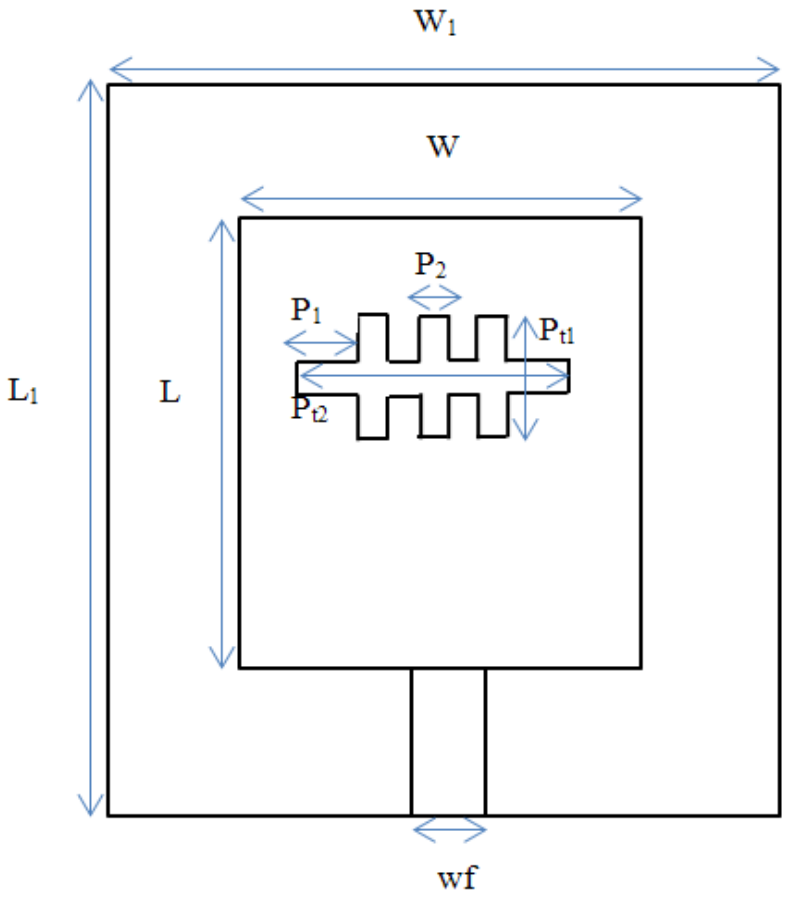


Figure 4: Antenna design geometry (top view).

Table 1: Dimensions of the antenna design.

Parameters	Units (mm)
Substrate length, L_1	50.0
Substrate width, W_1	35.0
Patch length, L	30.0
Patch width, W	26.5
Feedline width, wf	3.0
P_1	6.0
P_2	1.0
P_{t1}	5.0
P_{t2}	18.0
Ground plane thickness	1
Substrate thickness, h	1.6

4.2 Parametric analysis

The dimensions of antenna design from Table 1 (section 4.1) can be expressed with the following formulas:

$$L = \frac{c}{2f_0\sqrt{\varepsilon_{reff}}} - 2\Delta L \tag{1}$$

$$L_{eff} = \frac{c}{2f_0\sqrt{\varepsilon_{reff}}} \tag{2}$$

$$\varepsilon_{reff} = \frac{\varepsilon_r + 1}{2} + \frac{\varepsilon_r - 1}{2}[1 + 12\frac{h}{w}]^{-1/2} \tag{3}$$

$$\Delta L = 0.412h\frac{(\varepsilon_{reff} + 0.3)[\frac{w}{h} + 0.264]}{(\varepsilon_{reff} + 0.258)[\frac{w}{h} + 0.8]} \tag{4}$$

$$w = \frac{1}{2f_0\sqrt{\mu_0\varepsilon_0}}\sqrt{\frac{2}{\varepsilon_r + 1}} \tag{5}$$

where L is the patch length, L_{eff} is the effective patch length, c is the speed of light, f_0 is the resonant frequency, ε_{reff} is the effective dielectric constant, ε_r is the dielectric constant of substrate, h is the height of dielectric substrate, w is the width of the patch, μ_0 is the permeability ($4\pi \times 10^{-7}$ H/m), and ε_0 is the permittivity of free space (8.85×10^{-12} F/m).

4.3 Return Loss, *S11*

The return loss (RL) is a measurement of power being transferred from micro strip transmission line to the patch antenna. Based on the simulated results in Figure 5, the antenna design shows that the operating frequency, commonly referred to resonant frequency at 5.48GHz with S11 of -23.56 dB. This frequency is due to the geometries of the antenna design such as the patch length, L and the slots, P_1, P_2, P_{t1}, and *Pt2* at the patch antenna. The capacitive coupling between the patch of micro strip

antenna and the ground plane are being regulated as the result of the changes in the patch geometry and narrowband characteristics are amended [14]. Figure 6 shows the impedance being matched to 50 Ω. Overall, the results simulated are satisfactory.

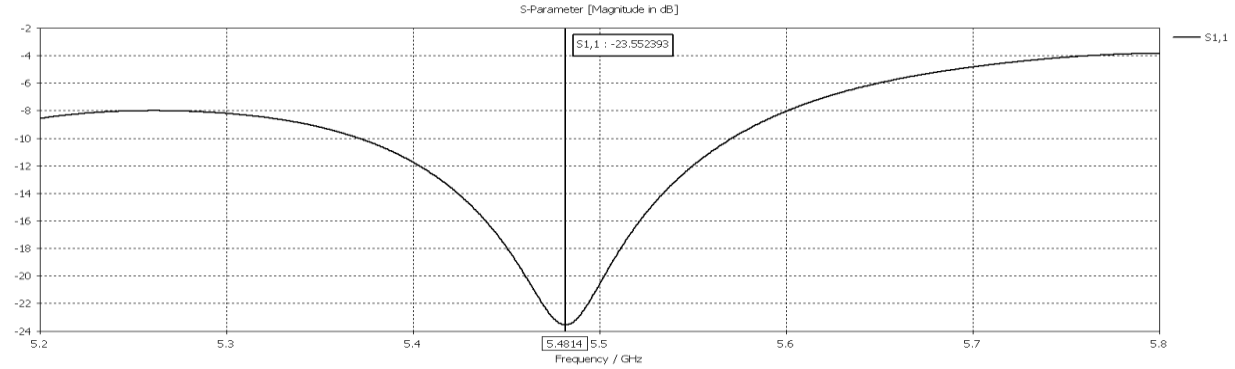


Figure 5: Simulated results of return loss S11 (dB) against Frequency (GHz).

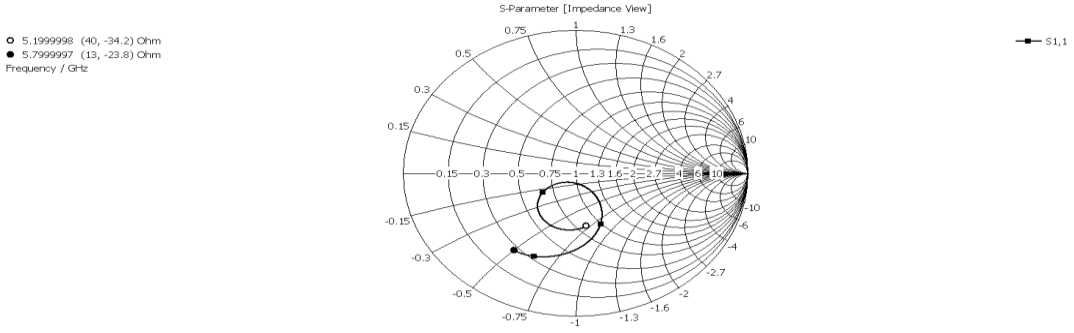


Figure 6: Smith chart of S-Parameter.

4.4 Voltage Standing Wave Ratio (VSWR)

Voltage Standing Wave Ratio (VSWR) is the measurement of bandwidth impedance mismatch between the antenna line feeder and micro strip patch. Therefore, the smaller the value of VSWR, the greater the micro strip patch antenna is matched to the micro strip transmission line and the power is delivered to the antenna more effectively. The ideal VSWR value for antenna is 1. The simulated result shown in Figure 7 displays that the VSWR value of this antenna designs is 1.14. The real part of the curve indicates the input impedance of the antenna whereas the imaginary part of the curve indicates the reactance impedance of the antenna.

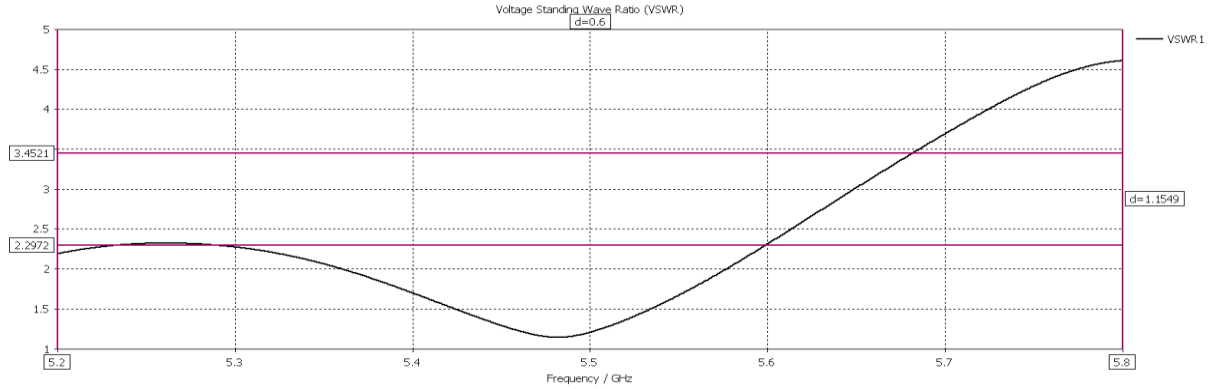


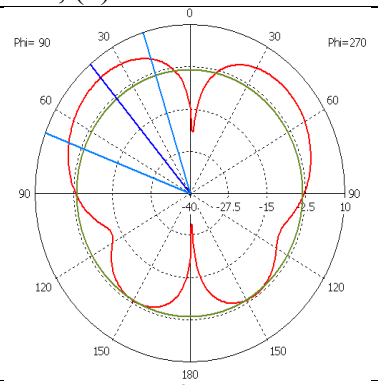
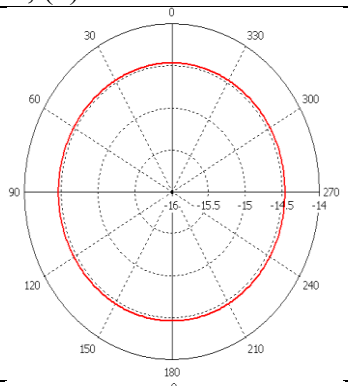
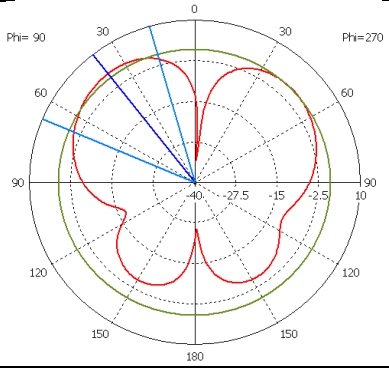
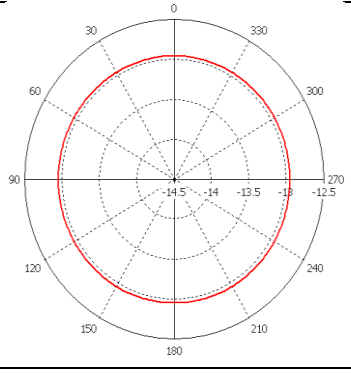
Figure 7: Voltage Standing Wave Ratio (VSWR).

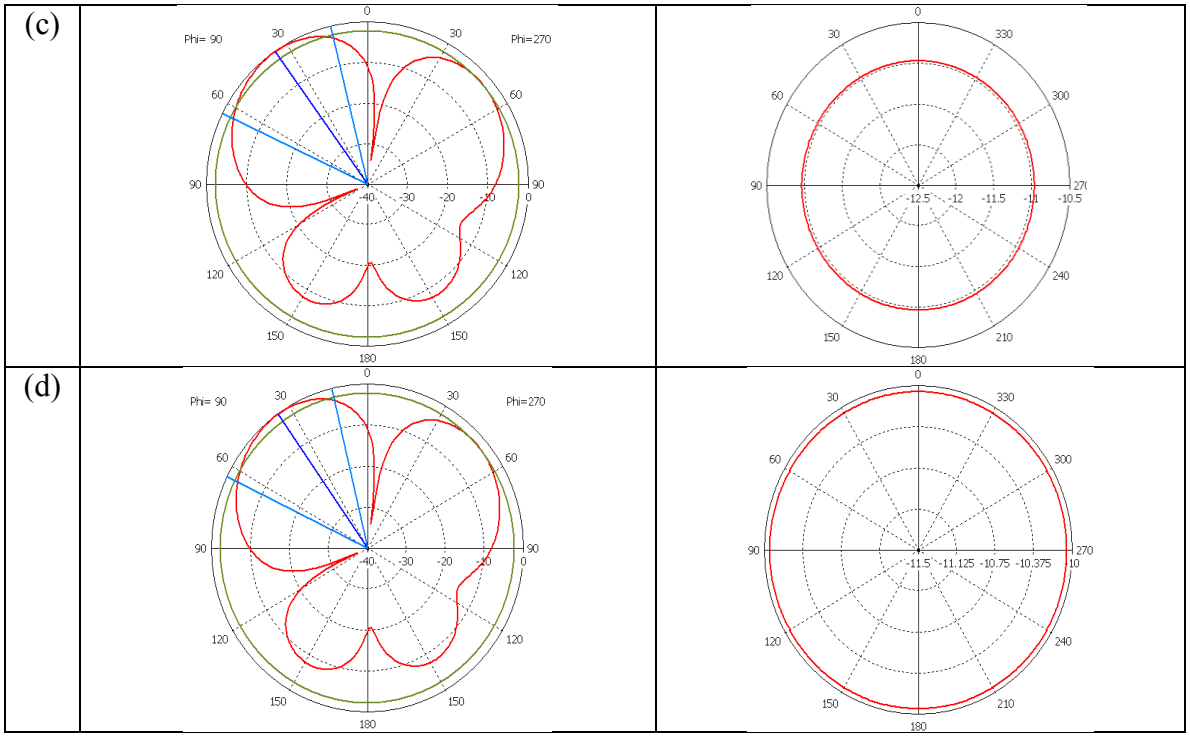
4.5 Radiation Pattern

The Table 2 below shows the simulated radiation pattern at different frequencies from 5.3GHz to 5.6GHz of 90° theta cut from the E-plane of the farfield representation. The incremental of the step size is 0.1GHz. The directivity of antenna defines that it is a fundamental antenna parameter, which measures the power density that the antenna radiates in the direction against radiated isotropic source which emits in equal amount in all directional [15]. The simulated results indicate that the concentration of field mainly being focused on the side of the patch. Upon that, most antennas applications should have a side lobe level not lesser than -20 dB. The directivity of the antenna is directly perpendicular to the frequency. Table 2 shows that with increasing values of frequency, the directivity of the antenna also increases. This is due to the fields that concentrate on the front part of the micro strip patch antenna. It is observed that the number of lobes also increases along with frequency.

Table 2 also displays the simulated radiation pattern at different frequencies of 0° phi cut from the H-plane. The incremental of step size is similar to the E-plane and it can be recognized that the radiation pattern exhibit omnidirectional radiation behavior.

Table 2: Simulated radiation patterns.

	Simulated Radiation Pattern with a 90° theta cut at (a) 5.3GHz, (b) 5.4GHz, (c) 5.5GHz, (d) 5.6GHz.	Simulated Radiation Pattern with a 0° phi cut at (a) 5.3GHz, (b) 5.4GHz, (c) 5.5GHz, (d) 5.6GHz.
(a)		
(b)		



6. Conclusions

This paper illustrates the proposed micro strip patch antenna design, with the simulated result operating from 5.2GHz to 5.8GHz. The antenna design has achieved the return loss of (*S11*<-10dB) and impedance of 50 Ω. Besides that, it also complies with the Voltage Standing Wave Ratio (VSWR) ranged from 1 to 2. This antenna design is suitable for most wireless applications such as the Wi-Fi/WLAN application in accordance to the wireless 802.11a standard, which runs in the band of 5GHz [16]. The impedance bandwidth of the proposed antenna design is fulfilling the requirements for the WLAN frequency bands. In addition, necessary improvements or enhancements are taken into consideration for possible future works in terms of design and its parameters. Thus, designing and creating a more enhanced micro strip patch antenna that exhibits optimal antenna performance at different range of operating bands.

References

[1] H. Kumar, Varshney, M. Kumar, A. K. Jaiswal, R. Saxena, and K. Jaiswal, 'Design Characterization of Rectangular Micro Strip Patch Antenna for Wi-Fi Application', pp. 2347-5161.

[2] A.S. Elmezughi, W.S.T Rowe, and R.B. Waterhouse, 'Edge-fed cavity backed patch antennas and arrays', pp. 614–620, May-2008.

[3] D. R. Jackson, J. T. Williams, A. K. Bhattacharyya, R. L. Smith, S. J. Buchheit, and S. A. Long, 'Microstrip patch designs that do not excite surface waves', *IEEE Transactions on Antennas and Propagation*, pp. 1026–1037.

[4] W. S. T. Rowe and R. B. Waterhouse, 'Edge-fed patch antennas with reduced spurious radiation', *IEEE Transactions on Antennas and Propagation*, pp. 1785–1790, 2005.

[5] R. Abdullah, D. Yoharaaj, and A. Ismail, 'Bandwidth Enhancement Technique in Microstrip Antenna for Wireless Applications', *PIERS Online*, pp. 633–639, 2006.

[6] D. Yoharaaj, R. S. Azmir, and A. Ismail, 'A New Approach for Bandwidth Enhancement Technique in Microstrip Antenna for Wireless Applications', *2006 International RF and Microwave Conference*, 2006.

[7] S. Panwar and B. S. Sharma, 'Microstrip Patch Antenna: Analysis of Surface Area for Bandwidth Improvement', *Journal of Engineering Research and Applications*, pp. 996–999, 2013.

[8] H. Kumar, Varshney, M. Kumar, A.K. Jaiswal, R. Saxena, and K. Jaiswal, 'A Survey on Different Feeding Techniques of Rectangular Microstrip Patch Antenna', *International Journal of Current Engineering and Technology*, pp. 1418–1423, 2014.

[9] M. Kiroriwal and S. Rawat, 'Improvement in Radiation Parameters of Rectangular Microstrip Patch Antenna', *International Journal of Engineering Research and General Science*, pp. 393-397, 2014.

[10] A. T. Hussein and S. Luhaib, 'Designing E-shape Microstrip Patch Antenna in Multilayer Structures for Wi-Fi 5GHz Network', 2012.

[11] S. Yeap and Z. Chen, 'Microstrip Patch Antennas With Enhanced Gain by Partial Substrate Removal', *IEEE Transactions on Antennas and Propagation*, 2010.

[12] M. H. Tariq, S. Rashid, and F. A. Bhatti, 'Dual Band Microstrip Patch Antenna for WiMAX and WLAN Applications', *International Journal of Multidisciplinary and Current Research*, 2014.

[13] D. Orban and G. J. K. Moernaut, 'The Basics Of Patch Antennas', *Obran Microwave Products*.

[14] Y. Rahayu, 'Reconfigurable Ultra Wideband Antenna Design and Developtment for Wireless Application', 2008.

[15] K. N. Modha, B. Gill, and I. Harrison, 'A compact Low Loss Ice Cream Cone Ultra Wideband Antenna', pp. 165-168, 2006.

[16] B. H. Walke, S. Mangold, and L. Berlemann, *IEEE 802 Wireless Systems Protocols, Multi-hop Mesh/relaying, Performance and Spectrum Coexistance*, 2006.

Effectiveness of Digital Media in Developing a 3D Model from 64 Detector CT Scan Images

P. Mohankumar, Leong Wai Yie

School of Engineering, Taylor's University, Taylor's Lakeside Campus, No 1, Jalan Taylor's, 47500 Subang Jaya.

mohanphysionix06@gmail.com, waiyie@gmail.com

Abstract

The development of science have always made medical field to reach its extreme which in turn have extended the life span of human race. When X-rays were discovered, it helped the physicians and orthopedicians in treating patients with fracture. When Computed Tomography (CT) and Magnetic Resonance Imaging (MRI) scanners were invented, it created a boon to the medical society. CT and MRI are far more advanced than the X-rays. In recent years, with the help of 256 and 320 detector CT scanners, scientists and researchers are trying to create the exact model of the bones and organs of our human body, which will diminish the dependency of researchers on cadaver models to conduct their study. The older 64 detector, helps in detecting the tumor cells in our body. At the same time, the radiation emitted from this scanner is also low. Hence, 64 detector scanner is still used in many hospitals and scan centres. Thus, in this study, we tried to create 3D model with the images obtained from the 64 detector CT scanner using the digital media tools. 5 complete set of 64 detector CT scan files were obtained from the internet and processed. The initial 3D model which was created initially had much noise. But after processing it, the edges and the outline of the bones were clearly visible. Several software's, both open source and paid software's are helpful in creating 3D models from CT scan files.

Keywords: DICOM files, CT scan, SSCT, MSCT, Detector.

1. Introduction

In the olden days, scientists and researchers used human cadavers for their medical research studies. The dependency on cadavers were high while the availability of cadavers were low. In order to solve this problem, science came up with a new technology called 3D modelling and Finite Element Analysis (FEA).

Finite element analysis is a method to solve equations of applied areas to understand how the system works or behaves. It is a simulation technique used in various scientific fields. A 3D model can be developed with the computed tomography scan (CT scan) and magnetic resonance imaging (MRI scan) files. These radiographic files are called as Digital Imaging and Communications in Medicine (DICOM) files. DICOM is the standard method or technique to handle, store, print or transfer medical images. This DICOM files can be obtained when a patient undergoes CT or MRI scan. The history and development of CT scan is remarkable.

1.1. Evolution of CT Scanner

Computed Tomography scanners were available from the mid of 1970 and have reached a remarkable place in medical imaging till today's date. The images obtained were taken from different angles around the body and uses computer to process it. The basic components of the CT scanner are x-ray source, detectors and computer. CT scan provide a high resolution, cross sectional images of our body in the shades of grey [1]. Bone appears white, while air appears black and other tissues in the different shades of grey.

CT scanning technology had developed to a significant level since its invention and started using advanced technology in the recent years. The development in the CT scanning were mainly focused on the faster scanning using finer slices. The very first conventional CT scanning machines at 1989 had only single detector with it. They were called as 'Single Slice spiral Computed Tomography' (SSCT). When the x-ray tube makes one complete rotation around the patient, it took only one slice or image of that patient and took more time to complete the scan. Latter in 1998, 'Multi Slice spiral or Multi Detector Computed Tomography' (MSCT or MDCT) was introduced. The initial multi detector computed tomography had 4 detectors. As days passed, more detectors were used. As of now MDCT comes with different configurations like 4, 6, 8, 16, 32, 40, 64, 128, 256 and 320 detectors [2]. The number of detectors in a CT scanner is equal to the number of slices taken per rotation (refer figure 1). Among these detectors, 64 detector CT scan is quite popular.

1.2. 64 Detector CT scan

64 detector CT scanner can take up to 64 images per rotation. This particular technology is useful for cardiologists. 64 detector has significantly improved the field of Angiography. The sensitivity and speed of this detector provides a broad outlook to the cardiologists on how well the heart is contracting and its blood vessels. It produces fine

images with sharp details within a very few seconds. Thus, 64 detector scanner is used in most of the hospitals and scan centres.

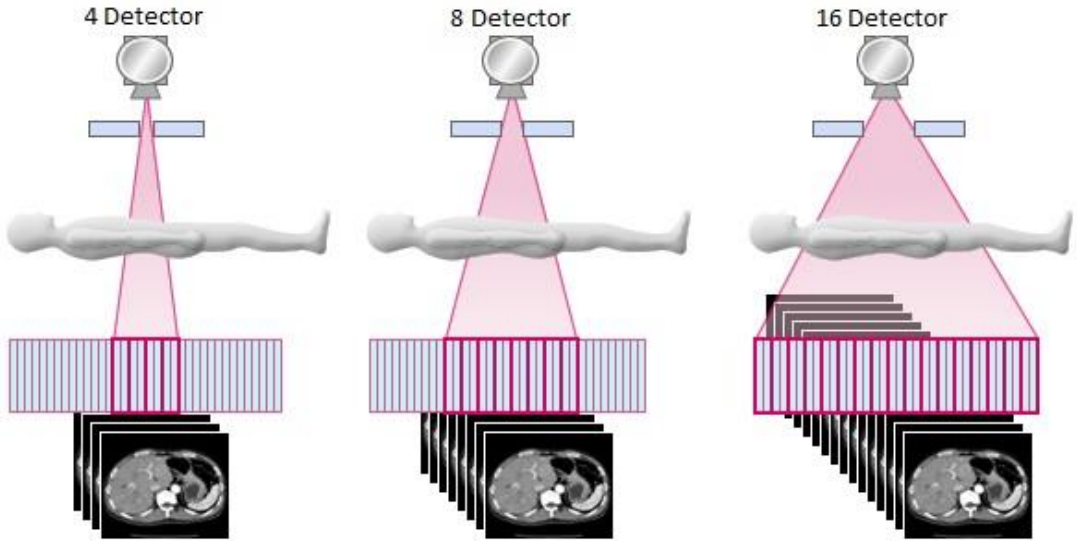


Figure 1: Types of Detector [3]

CT scan images (DICOM) plays a major role in developing 3D models of the patient. With the recent advancement of 3D printing technology, researchers use 256 and 320 detector CT scanned images to do 3D printing, since the images obtained from 256 and 320 detector are with high resolution and more accurate. In order to create a 3D model of the patient's bone or organ, several tools are available in the internet. Both open access and paid versions of software's. Thus, in this study, using digital media tool we try to create a fine 3D model using the DICOM files acquired from the 64 detector CT scanner.

1.3. Importance of 3D model in Research

Several studies are done by researchers and scientists on 3D modelling and 3D printing. Using 3D printers, researchers at Washington State University developed a hybrid material that has same properties (strength and flexibility) as of human bone. This model can be placed at the site of fracture, which can disintegrates latter once the bone is healed. In order to get an absolute, exact 3D printed model of a bone or organ of the human, a complete set of CT scanned DICOM files are required. Ai Min Wu, et al., in 2015 conducted a study on accuracy of a method for printing 3D spinal models using CT scans which revealed the possibility of 3D printing using DICOM files [4]. Atif N. Khan, et al., in 2014 conducted a study on radiation in organs using 64 and 320 detector, to determine absorbed radiation dose in radiosensitive organs [5]. Atif Khan, et al., in 2011 done a comparative study on image quality using 320 and 64 multi detector computed tomography and found that the image quality of both the 320 and 64 MDCT were good [6]. Clayton J Adam, Sara C Cargill and Geoffrey N Askin in 2007 conducted a study on CT based volumetric reconstruction of the pulmonary system in scoliosis. Where they created a 3D model using the DICOM files of 28 pre-operative 4 detector CT scan (Toshiba Aquilion Multi with 100kV, 50mA source) and found that the model created can be used as an alternative for performing pulmonary function test in infantile or juvenile patients with scoliosis [7]. Hendrik Schmidt, Annette Kettler, Frank Heuer and Ulrich Simon in 2007 done a study using DICOM files obtained from

16 detector CT scan and MRI to create a 3D model and find stress, strain and pressure in intervertebral disc [8]. Even in our previous study, we created a 3D model of a vertebrae using DICOM files obtained from different detectors [9].

2. Method

Five complete sets of DICOM files of the 64 detector Computed Tomography scanner (Siemens - SOMATOM Definition AS) were obtained from the internet [10] [11]. These DICOM files were initially imported into the software called InVesalius, version 3.0 [12]. InVesalius is a medical imaging program for 3D reconstruction developed by Brazilian Ministry of Health. It uses a sequence of 2D DICOM image files acquired from CT or MRI scanners and exports it in to 3D volumes or surfaces.

2.1. Processing

Depending upon the area of scan (brain, heart, bone) the number of DICOM files (slice) in the data set varies. Generally it varies from 100 to 900 or even more. Once the files are loaded in InVesalius, it is displayed in three planes in three windows namely axial, sagittal and coronal plane (refer figure 2). The 3D model created in InVesalius without doing any change in properties is shown in figure 3. Figure 3 has more noise and model is not complete. The vertebrae looks corrupted. In order to get the exact model, manual changes had to be done. Now, mask properties and manual threshold are adjusted in the selected region of interest. Predefined threshold can also be set according to the need or manual edition can also be done using the threshold which ranges between -1024 to +1734. If the number of slices are low, even each and every slices can be manually edited for more perfection. In case if it is high, the possibility of editing each and every slices becomes low. Once the editing work is done, a 3D surface is created where the surface property like transparency and other advanced properties can be adjusted. With this, a final 3D surface model can be exported (refer figure 4) in predefined file formats.

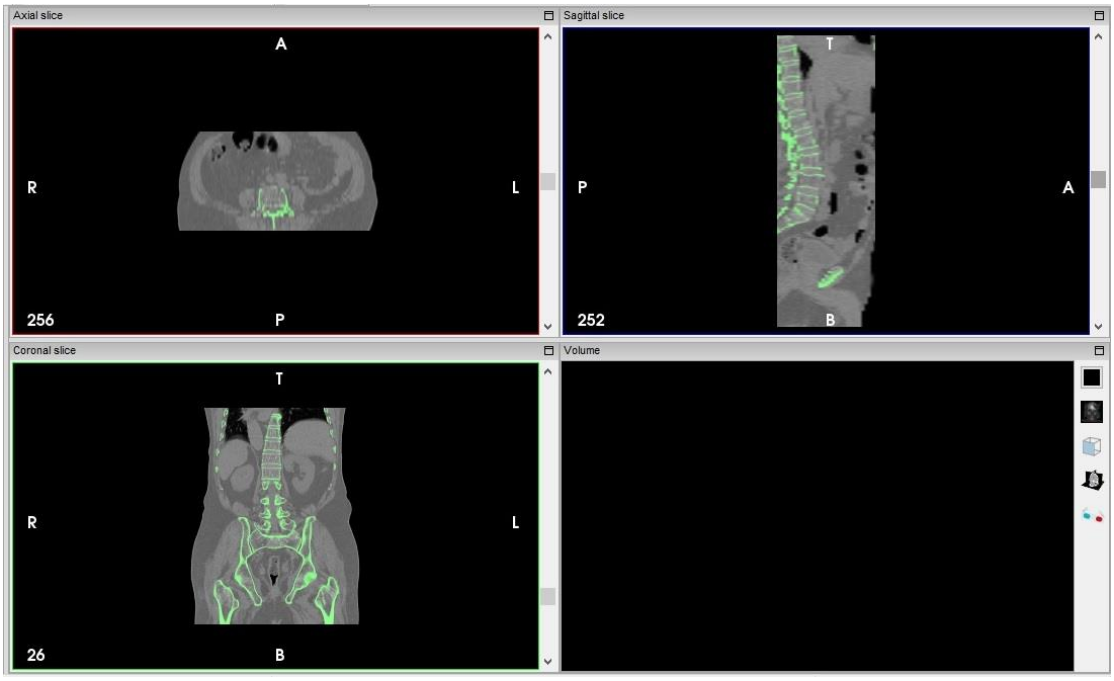


Figure 2: Three planes in InVesalius

3. Results and Discussion

The 3D model exported without doing any changes or manual corrections looked like a noisy, corrupted and untidy 3D model (figure 3). Most of the edges and curves of the vertebrae were not clear. Whereas, the 3D model exported with manual changes in the mask properties and threshold properties looked clearer than the previous. The edges and curves are clearly visible with very less or no noise. These differences can be noted in the histograms as well (refer figure 5 and 6). The X axis represents the level of intensity whereas the Y axis represents the number of pixels of a particular intensity with that of X axis.



Figure 3: Pre processing

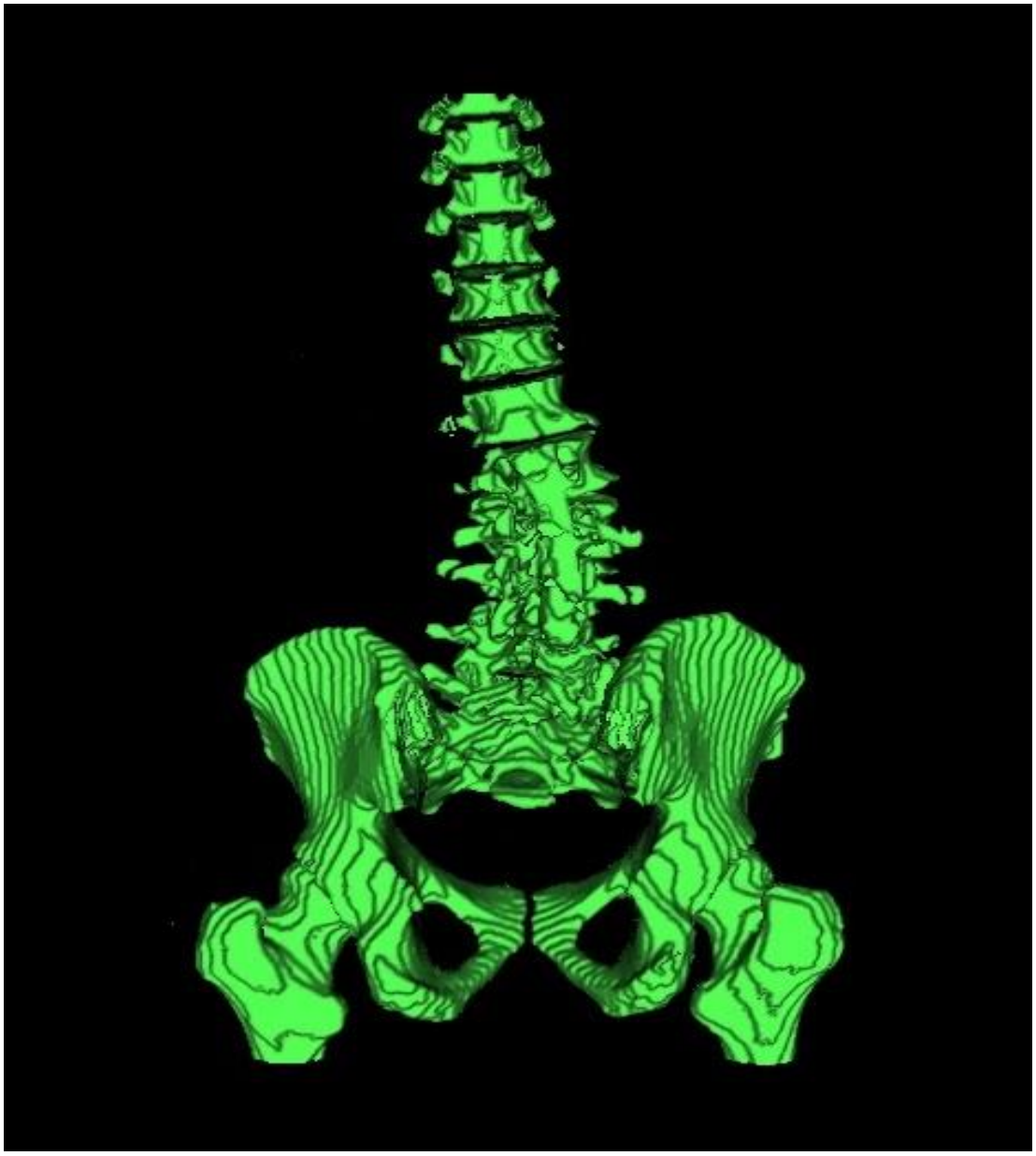


Figure 4: After processing

The manually edited 3D model (refer figure 4) looks complete when compared with the fully automated 3D model (refer figure 3).

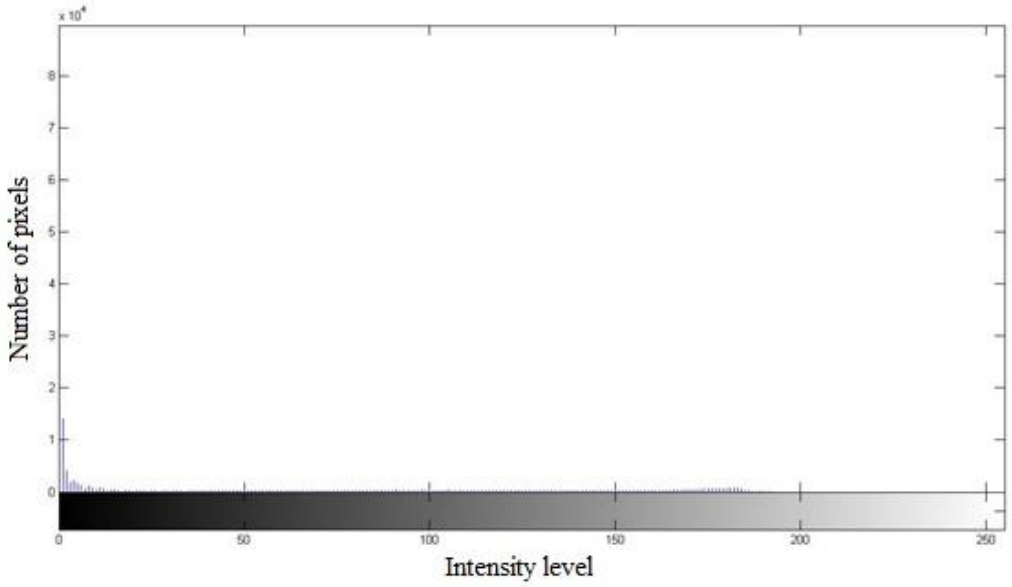


Figure 5: Histogram before processing

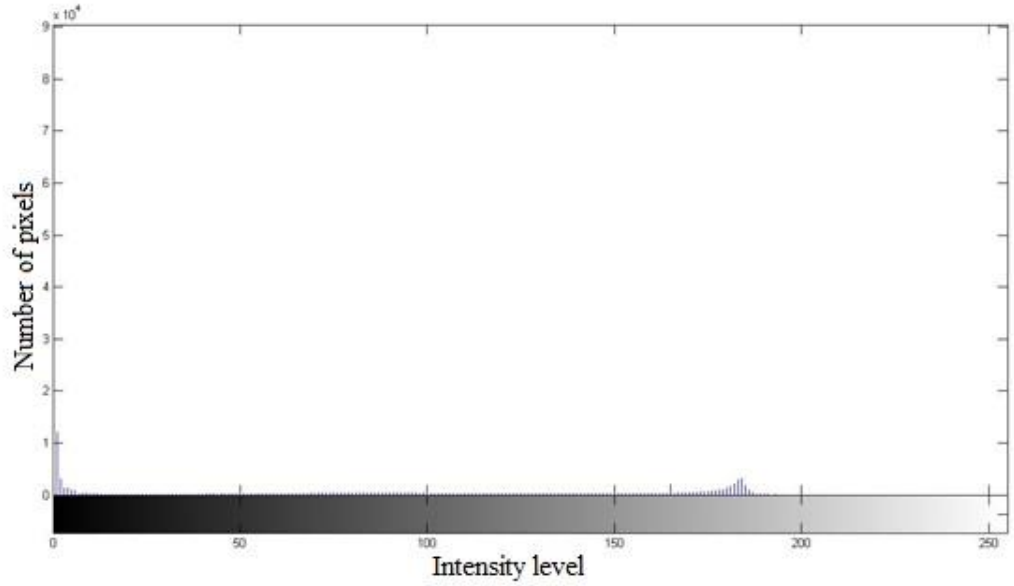


Figure 6: Histogram after processing

There are other freeware open access software's like ITK Snap, Slicer, MeshLab which can convert DICOM files into 3D model. But, as a researcher, when we tried to create 3D model using those software's, the final output was not satisfactory and adding to that, we also felt that the user interference of InVesalius was more convenient and easy to use. We tried to create a 3D model using ITK software. Initially, region of interest (ROI) was selected. Then followed by Pre-processing- which includes upper and lower threshold, Initialization- placing bubbles in the ROI and Evolution- contour evolution. Once all the editing is done, the final 3D model was obtained. The 3D model appears to be like a stack of bubbles placed one above the other (refer figure 7). Marking the vertebrae and ribs using bubbles in a noisy image is merely impossible or highly difficult.

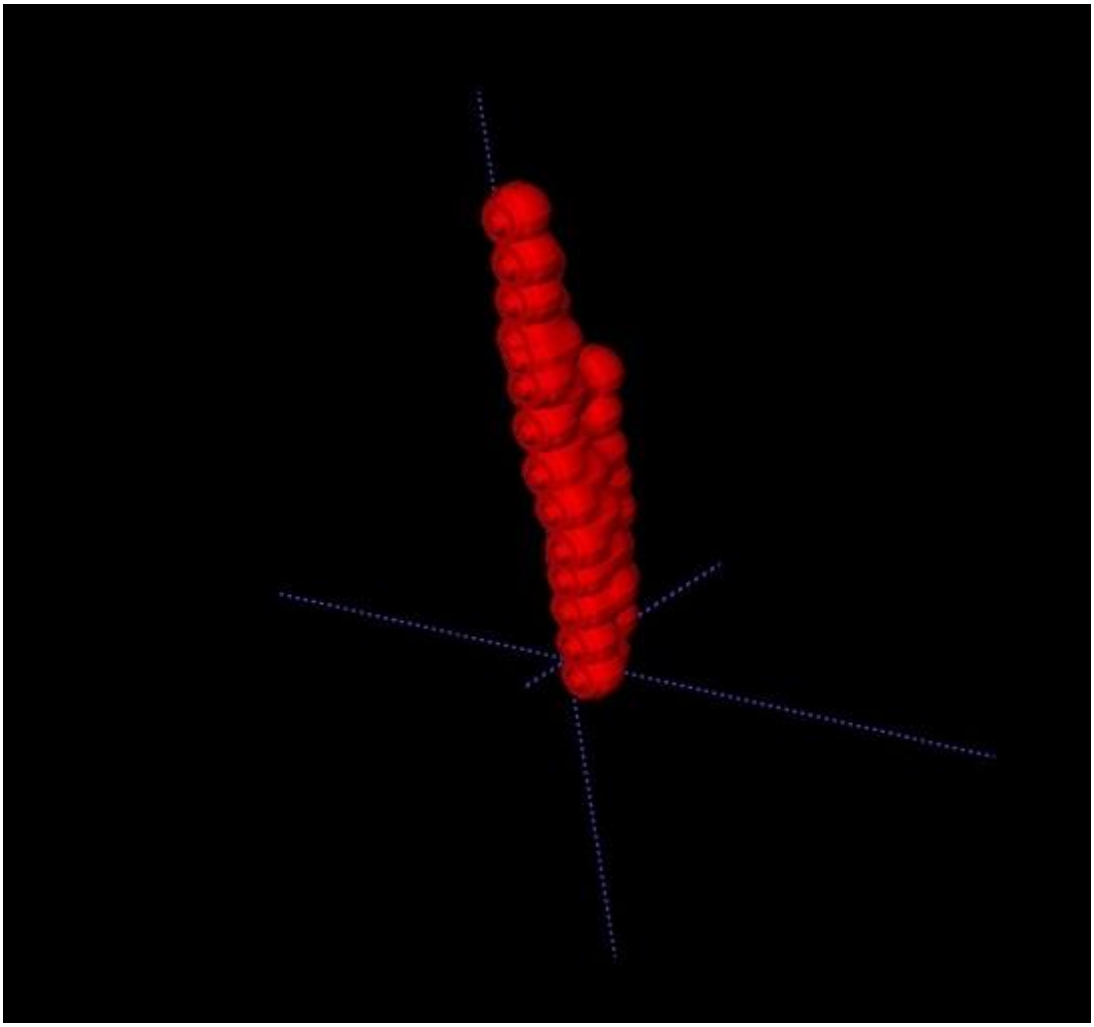


Figure 7: 3D model from ITKSnap

With the ability to create 3D models from CT scans, the dependency on cadaver models are greatly reduced. Instead of waiting for cadaver models, scientists and other medical researchers can rely on the 3D models. A depository for CT and MRI scan files can be initiated in every hospital, so that the patient's data can be used or converted into 3D model and finite element analysis can be applied for medical research purposes. Previously, Janko D. Jovanovic and Miomir Lj. Jovanovic in 2010 created a finite element modelling of the vertebrae with its geometrical and material properties retrieved from the CT scan data using the program Mimics (materialize software) [13].

4. Conclusion

Even though with the rapid advancement in the CT scan technology, 64 Detector CT scanners are still in commercial use at hospitals and scan centers. It is also significant in detecting the cardio abnormalities and plays a vital role in detecting cancer. With the possibility of creating a 3D model in 64 detector DICOM files, in future many medical studies can be done in 3D printing and enhance our understanding. Thus, digital media have a strong influence in creating a 3D model from CT scanners.

References

[1] L. Stephens, "The Evolution of CT Scanner Detectors," 11 May 2011. [Online]. Available: http://ezinearticles.com/?The-Evolution-of-CT-Scanner-Detectors&id=6261517. [Accessed 27 October 2015].

[2] N. Welch, "Types of CT scanners," 2 November 2013. [Online]. Available: http://www.amberusa.com/dmxreadyv2/blogmanager/blogmanager.asp?post=types_of_ct_scanners. [Accessed 27 October 2015].

[3] P. t. Pin, "MDCT 16 Slice CT Scan Picture," [Online]. Available: http://www.picstopin.com/901/mdct-16-slice-ct-scan/http:||jnch*nic*in|CT-Scan*jpg/. [Accessed 28 October 2015].

[4] A. M. Wu, Z. X. Shao, J. S. Wang, X. D. Yang, W. Q. Weng, X. Y. Wang, H. Z. Xu, Y. L. Chi and Z. K. Lin, "The Accuracy of a Method for Printing Three Dimensional Spinal Models," *PLoS ONE,* p. 12, 27 April 2015.

[5] A. N. Khan, W. Shuaib, B. Nikolic, M. K. Khan, J. Kang and F. Khosa, "Absorbed Radiation Dose in Radiosensitive Organs Using 64 and 320 Row Multidetector Computed Tomography: A Comparative Study," *Scientifica,* vol. 2014, p. 6, 6 August 2014.

[6] A. Khan, F. Khosa, K. Nasir, A. Yassin and M. E. Clouse, "Comparison of Radiation Dose and Image Quality: 320 MDCT Versus 64 MDCT Coronary Angiography," *AJR AM J Roentgenol,* no. 1, pp. 163-168, July 2011.

[7] C. J. Adam, S. C. Cargill and G. N. Askin, "CT based Volumetric Reconstruction of the Pulmonary System in Scoliosis: Trends in Lung Volume and Lung Volume Asymmetry with Spinal Curve Severity," in *Procedings Annual Scientific Meeting of the Spine Society of Australia*, Hobart, 2007.

[8] H. Schmidt, A. Kettler, F. Heuer, U. Simon, L. Claes and H. J. Wilke, "Intradiscal Pressure, Shear Strain and Fiber Strain in the Intervertebral Disc Under Comined Loading," *SPINE,* vol. 32, no. 2, pp. 748-755, 2007.

[9] P. Mohankumar and W. Y. Leong, "3D modelling with CT and MRI images of a scoliotic vertebrae," *Journal of Engineering Science and Technology,* 2015.

[10] OsiriX, "DICOM sample image sets," [Online]. Available: http://www.osirix-viewer.com/datasets/. [Accessed 28 October 2015].

[11] "DICOM Library," [Online]. Available: http://www.dicomlibrary.com/. [Accessed 28 October 2015].

[12] InVesalius, "InVesalius 3," [Online]. Available: http://www.cti.gov.br/invesalius/. [Accessed 28 October 2015].

[13] J. D. Jovanovic and M. L. Jovanovic, *Finite element modelling of the vertebrae with geometry and material properties retrived from CT Scan data,* vol. 8, Facta Universitatis, 2010, pp. 19-26.

A Practical Implementation for Technique of Self Timed Circuit Synthesis (TSCS) with Timing Constraints for Backend Hardware Synthesis

Tee Kok Khim teekokkhim@sd.taylors.edu.my

Edwin Chung Chin Yau ChinYau.EdwinChung@taylors.edu.my

Taylor's Graduate School
Research Programmes Unit (RPU)
Taylor's University Lakeside Campus
No. 1 Jalan Taylor's, 47500 Subang Jaya
Selangor Darul Ehsan, Malaysia

Abstract
This paper presents the software and hardware implementation of an asynchronous circuit in Field Programmable Gate Array (FPGA) using Technique of Self Timed Circuit Synthesis (TSCS) [1] to derive the timing constraints needed for backend hardware synthesis. Timing constraints and analysis is critical in Asynchronous Circuit design to ensure no hazards would happen and cause the circuit to be malfunctioned. However, most of the published popular techniques on asynchronous circuit design lack of timing analysis for backend hardware synthesis. TSCS functions as an analytic tool used in hazard removal stage to detect and eliminate functional hazards by deriving the timing constraints that are essential for backend hardware flow, in addition it also provides a generic approach which does not require any custom designed of asynchronous logic gates cells in hardware implementation [2]. The circuit is designed and used in any standard Electronic Design Automation (EDA) logic simulations tools written in Hardware Description Language (HDL) to validate its logic functionalities, furthermore gate-level simulation with timing information of gate delay and routing delay can be back-annotated from backend EDA tools to ensure functionalities are intact between pre and post implementation. Even though the proposed method is implemented in FPGA, it can be extended to designing more complex and larger function blocks in Application Specific Integrated Circuit (ASIC) design flow.

Keywords: Asynchronous Circuit, Technique of Self Timed Circuit Synthesis (TSCS), Timing Constraints, Hazards Detection and Removal, Functional Hazards

1. Introduction

Synchronous Circuit depends on global synchronization clocks or latches to sample the data at clock or latch enabled edges. In contrast, Asynchronous Circuit depends on local synchronization between communicated units to ensure data validity and readiness, timing relationship between local communicating signals must be validated to ensure circuit functionality is intact. Therefore, timing constraints and analysis is critical in Asynchronous Circuit design to ensure no hazards would happen and cause the circuit to be malfunctioned. However, most of the published popular techniques on asynchronous circuit design lack of timing analysis for backend hardware synthesis. Papers [3]–[5] showed how timing analysis is used in high-level synthesis. To avoid any circuit malfunction in asynchronous circuit, any hazards are not allowed and must be avoided and eliminated. A lot of researches and published papers focus on hazards detection and avoidance to eliminate hazards. Nonetheless, those techniques are unable to detect all the possible hazards conditions, and this means functional hazards will still persist in circuit implementation.

Technique of Self Timed Circuit Synthesis (TSCS) [6] provides a method for hazard detection and removal to derive the essential timing constraints that are required for FPGA hardware implementation. Since it has very strict sets of timing constraints that need to be fulfilled, therefore there are needs to find an optimum sets of relax constraints that is minimum and yet practical for hardware implementation. Commercial FPGA providers has a complete suites of Computer-Aided-Design (CAD) tool that provides design entry, logic simulation, logic synthesis to technology gates Place and Route (PNR) flow which is useful as a prototype platform to validate a practical implementation of using TSCS in asynchronous circuit design. In additions, the design can be validated using Hardware Description Language (HDL) Testbench on the logic functionalities as in a standard synchronous digital logic design flow. This methodology is seamlessly applied in FPGA flow which does not require additional custom logic gates specific for asynchronous design and can be further extended to apply on ASIC design flow as well.

1.1 TSCS Overview

TSCS is a type of Signal Transition Graph (STG) Synthesis approach [7]. The synthesis procedure requires design specifications to be defined in STG which can further be translated to State Graph (SG) and tabular minterm/maxterm, From tabular minterm/maxterm, QM method is then used to generate the Boolean Equations for states and output variables target to hardware implementation.

TSCS is an important technique to eliminate potential function hazards in asynchronous circuit. Nonetheless, to enable practical hardware implementation, finding the optimum or reduced timing constraints are necessary. TSCS is based on two fundamental algorithms for hazards detection and removal, which consist of

- Algorithm 1: Algorithm for detecting hazard susceptibility conditions, and
- Algorithm 2: Derivation of timing constraints necessary to avoid function hazard.

In [1] Chapter 7, Theorem 7.3, the restriction to have all the ordering constraints required for hazard avoidance can be relaxed by reducing the number of constraints required due to the effect of each transitions that shift away from subspace will have the reverse effect with the transitions which is shifting towards the subspace. Hence, transition of signals will not result in a shift into subspace if:

1. Transition that shift away from subspace (Tup), Or
2. There exists an earlier transition that has the reverse effect.

With the relaxed constraints taken into account in the TSCS solver, the initial signal state is critical to be in Tup region, this will ensure the condition of having the transition that shift away from subspace as the starting point. Hence, by cycling through the longest possible critical paths and computing the sequences, a set of ordering constraints can be derived which will provide a relaxed or minimum sets of timing constraints essential for backend synthesis.

2. Proposed Work

The primary goal for this work is to translate TSCS theories into practical software implementation, it will make use of TSCS as a critical ordering analysis tool to determine the required timing constraints for backend logic implementation, in which most of the popular tools do not or lack of timing constraints used for backend hardware synthesis. To enable TSCS in logic implementation, Quine-McCluskey (QM) algorithm is to be developed to facilitate the control abilities and visibilities into the Boolean equation derived from STG specifications.

Secondary goal is to find out an optimal solution as if there are possibilities to relax the timing constraints, such as for a larger and more complex circuit, there will be multiple sets of critical orderings derived from TSCS analysis, and if there exists conditions that require only selective of timing orders that will meet the TSCS timing constraints and requirements. Alternatively, it is yet to be concluded if there remains a possibility that there are conditions where timing constraints found from the TSCS analysis will contradict each other, which implies that there exists orders that are conflicting with earlier orders derived.

Final goal is to utilize the timing constraints derived from TSCS and implement the design in FPGA technology cell libraries. A circuit example is used throughout the work, from TSCS hazard detection and removal to timing constraints derivations. The Boolean equations is then generated with QM method and translated into Hardware Description Language (HDL) to facilitate design entry into FPGA EDA tools. A behavioural testbench is developed and written in HDL to verify the logic functionalities which include behavioural logic simulation and gate-level netlist simulation. In gate-level netlist simulation, gate delay and routing net delay is back-annotated from FPGA EDA tool in Standard Delay Format (SDF) and logic functionalities is validated to be intact between pre and post implementation, i.e between behavourial simulation and gate-level netlist simulation.

There are few important solvers needed to be developed in software for TSCS on top of hardware implementation with HDL coding. Figure below show the work flow and tasks required.

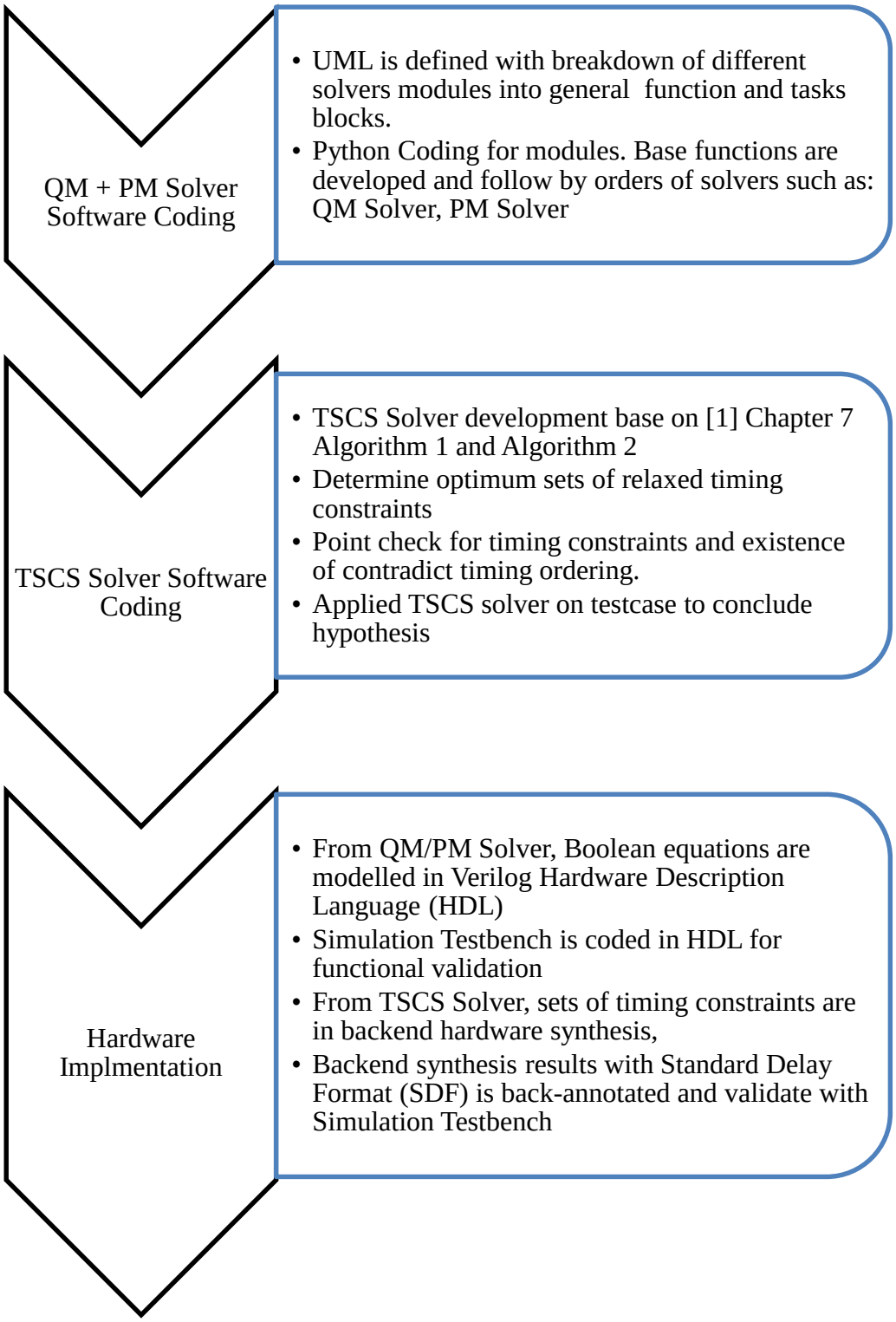


Figure 1. Work flow and tasks for Software and Hardware implementation.

3. Implementation

This section provides the overviews of modules or function blocks for software implementation and FPGA hardware implementation flow. Even though the hardware implementation is targeted at FPGA technology, it can be extended to

designing more complex and larger function blocks in Application Specific Integrated Circuit (ASIC) design flow. Most of the workflow share the same commonality in design entry, logic simulation and testbench validation.

3.1 Software

There are 2 major solvers that need to be developed in this thesis. The first solver is Quine-McCluskey (QM), it is used to derive the Boolean equation functions in Sum-Of-Products (SOP) terms from STG and State Graph specifications inputs. Second solver is based on Technique for Self-Timed Circuit Synthesis (TSCS), which is used for analyzing the hazard susceptibility of a circuit and finding the critical timing constraints that are needed towards a hazard free circuit implementation.

3.1.1 QM Solver

There are 2 major functions modules, the former QM module is used for prime implicants tables generation, reduction, and find the solution. The latter is Petrick's method module which provides a branching method to resolve cyclic problem from QM module if it exists. Below are the list of functions blocks.

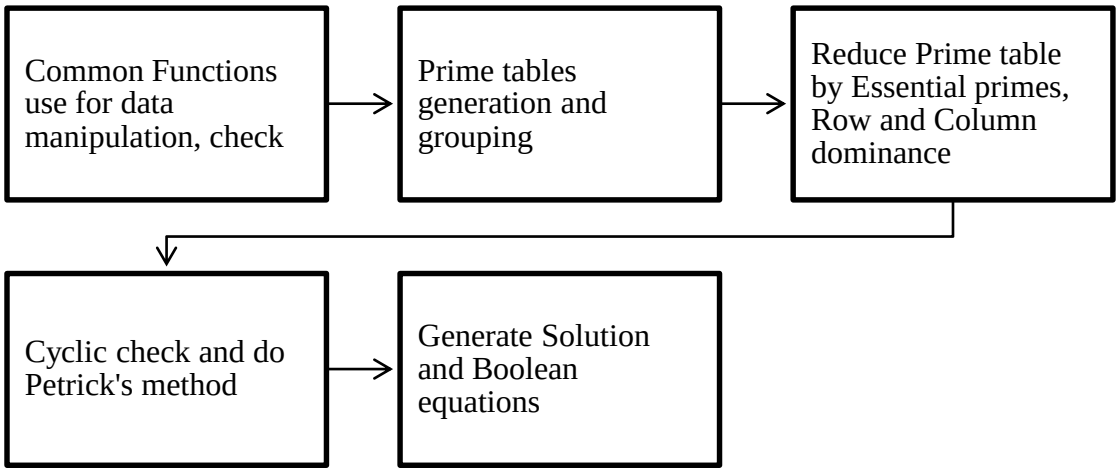


Figure 2. QM Solver and its modules group by functions

3.1.2 TSCS Solver

TSCS modules perform the timing analysis based on inputs from QM module solution in the result forms of Boolean equations. The function blocks listed below are developed based on Algorithm 1 and Algorithm 2 as in Section 1.1. Besides translating the theory into software implementation, some additional enhancements are added to the existing TSCS algorithm, these include a constraint solver for finding all the longest critical paths, optional input parameter to specify the offsets for the orders sequence, optional maxterm analysis, and finding the optimum result from the compute of critical orderings from numerous critical paths. It is due to existing TSCS's restriction on the timing constraints are too strict and not practical for hardware implementation. The goal is to find a reduced set or optimum set of timing constraints that is practical for backend hardware synthesis.

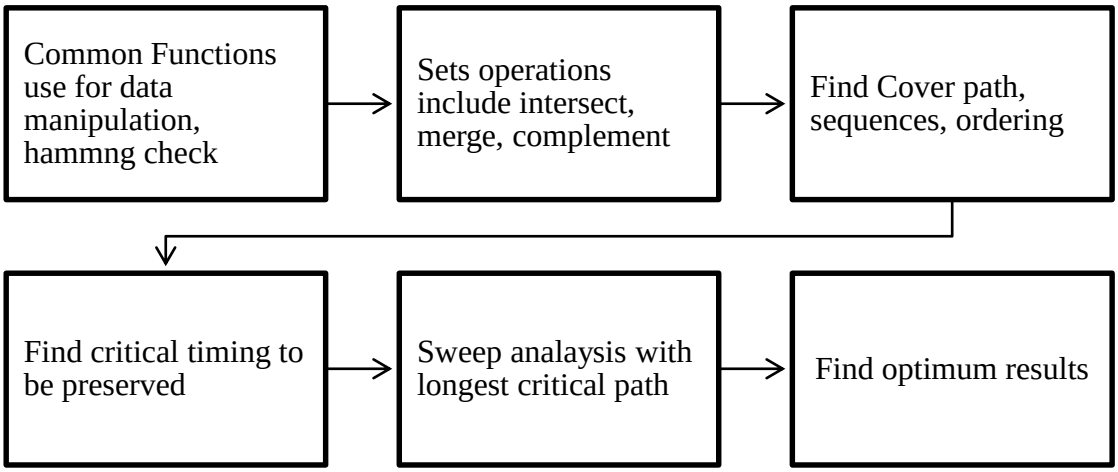


Figure 3. TSCS Solver and its modules group by functions

3.2 Hardware

The timing constraints derive from TSCS specify the critical orderings of the signals arrival at the inputs of the logic cells, inclusive of feedback paths that loop back to the inputs of the cells as well. In other words, the orderings between the signals are to be modelled as delays cells and constrained to meet the required delays for signals arriving at the logic gates inputs. FPGA vendors provide technology cells libraries which support configuration of different delay granularity for input and output signals. The macros are useful to model the timing constraints from TSCS by configuring the required delays in the design, hence the delays requirements can be incorporated into the design to facilitate simulation and backend implementation flow.

As an example, from the Boolean equations generated by QM Solver, an equivalent HDL design is coded as design entry to FPGA EDA tools. HDL testbench is developed to validate the design logic functionalities. By incorporating the delays constraints into the design, FPGA synthesis and place and route are executed to generate the netlist and timing information on delays for logic gates and routing nets are back-annotated to HDL testbench for validating the logic functionalities are still intact between the pre and post implementation.

Nonetheless, for asynchronous circuit implemented in FPGA hardware, there are certain guidelines that need to be strictly follow as listed below:

1. Avoid Look-Up-Table (LUT) optimization as it will cause TSCS to lose the timing constraints requirements as the logic is no longer preserves the prime implicant switching information with respect to the tabular minterm/maxterm.
2. Input and output delays constraints are not applicable to enforce the TSCS timing constraints, as the routing net delays in the circuit is controlled by FPGA vendors Place and Route (PNR) algorithm, and it is not able to produce the require delay granularity needed for hazard avoidance.
3. Virtual clock are used for Static Timing Analysis Check.
4. Dummy clock are used for FPGA delay cells macros to configure the required delays.

Figure below show the hardware implementation work flow.

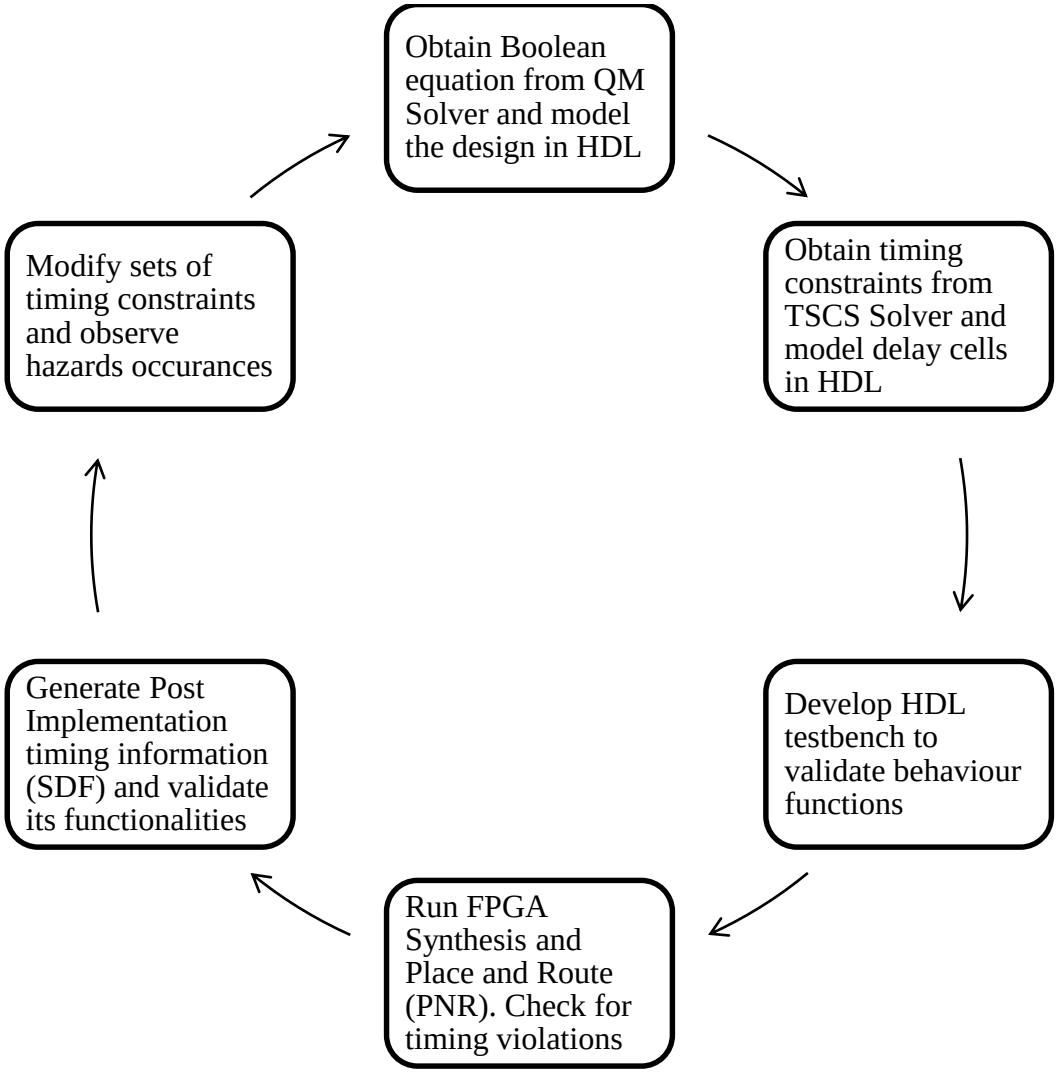


Figure 4. FPGA Hardware implementation by tasks

4. Result

An example of asynchronous circuit with the following STG is used in the derivation of State Graph that can be mapped into Karnaugh-map space. Boolean equations can be computed with tabular method using Quine-McCluskey (QM) Solver. QM is an algorithm to find minimum-cost Sum-Of-Product (SOP) implementation of a Boolean function. The Boolean equations generated from QM Solver is as Eq. (1) below,

$$c = d + \overline{a}b + bc \quad (1)$$

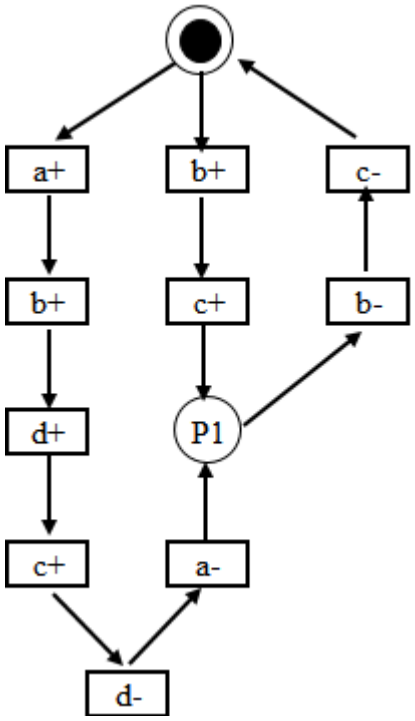


Figure 5. STG Specification

This sections list the simulation run waveform from FPGA EDA tool inclusive of behavioral logic simulation and gate level netlist simulation with Standard Delay Format (SDF) timing information back-annotated.

It can be seen from Figure 5 that even with reduced sets of TSCS timing constraints, the output of the logic blocks has glitch at marker 1 due to delays introduced at the inputs cause momentary switch of functions at the output.

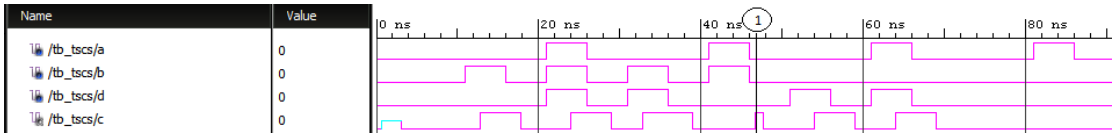


Figure 5. FPGA Behavioral Simulation

However, functional hazards are detected if the timing constraints are not set as per TSCS requirements, in this run, the constraints are set such as violating the TSCS, as shown in markers 1, and markers 2 in Figure 6

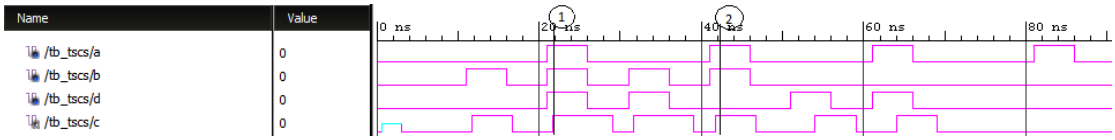


Figure 6. FPGA Behavioral Simulation with wrong TSCS constraints

There is a requirement to have glitch-filter logic at the output path or feedback path logics to ensure hazard free design is confined in its boundary than propagating the glitch to the next level of logic blocks. It can be seen from Figure 7 and Figure 8

that both of the pre and post implementation of the simulation result with reduced sets of TSCS timing constraints, the output of the logic blocks are hazard free no matter what are the combinations of the inputs stimulus. The waveform in Figure 8 shown the output has larger delays due to SDF timings is back-annotated in gate level simulation run.

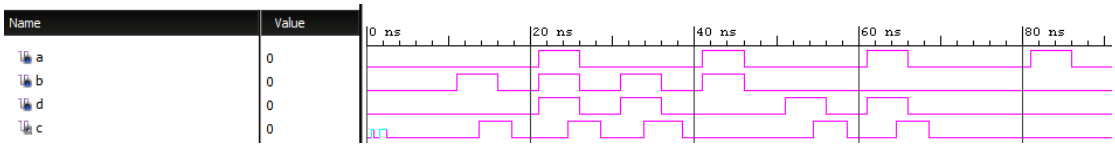


Figure 7. FPGA Behavioral Simulation with glitch filter

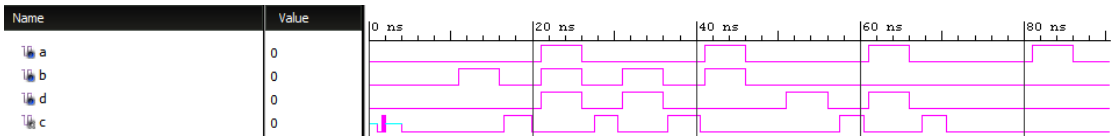


Figure 8. FPGA Gate-Level Simulation with glitch filter

5. Conclusions

This paper proposed a practical implementation of hazard free asynchronous design in FPGA hardware. An example of asynchronous design is implemented using TSCS for hazards detection and reduced sets of timing constraints are derived for backend implementation. TSCS provides a generic approach which does not require any custom designed of asynchronous logic gates cells in hardware implementation. The simulation results showed consistent logic functionalities between the pre and post implementation. Even though the hardware implementation is targeted at FPGA technology, it can be extended to designing more complex and larger function blocks in Application Specific Integrated Circuit (ASIC) design flow.

References

[1] E. Chung Chin Yau, "Synthesis of Hazard-free Metastable-robust Self-timed Digital Circuits from Live-Safe Simple Signal Transition Graphs. PhD Thesis," Monash University, Australia, 1995.

[2] I. P. Dugganapally, W. K. Al-Assadi, T. Tammina, and S. Smith, "Design and Implementation of FPGA Configuration Logic Block Using Asynchronous Static NCL," *2008 IEEE Reg. 5 Conf.*, pp. 1–6, Apr. 2008.

[3] C. J. Myers, T. G. Rokicki, and T. H.-Y. Meng, "Automatic synthesis of gate-level timed circuits with choice," *Proc. Sixt. Conf. Adv. Res. VLSI*, pp. 42–58, 1995.

[4] C. J. Myers, T. G. Rokicki, and T. H.-Y. Meng, "POSET timing and its application to the synthesis and verification of gate-level timed circuits," *IEEE*

Trans. Comput. Des. Integr. Circuits Syst., vol. 18, no. 6, pp. 769–786, Jun. 1999.

[5] C. J.Myers, *Asynchronous Circuit Design*, vol. 6. John Wiley & Sons, Inc, 2001.

[6] E. C. Y. Chung and L. Kleeman, "Avoiding Hazards in Self-timed Digital Circuits Derived from Signal Transition Graphs," *Aust. Telecommun. Res.*, pp. 1–29, 1995.

[7] T.-A. Chu, "Synthesis of Self-Timed VLSI Circuits from Graph-Theoretic Specifications. PhD thesis, MIT Laboratory for Computer Science, June 1987."

Smart Light Signal for Motorcyclists

Jia Chen Sim[1], Mohsen Nabipoor[2]

[1]*Student, School of Engineering, Taylor's University, Malaysia*
[2] *Lecturer, School of Engineering, Taylor's University, Malaysia*

[*]*Jiachen.sim@sd.taylors.edu.my*

Abstract
The accident rate involving motorcycles has raised a growing concern of the public and additional safety measures are strongly advisable to be implemented. Hence the idea of creating smart light signal for motorcycles is proposed. Smart light for motorcycle is a device which can be implemented in the helmet/ jacket of the rider. It can detect the movement of the motorcycle and signal other road users to reduce the chances of collision. The working principle of the device is based on a microcontroller and accelerometer. The sensor will collect data from the environment, and the microcontroller will process and analyze the data. The analyzed data will be used to identify the possible outcome and turn on the LED to signal other road user. The project is divided into two phases; under Phase 1 the specification of all components used in the project will be identified. Besides, a data logger circuit will be designed and constructed. The circuit will be attached to a motorcycle and the motorcycle will be travelling around to collect sensor data and store it in a SD card, video recording will also be done when the bike is travelling. These data will be retrieving from the SD card and imported into MATLAB. By applying three types of filter the graphs can be plotted in MATLAB. The plotted graph will be transformed into an animated plot and synchronize with the experiment. From the video the basic rule to form the algorithm will be defined. Phase 1 is to increase the accuracy of data collection due to different basic rule; Phase 1 will only end when the precision of the basic rule is high. On the other hand, Phase 2 is about prototype of the project, during this phase an algorithm based on the rule will be written and implemented into an embedded microcontroller. Finally, the main focus of this paper will be Phase 1 of the project.

Keywords: Motorcycle, detect, Accelerometer, Embedded microcontroller, Safety measure

1. Introduction

Transportation is important in human life; people often use transportation as a tool to reduce the time taken to travel from one place to another. Various types of transportation is available in the market and motorcycles are one of the popular transportation used by many people. Due to the low-cost of motorcycle and affordability to most people, motorcycles have become a priority transportation tool in many countries. For example, in East Africa countries like Kenya and Uganda, instead of using cars as taxis, they use motorcycles as taxis and name it as Boda-bodas [1]. On the other hand, motorcycles makes more economical sense compare to an automobile as it consumes less fuel which in turn saves more money.

Although motorcycles had many benefits it also comes with equal amount of risks. Motorcycles are more likely to get involved in an accident thus resulting in serious injuries to the riders. The accident is caused by two factors; external and internal. External factors refer to objects which are out of rider control, for example, the automobile drivers' lack of attention to the motorcycle or the road condition that motorcycle travels on. Internal factors on the other side are due to the rider himself, for example, the driving skill of the rider, the lack of personal protective equipment, the absent of signal lights to inform other when changing lane and the brightness of the signal lights is dim[2]. However the accident rate of motorcycles has raised a growing concern by the public and additional safety measures are strongly advisable to be implemented.

There are many products in the market that helps to reduce the motorcycles accident rate, for example, smart jacket by Clad Light. It is a reflective jacket equiped with LED's to increase the visibility of the rider on the road. The working principle of this product is a circuit with wireless capability and is connected to the indication system of the motorcycle. When the riders use the indication system, it will send a signal to the jacket and light up the LED to alert others [1]. Besides that, HelStar by Third Eye Design also serve the same function as the jacket but instead of putting the LED light on the jacket they put it in the back of the helmet to increase the visibility of the light and make it easier to alert other since it is more prominent [3].Although these products serve the purpose of reducing the accident rate but the effect is not significant. The main reason is some motorcyclists do not use the indication system before changing lanes or steering thus other road user may not know the direction they are heading towards, eventually resulting in an accident.

Hence, to further reduce the accident rate, the idea of creating smart light for motorcyclist is proposed. Smart light for motorcyclist is a device implant in the helmet or jacket or the rider. The device is able to detect the movement of the rider and signal other road user thus reduce the chances of a collision occurring. For example, when the device senses deceleration in the bike, it will turn on the light on the jacket or helmet to indicate that the bike is stopping. The process of indication is fully automatic and independent; it does not require any rider input or signal from the indication system of the bike. The device is based on two main components; a microcontroller and an accelerometer sensor. The sensor is used to collect data from the environment when the bike is travelling. These collected data is processed and analyzed by the microcontroller thus identifying the possible outcome and turning on the LED to signal other road users.

Consequently, the possibility of using an accelerometer and microcontroller to detect the movement of the motorcycle is discussed. This project consists of two phases. In phase 1, relevant data such as deceleration or tilting of a bike travelling in a pre-determined distance will be collected by a data logging circuit and save it in a SD card. Besides, a video of the bike travelling will also be recorded by camera and stored in a SD card. These data are transferred to a personal computer for further processing such as applying filters and synchronized with the video to determine the basic rule of the algorithm. The basic rule is the baseline of turning on the light of the device. For example, from the experiment it defines the rule as when it passes the threshold of -2g it will turn on the brake light, thus is real time when the sensor detected the value is below -2g it will turn on the brake light. On the other hand, Phase 2 consists of building a prototype of the device. In this paper, the main focus only is on Phase 1 of the project.

2. Methodology

The main focus of this paper is the method of identifying the basic rule thus figure 1 indicated the flow for Phase 1.

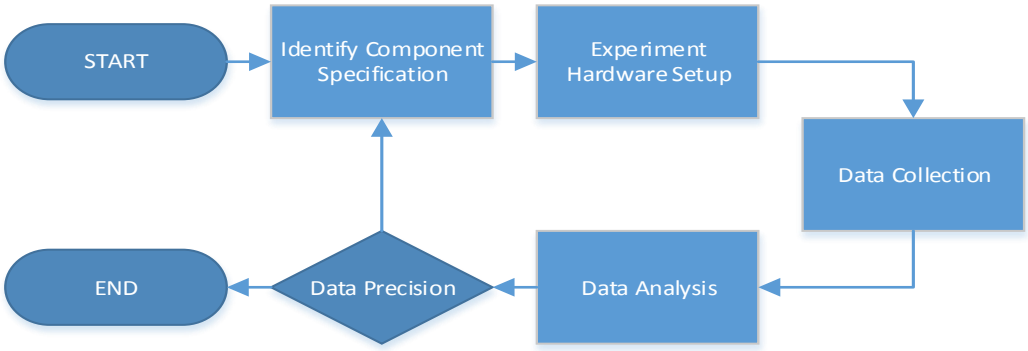


Figure 1: Flowchart for Phase 1

2.1 Identify Component Specification

The specification of an accelerometer sensor is determined by considering several situations of motorcycle deceleration. Based on the deceleration situation, Kinematic equation is used to calculate the approximated values of deceleration of the bike thus identify the suitable range of accelerometer.

After an accelerometer is decided, a media is needed to process the generated data; therefore Arduino is selected as the microcontroller. The reason Arduino are choose instead of a PIC microcontroller is because Arduino allow fast and easy testing. Arduino provided a platform for the user to concentrate on testing the idea instead of spending time building support circuitry, thus implementing Arduino shortens the time needed to execute an experiment. However, when more control is needed or the testing prototype is converted into a real product, a PIC microcontroller will still be needed. When a PIC microcontroller is implemented, the support circuitry can be build based on the application thus the size and price of complete circuit is smaller and cheaper compare to using an Arduino.

On the other hand, storage is needed to store the data processed by Arduino. However Arduino had limited space in its EEPROM, hence, an external storage media is needed. In this case, Adafruit data logger shield is suggested to be implemented. Adafruit data logger shield is an external feature which can attach to an Arduino. The shield provide a SD card interface which allow the user to insert FAT 16 or FAT 32 SD card and it had a Real time clock which will keep the time record even when the Arduino is not running. By implementing this shield it saved the time needed to build a SD card interface and real time clock for Arduino.

Finally, the type of SD card is identified. Variety type of SD card is available in the market and each type of SD card had its own write and transfer speed. The speed of the SD card can be determine by continuously writing data into it and read it in a period of time. Furthermore, having a high writing speed SD card increase the number of sample stored, which means the precision of data collection is higher.

2.2 Experiment Hardware Setup

After identifying the components needed, the data sheet of each component is studied. All identified components are then assembled into one product and shown in figure 2. Adafruit data logger is attached above the Arduino and SD card is inserted into the SD interface. Accelerometer is soldered on the prototyping area of the shield and directly connected to the Arduino. Figure 3 illustrated the program flow of the circuit. Accelerometer is generating three axis data, these data is process by the Arduino and stored in SD card.

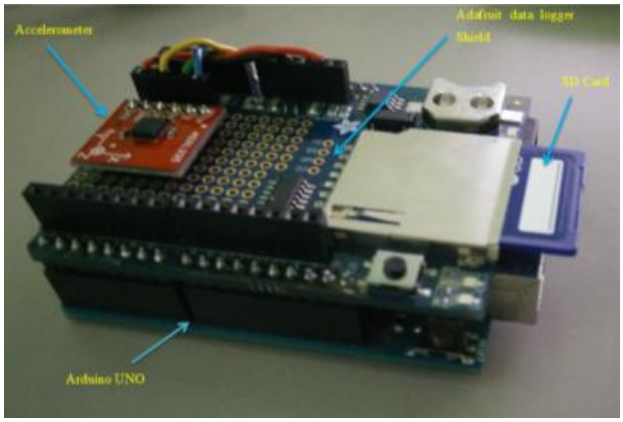


Figure 2: Hardware Connection

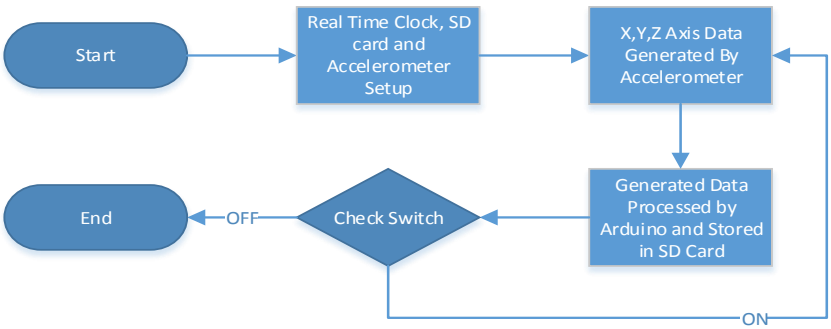


Figure 3: Data Logging Program Flow

2.3 Data Collection

Before the start of the experiment, an experiment plan is proposed. Experiment plan is a flow of procedures indicating the following items.

a) Road condition
b) Total duration and the distance the bike travelled
c) Time needed to change gears
d) Time taken for the bike to stop

The purpose of experiment plan is to increase the accuracy of data collection throughout the experiment.

The experiment plan is showed in Figure 4. The bike will travel from the start to stop marker and a camera will be used to record the whole experiment process. Before the bike start, the rider will tilt the bike to left for 5 second and tilt to right for another 5 second, this is to ensure that the video and the data is synced. The rider will repeat same set of action when the rider reaches the end point. The color strips shown in the figure is the action taken by. In real time, a ribbon with the same color will be used to represent these color strips. When the rider observes a green ribbon on the road the gear of the bike will be changed. When the rider observes the purple ribbon on the road, the throttle will be released for few second this will be representing coasting of the bike and finally when the rider observes the red ribbon the brake will be applied. Lastly the bike will stop at the end.

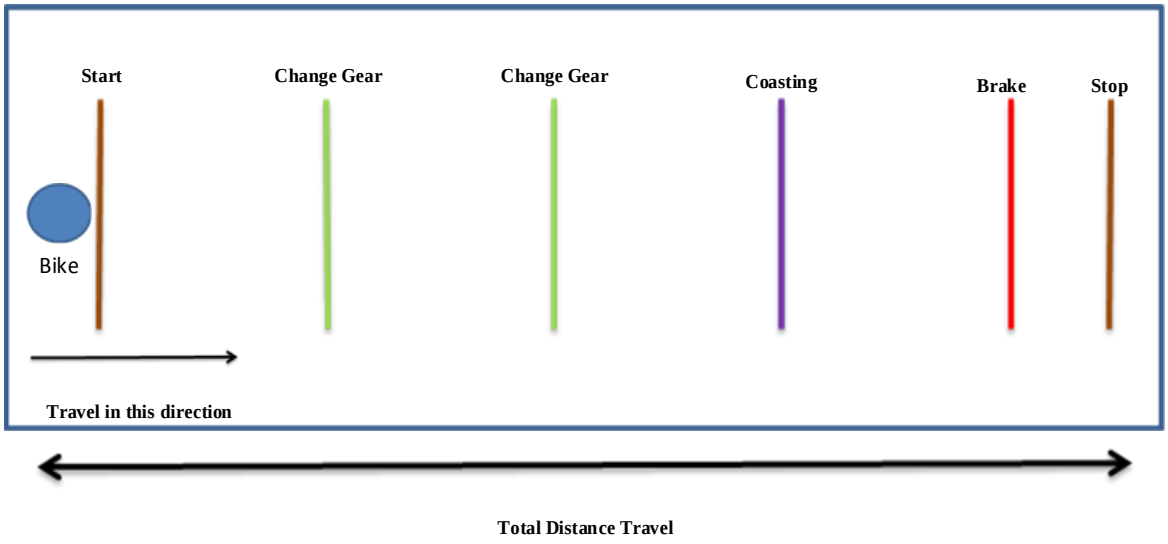


Figure 4: Experiment illustration

Steps listed below indicated the procedures to conduct the experiment

I. Rider started the video recording and switch on the Arduino simultaneously.
II. Rider tilting bike left for 5 second, then tilting bike right for 5 second.
III. Rider started to accelerate the bike.
IV. Rider observed green ribbon change to second gear and continue accelerating.
V. Rider observed another green ribbon and shifted to third gear continue accelerating.
VI. Rider observed purple ribbon started to coast.
VII. Rider observed red ribbon started apply brake and stopped on the ribbon.

2.4 Data Analysis

In order to identify the basic rule for the algorithm, the collected data and video regarding the whole experiment process is retrieved from the SD card and transferred into a personal computer with MATLAB loaded. There are 6 sets of data imported into MATLAB from SD card.

a) Time for each data recorded
b) X-axis value
c) Y-axis value
d) Z-axis value
e) Arduino turn on time
f) Video regarding the experiment process

Three types of filter will be applied to the raw collected data, one is known as the moving average filter which is a low pass filter, the other one is known as a differential filter and the final filter is known as the shifted window filter. The moving average filter is a filter which will average every 25 sets of data until the end of the data, this filter is use to smoothen the graph and remove the unwanted noise in the original data. Differential filter is used to determine the change of current stage and next stage. By using differential filter it is possible to identify the time when the bike is decelerating then turn on the LED which indicates braking. Lastly, the recorded video and data may started at different time thus to make sure video and data is synchronized shifted window filter is applied, shifted window filter will add zero to the start and end point of the data to make sure that the turn on time of the Arduino in real time is synchronize to the turn on time of the Arduino in the video.

-Mathematical Model for Moving Average Filter

$$Ave = \frac{\sum_{i=1}^{n} RD_i}{n} \quad (1)$$

RD = Raw Data

n = Total Number of Raw Data

Ave = Average value for Raw data

-Mathematical Model for differential filter

$$\Delta MA = MA(t) - MA(t - L) \quad (2)$$

ΔMA = Change of Current State with Respects to Previous State

$MA(t)$ = Current State

$MA(t - L)$ = Previous State

-Mathematical Model for Shifted Window Filter

$$ND = N1 + RD + N2 \quad (3)$$

ND = Total Video Period

$N1$ = Number of Second for Zero Added to Start Point

$N2$ = Number of Second for Zero Added to End Point

RD = Total Raw Data Period

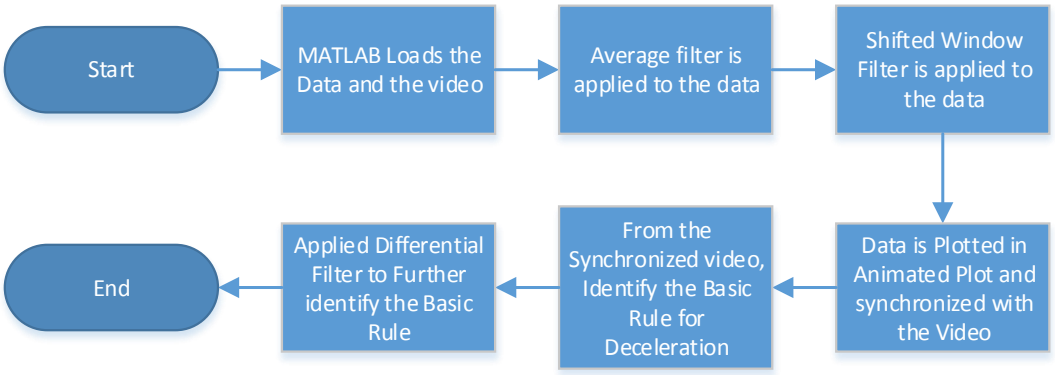


Figure 5: MATLAB Program Flow Chart

Figure 5 showed the program flow in MATLAB. At the beginning, MATLAB will find the video and the raw data from an excel file based on location given. After that, MATLAB will load the file and average and shifted window filter to the data. These data will transform into an animated plot. MATLAB will generate a new video which consists of the animated plot and the video. From the video, the basic rule is possible by visual observation. Lastly, MATLAB will apply the differential filter to the data and display a graph which helps to identify clearer when the braking period is.

3. Result and Discussion

Two sets of results will be presented in this paper and from the results the basic rule for braking is identified. First result is obtained by applying the moving average filter and shifted window filter to the raw data and transformed the data into an animated graph then synchronize with the experiment process video which also showed in figure 6.

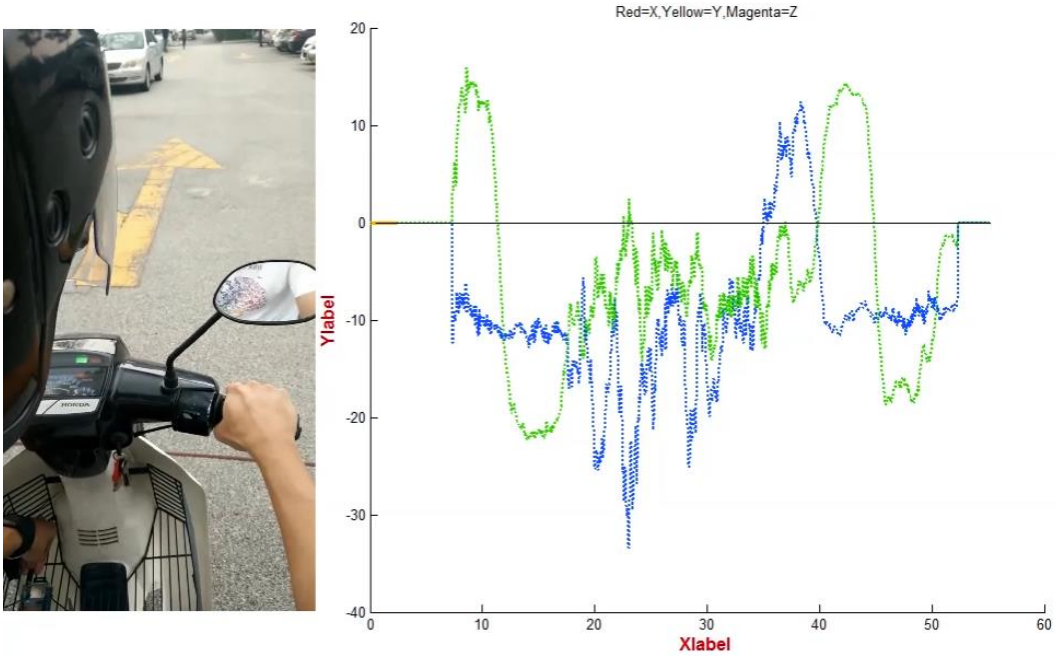


Figure 6: Animated plot synchronize with experiment process video.

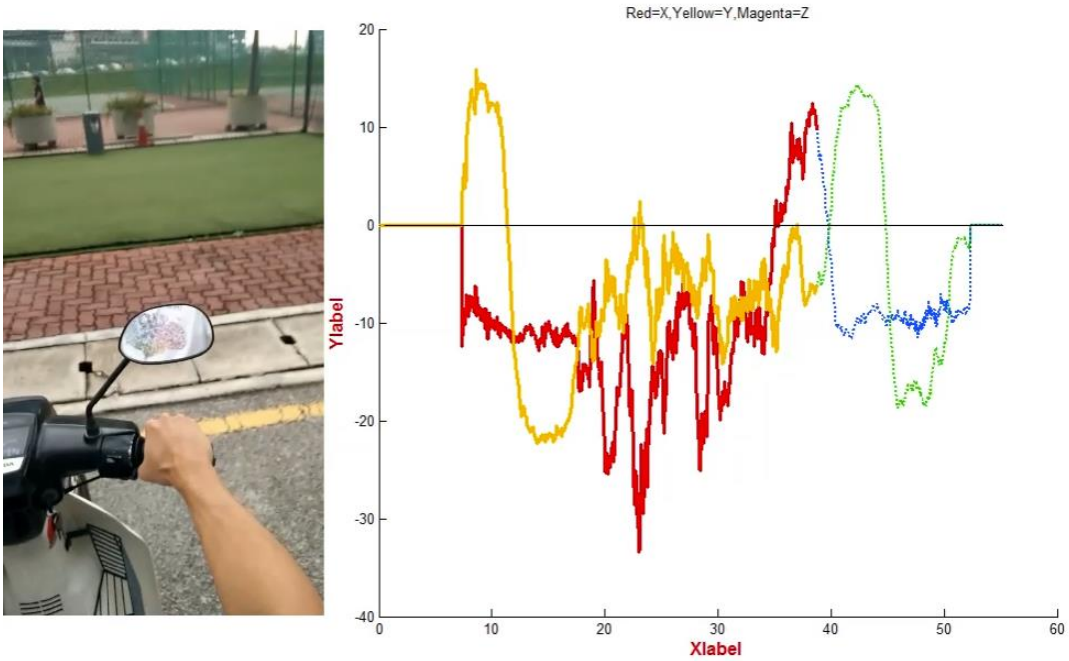


Figure 7: Deceleration of the bike

From figure 7 it can observed that the red line is reached the peak and started drop down, this situation showed that the bike is decelerating but it is not clear thus differential filter is applied to this graph to observe the deceleration much clearer.

The result after applying the differential filter can be seen in figure 8. From the figure it can see that the negative represents the braking period of the bike, thus it can assume that when the value drop under the green line in the figure the LED will be turn on and when it reach the blue line in the figure it will turn off the LED.

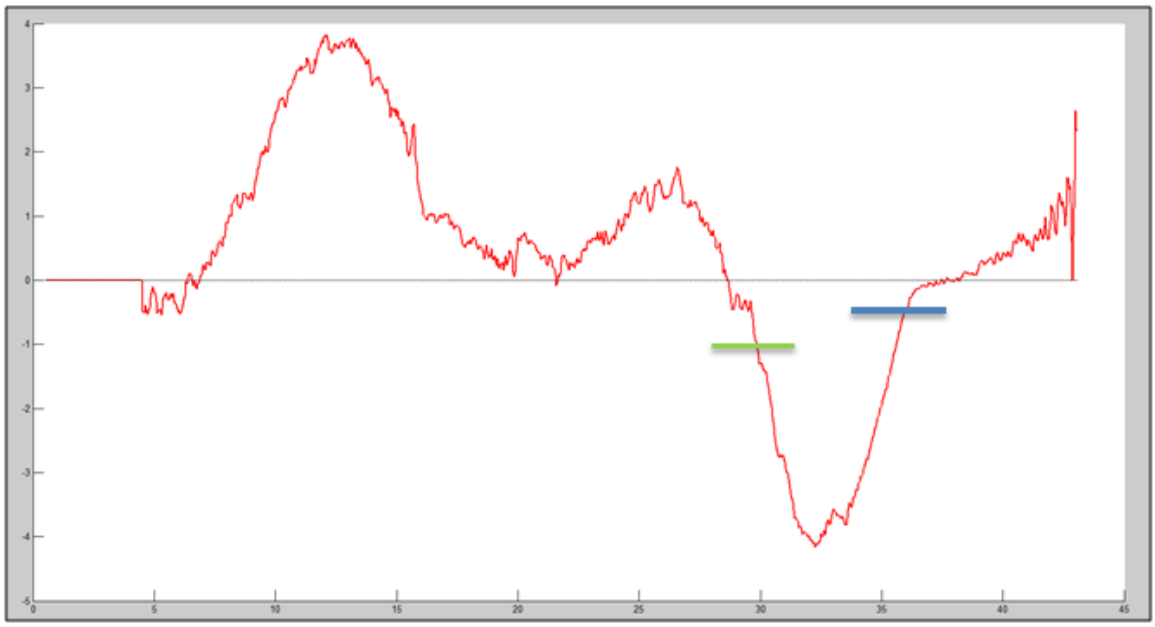


Figure 8: Result after applying differential filter

4. Conclusion

In conclusion, this project is to create a fully automatic and independent indication system, which can detect the movement of the motorcycle. The device will signal other road user the direction of the rider heading towards, thus reducing the chances of a motorcyclist getting involved in an accident.

In this paper the main focus will only be phase 1 of the project, the three filters is the key to identifying the basic rule. Upon identified the rule, it shall be tested in other situations such as the bike travelling up to fourth gear. If the basic rule is suitable for all cases it shall be used to form the algorithm and proceed to Phase 2 of the project. In Phase 2 of the project, a prototype will be created. The prototype is consists of embedded microcontroller, accelerometer, LED, battery and jacket or helmet. The algorithm will embedded into the microcontroller and eventually the prototype should be able to detect the movement of the bike and give appropriate signal to other road user.

References

[1] "Bringing wearable tech to Kenya", *CNN News*, October1, 2014. [Online]. Available: http://edition.cnn.com/videos/business/2014/10/01/spc-african-start-up-clad-light-limited.cnn [Accessed: October 10, 2015]

[2] F. Manering, L. Grodsky, "Statistical analysis of motorcyclists' perceived accident risk", "*Accident Analysis & Prevention*", vol. 27, no. 1, pp. 21-31, February 1995.

[3] "David Werner's Bright Idea", *S. Lahman, Democrat and Chronicle,* Nov 1, 2013. [Online]. Available: http://www.thirdeyedesigninc.com/in-the-news [Accessed: October 10, 2015]

Parametric Study of Microstrip Patch Antenna for Ultra wideband (UWB) Applications

Tang Ju Yuan, Lee Chia Ping*

School of Engineering, Taylor's University, Malaysia

*ChiaPing.Lee@taylors.edu.my

Abstract
This paper is about the parametric study of the microstrip patch antenna for UWB application. It is designed and simulated in CST Microwave Studio software. The frequency region is set between 2GHz-12GHz. The designed antenna meet the three main conditions which are return loss (S_{11}<-10dB), impedance of 50Ω and fractional bandwidth (FBW) of more than 0.2 or 20%. The analysis of each parameter (length and width for the patch, ground plane and feed line) are presented in this paper. Furthermore, the successfully designed microstrip patch antenna has fulfilled the UWB frequency range (3.1-10.6GHz), return loss, impedance and the Fractional Bandwidth.

Keywords: microstrip patch antenna, Ultra Wideband (UWB), Parametric Study.

1. Introduction

Microstrip patch antenna is basically a patch which is centralized at the substrate and the bottom is the ground plane as shown in Figure 1. In addition, there will be a feed line attached directly to the patch antenna.

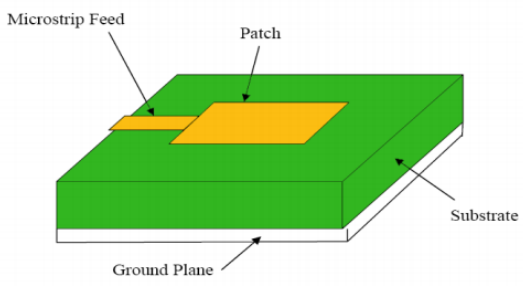


Figure 1. Basic Design of the Microstrip Patch Antenna [1].

The Federal Communications Commission (FCC) had defined UWB frequency range from 3.1-10.6GHz and the FBW is more than 0.2 or 20% [2]. Therefore, the microstrip patch antenna should have these basic characteristics. However, the main challenge is that the fundamental theory is derived based on the narrow band. It

means that the theory may not applicable to the UWB. Therefore, the research objective is to investigate the relationship of each parameter with the return loss and impedance matching. The performance also can be analyzed based on the FBW for each parameter. The three parameters of the length and width of the patch antenna, ground plane and feed line are selected to be studied. It will be start by design a basic microstrip patch antenna which has fulfilled the UWB application which then will undergo simulation for each parameter for evaluation and analysis. Besides that, the motivation of perform this research project is to analyze the relationship between each parameter and the return loss, impedance and FBW. Therefore, it is a great opportunity and potential as it is widely used in many fields and wireless technology that has become a part of our life.

2. Literature Review

According to [3, 4], the microstrip patch antenna has many applications due to the advantages. The main advantages include being small in size, easily mounted on any surface, ease of manufacturing and cheap. However, it also has drawbacks such as it being used in narrow band, low power handling capacity, efficiency reduced by the excitation of the surface wave. S. M. Vanam and R. P. Labade stated on the general shape of the radiating patch are square, rectangular, circular and strip line [5]. This is because of low cross polarization [6]. According to [5], the impedance matching is necessary to ensure the microstrip patch antenna has better performance over the frequency range of UWB. The impedance matching of 50Ω is very important criterion as it will minimize power loss in feed line and maximize power delivered [7, 13].

According to [8], the return loss must be less than -10dB for the UWB which is allocated for ultra wide range of bandwidth. It also stated that the size of antenna should be as small as possible as UWB is applicable in indoor and portable device and mobile phone [9, 10, 11, 12].

Based on [3, 13], the microstrip patch antenna is widely used compared to the conventional type antenna due to its advantages such as low cost, small size, light weight and easy of fabrication. It also can be incorporated with the printed circuit board. Based on [3], the main challenge is the microstrip patch antenna is only widely applicable in narrow band.

From [15], it stated that UWB has been widely used in different field such as mobile satellite communication system, Radio Frequency Identification (RFID) Direct Broadcast Television (DBTV), Wireless LAN's, Global Positioning System (GPS) , Ultra High Frequency (UHF) Patch Antenna for space, medical imaging, radar, indoor processing and in military system like rockets, aircrafts missiles etc. This is mainly due to low cost of the substrate material and fabrication which has increases the usage of microstrip patch antenna in different applications [15].

Furthermore, based on [16], there are 4 main feeding techniques which are Microstrip Line Feed, Coaxial Feed, Aperture Coupled Feed and the Proximity Coupled Feed. The comparison of feeding techniques is been summarized in Table 1. From the Table 1, Microstrip Line Feed will be chosen as the feeding technique for this research project as it can etch in the same substrate and ease of fabrication

as other only applicable on narrow band or need alignment which required more experiences.

Table 1. Comparison of Different Feeding Techniques [16].

	Microstrip Line Feed	Coaxial Feed	Aperture Coupled Feed	Proximity Coupled Feed
Advantages	-Can etch in the same substrate to provide a planar structure. -Easy to be fabricated.	-Can be placed in any place in the patch.	- Eliminate the spurious radiation. -Provide high bandwidth (as high as 13%). -Reduce harmonic radiation	-Can use different thickness or permittivity of the substrate to optimize the antennas and feed network.
Disadvantages	-Spurious feed radiation increases as the thickness of the substrate increase.	-Narrow Bandwidth. -Difficult to model.	-Required alignment as two substrate is needed.	-Required alignment as two substrate is needed.

3. Methodology

There are two phases of development which are Research Phase and Simulation Phase. The Research Phase is where the literature review is carried out to identify the fundamental theory and design on a microstrip patch antenna while Simulation Phase is done after Research Phase where it applies the fundamental theories behind antenna geometry into the design process before proceeding into analysis of the simulated results of each parameter.

3.1 Design Process

The Figure 2 shows the flow chart of the Overall Research and Design Process. The 1st phase includes only the Research Phase while the 2nd phase includes the Design and Simulation, Evaluation and Analysis and Conclude the Project.

During the 1st phase, it only includes the Research Phase. In this phase, the fundamentals theory is firstly understood. The fundamental theory will then be used during Evaluate and Analysis stage. During the process of literature review, the boundaries and equations are identified, followed by the understanding of the general design by other researchers for UWB applications. The general design will be used as a guide to design a basic microstrip patch antenna before proceeding with

parametric study by changing the length and width of each parameter during the Design and Simulation stage. All the findings need to be summarized and concluded before the next phase.

During the 2nd phase, a basic microstrip patch antenna is designed which is below -10dB and has the impedance of 50Ω for the entire frequency bands in CST Microwave Studio software. The software is a 3D simulation which has *x-y-z* plane. Then, the design can be verify through the simulated result. After the microstrip patch antenna achieves below -10dB then the parameter sweep is performed for each parameters. Parameter sweep is able to set a range of the parameter value and the step size of the range value which it can simulate multiple value of each parameter. Then, the result will be plotted in the same graph for evaluation and analysis purposes. The detail of the simulation process is explained in section 3.2.

After the 1st microstrip patch antenna design and the parameter sweep were done, the results will undergo evaluation and analysis through justification with the fundamental equations and principals. The results are simulated form the Time Domain Solver which shows the return loss, VSWR, impedance, radiation pattern and directivity. Next, the results of each parameter is being evaluated and analyzed through the FBW, resonant frequency, return loss, impedance and how it changes across the frequency.

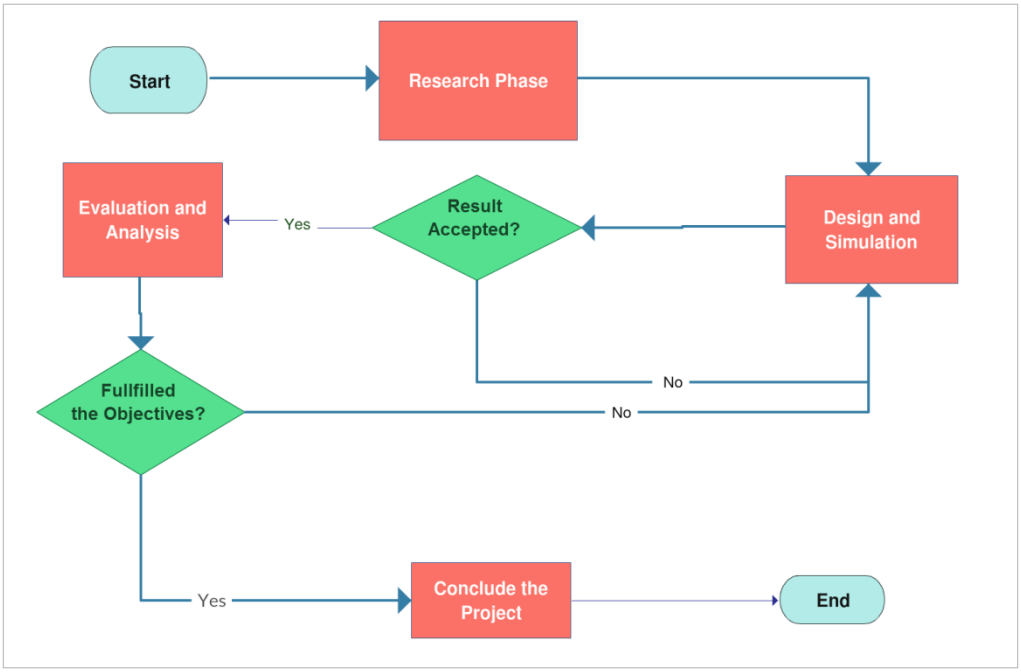


Figure 2. Design Process Flow Chart.

3.2 Simulation Process

Figure 3 is the flow chart for the Simulation Process. Since, it has three parameters such as length and width of the patch, ground plane and feed line. Therefore, there will be 2 sets of results for each parameter out of 6 sets, which is the total number of results. From the Figure 3, the design process begins with a basic microstrip patch antenna design and perform parameter sweep for the length and width of the patch and evaluate the result whether is acceptable; if not the

change the design of the microstrip patch antenna and re-simulate again. This is repeated for the ground plane and feed line. Then, from the results it can identify the parameter has below -10dB, impedance of 50Ω and fractional bandwidth of more than 0.2. Then, the results will be needed to fulfill the characteristic of the UWB. If not, then the basic microstrip patch antenna will need to verify the error and correct it and restart the whole process for the parameter sweep.

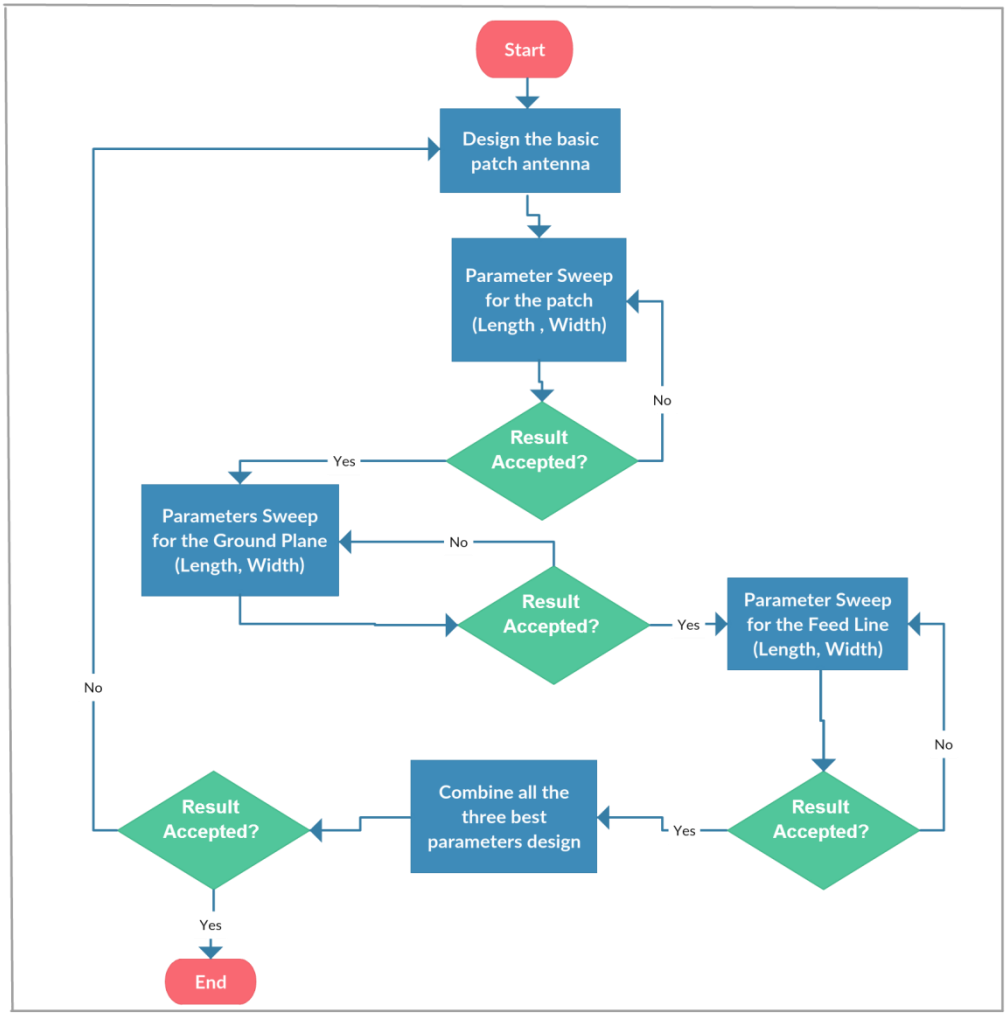


Figure 3. Simulation Process Flow Chart.

4. Result and Discussion

a) Ground Plane Length

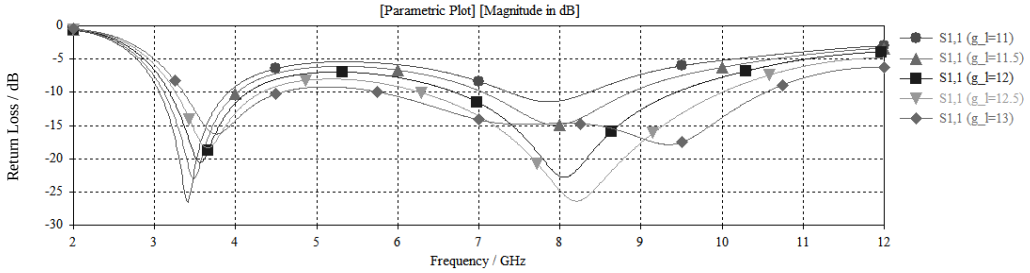


Figure 4. Return Loss for the Parametric Plot for the Ground Plane Length.

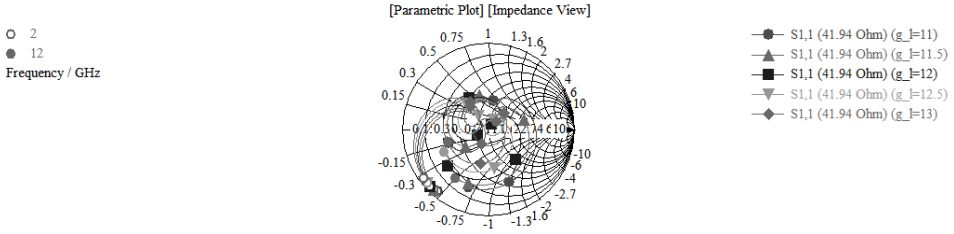


Figure 5. Impedance for the Parametric Plot for the Ground Plane Length.

The Figure 4 and Figure 5 are the results from the parameter sweep of the Ground Plane Length (*g_l*) which are from 11-13mm with similar step size width of 0.5mm. According to Figure 4, it can be concluded that the Ground Plane Length has significant effect on the return loss but the impedance remains constant at 41.94 Ω throughout the frequencies. The return loss decreases as the frequency decreases until 3.4934GHz and increases until 5.0227GHz before it decreases until 8.0932GHz then increases until 12GHz. Although the trend is similar throughout the Ground Plane Length but the rate of change is not constant and fluctuate between 7.6511mm and 9.5269mm. Hence, the Ground Plane length also not fulfilled the UWB characteristic as the impedance is remains constant at 41.94Ω and the return loss did not show stable performance while the return loss is still above -10dB and the FBW is not constant such as for *g_l* = 11mm, the FBW is 0.9207 and *g_l* = 12mm, the FBW is 0.9500 . Furthermore, the resonant frequencies are 3.4934GHz and 8.0932GHz.

The fractional bandwidth (F*BW*) [17]:
For *g_l* = 11mm:

$$FBW = 2\frac{(F_h - F_l)}{(F_h + F_l)} \tag{1}$$

$$= \frac{2(8.356 - 3.0872)}{8.356 + 3.0872}$$

$$= 0.9207$$

For g_l = 12mm:
By using Eq. (1):

$$FBW = \frac{2(9.4791 - 3.374)}{9.4791 + 3.374}$$

$$= 0.9500$$

b) Ground Plane Width

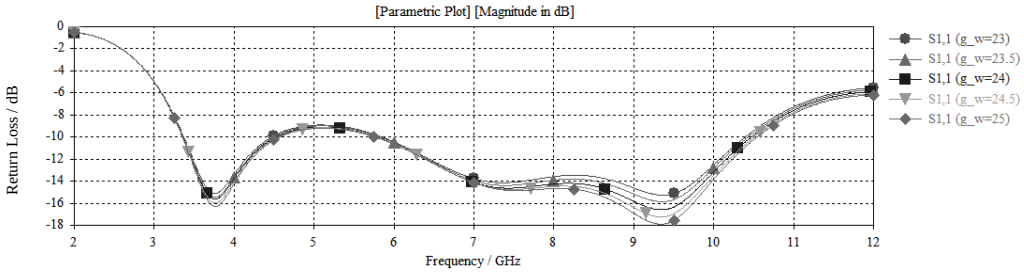


Figure 6. Return Loss for the Parametric Plot for the Ground Plane Width.

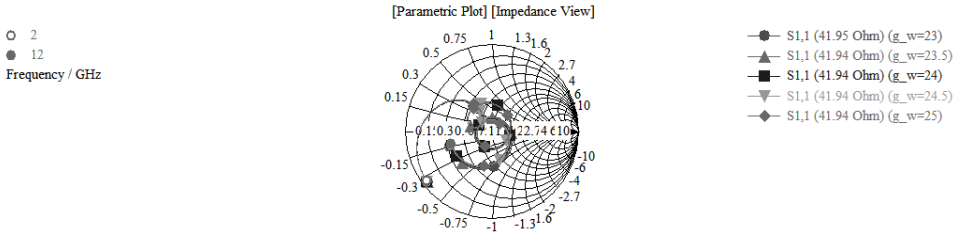


Figure 7. Impedance for the Parametric Plot for the Ground Plane Width.

The Figure 6 and Figure 7 are the results from the parameter sweep of the Ground Plane Width (g_w) which are from 23-25mm with similar step size width of 0.5mm. According to Figure 6, it can be concluded that the Ground Plane Width has lesser effect on the return loss. The return loss decreases as the frequency increases until 3.7411GHz before the return loss increases until 5.0197GHz. Then, it continues decreases until 9.4387GHz before it increases until 12GHz. The return loss trend is almost similar but after 6.7849GHz the rate of change is not constant. Furthermore, it impedance remain constant at 41.94Ω across the frequency. The resonant frequencies are 3.7411GHz and 9.4387GHz. Although the return loss is less than -10dB and the FBW is 1.0321 which is more than the UWB's FBW but the impedance is constant at 41.94Ω which do not fulfilled the UWB characteristic.

The fractional bandwidth (FBW):
By using Eq. (1):

$$FBW = \frac{2(10.548 - 3.3671)}{10.548 + 3.3671}$$

$$= 1.0321$$

c) Patch Length

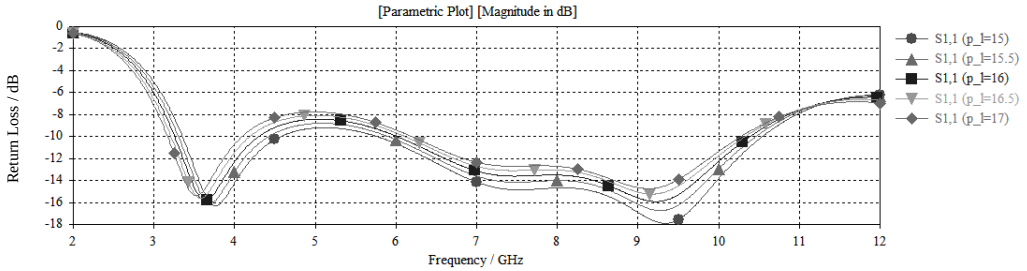


Figure 8. Return Loss for the Parametric Plot for the Patch Length.

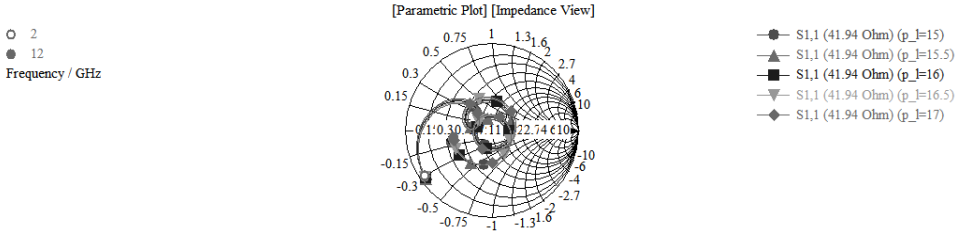


Figure 9. Impedance for the Parametric Plot for the Patch Length.

The Figure 8 and Figure 9 are the results from the parameter sweep of the Patch Length (*p_l*) which are from 15-17mm with similar step size width of 0.5mm. According to Figure 8, it can conclude that the Patch Length has significant effect on the return loss but not for the impedance. The return loss decreases as the frequency increases until 3.4934GHz and the return loss increases until 4.7957GHz. Then, it continues decreases until 9.3357GHz before it increases until 12GHz. The return loss trends between each Patch Lengths are almost the same. Furthermore, it impedance remains constant at 41.94Ω across the frequency. The resonant frequencies are 3.4934GHz and 9.3357GHz. The FBW is 1.0061 which is in the UWB's FBW. This parameter will not achieved the UWB characteristic as the impedance is only 41.94Ω and the major region of the return loss is still above -10dB although the FBW is fulfill for the UWB.

The fractional bandwidth (F*BW*):
By using Eq. (1):

$$FBW = \frac{2(10.566 - 3.4934)}{10.566 + 3.4934}$$

$$= 1.0061$$

d) Patch Width

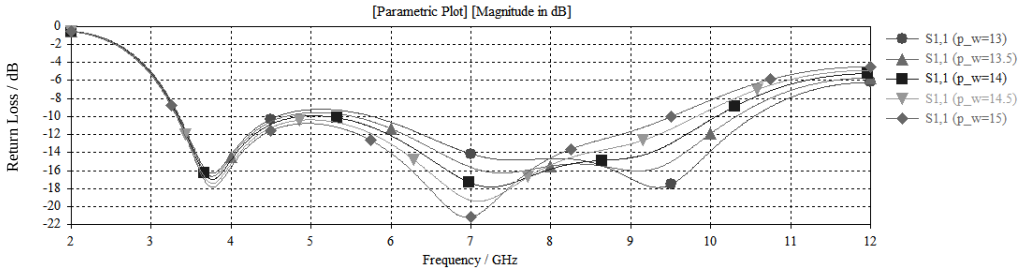


Figure 10. Return Loss for the Parametric Plot for the Patch Width.

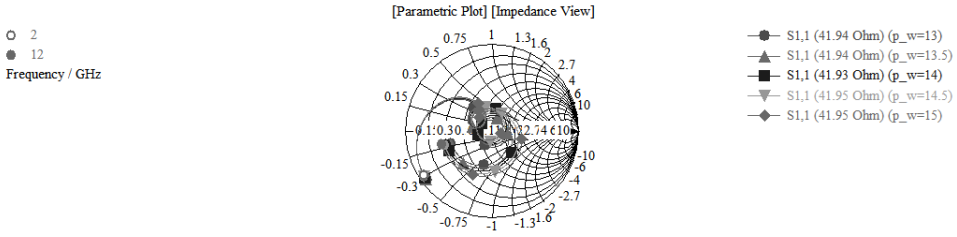


Figure 11. Impedance for the Parametric Plot for the Patch Width.

The Figure 10 and Figure 11 are the results from the parameter sweep of the Patch Width (*p_w*) which are from 13-15mm with similar step size width of 0.5mm. According to Figure 10, it can conclude that the Patch Width has lesser effect on the return loss on the beginning and start changes from 3.5601GHz. Then, the return loss increase slightly until 4.996GHz and decreases until 7.002GHz before it increases until 12GHz. However, after 4.996GHz, the rate of change does not follow the trend as before as it diverges and it also fluctuates with random trend at 7.7101GHz – 8.6506GHz. Furthermore, the impedance also fluctuate slightly from 41.94Ω to 41.93Ω and to 41.95Ω across the frequency but the changes are not significant and remain constant for *p_w* = 13 and 13.5mm, 14.5 and 15mm with two different values which are 41.94Ω and 41.95Ω. These parameter has not meet the UWB characteristic as the impedance is around 41.95Ω and the return loss has more than -10dB for the major frequency. The resonant frequencies are 3.5601GHz and 7.0467GHz. However, the return loss is not the same at the resonant frequency. The FBW is about 1.0370 which is within UWB's FBW. Although this parameter has major frequency that has less than -10dB and fulfilled the FBW but the impedance has not reach the impedance of 50Ω.

The fractional bandwidth (FBW):
By using Eq. (1):

$$FBW = \frac{2(10.544 - 3.3434)}{10.544 + 3.3434}$$

$$= 1.0370$$

e) Feed Line Length

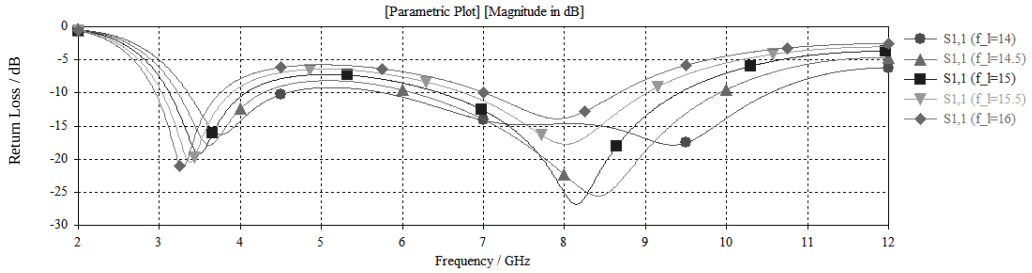


Figure 12. Return Loss for the Parametric Plot for the Feed Line Length.

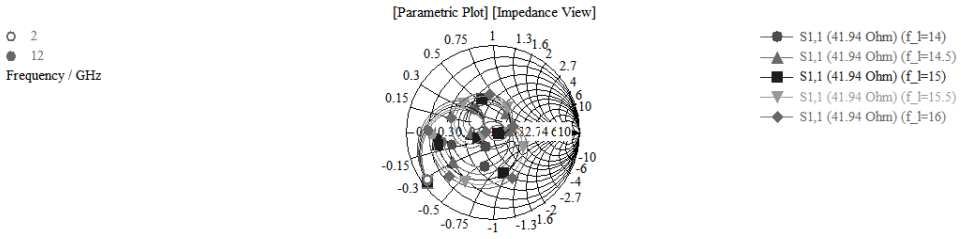


Figure 13. Impedance for the Parametric Plot for the Feed Line Length.

The Figure 12 and Figure 13 are the results from the parameter sweep of the Feed Line Length (*f_l*) which are from 14-16mm with similar step size width of 0.5mm. The return loss decreases as the frequency increases until 3.2714GHz but it had shift toward the left as the Feed Length increases. Then, the return loss increases until 5.0115GHz and then it decreases until 8.0151GHz before it increases until 12GHz. However, after 8.027GHz fluctuate by shifting to the left as the Feed Length increases. Furthermore, it impedance remains constant at 41.94Ω across the frequency. This result of this parameter is not satisfied has the return loss is still have above -10dB especially in the UWB range and the impedance is has not achieved 50Ω. Moreover, it shows unstable performance on the return loss. The resonant frequencies are 3.2714GHz in generally but for *f_l* =15mm is 8.1661GHz, *f_l*= 14.5mm the resonant frequency is 8.4521GHz and 8.011GHz for *f_l* =15.5mm and 16mm while *f_l* =14mm the resonant frequency is 9.501GHz. Besides that, the FBW increase is not stable as *f_l* = 14mm, FBW= 0.8919 while the *f_l* = 15.5mm and 16mm are 0.8971 and 1.122.

The fractional bandwidth (*BW*):
For *f_l* = 14mm:
By using Eq. (1):

$$FBW = \frac{2(9.501 - 3.6405)}{9.501 + 3.6405}$$

$$= 0.8919$$

For *f_l* = 15.5mm:
By using Eq. (1):

$$FBW = \frac{2(9.0004 - 3.4263)}{9.0004 + 3.4263}$$

$$= 0.8971$$

For *f_l* = 16mm:
By using Eq. (1):

$$FBW = \frac{2(10.609 - 2.9853)}{10.609 + 2.9853}$$

$$= 1.122$$

f) Feed Line Width

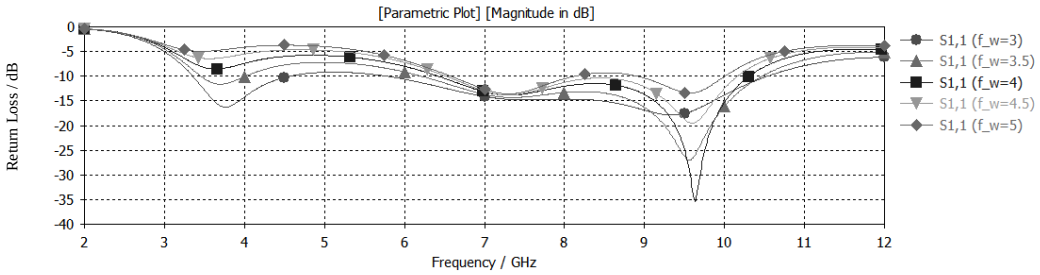


Figure 14. Return Loss for the Parametric Plot for the Feed Line Width.

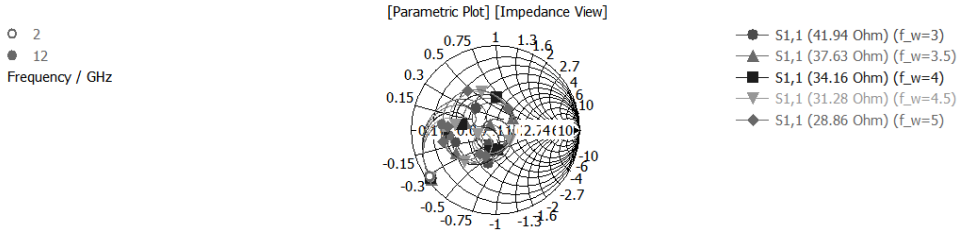


Figure 15. Impedance for the Parametric Plot for the Feed Line Width.

The Figure 14 and Figure 15 are the results from the parameter sweep of the Feed Line Width (*f_w*) which are from 3-5mm with similar step size width of 0.5mm. According to Figure 14, the return loss fluctuates across the frequency. However, the return loss decreases as the frequency increases until 3.748GHz, then it increases until the peak at 5.0163GHz before it decreases until 7.0163GHz. Then, it increases slightly and decreases until 9.6382GHz and increase until 12GHz. Furthermore, it impedance clearly shows that the impedance is inversely proportional to the Feed Width. From the Figure 15, the resonant frequencies are 3.748GHz and 9.6382GHz. The FBW is 1.0444 which is more than 0.2 which mean it is a UWB. Therefore, the Feed Line Width has the significant changes of the impedances while the fractional bandwidth is fulfilled the UWB characteristics. The return loss is not all the Feed Line Width is fulfilled the UWB characteristic.

The fractional bandwidth (F*BW*):
By using Eq. (1):

$$FBW = \frac{2(10.581 - 3.3211)}{10.581 + 3.3211}$$

$$= 1.0444$$

g) 50Ω Impedance:

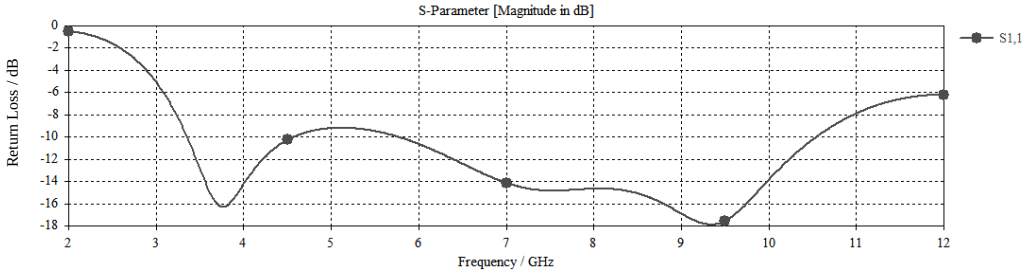


Figure 16. 50Ω's Return Loss.

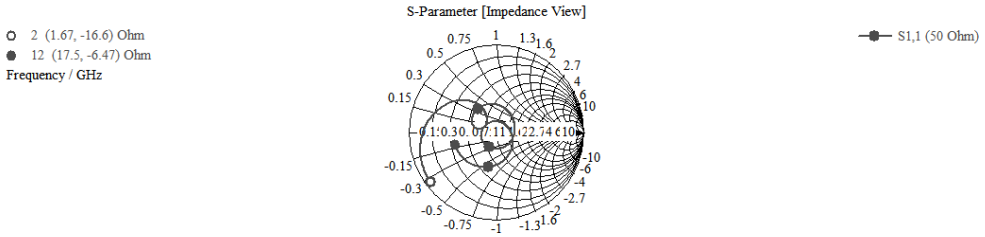


Figure 17. 50Ω 's Impedance.

The Figure 16 and Figure 17 are the results from the basic design. The return loss is fall below -10dB for the major UWB range and the impedance is also at 50Ω which is the impedance matching. This is important as impedance matching is measure between the input receiver and antenna which means if the impedance matching is archived, then, it will minimize the reflection and hence maximize the power transfer from antenna to receiver [18]. The resonant frequency is at 3.7701GHz and 9.3762GHz. As the return loss is below -10dB for the UWB range, the impedance of 50Ω and the FBW is 1.0355 which is also fulfilled the UWB characteristic. Table 2 and Table 3 show the optimized design of the microstrip patch antenna and the geometry.

The fractional bandwidth (F*BW*):
By using Eq. (1):

$$FBW = \frac{2(10.574 - 3.3599)}{10.574 + 3.3599}$$

$$= 1.0355$$

Table 2. Optimized Design of Microstrip Patch Antenna.

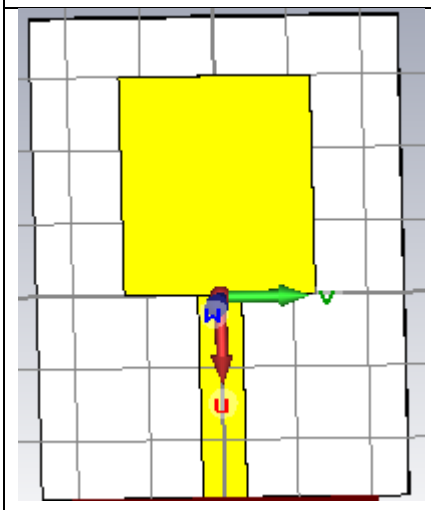
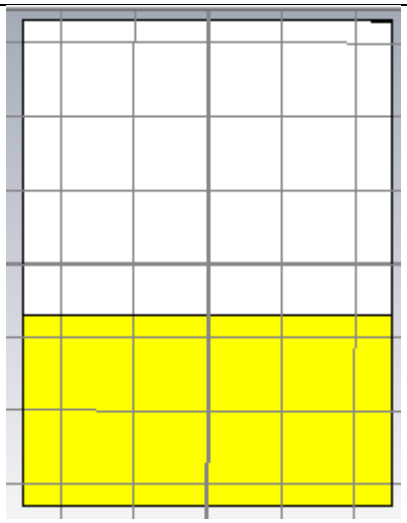
Front View	Back View
	
- The yellow square is the patch antenna which is made up of copper (annealed). - The yellow vertical rectangular is the feed line which is made up of copper (annealed) and feeding technique is microstrip line feed as it is the easier for impedance matching. - The white rectangular is the substrate which is made up of Roger RT 5880.	- The yellow rectangular is the ground plane which is made up of the copper (annealed). - The white rectangular is the same substrate as the front view and same material.

Table 3. Parameter Value for the Optimized Design.

Parameter	Symbol	Value (mm)
Feed line length	*f_l*	14
Feed line width	*f_w*	3
Feed line thickness	*f_t*	0.035
Ground plane length	*g_l*	13
Ground plane width	*g_w*	25
Ground Plane thickness	*g_t*	0.035

Patch Length	*p_t*	15
Patch width	*p_w*	13
Patch thickness	*p_t*	0.035
Substrate length	*s_l*	33
Substrate width	*s_w*	25
Substrate thickness	*s_t*	0.787

5. Conclusions

The parametric study of the microstrip patch antenna design is been analyzed. The Feed Line Width has shown stable return loss below -10dB and the significant changes of the impedance. The basic design of the microstrip patch antenna has achieved the performance of UWB where the FBW is 1.0355 (>0.2), return loss (*S11<-10dB)* and impedance is 50Ω. The future works are the parametric study of the different feeding methods and different materials for the substrate, feed line, patch and ground plane and experimental. It also can perform experimental on the Micro strip Patch Antenna for UWB Applications and compare the performance with the simulated result.

6. References

[1] C. V. V. Reddy and R. RANA, 'Design of Linearly Polarized Rectangular Microstrip Patch Antenna Using IE3D/PSO', 2009.

[3] FCC report and order for part 15 acceptance of ultra wideband (UWB) systems from 3.1– 10.6GHz, Washington, DC, 2002.

[3] I. Singh and V.S. Tripathi, " Micro Strip Patch Antenna and its Applications: A Survey", Indrasen Singh et al, Int. J. Comp. Tech. Appl., Vol 2 (5), 1595-1599, 2011. [Online]. Available: http://citeseerx.ist.psu.edu/viewdoc/download?doi=10.1.1.208.7887&rep=rep1&type=pdf . [Assessed 06- June - 2015].

[4] R. Poisel, "Antenna Systems and Electronic Warfare Applications*"* United Stated: Artech House, 2012, p. 766.

[5] S. M. Vanam and R. P. Labade, "Parametric Analysis And Design Of Rectangular Microstrip Patch Antenna for Ultra-wideband Application", *International Journal of Microwaves Applications*, vol. 3, no. 3, p. 17-20, 2014.

[6] C.Balanis, Antenna Theory Analysis and Design, 2nd ed: John Wiley & Sons, Inc., 1997.

[7] H. -R. Chuang, 'Chapter 5: Impedance Matching and Smith Chart', National Cheng Kung University, 2011.

[8] Q. Ain and N. Chattoraj, 'A Compact Novel Tapered U Slot Ultra Wideband Antenna', *International Journal of Applied Science and Engineering*, vol. 11, no. 3, pp. 301-315, 2013.

[9] Lim, E. G., Wang, Z., Lei, C. U., Wang, Y., and Man, K. L. 2010. 'Ultra Wideband Antennas- Past and Present', *IAENG International Journal of Computer Sciences*, 37, 3:304-314.

[10] Khalilpour, R., Nourinia, J., and Ghobadi, C. 2010. 'An Optimized Monopole Microstrip Antenna with Gradual Steps for Ultra Wideband Applications', *Progress In Electromagnetic Research Symposium Proceedings*, 1072-1076.

[11] Song, H. W., Park, J. K., and Yoo, J. H. 2008. 'A Novel Ultra-wideband Monopole Antenna with Two Symmetrical Strips', *Microwave and Optical Technology Letters*, 50, 11: 2845-2848.

[12] Yin, X. C., Ruan, C. L., Ding, C. Y., and Chu, J. H. 2008. 'A Planar U Type Monopole Antenna for UWB Applications', *Progress In Electromagnetic Research Letters*, 2: 1-10.

[13] S. Rastogi and M. Paliwal, 'Comparative Analysis of Microstrip Patch Antenna in Various Clime', *Advance in Electronic and Electric Engineering*, vol. 3, no. 8, pp. 1031-1038, 2013.

[14] A. Yadav and K. Pahwa, 'Design & Parametric Study of Rectangular slot Micostrip Patch Antenna for UWB Applications', *International Journal of Electrical Engineering Education*, vol. 1, no. 3, pp. 4-8, 2014.

[15] I. Singh and V.S. Tripathi, " Micro Strip Patch Antenna and its Applications: A Survey", Indrasen Singh et al, Int. J. Comp. Tech. Appl., Vol 2 (5), 1595-1599, 2011. [Online]. Available: http://citeseerx.ist.psu.edu/viewdoc/download?doi=10.1.1.208.7887&rep=rep1&type=pdf. [Assessed 09- Novemeber - 2015].

[16] A. Kumar, J. Kaur and R. Singh, 'Performance Analysis of Different Feeding Techniques', *International Journal of Emerging Technology and Advanced Engineering*, vol. 3, no. 3, pp. 1-2, 2013.

[17] B. Luther, 'Ultra Wide Bandwidth', Washington, DC, 2005.

[18] K. W. Whites, 'Transmission Line Matching Using Lumped L Networks', South Dakoda, U.S., 2005.

Portable Lightning Protection Structure

Teo Jian Hong[1*], Dr. Siow Chun Lim [2]

School of Engineering, Taylor's University, Malaysia

[*]*jianhong_1018@hotmail.com*

Abstract

A lightning strike is a hazardous natural phenomenon which can cause death to the human being. Hence, a lightning protection system is developed to provide protection against the lightning strike. However, the current lightning protection technique is mostly focused on building. There are situations whereby the human is unable to get into the building when a thunderstorm is approaching. This situation may occur in a large open area which has limited closed shelters. Therefore, personal lightning protection is vital during the mentioned situation. In this paper, the theory, method and design of a portable lightning protection structure are presented. The design structure must be able to protect human from a direct lightning strike. Besides that, the structure needs to be in small scale and light in terms of weight to enhance its portability. The functionality of design structure was examined by using PSCAD software. The circuit representation of design structure was modelled and simulated with a human model circuit. The simulation was done to obtain the data of potential difference and current flows into the human body when in contact with the structure that struck by lightning. The maximum current value will determine the insulation level of the structure. After that, the structure was constructed and tested by conducting high voltage testing. The structure was subjected to high impulse voltage by using Marx high impulse voltage generator at high voltage lab located in UPM. No sparking was observed throughout the surface of the structure when it was subjected to high impulse voltage. This indicated that the high impulse current was effectively grounded through the structure. Hence, the designed structure is working as expected and has a potential to be used as portable lightning protection structure.

Keywords: Lightning strike, Protection, Portable, PSCAD, Human safety, Impulse voltage.

1. Introduction

Lightning is a natural phenomenon that is caused by instability charge distribution within a cloud. The negative charges will repel from the cloud and form a downward step leader. As the step leader approaches the ground, the tallest object on the ground will form an upward step leader with positive charges and attach with the downward step leader. The attachment process then created a conductive path which allows a surge of electrons rapidly falls to the ground. This phenomenal is referred as lightning [1].

National Lightning Safety Institute (NLSI) has conducted lightning density measurement around the world and concluded that Kuala Lumpur is having 48.3 lightning strikes to the ground for every square km of real estate. With this result, Kuala Lumpur was ranked fifth in the world in the year of 2009 [2]. Based on the analysis done by Malaysian Meteorological Department, the highest mean annual number of days with lightning which was recorded at KLIA, Sepang is 309 days. On the other hand, the highest mean annual number of days with thunderstorm which was recorded at Subang is 211 days [3]. This data indicates that almost 60 % of the days per year in Subang is undergoing thunderstorm and 80% of the days per year is having lightning strikes in Sepang.

A lightning strike can cause victim to experience a cardiac arrest (heart stopping) and died on the spot. Recent years, the technology of identifying and locating lightning has been developed to minimize the damage that caused by lightning strikes. A commercial network of lightning sensors with a wideband magnetic direction-finding to generate lightning location in real time is being operated at many countries. This network is used to provide lightning warning for various applications [4]. Moreover, lightning protection system is also being developed to enhance the capability of facilities, vehicles and buildings in order to withstand the effect of lightning strikes [1]. Although lightning protection technology has been developed, the research on portable lightning protection is still limited. Even though human is always protected by a properly grounded building, but there are some situations that human might not have sufficient time to get into a building especially when they are located at large open areas such as construction site and agriculture field. The current research progress is still insufficient to address this issue.

Therefore, this research is conducted to study and design a portable lightning protection structure. The structure must be able to provide lightning protection conveniently in an open area where properly grounded closed structures are not available for protection. Other than that, the structure has to be designed based on the criteria of portability.

2. Methodology

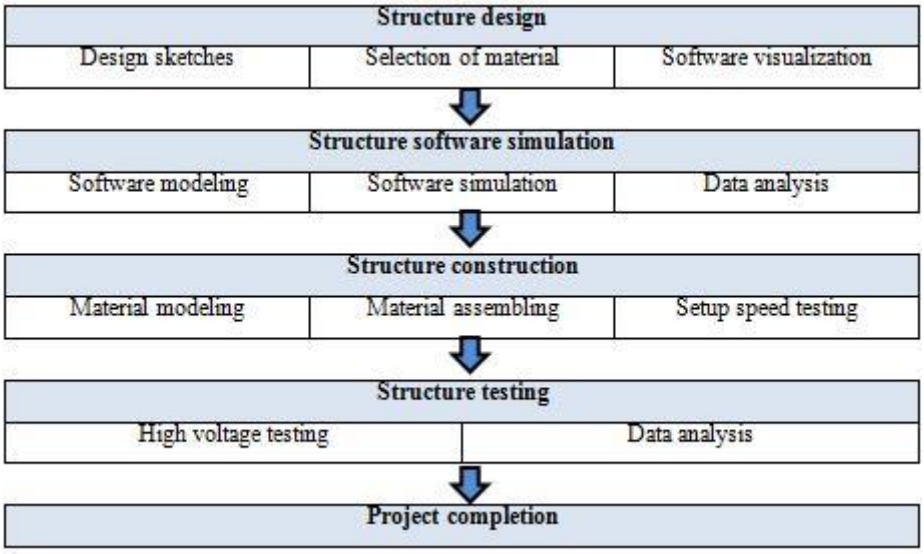


Figure 1. Project overall flowchart.

2.1 Structure design

The basic design concept is aiming for a structure that is having stable base with minimum pointy part. Therefore, a tripod structure design is selected as it fulfills the requirement. The reason of having minimum pointy part as one of the design criteria is because of the current will tend to accumulate more densely in the pointy part or sharp edges. Hence, pointy part will have more charge per unit surface area and also higher charge density. The lightning will be most likely attracted by the area that has higher charge density [5]. Sharp edges may also trigger sparking in the structure in the event of it being struck by lightning. Therefore, the design of the structure that consists of less pointy area will decrease the chances of being strike by lightning.

Table 1. Properties of copper, aluminium and steel [6]

Characteristics	Pure Copper	Pure Aluminium	Low-alloy Steel
Tensile strength (Ib/in2)	25000	13000	75000 to 90000
Corrosion resistance	Good	Very good	Poor
Density (g/cm^3)	8.96	2.7	7.83
Electrical conductivity (by volume at 20'C)	100%	62%	12%

To provide adequate lightning protection, the structure is made up by metal which has excellent conductivity, good resistance against corrosion and feasible mechanical strength. Table 1 shows the comparison between copper, aluminum and steel. By comparing each of the characteristics, aluminum is chosen as its conductivity and tensile strength is sufficient to offers lightning protection. Most importantly, aluminum has the lowest density which makes it become the lightest material among all the three metals. Apart from this, insulating material also has been studied. IEC 62305-3 states that even though the design of lightning protection system has fulfilled the criteria, the hazard due to touch or step voltage in the vicinity of the

down conductor system is still present [7]. Hence, specific level of insulation will be applied on structure to protect person from the high voltage built up in lightning strike event. It is mandatory to ensure the suitable insulation level for the structure because if the voltage successfully punctures the insulating material, a partial of lightning current can flow into human body [8]. In order to determine the insulation level, software simulation was conducted to indicate the maximum potential difference between structure and human.

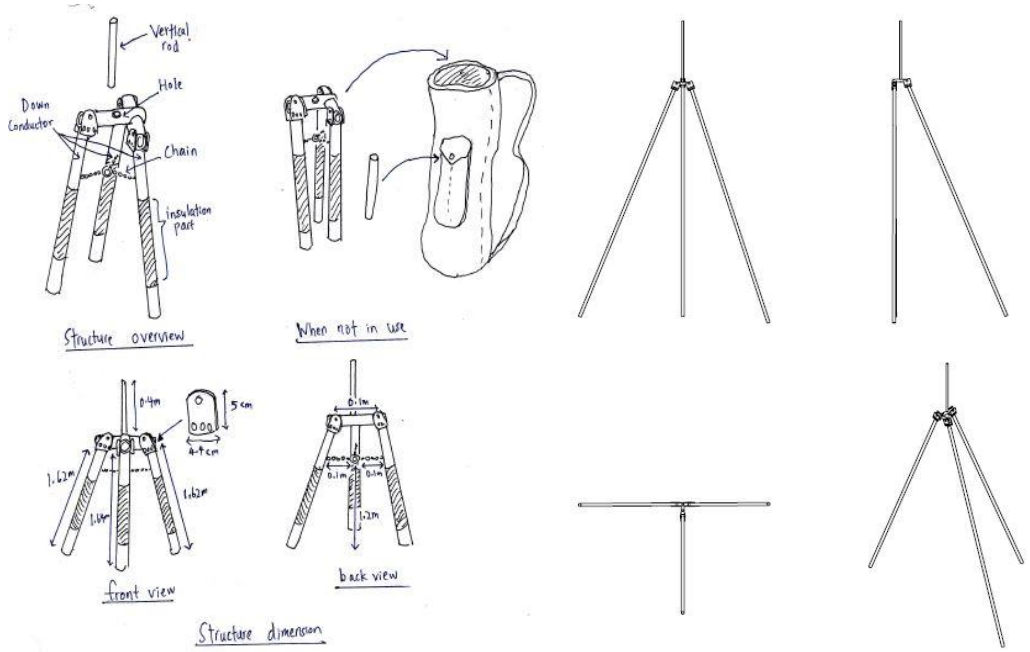


Figure 2. Structural design by hand sketch and Solidworks representation of proposed structure.

Fig. 2 shows the proposed design of portable lightning protection structure. The design is a tripod structure. A vertical rod was installed on the top of the structure. The vertical rod will intercept the discharge current from lightning strike and dissipate it to the ground harmlessly via down conductor. The down conductor is flexible, and a chain is installed to prevent the conductors from extending too far. Each of them is covered with a layer of insulating material for safety purpose. The structure is portable and convenient to carry. When not in used, the person can carry the structure around by folding and keeping it inside a bag as shown in the Fig. 2. The total height of the structure is 1.73 m, based on the studies carried out by M. A. Uman [22], the area protected by a single vertical rod is assumed to have a 45 °angle cone of protection. Therefore,

$$A_c = \pi(2 * H)^2 \quad (1)$$

(Where A=coverage area, H=total height of lightning protection structure)

By using equation (1), the coverage area of portable lightning protection structure in this study can be calculated:

$$A_c = \pi(2 * 1.73)^2 = 37.61m^2$$

Thus, it can be concluded that the design structure has a cone protection zone area of 37.61m^2 with a radius of 3.46 m.

2.2 Software modeling

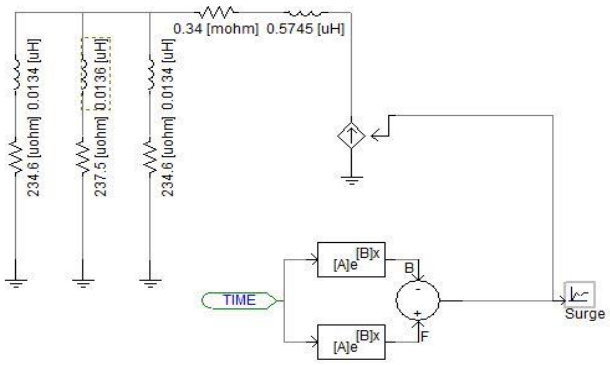


Figure 3. Structure circuit presented in PSCAD software.

The design of the structure was simulated by using PSCAD software. PSCAD is a simulation tool that is used to build, simulate, and model the power system. By using the software, lightning current source will be modified through the laboratory parameter defined by International standard. Fig. 3 shows the structure circuit subjected with an impulse current source. The applied impulse current was 10 /350 μs waveform based on IEC 62305-1 [9]. The value of impulse current can be approximated by using double exponential function [10]:

$$i(t) = \frac{I_o}{\eta}.(e^{-\alpha t} - e^{-\beta t}) \quad (2)$$

(Where I_o is the peak current, η is the correction coefficient of the current peak value, α and β are the parameters of the double-exponential function)

The structure circuit was modelled as resistor and inductor which are dominant characteristics of an electrical conductor. It is noted that capacitances have been neglected in this study. This is because the simulation is conducted under high frequency. Under this frequency, the capacitive effect is insignificant compared to inductive effect [19]. The value of resistance and inductance is calculated by using the equation (3) and (4). Equation (4) was derived by using electromagnetic approach.

$$R = \frac{\rho l}{A} \quad (3)$$

(Where ρ=resistivity, l=length, A=surface area)

$$L = \frac{\mu l}{2\pi}\left[\frac{4a^4 \ln\left|\frac{b}{a}\right| + a^4 - b^4}{4(a^4 - b^4)}\right] \quad (4)$$

(Where μ=permeability, l=length, a=inner radius, b=outer radius)

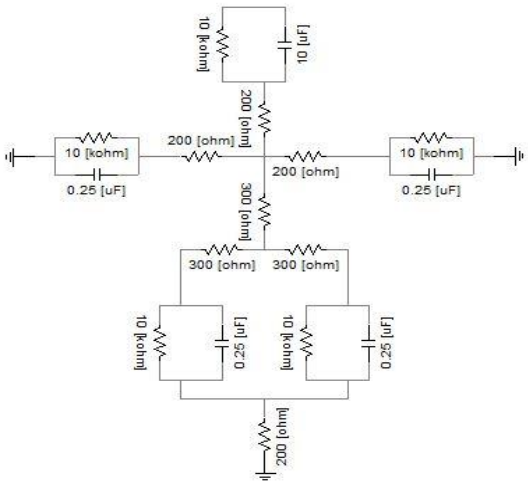


Figure 4. Human body model. [11]

In addition, the human body was electrically modeled as shown in Fig. 4. The circuit is formed by few lumped circuit that consists of resistor and capacitor which were arranged according to the impedance of each part of human body. The values of every component are obtained from literature review.

2.3 Software simulation

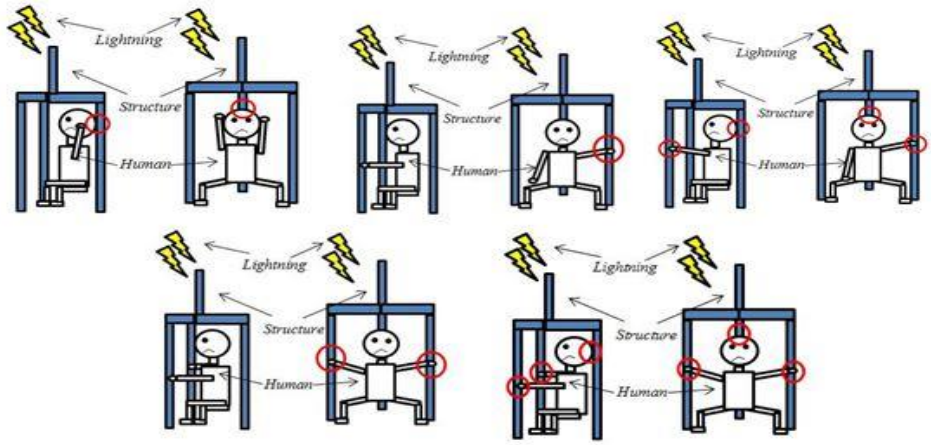


Figure 5. Five different human positions under the structure.

In the process of software simulation, the modeling for structure and human body model was first to be done. After that, a total of five different types of scenarios with different position of human under the structure will be simulated to examine the validity of lightning protection under various circumstances. The configuration of the structure remains constant throughout all the scenarios. All types of scenario are presented in Fig. 5 and the circle on the figure is indicating the human contact point with the structure. The scenarios are described as:

- Human is touching the structure with head.
- Human is touching the structure with one hand.
- Human is touching the structure with head and one hand.
- Human is touching the structure with both of the hands.
- Human is touching the structure with head and both of the hands.

2.4 Structure construction



Figure 6. Structure parts.

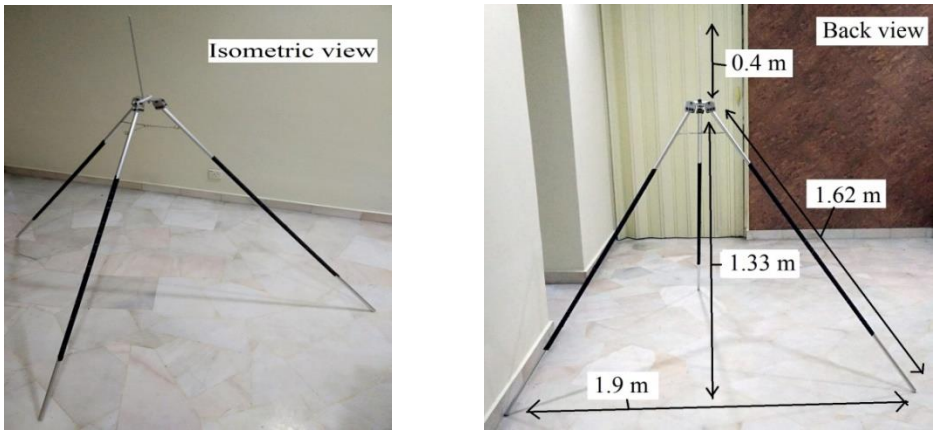


Figure 7. Assembled lightning protection structure.

The construction process was carried out in manufacturing lab located in Taylor's University Lakeside Campus. Cutting machine, milling machine, grinding machine, lathe machine and other tools such as jigsaw and hand grinder were used to manufacture and fabricate the structure parts shown in Fig. 6. The complete assembled structure with insulation is presented as isometric view and back view in Fig. 7. The total height of the complete structure is 1.73 m with the maximum extension length of 1.9 m.

2.5 High voltage testing

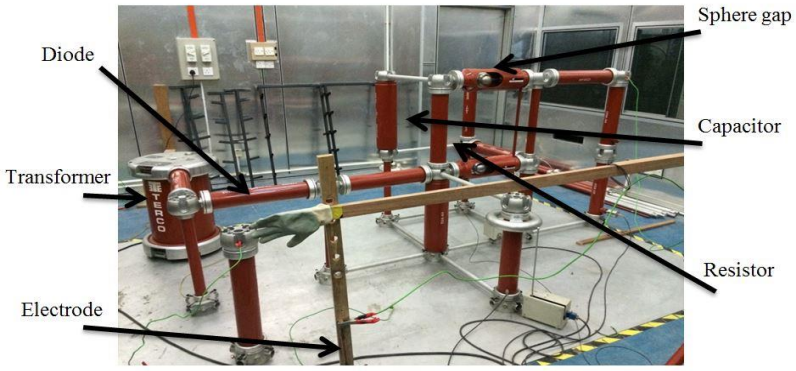


Figure 8. Marx high impulse voltage generator.

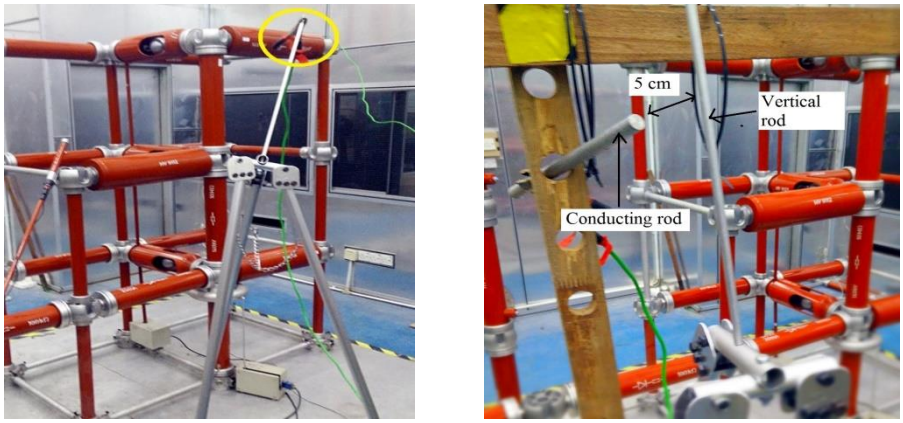


Figure 9. The setup of high voltage testing.

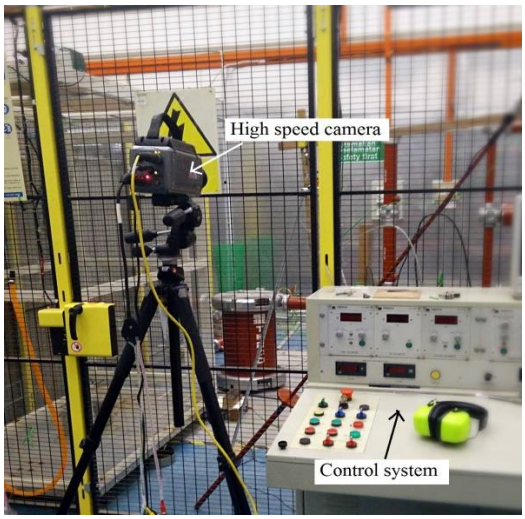


Figure 10. High speed camera setup and control system of generator.

The high voltage testing was carried out by using Marx high impulse voltage generator as shown in Fig. 8. The Marx generator has the capability of generating standard high impulse voltage (1.2/50 μs) following the IEC standard [12] up to magnitude of 400 kV. In this study, a total of 8 stages of high impulse have been applied to the structure. The range of impulse voltage applied was 100 kV to 275 kV with 25 kV increment per stage. A control system was used to manipulate the value of impulse voltage produced by Marx generator. There are two different methods applied in the testing. In the first method, the impulse current was directly injected to the structure through the tip of the vertical rod of the structure. In the second method, a 5 cm length of impulse voltage spark was created and transfer from the conducting rod of the Marx generator to the vertical rod located at the top of the structure. Both of the setups are shown in Fig. 9. The surface activities were observed by using high-speed camera. The testing was conducted in a low light intensity environment. Hence, if there is any flashover or sparks occur on the structure surface, the camera will be able to capture those events. Fig. 10 shows the setup of high-speed camera and control system.

3. Result and Discussions

3.1 Software simulation

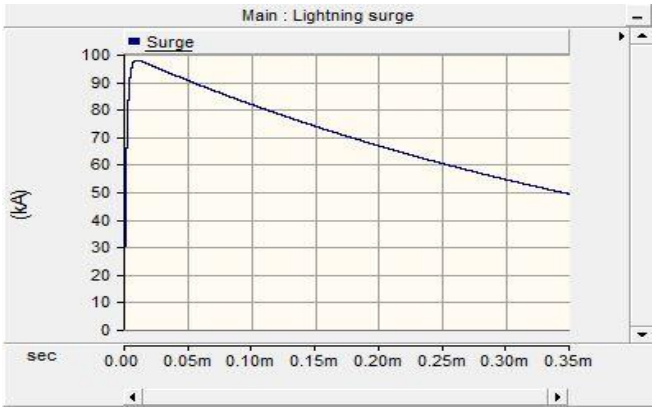


Figure 11. Waveform of impulse current generated.

The lightning impulse current subjected to the circuit is constant regardless of the scenario. Lightning is classified as a high transient current discharge [1]. Hence, it increases rapidly and reaches the peak within a short period of time. The waveform of impulse current generated by PSCAD software is shown in Fig. 11. In this study, 10/350 μs lightning waveform with 100 kA peak current was employed as the impulse current source. This type of waveform is taken from the standard IEC 62305-1, which is used to determine the maximum values of lightning current quantities of the first return stroke for lightning protection [9]. The types of waveform are determined by the front time and tail time of the waveform [10]. A 10/350 μs lightning waveform indicates that the current will reach the peak within 10 μs and drops to half of the peak current by the time of 350 μs.

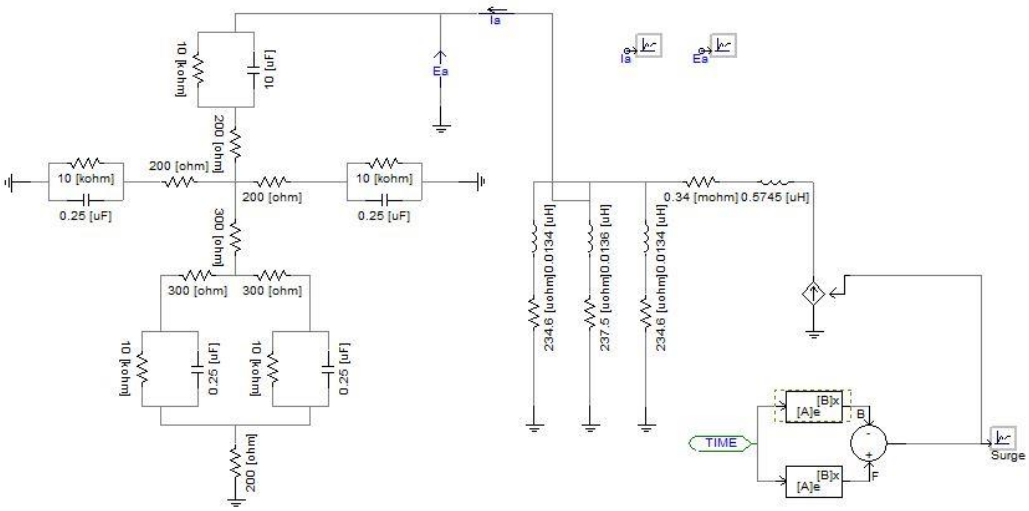


Figure 12. Circuit connection under Scenario 1 simulation.

Fig. 12 shows the circuit connection presented in PSCAD software between human body model and lightning protection structure with impulse current source under one of the scenarios. When lightning strikes an object, the current will flow in and generate a potential difference between two parts of the object [13]. In this study, when a lightning impulse current source with amplitude of 100 kA is applied to the structure, a potential difference is generated between the structure and human body.

This is because human is touching the structure which is being struck by the lightning. The higher the value of the potential difference, the larger the damage resulted from lightning.

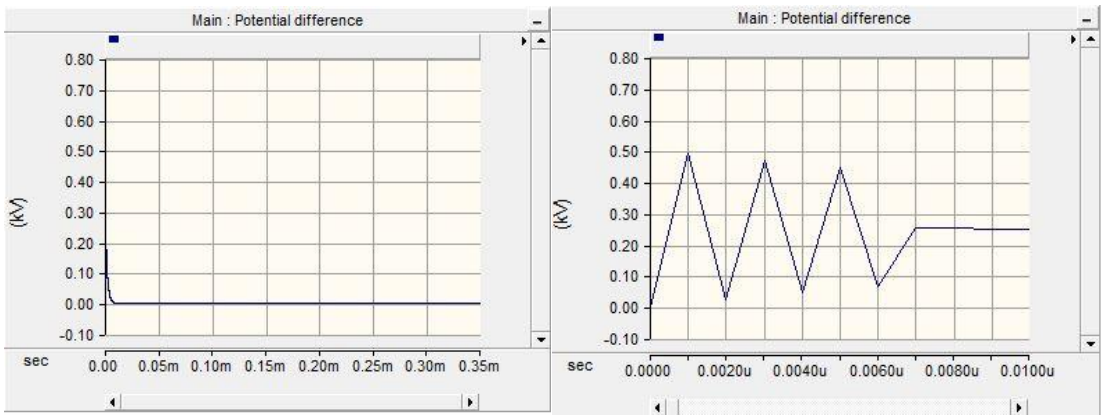


Figure 13. Potential difference waveform.

Table 2. Potential data collected from the waveform.

Potential difference between structure and human	Voltage value (kV)	Time (μsec)
Peak	0.492	0.001
End of oscillation	0.251	0.007
Zero	0.000	9.982

Fig. 13 shows the waveform of the potential difference generated between lightning protection structure and contact point of human body model. The result is presented in two different timeframes, which are millisecond and microsecond. The voltage waveform is oscillating with decreases of amplitude within a short period of time. Based on Table 2, the potential difference between lightning protection structure and human body model is approximately 492 V. The waveform achieves its peak voltage instantly, but it requires longer time to reaches zero during the decay process. It reaches peak voltage in 0.001 μs. There is an oscillation with decreasing voltage and it ended when the time approaches 0.007 μs. The waveform undergoes a slow decay and reaches 0 kV in 9.982 μs. The potential difference has a similar value under different scenario as the value of current flow within the structure and impedance of human body model remains constant.

It is observed that the waveform is oscillating in a short period of time due to high transient lightning which is capable of exciting the natural frequency of conductor and produces oscillatory transients during the striking process [14]. On the other hand, the value of potential difference fades to zero when the time reaches 9.982 μs. This is because the voltages are induced in the magnetic field of a closed conductor loop that carrying lightning current. The lightning current subjected has 10 μs front times and 350 μs tail time. Hence, the duration of potential difference is 9.982 μs, which approximately equal to 10 μs.

Table 3. Current data obtained from simulation under five scenarios.

Current flows		Current value (mA)	Time (μsec)
Scenario 1	Peak	1707	0.001
	Oscillation	876.7	0.007
	End	0	7.665
Scenario 2	Peak	1394	0.001
	Oscillation	712.1	0.007
	End	0	6.123
Scenario 3	Peak	963.4	0.001
	Oscillation	496.7	0.007
	End	0	6.399
Scenario 4	Peak	332.5	0.001
	Oscillation	167.6	0.007
	End	0	7.389
Scenario 5	Peak	231.8	0.001
	Oscillation	116.9	0.007
	End	0	6.838

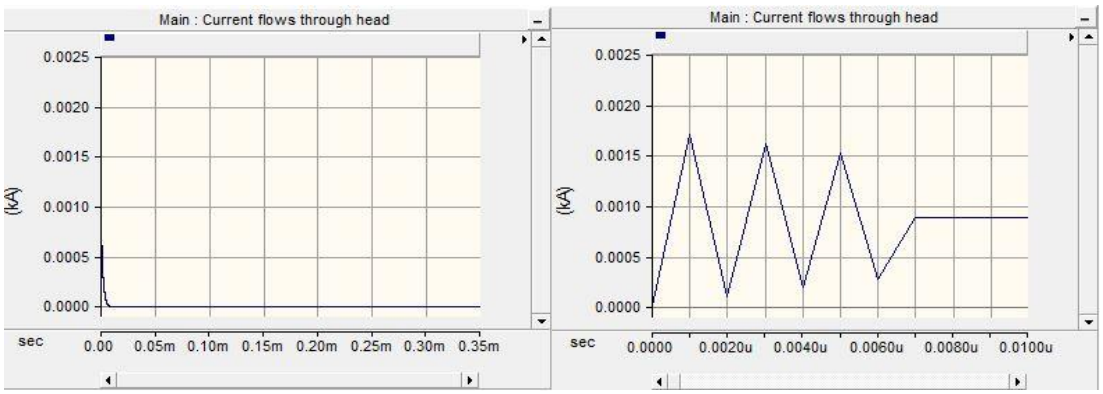


Figure 14. Simulated current waveform in scenario 1.

By comparing the results obtained in Table 3, scenario 1 has the highest value among all. Fig. 14 shows the simulated current waveform under scenario 1. In the first scenario, the structure circuit is directly connected to human head as shown in Fig. 12. This is the most lethal condition as there is no any other pathway to separate the current that flowing into human body. Furthermore, the current is directly flow into head and every part of the human body which are connected to ground. This results in a most deathly condition as the current could damage brain and heart. Meanwhile for another scenario, as there are several current paths provided, the current is able to divide into smaller value.

Apart from that, current pathway is one of the major factors that need to be taken into account because it will determine the type of injury which is caused by lightning. There are different types of pathway such as hand-to-hand, hand-to-foot and head-to-foot. The worst-case scenario is when the current is lead directly to the heart through the vessels and probably conducted through the veins [15]. Hence, it is not advisable to touch the lightning protection structure, because even hand-to-hand pathway has the possibility to lead the current into heart.

Based on the standard, the human body impedance under the wet condition is approximately 500 ohm [16]. The minimum current which can cause ventricular fibrillation is 370 mA. Ventricular fibrillation is defined as rapid and repeated uncoordinated contractions of the heart ventricles. This symptom can alter the heart pumping action, which probably cause fatal in human [20]. By using Equation (5) and (6) below [21], the minimum step voltage and touch voltage can be calculated.

$$U_s = (R_b + 2 * 3\rho)I_0$$
$$= (500 + 2 * 140.63)(370\ mA) = 289.07\ V \quad (5)$$

$$U_t = (R_b + 0.5 * 3\rho)I_0$$
$$= (500 + 0.5 * 140.63)(370\ mA) = 211.02\ V \quad (6)$$

Where U_s is step voltage, U_t is touch voltage, R_b is human body impedance, ρ is soil resistivity (assumed as $45\ \Omega m$ [23]), I_0 is minimum current which can cause ventricular fibrillation

The calculated minimum lethal step voltage and touch voltage is 289 V and 211 V respectively. Besides, the minimum current that can cause ventricular fibrillation is 370 mA. Based on the software simulation result, both the potential difference and current flow has exceeded the value calculated above. The potential difference value is 492 V while the highest current flow is 1707 mA. However, the exposed conductor parts will be insulated by using electrical insulation tape with a voltage breakdown of 24 kV. Since the generated potential difference (492 V) does not exceed the voltage breakdown of insulating material, the voltage would not able to puncture the insulation and allow the partial lightning current from entering the human body. Thus, it can be concluded that the person will be protected from electrocuting even if he/she accidentally touches the structure that is struck by lightning.

3.2 Hardware function testing

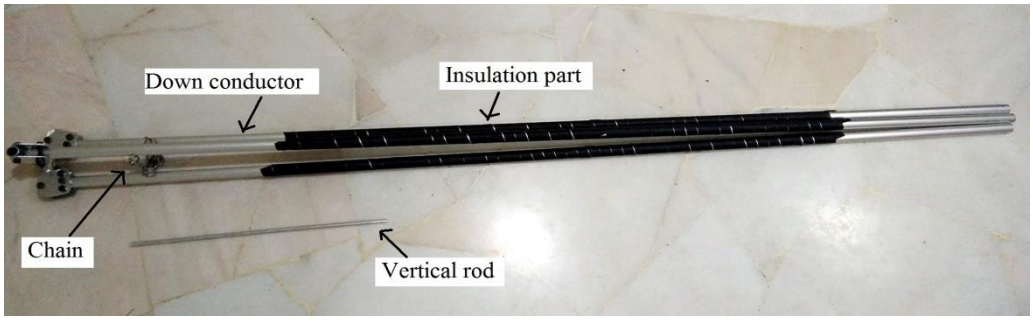


Figure 15. Parts of portable lightning protection structure.

The total assemble parts of design structure consists of a vertical rod and down conductor as shown in Figure 4.20. The setup procedure is simple, user only needs to set up the down conductor tripod and put the vertical rod into a hole located at the upper part of the structure. The chain was pre-installed to prevent the structure from extending too far. It also serves a purpose in improving the stability of the structure. The insulation was properly done on exposed part which might be in contact with the user.

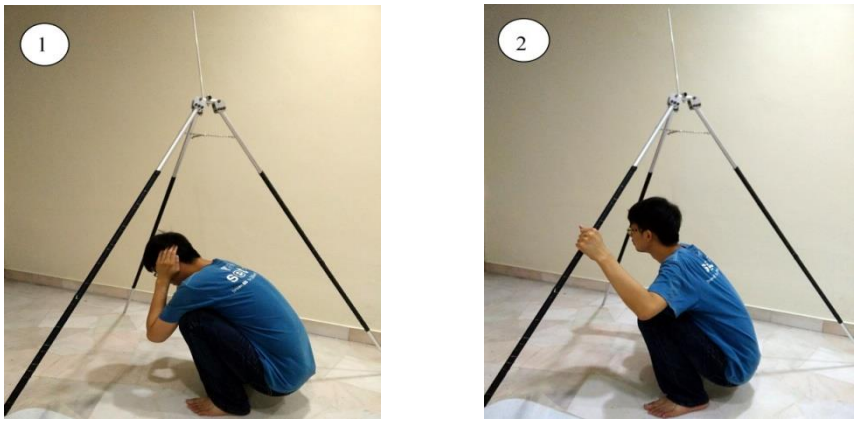


Figure 16. Structure usage demonstration.

Figure 4.21 shows the demonstration of user operating the structure. According to lightning safety handbook [17], the safety position should be practice during the thunderstorm. The person should crouch down, duck the head as low as possible, put the feet close together and cover the ears by hand. Therefore, when operating the structure, the user is advised to practice the first position in Figure 4.21. However, if the user is forced to be in contact with the structure, he/she must hold the insulated part as shown as the second position in Figure 4.21. Besides that, it is expected for the user to stay under the structure all the time during the thunderstorm for the intended protection. This is because the lightning will have the chance to strike the user instead of the structure if the user is standing outside of the protection coverage area.



Figure 17. Sparks emitted from conducting rod to vertical rod.

In the process of high voltage testing, the structure was subjected to a high impulse voltage up to 275 kV. During the injection of impulse voltage, the activity of structure surface was observed by using a high-speed camera. The moment when impulse voltage hits the structure was captured as shown in Fig. 17. The flashover event should not happen on the structure surface. This is because flashover occurs when the electric field strength exceeds the dielectric field strength in the air [18]. The high electric field strength indicates high potential differences in the structure. Yet, from the result shown in Fig. 17, it can be noticed that the structure surface did not trigger any spark or flashover event. Thus, it can be concluded that the structure is able to transfer the high impulse voltage to ground safely without trigger any spark.

4. Conclusions

Malaysia is geographically situated in close proximity with the equator. As the result, it is a zone with high lightning density. Therefore, it is necessary to emphasize the importance of personal lightning protection. The study based on lightning protection technologies has been conducted. A tripod design was proposed, sketched and visualized by Solidworks. By using PSCAD, the design is presented in circuit model and simulated with an impulse current source to determine the potential difference and current flows of the structure. After confirmed the validity of the structure and insulation level, the structure has been constructed. To further examine the functionality of the structure, high voltage testing is conducted to observe the possibility of spark occurrence on structure surface. The outcome was satisfying as there is no flashover occurs on the structure during the testing.

In a nutshell, a portable lightning protection structure had been constructed and tested. The design structure is aiming to provide personal lightning protection. Hence, it is presented in small scale design which only able to cover one person. The future improvement should be focused on more detailed simulation and enhancement of the portability of the structure. Other than 10 /350 μs waveform, different types of waveform based on another standard also will be applied in the simulation. The additional scenario of different human positioning within the structure can be considered in the simulation also. Moreover, to further enhance the structure portability, the leg of the structure will be designed to be retractable for more convenient transport.

References

[1] M. A. Uman, "Natural lightning," *IEEE Transaction on Industry Applications*, vol. 30, no. 3, pp. 785-789, May 1994.

[2] S. Andrew, T. Elizabeth, "Land of lightning," *The Star Online*, May 17, 2009. [Online]. Available: http://www.thestar.com.my/story/?file=/2009/5/17/lifefocus/3895023. [Accessed: June 9, 2015].

[3] Malaysian Meteorological Department, "General climate information," 2013. [Online]. Available: http://www.met.gov.my/index.php?option=com_content&task=view&id=30&Itemid=1090. [Accessed: June 9, 2015].

[4] R. E. Orville, "Development of the national lightning detection network," *Bulletin of the American Meteorological Society*, vol. 89-2, pp. 181-190, February 2008.

[5] A. V. Meier, "*Electric Power Systems: A Conceptual Introduction*," Hoboken, New Jersey: John Wiley & Sons Inc, pp. 11-13, 2006.

[6] "Electrical connections for power circuits," *Facilities Instructions, Standards, and Techniques*," vol. 3-3, pp. 1-17, November 1991.

[7] BS EN/IEC 62305-3, *Physical damage to structures and life hazard*, Standard, 2006.

[8] *Lightning protection guide*, 3rd ed. Germany, Neumarkt: DEHN, 2014.

[9] BS EN/IEC 62305-1, *General principles of lightning protection*, Standard, 2006.

[10] D. Lovric, S. Vujevic, T. Modric, "Least square estimation of double-exponential function parameters," *11th International Conference on Applied Electromagnetics*, Niš, Serbia, September 01-04, 2013.

[11] V. Cooray, *The lightning flash-cooray*, 1st ed. United Kingdom, London: The Institution of Engineering and Technology, 2003.

[12] IEC 60-1, *Guide on high-voltage testing technique,* Standard, 1989.

[13] A. M. Mousa, "Safety against lightning for linemen working on de-energized power lines," *IEEE Transactions on Power Delivery*, vol. PWRD-1, pp.245-250, January 1986.

[14] R. C. Dugan, M. F. McGranaghan, S. Santoso, H. W. Beaty, "Terms and definitions: transients," in *Electrical power system quality*, 2nd ed. McGraw-Hill, pp. 15-17, 2004.

[15] J. He, R. Zeng, B. Zhang, "Body Safety and Permitted Potential Difference," in *Methodology and technology for power system grounding*, 1st ed. Singapore: John Wiley & Sons, pp. 19-22, 2003.

[16] NFPA 70E, *Electrical safety requirements for employee workplace*, Standard, 2004.

[17] C. Gomes, *Handbook on lightning safety*. South Asian Technology Research and Information Centre, 2008.

[18] S. Nell, *Bungaroo Creek lightning resilience study*. Perth, Western Australia: Murdoch University, School of Engineering and Information Technology, 2014.

[19] M. Sadiku, *Elements of electromagnetics*. New York, United States: Oxford University Press, 2007.

[20] *High Voltage Safety Manual*. Colorado, Western United States: Colorado State University, NSF Engineering Research Center.

[21] IEEE-80, *Guide for safety in AC substation grounding*, Standard, 2000.

[22] M. A. Uman, *How does a lightning rod works*?. New York: All About Lightning Publications, 1986.

[23] R. Saad, "Groundwater detection in Alluvium using 2-D Electrical Resistivity Tomography (ERT)," *Electronic Journal of Geotechnical Engineering*, vol. 17, pp.369-376, 2012.

Minimal Instruction Set CPU

Wong June Keat[1], Dr. Edwin Chung Chin Yau [2*]

[1]*Research Student, School of Engineering, Taylor's University, Malaysia*
[2]*Lecturer, School of Engineering, Taylor's University, Malaysia*

[*]*junekeat.wong@sd.taylors.edu.my*

[*]*ChinYau.EdwinChung@taylors.edu.my*

Abstract

In the current world, computer is very important in human daily life and computer is almost impossible to imagine that human can live without computers. Computers have become electronic devices of almost every day use for individuals of every age as well as industry field. Today, everything related to human daily life almost can be done by using computers therefore computer really help human reduce a lot of burden in daily life. In order to enhance the performance, the minimal instruction set CPU is one of the solutions. The clock per instruction of simple instruction is small so that if the instructions per program can be narrow down which mean that the speed of the processor can be increase. In this paper, the theory, method and design of minimal instruction set for practical CPU is presented. This CPU is designed based on the MISC, the objective of this project is determine the minimal instruction set for a practical CPU therefore this CPU should design with few instruction set and it is able to working with the CPU. In the current stage, there are six different type instructions for this CPU. EEPROM memory are chosen for the memory part of this CPU, the reason to choose this memory is because of the EEPROM is easy to program and erasable. The number of registers can be decided by the designer when the number of register is less, the size of the memory should be larger. There are few improvements for this project which are implement an alphanumeric LCD display to show the instruction during execution and implement the working design into circuitry.

Keywords: CPU, RISC, CISC, MISC, Instruction set, Computer Architecture, Opcode.

1. Introduction

In the current world, computer is very important for human daily life and computer is almost impossible to imagine human can live without computers. Computers have become electronic devices of almost every day use for individuals of every age as well as industry field. Today, everything related to human daily life almost can be done by using computers therefore computer really help human reduce a lot of burden in daily life.

Computer architecture can be separated into two parts which is Instruction set architecture (ISA) and Hardware System Architecture (HSA). ISA is the part of the computer architecture and it is related to programming. An ISA includes a specification of the set of opcodes (machine language) and the native commands implemented by a particular processor. Besides that, hardware system architecture basically includes central processing unit (CPU) and Input/Output (I/O) system [1].

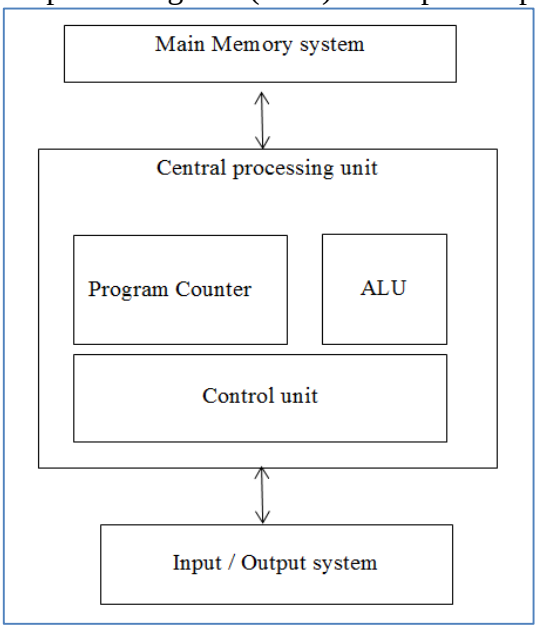


Figure 1: Von Neumann Machine

As described in Von Neumann Architecture, the design of Von Neumann machine is consist of three main systems which are main memory, input or output and central processing unit. Central processing unit (CPU) is the brain of a computer. The program which is use to execute is stored in the main memory of the computer. A program is a sequence of instructions to perform a specified task. Besides, the CPU is made up by few major parts which are Arithmetic and logic unit (ALU), Control unit (CU) , Program counter (PC) and Register set [1,2]. The working principle of CPU is CU fetches the instructions set from the main memory. In the same cycle, the CU is increments PC by one. The PC will read and send the instruction set of the address which is PC currently holding to Instruction register (IR). After that, CU will decodes the instruction set and perform specified task [3, 4, 5].

Complex Instruction Set Computing (CISC) processor began with straightforward hardware and relatively simple instruction set. The goal of CISC architecture is to complete a task with few lines of assembly code as possible therefore the complex instruction set is needed for this architecture. For example, the complex instruction “ADD” is used to addition the operands in the execution unit and “STORE” is the command to stores the result in the register. Thus, the entire task of

addition two data can be done with only two lines of instruction which is shown below [6].

```
ADD     5, 4
STORE   A
```

Figure 2: Example of CISC

From the Figure 2 the example program of CISC, the length of the program is short but the number of execution cycles of the CISC instruction is more than the RISC instruction. Besides, the addressing mode is more complex compared with RISC. Although the CISC program is simple but the instruction need to go through the complex addressing mode to get the data from memory.

Reduced Instruction Set Computing (RISC) is a design philosophy based on the premise that system performance could be greatly enhanced by reducing the complexity of the hardware. The RISC processor can be defined as a CPU with simplified, simplest and fixed-length instruction set. RISC processor only uses the simple instructions that can be executed within one clock cycle. For example, "LOAD" which is load the data from memory to register, "ADD" which is finds the values of addition of two data, "STORE" which is store the data from register back to the memory. Thus, the entire task of multiplying two data can be done in few lines of instruction and it is longer than CISC system [6].

```
LOAD    A, 5
LOAD    B, 4
ADD     A, B
STORE   A
```

Figure 3: Example of RISC

From the example program of RISC, the number of execution cycle per instruction is one therefore the program can be done in four execution cycles. Although the execution cycle per instruction is less but the length of the program is longer than CISC. Based on the performance equation of CPU, if the programmer can create the program will shorter length then the speed of the CPU will be faster.

This research is conducted to study and design a minimal instruction set CPU. The objective of this project is to determine the smallest numbers of instructions set for a practical CPU.

2. Literature Review

2.1 RISC versus CISC and MISC

Complex Instruction Set Computing (CISC) processor began with straightforward hardware and relatively simple instruction sets. The single instructions of CISC can execute several low-level operations such as arithmetic operation, load data from memory, data storing, address modes as well as multiple operations within single instruction. Three main factors that will affect the performance which is the speed of clock, how many cycle to perform a task and how many instructions needed to perform a task. Besides, CISC processor has most of the following properties:

- "Smart" instruction set (some of the instructions are simple and some very complex).
- Instructions generally take more clock cycle to execute.
- Instructions of variable size
- Small numbers of registers
- No pipelining technique
- Microcode control
- Segmented memory model

CISC has a large amount of different and complex instructions therefore the length of program is always shorter compare to RISC but the instructions will take more than one clock cycle to execute [7, 8, 9].

Reduced instruction set computing (RISC) is a design philosophy based on the insight that simplified instructions can provide higher performance if the simplified instructions enables much faster execution of each instruction. The general concept of RISC system is uses a small and highly optimized set of instruction rather than the complex instructions. RISC system only used the load and store architecture therefore it is simpler than a CISC system. RISC has the following common properties:

- Simple instructions and addressing modes
- Most of the instructions can be execute less than two clock cycles
- Uniformed length instructions
- Fixed instructions format
- Pipelining technique
- Large number of registers
- Instructions interface with memory via load or store

Most of the instructions of RISC system can be execute in one clock cycle therefore in order to enhance the performance of RISC system, the length of the program need to reduce as much as possible to increase the performance of RISC system [7, 8, 9].

Minimal Instruction Set Computing (MISC) is computer architecture with a very small number of basic instructions. It could be less than 15 instruction sets. Besides that, the characteristics of MISC are similar to RISC. For RISC, the number of instructions could be maximum up to 50 therefore MISC is called minimal instruction set computing because it has small number of instructions. On the other hand, there is

a computer architecture called One Instruction Set Computing (OISC), this computer will working with only one instruction. The properties of MISC are shown below:

- Simple instructions and addressing modes
- Most of the instructions can be execute less than two clock cycles
- Fixed length instructions
- Fixed instructions format
- Pipelining technique
- Larger size of memory
- Large number of registers
- Instructions interface with memory via load or store

Table 1: Comparison between RISC, CISC and MISC

RISC	CISC	MISC
Simple instruction	Complex instruction	Simple instruction
Single-cycle instruction	Multi-cycle instruction	Single-cycle instruction
High level language is done in software	High level language done in hardware	High level language is done in software
Register to register	Memory to memory	Register to register and Memory to register
More register	Less register	More register and larger size of memory

2.2 Instruction Set Architecture

Instruction Set Architecture (ISA) is one of the parts of the computer architecture and it is related to programing which is basically machine language. The ISA serves as the boundary between software and hardware. Besides, the instruction set provides commands to the system and communicate with the system and tell the system what needs to do. Few examples of instruction set are shown below.

- ADD (Add two number together)
- LOAD (load data from memory)
- STORE (store data from register to memory)
- MOVE (move the data from memory to memory)
- INCREMENT (data increment by 1)
- DECREMENT (data decrement by 1)

One of the components called Arithmetic Logic Unit (ALU) is used for this project. The ALU can perform several arithmetic tasks such as *ADD, AND, OR, INCREMENT and MULTIPLY* operations. The Instruction Set can be created by creator [10].

This Journal showed 16 different instructions for ALU which created by the creator.

Instruction	Opcode
Add	0000
Sub	0001
Mul	0010
Logical AND	0011
Logical OR	0100
Left Shift	0101
Right Shift	0110
NOT	0111

NAND	1000
NOR	1001
Bitwise AND	1010
Bitwise OR	1011
Bitwise NAND	1100
Bitwise NOR	1101
Move	1110
Compare	1111
Power Down Mode	zzzz

Figure 4: Example of Instructions with Opcode

Based on the understanding in this journal, the Opcode of the instruction can be design by the creator based on the creator how to design the control logic [10].

2.3 Performance Equation

The performance equation analyses execution time as a product of three factors which is shown below.

$$\frac{\text{seconds}}{\text{program}} = \frac{\text{instructions}}{\text{program}} \times \frac{\text{clocks}}{\text{instruction}} \times \frac{\text{seconds}}{\text{clock}} \quad (1)$$

The CISC approach attempts to minimize the number of instructions per program but the clocks per instruction of CISC always more than RISC. The opposite site, RISC reducing the clocks per instruction therefore the performance of the CPU can be enhance by reducing the instructions per program. However the instructions per program of RISC always longer than CISC but the instruction set designer can reduce the instruction as much as possbile to enhance the performance of CPU. The time per program is lesser which mean the speed of the CPU is faster therefore it is possible to enhance the performance of CPU by reducing the instructions per program. [5, 11]

One of the example provided from book about the performance between RISC and CISC. The results showed that the performance of RISC system is faster than CISC system. Both system are running the same program. [11]

The same program is compiled for a CISC machine (like a VAX) and for a pipelined RISC (like a SPARC based computer). The following data is available:

$IC_{CISC} = 500000$
$IC_{RISC} = 1100000$
$CPI_{CISC} = 6.8$
$CPI_{RISC} = 1.4$
$T_{ck\ CISC} = 25\ ns\ (25*10^{-9}\ s)$
$T_{ck\ RISC} = 30\ ns$

What is the relative performance of the two machines?

Answer:

$$\frac{CPU_{timeCISC}}{CPU_{timeRISC}} = \frac{5 * 10^5 * 6.8 * 25}{11 * 10^5 * 1.4 * 30} = \frac{850}{462} = 1.83$$

The RISC machine is by 83% faster than the CISC one.

Figure 5: Performance of RISC and CISC

From Figure 5, the results showed that the performance of RISC is much faster than CISC. Based on the performance equation of CPU, CPU_{time} = IC*CPI*T_{ck} where IC is instruction per program, CPI is clocks per instruction and T_{ck} is time per clock. The results showed that the time needed for RISC program is 46.2 ms and CISC need 85 ms therefore the performace of RISC is faster than CISC. However, most of the softwares available in market is only suitable for CISC system therefore the market value of CISC is bigger than RISC system [11].

3. Research Methodology

The planning for the research methodology is described on this chapter. The flowchart of the project is presented and explained in detailed.

3.1 Project flowchart

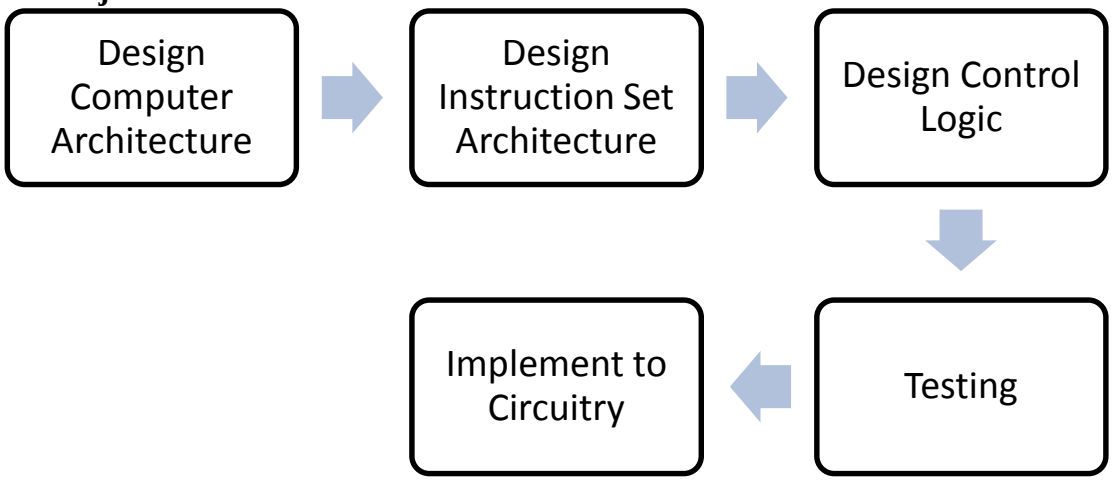


Figure 6: Flow chart of project

3.2 Design Computer Architecture

During design computer Architecture stage, the computer architecture is designed by part by part such as program counter, instruction fetch logic, data fetch logic, address fetch logic and the memory which store the instructions. Design stage is separated into two parts which is hand drawing and simulation. MULTISIM simulation is used to simulate the design. The first design which is program counter is shown in Figure 7 and Figure 8.

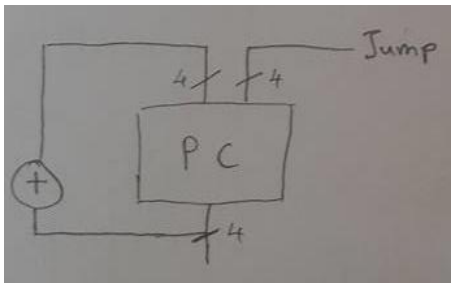


Figure 7: Design of Program Counter

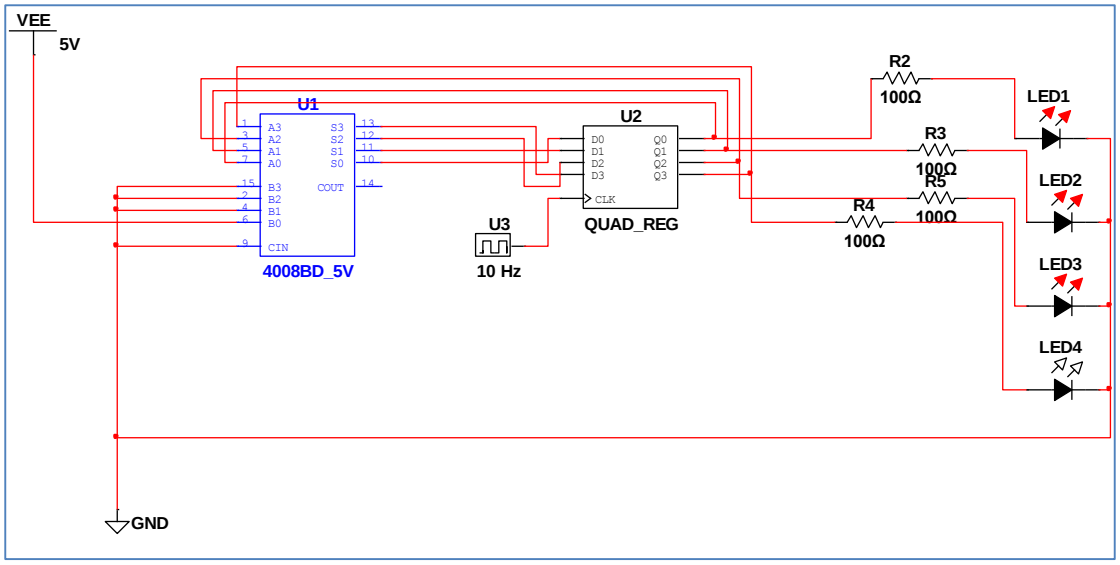


Figure 8: Design of Program Counter by Multisim software

From Figure 8, component U1 is 4-bits binary full adder and U2 is 4-bits register. The purpose of this design is the program counter able to increment by one which mean when the address pass through the register, the address will increament by one. Besides that, the four LED just to show the binary number is increment by one for each clock cycle (from 0000 to 1111).

Second design included program counter, data fetch logic as well as address fetch logic is shown in Figure 9 and Figure 10.

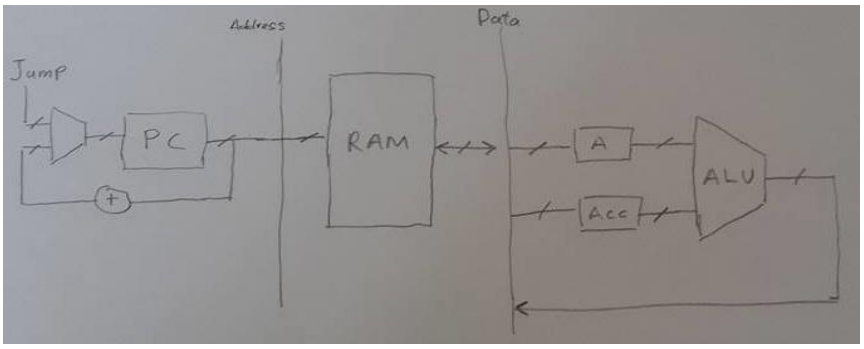


Figure 9: Second design of CPU architecture

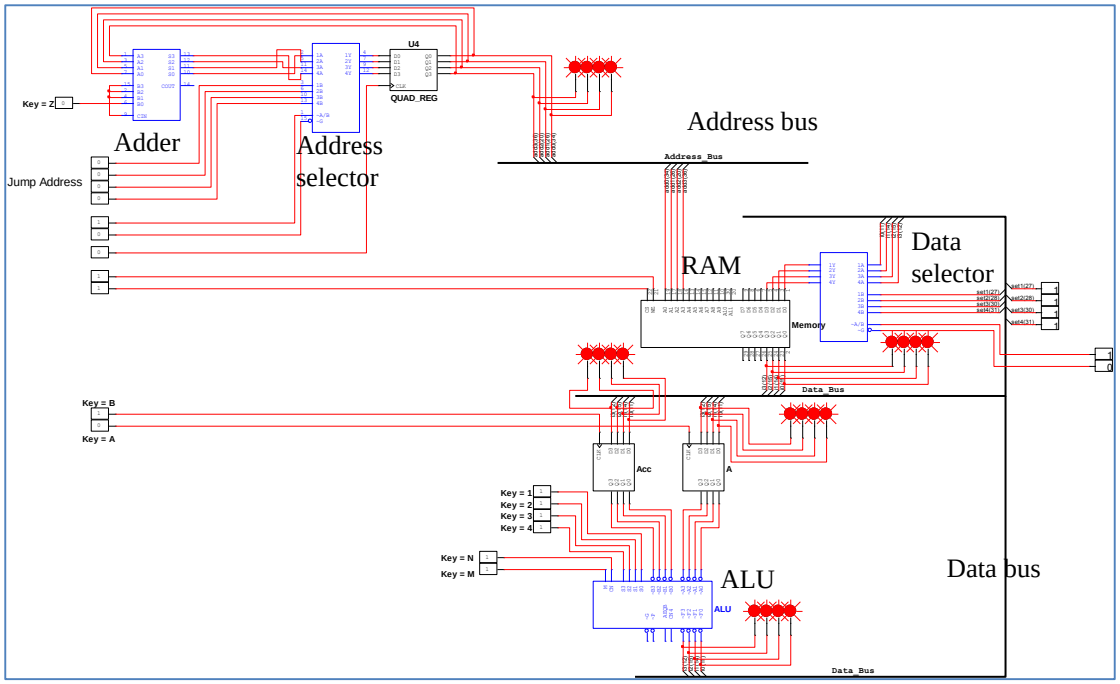


Figure 10: Second design of CPU architecture by Multisim software

From the Figure 10, top left corner is program counter. The design of program counter slightly different compare with first design. The address selector is use to choose which address go through the register either the current address with increment by one or the jump address. Besides, the middle of the figure is the RAM. In theorectical, the data is store inside the RAM with address. When the address is call, data inside the RAM will be take out and send to register. Furthermore, the bottom part of the figure is ALU. ALU will perform the arithmetic or logic function based on the instruction. All the LED lights just used to show the results and compare to the expected results.

The basic concept of this circuit is program counter will send the address through the address bus and the RAM will receive the address. Once the RAM receive the address, it will send the data with the same address to register. The address can be select in address selector and also the data can send to either accumulator register or normal register. The data will pass to the ALU and perform either arithmetic or logic function and at the end the data send to RAM by data bus and store inside the RAM.

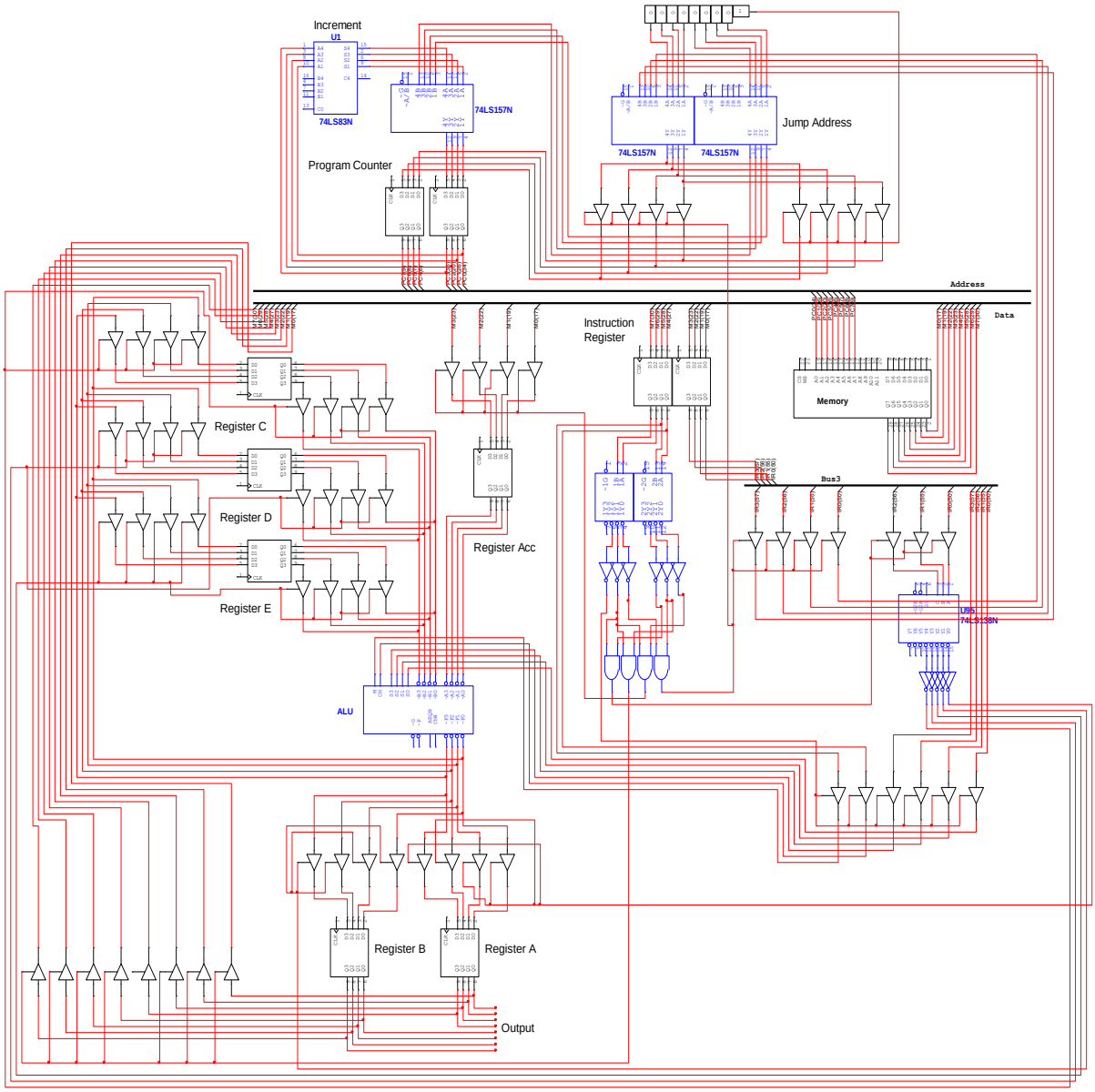


Figure 11: Final Design of CPU architecture by Multisim Software

Figure 11 is the final design of CPU architecture of this project. Each part of the CPU architecture is discussed on the results and discussion part.

3.3 Design Instruction Set

In the stage of design instruction set, different ideas of instruction set design will be proposed through brainstorming activitiy. The design of instruction set must meet the following criteria:

i. Instruction as short as possible
ii. Able to perform normal task for example like tic-tac-toe

During the designing process, the number of bit of the instruction set is the main element in this project. The student have to decide what is the number of bit is the best design for this project. For example the 7-bits register is shown below.

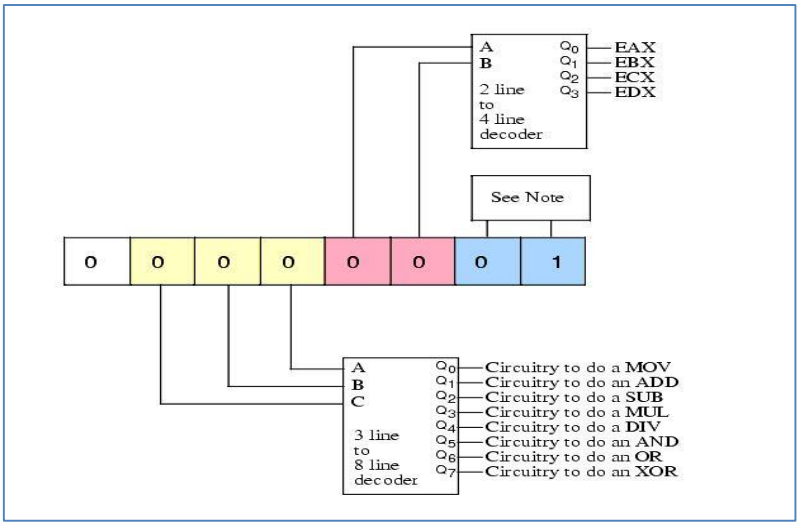


Figure 12: Example of Instruction set

In Von Neumann architecture CPU, the computer encodes CPU instruction as numeric values and stores the numeric values into memory. With the number of bit, there are 2^n different possible opcodes, so to encode m instructions the opcode need at least $\log_2(m)$ bits long. For example, the number of bits is seven therefore the opcodes of this size could encode 128 different instructions. For the figure above, the 3-bits (yellow) are used as operand, the operand could function as move, add, subtraction, multification and more. Besides that, the following 2-bits (pink) could used as a destination which mean save the data to the register after the operand. Furthermore, the other bits could also used as a addressing which mean to load the data from main memory which is same address with the register. The design of instructions and opcodes is based on the designer how to achieve the goal of project [12].

3.4 Design Control Logic

Control Logic basically is a key part of software that control the operations of the program. The control logic will responds to commands which input from the user. Besides, it also can perform automated tasks that have been structured into the program. There is one lecture class needed from project supervisor about the basic and knowledge on what is control logic and how to design it.

3.5 Testing and debugging

There are two times of testing and debugging. First time is to test the instruction set with the computer architecture. Once there is no error and able to get the expected outcome then the project will move to next stage which is called confirm the instruction set. Second time of testing is happen after design the control logic. The purpose is test the computer architecture is working with the control logic and can get the expected outcome.

3.6 Implement to Circuitry

This stage is implement the design of CPU architecture into circuitry. Most of the components of the design is use 7400 series intergrated circuit. When the board is developed and completed, the circuit board will be use to fetch the instruction and data from the memory to register and also from register to memory. To ensure the circuit board is working, the LCD display will be implemented to show the instruction. After the circuit board is done and working properly will try to implement a tic-tac-toe algorithm using this circuit board to allow play tic-tac-toe with user.

3.7 Limitation of the project

As earlier mentioned, most of the software in the market is available for CISC processor which mean those software is not capable for RISC processor. However, the performance of RISC is much faster than CISC as proven earlier. If the instruction set is powerful enough and can perform normal task as practical CPU, RISC and MISC can be one of the powerful machine in the world.

Besides, the MAR and MDR are not using for the MISC processor the reason is try to build the MISC processor as simple as possible therefore there is just only from register to memory or memory to register.

4. Results and Discussion

4.1 Design of CPU architecture

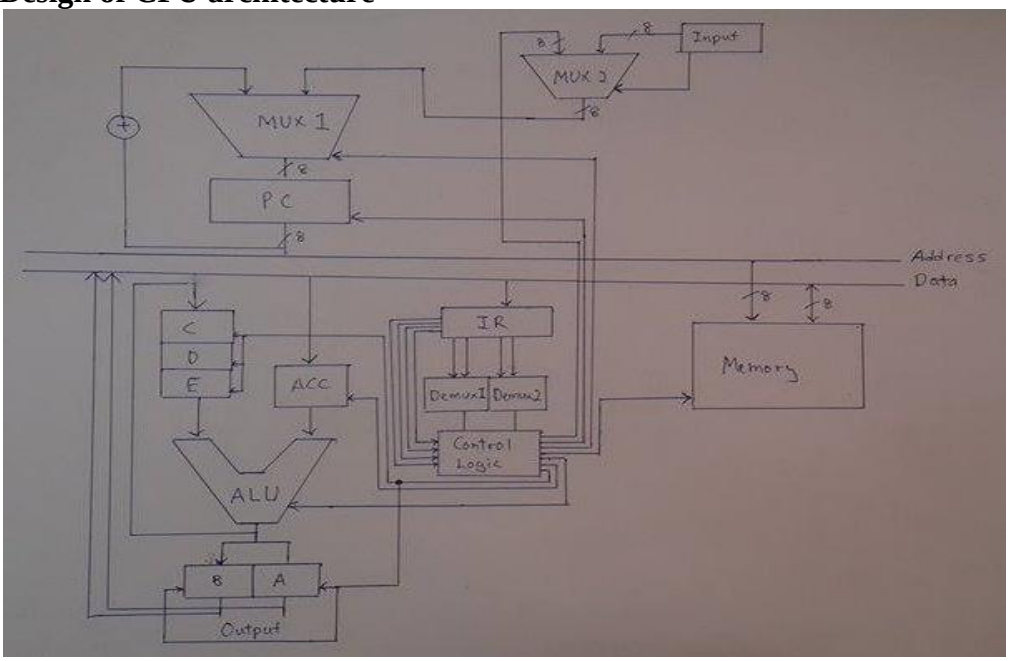


Figure 13: Latest design of CPU architecture

In figure 13 above is latest design of CPU architecture. For the Program Counter (PC) part, there are 8-bits input and 8-bits output for address and this 8-bits output address will send to memory to call out the data which stored in memory. There is first Multiplexer (MUX 1), this multiplexer is to choose which address to go in PC either the increment address or jump address. Besides that, there are two types of jump address which are imput jump address and memory jump address. Input jump address will send to MUX 1 by press the input key. On the other hand, MUX 2 is to choose either input jump address or memory jump address to send to MUX 1. There are two types of buses which are address bus and data bus.

For memory part, there are 8-bits input memory address and 8-bits memory data. When the input address is send to memory then it will call the data which is stored in the same address. After the memory data is send to data bus, the Instruction Set Register (IR) will receive the data and decode the data. After the decoding the IR will choose which Control Logic to use.

Furthermore, there are six Working Registers in this design which are called A, B, C, D, E and Accumulative (Acc). Each of the register is 4-bits parallel shift register. in this design, the data from memory will always send to Acc. The reason of data always send to Acc is because lack of memory data output bit.

4.2 Instruction Set Architecture

Table 2: Instruction with Opcode of this project

Operation Code	Instruction
0000 0000	NOP
0001_ _ _ _	Jump address
0100_ _ _ _	Move (Memory to register Acc)
0101_ _ _ _	Move (Register to Memory)
0110_ _ _ _	Move (Register to Register)
10_ _ _ _ _ _	Logic/Arithmetic

From the table 2, there are six types of instructions for this project. The highest two bit of memory data is chose for Operation Code (Opcode). When the Operation Code (OP) are all zero, the instruction is no operation the CPU will do nothing when receive this instruction. For jump instruction, the highest four bit are jump instruction Opcode and the rest of four bit are the address. This four bit of address will send to program counter. For move instruction, there are three different types of move instruction. The first move instruction is move the data from memory to register Acc. The highest four bit are the opcode and the rest of four bit are use to enable the register Acc. Second move instruction is move the data from register to another memory. The highest four bit are opcode, the rest four bit are use to enble register A to E and memory write enble. Third move instruction is move the data from register to another register. The highest four bit are opcode, the rest four bit are used to enable the registers. The last instruction is Logic/Arithmetic. The highest two bit are opcode, the rest of six bit are used to select the operation of the ALU.

The Figure 14 is part of the CPU architecture to show the connection from memory to control logic through IR and Demultiplexer (DEMUX).

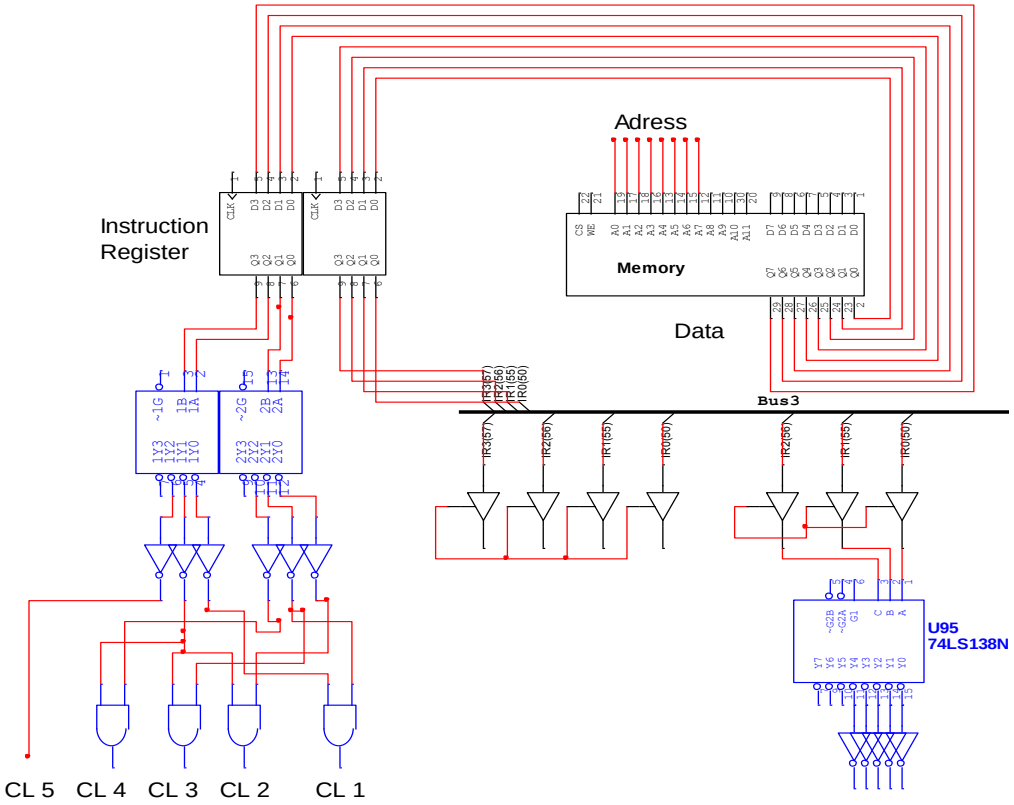


Figure 14: Circuit of architecture from memory to Control logic through IR and DEMUX

From the figure 14, the 8 bits memory data will send to IR and the highest 2 bits of IR are connected to DEMUX 1 and the following 2 bits are connected to DEMUX 2 and the rest of 4 bits are connected to a bus.

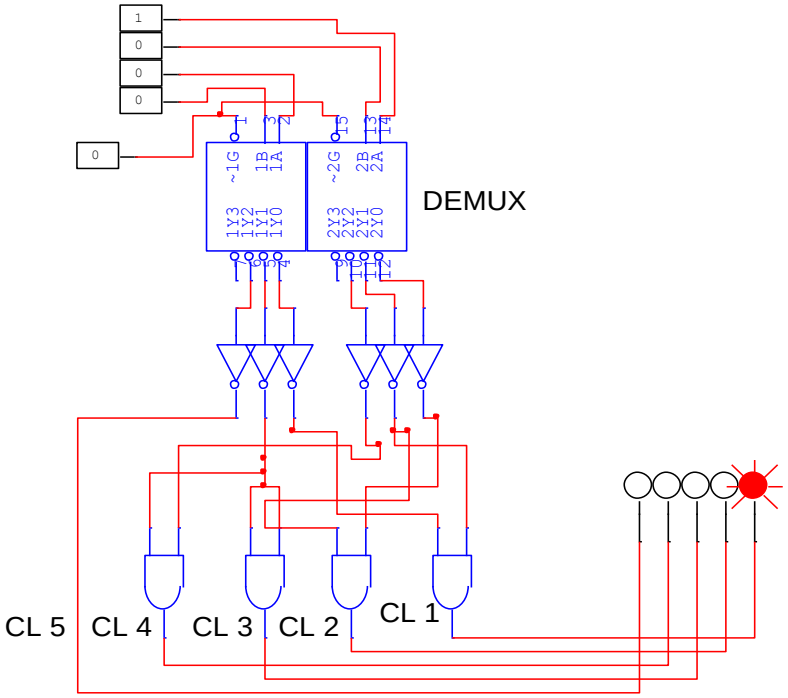


Figure 15: Example of instruction

From Figure 15, the input of the DEMUX is 0001, from table 2, the opcode 0001 is the jump instruction . The control logic 1 (CL1) is on therefore the control logic 1 will enable and the rest four bit of IR are send to PC to perform jump instruction.

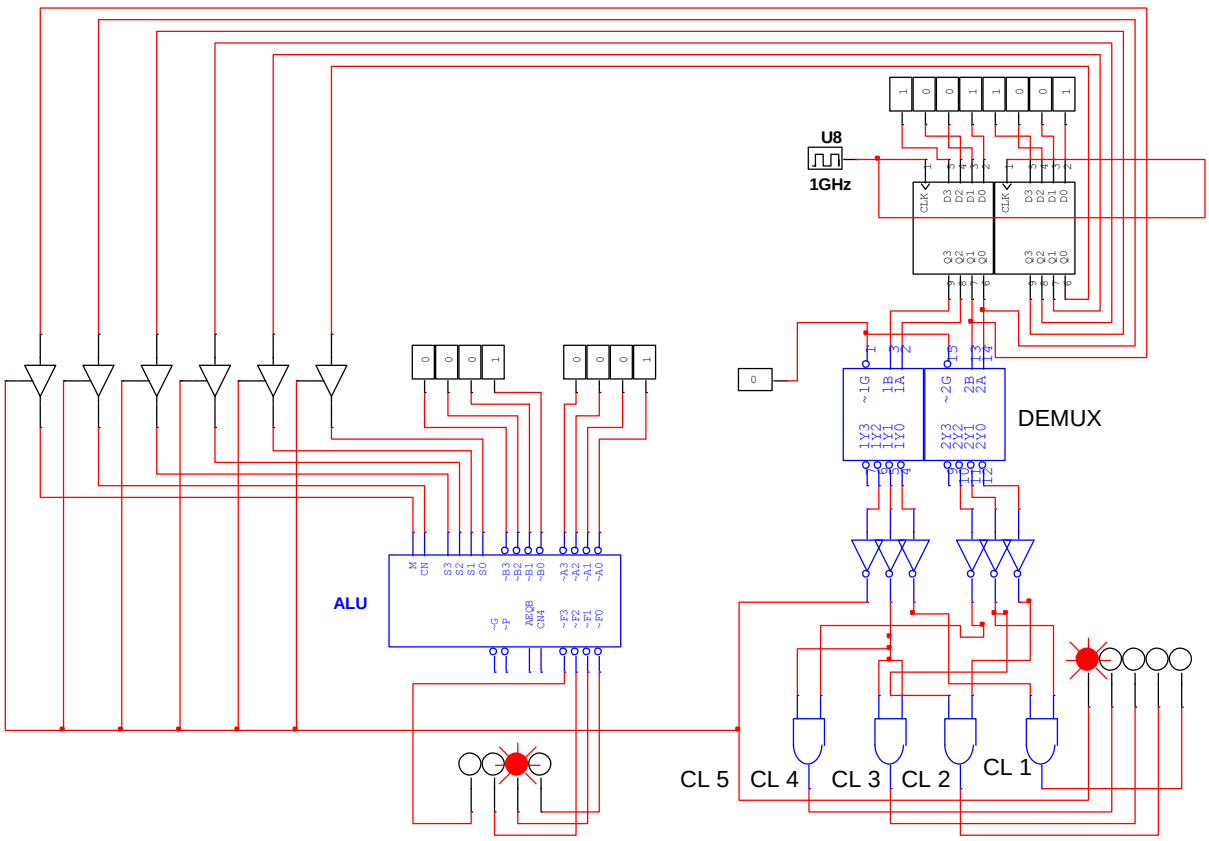


Figure 16: Example of logic/Arithmetic instruction

From Figure 16, the input of IR is 10011001, the highest two bits are 10 which is Logic/Arithmetic instruction and control logic 5 is enable. The rest six bits of IR are connected to ALU to control the operation of ALU. The addition instruction is used in this example, two inputs of ALU both are 0001 and the operation of the ALU is addition therefore the output of ALU should equal to 0010. The LED showed that the result of ALU is 0010.

Table 3: Function table of ALU

Mode Select Inputs				Active LOW Operands & F_n Outputs		Active HIGH Operands & F_n Outputs	
				Logic	Arithmetic (Note 2)	Logic	Arithmetic (Note 2)
S3	S2	S1	S0	(M = H)	(M = L) (C_n = L)	(M = H)	(M = L) (C_n = H)
L	L	L	L	$\overline{A}$	A minus 1	$\overline{A}$	A
L	L	L	H	$\overline{AB}$	AB minus 1	$\overline{A}+\overline{B}$	A + B
L	L	H	L	$\overline{A}+\overline{B}$	$A\overline{B}$ minus 1	$\overline{A}$ B	$A+\overline{B}$
L	L	H	H	Logic 1	minus 1	Logic 0	minus 1
L	H	L	L	$\overline{A}+\overline{B}$	A plus $(A+\overline{B})$	$\overline{AB}$	A plus $A\overline{B}$
L	H	L	H	$\overline{B}$	AB plus $(A+\overline{B})$	$\overline{B}$	$(A+B)$ plus $A\overline{B}$
L	H	H	L	$\overline{A}\oplus\overline{B}$	A minus B minus 1	$A\oplus B$	A minus B minus 1
L	H	H	H	$A+\overline{B}$	$A+\overline{B}$	$A\overline{B}$	AB minus 1
H	L	L	L	$\overline{A}$ B	A plus (A + B)	$\overline{A}+B$	A plus AB
H	L	L	H	$A\oplus B$	A plus B	$\overline{A}\oplus\overline{B}$	A plus B
H	L	H	L	B	$A\overline{B}$ plus (A + B)	B	$(A+\overline{B})$ plus AB
H	L	H	H	A + B	A + B	AB	AB minus 1
H	H	L	L	Logic 0	A plus A (Note 1)	Logic 1	A plus A (Note 1)
H	H	L	H	$A\overline{B}$	AB plus A	$A+\overline{B}$	$(A+B)$ plus A
H	H	H	L	AB	$A\overline{B}$ minus A	A + B	$(A+\overline{B})$ plus A
H	H	H	H	A	A	A	A minus 1

Based on the datasheet of ALU, four functions of ALU are chosen for this project. The four functions are list in table 4.

Table 4: Function table of ALU

Input						Output
S_3	S_2	S_1	S_0	M	C_n	
H	H	H	H	H	x	A
H	L	H	L	H	x	B
H	L	L	H	L	H	A plus B
H	H	H	H	L	H	A minus 1

*H = High, L = Low, x = Don't Care

4.3 Sequence of Instructions

Table 3: Table of sequence of each instruction

Instruction	Clock		
	T0	T1 & T2	
Jump	**Fetch** • PC OE • Memory OE	**Decode** • IR IE • IR OE **Execute** • DEMUX 1 EN • DEMUX 2 EN • Control logic 1 EN • MUX 2 EN • MUX 1 EN • PC IE	
Move (Register to Register)	**Fetch** • PC OE • Memory OE	**Decode** • IR IE • IR OE **Execute** • Acc OE • Register IE • Control logic 2 EN • ALU command	**Decode** • IR IE • IR OE **Execute** • Register OE • Register IE • Control logic 4 EN • ALU command
Move (Memory to Register)	**Fetch** • PC OE • Memory OE	**Decode** • IR IE • IR OE **Execute** • Acc IE • Control logic 2 EN	

Move (Register to Memory)	**Fetch** • PC OE • Memory OE	**Decode** • IR IE • IR OE **Execute** • Register OE • Memory WE • Control logic 3 EN
Logic or Arithmetic	**Fetch** • PC OE • Memory OE	**Decode** • IR IE • IR OE **Execute** • Acc OE • Register OE • Control logic 5 EN • ALU command

*EN = Enable, IE = Input Enable, OE = Output Enable, WE = Write Enable

5. Conclusion & Future work

As earlier mentioned in section 2 the performance of RISC is much faster than CISC processor. Based on the performance equation, each instruction of RISC is one clock cycle therefore in order to increase the performance of RISC processor, the length of program should reduced as much as possible. Besides that, if the system without using the pipeline technique, the clock cycle for each instruction is impossible equal to one therefore pipeline is a key technique to increase the performance of processor. Although the performance is faster but most of the software available in market is only suitable for CISC processor which mean the RISC processor only can perform the task based on the instruction set which designed by the instruction designer. However, as long as the instruction set is powerul enough, the RISC processor still can perform a lot of tasks.

5.1 Future work

The progress of this project is just until the first stage of designing. There are few tasks need to done for this project which is earlier mentioned the missing part of the computer architecture. Memory of instruction will be put in to complete the computer architecture. After that, the design of instruction set will be testing with the computer architecture. Besides that, when the Boolean expression of control logic is found, the control logic will be implement into the computer and do testing. Once the circuitry is working, the final product is done and the objective of this project which is develop the minimal instruction set for practical CPU will be achieve.

References

[1] R.J.Baron & H.Lee, *Computer Architecture*. USA: Addison-Wesley Publishing Company, 1994.

[2] N.Sharma, *Computer Architecture*. New Delhi, India: Pinnacle Technology, 2009.

[3] J.L.Hennessy, D.A.Patterson & A.C.A.Dusseau, *Computer Architecture: A Quantitative Approach*, 4th ed. Amsterdam, Boston: Morgan Kaufmann, 2007.

[4] G.Blanchet & B.Dupouy, *Computer Architecture*. London: Iste, 2013.

[5] J.L.Hennessy, D.A.Patterson, *Computer Architecture: A Quantitative Approach*, 5th ed. Amsterdam, Boston: Morgan Kaufmann, 2012.

[6] B.Gerard, D.Bertrand, *Computer Architecture*, In Computer Engineering Series. London: Iste, 2013

[7] E.Blem, J.Menon, T.Vijayaraghavan and K.Sankaralingam, "ACM Transactions on Computer Systems", "*Understanding the Relevance of ISA being RISC or CISC to Performace, Power, and Energy on Modern Architectures*", Vol. 33, No. 1, Article 3, March 2015.

[8] Sanford C. Bernstein & Co. LLC, "Bernstein Research", "RISC- Maintain Advantage Over CISC, Improvements Slow, Shakeout Anticipated", pg 33

[9] Sanford C. Bernstein & Co. LLC, "Bernstein Research", *"RISC Versus CISC"*, pp 27

[10] R. Kumar, M. Kaur, "International Journal of Advanced Research in Computer Engineering & Technology", *"Design & Implementation of 64 bit ALU for Instruction Set Architecture & Comparison Between Speed/Power Consumption on FPGA",* Vol. 1, Issue 4, June 2012.

[11] V. Bistriceanu, *Instruction Set Design.* Illinois Institute of Technology, Unknown year.

[12] Art of Assembly, *"Chapter Five Instruction Set Architecture"* [Online]. Available: http://www.plantation-productions.com[Accessed 4 May 1025]

Preparation and Characterization of Cu-, Fe-, Ag-, Zn- and Ni- Doped Gelatin Nanofibers for Possible Applications in Antibacterial Nanomedicine

Tamrin Nuge[1], Tshai Kim Yeow[1*], Lim Siew Shee[1], Norshariza Nordin[2], Md Enamul Hoque[1]

[1]*Department of Mechanical, Materials and Manufacturing Engineering, University of Nottingham Malaysia Campus, Jalan Broga, 43500 Semenyih Selangor, Malaysia.*

[2]*Faculty of Medicine and Health Science, University Putra Malaysia, Lorong Asam Jawa 1, 43400 Serdang Selangor, Malaysia.*

[*]Kim-Yeow.Tshai@nottingham.edu.my

Abstract

A facile and efficient approach to prepare metal nanoparticles doped electrospun (espun) gelatin from metal salts precursors was successfully developed. The incorporation of metal ions with antimicrobial activity into electrospun gelatin is an attractive approach to control the inflammatory reaction and prevent infection in wound. In this study, metal salts precursors $AgNO_3$, $Fe(NO_3)_3.9H_2O$, $Cu(NO_3)_2.3H_2O$, $Zn(NO_3)_2.6H_2O$ and $Ni(NO_3)_2.6H_2O$ were reduced to metal nanoparticles with acetic acid as a solvent and reducing agent. The agglomeration of nanoparticles was inhibited by the gelatin polymer matrix. Electrospinning of both neat electrospun gelatin and metal-nanoparticles/Ge-espun resulted in the formation of smooth fibers with average diameters of ~280 nm and ~ 40 nm - 150 nm, respectively. The efficacy of metal nanoparticles/Ge-espun against bacteria commonly found on the wounds: *Escherichia coli* (Gram negative: ATCC 25922), *Pseudomonas aeruginosa* (Gram negative: ATCC 27853); and *Staphylococcus aureus* (Gram Positive: ATCC 25023) were tested with different metal loading by measuring the inhibition of colony forming units. The results indicated a broad spectrum of antibacterial activity showed by Ag/Ge-espun, followed by Fe/Ge-espun and Zn/Ge-espun. An interesting finding on the efficacy of Cu/Ge-espun and Fe/Ge-espun against the Gram's positive bacteria is worth exploring to further investigate the potential application of metal-based antibiotics against the antibiotic-resistant bacterial strains.

Keywords: Electrospinning, Antibacterial Activity, Metal-nanoparticles, Electrospun.

1. Introduction

In recent years, electrospinning has gained much attention as a useful method to prepare fibers in nanometer diameter range. The unique combination of high specific surface area, extremely small pore size, flexibility and superior mechanical performance makes electrospun nanofiber a preferred material for many applications especially in biomedical fields such as enzymes immobilization, tissue engineered scaffolds and drugs deliveries [1]. In an electrospinning process, a polymer solution held by its surface tension and a high voltage is applied to the liquid solution at the end of a capillary tube. Charge is induced on the liquid surface by an electric field. Mutual charge repulsion causes a force directly opposite to the surface tension. As the intensity of the electric field is increased, the hemispherical surface of the solution at the tip of the capillary tube elongates to form conical shape known as the Taylor cone [2]. When the electrical field reaches a critical value at which the repulsive electric force overcomes the surface tension force, a charge jet of the solution is ejected from the tip of the cone [3]. Since this jet is charged, its trajectory can be controlled by an electric field. As the jet travels in the air, the solvent evaporates, leaving behind a charged polymer fiber which lays itself randomly on a collecting metal plate. Thus, continuous fibers are laid to form nonwoven fabric.

Overall, this is a relatively robust and simple technique to produce nanofibers from a wide variety of polymers including gelatin. Gelatin is a natural biopolymer derived either by partial acid (gelatin type A) or alkaline hydrolysis (gelatin type B) of animal collagen from skins, bones and tendons [4]. The differences in collagen sources and preparation techniques make gelatin present a structure with variable physical properties and chemical heterogeneity [5]. Due to its natural abundance and inherent biodegradability in physiological environments, gelatin is widely used in food, cosmetic, pharmaceuticals and medical applications [6]. Gelatin can be processed into hydrogels, three dimensional (3D) microporous scaffolds and electrospun into non-woven nanofibrous matrices due to its inherent properties such as triple helix conformational structure [6]. The electrospun gelatin nanofibers are ideal materials to be used as scaffolds for cell and tissue culture, carriers for tropical /transdermal delivery of drugs and wound dressing. Owing to its remarkable properties, such as high surface area to volume ratio, high porosity of the electrospun

matrices and flexibility for surface functionalization (via pendant free amine groups), the electrospun gelatin matrices are of interest here [7].

The high water absorption capacity and ability to activate macrophages and homeostasis in bleeding wounds are highly desired properties for wound dressing [8]. More recent strategies on controlling the inflammatory reaction and preventing infection in wounds are achieved via the incorporation of metal-based antibiotics into nanofibrous matrix [9]. Wound infection delays wound closure, diminishes tensile strength of the healing wound tissue, increases the length of hospital stay and cost, and increases the patient's risk of bacteremia, sepsis, multisystem organ failure and death [10]. With the increased prevalence and the emergence of antibiotic-resistant bacterial strains, there is mounting need to reduce and eliminate wound infection using methodologies that limit the ability of bacteria to evolve into further antibiotic resistant strains.

Klinkajon and Supaphol [11] investigated the use of copper (II) ions in hydrogel alginate dressing. The results showed that the copper (II) ions exhibited bacterial disinfection and displayed potentiating effect on prothrombotic coagulation and platelet activation. Additional work by Chaturvedi and coworkers demonstrated that the copper ions were successfully impregnated onto PVA-based cryogels nanocomposites and exhibited high antibacterial activity against Gram-positive and Gram negative bacteria. The nanocomposites also offered fair blood compatibility and good mechanical strength [12]. A study by Lin et al. [13] aimed to investigate the efficacy of silver containing dressings on controlling wound infection and wound healing. Silver ions and silver based compounds are known to have broad antibacterial spectrum (highly toxic to 16 major species of bacteria) [14] and are relatively safe, which makes silver an excellent choice for clinical care and consumer products. The impregnation of silver ions onto scaffolds could enhance reduction in the levels of pro-inflammatory cytokines [15] and inhibit the activities of interferon gamma and tumor necrosis factor alpha which are involved in inflammation [16]. Recent investigations have been extended to study other metal nanoparticles such as Zn, Ni and Fe that could have antibacterial activity and are economically cheaper than Ag and Au.

This works describes the preparation and characterization of electrospun gelatin chelates with metal ions (Cu^{2+}, Zn^{2+}, Ag^{+}, Ni^{2+} and Fe^{3+}) by electrospinning technique to explore the role of metal-based antibiotics as potential antibacterial agents. In the present study, the chelation of metal ions in the gelatin solution was extensively investigated, with the aim of understanding the effects of aging time on chelation. The nanofibers features produced during the electrospinning were studied and the efficacy of the doping process onto the nanofibers was characterized systematically. In order to evaluate the antibacterial activity, the electrospun nanofibers doped with metal ions were subjected to antibacterial screening against three bacterial strains that are commonly found on burn wounds, of which two were gram negative (*Escherichia coli* and *Pseudomonas aeruginosa*) and one Gram positive *Staphylococcus aureus*.

2. Experimental Details

2.1 Materials

Gelatin powder and silver nitrate ($AgNO_3$) were purchased from Merck (Germany). Iron nitrate ($Fe(NO_3)_3.9H_2O$), copper nitrate ($Cu(NO_3)_2.3H_2O$) and nickel nitrate ($Ni(NO_3)_2.6H_2O$ were purchased from Systerm®. Zinc nitrate ($Zn(NO_3)_2.6H_2O$) was purchased from R&M chemicals (UK). The solvent used was analytical grade glacial acetic acid obtained from Fisher Chemical (UK) and deionized distilled water (ddH_2O) which was filtered by Milli-Q integral water purification using 0.22 µm Millipak membrane filter. All chemicals were of analytical grade and used without further purification.

2.2 Preparation and characterization of gelatin solutions containing metal ions

The metal ions chemical reagents were first dissolved in a quantity of 10 % (w/v) in 90:10 glacial acetic acid/distilled water, respectively. 1 % (v/v) of the metal ion mixtures were then transfer into the 18 % (w/v) gelatin solution of acetic acid/ddH_2O at the ratio of 90:10. The mixture was then stirred to homogenize and allow the chelation of metal ions into the gelatin/acetic acid/water solution. In this system, gelatin was used as a stabilizer and dispensing agent for the metal ions. The gelatin solution containing metals ion were stirred for a varied period in order to investigate the effect of aging time on the formation of metal ions. The diffusion of

metal ions into the gelatin/acetic acid/water solution was confirmed by monitoring the surface plasmon absorption band using UV-Vis Lambda 35 spectrophotometer (Perkin Elmer, USA).

2.3 Preparation of neat and doped electrospun gelatin matrices

The neat gelatin solution and the metals ion-containing gelatin solution that had been aged for 12 hours were fabricated into nanofibers matrices by electrospinning. The experimental set-up used for electrospinning process (Fig.1) consisted of a syringe and a needle, a ground electrode (aluminum collector plate of 20 cm × 20 cm wrapped with aluminum sheet) with a distance of 10 cm from the needle and a high voltage adjustable DC power supply (Gamma High Voltage Research, USA). A positive voltage (15 kV) was applied to the gelatin solutions. The solutions were delivered via syringe pump to control the mass flow rate. The feed rate was maintained at 0.42 ml/h throughout the study. As the electrical potential was applied, a jet was created. The resulting nanofibrous matrices were collected on an aluminum plate after 18 hours of electrospinning process. After the process, all the matrices collected with the aluminum foils on the collector were kept at room temperature for 24 hours before being place in a vacuum drying oven for a couple of days for drying treatment. After the aluminum foil was carefully peeled off, the specimens' thickness were measured using a digital micrometer, having a precision of 1 µm. The thickness of the neat and the metals-ion containing gelatin matrices were between 320 µm to 340 µm.

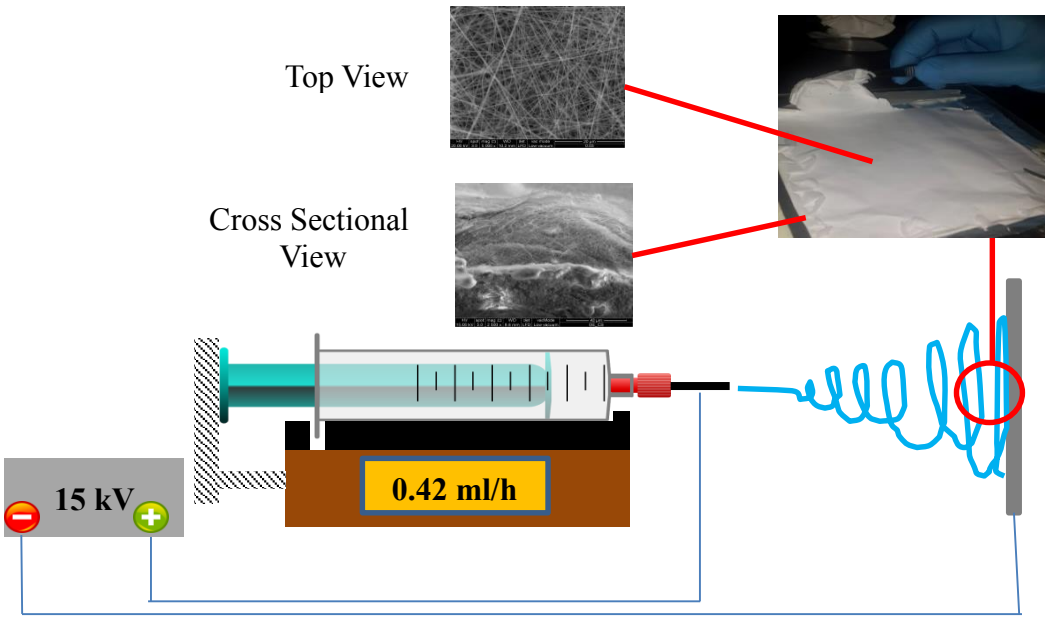


Figure 1. Schematic of electrospinning system

2.4 Characterization

The nanofibers morphology was observed under scanning electron microscopy (SEM) using a FEI Quanta 400 F (USA) with acceleration voltage of 20 kV. Before SEM observation, a small section of the nanofiber mat was cut at three different positions and placed on the SEM sample holder. The diameter of at least 100 different positions on the nanofiber mat was analyzed using image visualization software ImageJ developed by Upper Austria University of Applied Sciences and available for free at http://imagej.nih.gov/ij/download.html.

2.5 Antibacterial Evaluation

The antibacterial activity of the electrospun gelatin with both the neat and loaded metal nanoparticles were tested against bacteria commonly found on wounds: *Escherichia coli* (Gram negative: ATCC 25922), *Pseudomonas aeruginosa* (Gram negative: ATCC 27853); and *Staphylococcus aureus* (Gram Positive: ATCC 25023). The assessment was conducted based on the discs diffusion method of the US Clinical and Laboratory Standard Institute (CLSI). Both the neat and metal loaded gelatin matrices were cut into circular disks (7 mm in diameter). The bacteria were cultured on Luria Bertani agar (Merck, Germany) in a plastic petri dish. The nanofibrous disks were placed in the middle of culture and then incubated at 37 ℃ for 24 hours. If inhibitory concentration was reached, there would be no bacteria growth and could be observed as a clear zone around the disc specimens. These were photographed for further evaluation.

3. Results and Discussion

3.1 Formation of metal nanoparticles in gelatin solutions and effect of aging time

The liquid phase chemical reduction technique discovered by Faraday more than 150 years ago has been widely used for the production of metal nanoparticles. The chemical reduction method is based on mixing of a reducing agent with a metal salt precursor in the presence of stabilizing agents (ligands, polymers and surfactant). The stabilizing agent is confined to prevent the undesirable particle agglomeration and the formation of stable nanoparticles depends on the properties of stabilizing

agent [17]. In this study, the metal salts were reduced to metal nanoparticles with acetic acid as a solvent and reducing agent. The gelatin polymer matrix was used as stabilizer to prevent further growth and particle agglomeration of metals. The metal ions were reduced directly into metal nanoparticles through a series of steps including nuclei formation, crystal growth via diffusion mechanism to give primary particles and spontaneous self-organization of primary particles to form clusters. The formation of metal nanoparticle nuclei was postulated to originate from ionic interactions between metal ions and amino, carboxyl and hydroxyl groups on gelatin. The metal nanoparticles – gelatin matrix clusters can be expressed according to Eq. (1);

$$x\mathrm{M}^{\mathrm{n}+} + \mathrm{n}xe^{-} + \mathrm{Gelatin} \rightarrow \mathrm{M}_n^0\,(\mathrm{Cluster}) \qquad (1)$$

The reduction of metal ions into metal nanoparticles in metal salts-containing gelatin solutions at different aging time could be visualized from the solution color intensity, from light color of the neat solution to dark color after the completion of aging. The UV/visible absorption spectra of metal salt- containing gelatin solution that had been aged for various time of intervals after preparation are displayed in Fig. 2. The surface plasmon absorption bands for $Cu(NO_3)_2$ –containing gelatin solutions exhibit two peaks in the range of 370 nm to 390 nm and 690 nm to 710 nm (Fig. 2A). Upadhyaya et al. [18] observed the same pattern described that the spectral shift was due to the complexation between Cu^{2+} ions and stabilizing agents (polyaniline) and depended on the concentration of Cu^{2+} ions. Evidently, an increase in the aging time resulted in the observed color change in solution from blue to yellowish green and finally to dark green. It can be assumed that the cupric ions were bound to gelatin chains. Similar redox behavior was observed with Fe^{3+}, Ni^{2+} and Zn^{2+} ions in this study.

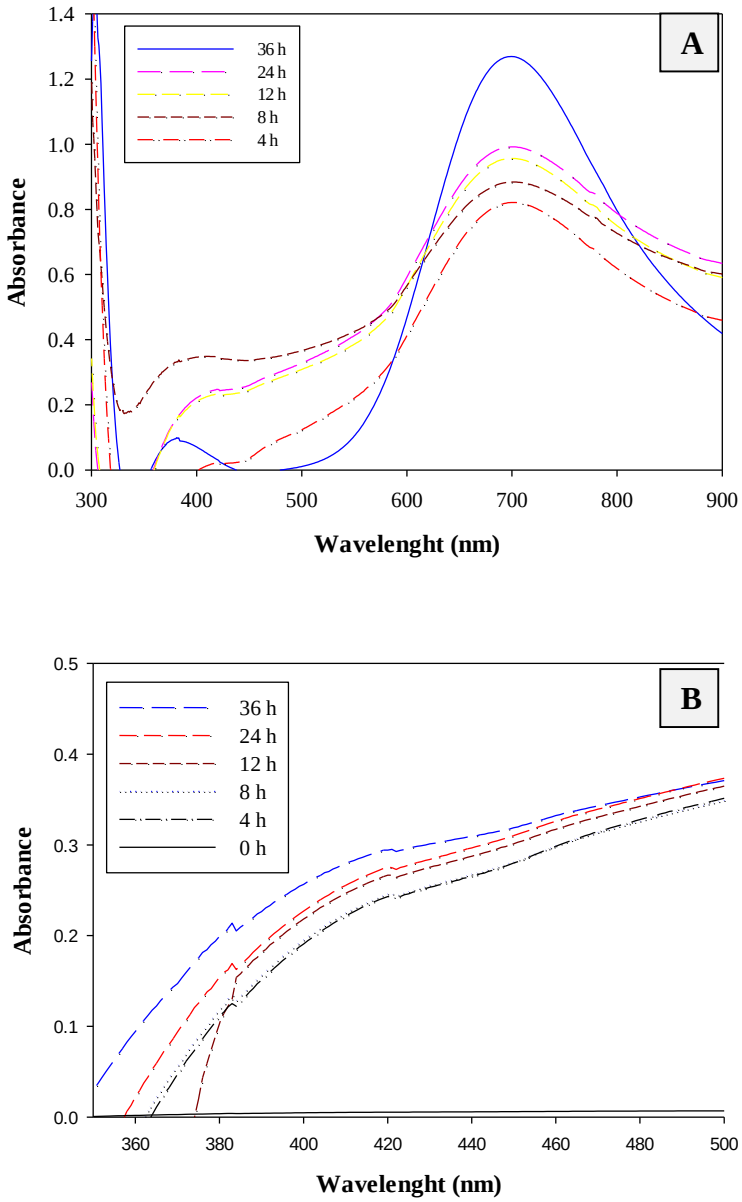


Figure 2. Surface plasmon absorption band of aged (A) $Cu(NO_3)_2$ and (B) $AgNO_3$ containing gelatin solution using UV-Vis spectrophotometer at different time intervals. The concentration of gelatin solution was 18% (w/v) and the metal salt precursor was 1 % (w/w) based on the weight of gelatin.

The reduction of Ag^+ to Ag^0 (silver nanoparticles) by acetic acids and the formation of silver nanoparticles-gelatin matrix follows the following schemes (Eq. (2) and Eq. (3)) [19]:

$$H_2N - COOH + AgNO_3 \leftrightarrow H_2N - COOAg + HNO_3 \quad (2)$$

$$H_2N - COOH + AgNO_3 \leftrightarrow AgHN - COOH + HNO_3 \quad (3)$$

Silver nanoparticles have a surface plasmon resonance absorption in the UV-visible region and the band arises from the coherent existence of free electrons in the conduction band due to small particle size [20]. The band shift is dependent on the particle size, chemical surrounding, adsorbed species on the surface and dielectric constant [19]. Fig. 2B shows the UV-Vis spectra gradually increased over time and the peak position was slightly shifted to a longer wavelength. This indicates that the number of Ag^+ ions that converted into silver nanoparticles increased with an increase of reaction time. The absorption peaks were observed at 382 nm and 420 nm, which correspond to two particle population of silver nanoparticles.

3.3 Morphology of metal nanoparticles /gelatin- electrospun nanofibers

While electrospinning has proven to be a versatile and powerful means of fabricating nanofibers, the applicability to obtain smooth, uniform fibrous structure is not straightforward. The morphology and diameter of electrospun fibers are dependent on a number of parameters including properties and composition of the polymer solution such as viscosity, concentration, conductivity and surface tension [21]. The optimum parameters for fabricating smooth and uniform neat electrospun gelatin nanofibers were discussed in our previous work [22].

Fig.3 shows the selected SEM images of the samples generated using electrospinning from gelatin solution and gelatin solutions containing different metal salts as a precursor. The conductivities of the metal nanoparticles-gelatin solutions linearly increased, while the viscosities and surface tensions did not change with increase content of metal salts. Since the metal salts increased the charge density in gelatin solutions, stronger stretch forces were imposed on the ejected jets under the

electrical field, resulting in substantial formation of finer ultrafine fibers [23]. The average diameter of neat electrospun gelatin and electrospun loaded with metal nanoparticles are shown in Fig. 3. Smooth and uniform nanofibers with average diameter of 280.60 ± 35.92 nm were observed on the neat electrospun gelatin (Fig. 3A). The fiber diameters tended to decrease, when the nanometals loaded onto the fibers. The average diameters of Ag/Ge-espun and Cu/Ge-espun were 147.33 ± 96.43 nm and 41.43 ± 8.05 nm, respectively (Fig. 3B and 3C). The average diameters of Fe/Ge-espun, Ni/Ge-espun and Zn/Ge-espun were ranging from 45.21 ± 12.43 nm to 102.05 ± 26.12 nm (data not shown). Wide variation of nanofiber size was observed on the Ag/Ge-spun. The diameter of Ag/Ge-spun obtained was much smaller compared to the study reported by Rujitanaroj et al. [24] with the diameter ranging from 280 ± 40 nm.

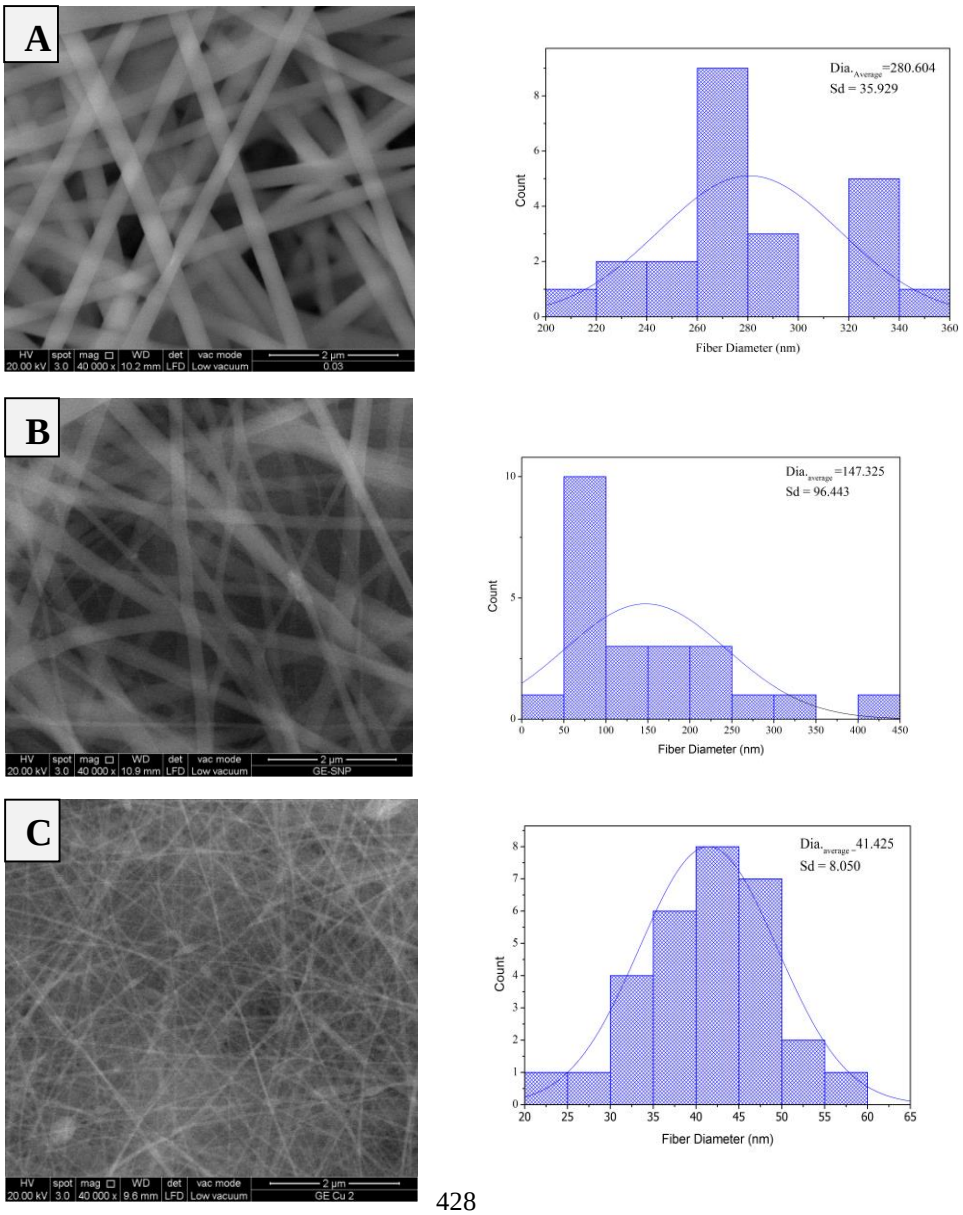


Figure 3. Selected SEM micrograph of the electrospun gelatin nanofibers and diameter distribution of (A) neat electrospun gelatin (B) Ag/Ge-espun (C) Cu/Ge-espun.

The presence of metal nanoparticles in the nanofibers was further assessed with energy-dispersive X-ray (EDX) spectroscopy analysis. The assessment proved the presence of metal nanoparticles in electrospun. The quantitative analysis of the presence of metal nanoparticles in electrospun gelatin is highlighted in the Table 1. The EDX pattern of elements detected in nanofibers is available as **supplementary data**.

Table 1. Quantitative EDX analysis of the presence of nanometals in the electrospun gelatin nanofibrous matrix.

Metal nanoparticles/Ge -espun	**Elements (w/w)%**				
	Ag	**Cu**	**Fe**	**Ni**	**Zn**
Neat-espun	-	-	-	-	-
Ag/Ge-espun	0.41	-	-	-	-
Cu/Ge-espun	-	0.44	-	-	-
Fe/Ge-espun	-	-	0.42	-	-
Ni/Ge-espun	-	-	-	0.45	-
Zn/Ge-espun	-	-	-	-	0.41

3.4 Antimicrobial activity

The antibacterial activity is a demonstration of release of metal ions from nanofiber matrix. Metal nanoparticles exhibit relatively large surface area, thus increasing their contact with bacteria. Fig. 4 shows the results of antibacterial efficacy of gelatin electrospun loaded with metal nanoparticles against some common bacteria found on wounds*: Escherichia coli* ATCC 25922, *Pseudomonas aeruginosa* ATCC 27853, and *Staphylococcus aureus* ATCC 25023. The antibacterial activity is based on the disc diffusion method and expressed as a ratio of clear inhibition of microorganisms in contact with all metal nanoparticles loaded on the nanofibers and

the neat electrospun gelatin. It should be noted that the initial diameter of all the specimens was fixed at 0.7 cm. The relative zone of inhibition was calculated from Eq. (4).

$$\text{Relative Zone of Inhibition} = \frac{\text{B}-\text{A}}{\text{A}} \times 100 \quad (4)$$

where A and B are the diameter of the clear inhibitory zone of the neat electrospun and the clear inhibitory zone of electrospun loaded with metal nanoparticles, respectively.

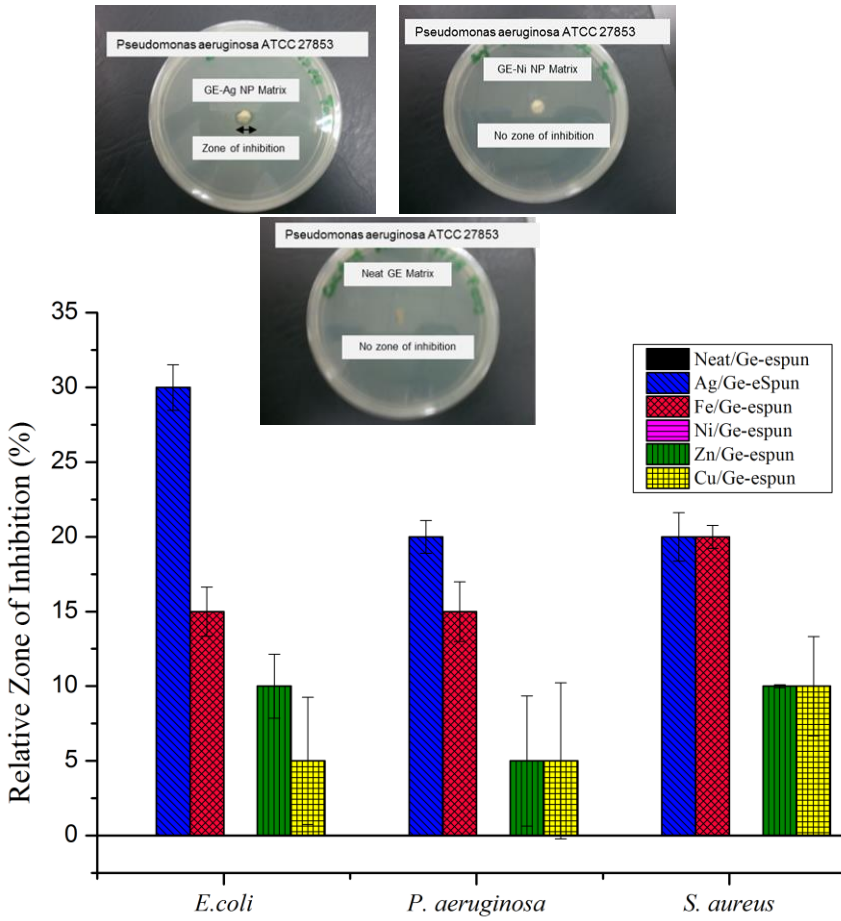


Figure 4. Bar diagram showing the antibacterial effect of the different metal loaded electrospun gelatin on commonly found bacteria on wounds. *Notes*: E.coli – Escherichia coli ATCC 25922; P. aeruginosa – Pseudomonas aeruginosa ATCC 27853; S. aureus – Staphylococcus aureus ATCC 25023

According to the data obtained, no antibacterial activity was detected for the neat Ge-espun nanofibers and Ni/Ge-espun against the bacteria tested. The poor inhibition by the Ni/Ge-espun was contradicted with the study reported by Popova et al. They found that the nickel ion complexes with ligands manifested good antibacterial activity against the tested bacteria, especially towards the Gram's positive strains [25]. In the recent years, focus on the bimetallic complexes of Ni with other metal nanoparticles has gained more attention in the area of dental materials. Argueta-Figueroa reported that the Ni-Cu complexes showed broad antibacterial spectrum and potentially being employed in dentistry for formulation of bone cements, irrigating the root canal and devices coating [26].

Evident bacteria inhibition zones were observed on the Ag/Ge-espun, Fe/Ge-espun, Zn/Ge-espun and Cu/Ge-espun. Metal nanoparticles except nickel exhibited broad spectrum antimicrobial activity. The bacterial inhibition zone on Ag/Ge-espun nanofiber was the greatest but its antibacterial efficacy reduced towards the *S. aureus* (gram positive bacteria). This can be explained by the difference in structure of the envelope of Gram-positive and Gram-negative bacteria. Gram positive bacteria have a thick peptidoglycan layer below the cell membrane that protects bacteria from external stresses and is believed to reduce the penetration of silver nanoparticle [27]. In contrast, the Fe/Ge-espun and Cu/Ge-espun displayed greater inhibition on Gram positive bacteria than Gram negative bacteria. The same pattern was also reported by Klinkajon and Supaphol [11] on the ability of the cooper alginate hydrogel to inhibit Gram positive bacteria. This can be explained due to the greater abundance of amines and carboxyl groups on cell surface of Gram positive bacteria and greater affinity of cooper towards these groups [28]. The cooper ions are targeting the antisense that involves in gene coding and lead to DNA molecules disruption [29]. In the case of Fe/Ge-espun, the bacterial inhibition was driven by iron chelation by the chelator. Based on this concept, the higher the iron binding constant to the chelator (Ge-espun), the stronger the predicted antimicrobial activity [30]. The composition of the microorganism's cell wall and the physical nature of the iron chelator also affect the inhibition of the bacterial growth [31]. The exact mechanism behind bactericidal effect of iron nanoparticles is not known and needs to be studied further.

4. Conclusion

In this work, copper, iron, nickel, silver and zinc were successfully impregnated onto electrospun gelatin nanofibers using electrospinning technique from 1% (v/v) solutions of their salts precursor and 18% (w/v) of gelatin solution. The presence of the metal nanoparticles was confirmed using the surface plasmon absorption band and energy-dispersive X-ray (EDX) spectroscopy. The amount of metal nanoparticles increased with the increase of aging time. Both neat and metal nanoparticles/Ge-espun were spun into smooth nanofibers matrices. The average diameter of nanofiber tended to decrease with nanometals loaded fibers. The average diameter of metal nanoparticles ranged from 40 nm to 150 nm. Wide variation of nanofiber diameter was observed on the Ag/Ge-espun. Metal nanoparticles doped gelatin nanofibers manifested good antibacterial effects except Ni/Ge-espun. The nanocomposite of Ag/Ge-espun showed greater inhibition against the Gram's negative bacteria but exhibited lower efficacy on the Gram's positive bacteria. In contrast, the Cu/Ge-espun and Fe/Ge-espun displayed high efficacy on the Gram's positive bacteria. Bimetallic complexes of Ag-Cu doped electrospun gelatin could be explored in the future for potential metal-based antibiotics that could prevent the emergence of antibiotic-resistant bacterial strains.

Acknowledgement

The authors would like to thank the researcher in the Faculty of Engineering and the Faculty of Science, University of Nottingham Malaysia Campus for the facilities and the helpful discussion. This study was supported by a research grant (NER40002) from the Ministry of Higher Education (MOHE) and partially supported by the Faculty of Engineering, University of Nottingham Malaysia Campus.

References

[1] Ziabari, M., Mottaghitalab, V., Haghi, A. ., and McGovern, S. T., 2009, "Control of Electospun Nanofiber Diameter Using Distance Transform Method: A Novel Approach," Electrospun Nanofibers and nanotubes Research Advances, A.. Haghi, ed., Nova Science Publishers, Inc, New York, pp. 69–94.

[2] Teo, W. E., and Ramakrishna, S., 2006, "A review on electrospinning design and nanofibre assemblies.," Nanotechnology, **17**(14), pp. R89–R106.

[3] Fong, H., Chun, I., and Reneker, D. ., 1999, "Beaded nanofibers formed during electrospinning," Polymer (Guildf)., **40**(16), pp. 4585–4592.

[4] Schrieber, R., and Gareis, H., 2007, Gelatine Handbook: Theory and Industrial Practice, Wiley-VCH Verlag GmbH & Co. KGaA, Germany.

[5] Schrieber, R., 2007, "From Collagen to Gelatin," Gelatin Handbook, Wiley-VCH Verlag GmbH & Co. KGaA, Germany, pp. 113–114.

[6] Hoque, M., Nuge, T., Yeow, T. K., and Nordin, N., 2013, "Electrospinning of Gelatin Nanofibre: Current Trends in Tissue Engineering Applications," J. Appl. Mech. Eng., **02**(04), p. 9873.

[7] Nuge, T., Hoque, M., Yeow, T., Nordin, N., and Chowdhury, M., 2013, "Electrospun Gelatin Composite Nanofibres : A Review On Structural and Mechanical Characterizations," Regen. Res., **2**(2), pp. 39–42.

[8] Gao, Y., Bach Truong, Y., Zhu, Y., and Louis Kyratzis, I., 2014, "Electrospun antibacterial nanofibers: Production, activity, and in vivo applications," J. Appl. Polym. Sci., **131**(18), p. 40797.

[9] Yang, H., Gao, P. F., Wu, W. B., Yang, X. X., Zeng, Q. L., Li, C., and Huang, C. Z., 2014, "Antibacterials loaded electrospun composite nanofibers: release profile and sustained antibacterial efficacy," Polym. Chem., **5**(6), p. 1965.

[10] Mohiti-Asli, M., Pourdeyhimi, B., and Loboa, E. G., 2014, "Skin tissue engineering for the infected wound site: biodegradable PLA nanofibers and a novel approach for silver ion release evaluated in a 3D coculture system of keratinocytes and staphylococcus aureus.," Tissue Eng. Part C. Methods, **20**(10), pp. 790–7.

[11] Klinkajon, W., and Supaphol, P., 2014, "Novel copper (II) alginate hydrogels and their potential for use as anti-bacterial wound dressings.," Biomed. Mater., **9**(4), p. 45008.

[12] Chaturvedi, A., Bajpai, A. K., Bajpai, J., and Sharma, A., 2015, "Antimicrobial poly(vinyl alcohol) cryogel–copper nanocomposites for possible applications in biomedical fields," Des. Monomers Polym., **18**(May 2015), pp. 385–400.

[13] Lin, Y. H., Hsu, W. S., Chung, W. Y., Ko, T. H., and Lin, J. H., 2014, "Evaluation of various silver-containing dressing on infected excision wound

healing study," J. Mater. Sci. Mater. Med., **25**, pp. 1375–1386.

[14] Prabhu, S., and Poulose, E. K., 2012, "Silver nanoparticles : mechanism of antimicrobial action , synthesis , medical applications , and toxicity effects," Int. nano Lett., **2**(32), pp. 1–10.

[15] Tian, J., Wong, K. K. Y., Ho, C.-M., Lok, C.-N., Yu, W.-Y., Che, C.-M., Chiu, J.-F., and Tam, P. K. H., 2007, "Topical Delivery of Silver Nanoparticles Promotes Wound Healing," ChemMedChem, **2**(1), pp. 129–136.

[16] Shin, S.-H., Ye, M.-K., Kim, H.-S., and Kang, H.-S., 2007, "The effects of nano-silver on the proliferation and cytokine expression by peripheral blood mononuclear cells.," Int. Immunopharmacol., **7**(13), pp. 1813–1818.

[17] Bonnemann, H., and Richards, R. M., 2001, "Nanoscopic metal particles - synthetic methods and potential applications," Eur. J. Inorg. Chem., (10), pp. 2455–2480.

[18] Upadhyaya, M., Ahmed, N., Deka, R., and Kakati, D. K., 2012, "Studies on Cu +2 ion doped polyaniline," Iran. Polym. J. (English Ed., **21**(9), pp. 601–607.

[19] Sharma, V. K., Yngard, R. A., and Lin, Y., 2009, "Silver nanoparticles: Green synthesis and their antimicrobial activities," Adv. Colloid Interface Sci., **145**(1-2), pp. 83–96.

[20] Jeong, L., and Park, W. H., 2014, "Preparation and characterization of gelatin nanofibers containing silver nanoparticles.," Int. J. Mol. Sci., **15**(4), pp. 6857–79.

[21] Haghi, A. ., and Zaikov, G., 2011, "Polymeric Nanofibre fabrication Via Electrospinning Process," Advances in Nanofibre Research, iSmithers, Shropshire, pp. 11–39.

[22] Hoque, M. E., Nuge, T., Yeow, T. K., Nordin, N., and Prasad, R. G. S. V, 2014, "Gelatin Electrospun Nanofibre Scaffold for Potential Wound Healing Application," 9th International Materials Technology Conference and Exhibition.

[23] Madhumathi, K., Sudheesh Kumar, P. T., Abhilash, S., Sreeja, V., Tamura, H., Manzoor, K., Nair, S. V., and Jayakumar, R., 2010, "Development of novel chitin/nanosilver composite scaffolds for wound dressing applications," J. Mater. Sci. Mater. Med., **21**(2), pp. 807–813.

[24] Rujitanaroj, P. O., Pimpha, N., and Supaphol, P., 2008, "Wound-dressing materials with antibacterial activity from electrospun gelatin fiber mats containing silver nanoparticles," Polymer (Guildf)., **49**(21), pp. 4723–4732.

[25] Popova, T. P., Alexandrova, R. I., Tudose, R., Mosoarca, E. M., and Costisor, O., 2012, "Antimicrobial activity in vitro of four nickel complexes," Bulg. J. Agric. Sci., **18**(3), pp. 446–450.

[26] Argueta-Figueroa, L., Morales-Luckie, R. A., Scougall-Vilchis, R. J., and Olea-Mejía, O. F., 2014, "Synthesis, characterization and antibacterial activity of copper, nickel and bimetallic Cu–Ni nanoparticles for potential use in dental materials," Prog. Nat. Sci. Mater. Int., **24**(4), pp. 321–328.

[27] Quirós, J., Borges, J. P., Boltes, K., Rodea-Palomares, I., and Rosal, R., 2015, "Antimicrobial electrospun silver-, copper- and zinc-doped polyvinylpyrrolidone nanofibers," J. Hazard. Mater., **299**, pp. 298–305.

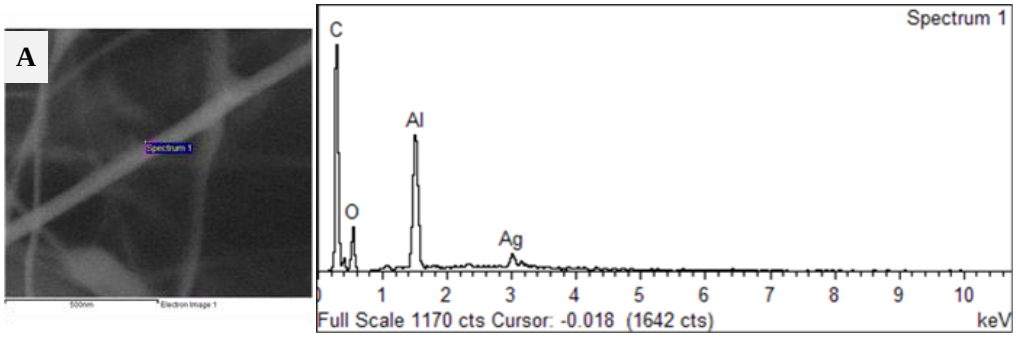
[28] Ruparelia, J. P., Chatterjee, A. K., Duttagupta, S. P., and Mukherji, S., 2008, "Strain specificity in antimicrobial activity of silver and copper nanoparticles," Acta Biomater., **4**(3), pp. 707–716.

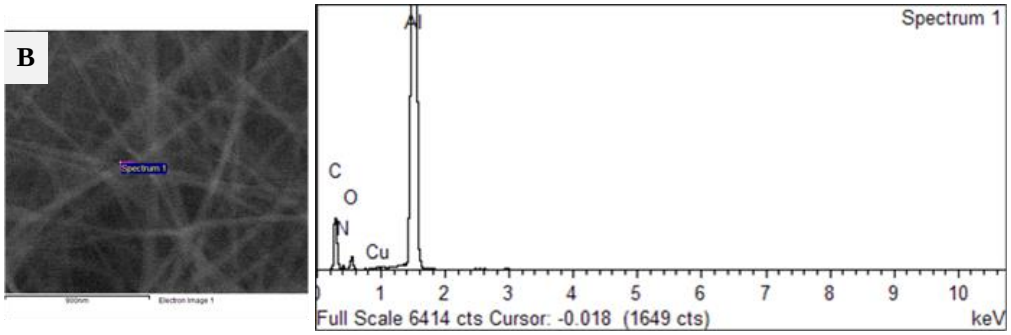
[29] Bai, H., Sang, G., You, Y., Xue, X., Zhou, Y., Hou, Z., Meng, J., and Luo, X., 2012, "Targeting RNA polymerase primary σ 70 as a therapeutic strategy against methicillin-resistant Staphylococcus aureus by antisense peptide nucleic acid," PLoS One, **7**(1), pp. 1–10.

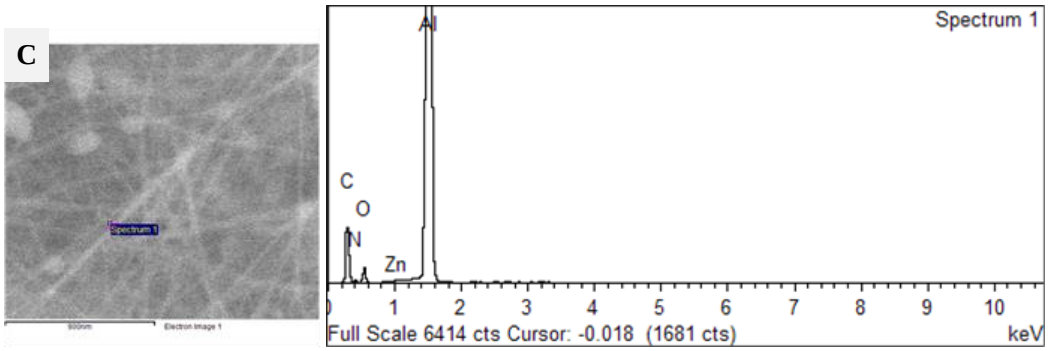
[30] Qiu, D.-H., Huang, Z.-L., Zhou, T., Shen, C., and Hider, R. C., 2011, "In vitro inhibition of bacterial growth by iron chelators.," FEMS Microbiol. Lett., **314**(2), pp. 107–11.

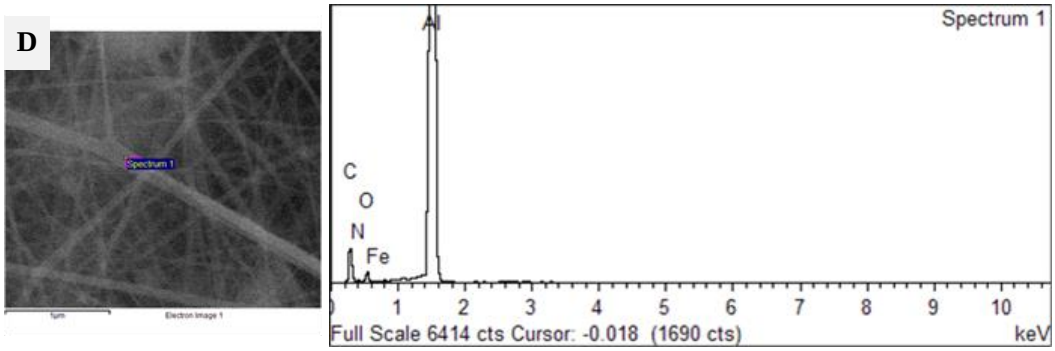
[31] Chew, B. P., Tjoelker, L. W., and Tanaka, T. S., 1985, "In Vitro Growth Inhibition of Mastitis Causing Bacteria by Phenolics and Metal Chelators," J. Dairy Sci., **68**(11), pp. 3037–3046.

SUPPLEMENTARY DATA









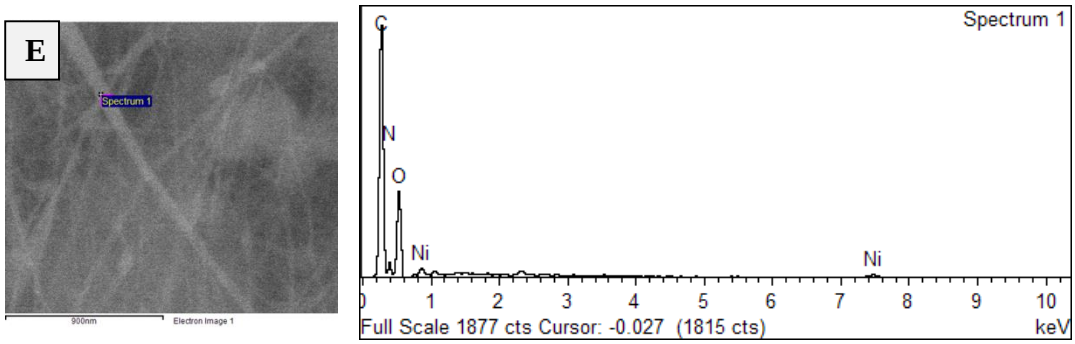


Figure 1. Energy dispersive X-ray analysis of (A) Ag/Ge-espun; (B) Cu/Ge-espun; (C) Zn/Ge-espun; (D) Fe/Ge-espun and (E) Ni/Ge-espun.

Mixing Using Synthetic Jets and Its Application in Enzymatic Reactions

Ferng Lin Ooi[1*], Mushtak Al-Atabi[1], Marwan M. Shamel[1], Yeong Leong Lim[1]

[1]*Taylor's University, Malaysia*

[*]fernglin.ooi@taylors.edu.my

Abstract

Mixing is a curial process in various industry. It is typically achieved through mechanical agitators. While this may be the most versatile means of achieving mixing, it is normally associated with shortcomings such as high power requirements, blind spots, difficulty with cleaning, and high shear rates, which can be detrimental to shear sensitive applications. This research describes the use of synthetic jets for mixing and its application in assisting enzymatic reactions. Synthetic jets are fluid jets that are synthesised from its surrounding fluid and it has zero net mass flux. Its current applications include focused cooling of electronic components such as high-power LEDs and microprocessors, boundary layer control and underwater propulsion. Synthetic jets also possess a characteristic of creating a series of successive vortices that can be used for effectively entraining adjacent fluid, which gives rise to its implications in mixing applications.

To assess the viability of mixing using synthetic jets, flow visualisation and Particle Image Velocimetry (PIV) techniques are used to assess the flow structure within the mixer. Time for complete mixing and power consumption is also measured to assess its performance. The effects of synthetic jet mixing on enzymatic reactions are studied by observing the change in enzyme denaturalisation rate under various displacement, oscillation, frequency and operating temperature. The results show that it is viable to use synthetic jets for mixing with an improvement in power consumption utilising lesser than 5% of the power used by conventional mixers. Moreover, its applications in enzymatic reactions show an improvement in enzymatic reaction rate of up to 10% compared to conventional means and an improvement in denaturalisation rate of up to 9%.

Keywords: synthetic jet, mixing, process engineering, enzymatic reactions, particle image velocimetry, coefficient of variance, flow visualisation.

1. Introduction

In the context of process engineering, mixing is defined as the operation of achieving homogeneity in a heterogeneous physical system through some means of physical manipulation which in the industry, are typically agitators such as impellers and blades. Other means of mixing in the industry include static mixers which uses baffles on vessels or pipes to agitate fluid as it passes and jet mixers that cycles the working fluid allowing mixing to occur. These are illustrated in Figure 1. [1]

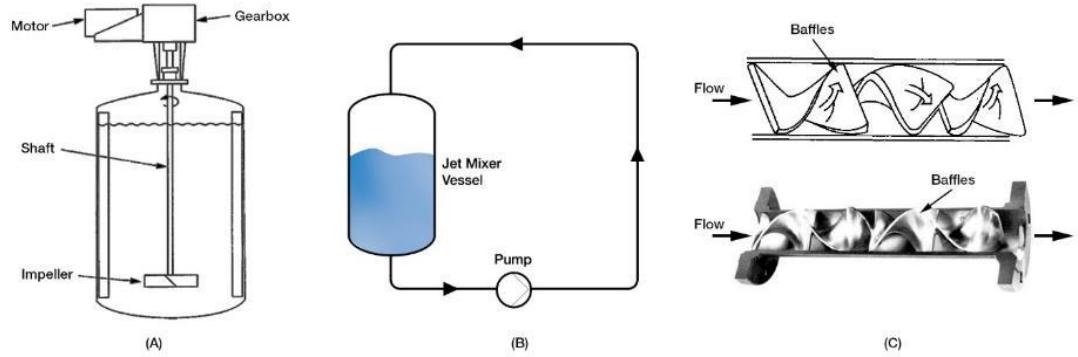


Figure 1: Typical mixers in the industry. (A) Conventional mixer with mechanical agitator (B) Jet Mixer (C) Static Mixer [1]

Mixing of enzyme and microorganisms is applied in pharmaceutical and biological processes. Conventional mixing process is normally involved with high shear stresses which able to deteriorate the protein structure of enzyme. Besides that, it consumes high electrical power. Other than that, when high shear rates are applied enzyme and microorganisms tend to denature and degrade respectively.

Fluid mechanics define jet flows as an efflux of fluid that has been forced through a nozzle or restrictor into an ambient medium and it typically has a mass inflow or fluid influx which is the source for projection. [2] However, a synthetic jet has its flow generated from the ambient fluid instead of a fluid influx. [3][4]

In contrast to conventional mixers that create currents and vortices in the fluid using blades and impellers, synthetic jet mixers induce fluid flows through the synthesised flow from an aperture in the mixer. This induced flow is ejected from the orifice at considerable velocity hence it entrains the surrounding fluid causing vortices to propagate throughout the mixer space allowing mixing to occur. [1][2]

A typical synthetic jet contains an enclosed space called the cavity and an orifice on one side of the enclosed space and a flexible diaphragm on the other side. The diaphragm is displaced in an oscillating manner which will vary the volume in the enclosed space causing fluid to be ejected from the space through the orifice when the volume decreases and pulled in when the volume returns to normal. When this motion is repeated, a jet flow will be created at the orifice. A cross-sectional view of the synthetic jet can be seen in Figure 2. [5]

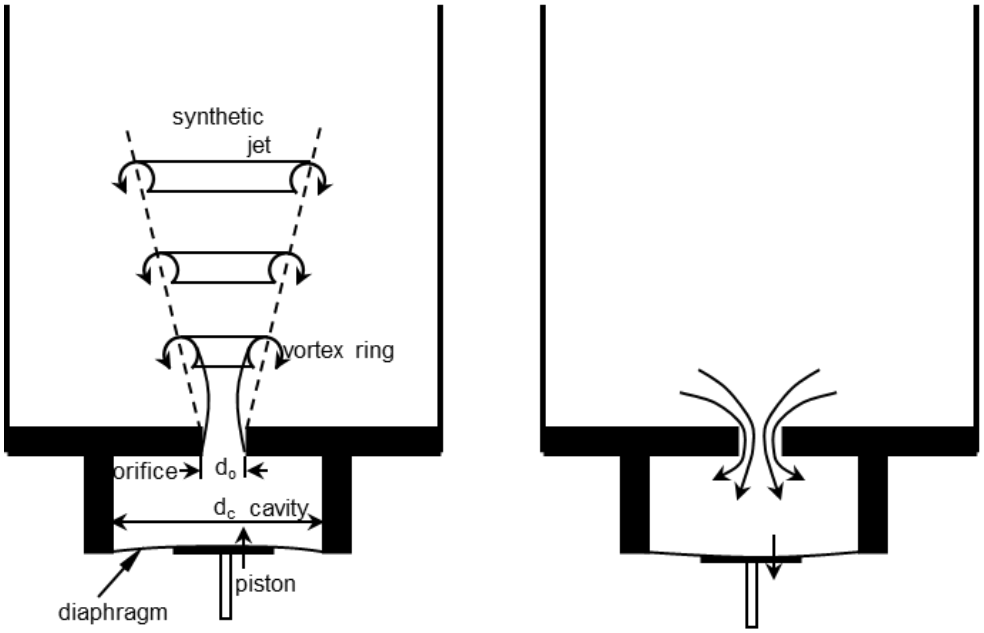


Figure 2: Cross-sectional View of a Synthetic Jet. [5]

In this paper, the performance of a synthetic jet mixer at various actuation frequencies and oscillation amplitudes are studied. In addition to that, the use of synthetic jet actuators in the place of typical rotating blades for enzymatic reaction agitation was also studied and comparison between power consumption, enzyme kinetics and rate of denaturalisation were studied as well.

2. Methodology

A synthetic jet mixer was constructed and its mixing performance was assessed by means of coefficient of variance analysis via flow visualisation and 2D particle image velocimetry. In addition to that, to determine the effectiveness of synthetic jet mixers for enzymatic reactions, a biological hydrolysis reaction with a lipase catalyst was utilised. The rate of butyric acid production was measured in the reaction. Power consumption was also measure and compared to the power consumption of an overhead stirrer.

2.1 Coefficient of Variance Analysis

To gauge the effectiveness of a mixing technique, a typically used method in the industry, is the calculation of the Coefficient of Variance. Which statistically represents the degree variance among a number of samples from the mean of those samples. This can be used to calculate degree of homogeneity of a mixture by dividing the mixture into a series of zones and adding a tracer into the system. In essence, the lower the CoV value, the more homogeneous the mixture is. The ideal CoV for industrial mixing applications is 0.2 where a mixture is assumed to be homogenous. [1] In this research, the amplitude and frequency of the oscillation was manipulated and the effects on the time taken to attain a stable CoV was observed.

The analyses were carried out using a digital camera that is capable of taking photographs at 5 frames per second (FPS). A laser sheet was used to illuminate a 2-dimensional plane in the mixer and 10 micron silver-coated hollow glass beads were

used as tracers. The photographs taken were broken down into 100 individual zones (Fig. 2) and processed in Matlab using the CoV equation (1).

$$CoV = \frac{Standard\ Deviation}{Average} \quad (1)$$

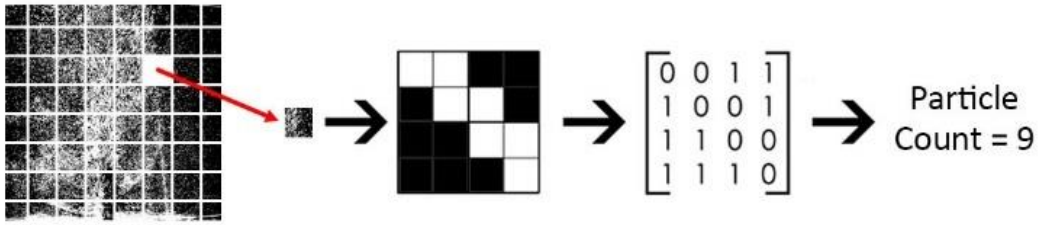


Figure 3: CoV analysis processing flow

The CoV values can be recorded and plotted as a function over time to produce a graph that would have a progressively downwards trend which eventually stops decreasing and fluctuating. An example of this is illustrated in Figure 4. The point where the CoV has stopped fluctuating and decreasing is known as the time for complete mixing or time to homogeneity. A lower value would signify that the mixer is able to achieve homogeneity faster.

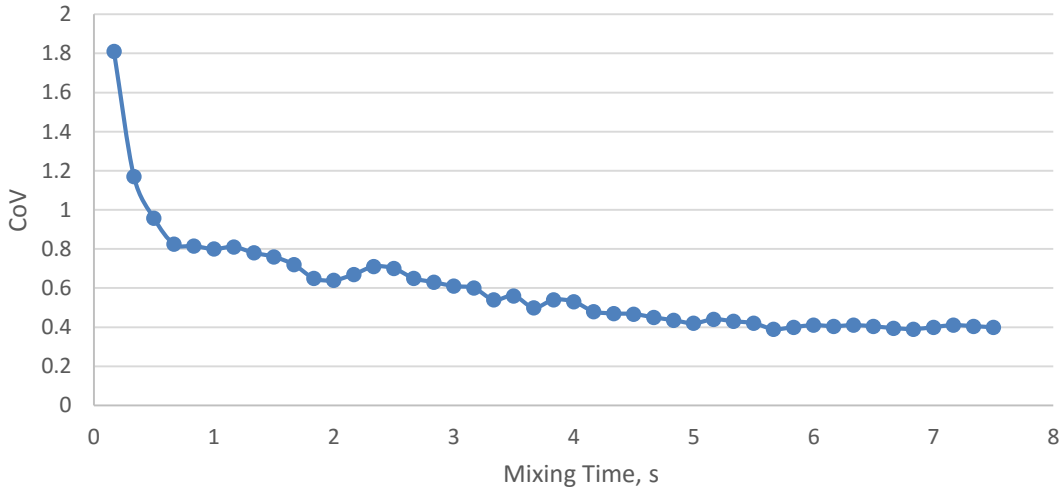


Figure 4: A typical example of a Coefficient of Variance against Mixing Time graph.

2.2 Particle Image Velocimetry Analysis

In addition to CoV, particle image velocimetry (PIV) analysis was also performed on the mixer to quantitatively determine the flow field within the mixer. PIV analysis allows the properties such as vorticity and both instantaneous and averaged velocities to be measured within a flow field. PIV analysis involves the use of a setup similar to CoV analyses with the exception of the camera being replaced with a special monochromatic camera that is extremely high speed and has low signal noise. Additionally, the laser is also replaced with a water-cooled microsecond pulse laser. [6] The working principle of a PIV setup is illustrated in Figure 5.

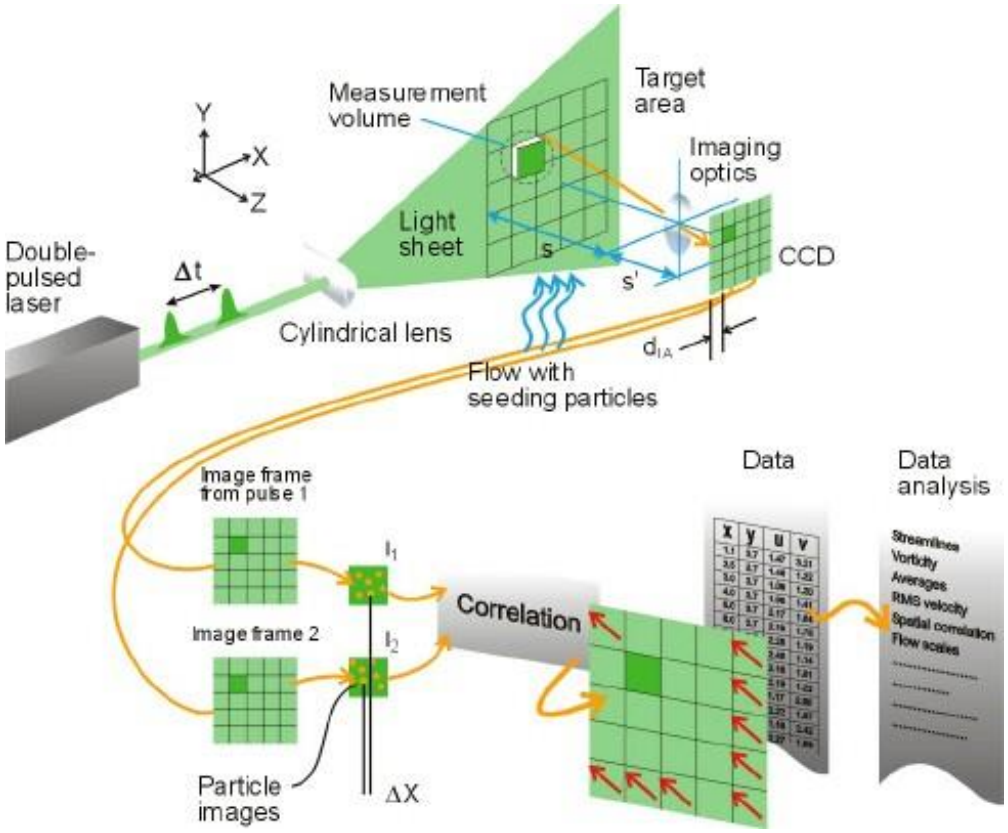


Figure 5: Working principle of a PIV setup.

The laser was pulsed twice in quick succession where a pair photographs are taken as well. The positions of individual particles are compared and the velocities for each particle are computed through the software which will build a velocity map of the region of interest. PIV analyses can be performed as a 2D or stereoscopic PIV where the analysed region is either a sheet or a 3 dimensional region. Stereoscopic PIV require multiple cameras whereas 2D require only one camera. [6]

The PIV analysis in this study was a 2D PIV study where the flow structure centre cross section of the synthetic jet mixer was analysed. The region of interest is the mixer region above the cavity. The laser pair was pulsed at 133ms intervals with 350µs delay between the pulse pairs. The images are exposed for 400µs.

2.3 Enzymatic Reaction

The enzymatic reactions require the preparation of a substrate emulsion before the study on enzyme kinematics and enzyme deactivation can be studied. For enzyme kinetics analyses, sodium hydroxide (NaOH) will be used to neutralise the butyric acid produced from the enzymatic reaction through titration. Whereas for enzyme deactivation analyses, the enzyme activity was analysed over time to determine activity loss of the enzyme. The preparation instructions for the substrate emulsion and experimental procedures for enzyme kinetics and enzyme deactivation is detailed below.

2.3.1 Substrate emulsion

8.95 g of NaCl and 0.2 g of KH2PO4 was dissolved in 230 mL of distilled water with 270 mL of glycerol. 3.0 g of Gum Arabic was added to the mixture with vigorous stirring until homogenised. In addition, 50 mL of emulsifying reagent, 3 mL of tributyrin oil and 298 mL of distilled water was also added under vigorous stirrer. [7] Fresh emulsions were prepared before every experimental run.

2.3.2 Enzyme kinetics

For each run, 2 L of substrate emulsion solution was added into the synthetic jet mixer while the actuator was simultaneously activated. With a sampling frequency of 10 minutes, 20 mL of the samples were taken and heated for 5 minutes to deactivate the enzyme to halt any further reaction. Titration was performed with 0.05 M NaOH and the volume of NaOH required to neutralise the sample (pH 7) were recorded. The enzyme kinetics analyses were repeated with a conventional overhead stirred mixer. [8]

2.3.3 Enzyme deactivation

The reactor was charged with 2 L of distilled water and 500 µL of pure lipase. Samples were collected for activity test to determine the enzyme activity lost over time for various synthetic jet oscillation frequencies and actuation amplitude. This analysis was also repeated on a conventional mixer. [9][10]

2.4 Power consumption

The power consumption is the product of the voltage and current of a mixer. Voltage and current values were extracted and recorded using a data acquisition instrument.

2.5 Experimental Design

The synthetic jet mixer consist of an orifice of 4mm, a cavity of 80mm and a mixing space dimension of 170mm height and 150mm diameter. The mixing rig can be seen in Figure 6 and Figure 7.

A jacket that is cube-shaped rather than cylindrical was added to the synthetic jet mixer using flow structure analyses to enable the laser sheet to be better transmitted during these analyses. The flat surface of the jacket would be positioned normal to the projected laser sheet and will minimise the risk of refraction. During the enzymatic reaction study, the jacket was not used.

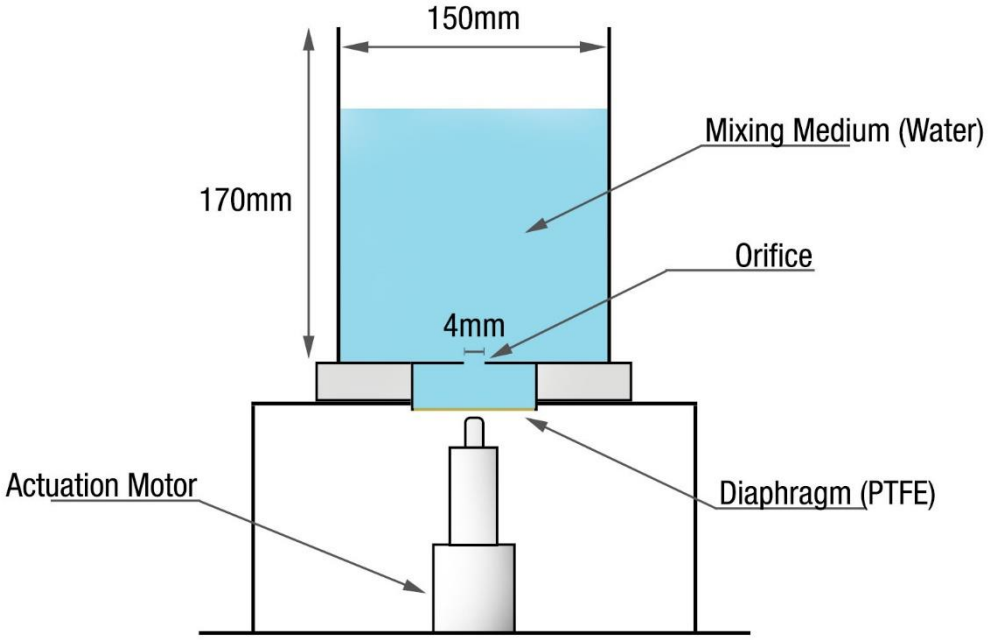


Figure 6. Experimental setup (without jacket)



Figure 7. Experimental rig with and without jacket.

2.6 Materials

The materials used during the study include tap water as the working fluid and 10 micron variable density silver-coated hollow glass beads (SC-HGB) as the tracer during flow structure analyses.

For the enzymatic reaction, Lipase from Aspergillus niger (Lipozyme CALB-L) with an activity of 100 kLU/ml supplied by Novozymes Denmark was used as a testing sample, analytical grade tributyrin oil (98%) from Fisher Scientific (M) Sdn Bhd, Anhydrous glycerine (99.5 v/v%) from Sigma Aldrich Malaysia, and sodium hydroxide pallets from Sigma Aldrich Malaysia were used.

3. Results and Discussion

The experimental parameters that were explored in this study which are flow structure analyses and enzymatic reaction analyses are tabulated in Table 1 and Table 2 respectively. The reference set of 15Hz and 1.5mm for the flow structure analyses was chosen based on previous work. [11]

Table 1. Tabulation of experimental sets for flow structure analyses

		Amplitude (mm)					
		0.5	1.0	1.5	2.0	2.5	3.0
Frequency	5Hz			●			
	10Hz			●			
	15Hz	●	●	●	●	●	●
	20Hz			●			
	25Hz			●			
	30Hz			●			

Table 2. Tabulation of experimental sets for enzymatic reaction analyses

		Amplitude (mm)	
		0.5	1.0
Frequency	5Hz	●	●
	10Hz	●	●
	15Hz	●	●

3.1 Effect of Oscillating Amplitude and Frequency on Time to Homogeneity

Figure 8 and Figure 9 illustrates how the oscillation amplitude and oscillation frequency affects the time required for complete mixing. It can clearly be seen that the mixing time will decrease with increasing oscillating frequency. However, from observing the trend, further increase in amplitude will eventually not have any improvement to the mixing time.

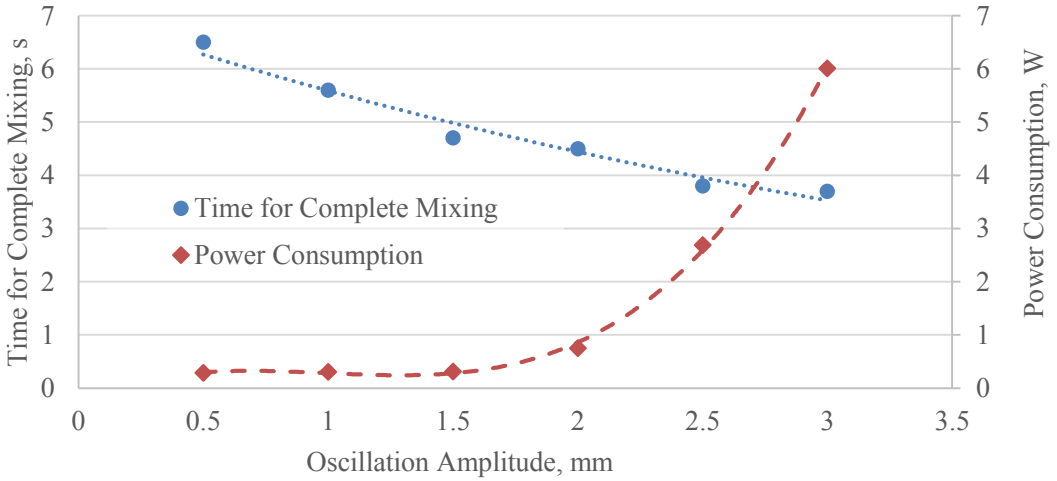


Figure 8: Effects of oscillation amplitude on power and mixing time.

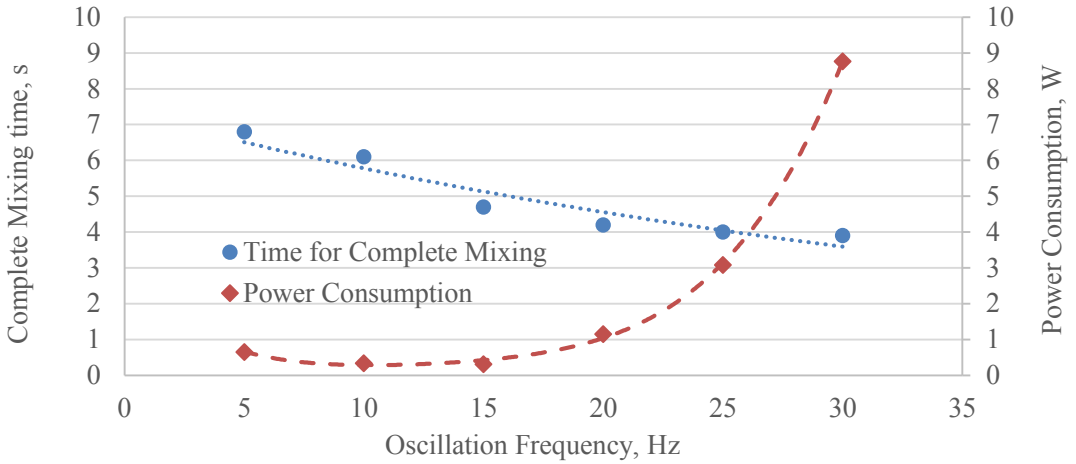


Figure 9: Effects of oscillation frequency on power and mixing time.

In addition to not having further benefits, increasing the frequency and amplitude will also cause the power consumption to increase exponentially which can also be seen in Figure 8 and Figure 9.

From the study, it is determined that at 15Hz and 1.5mm oscillating amplitude, the mixer has a good balance between efficiency and power consumption where there is a slight dip in time for complete mixing but the power consumption remains largely the same.

The PIV analysis results for the 15Hz, 1.5mm amplitude set, both at time averaged and instantaneous (eject cycle) can be seen in Figure 10 and Figure 11. The results show a good agreement with previous works and clearly shows the formation of vortices. [11]

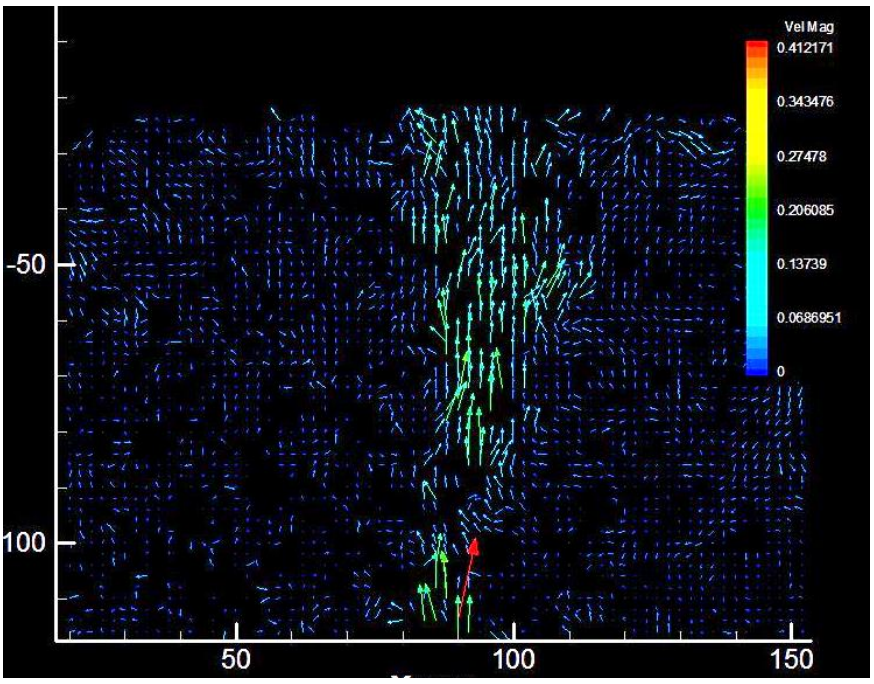


Figure 10: Instantaneous velocity during an eject cycle at 15Hz, 1.5mm

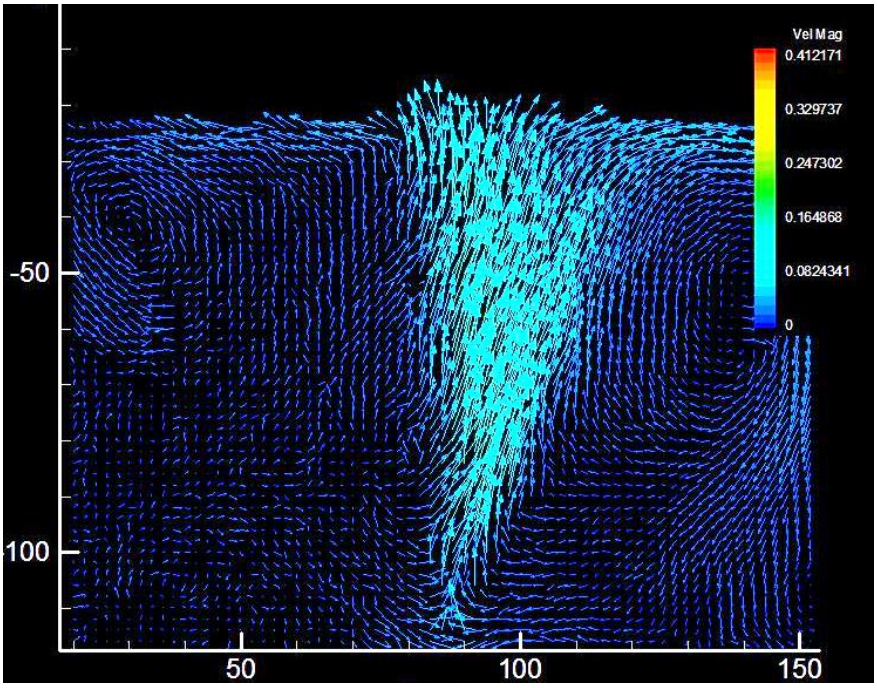


Figure 11: Time averaged velocity at 15Hz, 1.5mm

3.2 Effect of synthetic jet mixing on enzyme kinetics

Enzyme kinetics are affected by various factors such as enzyme concentration, substrate concentration, operating temperature as well as the effectiveness of the agitation mechanism (effect on the external mass transfer and convective molecular diffusion). In this study, the operating conditions were kept constant with the following conditions: enzyme concentration of 25 LU/ml, change of substrate concentration was negligible as the initial substrate concentration was set to 0.85% (v/v) and finally the operating temperature of 25oC. Hence the mixing effectiveness of the proposed mixer was tested based on the production of butyric acid inside the reactor as a function of time. The effects of oscillating frequency between 5 Hz and 15 Hz with 5 Hz increments and oscillating amplitude of 0.5 mm and 1.0 mm on the total moles of substrate consumed was studied.

Figure 12 illustrates the butyric acid produced over time while utilising a synthetic jet mixer as the agitator in the enzymatic reaction for both 0.5 mm and 1.0 mm. It can be seen that, in general, a lower amplitude of 0.5 mm has the higher amount of butyric acid produced with approximately double the amount produced compared to the higher 1.0 mm amplitude. This could be attributed to a higher shear stress produced by the higher amplitude. However, in contrast to this trend, the 1 mm, 5 Hz configuration actually causes the highest production of butyric acid. Hence, this data set is used in comparison to the conventional overhead stirrer.

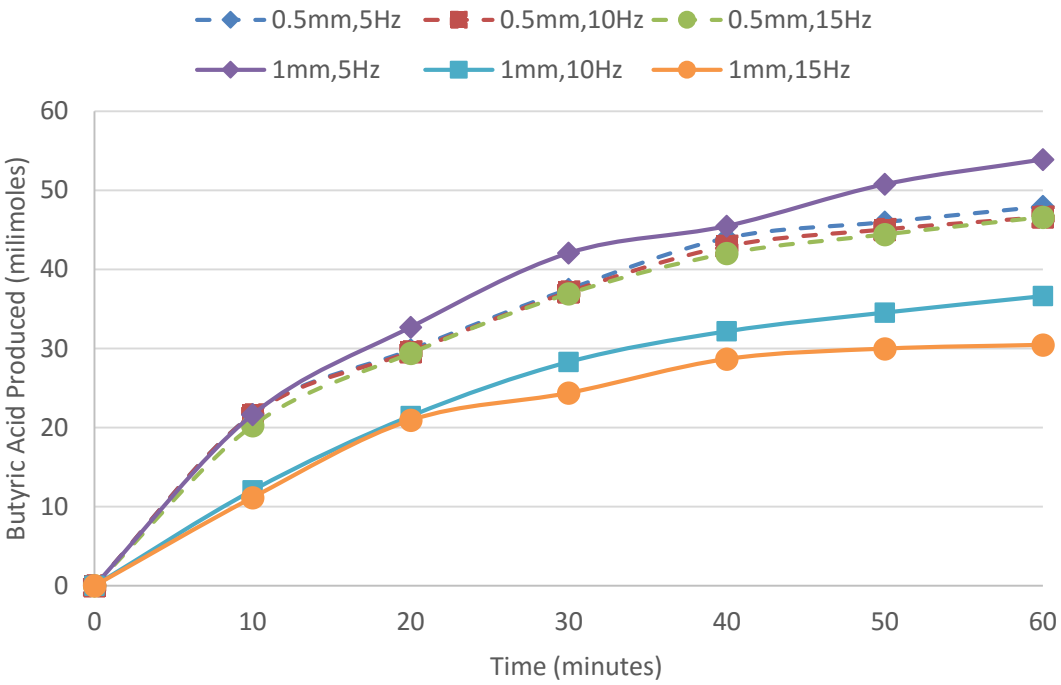


Figure 12: Butyric acid produced over time for various oscillation amplitudes and frequencies of the synthetic jet mixer.

Figure 13 illustrates the comparison between the synthetic jet mixer with a configuration of 1 mm, 5 Hz and the conventional overhead stirrer at 300 and 600 rpm whereas Table 3 tabulate these results. It is clear that while early on in the reaction, the 300 rpm conventional stirrer produces a higher amount of butyric acid, the final total amount is similar with the 600 rpm stirrer and they both produce approximately 9.5% lesser butyric acid when compared to the synthetic jet mixer.

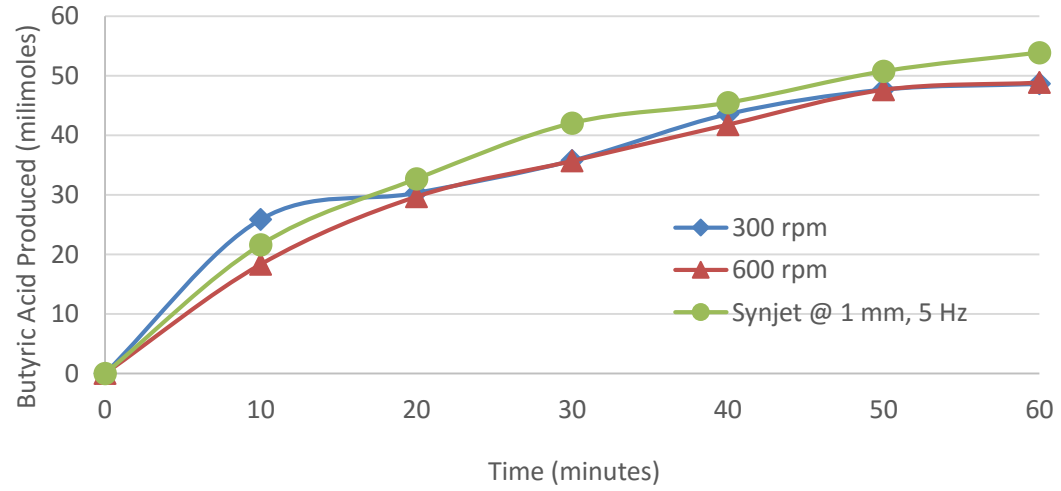


Figure 13: Butyric acid produced over time for synthetic jet mixer at 1 mm, 5 Hz and conventional mixer at 300 rpm and 600 rpm.

Table 3. Data tabulation for Synthetic Jet mixer at 1 mm, 5 Hz and conventional mixer at 300 rpm and 600 rpm.

Agitation device	Overhead Stirrer		Synthetic Jet
Time (minutes)	300 rpm	600 rpm	1.0 mm, 5 Hz
10	25.87	18.34	21.62
20	30.33	29.7	32.68
30	35.75	35.69	42.05
40	43.56	41.79	45.47
50	47.67	47.63	50.74
60	48.63	48.84	53.88

3.3 Effect of synthetic jet mixing on enzyme denaturalisation

The effect of synthetic jet mixer and overhead stirrer mixer on the denaturalization rate of the enzyme was investigated for 150 minutes and a 1 mL sample was taken every 30 minutes and tested for loss of enzyme activity. An enzyme solution with similar concentration but without any agitation was used as a control. The control has an 8.10% activity loss at the end of the 150 minutes whereas the synthetic jet mixer has the lowest enzyme loss of 10.13% at 150 minutes. The overhead stirrer mixer with 300 rpm has an activity loss of 15.95% at 150 minutes and the 600 rpm setting has an activity loss of 18.98% at 150 minutes. This indicates a high shear rate from the overhead stirrer as high shear stresses can deactivate enzymes in a solution. Figure 14 illustrates the information presented above.

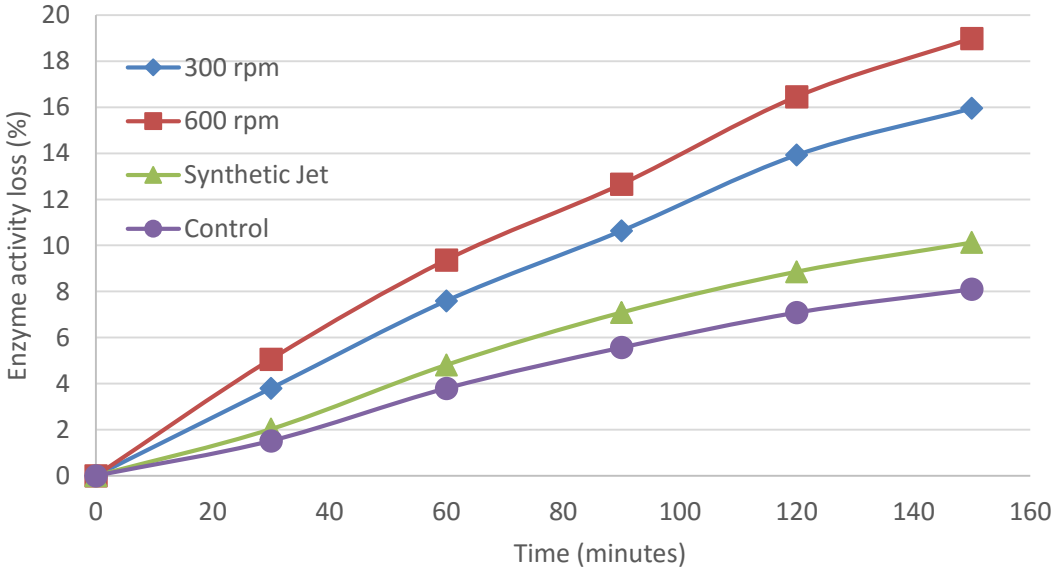


Figure 14: Effects of synthetic jet mixer and overhead conventional mixers on enzyme activity loss.

3.4 Power consumption comparisons

The power consumption of the synthetic jet mixer at 5 Hz and 1.0 mm oscillating amplitude was compared to the conventional overhead stirrer at 300 rpm and 600 rpm. Table 4 shows the voltage, current and power consumption of the mixer.

Table 4: Voltage, current and power consumption of the mixers expressed as root mean square (R.M.S.) values.

Device	Voltage (V)	Current (A)	Power (W)
Overhead Stirrer @ 300 rpm	240.0	0.094	22.51
Overhead Stirrer @ 600 rpm	240.0	0.111	26.64
Synthetic Jet @ 5Hz, 1.0 mm	1.654	0.350	0.578

The synthetic jet consumes at least a magnitude lesser power than an overhead stirrer making it extremely power efficient to use.

7. Conclusions

The mixing performance of a synthetic jet mixer have been analysed and it is found to be a feasible alternative to conventional mixing. Power consumption has been shown to rise exponentially when both frequency and amplitude are increased while the mixing time is decreased. However, the trend indicates that the mixing time will be constant after a certain amplitude and frequency.

The synthetic jet mixer has been shown to have a better performance in aqueous enzymatic reactions when compared to conventional overhead stirrers. Conventional overhead stirrer at both 300 rpm and 600 rpm has total butyric acid production of 48.8 millimoles compared to 53.9 millimoles in a synthetic jet mixer (1.0 mm amplitude with 5 Hz oscillating frequency) at the end of 60 minutes. Besides that, the loss of enzyme activity was found to be 10.1%, 15.9% and 19.0% for synthetic jet and overhead stirrer at 300 rpm and 600 rpm, respectively. Thus it is concluded that synthetic jet mixer has better performance in enzyme kinetics, lower rate of denaturalization of enzyme and lower power consumption when compared with conventional overhead stirrer mixers.

Future work could focus on the optimization of the oscillating amplitude, frequency as well as modifying the waveform of the oscillation. The change of enzyme concentration with varying temperature can be considered where both of these are one of the main factor that affecting the enzyme kinetics. Other future work that can be considered include varying the orifice geometry, identifying the viscosity limits of a synthetic jet mixer and implications of scaling up.

References

[1] Paul E., Atiemo-Obeng V., & Kresta S. (2004). Handbook of Industrial Mixing. New Jersey, USA. John Wiley & Sons, Inc.

[2] Kundu P. K., Cohen I. M., & Dowling D. R. (2012). Fluid Mechanics. 5th ed. Oxford, UK. Elsevier.

[3] Glezer A., & Wiltse J. W. (2000). Synthetic Jet Actuators for Mixing Applications. Patent No. 6056204, United States.

[4] Glezer A., & Amitay M. (2002). Synthetic Jets (Review Paper). Annual Review of Fluid Mechanics, Volume 34, pp. 503-529.

[5] Al-Atabi M., & M. Shamel. M. (2010). Mixing in Tanks Using Synthetic Jets. Daegu, ISFV 14.

[6] Raffel M., Willer C., Wereley S., & Kompenhans J. (2007). Particle Image Velocimetry: A Practical Guide. 2nd Ed. New York, US. Spinger.

[7] M. Shamel, M., Ramachandran, K.B., Hasan, M., Al-Zuhair, S. (2007). Hydrolysis of palm and olive oils by immobilised lipase using hollow fibre reactor. Biochemical Engineering Journal, 34(3), 228-235.

[8] Lawson, N.J.; Arruda, M.P.; and Davidson, M.R. (2005). Control of a submerged jet in a thin rectangular cavity. Journal of Fluid and Structures, 20(8), 1025-1042.

[9] Stein, R.L. (2011). Kinetics of enzyme reaction. Hoboken: John Wiley & Sons, Inc.

[10] Al-Zuhair, S. (2006). Kinetics of hydrolysis of tributyrin by lipase. Journal of Engineering Science and Technology (JESTEC), 1(1), 50-58.

[11] Al-atabi M., Liang H. C., Ng K. K., Hia I. L., Chin J. J., Ooi F. L. (2011). Particle Image Velocimetry Study of Mixing in Tanks Using Synthetic Jets. Kuantan, ICCEIB 2011.

Potential application of deep eutectic solvents in heat transfer application

Yan Y.C[1], Rashmi W[1*], Khalid M[2], Kaveh S[3], Gupta T.C.S.M[4], Mariam A.H[1]

[1]*Energy Research Group, School of Engineering, Taylor's University Lakeside Campus, Malaysia*
[2]*Division of Manufacturing and Industrial Processes, Faculty of Engineering, University of Nottingham, Malaysia Campus*
[3]*Department of Chemical and Materials Engineering, Faculty of Engineering, The University of Auckland, New Zealand*
[4]*Apar Industries, Research and Development, Mumbai, India*

*Corresponding Author: RashmiGangasa.Walvekar@taylors.edu.my

Abstract

Deep eutectic solvents (DESs) are termed as green solvents due to their excellent solvent properties such as low vapor pressure, non-corrosive, cheap, biodegradable and tunable which has a potential to be applied in variety of engineering applications such as extraction, electrodeposition, electrochemical synthesis and nanotechnology. Thus, this paper explores the possibility of utilizing DES as a heat transfer fluid due to their enhanced thermal stability compared to conventional fluids. Thermal conductivity of three types of DES comprising of methyl triphenyl-phosphonium-bromide (MTPB) and choline chloride (ChCl) as salts, and glycerol (GLY), ethylene glycol (EG), and triethylene glycol (TEG) as the hydrogen bond donor (HBD), are measured from 25°C to 70°C using KD2 Pro thermal properties analyser. The obtained results show that the DESs alter the thermal conductivity behavior of the organic fluids at higher temperature (70°C) with the maximum enhancement of 172% for MTPB:GYL-DES and 93% for MTPB:EG-DES. No obvious enhancement was observed for ChCl:TEG-DES. Nevertheless, these results provides good indicator that DESs has a good potential in heat transfer application such as coolants and lubricants.

Keywords: deep eutectic solvents, thermal conductivity, glycol, glycerol

1. Introduction

Deep eutectic solvent (DES) (a type of ionic liquid - IL) is a mixture of two or more economic components that are formed by the hydrogen bond interactions resulting in an eutectic mixture [1, 2]. In general, DES is synthesized by incorporating organic halide salts and hydrogen bond donors (HBD) in a particular molar ratio. The particular molar ratio should allow the mixture to reach eutectic point [3, 4]; hence, DES. The molar ratio of the salts and HBD is dependent on the amount of HBD molecules required for each halide ion in the mixture [5]. For instance, the eutectic point of choline chloride (ChCl) and carboxylic acid is detected at the molar ratio of 1 mole ChCl and 2 moles carboxylic acids (which is equivalent to 67mol% of carboxylic acid). This indicates that two moles of acid are needed to develop complex with each mole of halide ion; in order to produce the eutectic mixture [6]. The discovery of DES as a substitute to ILs was introduced by Abbott et al. [7] with the production of the first generation DESs from quaternary ammonium salts and amines or carboxylic acids as the hydrogen bond donors [5, 7, 8]. The resulting DES exist in liquid phase at temperature below 100℃ due to the reduction in freezing point as a result of hydrogen bonds formation [4].

The conventional applications of DES are metal oxides dissolution [5, 6], electro-polishing [9, 10], catalysis [11, 12], extraction [13-15] and electrodeposition [4]. Till date there are no literatures available that studies DES as heat transfer fluid. However, since DES belongs to a class of ionic liquid; research done on ionic liquid can be used as reference to explore the potential of DES in heat transfer application. In the past few years, ionic liquids (ILs) have been researched as a viable replacement of the present working heat transfer fluid. In comparison to the conventional heat transfer fluid, ILs has wide liquid temperature range, high heat capacity, high density, high thermal and chemical stability, and low vapor pressure [16]. Hence, the objective of this paper is to review research done on ILs as heat transfer fluid and explore the potential of DES in the heat transfer application and as a replacement for conventional heat transfer fluid by measuring thermal conductivity with respect to molar ratio and temperature. This would open up more research opportunity to the scientific community to research on DES for future application.

2. Ionic Liquids in Heat Transfer Application

In this section, literature reviews are conducted on ILs in the field of heat transfer. Various research studies done on ILs can be used to fortify the potential of DES in the heat transfer application.

The application of silicon oil and diphenyloxide/biphenyl as working heat transfer fluid are limited by various disadvantages such as low density, high vapor pressure, low chemical stability, and low decomposition temperature [17]. Studies conducted by Valkenburg et al. [18] show ILs are able to overcome the various disadvantages of silicon oil and diphenyloxide/biphenyl, and serve as a more suitable working heat transfer fluid. Another study by He et al. [16] on the heat transfer

performance of 1-hexyl-3-methylimidazolium tetrafluoroborate in microfin tubes has shown that the initial decomposition of the IL is 440.6°C which overcomes the low decomposition temperature of silicon oil and diphenyloxide/biphenyl as working heat transfer fluid. This implies that the IL is suitable to be used in mid to high temperature applications. Additionally, from the study, thermal conductivity of the IL measured increase linearly with increasing temperature. Fox et al. [19] investigated the thermal stability of 1-butyl-2,3-dimethylimidazolium hexafluorophosphate by using thermogravimetric analysis (TGA). The result shows that the IL starts to decompose at the temperature of 200°C. Another study by Liaw et al. [20] investigate the effect of heating temperature on the flash point of 1-hexyl-3-methylimidazolium chloride and 1-ethyl-3-methylimidazoliumbis (trifluoromethylsulfonyl)imide. From the study, heating the IL below 180°C for one hour does not affect the flash point of the IL. However, heating the IL above 200°C reduces the flash point of the IL. These results correspond to the outcome of the investigation by Fox et al.

In the application of solar thermal application, Paul et al. [21] has investigated the potential of N-butyl-N,N,N-trimetylammoniumbis(trifluormethylsulfonyl)imide. In this study, it is shown that the thermal conductivity of IL (approximate 0.124 W/m.K) is lower than de-ionized water by 20% at room temperature. Additionally, it is also indicated the thermal conductivity of the IL decreases with temperature. This ultimately reduces the heat transfer coefficient of the IL in solar thermal application. In absorption heat transformer application, mixture of water and lithium bromide was used as the working heat transfer fluid. This is due to exceptional properties of the mixture such as non-toxic, non-flamable, and high latent heat [22]. However, the presence of corrosion inhibitors, low thermal stability, high volatility, high vapor pressure of water and the occurrence of crystallization in this mixture limited the use of absorption heat transformers to only air-conditioning applications [23]. Besides water and lithium bromide, ammonia and water, and 2,2,2-trifluoroethanol and tetraethylene glycol dimethyl ether are also some of the conventional working heat transfer fluid used in heat absorption [19-20]. However, these working heat transfer fluids also poses impractical application due to the high vapor pressure of water and low system performance [18-19]. Therefore, ILs can be used in this application to overcome the conventional constraint of organic working heat transfer fluid such as thermal instability and high volatility. A study conducted by Zhang and Hu [26] using water and 1-ethyl-3-methylimidazolium dimethyl phosphate in a single stage absorption heat transformer shows that the usage of ILs is able to perform similarly to the conventional water and lithium bromide working heat transfer fluid. Another study by Ayou et al. [23] on single stage absorption heat transformers and double absorption heat transformer compares the performance of 2, 2, 2-trifluoroethanol and 1-ethyl-3-methylimidazolium tetrafluoroborate, 2, 2, 2-trifluoroethanol and 1-butyl-3-methylimidazolium tetrafluoroborate, 2, 2, 2-trifluoroethanol and tetraethylene glycol dimethyl ether, and water and lithium bromide. From the study, it is concluded that in the single stage heat transformer, the ILs mixture, although has lower efficiency, has higher gross temperature lift than the conventional working heat transfer fluid which

is superior for recovery of low temperature waste heat or heat transfer application in cold weather. As for the double stage heat transformer, ILs mixture also shows higher ability to increase the waste heat temperature (by approximate 60°C) compared to conventional 2, 2, 2-trifluoroethanol and tetraethylene glycol dimethyl ether mixture. In addition, the ILs does not exhibit corrosion and crystallization issue at higher temperature.

In summary, ILs have high thermal stability up to 200°C and are stable to the effect of heating temperature [16, 19, 20]. Study by He et al. [16] shows that ILs have increasing thermal conductivity with temperature. However, study by Paul et al. [21] states that the thermal conductivity of does not differ with temperature. The contradiction in these results may due to the difference in the ILs used in the study. Nevertheless, application studies on absorption heat transformer by Zhang and Hu [26] shows that, even with lower energy conversion efficiency, ILs show good promises in heat transfer application for low temperature waste heat recovery and cold temperature environment heat waste recovery. From the industrial standpoint, it is prudent for researchers to investigate more in the heat transfer application using ILs as working heat transfer fluid to provide fundamental understanding as a replacement of the conventional working heat transfer fluid.

3. Research Methodology

3.1 Synthesis of Deep Eutetic Solvents

In this study, methyl triphenyl-phosphonium-bromide (MTPB) and choline chloride (ChCl) were selected as the salts while glycerol (GLY), ethylene glycol (EG) and triethylene glycol (TEG) were used as HBDs. The DESs are prepared according to the molar ratio as shown in Table 1.

Table 1: Molar ratio of the synthesized DESs and their abbreviations.

Salt	HBD	Molar ratio (Salt : HBD)	Abbreviation
MTPB	GLY	1 : 2.5	DES 1
		1 : 3.0	DES 2
		1 : 4.0	DES 3
		1 : 5.0	DES 4
	EG	1 : 3.0	DES 5
		1 : 5.0	DES 6
ChCl	TEG	1 : 3.0	DES 7
		1 : 4.0	DES 8

Salt and HBD were accurately measured and transferred into Schott bottle with magnetic stirrer. The contents were vigorously mixed at 600rpm on a hot plate stirrer at 90°C for 3 hours until a colorless, clear and homogeneous solution was obtained as shown in Fig. 1 and Fig. 2. During this process the bottle was wrapped with parafilm to avoid contact with moisture from surrounding.

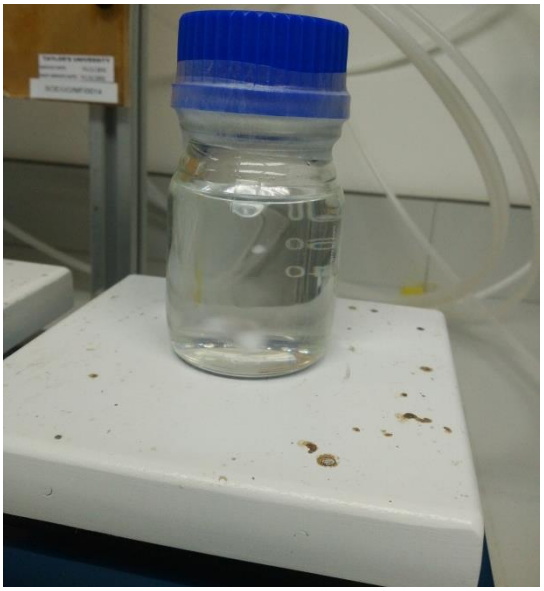


Figure 1: Preparation of DES.

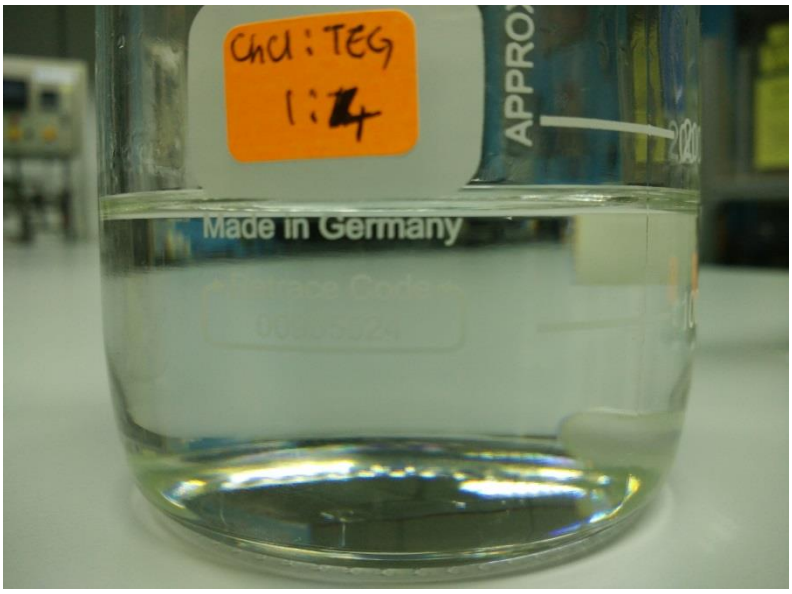


Figure 2: Colorless, clear and homogenous mixture of DES.

3.2 Thermal Conductivity

The thermal conductivity was measured using the KD2 Pro thermal properties analyzer (Decagon Devices, Pullman WA, USA) with an accuracy of ± 5% and measuring range up to 2 W/m.K. KD2 Pro thermal properties analyzer measures thermal conductivity of the samples based on the principle of transient hot-wire method. In this method, the analyzer dynamically measures the increase in temperature of a linear heat source immersed into the sample [27].

In this study, the thermal conductivity of the DESs was measured using a single 6cm long needle from 25°C - 70°C in a vial bottle. The temperature of the DESs was controlled by using digital water bath (Daniel Digital Water Bath) as shown in Fig. 3. A hole was made on the cap of the vial bottle to reduce unwanted heat convection from the surrounding as the transient hot-wire method operates under the assumption that convection is absence [27], [28]. Before any measurements were taken, the needle was calibrated using standard glycerine at 20°C. In order to minimize the experimental errors, for each sample 5-10 readings were recorded at an interval of 15 minutes between each reading and the average value was used for data analysis. Additionally, the DESs were filled to the brim of the vial bottle in order to immersed at least 75% of the needle into the samples.



Figure 3: Measuring thermal conductivity in digital water bath.

4. Results

It was observed that MTPB:GLY-DESs exhibited the highest increment in thermal conductivity. In Fig. 4, the thermal conductivity of the DESs corresponds to the amount of salt (in this case MTPB). With decreasing salt content in the DES, thermal conductivity of the MTPB:GLY-DES increased as a result of reduction in the general mobility and the amount of effective charge carriers due to aggregation of ions which causes the DES to have higher thermal conductivity [29]. Overall, thermal

conductivity of MTPB:GLY-DES increases by approximate 230% to 360% from 25°C to 70°C. On other hand, pure GYL shows constant thermal conductivity (0.285W/m.K) with increasing temperature as shown in Fig. 4 [30]. At 25°C, MTPB:GLY-DES shows negative thermal conductivity enhancement (DES 1: -52%, DES 2: -30%, DES 3: -21% and DES 4:-19%) as shown in Fig. 5. However, as the temperature increases to 70°C, the DESs enhanced the thermal conductivity up to 123% (DES 1), 145% (DES 2), and 172% (DES 3 & DES 4).

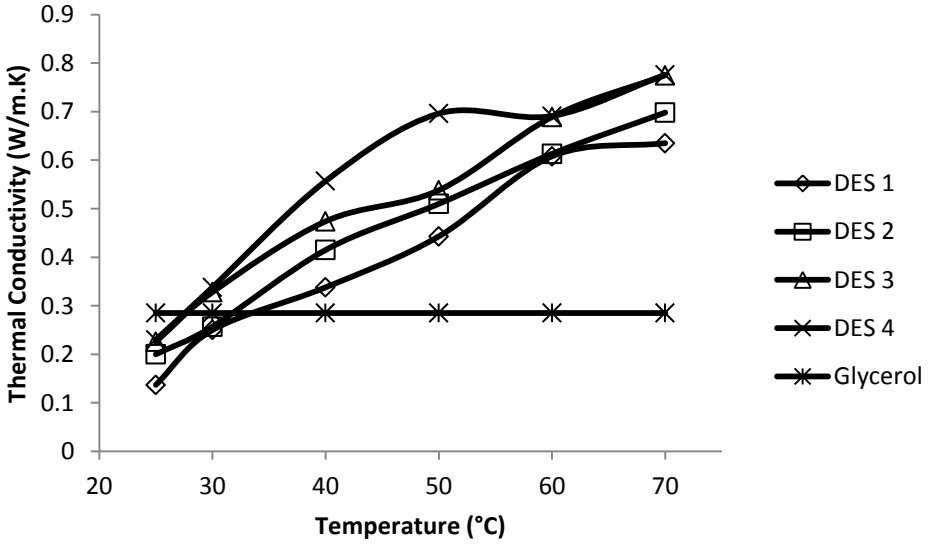


Figure 4: Thermal conductivity of MTPB:GLY with respect to temperature.

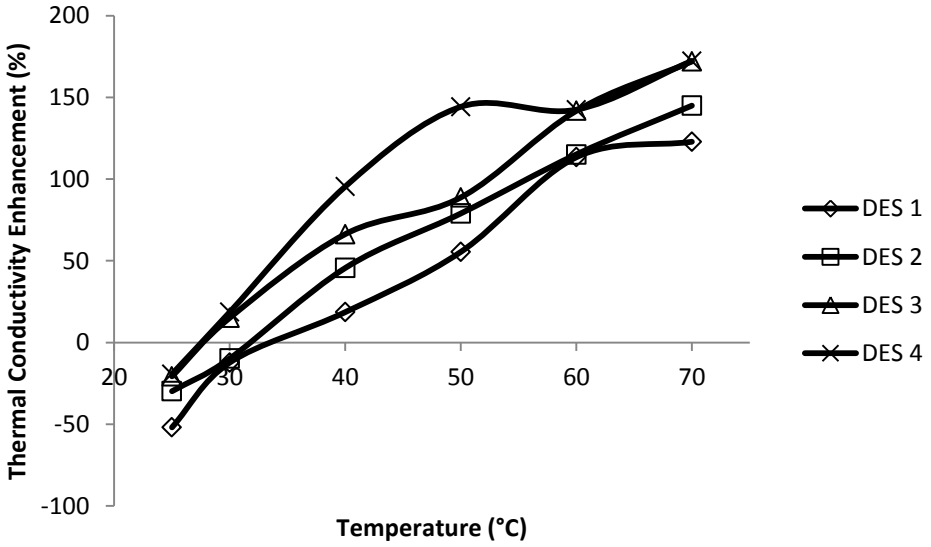


Figure 5: Thermal conductivity enhancement of MTPB:GYL over pure GYL with respect to temperature.

Compared to MTPB:GYL-DESs, contradicting results were observed for MTPB:EG-DESs with the same molar ratio of salt as shown in Fig. 6. The thermal conductivity decreased with the decrease in salt content which could be due to low hydrogen bonding between EG and MTPB. Thermal conductivity of MTPB:EG-DES increases with temperature whereas pure EG has decreasing thermal conductivity [31]. Fig. 7 shows that MTPB:EG-DES has negative enhancement of 68% (DES 5) and 60% (DES 6) over the pure EG at room temperature (25°C). However, MTPB:EG-DES makes up for the loss in thermal conductivity enhancement at higher temperature (70°C) with 23% higher thermal conductivity in DES 5 and 93% in DES 6.

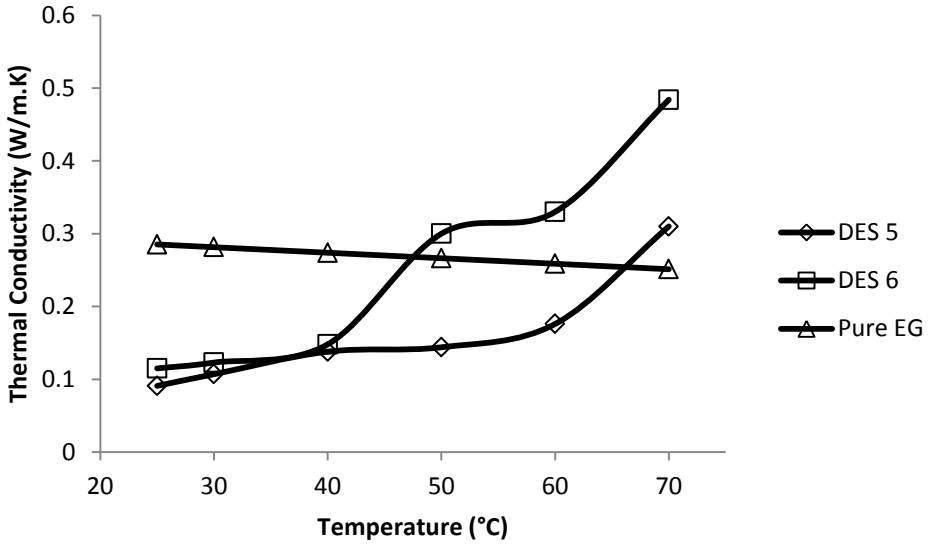


Figure 6: Thermal conductivity of MTPB:EG with respect to temperature.

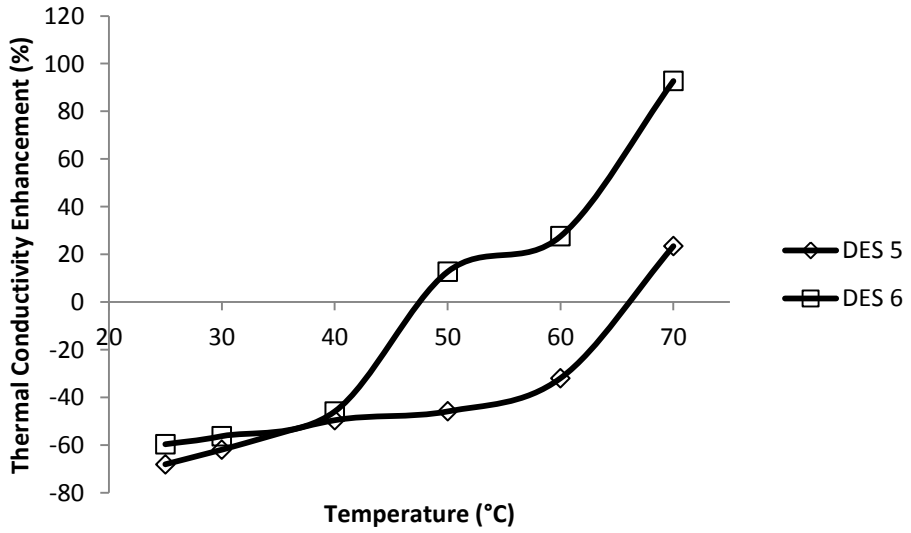


Figure 7: Thermal conductivity enhancement of MTPB:EG over pure EG with respect to temperature.

Lastly, the thermal conductivity of ChCl:TEG-DESs shows relatively little increment in thermal conductivity (approximately 5% to 7%) when the temperature rises from 25°C to 70°C as shown in Fig. 8. In comparison with the pure TEG, ChCl:TEG-DES shows increasing thermal conductivity with increasing temperature whereas pure TEG shows reducing thermal conductivity [32]. It is also observed that increasing the amount of ChCl salt reduces the thermal conductivity of the resulting DES. In term of thermal conductivity enhancement, ChCl:TEG-DES does not show a lot of thermal conductivity enhancement as shown in Fig. 9 in which the only positive enhancement is observed at 70°C in DES 8 (2%).

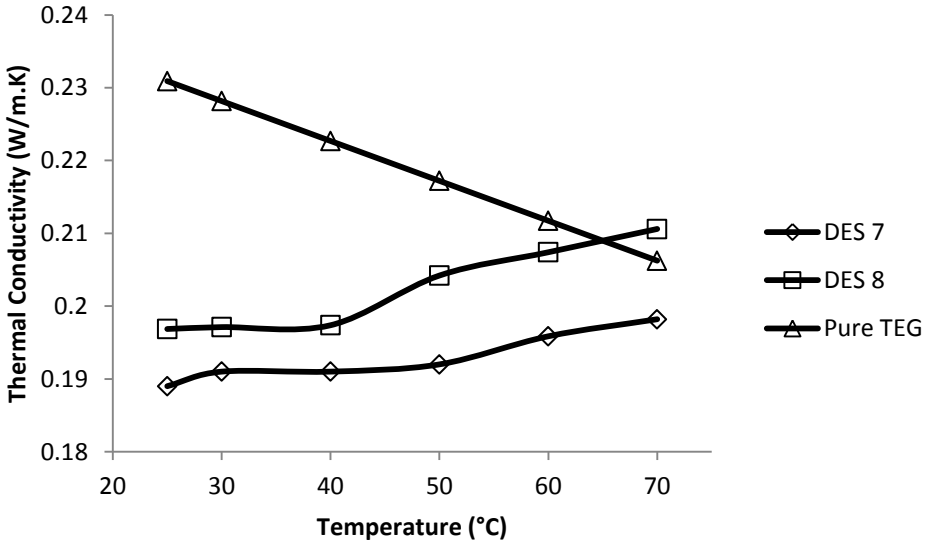


Figure 8: Thermal conductivity of ChCl:TEG with respect to temperature.

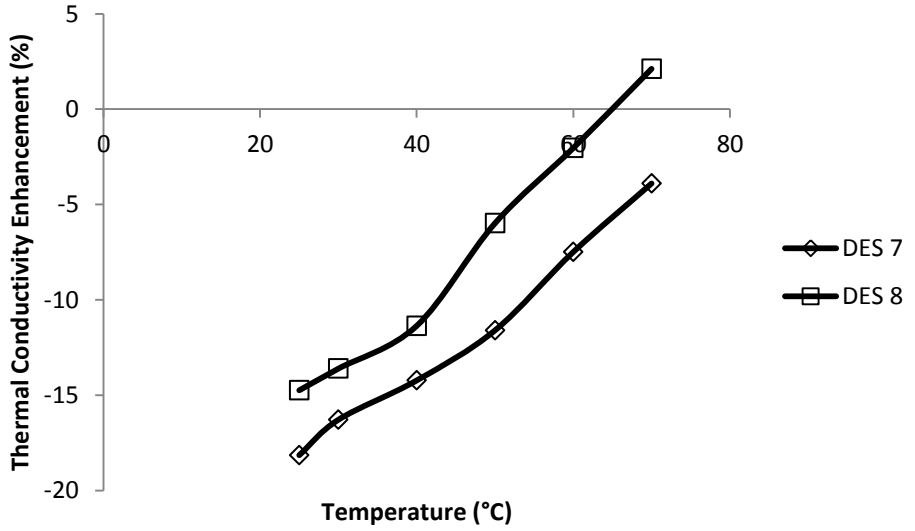


Figure 9: Thermal conductivity enhancement of ChCl:TEG over pure TEG with respect to temperature.

5. Conclusions

This paper presents an overview on DESs and their engineering applications. As there is no work reported on application of DES as an heat transfer fluid, this study attempts to measure the important physical property (i.e thermal conductivity) of DES to explore its potential in heat transfer application. Based on the observations it can be concluded that DESs can be successfully applied in various applications were faster heat removal is desirable with further enhancing the performance, reducing the cost and size of the equipment. At room temperature, all the DESs showed negative thermal conductivity enhancement over the pure organic fluids. However, at 70°C, a maximum of 172% thermal conductivity enhancement is observed in MTPB:GLY-DES and a maximum of 93% in MTPB:EG-DES. ChCl:TEG-DES on other hand shows very little increase (approximate 2%) in thermal conductivity at 70°C. The addition of small amount of salt is able to alter the thermal conductivity of conventional heat transfer fluids. More detailed work is required to further measure the other thermo-physical properties of such DESs.

References

[1] C. Yue, D. Fang, L. Liu, and T. . Yi, "Synthesis and application of task-specific ionic liquids used as catalysts and/or solvents in organic unit reactors," *J. Mol. Liq.*, vol. 163, no. 3, pp. 99–121, 2011.

[2] Y. Dai, G. . Witkamp, R. Verpoorte, and Y. . Choi, "Natural Deep Eutetic Solvents as a New Extraction Media for Phenolic Metabolites in Carthmux Tinctorius L," *Anal. Chem.*, vol. 85, pp. 6272–6278, 2013.

[3] K. Shahbaz, F. . Mjalli, M. . Hashim, and I. . AlNashef, "Prediction of deep eutetic solvents densities at different temperatures," *Thermochim. Acta*, vol. 515, no. 1–2, pp. 67–72, 2011.

[4] E. . Smith, A. . Abbott, and K. . Ryder, "Deep Eutectic Solvents (DESs) and Their Applications," *Chem. Rev.*, vol. 114, pp. 11060–11082, 2014.

[5] A. . Abbott, D. Boothby, G. Capper, D. . Davies, and R. . Rasheed, "Deep Eutetic Solvents Formed between Choline Chloride and Carboxylic Acids: Versatile Alternatives to Ionic Liquids," *J. Am. Chem. Soc.*, vol. 126, pp. 9142–9147, 2004.

[6] Q. Zhang, K. Oliveir, Dea Vigier, S. Royer, and F. Jérôme, "Deep eutectic solvents: syntheses, properties and applications," *Chem. Soc. Rev.*, vol. 41, no. 21, p. 7108, 2012.

[7] A. . Abbott, G. Capper, D. . Davies, R. . Rasheed, and V. Tambyrajah, “Novel Solvent Properties of Choline Chloride/Urea Mixtures,” *Chem. Commun.*, pp. 70–71, 2003.

[8] M. . Kareem, F. . Mjalli, M. . Hashim, and I. . AlNashef, “Phosphonium-Based Ionic Liquids Analogues and Their Physical Properties,” *J. Chem. Eng. Data*, no. 11, pp. 4632–4637, 2010.

[9] A. . Abbott, G. Capper, K. . McKenzie, A. Glidle, and K. . Ryder, “Electropolishing of stainless steels in a choline chloride based ionic liquid: an electrochemical study with surface characterisation using SEM and atomic force microscopy,” *Phys. Chem. Chem. Phys.*, no. 36, pp. 4214–4221, 2006.

[10] A. . Abbott, K. . Ttaib, G. Frisch, K. . Ryder, and D. Weston, “The electrodeposition of silver composites using deep eutectic solvents,” *Phys. Chem. Chem. Phys.*, no. 7, pp. 2443–2449, 2012.

[11] D. Lindberg, M. Fuente Revenga, and M. Widersten, “Deep eutectic solvents (DESs) are viable cosolvents for enzyme-catalyzed epoxide hydrolysis,” *J. Biotechnol.*, no. 3–4, pp. 169–171, 2010.

[12] H. Zhao, C. Zhang, and T. . Crittle, “Choline-based deep eutectic solvents for enzymatic preparation of biodiesel from soybean oil,” *J. Mol. Catal. B Enzym.*, vol. 85–86, pp. 243–247, 2013.

[13] A. . Abbott, P. . Cullis, M. . Gibson, R. . Harris, and E. Raven, “Extraction of glycerol from biodiesel into a eutectic based ionic liquid,” *Green Chem.*, no. 8, pp. 868–872, 2007.

[14] R. . Leron and M. . Li, “Solubility of carbon dioxide in a choline chloride–ethylene glycol based deep eutectic solvent,” *Thermochim. Acta*, vol. 551, pp. 14–19, 2013.

[15] R. . Leron, A. Caparanga, and M. . Li, “Carbon dioxide solubility in a deep eutectic solvent based on choline chloride and urea at T = 303.15–343.15 K and moderate pressures,” *J. Taiwan Inst. Chem. Eng.*, no. 6, pp. 879–885, 2013.

[16] G.-D. He, X.-M. Fang, T. Xu, Z.-G. Zhang, and X.-N. Gao, “Forced convective heat transfer and flow characteristics of ionic liquid as a new heat transfer fluid inside smooth and microfin tubes,” *Int. J. Heat Mass Transf.*, vol. 91, pp. 170–177, 2015.

[17] B. . Wu, R. . Reddy, and R. . Rogers, “Novel ionic liquid thermal storage for

solar thermal electric power systems," in *International Solar Energy Society World Congress*, 2001, pp. 445–451.

[18] M. E. . Valkenburg, R. . Vaughn, M. Williams, and J. . Wilkes, "Thermochemistry of ionic liquid heat-transfer fluids," *Thermochim. Acta*, vol. 425, pp. 181–188, 2005.

[19] D. . Fox, J. . Gilman, H. . De Long, and P. . Trulove, "TGA decomposition kinetics of 1-butyl-2,3-dimethylimidazolium tetrafluoroborate and the thermal effects of contaminants," *J. Chem. Thermodyn.*, vol. 37, pp. 900–905, 2005.

[20] H.-J. Liaw, K.-Y. Chen, H.-Y. Chen, and S.-N. Liu, "Effect of heating temperature on the flash point of ionic liquids," *Procedia Eng.*, vol. 84, pp. 293–296, 2014.

[21] T. C. Paul, A. K. M. M. Morshed, E. B. Fox, A. E. Visser, N. J. Bridges, and J. A. Khan, "Thermal performance of ionic liquids for solar thermal applications," *Exp. Therm. Fluid Sci.*, vol. 59, pp. 88–95, 2014.

[22] B. Bakhtiari, L. Fradette, R. Legros, and J. Paris, "A model for analysis and design of H2O-liBr absorption heat pumps," *Energy Convers. Manag.*, vol. 52, pp. 439–449, 2011.

[23] D. S. Ayou, M. R. Currás, D. Salavera, J. García, J. C. Bruno, and A. Coronas, "Performance analysis of absorption heat transformer cycles using ionic liquids based on imidazolium cation as absorbents with 2,2,2-trifluoroethanol as refrigerant," *Energy Convers. Manag.*, vol. 84, pp. 512–523, 2014.

[24] S. . Chaudhari, K. . Patil, J. Allepus, and A. Coronas, "Measurement of the vapour pressure of 2,2,2 –trifluoroethanol and tetraethylene glycol dimethyl ether by static method.," *Fluid Phase Equilib.*, vol. 108, pp. 159–165, 1995.

[25] M. Medrano, M. Bouronis, and A. Coronas, "Double-lift absorption refrigeration cycles driven by low-temperature heat sources using organic fluid mixtures as working pairs," *Appl. Energy*, vol. 68, pp. 173–185, 2001.

[26] X. Zhang and D. Hu, "Performance analysis of the single-stage absorption heat transformer using a new working pair composed of ionic liquid and water," *Appl. Therm. Eng.*, vol. 37, pp. 129–135, 2012.

[27] B. Merckx, P. Duoignon, J. . Garnier, and D. Marchand, "Simplified transient hot-wire method for effective thermal conductivity measurement in geo materials: Microstructure and saturation effect," *Adv. Civ. Eng.*, vol. 2012,

2012.

[28] W. . Wakeham, A. Nagashima, and J. . Sengers, “Measurement of the transport properties of fluids,” *Exp. Thermodyn.*, vol. 3, 1991.

[29] F. . Ghareh Bagh, K. Shahbaz, F. . Mjalli, I. . AlNashef, and M. . Hashim, “Electrical Conductivity of Ammonium and Phosphonium Based Deep Eutetic Solvents: Measurements and Artificial Intelligence-Based Prediction,” *Fluid Phase Equilib.*, vol. 356, pp. 30–37, 2013.

[30] OPTIM, “Synthetic glycerin - thermal conductivity.” 2015.

[31] MEGlobal, “Ethylene glycol: Product guide.” 2008.

[32] DOW, “Triethylene glycol.” 2007.

Biodegradability Study of Controlled Released Fertilizer by starch-derivative-alginate based Formulation

Xin Ying Tan[1], Siew Wei Phang [1,2], Lee Tin Sin[2], Soo Tueen Bee[2]*

[1] School of Engineering, Taylor's University Lakeside Campus, Malaysia.

[2]Department of Chemical Engineering, Faculty of Engineering and Science, Universiti Tunku Abdul Rahman, Kuala Lumpur, Malaysia.

[*]r_ying715@hotmail.com

Abstract

Controlled released fertilizers (CRF) play an interesting role in improving the quality of fertilizer and protecting the ecosystem. Under this point of view, new technology is developed by combining starch and alginate as both of the materials are eco-friendly and biodegradable. Starch-based-alginate beads are believed to overcome environment issues by delivering plant nutrients in a delayed or controlled-manner with less energy consumption and has no negative impacts on the environment [1]**. By reacting with a cross-linker calcium chloride, gelation process occurs and alginate beads are formed immediately when alginate is interacted with divalent metal ions solution, Ca2+. To outstanding the achievement of starch-based-alginate beads, biodegradability is tested in natural settings by using soil burial test. However, there are many aspects involved in the process of biodegradation of starch-derivative-alginate beads such as chemical properties of the polymer such as nutrients, oxygen, pH value, composition, concentration and bioavailability of the contaminants, and the pollution history of the contaminated environment** [2]**. No research has been done on biodegradation of starch-derivative-alginate beads at the moment. In this project, Taguchi method is applied to obtain the formulations of starch-alginate-Ca2+ beads. The experiment is carried out by burying the beads in the mixture of soil and waste water treatment sludge to study the biodegradability. Each sample of beads is weighed before and after the test by using a weighing balance to obtain the weight loss percentage. This research is intended to study the biodegradability of the beads using Taguchi Method and to determine the beads formulation which has the highest degree of biodegradability. By contrast, alginate-derivative-starch beads have provided us more practical and cheaper formulation of CRF which allowed promoting the sustainability development in agriculture field.**

Keywords: Controlled-release-fertilizers, biodegradability study, biodegradation behaviour, starch alginate formulation.

1. Introduction

According to Food and Agriculture Organization, the world's population has risen and expected to reach about 8 billion people by 2030. Besides, the growing demand for cereal production has grown as cereals are by far the most significant food sources for human. Nevertheless, there is only 7% of arable land is available worldwide which limits the crop yields in most of the countries [3]. Hence, higher production for fertilizer is essential for increase input application crop productivity.

Urea, a white crystal-like granular solid that carries more than 40% of nitrogen [4]. It is found that high input of nitrogen content has generally reduced soil microbial activity when ammonia (NH_3) is oxidized to NO_3^- [4]. The use of conventional urea fertilizers has thus far demonstrated environmental pollution by releasing hazardous emissions such as ammonia, nitrous oxide and nitrogen dioxide. The emission rate of nitrous oxide (N_2O) in the United State for various fields from 1990 to 2009 which leads to greenhouse effect [5].

Furthermore, excessive usage of urea fertilizer is rinsed off by heavy rain into the lake or ocean which causes eutrophication, a process that will damage the coastal marine ecosystems [6]. Therefore, several technologies have already been modified worldwide to improve the quality of urea fertilizer while alleviating the environmental footprints of fertilizer production systems [6]. In this context, starch based formulation of controlled release fertilizer (CRF) with the presence of urea as active ingredient is potentially obligated to be studied in order to encounter the situation.

CRF is designed to deliver active fertilizing nutrients to a specific area in a delayed manner automatically over a long period of time [7]. The design parameters of CRF are tuned appropriately to optimize nutrient use efficiency by coinciding with the sequential nutrient needs of a plant [7]. The idea of coating the fertilizer with natural, environmentally friendly macromolecules improves the quality of the soil while minimizes ecological or biological side effects to the surrounding [7]. As a result, crop yields can be increased under better soil condition and hence increase the production of foodstuffs.

Despite all the advantages of CRF, a combination of fertilizer with polymeric coating has a major limitation. Huge quantities of polymers are left in the soil when the nutrients are drained [8]. Environmental issue might arise if these polymers are non-biodegradable and hence further researches are required in this project to improve the performance of starch based formulation CRF by testing the biodegradability of polymers. Due to the rising concern over the reduction of non-renewable, fossil-based resources in the recent years, the production of biodegradable polymers has gradually increased and has highly promoted the sustainable development based on their biocompatibility and biodegradability characteristics [9]. Both the academic and the industry have massively produced environmentally-friendly biodegradable polymers that can be obtained from alternative and renewable resources, with less energy consumption and has no negative impacts on the environment [10].

From environmental aspect, biodegradation or mineralization takes place when polymers are converted under the influence of living organisms into carbon dioxide, methane, water, inorganic compounds or biomass [11]. Thus, the extent of polymers' life cycle, biodegradability of polymers and their interaction with the environment need to be justified when handling with biodegradable polymer wastes. From engineering aspect,

biodegradability of polymers is preferably used for short lifespan applications, such as packaging materials, but are non-favourable for long lifespan applications, such as automotive and construction uses [11].

Starch, an agro-sourced polymer is chosen because it is relatively economy and easy to access from market. However, the existent of hydrogen bonds between the hydroxyl groups has weakened the suspension stability and mechanical properties of the starch [12]. Therefore, alginate, an anionic biopolymer that is made up of linear chains of α-L-guluronic acid and β–D-mannuronic acid residues combined with 1, 4- glycosidic linkages is brought into the formulation [13]. Both alginate and starch are served as core materials for controlled release formulation to prepare starch-based-alginate beads due to its advantages such as great biocompatibility, biodegradability, non-toxicity, gelation and film formation properties [13]. On the other hand, by adding cross-linker calcium chloride into the formulation, gelation process occurs and alginate beads can be easily formed when alginate is interacted with divalent metal ions solution such as Ca^{2+} [14]. In the presence of calcium, sodium alginate can form resilient gels without the need of heat to make spheres. The bonding of starch-alginate-Ca^{2+} beads is illustrated in **Figure 1** below.

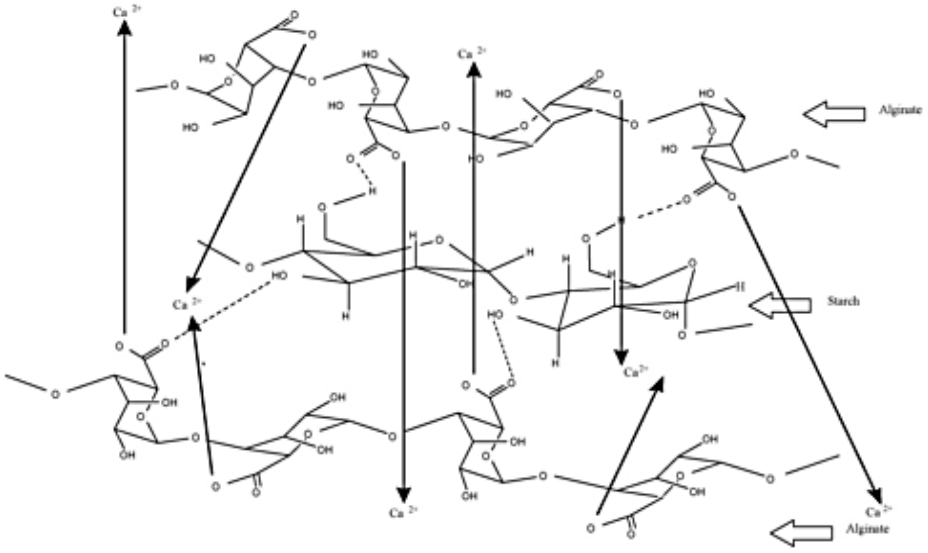


Figure 1: Structure of starch-alginate-Ca^{2+} beads [14]**.**

The formulation of starch-alginate beads [14] was used in this biodegradability study is presented in Table 1 below with starch ranging from 3 to 5% w/v, alginate ranging from 0.5 to 2.5% w/v and calcium chloride ranging from concentration of 0.1 to 0.5M to look into their effects on bead diameter and biodegradability.

Table 1: Formulation Parameters for the Production of Starch-Alginate-Ca^{2+} beads [14].

Formulation Code	Starch (%, w/v)	Alginate (%, w/v)	Thiram (mg)	Crosslinker Concentration (M)	Beads Formed (g)	Yield (%)
SA1	3	1	30	0.1	0.66	64.08
SA2	6	1	30	0.1	1.06	59.55
SA3	9	1	30	0.1	1.42	56.13
SA4	12	1	30	0.1	2.12	64.63
SA5	15	1	30	0.1	2.56	63.52
SA6	12	0.5	30	0.1	No Product	
SA7	12	1.5	30	0.1	2.38	69.79
SA8	12	2	30	0.1	2.44	69.12
SA9	12	2.5	30	0.1	3.18	86.88
SA10	12	1	30	0.2	1.97	60.06
SA11	12	1	30	0.3	2.63	80.18
SA12	12	1	30	0.4	2.7	82.32
SA13	12	1	30	0.5	2.58	78.66

The increase of alginate amount and cross-linker concentration increase the size and diameter of starch-alginate-Ca^{2+} beads because there are more available alginate and calcium ions to perform crosslinking within the networks. Based on samples SA1 to SA5 where the amount of alginate is constant, starch does not affect the size of the beads as most of the interactions have been used up in crosslinking rather than hydrogen bonding between starch and alginate and hence, not affecting the yield. However, when the starch and alginate contents reach 12% w/v and 0.5% w/v respectively, no product is formed [14]. As for calcium chloride cross-linker, bead size and equilibrium swelling percentage will decrease due to cavity type of network which is formed by bivalent calcium ion. Nevertheless, thiram properties are different with urea therefore no accurate assumption can be made about the effect of starch-derived-alginate based formulation for urea coating.

The current study suggests that the biodegradation characteristics varied significantly with different starch content in the biodegradable polymers. The biodegradation of two starch based polymers: 100% pure poly-butylene succinate (PBS) and poly-caprolactone (PCL) consisting of 55% of PCL, 30% of starch and 15% of aliphatic polyesters were studied under both anaerobic and aerobic conditions [15]. PCL has biodegraded 88% in 44 days under aerobic condition whereas PBS only degraded 31% in 80 days [15]. However, PBS is barely biodegrade under anaerobic condition by soil burial test and the biodegradability of PCL is moderately low under the same conditions for 180 days.

There are many factors involved in the process of biodegradation of starch-derivative-alginate beads including properties of the polymer such as the composition of starch and crosslinker concentration. Moreover, bioavailability of the soil, soil pH, surrounding temperature and the pollution history of the soil environment should be taken into account in the biodegradation study as well [16]. Hence, this research is carried out to further understand the extent to which starch-derivative-alginate beads will be biodegraded by using soil burial tests by observing weight loss as a function of incubation time in soil. The physical properties in this research are affected by this four parameters, sodium alginate (g/L), starch (g/L), calcium chloride cross-linker concentration (M) and urea (M) that will be selected as the manipulate variables for studies. One of the objectives of this research is to study the factors influencing the beads size formation and the biodegradability of the beads using Taguchi Method. Last but not least is to investigate the biodegradability of the starch-derivative-

alginate beads by weight loss analysis at specific time intervals throughout 15 days of soil burial.

2. Experimental

Starch, alginate, urea and calcium chloride are the four main parameters with three levels on each parameter. With the application of fractional factorial design, a total of $3^4 = 81$ experimental settings are required to investigate the interaction between variables which is not possible as it is time consuming and cost ineffective. Hence, Taguchi method is introduced to perform experimental design in a much simpler and cheaper way by narrowing the scope down for this research project. By applying Taguchi method of L9 (3^4 Series), a total of 9 sampling formulations are needed to produce high quality beads instead of running all possible arrangements proposed by factorial design to fully understand the relations between variables at low cost.

Biodegradability study of controlled release fertilizers of starch-derivative-alginate beads is conducted with soil burial test for 15 days. A soil burial test is designed to simulate and determine the degree of biodegradation of starch-derivative-alginate beads exposed to soil composition environment [17]**.** Before burying in the soil, starch-derivative-alginate beads are weighed, wrapped with fabric net and tied with thread to minimize physical damage coverage [18]. After intervals of 1, 2, 3, 5 7, 10, 15 days duration, the beads are removed from the soil, cleaned, and weighed again. Triplicate of each sample with different amount of beads will be done in order to gain higher accuracy and precisions.

2.1 Materials

The main ingredient, *cassava* starch powder, normally described as tapioca starch that contains 17 % of amylosewas was manufactured by Malaybis Sdn. Bhd., Kuala Lumpur while sodium alginate powder, a natural polysaccharide product extracted from brown seaweed was manufactured by Bis Chemicals Sdn. Bhd. which located in selangor as gelation ingredient. The active ingredient, urea powder was manufactured by Al Asia Chemical Industry Sdn. Bhd., Kuala Lumpur. Lastly, crosslinker calcium chloride powder was manufactured by Export Solution Sdn. Bhd., Selangor.

2.2 Synthesis of Starch-derivative-Alginate beads

The beads are synthesized with calculated volume of starch and alginate into hot distilled water and the content is agitated and uniform throughout for about 10 minutes [19]. Then the urea is added into the solution and stirred constantly to make sure there is no variation in concentration [19]. A syringe with needle size of 1.2 mm is placed into the mixture followed by suction until the syringe is sterility packaged. Beads are formed when it is added dropwise into 100ml of $CaCl_2$ cross-linker solution from a 30m height with moderate stirring [19]. Then, the beads are removed from cross-linker solution and cleansed by soaking them in water for 7 days. Oven is needed to dry all the beads at 30ºC for several days after purification. Beads are constantly weighed while drying until there is no further drop in mass and readily kept in airtight polyethylene bags.

Table 2 shows the four main factors which are mass concentration of cassava starch (g/ml), sodium alginate (g/ml), urea (g/ml) and concentration of calcium chloride cross-linker solution (M) and each one has 3 levels of low, moderate and high values set.

Table 2: Composition for 4 factors with 3 possible levels Taguchi method [14]**.**

Factor	Low (1)	Medium(2)	High (3)
Starch (g/ml)	0.04	0.08	0.16
Alginate (g/ml)	0.04	0.08	0.16
Urea (g/ml)	0.30	0.50	0.70
Crosslinker (M)	0.20	0.50	1.00

Based on Table 2, 4g of alginate and starch are mixed and dissolved in 20 ml of distilled water to make a maximum concentration of 0.2 g/ml. Next, 1kg of urea is dissolved in 1L of distilled water to give a maximum concentration of 1 g/ml with nitrogen content of 46%. The mass concentration is set to 0.04, 0.08 and 0.16 for starch and alginate, 0.3, 0.5 and 0.7 for mass concentration of urea while the concentration of corsslinker is set to 0.2, 0.5 and 1.0 as stated in journal papers to give best outcome in beads formation ranging from 0.1 M to 0.5 M [14]. The parameter to formulate 9 sets of sample (SA1 to SA9) is tabulated in Table 3 by using Taguchi method.

Table 3: Reaction Parameter for the Synthesis of Starch-Alginate beads [14]**.**

Experiments	Factors			
	Starch (g/ml)	**Sodium Alginate (g/ml)**	**Crosslinker (M)**	**Urea (g/ml)**
SA1	0.02	0.02	0.2	0.3
SA2	0.02	0.06	0.5	0.5
SA3	0.02	0.08	1.0	0.7
SA4	0.06	0.02	0.5	0.7
SA5	0.06	0.06	1.0	0.3
SA6	0.06	0.08	0.2	0.5
SA7	0.08	0.02	1.0	0.5
SA8	0.08	0.06	0.2	0.7
SA9	0.08	0.08	0.5	0.3

2.3 Preparation of Soil

Gardening soil is chosen as the material of incubation. In this paper, soil is obtained from Annway Garden Centre**,** Sunway and mix with 100mL of waterwater treatment sludge due to the simulation of real soil condition including the action of microorganisms [20]. Besides, soil is dried under the sun after mixing for 24hr. Next, it is sieved to less than 2mm and big pieces of solid such as crystals, pebbles and metals should be removed to produce a uniform soil inoculum [21].

2.4 Data Analysis of Biodegradability Rate

2.4.1 Determination of the Beads Size (mm) and Weight (g)

Beads are first removed from the oven after drying and measured using a vernier caliper. Diameter of the beads is taken at different position and average reading is calculated for each samples. The dried beads are weighed before and after burying in the soil. Weighing of the beads can be done by using weighing balance. The percentage weight loss can be obtained by the following eq. (1) [22]:

$$\text{Weight loss (\%)} = [(M_o - M_d) / M_o] \times 100 \qquad (1)$$

Where,
M_o = initial mass
M_d = degradation mass

4. Result & Discussion

4.1 Bead size measurement

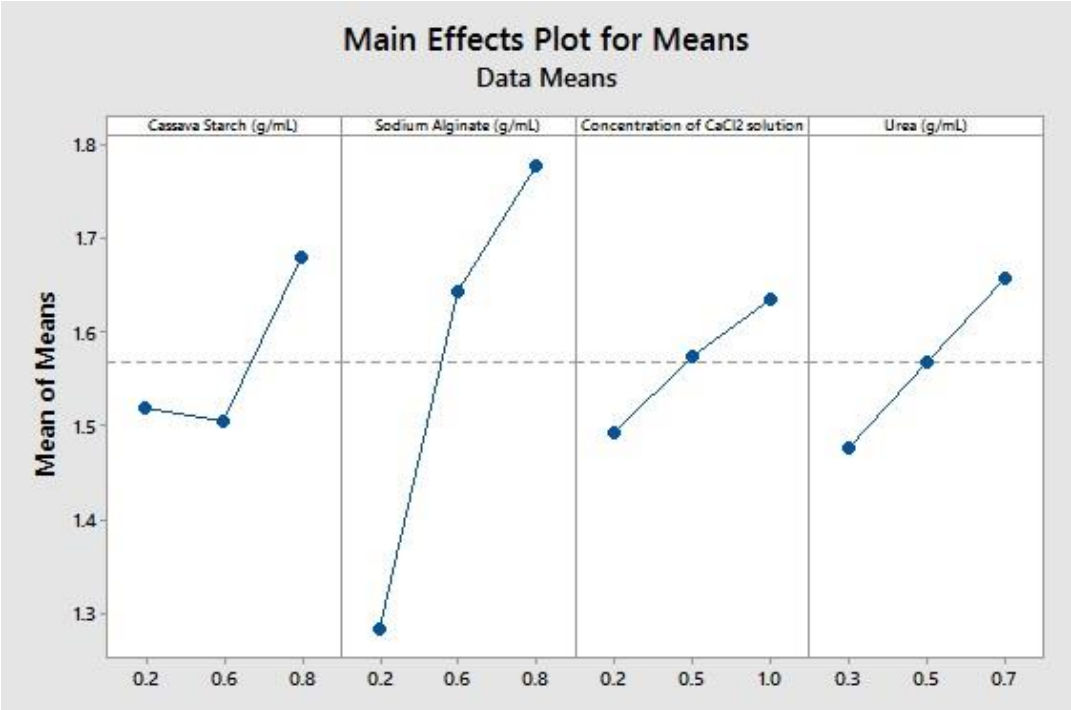


Figure 2: Taguchi Analysis Result of Bead Diameter with MiniTab 17.

Based on Figure 2, it is clearly shown that sodium alginate serves as the most significant factor in shaping of the beads as the graph shows a sharp increment of bounding line from 0.02 g/mL to 0.06 g/mL for sodium alginate. Beads are formed in spherical shape for higher content of sodium alginate. However, beads that contain low concentration of sodium alginate such as SA1, SA4 and SA7 give asymmetrical shape and they are very gummy even after being air-dried for 24hr which makes them tougher to pull apart from each other. Without sodium alginate, it is almost impossible to obtain perfect spherical shape even with high content of starch and $CaCl_2$ crosslinker. This is because the carbonyl group of the sodium alginate acts as a support and forms bond between the hydroxyl group and Ca^{2+} ion which are obtained from starch and $CaCl_2$ crosslinker respectively [14]. On the other hand, urea which consists of a pair of valence electrons also reacts with carbonyl group of sodium alginate to form hydrogen bond between them. Nevertheless, Ca^{2+} ion produces greater hydrogen bonding with carbonyl group as compared to urea in this case.

4.2 Weight loss analysis

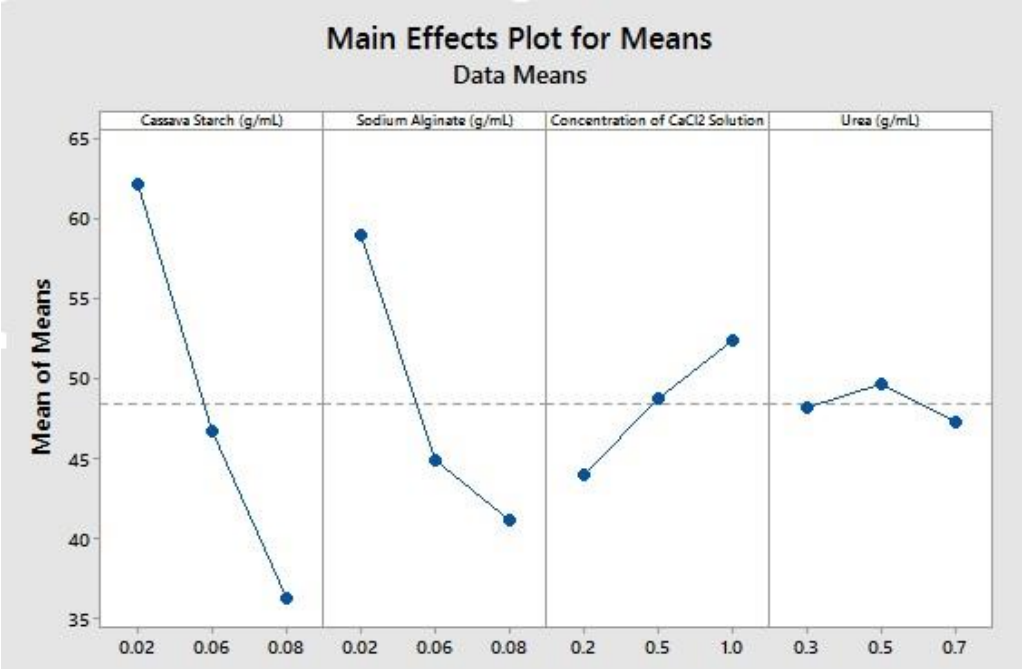


Figure 3 Taguchi Analysis Result of Biodegradability of Starch-Derivative-Alginate beads with MiniTab 17.

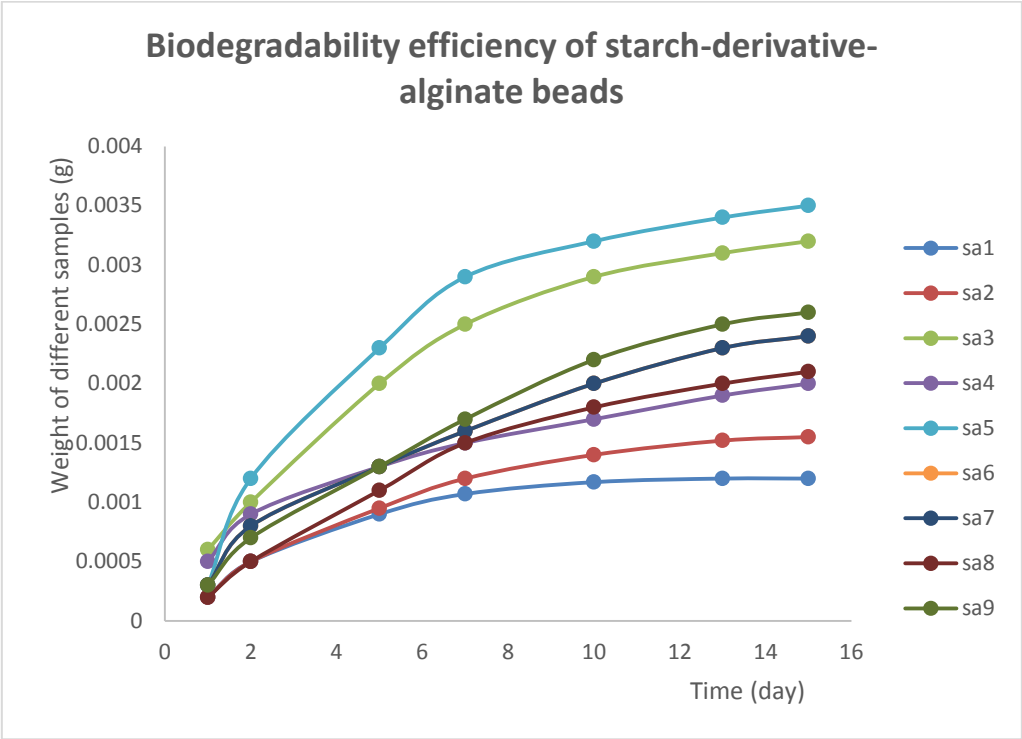


Figure 4: Biodegradability efficiency of starch-derivative-alginate beads throughout 15 days.

Waste water treatment sludge generally contains various types of microorganism which contributes to the presence of biodegradation. Based on Figure 4**,** it shows that starch-derivative-alginate beads are readily used as a carbon source by microorganisms. It can be observed that there is a steady increment in the weight loss with increasing time. At the 15th day, the percentage of biodegrading for SA1 was found to be 92.3%. In general, the biodegradation mostly occurs in the unstructured areas due to the greater mobility of the chains and hence, higher accessibility to the microorganism [23]. Based on Figure 3, the phenomena explains with lower concentration of sodium alginate, such as SA1, SA4 and SA7 which give irregular shape and make them more destructible and therefore, higher degree of biodegradability. The degradation of starch might be devoted to its crystallinity and hydrophobicity nature which allows outbreak from the microbial at the same time enhancing the rate of biodegradation [23]. However, the observed higher starch and sodium alginate content reduces the biodegradation rate in soil because the anionic polymer increasing the number of polar chains causing greater intermolecular interaction between sodium alginate and starch macromolecular and hence, starch and alginate hold tightly together at the same time retard the penetration of microorganisms into the surface [23]. Both the components form strong hydrogen bond between carbonyl group of the sodium alginate and hydroxyl group from the starch. On the other hand, the increase in alginate content is observed with lower biodegradability. This may be attributed to the increase in crosslinking between the alginate and Ca^{2+} ion in the beads which results into a more compact structure and hence leading to slow biodegradation [14]. On top of that, increasing the concentration of $CaCl_2$ improves the biodegradability as it is highly soluble and it attracts the microorganisms to penetrate the surface. As for urea, the degree of biodegradation seems to be the highest at the concentration of 0.5 g/m. In fact, 2nd amines group with N-H bend should be increase with increasing of urea concentration and hence, increasing the biodegradability [23]. Some errors might be encountered while conducting the experiment.

7. Conclusions

In conclusion, starch has become the focus of biodegradable material as it is renewable, inexpensive and can be easily obtained from plant with no releasing of chemical which gives zero pollution to the environment. The combination of alginate and starch offers the opportunity for testing bead coating in CRF application. In this context, biodegradation test is carried out to investigate the by soil burial test. It has been found that SA1 has the highest rate of biodegration which is 92.7% at the 15th day with cassava starch content of 0.02 g/mL, sodium alginate content of 0.02 g/mL, 0.2 M of calcium chloride and 0.3 g/mL of urea. Results of bead diameter and biodegradability properties are majorly depending on the concentration of cassava starch and sodium alginate.

References

[1] M. Zhang, B. Gao, J. Chen, Y. Li, A. E. Creamer, and H. Chen, "Slow-release fertilizer encapsulated by graphene oxide films," *Chem. Eng. J.*, vol. 255, pp. 107–113, 2014.

[2] Y. Zhang, F. Wu, L. Liu, and J. Yao, "Synthesis and urea sustained-release behavior of an eco-friendly superabsorbent based on flax yarn wastes," *Carbohydr. Polym.*, vol. 91, no. 1, pp. 277–283, 2013.

[3] Y. Xu, P. McNamara, Y. Wu, and Y. Dong, "An econometric analysis of changes in arable land utilization using multinomial logit model in Pinggu district, Beijing, China," *J. Environ. Manage.*, vol. 128, pp. 324–334, 2013.

[4] B. Ni, M. Liu, and S. Lü, "Multifunctional slow-release urea fertilizer from ethylcellulose and superabsorbent coated formulations," *Chem. Eng. J.*, vol. 155, no. 3, pp. 892–898, 2009.

[5] "EMISSIONS OF GREENHOUSE GASES IN THE U. S.," *US department of energy*, 2011. [Online]. Available: http://www.eia.gov/environment/emissions/ghg_report/ghg_nitrous.cfm. [Accessed: 15-Jun-2015].

[6] R. Dupas, M. Delmas, J.-M. Dorioz, J. Garnier, F. Moatar, and C. Gascuel-Odoux, "Assessing the impact of agricultural pressures on N and P loads and eutrophication risk," *Ecol. Indic.*, vol. 48, pp. 396–407, 2015.

[7] M. Tomaszewska and A. Jarosiewicz, "Polysulfone coating with starch addition in CRF formulation," *Desalination*, vol. 163, no. 1–3, pp. 247–252, 2004.

[8] B. Singh, D. K. Sharma, and A. Gupta, "In vitro release dynamics of thiram fungicide from starch and poly(methacrylic acid)-based hydrogels," *J. Hazard. Mater.*, vol. 154, no. 1–3, pp. 278–286, 2008.

[9] F. P. La Mantia, R. Arrigo, and M. Morreale, "Effect of the orientation and rheological behaviour of biodegradable polymer nanocomposites," *Eur. Polym. J.*, vol. 54, pp. 11–17, May 2014.

[10] H. Tian, Z. Tang, X. Zhuang, X. Chen, and X. Jing, "Biodegradable synthetic polymers: Preparation, functionalization and biomedical application," *Prog. Polym. Sci.*, vol. 37, no. 2, pp. 237–280, 2012.

[11] A. K. Lau, W. W. Cheuk, and K. V Lo, "Degradation of greenhouse twines derived from natural fibers and biodegradable polymer during composting.," *J. Environ. Manage.*, vol. 90, no. 1, pp. 668–71, Jan. 2009.

[12] Y. M. Z. Ahmed, E. M. M. Ewais, and S. M. El-Sheikh, "Potato starch consolidation of aqueous HA suspension," *J. Asian Ceram. Soc.*, vol. 3, no. 1, pp. 108–115, 2015.

[13] P. Lertsutthiwong, K. Noomun, N. Jongaroonngamsang, P. Rojsitthisak, and U. Nimmannit, "Preparation of alginate nanocapsules containing turmeric oil," *Carbohydr. Polym.*, vol. 74, no. 2, pp. 209–214, 2008.

[14] B. Singh, D. K. Sharma, and A. Gupta, "A study towards release dynamics of thiram fungicide from starch-alginate beads to control environmental and health hazards," *J. Hazard. Mater.*, vol. 161, no. 1, pp. 208–216, 2009.

[15] H. S. Cho, H. S. Moon, M. Kim, K. Nam, and J. Y. Kim, "Biodegradability and biodegradation rate of poly(caprolactone)-starch blend and poly(butylene succinate) biodegradable polymer under aerobic and anaerobic environment," *Waste Manag.*, vol. 31, no. 3, pp. 475–480, 2011.

[16] F. Flores Céspedes, S. Pérez García, M. Villafranca Sánchez, and M. Fernández Pérez, "Bentonite and anthracite in alginate-based controlled release formulations to reduce leaching of chloridazon and metribuzin in a calcareous soil," *Chemosphere*, vol. 92, no. 8, pp. 918–924, 2013.

[17] E. Bååth and T. H. Anderson, "Comparison of soil fungal/bacterial ratios in a pH gradient using physiological and PLFA-based techniques," *Soil Biol. Biochem.*, vol. 35, no. 7, pp. 955–963, 2003.

[18] Z.-H. Hu, G. Wang, and H.-Q. Yu, "Anaerobic degradation of cellulose by rumen microorganisms at various pH values," *Biochem. Eng. J.*, vol. 21, no. 1, pp. 59–62, 2004.

[19] K. Muda, A. Aris, M. R. Salim, Z. Ibrahim, M. C. M. van Loosdrecht, M. Z. Nawahwi, and A. C. Affam, "Aggregation and surface hydrophobicity of selected microorganism due to the effect of substrate, pH and temperature," *Int. Biodeterior. Biodegradation*, vol. 93, pp. 202–209, 2014.

[20] Astm, "Standard Test Method for Determining Aerobic Biodegradation of Plastic Materials in," *Astm D5988 − 12*, pp. 1–6, 2014.

[21] Suherman and D. D. Anggoro, "Producing Slow Release Urea by Coating with Starch/Acrylic Acid in Fluid Bed Spraying," *Int. J. Eng. Technol.*, vol. 11, no. 6, pp. 77–80, 2011.

[22] B. Azeem, K. Kushaari, Z. B. Man, A. Basit, and T. H. Thanh, "Review on materials & methods to produce controlled release coated urea fertilizer," *J. Control. Release*, vol. 181, no. 1, pp. 11–21, 2014.

[23] I. M. Thakore, S. Desai, B. D. Sarawade, and S. Devi, "Studies on biodegradability, morphology and thermo-mechanical properties of LDPE/modified starch blends," *Eur. Polym. J.*, vol. 37, no. 1, pp. 151–160, 2001.

Capturing Cold Energy from Regasification of LNG

Yi Jin Tan[*], Mushtak Al-Atabi[2], Veena A Doshi Arun Kumar Doshi[3]
[1,2,3]*School of Engineering, Taylor's University, Malaysia*

[*]tan_yijin@hotmail.com
[2]mushtak.t@taylors.edu.my

Abstract
Natural gas is known as the clean fuel due to its low emission. For transportation, natural gas are often liquefied into liquefied natural gas (LNG). During the regasification, tremendous amount of cold is released. Recent innovation designed a LNG refrigerated vehicle to utilize LNG as both fuel and refrigerant. Due to fluctuation of LNG flowrate, a cold storage system (CSS) is required. For this research, PCM is used and heat transfer properties of the discharge process is the focus of this research. $CaCl_2$, $Mg(NO_3)_2$, K_2CO_3 eutectic water-salt PCM are chosen based on safety, health and environmental concerns. A tube in a tank design and its effectiveness is measure as a heat exchanger. Though UniSim simulation, the cold generated by LNG is 260% more than sufficient. Samples of PCM were prepared by mixing salt in distilled water then analysed with DSC. Result shows that $Mg(NO_3)_2$ has the most suitable phase change temperature for food refrigeration purpose at -25.92 ^oC and the highest energy density which is 165.28 J/kg. Discharge process shows that the effectiveness NTU of $CaCl_2$, $Mg(NO_3)_2$ and K_2CO_3 are 0.5146, 0.4880 and 0.5053 respectively. $Mg(NO_3)_2$as PCM is suitable for the CSS facility of a LNG refrigerated vehicle.

Keywords: Liquefied Natural Gas, Phase Change Material, Effectiveness NTU, LNG Refrigeration Vehicle, Heat Transfer.

Nomenclature

$Cp,_{HTF}$	Specific Heat Capacity of HTF (J/kg K)
CSS	Cold Storage System
HTF	Heat Transfer Fluid
LHCES	Latent Heat Cold Energy Storage
LNG	Liquefied Natural Gas
m_{HTF}	Mass of HTF (kg)
NG	Natural Gas
NTU	Number of Transfer Unit
PCM	Phase Change Material
Q_{Actual}	Actual Cold Discharged (J)
$Q_{Theoretical}$	Theoretical Cold Discharged (J)
TES	Thermal Energy Storage
$Tw,_f$	Final Temperature of HTF (K)
$Tw,_i$	Initial Temperature of HTF in (K)
ε	Effectiveness NTU

1. Introduction

Nature gas (NG) is commonly known as clean fuel due to its lower emission compared to the other source of fuel such as petroleum and diesel. However, NG comes in gas form that occupy large volume of space which causes difficulties in transportation from the extraction site to user. To improve transport efficiency, one of the few methods is to convert NG to liquefied natural gas (LNG) by cooling NG to -160^{o}C at pressure slightly lower than atmospheric pressure. In the process of liquefaction, large amount of electrical energy is used to reduce the volume of NG by folds. However, prior distribution to customers, LNG needs to be regasified and the process releases tremendous amount of cold, as much as 240 kWh per tonne of LNG, and the global LNG trade is expected to double in 2030 to 500 million tonnes per year, equivalent to fourteen 1GW nuclear plant [1]. Instead of releasing these energy to the environment, a better approve is to capture, store or utilize these cold. In recent years, many researches has been developing new methods to utilize cold energy, such as generating electricity through the Rankine, Bryaton and Kalina cycle [2], greenhouse gaseous sequestration [3], and the desalination of seawater [4]. Although most of these researches focus on the utilization of cold energy in a large scale, it is also important to scale down the process to improve efficiency at its fundamental.

In year 2010, an innovative design of a refrigerant vehicle is developed by Tan et al. [5] to utilize LNG in the process. This vehicle uses LNG as both refrigerant and fuel, providing cold to the refrigeration space in the process of regasification and uses the NG, product of regasification, to power the engine of the vehicle as shown in Fig. 1. Through simulation using Honeywell's UniSim software, the amount of cold generated by regasification of LNG based on the fuel consumption of a refrigeration vehicle is more than sufficient to maintain the temperature of the vehicle's refrigeration space. Despite the large amount of cold generated from regasification of LNG, the energy flux fluctuate along with the fuel consumption of the vehicle, which mean cold is generated during the drive but none when the engine is turned off. Due to this issue, the LNG refrigerated vehicle requires a cold storage system (CSS) to manage the cold released from the regasification of LNG. Apart from managing the

cold, CSS also avoid unhelpful or harmful cooling caused by LNG. Therefore, the need for a system to control and balance cold energy between supply and demand is unavoidable.

One of the most common CSS method is the latent heat cold energy storage (LHCES) that uses solid-liquid phase change material (PCM) to store energy and release the required amount when needed. Solid-liquid PCM is liquid in room condition, changes to solid when exposed to cold and back into liquid when the stored cold is released. The melting and freezing of PCM gives PCM the advantage store large amount of energy in small temperature change. Due to these advantages, PCM became very important in field of thermal energy storage (TES), to conserve and adjust energy difference between supply and demand, or for peak shaving. In the pass decades, PCM has been used for many applications such as energy storage [6], building cooling [7], heat storage system in solar power generation [8] etc.

In recent years, many researches has been conducted on PCM to improve its performance in respective applications. Tan et al. uses water as PCM to perform the thermal resistance analysis for food transportation [9]. Altohamy et al. added Al_2O_3 nanoparticle in PCM to improve the thermal properties for air conditioning system [10]. Chandrasekaran et al. similarly conducted the same experiment with CuO additive [11]. As for He et al. measure multiple thermal properties such as thermal conductivities, supercooling etc of $BaCl_2/H_2O$ PCM solution for the application in refrigeration system [12]. Oro et al. on the other hand conducted corrosion analysis on multiple PCM solutions for food transportation and storage application [13].

Despite have many type of PCM available in the market, researches investigating the CSS in LNG refrigerated vehicle uses pure water as PCM in the design. Generally, PCM are classified into organic and inorganic PCM, then both of these PCM are further divided into eutectic and mixture PCM. In the work of Li et al. [14], an excellent PCM satisfy the following conditions: proper phase change temperature, large fusion heat, excellent cycling stability, high thermal conductivity, low super cooling, chemically stable, easy to manufacture and cheap. However, there is no ideal PCM that satisfied all of the above mentioned properties. Instead, these properties are simplified into 3 positive and 3 negative properties, being thermal conductivity, fusion heat and density as positive properties; corrosion, supercooling and flammability as negative properties. In this research, the eutectic water-salt solution is selected as the scope of investigation due to its high fusion heat and suitable phase change temperature despite having issues with phase separation and supercooling.

In a list of commercialized eutectic water-salt solution for sub-zero applications, a few PCM are selected for the application in the CSS of LNG refrigerated vehicle. $CaCl_2$, K_2CO_3 and $Mg(NO_3)_2$ water-salt solution is selected considering safety, health and environmental condition. The selected PCM all have relatively less hazardous properties compared to the other PCM in the list of commercialized eutectic water-salt solution for sub-zero applications. Moreover, these PCM has phase change temperature lower than water, which are -55 ^oC, -36.5 ^oC and -29 ^oC respectively, making it more suitable to capture the energy release by LNG at -160 ^oC. In addition, these PCM also have higher fusion heat compared to water, which is 163.93 kJ/kg, 165.36 kJ/kg and 186.93 kJ/kg respectively. Being one of the

main positive properties, heat transfer is one of the most famous topic in the study of PCM, the LNG refrigerant vehicle is not exceptional. Thus in this research, the heat transfer properties of the 3 PCM in a simple shell and tube heat exchanger is investigated to obtain the most suitable PCM for the LNG refrigerated vehicle.

2. Experimental Setup

2.1. LNG Refrigerated Vehicle

A schematic diagram of a the LNG refrigerated vehicle along with its adopted CSS that is patented in 2010 by Tan et al. [5] is shown in Fig 1. In this system, LNG, stored in the fuel storage tank which is essentially a Dewar to prevent boil off, flows into the CSS controlled by the valve box. The CSS is a heat transfer tank filled with PCM will be cooled and solidified by the energy emitted by the flowing LNG. In exchange, LNG absorb the heat from the CSS to raise its temperature and eventually vaporizes into gas. However at this refrigerated condition, usually 20 ^{o}C, the fuel is not suitable to be used as in a motor engine for combustion, thus, it is superheated in a heat exchanger, then flows into the engine at normal condition.

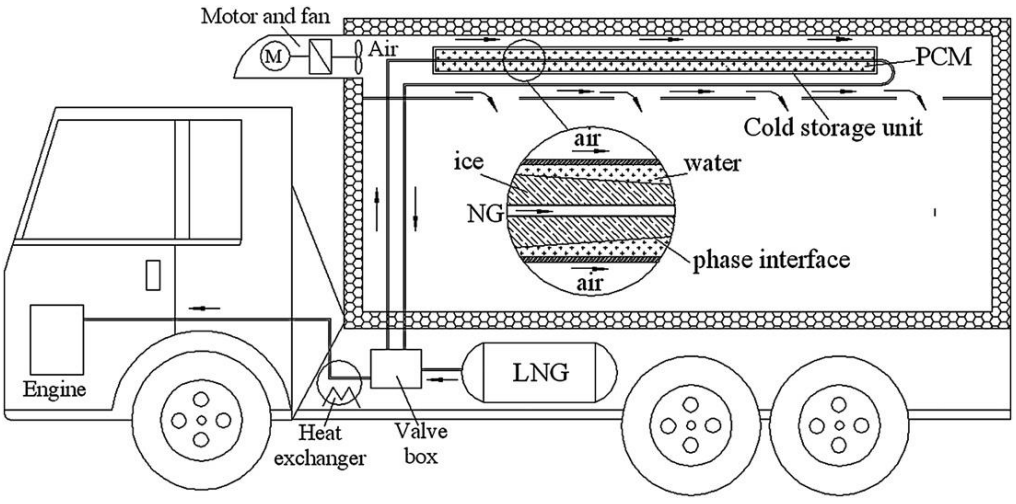


Figure 1. Schematic diagram of LNG refrigerated vehicle

2.2. Simulation of Cold Generated from LNG

The simulation of cold generated from LNG is performed using the UniSim software developed by Honeywell. A diagram of the simulation environment is shown in Fig. 2. In the simulation methane (CH_4) is used as the working fluid of the system. As for fluid package, the Peng-Robinson package is used because the system only contain hydrocarbons. In the simulation environment, a heater is used to represent the CSS unit in the LNG refrigerated vehicle. The feed condition of methane is set to the condition of LNG, which is -162 ^{o}C and atmospheric pressure at 101.325 kPa. The flowrate of the feed is 123 kg/hr of pure methane, having equivalent heating value to the average fuel consumption of a basic enclosed van as reported by Gaines et al. [15]. At the outlet, the temperature is set to -25 ^{o}C when the system achieved thermal equilibrium with the condition of the refrigerated space.

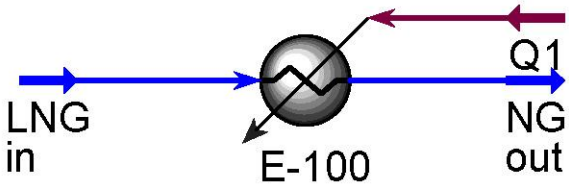


Figure 2. Simulation environment of cold generation of LNG

2.3. Sample Preparation

PCM used in this research are $CaCl_2/H_2O$, $Mg(NO_3)_2/H_2O$, and K_2CO_3/H_2O eutectic water-salt solution. These PCM are prepared by dissolving the respective salt into distilled water. Salt are purchased from Evergreen, $CaCl_2$ and K_2CO_3 being anhydrous salt while $Mg(NO_3)_2$ is purchased in the hexahydrate form. The weight of salt added into distilled water is based on the eutectic point of respective salt. 1.5 litres of each PCM samples are transferred into the test rig and cooled to approximately -60 ^oC in a cooler box using dry ice as the cooling source.

2.4. Differential Scanning Calorimeter (DSC)

The phase change temperature of the selected PCM are analysed using the DSC model DSC 8500 by PerkinElmer. 9-12 mg of each sample is sealed in an aluminium sample pan using a crimper and transfer into the DSC, blanketed with platinum disc. Cooling is supplied to the DSC using IntraCooler II to supply cooling as low as -100 ^oC. The analysing method is performed from -70 ^oC to 25 ^oC at a rate of 10 ^oC/min. Data recording is taken at an interval of 0.2 sec. The data recording and analysis is performed using Pyris Series – DSC 8500 software.

2.5. Experiment Apparatus and Procedures

A schematic diagram of the experiment apparatus is shown in Fig. 3. The setup consist of an insulated tank, water pump, PCM solidification test rig and temperature measuring apparatus. The insulation tank has inner dimension of 380 x 280 x 250 mm and insulated with 25 mm thick of polystyrene. The insulation tank is filled with 7 litres of water as heat transfer fluid (HTF). The HTF is circulated to increase heat transfer rate using a water pump capable of producing pressure equivalent to 0.85 mH_2O. The PCM solidification test rig is placed on the centre floor of the insulation tank, with inner dimension of 200 x 100 x 100 mm, made of 15 mm thick of mild steel. 4 temperature measurement points in the test rig, T_1, T_2, T_3 and T_4 is used for temperature recording, from the centre of the PCM solidification test rig towards the furthest end of the tank, at x = 0, 33.3, 66.6 and 100 mm using type T thermocouple. The temperature of HTF is measure as T_w.

The test rig is transferred to the insulation tank filled with HTF when the initial temperature is achieved. The PCM is left to discharge its energy and temperature reading is taken at an interval of 5 min until all the PCM melted.

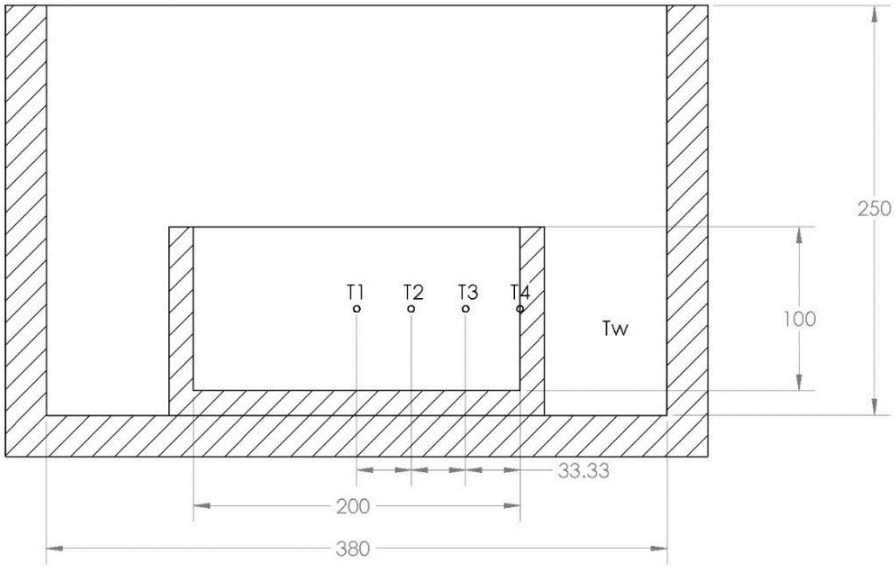


Figure 3. Schematic diagram of experiment apparatus

3. Result and Discussion

3.1. UniSim Simulation

Following the procedure from Sub-section 2.2 the amount of cold generated from heating of LNG from storage condition to refrigerated condition is approximately equals to 27 kW. As reported by Tassou et al. [16], the refrigeration duty to maintain a 90 m^3 rigid semi-trailer at 20 ^oC is 5250 W. In comparison to 27 kW, the cold generated from LNG consumption of a LNG refrigerated vehicle has as much as 260% excess energy to maintain a 90 m^3 refrigerated space at -20 ^oC and still allow a pinch temperature of 5 ^oC. Table 1 shows the result reported by Tassou et al. [16]. As seen from the table, energy released by LNG, 27 kW, is much more than sufficient to cool all truck type at a temperature well below needed, proving the efficiency of the innovation to use LNG as both fuel and refrigerant.

3.2. DSC Analysis

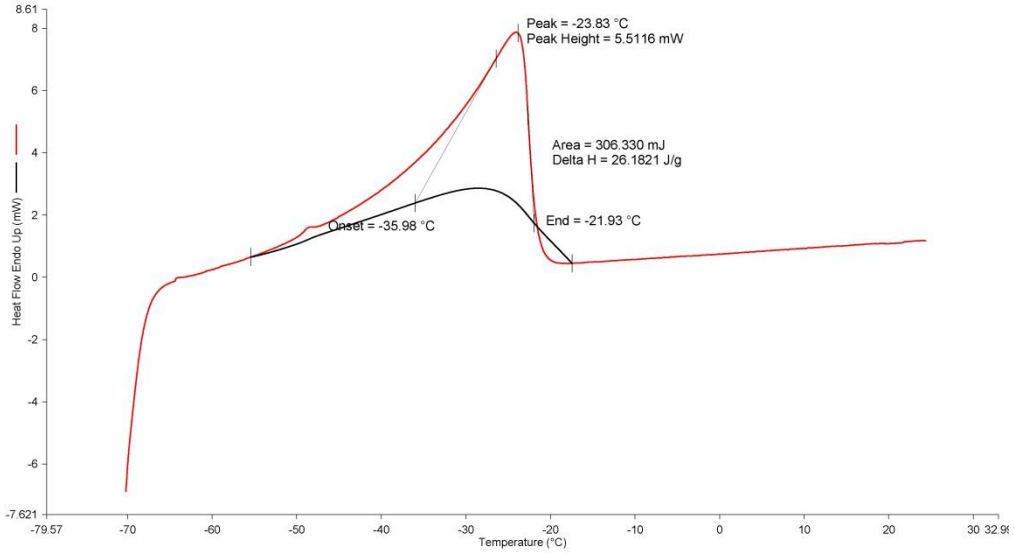
By completing the procedure from sub-section 2.4, analysis yields the graph of heating value against temperature of the PCM. Fig. 4 (a), (b) and (c) show the obtained result from DSC analysis. Since curve (a) and (b) do not have obvious peak, the curves are analysed using the sigmoidal analysis method to calculate the peak height and the area under the curve. Curve (c) on the other hand has an obvious peak, thus it is analysed using the standard analysis method. Table 2 shows the summary of the melting temperature and the latent heat as obtained from these analysis. These graphs shows the onset, which is the temperate when the PCM start melting and the end, which is the final temperature where the last solid exist. Based on these information, it can be concluded that $Mg(NO_3)_2$ is most suitable for refrigeration space as the melting temperature range is most appropriate for food refrigeration, melting from -30.69 ^oC to -23.6 ^oC. As compared to water, the system with $Mg(NO_3)_2$ is able to maintain food in refrigerated space at a temperature well below 0 ^oC. At the

melting temperature, the energy storage system will release the most amount of energy to provide refrigeration for the food storage space.

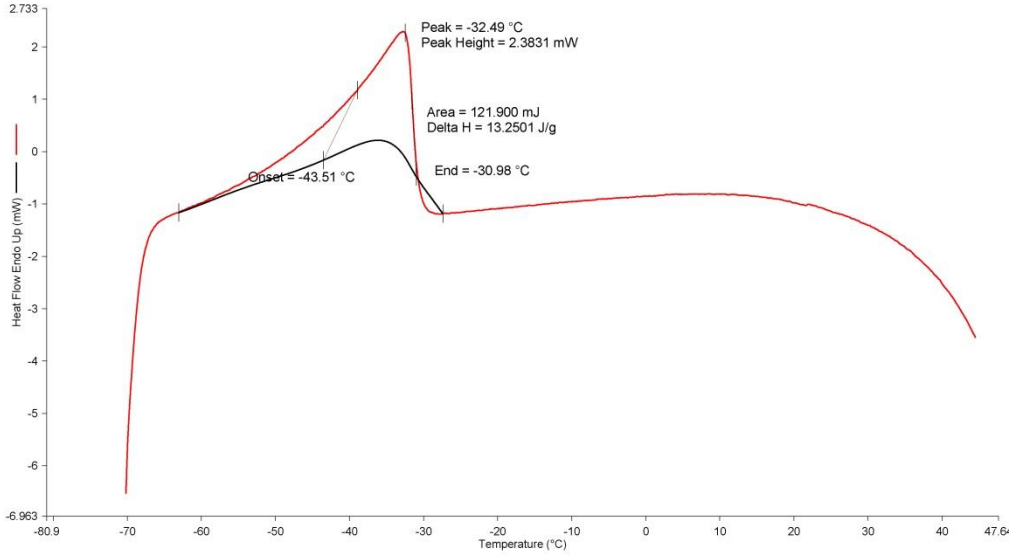
Another analysis conducted on the curves is to obtain the theoretical amount of energy used in the experiment conduct in sub-section 2.5. These temperature ranges are obtained after conducting the main experiment. The area under the curve representing the amount of heat provided by the heating furnace of the DSC to the sample and is shown in fig. 5. As seen from the figure, $Mg(NO_3)_2$ releases the most amount of energy as it melting from -60 ^oC until all of the material is melted, at 165.28 J/g.

Table 1. Refrigeration duties of self-contained mechanical transport food refrigeration units

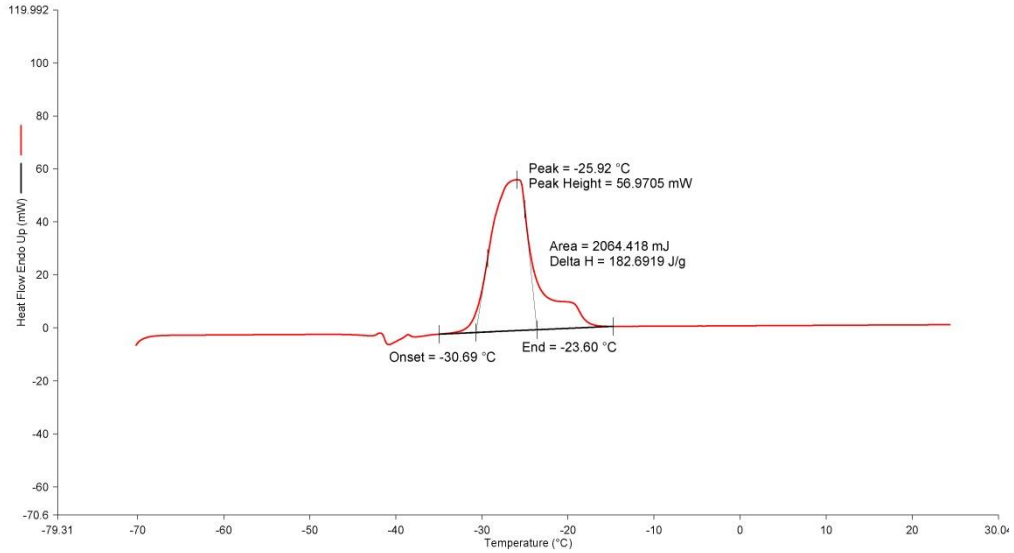
Body Length/Volume/Type	Minimum refrigeration duty (W) for ATP based on 0.4 W/m^2 K	
	-20 ^oC	0 ^oC
6 m/ 30 m^3/ Rigid Lorry	2380	1428
<9 m/ 30 m^3/ Rigid Lorry	3850	2310
13.6 m/ 90m^3/ Rigif Semi Trailer	5250	3150



(a)



(b)

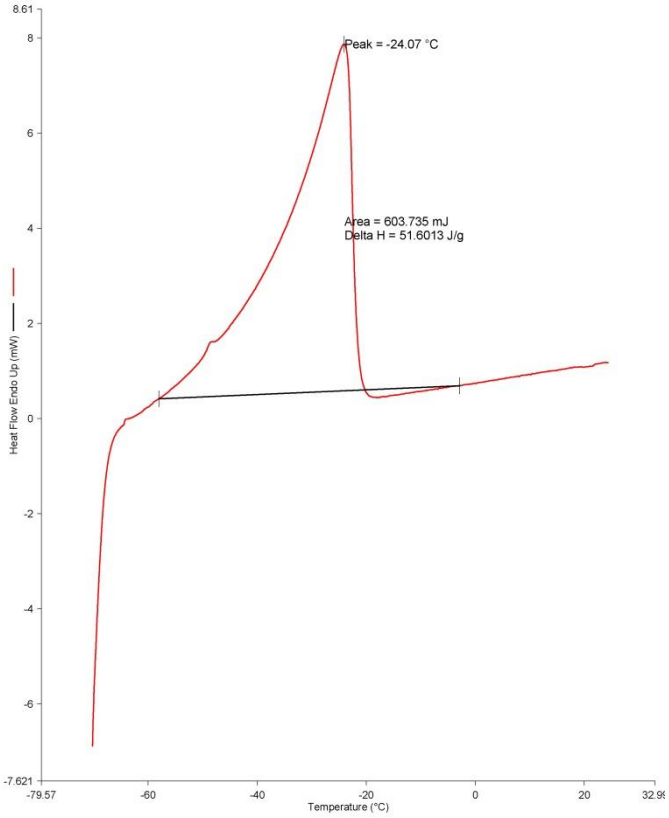


(c)

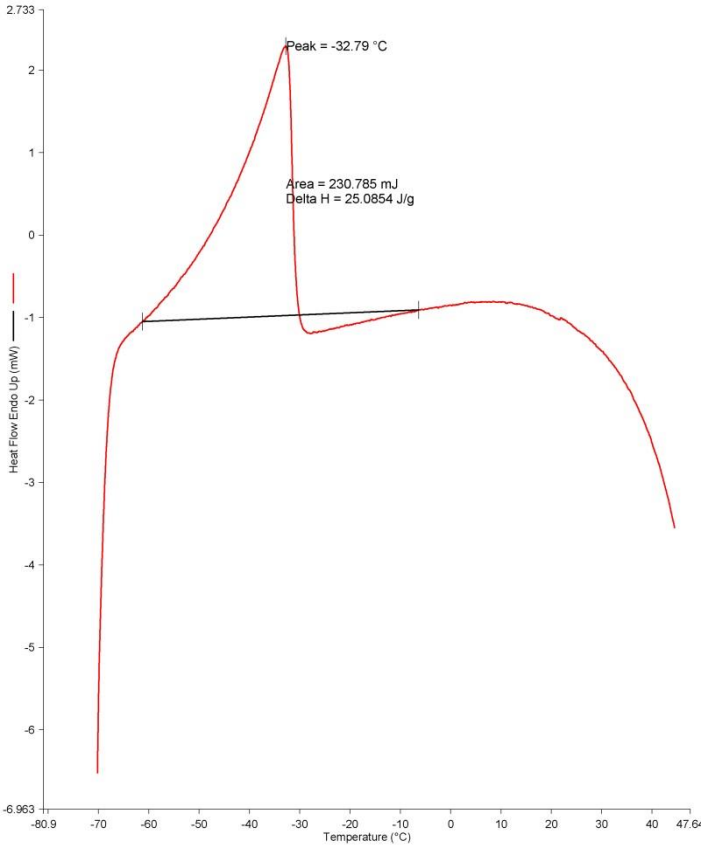
Figure 4. Melting temperature of (a) $CaCl_2$ (b) K_2CO_3 (c) $Mg(NO_3)_2$

Table 2. Melting temperature and latent heat of PCM

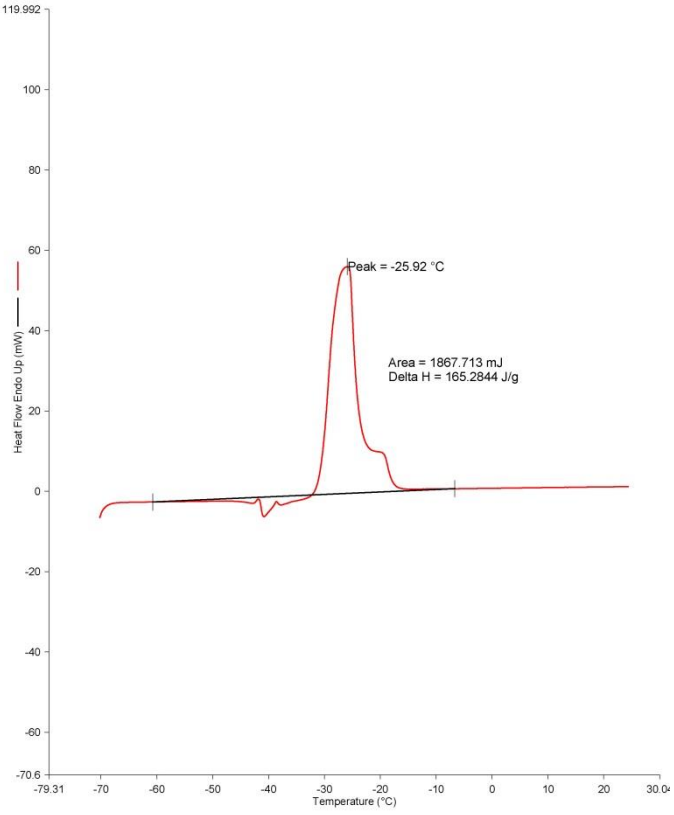
PCM	Melting Temperature (^oC)	Latent Heat (J/g)
$CaCl_2$	-32.49	25.09
K_2CO_3	-23.83	51.60
$Mg(NO_3)_2$	-25.92	165.28



(a)



(b)



(c)

Figure 5. Change in enthalpy of (a) $CaCl_2$ (b) K_2CO_3 (c) $Mg(NO_3)_2$

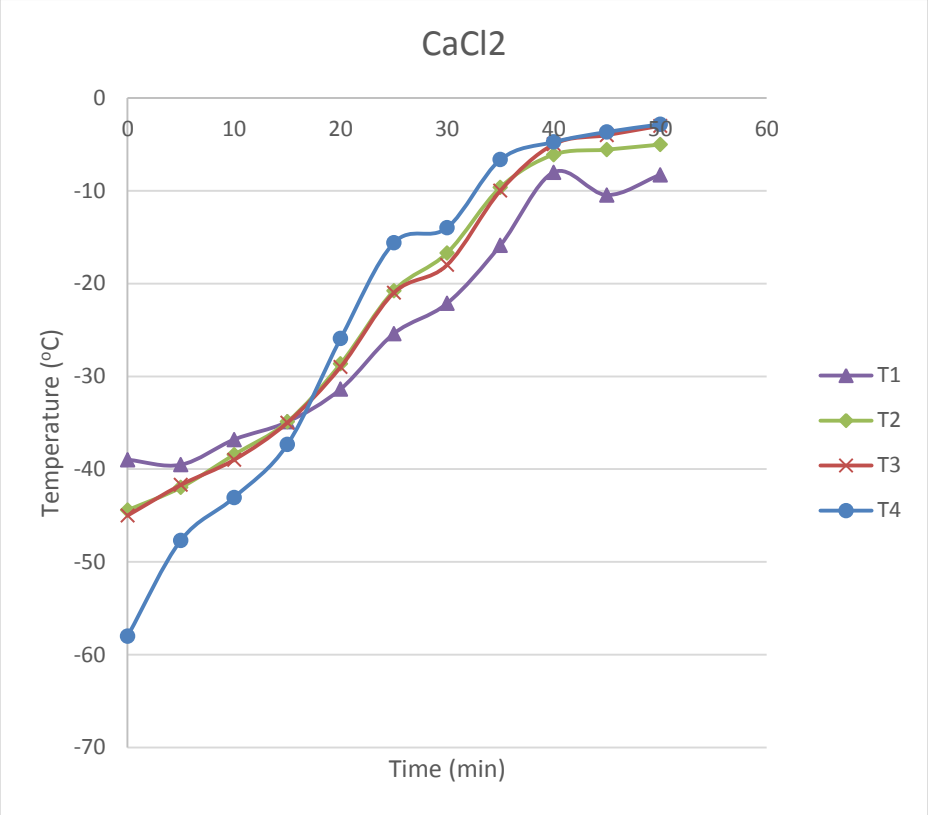
3.3. Effectiveness Number of Transfer Unit (NTU) Analysis

By completing the experiment in sub-section 2.2, the temperature distribution in the CSS and change in HTF temperature is obtained to calculate the effectiveness NTU of the CSS. Fig. 6 shows the temperature distribution of CSS with different PCM throughout the discharging process. Consistently, all experiments begin with similar temperature at position 4, which is approximately -60 ^{o}C. During the melting process, the temperature of the material in the test rig increase steadily towards the melting temperature and rapidly increase after the melting point. The graph shown in fig. 6 is essentially a typical temperature time curve of a melting process. At the initial stage, the curve increases steadily representing the sensible heating of the PCM as a solid, temperature flat out for a small amount of time, representing the latent heating of a melting process and the end of the curve representing the sensible heating of PCM as a liquid. Measurement of temperature of all three PCM follows the same increasing pattern for all points in the test rig. Fig. 6 (b) shows that the melting occur at -35 ^{o}C and a rapid raise in temperature after melting. Fig. 6 (c) on the other hand, also shows that melting occur at -35 ^{o}C and increase rapidly after melting. At time 55 to 65 min, T_1 and T_2 shows a rapid bounce in temperature, this is due to the floating of ice that happens to migrate to point 1 and 2 at the given time and causes the temperature fluctuation. The change in temperature against time at position 1 is shown in figure 7 to provide a clearer comparison between the different PCMs.

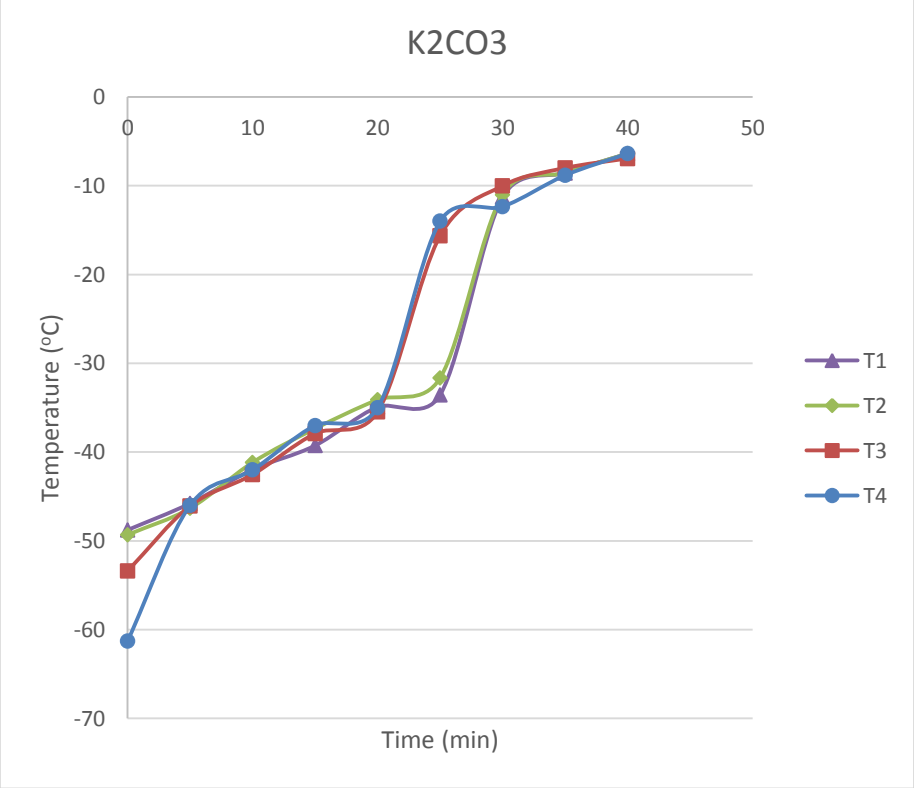
The PCM storage tank, absorbing the cold energy from LNG during the charging process and release cold during the discharging process is equivalent to a heat exchanger transferring heat energy between the PCM and HTF on the container surface. Therefore, the analytical method of the storage tank can be similar to a heat exchanger. In this research, the result is analysed using one of the most famous analytical method, which is the effectiveness NTU method to evaluate the performance of the system when the log mean temperature is not available. The effectiveness of a heat exchanger is define as the ratio of actual heat release to the theoretical heat release and is shown in the formula below.

$$\varepsilon = \frac{Q_{Actual}}{Q_{Theoretical}} = \frac{m_{HTF} C_{p,HTF} (T_{w,f} - T_{w,i})}{Q_{Theoretical}} \quad (1)$$

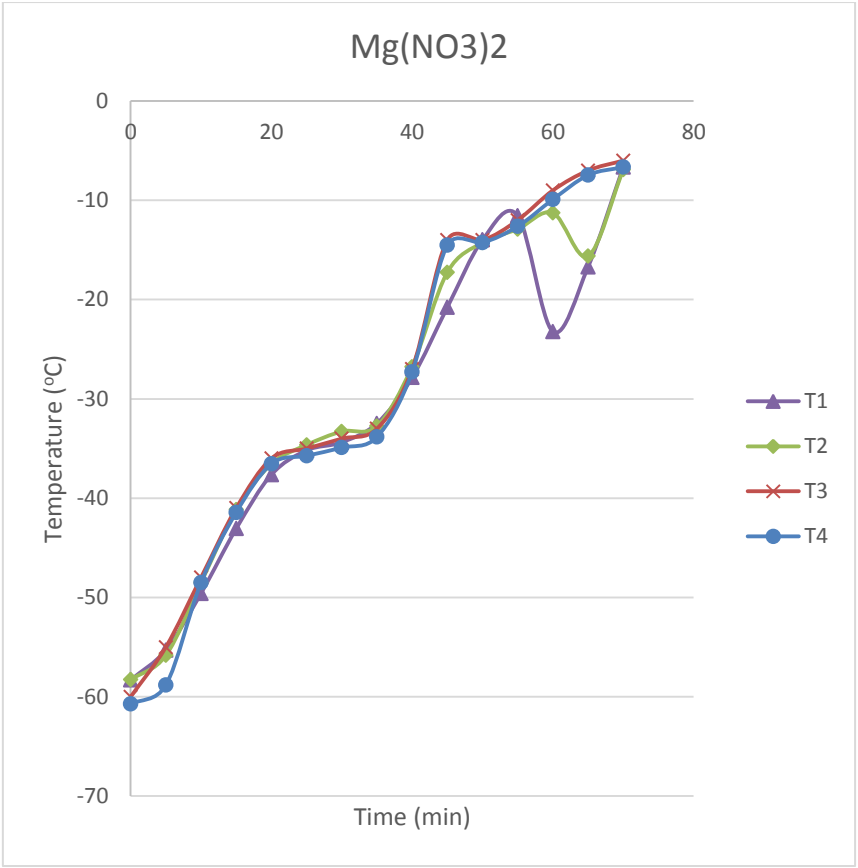
Where ε is the effectiveness NTU, Q_{Actual} is the actual cold discharged from CSS in J, $Q_{Theoretical}$ is the theoretical cold released by the system in J, m_{HTF} is the mass of HTF in kg, $Cp_{,HTF}$ is the specific heat capacity of HTF in J/kg K, $Tw_{,f}$ is the final temperature of HTF in K and $Tw_{,i}$ is the initial temperature of the HTF in K. By calculation, it is found that the effectiveness NTU of $CaCl_2$, $Mg(NO_3)_2$, K_2CO_3 are 0.5146, 0.4880 and 0.5053 respectively, which indicates that the CSS with $CaCl_2$ has the best effectiveness. However, $Mg(NO_3)_2$ is merely slightly less effective, considering on the justification on melting temperature and energy storage density, is can be concluded that the most suitable PCM to be adopted in the CSS of an LNG refrigerated vehicle is $Mg(NO_3)_2$.


CaCl2
0
-10
-20
-30
-40
-50
-60
-70
0
10
20
30
40
50
60
Temperature (°C)
Time (min)
T1
T2
T3
T4

(a)


K2CO3
0
-10
-20
-30
-40
-50
-60
-70
0
10
20
30
40
50
Temperature (°C)
Time (min)
T1
T2
T3
T4

(b)



(c)

Figure 6. Temperature of (a) $CaCl_2$ (b) K_2CO_3 (c) $Mg(NO_3)_2$ during the discharging process

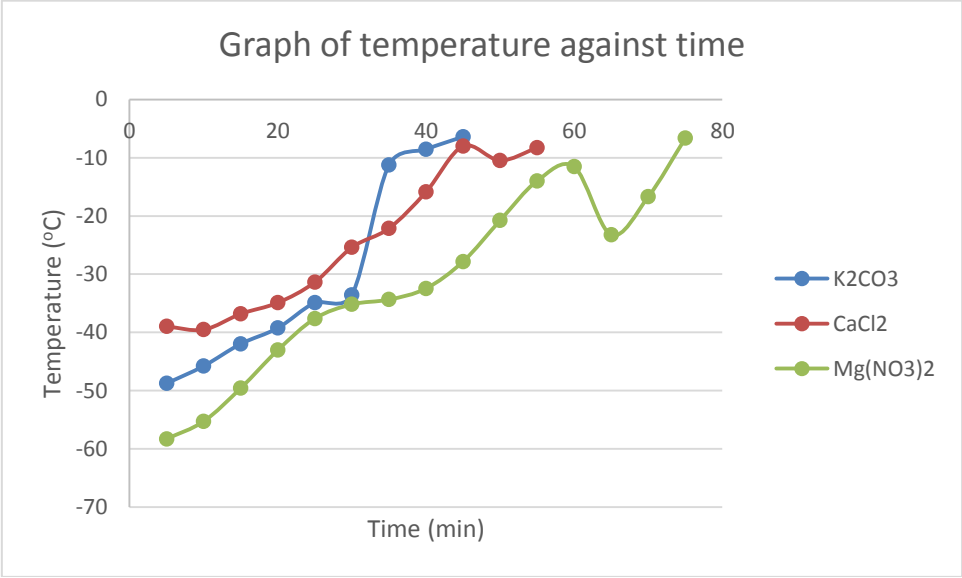


Figure 7. Graph of temperature against time

4. Conclusion

In this research work, PCM material used in the CSS of a LNG refrigerated vehicle is studied. The research treat the CSS as a heat exchanger and focuses on the

heat transfer properties of the discharging process where energy is release to refrigerate an enclosed volume for food transportation purposes. Though UniSim simulation, the cold generated by LNG is 260% more than sufficient to cool the refrigerated space. 3 PCM were tested in the experiment to characterize the behaviour of these PCM in the adaptation on CSS. The DSC result shows that $CaCl_2$, K_2CO_3, $Mg(NO_3)_2$ has latent heat of 25.09, 51.6, 165.28 J/kg respectively and melting temperature of -32.49, -23.83, -25.92 ^oC respectively. Through the discharging process, the effectiveness NTU of $CaCl_2$, K_2CO_3, $Mg(NO_3)_2$ are 0.5146, 0.4880 and 0.5053 respectively. This shows that $Mg(NO_3)_2$ has the largest latent heat and the most suitable melting temperature for the application of food refrigeration and $CaCl_2$ has the best effectiveness in the CSS of a LNG refrigerated vehicle. A good PCM would have fulfilled all the criteria, however in this case, since $Mg(NO_3)_2$ inherit most of the positive properties, it is safe to conclude that the $Mg(NO_3)_2$ is the most suitable PCM to be adopted into the CSS of LNG refrigerated vehicle. As for future work, one shall consider the use of additive in $Mg(NO_3)_2$ water-salt solution or a different tank design to increase heat transfer effectiveness of the CSS in LNG refrigeration vehicle.

Acknowledgment

The authors gratefully acknowledge the Ministry of Education Malaysia, Fundamental Research Grant Scheme (Grant no: 320201-TK61-321-C31), School of Engineering of Taylor University, School of Bioscience of Taylor's University for the usage of DSC, KGC Resources Sdn Bhd for the design of the test rig, Alpha Gas Solution Sdn Bhd as the supplier of dry ice and Evergreen Engineering & Resources as the supplier of chemical.

References

[1] Dearman Company, *The Cold Economy*. 7 Henrietta Street, 2014.

[2] M. Romero Gómez, R. Ferreiro Garcia, J. Romero Gómez, and J. Carbia Carril, "Review of thermal cycles exploiting the exergy of liquefied natural gas in the regasification process," *Renew. Sustain. Energy Rev.*, vol. 38, pp. 781–795, 2014.

[3] A. Alabdulkarem, Y. Hwang, and R. Radermacher, "Energy consumption reduction in CO 2 capturing and sequestration of an LNG plant through process integration and waste heat utilization," *Int. J. Greenh. Gas Control*, vol. 10, pp. 215–228, 2012.

[4] W. Cao, C. Beggs, and I. M. Mujtaba, "Theoretical approach of freeze seawater desalination on flake ice maker utilizing LNG cold energy," *Desalination*, vol. 355, pp. 22–32, 2015.

[5] H. Tan, Y. Li, H. Tuo, M. Zhou, and B. Tian, "Experimental study on liquid/solid phase change for cold energy storage of Liquefied Natural Gas (LNG) refrigerated vehicle," *Energy*, vol. 35, no. 5, pp. 1927–1935, 2010.

[6] A. Sarı, C. Alkan, and A. N. Özcan, "Synthesis and characterization of micro/nano capsules of PMMA/capric–stearic acid eutectic mixture for low

temperature-thermal energy storage in buildings," *Energy Build.*, vol. 90, pp. 106–113, 2015.

[7] J. Zhang, X. Guan, X. Song, H. Hou, Z. Yang, and J. Zhu, "Preparation and properties of gypsum based energy storage materials with capric acid–palmitic acid/expanded perlite composite PCM," *Energy Build.*, vol. 92, pp. 155–160, 2015.

[8] F. C. Porisini, "Salt hydrates used for latent heat storage: Corrosion of metals and reliability of thermal performance," *Sol. Energy*, vol. 41, no. 2, pp. 193–197, 1988.

[9] H. Tan, C. Li, and Y. Li, "Simulation research on PCM freezing process to recover and store the cold energy of cryogenic gas," *Int. J. Therm. Sci.*, vol. 50, no. 11, pp. 2220–2227, 2011.

[10] A. a. Altohamy, M. F. Abd Rabbo, R. Y. Sakr, and A. a. a. Attia, "Effect of water based AL2O3 Nanoparticle PCM on cool storage performance," *Appl. Therm. Eng.*, vol. 84, pp. 331–338, 2015.

[11] P. Chandrasekaran, M. Cheralathan, V. Kumaresan, and R. Velraj, "Enhanced heat transfer characteristics of water based copper oxide nanofluid PCM (phase change material) in a spherical capsule during solidification for energy efficient cool thermal storage system," *Energy*, vol. 72, pp. 636–642, 2014.

[12] Q. He, S. Wang, M. Tong, and Y. Liu, "Experimental study on thermophysical properties of nanofluids as phase-change material (PCM) in low temperature cool storage," *Energy Convers. Manag.*, vol. 64, pp. 199–205, 2012.

[13] E. Oró, L. Miró, C. Barreneche, I. Martorell, M. M. Farid, and L. F. Cabeza, "Corrosion of metal and polymer containers for use in PCM cold storage," *Appl. Energy*, vol. 109, pp. 449–453, 2013.

[14] G. Li, Y. Hwang, R. Radermacher, and H. H. Chun, "Review of cold storage materials for subzero applications," *Energy*, vol. 51, pp. 1–17, 2013.

[15] L. Gaines, A. Vyas, and J. Anderson, "Estimation of Fuel Use by Idling Commercial Trucks," *Transp. Res. Rec.*, vol. 1983, no. 06, pp. 91–98, 2006.

[16] Tassou, De_Lille, and Lewis, "Food transport refrigeration," no. 853, pp. 1–25.

Application of Deep Eutectic Solvent (DES) in Chitosan-Cellulose Blend Film for Proton Exchange Membrane

Wong Chun Yik*, Wong Wai Yin, Rashmi W. Walvekar

School of Engineering, Taylor's University, Malaysia

*chunyik.wong@sd.taylors.edu.my

Abstract
Chitosan and carboxymethyl cellulose (CMC) are abundant natural polymers that are known as renewable and biodegradable sources. Formation of blend polymeric film requires plasticizer to cross-link with natural polymers to improve the mechanical strength. In the past, ionic liquid was selected for this purpose despite its high toxicity and high costs. For the first time, an investigation on potential of choline chloride (ChCl) and urea deep eutectic solvent (DES) serving as the plasticizer for chitosan-carboxymethyl cellulose (CMC) blend film as proton exchange membrane is reported herein. The novelty of this work lies within the interaction of deep eutectic solvent (DES) as a plasticizer to interact with the chitosan-carboxymethyl cellulose (CMC) blend film without any common solvent for the dissolution of both polymers. Several analytical test include FT-IR, electrochemical impedance test (EIS), water uptake and film thickness measurement were conducted on the blend film membranes. Through the FT-IR analysis, an interaction between chitosan and carboxymethyl cellulose (CMC) occurred at the characteristics peak of 1641 cm^{-1}. The peak at the characteristics peak will be sharpen due to an overlapping of amino groups and carboxyl groups, while the peak at 3370 cm^{-1} will become weaker. Besides that, the ion conductivity under samples with plasticizer shows a positive sign as those without plasticizer tended to shrank throughout the test. The sample of blend film that contains 50 wt% of chitosan had the highest proton conductivity of 1.57×10^{-2} S/cm, which was slightly lower compared to Nafion-117 membrane (8.6×10^{-2} S/cm). Lastly, the blend film containing 75 wt% of chitosan shown to be a potential polymer electrolyte membrane (PEM) with water uptake of 49.4%, which was comparable to the commercial Nafion-117 membrane (34.0%).

Keywords: Deep eutectic solvent (DES), biocomposite blend film, plasticizer, polymer electrolyte membrane (PEM), fuel cell.

1. INTRODUCTION

Proton exchange membrane fuel cells (PEMFCs) are a state-of-art energy generation device in transportation, portable and stationary devices. The application of proton exchange membrane fuel cells (PEMFCs) had caught the eyes of researchers with various advantages compared to conventional power sources, such as higher efficiency, lesser maintenance cost and virtually pollution-free. In a study on performance of proton exchange membrane fuel cells (PEMFCs), Braga et al. [1] has discovered that proton exchange membrane fuel cells (PEMFCs) is more efficient than internal combustion engine in term of exergetic efficiency. The fundamental operating concept of proton exchange membrane fuel cells (PEMFCs) is mainly contributed by a polymer electrolyte membrane (PEM). The conventional polymer electrolyte membrane (PEM) available is Nafion-117 membrane, it comprises side chains of sulfonic group and polytetrafluoroethylene backbone that allows high current density to be obtained [2]. However, the manufacture cost of Nafion-117 membrane is relatively expensive and this channels the interests in using biocomposite materials as a replacement.

Cellulose is the most abundant natural polymer in the world and it could serves as one of the future mainstream in industrial process, such as pharmaceutical, food, textile, fuel cell application and more. One of derivative which retains some special characteristics of cellulose such as biodegradable, hydrophilicity, broad chemical-modification capacity, and the formation of of versatile semicrystalline fiber morphologies is carboxymethyl cellulose (CMC) [3]. It has a chemical structure that similar to cellulose, but it has a carboxymethyl groups in place of hydroxyl groups. Besides that, chitosan is the second most abundant natural polymer in the world and it obtained by further treatment on shrimp shells. It possess similar characteristics to cellulose which made it feasible to prepare a biocompatible composites from both chitosan and carboxymethyl cellulose (CMC). **Figure 1** and **Figure 2** show the chemical structure of both carboxymethyl cellulose (CMC) and chitosan respectively [4, 5].

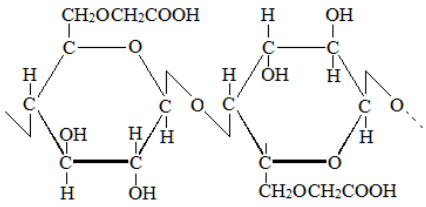


Figure 1. Monomer segments of carboxymethyl cellulose (CMC) [4]

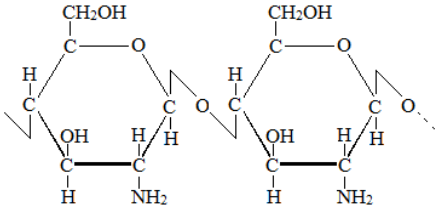


Figure 2. Monomer segments of chitosan [5]

The blending of both biopolymers offer a modification on both amino groups and hydroxyls groups of carboxymethyl cellulose (CMC) and chitosan. Such a way is often known as cross-linking, whereby one polymer chain is link through another polymer chain by either covalent or ionic bond in nature [6]. Through the cross-linking between both biopolymers, it promotes significant changes in physical properties (such as mechanical strenght [7]) as each individual polymer chains losing its ability to slide past each other and forming a close packing structure.

The objective of this work is to investigate the performance of chitosan-carboxymethyl cellulose (CMC) blend film through the usage of deep eutectic solvent (DES) as plasticizer. A plasticizer is usually a low-molecular organic compounds that possess low vapor pressure, it capables in shifting the glass transition temperature, t_g of polymer to a lower side while preserving its rubbery properties [8]. In the study of plasticizer effect on polymer, Singh et al. [9] reported with the usage of polyethylene glycol (PEG) as plasticizer into polyethylene oxide (PEO) matrix to reduce crystallinity.

Deep eutectic solvent (DES) is the next promising green solvent to replace the current usage of ionic liquids (ILs) [10]. The term “green solvents” define that it will not or less likely to cause any environmental impact while in use. DES is a mixture of hydrogen bond donor systems with simple salts to produce liquids which consist of physicochemical properties similar to ionic liquids (ILs) [11]. Based on the study of types of deep eutectic solvent (DES), Abbott et al. [12] discovered 3 different types of deep eutectic solvent (DES) with a general formula $R_1R_2R_3R_4N^+X^-Y^-$.

Type I DES: Y = MCl_x, where M = Zn, Sn, Fe, Al, Ga
Type II DES: Y = $MCl_x \cdot yH_2O$, where M = Cr, Co, Cu, Ni, Fe
Type III DES: Y = R_5Z, where Z = -$CONH_2$, -COOH, -OH

The use of deep eutectic solvent (DES) as plasticizer is studied by Zdanowicz et al. [13], where they revealed choline chloride (ChCl) based deep eutectic solvents (DES) are one of the potential candidates by decreasing the polymer chains interaction and bind them together. Based on the work from Leron et al. [14], a mixtures of choline chloride (ChCl) and urea, at the molar ratio 1:2 will hold an optimum melting point of 12℃. As a results, the mixtures of deep eutectic solvent (DES) possess characteristics such as high thermal stability, low vapor pressure and low melting point, which satisfied the criteria of a plasticizer.

This work presents results of choline chloride (ChCl) and urea mixtures deep eutectic solvent (DES) as the plasticizer for chitosan-carboxymethyl cellulose (CMC) blend film.

2. EXPERIMENTAL

2.1 Materials

Chitosan (low-molecular weight) was received in the form of powder from Sigma-Aldrich Corporation with a claimed viscosity of 20-300 cP for 1 wt% of chitosan in 1 wt% of acetic acid. Carboxymethyl cellulose (CMC) was also received in the form of powder from Sigma-Aldrich Corporation. The following chemicals were all obtained and used as reagent grades from Merck Sdn Bhd: choline chloride, urea (99.5%), acetic acid. Deionized water with a pH level of 7.4 was used for all the samples.

2.2 Synthesizing Deep Eutectic Solvent (DES)

The mixture of choline chloride (ChCl) and urea deep eutectic solvent (DES) was prepared according to the procedure being described by Abbott et al. [15]. Both choline chloride (ChCl) and urea are measured with a molar ratio of 1:2 and added gently into 100 ml DURAN Laboratory bottle with spatula. The bottle is sealed with parafilm to prevent moisture trap inside the mixture that may changes its physical properties. Then, it follows by a heating under continuous stirring at the temperature of 90 ˚C until a homogeneous liquid (transparent viscous liquid) is obtained.

2.3 Dissolution of Biopolymers

The dissolution of chitosan and carboxymethyl cellulose (CMC) in 0.1 M of acetic acid and deionized water are performed respectively. 1 wt% of chitosan is added to 100 ml of 0.1 M acetic acid solution in 100 ml DURAN Laboratory bottle under nitrogen purge. It followed by heating the system under 47 ˚C and continuous stirring at the speed of 300 rpm for 24 hours. At the end of dissolution experiment, a homogeneous solution of chitosan was obtained. As for the dissolution of carboxymethyl cellulose (CMC), a similar procedure was performed by stirring it at 500 rpm for about 4 hours and room temperature to obtained 1 wt% carboxymethyl cellulose (CMC) solution.

2.4 Preparation of Chitosan-Carboxymethyl Cellulose (CMC) Blend Film

The preparation of chitosan-CMC blend film was performed by mixing both chitosan (1 wt%) and carboxymethyl cellulose (CMC, 1 wt%) solution prepared as described in **Section 2.3** under gentle stirring. Different proportion of both dissolved polysaccharide solutions were mixed with the chitosan to CMC ratio of 5:95, 10:90, 25:75, 50:50 and 75:25. The procedure for preparation of blend film was conducted accordingly as per described by Kuzmina et al. [16]; the blended solution of 50 ml under different proportion will be casted on a glass petri dish, while temperature of the oven was set at 60 ˚C. Since both chitosan and carboxymethyl cellulose (CMC) were not carried out under a common solvent, homogeneous solution will not be formed and resulting differences in film thickness. Besides that, pure chitosan film was fabricated using the abovementioned procedure to verify the advantages of composite materials.

Table 2.1 shows all the test samples that being conducted under this work, whereby each set of the samples were carried out for both with and without deep eutectic solvent (DES) respectively.

Table 2.1. Test samples performed with and without DES as plasticizer

Description	Sample(s)
With deep eutectic solvent	Pure chitosan

(DES) as plasticizer / Without deep eutectic solvent (DES) as plasticizer	Chitosan : CMC (5:95) Chitosan : CMC (10:90) Chitosan : CMC (25:75) Chitosan : CMC (50:50) Chitosan : CMC (75:25)

2.5 Film Thickness Measurement

The thickness of chitosan-CMC blend films produced were measured with a micron scaled film thickness gauge.

2.6 Fourier Transform Infrared Spectroscopy (FT-IR) Analysis

Fourier transform infrared spectroscopy (FT-IR) (PerkinElmer, Spectrum 100 FT-IR Spectrometer) was used to identify the chemical functional groups of the chitosan-CMC blend films. The particular analysis was driven by a software called "Spectrum" to plot and analyze the data generated. Wavenumber of the analysis was carried out between the range of 4000 to 650 cm^{-1} [16]. Attenuated total reflectance (ATR) sampling techniques were conducted for all the samples.

2.7 Electrochemical Impedance Spectroscopy (EIS) Analysis

Electrochemical impedance spectroscopy (EIS) (Autolab PGSTAT128N potentialstat) analysis was thought to provide information regarding on electrical properties of the biocomposite film and its interface with conducting electrodes [17]. In this work, electrochemical impedance spectroscopy (EIS) test was carried out by sandwiching the samples in between stainless steel electrode in a measurement cell through alternative current (AC) mode (frequency range of 1000 kHz and signal amplitude of 0.1 V) [17]. The diameter taken for circle of measurement cell was 16 mm.

Analysis was then performed using NOVA software for every samples by applying electrochemical circle fit to determine its electrolyte resistance, R_s. The criteria to employ the electrolyte resistance, R_s value was to obtained a convergence curve. Proton conductivity of the samples were calculated with the following Equation:

$$\lambda = \frac{t}{A \times R_s} \quad (1)$$

Where;

λ is the proton conductivity, S/cm

t is the thickness of blended film, m

A is the area of the blended film, m^2

R_s is the electrolyte resistance, Ω

2.8 Water Uptake Rate

Water uptake rate is an important parameter to identify the suitability of blend film in fuel cell application as proton transfer needs to be facilitated with the presence of water in the membrane. It measures the interaction between biocomposite membrane and liquid. Hence, the membrane should possess adequate water uptake and dimensional swelling in order to reduce the stress acting towards it throughout the operation [18].

First of all, the mass of the dry chitosan-cellulose biocomposite membrane is weighed, followed by soaking it in distilled water. Then, the wet membrane is removed with tissue paper and immediately weighed to estimate the amount of water absorbed at a given time [19]. Equation 2 is used to calculate the percentage sorption or water uptake in term of percentage (%).

$$Water\ Uptake\ (\%) = \frac{M_s - M_d}{M_d} \times 100 \quad (2)$$

Where;

M_s is the mass of wet blended film in gram, g

M_d is the mass of dry blended film in gram, g

3. RESULTS AND DISCUSSION

3.1 Thickness of blend film

The thickness of the blend films were measured with micron scaled film thickness gauge. A table was tabulated as follow to present the data collected:

Table 3.1. Thickness of chitosan membrane and chitosan-CMC blend films

Samples	Measurement, mm	
	With DES as plasticizer	Without DES as plasticizer

Pure Chitosan	0.300	0.033
Chitosan:CMC (5:95)	0.060	0.025
Chitosan:CMC (10:90)	0.175	0.070
Chitosan:CMC (25:75)	0.510	0.350
Chitosan:CMC (50:50)	0.590	0.155
Chitosan:CMC (75:25)	0.460	0.450

Based on the results tabulated in **Table 3.1**, larger thickness was examined for the blend films with plasticizer. The addition of plasticizer will increase the overall film thickness while offering higher flexibility for the film. More information regarding to plasticizer will be further discussed under latter section.

3.2 Fourier Transform Infrared Spectroscopy (FT-IR) analysis of blend film

The formation of biocomposite film was mainly caused by the strong interaction of hydrogen bonds through the blending of chitosan and carboxymethyl cellulose (CMC). These interactions between both polymers were determined by performing fourier transform infrared spectroscopy (FT-IR) analysis. **Figure 3** presents the spectra of chitosan and carboxymethyl cellulose (CMC) solutions. The peak within a range of 1000 to 1200 cm^{-1} shows the presence of saccharide ring (C-O-C) [20]. An C-O-C bond also known as glycoside bond refers to the connection that held between two monosaccharides (Chitosan and carboxymethyl cellulose(CMC)) [21]. The absence of this band refers that the polysaccharide chains of biopolymer were dissapeared under dissolution solvent.

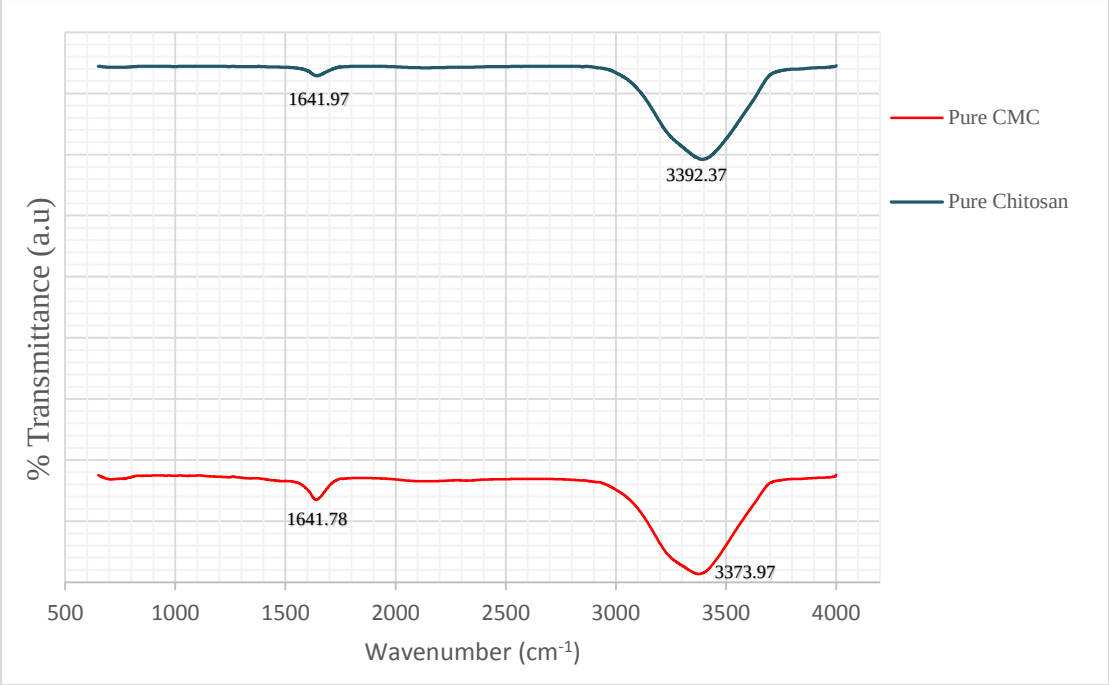


Figure 3. Spectra of chitosan and CMC solutions

Figure 4 shows the spectra of chitosan-CMC blend films with deep eutectic solvent (DES) as plasticizer. The characteristic peaks within a range of 1200 to 1700 cm^{-1} shows the presence of amino (N-H) and carboxyl (C=O) groups from chitosan and carboxymethyl cellulose (CMC) respectively. Here, we can observed that all the blend films do possess that particular characteristics within the interaction between chitosan and CMC. Besides that, characteristic peak within range of 1000 to 1200 cm^{-1} is present for all the blend films except for 25 wt% chitosan blend film.. The absence of this characteristic peak imply that cross-linking between chitosan and carboxymethyl cellulose (CMC) did not take place through the blending of both solutions as observed from the physical state of this film (gelatin form at room temperature).

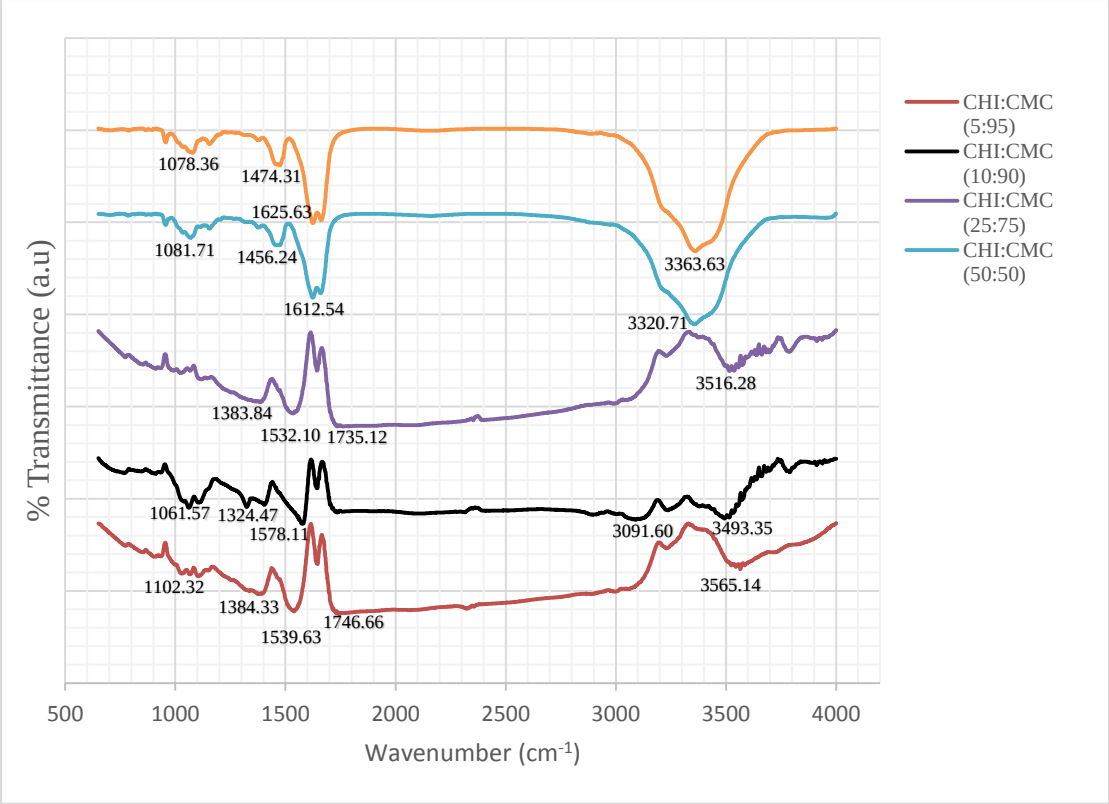


Figure 4. Spectra for different proportion of blend films with plasticizer

According to Yu et al. [20], the characteristic peak of amino groups (1200 to 1700 cm^{-1}) will become sharper while the band of hydroxyl groups will become weaker (3200 to 3400 cm^{-1}) due to the formation of intermolecular interaction between biocomposite polymers. From **Figure 4**, an obvious stretch for amino bands was observed for both 50 wt% and 75 wt% of chitosan containing blend films. The sharper peak in the amino groups (chitosan) was though to be overlapping with the carboxyl groups in carboxymethyl cellulose (CMC) and interact via hydrogen bonding.

3.3 Electrochemical impedance spectroscopy (EIS) analysis of blend film

The proton conductivity of chitosan membrane and chitosan-CMC blend films were measured using complex impedance method. All the samples were performed under dry and wet state to compare the differences in term of conductivity. A Nyquist plot of real impedance, -Z'' against imaginary impedance, Z' was performed for the analysis while carrying out the test under room temperature. **Figure 5** demonstrated a sample of graphical representation under Nyquist plot with electrochemical circle fit feature to specify the corresponding high frequency zone. A high frequency zone in

Nyquist plot was referred as the response from grains, which is the conduction process through the bulk of blend film [22]. The tail of the plot is often represents as the electrode effect, which determined from the stainless steel electrode that sandwiched the blend film.

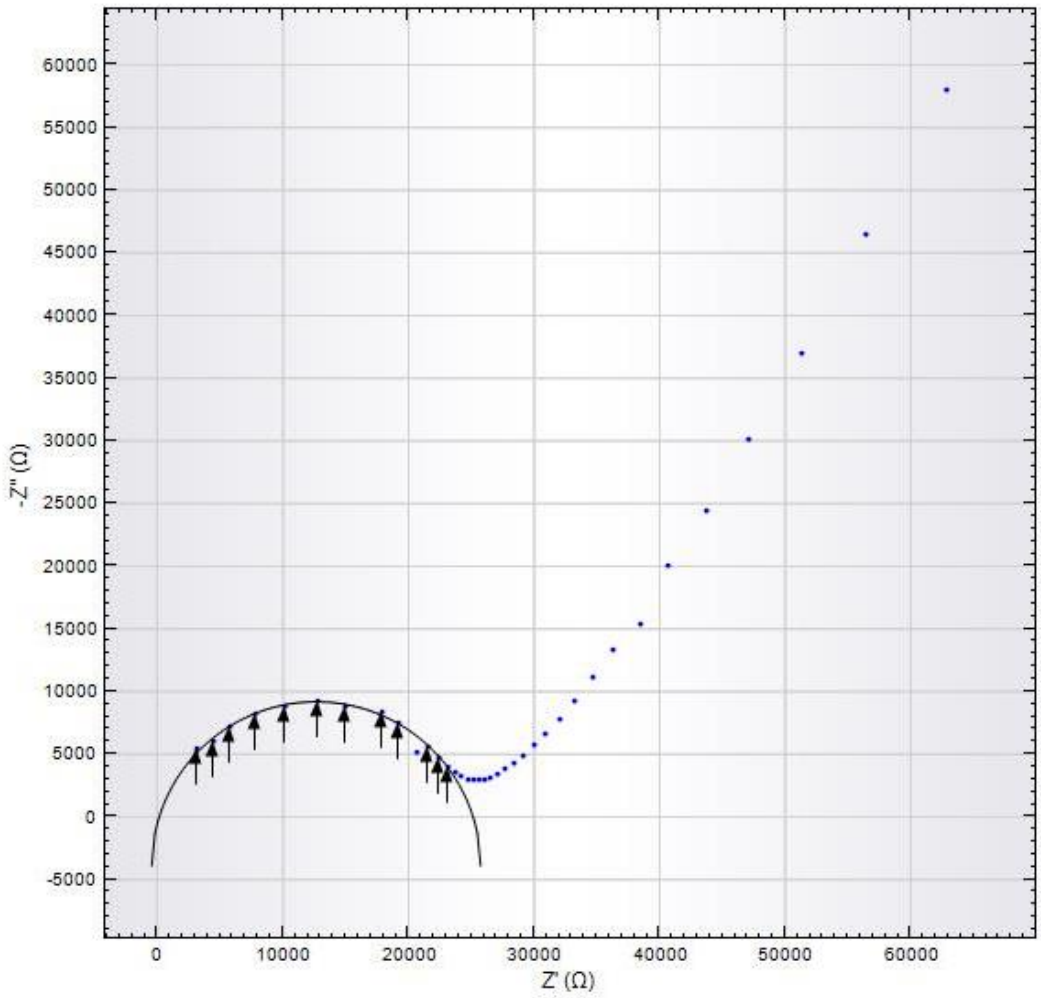


Figure 5. Sample of impedance spetra with electrochemical circle fit

The proton conductivity of all the samples were calculated by applying Equation 2 as stated in **Section 2.7**. A list of table was tabulated as follow to demonstrate the proton conductivity for all samples. An increasing trend was determined with a higher proportion of chitosan in the blend film.

Table 3.2. Proton conductivities of samples under dry and wet state

Sample	Conductivity, S/cm (With plasticizer)		Conductivity, S/cm (Without plasticizer)	
	Dry State	Wet State	Dry State	Wet State

Chitosan:CMC (5:95)	1.24×10^{-5}	1.31×10^{-4}	1.46×10^{-6}	Break
Chitosan:CMC (10:90)	7.08×10^{-4}	1.68×10^{-3}	Break	Break
Chitosan:CMC (25:75)	Break	Break	1.19×10^{-4}	Break
Chitosan:CMC (50:50)	2.00×10^{-3}	1.57×10^{-2}	Break	Break
Chitosan:CMC (75:25)	2.47×10^{-3}	4.44×10^{-3}	6.22×10^{-5}	Break
Pure Chitosan	2.29×10^{-3}	7.42×10^{-3}	Break	Break

The term “Break” refers that the film was either shrank when hydrated or not capable to exhibit proton conductivity in wet state. In nature form, carboxymethyl cellulose (CMC) is a water-soluble cellulose derivative that appeared to be easily dissolved out of the cross-linking media between chitosan. Based on the results tabulated, it concluded that choline chloride (ChCl) and urea deep eutectic solvent (DES) as a plasticizer could potentially interact with the blend film via hydrogen bonding. From a study of plasticization, Ma et al.[23] reported that C-O group of starch formed hydrogen bond interactions with glycerol or formamide as plasticizer. Hence, plasticizer will allows higher flexibility until certain extent while preventing the film over swelt.

Results shown here for dry state were relatively high and could be able to compatible with results reported by Y. Wan et al.[24] after hydrated. Based on the study of proton conductivity, the group had reported an optimum proton conductivity of 1.4×10^{-3} S/cm (After hydration) with 35 ml of 2-chloroethanol used in hydroxyethylation of chitosan. The relatively high in proton conductivity of blend film could be due to the existence of plasticizer. It assisted the blend film in decreasing the crystallinity while promoting amorphous phases for ions transport. The results shown that increasing in composition of chitosan formulates a tougher backbone, while allowing the blend film to sustain its physical appearance and promotes higher proton conductivity. In conclusion, blend film that containing 50 wt% of chitosan shows the highest proton conductivity under hydrated state with a figure of 1.57×10^{-2} S/cm, which was just slightly lower compared to Nafion-117 membrane (8.6×10^{-2} S/cm) [25]. Thereby, these biocomposite blend film shows the sign of interest in advancing in term of fuel cell application.

3.4 Water Uptake Rate

Water uptake rate of the films were studied and presented in **Table 3.3**. The test was carried out under room temperature.

Table 3.3. Water uptake of samples

Sample	Water uptake rate (%)	
	With plasticizer	Without plasticizer
Chitosan:CMC (50:50)	86.7	129.1
Chitosan:CMC (75:25)	49.4	156.9
Pure Chitosan	63.3	105.2

Based on the results shown, it can further justified that samples without addition of plasticizer will be completely swelt and shrank. This indicates the film was not suitable to be used as proton exchange membrane (PEM). Particularly, a PEM is expected to spontaneously absorbs water to allow ionic aggregrates within the film to swell. Once the water concentration or water uptake was high enough, percolated water-rich channels were expected to form and promotes proton transport mechanism [26]. In comparison with commerical Nafion-117 membrane with water uptake of 34% [27], the water uptake obtained in our study were higher, with nearest value obtained at 49.4% for Chitosan:CMC (75:25) indicating the potential of our novel biocomposite film as proton exchange membrane (PEM) despite a lower proton conductivity obtained for this sample. The lowest and highest water uptake among samples with plasticizer were 75 wt % chitosan containing film and 50 wt% chitosan cointaining film respectively. This trend was matched with the proton conductivity obtained through electrochemical impedence spectroscopy (EIS) analysis, with an order of Chitosan:CMC (50:50) > Pure Chitosan > Chitosan:CMC (75:25). The low proton conductivity of 75 wt % chitosan containing film might due to the lack of hydrophilic groups, where it directed to a lower water uptake compared to the remaining two samples. Although the actual synergy effect between DES and dissolved polymers in forming the blend film is yet to be fully understood, this new finding has indeed opens new window for us to further investigate into the use of other DES as plasticizer for biocomposite film to be used as proton exchange membrane (PEM) at much lower cost as compared to commercial Nafion membrane.

4. CONCLUSION

Several important findings from this study are summarized as below:

a. The study reveals that choline chloride (ChCl) and urea deep eutectic solvent (DES) can be acted as a plasticizer for chitosan-CMC blend film with a considerably high proton conductivity and good water uptake to be used as proton exchange membrane (PEM).
b. The blend film containing 50 wt% chitosan with DES as plasticizer possess highest proton conductivity (1.57×10^{-2} S/cm) out of all the samples and was shown comparable to the commercial Nafion-117 membrane (8.6×10^{-2} S/cm).
c. Water uptake rate for the blend film containing 75 wt% of chitosan (49.4%) was shown to be a potential membrane due to its comparable value with commercial Nafion-117 given at 34.0% despite a lower proton conductivity obtained.
d. Through the ionic conductivity and water uptake test, it was found that the blend film without DES as plasticizer tended to shrank and was found not suitable to be used as proton exchange membrane.

Future studies will be focused on optimising the ratio of chitosan to carboxymethyl cellulose (CMC) and selecting co-solvent prior to blending with DES to improve the properties and homogeneity of the film to be used as proton exchange membrane (PEM).

REFERENCES

1. L. Braga, J. Silveira, M. Evaristo da Silva, E. Machin, D. Pedroso and C. Tuna, "Comparative analysis between a PEM fuel cell and an internal combustion engine driving an electricity generator: Technical, economical and ecological aspects," *Applied Thermal Engineering*, vol. 63, no. 1, pp. 354-361, 2014.

2. J. Ma and Y. Sahai, "Chitosan biopolymer for fuel cell applications," *Carbohydrate Polymers*, vol. 92, no. 2, pp. 955-975, 2013.

3. M. Islam., M. Alam and M. Zoccola, "Review on modification of nanocellulose for application in composites," *International Journal of Innovative Research in Science, Engineering and Technology*, vol. 2, no. 10, pp. 5444-5451, 2013.

4. S. Manahan, "*Fundamentals of Environmental Chemistry*," Taylor & Francis Group, LLC. pp.348, 2013.

5. S. Kim, "*Chitin, Chitosan, Oligosaccharides and Their Derivatives*," Taylor & Francis Group, LLC. pp.150, 2011.

6. M. Adikwu, "*Biopolymers in Drug Delivery: Recent advances and challenges*," Bentham Science Publishers Ltd, pp.96, 2009.

7. C. Tran, S. Duri, A. Delneri and M. Franko, "Chitosan0cellulose composite materials: Preparation, characterization and application for removal of microcystin," *Journal of Hazardous Materials*, vol. 252-253, pp.355-366, 2013.

8. G. Zaikov and Y. Mikheev, "*Kinetics and Mechanisms of Chemical Reactions*," New York, Nova Science Publishers Inc, pp.286, 2004.

9. P. Singh, B. Bhattacharya, R. Mehra and H. Rhee, "Plasticizer doped ionic liquid incorporated solid polymer electrolytes for photovoltaic application," *Current Applied Physics*, vol. 11, no. 3, pp.616-619, 2011.

10. Y. Dai, J. Spronsen, G. Witkamp, R. Verpoorte and Y. Choi, "Natural deep eutectic solvents as new potential media for green technology," *Analytica Chimica Acta*, vol. 766, pp.61-68, 2013.

11. K. Shahbaz, S. Baroutian, F. Mjalli, M. Hashim and I. AlNashef, "Densities of ammonium and phosphonium based deep eutectic solvents: Prediction using artificial intelligence and group contribution techniques," *Thermochimica Acta*, vol. 527, pp. 59-66, 2012.

12. A. Abbott, J. Barron, K. Ryder, D. Wilson, "Eutectic-based ionic liquids with metal containing anions and cations," *Chemistry*, vol. 22, pp.24-30, 2007.

13. M. Zdanowicz and T. Spychaj, "Ionic liquids as starch plasticizers or solvents," Poland, Szczecin: *West Pomeranian University of Technology*, Polymer Institute, pp.861-864, 2011.

14. R. Leron, A. Caparanga and M. Li, "Carbon dioxide solubility in a deep eutectic solvent based on choline chloride and urea at T=303.15–343.15K and moderate pressures," *Journal of the Taiwan Institute of Chemical Engineers*, vol. 44, no. 6, pp.879-885, 2013.

15. A. Abbott, D. Boothby, G. Capper, D. Davies and R. Rasheed, "Deep Eutectic Solvent formed between Choline Chloride and Carboxylic Acids: Versatile alternative to ionic liquids," *J. Am. Chem. Soc*, vol. 126, no. 29, pp.9142-9147, 2004.

16. O. Kuzmina, T. Heinze and D. Wawro, "Blending of Cellulose and Chitosan in Alkyl Imidazolium Ionic Liquids," *ISRN Polymer Science*, vol. 2012, pp.1-9, 2012.

17. S. Aziz and Z. Abidin, "Electrical Conduction Mechanism in Solid Polymer Electrolytes: New concepts to Arrhenius equation," *Journal of Soft Matter*, vol. 2013, pp.1-8, 2013.

18. B. Smitha, S. Sridhar and A. Khan, "Chitosan–poly(vinyl pyrrolidone) blends as membranes for direct methanol fuel cell applications," *Journal of Power Sources*, vol. 159, no. 2, pp.846-854, 2006.

19. K. Peinemann and S. Nunes, "*Membrane Technology*," Weinheim: Wiley-VCH. pp.23, 2008.

20. S. Yu, H. Hsieh, J. Pang, D. Tang, C. Shih, M. Tsai, Y. Tsai and F. Mi, "Active films from water soluble chitosan/cellulose composites incorporating releasable caffeic acid for inhibition of lipid oxidation in fish oil emulsions," *Food Hydrocolloids*, vol. 32, no. 1, pp.9-19, 2013.

21. L. Malone and T. Dolter, "*Basic Concepts of Chemistry*," New York: Wiley, pp.51, 2008.

22. X. Yuan, C. Song, H. Wang and J. Zhang, "*Electrochemical Impedance Spectroscopy in PEM Fuel Cells*," New York: Springer, pp.81, 2010.

23. X. Ma and J. Yu, "The Effects of Plasticizers containing Amide groups on the properties of Thermoplastic Starch," *STARCH-STARKE*, vol. 56, no. 11, pp.545-551, 2004.

24. Y. Wan, K. Creber, B. Peppley and V. Tam Bui, "Proton conductivity and Tensile Properties of Hydroxyethyl and Hydroxypropyl Chitosan Membranes*," J. Polym. Sci. B Polym. Phys*, vol. 42, no. 8, pp.1379-1397, 2004.

25. B. Smitha, S. Sridhar and A. Khan, "Chitosan–poly(vinyl pyrrolidone) blends as membranes for direct methanol fuel cell applications," *Journal of Power Sources*, vol. 159, no. 2, pp.846-854, 2006.

26. N. Balsara and K. Beers, "Proton conduction in materials comprising conducting domains with widths less than 6 nm," *European Polymer Journal*, vol. 47, no. 4, pp.647-650, 2011.

27. J. Kolde and B. Bahar, "Advanced composite polymer electrolyte fuel cell membranes," in *Proceedings of the First International Symposium on Proton Conducting Membrane Fuel Cells I Electrochemical Society Proceedings, South Main Street, Pennington*, vol. 95-23, pp.193-201, 1995.

Effect of Low Combustion Temperature and Alkaline Treatment on Biochar Properties from Rice Husk

Woanlin Yeoh[1*], Wai Yin Wong [2], Ting Lee[3], Veena Doshi

[1] *Discipline of Chemical Engineering, School of Engineering, Taylor's University Malaysia, No.1 Jalan Taylors, 47500, Subang Jaya, Selangor Darul Ehsan, Malaysia.*

[*]woanlin.yeoh@sd.taylors.edu.my

Abstract

Biochar is a form of carbon that is produced by heat decomposition of biomass. Pyrolysis under the inert atmosphere is a well-established method to produce biochar with high carbon yield. However, the technology is yet to be fully developed to become viable for commercial applications due to the need of utilisation of inert conditions. In this study, combustion technique was adapted as the novel method to produce biochar from rice husk with low cost. Rice husk is an excellent source for production of biochar due to its high lignin and carbon content. Alkaline treatment of rice husk was carried out with the aim to improve its pore characteristics and physicochemical properties. Hence, rice husk has been subjected to a combination of various treatments, including combustion at different temperatures (200, 300 and 400 ºC) and NaOH treatment. Several analytical techniques such proximate analysis, ultimate elemental analysis (CHNS), X-ray diffraction (XRD) and Brunauer-Emmett-Teller (BET) were employed to analyse the characteristics of different biochar samples. Highest carbon content obtained was about 44.25%. All the tested samples exhibited amorphous structure. It has been found that specific surface area values between 305.25 and 466.67 m^2 g^{-1} were obtained when alkaline treatment of the RH showing the viability of combustion method for biochar production.

Keywords: Combustion, Alkaline treatment, Rice husk, Biochar, Direct carbon fuel cell

1. Introduction

Recently, biomass utilisation is receiving great attention as an energy source for providing approximately 14% of the world's energy need. Among all the biomass sources, rice husk (RH) offers the most promising option because the annual world RH production is approximately 140 million tonnes per year [1]. RH is an agricultural waste material removed in the first stage of the milling process [2]. The commercial use of RHs has been limited due to their low density, which makes transportation of husks problematic. As a result, RH has been disposed of by open-field burning, creating more environmental issues. Therefore, suitable combustion technology has been developed to convert RH into useful energy since RH has high heating value of 16.3 MJ/kg, indicating that it could be a source of good fuel [3]. Additionally, RH is a great source for biochar production due to its high lignin content (22%) and carbon content (42.2%). There is an increased interest to fuel a direct carbon fuel cell (DCFC) using biochar because they are cheap, abundant and readily available [4]. DCFC is regarded as a highly efficient energy conversion device in which the chemical energy of a carbonaceous fuel is converted directly into electricity [5]. Amorphous structure, high surface area and high carbon content are the desired carbon fuels characteristics to attain high power density in DCFC operation [6,7]. The feasibility of using biochar as carbon fuel for application in DCFC has been discussed in several studies. Kacprzak et al. [8] proved the potential of DCFC to be operated with biochar prepared from biomass including apple, energetic willow, sunflower husks and pine. Dudek et al. [9] showed that there was increased interaction between carbon particles with large surface area and electrolyte, thereby promoting electrochemical reactions in DCFC due to efficient electron transfer [10].

Pyrolysis is the process involving thermal destruction of organic matter for the production of biochar, where the volatiles are released leaving the solid char [11]. However, pyrolysis process is usually carried out at moderate temperature of around 600 °C in inert (nitrogen) atmosphere [12,13]. Therefore, the cost for mass production of biochar using pyrolysis process is high, preventing the widespread application of this method. Combustion, which is another thermochemical process, offers an alternative to produce biochar [14]. Burning of RH at high temperature has resulted in the formation of rice husk ash (RHA), primarily consists of ~90 wt% silica and other metal oxides [15]. To date, an increasing application of RHA is as raw material for production of high quality silica [16]. The study on the production of RH biochar using combustion technique is yet to be reported. Low combustion temperature method appears to be an attractive option to produce biochar, where careful selection of temperature is required to obtain biochar with high carbon content.

To improve the biochar properties of RH, chemical treatment of RH can be carried out. Heating of the NaOH-treated sample for a certain time have been found to cause swelling of the pores, resulting in higher internal surface area and less crystalline structure which are the desired characteristics to achieve high power density in DCFC [17-19]. In addition, Markovska et al. [20] has proven that application of NaOH treatment showed effectiveness in removing ash from RH. However, limited work has been published concerning the influence of NaOH and its application before and after combustion on the RH biochar properties.

In the present research, production of RH biochar using low combustion temperature method and alkaline treatment were proposed to produce carbon fuels without the need of high temperature and inert treatment condition targeted for DCFC application. RH biochar was prepared with combustion temperature at 200, 300 and 400 °C. Changes in the colour of the biochar and the biochar yield were observed, followed by chemical analysis of samples. The effect of the combustion alone or combination of alkaline treatment and combustion on RH biochar was evaluated by X-ray diffraction (XRD) and Brunauer-Emmett-Teller (BET) to determine the structure and pore characteristics of samples.

2. Materials and methods

2.1 Materials and Sample Preparation

Rice husk was collected from the Oblique Titi Rice Mill Co., Inc., Perak, Malaysia, followed by washing with distilled water few times and drying at 105 °C for 24 h. The dried RH was grind, and then sieved to obtain particles within the indicated size range (2 mm to 500 μm). Laboratory grade (Friendemann Chmidt) NaOH was used for treatment of samples.

The process of preparing biochar from RH can be divided into three sets, which are illustrated as follows. In first set, about 25 g of dried RH was placed in a crucible and combusted at 200, 300 and 400 °C for 2 h in a muffle furnace of ambient atmosphere without any external gas supply. In the second set, about 30 g of dried RH was stirred with 0.1 M NaOH for 12 h in conical flask. After treatment, RH was washed with distilled water few times until constant pH was achieved, and then dried for 24 h at 105 °C. The NaOH-treated RH was combusted at temperature following the same procedure as above. In the last set, the procedures were similar to the first and second sets, except combustion was carried out prior to alkaline treatment. All the samples were assigned with sample codes as presented in Table 1.

Table 1. Experiment sets.

	Combustion temperature (°C)		
	200	300	400
Untreated	Set A1	Set A2	Set A3
Pre-treatment	Set B1	Set B2	Set B3
Post-treatment	Set C1	Set C2	Set C3

2.2 Characterisation of biochar

The biochar yield from RH was calculated by measuring the weight of the samples before and after combustion. The weight percent of biochar as the product formed was calculated using eq.1.

$$\text{Biochar yield } \% = \frac{\text{Biochar mass}}{\text{Biomass inital mass}} \times 100\% \quad (1)$$

The amount of main constituent of biochar was determined by proximate analysis through a thermogravimetric analyser (Mettler Toledo). Samples were heated in nitrogen atmosphere from room temperature to 110 °C at a heating rate of 10°C min^{-1}, followed by holding them for 10 min at the same temperature until constant weight was reached. The amount of the moisture content was observed from the first weight loss. Under the same flowing gas, the samples were heated from 110 to 950 °C where the amount of volatile matter was estimated by observing the second weight loss. The atmosphere was then switched to air and the temperature was maintained at 950 °C. Ash content was determined from the amount of residue remained. Gas flow rates of 20 ml min^{-1} were used in all cases. Elemental analysis of RH biochar was performed using a CHNS elemental analyser to obtain the weight percent of carbon, hydrogen, nitrogen and sulphur elements.

XRD characterisation was carried out with a diffractometer (D8 Bruker Discover) for crystal structure identification of RH biochar at 40 kV and 40 mA. The analysis was performed with Cu-K$\propto$ radiation at a scan speed of 2 ° min^{-1} within the 2θ range from 10 to 90°.

Nitrogen adsorption isotherms were investigated using a surface area and porosity analyser (Micromeritics ASAP 2020) at -196 °C. The specific surface area was calculated using BET model at relative pressure (P/P_o) ranging from 0.01 to 0.99. Barrett–Joyner–Halenda (BJH) model was applied to determine the diameter of the pore (D_{pore}), while the total pore volume (V_{total}) was estimated based on the amount of the nitrogen gas adsorbed on the sample surface.

3. Results and discussion

3.1 Visual Analysis

The colour changes of the samples were observed when RH was prepared under different combustion temperatures and treatment of NaOH, as shown in Fig. 1.

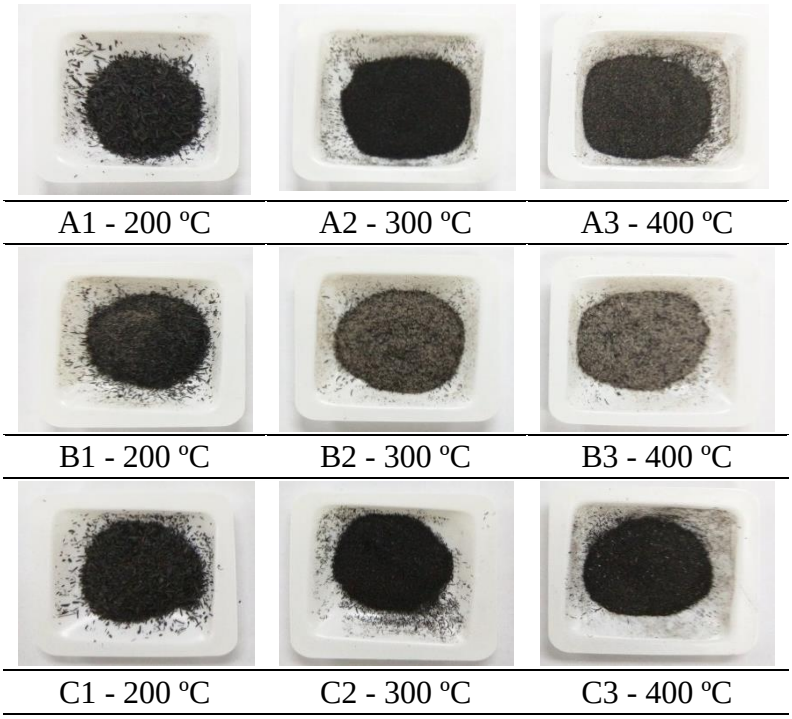


Figure 1. Visual images of RHA.

The colour for three sets of samples became more greyish as the combustion temperature increased from 200 to 400 ºC. Burning of RH in air up to 200 °C produced powder almost black in colour, indicating that the presence of carbon in RH which had not been oxidised completely yet. With the temperature increasing to 300-400 °C, the non-oxidised carbon started to decompose, transforming the black powder into grey-white ash. The effect of alkaline treatment on biochar was analysed in the subsequent analyses.

3.2 Biochar Yield

Determining the yield of RH biochar will affect the possibility to be applied as carbon fuel in DCFC. Increasing combustion temperature significantly decreased the biochar yield, as shown in Fig. 2. The decrease for the untreated RH was 30.6% (from 48.44 to 17.84%) when temperature was increasing from 200 to 400 ºC. Similarly, the decrease for the pre-treated RH was 17.16% (from 33 to 15.84%) under the same condition, while reduction for post-treated RH was 28.58% (from 45.5 to 16.92%). The yield reduction was caused by the transformation of carbon component of biomass to biochar and simultaneously combustion of volatile matter occurred during the burning process [21]. Lee et al. [22] reported that thermal degradation of hemicellulose and cellulose of RH occurred in the temperature range of 210 to 360 °C. As a result, more volatiles evolved within the temperature range, reducing the biochar

yield. Compared to biochar from other carbonaceous material which yielded lesser than 35 wt% [23], RH produced at 200 ºC seems to be an attractive resource as carbon fuel because the biochar yield was about 48%, 33% and 45.5% for untreated, pre-treated RH and post-treated RH respectively.

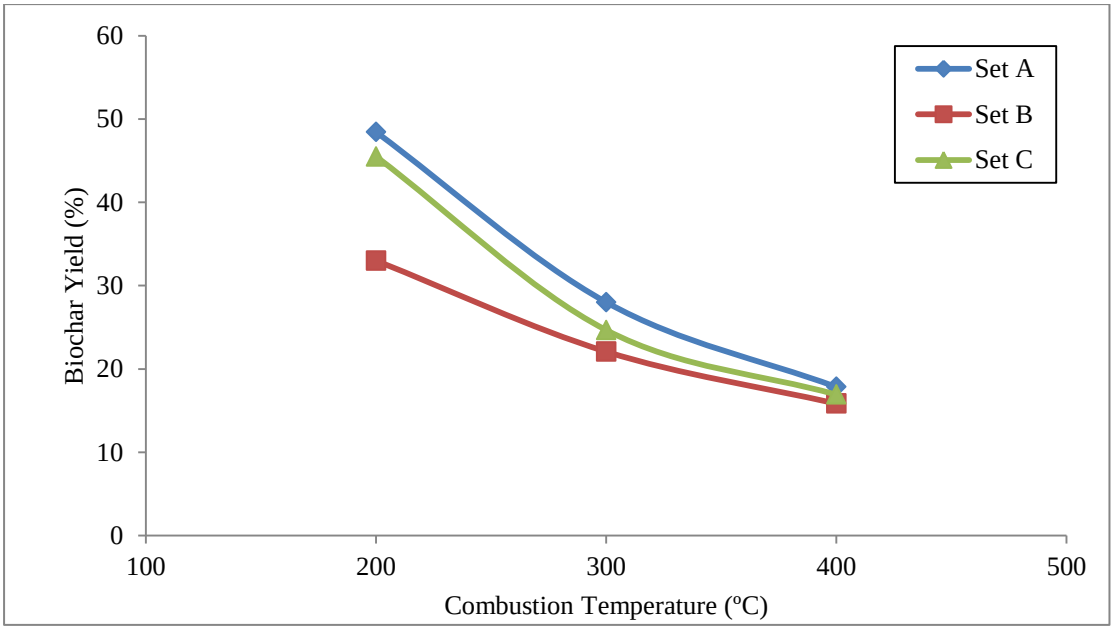


Figure 2. Biochar yield for untreated (Set A) and NaOH-treated (Set B and C) sample

3.3 Characterisation of biochar

3.3.1 Chemical analysis of biochar

Table 2 compares the four main components of each of the biochar sample, including moisture, volatile matter, fixed carbon and ash content.

Table 2. Constituent component of each biochar determined by proximate analysis.

Biochar	Moisture (% wt)	Volatile matter (% wt)	Fixed carbon (% wt)	Ash (% wt)
A1	2.79	22.28	34.10	40.83
B1	2.96	23.01	37.12	36.94
C1	2.15	21.11	33.26	43.48

As shown in Table 2, RH biochars consist of volatile matter contents of about 21.11 to 23.01%, which was slightly higher than volatile content of coal (less than 20%) [24]. Generally, raw biomass has high volatile matter content where 80-90% of biomass is combusted in the form of volatiles. Since most of the energy is stored in the volatiles, volatile matters are highly reactive, which makes the combustion process more difficult to be controlled [25]. Hence, lower content of volatile matter is desirable because it is an indication that the combustion process is easier to be controlled.

The fixed carbon content obtained in this work ranged from 33.26 to 37.12%. The result suggested that the fixed carbon content was affected by the higher ash content of RH, which inhibited the formation of aromatic carbon during the thermochemical conversion process [26].

Among all the three samples, the ash content of sample B1 was the lowest (36.94%). Biomass treatment using diluted acid or alkali has been regarded as one of the effective ways in removing inorganic elements under influence of mineral dissolution and desorption [27]. Hence, the reduction in ash content after treatment of RH with NaOH was caused by the reaction of silica in RH with NaOH, and the silica was extracted out as a form of Na_2SiO_3[20]. It was observed that post-treatment of RH biochar with NaOH was inefficient in leaching out ash-forming elements, since sample C1 exhibited the highest ash content. High ash content is likely to cause fouling at the current collector in DCFC [28]. Hence, further study is required to reduce the ash content.

Next, compositions of the selected samples were examined by analysing the main elements (carbon, hydrogen, nitrogen, sulphur) as illustrated in Table 3. At the same combustion temperature, only slight composition difference was observed in samples A1, B1, and C1. Sample B1 has the carbon content of about 44.254%, which was the highest among all the tested biochar samples. The increase in carbon content after the alkaline treatment was probably due to the extraction of impurities by NaOH. The results also showed that the nitrogen and sulphur content in the biochar prepared were considerably lower, which was an indication that deposit formation was unlikely to occur in the operation of the DCFC [25].

For comparison, the carbon content of RH combusted at 300 °C was 34.03%, indicating that combustion temperature had significant effect on the contents of organic component. It was found that treatment of RH before combustion at 200 °C appeared to have positive effect on the carbon content, where high carbon content was one of the desired characteristics to be used as carbon fuel in DCFC [7].

Table 3. Elemental composition of A1, B1, C1 and C2.

Sample	C (%)	H (%)	N (%)	S (%)
A1	43.709	2.946	7.529	0.109
B1	44.254	2.798	6.615	0.079
C1	42.812	3.324	5.986	0.064
C2	34.030	2.146	5.538	0.034

3.3.2 Graphitic structure of biochar samples

Figure 3 shows the XRD patterns of untreated, pre-treated and post-treated biochar prepared at combustion temperature of 200 ºC. All the samples exhibited the same diffraction patterns, where broad peaks were observed between 15 and 35º 2 θ. According to Krishnarao et al. [29], the range corresponded to the presence of amorphous silica. Also, the XRD patterns revealed the absence of any ordered crystalline structure [30]. It was reported that the broad peak at 22 º corresponded to the contribution from both amorphous carbon and silica [31]. Therefore, it could be concluded that the amorphous structure of untreated and treated RH were retained after combustion. It is desirable to have amorphous carbon as the carbon fuel for

DCFC [32], nonetheless, we are unable to tell the percentage of amorphous carbon and silica in the biochar.

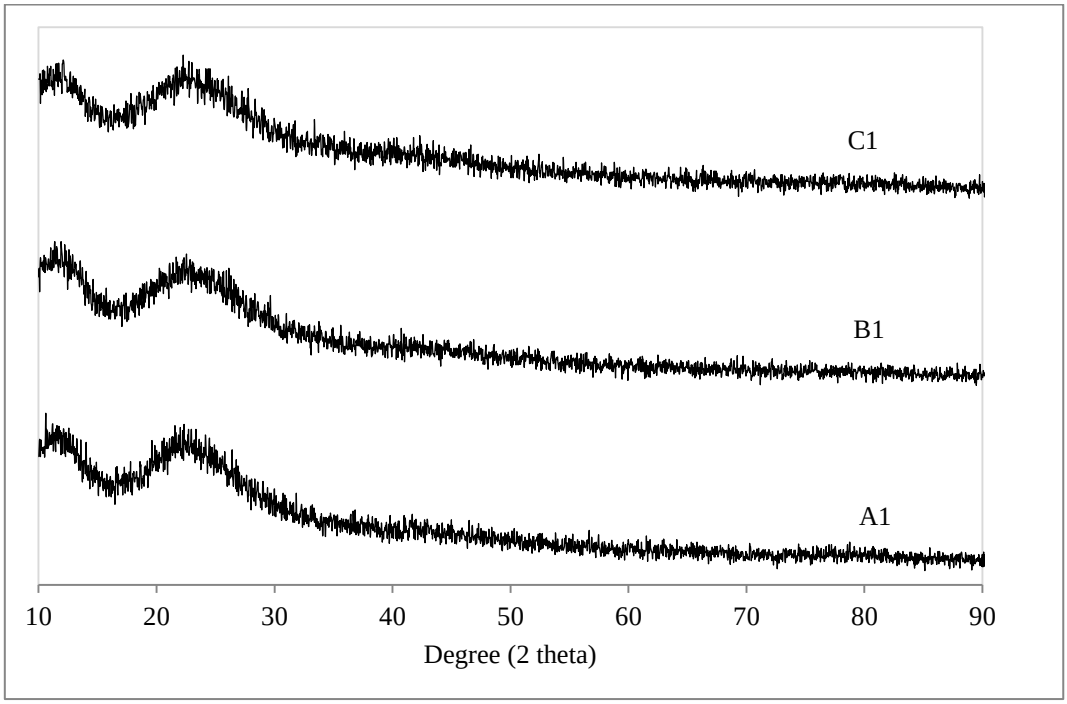


Figure 3. X-ray diffraction patterns for samples A1, B1 and C1.

3.3.3 Textural properties of biochar samples

The pore structures of the biochars obtained by BET analysis are summarised in Table 4. Specific surface area, total volume and pore size of biochars treated with alkali were generally higher than the untreated biochar. The pore structure of sample A1 was insufficiently developed, with surface area and total volume of 50.13 $m^2 g^{-1}$ and 0.037 $cm^3 g^{-1}$, respectively. Combustion process alone seemed to be insufficient to enhance the pore structures. On the other hand, sample B1 exhibited the highest specific surface area of about 466.67 $m^2 g^{-1}$ with pore volume of 0.414 $cm^3 g^{-1}$. Alkaline treatment is usually conducted to remove the inorganic matters in the biomass, allowing the generation of more developed pore network [33]. In this study, NaOH pretreatment was found to decrease the ash content, as demonstrated in section 3.3.1. Therefore, the combined effect of combustion and alkaline treatment improved the pore structures significantly.

Additionally, the sequence of alkaline treatment on RH greatly influences the pore characteristics developed. It can be seen that specific surface area and pore volume of biochar was higher for pre-treated sample than post-treated sample. When alkaline treatment was conducted after combustion, the post-treated biochar experienced porosity shrinkage where the pore shrank to narrower size, leading to pore size reduction [34]. The shrinkage effect was not obvious in pre-combustion-treatment sample, since combustion process helps to generate pores.

Table 4. Pore characteristic of the untreated and treated biochars.

Biochar	S_{BET} (m^2 g^{-1})	V_{total} (cm^3 g^{-1})	D_{pore} (nm)
A1	50.13	0.037	2.91
B1	466.67	0.414	3.57
C1	305.25	0.202	2.65

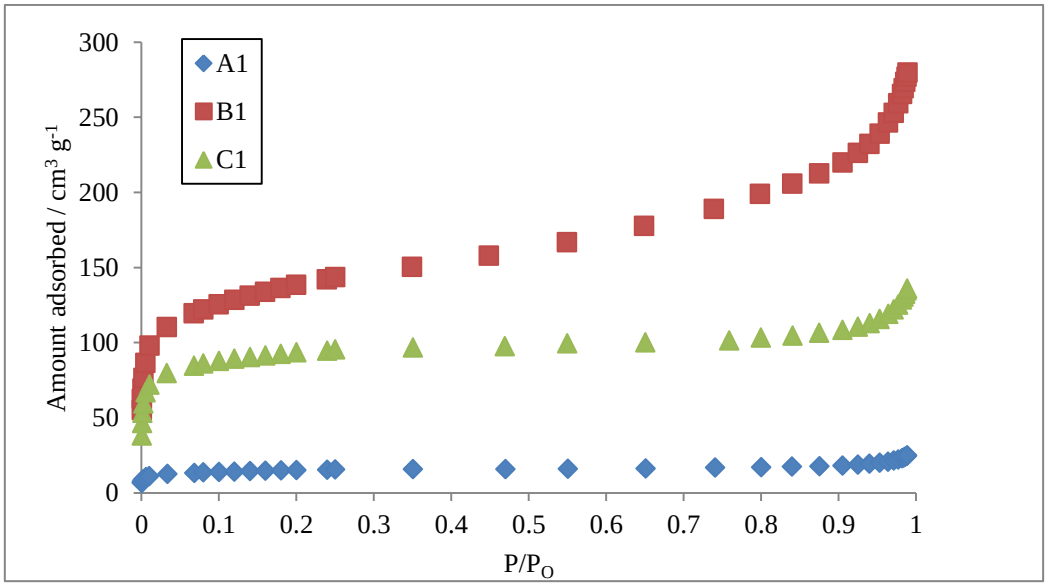


Figure 4. Nitrogen adsorption isotherms of A1, B1 and C1.

The nitrogen adsorption isotherms of A1, B1 and C1 are shown in Fig. 4. The adsorption curves of samples B1 and C1 showed a better adsorption performance than sample A1. At low relative pressure, steep adsorption in B1 and C1 isotherms confirmed the existence of micropores as a result of alkaline treatment [35]. Both the samples showed a gradual increase in isotherms after the initial micropores filling. At high relative pressure, large adsorption capacity took place which indicated that the presence of mesopores with wider porosity. However, the small adsorption capacity of the sample A1 proved an obvious decrease in the mesoporosity. The results suggested that combustion process alone was insufficient to produce microporous and mesoporous biochar.

4. Conclusions

This study reports the preparation of biochar from RH using low combustion temperature method and alkaline treatment. Combustion method is a viable method to produce biochar with high carbon content, large surface area and amorphous structure comparable to pyrolysis process despite of its high ash content. Especially with NaOH treatment followed by combustion, the treated biochar shows the highest carbon content (44.25%) and specific surface area (466.67 m^2 g^{-1}) compared to all of the tested samples. In the future work, the cost effective method can be further modified to reduce the ash content in order to meet the specification for DCFC fuel.

Acknowledgment
This research work was financially supported by the research funds from School of Engineering, Taylor's University.

References

[1] D. Kalderis, S. Bethanis, P. Paraskeva, and E. Diamadopoulos, "Production of activated carbon from bagasse and rice husk by a single-stage chemical activation method at low retention times.," *Bioresour. Technol.*, vol. 99, no. 15, pp. 6809–16, 2008.

[2] A. Bazargan, M. Bazargan, and G. McKay, "Optimization of rice husk pretreatment for energy production," *Renew. Energy*, vol. 77, pp. 512–520, 2015.

[3] L. Armesto, A. Bahillo, K. Veijonen, A. Cabanillas, and J. Otero, "Combustion behaviour of rice husk in a bubbling fluidised bed," *Biomass and Bioenergy*, vol. 23, no. 3, pp. 171–179, 2002.

[4] A. C. Rady, S. Giddey, S. P. S. Badwal, B. P. Ladewig, and S. Bhattacharya, "Review of fuels for direct carbon fuel cells," *Energy and Fuels*, vol. 26, no. 3, pp. 1471–1488, 2012.

[5] S. Giddey, S. P. S. Badwal, A. Kulkarni, and C. Munnings, "A comprehensive review of direct carbon fuel cell technology," *Prog. Energy Combust. Sci.*, vol. 38, no. 3, pp. 360–399, 2012.

[6] A. Kulkarni, S. Giddey, and S. P. S. Badwal, "Electrochemical performance of ceria-gadolinia electrolyte based direct carbon fuel cells," *Solid State Ionics*, vol. 194, no. 1, pp. 46–52, 2011.

[7] A. Elleuch, A. Boussetta, J. Yu, K. Halouani, and Y. Li, "Experimental investigation of direct carbon fuel cell fueled by almond shell biochar: Part I. Physico-chemical characterization of the biochar fuel and cell performance examination," *Int. J. Hydrogen Energy*, vol. 38, no. 36, pp. 16590–16604, 2013.

[8] A. Kacprzak, R. Kobyłecki, R. Włodarczyk, and Z. Bis, "The effect of fuel type on the performance of a direct carbon fuel cell with molten alkaline electrolyte," *J. Power Sources*, vol. 255, pp. 179–186, 2014.

[9] M. Dudek, P. Tomczyk, R. Socha, M. Skrzypkiewicz, and J. Jewulski, "Biomass fuels for direct carbon fuel cell with solid oxide electrolyte," *Int. J. Electrochem. Sci.*, vol. 8, no. 3, pp. 3229–3253, 2013.

[10] X. Li, Z. H. Zhu, R. De Marco, A. Dicks, J. Bradley, S. Liu, and G. Q. Lu, "Factors that determine the performance of carbon fuels in the direct carbon fuel cell," *Ind. Eng. Chem. Res.*, vol. 47, no. 23, pp. 9670–9677, 2008.

[11] J. Wannapeera, N. Worasuwannarak, and S. Pipatmanomai, "Product yields and characteristics of rice husk , rice straw and corncob during fast pyrolysis in a drop-tube / fixed-bed reactor," *Songklanakarin J. Sci. Technol.*, vol. 30, no. 3, pp. 393–404, 2007.

[12] J. H. Windeatt, A. B. Ross, P. T. Williams, P. M. Forster, M. A. Nahil, and S. Singh, "Characteristics of biochars from crop residues: potential for carbon sequestration and soil amendment.," *J. Environ. Manage.*, vol. 146, pp. 189–97, 2014.

[13] E. Pütün, F. Ateş, and A. E. Pütün, "Catalytic pyrolysis of biomass in inert and steam atmospheres," *Fuel*, vol. 87, no. 6, pp. 815–824, 2008.

[14] A. Demirbas, "Combustion characteristics of different biomass fuels," *Prog. Energy Combust. Sci.*, vol. 30, no. 2, pp. 219–230, 2004.

[15] S. C. Peterson, M. a. Jackson, and M. Appell, "Biochar: Sustainable and versatile," *ACS Symp. Ser.*, vol. 1143, pp. 193–205, 2013.

[16] H. Zhang, X. Zhao, X. Ding, H. Lei, X. Chen, D. An, Y. Li, and Z. Wang, "A study on the consecutive preparation of d-xylose and pure superfine silica from rice husk.," *Bioresour. Technol.*, vol. 101, no. 4, pp. 1263–7, 2010.

[17] X. Xu, W. Zhou, F. Liang, and Z. Zhu, "A comparative study of different carbon fuels in an electrolyte-supported hybrid direct carbon fuel cell," *Appl. Energy*, vol. 108, pp. 402–409, 2013.

[18] M. Galbe and G. Zacchi, "Pretreatment of lignocellulosic materials for efficient bioethanol production," *Adv. Biochem. Eng. Biotechnol.*, vol. 108, no. July, pp. 41–65, 2007.

[19] D. Cao, G. Wang, C. Wang, J. Wang, and T. Lu, "Enhancement of electrooxidation activity of activated carbon for direct carbon fuel cell," *Int. J. Hydrogen Energy*, vol. 35, no. 4, pp. 1778–1782, 2010.

[20] I. G. Markovska, B. Bogdanov, N. M. Nedelchev, K. M. Gurova, M. H. Zagorcheva, and L. A. Lyubchev, "Study on the Thermochemical and Kinetic Characteristics of Alkali Treated Rice Husk," *J. Chinese Chem. Soc.*, vol. 57, no. 3A, pp. 411–416, 2010.

[21] C. G. Vassileva and S. V. Vassilev, "Behaviour of inorganic matter during heating of Bulgarian coals," *Fuel Process. Technol.*, vol. 86, no. 12–13, pp. 1297–1333, 2005.

[22] T. Lee, R. Othman, and F. Y. Yeoh, "Development of photoluminescent glass derived from rice husk," *Biomass and Bioenergy*, vol. 59, pp. 380–392, 2013.

[23] T. R. Brown, M. M. Wright, and R. C. Brown, "Estimating profitability of two biochar production scenarios: slow pyrolysis vs fast pyrolysis," *Biofuels, Bioprod. Biorefining*, vol. 5, no. 1, pp. 54–68, 2011.

[24] P. Quaak, H. Knoef, and H. Stassen, "Energy from Biomass: A review of combustion and gasification technologies," *World Bank Tech. Pap.*, no. 422, pp. 1–78, 1999.

[25] Z. Liu, B. Fei, Z. Jiang, and X. Liu, “Combustion characteristics of bamboo-biochars.,” *Bioresour. Technol.*, vol. 167, pp. 94–9, 2014.

[26] A. Enders, K. Hanley, T. Whitman, S. Joseph, and J. Lehmann, “Characterization of biochars to evaluate recalcitrance and agronomic performance.,” *Bioresour. Technol.*, vol. 114, pp. 644–53, 2012.

[27] K. L. Chin, P. S. H’ng, M. T. Paridah, K. Szymona, M. Maminski, S. H. Lee, W. C. Lum, M. Y. Nurliyana, M. J. Chow, and W. Z. Go, “Reducing ash related operation problems of fast growing timber species and oil palm biomass for combustion applications using leaching techniques,” *Energy*, pp. 1–9, 2015.

[28] B. . Jenkins, L. . Baxter, T. . Miles, and T. . Miles, “Combustion properties of biomass,” *Fuel Process. Technol.*, vol. 54, no. 1–3, pp. 17–46, 1998.

[29] R. V. Krishnarao, J. Subrahmanyam, and T. Jagadish Kumar, “Studies on the formation of black particles in rice husk silica ash,” *J. Eur. Ceram. Soc.*, vol. 21, no. 1, pp. 99–104, 2001.

[30] G. Nallathambi, T. Ramachandran, V. Rajendran, and R. Palanivelu, “Effect of silica nanoparticles and BTCA on physical properties of cotton fabrics,” *Mater. Res.*, vol. 14, no. 4, pp. 552–559, 2011.

[31] N. Prakongkep, R. J. Gilkes, W. Wiriyakitnateekul, and A. Duangchan, “The Effects of Pyrolysis Conditions on the Chemical and Physical Properties of Rice Husk Biochar,” *Int. J. Mater. Sci.*, vol. 3, no. 3, pp. 97–103, 2013.

[32] G. a. Hackett, J. W. Zondlo, and R. Svensson, “Evaluation of carbon materials for use in a direct carbon fuel cell,” *J. Power Sources*, vol. 168, no. 1 SPEC. ISS., pp. 111–118, 2007.

[33] C. Deiana, D. Granados, R. Venturini, A. Amaya, M. Sergio, and N. Tancredi, “Activated carbons obtained from rice husk: Influence of leaching on textural parameters,” *Ind. Eng. Chem. Res.*, vol. 47, no. 14, pp. 4754–4757, 2008.

[34] I. Martin-Gullon, J. P. Marco-Lozar, D. Cazorla-Amorós, and a. Linares-Solano, “Analysis of the microporosity shrinkage upon thermal post-treatment of H3PO4 activated carbons,” *Carbon N. Y.*, vol. 42, no. 7, pp. 1333–1337, 2004.

[35] T. Lee, Z. A. Zubir, F. M. Jamil, A. Matsumoto, and F.-Y. Yeoh, “Combustion and pyrolysis of activated carbon fibre from oil palm empty fruit bunch fibre assisted through chemical activation with acid treatment,” *J. Anal. Appl. Pyrolysis*, vol. 110, pp. 408–418, 2014.

HARNESSING OF RENEWABLE ENERGY SOURCES FOR SUSTAINABLE FUTURE

NEELKANTH GOYAL*, SUDHNAY VERMA

Department of Electrical engineering
Chandigarh University,
Gharuan (Mohali), India
*Corresponding Author: neelkanthgoyal@gmail.com

Abstract

This paper describes the ideology for an energy efficient building. Day-by-day energy requirement is increasing, there is a huge gap between energy generation and energy consumption and we are not capable of producing at the rate at which demand of energy is increasing. So we have to choose an alternate source of production. Energy conservation is taken as new source of production as energy saved is energy produced. So in this paper, we are harvesting the simple day life non-conventional sources for producing energy. In this paper, some methodologies are discussed and structure is proposed with different materials for Smart and Futuristic Environment.

Keywords: Non-conventional sources; Energy Efficient Building; Smart Buildings, Auto-cad

1. Introduction

The utility electricity sector in India had an installed capacity of 278.733 GW as of 30 September 2015. Renewable Power plants constituted 28% of total installed capacity and Non-Renewable Power Plants constituted the remaining 72%. The available fossil fuels were about 65%. These fossil fuels will exhaust in coming few years estimated to be 35-40 years. These fossil fuels when used for the generation of electric power have an environmental impact as have carbon emission and other flue gases released. So it is advised to use non-conventional sources of energy or re-harvest the energy released by the machines. The day to day available non-conventional sources are thereby used in smart buildings or energy efficient buildings.40% body station.

2.Methodology

The Methodology involves Ventilation System for whole year comprising of two extreme environments. Energy Efficiency also pertain to use of Renewable Energy sources by making use of Solar Energy with in economic constraints, producing Pyroelectric effect harvested energy with recycling of water technique.

2.1. RESERVOIR & VENTILATION SYSTEM

It holds the rain water and has two major functions. From here we can provide water to the washrooms and for other such purposes like it can also be provided for fire protection. Water from reservoirs is also used for cooling purposes. For water cooling, the water through the reservoir is carried out to the tanks constructed over the roof [1, 2]. Here the water is cooled naturally during the night and is then used for cooling the building with fans moving in pipes. Now the warm and exhausted air is removed from the building using exhaust fans and

this heat can be exchanged with the cold water already available in the reservoir.
It also presented in Fig.1, 2 & 3.

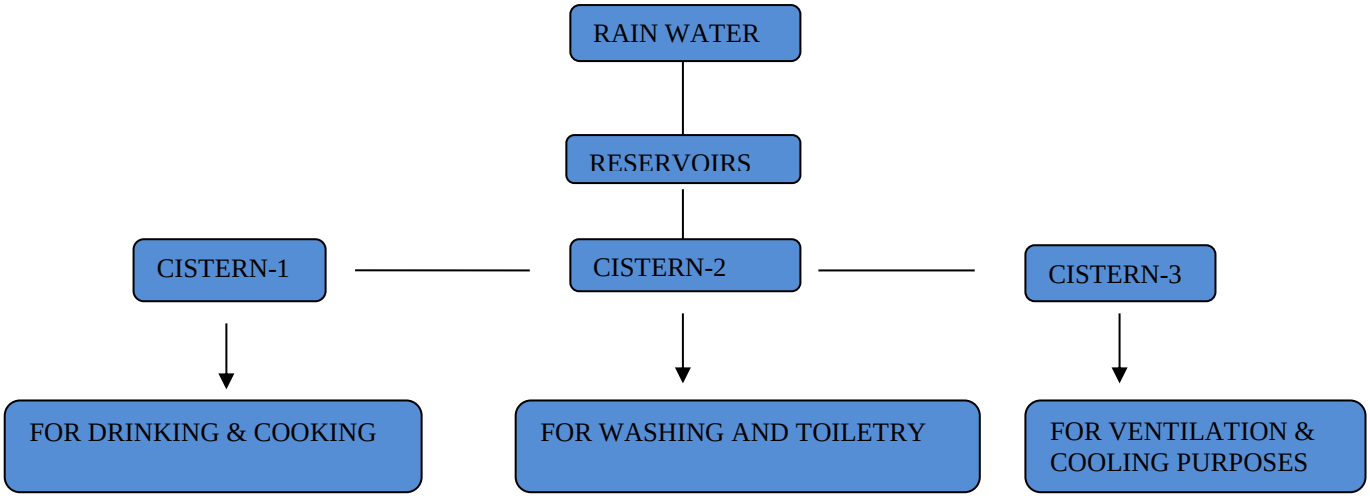


Fig. 1 WATER USAGE SYSTEM

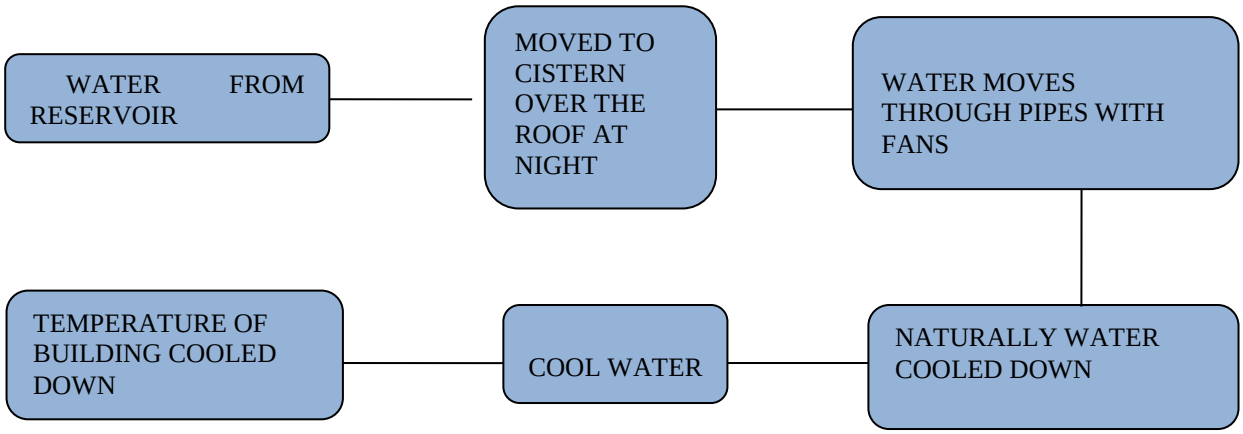


Fig. 2 VENTILATION SYSTEM (FOR SUMMERS)

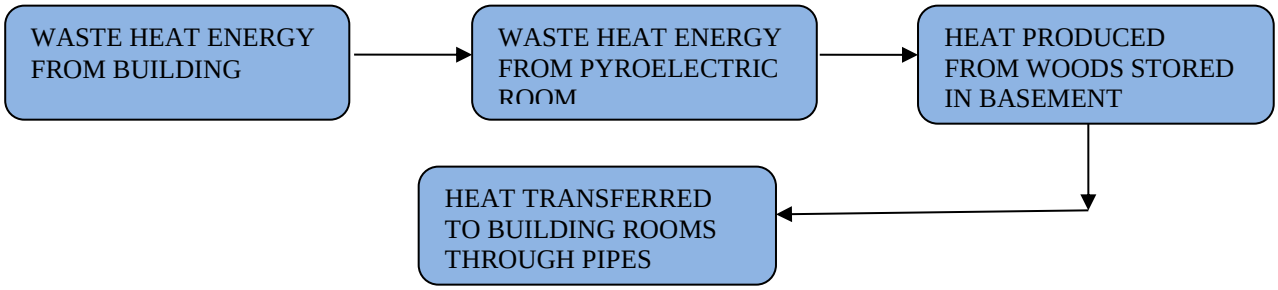


Fig.3 VENTILATION SYSTEM (FOR WINTERS)

2.2. RECYCLING OF WATER

Recycling of water and energy efficient usage of water are also a part of smart building. As the rain water is collected in the reservoir. From that reservoir the water is used for various purposes and is therefore divided into different sub cisterns [9].

One cistern is used for providing coolness to the building during hot seasons. While for providing warm heat to the building during winters, heat left from Pyroelectric energy room and heat energy produced from woods collected in basement of the building [5,6]. One cistern is used for providing water for drinking and cooking purposes while other cistern is used for toilets and other such activities. In toilets vacuum pumps and drain system is involved such that water used for washrooms is quite less. Here we have provided two types of drainage. One is where the waste drinking water is moved and recycled back such that it is used for gardening purposes and the water collected in the other drainage unit is recycled and used for making fertilizers and other organic compounds. The Proposed structure is shown in Fig. 4.

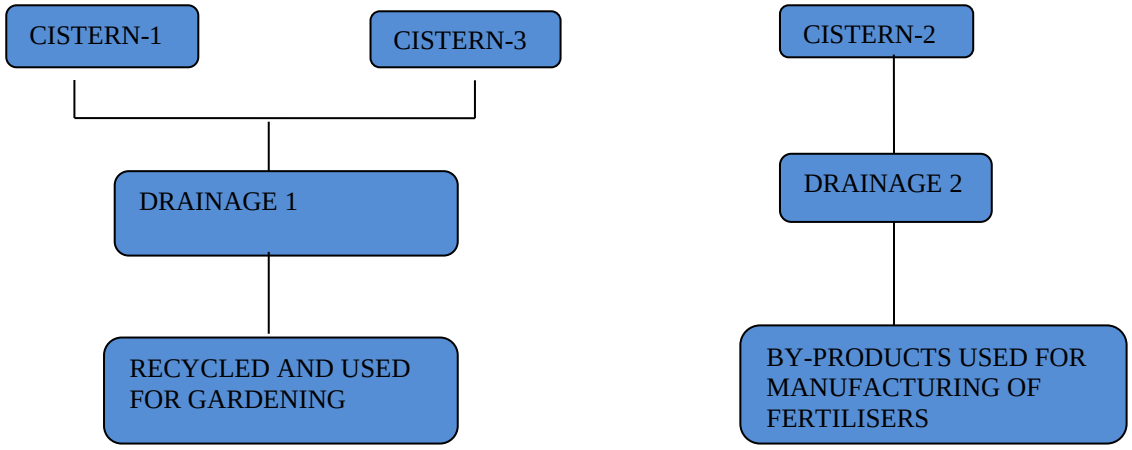


Fig. 4 Proposed Structure for Recycling of Water

2.3. Solar Energy

Solar power is a promising, carbon-neutral energy source. Solar power is produced in two ways: concentrating solar power (CSP) and photovoltaic. CSP utilizes focused sunlight to generate heat and steam that powers a standard turbine. When coupled with storage solutions, CSP may be able to provide dispatch able energy, for example, energy that can be stored for a several hours and called upon when needed. Solar PV systems convert sunlight directly into electricity. Starting in the early 2000s, demand for PV systems grew significantly when Germany and later Spain instituted significant Fits for solar-generated electricity. As considerable poly-silicon capacity has been added (largely in China) to serve such demand, PV module prices have fallen by 75%. As these costs have declined in recent years, solar capacity has grown dramatically. However, other costs remain – associated with the installation and efficient grid integration of this type of energy (e.g., permits, installation costs and materials) [7, 8]. The growth of solar PV might be affected by inexpensive shale gas in the US. At the same time, however, many parts of the world show favourable

irradiation conditions where the quick cost- reduction of PV is likely to lead to competitiveness in the short term.45 Also, as the industry continues to cut the costs of installation and the total system, PV will reach cost-levels that are financially viable for final consumers to displace some electricity purchased from the grid with power generated in their own PV systems. The better the match between load profile and solar irradiation, the higher will be the share of self-consumed output and the better will be the business case

The solar energy is abundant in nature. Here we are harvesting the solar energy using photovoltaic cells (solar panels). For this we have installed solar panels on the roof top of the buildings which here convert the solar energy into useful electric energy. From here, the converted electric energy is transferred to the battery rooms where the energy is stored and is used for various purposes like providing lightning and other such light loads. Solar panels are further installed on the roof of the parking lots. Similarly the converted energy is transferred to the same battery room in Fig. 4 [2].

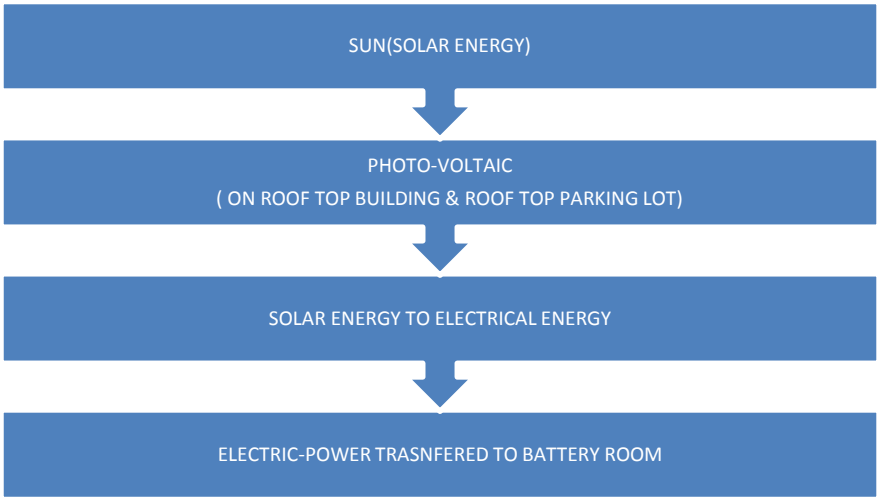


Fig. 5 Terminology for Transferring of Solar Energy

2.4. PYROELECTRIC EFFECT HARVESTED ENERGY

The Pyroelectric effect converts a temperature change into electric current or voltage. It is analogous to the piezoelectric effect, which is another type of ferroelectric behaviour. Pyroelectricity requires time-varying inputs and suffers from small power outputs in energy harvesting applications due to its low operating frequencies. However, one key advantage of Pyroelectric over thermoelectric is that many Pyroelectric materials are stable up to 1200 ^{0}C or higher, enabling energy harvesting from high temperature sources and thus increasing thermodynamic efficiency.

With help of this effect the thermal energy or the heat energy released from air conditioners or other such big machines can be harvested with the use of Pyroelectric transducers.

For this purpose we have used an idea of collecting the thermal energy in a single collecting duct. This duct is directly connected to the Pyroelectric energy room.

2.5. PIEZO POWERED AREA

The piezoelectric effect converts mechanical strain into electric current or voltage. For this purpose we have installed piezo electric transducers in the streets of the university and making university roads as smart roads producing electric energy with the help of piezo electric transducers. As the power developed is in milli-watts, so it is used for providing energy to the led notice boards for giving information related to university and current affairs. The mechanism and demonstration is shown in Fig.6



Fig.6 Demonstration and Mechanism of Piezo Powered Area

3. Design of Building

More glass windows are used for using the natural light and the material used is insulating material such that during summers coolness is maintained and during winters heat is maintained within the building [3, 4].(winters: space provided btw window panes).

Automatic lightning technique is used which further helps in saving energy.

3.1 Proposed Material for Building

3.1.1 Insulated glass

Insulated glazing, or double glazing, consists of a window or glazing element of two or more layers of glazing separated by a spacer along the edge and sealed to create a dead air space between the layers. This type of glazing has functions of thermal insulation and noise reduction. When the space is filled with an inert gas it is part of energy conservation sustainable architecture design for low energy buildings.

3.1.2 Cistern

Cisterns can be constructed from a variety of materials including cast-in-place reinforced concrete, cinderblock and concrete, brick or stone set with mortar and plastered with cement on the inside, ready-made steel tanks, precast concrete tanks, redwood tanks, and fibreglass. Cast-in-place reinforced concrete is considered best, especially for underground cisterns. However, cinderblock-walled cisterns with concrete floors are common and are quite satisfactory for below-ground construction; these will usually be somewhat less expensive than the all-concrete version. Concrete walls and floors should be at least 6 inches thick and reinforced with steel rods.

3.1.3 Mineral wool

Mineral wools, including rock and slag wools, are inorganic strands of mineral fibre bonded together using organic binders. Mineral wools are capable of operating at high temperatures and exhibit good fire performance ratings when tested.

Mineral wools are used on all types of pipe work, particularly industrial pipe work operating at higher temperatures.

3.1.4 Glass wool

Glass wool is a high-temperature fibrous insulation material, similar to mineral wool, where inorganic strands of glass fibre are bound together using a binder.

As with other forms of mineral wool, glass-wool insulation can be used for thermal and acoustic applications.

4. Conclusions

An investigation has been made on the conventional systems Some concluding observations from the investigation are given below.

- Rain Harvesting Technique is viable to conventional system and can reduce 40% of total Energy consumption along with Smart Ventilating System.
- Piezo Electric and Pyro Electric Effect Technique will complete their payback period in five years if implemented for replacing Conventional System.
- With the use of Solar Energy and right orientation of Building, Emergy Analysis can be calculated to improve the efficiency of building.

5.Future Aspects

Renewable Energy Sources are much costly in installation and gestation period dominates the environment LCA in various ways and are limited in use. So we have discussed some of the renewable energy sources in the manuscript. Like we can implement the use of mirrors at an angle of 45 degrees, use of snubbers, roof terracing. Various methods are already proposed, thus improvisation can be carried out in the research area.

Acknowledgement

The author would like to acknowledge Electrical Engineering Department of CHANDIGARH UNIVERSITY, Gharuan, India.

References

1. ASRHAE/IESNA Standards 90.1-2004, ASRHEA Standard - Energy Standards for Buildings except Low-Rise Residential Buildings. American Society of Heating Refrigerating and Air conditioning Engineers, Inc.
2. IECC 2004, International Energy Conservation Code 2004. Energy standard for Low-Rise Residential Buildings set by the International Code Council, ICC.
3. IEBC, International Buildings Code for Existing Buildings, International building code for energy efficiency in existing buildings set by ICC, International Code Council.

4. CEPHEUS project on Cost Effective Passive Houses as European Standard, Final Report July 2001.
5. R. Dones, C. Bauer, R. Bollinger, B. Burger, M. F. Emmenegger, R. Frischknecht, T. Heck, N. Jungbluth, A. Roder, and M. Tuchschmid, "Life cycle inventories of energy systems," Swiss Centre for Life Cycle Inventories, Duebendorf, Switzerland, Eco Invent Rep. No. 5, 2007.
6. S. Pfister, A. Koehler, and S. Hellweg, "Assessing the environmental impacts of freshwater consumption in LCA," Environ. Sci. Technol., vol. 43, pp. 4098–4104, 2009.
7. M. Held, "Life cycle assessment of CdTe module recycling," in Proc. 24th Eur. Photovoltaic Solar Energy Conf. Exhib., 2009, pp. 2370–2375.
8. V. Fthenakis and H. C. Kim, "Life-cycle uses of water in U.S. electricity generation," Renewable Sustainable Energy Rev., vol. 14, pp. 2039–2048, 2010.
9. J. F. Kenny, N. L. Barber, S. S. Hutson, K. S. Linsey, J. K. Lovelace, and M. A. Maupin, "Estimated use of water in the United States in 2005," U.S. Geological Survey, Reston, VA, Circular 1344, 2009.

Designing of TRANSMITTER CIRCUIT for GESTURE BASED ROBOT

Aniket Rai*, Vivek Kanwar and Anjali Thakur
Department of Electrical engineering
Chandigarh University,
Gharuan (Mohali), India
*Corresponding Author: aniket.india99@gmail.com

Abstract

In this paper TRANSMITTER CIRCUIT for a GESTURE BASED ROBOT is designed and implemented to propose a GESTURE BASED ROBOT. Circuits are designed using ELECTRICAL SIMULATION SOFTWARES. Applications and Algorithms have been studied thoroughly.

Keywords Gesture Based Robot, Microcontroller (8051), Gesture Devices

1. Introduction

Robotics is a branch of engineering which involves the mechanical, electrical as well as electronics study including a deep knowledge of software's [1.2]. It deals with the design construction and applications of robot as well as computer system for the feedback of control sensory system as well as for the processing of information.
Gesture based robot is a well equipped modernized robot which is not controlled by primitive ideas like pressing a button whereas it is controlled by the gesture of hands. Wearing a transmitting device (mainl ACCELOROMETERS) in the hand is the only thing which is required to control it. This transmitting chip or device will transmit the appropriate signals or commands to the robot to make it to do the work that we want it to do.the transmitting device which user need to wear consists of a COMPARATOR IC to convert the analog signals into digital signals, an ENCODER IC(HT12D) to encode the 4 bit data and after that an RF TRANSISTOR module is used to transmit that data. Receiving end is equipped with an RF RECEIVER module that receives the data from the transmitter and decode it by a DECODER IC(HT12D).The data then received by the decoder is processed by the MICROCONTROLLER(8051) and at last after all these processes MOTOR DRIVERS are used to control the motors flowchart is being drawn below to show how transmitting devices works in top to bottom manner.

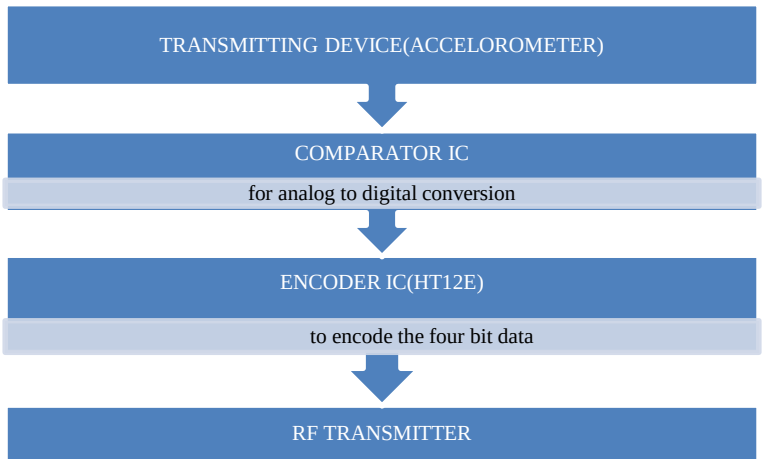


Fig. 1 Flowchart for Transmitting Devices

2. Methodology

The overall processes which were required to complete the project is divided into different modules to make it more easier and simpler as well as error free.
The module in which the project is divided is shown below with the help of a block diagram:

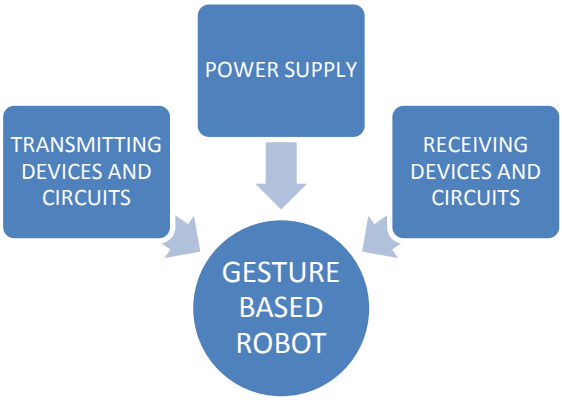


Fig.2 Block Diagram

The block diagram above depicts that the whole project i.e. GESTURE BASED ROBOT is made with the help of POWER SUPPLY, TRANSMITTING DEVICES and RECEIVING DEVICES.
Now, let's have a look towards the components that are required for making our transmitter circuit for the proposed gesture based robot through this table

Table.1 Components used and its specifications

SERIAL NUMBER	NAME OF THE EQUIPMENT	QUANTITY USED
1	7805 VOLTAGE REGULATOR	1
2	8051 MICROCONTROLLER	1
3	ACCELEROMETER	1
4	COMPARATOR	1
5	ENCODER(HT12E)	1
6	RF TRANSMITTER	1

Since this paper involves only the designing of transmitter circuit we will only discuss about the transmitting circuit and the devices which are used in the robot for the purpose.

VOLTAGE REGULATER:- A voltage regulator is used for maintain constant voltage level. To supply a constant voltage to different equipment voltage regulator are used.

MICROCONTROLLER:- An 8051 microcontroller is used in circuit to give decision capability .The data from the decoder now based on that data which have to make the decision .

ACCELEROMETER:- It is a sensor which provide analog data while moving in any direction if only depends on the type of sensor.

COMPARATOR:- The use of comparator is to change the analog voltage into digital voltage which compare that analog voltage to reference voltage and provide particular voltage whether it is high or low.

ENCODER(HT12E):- It is used to encode the data provided to it. The data provided by the user is stored in encoder.

RF TRANSMITTER:- RF transmitter is used to make robot wireless .it consists a transmitter or a receiver it also transmits encoded signal.

3. Origin of robot

As the idea of robot is very old but it is still in the process of advancement many new things are being discovered in robot. Earlier, the robots was not gesture based they can't be operated easily. As they are very much complex and difficult to handle they are large in size but as the time passes size and handling of robot is reduced . Now its easy to operate a robot as now a day's robots are gesture based. A **Gesture Controlled robot** is a robot which can be controlled by hand gestures not by old buttons. It needs to wear a small transmitting device in hand which included an acceleration meter [3, 4]. The transmitting device included a ADC for analog to digital conversion and an encoder IC(HT12E) which is use to encode the four bit data and then it will transmit by an RF Transmitter module.

4. Technical Gaps in Existing Work

a. Power supply:

It is well known by all that before making any electrical, mechanical or electronic device to work we need to design its power circuit that from where It will complete its power requirement. Similarly in the case of robot also it is necessary to make the power circuit foremost [4]. A power supply circuit consist of many parts like step down ,ac-dc conversion, voltage stabilizing etc but for making a robot the power will be given through a 12 volt adapter so we can say that our power supply consists of a voltage regulator, capacitor, diode, LED and connector .

7805 voltage regulator can be used and an image of that is shown below:

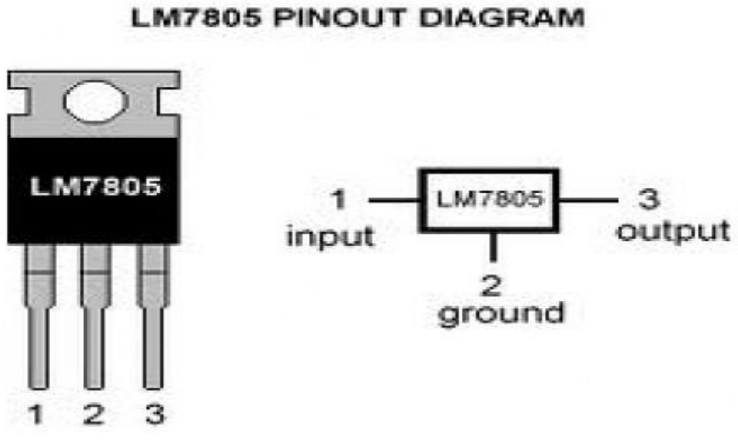


Fig.3 Pin Diagram

A 1000uF capacitor has been used in order to maintain the continuity and to reduce the ripple. A 2 pin male connector can be used to give the power. The positive should be connected to pin1 of 7805.

b. Microcontroller: An 8051microcontroller has 40 pins and the basic circuit of the microcontroller consists of reset circuitry and oscillator circuit. It has 32 inputs -output lines, four 8bit ports. For making the circuit one needs only 8 pins which are as follows:

- Pin no.9 is a reset pin which reset the program counter of 8051 and is highly active.
- XTAL1 and XTAL2 provides the oscillations to the controller
- For serial communication pin no.10 and 11 are used.
- 31st and 40th pin no. are used to provide Vcc(5V)
- Pin no. 20 is ground.

To make the above points more understandable and easy an image is shown below for the proposed microcontroller.

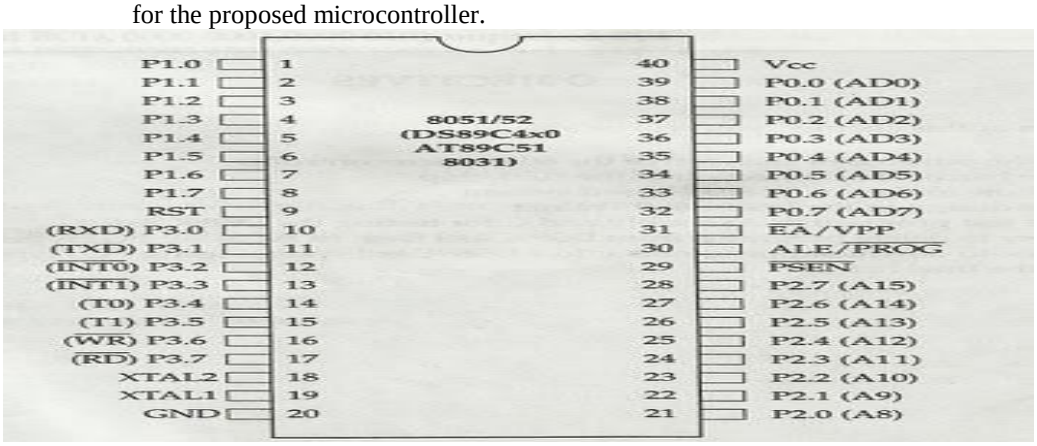


Fig.4 Configuration of Pin Diagram

The two basic circuits which can be referred for microcontroller are shown below:

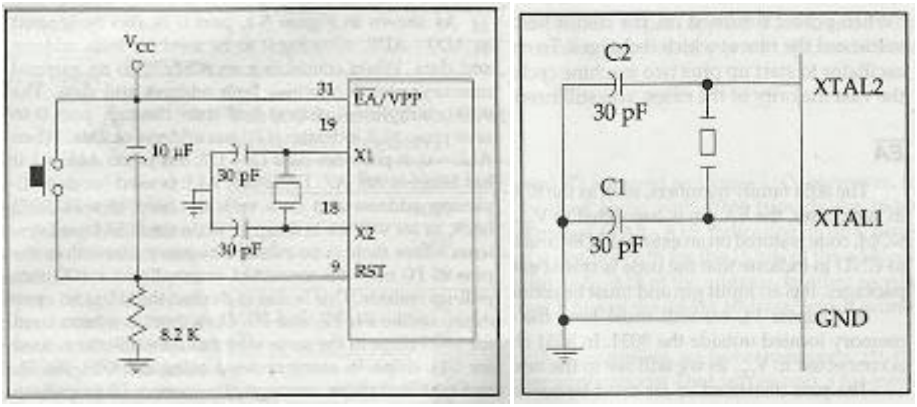


Fig.5 Circuit Diagram

c. Transmitter devices:

These are the devices which to different tasks from sensing the gesture of our hands, converting the analog signals into digital to transmit it to the receiver. Foremost device which has been used is ACCELEROMETER [5].

ACCELEROMETER: It is a type of sensor which provides an analog data while moving in X, Y, Z direction. An accelerometer consists of 6 pins

- Vdd is given the +5volt supply
- Pin GND is being connected to the ground for biasing
- X pin receives the analog data for x-direction movement
- Y pin receives the analog data for y-direction movement
- Z pin receives the analog data for z-direction movement
- ST is used to set the sensitivity of the device

Secondly, comparator is used for the conversion of analog voltage into digital. it compares the analog voltage to reference voltage and gives a particular high or low voltage. a proposed fig.of comparator IC is shown below Pins 1,7,8,14 are used to give the output to the microcontroller
ENCODER(HT12E):

- It is a 4-bit encoder IC which is used to encode the input data applied on it.
- Pins(1-8)are not needed to be considered as they are address bits.
- Pins(9-18) can be used to bias the IC. Pin18 is connected as Vcc and pin9 should be connected to ground.
- RF transmitter module is connected to pin17
- Pin14 is grounded to enable the transmission
- Pins13-pin10 contains 4bit data which is to be transmitted.

RF TRANSMITTER:

A positive terminal of the circuit has been connected to the pin Vcc. The ground terminal is being connected to the pin i.e. named as GND last pin i.e ANT is being connected to a small wire antenna.

RESULT

The complete transmitter circuit for the proposed gesture based robot is being studied and designed using different devices and computer software's. A complete circuit for the transmitter module is shown below:

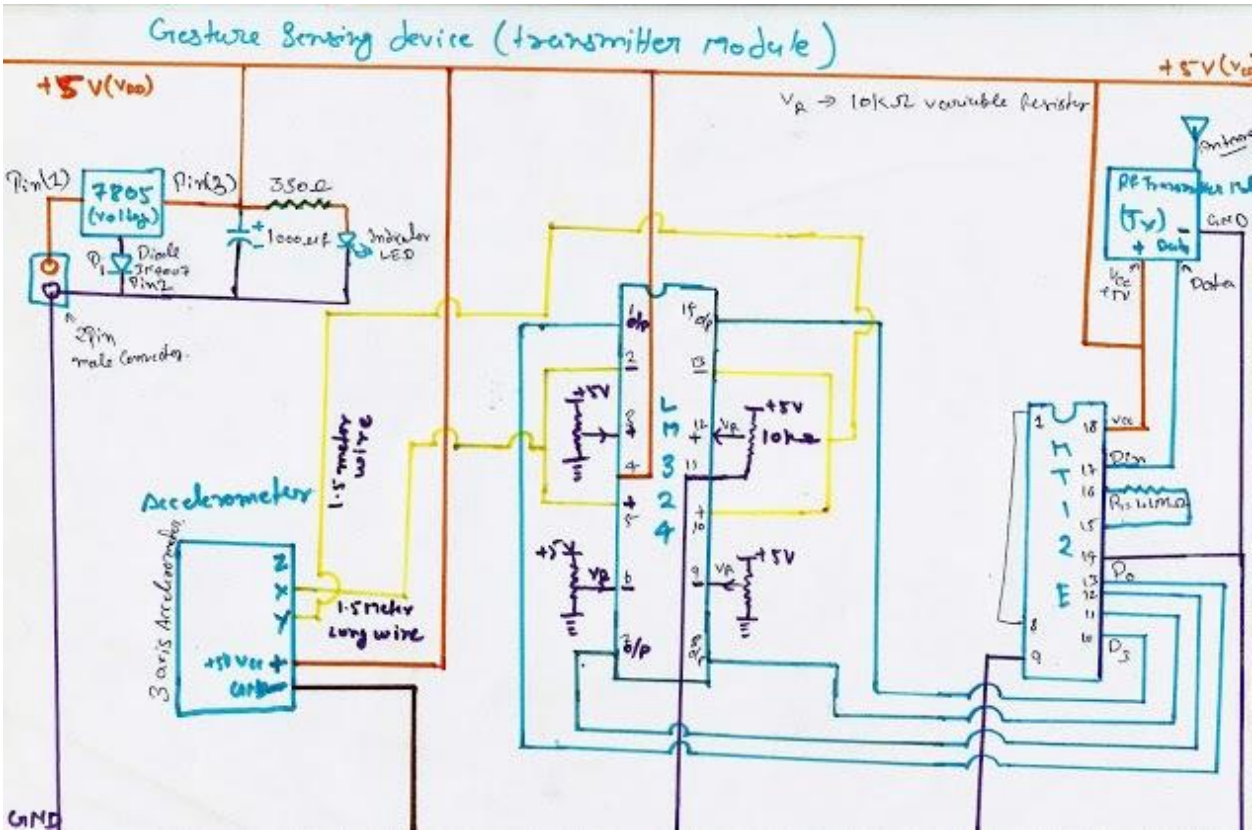


Fig. 6. Complete transmitter circuits

Conclusion

Gesture based Robotics is used to make line follower, edge avoider and implemented using Bluetooth technology.

Acknowledgement

The author would like to acknowledge electrical department of CHANDIGARH UNIVERSITY , Gharuan, India.

References

[1] Dai and Kampker, 2000] Wenrui Dai and M. Kampker. User oriented integration of sensor operations in a of- fline programming system for welding robots. In Proceedings of the IEEE Intl. Conf. on Robotics and Automation (ICRA ’00), volume 2, pages 1563–1567, apr 2000.

[2] Jeon, P.W., Jung, S.: Teleported Control of Mobile Robot Using Exoskeleton Type Motion Capturing Device Through Wireless Communication. In: Proceedings of the 2003 IEEE/ASME International Conference on Advanced Intelligent Mechantronics (AIM 2003), july 2003

[3] Sibert, L.E., Jacob, R.J.K.: Evaluation of Eye Gaze Interaction. In: Proceedings of the ACM SIGCHI Conference on Human Factors in Computing Systems (CHI 2000), pp. 281–288 (2000); The Hague Amsterdam. CHI Letters. 2(1), 1–6 (April 2000

[4] T. H. Speeter (1992), “Transformation human hand motion for tele manipulation,” Presence, 1, 1, pp. 63–79.

[5] W. M. Newman and R. F. Sproull (1979), Principles of Interactive Computer Graphics. New York: McGraw-Hill.

REVIEW ON WIND AND SOLAR ENERGY SOURCES

VANDANA*, SUKHLEEN KAUR

Department of Electrical engineering
Chandigarh University,
Gharuan (Mohali), India
*Corresponding Author: vandanamukhija09@gmail.com

Abstract

This research gives brief introduction about types of renewable Energy Sources mainly Solar and Wind energy. Renewable Energy Sources are of paramount importance as conventional Energy Sources are not in a position to cater the needs of changing demand scenario. Various Renewable Energy Technologies are not conversant with Conventional Energy Sources Technologies. Thus, to synchronize both past and present Energy Sources, advanced technologies need to address. This paper addresses the technologies used for Renewable Energy Sources and their prominent role in present scenario.

Keywords: Non-conventional sources; Efficient Technologies

6. Introduction

Energy is basic need of human beings of modern society. The primary resources available are used since past to convert them into useful forms of the energy. In ancient times the society was based on various forms for example:-wind, Hydro, bio and other energy. There was Continuous improvement in the technology for harnessing the energy from these resources and brought an industrial revolution .the fossil fuel such as coal, natural gas have been used in industrial world to produce needed for the society [1, 2].

Energy: Energy is the fundamental concept and is defined as the capability to produce an effect or capacity to do work. It has following characteristics:

- It can transformed from one form to another
- It can be stored
- An energy is associated with a potential
- It can neither be created nor be destroyed
- It doesn't have absolute values
- Energy is available in different forms

2. WIND ENERGY

Wind energy is extracted from air flow using wind turbines or sails to produce mechanical or electrical power. Windmills are used for their mechanical power, wind pumps for water pumping, and sails to propel ships Wind power as an alternative to fossil fuels is plentiful, renewable widely distributed, clean produces no greenhouse gas emissions during operation, and uses little land. The net effects on the environment are far less problematic than those of non-renewable power sources.

Wind farms consist of many individual wind turbines which are connected to the electric power transmission network. Onshore wind is an inexpensive source of electricity, competitive with or in many places cheaper than coal, gas or fossil fuel plants .Offshore wind is steadier and stronger than on land, and offshore farms

have less visual impact, but construction and maintenance costs are considerably higher. Small onshore wind farms can feed some energy into the grid or provide electricity to isolated off-grid locations [9].

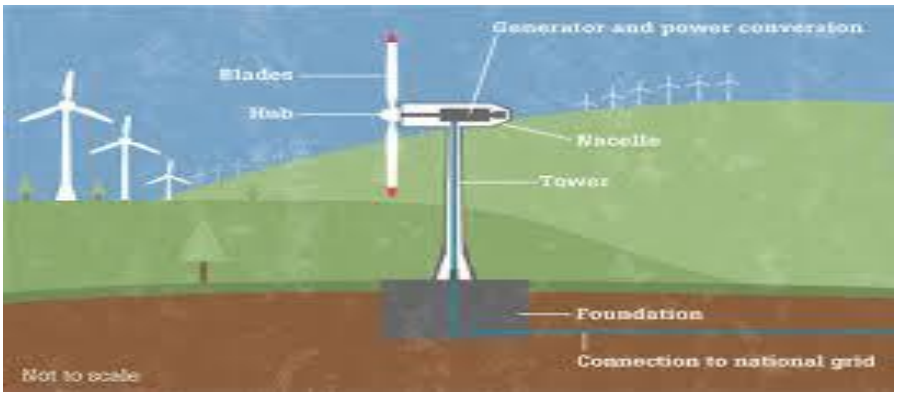


Fig. 1 Wind Energy Generation

- **WIND TURBINE**

It's a device that converts kinetic energy from the wind into electrical power the term appears to have migrated from parallel hydroelectric technology (rotary propeller). The technical description for this type of machine is an aerofoil-powered generator.

The result of over a millennium of windmill development and modern engineering, today's wind turbines are manufactured in a wide range of vertical and horizontal axis types. The smallest turbines are used for applications such as battery charging for auxiliary power for boats o or to power traffic warning signs. Slightly larger turbines can be used for making contributions to a domestic power supply while selling unused power back to the utility supplier via the electrical grid Arrays of large turbines, known as wind farms are becoming an increasingly important source of renewable energy and are used by many countries as part of a strategy to reduce their reliance on fossil fuels.

- **STEPS TO REMOVE CARBON CONTENT FROM AIR**

Plant trees and preserve the rain forests. A plant improves the process of photosynthesis to convert atmospheric CO2 into carbon-rich carbohydrates and sugars to feed them. They not only feed themselves, but also feed the whole chain of animal life. They also produce oxygen as a by-product of photosynthesis, an element essential for animal life.

- Operate power plants with improved technology to reduce the fuel input. Carbon dioxide is an unavoidable part of the combustion process. Small reductions are possible by process adjustments. Major reductions in CO2 can only be achieved by a drastic change in Power generation technology.
- Encourage people to promote energy efficient practices such as :-
- Insulating the house, and reducing the use of refrigerator, washing machine, and water heater. Buying products with minimal packaging. Less driving means fewer emissions.

- Replace regular light bulbs with compact florescent light (CFL) bulbs.
- Use less heat and air conditioning.
- Use less hot water. Warm or cold water to reduce your use of hot water and the energy required to produce it. That change alone can save at least 500 pounds of carbon dioxide annually in most households.
- Save electricity and reduce global warming by turning off lights when you leave a room, and using only as much energy as you need. And remember to turn off your television, stereo and computer when you're not using them. Utility companies provide free home energy audits to help consumers identify areas in their homes that may not be energy efficient.
- Share information about recycling and energy conservation with your friends, neighbours and co-workers, and take opportunities to encourage public officials to establish programs and policies that are good for the environment.
- Encourage the use of public transportation facilities instead of private vehicles.
- Chemical methods conversion of carbon dioxide to more reduced chemical species using electrical energy. when carbon dioxide was reduced to formic acid using a zinc cathode.
- Industry have recently begun to pay more attention to carbon capture and storage (CCS) — a process that traps CO2 produced by factories and gas or coal power stations and then stores it, usually underground.
- Reduce the consumption of carbon-based fuels (e.g., natural gas, oil, coal, or gasoline)
- Biochar is charcoal used as a soil amendment is emerging practice which converts agricultural waste into a soil enhancer that can hold carbon, boost food security and increase soil biodiversity, and discourage deforestation. The process creates a fine-grained, highly porous charcoal that helps soils retain nutrients and water.
- Ocean fertilization is a type of climate engineering based on the purposeful introduction of nutrients to the upper ocean to increase marine food production and to remove carbon dioxide from the atmosphere.
- Use the dissolution of natural or artificially created minerals to remove carbon dioxide from the atmosphere.

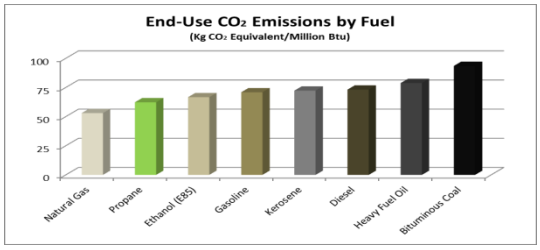


Fig. 2 Emissions of CO_2

In less than two centuries of industrial revolution, the man has managed to deteriorate his habitat, the Earth, beautiful and fragile result of millions of years or evolution. We have a duty of solidarity towards the next generations. We have to accept our heavy responsibility in the current situation. We have no right to leave to our children as unique heritage the administration of our mistakes. If we don't take immediate actions, we will be guilty of non assistance towards the humanity in danger [7, 8].

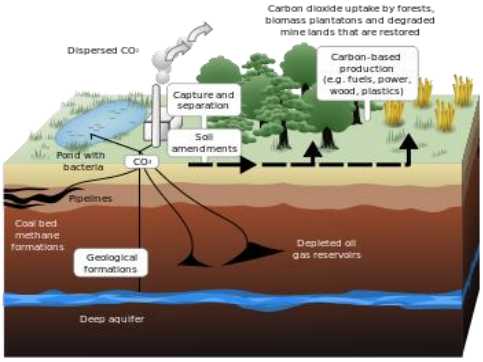


Fig. 3 Green House Effect

Few effective and simple methods for Carbon-free energy sources include solar power, wind power, geothermal energy, low-head hydropower, hydrokinetics (e.g., wave and tidal power), and nuclear power. Alternatively, switching from high-carbon fuels like coal and oil, to reduced-carbon fuels such as natural gas, will also result in reduced carbon dioxide emissions. Another option for reducing carbon dioxide in the atmosphere is carbon sequestration. Carbon sequestration involves the capture and storage of carbon dioxide that would otherwise be present in the atmosphere, contributing to the greenhouse effect.

3. SOLAR ENERGY

The sun is a large sphere of hot gases with its diameter which is 1100 times of earth diameter and because of this large distance the sun subtracts an angle of 30 min at the earth surface [3]. The sun is a sustainable source of providing inexhaustible renewable energy is the form of heat etc. The solar energy is produced by the sun due to nuclear fusion. The sun is like a nuclear reactor which generates enormous amount of heat

The solar energy we get on the earth’s surface directly is in the form of radiation, visible light and infrared radiation. This energy is absorbed by surface as well as ocean, plants and buildings .Although the amount of

solar enegy reaching is very large but there are also limitations to collect it efficiently and convert it into useful form

- **SOLAR CELL**

A solar cell is a device people can make that takes the energy of sunlight and converts it into electricity. In a crystal, the bonds [between silicon atoms] are made of electrons that are shared between all of the atoms of the crystal. The light gets absorbed, and one of the electrons that's in one of the bonds gets excited up to a higher energy level and can move around more freely than when it was bound. That electron can then move around the crystal freely, and we can get a current.

Imagine that you have a ledge, like a shelf on the wall, and you take a ball and you throw it up on that ledge. That's like promoting an electron to a higher energy level, and it can't fall down. A photon [packet of light energy] comes in, and it bumps up the electron onto the ledge representing the higher energy level and it stays there until we can come and collect the energy [4, 5].

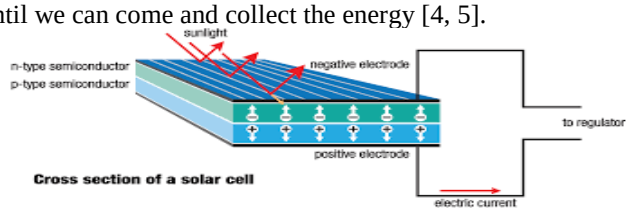


Fig. 4 Solar Cell

- **ECONOMIC ANALYSIS OF SOLAR ENERGY**

On average the total cost of solar installation can be between $15,000 to $29,000 for average sized systems sized between 4kW and 8kW.2
Sun run solar lets you get started for as little as $0 down and helps you lower your electric bill. If you want to own your system, we do that too. If you choose to buy your system, the graph shows an average breakdown of costs of a residential solar installation.

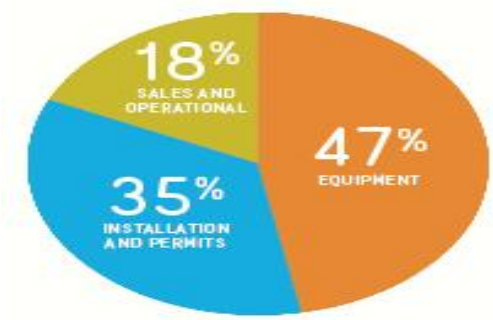


Fig.5 Graphical Analysis of Solar Energy

- Equipment costs: Solar panels , inverter, mounting hardware and wiring
- Installation and permits: Installation, supply chain, permitting and interconnection
- Sales and operational: Monitoring and maintenance costs, repairs, additional operational and overhead

- **STEPS TO REDUCE COST OF SOLAR ENERGY POWER SYSTEM**

1. RTI's solar cells are formed from solutions of semiconductor particles, known as "colloidal quantum dots" that can have power conversion efficiency competitive to traditional cells at a fraction of the cost. RTI and others are focused on solar cells due to the costs driving the technology out of competitiveness. Yet the lure of free energy remains. Solar energy has the potential to be a renewable, carbon-neutral source of electricity, endlessly replenishing itself each day.
2. The RTI developed solar cells were created using low-cost materials and processing techniques that reduce the primary costs of photovoltaic production, including materials, capital infrastructure and energy associated with manufacturing.

The preliminary analysis of the material costs of the technology show that it can be produced for less than $20 per square meter, which can be as much as 75% less than traditional solar cells. The cells, which are composed of lightweight, flexible layers, have the potential to be manufactured using high volume roll-to-roll processing and inexpensive coating processes, which reduces capital costs and increases production

- **QUANTUM DOT SOLAR CELL**

A quantum dot solar cell is a solar cell design that uses quantum dots as the absorbing photovoltaic material. It attempts to replace bulk materials such as silicon, CIGS). Quantum dots have band gaps that are tunable across a wide range of energy levels by changing the dots' size. In bulk materials the band gap is fixed by the choice of material(s). This property makes quantum dots attractive for multi-junction solar cells, where a variety of materials are used to improve efficiency by harvesting multiple portions of the solar spectrum. As of 2014 efficiency ranges from 7.0 to 8.7%.

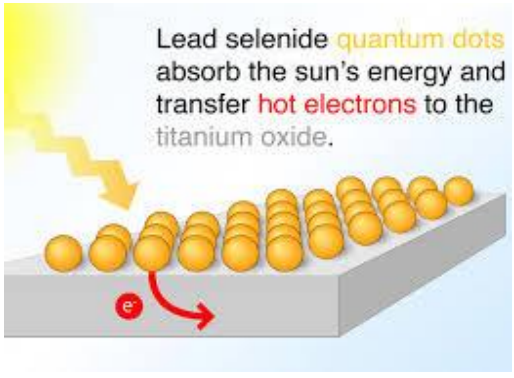


Fig.6 Quantum Dot Solar Cell

When energy is applied to an atom, electrons are energized and move to a higher level. When the electron returns to its lower and stable state, this additional energy is emitted as light corresponding to a particular frequency. Quantum dots work in much the same way but a quantum dot crystal acts as one very large atom. The energy source used to stimulate a quantum dot is commonly ultraviolet light. The frequency or colour of light given off is not related to the material used in the quantum dot, but by the size of the quantum dot. Quantum dots can be manufactured by a number of processes from colloidal synthesis to chemical vapour deposition (CVD). The cheapest and simplest method is bench top colloidal synthesis. Electrochemical techniques and CVD can be used to create ordered arrays of quantum dots on a substrate material.

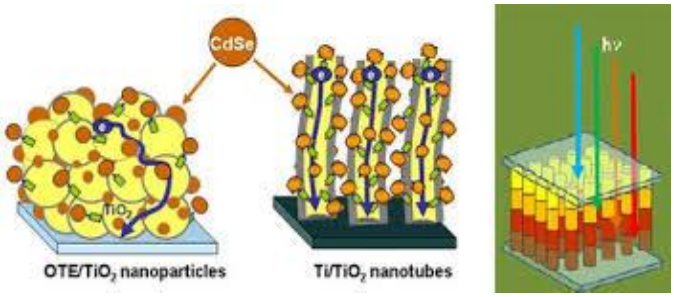


Fig.6 Working of Quantum Dot Solar Cell

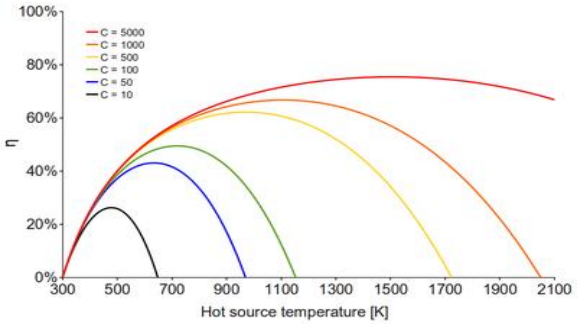
- **. CONCENTRATED SOLAR POWER PLANT**

Concentrated solar power systems generate solar power by using mirrors or lenses to concentrate a large area of sunlight, or solar thermal energy, onto a small area. Electricity is generated when the concentrated light is converted to heat, which drives a heat engine (usually a steam turbine) connected to an electrical power generator or powers a thermo chemical reaction. The core technology developed as part of the project is known as STEM, short for Solar Thermoelectric Magaldi, which is based on an air/sand fluidized bed solar receiver that is optimised for solar energy collection, transfer and storage. Concentrated solar technology systems use mirrors or lenses withtracking systems to focus a large area of sunlight onto a small area. The concentrated light is then used as heat or as a heat source for a conventional power plant (solar thermoelectricity). The solar concentrators used in CSP systems can often also be used to provide industrial process heating or cooling, such as in solar air-conditioning.Concentrating technologies exist in five common forms, namely parabolic trough, enclosed trough, dish Stirlings, concentrating linear Fresnel reflector, and solar power tower

Efficiency and cost of concentrated solar power plant :-

the cost of building a CSP station was typically about US$2.50 to $4 per watt, while the fuel (the sun's radiation) is free The current performance and cost of CSP plants varies by technology, configuration, solar resource, and financing parameters. However, it is possible to evaluate different plant designs and technologies in terms of a single index: the levelized cost of energy (LCOE). LCOE takes into account the available solar resource, upfront capital investment, plant capacity factor, operation and maintenance (O&M) costs, and financing parameters. The performance of a CSP plant is characterized by its annual solar-

to-electric conversion efficiency. This metric includes all of the energy losses that affect the annual electricity produced by the plant, Although higher efficiency often costs more up front, it may more than pay for itself over the operating life of the plant. Also, plants with higher efficiency require less land to produce a given amount of electricity



6. Conclusion

As discussed in the paper the reduction of carbon content can be done by various defined methods in article. these are easy to use and follow but for the solar energy the proposed system will be very effective or solving several situations where the solar panel is incapable and not worthy for the work. Whereas the usage of quantm dot cell is also helpful as it increase the efficiency and working of the system .these two system also reduces the cost of solar energy

7. Acknowledgement

We would also like to show our gratitude to Dr. Inderpreet Kaur for sharing their pearls of wisdom with us during the course of this research. We are also immensely grateful to her for their comments on an earlier version of the manuscript, although any errors are our own and should not tarnish the reputations of these esteemed persons.

References

1. Fridle fission, Ingvar B (2001), "Geothermal energy for the benefit of the people", Renewable and Sustainable Energy Reviews
2. World Energy Assessment (2001). Renewable energy technologies,
3. Green, Martin A. Solar Cells; Operating Principles, Technology, and System Applications, Prentice-Hall Inc, 1982 pp xii and pp 62-184 [2]
4. Fells I. The problem. In: Dunderdale J,(1990) editor. Energy and the environment. UK: Royal Society of Chemistry.
5. Abu Tariq, M. Asim, Mohd Tariq (2011) "Simulink based modeling, simulation and Performance Evaluation of an MPPT for maximum power generation on resistive load", 2nd International Conference on Environmental Science and Technology,Singapore.

6. Khan, B.H., (2006), Renewable energy resources, TataMcGraw-Hill Publishing Company Limited, New Delhi, India.
7. [Altas. I, A. M. Sharaf, 2007 "A photovoltaic array (PVA) simulation model to use in Matlab Simulink GUI environment." IEEE I-4244- 0632 -03/07. http://teeic.indianaffairs.gov
8. Electric Power Research Institute, EPRI. (2010). Solar Thermocline Storage Systems: Preliminary Design Study. Electric Power Research Institute, Palo Alto, CA: June 2010. 1019581.
9. Ellison, L.E. 2012. Bats and wind energy-A literature synthesis and annotated bibliography: U.S. Geological Survey Open-File Report 2012–1110. 57 p.
10. BTM-consult (several editions): 'International wind energy development – World market update'
11. NRC (2010). *Advancing the Science of Climate Change* . National Research Council. The National Academies Press, Washington, *DC, USA*
12. U.S. Department of State (2007). *Fourth Climate Action Report to the UN Framework Convention on Climate Change* Projected Greenhouse Gas Emissions. U.S. Department of State, Washington, DC, USA.

DESIGNING OF RECEIVER CIRCUIT FOR GESTURE BASED ROBOT

ANIKET RAI*, VIVEK KANWAR, SAKSHI KANWAR

Department of Electrical engineering
Chandigarh University,
Gharuan (Mohali), India
*Corresponding Author: aniket.rai.india@gmail.com

Abstract

In this paper RECEIVER CIRCUIT for a GESTURE BASED ROBOT is designed and implemented to propose a GESTURE BASED BOUT. Circuits are designed using ELECTRICAL SIMULATION SOFTWARES. Applications and Algorithms have been studied thoroughly. Gesture based Robotics involves the use of Arduino and helps the human Interactive system along with Artificial Intelligence very imperative. This paper also involves the components and their role in Gesture Based Robotics. The Interfacing with Microcontroller makes Gesture Based Bout to work as Obstacle Avoider, Photo Phobic, Photo Tropic, Obstacle and Line Follower Robot which is also play an Important role in Crucial applications.

Keywords: Arduino; Gesture Based Robotics; Animatronics, Microcontroller (8051), Gesture Receiving Devices

7. Introduction

Robotics is a branch of engineering which involves the mechanical, electrical as well as electronics study including a deep knowledge of software's. It deals with the design construction and applications of robot as well as computer system for the feedback of control sensory system as well as for the processing of information.

Gesture based robot is a well equipped modernized robot which is not controlled by primitive ideas like pressing a button whereas it is controlled by the gesture of hands. A receiving device in the hand is the only thing which is required to control it. Receiving device which consists of a RF RECEIVER MODULE which receives the signals which are transmitted from the transmitting devices, a DECODER IC(HT12D) to decode the 4 bit data and is used to convert that serial data into parallel which RF RECEIVER receives but the input data will only be decoded when no error is detected. .The data then received by the decoder is processed by the 8051 and at last after all these processes MOTOR DRIVERS are used to control the motors. The receiver circuit is followed by an algorithm to process, receive and to store the data provided by the user. This algorithm is used to design the program for a gesture based bout to make it run on the gesture or it can be said that a receiver circuit completes the gesture based bout and provides a human-machine interface A flowchart is being drawn below to show how receiving devices works in top to bottom manner in Fig. 1

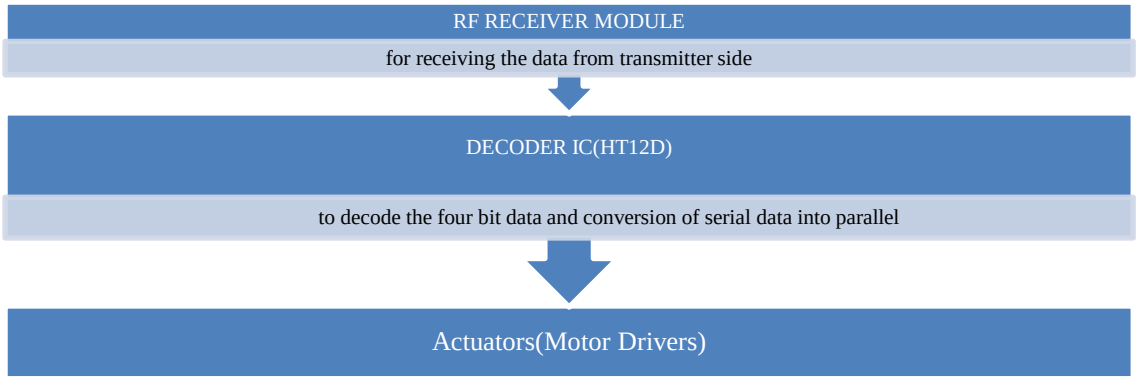


Fig. 1 Flow Chart for Hierarchy Level

8. Methodology

2.3. The overall processes which were required to complete the project is divided into different modules to make it more easier and simpler as well as error free. The module in which the project is divided is shown below with the help of a block diagram in Fig. 2

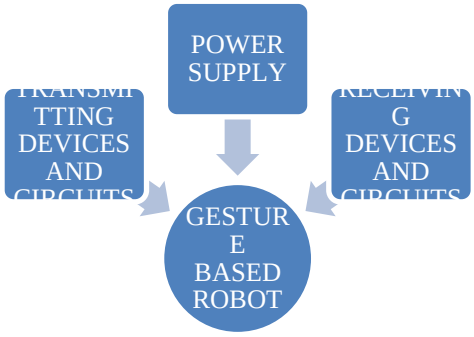


Fig.2 Block Diagram of Project Modules

The block diagram above depicts that the whole project i.e. GESTURE BASED ROBOT is made with the help of POWER SUPPLY, TRANSMITTING DEVICES and RECEIVING DEVICES.

The components that are required for making our transmitter circuit for the proposed gesture based robot through this table 1.

Table.1 List of Components

SERIAL NUMBER	NAME OF THE EQUIPMENT	QUANTITY USED
1	7805 VOLTAGE REGULATOR	1
2	8051 MICROCONTROLLER	1
3	RF RECIEVER MODULE	1
4	DECODER (HT12D)	1
5	ACTUATOR	1

Since this paper involves only the designing of receiver circuit we will only discuss about the receiving circuit and the devices which are used in the robot for the purpose

VOLTAGE REGULATER: - A voltage regulator is used for maintain constant voltage level. To supply a constant voltage to different equipment voltage regulator are used.

MICROCONTROLLER: - An 8051 microcontroller is used in circuit to give decision capability .The data from the decoder now based on that data which have to make the decision.

RF RECEIVER MODULE: - it is an embedded type system that is used to transmit and receive signals between any two devices.

DECODER:-It is used to change a code into sets of many signals. it is basically reverse of encoding

ACTUATOR: - it is used for moving or controlling purpose of robot. It is operated by hydraulic fluid pressure or pneumatic pressure.

3. Origin of robot

As the idea of robot is very old but it is still in the process of advancement many new things are being discovered in robot. Earlier, the robots was not gesture based they can't be operated easily. As they are very much complex and difficult to handle they are large in size but as the time passes size and handling of robot is reduced. Now its easy to operate a robot as now a day's robots are gesture based. A **Gesture Controlled robot** is a robot which can be controlled by hand gestures not by old buttons. It needs to wear a small transmitting device in hand which included an acceleration meter. The transmitting device included a ADC for analog to digital conversion and an encoder IC(HT12E) which is use to encode the four bit data and then it will transmit by an RF Transmitter module.

4. Technical Gaps in Existing Work

4.1.1 Power Supply

It is well known by all that before making any electrical, mechanical or electronic device to work we need to design its power circuit that from where It will complete its power requirement. Similarly in the case of robot also it is necessary to make the power circuit foremost. A power supply circuit consist of many parts like step down ,ac-dc conversion, voltage stabilizing etc but for making a robot the power will be given through a 12 volt adapter so we can say that our power supply consists of a voltage regulator, capacitor, diode, LED and connector .

7805 voltage regulator can be used and an image of that is shown below in Fig 3.

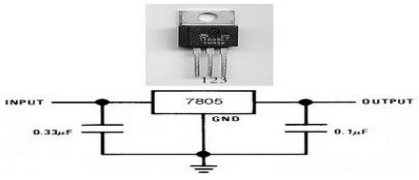


Fig.3 LM7805 Voltage Regulator

A 1000uF capacitor has been used in order to maintain the continuity and to reduce the ripple. A 2 pin male connector can be used to give the power. The positive should be connected to pin1 of 7805.

4.1.2Process Microcontroller

An 8051microcontroller has 40 pins and the basic circuit of the microcontroller consists of reset circuitry and oscillator circuit.It has 32 input -output lines, four 8bit ports. For making the circuit one needs only 8 pins which are as follows:

- Pin no.9 is a reset pin which reset the program counter of 8051 and is highly active.
- XTAL1 and XTAL2 provides the oscillations to the controller
- For serial communication pin no.10 and 11 are used
- 31st and 40th pin no. are used to provide Vcc(5V)
- Pin no. 20 is ground.

To make the above points more understandable and easy an image is shown below for the proposed microcontroller in Fig.4 and 5.

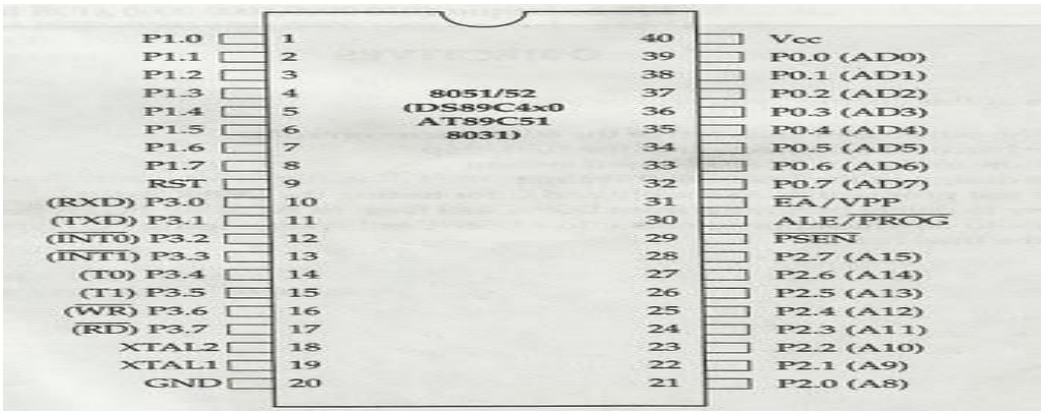


Fig .4 Pin Diagram of Microcontroller (8051)

The basic circuits which can be referred for microcontroller to initialize it is shown in Fig. 5

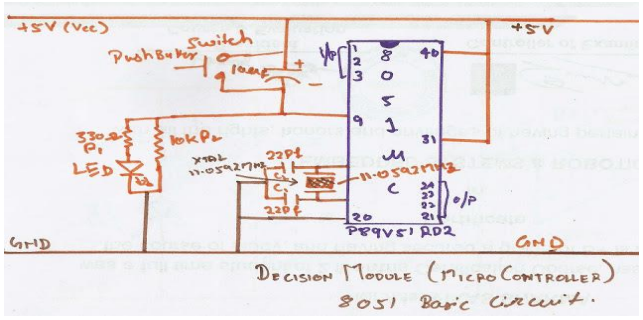


Fig.5 Basic circuit for Microcontroller

4.1.3 Receiving devices

These are the devices which are used to receive the data from transmitter devices which is mainly sent to this part of the circuit to make it work. Foremost device which has been used is RF RECEIVER MODULE

A. RF RECEIVER MODULE:

It is a type of sensor which receives the data or analog and digital signals transmitted through transmitter circuit. A receiver module work as same as transmitter module. The pictorial view is shown in Fig.6

- Vcc is given the +5volt supply
- Pin GND is being connected to the ground for biasing
- Data pin is connected to HT12D at pin number 14



Fig.6 Pictorial View of RF Receiver module

B. DECODER (HT12D):

A decoder is a device which we can say simply converts the serial data received by the receiver. It only decodes the data when there is no input error or unmatched codes are present. Transmission is indicated by a high signal at VT pin i.e. pin number 17

- It is a 4-bit decoder IC which is used to encode the input data applied on it.

- Pins (1-8) are not needed to be considered as they are address bits.
- Pins18 can be used to bias the IC. Pin 18 is connected as Vcc at +5volts
- Pin 17 is connected to an led for indication as this pin is high when the transmission is ok
- Pin14 is connected to the rf receiver module data pin for receiving the serial data
- Pins10-pin13 contains 4bit data which is transmitted by the gesture module or transmitter module.

The Connection Diagram of Decoder is shown in Fig.7

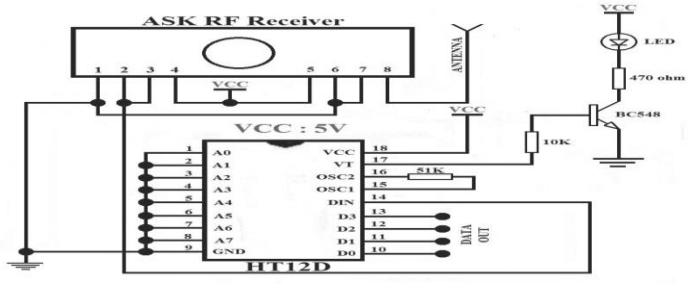


Fig.7 Connection Diagram of Decoder

C. Actuators(L293D):

Actuators are the devices which are used for the movement of the proposed bot and to do tasks like motor's.since there are variety of motors available which operates on different voltages so a motor driver is needed to run them through controller. To provide an interface between motor and microcontroller L293D motor driver is used in the circuit. Fig.9 shows the pictorial representation of actuators.



Fig.8 Actuator

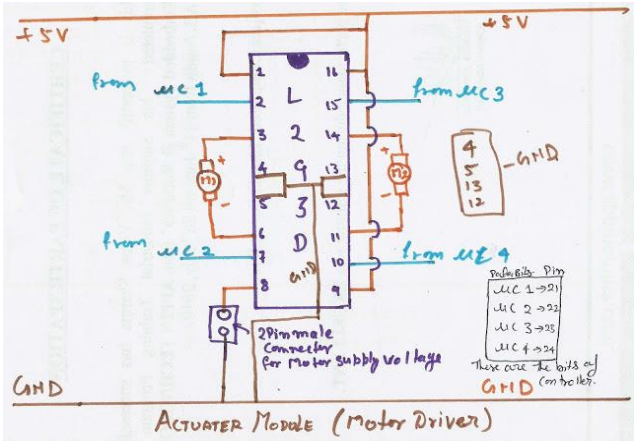


Fig.9 Actuator module (motor driver)

4.1.4 ALGORITHM

Step 1 start
Step2 declare a
Step 3 input 0 or 1
Step 4 while input=1
set a=P1&0x03
Step 5 (if a==0x00)
set P2=st;
else if(a==0x02)
set P2=rev;
Delay(150)
P2=rt
Delay(150)
else if (a==0x01)
set P2=rev
Delay(150)
P2=lt
else if (a==0x03)
set P2=rev
Delay(150)
P2=stp
Delay(200)

Step 6: End

5. RESULT

The complete transmitter circuit for the proposed gesture based robot is being studied and designed using different devices and computer software's. A complete circuit for the transmitter module is shown below in Fig.10

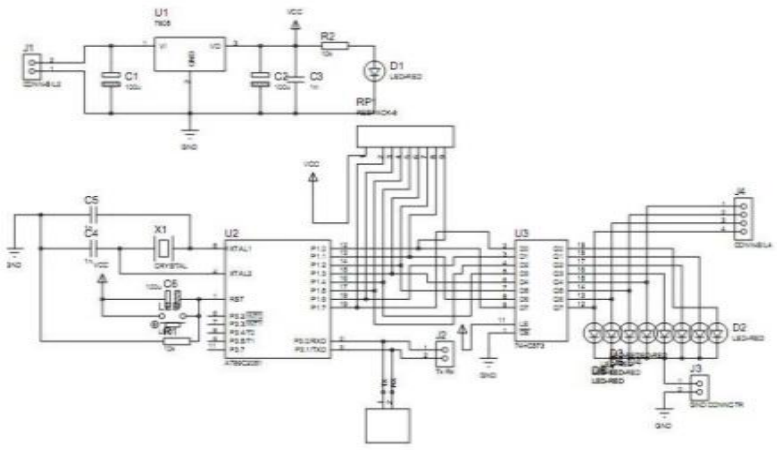


Fig. 10 A Complete Receiver Circuit

After all the works completed and circuits drawn a gesture based robot is proposed at the end and the images for the robot are shown in fig.11 (a) and Fig.11



Fig.11 (a) top view of the robot

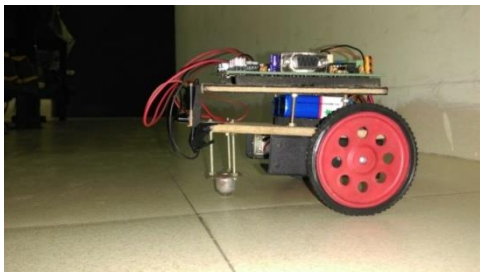


Fig.11 (b) side view of the robot

Acknowledgement

The author would like to acknowledge Electrical Engineering Department of CHANDIGARH UNIVERSITY, Gharuan, India.

References

1.Sturman, D.J. ; Medialab, Paris, France ; Zeltzer, D. "Computer Graphics and Applications, IEEE (Volume:14 , Issue: 1),Jan1994.

2. Dai and Kampker, User oriented integration of sensor operations in a of- fline programming system for welding robots. In Proceedings of the IEEE Intl. Conf. on Robotics and Automation (ICRA '00), Volume 2, pages 1563–1567, Apr 2000.

3. Jeon, P.W., Jung, S.: Teleoperated Control of Mobile Robot Using Exoskeleton TypeMotion Capturing Device through Wireless Communication. In: Proceedings of the 2003 IEEE/ASME International Conference on Advanced Intelligent Mechantronics (AIM 2003), July 2003

4. Sibert, L.E., Jacob, R.J.K.: Evaluation of Eye Gaze Interaction. In: Proceedings of the ACM SIGCHI Conference on Human Factors in Computing Systems (CHI 2000), pp. 281–288 (2000); The Hague Amsterdam. CHI Letters. 2(1), 1–6 (April 2000)

5 T. H. Speeter (1992), "Transformation human hand motion for tele manipulation," Presence, 1, 1, pp. 63–79.

6. W. M. Newman and R. F. Sproull (1979), Principles of Interactive Computer Graphics. New York: McGraw-Hill.

Attractive and Unconventional Conceptual Tripod Design to Support Hanging Objects as a Support System

Jang Kyungmoon[*], Hardie Hidayat[2], Alexander Chee[3]

[1]*School of Engineering, Taylor's University, Malaysia*

[2]*School of Engineering, Taylor's University, Malaysia*

[*]Hinaya_@hotmail.com

Abstract

The existing applications of a tripod are focused on photography, firearms and astronomy. This project is proposed with design based how to come up with new conceptual and implemental design of tripod. The users who have interest with taking photos sometimes face to the situation where they have to carry not only a heavy camera but also a tripod to help mount it on. Then, when the pictures could be taken at slope area, it is not easy to adjust the angle of the camera and position of the tripod because of the ground condition. So, this project is initiated from the idea that could help to solve this problem with a new design of the tripod which can be adjust on the slope ground such as mountain or hills and does not lost the balance of the camera position by applying Parallel Kinematic Mechanism (PKM) and gimble system so that user still can have the best photos. So, the new application is decided to design a new conceptual tripod deign concerning workspace, structural strengths and the degree of freedom, which is within the project scope. A new conceptual design of tripod is improved from a simple tripod design that can be found easily anywhere. The design of a new tripod as a support system can be drawn with the computer software, SolidWorks. The mainly focused aspects in terms of design are having small workspace area with having structural strengths of the tripod. Furthermore, by applying PKM, even if one of tripod legs is adjusted short, the camera and tripod would not fall down by the gravity force and the weight of both of them. A simple and widely used tripod design will be presented for the comparison by a new model of it. The new design is based on the technology and concept of the machine legs movement

Keywords: degree of freedom, gimbal system, parallel kinematic machine(PKM), structural strength, tripod, workspace.

1. Introduction

Literally, the term of a tripod has been defined as a support with three legs for a piece of equipment such as a camera. For example, a camera should be mounted on a tripod in order to have it balanced not to fall down for a photograph requiring not short exposure period. There are countless, strong tools or items that require extra other support components or tools to make them withstand and have a good balance of position without unforced error. Normally, two different kinds of tripod exist. The one is adjustable-leg tripod type and the other is fixed-leg tripod type. The former type of tripod is the most commonly used product in society. It is easy for users to set it up on the ground because the length of each leg can be adjusted by users to the level of ground. The latter type of tripod has the same length of each leg.

A tripod consists of several components which can be divided as legs part, points and head. The tripod legs are made of widespread materials such as steel, aluminum, wood or fiberglass. Steel is used to make tripod legs because of the advantage of it. Steel has properties that it is the most durable. However, it has disadvantage in aspect that that is too heavy to carry by users. A tripod having aluminum legs is widely used because of its lightweight and sturdy. If legs of tripod are made of wood or fiberglass, it would be the most accurate materials that they are not sensitive to the change in temperature. The head of a tripod normally is joined together with the legs. There is a leveling device that can change the height or surface level of machine on it.

Other application of tripods can be classified with firearms, photography and astronomy. This project is a further study, research and design implement from the idea of a tripod concept to bring out much more useful and a technically advanced model and outcome that can be used in the society with attractive and unconventional design to evaluate the new design and application of it.

2. Theoretical approach

It has been incorporated that a lot of the basic linkage configurations into machines designed centuries ago, and the terms currently used to describe them have changed as time goes. According *to C.Willson, J (1983),* it is defined that a link is one of the rigid bodies or members joined together to form a kinematic chain, the term of rigid link, or just simply link, is an idealization used in the study of mechanisms that does not take into account small deflections due to strains in machine members. A perfectly rigid or inextensible link is able to exist just as form of a model of a real machine member. In his study, it is scribed that for typical machine parts, the maximum changes in dimension are on the order of only one-thousandth the part length. The fixed or stationary link in a mechanism is called the frame. When there is no link that is actually fixed, the one should be considered as being fixed and determine the motion of the other links relative to it. In an automotive engine, for example, the engine block is considered the frame, even though the automobile may be moving. The connections between links that permit constrained relative motion are called joints. The joint between a crank and connecting rod, for instance, may be called a revolute joint or a pin joint. The revolute joint has one degree of freedom, in that, if one element is fixed, the revolute joint allows the other only to rotate in a plane. A sphere joint (ball joint) has three degrees of freedom, thus allowing relative motion in three angular directions [1].

There are well-known few of type of joint (pair). They are revolute, prism, helix, cylinder, sphere, plane, universal joint, gear pair, and cam pair. Revolute joint is a lower pair, having 1 degree of freedom. It is a pin joint that permits rotation only. Prism joint is a lower pair, having 1 degree of freedom. It is a straight spline that permits sliding only. Helix joint is a lower pair, having 1 degree of freedom. It is power screw or helical spline. Cylinder joint is a lower pair, having 2 degree of freedom. It is a sleeve that permits both rotation and sliding. Sphere is a lower pair, having 3 degree of freedom. It is a ball and socket joint permitting rotation in three angular directions. Plane is a lower pair, having 3 degree of freedom. It is a surface restraint permitting rotation and motion parallel to the plane of the surface. Universal join has 2 degree of freedom. It is the hooke-type universal joint that combines two revolute pairs. Gear pair is a higher pair, having 2 rolling and sliding degree of freedom. It is classified by spur gears, helical gears, and other gears. Lastly, Cam pair is also a higher joint, having 2 rolling and sliding degree of freedom. It consists of disk cam and follower.

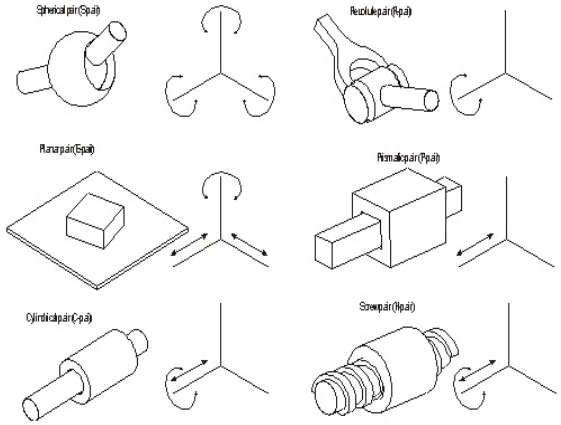


Figure 1.1 Lower order kinematic joints (pairs) [2]

The degrees of freedom of a certain linkage are considered as the number of independent parameters that must be specified to determine the spot of every link relative to the frame or fixed link. Also, the linkage mobility is considered as the degrees of freedom of a linkage, too. The system has only one degree of freedom when the instantaneous arrangement of a system may be completely defined by specifying one independent variable. The majority of practically used mechanisms have one degree of freedom [1]. The number of degrees of freedom of a mechanism depends on the types of joints or pairs and the number and arrangement of the links. Most practical closed-loop kinematic chains have one degree of freedom, while robots usually have six or more degrees of freedom. The actual motion of the linkage may depend on the transmission angle as well. Practical design and analysis of mechanisms is heavily dependent on computers. An unconstrained rigid body has six degrees of freedom: translation in three coordinate directions and rotation about three coordinate axes. A body that is restricted to motion in a plane has three degrees of freedom: translation in two coordinate directions and rotation within the plane [1].

Based on the research by *Chen, J (2004)*, it is clearly mentioned that Prallel Kinematic Mechanism machines (PKMs) have been discussed and studied for the past few years. This PKM was mainly focused on the improvement of indirect, non-accurate metrology system and weak stiffness. Static stiffness is the one of important

property in PKM that drives much better function [3]. The design of a tripod has been one of popular majority in the field of development of parallel kinematic machines because most machining operations need at least a maximum of five axes. It is known that a machine that has a five-axis with both of large workspace and dexterity is formed by the arrangement of a tripod with a gantry system forms. The current tendency towards the high-speed-machining (HSM) leads requirement to enhance machine tools with high both of static and dynamic performance, improved stiffness and reduced moving mass. To do so, parallel mechanisms are applied to enhance and widen a concept of parallel kinematic machines (PKMs). The beginning stage of PKMs advancement was centered on inverting the Stewart platform to have a hanging-down design pattern for machine tools. A tripod design with three axes, which is same as the Stewart platform based machine instruments, is getting to be well known. According to the research and study conduct by *F. Xi (2003),* it is written that one of the most prosperous successful developed model on Tri-cept emanates from Neos Bobotics AB. It has generally it's the purpose of the usage for cutting applications purpose. It can be mounted on variants of machine frames. There is another type of tripod unit which is the Z3 head from Cincinnati Machine is considered and reconfigured for the same application purpose. The main difference is that the extensible legs are considered in the design of the Tri-cept. In contrast with other PKMs, the Z3 Head is developed with fixed-length actuators. From the perspective of a PKM design, these tripod units represent different structures [4].

All of these tripod types are designed by applying three motion axes to get three degrees of freedom. But, few differences are found out. For example, kinematic constraints are the one of the difference due to different kinematic structures. It would be explained by the following the equation of mobility [4]:

$$M = d(n-g-1) + \sum_{i=1}^{g} f_i \qquad (1)$$

M = mobility or the system DOF
d = order of the system (d = 3 for planner motion, and d = 6 for spatial motion)
n = the number of the links including the frames
g = the number of joints
f_i = the number of DOFs for the *i* th joint.

Again, based on the research conducted by *D.Zhang, Z. Xu (2003),* the stiffness is described and defined as the capacity of the ability of a structure or body against the deformation because of the external forces action. The parallel stiffness matrix enables to characterize the parallel mechanism stiffness at a given point of its workspace. The parallel stiffness matrix relates with both of the forces and torques applied at the moving platform to its linear and angular displacements [4].

In order to measure the PKMs static stiffness of analytical modeling, few methods are recommended, for example, considering the contribution of each chain independently and combining. And also, from the boundary conditions of the joints study, the overall stiffness matrix of the PKM is tabulated and found out. According to the study of *Azulay, H (2014),* it is said that the Matrix Structural Analysis (MSA) method is used to find out the static stiffness of the PKM at the center point of the platform. This

MSA method has an advantage that it is easy to evaluate the stiffness distribution within the workspace [5].

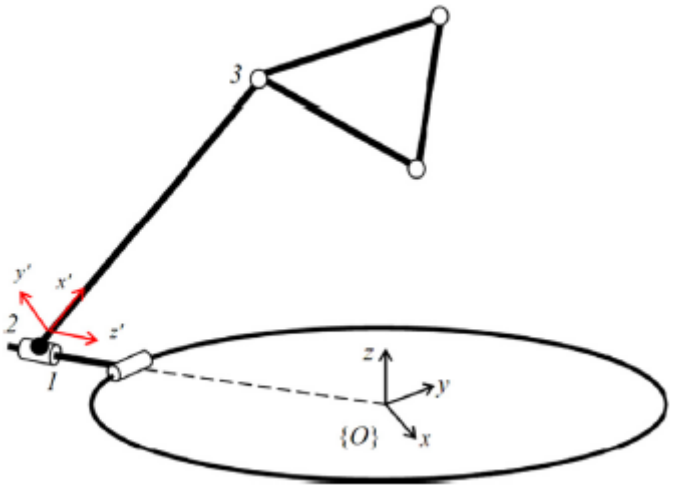


Figure 1.2 Coordinate notations for the proposed PKM static stiffness model [5]

The volume of workspace is identified by the three dimensional area where the center of the moving platform is able to reach. The method applied is called a discretization. The main three key kinematic constraints would have an effect on the available workspace of a tripod, namely, link length limitations, joint angel limitations and link interference. The volume of workspace, V, is calculated as below [4]:

- The workspace is divided into slices of thickness dz parallel to the X-Y plane.
- The boundaries of each slice are found and the volume of each slice is calculat ed.
- The volume of the platform workspace is computed by summing the volumes of all slices.

The volume of workspace is calculated as:

$$V = \sum_{i}^{n} A_i \, \Delta z \tag{2}$$

Whereby; A_i means the reachable region of the $_i$ th layer. Dz means the layer interval.

A set of location where a robot is able to reach is called robot workspace. It is the most widely used a method of measurement for the evaluation of a robot. In other words, it means the space where the end-effector enables to reach in Cartesian coordinate system. It refers to the coordinate system of the joint in way of the motion of the joint as well. The end-effector workspace that is called task workspace and the joint motions workspace is also meaning joint workspace. As an example, take three degrees of freedom (DOF) in tripod machine tool. And, a parallel kinematic machine (PKM) joint workspace is centered, too. Based on the research performed by *Z. Bi (2009)*, regarding other kinematic model in order to look into a tripod machine tool joint workspace, it should be set up. It is because that a kinematic model is applied so as to verify the joint workspace which engages with a partial domain of joint motion. The main contributions in this study are divided with a new concept of a new

optimization design and the control of PKM, joint workspace determination move that is based on a PKM structural constrains [6].

It should have a good quality of function for a robot to convert and deliver motions of the joint into motion of end-effector which executes given jobs correctly. When the design of a machine is effectively enhanced, the efficiency of transformation of the motion will increase so that the joint capacity, which is minimized, needs to execute a task. In short, the main two ideas should be evaluated. For instances, the contribution of joint motions to the expected and directed end-effector motion and the joint capacity utilization are those ideas. In the further research performed by *S. Lang (2009)*, the former can be classified as workspace, dexterous workspace, and service angle, Cartesian coordinate system. The utilization of the joint capacity has a few advantages in terms of a full capacity of joint motion unless self-interference among the linkages exists. It says that an open-loop robot is not much significant to evaluate. On the other hand, a closed-loop or hybrid robot has unreachable region in comparison with the domain of joint motions. The utilization of joint capacity of joint motion and the utilization of joint capacity are limited. Yet, any specific study to evaluate the joint capacity utilization has been found [6].

The most effective measure of a robot's capacity is workspace. Usually, workspace is defined in Cartesian coordinate system for the motion range of the end-effector, and it is called task workspace in the paper. It straightly point out the area where the end-effector motion can reach in the Cartesian coordinate system. But, it seems that it is impossible to measure how the motions of joint are operated to cover reachable region. So, workspace will be defined in joint coordinate system for the joint motion to overcome this limitation. That is called joint workspace. Studying on joint workspace is really having an important effect to a robot with a closed-loop or hybrid structure [6].

A tripod machine tool demonstrates as an example of the relation between the joint workspace and the structural constraints. It is because that joint workspace has not been named, yet [6].

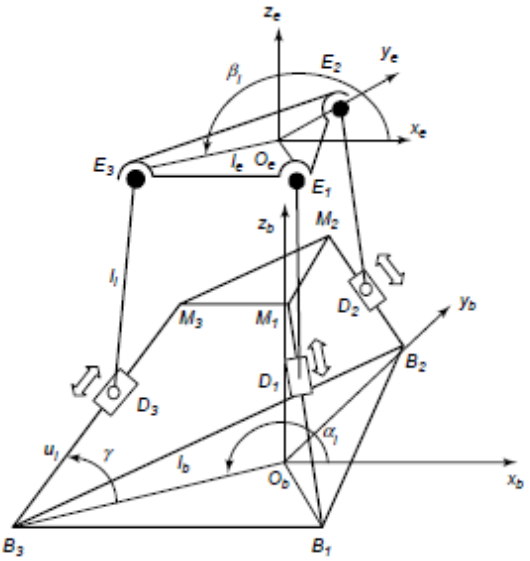


Figure 1.3 Simple Tripod Machine Diagram [6]

The PKM structural constraints are dependant factor to the joint workspace. They consist of light-metal cutting. There are three platforms, for examples, base platform (B1, B2 and B3), middle platform (M1, M2 and M3) and end-effector platform (E1, E2 and E3) are composing this tripod machine tool. The base platform must have a strong base and stick to the ground. The middle platform is supporting the guide-ways of prismatic joints. The end-effoctor platform is connected with the slide of a prismatic joint by a support bar D_i and E_i. A support bar has a spherical joint at E_i and a rotational joint at D_i. The middle platform is connected with the base platform by guide-way B_i and M_i of the prismatic joint statically. Three prismatic joints are actuating a tripod machine. In order to design a tripod machine device, a few limitation must be considered to design it; the base platform dimension, the end-effector platform dimension and the direction of a guide-way and the support bar length [6].

However, the accuracy of a tripod-Based PKM still needs improvement. And also, the rigidity problem from the ball- and the universal-joints, the poor floor span efficiency or no explicit forms of the kinematic analysis need enhancement, too.

This project is focused on the conceptual design of Tripod machine that is based on parallel kinematic mechanism (PKM). In short, it is required to understand the research of the mechanism in parallel kinematic mechanism that are used in the industry and the design a conceptual design of tripod-based parallel kinematic machine. The purpose of this project is to design a Tripod to increases the structure strength and workspace efficiency to widen the application scope in society in a way that a tripod does not fall down even if the user push it forward and it has ability to shrink and shorten its three legs automatically by applying PKM concept on those legs. Furthermore, the head part where a camera is usually mounted on would have a gimbal system on it so that the camera would not lost its horizontal position to take a shot and would not be shaken or fallen to the ground by unforced error.

As written in the literature part specifically, tripod machine based on parallel kinematic mechanism (PKM) has degree of freedom (DOF) of the tripod, components consisting of the tripod body structure and many factors. Its usage is simply expected to perform loading and withstanding heavier working load with higher speed, and higher precision.

But, tripod-Based PKM still have many lacking such as accuracy problem, rigidity problem from the ball- and universal-joints, poor floor span efficiency or no explicit forms of the kinematic analysis. How a Tripod-Based PKM can offer a more flexible in the service condition yet the workspace efficiency and reliability still sustained or even improved? The novel of this project is to create an innovative and new design from exist PKM tripod machine design. From the present situation, the expected outcome will be presenting better workspace, stronger stiffness and having at least, minimum, 3 DOF.

2. Research Methodology

This flow chart dedicates more clear and easy look of working process as shown in Fig 4.0. It will guide this project to be on time with correct action that conductor must follow to achieve maximum result out. The project has begun with the selection of the title. After that, to understand and approach the project, journal research and literature review and study must be conducted. Journal should be selected correctly and properly titled within topic. Journal study must be conducted in diverse ways. Finding out the boundary condition, scope, objectives, contribution of the body and expected outcomes all comes from the correct and deep study.

Then, it proceeds to the next stage of conceive and design a model based on degree of freedom, boundary condition. In this stage, the important factors will be discussed and studied. Because designing a tripod having smaller DOF point and its workspace making better performance has been one of objectives, this stage also is truly important. During the half of later project period, it will begin from the real design process of modeling a tripod in 3D model. In order to make it a real design, ability to draw a 3D design using computer software is permanently needed. Then, all of designed parts were assembled as one of new tripod model proposed.

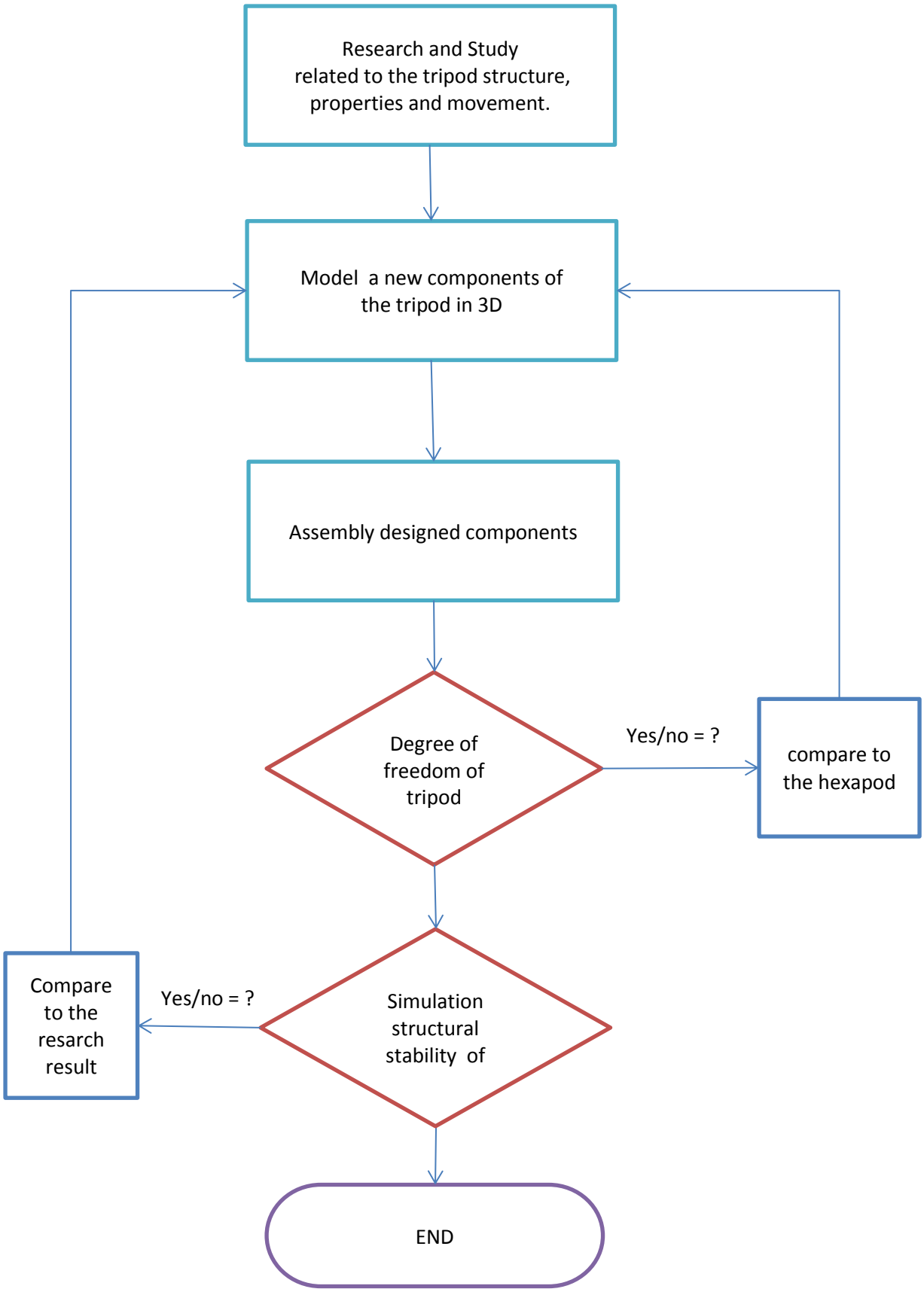


Figure 2.1 Flow Chart

3. Results and Discussions

3.1 Tripod design

In this project, a conceptual design of tripod was projected and come up with a different or unconventional type compared to the common tripods which are used in society. This idea was driven from the conceptual thought to design it.

First of all, a few parts of tripod would be described as figures below.

3.1.1 General type of tripod leg drawing.

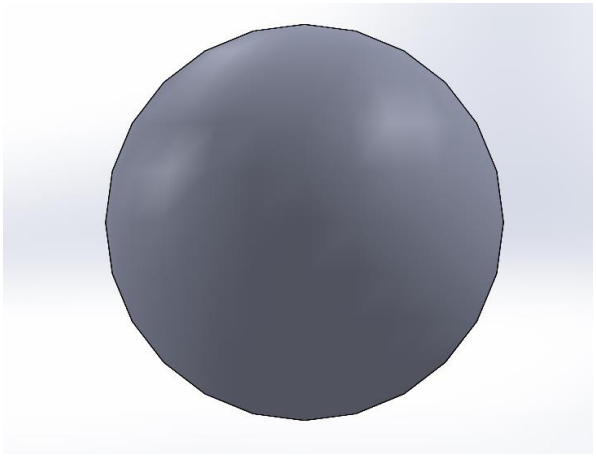
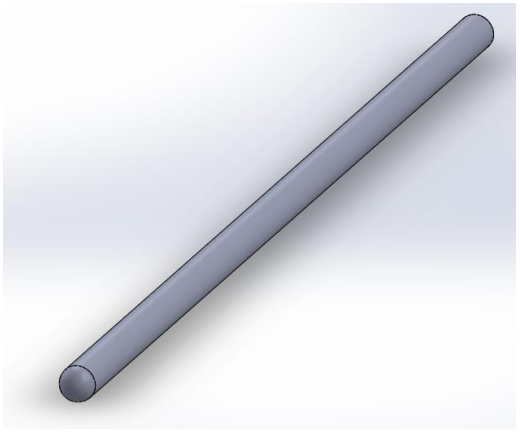


Figure 4.1.1 Bottom view of general tripod leg bar part design



Figure 4.1.2 side view of general tripod leg bar part design



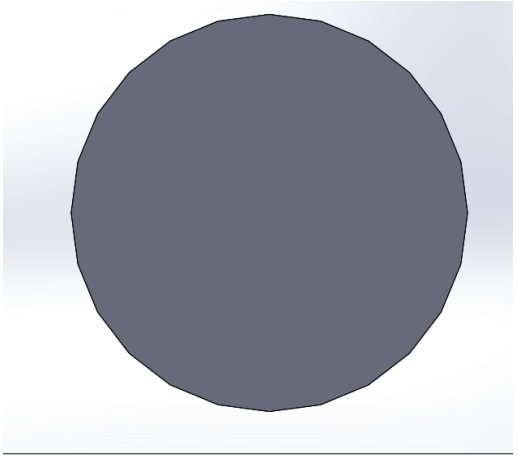


Figure 4.1.3 front view of general tripod leg bar part design

Figure 4.1.4 top view of general tripod leg bar part design

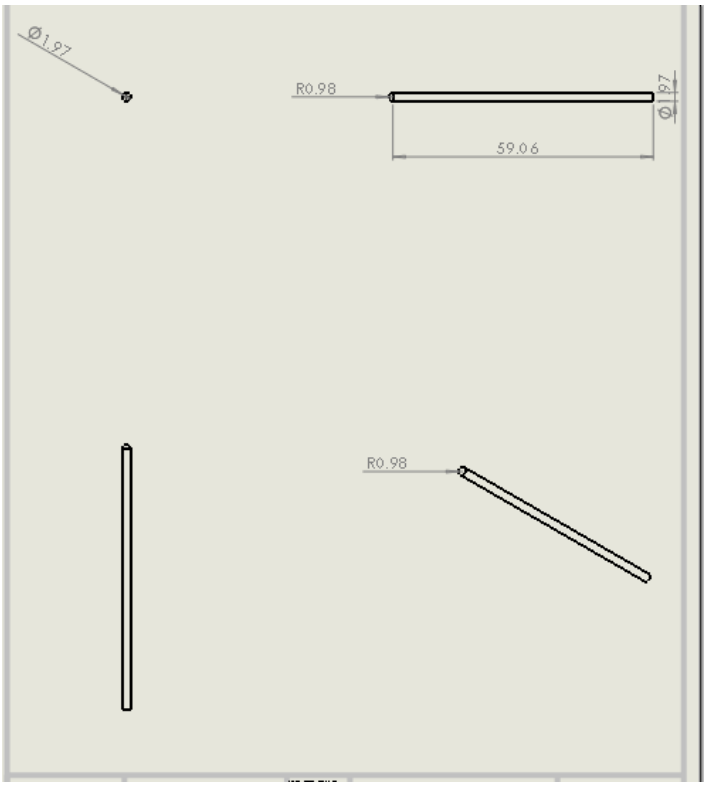


Figure 4.1.5 Scales of general tripod leg bar part design

3.1.2 A new conceptual type of tripod leg drawing.

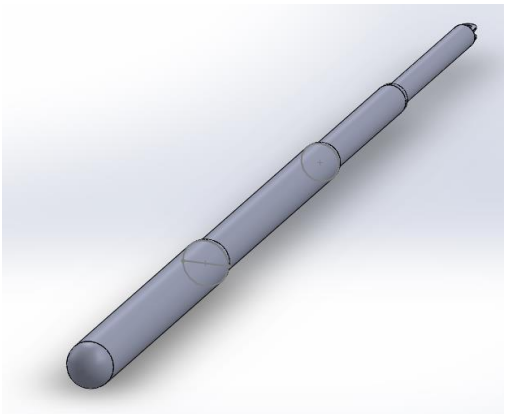


Figure 4.2.1 Side view of a new conceptual tripod leg bar part design

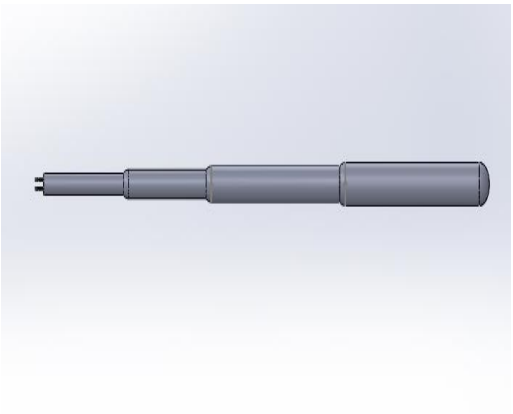


Figure 4.2.2 Side view of a new conceptual tripod leg bar part design



Figure 4.2.3 Front view of a new conceptual tripod leg bar part design

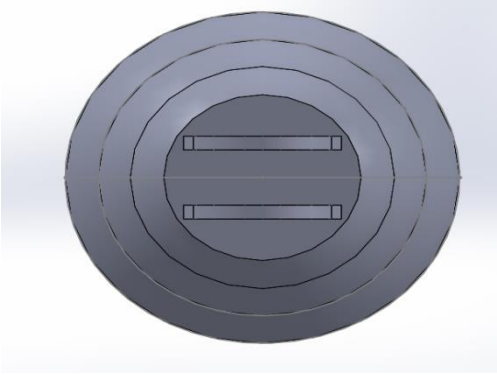


Figure 4.2.4 Top view of a new conceptual tripod leg bar part design

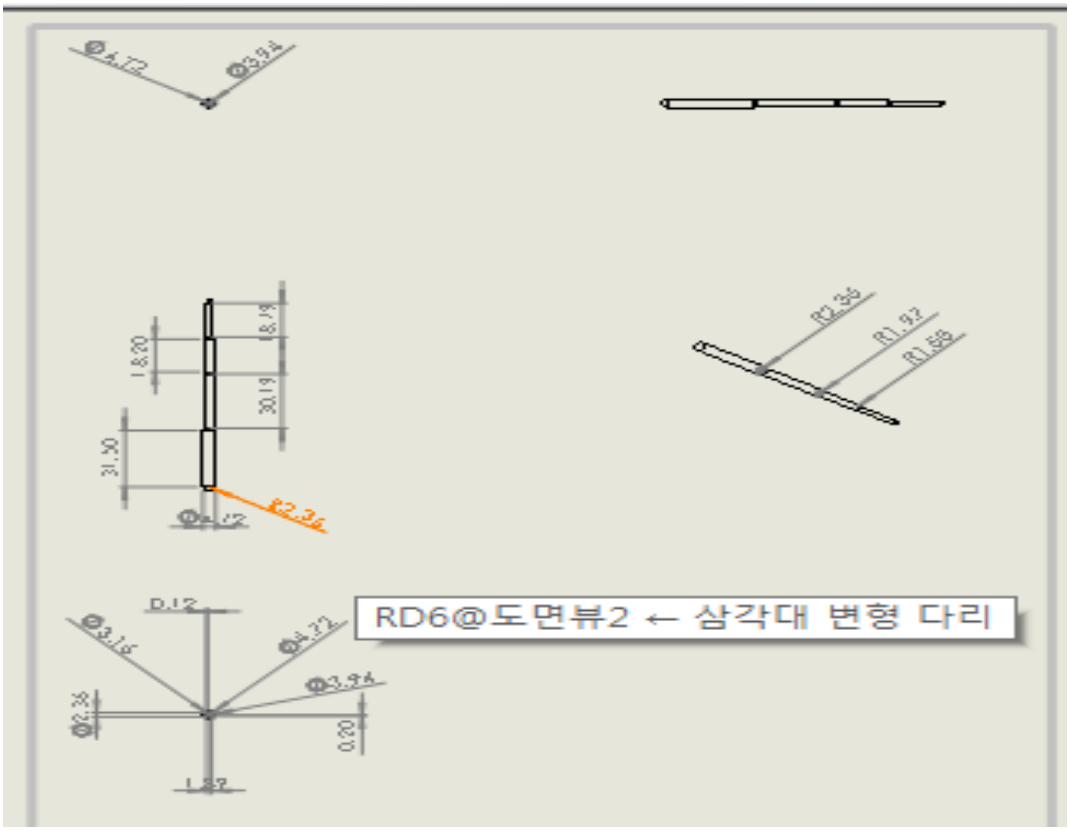


Figure 4.2.5 Scales of a new conceptual tripod leg bar part design

3.1.3 Bolt and nut drawing part of new conceptual tripod drawing.

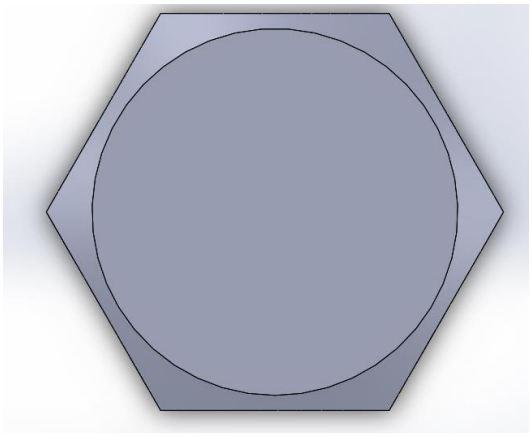


Figure 4.3.1 Top view of a new conceptual tripod nut part design

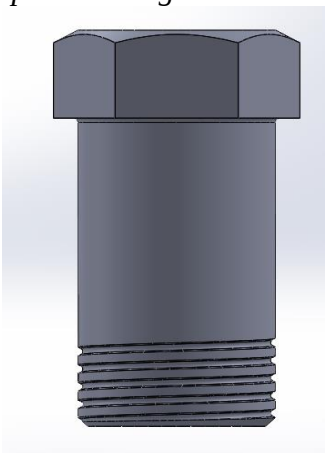


Figure 4.3.2 Front view of a new conceptual tripod nut part design

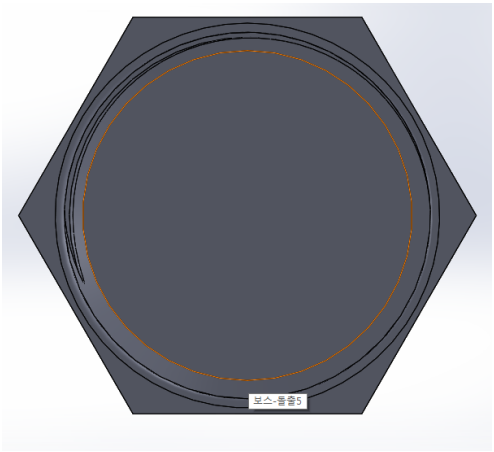


Figure 4.3.3 Bottom view of a new conceptual tripod nut part design

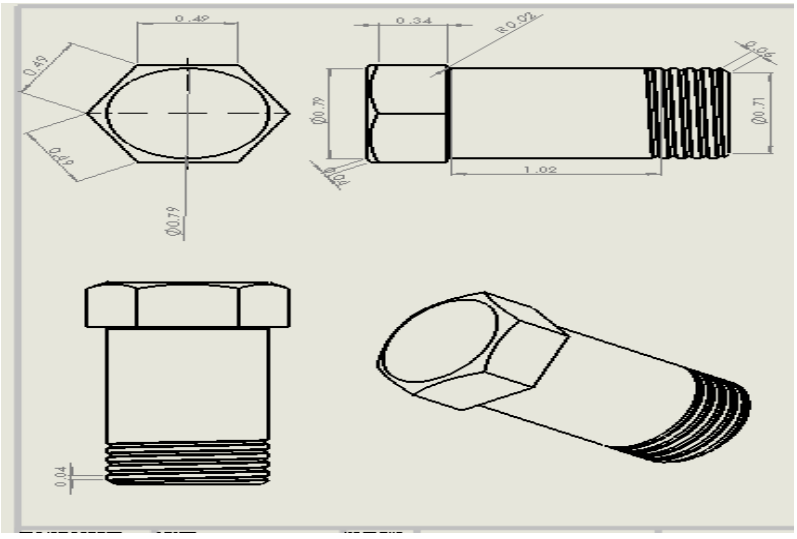


Figure 4.3.4 Scales of a new conceptual tripod nut part design

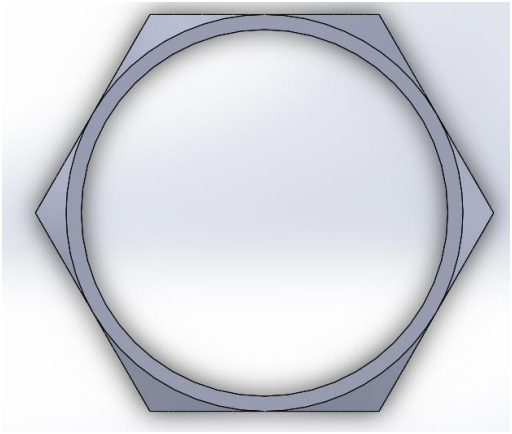


Figure 4.3.5 Top view of a new conceptual tripod bolt part design

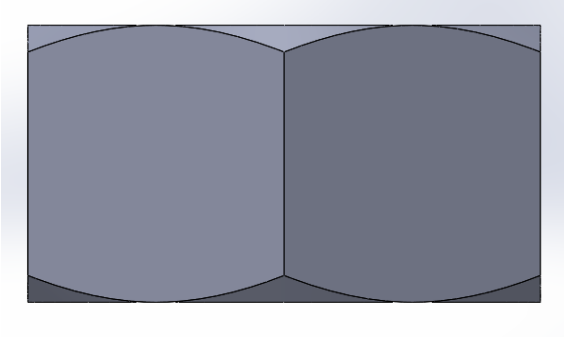


Figure 4.3.6 Top view of a new conceptual tripod bolt part design

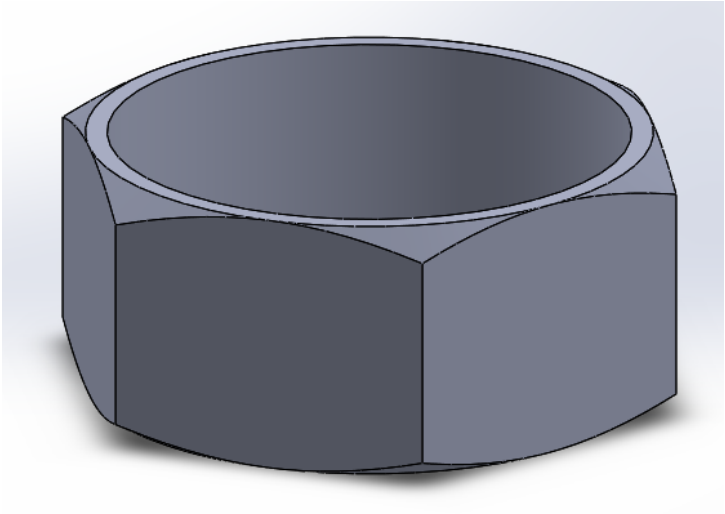


Figure 4.3.7 Top view of a new conceptual tripod bolt part design

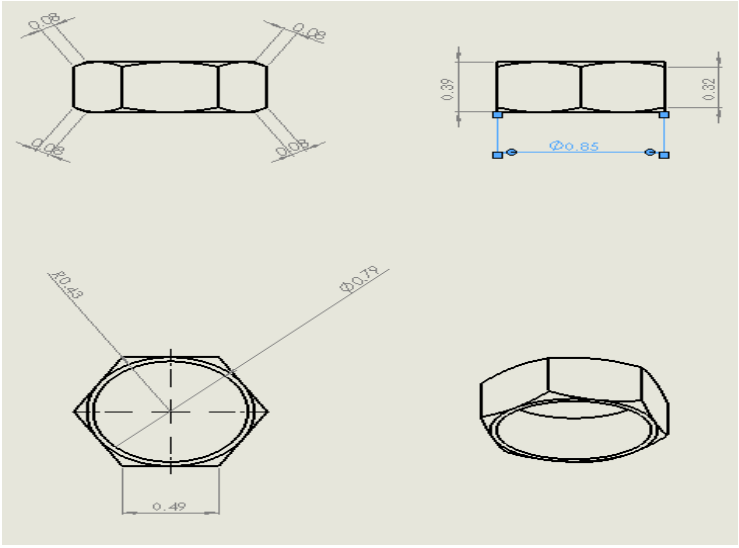


Figure 4.3.8 Top view of a new conceptual tripod bolt part design

3.1.4 A new conceptual type of tripod head part drawing.

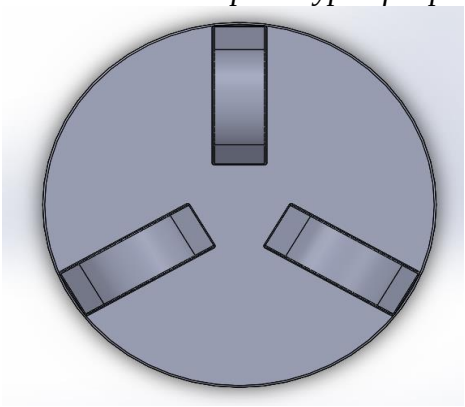


Figure 4.4.1 Bottom view of a new tripod head connecter part design

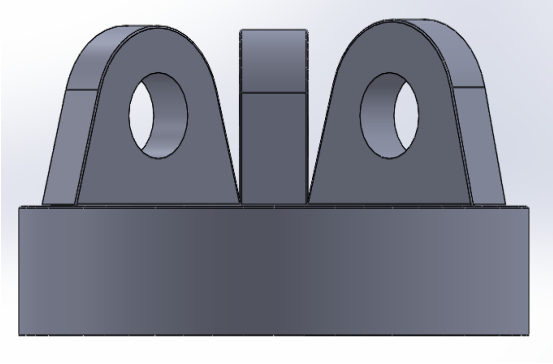


Figure 4.4.2 Side view of a new tripod head connecter part design

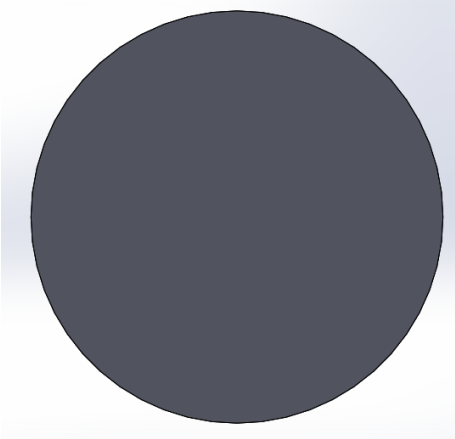


Figure 4.4.3 Top view of a new tripod head connecter part design

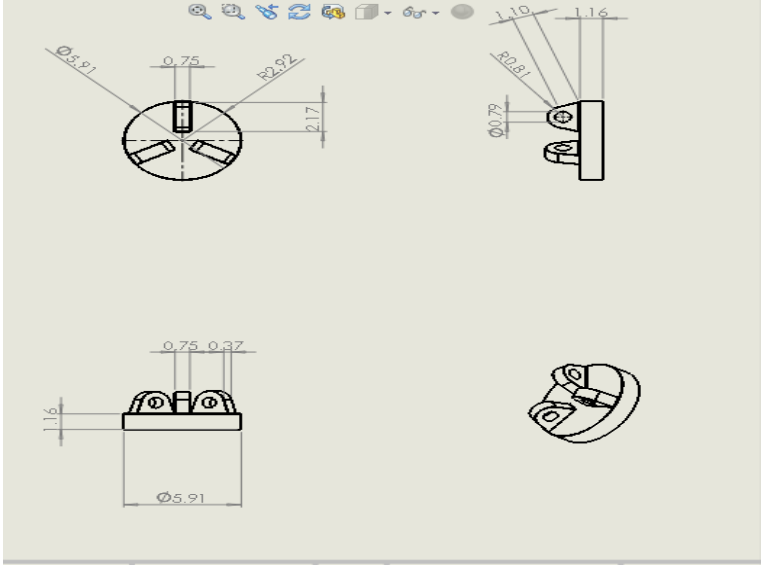


Figure 4.4.4 Scales of a new tripod head connecter part design

3.2.1 Assembly

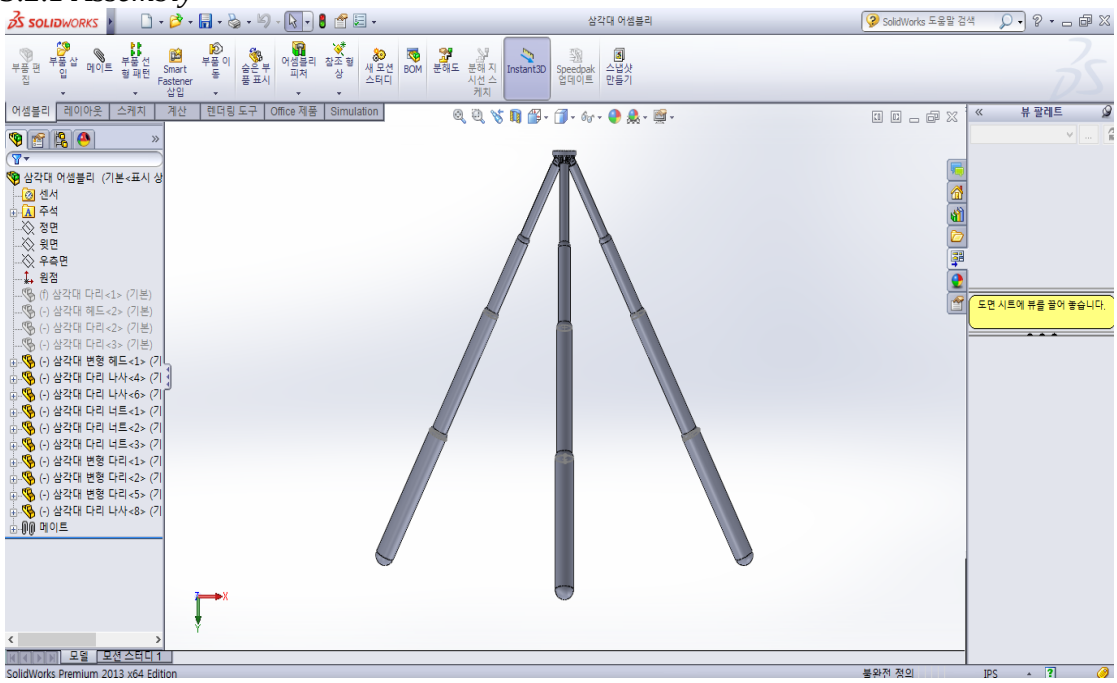


Figure 4.5.1 the Front View of Assembly feature of all of new part drawing

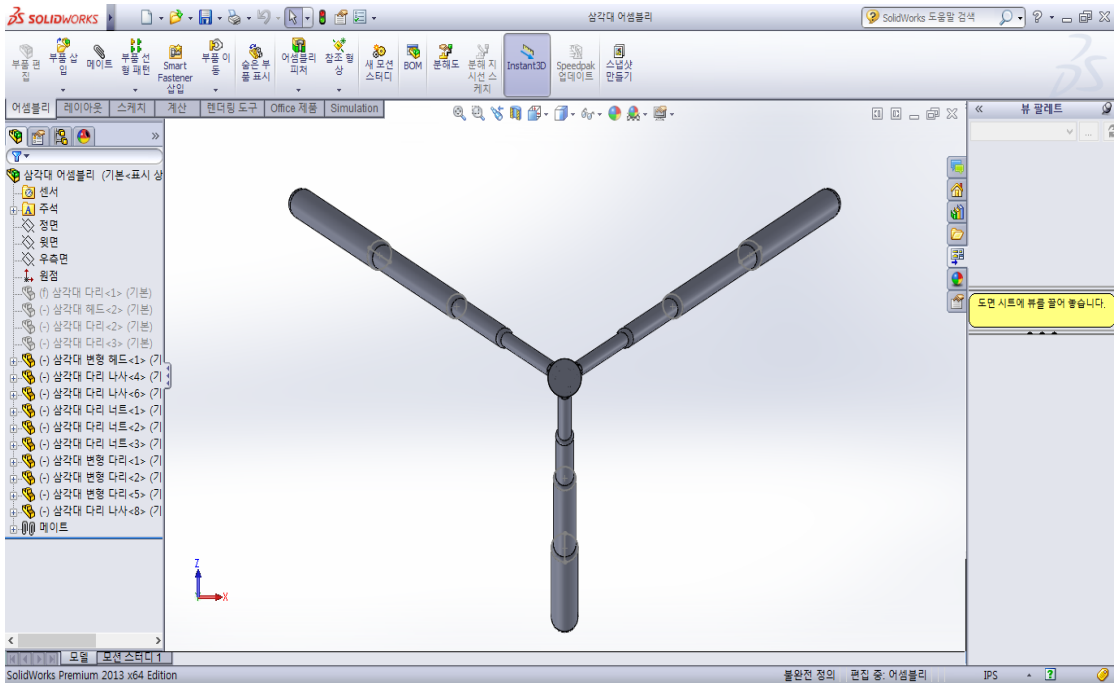


Figure 4.5.2 the Top View of Assembly feature of all of new part drawing

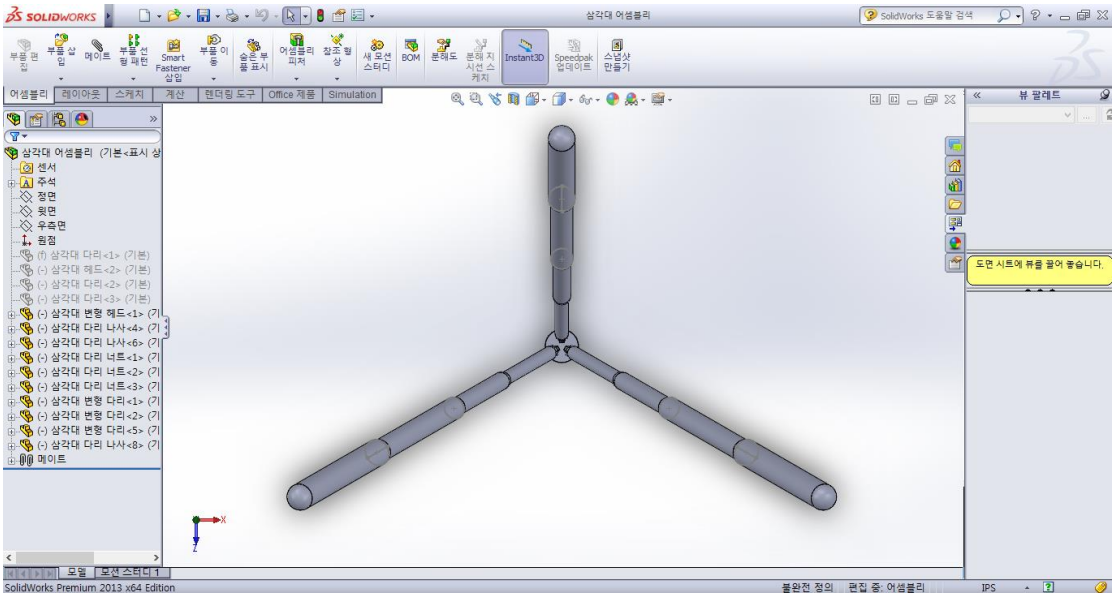


Figure 4.5.3 the Bottom View of Assembly feature of all of new part drawing

3.3.1Simulation of structural strength of new model

In this section of simulation of structural strength of new conceptual tripod assembly feature, in order to conduct this simulation, it is assumed that the camera and the Gimbal system which is holding the camera on are mounted on the head part of the new part design. So, the weight of both components will be also assumed to according to the research of those two units. Furthermore, the simulation to find out maximum force when the user pushes the tripod so that the camera and tripod are suitably positioned in order to take a photo or video clip with certain angle and even at the hill was conducted.

Additionally, the extra research on the material selection will be conducted in order to simulate the structural strength of newly designed conceptual tripod. Considered materials to be selected in the case of manufacture of it will be alloy steel, plastic and so on. The reason why these materials were selected is they are the most commonly used materials when it comes to the manufacture a custom stuff which are supporting a heavy weight of certain object on it with its minimum strength that can sustain the weight or stress forced on.

4. Conclusions

In order to develop the structural strength of the new tripod design model, deeper research regarding the properties of material for the manufacture and design is needed in the first place. The most important components that this project is aiming is to have a better design in terms of structural strength and workspace when it comes to compare an usual tripod model and newly designed tripod model.

This new type of tripod is designed for the user who would like to take a photo with having a better balanced position of camera and stand. Even if on the hill, the camera could maintain the horizontal position because of the Gimbal system application on the head part in the future. When the user wishes to have a low position of camera and stand, it is advised that the tripod can be pushed to the forward direction. Then, one of the legs of tripod stand will be shorten up based on the PKM system concept. Other legs will be automatically longer as the former leg goes shorten. The concept of the

leg design was based on the implement of tri-cept which is widely used in the industries. Those new design parts are the most important components to be changed from general shape or structure of tripod such as the legs, bolts and nuts and head part connecting to the legs and Gimbal system to hang the camera with balance.

These proposed new tripod design part by part was measured and described as figures posted above in result and discussion section. Unfortunately, the simulation of the structural strength and workspace was not conducted and tabulated. This is strongly recommended to do so.

More design of a conceptual design must be drawn and proposed in order to have the best design out of them. Moreover, further numerical and PKM with other methodology to maximize the movement effect of three tripod legs are advised to add and look for.

Acknowledgment (optional)
The author would like to express all his thanks to the reader of this EURECA 2015 conference paper and to the all support by the former supervisor of this project the latter supervisor of this project from Taylor's University Lakeside, Mr.Alexander Chee and Mr.Hardie Hidayat and even more to the university facility approved for the software.

References

[1] C. Wilson, J. Sadler and W. Michels, *Kinematics and dynamics of machinery*, 3rd ed. New York: Harper & Row, 1983, pp. 1-31.

[2] Brighthub Engineering, (2009). *Types of Kinematic Joints in the Design of Machines*. [online] Available at: http://www.brighthubengineering.com/machine-design/6577-types-of-kinematic-joints/ [Accessed 16 Jun. 2015].

[3] Chen, J. and Hsu, W. (2004). Design and analysis of a tripod machine tool with an integrated Cartesian guiding and metrology mechanism. *Precision Engineering*, 28(1), pp.46-57.

[4] F. Xi, D. Zhang, Z. Xu and C. Mechefske, 'A comparative study on tripod units for machine tools', *International Journal of Machine Tools and Manufacture*, vol. 43, no. 7, pp. 721-730, 2003.

[5] Azulay, H., Mahmoodi, M., Zhao, R., Mills, J. and Benhabib, B. (2014). Comparative analysis of a new 3×PPRS parallel kinematic mechanism. *Robotics and Computer-Integrated Manufacturing*, 30(4), pp.369-378.

[6] Z. Bi and S. Lang, 'Joint workspace of parallel kinematic machines', *Robotics and Computer-Integrated Manufacturing*, vol. 25, no. 1, pp. 57-63, 2009

Numerical Modal Analysis of Classical Guitars

Joel Ryan Imanuel (joelryan888@gmail.com), Mohammad Hosseini Fouladi, Satesh Narayana Namasivayam

Mechanical Engineering Programme, School of Engineering, Taylor's University, Jalan Taylor's, Subang Jaya, Selangor Darul Ehsan, Malaysia.

Abstract
This research study is a part of the musical acoustics field and the sciences behind the acoustic radiation of a classical guitar. The acoustic radiation is aimed to be increased by using numerical modal analysis and harmonic analysis on the different parts of a classical guitar. There are three main objectives that are aimed to be accomplished as the research progresses, which are to perform numerical modelling to study the vibration response of a classical guitar, to investigate the correlation between the vibration response of a classical guitar and the sound it produces, and to study the dependence of acoustic radiation on a specific design attribute of a classical guitar. As for research methodology, initially critical literature review was carried out in the first few weeks regarding the field of musical acoustics, analysis of the propagation of sound waves through a variety of materials, then applying this knowledge to the context of a classical guitar. The next stage is for current and new guitar components to be 3D modelled on a CAD design software (Solidworks) using the bottom-up assembly approach. The 3D model is then transferred to an engineering software made for analyses (ANSYS) to run modal analysis, and hence a harmonic analysis to gauge how it behaves during vibration, and its acoustic radiation patterns. With the data collected, it is then compared to the acoustic radiation that a current guitar generates and how the design attributes can be modified via simulation to test for improvements in acoustic radiation of the classical guitar. At the end of the research, the natural frequencies of the individual components of a classical guitar is identified, and is then utilised to vary the acoustic radiation that is produced by that specific guitar. According to the simulation conducted, modified guitar designs with a wider bridge and also added sound holes produced an increase in sound pressure levels by an average of 1 decibel, and also an improvement in the scattering of acoustic radiation is found.

Keywords: Musical acoustics, classical guitar, stringed instruments, acoustic vibration and modal analysis.

1. Introduction

The study of vibrational and acoustical properties of stringed instruments has gained in popularity over the past decade, and the classical guitar is no exception. This is due to the recent introduction of various computer-aided engineering (CAE) software that has spurred researchers to pursue acoustical studies with greater depth. A classical guitar is made out of several components: a soundboard, bridge, sides, back plate, etc. Upon a given string excitation, the vibratory relationship between these components will then determine the characteristics of the sound produced by that specific guitar. Among these components, the soundboard plays the biggest role in terms of sound production of a guitar [1].

In this paper, numerical and harmonic methods were utilised to study the vibrational characteristics of a classical guitar. Modal analysis is a study of the dynamic properties of structures that undergo vibrational excitation, and also the measurement of the dynamic response of structures when excited by a particular input [2]. Initially in this research, numerical modal analysis was used to identify the natural frequencies of each classical guitar body with varying soundboard designs. This method was also used to determine the vibrating patterns of each design that is associated with each of their mode shapes. Upon grasping the vibrating patterns of

each design, a harmonic response analysis then follows to study how the sound production is affected between the different designs in a real-world-usage scenario.

2. Literature Review

As mentioned in Section 1 of this paper, the study of acoustical properties of stringed instruments has gained in popularity over the past few years. In 2012, Gorrostieta-Hurtado [2] ran modal analyses on violins to study its vibrational behaviour and also the sound it produces. Experiments conducted showed that the results obtained for the experiments proved the possibility of further development of methods and techniques that can be used to collect vibratory and acoustic information from violins. According to Gorrostieta-Hurtado, the primary object of a dynamic identification of a harmonic plate in a violin is to detect its vibration performance, and to visualize the resulting mode shapes which can be seen in Figure 2.1. Figure 2.1 shows the numerical mode shapes of the soundboard and back of a violin, constructed in ANSYS.

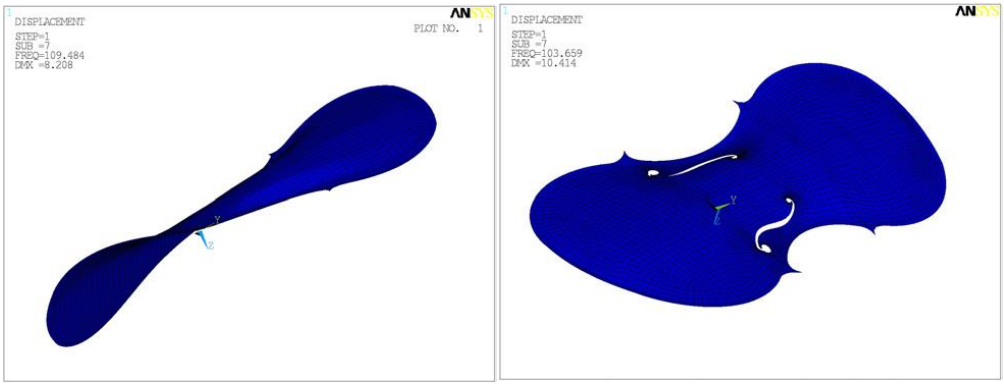


Figure 2.1: Numerical mode shapes of the soundboard and back of a violin [2].

Numerical model analysis of these two components of a violin were performed based on Lanczos method. Lanczcos method is used for large symmetric eigenvalue problems, with over five hundred thousand degrees of freedom, and is utilized to obtain solutions for the lowest possible modes to learn the particular behavioural patterns of a model [3]. The eigenvalues and eigenvectors are then extracted by the analysis using the code formed by ANSYS. Based on Gorrostieta-Hurtado, a larger number of meshing elements will result in a more detailed schematization, which will result in a better comprehension in its structural behaviour. The more detailed meshing would ideally involve more than 4000 elements for this case. To conclude this analysis, the main occurrence that influences the dynamic and acoustic performance of this violin is force-transmission that resides in the bridge-soundboard contact according to Gorrostieta-Hurtado. By modifying the design of the bridge-soundboard, the force-transmission can be improved, resulting in better sound production in the violin.

In 2007, Tippner *et al* [4] carried out studies that also involved numerical modal analyses to identify the change in eigenfrequencies and eigenmodes of the vibration of a soundboard in an upright piano. This change in eigenfrequency and eigenmode are affected by the change in material properties and qualities, change of

geometry and the way the soundboard is anchored. The results of this analysis suggested that the most effective way to improve the sound production of the upright piano is via the change of geometry, which is by increasing the density of the material used in the construction of the soundboard. Besides that, this study also shows that the values of eigenfrequencies will increase whenever the plasticity of the studied system increases. The plasticity can be varied by the placement of ribs, blanks and anchoring. The eigenmodes of vibration can then be varied by changing the position of the soundboard of the upright piano [4].

Another study conducted by Ezcurra *et al* [5] researched into the fluid-structure coupling in guitar boxes to determine how the coupling affects the sound radiation that is produced by it. Three different gases, which are helium, air and krypton, were filled into the guitar box as the only variable, which keeping the remaining characteristics of the guitar constant. Ezcurra *et al* arrived with several conclusions regarding the fluid-structure coupling in a guitar which are that modal patterns and also frequencies of the whole guitar box are heavily dependent on the type of fluid that was used during the analysis, and that the measurements obtained from the individual experiments prove that the only affected outcome was the quality of sound produced, and is very sensitive to the fluid type that was used [5].

In 2012, Brémaud [6] conducted a research on the acoustical properties of wood for stringed musical instruments, with the purpose analysing the diversified properties of various types of wood and their application in musical instruments. A total of 452 species of wood was studied, thorough a variety of projects and theoretical analysis. As a result of this, a wide database was created regarding the diversity of axial vibrational wood properties which makes it easier for instrument-makers to refer and compare the various wood species which is to be used in the components of the instruments they make. Besides that, Brémaud also concludes that the only shared characteristic that is similar between the various types of woods used for the top plate is that they possess a moderate density [6]

On the subject of wood variability, in 2014 Shepherd *et al* [7] researched into the free vibration of acoustic guitars while varying the properties of wood but keeping the braces and bridge properties as a constant throughout the study. Shepherd *et al* also included the varying moisture content of wood into the analysis, and has found that the modes and natural frequencies that have been identified are comparable to the theoretical measurements that were done beforehand, and concluding that the obtained outcomes strongly stresses the importance of properly studying the material properties before modelling an acoustic guitar [7].

In 2002, Boullosa [8] used three isolated classical guitar soundboard which were made out of different types of wood, and studied the differences between them with regards to their early decay times and also to measure their vibrational impulse responses. This was done to investigate all the different ways of measuring the reverberation time of different types of plates. Boullosa proposed that the outcome of the analysis suggests that high frequency vibrations and also radiation notably takes place between 1 to 14 kilohertz, and that the sound radiation has harmonical properties at frequencies up to 20 kilohertz [8].

One of the most vital components of a classical guitar in terms of support is the bracing within the guitar sound box. In 2008, Okuda *et al* [9] investigated and compared the roles and effects a bracing would have on the vibration of a classical guitar through a vibration experiment and also utilizing modal analysis. Figure 2.2 shows the two different guitar top plate models used in the experiment, one with an "X" type bracing and one without.



Figure 2.2: Two modelled guitar top-plates with and without braces [9]

Okuda *et al* has found that the usage of bracing in a particular soundboard would result in a higher resonant frequencies experienced as shown in Figure 2.3, and also results in a smoother frequency response characteristic. This analysis then concluded by Okuda *et al* proposing that the usage of bracing on a soundboard of a guitar is only beneficial in the high frequency range, and does not influence the sound in the lower frequency bands [9]

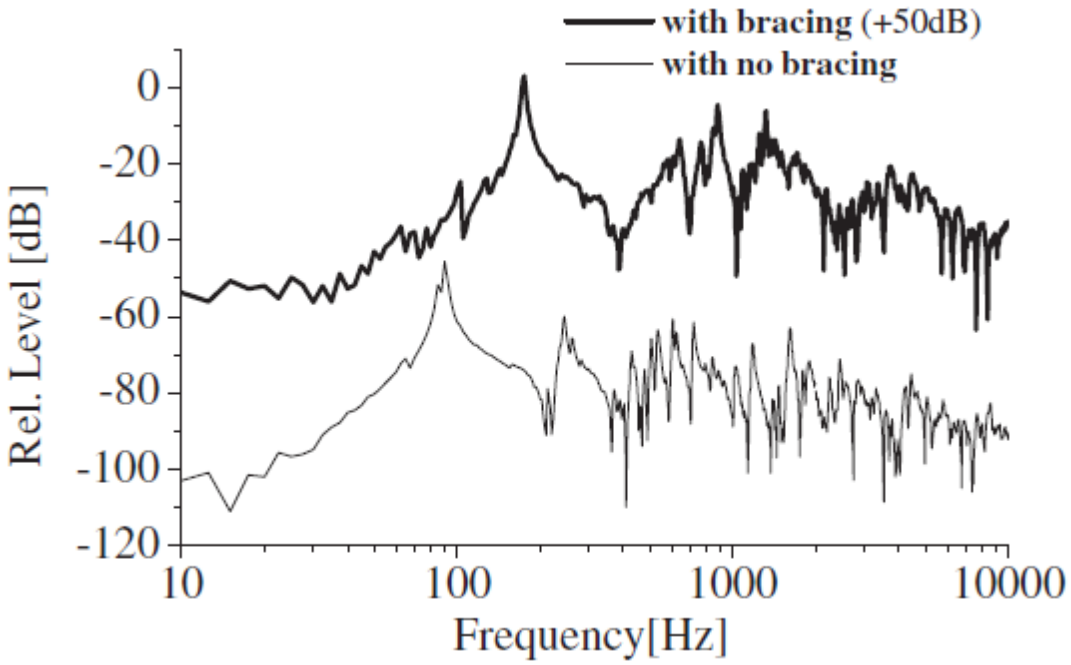


Figure 2.3: Frequency responses of guitar soundboards [9]

3.0 Research Methodology

3.1 Geometric Modelling of the classical guitar

To begin modelling the guitar body as a part, a rough sketch was drawn according to the outline of a guitar body. The dimensions used for the sketch were obtained from the authors' personal classical guitar, which is a model named Yamaha C315. The method which was utilized for modelling is the bottom-up method, whereby a sketch is extruded into the final shape [10]. Once the measurements were obtained, points were plotted onto a blank sketch according to the aforementioned measurements.

After plotting, each of the points were then connected using the "Spline" function to form a singular line from one edge of the sketch to the other. Figure 3.3 shows the spline connecting all the points to form the first half of the sketch. Once the spline function was used, the first half of the sketch was complete. For the second half of the sketch, the "Mirror Entities" function was used to mirror the spline of the first half of the sketch, which was then mirrored along the centerline of the sketch. Figure 3.1 shows the mirrored half along with the original half that was sketched before that, forming the initial outline of the guitar body, which completes the sketching phase of the 3D model. Figure shows the completed sketch which is the outline of the guitar body.

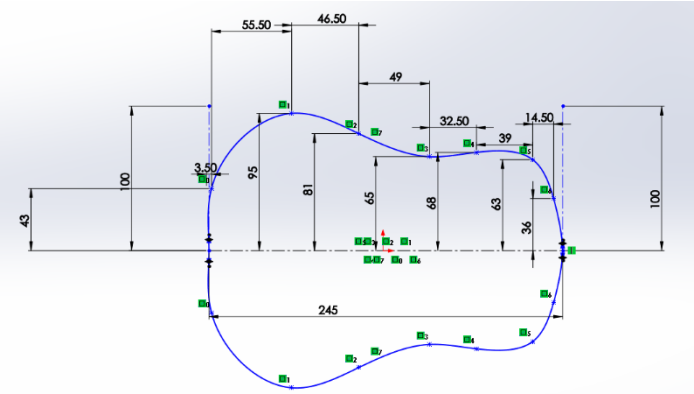


Figure 3.1: Mirrored spline function completing the initial outline of the guitar body

Once the initial sketching of the guitar body outline is formed, the sketch is then extruded to form a block with the shape of the guitar body. The sketch is extruded by 45mm based on the body thickness of an actual classical guitar. After extruding the sketch, a solid guitar-shaped block is formed, which will then need to be made hollow. The "Shell" function is then used to make the block hollow, with the thickness of each side set to 3mm. The next stage is for the bridge, sound hole and bracing to be modelled onto the newly extruded guitar body. Figure 3.6 shows the sound hole sketch and the "Extrusion cut" feature to create the sound hole. After forming the sound hole feature on the guitar body, the bridge is then modelled according to the available measurements. The sketch was drawn on the surface of the body and is then extruded by 3mm to form the bridge. Figure 3.2 shows the completed model of the guitar body.



Figure 3.2: Classical guitar body modelled on Solidworks

For this research, the bracing used is Ladder bracing, and is kept constant throughout the whole research to simplify the validation process in the end of the analysis with an actual classical guitar that uses a ladder bracing.

3.2.3 Modelling of the modifications to the guitar sound box

In order to achieve the third objective of this research, which is to study the dependence of acoustic radiation on a specific design attribute of a classical guitar, the main design of the modelled guitar body from section 3.2.2 was then modified with added and different features. These modified designs was then benchmarked against the original design to test for changes in the measured sound pressure level which will be detailed in the coming sections. The methods used for these modifications are extrusion and extrusion cut, which are similar to that of the previous section. Figure 3.3 shows the two modified designs with added features which are additional symmetrical sound holes, and a wider brace design.

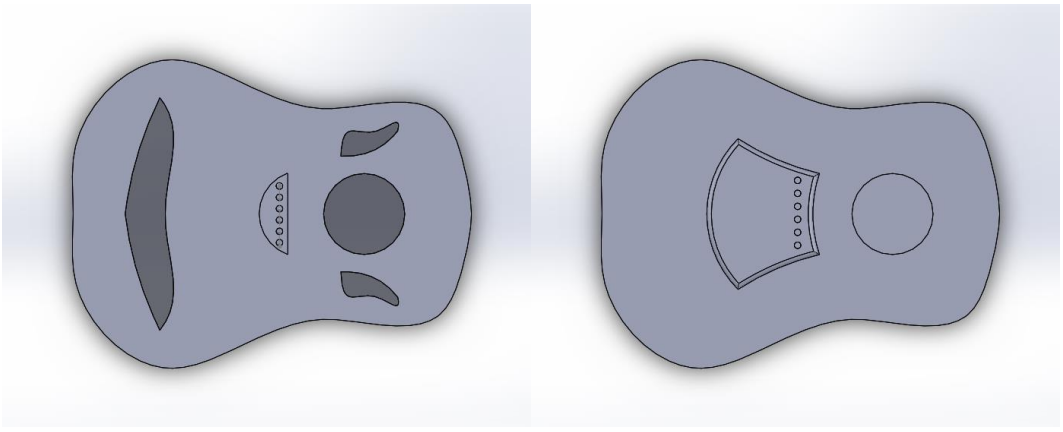


Figure 3.3: Additional sound holes (left) and wider bridge (right)

3.3 Numerical Modal Analysis in ANSYS

3.3.1 Meshing

Upon completing the modelling phase of the guitar, all of its vibrational patterns would then be analysed numerically via ANSYS. The first step of the numerical analysis is to mesh the model into elements. This can be performed in ANSYS through the "Mesh" feature in ANSYS Mechanical. Tetrahedral meshing was utilised with a meshing element size of 5mm as it was the most suitable meshing method for the classical guitar body, while also providing the maximum number of element count. According to a recent study, element sizes between 1mm and 3mm has no difference in the accuracy of the results obtained [11]. Figure 3.4 shows the example of mesh created on the top of the guitar sound box.

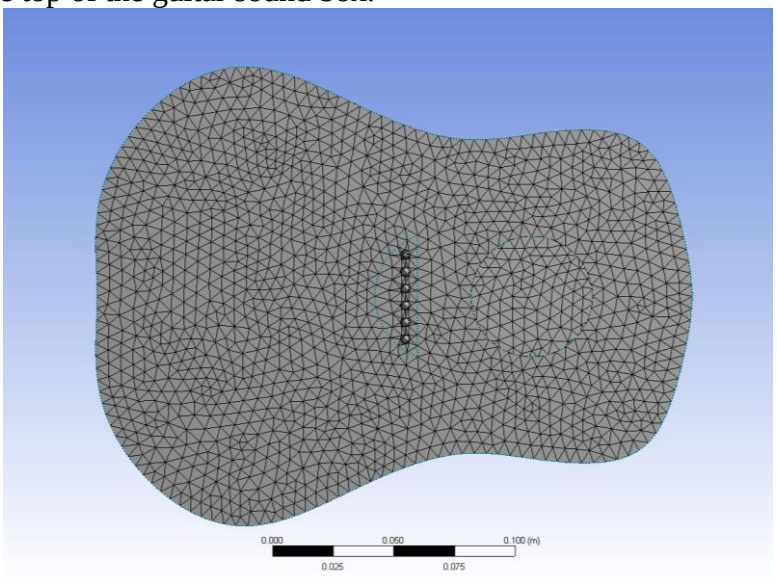


Figure 3.4: Example of tetrahedral mesh on a guitar sound box

3.3.2 Fixing boundary conditions

For all the analysed designs, the material used was constant with properties akin to Mahogany Wood which material properties were obtained from [12]. The only boundary condition applied to all the guitar designs is a fixed point on each design at the left most of the guitar, where the neck of the guitar would be situated. This is to simulate the placement of the guitar body that's hanging by the neck during analysis. Besides that, the number of modes set for the analysis to run was 4, since only the first and lowest natural/resonant frequency will be extracted to be reviewed along with its corresponding mode shape.

3.4 Harmonic Response Analysis in ANSYS

After identifying the natural frequencies and mode shapes of all the guitar bodies, each design was then subject to harmonic response analysis to simulate a real-world-usage scenario. This analysis will provide readings on sound pressure levels in decibels, acoustic pressure, sound power and etc, which will then be used to formulate the acoustic radiation pressure using the equation from [13]. This part of the analysis also warrants the usage of the Acoustics ACT Extension on ANSYS Workbench which is an acoustic FEM solver, designed to provide an integrated environment to solve acoustical and vibroacoustical analyses [14]. This extension enables the author to create mass source excitations to simulate the strumming of guitar strings, and also to display the various results needed to manually compute the acoustical radiation pressure.

3.4.1 Acoustical simulation set-up

Upon importing the geometric models from Section 3.2 into ANSYS Workbench, the "Harmonic Response" component was then selected in place of the "modal" component which was used in Section 3.3. Two enclosures were then required to be modelled surrounding each design, with the first enclosure being an acoustic medium in which the acoustic waves would propagate, and the outermost enclosure is to absorb any outgoing acoustic radiation without reflection [14]. Each of the enclosure has a uniform distance of 0.025 meters from each side of the geometry to maintain a symmetrical domain. Figure 3.5 shows the first and second enclosure surrounding the imported geometry.

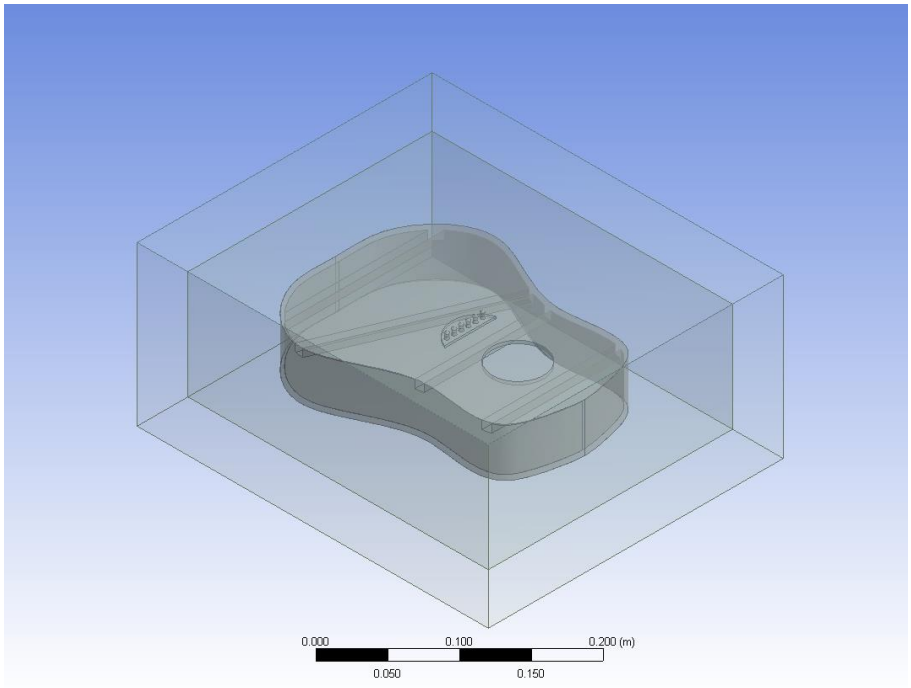


Figure 3.5: Both the enclosures surrounding the imported guitar body geometry

Material properties were then assigned to each geometry, Mahogany wood for the guitar sound box, and structural steel for the two enclosures. The material property of the two enclosures will be overridden further into the analysis once they've been set as "Acoustical Body" in the extension. The frequency range chosen for the analysis is between 0 Hz to 20 kHz because according to the findings of Boullosa [8], although high frequency vibrations and radiation occurs usually between 1 to 14 kHz, sound radiation has harmonics at frequency levels of up to 20 kHz. The next step is then to

define both the enclosures as an acoustic body, by synchronising their mass density and also their speed to the properties of air. The outermost enclosure was also made to have zero pressure on its outer surfaces to ensure outgoing wave absorption [14].

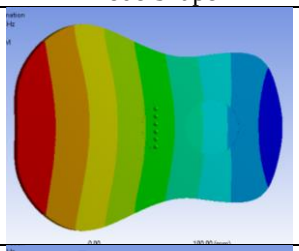
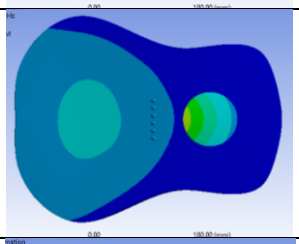
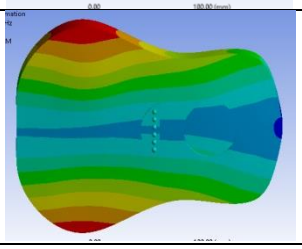
The final step is to define the excitation source for the simulation. Since the model is without any guitar strings to reduce variability, the excitation source is set as the pins on the bridge of the guitar body. The type of excitation that was chosen is mass flow acoustic excitation with an amplitude of 0.01 kg/m^{2}s [14]. Meshing settings used in this analysis were identical to that of the settings used in the numerical modelling analysis in Section 3.3.
Once all the conditions have been set, the simulation results obtained will be in the form of sound power level in decibels, acoustic pressure experienced in the inner enclosure, sound power and etc. These data can then be used to calculate the acoustic radiation pressure that each of the designs emit after excitation.

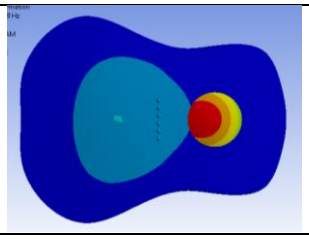
4.0 Results and Discussion

4.1 Obtained results using NMA on multiple guitar designs

The designed guitar models were first subjected to NMA through ANSYS to have their natural frequencies identified, and also their vibrational patterns and mode shapes studied. This analysis gives an insight to how each design responds to particular resonant frequencies, and also how the change in design can vary the way it vibrates. Table 4.1 shows the first 4 modes of the main classical guitar design without any modifications, along with their natural frequencies.

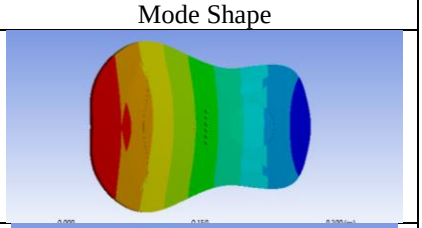
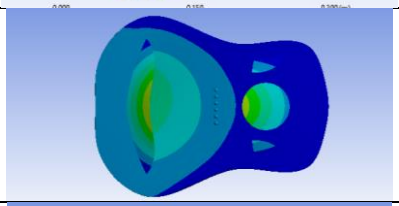
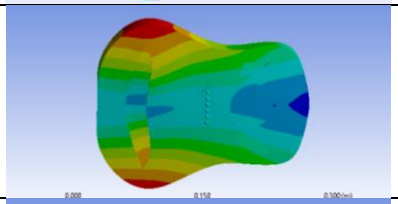
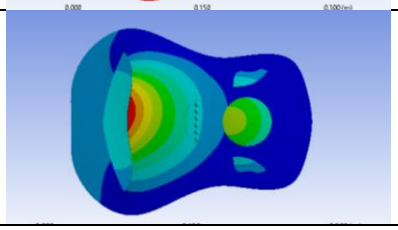
Table 4.1: First 4 modes of the main design

Mode no. *n*	*F* [Hz]	Mode Shape
1	183.37	
2	568.25	
3	654.80	

4	809.49	

According to Table 4.1, modes number 1 and 3 share a similar vibrating pattern but in the opposite direction, while the same can be said for modes number 2 and 4. The mode that will be extracted as reference is the first mode which has a natural frequency of 183.37 Hz. Table 4.2 shows the first 4 modes of the first modified guitar design, which is the added sound holes.

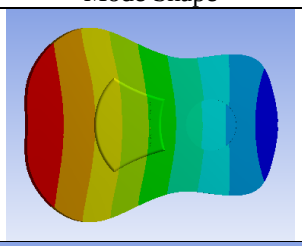
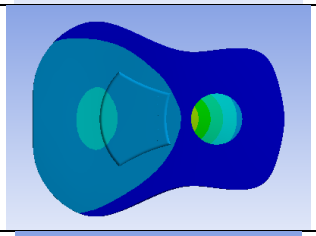
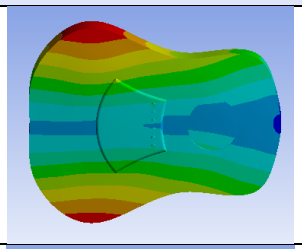
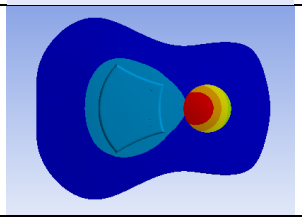
Table 4.2: First 4 modes of the modified design with added sound holes

Mode no. *n*	*F* [Hz]	Mode Shape
1	179.32	
2	567.39	
3	622.21	
4	772.43	

Based on Table 4.2, the results are comparable to the mode shapes in Table 4.1. Modes 1 and 4 have the same vibrational behavior albeit in opposing directions, while modes 2 and 4 have the opposite vibrational behavior between the two. The mode that will be extracted from this data is the first mode which is 179.32 Hz.

Lastly, Table 4.3 shows the first 4 modes for the second modified guitar design, which is with the wider bridge.

Table 4.3: First 4 modes of the modified design with wider bridge

Mode no. *n*	*F* [Hz]	Mode Shape
1	181.33	
2	566.43	
3	654.09	
4	810.61	

Data in Table 4.3 also suggests that the vibrational patterns of mode 1 and 3 are similar but with opposite directions, while modes 2 and 4 have the opposite patterns. Based on all the obtained information from Table 4.1, 4.2 and 4.3, it can be deduced that even by changing or tweaking the design of the soundboard, the vibrational pattern remains unchanged, and only affects the vibrational intensity. Since the design with the added sound hole has the lowest natural frequency among the three, it will be the easiest to excite whenever it's used with proper guitar strings but not by a large margin.

Since the author is unable to validate these modal analysis data through the means of Experimental modal analysis, literature is used as a benchmark for validation purposes. According to Curtu *et al* [15] the guitar model that has the most similar bracing and overall design had the lowest natural frequency of 110 Hz through Experimental Modal Analysis, and 143 Hz through FEM Analysis. This shows that the results obtained in this paper only has a deviation of 20% which could be due to a variety of reasons such as type of wood, and actual measurements used.

4.2 Harmonic Response Analysis

After identifying the natural frequencies and mode shapes of the individual designs, they were then subject to harmonic analysis to study their sound production in a simulated environment. The analysis that was done for the models were for Sound Pressure Level in decibels, and to identify the maximum acoustic pressure in the innermost enclosure of the simulated environment.

4.2.1 Sound Pressure Level analysis

In the simulated environment, a microphone was placed 25cm above the models individually to measure the sound levels produced by each design. Figure 4.1 shows the obtained results plotted through an Excel graph.

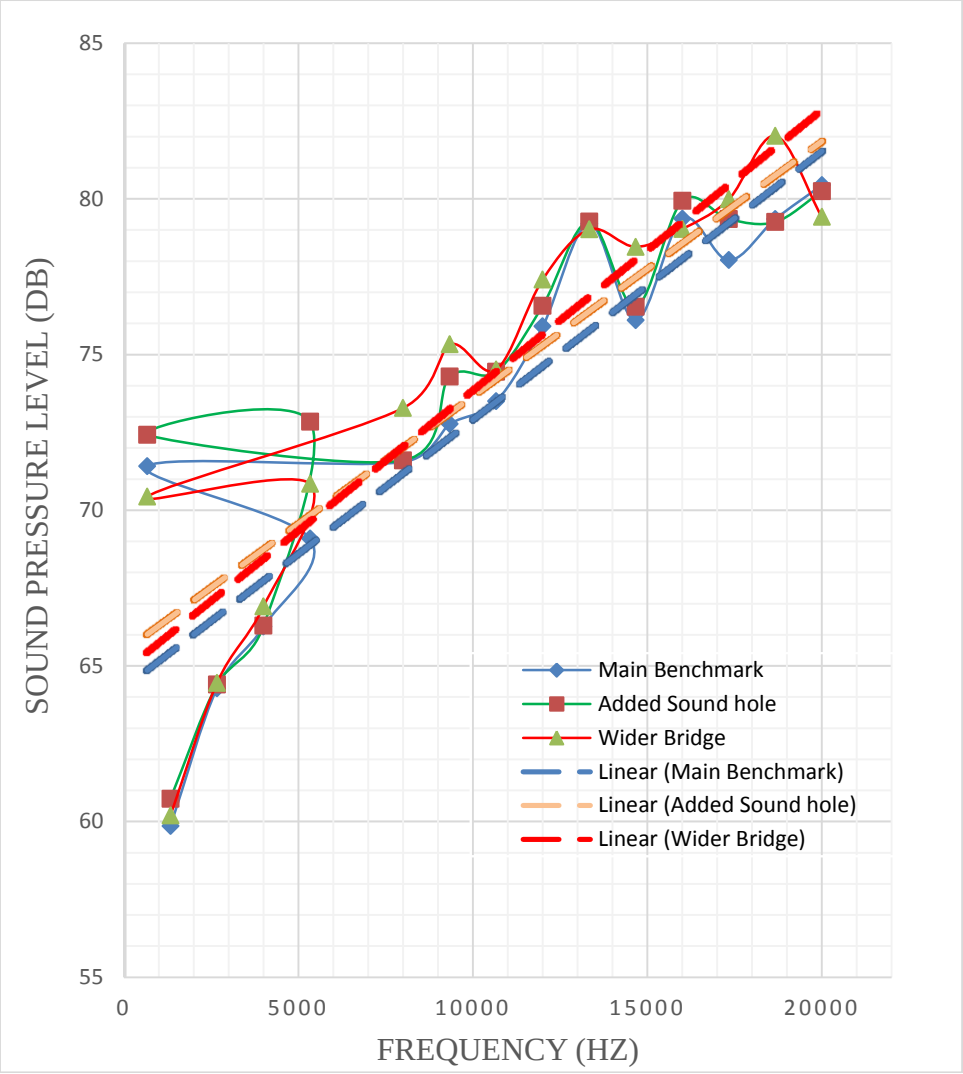


Figure 4.1: Graph of Frequency tested against SPL produced for each design

Based on the individual plots, three trend lines were created to study the trend of each analysis, and to identify which was the most effective design in terms of sound volume. Based on the graph, it can be clearly seen that the design with the widened bridge produced an overall louder volume added sound hole. Though the difference may only be approximately by 1 decibel, the results in reality may be quite significant.

4.2.2 Acoustic Pressure analysis

Besides sound pressure level testing in the ANSYS Workbench utility, the acoustic pressure experienced by each design was also measured and tested. The first (innermost) enclosure was probed after the analysis to simplify the identification of the maximum and minimum acoustic pressure faced by the enclosure. Figures 4.2, 4.3 and 4.4 shows the individual maximum acoustic pressure measured, and also a visual representation of the acoustic pressure on the enclosure.

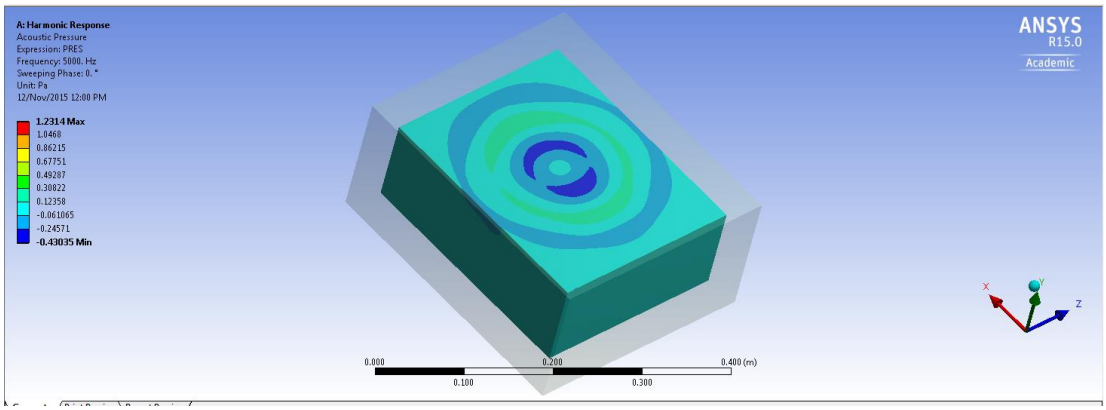


Figure 4.2: Scattering of acoustic pressure on the inner enclosure for the Main Design

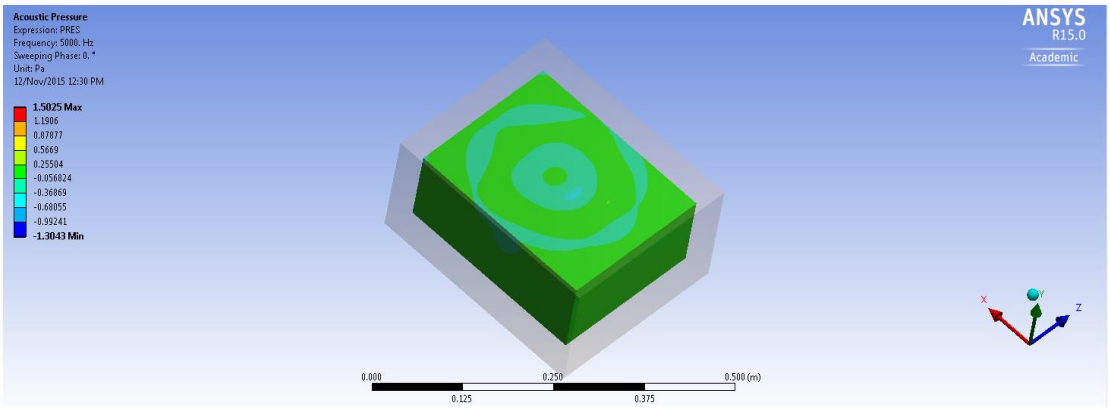


Figure 4.3: Scattering of acoustic pressure on the inner enclosure for the Design with Added Sound Hole

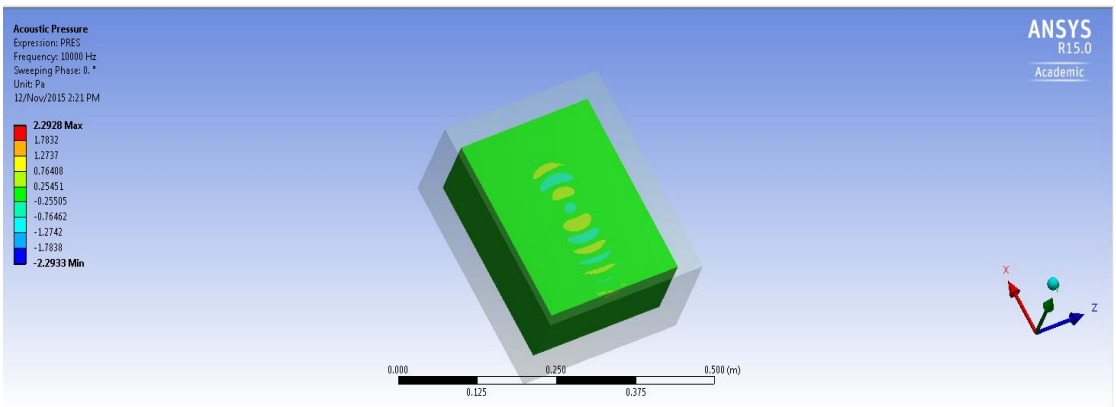


Figure 4.4: Scattering of acoustic pressure on the inner enclosure for the Design with Widened Bridge

As per assumption, the design with the highest acoustic pressure reading is the model with the widened bridge at 2.3 Pascals, followed by the design with the added sound holes at 1.5 Pascals, and with the original unmodified design at 1.2 Pascals. By observing the acoustic pressure scattering in each figure, the two modified designs scatters the pressure more effectively and is more apparent than that of the original design.

4.3 Acoustic Radiation calculations

According to Cox [13], acoustic radiation pressure, which is the apparent pressure difference between the average pressures at a surface, can be computed with the formula:

$$P_{rad} = \frac{I_{av}}{c_0} = \frac{1}{2}\frac{{p_a}^2}{p_0{c_0}^2}\ Pa \tag{5}$$

By using this formula and substituting the sound pressure levels to obtain acoustic radiation pressure readings, Figure 4.5 shows the relationship between sound pressure level in decibels and acoustic radiation pressure in Pascals.

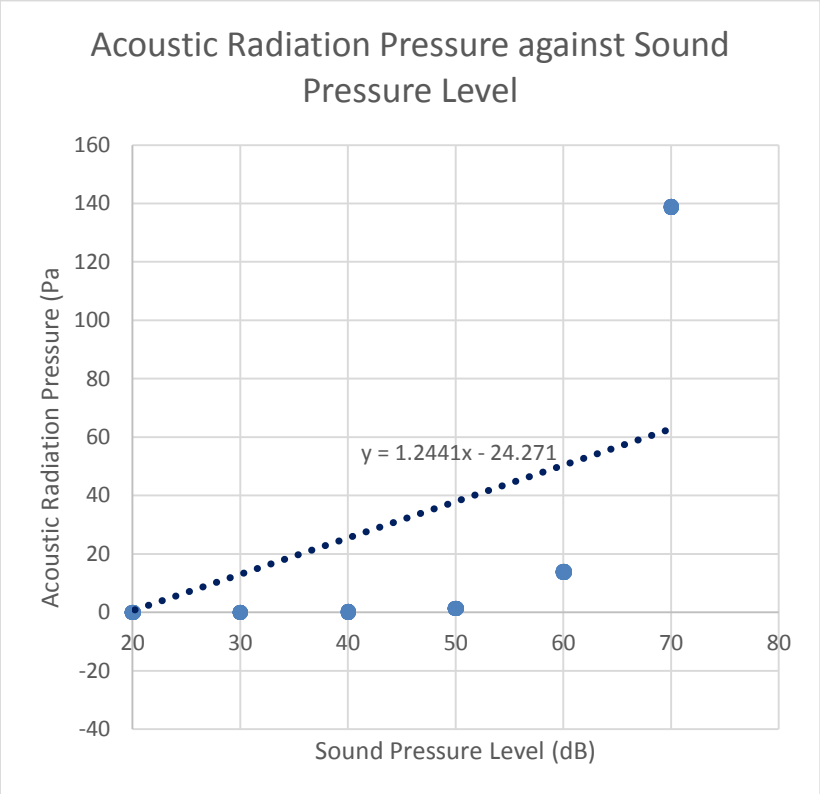


Figure 4.5: Trend line of ARP vs SPL

5.0 Conclusion

This research will help the music industry, specifically guitar manufacturers, as they can make use of this research to improve the acoustic radiation in their products. With the data obtained from this study, the design characteristics of the classical guitar can be changed to improve the sound production from it, resulting in a louder musical instrument.

At the end of this research, several outcomes that is planned to be attained which is to be able to successfully model the vibration response of a classical guitar through the relevant software, to be able to vary the acoustic radiation by modifying its design characteristics, and lastly to be able to relate the modal analysis with actual acoustic radiation of a component in a classical guitar. Designs have been modified and have proven to be able to improve the sound pressure level and also the acoustic radiation when measured.

References

[1] S. Goutham, N. SD Satadeep, T. Prasad and G. Babu, 'Modal Analysis of Chassis', *International Journal of Engineering and Advanced Technology (IJEAT)*, vol. 2, no. 4, pp. 789-795, 2013.

[2] L. Beranek and T. Mellow, *Acoustics*. [S.l.]: Academic Press, 2012.

[3] Efren Gorrostieta-Hurtado, 'Vibration analysis in the design and construction of an acoustic guitar', International Journal of Physical Sciences, vol. 7, no. 13, 2012.

[3] *ANSYS Mechanical APDL Structural Analysis Guide*, 15th ed. ANSYS Inc., 2013, pp. 39-75.

[4] J. Tippner and P. Koňas, 'Finite-element model and modal analysis of grand piano soundboard', *Acta Universitatis Agriculturae et Silviculturae Mendelianae Brunensis*, vol. 55, no. 4, pp. 111-118, 2007.

[5] A. Ezcurra, M. Elejabarrieta and C. Santamaría, 'Fluid–structure coupling in the guitar box: numerical and experimental comparative study', *Applied Acoustics*, vol. 66, no. 4, pp. 411-425, 2005.

[6] I. Brémaud, 'Acoustical properties of wood in string instruments soundboards and tuned idiophones: Biological and cultural diversity', *The Journal of the Acoustical Society of America*, vol. 131, no. 1, p. 807, 2012.

[7] M. Shepherd, S. Hambric and D. Wess, 'The effects of wood variability on the free vibration of an acoustic guitar top plate', *The Journal of the Acoustical Society of America*, vol. 136, no. 5, pp. EL357-EL361, 2014.

[8] R. Boullosa, 'Vibration measurements in the classical guitar', *Applied Acoustics*, vol. 63, no. 3, pp. 311-322, 2002.

[9] A. Okuda and T. Ono, 'Bracing effect in a guitar top board by vibration experiment and modal analysis', *Acoust. Sci. & Tech.*, vol. 29, no. 1, pp. 103-105, 2008.

[10] S. Tickoo, *SOLIDWORKS 2015 for designers*. Schererville, Indiana: CADCIM Technologies, 2015.

[11] D. Lim, M. Hosseini Fouladi and K. Yap, 'Develop An integrated approach to FE model correlation on multi-bent deoxidized copper phosphorus tubes', in *EURECA Conference*, 2013

[12] *Wood Handbook: Wood as an Engineering Material*. Madison, Wisconsin: Forest Products Laboratory, United States Department of Agriculture Forest Service, 2010.

[13] B. Cox, *Acoustics for Ultrasound Imaging*. London: University College London, 2013, p. 56.

[14] *Acoustics ACT Extension Workshop 3: Audio Speaker and Plate*. ANSYS Inc, 2013.

Modelling and Optimisation of Human Arteries Stent

Lee Chun Tat, Thein Chong Ket*

School of Engineering, Taylors University Lakeside Campus
No. 1 Jalan Taylor's, 47500 Subang Jaya, Selangor, Malaysia

chungket.thein@taylors.edu.my

Abstract

Coronary stent are used to unblock or enlarge the narrowed or blocked coronary artery. Stent implantation may injure the vessel wall due to the shape and design of the stent. Hence the design of the stent has to be optimize to reduce the chance of injury. This research is to optimize the size and shape of the coronary stent and to investigate and reducing the dogboning rate while stent expand. The coronary stent available on market have improved over the decade but in some cases which the artery begin to narrowed after some times which known as restenosis. In addition dogboning effect will causes mechanical injury to the vessel wall during the non-uniform expansion of balloon-stent. This will cause to induce an inflammatory response which results in thrombosis. Hence, this research is conducted to reduce injury causes by stent during angioplasty process and reduce the effect of dogboning. This research will be conducted by using ANSYS software which a stent CAD will be model with SOLIDWORKS. Boundary conditions are applied on stent model and simulations are run to obtain the stress and displacement of the stent model. Then modifications are done by analyzing the relation between stress and radial expansion to improve the overall performance of the stent. Dogboning rate of the stent are observe by running the simulation with applied internal pressure on the inner balloon surface. The effect of different stent design on the restenosis rate can be study by comparing different stress distribution on the artery wall. To reduce the dogboning and restenosis rate, a better and optimized design has to be done. At the ends of the research, a better stent design which is stent 3 has dogboning value which is 70.45% lower than Stent 1. Furthermore, Stent 3 stress concentration on artery wall is 67.31% lower than Stent 1 which led to a lower restenosis rate.

Keywords
Stent, coronary artery, shape optimization

1. Introduction

Coronary artery disease is the most common type of cardiovascular diseases. When the coronary artery is blocked or narrowed due to plaque buildup on the artery wall, it affects the blood flow into the heart and causes heart attack. Atherosclerosis which is another term of the coronary artery disease are causes by the fatty material, which known as plaque built up on the wall of the arteries. Coronary arteries are the only source of blood supply to the myocardium. When oxygen-rich blood stopped flow into myocardium due to blockage of coronary artery, angina or heart attack will endure by that person and may causes death.

In order to prevent this disease, coronary stents are being use to unblock or enlarge the narrowed coronary artery causes by the buildup of cholesterol-laden plaques. Coronary stent are tube-shaped device which placed on the coronary arteries to keep the blood flow and supply for myocardium. The stent are inserted into the narrowed artery and a balloon place within the stent is inflated. The stent expands to the size of the artery and holds it open. Then the balloon is deflated and removed leaving the stent supporting the narrowed artery [1].

Stent is a tubular medical implement used to support or expanded the narrowed or blocked artery due to plaque. Shape and design of the stent used in most cases are devised according to the experience of doctors and designers. The measurement of the most relevent mechanical and dimensional parameters for a given stent design are summarize by Schmitz *et al*. [2]. Theres 1.2 million of patients undergo stent implantations each year in United States only [3].

There are two methods used to analyze the behavior of stent during the stent deployment: experimental methods and numerical simulations. Numerical simulations are preferred to be used compared to experimental methods due to its flexibality and cost. Different numerical simulations model has published recently with different level of complexity and accuracy to simulate the stent deployment. Single stent model were use to simulate the expansion of stent in the early work without considering the contact effect of stent with the ballon and artery wall [3,4]. To increase the accuracy of the simulation, a better and more complicated model has been proposed, balloon-stent model [5,6], stent artery model with plaque [7], ballon-stent-artery model without plaque [8] and balloon-stent-artery model with plaque [9]. Model of artery and plaque with different formulation has been proposed in the literature including linear isotropic [8] and hyperelastic material models [7]. Mechanical properties of balloon-stent system expansion were simulated by the loading of radial displacement applied on inner surface of balloon. The loading are simplified and can reduce the amount of computation. Time-related pressure was applied on balloon inner part surface to analyze the balloon-stent system dilation and this loading method is more accurate. But in both condition, interaction between the stent and vessel wall was not consider and this might affect the overall simulated results[10]. Design optimization in present paper are mostly emphasize on reducing dogboning effect.

Dogboning phenomenon which is due to non uniform balloon-stent expansion will causes the development of thrombosis which is the formation of blood clot inside a blood vessel. This will narrowed or blocked the vessel. Mechanical injured on the vessel wall causes by the dogboning phenomenon as the stent expand unevenly throughout the process and critical pressure point on the stent act on the vessel wall will results in thrombosis. The design of the stent are believe to affect the stent expansion performance which including the dogboning phenomenon. The mechanical properties of stent expension are investigated in

previous study and simulated by the loading of redial displacement applied on inner surface of balloon. Time-related pressure was applied on the balloon-stent expension system to analyze the pattern of the expansion and observe the effect of stent design on dogboning phenomenon. Quality of stent expansion are define by the dogboning rate. Dogboning rate is a nonlinear implicit function of the geometrical parameters and are tpically evaluated by the solution of the finite element method. Depending on the complexity of the simulation for stent expansion, the simulation can be computatuionally expensive. Hence the challenge is to reduce the computational cost of simulating the dogboning rate during the optimization process [11]. By reducing the computational cost of simulating dogboning rate, the process of the modification of the stent design can shorten as the result of the dogbone phenomenan can be observe within a short time.

The stent on the market now days are safe to use but still there is some problem that will injured the vessel while in use. The artery that was open by using the stent begins to become narrowed again within month of the procedure due to arterial injury and inflammatory response. A good shape design stent is important in avoiding the injury when the stent is implanted into the vessel.

However, bad stent shape design may causes the stent to undergo dogboning and have a high pressure point and acted on the vessel wall [12]. The pressure point acted on the wall will causes injury and damages the vessel wall. Dogboning phenomenon also contributes to the injury of vessel wall. Dogboning effect is causes by non uniform balloon-stent expansion and causes the stent to have a high pressure point acted on the vessel wall. Non uniform balloon-stent expansion has significant impact on thrombosis and hyperplasia development. Mechanical injury due to non uniform expansion will induce an inflammatory response which results in thrombosis and affects artery restenosis [13]. Artery restenosis is re-narrowing or blockage of the artery after the stenting process has taken place. Artery restenosis rate is related to the stress distributed and concentrated on the stent-artery wall contact [3]. Stent design affect the artery restenosis rate after the stent implantation process as the stent design causes different stress concentrate and distribute on the artery wall [14].

The scope of this project is to optimize the design of the stent to reduce the chance of injury occur at the vessel wall and reduce the artery restenosis rate. This can archive by improving stent design and performing finite element analysis and simulation on the stent to seek an optimum designs.

The coronary stent available on market have improved over the decade but in some cases which artery restenosis occurs. In addition dogboning effect will causes mechanical injury to the vessel wall during the non-uniform expansion of balloon-stent. This will causes to induce an inflammatory response which results in thrombosis. Hence the main objective of this research is to reduce injury causes by stent during stent implantation process by reducing the dogboning effect and reduce the restenosis rate by optimizing the current available stent model. Two commercially available stent are chosen which have the same materials properties to run a finite element analysis. The simulation of both two model are compared in terms of stress distribution, radial gain and dogboning. Restenosis rate of the stent are studied by observing the stress distribution on the artery wall after the stent implanted on it.

2. Methodology

This research is conduct by analyzing the performance of two different commercial available stent and optimize the design which result in a better stent design. SOLIDWORKS software are used to model the stent, balloon, vessel and plaque and ANSYS software are used to run the finite element analysis.

2.1 Stent

A stent design available from the market are chosen to analyze. Optimization of the stent design are then done. Palmaz-Schatz coronary stent is a commercial available stent and is chosen to simulate in this research. Palmaz-Schatz coronary stent will be referred as Stent 1. The optimized stent design will be referred as Stent 2 and Stent 3. Stent 2 and Stent 3 has round corner geometry properties and have smaller link or bridging members between the structures. Round corner geometry properties reduce the stress concentration of the stent structure and smaller bridging members increase the flexibility of the stent structure.

All three stent models are modelled using SOLIDWORKS software. The geometry properties of three stent are assume to be both same to simulate and compare the results. Outer diameter of both stents are 3mm with thickness of 0.05mm and length of 5mm. Fig. 1 below shows the CAD of the three stent in the original unexpanded condition.

(a) Stent 1 (b) Stent 2 (c) Stent 3

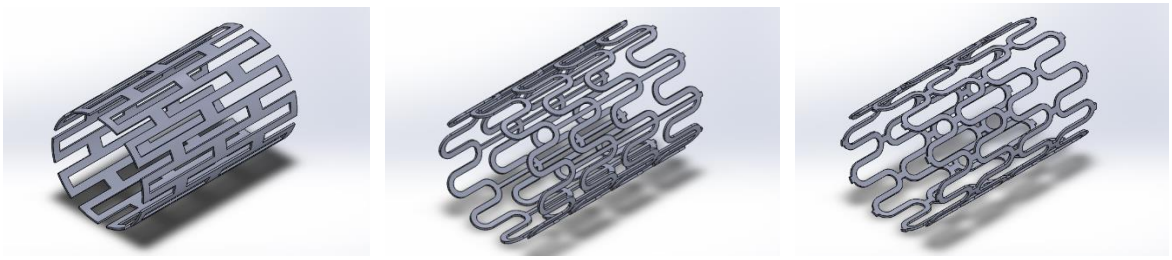


Figure 1. Geometry of stent models in unexpanded condition (a) Stent 1, (b) Stent 2, (c) Stent 3

The stents are assumed to make of same materials as the previous two stent, stainless steel 304. The material model for the stents are bi-linear elasto-plastic which chosen due to the stent will undergo plastic deformation and expanded to the desire diameter. Material properties of the stents were assume as same as the literature [5] where: Young's modulus = 193GPa; shear modulus = 75GPa; tangent modulus = 692MPa; density = $7.86.10^{-6}$kg/mm^3; yield strength = 207 MPa; Poisson's ratio = 0.3.

2.2 Artery with plaque

The coronary artery are assumed to be a homogenous and isotropic materials and modelled as an idealized vessel which have same inner and outer diameter all along. The geometry property of the artery and plaque are: artery length = 10 mm; outer diameter = 5 mm; inner diameter = 4 mm; plaque length = 7 mm; plaque inner diameter = 3 mm. Fig. 2 shows the model of the artery with plaque.

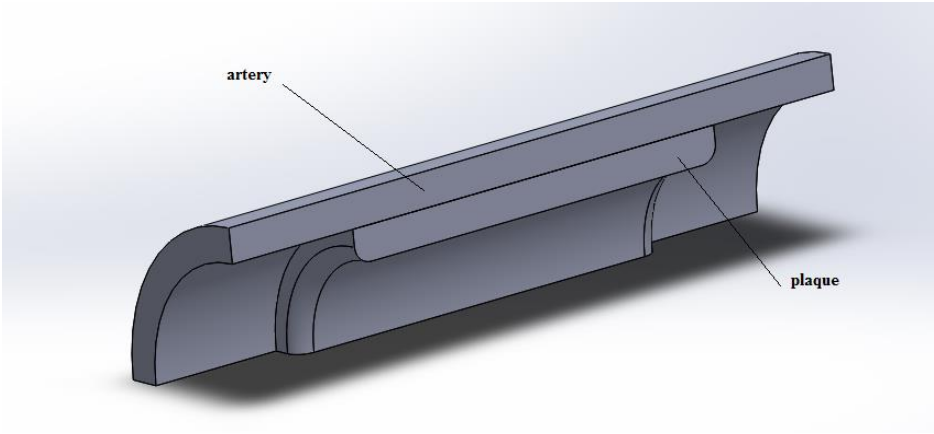


Figure 2. Artery with plaque model.

The material model used for the artery and plaque are hyperelastic material models. Mooney-Rivlin hyperelastic equation was used to define the artery and plaque tissue. Carew *et al.* [15] describe the general polynomial form of the strain-energy density function for an isotropic hyperelastic materials can be written as:

$$W(I_1, I_2, I_3) = \sum_{i,j,k=0}^{\infty} C_{ijk} (I_1 - 3)^i (I_2 - 3)^j (I_3 - 3)^k \quad (1)$$

Where, W is the strain energy density function of hyperelastic material, C_{ijk} is the hyperelastic constant, $C_{000} = 0, \lambda_1, \lambda_2, \lambda_3$ are principal stretches of the material and I_1, I_2, I_3 are the invariant of strain. The invariant of strain can be define by:

$$I_1 = \lambda_1^2 + \lambda_2^2 + \lambda_3^2 \qquad I_2 = \lambda_1^2\lambda_2^2 + \lambda_1^2\lambda_3^2 + \lambda_2^2\lambda_3^2 \qquad I_3 = \lambda_1^2\lambda_2^2\lambda_3^2 \quad (3)$$

Five parameter Mooney-Rivlin model as shown in Eq. (4) was used for the artery and plaque model.

$$W = C_{10}(I_1 - 3) + C_{01}(I_2 - 3) + C_{20}(I_1 - 3)^2 + C_{11}(I_1 - 3)(I_2 - 3) + C_{30}(I_1 - 3)^3 \quad (4)$$

The hyperelastic constant of Eq. (4) are stated in Table 1 [7]. Stress component of the model can be derived by differentiating the strain energy density function with respect to strain.

Table 1. Hyperelastic coefficients of artery and plaque tissue

	Artery wall tissue (kPa)	**Plaque tissue (kPa)**
$\boldsymbol{C_{10}}$	18.90	-495.96
$\boldsymbol{C_{01}}$	2.75	506.61
$\boldsymbol{C_{20}}$	85.72	1193.53
$\boldsymbol{C_{11}}$	590.43	3637.80
$\boldsymbol{C_{30}}$	0	4737.25

2.3 Balloon

A balloon is put in the inner wall of the stent and pressure are applied on the balloon to expand the stent during stent implantation process. The balloon modelled has length of 7mm, with outer diameter of 7mm and thickness of 0.1mm. The expandable balloon are represent with a polyurethane rubber material which is an incompressible material and was define by Mooney-Rivlin two parameter hyperelastic model. The strain-energy density function of the balloon are:

$$W = C_{01}(I_2 - 3) + C_{10}(I_2 - 3) \quad (5)$$

The hyperelastic coefficient of the strain-energy density function of ballo0n are as stated in Table 2 below and the density of the balloon material is 1079kg/m^3 [5].

Table 2. Hyperelastic coefficient of balloon

	Pressure (MPa)
$\boldsymbol{C_{01}}$	0.710918
$\boldsymbol{C_{10}}$	1.06881

2.4 Meshing and boundary conditions

The model of the stent-balloon-artery with plaque is meshed with eight-node linear 3D block elements. Model 1 simulate the condition for Stent 1 implantation while Model 2 simulate the condition for Stent 2 implantation and Model 3 simulate the condition for Stent 3 implantation. Model 1 has 9099 elements, Model 2 has 9228 elements and Model 3 has 9943 elements. The model consist of four layer as shown in Fig. 3.

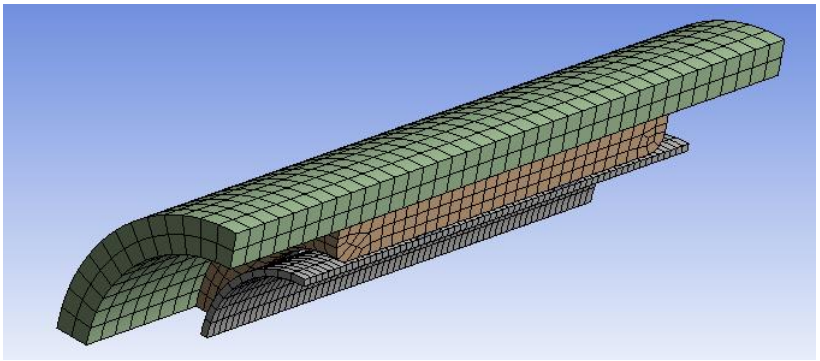


Figure 3. Assemble model for Stent 1.

The outer first layer of the model is the artery wall, the second layer is the plaque, third layer is the stent and fourth layer is the balloon. To perform a steady-state analysis to avoid rigid body motion, both end of the balloon model are set where the displacement to be fixed in all direction. The artery model are set so that only radial movement is allowed. The stent model are tethered so that only radial displacement is allowed. Contact between the stent-balloon and stent-artery with plaque wall are assumed to be frictionless, while contact between artery-plaque are assumed to be bonded. Special attention must be taken in parameters like contact algorithm, penetration factors, time step and stiffness as the simulation involve large displacement and complex contact analysis.

2.5 Loading and solutions

There are two approaches to simulate the stent implantation process. First method consider uniform increases pressure applied on the inner surface of the balloon. Second method is the radial displacement is directly enforced on the inner surface of the balloon causing the stent to expand to the desire diameter [16]. In this research, the simulation is carried in by using first method. Constant pressure are applied on the inner wall of the balloon to simulate the expansion of the stent model. Pressure applied on the model increases in a constant rate in 1.635s and for Model 1 the pressure varied from 0 to 0.75MPa while for Model 2 the pressure varied from 0 to 0.48MPa lastly for Model 3 the pressure varied from 0 to 0.365MPa. The pressure are set as stated so that the maximum radial expansion for both model are 0.5mm.

3. Results and Discussion

3.1 Stress distribution

Distribution of von Mises stress in the stent models are as shown in Fig. 4, Fig. 5 and Fig. 6. For Stent 1, Stent 2 and Stent 3, the maximum stress on the stent model are 322MPa, 287MPa and 274MPa which doesn't exceed the ultimate tensile strength of the materials which is 460MPa. Hence the stent wont fail n structure.

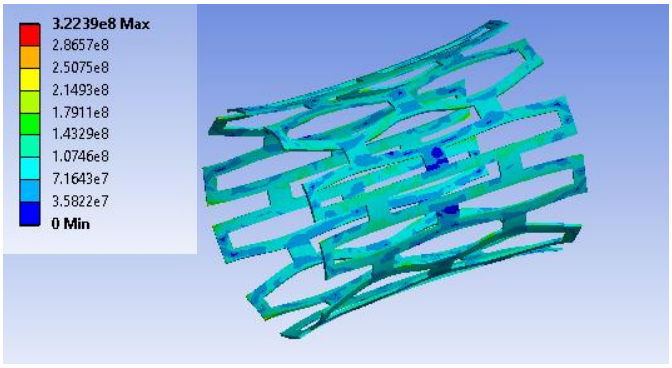


Figure 4. Von Mises stress distribution of Stent 1.

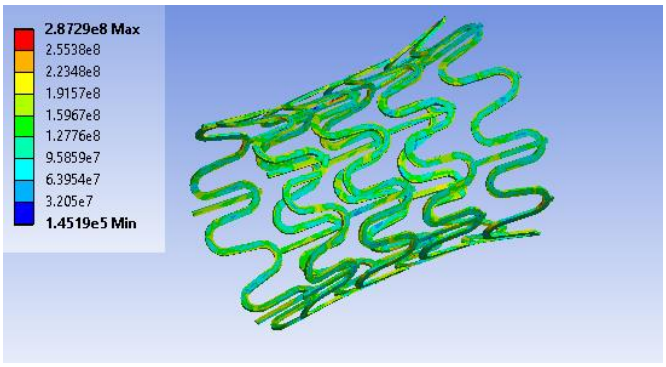


Figure 5. Von Mises stress distribution of Stent 2.

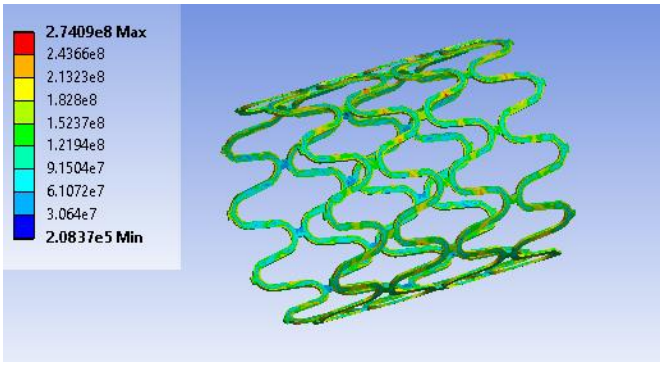


Figure 6. Von Mises stress distribution of Stent 3.

Von Mises stress distribution on the artery wall of 3 models are shown in Fig. 7. For Model 1, Model 2 and Model 3, the maximum stress acted on the artery wall are 8.32MPa, 2.94MPa and 2.72MPa respectively. On the critical stress point, possible injury might occurs at the artery wall and causes thrombosis. Stress distribute on the artery wall is different from the literature by Misagh *et al*. [17] which have different plaque composition on the artery wall. This study has more plaque composition compare to Misagh *et al.* study, hence the stress distribution will different from it. More plaque composition artery is simulated in this study to approach a more severe coronary artery blockage condition.

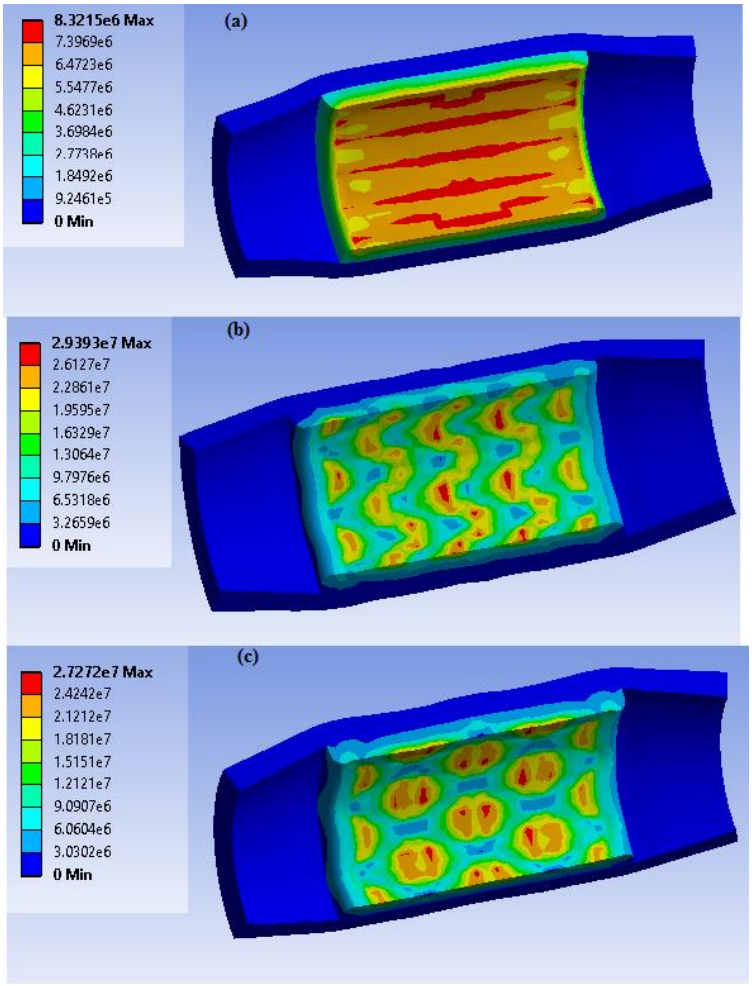


Figure 7. Von Mises stress distribute on (a) Model 1; (b) Model 2; (c) Model 3

According to Gu *et al.*, stress concentration on the wall is the main factor contribute to the restenosis rate [3], as the stress concentration on the artery wall is high, the more likely the restenosis rate will be high too. Different geometry property of the stent may lead to different stress concentration acting on the artery wall and influences the restenosis rate.

Clinical trials by different researcher has confirm that different stent design will influences the restenosis rate of the stent after implantation process. Those researchers are Kastrati *et al*. [14] and Miketic *et al*. [18]. In this study, the Palmaz-Schatz coronary stent available commercially in market, which is Stent 1 has higher stress concentration on the artery wall when compare to Stent 2 and Stent 3. Hence the restenosis rate of Stent 2 and Stent 3 is lower than Stent 1. Optimization of the stent design has successfully reduce the restenosis rate. In this study, Stent 3 which is the final optimized stent design has lowest stress concentration acting on artery wall which means it has the lowest restenosis rate.

3.2 Radial gain and diameter changes

Radial gain is the main parameter to evaluate the performance of the stent. Radial gain can be calculate by using Eq. (6) as shown:

$$Radial\ Gain = R_{expansion} - R_{original} \tag{6}$$

where $R_{expansion}$ is the radius in a given point after the expansion process ongoing and $R_{original}$ is the original radius length. Radial Gain determine the radius expanded during the balloon-stent expansion process. Radial gain are measure in the centre part and tail part of the stent as shown in Fig. 8.

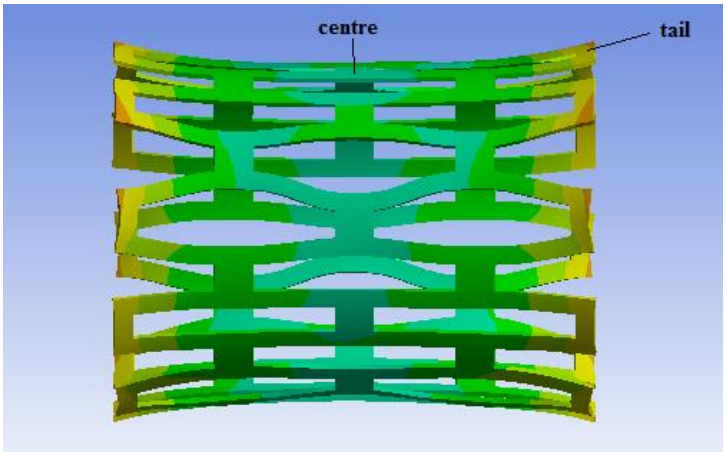


Figure 8. Stent 1 with overall radial gain

Radial Gain of the centre and tail part of the stent are used to calculate the centre and tail diameter of the stent by adding the Radial Gain with the original radius length. Diameter of the tail part of Stent 1, Stent 2 and Stent 3 are 4mm, 3.98mm and 4mm. All three stent model has similar tail diameter at the end of the balloon-stent expansion process to compare the results. Fig. 9 below shows the centre and tail diameter plot of the stent over 1.635s of expansion period.

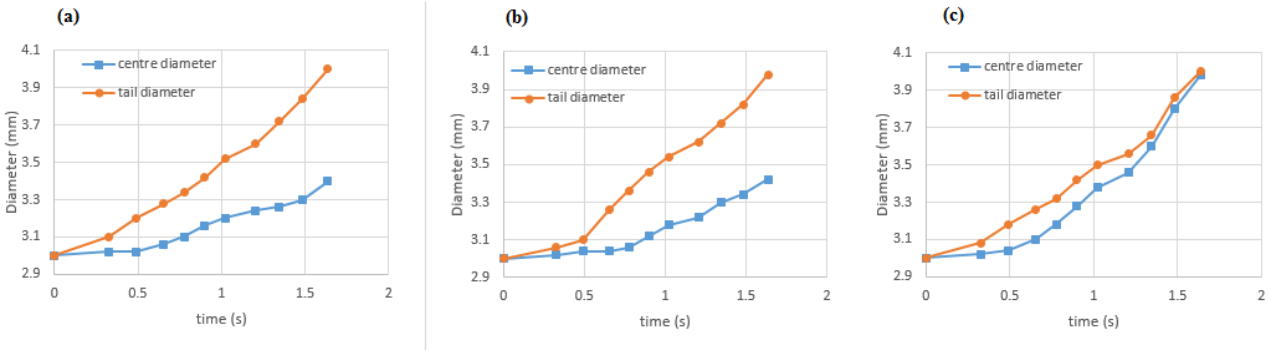


Figure 9. Centre and tail diameter data of (a) Stent 1; (b) Stent 2; (c) Stent 3

Centre and tail radial change of Stent 1 and Stent 2 start to differ when the balloon-stent expansion process begin while Stent 3 remain consistent over the whole balloon-stent expansion process. This phenomena is causes by different stent geometry properties lead to different stent expansion pattern.

3.3 Dogboning

The different between the centre and tail expansion rate are known as dogboning. Dogboning occurs during the balloon-stent expansion process are due to different geometry properties of different stent. Dogboning of the stent is defined as

$$Dogboning = \frac{Tail\ Diameter - Centre\ Diameter}{Centre\ Diameter} \quad (7)$$

Fig. 10 plots the relation of dogboning against time. As shown in Fig. 10, maximum dogboning for Stent 1, Stent 2 and Stent 3 are 0.176, 0.163 and 0.052. Stent 1 and Stent 2 has similar dogboning rate across the time as both of it are increasing. Stent 3 has lower dogboning rate when compare to Stent 1 and Stent 2. Dogboning rate of Stent 3 started to decrease at the time of 0.6s. This mean that Stent 3 has more uniform balloon-stent expansion process and with this condition, it can reduce the injury chances of the artery wall and causes thrombosis. When the stent expanded with non-uniform pattern and have high dogboning rate, it will create a pressure point acting on the artery wall and causes mechanical injury. Mechanical injury will induce an inflammatory response which results in thrombosis and affects artery restenosis [13]. In this case, Stent 3 has a better performance when compare to Stent 1 and Stent 2.

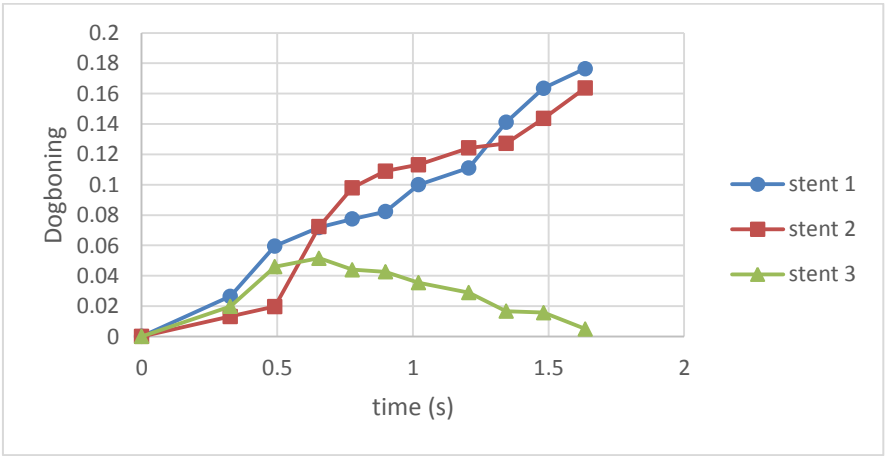


Figure 10. Relation of dogboning against time for Stent 1, Stent 2, Stent 3

4. Conclusion

Referring to this study, a commercial available Palmaz-Schatz coronary stent, Stent 1 is use as a reference for the optimized stent design which are Stent 2 and Stent 3. Stent 2 and Stent 3 has better performance in terms of stress distribution on stent, stress distribution on artery wall, restenosis rate and dogboning rate. Stent 2 maximum stress on stent is 10.86% lower than Stent 1 and Stent 3 maximum stress on stent is 14.91% lower than Stent 1. Also Stent 2 stress concentration on artery wall is 64.66% lower than Stent 1 and Stent 3 stress concentration on artery wall is 67.31% lower than Stent 1. Lower stent concentration lead to lower restenosis rate. Furthermore, maximum dogboning value of Stent 2 is 7.39% lower than Stent 1 and Stent 3 maximum dogboning value is 70.45% lower than Stent 1. Overall, Stent 3 has a better performance when compare to Stent 1 and Stent 2. Hence the design optimization for this study is successful.

Stent 3 can be used as a replacement for Stent 1 as it has better performance refer to this study.

References

[1] Cleveland Clinic ,"Angioplasty and Stent Interventional Procedures" ,*Cleveland clinic,* 12/11/2013. [Online]. Available: http://my.clevelandclinic.org/services/heart/services/hic_Cardiac_Catheterization_and_Coronary_Interventional_Procedures [Accessed: 5/4/2015].

[2] Schmitz, K.P., Behrend, D., Behrens, W., Schmidt, W. Comparative studies of different stent design. *Progress in Biomedical Research*, 1999, p. 52-58.

[3] Gu L., Zhao S., Muttyam A.K., Hammel J.M., 2010, The relation between the arterial stress and restenosis rate after coronary stenting, *Journal of Medical Devices*, **4**, 031005

[4] Chua S.N.D., MacDonald B.J., Hashmi M.S.J., 2002, Finite-element simulation of stent expansion, *Journal of Materials Processing Technology*, **120**, 335-340

[5] Chua S.N.D., MacDonald B.J., Hashmi M.S.J., 2003, Finite element simulation of stent and balloon interaction, *Journal of Materials Processing Technology*, **143/144**, 591-597

[6] Chua S.N.D., MacDonald B.J., Hashmi M.S.J., 2004a, Effects of varying slotted tube (stent) geometry on its expansion behaviour using finite element method, *Journal of Materials Processing Technology*, **155/156**, 1764-1771

[7] Lally C., Dolan F., Prendergast P.J., 2005, Cardiovascular stent design and vessel stresses: a finite element analysis, *Journal of Biomechanics*, **38**, 1574-1581

[8] Walke W., Paszenda Z., Filipiak J., 2005, Experimental and numerical biomechanical analysis of vascular stent, *Journal of Materials Processing Technology*, **164/165**, 1263-1268

[9] Wu W., Wang W.Q., Yang D.Z., Qi M., 2007, Stent expansion in curved vessel and their interactions: A finite element analysis, *Journal of Biomechanics*, **40**, 2580-2585

[10] Hongxia Li, Tianshuang Qiu, Bao Zhu, Jinying Wu and Xicheng Wang, "The Scientific World Journal", *Design Optimization of Coronary Stent Based on Finite Element Models*, vol. 2013, no. 630234, pp. 1-10, September 2013.

[11] F. Etave, G. Finet, M. Boivin, J.C. Boyer, G. Rioufol and G. Thollet, "Journal of Biomechanics", *Mechanical Properties of Coronary Stents Determined by Using Finite Element Analysis*, vol. 34, no. 2001, pp. 1065-1075, February 2001.

[12] De Beule M., Van Impe R., Verhegghe B., Segers P., Verdonck P., 2006, Finite element analysis and stent design: Reduction of dogboning, *Technology and Health Care*, **14**, 233-241

[13] W.-Q. Wang, D.-K. Liang, D.-Z. Yang, and M. Qi, "Analysis of the transient expansion behavior and design optimization of coronary stents by finite element method," *Journal of Biomechanics*, vol. 39, no. 1, pp. 21–32, 2006

[14] Kastrati A., Mehilli J., Dirschinger J., Pache J., Ulm K., Schuhlen H., et al., 2001, Restenosis after coronary placement of various stent types, *American Journal of Cardiology*, **87**, 34-39

[15] Carew T.E., Vaishnav R.N., Patel D.J., 1968, Compressibility of the arterial wall, *Circulation Research*, **22**, 61-68

[16] Gervaso F, Capelli C, Petrini L, et al., 2008, On the effects of different strategies in modelling balloon-expandable stenting by means of finite element method. J Biomech 41:1206-12

[17] Misagh Imani, Ali M. Goudarzi, Davood D. Ganji, Amir L. Aghili, et al., 2013, The comprehensive finite element model for stenting the influence of stent design on the outcome after coronary stent placement, *Journal of Theoretical and Applied Mechanics*, **51**, 3, pp. 639-648

[18] Miketic S., Carlsson J., Tebbe U., 2001, Randomized comparison of J&J Crown stent versus NIR stent after routine coronary angioplasty, *American Heart Journal*, **142**, E8

Numerical and Experimental Assessment of Velocity with/without model inside Taylor's Wind Tunnel Test Section

Low Heng Yang[1*], Abdulkareem Shafiq[2]

[1,2]*Department of Mechanical Engineering, School of Engineering, Taylor's University*

[*] hengyang.low02@sd.taylors.ed

Abstract
A wind tunnel is a tool designed to determine the flow characteristics of air around a solid object that replicate the actual flow condition with designated similarities. It is important to study and analyse the flow conditions, such as velocity in the test section which is supposed to simulate the real flow conditions exactly. This research aims to assess the air flow velocity and velocity distribution in the test section of the subsonic suction-type wind tunnel available in Taylor's University by determining the error percentage. There are difference between the flow pattern in the test section and the ideal case simulated using numerical analysis model, in this case, computational fluid dynamics. The differences are compared to assess the accuracy and precision by determining the percentage error from the ideal flow conditions. For experimental analysis, the flow velocity of different data points in the Taylor's Wind tunnel were measured using the hot wire anemometer and the DAQ system which are tabulated and visualised in plotted graphs. As for numerical analysis, ANSYS FLUENT is used to model the flow in the test section using the SST k-ω turbulent model. The post processing unit of the software helped in the interpretation of the data collected in the simulation. The same was done with an aluminium NACA 0012 airfoil model inside Taylor's Wind tunnel test section. Results shows that the maximum error percentage is -6.96% and -3.16% when frequency is adjusted 15Hz and 25Hz to for case without model. For the case with model, the velocity varies at a maximum up to 2.94% and -3.16% when the frequency is 15Hz and 25 Hz respectively. There is also a notable negative trend of velocity approaches the bottom wall may be due to the air flow into the test section and elevated roughness of test section wall.

Keywords: Low-Speed Wind Tunnel, Test Section, Flow Velocity, Computational Fluid Dynamic (CFD)

1. Introduction

A wind tunnel is a tool designed to measure the flow characteristics of air around the solid object that replicate the actual flow condition with designated similarities. Low-speed wind tunnels are wind tunnels that are capable with the operational flow speed of 134 m/s or Mach = 0.4 [1].

One of the first wind tunnels was invented around the 19th century [2]. In 1901, the Wright brothers used it to study the flow behavior around the different shapes to make their Wright Flyer [3]. Wind tunnels are designed based on different applications. There is one field that uses wind tunnels is the testing for atmospheric boundary conditions [4]. Ghani *et al.* analysed the performance of different critical components of a closed-loop full-scale climatic wind tunnel for road vehicle natural environment using CFD [5]. In aeronautics, wind tunnel nozzles are designed using CFD [6]. CFD was also used to interpret wind tunnel measurement result [7,8].

Despite large improvement in computational power and capabilities so far, Wind tunnel has not been replaced by CFD but CFD had reached a point whereby the experimental and numerical results complement each other. Moonen *et al.* came up with a method of numerical model that simulates the steady-state conditions in a closed-loop wind tunnel using standard and realisable k-ε equation [9]. Their work provided a new benchmark to the accuracy of the wind tunnel model simulation. Gordon and Imbabi utilized CFD to model the flow inside critical sections of closed-loop wind tunnel [10]. The results obtained in this research demonstrated that proper classification of required improvement could improve the cost effectiveness and reduce the size of wind tunnels. Moonen *et al.* achieve six indices of similar characteristics to evaluate the flow quality in the test section in 3D in the CFD simulation [11].

In year 2010, another research is done by Guzella *et al.* to numerically and experimentally assess the airflow inside a wooden-made low-speed wind tunnel [12]. This test section has a length of 0.79 m and side and width of 0.2 m. Reynolds-Averaged Navier–Stokes (RANS) equations were solved numerically utilising ANSYS-CFX simulation software and the model used is the SST k-ω turbulence model. The velocities of the tunnel outlet were measured using a hotwire anemometer and a Pitot tube were compared with the numerical values of axial velocity. However, this research only focuses on the airflow exiting the tunnel test section which is not as accurate as the flow measure within the test section.

The wind tunnel that is used in this project is the subsonic open-type wind tunnel which has a suction fan to draw air. It has a better flow quality as compared to the blow-down wind tunnel. Figure 1 depicts the Taylor's Wind Tunnel.

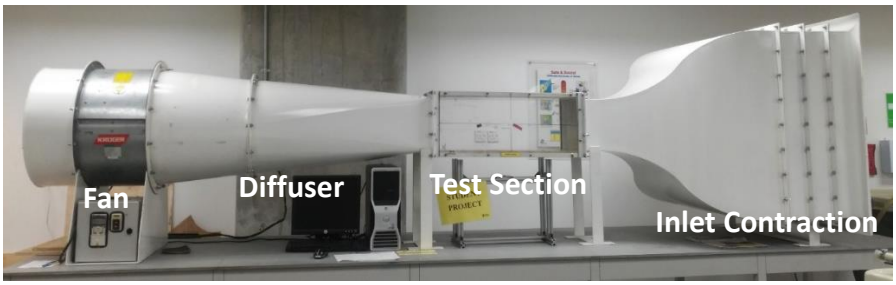


Figure 1. Taylor's Wind Tunnel

From Table 1shows the percentage error of the wind tunnel experiment results from Lim in Taylor's Wind tunnel is up to 49% as when compared to the results published by Abbott and Von Doenhoff [13,14].

Table 1. Percentage error in lift and drag coefficients obtained from wind tunnel tests at different Reynolds number [13,14].

Alpha	Percentage Error (%)					
	Re = 200000		Re = 100000		Re = 50000	
	CL	CD	CL	CD	CL	CD
-10	16.600	3.791	6.800	18.56	28.942	8.732
-5	11.735	27.518	16.970	48.79	26.033	30.795
0	7.393	3.901	10.000	28.59	2.715	6.514
5	15.320	19.789	1.160	37.66	5.617	27.398
10	25.173	17.478	14.840	10.00	9.800	13.015

To show a more comprehensive visualisation of sub-sonic wind tunnels, Table 2 is presented to compare the specifications of the existing facilities at different places around the world.

Table 2: Specification of existing subsonic wind tunnels [13,15,16,17]

University	UNNE (Wittwer and Möller 2000)	IPT WT (Nader et al. 2006)	University of Leeds (Calautit et al. 2014)	Taylor's University (Lim 2014)
Location	Chaco, Argentina	SaoPaulo, Brazil	Leeds, United Kingdom	Selangor, Malaysia
Circuit type	Opened-loop	Opened-loop	Closed-loop	Opened-loop
Application	Structural Engineering	Calibration	Civil Engineering	Calibration
Test section (m)	2.4 × 1.8	0.5 × 0.5	0.5 × 0.5	0.303 × 0.303
Air Velocity (m/s)	-	2.5 - 20	42036	3.3 - 38.4

Achieving accurate measurement of aerodynamic characteristics in the wind tunnel is challenging. It is subject to many factors, for instant the flow conditions in the test section. One important condition is to ensure that the flow velocity inside the test section is similar to the velocity of the prototype in real situation. The current research addresses the challenge by numerical and experimental study and analysis of the flow velocity and the velocity distributions with or without a model inside the test section of Taylor's wind tunnel. It aims to achieve uniformity of mean air velocity so that it can contribute directly to the accuracy of the tests in future.

2. Methodology

The research design of this project involves numerical and experimental approach. This research will compare the experimental data with the numerical result of the flow velocity in with and without a model inside the test section. The numerical approach will take advantage of the ANSYS FLUENT software available to generate the geometry, discretize the domain and solve the cases in ideal manner. On the other hand, for the experimental approach, the flow velocity is measured from 25 data point distributes across the test section by using a hotwire anemometer. The experimental data will then be compared with the numerical results to identify the error percentage in terms of velocity and velocity distribution.

2.1 Numerical Method

In this paper the numerical approach used is Computational Fluid Dynamics (CFD) which is useful in preforming engineering problem solving especially in flow studies. CFD provides the researcher the understanding of engineering designs and give a rough overview on the efficiency of the newly developed systems. ANSYS FLUENT is used in this research [18].

Here, only uses two governing equations which are used the conservation of momentum and conservation of mass[1]:

$$\frac{\partial \rho}{\partial t} + \vec{\nabla} \cdot (\rho U) = 0 \quad (1)$$

$$\frac{\partial (\rho U)}{\partial t} + \vec{\nabla} \cdot (\rho U \times U) = -\overrightarrow{\nabla p'} + \vec{\nabla} \cdot (\mu_{eff}(\vec{\nabla} U + (\vec{\nabla}\, U)^T) + B \quad (2)$$

where U is mean velocity vector, ρ is fluid density, μ_{eff} represents effective viscosity contributing to turbulence, p' stands for modified pressure. The equation for μ_{eff} and p' are also given in as (3) and (4) respectively.

$$\mu_{eff} = \mu + \mu_t \quad (3)$$

$$p' = p + \frac{2}{3}\rho k \quad (4)$$

Equation for $\mu_t$can be describe as

$$\mu_t = C_\mu \rho \frac{k^2}{\varepsilon} \quad (5)$$

where μ is molecular viscosity, k represents turbulent kinetic energy, ε is the turbulent dissipation rate and C_μ stands for the model constant. The model constant is preset by ANSYS FLUENT beforehand.

Since wind tunnel is an enclosed channel, it is considered as an internal flow. The common model used to solve internal flows is the standard k- ε turbulence model. However, this model does not produced accurate results when it comes to capturing

the boundary layer effect thus it is not suitable for this simulation. Realizable *k*- *ε* turbulence model an improved version of the k- *ε* turbulence model. On the other hand, despite its better accuracy in solving the boundary layer effect, it uses the enhance wall treatment as default which will not allow the input of wall roughness later in the research.

There is another model that is suitable for aerodynamic which is the realizable *k*- *ω* turbulent model. It has the best accuracy when it comes to capturing the boundary layer but the SST *k*- *ω* turbulence model is final choice as it combines the benefit of both the *k*- *ω* turbulence and the *k*- *ε* turbulence model. This two-equations model are very versatile and robust.

This numerical research is done using a 3-dimentional model instead of a 2-dimentional one. The basic test section model has dimension based on the position at which the velocity is measurable using the hotwire anemometer in the experiment. The air flow in the test section is assumed to be fully developed. While FUELNT does provide an option in replacing the uniform inlet velocity with a velocity profile, the process of doing so is tedious and does not justify the amount of time and unnecessary effort spent in this research.

Therefore, extra length can be added so that the fully developed flow can be modelled. Figure 3.4 shows the side view of the expected geometry of the test section. The section drawn in blue is the added section for numerical simulation while the section drawn in black is the follows the actual dimension of the controlled test section. The origin where x = 0.00 m is set 0.75 m away from the numerical inlet while the actual inlet and the actual outlet is 0.35 m away from the origin.

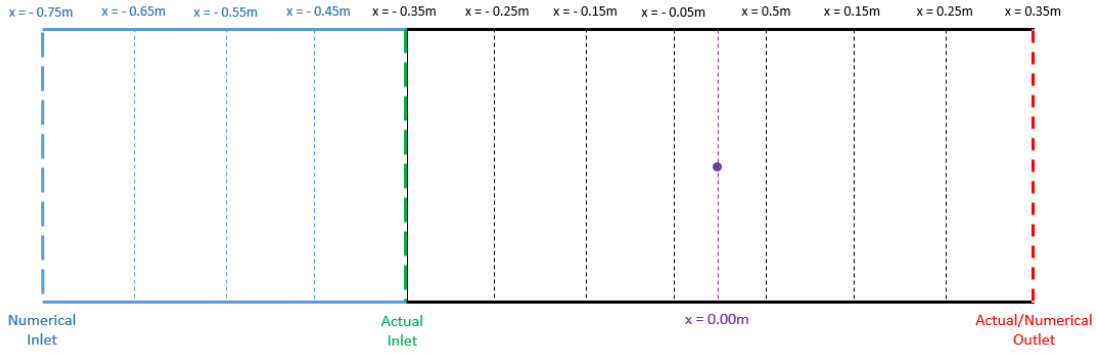


Figure 2. Layout of geometric model of test section for numerical simulation.

To reduce the processing time, only half of the geometry is modelled. The middle plane is set as symmetry and the working domain is set to be fluid. The final empty test section that is modelled in FLUENT as shown in Figure 3 and Figure 4. The final test section with model is also modelled in FLUENT as shown in Figure 5 and Figure 6 show the mesh.

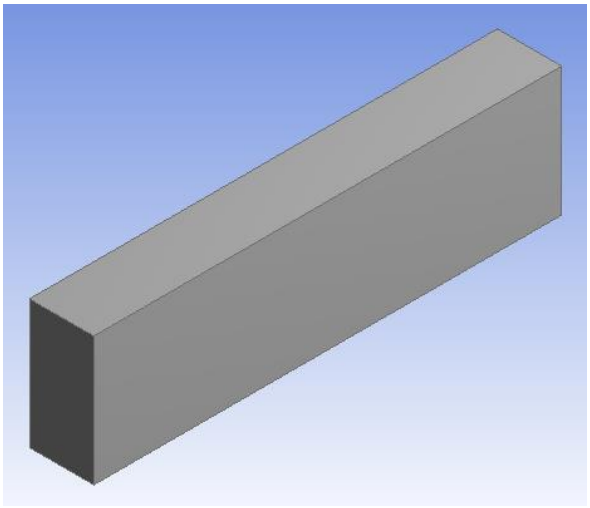
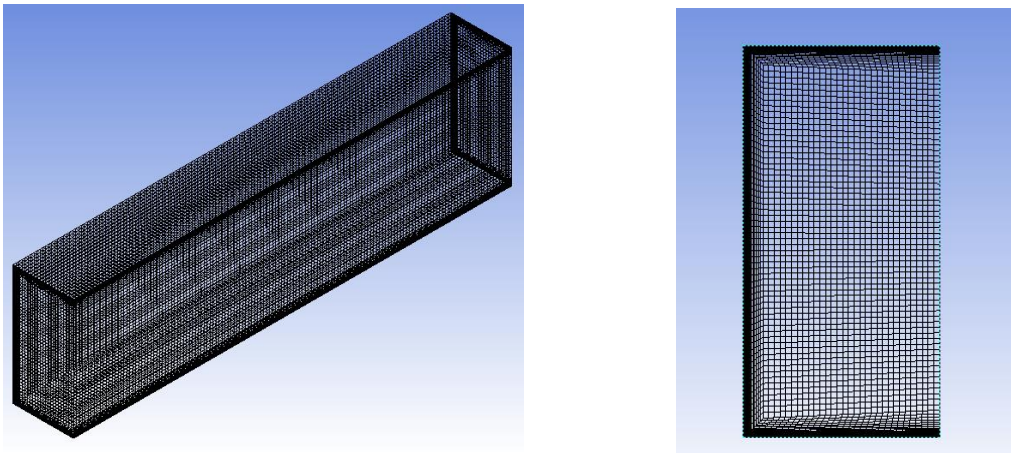


Figure 3. Geometric model of test section without model.



(a) Isometric view (b)Front View

Figure 4. Mesh results for test section without model.

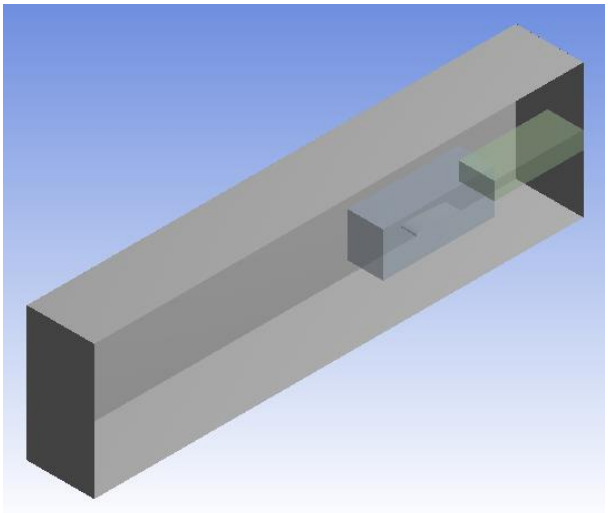
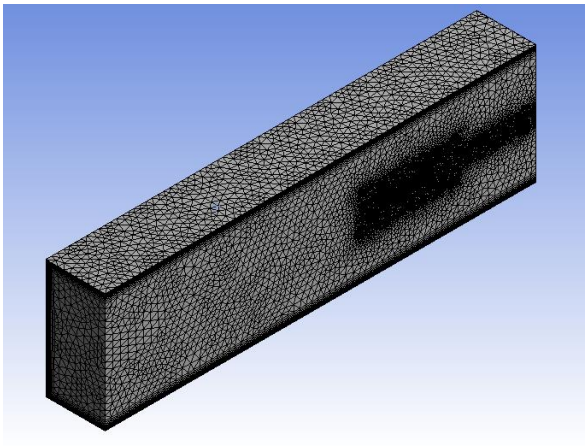
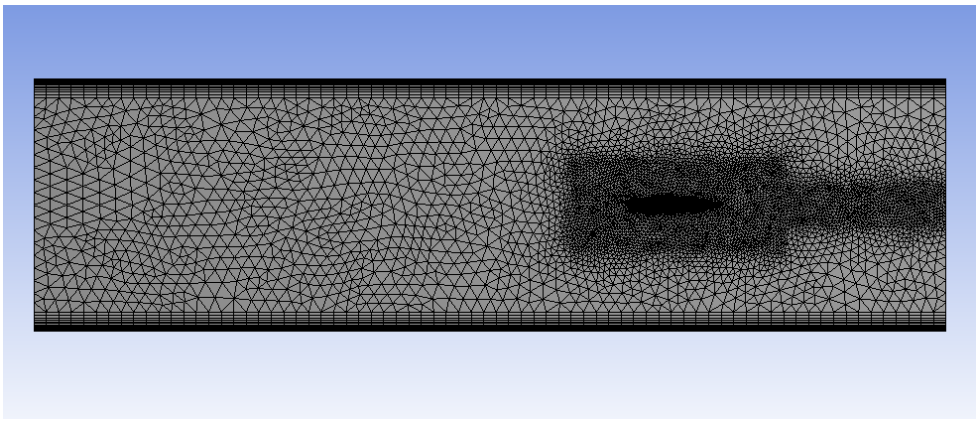


Figure 5. Geometric model of test section with model.



(a) Isometric view



(a) Side View

Figure 6. Mesh results for test section with model.

Different mesh types are used in this numerical simulation to acclimatize to specific conditions. Abbreviations are given to these different mesh cases for the ease of reference as shown in Table 3. Different mesh cases are given different input in term of element size and inflation. Mesh dependency is done and the results are futher explained in results and discussion.

Table 3. Abbreviations for different mesh type.

Abbreviations	Conditions	Cell Shape
EM	Empty, Multi-zone	Hexahedral
WMAB	With model, Automatic, Body of Influence	Tetrahedral

Boundary conditions that will be set include the inlet and outlet of the test section other than the wall of test section. To acquire the inlet velocity, the initial input is obtained from the calibration graph shown in Figure 7. From this graph, it can be seen that the calibration done recently has a slight difference compared to the data collected back in 2009 [19]. To achieve the more accurate input for the numerical simulation, the gradient, m of the straight lines are calculated in average and the offset, c is ignored. With the averaged gradient, the velocity for 15 Hz and 25 Hz are found to be 9.801 m/s and 16.335 m/s respectively.

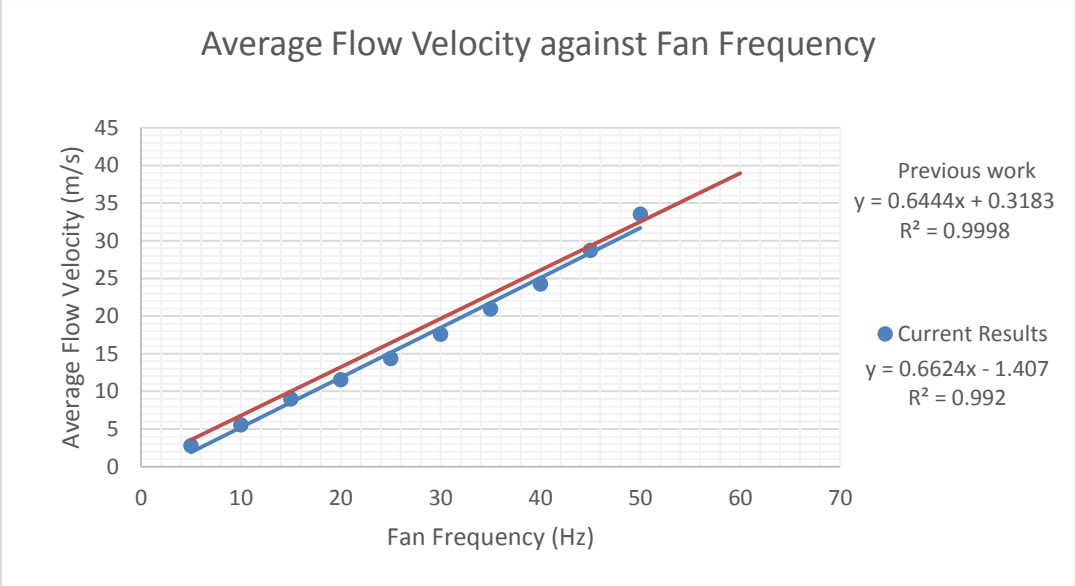


Figure 7. Calibration Graph of Test Section [19]

However, all the velocities from this graph are obtained from the exact center of the test section with the coordinates of (0, 0, 0). These values are not accurate when it is used as the velocity of the inlet because this is the not the inlet velocity. To determine the inlet velocity for the simulation, estimation and trial an error is done until the velocity at the center of the test section is 9.801m/s and 16.335 m/s for 15 Hz and 25 Hz respectively. The results are shown in Table 4.

Table 4. Numerical velocity test across empty test section

Fan Frequency (Hz)	Numerical Inlet Velocity (m/s)	Velocity At centre of test section (m/s)
15 Hz	9.801	9.922
	9.714	9.833
	9.682	9.801
25 Hz	16.335	16.468
	16.270	16.405
	16.201	16.335

From this table, the numerical inlet velocity is determined to be 9.862 m/s and 16.201 m/s for 15 Hz and 25 Hz respectively.

As mention by ANSYS [20], when Mach numbers is equal to 1.0 or less, the effect of the compressibility may be neglected other that the deviation of the gas density against pressure is negligible. Therefore, the density is set at a constant of 1.225 kg/m^3.

For the walls, it is impractical not to consider non-slip condition as it will affect the flow velocity at a relatively significant manner. Therefore, the assumption of non-slip condition is made. This shows that the friction along the wall is the highest resulting in the airflow velocity at the wall has zero value [21]. In the simulation, this means that the first layer of the mesh that have one of its sides connected to the solid wall will have zero velocity.

Since the wall of test section were made up of Plexi-glass, it is defined to have a roughness of 0.0000015 m roughness height. Moreover, for the case with CNC-machined aluminum model of NACA0012 airfoil inside, the wall of the model is set to have a roughness height of 0.00000984 m [22]. The walls of all test section and the surface of the airfoil model is assume to have an even surface with 0.5 roughness constant.

As for the outlet, the relative static pressure is assumed to be 0 Pa and the turbulent intensity is 5% which is originally set by FLUENT when initiated. Isothermal condition is assumed in this flow conditions. The simulation type is 3D pressure based for the solution method. The simulation is also considered to be a steady state flow which is independent of time. The pressure-velocity coupling scheme will be tested to identify the solver that requires the less time to achieve convergence in the results.

Table 5. Time taken for different solvers to solve WMAB 3

Case	Solver	Time Taken (min: sec)
WMAB 3	SIMPLE	10:23
	SIMPLEC	14:30
	Coupled	10:43

From Table 5, it can be seen that the SIMPLE scheme requires the least time for the solution to converge which is only 10 minutes and 23 seconds. Hence, it is chosen to compute the all the simulations results because of it provides faster and easier convergence. The skewness correction is set to be 0. The spatial discretisation include the gradient of Least Square Cell Based. The Pressure, Momentum, Second Order while the Turbulent Kinetic Energy and Turbulent Dissipation rate is set to be First Order.

2.2 Experimental Method

The experimental equipment used is the Taylor's Wind Tunnel which has a contraction ratio of 3:4:1. The achievable air velocity by this low speed wind tunnel is from 3.33 m/s up to 38.35 m/s. The velocity can be controlled by adjusting the fan frequency with a recommended range of 10 Hz to 50 Hz. It is operated using a 3 HP, 415 V/50 Hz motor and 0.63 m of fan diameter. The square cross section of the test section is measured 0.303 m at the sides and it has a total length of 0.885 m. However, in this research, the inlet and outlet of the test section are considered to be located 0.35 m away from the center datum of the test section in the longitudinal direction. This is because there are holes drilled on the plexi-glass and the farthest holes are there. These holes are drilled so that the data for velocity can be collected when the hotwire anemometer is inserted into them.

For data collection, a hotwire anemometer with HVACR Datalogger which measures real time data will be used to obtain the flow velocity Holes had been made through the bottom of the test section wall for the hotwire to position through. The flow distribution had been measure by collecting set of data of flow velocity in

different data points located at position distributed across the test section. The test section is separated by 5 sections which result in 5 plane including the inlet and outlet of the test section as shown in Figure 8. As the minimum data points established by ISO 3966:1977 to characterized the flow profile is 25, 25 data points is set on each planes from x = -0.35 to x = +0.35 as shown in Figure 9.

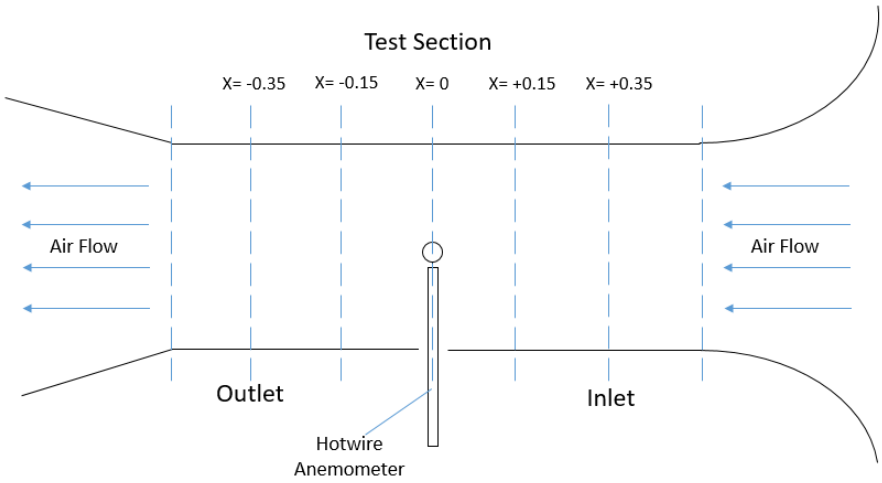


Figure 8. Experimental setup

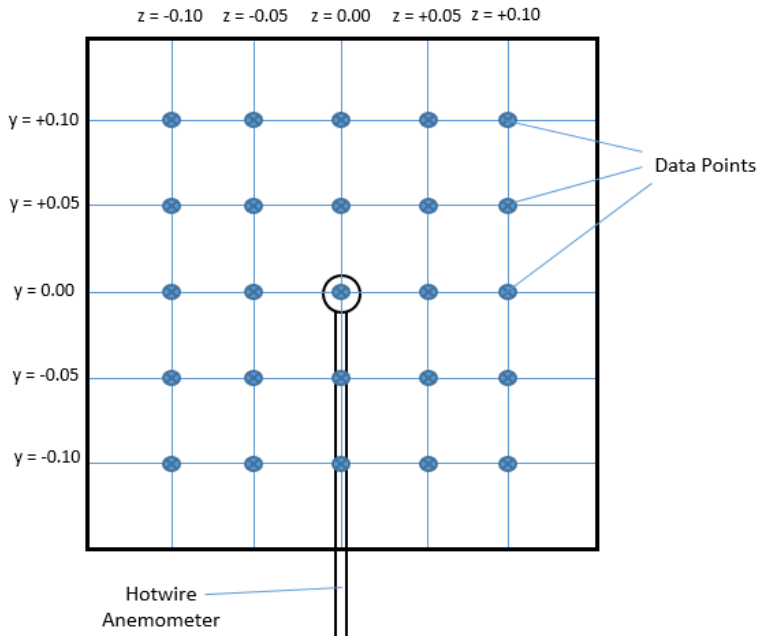


Figure 9. Data points acquired from the cross section of the wind tunnel

The data of velocity profile is collected initially without a model in the test section and later with a NACA0012 placed in at the coordinate (0, 0). The NACA0012 model is machined from a single block of aluminum which has a span of 0.068 m and a chord length of 0.10m.

For the empty test section, velocity readings are collected from a total of 125 data points. Then, for the test section with NACA0012 model, the total number of data points that is needed to have velocity reading collected is 122 points. This is because the point located at the origin of the test section is occupied by the model

while the 2 other points are occupied by the structure supporting the model. For each data points, 3 readings of velocity are taken over a period of 10 seconds to reduce the random error.

3. Results and Discussion

The experimental data are collected accordingly and the final data is presented in the form of mean velocity at different vertical position as shown in Table 6 which are later compared with the numerical results.

Table 6. Experimental mean velocity across test section

y/H	Mean Velocity (m/s)			
	Empty Test Section		Test Section With Model	
	15Hz	25Hz	15Hz	25Hz
+0.33	9.83	16.40	10.01	16.22
+0.17	9.89	16.34	10.04	16.25
0.00	9.98	16.51	9.96	16.14
-0.17	9.59	16.04	9.88	16.24
-0.33	9.31	15.20	9.58	15.84

Mesh analysis is done and the suitable mesh identified are MWAB 3 and EM 3 as these two mesh shows mesh independence. The final numerical results are taken from the mesh EM 3 and WMAB 3. These results are then used as a benchmark of the ideal flow in the test section when there are no external forces subjected to it. The results obtained from the experiment are compared to these data and the difference between the results are analysed.

Figure 10 and Figure 11 illustrate the comparison of the experimental data of velocity obtained using the hotwire anemometer with the numerical results of the average velocity profile. Overall, it shows that there is a well agreement between the numerical result and the experimental data for both 15 Hz and 25 Hz of fan frequency. However, there are still some slight variations. For the case without model, the experimental data shows an increasing trend when y approaches the top wall. Flow velocity also decreases as y approaches the bottom wall.

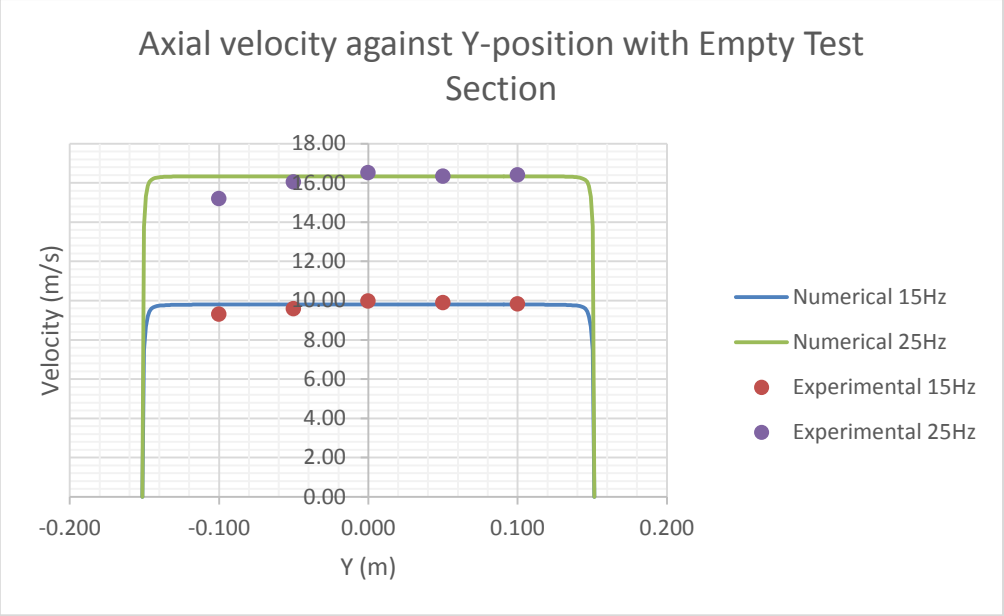


Figure 10. Comparison of Experimental and Numerical Results for Empty Test Section

Figure 11 shows that there is a fluctuation of velocity near y = 0.00. This fluctuation is caused by the existence of model inside the test section. This can be explained with the aid of Figure 12 and Figure 13.

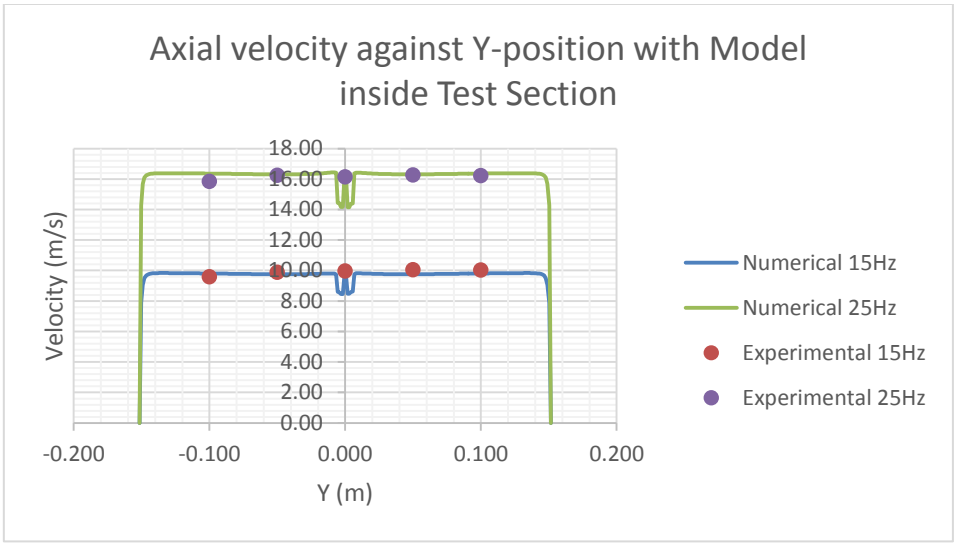


Figure 11. Comparison of Experimental and Numerical Results for Test Section with Model

Figure 12 depicts the velocity contour along the test section with NACA0012 at 15 Hz. The yellow vertical lines are where the data points are collected. It can be seen that two out of seven yellow lines intersects the air foil model and there is a very thin has boundary layer along the top and bottom surface of the airfoil. This boundary layer which is shown in Figure 13 is the blue layer around the airfoil is where the air is slowed down by the viscous force with the no-slip condition. The same can be said for the case of 25 Hz (16.335m/s)

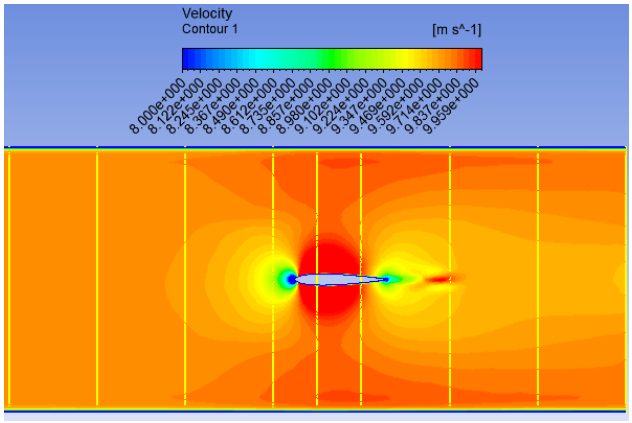


Figure 12. Velocity contour in the symmetry plane of test section with model at 15 Hz (9.801 m/s)

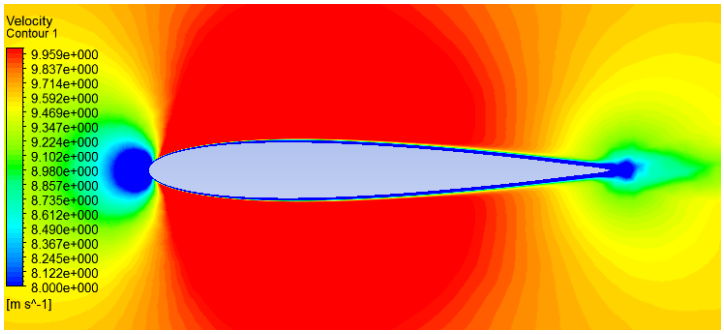


Figure 13. Boundary layer around NACA0012 model at 15 Hz (9.801 m/s)

Table 7. Percentage error of the velocity across the vertical position of test section

y/H	Percentage Error (%)			
	Empty Test Section		Test Section With Model	
	15 Hz (9.801 m/s)	25 Hz (16.335 m/s)	15 Hz (9.801 m/s)	25 Hz (16.335 m/s)
+0.33	0.30	0.43	2.10	-0.86
+0.17	0.97	0.01	2.89	-0.32
0.00	1.81	1.11	2.94	-0.32
-0.17	-2.14	-1.82	1.30	-0.43
-0.33	-4.99	-6.96	-2.30	-3.16

In general, the correlation is considered to be fairly good. From Table 7, the experimental data only varies from the numerical results by a maximum of 6.96% and 3.16% at *y*/H = -0.33 for case without model when frequency is adjusted to 15 Hz and 25 Hz. For the case with model, the velocity varies at a maximum 2.94% at *y*/H = 0.00 and -3.16% at *y*/H = -0.33 when the frequency is 15 Hz and 25 Hz respectively.

As seen from the table and the graph, regardless of the existence of a model inside the test section, there is a negative trend of velocity towards the bottom of the test section wind based on the experimental data. This means as the position of the tunnel approaches the bottom wall of the wind tunnel; the measurement of velocity will be lower also.

The negative trend of the results when vertical position approaches the bottom wall of the wind tunnel may be caused by few possible reasons. One of the reasons that might cause this error is the inflow of air through the hole where the hotwire anemometer is placed through. This phenomenon occurs because of the pressure difference whereby the air pressure in the test section is lower than the air pressure outside it due to its high higher velocity of air. The holes allowed the surrounding air to enter the test section to compensate this difference thus reducing the velocity.

Despite the effort to seal the drilled holes on the bottom wall with cellophane tape to reduce the inflow flow of air, it is very likely that it is not air tight enough. Other than that, the surface of the bottom test section wall also has elevated roughness as the repeated used of cellophane tapes to cover the drilled holes left residues on it.

Another phenomena that may cause the errors in this research is the rapid fluctuation of the velocity reading from the datalogger that obtains the data from the hotwire anemometer. This fluctuation is cause by the turbulence in the flow. Therefore, it is better to collect the experimental data with more number of readings to in the future when the time constrain is less. Another source of error may be due to the insufficient data points for reading to be collected to achieve a mean results whereby random errors are negligible

7. Conclusions and Future work

In a nut shell, this research shows a comprehensive and clear comparison between the numerical and experimental correlations of velocity profile in the test section of Taylor's opened-loop suction type low-speed wind tunnel. Detail measurements done using hotwire anemometer and HVAC Datalogger were used to examine the flow velocity profile along center plane of the test section. SST k-ω turbulence model was used to compute the numerical results and were compared with the experimental data. Mesh independence was ensured for accurate results. The amount of variation of experimental data from the numerical result is computed to illustrate the accuracy of the wind tunnel when it is put into practical operation. In general, the correlation is considered to be fairly good. Experimental data only varies from the numerical results by a maximum error of 6.96% and 3.16% for case without model when frequency is adjusted to 15Hz and 25Hz. For the case with model, the velocity varies at a maximum up to 2.94% and -3.16% when the frequency is 15Hz and 25 Hz respectively. The negative trend is evident when the vertical position approaches the bottom wall. It is very likely to be cause by the inflow of air flow to the test section and elevated roughness.

Further study should be done on the boundary layer by measure velocity near the wall of test section in the experimental part since the results for the numerical simulation already includes the boundary layer. The effect of the orientation of model towards the velocity profile may also by an interesting subject to be studied as well as the effect of different size of the model. This will help to identify the best orientation and size needed to achieve the most accurate results.

The supporting structure for the model may also be taken into consideration in the numerical simulation in the future to achieve more accurate results. This is

because the supporting structure will also alter the flow velocity within the wind tunnel.

Acknowledgment

The author of this present paper would like to thank his constitution Taylor's University which provided him an opportunity to utilise Taylor's wind tunnel and the ANSYS FLUENT 15.0 available to complete this research.

References

[1] Barlow, J.B., William, H.R., Pope, A. (1999). *Low-speed wind tunnel testing (3rd Edition.)*. John Wiley & Sons

[2] Nguyen, Q.Y. (2014). Designing, constructing, and testing a low-speed open-jet wind tunnel, *Ijera*, *4*, *1(*2), 243-246.

[3] Technology, T. M. I. of. 2002. *Wind Tunnel Wright Brothers*.

[4] Maurer, T., Herrmann, L., Gaiser, T., Mounkaila, M., Stahr, K. (2006). A mobile wind tunnel for wind erosion field measurements, *Journal of Arid Environments*, 66, 257–271.

[5] Ghani, S.A.A.A., Aroussi, A., Rice, E. (2001). Simulation of road vehicle natural environment in a climatic wind tunnel, *Simulation Practical Theory*, *8*, 359–375.

[6] Korte, J.J. (1992), Aerodynamic design of axisymmetrical hypersonic wind-tunnel nozzles using a least-squares parabolized navier-stokes procedure, *Journal of Spacecraft Rockets*, *29*(5), 685–691.

[7] Moreau, S., Henner, M., Roger, M. (2003). Analysis of flow conditions in freejet experiments for studying airfoil self-noise, *AIAA Journal*, *41(10)*, 1895–1905.

[8] Cockrell, C.E. (1994). Interpretation of waverider performance data using computational fluid dynamics, *Journal of Aircraft*,*31*(5), 1095–1100.

[9] Moonen, P., Blocken, B., Roels, S., Carmeliet, J. (2006). Numerical modeling of the flow conditions in a closed-circuit low-speed wind tunnel, *Journal of Wind Engineering and Industrial Aerodynamics*, *94*, 699–723.

[10] Gordon, R., Imbabi, M. (1998). CFD simulation and experimental validation of a new closed circuit wind/water tunnel design, *Journal of Fluids Engineering*, *120(*2), pp. 311–318.

[11] Moonen, P., Blocken, B. & Carmeliat, J. (2007). Indicators for the evaluation of wind tunnel test section flow quality and application to a numerical closed-circuit wind tunnel", *Journal of Wind Engineering and Industrial Aerodynamics*, *95*, 1289–1314.

[12] Guzella, M.S., Manto, D., Soares, C.B., Maia, C.B., Hanriot, S.M., Cabezas-Gómez L. (2010), Airflow CFD Modeling in the Test Section of a Low-Speed Wind Tunnel, *Journal of Advanced Research in Mechanical Engineering, 1(4*), 210-225.

[13] Lim, WK 2013, *Taylor's Wind Tunnel Manual*, Taylor's University Subang Jaya, Malaysia.

[14] Abbott, I.H., Von Doenhoff, A.E. (1999). *Theory of Wing Sections: Including Summary of Airfoil data*. Mineola: Dover Publications.

[15] Wittwer, AR & Moller, SV 2000, "Characteristics of the low-speed wind tunnel of the UNNE", *Journal of Wind Engineering and Industrial Aerodynamics*, Vol. 84, pp.307-320.

[16] Nader, G., DosSantos, C., Jabardo, P.,Cardoso, M., Taira ,N., Pereira, M. (2006). *Characterization of low turbulence wind tunnel*, Metrology Sustainability Development, Rio de Janeiro, Brazil, 17–22.

[17] Calautit, J.K., Hughes, B.R., Chaudhry, H., Sim, L.F (2014). A Validated Design Methodology for a Closed loop Subsonic Wind Tunnel. *Journal of Wind Engineering and Industrial Aerodynamics, 125,* 180-194

[18] Versteeg, H.K., Malalasekera, W. (1995). *An Introduction to Computational Fluid Dynamics. The Finite Volume Method*, Longman Group Ltd.

[19] Al-Obaidi, A., Lee, C. S., Tan, K., Lee, H. I., Singh, K., Foo, T. (2009), Velocity – Frequency Calibration Curve, Taylor's College, Subang Jaya, Selangor.

[20] ANSYS (2013), *ANSYS Fluent User's Guide*, Southpointe, Pennsylvania: ANSYS Inc.

[21] Young, D.F., Munson, B.T., Okiishi, T.H., Huebsch, W.W. (2012), *Introduction to Fluid Mechanics*. John Wiley & Sons, Inc.

[22] Dilworth, R.L. (1967), Aerospace metals, general data and usage factors, *Technical Manual Engineering for Aircraft repair*, United States Army.

Analysis of Footform Effects on Traction Characteristics of Shoe Sole-Playing Surface Interface

Marcus Lim Bo Shen*, Mohd Hardie Hidayat Mohyi

School of Engineering, Taylor's University, Malaysia

*marcuslimboshen@gmail.com

Abstract

This Study was conducted to study the system of footwear traction testing devices. The lack of standardised foorforms led to the focus on the study of footform designs and its effects on traction characteristics. Traction characteristics of shoe sole-playing surface interface governs the performance of athletes and injury risks. Many studies have been done, but we are yet to fully understand the characteristics of traction for athletic performance. Traction characteristics of shoe sole-playing surface interface is a major challenge to be solved as it does not fully obey the classical laws of friction which is also known as coulomb friction. Although, the laws of coulomb friction are required to understand traction, traction of shoe sole-playing surface are highly dependent on the shoe pattern and the surface of the playing surface. A series of studies were done with 3 types of footform that were modelled in SolidWorks and simulated in Ansys Static Structural Analysis. Conventional footforms that are used usually have a totally flat and linear surface as long as the shoe sole is able to be tightly fitted without moving, hence a cuboid was used. The first design and second was modelled according to the foot sole of a human. However the second design experience meshing problems and is yet to be analysed. Normal stress on the surface of the shoe sole in the direction of the Y component was analysed and compared between the two models that were analysed with Static Structural Analysis. The footform that was designed based on shape of a human foot sole causes the shoe sole to experience greater normal stress. Results also show that the normal stress is more evenly distributed with the footform designed according to the shape of a human foot sole.

Keywords: Traction, Footwear Traction Device Friction, Shoe Sole, Footform, Static Structural Analysis, Normal Stress.

1. Introduction

Traction is the maximum frictional force that can be reached before an object starts to slip off a surface. It is a much vital component of footwear design in sports as it is the major factor that affects an athlete's performance. Many studies have about shoe traction and surface interface but it is yet to be understood as a whole. A study was done by Thorsten Sterzinga, Clemens Mullera, Ewald M. Hennigb and Thomas L. Milania to confirm actual and perceived factors that are affecting running performance in soccer shoes, and the results obtained shows that stud geometry and surface conditions influence the performance of the athletes significantly proving that traction is the main factor over shoe weight and comfort [1]. The amount of traction between the outsole of the shoe and playing surface has great implications on injuries as shown in a study by John W. Wannop, Geng Luo, and Darren J. Stefanyshyn to study the connection between athletes' footwear traction and lower extremity non-contact injury in high school football. Findings show of how rotational and translational traction affects the rate of injury. Results from this study shows that low rotational traction footwear has lower rates of injuries than that of mid and high rotational traction. However, increase in translational traction proves otherwise [2]. Although, traction devices do not carry out dynamic movements such as of an athlete, it provides a constant set of data that we can study to analyze the traction characteristics of shoe outsole and playing surface interface. The QDPI&F (Queensland Department of Primary Industries and Fisheries) automated turf tester was developed by Dr Don Loch a QDPI&F agronomist and engineer Les Zeller in the year 2002, which has been used to study of thatch on traction and injury occurrence to athletes participating on natural turf sporting surfaces. Results from this study indicate that the main contribution to traction is the stolon or rhizome and general root growth on and just within the playing surface [3]. The ASTM International has published a technical standard method for testing traction characteristics of athletic shoes, which encompasses simple and straight forward procedures for translational and rotational traction testing in which traction devices can be constructed according to these procedures. The load conditions based on field studies of athletes performing specific movements are provided for translational and rotational test [4]. However, there is no specific standard of footform that is required to be used during testing procedures. The challenge of this project is to analyze the effects of foot forms that are used by traction devices. This study can potentially Studying the effects of traction characteristics with loadings from different configurations of footform will provide future researchers with a clearer view of how results obtained from their studies are affected by the configurations of footform that they use.

2. Theoretical Approach

2.1 The classical laws of friction and Traction

2.1.1 Coulomb Dry Friction

The classical laws of friction is defined by the Coulomb Dry Friction, which stated that "a force of resistance acting on a body which prevents or retards slipping of the body relative to a second body or surface with which it is in contact. This force always acts tangent to the surface at points of contact with other bodies and is directed so as to oppose the possible or existing motion of the body relative to these points" [5]. Friction exist in the form of static and kinetic friction in which static friction is the force applied to an object which does not create movement, while kinetic friction is when the object starts to move . Friction is often expressed in the form of coefficient of friction which is the frictional force between the contact surface and object divided by the normal force exerted on or by the object on the surface it is in contact with.

The coefficient of static friction can be expressed as,

$$\mu_s = F_s/N$$

Where,

μ_s is the coefficient of Static Friction,
F_s is the static friction,
And N is the normal force.

The coefficient of Kinetic Friction,

$$\mu_k = F_k/N$$

Where,

μ_k is the coefficient of Kinetic Friction,
F_k is the kinetic friction,
And N is the normal force.

The motion of friction consist of two main parts, which are translational and rotational. The project which mainly focus on translational friction can be expressed as,

$$F = \mu W$$

Where,

F is the Frictional Force,
μ is the Coefficient of friction,
and W is the Vertical Load applied.

2.1.2 Traction

In classical friction, kinetic friction is always greater than that of static friction. However, in a study done by Benjamin S. Cooper (2009), for the case of traction the static friction maybe greater than dynamic friction at times. The frictional force can always exceed the normal force and therefore giving coefficient of traction that is greater than 1. This main cause it the interference of playing surfaces and the patterns on the outsole of the shoe [6].

The Coulomb laws of dry friction relevant to an understanding of traction are:

(i) The friction force is dependent on the kinds of materials in contact and their roughness;
(ii) The static friction force developed at the point of sliding is dependent upon the normal force applied to the surfaces;
(iii) The friction force is independent of the apparent geometric area of contact; and
(iv) The friction force is inversely dependent on the velocity - decreasing as velocity increases [7].

2.2 Design of Footwear Traction Devices

2.2.1 ASTM International Standards

ASTM International, provide simple procedures for footwear traction testing. There are a few important areas in which the standard encompasses, which are:

(i) The test specifies methods for linear translation and rotational motion. However, translational and rotational motions are not tested simultaneously.
(ii) Test results obtained by this method shall be qualified by the characteristics of the specimen.
(iii) Comparative tests of surfaces shall be qualified by the characteristics of the shoes used to test the surfaces, including the cushioning, outsole material, and sole design.
(iv) Comparative tests of shoes shall be qualified by the pertinent characteristics of the surfaces on which shoes are tested, including the surface type, material, condition, and temperature [4].

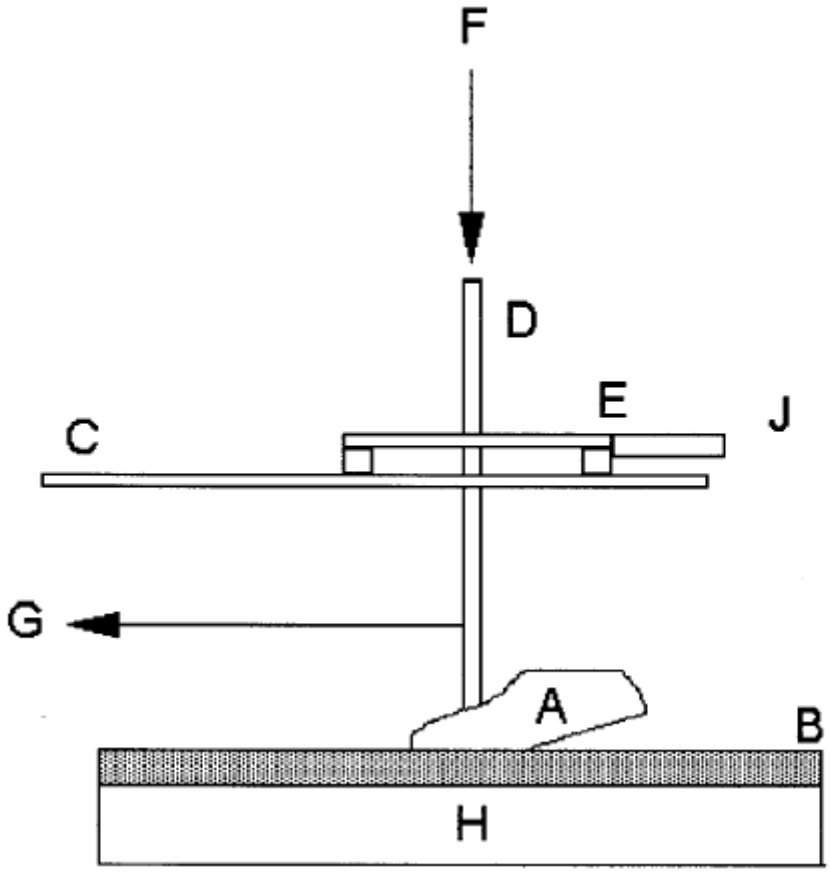


Figure 1: Schematic Diagram of a Generic Device for Measuring Linear Traction [4].

A. Shoe under test, mounted on a footform.
B. Surface under test.
C. Guide rails with linear bearings or other means of maintaining rectilinear motion.
D, E. Vertical shaft and bearing mounted carriage or other means of maintaining motion parallel to the plane of the shoe-surface interface.
F. Weights, actuator or other means of applying a downward vertical force.
G. Actuator or other means of applying a horizontal force.
H. Force plate or other means of measuring vertical and horizontal forces.
J. Velocity transducer [4].

3. Methodology

Three two foot forms were designed to analyze how it affects the normal load on the shoe sole and compared with commonly used footform. The normal stress that is acting on the shoe sole is analyzed. Two foot forms were designed to analyze how it affects the normal load on the shoe sole with SolidWorks and simulated with Ansys Static Structural Analysis. The second design is in the process of some changes and yet to be analyzed due to poor quality mesh that resulted in inaccurate results. Meshes for the second design result in obsolete mesh mainly due to the geometry of the design.

3.1 Design of foot form

Two foot forms were designed to analyze how it affects the normal load on the shoe sole with SolidWorks, both according to the shape of a human foot sole. Dimensions of the footfroms are the same with 32cm in length which is about the average footsize to an NBA basketball player [8]. Another design used as conventional traction testing footforms which is a solid cuboid is modeled in SolidWorks.

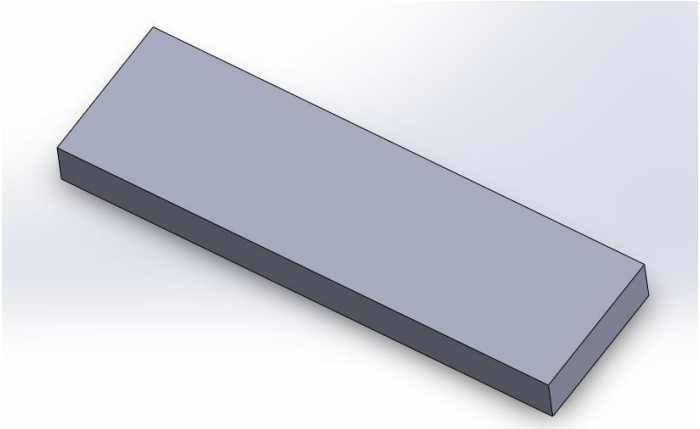


Figure 2: SolidWorks 3D model of Conventional footforms

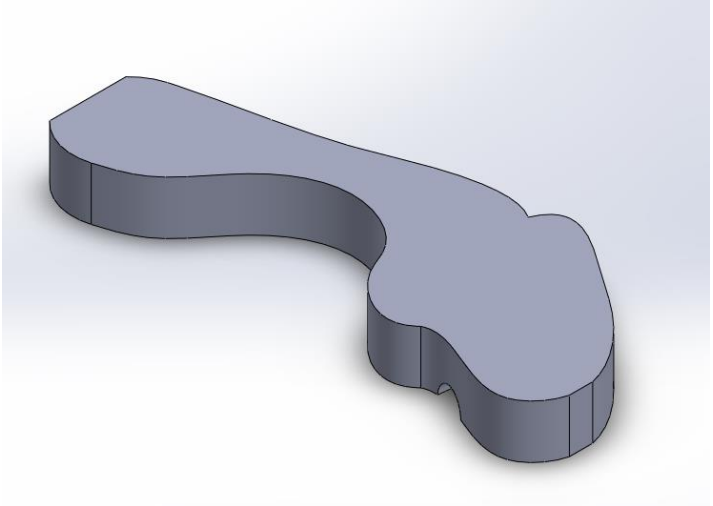


Figure 3: SolidWorks 3D model of First Design

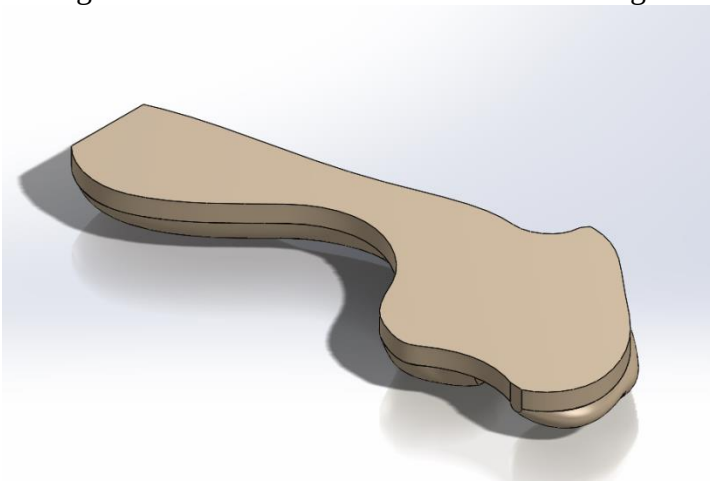


Figure 4: SolidWorks 3D model of Second design

3.2 Static Structural Analysis

3.2.1 Contacts

Contact faces between the shoe and the foot form were selected and defined to be bonded to prevent sliding as an athlete's foot and the sport shoe are assumed to be a single body. Augmented Lagrange contact formulation was used as it use integration point detection which results in more detection points compared to Normal Lagrange and multi-point constraint formulations which uses nodal detection. However, Augmented Lagrange was chosen over pure-penalty formulations for large deformation problems and to provide additional control to reduce penetration.

3.2.2 Meshing

Meshing plays an important role to obtain an accurate result. Higher mesh elements provide higher accuracy as denser meshes allow more detection points to occur. Contact formulations are also highly dependent on mesh density to obtain accurate results. However geometrical problems can result in limited mesh elements or obsolete meshes. Mainly geometry to multiple curved surfaces or deep patterns can cause meshing problems.

Mesh size of 0.01m for conventional and first design of footform was used and default mesh size was used for second design of foot form due to occurrence of obsolete mesh because of the geometry.

Table 1: Mesh properties

	Conventional	First Design
Mesh size	0.01m	0.01m
Elements	38689	43751

3.2.3 Analysis

The settings of analysis was set to 30 numbers of step time which ends in 30s. The magnitude of the force on the top face of the foot form was set to be in a tabular form where force was set to increase from 0N to 3000N in 30 step time in the negative Y axis direction. The floor was set to be a fixed support.

The normal stress of the shoe sole to the ground was obtained and analyzed.

4. Results and Discussion

The graph below shows the normal stresses at the bottom of the shoe sole.

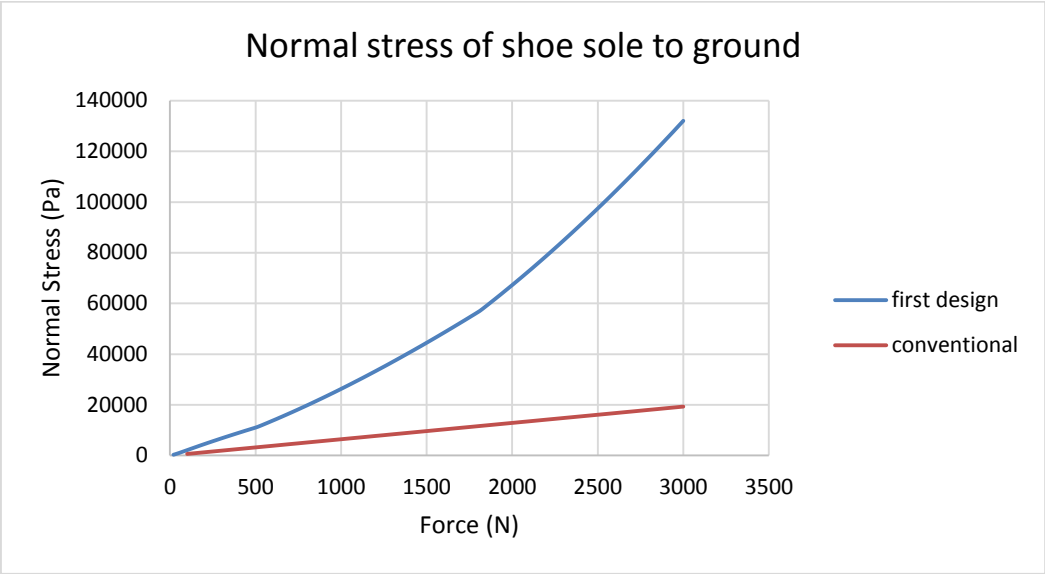


Figure 5: Graph of normal stress of shoe to ground.

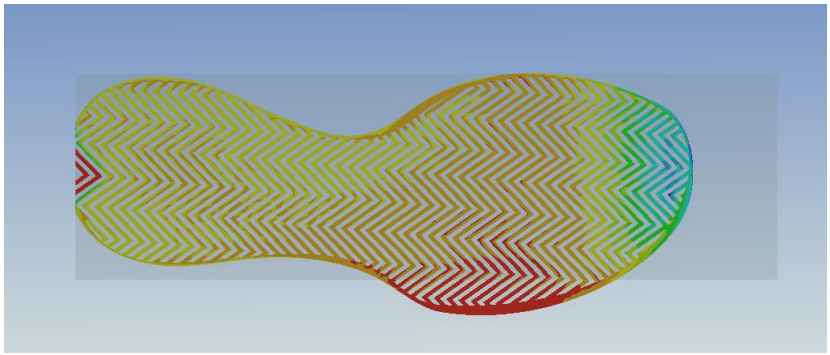


Figure 6: normal stress contours at the bottom of the shoe sole with compression from conventional footforms.

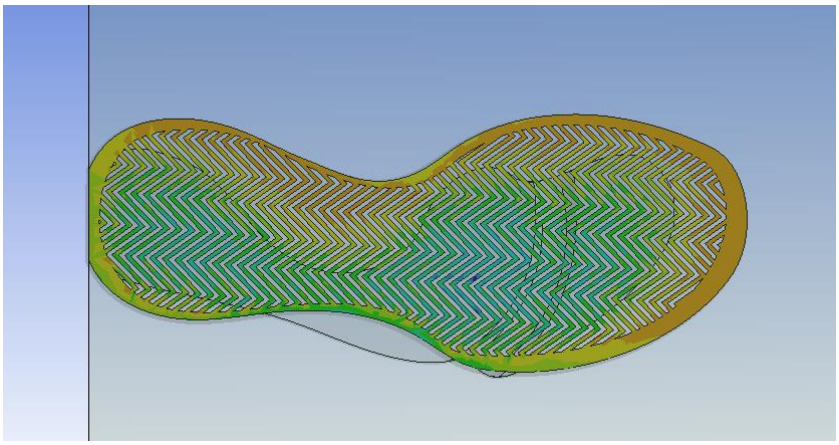


Figure 7: normal stress contours at the bottom of the shoe sole with compression from the first footform design

From figure 5, we can see that the normal stresses experienced by the shoe sole with the first design is much higher than conventional footforms. The trend of the normal stress with the first design is seen to be in an exponential behavior while the normal stress with the conventional footfrom have a more linear behavior. The increase in normal stressed on the shoe sole can potentially give rise in affecting the coefficient of friction. In most studies, the behavior of the coefficient of friction decreases as the normal force increases, which indicates that the frictional force becomes relatively small compared to the normal load applied [9], [10].

Figure 6 and 7 shows the contours of the normal stresses that are acting on the shoe sole. Figure 7 with the first design can be seen to have more evenly distributed contour colors as compared to figure 6 with the conventional footform.

5. Conclusion

This study is still on going and is yet to confirm the effects of footform on footwear traction. Although, simulation results show difference in normal stresses that will contribute to the normal loads in which will affect the traction characteristics. Further analysis has to be done on the shear stresses on the shoe sole by friction to understand effects of footfrom designs that will affect traction study.

Reference

[1] T. Sterzing, C. Müller, E. M. Hennig, and T. L. Milani, “Actual and perceived running performance in soccer shoes: A series of eight studies,” *Footwear Sci.*, vol. 1, no. 1, pp. 5–17, 2009.

[2] J. W. Wannop, G. Luo, and D. J. Stefanyshyn, “Footwear Traction and Lower Extremity Noncontact Injury,” *Med. Sci. Sport. Exerc.*, vol. 45, no. 11, pp. 2137–2143, 2013.

[3] L. C. Zeller, “Leslie Charles Zeller,” no. December, 2008.

[4] Astm, “Standard Test Method for Traction Characteristics of the Athletic Shoe – Sports Surface Interface,” vol. 04, no. Reapproved 2011, pp. 1–9, 2013.

[5] P. M. Insel and W. T. Roth, “Twelfth Edition,” pp. 0–7, 2012.

[6] B. S. Cooper, “Traction Characteristics of Cleated Athletic Shoes At Various,” 2009.

[7] G. W. Housner and D. E. Hudson, “Applied Mechanics Dynamics,” 1980.

[8] "SLAM Footwear Database Breakdown | SLAMonline." [Online]. Available: http://www.slamonline.com/nba/slam-nba-footwear-database-breakdown-sneakers-nba-players/#FJyIlFuOUAjezCMM.97. [Accessed: 18-Oct-2015].

[9] S. Kuhlman, M. Sabick, R. Pfeiffer, B. Cooper, and J. Forhan, "Effect of loading condition on the traction coefficient between shoes and artificial turf surfaces," *Proc. Inst. Mech. Eng. Part P J. Sport. Eng. Technol.*, vol. 224, no. 2, pp. 155–165, 2009.

[10] J. Clarke, M. Carré, A. Richardson, Z. Yang, L. Damm, and S. Dixon, "Understanding the traction of tennis surfaces," *Procedia Eng.*, vol. 13, pp. 402–408, 2011.

Mechanical Properties of Polycaprolactone Blended Biomaterials.

Muhammad Fuad Abry[1*], Yong Leng Chuan[1]

[1]Taylor's University Lakeside Campus, Malaysia

[*]muhammad_abry @hotmail.com

Abstract
Ongoing research on tissue engineering has grown in the past few years, with great challenges emerging as many different scaffolds are being designed; tissue engineering could play a great impact in the success of health research. One of the great challenges in designing these scaffolds is their ability to withstand the forces exerted during nerve regeneration, where the mechanical properties are important properties which should be considered when designing these scaffolds. Different materials possess different properties which could be used in designing neural scaffolds, The existence of two essential polymers; polycaprolactone (PCL) and polylactic acid (PLA) have a high possibility of becoming a solution towards the challenges in designing neural scaffolds, hence their mechanical properties are an important focus with the need of engineers to be a part of this ongoing research. These two essential polymers blend well; the main focus on these blends is their mechanical properties and their impact towards designing scaffolds with better mechanical properties. The individual properties of each of these polymers has allowed them to form a good blend, where PCL is known to be ductile and PLA is a brittle material with a good elasticity allowing it to be flexible, which is one of the important features of a neural scaffold. This study focuses on the mechanical properties of blending PCL with PLA using different ratios, these prepared blends were tested for their strains and were compared. Three different concentrations of PCL were used for electrospinning; 5%, 10% and 15%, and a scanning electron microscope (SEM) was used for these different concentrations.

Keywords: Scaffold, Mechanical properties, Electrospinning, Scanning electron microscope (SEM).

1. Introduction

Many people suffer from damaged tissues due to different causes such as; accidents, wars, and other devastating causes, hence the need for tissue engineering has merged highly in the past decade, to allow these people to have a good normal life. Tissue engineering can help ensure society meet their achievements without being affected by their injuries, there are many challenges in tissue engineering hence to ensure these challenges are overcome, an ongoing research is taking place. This ongoing research has allowed doctors and engineers to work together to overcome these challenges, the main reason on why engineers have been notified in taking part in this research is; when designing neural scaffolds. The material used play an important role, understanding these roles can allow engineers to come up with solutions to overcome the great challenges such as the flexibility of these neural scaffolds, tissues consists of nerves. Nerve regeneration is a phenomenon that occurs to repair the dead nerves, therefore during injuries nerve regeneration needs to occur and these neural scaffolds should not kink during bending in order to allow nerve regeneration. The main concern with designing scaffolds in tissue engineering is to satisfy many different characteristics which include;

- **Biocompatibility;** this characteristic of scaffolds involves the behavior of cells, and the process of nerve generation where the scaffolds do not have any negative impacts on the tissue during nerve regeneration. The biocompatibility includes three main features which are; mechanical compatibility, blood compatibility and histocompatibility. The mechanical compatibility focuses on the scaffold's mechanical properties, the blood compatibility ensures that the scaffolds designed have no effect on the blood and the histocompatibility is the focus of no toxic effects on the tissues.
- **Biodegradability;** this is an important feature which scaffolds should have, normally scaffolds are used in nerve regeneration, and hence after these nerves have been repaired the scaffold should decompose by themselves after nerve regeneration is over this means that the materials used in designing scaffolds should be biodegradable.
- **Permeability;** this feature is concerned with the scaffold being capable of allowing gas and nutrients exchange since these are needed as a source of energy for nerve regeneration, there are various techniques used in designing scaffolds to ensure permeability is achieved.
- **Biomechanical properties;** these properties are essential for ensuring that the scaffolds do not fracture or break since during nerve regeneration, since there are forces exerted on these scaffolds which can cause them to fracture or break, another important aspect is the flexibility of the scaffolds during nerve regeneration [1].

These features are important when selecting the material used to design scaffolds, the materials used to design these scaffolds must possess certain mechanical properties to ensure the enhancement of these scaffolds, thus allowing a forgotten polymer "polycaprolactone" to find its way back. Polycaprolactone is known to be a good ductile polymer which can contribute to designing strong scaffolds in tissue engineering, the main challenge with Polycaprolactone (PCL) is its low flexibility which is an important mechanical property when designing tissue scaffolds. Moreover to ensure flexibility is taken into consideration when designing scaffolds PCL is blended with other polymers, this allows the blend to possess more mechanical properties essential for designing scaffolds. PCL is an aliphatic polymer which was almost forgotten, hence its mechanical properties and biodegradability has allowed it to become an important polymer in the ongoing research on tissue engineering [2].

It is known that PCL is the product of a chemical reaction of its petroleum based polymer which undergoes esterification to produce PCL with a chemical formula of $(C_6H_{10}O_2)_n$. The advantages of PCL can allow a good blend to be produced out of it, which can ensure the enhancement of tissue engineering thus blending it with another polymer known as polylactic acid (PLA) can produce a blend with better mechanical properties. PLA is a polymer commonly found in the substrate of cassava, sugar cane and maize, both PLA and PCL are biodegradable materials, where PCL degrades slowly and PLA

degrades fast, blending these two materials can produce a blend with a high strength, high modulus, and better fracture toughness and better impact resistance [3]. PLA possess good mechanical properties with an elastic modulus of between 600-800 Mpa and a tensile strength between 22-50 Mpa, however it is known to have a poor brittle behavior, and this can cause it to fracture easily when high forces are exerted to it [4].

PLA is also a biodegradable polymer which has two structures; poly (L-lactide) acid (PLLA) and poly (D-lactide), blending is a method used to mix two polymers and achieve the advantages of each to a certain extent depending on the ratio. PCL is a strong material with a high ductility whereas it has a low modulus of elasticity with also a poor flexibility hence blending of these materials can produce a blend which possess both of these mechanical properties required in designing scaffolds. An important aspect in blending these polymers is achieving the best mechanical strength, which means it is important to analyze which ratio of PCL/PLA can produce the best mechanical strength this can be done by using different ratios of PCL and PLA. Figure 1 below shows the decrease of strain at failure when the mass fraction of PLA increases in the PCL/PLA blends. This graph can help in demonstrating the relationship between PCL and PLA; it clearly shows that an increase in PLA tends to decrease the ductility of the blend thus decreasing the strain at failure [5].

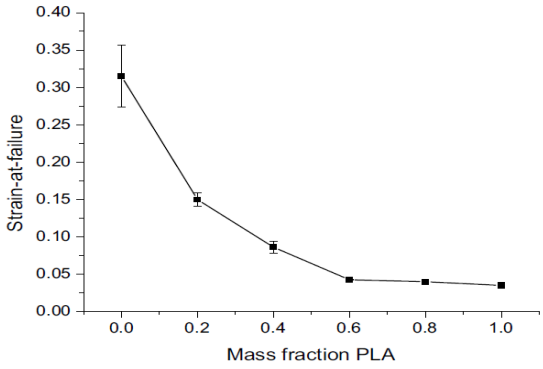


Figure 1. The decrease in strain at failure when the mass fraction of PLA increases in the PCL/PLA blends.

Figure 2 below shows the increase of the yield stress when the mass fraction of PLA increases in the PCL/PLA blend. This behavior is highly noticeable for ranges 0.4-1.0 where the mass fraction of PLA increase this could have been caused due to the good interaction of the PLA thus contributing to the yield stress of the blend [5].

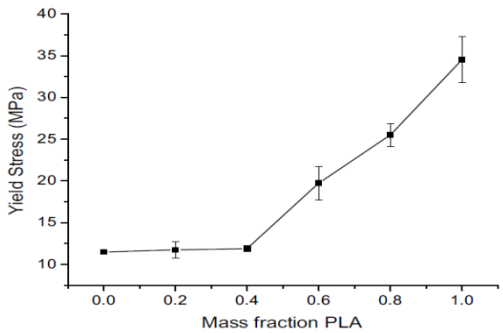


Figure 2.The increase in yield stress when the mass fraction of PLA increases in the PCL/PLA blends.

PCL/PLA is a biodegradable polymer blend, which has been created to; improve the fracture mechanism of PLA which is brittle as well as improving the flexibility of PCL since it is known to have a poor flexibility, both of these polymers; PCL and PLA have been approved by the food and drug administration (FDA) as safe polymers which can be used in medicine devices and designing scaffolds

[6]. Many ongoing researches are taking place to ensure a success in producing the best PCL/PLA blend, the main focus is the ability to produce a blend with the best mechanical strength which can be used in designing scaffolds for tissues allowing nerve regeneration, another main reason why these polymers have managed to receive great attention in the past decade is because they come from renewable energy sources hence making them more sustainable in comparison to non-renewable energies. The study of these polymers allows one to understand how blending can have improve the mechanical properties, which can help in the enhancement of tissue engineering as these polymers offer a good respond towards the current challenges of tissue engineering where for the past years many researchers have concentrated with blending PCL with other polymers as not much attention has been given to blending PCL with PLA a few good research papers have shown that there is a potential of a good blend when using PCL with PLA, the mechanical properties of each polymer needs to be addressed before deciding which ratios to be used for testing and analysis as there will be at least three different blends furthermore this blend can allow patients to benefit from tissue engineering which can help them recover faster as well as allow them to perform their daily chores normally.

To understand the phenomena and behaviour of Polycaprolactone and its blends we must understand the behaviour of materials in relevance to the stress-strain curves which represent the most essential mechanical properties of a material, which is based on the applied load and the deformation of the material at a fixed rate the graph of a stress-strain curve can be used to identify the deformation of a material as it is known that materials tend to have three types of deformations which are;

1) Elastic deformation; this is the area under the stress-strain curve where deformation occurs but the material can return to its original shape after the load is removed this occurs just below the yield point.

2) Plastic deformation; in this phase higher than the yield point the material will deform and cannot retain its original shape after the load is removed plastic deformation lies between the yield point and the ultimate tensile point.

3) Unstable deformation; this is when the load applied is higher than the ultimate tensile point causing necking and the material is most likely to undergo fracture[7].

The strain rate plays a big role in analysing the mechanical properties of a material, thus there is a certain relationship between strain rate and mechanical strength of a material, this relationship is essential in understanding the behaviour of materials. The increase in strain rate causes an increase in the tensile strength of these polymers hence based on the study of materials it is possible to state that polymers tend to inhibit a certain relationship between the strain rate and the tensile strength, this relationship further emphasizes that strain rate can be a key to enhancing the mechanical strength of a material [8]. This study aims to synthesize PCL-PLA blends using different ratios and investigate their mechanical properties.

2. Research Methodology

2.1 Specimen Design

2.1.1 Solid Works Design

The design of the specimen was done using a computer aided design known as solid works, a 3D design of the specimen was produced with the dimensions in accordance with the ASTM D638-03. The ASTM D638-03 is the preferred standard in the design of specimen for mechanical testing, the dimensions of the specimen are shown in figure 3 where the thickness is 2mm since ASTM D638-03 specification is used for polymers using different thickness the preferred thickness adopted from previous research for testing the mechanical strength is suggested to be 2mm which follows the ASTM D638-03 [17].

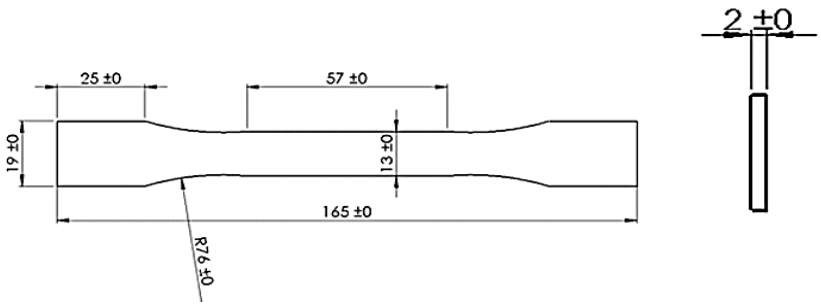


Figure 3. Specimen dimensions in mm

2.1.2 Volume of Specimen

The volume was required to ensure that the calculations were as accurate as possible hence the importance of identifying the volume is to ensure that the mass of the blends can be calculated using the formula; Mass = Density × Volume, the volume obtained from solid works which is 5018.17mm^3.

2.1.3 Solid Works Modification

After the research was progressing it was noticed that there was a need of redesigning the specimen to ensure it matches with the specifications of the equipment that was used which a creep test equipment; therefore the specimen was redesigned to ensure the dimensions match the equipment where the modification matched the ASTM D638-03 standard for polymers and plastics. The dimensions of the new design are shown in figure below. The volume of the new design was determined which is 1705.83 mm^3 (1.70583ml), figure 4 below shows the new modified specimen.

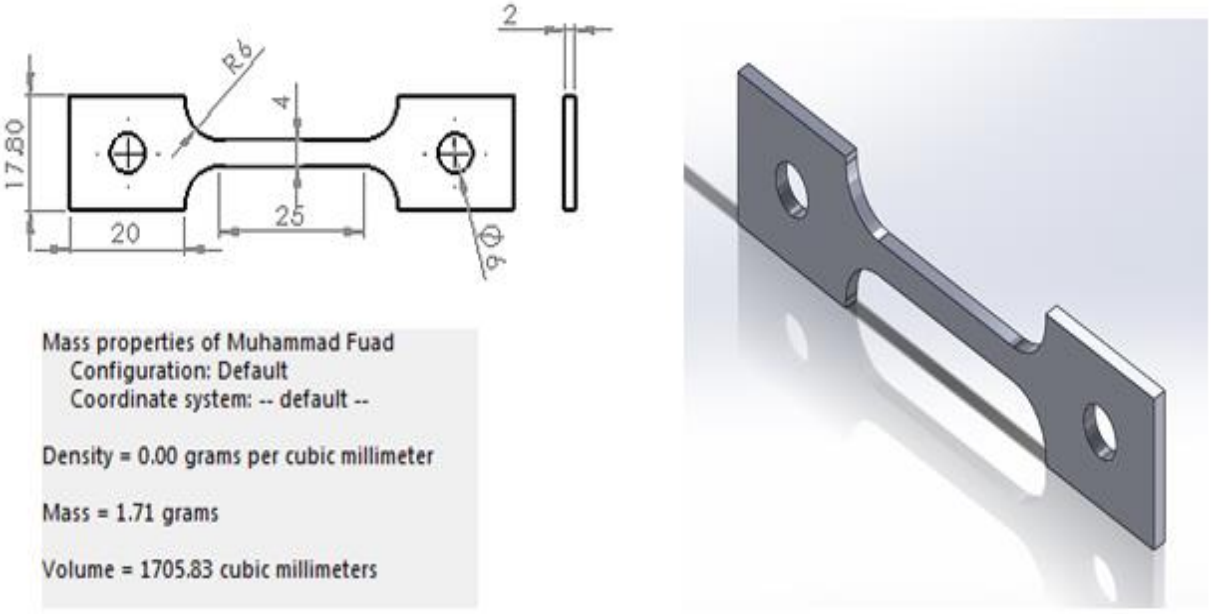


Figure 4. Modified specimen with dimension in mm

2.2 PCL and PLA

2.2.1 Blend Selection

Initially 5 blends were selected, these selected blends were based on previous research results however it was necessary to observe the compatibility and mixing of these blends, the blends that were first selected and mixed together were 100% PCL, 80:20 PCL-PLA 50:50 PCL-PLA, 20:80 PCL-PLA

and 100% PLA. The selection of the blends is an important phase of this research since the results of the mechanical properties hugely depend on the selected blends where a discussion on these results contributes a lot to the research of the mechanical properties of Polycaprolactone blended materials. The PCL used had an average Mn 80,000 with the PCode 1001607304 440744-250G and the PLA was supplied by the department of Applied chemistry and Biochemical engineering in Shizouka University, Japan. Figure 5 below shows the first selected blends, from left to right 100% PLA, 100% PCL, 80:20 PCL-PLA, 20:80 PCL-PLA and 50:50 PCL-PLA.



Figure 5 first prepared blends

2.2.2 Blend Calculations

For every blend it is important to calculate the mass of each material i.e. PCL and PLA this is done by using the density of each material and multiplying the volume of the specimen for instant based on the second volume of the specimen which was found to be 1705.83mm^3 (1.70583ml) for a 80:20 PCL-PLA ratio the PCL would be taken as 0.8 multiplied by its density and multiplied by the volume ($m = \rho \times v$) whereas for the PLA 0.2 would be used instead of 0.8, the density of PCL is 1.145g/ml and PLA is 1.25g/ml Table 1 shows the blend calculations.

Table 1. Blend masses.

blend	Mass of PCL (g)	Mass of PLA (g)
100% PCL	1.95	-
100% PCL-PLA	2.13	-
80:20, PCL-PLA	1.56	0.43
50:50, PCL-PLA	0.98	1.07
20:80 PCL-PLA,	0.39	1.71

2.3 Blend preparation

2.3.1 Heating PLA using a Water Bath

The PLA was first heated using a water bath in order to remove it from its container, PLA is known to be a tricky polymer as it possess different physical properties at different temperatures. The first procedure used to remove the PLA from its container was by using a water bath, the apparatus was set up safely and ensured to be working properly. Since the PLA container was not stable a Pyrex beaker was used because of its high resistance to high temperatures where the PLA container was placed inside the Pyrex beaker filled with some water allowing the PLA container to float the Pyrex beaker was then placed in the water bath and the temperature of the water was recorded. The maximum temperature achieved by using the water bath was 82°C. Figure 6 represents the graph to show the increase in the temperature against time.

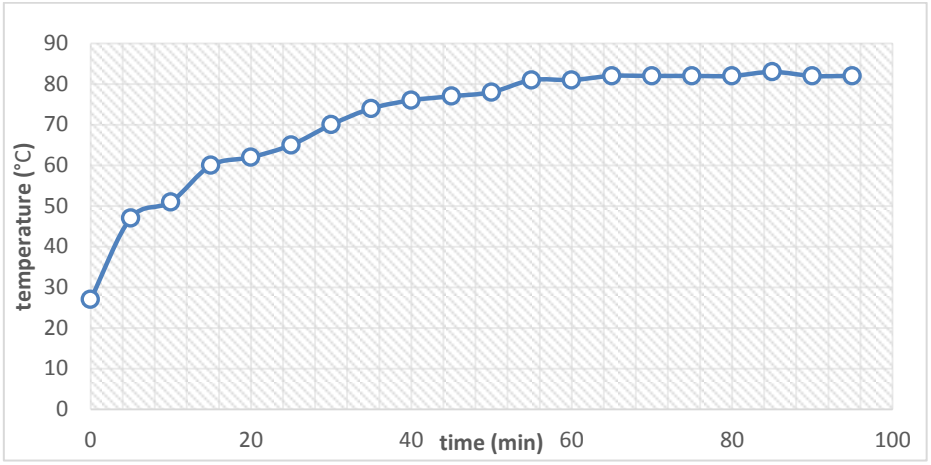


Figure 6. Increase in temperature using water bath.

2.3.2 Heating PLA Using a Hot Plate.

The PLA did not melt and it could not be removed from its flask, therefore a hot plate was used. The hot plate was set at a high temperature of 200°C and left to heat up for more than an hour to ensure the plate was hot enough. Using the same procedures as the water bath the PLA was placed on a hot plate, and the temperature was recorded where the maximum temperature achieved was 68 which was lower than the maximum temperature achieved by using the water bath, the plotted graph is shown in figure 7.

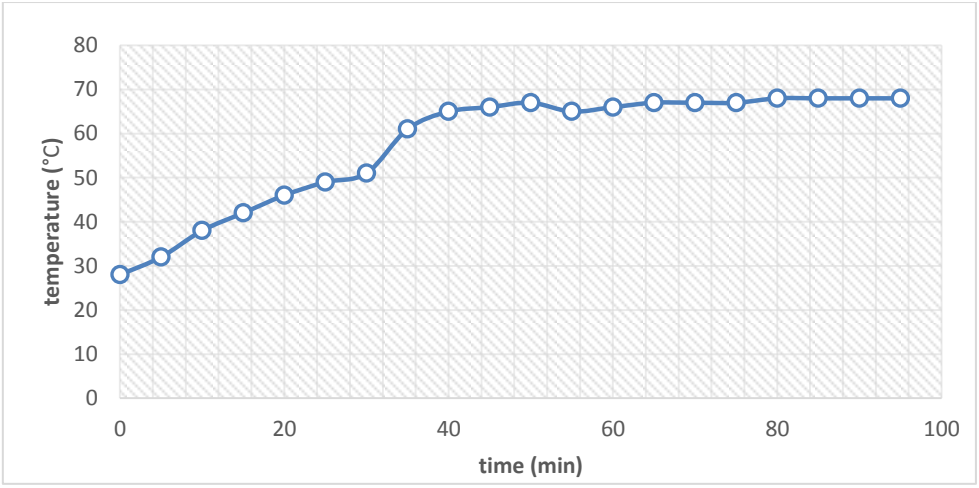


Figure 7. Increase in temperature using hot plate.

2.3.3 Heating PLA Using an Oven

The third method used to heat the PLA was by using an oven where the temperature was first set at 50°C and allowed to heat up once the oven temperature had reached 50°C the PLA was placed on a pyrex beaker and placed in the oven and allowed to heat up for 15 minutes the oven temperature was then increased to 70°C a further 20°C was increased after 15 minutes, this was repeated until a temperature of 150°C was reached. The reason the set temperature of the oven was increased by 20°C every 15 minutes was to ensure that the PLA did not undergo temperature shock where a sudden increase of the temperature of PLA could allow room for thermal to occur which can affect the properties of the PLA.

2.3.4 Blending PCL and PLA

After heating the PLA in an oven it was possible to remove it from its container, a metal spatula was used to scoop it out where the removed PLA was removed safely and placed in a Pyrex beaker, sufficient PLA for all the 5 blends was obtained. A scale was used to measure the required masses of the PCL and PLA and the granules of PLA and PCL were placed on 5 separate beakers each beaker consisting of one blend. The blends were then placed in an oven and heated using the same procedures used to heat the PLA. At a temperature of 90°C the PCL had started and the 100% PCL was removed from the oven. The rest of the blends were left to heat up where every 20°C they were mixed using a metal stirring rod to ensure proper blends were achieved after reaching the maximum temperature which was 150°C the material had melted well however mixing them was not easy due to their stickiness therefore it was necessary to do it separately for each blend where 1 was removed from the oven and the rest were left to prevent them from cooling while one is being mixed after the mixing process was done these blends were cut into smaller granules to see if the blends had mixed well. The 3 blends that were selected were 100% PCL, 80:20 PCL-PLA and 50:50 PCL-PLA, these 3 blends had produced the best blends.

2.4 Fabricating the Blends

2.4.1 Electrospinning Mechanism

The electrospinning technique is a technique where polymer solutions are used to produce fibers by using electrostatic forces the fibers are deposited on the collector which is normally place in front of the syringe containing the polymer solution. PCL was used for electrospinning where it was first dissolved in N,N-Dimethylformamide (C_3H_7NO) and using a magnetic stirrer it was allowed to dissolve for 30 minutes. Three different PCL solutions were produced which were 5%(5g/100ml),10%(10g/100ml) and 15%(15g/ml), for a small scale the Dimethylformamide (C_3H_7NO) was decreased to 5ml therefore the mass of the PCL had to be decreased by the same ratio (5:100) as the solvent. Therefore the 3 solutions were 5% (0.25g/5ml), 10% (0.5g/5ml) and 15% (0.75g/5ml). the setup of the electrospinning machine is shown in figure 8.

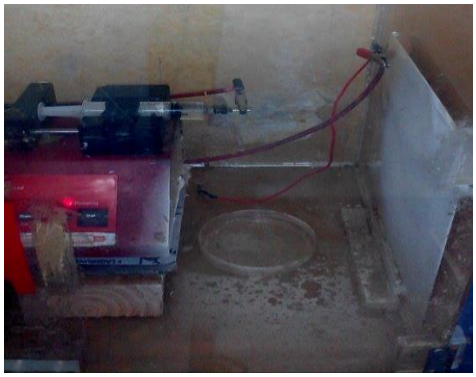


Figure 8. Electrospinning setup.

2.4.2 Fabricating the Blends on a Metal Plate.

The electrospinning technique requires a lot of time to fabricate a single blend, therefore the blends had to be fabricated on a metal plate where the blends were heated until they melted, removed from the oven one at a time, then removed from the beaker and placed on the metal plate and shaped as nicely as possible using the shape of a nylon specimen as a reference and finally allowed to cool. Figure 9 below shows the fabricated specimens.



Figure 9. Fabricated PCL-PLA specimens bottom to top; 100% PCL, 50%PCL and 80%PCL.

2.5 Strain Testing

2.5.1 Equipment and Blend Testing

To ensure accurate results are obtained in this study, it is necessary to ensure that the equipment is functioning well therefore the equipment was first tested using different polymers, since PCL and PLA was limited and could not be used ensure the equipment is functioning properly, the availability of two polymers; nylon and Teflon were an assurance to the testing of the machine. The Nylon specimen was placed in the equipment then the 5N load was applied on the end of the lever and the gauge was ensured to be at zero where the lever was raised up and released slowly a video was recorded and readings at different intervals were taken the same was repeated for Teflon. After ensuring that the equipment was working properly, PCL and its blends were tested using the creep testing machine

3. Results and Discussion

3.1 Strain Results of Nylon and Teflon

The results obtained from the first experiment using nylon and Teflon showed that initially nylon had a higher strain, then later on Teflon managed to obtained a higher strain, this could be due to nylon having a low resistant to sudden loads being applied to it causing the forces of attraction between the molecules to be weaker hence this weakness could have caused sudden elongation in the specimen, however for Teflon initially the elongation was low and managed to go higher than that of Nylon. The results obtained in this experiment were validated [9][10], which helped in ensuring the machine was operating properly since the PCL and PLA materials were limited the in testing the machine were plotted on a graph which is shown in figure 10.

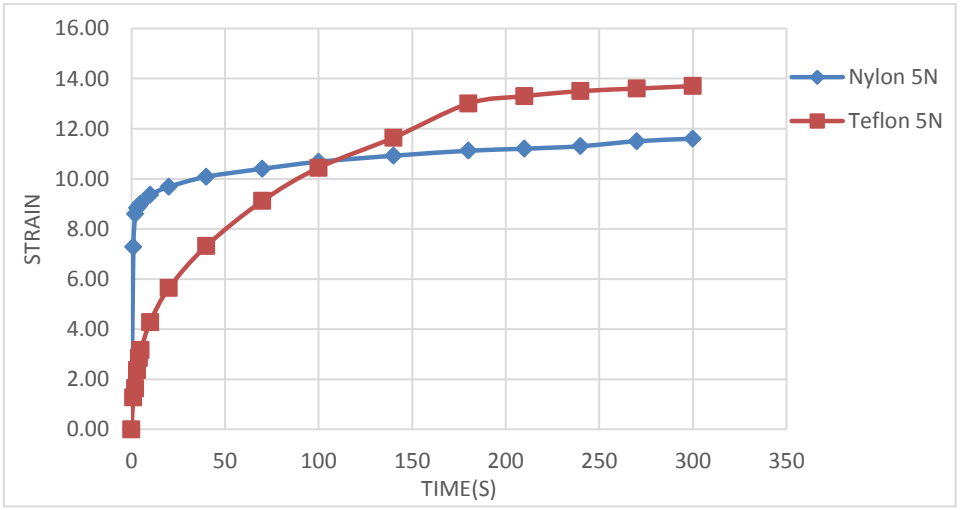


Figure 10. Strain vs. time graph for nylon.

3.2 Strain Results of PCL and its Blends

The three different specimens achieved three different results, where the 100% PCL achieved the highest values, based on the high strain energy it is possible to state that PCL contributed a lot toward the strain of the specimen it also managed to contribute a lot to the elongation of the specimen, this is justified by comparing the 100% PCL to the 50:50 PCL-PLA. Firstly the 100% PCL specimen showed a higher elongation especially when the time increased this is because PCL tends to be ductile unlike PLA which is brittle and its brittleness contributed to lower the strains of the specimen, but the advantage of the PLA is its high yield strength. The theoretical assumption of blending these two polymers to produce a blend which possess good mechanical properties is further emphasized in this study, where considering the 80:20 PCL-PLA blend did show some features of the PLA which is the low elongation as well as the strain was lower than that of 100% PCL, further analyzing this based on where PLA tends to become tuned from brittle to ductile as it did allow the strain energy to increase with time but there were certain contradictions to how much the PLA contributed in the blend, this could have occurred due to the low ratio of PLA, this can also be justified by a possibility of immiscibility occurring between the blends, since PLA and PCL tend to be immiscible at certain ratios. The comparison of the 50:50 PCL-PLA specimen and 80:20 PCL-PLA leads to one similarity which is the increase in strain despite the two blends having different values where higher values were obtained for the 80:20 PCL-PLA, certainly at the end of the recorded time both blends had almost reached a constant value which is also visible in the graph, whereas the 100% PCL did show a smaller increase but the tendency to increase was lower as time increased. Based on the graph in figure 11, it is possible to state that the 100% PCL specimen will eventually reach a constant strain level, this could be ideally true but as long as certain amount of load is applied there is a certain impact on the strain level which could not be measured experimentally. Table 1 below shows the elongation of the specimen which were obtained from the experiment conducted, table 2 shows the strain of the specimen.

Table 2 results obtained from the experiment.

time (s)	Strain (10^{-3})		
	100% PCL	80:20, PCL-PLA	50:50, PCL-PLA
0	0.000	0.000	0.000
1	2.840	2.680	2.200
2	2.880	2.720	2.240
3	2.920	2.740	2.280
4	2.940	2.748	2.300
5	2.960	2.760	2.308
10	3.000	2.780	2.360
20	3.008	2.788	2.400
40	3.040	2.800	2.432
70	3.060	2.808	2.448
100	3.080	2.816	2.480
140	3.088	2.820	2.500
180	3.120	2.828	2.520
210	3.124	2.828	2.524
240	3.128	2.828	2.524
270	3.140	2.832	2.528
300	3.160	2.832	2.540

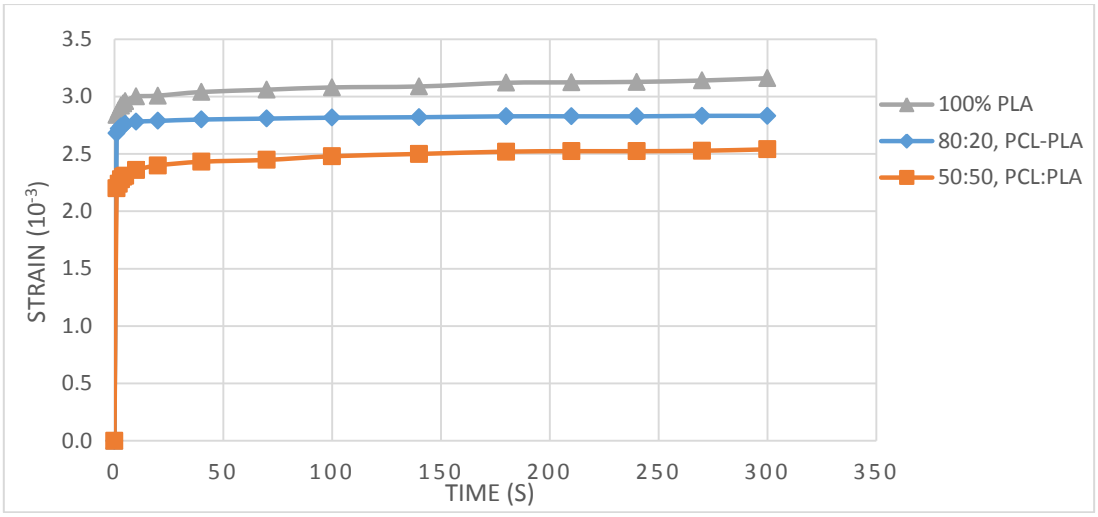


Figure 11. Strain vs.time graph for PCL and its blends.

The scanning electron microscope (SEM) images described the three different concentration used by the electrospinning mechanism which were 5%, 10%, and 15%. The best SEM image produced was by the 10% this showed proper 3D Nano fibres in the PCL which are not only suitable for ensuring the fabrication of a polymer with good mechanical properties but also the most suitable conditions for cell cultivation in the enhancement of biocompatibility. One of the two main focuses in the SEM results are; concentration and viscosity. The formation of the fibers hugely depend on the concentration of the solution, thus a low concentration is more likely to produce polymeric microparticles whereas a high concentration allows beads to form thus the results are not 100% fibers this is visible in the SEM results where 10% was the optimum concentration. The viscosity of the solution is an important factor as far as the formation of fibers is concerned, where low viscosity prevents the formation of smooth fibers and triggers the formation of beads where surface tension is the major factor, when the viscosity level is high, it is hard for the solution to be ejected therefore formation of fibers is also hard. When the ejection of the solution is hard the concentration level is also affected since lower concentration is ejected, there is an interrelation between concentration and viscosity where both affect each other that is why it is important to ensure the optimization of these two factors. Figure 12, 13 and 14 show the SEM images of 5%,10% and 15%.

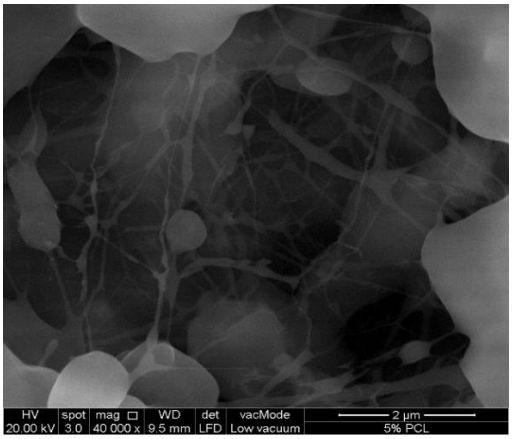


Figure 12. 5% PCL concentration SEM image.

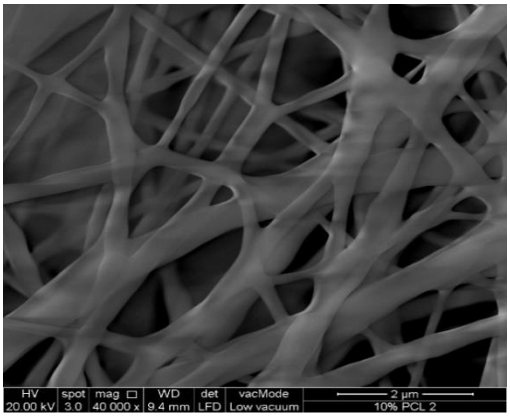


Figure 13. 10% PCL concentration SEM image.

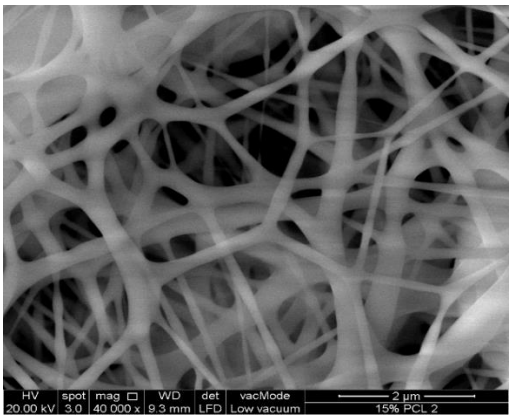


Figure 14. 15% PCL concentration SEM image.

Using similar procedures as the 100% PCL to produce electrospun fibres SEM images were obtained for 80:20, PCL;PLA and 50:50, PCL;PLA using 10% concentration as it had produced the best results for all different ratios. The SEM images showed a variation in the nanofibres in all three different blends, hence the morphology was also different for all three blends, figure 4.6 shows the SEM images of 80:20 PCL:PLA using a 5 µm scale at 10% concentration, and the SEM image of 50:50 PCL:PLA is shown in figure 4.7 using a 5 µm scale at 10% concentration.

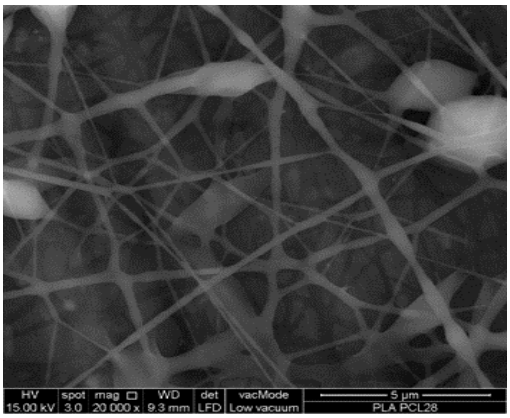


Figure 15. SEM image of PCL:PLA 80:20 at 10% concentration**.**

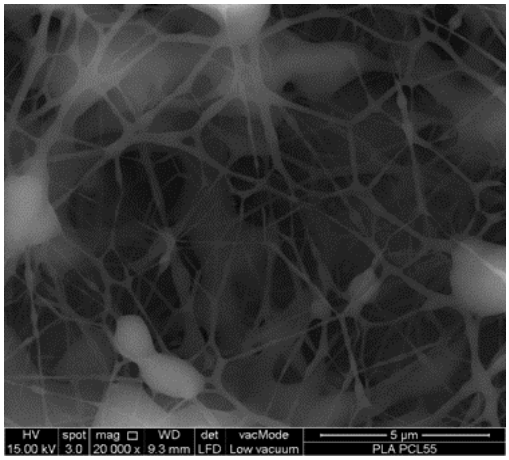


Figure 15. SEM image of PCL:PLA 50:50 at 10% concentration.

4. Conclusion

The importance of this study was to analyze how blending PCL with PLA can affect its mechanical properties, and provide enhancement of tissue engineering. The different blends produced different strain results, their applications in designing scaffolds hugely depends on the amount of forces exerted on them as well how much kinking is required for nerve regeneration. Biocompatibility plays a huge role in the design of the scaffolds, therefore it is important to analyze not only the mechanical properties but also the biocompatibility of these blends, and similar blending methods can be used to perform this analysis. The electrospinning method is suitable for both PCL and PLA, the obtained SEM images showed that these blends can produce a successful biocompatible scaffold where certain factors are to be considered to ensure optimum results of the scaffold designs are achieved. The SEM results showed that there is a possibility of achieving nanoscaffolds using PCL and PLA blends, hence the combination of this research with research on nanoscaffolding could be a key to achieving nanoscaffolds with good mechanical properties. Furthermore, the results obtained by using different ratios of PCL and PLA can be useful for further research on the mechanical properties of polycaprolactone blended material and its application in tissue engineering, hence certain factors could also be considered when analyzing the results where a certain degree of immiscibility could have occurred which could have had an impact on the results.

Reference

[1] X. Gu, F. Ding, Y. Yang, and J. Liu, “Construction of tissue engineered nerve grafts and their application in peripheral nerve regeneration,” *Prog. Neurobiol.*, vol. 93, no. 2, pp. 204–230, 2011.

[2] M. A. Woodruff and D. W. Hutmacher, “The return of a forgotten polymer - Polycaprolactone in the 21st century,” *Prog. Polym. Sci.*, vol. 35, no. 10, pp. 1217–1256, 2010.

[3] K. Chavalitpanya and S. Phattanarudee, “Poly(Lactic Acid)/Polycaprolactone Blends Compatibilized with Block Copolymer,” *Energy Procedia*, vol. 34, pp. 542–548, 2013.

[4] M. Zuideveld, C. Gottschalk, H. Kropfinger, R. Thomann, M. Rusu, and H. Frey, “Miscibility and properties of linear poly(l-lactide)/branched poly(l-lactide) copolyester blends,” *Polymer (Guildf).*, vol. 47, no. 11, pp. 3740–3746, 2006.

[5] M. E. Broz, D. L. VanderHart, and N. R. Washburn, “Structure and mechanical properties of poly(D,L-lactic acid)/poly(??-caprolactone) blends,” *Biomaterials*, vol. 24, no. 23, pp. 4181–4190, 2003.

[6] M. Todo, K. Arakawa, H. Tsuji, and Y. Takenoshita, “TOUGHENING MECHANISM OF BIOABSORBABLE PLA / PCL POLYMER BLEND,” vol. 3, no. 1, pp. 3–8.

[7] R. K. Roeder, *Mechanical Characterization of Biomaterials*. Elsevier Inc., 2013.

[8] M. Schoßig, C. Bierögel, W. Grellmann, R. Bardenheier, and T. Mecklenburg, “Effect of Strain Rate on Mechanical Properties of Reinforced Polyolefins,” pp. 2–7.

[9] Dupont, “Teflon PTFE ® Properties Handbook,” p. 38, 1996.

[10] B. Corporation, “BASF Corporation AN ADVANCED HIGH MODULUS (HMG) SHORT GLASS – FIBER REINFORCED NYLON 6 : PART II - MECHANICAL,” *Corporation*, 2003.

The Analysis and Comparison of Parallel Configuration of Single and Dual Inlet Designs in Proton Exchange Membrane Fuel Cell using CFD approach

Muhammad Hidayat Hamzah[1], Hardie Mohyi[2]
[1]*Taylor's University, Malaysia*
[2]*Taylor's University, Malaysia*

*hidayat_hamzah@yahoo.com

Abstract
Proton exchange membrane (PEM) hydrogen fuel cell is a type of clean alternative energy that produces power through chemical reaction and released clean exhaust, which is water. Currently fossil fuel is one of the main energy source used in the world that produces high pollution and greenhouse gas that could result into global warming. Contribution in the PEM fuel cell research could further its development to produce more efficient and sustainable models thus replacing the dependent of fossil fuel. There are many factors affecting the efficiency of PEM fuel cell among them are the design of the flow configuration. Different designs produce different pressure and velocity distributions. Furthermore the accumulation of water within the channels could create blockage thus limiting the gas flow within it. Hence optimum design must be develop to reach optimal efficiency. This research analyze on the different design focusing on the parallel concept. Comparison between the dual and single inlet are done to determine the advantage/disadvantage of both. A total of 7 designs were model using SOLIDWORKS software and analyzed using the computational fluid dynamics ANSYS software. The results obtain were recorded. These were maximum and average pressure and velocity values. Contour profile of the pressure distribution result has been illustrated. Pressure drop largely discuss together with the ideal design choice. Overall conclusion is that dual inlet of the particular design produces the best pressure distribution as well as sufficient velocity distribution. These are due to the big channel of the outlet located at the center bridging the flow from the two inlet big channel located on the sides reducing the flow pressure stress. Additionally dual inlet design has high active volume promoting more reaction to increase efficiency.
Keywords: PEM fuel cells, Flow Field, Single Inlet, Dual Inlet, Parallel Design.

1. Introduction

1.1 Fuel Cell Concept

Fuel cell is a device that converts the chemical energy of two chemical through the chemical reaction into electrical energy with one of the chemical being an oxidizing agent usually oxygen. The process are basically reverses electrolysis as current is being produce through the chemical reaction. Hydrogen fuel cell consist of hydrogen gas and oxygen gas that react or recombining to produce current and water as shown below in the simple reaction equation (1) ,(2) and (3).

$$2H_2 + O_2 \rightarrow 2H_2O \quad (1)$$

$$2H_2 \rightarrow 4H^+ + 4e- \quad (2)$$

$$O_2 + 4H^+ + 4e- \rightarrow 2H_2O \quad (3)$$

The current produce however is small due to low contact area between the gas, the electrode and the electrolyte. Furthermore large distance between the electrode make the electrolyte resist the electric current flow. Hence electrodes are design to be flat with a thin layer of electrolyte as illustrated in Figure 1. With the electrode structure being porous, both electrolyte and gas on each side could penetrate it. Equation (2) shows that anode of an acid electrolyte fuel cell ionizes the hydrogen gas releasing electrons and creating protons (H+ ions). As the reaction releases energy, equation (3) shows that at the cathode oxygen react with the electrons and protons to form water. Both of these reactions occur constantly. Certain polymer could be made to provide mobile H+ ions and the material is known as proton exchange membranes (PEM). To keep the system in balance, two hydrogen molecules is needed for one oxygen molecules as illustrated in equation (1). [1]

1.2 Proton Exchange Membrane Fuel Cell

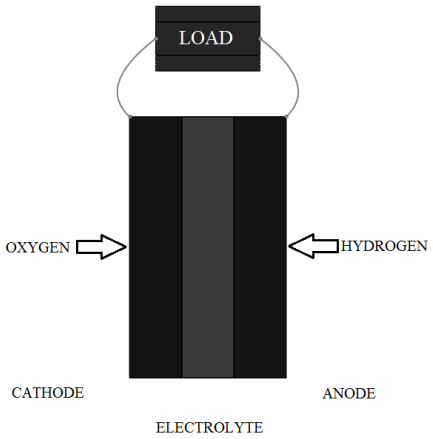


Figure 1. Basic cathode-electrolyte-anode fuel cell structures

PEM fuel cell is among the most efficient energy conversion devices. The advantage of PEM fuel cell is that it could be operated under low operating temperature, high power density, rapid start up and high in endurance. The assembly components are shown in figure 2. [2]

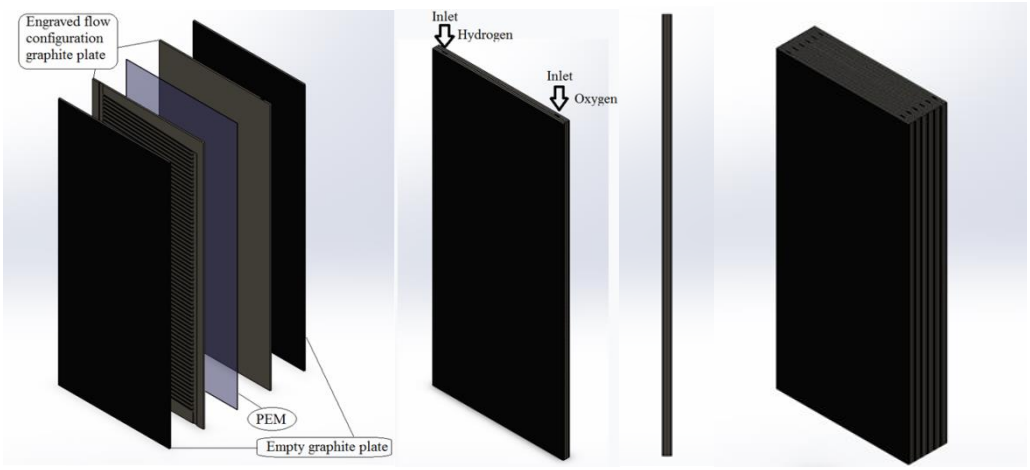


Figure 2. PEM hydrogen fuel cell component and assembly.

1.3 PEM Fuel Cell Challenge

The main issues that affect the efficiency and life of PEM hydrogen fuel cell are the accumulations of water inside the channels of the plates. It occurred due to low pressure zone inside the flow configuration plates as when water produces from the chemical reaction, it remain accumulated inside the low pressure zones. Beside that capillary effect of the water could occur in the outlet when the pressure inside the system is not sufficient to purge it out. Nevertheless very high pressure inside the system will resulted in wasted energy from incomplete reaction between the gases as well as possible damaging the plates and membrane. Finding the optimal flow pressure and velocity distributions are the key.

Others factors that affect the efficiency of PEM hydrogen fuel cell including material type, chemical composition, orientation, fluid mechanics, temperature and others. The scope of studies will focus on the fluid mechanics aspect to be specific the flow field configurations of PEM fuel cells. The studies will largely focus on the flow configuration design analysis of multiple parallel model concepts both single and dual inlet, as well as its comparison. The main target is to review the pressure distribution, pressure drop and velocity of the hydrogen gas on the various designs of the flow field configuration.

1.4 Literature Review

There are various studies that are done on the PEM fuel cell. Among the studies are related to comparison of various typical flow field designs. The authors did actual experimental test on PEM fuel cells to investigate the effect of gas flow fields on fuel cell performance. Graphite plate was used with effective membrane area of 23.5cm^2. The authors compare between all the typical basic flow channel designs. A total of 7 designs were tested. The design concepts are one serpentine, two parallel, two pin, one interdigitated and one spiral. The final conclusion is that serpentine design obtained the best performance and spiral design being the worst. This resulted in the authors focusing on refining only the serpentine design. Though the parallel design received an above average performance rating, the authors did not refine the design further. Thus a gap in refine and modify for improvements for parallel concept is still present. [2]

As for the effect of corners, there is a CFD study on flow distribution uniformity in fuel distributors having multiple structural bifurcations of flow channels. The authors study the issues of uniform flow distribution. The studies primarily touch on the effect of corners angle and shape i.e. sharp or rounded. Furthermore detail radii size of the outer and inner corner was tested and the data tabulated. The results from this journal are very useful in reviewing the effect of fillet at the corners of the flow channels. [3]
The study of nature or biomimicry to determine the effect it has on the performance of the flow, the author flow field design is inspired from the flow patterns in the leaf. Though the flow is not the author main scope of studies, his concept idea using nature inspire design could spark breakthrough design notions especially for the dual inlet concept. [4]

1.5 Computational Fluid Dynamics (CFD)

The computational fluid dynamics (CFD) uses the numerical analysis and algorithms implementing various governing formula such as Continuity equation (4) and Navier-Stoke equation (5), (6) and (7); these equations are used to analyze and guess the accurate results of a particular studies that involve fluids flow.

Continuity equation,

$$\frac{\delta \rho}{\delta t} + \nabla \bullet (\rho U) = 0 \quad (4)$$

Navier-Stoke equation,

$$\text{X-component: } \frac{\delta \rho u}{\delta t} + \nabla \bullet \rho u V = -\frac{\delta P}{\delta x} + \nabla \bullet (\mu \nabla u) + S_{mx} \quad (5)$$

$$\text{Y-component: } \frac{\delta \rho u}{\delta t} + \nabla \bullet \rho u V = -\frac{\delta P}{\delta x} + \nabla \bullet (\mu \nabla u) + S_{mx} \quad (6)$$

$$\text{Z-component: } \frac{\delta \rho u}{\delta t} + \nabla \bullet \rho u V = -\frac{\delta P}{\delta x} + \nabla \bullet (\mu \nabla u) + S_{mx} \quad (7)$$

With the current advance development of CFD technology, more and more accurate result could be achieved. Thus using CFD approach is an alternative to multiple full scale prototyping testing that may be high in cost. Many difference designs could be tested beforehand in CFD before actual experimental validations are done.

1.6 Closing

In world current states of high carbon footprint from fossil fuel which lead to possible global warming, alternative clean energy is required such as PEM hydrogen fuel cell. By contributing in this research field, more efficient PEM hydrogen fuel cell could be develop thus replacing the need for fossil fuel. The possibility to preserve planet earth further motivate in research for this project.

2. Methodology

2.1 Design Modelling

The 3 dimensional design models are created using the SOLIDWORK software. There are a total of 7 parallel concept designs illustrate in figure 3 that are created to analyze and form comparison. The designs must be able to engrave on to graphite plate with the dimension of 190mm×80mm×1mm. Design A are the typical single inlet parallel design where the inlet and outlet are opposite end of each other. Both of them contain two main channels with multiple parallel small channels in between in a horizontal orientation. Design B follow the same concept as design A but with a slanted (3º angle from horizontal plane) small channels design. Design C add fillet with radius of 1mm at every corner of the small channels in design A. Design D employs the inverted orientation making the central small channels in a vertical orientation. For design E splines are created on the small channels. Design F are dual inlet design with one central big channels located on the center of the plate that lead to the outlet, where then the small channels that link the two outer big channels to the center big channel are in horizontal orientations. Same concept design is done with design G but with the smaller channel being in slanted orientations (3º angle from horizontal plane). All of the designs are illustrated in figure 3 and the parameter shown in table 1.

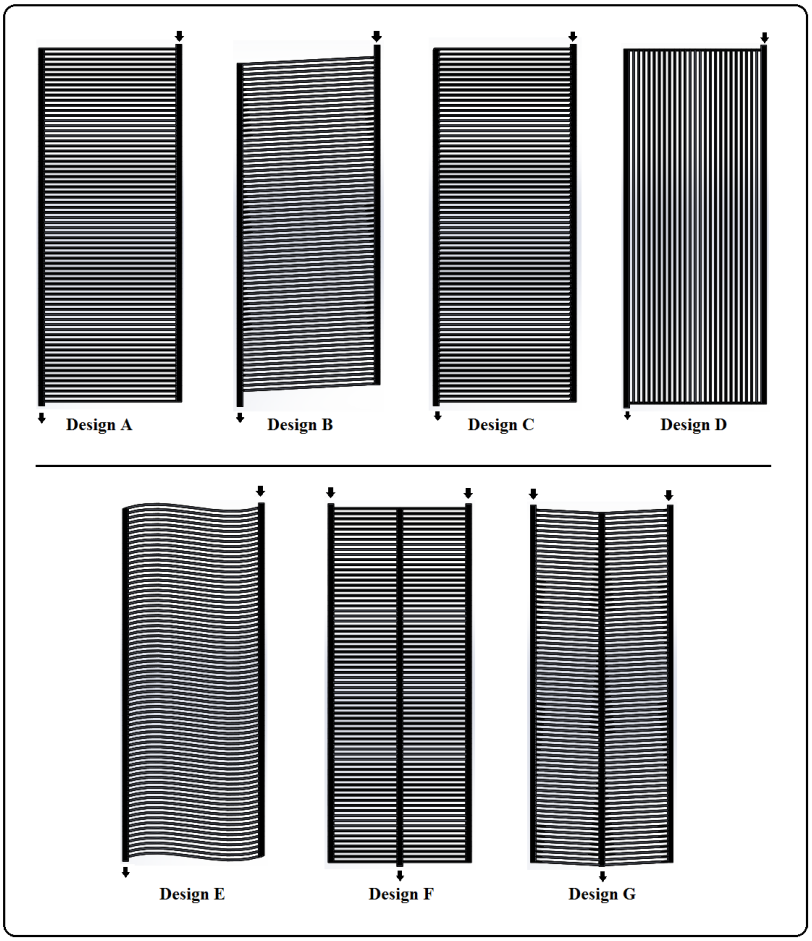


Figure 3. Parallel flow configuration designs. (A) Initial-Single; (B) Slanted-Single; (C) Fillet-Single; (D) Vertical-Single; (E) Spline-single; (F) Initial-Dual; (G) Slanted-Dual.

Table 1. Design modelling parameters.

	Design						
	A	B	C	D	E	F	G
Plate dimensions	80 mm × 190 mm × 1 mm						
Channels dimension	75 mm × 190 mm × 0.5 mm						
Main channel width	3mm						
Small channel width	1mm						
Gap between small channel	1.68mm						
Active Volume (mm^2)	2980	2782	2994	2932	2977	3156	3161
Number of inlet	1	1	1	1	1	2	2

2.2 Meshing

Meshing is done to create small element within the geometry domain. The purpose of these elements is the present of cell/node within its geometry. Equations are solved at nodal location. ANSYS meshing software are used for the project. There are various factors that need to observe during the meshing process; among them are cells size, quality and types. Bigger cell created will have high efficiency in the calculation process due to its smaller element numbers but produce less accurate results due to its lower quality coarse mesh. The Smaller or refined mesh produce high accuracy results due to its fine geometric detail but at the cost of higher element numbers. As for the types, tetrahedrons are the common mesh used, but the element counts tend to be high due to its size in comparison to the hexagonal mesh. Hexagonal mesh are done using sweep to produce less element and low skewness mesh, however not all geometry could be sweep. Balance in the efficiency and accuracy must be done to ensure the optimal simulations data are achieved.

For the project, the mesh setting is done using the proximate size setting with fine relevance center. Smoothing is set to medium. Inflation uses program controlled with maximum layer of 3-5 and growth rate of 1.2. Collision avoidance setting of stair stepping is done. Skewness and orthogonal quality are monitored. All of the mesh quality must be below 0.97 for maximum skewness and above 0.2 for minimum orthogonal quality. The meshes for the designs are all within range. [5]

2.3 Simulation Parameters Settings

ANSYS FLUENT program is used for the CFD simulation in this project. The boundary conditions are set using inlet mass flowrate of 3.0×10^{-7} kg/s for single inlet and 1.5×10^{-7} kg/s for dual inlets. The outlet pressure is set to 0 Pa. Surface monitor are set to view the area-weighted average of pressure and velocity. Volume monitor are set to view the pressure. Standard initialization is set and calculation will run until convergent occurred. Table 2 shows the parameters for all the designs. [5]

$$Re = \frac{\rho v D}{\mu} = 20.36 \quad (8)$$

$$\text{Rectangular pipe, } \mathrm{D} = \frac{4\mathrm{A}}{\text{Circumference}} \quad (9)$$

Laminar for rectangular pipes $\mathrm{Re} < 500$.

Following equation (8) and (9) the fluids flows are determine to be laminar, thus the models used are laminar.

Convergent occurred when continuity and velocity residual reach below 1.0×10^{-3} during iteration and energy below 1.0×10^{-6}.

Table 2. Boundary condition and simulation parameters.

	Design						
	A	B	C	D	E	F	G
Inlet mass flowrate (kg/s)	3.0×10^{-7}					1.5×10^{-7}	
Outlet back pressure (Pa)	0						
Gravity (m/s^2)	9.81 (outlet direction)						
Working fluid	Hydrogen (h_2 from Fluent database)						
Fluid temperature (K)	300						

2.4 Qualitative Assessment

Table 3 Quality assessment criteria.

	Good	Bad
Low Pressure Zone	Small	Large
Pressure Drop	Low -Must be sufficient to push the water accumulation or the capillary effect.	Too High

3. Results and Discussions

3.1 Simulation Data Results

Table 3 illustrates the data obtained from the simulations. The data taken are all the convergent values of pressure and velocity of each data from ANSYS FLUENT solution.

Table 3. Pressure and velocity data results.

	Design						
	A	B	C	D	E	F	G
Maximum pressure (Pa)	121.64	123.20	115.05	183.39	122.66	77.15	75.54
Average pressure (Pa)	60.47	62.11	57.25	90.88	60.98	41.54	39.79
Maximum velocity (m/s)	4.13	4.14	3.99	10.70	4.23	4.17	4.02
Average velocity (m/s)	0.2999	0.3352	0.3241	0.3350	0.3157	0.2431	0.2398

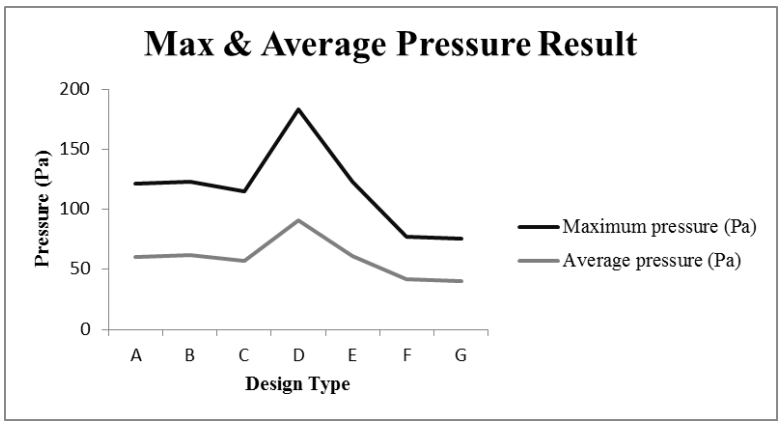


Figure 4. Maximum and Average Pressure Graph

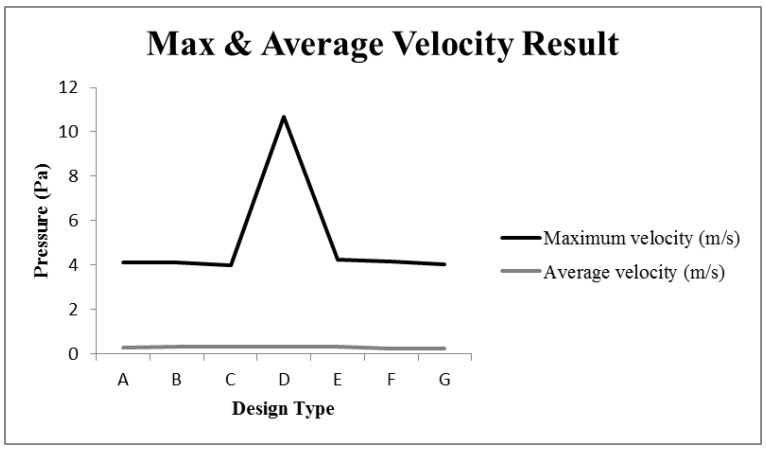


Figure 5. Maximum and Average Velocity Graph

3.2 Single Inlet Analysis

3.2.1 Design A

Figure 6 illustrate the pressure contour throughout design A flow configuration model. The pressure distribution display are expected and of a good quality spread. The maximum pressure of 121.64 Pa could be seen at the inlet and slowly reduce as the fluid gradually lose its momentum. Due to the parallel concept, many channel are present for the fluid to travel thus the dispersion are more vast in comparison to the one channel design of serpentine. Relating to pressure drop, the design does not have low pressure zone in the center hence any water development could be expunge out at the outlet. Closely examining the pressure distribution, the pressure drop "radially" slightly from the top right side of the plate where the inlet is located and same thing could be seen on the bottom left side where the outlet is located. However these are only happen on the top and bottom 25% of the plate, whereas the center of the plate has the pressure drop in vertical distribution going down. The average pressure taken is 60.47 Pa which is enough for continuous flow.
From Table 3, maximum velocity achieved is 4.13 m/s and in theory it is located at the low pressure zone near the outlet. The average velocity of the working fluid is 0.2999 m/s. The effect of velocity will further explain during the comparison of designs.

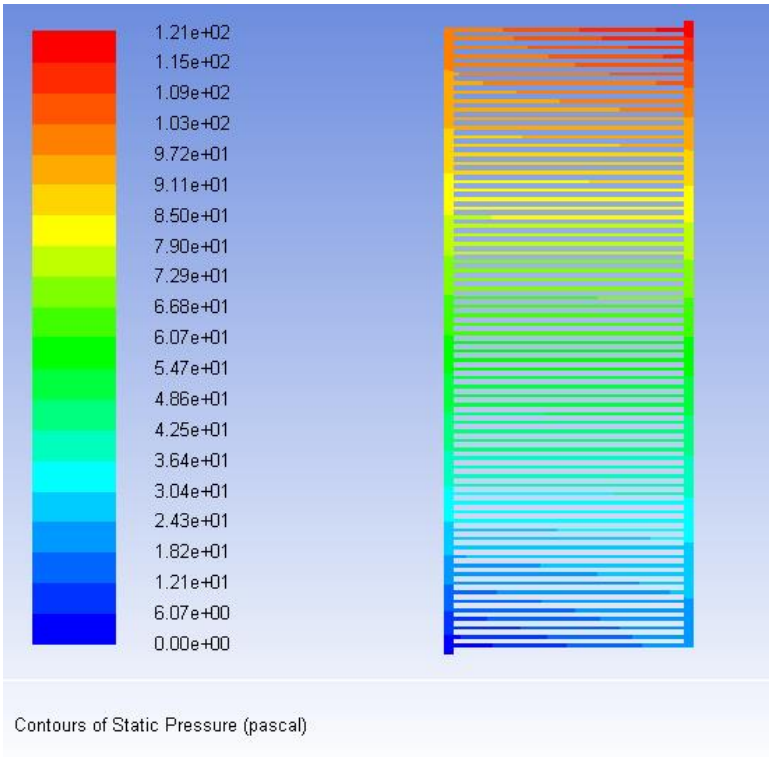


Figure 6. Pressure contour for design A.

3.2.2 Design B

Figure 7 show the pressure contour of design B model. The slanted angle of 3º in theory due to gravitational force setting, the flow will travel faster due to acceleration than design A. However the result show that it is not really noticeable as the maximum pressure of 123.20 Pa, average pressure of 62.11 Pa and the maximum velocity of 4.14 m/s are similar to design A reading. The average velocity shows a slight increase with the value of 0.3352 m/s. The possible explanation is the volume of design B which is 2782.28 m^2 is smaller than design A of 2979.88 m^2 thus even when the average velocity increased, the peak pressure and velocity does not. The distribution of pressure are identical to design A and considered a good quality spread.

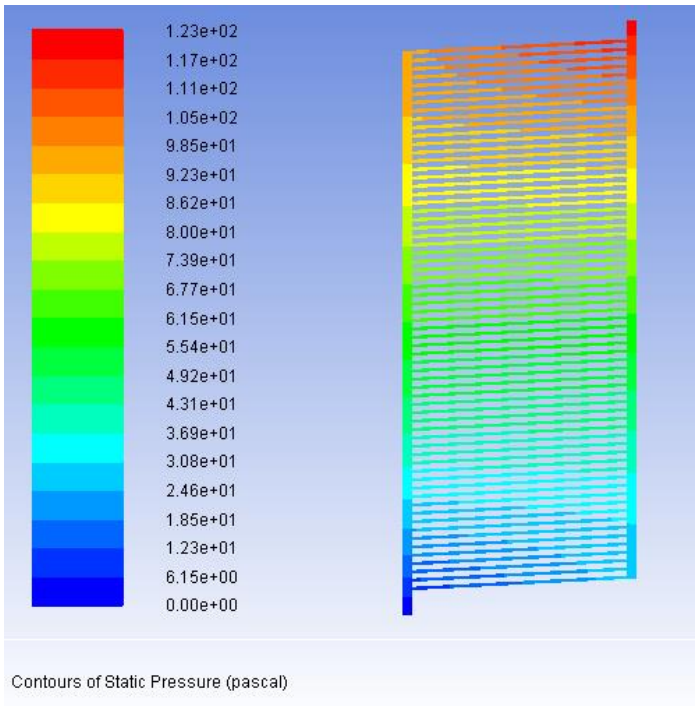


Figure 7. Pressure contour for design B.

3.2.3 Design C

Figure 8 display the pressure contour of design C model. The corner fillet design ensure that the fluid enter the corner smoothly with less corner friction. The maximum pressure value of 115.05 Pa is obtained which is slightly lower than design A. The maximum velocity of 3.99 m/s are slightly lowered also in comparison to design A. However the average velocity of 0.3241 m/s is higher than design A. This mean that the velocity distributions throughout the model are well distributed as it is not disrupted at the corner due to friction of the small channel opening. Furthermore the pressure contour shows a better pressure distribution overall as the vertical pressure drop zone are bigger in the center.

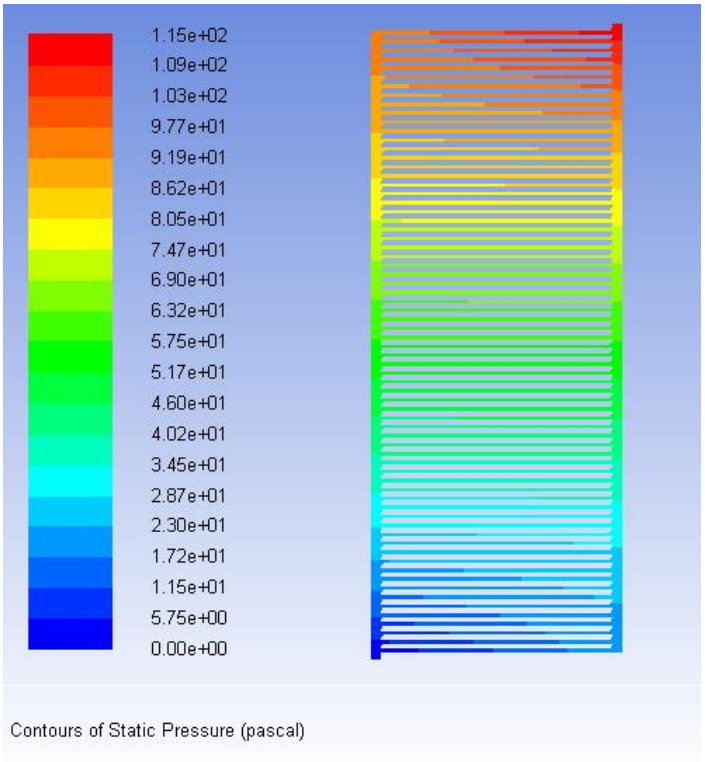


Figure 8. Pressure contour for design C.

3.2.4 Design D

Figure 9 demonstrate the pressure contour of design D model. It is noticeable that the pressure contour defer greatly from design A as pressure drop now occur from right to left. The max pressure is at the highest with the value of 183.39 Pa with is 50% more than design A. The low pressure zones are large and located at the left side on the big channels. Large low pressure zones may increase the chance of water capillary effect. Overall pressure distributions are not really good in design D. As for the velocity, the maximum value of 10.7 m/s is 159% more than design A due to the multiples vertical small channels of design D. However the average velocity of 0.3350 m/s is similar to design B. This means that the velocity distributions are also considered bad.

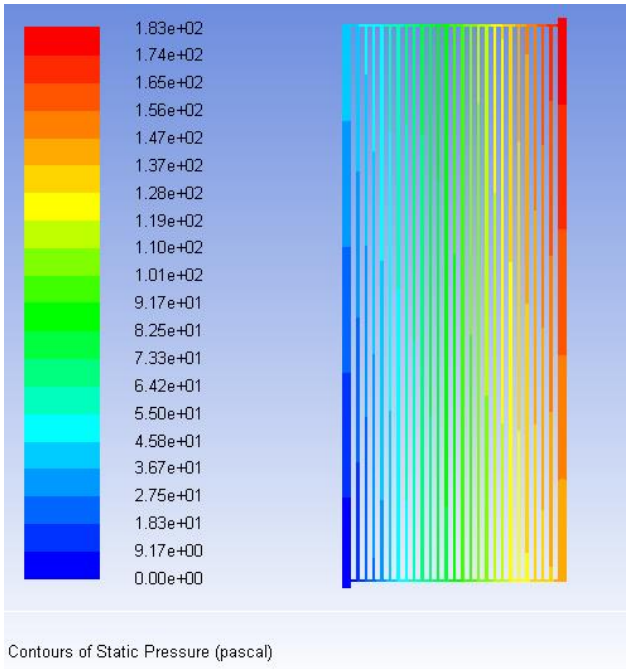


Figure 9. Pressure contour for design D.

3.2.5 Design E

Figure 10 illustrates the pressure contour of design E model. The maximum and average pressure values are similar to design A as well as the pressure distribution contour. The maximum and average velocities are slightly higher giving the impression that the spline concept design E promotes minor increase in better velocity distributions.

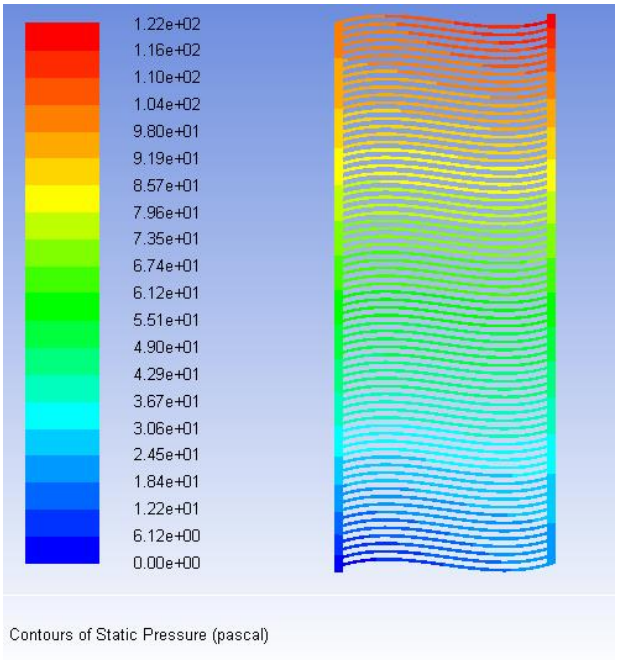


Figure 10. Pressure contour for design E.

3.3 Dual Inlet Analysis

3.3.1 Design E

Figure 11 illustrates the pressure contour of design F model of dual inlet concept. The two inlets located on opposite end promote a very good pressure distribution with low pressure drop as the maximum pressure located at the inlets are only 77.15 Pa with the average pressure being 41.54 Pa. From the pressure contour image, the pressure drop zones are mostly drop in vertical motion from top to bottom. These further show that design E has good pressure distributions. The maximum velocity is 4.17 m/s and the average velocity is at 0.2431m/s. By considering the low pressure drop of the design, the velocity nonetheless is quite high with good distributions. Overall the dual inlet design with center big channel for the outlet provides one of the best results currently for pressure distribution and pressure drop.

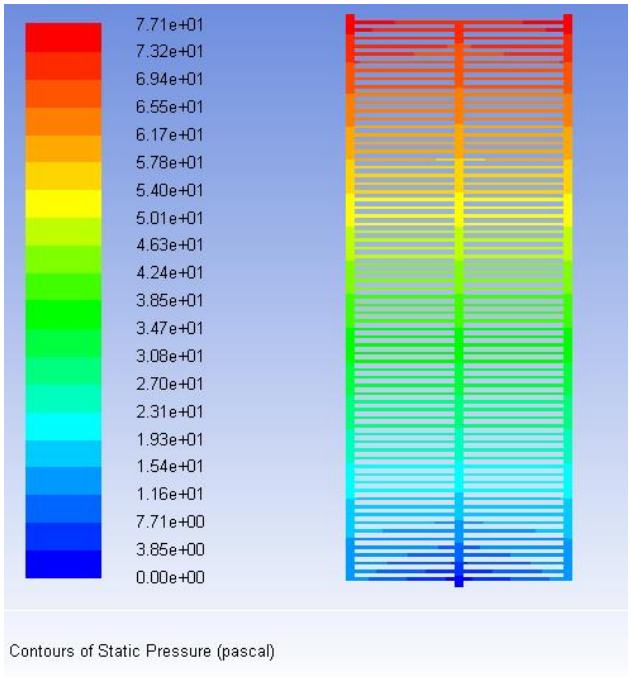


Figure 11. Pressure contour for design F.

3.3.2 Design G

Figure 12 displays the pressure contour of design G model. The slanted design achieved the maximum pressure of 75.54 Pa and average pressure of 39.79 Pa. The maximum velocity attained is 4.02 m/s and average velocity attained 0.2398 m/s. As per stated in section 3.2.2 design B, design G is similar to design F in the result obtained with, but with slightly lower stats as the active volume for design F and design G a similar.

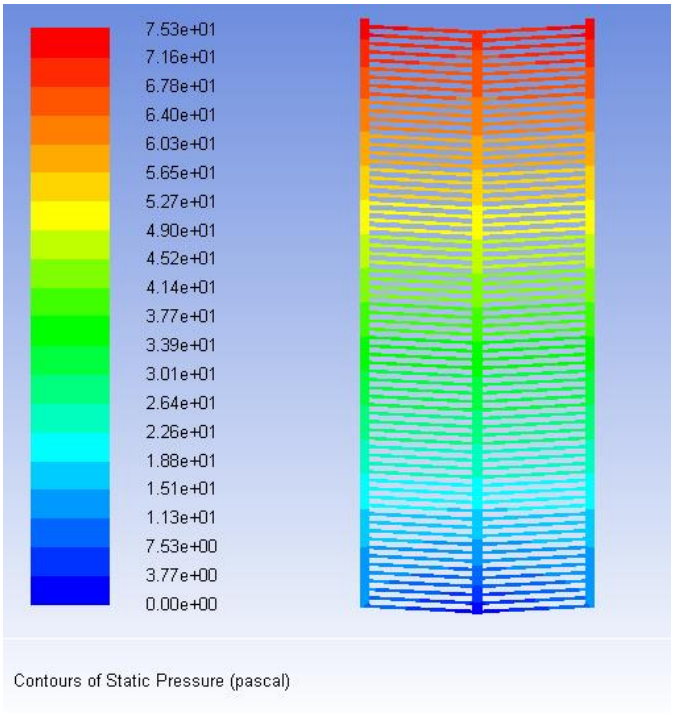


Figure 12. Pressure contour for design G.

3.4 Comparison of Single and Dual Inlet Designs

Figure 13 display the comparison of two pressure contour results of design A and design E using the pressure range of 0 Pa to 130 Pa to clearly show the pressure difference between the two. Design A have a higher maximum and average pressure when comparing to design E. This mean pressure drop is higher for design A. However, the maximum velocity and average velocity are similar for both designs with design E having higher maximum velocity and design A having higher average velocity.

As shown in figure 14 the gradient of the pressure drop of design A are higher than design E. These possibly suggest that flow inside design A may have some restriction that produce high stress, among them could be flow channel bottleneck between the big and small channels near the inlet. Beside that single inlet design has longer distance on which the flow travels from the inlet to the outlet location, thus the pressure drop greatly increases. The main concern regarding high pressure drop is it create large unutilized section of the plate reducing gases reaction thus lowering the fuel cells efficiency.

With the present of the big channel located in the center of the design E and the two inlet channels located on the sides, less distance are required for the flow to travels thus reducing pressure drop. Pressure losses are lowered as less restriction is present in the channel. More active volumes are present in the dual inlet design largely due to the center big channel promoting more reaction between the gases increasing the efficiency.

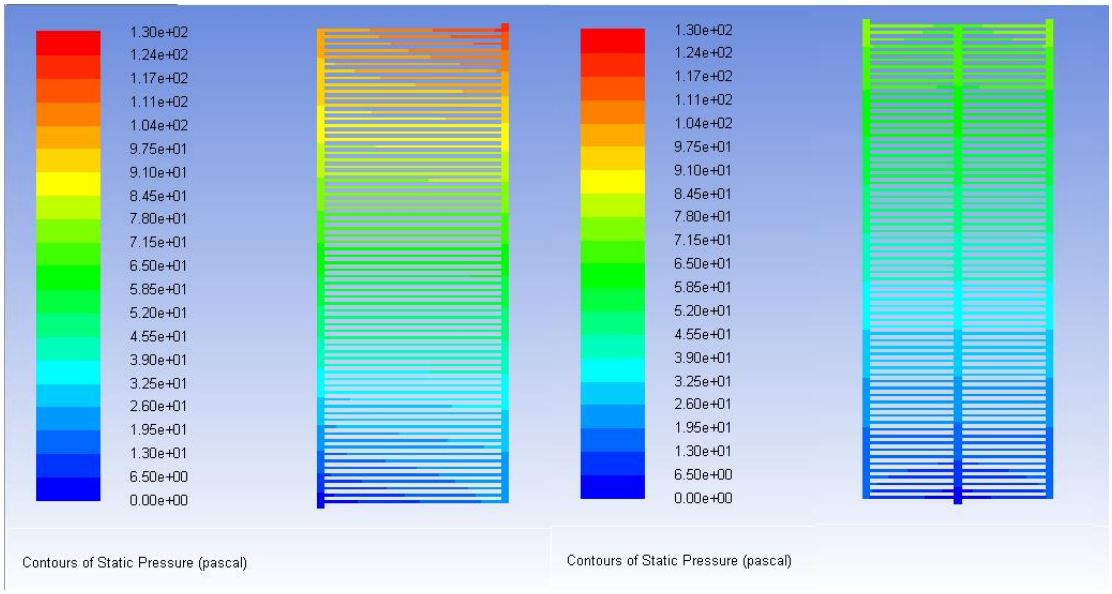


Figure 13. Pressure contour comparison between design A and design E. (130Pa Max)

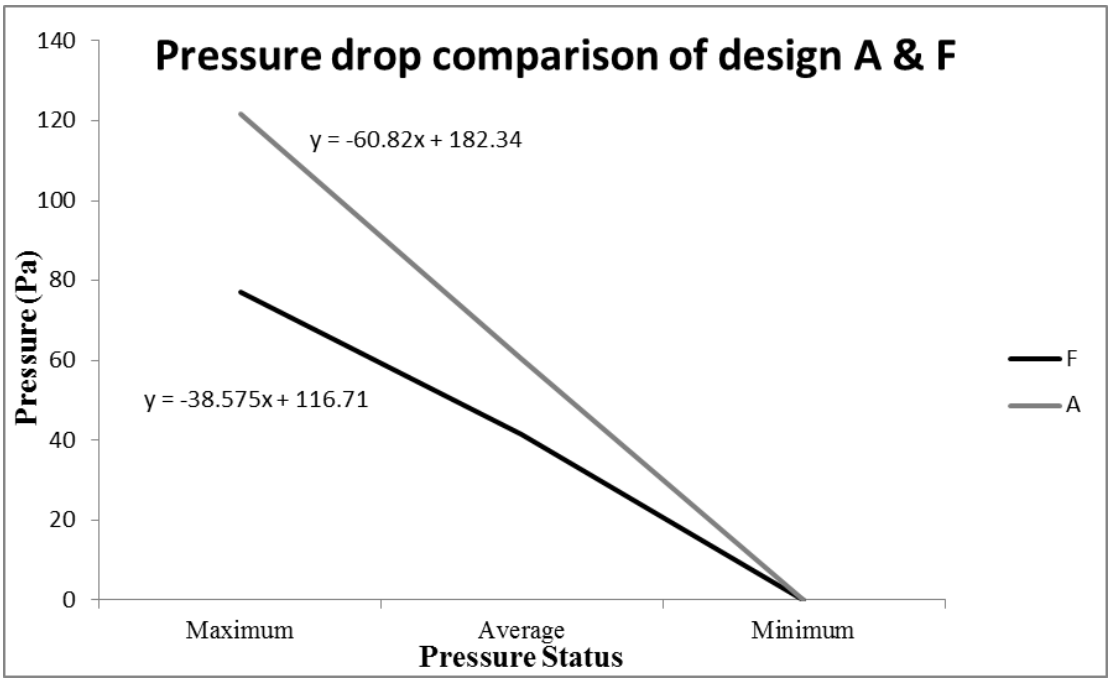


Figure 12. Graph of pressure drop comparison of design A and design F.

4. Conclusion

The pressure and velocity distribution largely affect the effective flow and reaction within the model channels. Pressure drop is one of the main factors that affect the efficiency of the fuel cells hence finding the optimal flow field design are the target. Some of the single inlet designs show remarkable characteristic. Such example are the additions of fillet in design C reducing its overall pressure while increasing the average velocity within due to less friction experience by the fluid during the turning of the corners. The worst results come from the inverted channel design D as low pressure zones are largely present near the outlet channel. As for the comparison of single and dual inlet, the dual inlet for these particular design exceed in the flow pressure distribution and effective active volume promoting high rate of gas reaction increasing the fuel cells efficiency.
Further refinement of the research could be to design more dual inlet concepts to be analyzed such as implementation of fillet. The search for the best optimal design continues. Experimental validation and theoretical validation for confirmation could be planned for future works.

References

[1] Larminie, J., Dicks, A. (2003). *Fuel Cell Systems explained.* West Sussex, England: John Wiley & Sons Ltd.

[2] Liu, H., Li, L., Juarez-Robles, D., Wang, K., Hernandez-Guerrero, A.(2014). Front. Energy Res: *Experimental Study and Comparison of Various Designs of Gas Flow Fields to PEM Fuel Cells and Cell Stack Performance*, 2, 1–8.

[3] Liu, H., Li, P., Van Lew, J., (2010). Int. J. Hydrogen Energy: *CFD study on flow distribution uniformity in fuel distributors having multiple structural bifurcations of flow channels,* 35, 17, 9186–9198.

[4] Maher, A.R.(2015). J. Energy Environ: *Analysis of transport phenomena and electrochemical reactions in a micro PEM fuel cell with nature inspired flow field design,* 6, 1, 1–16.

[5] Canonsburg, T. D.(2012). Knowl. Creat. Diffus. Util: *ANSYS FLUENT Fuel Cell Modules Manual,* 15317,724–746.

Design and prototyping of an automated mechanism to prevent bedsore

N.T. Saidy[1*], A. Ghadimi[1], Mohammad Jaweed[2]

[1]*School of Engineering, Taylor's University Lakeside Campus, Malaysia*
[2]*School of Medicine, Taylor's University Lakeside Campus, Malaysia*

[*] Navid.toosi@gmail.com

Abstract
Pressure ulcers or commonly known as bedsores are areas of concentrated injuries on the skin and the structure of the soft tissue of the patient mainly cause by excessive pressure and shear force applied at the 3 main bony premises of the patient's body such as the sacrum, heel and the occiput area. Accumulation of blood due to the extreme pressure results into inadequate nutrition supplied to the soft tissues, which eventually causes tissue breakdown. Continues repositioning of the patient in a fixed time interval is currently practiced by caregivers where this requires at least 2 nurses to perform this operation. The main purpose of this project is to conceive, design, implement and operate an automated mechanism to prevent pressure ulcers by repositioning the patient. A mechanism consisted of 12 plates and 17 hinges integrated with a 3-piece mattress is introduced in this project at which it is designed by "Solidworks 2014" to be installed on to an available hospital bed. This 12 mechanism is driven by an automated power screw that is devised to reposition the patient from supine to any intended position by the user. These proposed designs are then manufactured using the defined materials and components and eventually installed on to the purchased hospital bed to perform the repositioning operation. Pressure mapping studies is done in order to measure the interface pressure applied at the critical locations of the body where in this research an array of 10 Interlink Force Sensitive Resistor (FSR) sensors are used to measure the interface pressure at the sacrum area of the patient. The interface pressure is measured for a duration of 5 minutes at the supine position as well as 15,30 and 60 degree of lateral rotation to compare the pressure applied at these positions. The sensing area of this sensor array is 27×14cm which is anticipated to cover the sacrum area of the subject in this experiment . The interface pressure of the supine and 4 lateral positions are represented in this research where 30-degree lateral position is identified as the most suitable lateral repositioning angle. Moreover, the time –pressure relationship of the patient is investigated for both positions at every 10 seconds to gauge the change in the interface pressure value across time. The interface pressure experienced a minor fluctuation across this 5 minutes' period which is mostly affected by the minor movement of the subject. Interface pressure measurement is performed on 3 different volunteers in order to asses the effect of BMI on the resultant interface pressure.

Keywords: pressure ulcer prevention, repositioning, interface pressure, lateral position

1. Introduction

Pressure ulcers commonly known as bedsores are areas of confined injuries on the skin and its beneath tissue structure mostly caused by prolonged static pressure and shear stress applied at the critical areas of body [1]. Pressure ulcers mostly occur at the bony locations of the patient that is in direct contact with the surface of the mattress, which is mostly due to the greater amount of pressure applied at these locations [2]. There are a few factors that lead to the occurrence of pressure ulcers such as excessive pressure for a long duration of time, shear stress and also moisture at the critical regions. The accumulation of blood due to prolonged extreme pressure applied at the skin results into restriction of nutrition delivery to the tissue cells of the skin. Inadequate nutrition supplied to the tissue cells results into the break down of skin. [3]. In addition daily medical practices may result into a further shear stress and friction force applied at the critical areas of body causing the distortion of dermal veins and eventually formation of the pressure ulcers.

Pressure decubitus are divided into 4 categories based on its development stage, which is identified by comparing the severity of ulcers to a set of fixed rules and regulations. Mild redness and a firm skin are the first symptoms of a pressure ulcer that falls into stage 1 of the bedsore development. Further application of pressure for a longer duration of time causes the skin to wear away and break open and eventually it forms an ulcer at this affected area. This can cause an excruciating pain for the patient and it needs an extensive care and nursing practice to be stopped. At the third stage this pressure penetrates its way through the tissue cells to the fats that is only one layer before the muscles and bones of the patient. Ultimately, at the last stage, pressure ulcer deepens its way to the muscles and bones and it creates a widespread damage where at this stage the patient may not even feel the pain as the tissue have been broken away. Majority of bedsore patient are the elderly and the patients which have been paralyzed due to different reasons like accidents. The age group and the situation of the patients define the type of treatments that should be given to these patients [4].

There is a set of different bedsore treatments, which is done depending on the development of the ulcers as well as the general condition of the patient where in the case of a first and second stage pressure decubitus, treatment is solely done by cleaning and rotating the patient by the nurse. This is done to relieve the pressure from the critical areas of the body while avoiding any sort of dirt and moisture at these areas. Bedsore treatment is a very costly procedure at the third and fourth stage of its development where skin flap surgery is necessary with a cost of about 63000 $ [5]. In addition to these costly procedures, pressure decubitus can lead to life threatening situations, extended stay in the hospitals and unbearable pains where all these can be avoided by the right practice of repositioning and distributing the pressure. This shows the importance of this research in order to develop a better mechanism to prevent bedsores from happening. The current practice of bedsore prevention involves 2-3 nurses in order to reposition and clean the patient, which is a very exhausting procedure. Based on the data collected in the hospital visitation patients are repositioned every 2-3 hours to ease the pressured parts where lack of knowledge, poor intentions and attitude among the caregivers about bedridden patients may boost the probability of this incident [6].

Pressure ulcer is a localized injury mostly occurring at the bony locations in contact with the mattress. Identification of these locations plays an important role in solving this life-threatening matter. A study done by Mallah et al [7] shows that in 50% of the cases pressure ulcers occur at the coccyx sacrum followed by the heel and occiput area [7].

According to the research done by the European Pressure Ulcer Advisory, frequent repositioning of the patient can result to a better pressure distribution at the contact surface of the body and this can eventually eliminate the prolonged excessive pressure applied at the occiput and sacrum area [1]. Patients with lack of mobility require help from the caregivers in order to rotate and reposition based on a defined duration of time. Frequently repositioning the patient based on a fixed interval of time is a very costly and time-consuming act. There are two major things that have a vital effect on the formation of the pressure ulcers where those are the lateral angle of the patient after the act of repositioning as well as the time interval that this act is done.

Rosmar et al [8] conducted a research on 49 healthy individuals in order to compare the effect of double regression hospital bed and the normal hospital bed. In addition, the interface pressure at different lateral angles is compared to find the best lateral position of the patient in the act of repositioning. Interface pressure results are taken at four supine positions of 0, 30, 45 and 65 degrees where they are called the supine, semi follower, follower and seated positions respectively. The generated outcome from this study shows that the 0 and 30^{o} lateral positions result into a lower interface pressure in compare with the other lateral positions in the experiment.

One of the major considerations in designing the mattress is how often should the patient be repositioned in the bed to prevent bedsore from creating. A literature review study done by Hagisawa et al [9] shows that there are a set of different studies done on this matter which they mostly resemble a 2-hour turning period based on medical practice that is not established on critical pressure versus tissue breakdown studies. This 2-hour period have initiated from 1870's where it was stated that this is the duration that takes for a nurse to go around on one side of the ward [10]. This has followed by several critical studies by Guttmen et al [11], which suggests a 30 minutes to 1-hour period for the daytime and 2-hour for the nighttime. In addition a study done by Reswick and Rogers reveals a graph about the hours of continues pressure against the applied pressure, which shows that 2-3 hour is the most suitable period to be considered for repositioning the patient [12]. However, the suitable duration is not identified for different individuals with different conditions, which can be taken into consideration for future studies. Figure 1 demonstrates the graph of pressure versus the duration of its application.

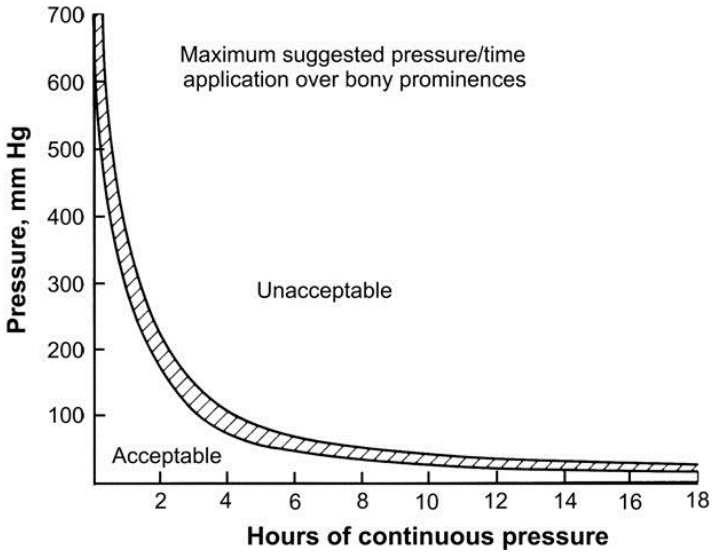


Figure 2: Pressure versus the hours of continues pressure [12]

Study done by Nixon [13] illustrates that the pressure and the shear force can be reduces by considering preventive measures such as alternating the region under pressure or repositioning the patient. This can result into a better supply of oxygen to the tissue cells and avoids any break of the tissue cells. Accordingly, there are a few products that are designed to prevent pressure ulcers such as Alternating Pressure Mattress (APM), Alternative Pressure Low Air Loss Mattress (APALMs), gel overlay and ripple mattresses but a comparative study done by McInnes et al. [14] shows that there are not enough studies to show which type of mattress is more effective to prevent bedsores. As a result of that repositioning of the patient is practiced by the caregivers in the hospitals in order to ensure a good blood circulation at the critical areas. According to the study done by Moore et all [15] constantly repositioning the patient can cost about 200 to 250 £ per month, which can only be saved by creating a mechanism that can replace this manual procedure with an automated or assisted operation. On the other hand, critical comparison has to be done to compare the effectiveness of the automated repositioning mechanism in compare with the normal repositioning done by the caregivers.

One of the major uncertainties in using a new automated device to deal with a variety of patients is the question of its effectiveness in solving that particular challenge. A study done by Woodhouse [16] shows that there is no substantial difference in terms of the interface pressure between the automated and manual way of repositioning. This interface pressure is the primary factor to focus on, in this area of research where by reducing the interface pressure the probability of bedsores decreases significantly. This interface pressure varies at different lateral positions defined by the caregiver or the automated mechanism. Despite the fact that the generated results from the automated system seems promising, other factors have to be considered such as the safety of the patient and the angle of rotation. These factors are in a close relation with the interface pressure of the patient's body and have to be taken into consideration in the design stage to fully satisfy the requirements of the design.

The identified research gap for this research is to design and manufacture a hospital mattress compatible mechanism that is capable of repositioning the patient and to quantify its effectiveness with the current accepted methods. Hence in order to address this issue, this research is conducted to design and prototype an automated mechanism that simulates the current nursing practice to prevent pressure ulcers from happening. Moreover, the main advantage of this mattress over the current products is the flexibility of the usage and the possibility of employing it on to the current hospital beds. 3D design of the proposed mechanism is modelled in "Solidworks 2014" by setting the dimensions based on the current literature review in relation with the human body dimensions. As a result of that this design is manufactured with the defined materials and components in an actual scale and implemented on to a hospital bed in order to assess the adoptability of the design in accordance with the current hospital beds. Lastly the interface pressure is measured using a pressure mapping system that is specifically developed in this project. A pressure mapping system is consisted of multiple pressure sensors where in this case Force Sensitive Resistor (FSR) is used to perform this task.

2. Research Methodology

As this project involves designing and prototyping a product, CDIO framework is used as an approach to tackle the issue of pressure ulcers. It all starts with conceiving on methods to prevent pressure ulcers based on basic medical knowledge that is attained through literature review and Sungai Buloh hospital visitations. Several ideas are generated at this stage through sketches in order to have an overall idea on the methods that can be used to prevent pressure ulcers. These ideas are evaluated based on the fundamental theories from engineering and medical perspective in order to be filtered before the computer aided design stage. Lack of effectiveness in the current preventive products imposes the caregivers to perform continues repositioning of patient at a defined time interval which makes repositioning method as the most effective approach of prevention. In addition, time and budget constraint are important factors that can eliminate a conceptual design before the stage of manufacturing.

In fact, the mattress is designed to perform the repositioning practice where preliminary ideas are given and final design is modelled progressively by compiling all the necessary factors. Therefore, the final design of the mattress and its mechanism is prototyped using the defined materials and components where the manufactured model is implemented on a manual hospital bed to prove the functionality of this proposed product.

Interface pressure study is performed based on the pressure mapping method in order to evaluate effectiveness of the proposed model in preventing pressure ulcers. Pressuring mapping is defined as measuring the applied pressure at different locations of the patient's body in order to assess the effectiveness of repositioning performed by the developed product in this project. Force Sensitive Resistor (FSR) is used to measure the force applied at different positions of the body where a FSR 402 with a force sensitivity of 1 to 100 N and sensitivity area of 0.5 inch is used in the context of this project. An array of 10 sensors are positioned in an arrangement of 5 columns and 2 rows on a 33×30 cm pleksi board and connected to an Arduino microcontroller board in order to interface pressure of the mattress and the body. This plate is

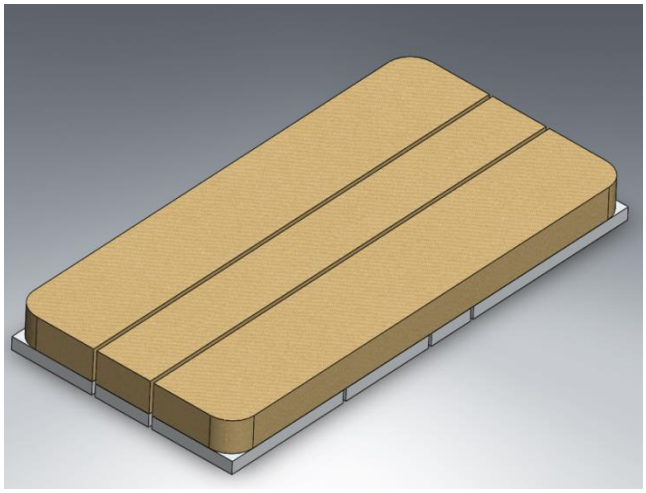
positioned at the sacrum region which is identified as the most critical location in the current literatures. This interface pressure is measured at the supine position as well as 30 ^{o} of lateral rotation in order to assess the effectiveness of this lateral rotation.

2.1 Conceive and design of the proposed mechanism

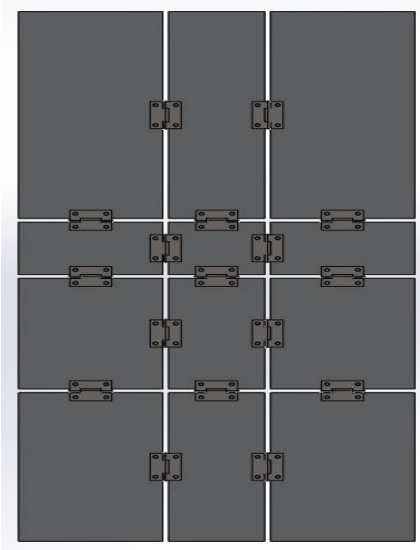
Several ideas are generated at this stage with the core purpose of preventing the formation of pressure ulcers. These ideas are such as removing the contact interface of the supporting surface at the critical points, cooling down the critical points to avoid sweat and moisture, continues cooling and heating to provide better blood circulation and mimicking the repositioning of the patient performed by the nurses. However, repositioning the patient according to a fixed time interval seems to be more effective as it is widely practiced in the hospitals all around the world. Despite the effectiveness of this act, repositioning is a time consuming, expensive, and exhausting process which is not done in accordance of the required time interval, causing the creation of bedsores all around the world. This issue can be solved by introducing a mechanism to perform this repositioning practice. This mechanism is aimed to be implemented on the current hospital beds in order to allow lateral movement without discretizing the basic movement of the bed to elevate the upper body and the legs. Moreover, the cost of the proposed product has to be up to a limited budget to be provided to the lower level of the community where expensive products such as the freedom bed with a cost of 30000 $ is not affordable by the hospitals and the patients.

The standard size of the hospital bed is 1×2 meters which means that the overall size of this mechanism have to be limited to this dimension. Preliminary a 2-piece plate with the defined size is modelled in order to prepare a platform for the repositioning of the patient. After further analysis and hospital visitation it was found that, the patients are mostly positioned in the middle of the mattress and having a 2-piece mechanism does not reposition the patient on its side. This may also cause the patient to be stuck in the middle of these 2 sections which may create further medical issue for the patient. Therefore, in order to prevent this from happening it was decided to divide the mechanism into 3 sections in order to use the middle section as a medium of repositioning and the side section to secure the patient on the bed.

This 3-section mechanism can be integrated with a 3-piece mattress to provide the necessary comfort for the patient. However, implementing this 3-section mechanism compromises the required back and leg elevation performed by the bed. This is resolved by defining a 12-piece plate with an arrangement of 4 rows and 3 columns in order to create the required degree of freedom upper body, leg and lateral movements. These 12 pieces are connected with 17 hinges and integrated with a 3-piece mattress at every column of this structure shown in Figure 2. A 9mm plywood is used in the manufacturing stage to allow an easier prototyping process.



(a) Design overall assembly



(b) Design of the hinge and plate connections

Figure 3: The 12-piece mechanism

This 12-piece mechanism is designed to perform the repositioning practice based on the defined time interval where the rotation of the middle section in a clockwise manner results in to the repositioning of the patient to the left arm. Similarly, after a period of 2 hours' patient is brought back to to his/her neutral position and repositioned again with an anticlockwise rotation of the middle section causing the patient to land on the right arm. This have to be done every 2 hours in order to relocate the pressure from the left side of the body on to its right side as it is defined by Reswick [12] and many other researchers in this field. This period is in a direct relation ship with the accumulation of the blood flow and the creation of the pressure ulcers. Moreover, the patient has to be repositioned to the most efficient angle that results into the least amount of interface pressure applied at the patient's critical areas. A study done by Romsar et al [8] demonstrates that 30^o lateral position yields the least interface pressure applied at the coccyx sacrum, heel and the occiput area. Therefore, this 12-piece mechanism is set to perform lateral repositioning up to 30^o and in a 2-hours time interval. The result of this 30^o repositioning for clockwise rotations is shown in Figure 3.

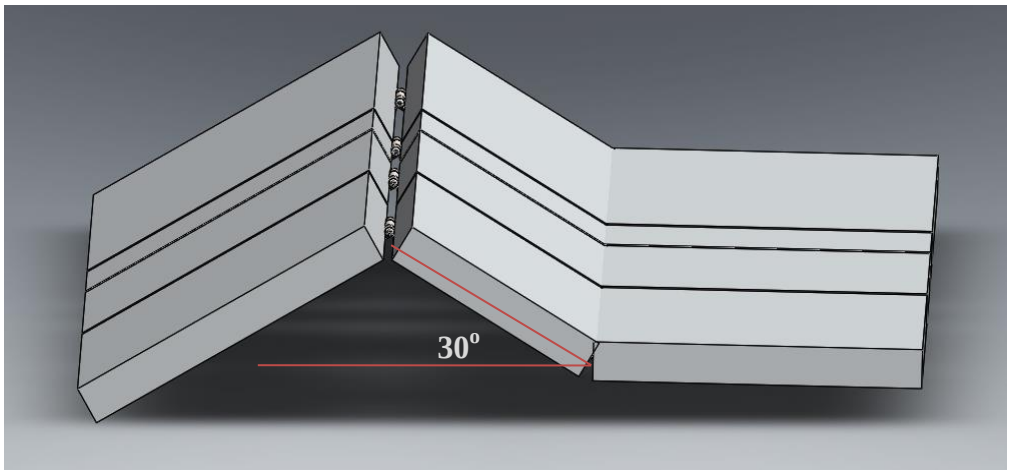


Figure 4: 30 degree clockwise lateral position

Subsequently this 12-piece mechanism requires a system to perform the lateral repositioning based on the defined criteria where initially a linear actuator is selected to drive the targeted pieces by contacting the middle and the side plates. However, a heavy duty linear actuator with a maximum load of 100-150 kg was found to be very expensive. Hence, an automated power screw is designed to perform a similar task with a much lower cost in compare with a linear actuator (figure 4). This automated power screw is similar to a car hydraulic jack implemented with a 120W electric motor which is used to perform this action automatically based on a 2-hours time interval. In addition, a structure is added on to the arm of this hydraulic jack in order to drive the first 2 rows separately rather than using 2 automated power screws at each side of the mechanism. The stroke of this automated power screw is in direct relation with the repositioning of the mechanism where in this case the power screw is designed to have a maximum stroke of 30mm allowing the bed to reposition from 0 to $90^{o.}$ One automated power screw is implemented on each side of the mechanism to perform clockwise and anticlockwise rotations.

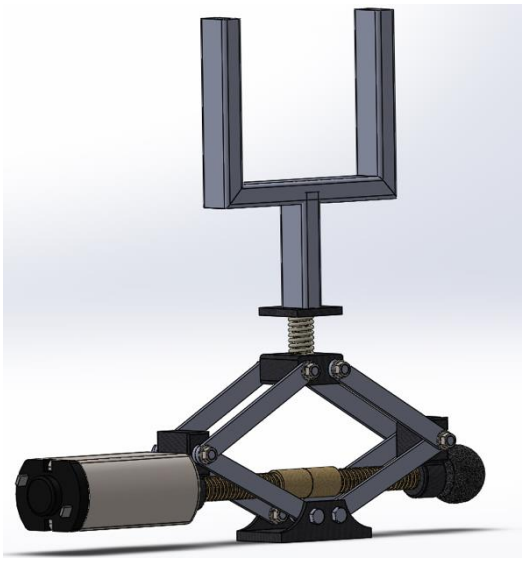


Figure 5: The automatic power screw

The mattress mechanism and the automated power screw system are implemented on to a normal hospital bed to indicate the adoptability of the proposed design on to the available hospital beds. The design of the hospital bed is in accordance with the purchased hospital bed that is discussed more in the manufacturing section. The design of the bed may slightly affect the structure on the automated power screw where in this case the distance between the 2 opening underneath the bed is about 26 cm which is the same size as the length of the mentioned structure. In addition, existence of side protectors has to be assured as it is important for the safety of the patient when the repositioning practice is performed. Clockwise and anticlockwise lateral rotation of the patient on the hospital bed using the automated powers screws is shown in Figure 5.

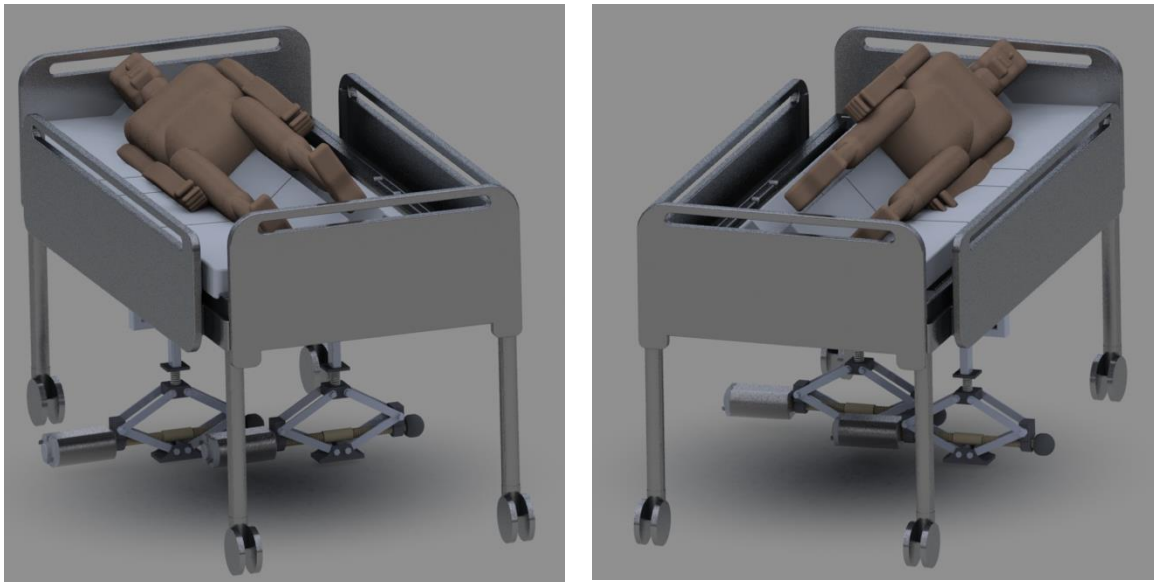


Figure 6: Clockwise and Anticlockwise lateral rotation

2.2 Implementation

The designed components are manufactured precisely in a 1:1 scale based on the defined dimensions in the conceive and design stage. The 12-piece mechanism is manufactured initially by printing the 2D drawing of the mechanism from the Solidworks 2014 model. This 2D drawing is then attached on to the wood pieces in order to cut the exact dimension of of the selected piece. All the 12 pieces of this mechanism are constructed and then assembled using 12 mm steel hinges in order to allow the plates to rotate at every orientation that is required. It is very important to ensure that aligned hinges are concentric as it can strongly affect the lateral rotation of the plates as well as the upper body and leg elevation. This is done by assembling each part individually and drilling on the next plane in accordance with the first assembled part.

Subsequently the 3-piece mattress is attached on to the 12-piece mechanism and a cover sheet is used to cover this mattress. The 12-piece mechanism and the 3-piece mattress are shown in figure 6. This combination is then placed on the purchased hospital bed to verify the adoptability of this manufactured mattress mechanism on to

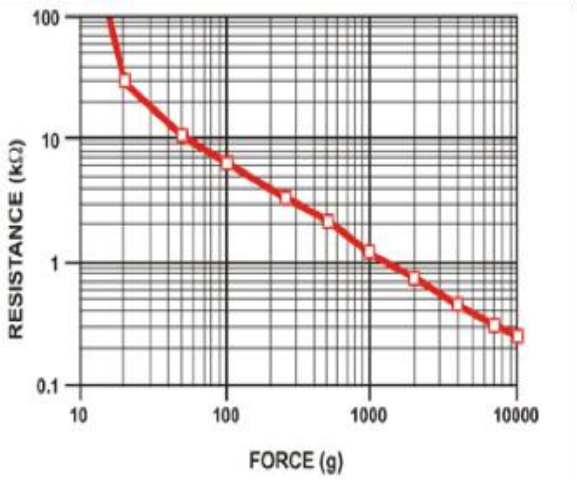
an available hospital bed in the market. Lastly the automatic power screw is prototyped by manufacturing the structure that was designed in the first stage and assembling it on to an available car scissor jack. This scissor jack is then automated by integrating a 120 W electric motor with the built structure that was mentioned.



Figure 7: 12-piece mattress mechanism implemented with the 3-piece mattress

2.3 Pressure mapping

It is established that pressure ulcers are formed due to the high interface pressure causing the accumulation of the blood flow at the bony premises of the body. Therefore, pressure mapping studies is done in order to measure the interface pressure applied at the critical locations of the body. In this project pressure mapping is carried out using an Interlink Force Sensitive Resistor (FSR) which shows a drop in resistance with a rise in the amount of force applied to the surface of the FSR. The unique feature of this sensor is the attachment of its resistive polymer onto the thin-film conductive traces where the FSR material is not in contact with electrodes when no force is applying. Therefore, the resistance of this sensor is infinity when there is zero force applying on its active area. The resistance to force relationship of the force resistive sensor is shown in graph 1 where the sensitivity of this sensor is from 0.1 to 100 N.



Graph 1: Force versus resistance of FSR [17]

The interface pressure is measured by connecting one end of this FSR to power and the other end to 10Kohm resistor where this pull down resistor is eventually connected to the ground. In this arrangement the point between the FSR and the 10 Kohm resistor is connected to an Arduino DUE to to read the output of the employed sensor. The resistance of the FSR decreases with an increment of the force applied on to its active area hence reducing the total resistance of the FSR and the pull-down resistor from about 100Kohm to 10Kohm. On the other hand, this results into a larger current flowing through both FSR and the 10 Kohm resistor which eventually causes an increment in the voltage between the FSR and the fixed resistance. It is clearly shown in equation 1 that the output voltage is inversely proportional to FSR resistance.

$$V_o = V_{cc}(\frac{R}{R+FSR}) \quad (1)$$

In this project ten FSR 402 series sensors are arranged in five columns and two rows on a 33×30 cm pleksi sheet with a sensing area of 27×14 cm (figure 7) in order to measure the interface pressure at the sacrum area of the patient. Sacrum region is selected as the controlled pressure mapping area as it is the most critical region for the occurrence of pressure ulcers. This array of sensors is connected to an Arduino controller in order to process the generated data from the sensors. The interface pressure is measured at the supine position as well as 30^o of lateral rotation to compare the pressure applied at these 2 positions. In addition, this measurement is done for a duration of 6 minutes to investigate about the relationship between the pressure and duration that this pressure is applied. A healthy 27 years old male with a weight of 90Kg is the subject of this experiment.

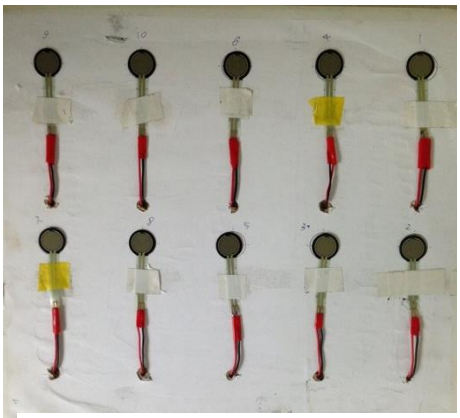


Figure 8: FSR sensor arrangement

2.4 Operation

Finally, the assembled components are used to accommodate volunteers in order to assess the final prototype of the mechanism in terms of the repositioning practice. The repositioning practice is performed for 3 different individuals with BMI values of 28,24 and 18 who are categorized in the overweight, average and underweight category. These subjects are successfully repositioned from supine position to a range of angles between 0 and 60 which is the operating range of the APS system. The safety aspect of this product is taken care of by the available side protectors in the hospital bed, which can stop the patient in the necessary cases (figure 8). However, the speed of the repositioning practice is set as only 11.5 centimeters per

minute where based on the performed operation on the prototype it did not result into any sudden movement of the patient. This can be further investigated where multiple patients can be repositioned and the feedback by the patients can be recorded in a form of a survey. The repositioning of the three subjects are further discussed in the following section of the report.



Figure 8: Patient laying down at supine position

3.0 Results and Discussion

The designed and prototyped components are operated in the last stage of the process where interface pressure measurement is done for 3 volunteers from overweight, average and underweight Body Mass Index (BMI) subclass. The interface pressure of the first volunteer is initially measured for the supine position where this value is then compared with the measured interface pressure for 15,30,45 and 60 degrees of lateral rotation. This is done in order to assess the effect of lateral positioning of the patient on the created interface pressure. Subsequently interface pressure measurement is done for the second and third volunteer with BMI values of 24 and 18 respectively. This measurement is done for two position in order to investigate about the correlation between the interface pressure and the BMI value. Lastly the interface pressure for the second and the third volunteers are compared as supine and lateral repositioning angle in order to assess the effectiveness of the repositioning preformed for the mechanism on multiple individuals

Pressure mapping studies are done using the developed FSR array where measurement is done for a duration of 5 minutes and a sampling rate of 10 seconds for every case of this experiment. The error analysis of every experiment is discussed at its respective section which means that there is no separate section showing the error analysis of the data measurement

3.1 Interface pressure measurement at supine position

The interface pressure of the patient is measured for the first volunteer at supine position with a Body Mass Index (BMI) of 28.1 where the average and the standard deviation of pressure applied at supine is presented in table 1. It is clearly shown that highest amount of interface pressure for the supine position is applied at the sensor located at Column 3, Row 1 that is positioned exactly at the middle of the patient's sacrum. Moreover, the interface pressure of the middle sensors is much higher that the side sensors, which means that there is higher, amount of pressure applied at the sacrum region in compare with pressure applied at the sides and the pelvis region. It is clearly shown that the pressure distribution for the 15 degrees of

lateral position is different from the interface pressure at supine position. The standard deviation of the collected data across the time is calculated where it is in a range of 1 to a maximum of 2.58 calculated at the sensor located at Column 1, Row 2 of the array.

It is established that the occurrence of pressure ulcers is highly dependent on the duration of the pressure applied at a certain location. Therefore, a repositioning interval of 2-3 hours is suggested by comparing the measured interface pressure with the graph generated by Reswick and Rogers shown in graph 1 [12]. According to this graph and considering the highest pressure point of 110.97 mmHg the patient has to be repositioned in a duration of 2-3 hours as any repositioning interval more than this falls in to the unacceptable region defined by Reswick and Rogers [12].

Table 3: Interface pressure at supine position

Position	Mean pressure at supine position (mmHg)	Standard deviation at supine position
Column 1, Row 1	37.97	2.46
Column 2, Row 1	88.35	2.08
Column 3, Row 1	110.97	2.42
Column 4, Row 1	30.39	2.07
Column 5, Row 1	38.92	2.20
Column 1, Row 2	42.42	2.58
Column 2, Row 2	29.05	2.49
Column 3, Row 2	23.45	2.37
Column 4, Row 2	27.08	2.40
Column 5, Row 2	36.15	2.18

3.2 Investigation on the relationship of lateral repositioning angle and the interface pressure

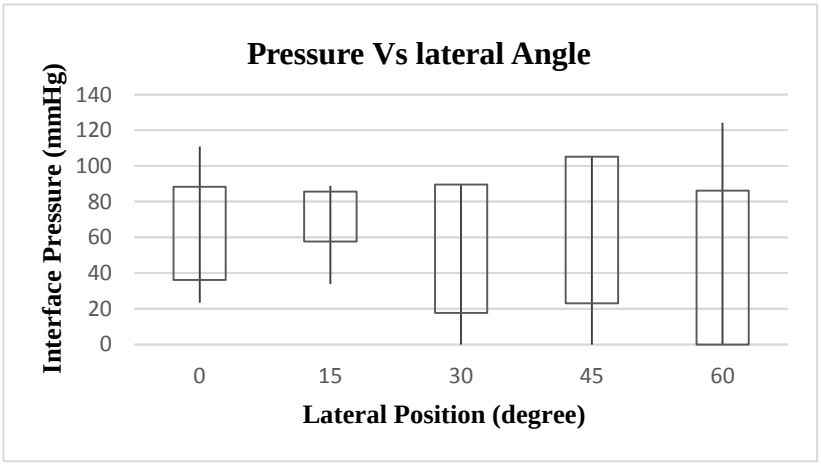
In the second stage of pressure mapping studies the patient is repositioned from the supine position up to 15, 30, 45 and 60 degree of lateral position. This is done to examine the effect of lateral repositioning on the interface pressure between the patient and the supporting surface. The average interface pressure of the supine position and the mentioned lateral positions are plotted in a candlestick graph in order to show the distribution of the pressure at different lateral angles as well as showing the highest pressure experienced by the patient at that certain location. This graph is displayed in graph 8. Based on the presented graph there is no specific pattern between the increase in the larteral position of the patient and the measured interface pressure at different positions. The pressure experienced by the patient at 15 degree of lateral position is mainly distributed from 60 to 80 mmHg with the highest interface pressure of 89 mmHg, which is lower than the highest interface pressure measured at the supine position. On the other hand, the distribution of the pressure at supine position ranges from 40 to 80 mmHg, which means the pressure, is more distributed in compare with the 15-degree lateral repositioning trial.

The interface pressure measured at 30 degrees lateral position is distributed from 15 to 80 mm hg with on high pressure point of 89.6 mmHg at the right side of the pressure-sensing array. This means that the 30-degree trial has a similar maximum pressure point as the 15-degree trial whereas the 30 degree lateral position is showing a better pressure distribution across the sensing array which makes it for favorable in that sense.

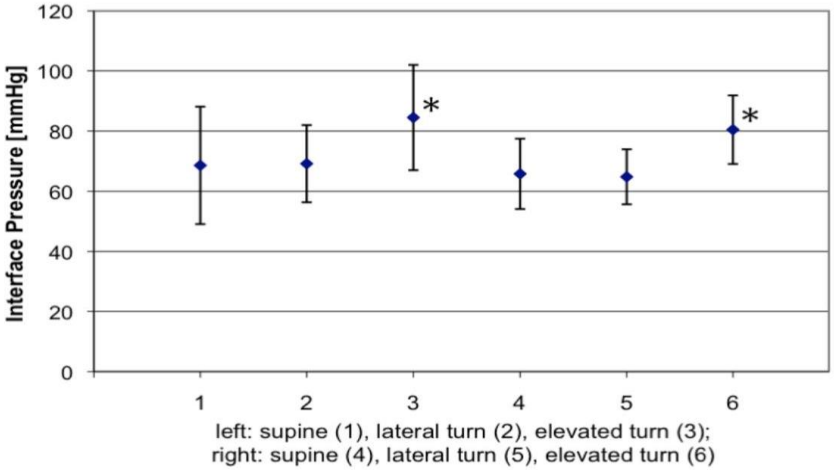
Lastly, the interface pressure measured for the 45 and 60 degrees of lateral rotation shows a maximum pressure point of 105.2 and 124.1 mmHg respectively,

which is higher than the supine, 15-degree and 30 degree of lateral position. According to this measurement, repositioning the patient to such angles may worsen the situation rather than relieving the pressure to prevent pressure ulcers.

According to a study done by James [18] the average interface pressure experienced by the patient at the supine position ranges from 45 to 90 mmHg, which is very similar to the interface pressure measurement done at this experiment. Moreover, the interface pressure is measured for a 30 degree lateral position where in the case of this experiment the patient is repositioned by placing a pillow under the patient in order to elevated the patient to the required position. The pressure measured for the 30-degree lateral turning is shown in graph 2 where it ranges from around 60 mmHg to 84 mmHg. The maximum interface pressure at the lateral repositioning performed by James is very similar to the measurement done at this experiment whereas the distribution of the pressure shown in graph 6 is in a wider range in compare with the measurement done by James. There is no pressure measurement at 15, 45 and 60-degree lateral position reported at this paper. The other 4 bars presented in graph 9 shows the pressure measurement done at upper body elevation which is not related to this experiment.



Graph 2: Interface Pressure-Lateral position relationship



Graph 3: effect of lateral position on interface pressure done by James

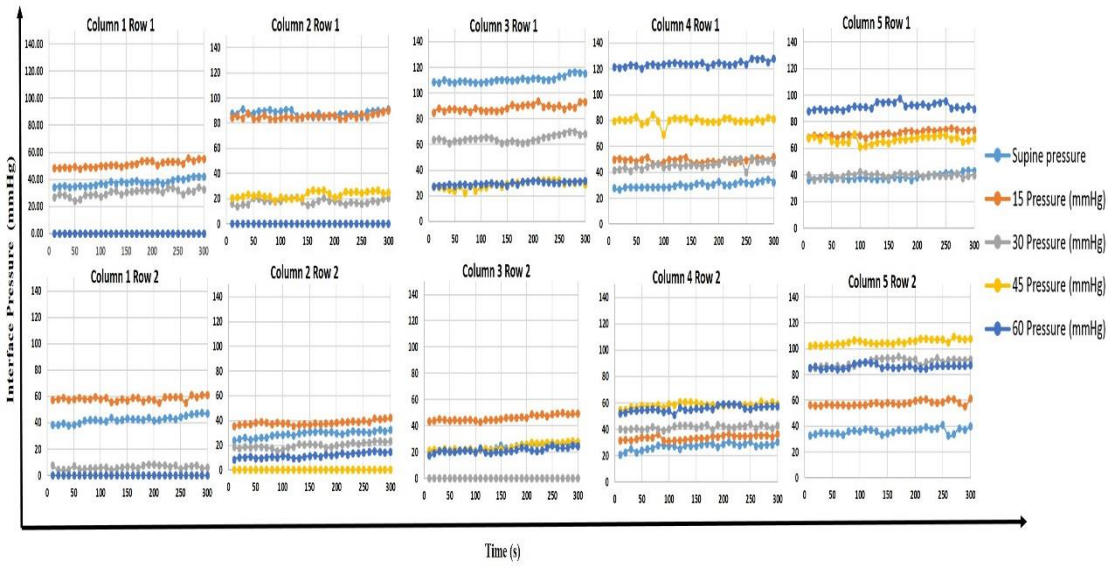
According to a study done by Rosmar et al. [8] pressure mapping study is done for a sample group of 49 healthy individuals where the maximum interface pressure measured at the supine position is reported as 42.8 mmHg for the case of a

standard hospital bed. The maximum interface pressure measured at supine position is higher than the pressure measurement reported at this experiment. This can be due to multiple factors such as the BMI of the patient, type of the mattress and the positioning of the force sensitive array performed at this experiment. Rosmar et al. also performed pressure-mapping study for lateral angles of 30, 60 and 90 degrees where this measurement is done for the shoulder, pelvis and the ankle area rather than the sacrum area of the patient. Nevertheless, lateral position of 30 degrees is preferred in compare with the other lateral angles due to the higher interface pressure reduction achieved at this angle. This proves the higher effectiveness of the 30 degree suggested at the current performed research.

3.3 Investigation on the interface pressure and time

Lastly the effect of time on the applied interface pressure is investigated on all 10 sensors for supine,15,30,35 and 60-degree lateral position in order examine the change in the interface pressure with respect to time. Time dependent interface pressure graph of supine and all the lateral positioning trials is shown in graph 8. As it is shown in graph 8 interface pressure measure at 5 minutes has a linear characteristic where the interface pressure measured for different positioning represents almost a straight line with a minor increase toward the end of the duration of the measurement. This minor change of the interface pressure may be due to the creep error of the sensor which is associated with most of the interface pressure measurement systems [19]. The pressure measured by the sensor exhibits a higher value with an increase in time where in reality there is no change in the interface pressure of the patient and the supporting surface. Creep is basically the distortion of material caused by a lifted temperature as well an excessive static pressure applied for a long duration of time [20]. It is mainly associated with the deformation of the sensor across time where in this case it is due to the static stress applied by the volunteer on to the sensor.

Moreover, slight fluctuations are measured across time, which may be due to the minor movement of the patient during the interface pressure measurement experiment. It is extremely hard to keep the subject of the experiment in a stand still position which is why minor fluctuation are expected across the time of the experiment.



Graph 4: Interface pressure measurement across time

4.4.5 Investigation on the interface pressure and BMI value

The interface pressure measurement is performed for 3 different volunteers from the overweight, average and underweight BMI categories. The Body Mass Index of these volunteers is shown in table 13.

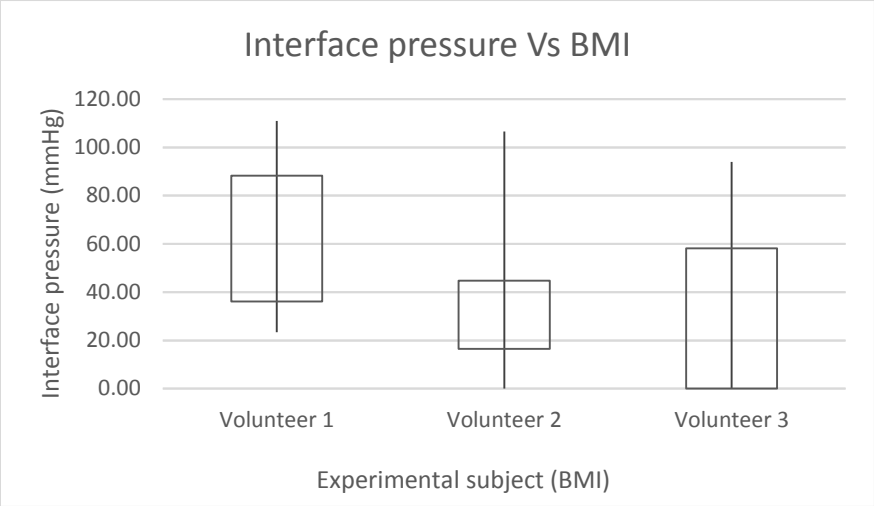
Table 4: Details of the experimental subjects

Experimental Subject	BMI	Wight (kg)	Height(cm)	BMI Category
Volunteer 1	28.1	90	179	Overweight
Volunteer 2	24.2	75	1.76	Average
Volunteer 3	17.96	55	1.75	Underweight

This is done in order to assess the effect of weight and mainly BMI value of the patient on the measured interface pressure. The interface pressure of the volunteers at supine position is shown in graph 9. The interface pressure measured for the third volunteer is done only with the first row of sensors due to the small contact area of the volunteer's buttock.

It is clearly shown that the maximum interface pressure increases with an increase in the value of BMI where in this case the first volunteer experiences a maximum interface pressure of 110.97 mmHg whereas the maximum interface pressure for the second and third volunteers are 106.8 and 94.05 (mmHg) respectively. Moreover, the interface pressure for the first volunteer is distributed at a higher range from 36 to 88.38 mmHg in compare with the second volunteer with a lower BMI which ranges from 16.56 to 44.81 mmHg. Since the height of these volunteers are in a close range, it can be concluded that there is a relationship between the weight the resultant interface pressure of the patient. A similar conclusion is made in a study done by James which shows that the interface pressure and eventually the risk of developing pressure ulcers is dependent on the BMI value of the patient.

This proves the developed measurement performed at the current research done for different BMI values. Qualitative results are only generated due to the small sample size of this experiment. However, measurement is done for 3 different subclasses of Body Mass Index in order to give an insight in the effect of this parameter on the measured interface pressure.



Graph 2: Effect of BMI value on the measured interface pressure

5.0 Conclusion

In a nutshell, a repositioning mechanism was successfully introduced in this research where the proposed components are compatible with the current hospital beds available in the market. A 12-piece mechanism integrated with a 3-piece mattress and an automated power screw are the main components that was presented in this research. The 12-piece mechanism is designed and manufactured according to the available hospital bed dimensions where every piece is dimensioned based on the available upper body elevation and leg elevation in the hospital beds. The repositioning mechanism is then implemented with a special 3-piece mattress that was dimensioned based on the 3 columns of the proposed design. Automatic Power Screw (APS) is proposed in this project in order to perform the repositioning practice by an application of linear force on the connection of the side and the middle plate. As a result of this linear force on the connection of the middle and the left section, the mechanism performs a clockwise rotation whereas with an application of a similar force on the right and middle section an anti-clockwise repositioning is performed. These 3 components are then assembled on to a standard hospital bed in order to assess the compatibility of the proposed designs. `

The repositioning action was successfully performed by repositioning 3 volunteer from supine to 15,30,45 and 60 degree lateral positions. Pressure mapping studies were done using the developed FSR array where measurement was done for a duration of 5 minutes and a sampling rate of 10 seconds for every case of this experiment. The interface pressure of the first volunteer was compared at supine,15,30,45 and 60-degree lateral positions where supine and 30 degree of lateral repositioning were identified as the most suitable options. This was backed up with 2 different literatures on the same area of study where 30 degrees results into the smallest maximum interface pressure as well as a better pressure distribution across the patient's sacrum. Pressure measured at supine position demonstrates its highest value at the middle sensors whereas the pressure measured by the side sensors is in the low margin of the interface pressure. This pressure distribution tends to relocate on to the side sensors with an increment of the lateral angle where the pressure at 30-degree lateral position exhibits the best distribution and relocation of pressure across the study area.

In addition, the effect of time on the applied interface pressure is investigated on all 10 sensors for supine,15,30,35 and 60-degree lateral position in order examine the change in the interface pressure with respect to time. It was concluded that the pressure measured at 5 minutes has a linear characteristic where the interface pressure measured for different positioning represents almost a straight line with a minor increase toward the end of the duration of the measurement. This minor change of the interface pressure may be due to the creep error of the sensor which is associated with most of the interface pressure measurement systems.

Lastly the effect of the BMI value on the interface pressure is investigated for 3 volunteers from 3 different BMI subclasses. It is concluded that the interface pressure increases with an increment in the Body Mass Index of the patient which in this case it is mostly associated with the growth in the weight of the patient.

References

[1] European Pressure Ulcer Advisory Panel and National Pressure Ulcer Advisory Panel (2009). Prevention and treatment of pressure ulcers: quick reference guide. Washington DC: National Pressure Ulcer Advisory Panel.
[2] M. Ciliberti, F. De Lara, G. Serra, F. Tafuro, F. Iazzetta, V. De Martino, A. Filosa, R. Scognamiglio, G. Ciliberti and M. Veneri (2014), 'Effective management of pressure ulcers using Hydrofibre technology with silver ions', *Wound Medicine*, vol. 5, pp. 40-44.

[3] S. Derler, G. Rotaru, W. Ke, L. Issawi-Frischknecht, P. Kellenberger, A. Scheel-Sailer and R. Rossi (2014), 'Microscopic contact area and friction between medical textiles and skin', *Journal of the Mechanical Behavior of Biomedical Materials*, vol. 38, pp. 114-125.
[4] S. Derler and L. Gerhardt (2011), 'Tribology of Skin: Review and Analysis of Experimental Results for the Friction Coefficient of Human Skin', *Tribology Letters*, vol. 45, no. 1, pp. 1-27.

[5] C. Mathewson, M. Nemeth and H. Murray (2000), 'Pressure Ulcers: Interdisciplinary Approach Across the Continuum', *Topics in Spinal Cord Injury Rehabilitation*, vol. 6, no. 1, pp. 91-95.
[6] M. Saleh, J. Qaddumi and D. Anthony (2012), 'An Interventional Study on the Effects of Pressure Ulcer Education on Jordanian Registered Nurses' Knowledge and Practice', *Procedia - Social and Behavioral Sciences*, vol. 47, pp. 2196-2206.

[7] Z. Mallah, N. Nassar and L. Kurdahi Badr (2015), 'The Effectiveness of a Pressure Ulcer Intervention Program on the Prevalence of Hospital Acquired Pressure Ulcers: Controlled Before and After Study', *Applied Nursing Research*, vol. 28, no. 2, pp. 106-113.

[8] R. Ros-Mar and M. Martínez-Gamarra (2011), 'The effect of a double-regression hospital bed on interface pressure', *Applied Nursing Research*, vol. 24, no. 4, pp. e79-e85.
[9] S. Hagisawa and M. Ferguson-Pell (2008), 'Evidence supporting the use of two-hourly turning for pressure ulcer prevention', *Journal of Tissue Viability*, vol. 17, no. 3, pp. 76-81.

[10] Nightingale F (1969). Notes on nursing; 1860 (reprinted by Dover Publications, New York;127). [11] 'Book Reviews : Community Work: Theory and Prac tice: Ed. Philip Evens (various contributors) Alistair Shomach Ltd., Oxford, 2.25', *Probation Journal*, vol. 21, no. 3, pp. 95-95, 1974.

[12] A. Gefen, 'Reswick and Rogers (2009), pressure-time curve for pressure ulcer risk. Part 1', *Nursing Standard*, vol. 23, no. 45, pp. 64-74.

[13] J. Nixon (2006), 'Randomised, controlled trial of alternating pressure mattresses compared with alternating pressure overlays for the prevention of pressure ulcers: pressure relieving support surfaces trial', *BMJ*, vol. 332, no. 7555, pp. 1413-0.

[14] E. McInnes, A. Jammali-Blasi, N. Cullum, S. Bell-Syer and J. Dumville (2013), 'Support surfaces for treating pressure injury: A Cochrane systematic review', *International Journal of Nursing Studies*, vol. 50, no. 3, pp. 419-430.

[15] Z. Moore, S. Cowman and J. Posnett (2013), 'An economic analysis of repositioning for the prevention of pressure ulcers', *J Clin Nurs*, vol. 22, no. 15-16, pp. 2354-2360.

[16] M. Woodhouse, P. Worsley, D. Voegeli, L. Schoonhoven and D. Bader (2015), 'The physiological response of soft tissue to periodic repositioning as a strategy for pressure ulcer prevention', *Clinical Biomechanics*, vol. 30, no. 2, pp. 166-174.

[17] Interlink Electronics. (2014). *FSR 400 series data sheet*, Camarillo, USA: Interlink Electronics Incorporation, Force Sensitive Resistor Research Centre.

[18] M. James Peterson, 'Pressure ulcer prevention research', Doctor of philosophy, University of Florida, 2009.

[19] A. Abdul Razak, A. Zayegh, R. Begg and Y. Wahab, 'Foot Plantar Pressure Measurement System: A Review', *Sensors*, vol. 12, no. 12, pp. 9884-9912, 2012.

[20] Madoum. Mems fabrication.In the mems handbook; Crc press: Bocaraton,Fl, USA, 2001.

EURECA 2015 – Conference Paper
Paper 2ME17

CFD Simulation and Experimental Correlation for Fluid Flowing in Different Pipe Designs

Wei Tar Tan[1], Chin Hong Lim[2*], Kim Haw Yap

[1,2]*School of Engineering, Taylor's University, Malaysia*

[3]*Panasonic Appliances Air-Conditioning R&D Malaysia Sdn. Bhd. (PAPARADMY1)*

*ChinHong.Lim@taylors.edu.my

Abstract

Air-conditioning and refrigeration system is one of the greatest engineering inventions in the 20th century as it can provide cooling load and make people feel comfortable even during summer time. There are four main components in an air-conditioning system, namely the compressor, condenser, evaporator and expansion valve. Many researches have been done on the heat exchanger, but not much study was done previously on discharge tube that serves to transport refrigerant from the compressor to the condenser. In this research, CFD simulation was performed on the discharge tube using realizable k-ε turbulence model with Enhanced Wall Treatment to model the turbulent flow and solve for the boundary viscous sub-layer. Water was used in this study because of the ease of experimental handling and it is a simple representation of the refrigerant which is assumed to be incompressible within the normal working range of temperature and pressure. Mass fluxes between 1000 kg/m^2s to 1500 kg/m^2s were simulated for the pressure losses. Theoretical calculation and simulation result shows a good agreement with a maximum deviation of 12.25% for the working mass flux range. Simulation was able to predict all of the experimental data within a maximum deviation of 7.61%. The recovery length was studied numerically and found to be located at approximately 30D as the pressure loss per unit length at further location only deviates by 0.65%. It was found that the highest turbulent kinetic energy is located at Bend 2, and contributes to the highest pressure loss per unit length. Meanwhile, sections after Bend 4 generally suffer from higher pressure loss per unit length, and these sections together with Bend 2 should be considered for design improvement.

Keywords: CFD simulation, Pressure loss, Discharge tube, Air-conditioner, Water

1. Introduction

An air-conditioner is a common household electrical appliance especially in countries with warm climate like Malaysia, Singapore and Indonesia. An air-conditioner provides space cooling which decreases the surrounding temperature and humidity while at the same time increasing the comfort of the people staying in the zone. It was quoted as the tenth greatest engineering achievement of the twentieth century as most people could hardly live comfortably without an air-conditioner nowadays especially during the summer time [1].

An air-conditioner consists of four major components, namely the compressor, condenser, expansion valve and evaporator. The compressor does work on the refrigerant by compressing vapour to high temperature and high pressure. The vapour flows to the condenser and this is the component where a fan is used to cool down the refrigerant into liquid form. Through the expansion valve, the pressure of the liquid refrigerant is reduced and its temperature drops as well. Low temperature refrigerant flows through the evaporator where it absorb enthalpy from the surrounding and changes its phase back to vapour again due to boiling, before going back to the compressor[2].

The components in an air-conditioner are connected using copper tubing due the ductile characteristic which allows it to be bent into different shapes easily. Numerous studies have been done by researchers on the condenser and evaporator, also known as the heat exchangers, regarding the heat transfer performance and pressure drop across the components. However, there are limited studies that had been done on both the discharge tube and suction tube of the compressor. The suction tube draws the refrigerant from the evaporator into the compressor, while the discharge tube transports the compressed refrigerant to the condenser for heat exchange.

In 1992, Paliwoda [3] has conducted a research to find out a general method that is capable of predicting the frictional pressure loss across common piping components such as bends, T-junctions, valves etc. His method was proven able to predict the pressure loss in most of the piping components with all kinds of refrigerant used in refrigeration cycles at various operating temperatures. Later, Chen *et al.* [4] conducted an experiment to study the frictional pressure loss in U-bend using R-410A refrigerant. The effects of diameter and curvature ratio of the U-bend were studied and the experimental result was compared the existing correlations. Experiment outcome showed that the frictional factor that contributed to the pressure loss showed an increasing trend when the curvature ratio was decreased. For single-phase flow, the experimental result was compared with three existing correlations [5][6][7] which showed a fair agreement among these results with highest mean deviation of 30.8%.

Domanski and Hermes [8] attempted improve the correlation for two-phase pressure drop for R-22 and R-410A refrigerants in U-bend by conducting experiments in pipes with different inner diameter, bending radius and curvature ratio. They have compared their experimental results with several researchers, including Chen *et al.* [4] mentioned previously, and their results showed dissimilar trend at segments with high vapour quality. The Chen *et al.* correlation showed a linear increasing trend of pressure drop with vapour quality while the new correlation proposed by Domanski and Hermes indicated that the pressure drop would continue to increase

up to vapour quality ≈ 0.8, after which the pressure drop would start to decrease until the fluid is fully saturated vapour. They explained this phenomenon due to the reduction of interference between the liquid and vapour phases when the liquid adhering to the wall became thinner as the vapour quality increases. Despite these differences, the proposed new correlation was shown able to predict 75% of the experimental data points with root mean square deviation of 25% for all data points [8].

Silva Lima and Thome [9] have proposed another prediction model that gives a better prediction results. The authors have studied similar experiments performed by previous researchers and have pointed out some factors that were not considered before, including the decrease of saturation temperature which leads to the increase of viscosity, orientation of the straight pipe and U-bend, and the flow pattern in the pipe. In order to account for the factors stated above, the authors have suggested a new modelling method for each of the flow pattern under different geometry orientations. This new model was able to predict more than 93% of the data in the database, with a deviation of ±30%. Later on, the authors conducted another experiment using similar experimental setup and successfully improved the prediction model to predict 97% of the results with a deviation of ±30% [10].

Some researchers have investigated other possible methods to reduce the pressure loss in a U-bend. Chen *et al.* [11] have performed an experiment to study the effect of lubricating oil concentration on the pressure drop across the U-bend. In this experiment, the internal diameter and the curvature ratio of the U-bend was fixed, so that the effect of lubricating oil concentration could be investigated. It was found that the oil concentration does not significantly affect the pressure drop, and it only became more noticeable at high vapour qualities. This finding was supported by Wen and Ho [12] as they have performed similar experiment that assessed the effect of oil concentration on pressure drop. Besides that, Wen and Ho [12] also found that the pressure loss would increase when there are more number of tube bends in the system.

On the other hand, Tran *et al.* [13] studied the effect of void fraction on the pressure drop along a straight tube and U-bend. Void fraction is the amount of vapour pocket over a cross-sectional area whereby 0 indicates a fully liquid filled channel and 1 represents a fully gas-occupied channel. Several parameters have been considered in this experiment, including the mass flux and vapour quality, while the inner diameter and inlet temperature of the test section are maintained constant. Experiment outcome showed that the effect of void fraction in the straight pipe was negligible. In addition, it was found that the increase of mass flux had resulted in the increase of pressure loss, and the pressure loss increases when the vapour quality increases as well. Also, orientation of the test section seemed to have significant effect on the pressure loss where it was found that a downstream to upstream flow orientation results in a higher pressure loss.

Apart from studying the effect of mass flow rate, tube diameter and curvature ratio on the pressure loss in the U-bend, Padilla *et al* [14] have also identified the required recovery length of the flow in a tube. The recovery length is determined by calculating the pressure loss per unit length where the flow is considered recovered when the rate of change of pressure with respect to length becomes constant. They have determined that the recovery length could be located before 20 *D*, where *D* denotes the hydraulic diameter, as the pressure losses at 20 *D* and 50 *D*

only deviate by 5%. However, results of the study from Kerpel *et al.* [15] did not agree with Padilla *et al.* [14]. Through their experiments, the flow was found yet to be fully developed at 30*D* after the bend. It is then believed that the rate of change of pressure loss with respect to length would continue to increase as the flow has not fully developed yet. This contradiction in results could be due to the different type of refrigerants and mass flux tested in the experiments.

Other than experimentation works, some researchers have assessed the pressure loss numerically, e.g. with Computational Fluid Dynamics (CFD) which uses discretization algorithms to analyse and solve for the fluid flow domains. Zhang et al. [16] have performed a CFD analysis on particle deposition in a curved pipe and they have compared the results with existing experimental result and established correlations. Standard k-ε model and linear pressure-strain Reynolds Stress Model (RSM) were compared and the RSM model was found to perform much better than the standard *k-ε* model. The standard *k-ε* model is a turbulence model proposed by Launder and Spalding [17], which is a semi empirical formula that models the transport equation with turbulence kinetic energy, *k*, which is obtained from an exact equation, and the turbulence energy dissipation rate, *ε* is modelled based on physical reasoning. The RSM on the other hand was introduced by Launder et al. [18] which solves for the Reynolds stresses together with the dissipation rate. The author found that by using Enhanced Wall Treatment (EWT) by combination with RSM model, the accuracy of the result predicted for a U-bend could be improved by up to 30% when compared with near-wall treatment on the pipe wall.

A single-phase water, oil and air pressure drop experiment and simulation performed by Edvardsen *et al.* [19] for a downhole shut-in valve was a good example to be studied for this project. Edvardsen *et al.* have studied their experiment using three turbulence models, namely the standard *k-ε* model, the RNG *k-ε* model, and lastly the realizable *k-ε* model. The RNG *k-ε* model was proposed by Orszag *et al.* [20] and it includes several refinement from the standard *k-ε* model including the introduction of an additional term in the *ε* equation which improve the accuracy of rapidly strained flow and provides an analytical formula for the turbulent Prandlt numbers instead of a constant value in the standard *k-ε* model. On the other hand, the realizable *k-ε* model proposed by Shih *et al.* [21] differs from both standard and RNG models that it satisfies certain mathematical constraints on the Reynolds stresses, and it conforms to the physics of turbulent flow. Three type of single-phase flow were examined, but only the water single-phase flow will be discussed since it is most related to this project. At a highest mass flow rate of 10 *kg/s*, the CFD result showed a deviation of only -6.1% from the experimental result using the realizable *k-ε* turbulence model. Though the result of other turbulence models were not mentioned in the journal, the realizable *k-ε* turbulence model was said to give the closest result to experimental value comparing with other models.

Most of the studies are done using refrigerant as the transport medium while limited studies have been done to assess the performance of water in a return bend. This is probably because refrigerants are commonly used in real life application with return bends such as in heat exchangers. The pressure loss in a pipe is known due to several factors, including the fluid viscosity, fluid density, flow velocity, elevation, pipe fittings, pipe length, hydraulic diameter and temperature.

For an experiment using the same discharge tube, the physical geometry parameters such that the hydraulic diameter and pipe length are constant. Besides, by conducting experiment at room temperature, the heat transfer through discharge tube pipe wall is assumed to be negligible. The main differences between refrigerant and water flowing in a pipe would be their respective fluid density and fluid viscosity. Water is considered as an incompressible fluid due to the negligible change of its volume when subjected to a change in pressure.

During operation, at ambient temperature of 50°*C*, the actual pressure of compressor outlet is about 1.8 *MPa* [22]. Under the same pressure of 1.8 *MPa*, and with refrigerant R-22, the density of the refrigerant at the pipe inlet would be 76.923 kg/m^3 [23]. Using the Domanski and Hermes [8] experimental result, the expected pressure loss through the discharge tube is estimated to be 4.25 *kPa* under the boundary condition of mass flux = 200 kg/m^2s, D = 5 *mm* and bending radius = 10 *mm*. With a small pressure drop of 4.25 *kPa*, the refrigerant density at the pipe outlet would become 76.647 kg/m^3, which is 0.358% in difference. Due to the small pressure gradient along the pipe, the refrigerant vapour is assumed to be incompressible. In addition, the viscosity of the refrigerant can be treated as a constant as well because the temperature change through the discharge tube is negligible. Therefore, water, which is an incompressible liquid, is substituted to be used for the experiment and simulation work of this study, and a correction factor, *C* can be implemented to account for the differences between the refrigerant and water pressure losses.

This research aims to correlate the result produced through the actual experiment and simulation, so that the simulation method can be employed for study in the future. Besides, the effect of the length of U-bend on the pressure loss will be studied as well. This is a collaborative project with the Panasonic Appliances Air Conditioning R&D Malaysia group (PAPARADMY1) to analyse and understand the flow behaviour of the current discharge tube design, and the knowledge gained from this project will be used to produce a better design of air-conditioner discharge tube with greater performance, lower cost of production and higher efficiency.

2. Research Methodology

2.1 Geometry Modelling and Theoretical Calculation

The schematic of the fluid of the original design of the discharge tube is shown as follows:

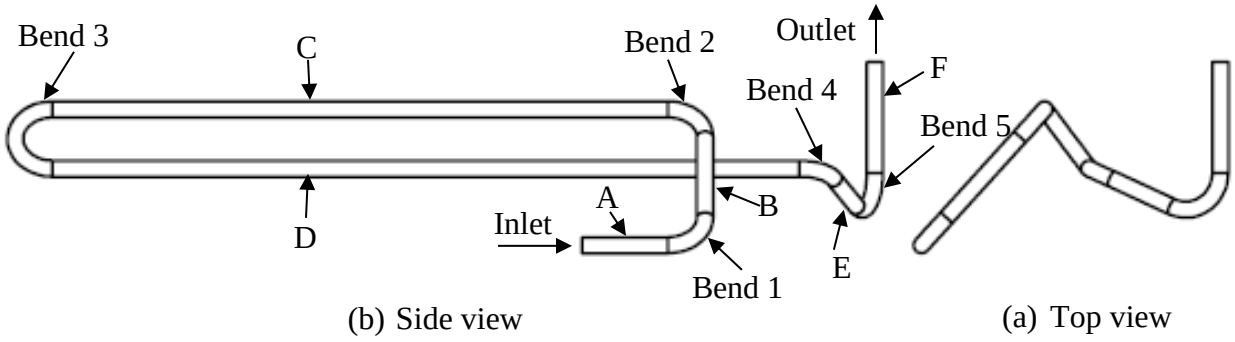


Figure 1. Schematic of the discharge tube fluid.

The empty channel of the discharge tube is modelled because only the fluid flowing in the tube is of interest for the CFD simulation.

The theoretical pressure loss across the discharge tube can be calculated using the Bernoulli's equation as shown below:

$$P_1 + \frac{1}{2}\rho V_1^2 + \rho g h_1 = P_2 + \frac{1}{2}\rho V_2^2 + \rho g h_2 + P_{loss} \quad (1)$$

Since the pressure difference is of interest, P_2 is taken as 0 *Pa* as a point of reference. The inlet velocity, v_1 and outlet velocity, v_2 are the same because there is no change in hydraulic diameter. Density, ρ and gravitational acceleration, g are constant as well. The frictional pressure loss, P_{loss} can be further divided into pipe major loss, $P_{l\text{-}major}$ which is due to the surface roughness of the pipe, and the pipe minor loss, $P_{l\text{-}minor}$ which is the pressures loss due to pipe geometry, i.e. bends. $P_{l\text{-}major}$ can be calculated using the *Darcy-Weisbach* equation as follows:

$$P_{l-major} = f\frac{l}{D}\frac{\rho V^2}{2} \quad (2)$$

This equation is only applicable to turbulence flow, which is Reynolds number > 10000:

$$Re = \frac{\rho V D}{\mu} \quad (3)$$

$P_{l\text{-}major}$ is also affected by the interval surface relative roughness:

$$Relative\ roughness = \frac{\varepsilon}{D} \quad (4)$$

The coefficient of friction, f can be obtained from the *Moody* chart with the known *Re* and relative roughness. On the other hand, $P_{l\text{-}minor}$ can be calculated by using the following equation:

$$P_{l-minor} = K_L\frac{\rho V^2}{2} \quad (5)$$

where K_L is the loss coefficient.

The final Bernoulli's equation for the discharge tube flow would be:

$$\Delta P = \rho g(h_2 - h_1) + \frac{\rho V^2}{2}\left(f\frac{l}{D} + K_L\right) \quad (6)$$

2.2 Meshing

Prior to deciding on the meshing method, both tetrahedron mesh and hexahedron mesh were assessed for the effect of meshing methods on the outcome of results.

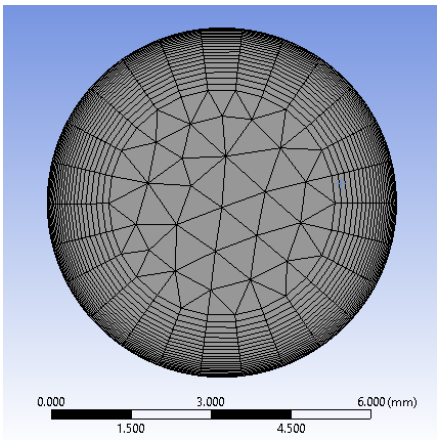


Figure 2. Tetrahedron mesh.

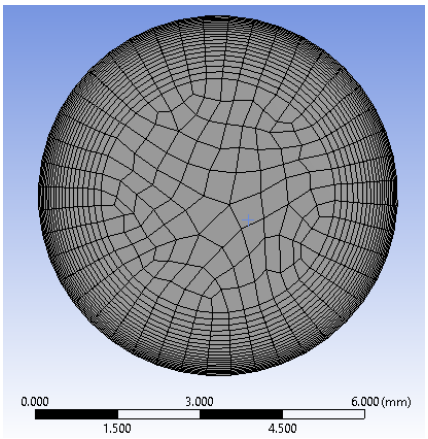


Figure 3. Hexahedron mesh.

In order to analyse the viscous flow on the near wall section of the pipe, a combination of fine and dense meshes are generated for the model. Generating fine mesh throughout the whole model would cause the total number of cells to be too high and as a result the total computational time will be long as well. To solve this issue, the inflation method is introduced into the model where the mesh generated would be the finest at the wall boundary, and increases in size at a constant rate of 1.1 towards the centre of the flow. The grow rate of inflation was set to 1.1 so that there is a smooth transition between the cells for a more accurate result.

The quality of mesh should always be assessed before proceeding to simulation stage. A good quality of mesh can produce a more accurate result and it can converge more easily. The quality of mesh can be assessed from several factors, one of the most important factors is the skewness. The skewness of mesh can be simply explained as the difference between the generated cell and the optimum cell in terms of the angle, with 0 = perfect quality and 1 = bad quality. Generally, the skewness value of <0.95 is applicable to most of the cases [24].

The flow model input of simulation required wall $y^+ \approx 1$ in order to the model the viscous sub-layer of the flow model. Different mass flux simulation requires different thickness of the first cell to achieve wall $y^+ \approx 1$. Therefore, for each different mass flux, the inflation layers are adjusted accordingly to fulfil the flow model criteria. It was found that the hexahedron mesh produces less cells as compared to tetrahedron mesh, thus the computational time is much shorter as well, while they are able to produce similar result.

2.3 Simulation Setup

A three-dimensional, steady state, incompressible hydrodynamic of fluid flowing in a copper discharge tube was simulated using ANSYS 15.0 FLUENT software program. The Lagrangian flow model was used to calculate the governing equations, including the mass balance continuity equations, Navier-Stokes equation, and two equations for the turbulence model. The energy equation is not switched on because there is no thermal mixing in the fluid, and the heat flux through wall is assumed to be negligible. The equations involved are shown as follows [25]:

Mass balance continuity equation:

$$\nabla \cdot (\rho \vec{v}) = 0 \tag{7}$$

Navier-Stokes equation:

$$\rho \vec{v} \cdot \nabla \vec{v} = \mu \nabla^2 \vec{v} - \nabla P \tag{8}$$

Realizable *k*-*ε* turbulence transport equation for turbulence kinetic energy, *k* and hydrodynamic dissipation, *ε* [20]:

$$\frac{\partial}{\partial t}(\rho k) + \frac{\partial}{\partial x_j}(\rho k u_j) = \frac{\partial}{\partial x_j}\left[\left(\mu + \frac{\mu_t}{\sigma_k}\right)\frac{\partial k}{\partial x_j}\right] + G_k + G_b - \rho\varepsilon - Y_M + S_k \tag{9}$$

And

$$\frac{\partial}{\partial t}(\rho \varepsilon) + \frac{\partial}{\partial x_j}(\rho \epsilon u_j) = \frac{\partial}{\partial x_j}\left[\left(\mu + \frac{\mu_t}{\sigma_\varepsilon}\right)\frac{\partial \varepsilon}{\partial x_j}\right] + \rho C_1 S_\varepsilon - \rho C_2 \frac{\varepsilon^2}{k+\sqrt{v\varepsilon}} + C_{1\varepsilon}\frac{\varepsilon}{k} C_{3\varepsilon} G_b + S_\varepsilon \tag{10}$$

where

$$C_1 = \max\left[0.43, \frac{\eta}{\eta+5}\right], \eta = S\frac{k}{\varepsilon}, S = \sqrt{2S_{ij}S_{ij}}$$

In addition, the enchanced wall treatment function was employed because it is best suited for the Realizable *k*-ε turbulence model [24]. The enhanced wall treatment function provides a better solution to resolve the viscous sublayer, which is typically at the first cell adjacent to the wall boundary. The y^+ of the first cell is suggested to be approximately 1, in order for the enhanced wall treatment to function at its optimium. The wall y^+ is a dimensionless measure of the distance from the wall. In fluid mechanics, any fluid moving along a boundary would have a vicsocity effect, and this is also commonly known as the no-slip condition of fluid, which states that any viscous fluid would have a zero velocity relative to the boundary. The enhanced wall treatment function and the measurement of wall y^+ value would help to model this no-slip condition and make the simulation more accurate.

Liquid water was set as the working fluid for this simulation, with default density of 998.2kg/m^3 and dynamic viscosity of 0.001003 *kg/m·s*. Boundary condition was set such that the inlet has a mass flow rate of 0.03333 *kg/s* to 0.125 *kg/s*, with 5% of turbulence intensity and hydraulic diameter, d_h of 6.54 *mm*. While for the outlet, it was defined as the pressure outlet with gauge pressure of 0 *Pa*, 5% of back flow turbulence intensity and d_h of 6.54 *mm*. The heat flux of the wall was set as zero as the heat transfer from the fluid to wall is assumed to be negligeble. For simulation of steady state condition for the fluid, a pressure-based solver was employed using the COUPLED scheme to compute for the pressure-velocity coupling. Pseudo transient was activated as well to solve for the flow. The residual of the solver, which represents the convergence, was set as 10^{-3} for continuity, while the convergence criteria for the velocity at all three axis, *k* and *ε* was set as 10^{-4}.

2.4 Experimental setup

The experimental test rig was constructed to validate the simulation result. Water is supplied to the test rig through a water pump which can supply a maximum pressure head of 3*m*. The mass flow rate of the system is measured and controlled using a rotameter with maximum mass flow rate of 20 *L/min* and accuracy of ±3%. Differential pressure sensor of ±0.2% accuracy is used in this test rig because only the pressure drop across the test section is of interest. The sensor is then calibrated to obtain a general equation for the calculation of differential pressure based on the voltage output. Schematic of the experiment test rig is shown in Figure 4 below:

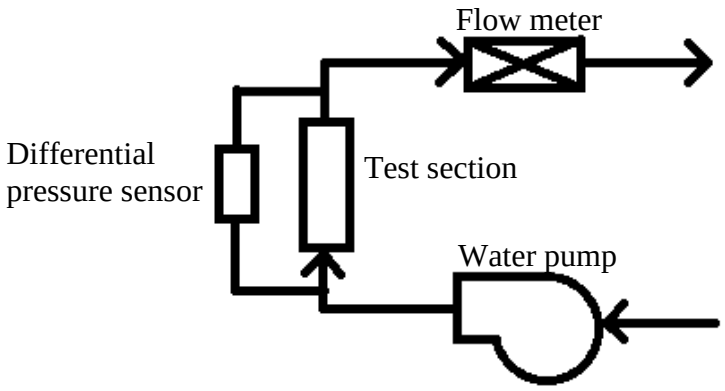


Figure 4. Schematic of experimental test rig.

3.0 Results and Discussion

3.1 Theoretical Calculation and CFD Simulation Comparison

The theoretical pressure drop of water across the discharge tube was calculated using Eq. (6), with the following parameters and assumptions:

Gravitational acceleration, $g = 9.81\ m/s^2$ Density of water, $\rho = 998.2\ kg/m^3$
Length, $l = 0.7\ m$ Hydraulic diameter, $D = 0.00654\ m$
Elevation, $h_2 - h_1 = 0.119\ m$ Pipe component loss coefficient, $K_L = 1$
Friction factor, $f = 0.0242 \sim 0.034$ as obtained from *Moody* diagram
Flow velocity, $v = \dot{m}/A$ where $\dot{m}$ = mass flow rate and A = cross sectional area
Dynamic viscosity of water, $\mu = 0.001003\ kg/m{\cdot}s$

Both the theoretical and simulation results show an increasing trend where the increase of mass flux would result in more pressure loss. The general trend shows an increasing gradient of pressure loss over the mass flux which indicates that the pressure loss would further increase at a higher rate after the tested maximum mass flux, and this agrees with the findings of Tran *et al.* [13]. In general, the theoretical calculation obtained a higher pressure loss result as compared to the simulation result with a maximum deviation of 12.25%. Then, trend of result intersect at approximately 1500 kg/m^2s, in which after this point, it is expected that the simulation result would predict a higher value as compared to theoretical calculation. The exist of marginal error between the theoretical calculation and the simulation result could be due to that the pipe component loss coefficient, K_L that is found from [26] being different from the actual discharge

tube, as the discharge tube diameter is different from the commonly used pipe diameters. Figure 5 below shows the result comparison between the theoretical calculation and simulation result.

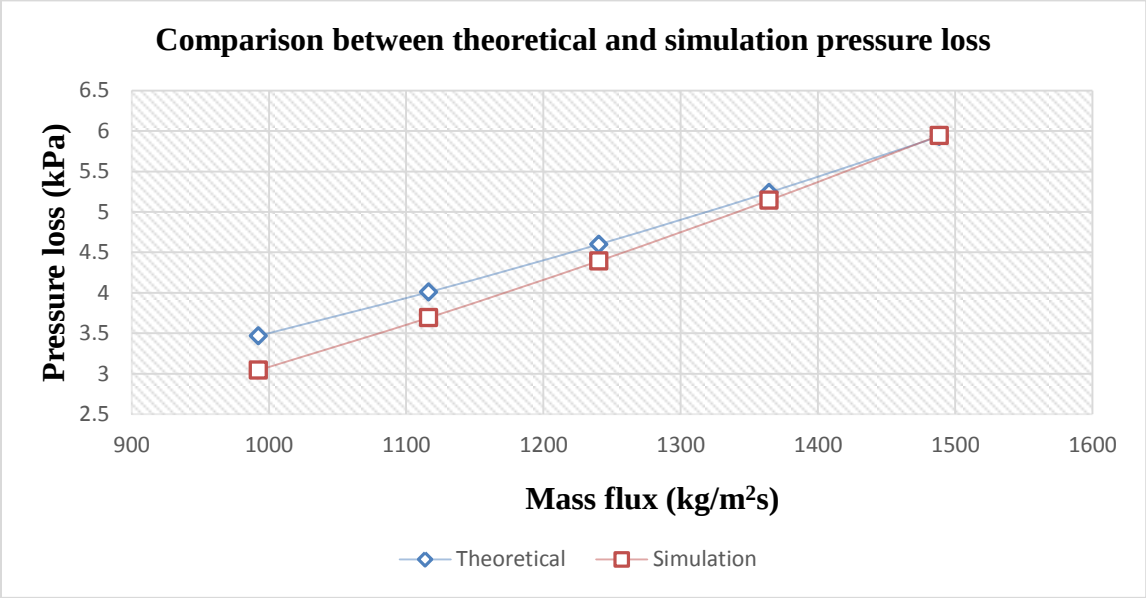


Figure 5. Pressure drop against mass flux for theoretical and simulation result.

3.2 Correlation between Simulation and Experimental Result

The experimental result is then compared with the simulation result, as shown in Figure 6 below. In general, the trend of pressure loss data obtained from the experiment agree with the simulation result with a maximum of 5.05% deviation. With this result, it is confident to state that for a mass flux of 992.28 kg/m^2s to 1488.42 kg/m^2s, the simulation study is able to predict the actual pressure loss of water inside the discharge tube. This shows that the simulation model used is capable of predicting actual pressure loss of water with a maximum deviation of 5.05%.

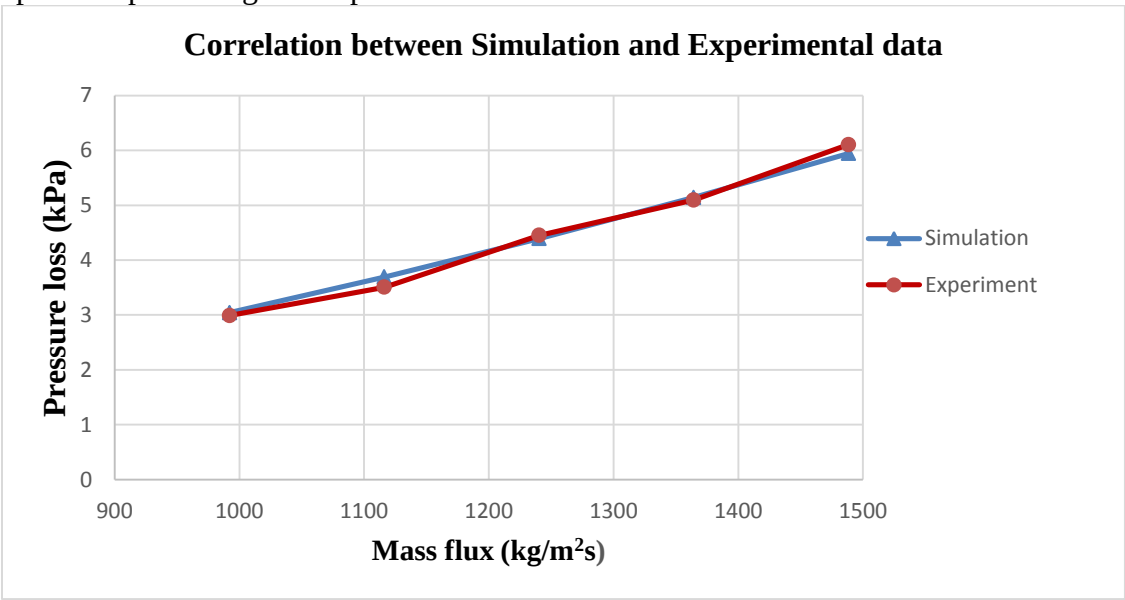


Figure 6. Correlation between simulation and experimental data.

3.3 Parameter study

Three discharge tubes of different length of section C were designed. i.e. 135*mm* $\approx$ 20*D*, 205*mm* $\approx$ 30*D* and 280*mm* which is the maximum allowable length for a discharge tube due to assembly constraint. The three discharge tube designs were tested experimentally as well, in order to verify the simulation result. Experimental data shows that the simulation result conforms to the experiment outcome. For the discharge tube with 150*mm* of section C length, the experimental data generally shows a higher pressure loss as compared to the simulation result, with a maximum of 7.6% deviation at mass flux of 1240.3 kg/m^2s. On the other hand, for the 220*mm* discharge tube, it shows that the experimental result is higher than the simulation by a margin of maximum 6.05% up to 1240.3 kg/m^2s, then the experimental result drops and lack behind the simulation result by 6.36% at maximum mass flux. Lastly, the 280*mm* discharge tube shows a higher outcome at minimum mass flux, with 6.14% of result deviation. Then, the trend of experimental result drops and fall behind the simulation outcome by 4.66% at maximum mass flux.

In general, the simulation model is capable of predicting the experimental outcome, with a maximum deviation of 7.61% from the experimental data. The error window of -6.36%~7.61% could be due to the parallax error when controlling the mass flux using the rotameter. Parallax error occurs when the eye level of the observer is not in-line with the scale of the rotameter and the float inside, which would result in inaccurate flow rate set for the experiment. Nonetheless, in overall, the simulation model is able to predict the pressure loss trend in the discharge tube accurately, with a maximum deviation of 7.61%. The comparison of simulation and experimental data is shown in Table 1 below:

Table 1. Comparison between simulation and experimental result for three discharge tube designs.

Mass flux (kg/m^2s)	**135*mm* discharge tube**			**205*mm* discharge tube**			**265*mm* discharge tube**		
	Sim. (*kPa*)	**Exp. (*kPa*)**	**Result difference (%)**	**Sim. (*kPa*)**	**Exp. (*kPa*)**	**Result difference (%)**	**Sim. (*kPa*)**	**Exp. (kPa)**	**Result difference (%)**
992.3	2.353	2.389	1.527	2.768	2.920	5.490	3.128	3.320	6.141
1116.3	2.853	2.950	3.381	3.358	3.369	0.330	3.795	3.798	0.078
1240.3	3.393	3.652	7.608	3.995	4.237	6.050	4.516	4.524	0.187
1364.4	3.972	4.012	1.022	4.677	4.383	-6.279	5.287	5.012	-5.208
1488.4	4.590	4.651	1.338	5.404	5.061	-6.361	6.111	5.826	-4.656

By changing the length of section C, the pressure loss across the discharge tube changes significantly. A reduction of section C length by 0.045*m* will result in reduction of pressure loss by 9.09%. Further reduction of section C to a length of 0.135*m* will result in an overall pressure loss reduction of 22.80% from the original design. On the other hand, an increment of 0.015*m* of length on section C only causes the pressure loss to increase by 2.79%. It is believed that the flow in the original design has reached a fully-developed condition at the end of section C, therefore further increment of length of section C will cause the pressure loss to increase by a smaller fraction. From the result shown in Table 2, decreasing the length of section C shows to effectively decrease the pressure loss. However, decreasing the length of section C will increase the overall stiffness of the discharge tube. The stiffness of the modified discharge tube should be assessed in the future to ensure that it is fit for purpose.

The 265 *mm* length of Section C discharge tube was taken to be studied for its recovery length, because it is the longest discharge tube sample. The average pressure at an equivalent distance of approximately 3*D* are taken to calculate the average pressure loss per unit length, dP/dL, in order to assess the location where the flow is fully-redeveloped. The flow is considered to be fully-redeveloped when the change of dP/dL becomes constant. It was determined that the dP/dL becomes constant starting from 28*D*. Therefore, it can be concluded that the recovery length is located at about 30*D*, which agrees with the finding of Kerpel *et al.* [15].

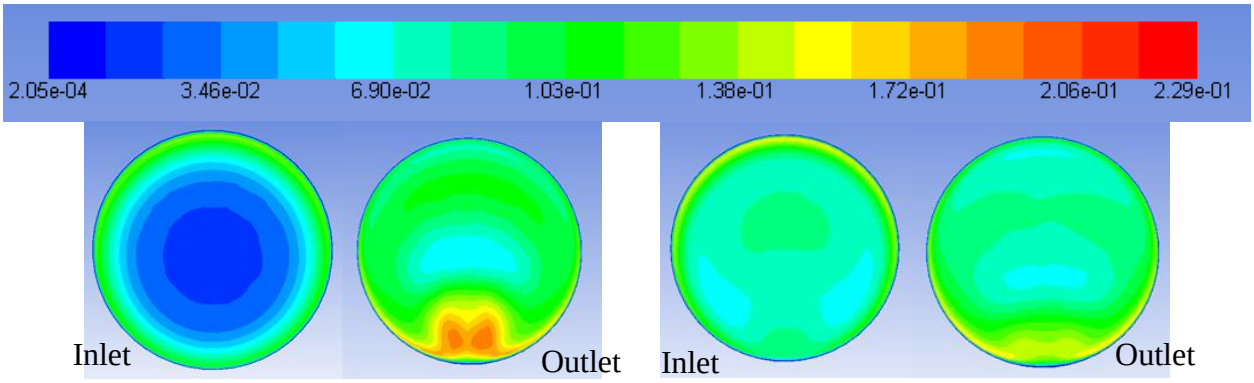
Table 2. Effect of section C length on overall pressure loss.

Mass flux (kg/m^2s)	**Section C length (m)**	**Overall pressure loss (kPa)**	**Percentage of difference (relative to original design)**
992.3	0.135	4.590	-22.80
992.3	0.205	5.404	-9.09
992.3	0.25 (Original design)	5.945	-
992.3	0.265	6.111	2.79

3.4 Flow Characteristics in Discharge Tube

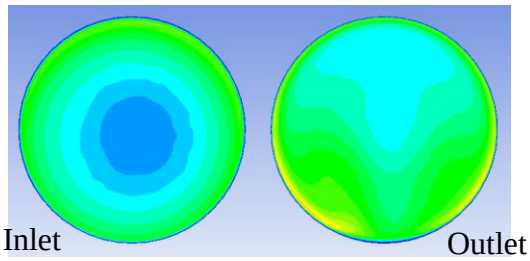
The pressure loss in a pipe is due to the excessive turbulent flow which resulted in energy loss in the pipe flow. By examining the turbulent kinetic energy in the discharge tube, it is possible to find out the critical areas that contributes to high pressure loss. From Figure 7, a common phenomenon that can be observed is that the turbulent kinetic energy at the near wall boundary is usually higher than the core. This is because for a turbulent flow, chaotic eddies and vortices are formed at near wall boundaries, and they act as obstructions to the main flow. As a result, kinetic energy in the fluid is lost in terms of pressure drop to overcome these obstacles.

For Bend 1, prior to entering the bend, it can be seen that the flow is fully-developed as it shows a smooth progression of very low turbulent kinetic energy at its core towards a higher turbulence at the boundary. After exiting the Bend 1, the flow has a high turbulence at the inner bend side, and this phenomenon can be seen in all the other bends as well, where it is most significant for Bend 1 and Bend 4. On the other hand, the inlet of both bend 3 and bend 4 show rather similar flow pattern as the inlet of Bend 1, which indicates that flow has recovered to a more developed flow after travelling along a straight tube. Lastly, after the flow exits Bend 4, it appears to remain at a high chaotic flow towards the outlet.

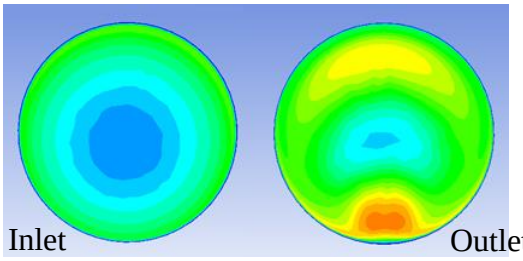


(a) Bend 1 (b) Bend 2

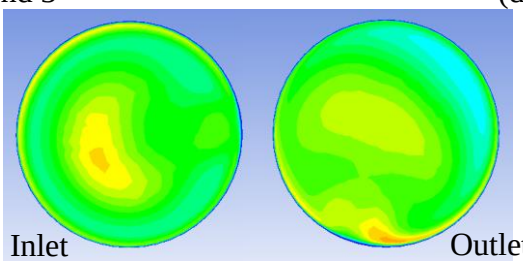
(b)



(c) Bend 3



(d) Bend 4



(e) Bend 5

Figure 7. Turbulent kinetic energy contour of the pipe bends.

In general, all the bends in the discharge tube are having larger pressure loss per unit length than the straight tube section as presented in Table 3 below. Bend 2 suffers from the highest pressure loss per unit length with 11.071 *kPa/m.* Section C and Section D experience the largest pressure loss with 1.554*kPa* and 1.839*kPa* respectively due to their longest section length in the discharge tube. However, the pressure loss per unit length of both Section C and Section D are the lowest, with only 6.215 *kPa/m* and 6.065 *kPa/m* respectively, and this is most probably due to that the flow has been fully-redeveloped. From Bend 4 onwards, the pressure loss per unit length is significantly higher than the previous sections, mostly probably due to that the recovery lengths are short, and the flows are not fully-redeveloped yet. Design improvement should focus on the Bend 2 section, as well as Bend 4 onwards as these sections suffer from the highest pressure loss per unit length.

Table 3. Pressure loss per unit length in discharge tube for mass flux = 1488.4 kg/m^2s.

Section	**A**	**Bend 1**	**B**	**Bend 2**	**C**	**Bend 3**
ΔP (*kPa*)	0.218	0.241	0.309	0.261	1.554	0.476
ΔP/ΔL	6.231	10.216	6.965	11.071	6.215	10.103
Section	**D**	**Bend 4**	**E**	**Bend 5**	**F**	
ΔP (*kPa*)	1.839	0.196	0.208	0.321	0.322	
ΔP/ΔL	6.065	10.501	7.319	10.836	7.200	

4.0 Conclusion and Future Work

This paper presents the studies on the correlation of experimental data and simulation result for the pressure loss inside discharge tube. The simulation was performed under the assumption of incompressible fluid, single phase flow and fluid is under a steady state. Water is chosen to be studied for both the simulation and experiment because of the ease of experimental handling. Also, this is a simple representation of the refrigerant gas which is assumed to be incompressible within the normal working range of pressure and temperature.. For the simulation, realizable *k-ε*

turbulence model with Enhanced Wall Treatment was employed to compute for the turbulent flow and the viscous sublayer. Key findings from this study can be concluded as follows:

1. Simulation result generally agrees with theoretical calculations with deviation of 12.25%.
2. The experimental data collected is well correlated with the simulation result with a maximum deviation of 5.05%, within the range of mass flux from 992.3kg/m^2s to 1488.4kg/m^2s.
3. Further experimental and simulation comparison on different discharge tube design length of Section C shows that the simulation is capable of predicting the experimental data with a maximum deviation of 7.61%.
4. The recovery length has been identified numerically to be approximately 30D, which further pressure drop per unit length only deviates by 0.65%.
5. Bend 2 shows to suffer from the highest pressure drop per unit length. All the sections from Bend 4 onwards suffer from relatively higher pressure drop per unit length, and this could be due to the flows are not fully-redeveloped.

In addition, the stiffness of the discharge tube after design modification should be assessed so that it is fit for purpose. In addition, experiment and simulation on performance of refrigerant in discharge tube should be done in the future, in order to find out a correction factor, C for the water to replace refrigerant in this experiment.

References

[1] National Research Council. *A Century of Innovation: Twenty Engineering Achievements that Transformed our Lives*. Washington, DC: The National Academies Press, 2003.
[2] Y.V.C Rao, *An introduction to thermodynamics*, 2nd ed. Hyderabad: Universities Press, 2004, pp. 366-369.
[3] A. Paliwoda, "Generalized method of pressure drop calculation across pipe components containing two-phase flow of refrigerants," vol. 1, no. 2, pp. 119–125, 1992.
[4] I. Y. Chen, C. C. Wang, and S. Y. Lin, "Measurements and correlations of frictional single-phase and two-phase pressure drops of R-410A flow in small U-type return bends," *International Journal of Heat and Mass Transfer*, vol. 47, no. 10–11, pp. 2241–2249, 2004.
[5] H. Ito, "Friction factors for turbulent flow in curved pipes," *ASME Journal of Basic Engineering*, pp. 123-134, 1959.
[6] C.O. Popieil, J. Wojtkowiak, "Friction factor in U-type undulated pipe," *Journal of Fluids Engineering*, pp. 260-263, 2000.
[7] I. Y. Chen, Y. K. Lai, C. C. Wang, "Frictional performance of small diameter U-type wavy tube," *Journal of Fluids Engineering*, pp. 880-886, 2003.
[8] P. A. Domanski and C. J. L. Hermes, "An improved correlation for two-phase pressure drop of R-22 and R-410A in 180° return bends," *Applied Thermal Engineering*, vol. 28, no. 7, pp. 793–800, 2008.
[9] R. J. Da Silva Lima and J. R. Thome, "Two-phase flow patterns in U-bends and their contiguous straight tubes for different orientations, tube and bend diameters," *International Journal of Refrigeration*, vol. 35, no. 5, pp. 1439–1454, 2012.

[10]R. J. Da Silva Lima and J. R. Thome, 'Two-phase flow pressure drops in U-tubes: Towards more accurate measurement methods and prediction models', International Journal of Refrigeration, vol. 36, no. 2, pp. 492-503, 2013.
[11] I. Y. Chen, C. L. Won, and C. C. Wang, "Influence of oil on R-410A two-phase frictional pressure drop in a small U-type wavy tube," *International Communications in Heat and Mass Transfer*, vol. 32, no. 6, pp. 797–808, 2005.
[12] M. Y. Wen and C. Y. Ho, "Condensation heat-transfer and pressure drop characteristics of refrigerant R-290/R-600a-oil mixtures in serpentine small-diameter U-tubes," *Applied Thermal Engineering*, vol. 29, no. 11–12, pp. 2460–2467, 2009.
[13] C. C. Tran, S. Gupta, T. a Newell, J. C. Chato, and H. Phoenix, "A study of refrigerant void fraction and pressure drop in return bends and development of a new two-phase experimental apparatus," 2000.
[14] M. Padilla, R. Revellin, P. Haberschill and J. Bonjour, 'Two-phase pressure drop in return bends: Experimental results for R-410A', *International Journal of Refrigeration*, vol. 34, no. 8, pp. 1854-1865, 2011.
[15] K. De Kerpel, B. Ameel, H. Huisseune, C. T'Joen, H. Canire, and M. De Paepe, "Two-phase flow behaviour and pressure drop of R134a in a smooth hairpin," *International Journal of Heat and Mass Transfer*, vol. 55, no. 4, pp. 1179–1188, 2012.
[16] P. Zhang, R. Roberts and A. Bénard, 'Computational guidelines and an empirical model for particle deposition in curved pipes using an Eulerian-Lagrangian approach', *Journal of Aerosol Science*, vol. 53, pp. 1-20, 2012.
[17] B. E. Launder and D. B. Spalding. Lectures in Mathematical Models of Turbulence. Academic Press, London, England. 1972.
[18] B. E. Launder, G. J. Reece, and W. Rodi. "Progress in the Development of a Reynolds-Stress Turbulence Closure". *Journal of Fluid Mechanics*, vol.68, no. 3, pp. 537–566, 1975.
[19] S. Edvardsen, C. A. Dorao, and O. J. Nydal, "Experimental and numerical study of single-phase pressure drop in downhole shut-in valve," *Journal of Natural Gas Science and Engineering*, vol. 22, pp. 214–226, 2015.
[20] S. A. Orszag, V. Yakhot, W. S. Flannery, F. Boysan, D. Choudhury, J. Maruzewski, and B. Patel. "Renormalization Group Modeling and Turbulence Simulations". In International Conference on Near Wall Turbulent Flows, Tempe, Arizona. 1993.
[21] T.H. Shih, W. W. Liou, A. Shabbir, Z. Yang, and J. Zhu. "A New *k-ε* Eddy-Viscosity Model for High Reynolds Number Turbulent Flows - Model Development and Validation". Computers Fluids. 24(3). 227–238. 1995.
[22] Inspectapedia.com, 'Air conditioner repair: Typical Air Conditioner Compressor & Refrigerant Pressure Readings', 2015. [Online]. Available: http://inspectapedia.com/aircond/Refrigerant_Pressures.php. [Accessed: 07- Aug- 2015].
[23] 'Thermodynamic Properties of DuPont™ Freon® 22 (R22) Refrigerants', 2005.
[24] ANSYS, 'ANSYS Meshing Application Introduction', 2009.
[25] Fluent, ANSYS Fluent Theory Guide, 15.0 Documentation. ANSYS Inc., 2013.
[26] B. Munson, T. Okiishi, W. Huebsch and A. Rothmayer, Fundamentals of Fluid Mechanics, 7th ed. Hoboken, New Jersey: John Wiley & Sons, Inc., 2013, p. 439.

Mechanical Properties and Inter-Vertebral Disc Pressure of the Pre-Operative Scoliotic Human Vertebrae

Teoh Wy Sean[1*],Jeffrey Chin Kong Leong, Leong Wai Yie

Health Research Group, School of Engineering, Taylor's Lakeside Campus, Malaysia

[*]wysean.dtp@gmail.com

Abstract

Scoliosis is a lateral or sideways curvature of the spine. There are various treatment methods for patients that are experiencing scoliosis such as external braces or via surgery. However, not much is known about the properties of the inter-vertebral discs that is experiencing deformities due to the fact that majority or previous studies were conducted on cadaver specimens and as such, the purpose of this research is to conduct a proper analysis to determine the properties of the inter-vertebral discs before treatment. Although there have been countless studies conducted on the mechanical properties of a normal human vertebrae, there has been minimal amount of study conducted on the mechanical properties of individuals experiencing scoliosis and other spinal deformities. As such, a more in depth knowledge is required in order to efficiently improve the lifestyle and social well-being of individuals experiencing such spinal deformities. To achieve the desired results, computational data analysis through simulation is conducted by obtaining various radiograph files which would be converted into a three-dimensional geometrical model for analysis via the finite element method using ANSYS. However, in order to convert the radiograph files into a three-dimensional model, an external software is used such as Magics and Invesalius. The desired results obtained of the mechanical properties of both the scoliotic human vertebrae and the inter-vertebral discs should prove to be fundamental in providing future practitioners and also researchers in determining the key areas at which scoliosis starts to take place before surgical operations are conducted.

Keywords: Scoliosis, DICOM, CT image, finite element approach.

1. Introduction

The human vertebral column consists of 33 vertebrae which are then sub-categorized to 7 cervical (C1-C7), 12 thoracic (T1-T12), 5 lumbar (L1-L5), 5 fused sacral vertebrae and 4 fused coccygeal vertebrae [1]. In the structure of the spinal column, each vertebrae is separated by inter-vertebral discs, which acts as a protection as well as a shock absorber for the spinal cord and spinal canal. However, there is a certain limit as to how much pressure and force that these inter-vertebral discs can sustain before it starts to experience a significant degenerative wear-and-tear effect. Of the various types of spinal degenerative effects, the effect of scoliosis was chosen as the foundation of this study. When the spine is affected by spinal deformity such as scoliosis, the shape and properties of the vertebrae and inter-vertebral discs are also affected.

The mechanical properties of the human vertebrae are important as its main function is to maintain the Range of Motion (ROM) and stability of the human body. The mechanical properties of the vertebrae include stress, strain, shear and torsion of the bone which varies between individuals. Although several studies have been conducted on cadavers in order to obtain the mechanical properties of the human vertebrae as well as the inter-vertebral discs, only a minimal amount was conducted using radiograph-converted images. This provides the necessary urge to conduct an analytical study on the mechanical properties of the inter-vertebral discs based on the radiograph-converted 3D model.

Scoliosis is a lateral or sideways curvature of the spine. There are various methods to detect scoliosis such as radiograph digital imaging (MRI or CT scan – DICOM files), rib hump tests, and many more. When scoliosis occurs, its appearance differs from the normal vertebrae whereby the spine can curve in either directions in the form of a “C” shape or even curve in both sides concurrently which results in an “S” shaped spine. Due to this curvature, the normal pressure (0.7 kg/cm^2) that is exerted uniformly on the inter-vertebral disc will be altered whereby it is mainly concentrated on either side of the disc [1]. From this, the mechanical properties of the vertebrae and the inter-vertebral discs will vary when compared between a healthy human spine and one which is currently experiencing scoliosis. Although scoliosis can be treated by placing external braces for teenagers or via surgical operations, patients are unable to revert back to their original range of motion.

The objective of this study is to provide a 3D model of a scoliotic human vertebrae using the existing MRI or CT scan files (DICOM files) provided and attempt to analyse the mechanical properties of the human scoliotic vertebrae.

2. Literature Review

2.1 Research based on cadaver specimens

Countless studies have been conducted over the past decade to determine the mechanical properties of the human spine. Ling H.Y. and Tan S.H. has used Dual-energy X-ray Absorptiometry (DEXA) to study the effect of the bone density on the mechanical properties of the human vertebrae trabecular [2]. Furthermore, Nicollela et al. has conducted a study on the measurement of microstructural strain in cortical bone by using a custom microscopy loading frame [3]. In addition to that, M.M. Trexler, A.M. Lennon, Q.T. Luong and A.C. Wickwire have incorporated a modified split Hopkinson pressure bar to determine the shear loading in soft materials and biological tissues [4]. Among other studies, Arno Bisschop, Jaap H. van Dieen and Idsart Kingma has conducted a study on the torsion biomechanics of the spine following a lumbar laminectomy using an instrument called Instron [5]. Besides that, Michalek, A.J. et al., has conducted a study using a Harrick Scientific Tissue Deformation Imaging Stage to measure the local strains in inter-vertebral disc annulus fibrosus tissue under dynamic shear using the inter-vertebral discs from cadaver specimens [6].

2.2 Research based on live human beings

Aside from various studies conducted on cadaver specimens, there are a few studies that were conducted on live human beings whereby subjects have voluntarily agreed after an explanation on the purpose was provided. One such study was the study on the biomechanical characteristics of the lumbar vertebrae of a speed skating athlete using finite element analysis by Qinghua Meng and Chunyu Bao [7]. During this study, a stacked digital imaging to the volunteer's fourth lumbar vertebrae (L4) to the fifth lumbar vertebrae (L5) was taken by means of a CT scan. The obtained CT images were then processed and a 3D geometrical model of the L4-L5 vertebrae was established by 3D calculations. It was concluded that the stress on the main disc has a higher concentration on the annulus fibrosus [7].

3. Methodology

3.1 Materials

Before proper analysis of the human vertebrae experiencing scoliosis can be conducted, it is necessary to acquire the materials needed before the study can commence. In this case, the MRI and CT radiograph files (Digital Imaging and Communications in Medicine - DICOM) of patients who are experiencing scoliotic spinal deformities from proper sources. The above stated files were provided by P. Mohankumar which has been acquired from India.

3.2 Method

3.2.1 Generating a 3D Geometrical Model

After obtaining the MRI and CT radiograph files, conversion of the DICOM file format is necessary as the radiograph files are a stack of image slices at varying angles. Hence, such files are to be converted into a geometrical model compatible file format such as STL through a series of procedures. As such, the DICOM files were then imported into a software called InVesalius 3.0 [8]. InVesalius is an open source software with a purpose of reconstructing computed tomography and Magnetic Resonance Images (MRI). It will generate a 3D medical imaging reconstruction based on a sequence of DICOM files.

After importing the files into InVesalius, the region of interest is then selected and the various properties such as mask properties, surface properties and threshold properties are adjusted accordingly. After necessary adjustments are done, a 3D model is generated and then exported in STL file format. Figure 1 shows the processing of the stacked DICOM files into a single 3D geometrical model.

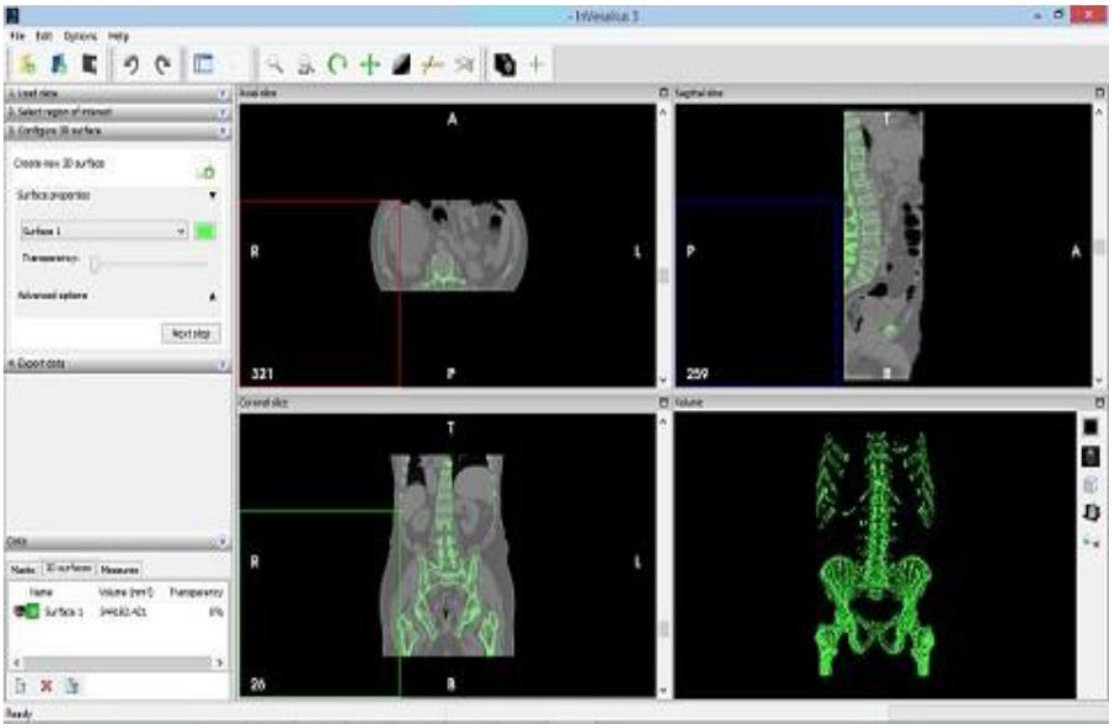


Figure 1: DICOM Processing in InVesalius.

After generating a 3D geometrical model, it is then imported into Magics 18.0 [9]. Magics is a data preparation software packaged with the STL editor feature developed by Materialize. It is mainly used in additive manufacturing and also in 3D printing. In here the STL editor was utilized to remove excess noise particles that have been generated in the model as well as filling up the holes that are present within the geometrical model as shown in Figure 2 and Figure 3.

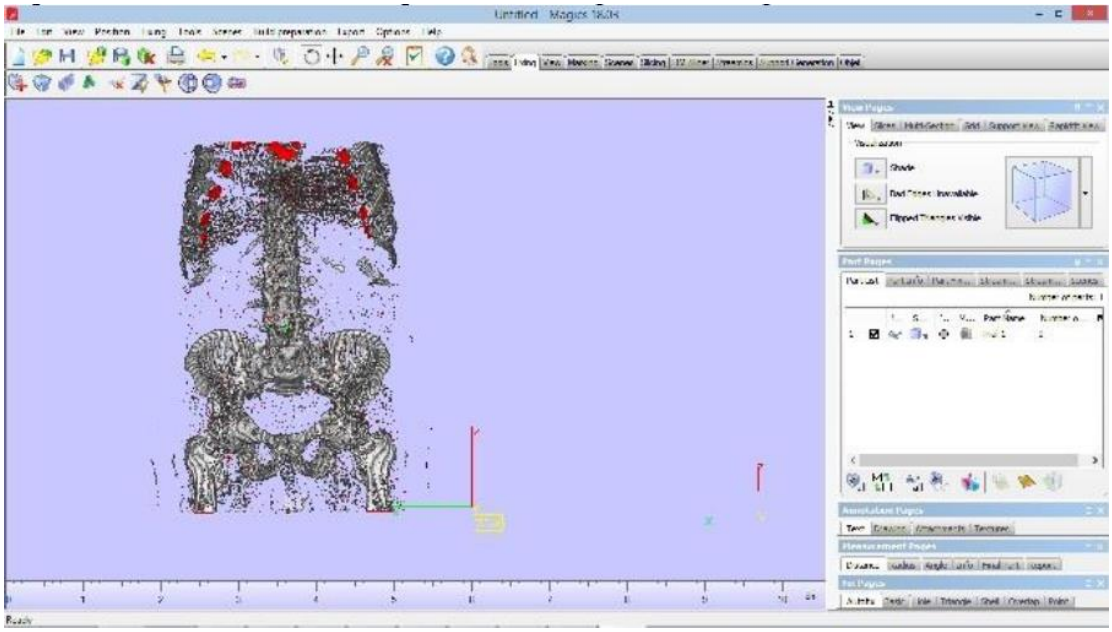


Figure 2: Before Editing in Magics.

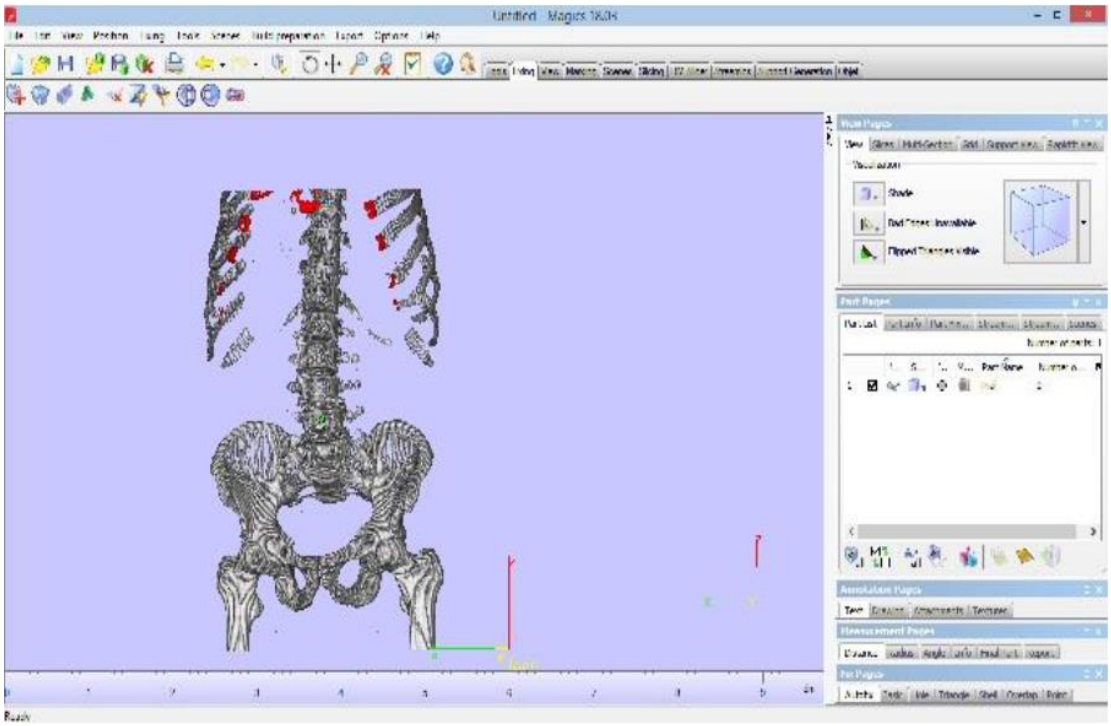


Figure 3: After Editing in Magics.

3.2.2 Analysis of the 3D Geometrical Model using ANSYS

After generating a 3D geometrical of the scoliotic spine, it was then imported into ANSYS to begin analysis of its mechanical properties of the scoliotic human vertebrae. An isotropic, 3D, non-linear finite element model of the spine was created. However, necessary boundary conditions must be applied onto the model whereby the compressive loading force applied on the model is based on the subject's weight in order to accurately determine the stress and strain experienced by the model.

A previous study conducted by Su, J.C., Li, Z.D., Cao, L.H., Yu, B.Q., Zhang, C.C. and Li, M. in regards to the three-dimensional finite element analysis of lumbar vertebrae loaded by static stress and its biomechanical significance using a similar method however, the study was done on a healthy pelvis of an adult female volunteer at the age of 39 years [12]. During their study, they have managed to analyse the lumbar spine model whereby it was divided into a total of 121 239 nodes, 112 491 units [12]. Based on their study, they have said that by converting CT scan images into a geometrical model to be analysed, it objectively reflect the true anatomy of lumbar spine and its biomechanical behaviour [12].

Another study conducted by Toosizadeh, N. and Haghpanahi, M. in generating a finite element model of the cervical spine: estimating muscle forces and internal loads [13]. In their study, they have used a similar method of model reconstruction from CT scan images. The results obtained showed an excessive increase in internal loads by increasing the angle of rotation in all directions [13].

Using necessary results that has been found from previous study, a comparison will be made for each vertebral segment of the scoliotic human vertebrae against a normal human vertebrae.

4. Results and Discussion

Conventionally, biomechanical experiments on bone structures were carried out on cadavers which may prove to be inconvenient as the shelf life of cadavers will affect the results obtained. Hence, with the emergence of various methods such as numerical analysis as well as finite element method are beginning to be beneficial to solve such issues.

During the 3D geometrical model conversion, there were issues on the accuracy of the model due to the noise in the existing CT scan files. As such, a large amount of editing was needed in Magics to remove the random noise as well as to fill up gaps in the structure. After editing, it was observed that the model was clearer with minimized noise and corruption. However, even after editing, the noise still exists although it is minimal, this is most likely due to the file provided as it could have been corrupted. As for the accuracy of the model, more radiograph images are required in order to have a detailed view of the model.

Although a vast majority of previous studies on the human bone structure; mainly the spine, have been conducted on cadaver specimens, there is a lack of research that have been conducted on spinal structures that is experiencing spinal deformities such as scoliosis. Hence, with the advancement in technology, researchers are able to utilize medical data of living subjects to conduct their necessary studies. One such study was conducted by Jovanovic, J.D. and Jovanovic, M.L. whereby they have created a finite element modelling of the vertebrae using CT scan images [10]. During their study, they have used Mimics – a software by Materialize; to generate the geometric model of the vertebrae. Based on their results, it was observed that the model was able to provide a detailed qualitative information on the biomechanical behaviour of the vertebrae [10]. Furthermore, another study was conducted by Haiyun Li and Zheng Wang on the intervertebral disc biomechanical analysis using the finite element modelling based on medical images [11]. In this study, they have used the VTK reconstruction software to generate a 3D geometrical model from CT and MRI data-based anatomical structure of the spine which was then imported into ANSYS 6.0 for analytical purposes [11]. Figure 4 shows the model reconstruction in VTK whereas Figure 5 shows the finite element model of the first and second lumber vertebrae segment (L1-L2).

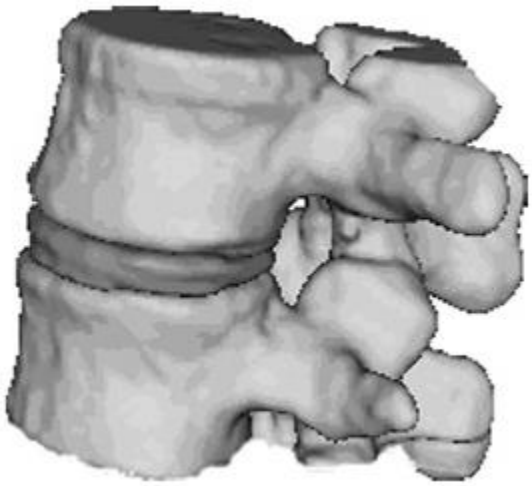


Figure 4: Model reconstruction in VTK [11].

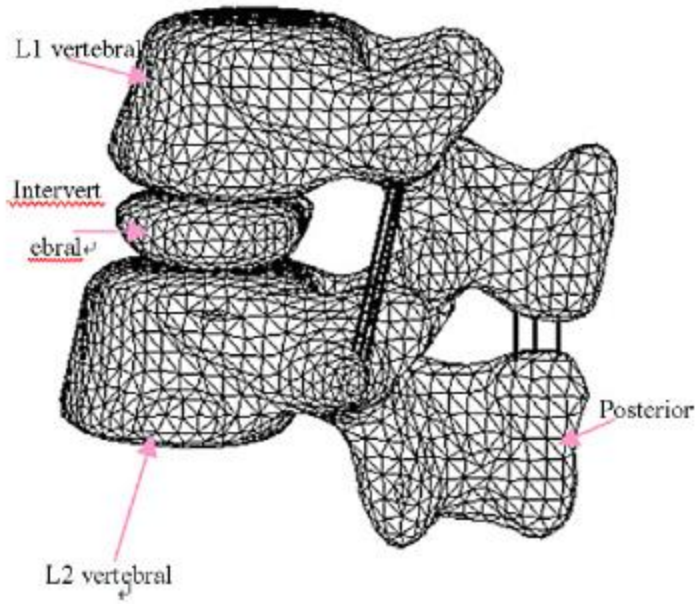


Figure 5: The finite element model of L1-L2 segment [11].

During the analysis of the scoliotic human vertebrae, several issues pertaining to the geometrical model have prevented the analysis from being conducted. Such issues that have risen could be due to the corruption of the DICOM files which leads to a massive loss of necessary information needed. Hence, there is no definite results obtained at the moment in terms of analysis. Once results have been achieved, it will then be compared with past studies that have been conducted on healthy bone specimens such as the results obtained by Toosizadeh, N. and Haghpanahi, M. in Table 1 and Table 2.

5. Conclusion

The concept of incorporating DICOM files into the generation of a 3D model can be used as a viable alternative to researchers as compared to using cadavers. With this, results obtained can be achieved with a closer proximity to actual conditions

which in turn will provide a deeper understanding on the mechanical properties and also the functionality of the scoliotic vertebrae. This will be able to aid medical practitioners and researchers in determining the root cause or initial degenerative areas of the spine which will lead to a more distinctive prescribed treatment method based on individual's conditions.

References

[1] Alison Middleditch and Jean Oliver. (2005). *Funtional Anatomy of the Spine*, 2nd Edition
[2] Ling, H.Y., Tan, S.H.. Effect of Bone Density on the Mechanical Properties of Human Bone (Vertebrae Trabecular), School of Mechanical and Production Engineering, Nanyang Technological University
[3] Nicolella, D.P., et al.. (2005) Measurement of Microstructural Strain in Cortical Bone. *European Journal of Morphology* 2005; 42(1-2): 23–29
[4] Trexler, M.M., Lennon, A.M., Luong, Q.T., Wickwire, A.C., Roberts, J.C., and Merkle, A.C. (2011) Modified split hopkinson pressure bar technique for characterizing soft materials and biological tissue under shear loading. *Injury Biomechanics Research*, Proceedings of the Thirty Seventh International Workshop. Epub Jun 23.
[5] Arno Bisschop et al., (2013). Torsion Biomechanics of the Spine following a Lumbar Laminectomy: a human cadaver study. *European Spine Journal 22: 1785-1793*
[6] Michalek, A.J. et al., (2009) Measurement of local strains in intervertebral disc anulus fibrosus tissue under dnamic shear: Contributions of matrix fiber orientation and elastin content. *Journal of Biomechanics 42 (2009) 2279-2285*
[7] Qinghua Meng, Chunyu Bao. (2009). Study on Lumbar Vertebrae Biomechanical Characteristics for Speed Skating Athlete based on Finite Element Method. *International Journal of Sports Science and Engineering*, Volume – 03, No. 03, pp. 169 - 174.
[8] *INVESALIUS*. (2015, 5 7). Retrieved 4 2015, from INVESALIUS: http://www.cti.gov.br/invesalius/
[9] *Materialise*. (2015, 5 7). Retrieved 5 7, 2015, from Materialise: http://software.materialise.com/magics
[10] Jovanovic, J.D. and Jovanovic, M.L. (2010). Finite element modelling of the vertebrae with geometry and material properties retrieved from CT scan data. Facta universitatis, *Mechanical Engineering*, Volume 8, No. 1, pp. 19-26
[11] Haiyun Li and Zheng Wang (2006). Intervertebral disc biomechanical analysis using the finite element modelling based on medical images. *Computerized Medical Imaging and Graphics 30 (2006) 363-370*.

[12] Su, J.C., Li, Z.D., Cao, L.H., Yu, B.Q., Zhang, C.C. and Li, M. (2009). Three-dimensional finite element analysis of lumbar vertebrae loaded by static stress and its biomechanical significance. *Chinese Journal of Traumatology 2009; 12(3):153-156*
[13] Toosizadeh, N. and Haghpanahi, M. (2011) Generating a finite element model of the cervical spine: Estimating muscle forces and internal loads. *Scientia Iranica B (2011) 18(6), pp 1237-1245*